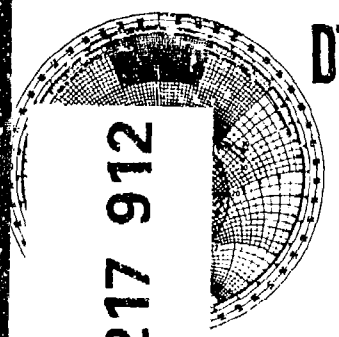
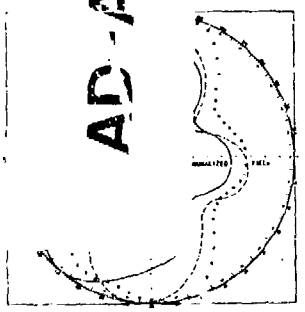
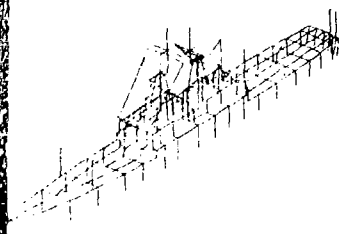
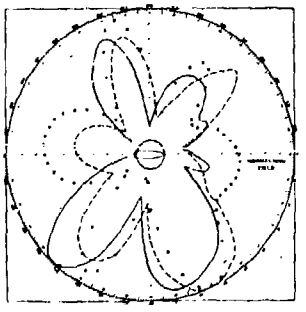
DTIC FILE COPY

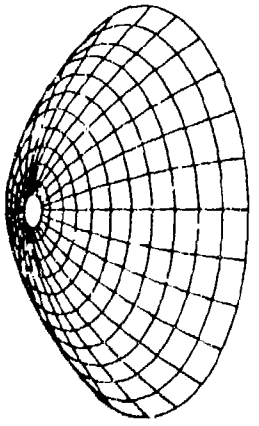
AD-A217 912











4th Annual Review of Progress in

APPLIED COMPUTATIONAL ELECTROMAGNETICS

at the
Naval Postgraduate School
Monterey, CA

DTIC
ELECTE
FEB 09 1990
S D
Co D

March 22-24, 1988

CONFERENCE PROCEEDINGS

Distributed by:

The Applied Computational Electromagnetics Society

DISTRIBUTION STATEMENT A
Approved for public release
Distribution Unlimited

ACES Secretary
R. W. Adler, Code 62AB
Naval Postgraduate School
Monterey, CA 93943

90 02 06 278

REPRODUCTION QUALITY NOTICE

This document is the best quality available. The copy furnished to DTIC contained pages that may have the following quality problems:

- Pages smaller or larger than normal.
- Pages with background color or light colored printing.
- Pages with small type or poor printing; and or
- Pages with continuous tone material or color photographs.

Due to various output media available these conditions may or may not cause poor legibility in the microfiche or hardcopy output you receive.

☐ If this block is checked, the copy furnished to DTIC contained pages with color printing, that when reproduced in Black and White, may change detail of the original copy.

AGENDA

The Fourth Annual Review of Progress in Applied Computational Electromagnetics
122 Ingersoll Hall
Naval Postgraduate School
March 22-24, 1988

Monday 21 March

1900-2030 REGISTRATION

Tuesday 22 March

0730-0830 REGISTRATION → Partial Contents:

0815-0900 ACES General Business Session and Spouses' Get-Together

0900-1030 Session I - FINITE DIFFERENCE & FINITE ELEMENT METHODS
Moderator: David Stein

"A Finite Element Analysis of Lightning Induced Maxwell Current Densities"
M.E. Baginski, F.J. German and L.S. Riggs Auburn University

"Transient Electromagnetic Coupling To A Cavity with Metallic Walls"
H.A. Sabbagh and Stephen A. Jenkins Sabbagh Associates

"Finite Element Computer Programs for Microstrip, Waveguides and Cavities"
Z. Cendes Carnegie Mellon University
Din Sun Ansoft Corp.

"A Time-Domain Differential Solver For Electromagnetic Scattering Problems"
V. Shankar and William Hall Rockwell International Science Center

"Electromagnetic Analysis by the Transmission Line Modelling (TLM) Method"
F.J. German, L.S. Riggs and M.E. Baginski Auburn University

"Object Oriented Scientific Programming - A Transmission Line Code Example of 'Smart' Arrays"
D.F. Higgins Consultant

10:30-1045 BREAK

1045-1130 Session I (Continued)

"Calculation of Antenna Input Impedance Using Finite Difference Time Domain"
K.S. Kunz and R.J. Luebbers Pennsylvania State University

"One-Dimensional Finite Difference Time Domain Demonstration for the Classroom"
R.J. Luebbers and K.S. Kunz Pennsylvania State University

"A High Frequency Reformulation of the FDTD Algorithm in Generalized Coordinates"
M.A. Fusco and M.V. Smith Lockheed R&D Division

1130-1215 Session II COMPUTATIONAL ISSUES
Moderator: Ed Coffey

"Using Impedance Matrix Frequency Derivatives for Estimating Broadband Transfer Functions"
G. Burke — Lawrence Livermore Lab
E.K. Miller — Rockwell Science Center

"The 7-Digit Precision Environment - A Numerical Challenge"
Ruediger Anders — Applied Electromagnetics Engineering

"Do We Need Double Precision For EM Applications in the 7-Digit PC and Workstation World?"
Ruediger Anders — Applied Electromagnetics Engineering

"A Block Elimination Equation Solver for Large Matrices in the 7-Digit Environment"
Ruediger Anders — Applied Electromagnetics Engineering

1215-1330 LUNCH

1330-1430 Session II (Continued)

"The MAFIA Approach to Solving Maxwell's Equations in Three Dimensions"
R.K. Cooper, M.J. Browman — Los Alamos National Laboratory
T. Weiland — Deutsches Elektronen-Synchrotron

"An Improved Exact Kernel for MININEC"
J.C. Logan and J.W. Rockway — Naval Ocean Systems Center
D. Wilton — University of Houston

"Numerical Integration Schemes In Calculating the Fourier Coefficiencies of the Free-Space Green's Function"
J.C. Peterson — Photon Research Associates Inc.

"Accurate and Efficient Numerical Computation of Sommerfeld Integrals for Layered Media Green's Functions"
B.L. Brim and David C. Chang — University of Colorado

1430-1445 BREAK

1445-1645 EM CODE USERS PANEL DISCUSSION. Chaired by Jim Breakall of LLNL.
User community suggestions on needed enhancements for EM Codes.
15 minute limit per participant - Use viewgraphs for maximum efficiency.

1645-1800 PC DEMONSTRATIONS. Coordinated by Chuck Vandeinent
Room 119.

Wednesday 23 March

0830-1030 Session III - SCATTERING
Moderator: Harold Sabbagh

"Numerical Aspects of Scattering by An Impedance Wedge"
Robert T. Brown — Grumman Corporation

"A Lattice Representation for Back Face Removal in Electromagnetic Scattering"
T.K. Pollock — Chirp Technical Services

"Protecting Scattering Computations from Effects of Interior Resonances"
F.X. Canning — Rockwell International Science Center

"Floquet Theory Based Modification to NEC-2 for Analysis of Very Large Periodic Planar Arrays"
R.M. Cribb — McDonnell Douglas Astronautics Company

"Singularity Expansion Method (SEM) Natural Modes as Efficient Entire Domain Expansion Functions in the Analysis of Frequency Selective Surfaces (FSS)"
L.S. Riggs, M.E. Baginski, F.J. German — Auburn University

"Optimal Loading"
B. Tomas and Elizabeth Yip — The Boeing Aerospace Company

"Numerical Difficulties and Software Validation Needs Associated with EFIE Formulations for Dielectric Scatterers"
A.F. Peterson — University of Illinois

"Computation of Frequency-Domain and Time-Domain Scattering from a Cross with the GEMACS and CASSANDRA Codes"
D.E. Thomas and G.R. Salo — BDM Corporation

1030-1045 BREAK

1045-1215 Session IV - INPUT-OUTPUT ISSUES
Moderator: Ruediger Anders

"An EM Language Translator and Macro Processor"
E.L. Coffey — Advanced Electromagnetics
A. Lockyer — Northrop Corporation

"Graphical Aids for Users of GEMACS (GAUGE)"
A. Lockyer, P. Tulyathan — Northrop Corporation
K.R. Siarkiewicz — Rome Air Development Center

"Graphics Programming for Electromagnetic Modeling"
G. Upshaw, M. J. Grage — Northrop Corporation
K.R. Siarkiewicz — Rome Air Development Center

"MATHPLOT - A Modeling Tool for Scientists and Engineers""
D.F. Higgins — Consultant

"PC Program for Plotting the Vector Fields"
D. Kajfez and J.A. Gerald — University of Mississippi

DTIC COPY INSPECTED 8

Accesion For
NTIS CRA&I ☑
DTIC TAB ☐
Unannounced ☐
Justification
By per call
Distribution /
Availability Codes
Dist | Avail and / or Special
A-1

STATEMENT "A" per Professor Adler
NPS, Code 62
TELECON 2/9/90 CG

"Scientific Visualization in Computational Electromagnetics"
S. Lamont San Diego Supercomputer Center

1215-1330 LUNCH

1330-1445 Session V - GEMACS
Moderator: David Thomas

"GEMACS – The Present and the Future"
K.R. Siarkiewicz Rome Air Development Center

"A GEMACS Source Book"
E.L. Coffey Advanced Electromagnetics
K.R. Siarkiewicz Rome Air Development Center

"Solution of Multi-Region, Aperture-Coupled Problems with GEMACS 4.0"
E.L. Coffey Advanced Electromagnetics
K.R. Siarkiewicz Rome Air Development Center

"Application of GEMACS-IV for Small Aperture Coupling"
R.J. Balestri Booz Allen & Hamilton, Inc.

"GEMACS on a Personal Computer"
E.L. Coffey Advanced Electromagnetics

1445-1500 BREAK

1500-1700 SOFTWARE VALIDATION. Chaired by Stanley Kubina of Concordia
(Same ground rules as NEC USERS Panel Discussion)

1700-1800 PC DEMONSTRATIONS. Coordinated by Chuck Vandament.
Room 118

1830 "Early Bird Special" (Dutch Treat) at Cannery Row Restaurant or NPS Officers Club

Thursday 24 March

0830-0930 ACES Concluding Business and Election.

0930-1045 Session VI - ANTENNA ANALYSIS
Moderator: Bob Evensse

"The Design of Antenna Matching Networks Using a Microcomputer"
S.T. Li and D.W.S. Tam Naval Ocean Systems Center

"Numerical Methods Used for Analysis of a Transmitting Biconical Antenna"
V. Badii, K. Tomiyama, D. Grimes Pennsylvania State University

"Design Program for Microstrip Antennas with a Dielectric Cover"
R. Bancroft Martin Marietta Astronautics Group

"Efficient Computation of the Far Field of Offset Dual Reflector Antennas with Offset Feeds"
J.S. Hoover and L.Q. Bowers Martin Marietta Astronautics

"Development and Validation of a New Version of the NEC-BSC"
R.J. Marhefka Ohio State University

1045-1100 BREAK

1100-1215 Session VI - (Continued)

"Prediction and Measurement of Transverse Wave Impedance in the Vicinity of Electrically Small radiating Structures"
M.E.G. Upton and A.C. Marvin University of York

"The Analysis of Two Inverted F-Antenna Structures on a Box Using NEC Wire Model"
M. Somersalo Technical Research Centre of Finland

"Synthesis Techniques for Circular Arrays"
K.J. Moeller and V.P. Cable California Microwave, Inc.

"Moment Method Analysis of Large Finite Phased Arrays"
H.K. Schuman and G.A. Bright Atlantic Research Services Corporation
S. Barbour Grumman Aerospace Corp.

"Application of the Network Approach to Electromagnetic Solutions Involving Apertures on a Body of Revolution"
J.R. Rogers Atlantic Aerospace Electronics Corporation

1215-1330 LUNCH

1330-1500 Session VII - CAVITIES INTERACTIONS & TRANSMISSION
Moderator: Dawson Coblin

"FITPAK - A Finite Integration Technique Package For Numerical Solution of Interior Electromagnetic Boundary Value Problems"
J. Lebaric Rose-Hulman Institute of Technology
D. Kajfez University of Mississippi

"A Computational Model for Electromagnetic Interactions with Advanced Composites"
H.A. Sabbagh, T.M. Roberts, J.C. Treece, L.D. Sabbagh Sabbagh Associates Inc.

"A Computational Model of Eddy-Current Probes Over a Stratified Composite Workpiece"
H.A. Sabbagh, L.D. Sabbagh, J.R. Bowler Sabbagh Associates Inc.

"Comparison of Soil Models with Frequency-Dependent Constitutive Parameters"
J.W. Williams and G.D. Rensner Science Applications International Corp.

"MULTINEC - A MININEC Modification For Analysis of Multiconductor Transmission Lines"
J.E. Lebaric, J.A. Allred, T.M. Cantrell, C. Pfeifer and D.W. Yergeau Rose-Hulman Institute of Technology

"Analysis of Large Parallel-Plate EMP Simulators Using the Numerical Electromagnetics Code (NEC)"
S. Gedney and R. Mittra University of Illinois

1500 BREAK OR LEAVE FOR MONTEREY AQUARIUM TOUR

1515-1630 Session VIII ANTENNAS NEAR GROUND
Moderator: George Hagn

"Relationships Between Base Drives and Fields in Broadcast Medium Wave Directional Antennas"
J.B. Hatfield — Hatfield & Dawson Consulting Engineers, Inc.

"HF Ground Constant Measurements at the Lawrence Livermore National Laboratory (LLNL) Field Site"
G. Hagn — SRI International

"Experimental Antenna Measurements for the Validation of the Numerical Electromagnetics Code (NEC)"
J.K. Breakall and A.M. Christman — Lawrence Livermore National Laboratory

"NEC Modeling of HF Monopole Antennas with Elevated Radials"
A. Christman and R. Radcliff — Ohio University

Field Tests of HF Monopole Antennas with Elevated Radials"
A. Christman and R. Radcliff — Ohio University
J.K. Breakall — Lawrence Livermore National Laboratory

"A Simplified Model of the Terminated, Sloping Long-Wire (AFW0NXX) Antenna"
B. Campbell and W. Stuart — IIT Research Institute

TENTATIVE PC DEMONSTRATIONS

* FINITE ELEMENT
* "FITPAK"
* "GAUGE"
* "GEMACS-PC"
* MATHPLOT"
* MICROSTRIP ANTENNA
* "MULTINEC"
* "NAC-3"
* TRANSMISSION LINES"
* VECTOR FIELDS

Special Demonstration:

GROUND-CONSTANT MEASUREMENTS

SESSION I - "FINITE DIFFERENCE & FINITE ELEMENT METHODS"

Moderator: David E. Stein
The LTV Aerospace and Defense Company

"A Finite Element Analysis of Lightning Induced Maxwell Current Densities"
M.E. Baginski, F.J. German and L.S. Riggs — Auburn University

"Transient Electromagnetic Coupling To A Cavity with Metallic Walls"
H.A. Sabbagh and Stephen A. Jenkins — Sabbagh Associates

"Finite Element Computer Programs for Microstrip, Waveguides and Cavities"
Z. Cendes — Carnegie Mellon University
Din Sun — Ansoft Corp.
* Paper was not submitted and is not published.

"A Time-Domain Differential Solver For Electromagnetic Scattering Problems"
V. Shankar and William Hall — Rockwell International Science Center

"Electromagnetic Analysis by the Transmission Line Modelling (TLM) Method"
F.J. German, L.S. Riggs and M.E. Baginski — Auburn University

"Object Oriented Scientific Programming - A Transmission Line Code Example of 'Smart' Arrays"
D.F. Higgins — Consultant

"Calculation of Antenna Input Impedance Using Finite Difference Time Domain"
K.S. Kunz and R.J. Luebbers — Pennsylvania State University

"One-Dimensional Finite Difference Time Domain Demonstration for the Classroom"
R.J. Luebbers and K.S. Kunz — Pennsylvania State University

"A High Frequency Reformulation of the FDTD Algorithm in Generalized Coordinates"
M.A. Fusco and M.V. Smith — Lockheed R&D Division

A FINITE ELEMENT ANALYSIS OF LIGHTNING INDUCED MAXWELL CURRENT DENSITIES

M.E. Baginski, F.J. German and L.S. Riggs Auburn University

INTRODUCTION

The use of Maxwell currents and current densities to describe the electromagnetic response of the atmosphere is a fairly recent development. Krider and Musser [1982], and Nisbet [1984] have suggested that the thunderstorm is fundamentally a current source and should therefore be investigated in terms of current densities rather than electric fields. The current densities generated by charge perturbations associated with lightning consist of either conduction (resulting from charge movement) or displacement ($\varepsilon_o \partial E/\partial t$) terms. The sum of these current densities are referred to as the Maxwell current density (J_m).

$$J_m = \nabla \times H = J_p + \varepsilon_o \partial E/\partial t \qquad (1)$$

J_m = Maxwell current density

J_p = the sum of all conduction current densities including source (impressed) terms

$\varepsilon_o \partial E/\partial t$ = displacement current density

The Maxwell current density has several properties that may be exploited to more accurately describe both the local and global effects of lightning transients on the atmosphere. Probably the most important

of these is that the divergence of the Maxwell current density is zero ($\nabla \cdot J_m = 0$) making it a solenoidal quantity. As a consequence of this, the lines of Maxwell current density (J_m) form closed loops. Along these Maxwell current density stream lines the displacement term is usually dominant at low altitudes ($J_p << \varepsilon_o \partial E/\partial t$) with conduction current densities dominating the high altitude Maxwell current density ($J_p >> \varepsilon_o \partial E/\partial t$).

This solenoidal character of the Maxwell current density ($J_m = \nabla \times H$, $\nabla \cdot [\nabla \times H] = 0$) infers that the electrical parameters of the entire path of circulation strongly affect its response and conversely; if the Maxwell current density along the streamline is mathematically describable, the corresponding streamline's electric fields may be formulated by simple time domain convolution [Stremler, 1977]. An analogy exemplifying this phenomenon can be made to a simple series RC circuit with the relative analogies (equivalences) as follows: current ~ J_m, elemental voltages ~ E, and elemental values $C\partial V/\partial t$ ~ $\varepsilon_o \partial E/\partial t$ and IR ~ σE. It is obvious that the largest elemental impedance limits the circuit's current response, analogous to the peak surge impedance along the streamline's path governing the behavior of the Maxwell current density [Krider and Musser, 1982]. Therefore, if the limiting factors (peak surge impedances) could be identified and incorporated in an atmospheric electrodynamic model simulating the Maxwell current density then the resulting current densities could plausibly be used as the basis for determining corresponding electric fields, power and energy deposition at all points along the streamline.

Previous attempts at investigating [Nisbet, 1983], via simulation, the Maxwell current densities generated by lightning have implicitly

assumed a conservative electric field ($\nabla \times E = 0$). The mathematical consequence of using this assumption in the solution of Maxwell equations is to constrain the electric field to decay exponentially in time; therefore, limiting the Maxwell current density to be time independent [Baginski, 1987]. This can be shown as follows:

Beginning with Maxwell's equations, a single equation is derived where the electric field is dependent on the charge density only.

$$\nabla \times E = -\mu_o \, \partial H/\partial t \qquad (2)$$

$$\nabla \times H = J + \partial D/\partial t + \text{any additional sources of charge movement} \qquad (3)$$

$$\nabla \cdot D = \rho \qquad (4)$$

$$\nabla \cdot H = 0 \qquad (5)$$

$$J = \sigma E \qquad (6)$$

$$D = \varepsilon_o E \qquad (7)$$

The general wave equation is developed using the above equations as follows:

1) taking the curl (2)

$$\nabla \times \nabla \times E = -\mu_o \, \partial(\nabla \times H)/\partial t \qquad (8)$$

2) using the vector identity

$$\nabla \times \nabla \times E = \nabla \nabla \cdot E - \nabla^2 E$$

3) substituting (3) for $\nabla \times H$ in (8)

4) substituting (4), (6), (7) in (8) results in the wave equation

$$\nabla \times \nabla \times E = - \mu_o \sigma \partial E/\partial t \; -\mu_o \varepsilon_o \partial E^2/\partial t^2 \qquad (9)$$

if $\rightarrow E = - \nabla\phi$

$\nabla \times E = \nabla \times (-\nabla\phi) \equiv 0$ (vector identity)

$\nabla \times \nabla \times E = 0$ (the curl of a constant = 0)

(9) reduces to

$$0 = - \mu_o \sigma \partial E/\partial t - \mu_o \varepsilon_o \partial E^2/\partial t^2$$

The general solution of this partial differential equation is:

$$E(\underline{x},t) = E_1(\underline{x})\exp(-t/\tau(\underline{x})) + E_o(\underline{x}) \qquad (10)$$

where

$\underline{x}$ is a position vector in any general coordinate system

$\tau(\underline{x}) = \varepsilon_o/\sigma(\underline{x})$

The Maxwell current density according to (10) is independent of time generally ($\nabla \times H = \sigma E + \varepsilon_o \partial E/\partial t = \sigma E_o(\underline{x})$) and zero if no DC ($E_o(\underline{x})$) term appears. All models based on a solution of the two Maxwell curl equations with a conservative electric field restriction would be unsuited for Maxwell current density characterizations.

DISCUSSION OF THE MODEL

Maxwell's Equations

The simulations described here do not account for the lightning return stroke current's (J_s) contribution to the transient. Lightning return stroke currents are usually considered the source of the propagating component (launched wavefront) of the induced field and involve time scales ~ 100 μsec [Baginski, 1987]. This type of sferic analysis emphasizes the wavefronts refraction and attenuation [Uman, 1969]. The focus of this study is on the late time [Hale and Baginski,

1987] induced field characterization in the relative proximity of the source.

The partial differential equations describing the electrodynamic response of the atmosphere are shown in the form required by PROTRAN for input data. The equations are developed from the fundamental Maxwell equations (1-7) previously stated and listed below:

$$\nabla \times \nabla \times E = -\mu_o(\sigma \partial E/\partial t + \partial J_s/\partial t) - \mu_o \varepsilon_o \partial E^2/\partial t^2 \qquad (11)$$

$$\nabla \rho/\varepsilon_o = \nabla^2 E - \mu_o(\sigma \partial E/\partial t + \partial J_s/\partial t) - \mu_o \varepsilon_o \partial E^2/\partial t^2 \qquad (12)$$

$$0 = \nabla \cdot (\nabla \times H) = \nabla \cdot (\sigma E + \varepsilon_o \partial E/\partial t + J_s)$$
$$0 = \sigma \nabla \cdot E + \nabla \sigma \cdot E + \varepsilon_o \partial(\nabla \cdot E)/\partial t + G_s$$
$$0 = \sigma \rho/\varepsilon_o + \nabla \sigma \cdot E + \partial \rho/\partial t + G_s \qquad (13)$$

$\nabla \cdot J_s = G_s$ = source of charge perturbation (deposition of return stroke charge)

$\partial \rho/\partial t$ = partial derivative of total charge density with respect to time

J_s = source current density associated with return stroke current, J_s is neglected in the simulations

ρ = charge density

It is important to underscore the fundamental difference in the forcing function (charge related G_s) used here relative to that of most previous lightning research (typically current related forcing functions involving J_s): a current related transient (e.g., current loop) is allowable in a charge neutral region (current implies charge

movement through space but not necessarily a non-zero volume charge density) and furthermore, a charge perturbation may be considered separately without currents or current densities present (charge perturbation implies charge generation at a point in space). In the latter case, movement of charge is required (conservation of charge), but the relative contribution of each (charge versus current) mechanism to the resulting total solution may be analyzed separately. Initially (prior to the first iterative time step), no charge is assumed displaced and the electric field and Maxwell current density everywhere assumed zero. A detailed discussion of the finite element code employed in the simulations is given by Baginski (1987).

Vertical (axial) symmetry is assumed in this study with spatial position being defined using a cylinder coordinate system (r,ϕ,z). The equations are developed as follows:

$$\nabla^2 E = [\nabla^2 E_r - E_r/r^2 - 2(\partial E\phi/\partial\phi)/r^2]a_r + [\nabla^2 E_\phi - E_\phi/r^2 + 2(\partial E_r/\partial_\phi)/r^2]a_\phi + [\nabla^2 E_z]a_z \qquad (14)$$

where $a_{(r,\phi,z)}$ is a unit vector in the respective direction

Axial symmetry eliminates all terms that vary with respect to, or are functions of ϕ. The above equation therefore reduces to:

$$\nabla^2 E = [\nabla^2 E_r - E_r/r^2]a_r + [\nabla^2 E_z]a_z$$

where

$$\nabla^2 E_z = \partial^2 E_z/\partial z^2 + 1/r(\partial^2/\partial r^2(r\partial E_z/\partial r))$$

$$\nabla^2 E_r = \partial^2 E_r/\partial r^2 + 1/r(\partial^2/\partial r^2(r\partial E_z/\partial r))$$

Only the vertical component (a_z) of equation 14, in conjunction with equation 13, is required for a unique solution, via simulation, of

the system. A more detailed discussion of this specific development is given by Holzworth and Chui (1982). The variables simulated in the study are E_z and ρ and the equations given as:

$$\mu_o \varepsilon_o \partial^2 E_z / \partial t^2 = - \nabla\rho/\varepsilon_o + \nabla^2 E_z - \mu_o \sigma \partial E_z / \partial t$$

$$U = \partial E_z / \partial t, \quad V = E_z, \quad P = \rho$$

$$\nabla^2 E_z = \partial(\partial E_z/\partial z)/\partial z + \partial(\partial E_z/\partial r)/\partial r + 1/r(\partial E_z/\partial r)$$

$$\nabla\rho = \partial\rho/\partial z, \quad \nabla\sigma = \partial\sigma/\partial z$$

program requires: $r \rightarrow x$, $z \rightarrow y$, $\partial U/\partial x \rightarrow UX$

$\partial U/\partial y \rightarrow UY$, $\partial V/\partial x \rightarrow VX$, $\partial V/\partial y \rightarrow VY$

Charging mechanisms

A thunderstorm is sustained by charge separation which yields a net positive and negative charge center in a dipole configuration. The height of the charge centers is somewhat affected by seasonal and geographic effects. Heights of 10 km for the upper and 6 km for the lower charge center are generally accepted [Chalmers, 1967] and will be used in this research [Baginski, 1987].

It is well known that the deposition of the return stroke current is responsible for the charge perturbation [Uman, 1969]. The rate of deposition of lightning return stroke current is proportional to the time derivative of the charge perturbation [Holzer and Saxon, 1952]. Therefore, the total charge deposited at time <t> may be expressed as the integral of the lightning return stroke current in time.

$$Q(t) = \int_0^t i_R(t')dt' \qquad (15)$$

where i_R = lightning return stroke current

Q = total displaced charge of the return stroke

Sunde's [1968] lightning return stroke model is selected for this study. Sunde's model is relatively simple compared to some [Uman, 1969], but includes all of the fundamental attributes necessary to predict the "average" electromagnetic field behavior [Sunde, 1968]. The charge generation may be expressed in terms of the temporal behavior of this current, as follows:

$$i(t) = I_0(\exp(-at) - \exp(-bt)) \qquad (16)$$

where i(t) = return stroke current (Sunde's model)

$a = 10^4$ seconds^{-1}

$b = 0.5 \times 10^6$ seconds^{-1}

I_0 = proportional to amount of charge displaced during return stroke

The temporal structure of the forced charge generator is given as:

$$\partial Q(t)/\partial t = I_0(\exp(-at) - \exp(-bt)) \qquad (17)$$

Cylindrical symmetry is assumed about the vertical (z) axis with the radial (horizontal) coordinate listed as (r). The spatial structure of the deposited charge is given by a modified spherical Gaussian profile:

$$\partial Q(r,z)/\partial t = (\exp(-RR/(2\lambda))/(2\pi\lambda)^{1.5} \qquad (18)$$

where λ = variance

$$RR = r^2 + (z - z')^2$$

z' = altitude of charge perturbation

The spatial distribution of the charge perturbation does not noticeably effect Maxwell current density signatures far from its interior; since transient phenomenology exterior to the cloud is of interest here a certain degree of freedom exists in the specification of the distribution.

Geometry of the Region

The region selected (Figure 1) is contained within a perfectly conducting right circular cylinder with a radius of 80 km and height of 110 km. The earth's surface is modeled electrically as a perfect conductor (lower plate). Typical values of 10^{-3} to 10^{-2} mhos/meter [Volland, 1984] are given for the earth's conductivity while 10^{-14} to 10^{-13} mhos/meter is the usual range of the adjacent atmosphere's conductivity. This is a difference of more than 11 orders of magnitude, making the earth's surface appear (electrically) as a perfect conductor with respect to the atmosphere. The simulations of interest were found to be insensitive to increases in either the vertical (110 km) or the radial (80 km) limits. The effects of both the Hall and Pederson components of the conductivity (above 70 km) and equating the global circuits surge impedance to zero ohms ($z \sim 0\ \Omega$) is based on worst case estimates (acknowledging the fact that only a passive global circuit is assumed) of the possible effects these parameters may have on the simulations. The conductivity used in the simulations is based on

measured data obtained August 8, 1981 during a thunderstorm campaign at Wallop's Island, Virginia [Baginski, 1987] and shown in Figure 2.

Discussion of the Simulations

The vertical component of the simulated Maxwell current density signatures are shown in Figure 3 for altitudes of 46, 53, and 60 km at a radial distance of 15 km from the vertical axis of symmetry. The waveforms show only slight differences in both magnitude and temporal character. Vertical electric field signatures at the same positions show a relatively large variation in both temporal character and magnitude (Figure 4).

Figure 5. and 6. identify the vector normalized Maxwell current density and electric field for altitudes of 40-60 km and radial distances of 15-30 km at t = 200 milliseconds. The interesting feature is that the Maxwell current density and the electric field are not aligned. This observation is of importance to experimentalists who typically infer field characteristics ($\vec{E}$ and J_m) from a single measured quantity.

The simulated vertical electric field signatures (Figure 4) are based on conductivity measurements obtained concurrently with transient electric field data (Figure 7). There are two traits common to both measurements and simulations that are not explainable in terms of simple relaxation time solutions [Baginski, 1987]: the significant time delay prior to the onset of maximum field strength, and the relatively long time duration of the transient. This fact indicates that the use of a

conservative electric field assumption ($E = -\nabla\phi$) is invalid for the study conducted.

CONCLUSIONS

The major contribution of the study of general importance is to emphasis the role modeling has in identifying allowable atmospheric transient behavior. This reduces the researchers need to rely on assumptions that in many cases are not rigorously justifiable. It is probable that the next major advances in atmospheric electricity will involve numerical simulation predictions of otherwise unexpected behavior.

Lightning researchers may benefit from the relative spatial and temporal invariance of the Maxwell current density with respect to the corresponding electric field signatures. It is likely that this type of characterization would provide an alternative fundamental description of the lightning event (e.g., forcing function required for single particle statistical solutions via the Maxwell Boltzman equation) that would greatly simplify the complexity of much current ionospheric phenomenology.

REFERENCES

1. Baginski, M.E., "Finite element simulation of the atmosphere's electromagnetic response to charge perturbations associated with lightning," Ph.D. thesis, Pennsylvania State University, 1987.

2. Chalmers, J.A., Atmospheric Electricity, 2nd ed., Pergamon, New York, 1967.

3. Gish, O.H., and R.G. Wait, "Thunderstorms and the earth's general electrification," J. Geophys. Res., 55, 473, 1950.

4. Hale, L.C., and M.E. Baginski, "Current to the ionosphere following a lightning stroke," Nature, 329, 814, 1987

5. Holzer, R.E. and D.S. Saxon, "Distribution of electrical conduction currents in the vicinity of Thunderstorms," J. Geophys. Res., 57, 207, 1952.

6. Holzworth, R.H., M.C. Kelly, C.L. Siefring, L.C. Hale, and J.D. Mitchell, "Electrical measurements in the atmosphere and ionosphere over an active thunderstorm: 2. Electric field and conductivity," J. Geophys. Res., in press, 1985.

7. Krider, E.P., and J. A. Musser, "Maxwell currents under a thunderstorm," J. Geophys. Res., 11, 171-176, 1982.

8. Nisbet, J.S., "A dynamic model of thundercloud electric fields," J. Atmos Sci., 40, 2855, 1983.

9. Stremler, F. G., Introduction to Communication Systems, Addison-Wesley, California, 1977.

10. Sunde, E.D., Earth Conduction Effects in Transmission Systems, Dover, New York, 1968.

11. Uman, M.A., Lightning, McGraw-Hill, New York, 1969.

12. Volland, H., Atmospheric Electrodynamics, Chemistry in Space, vol. II, Springer-Verlag, Berlin, Germany, 1984.

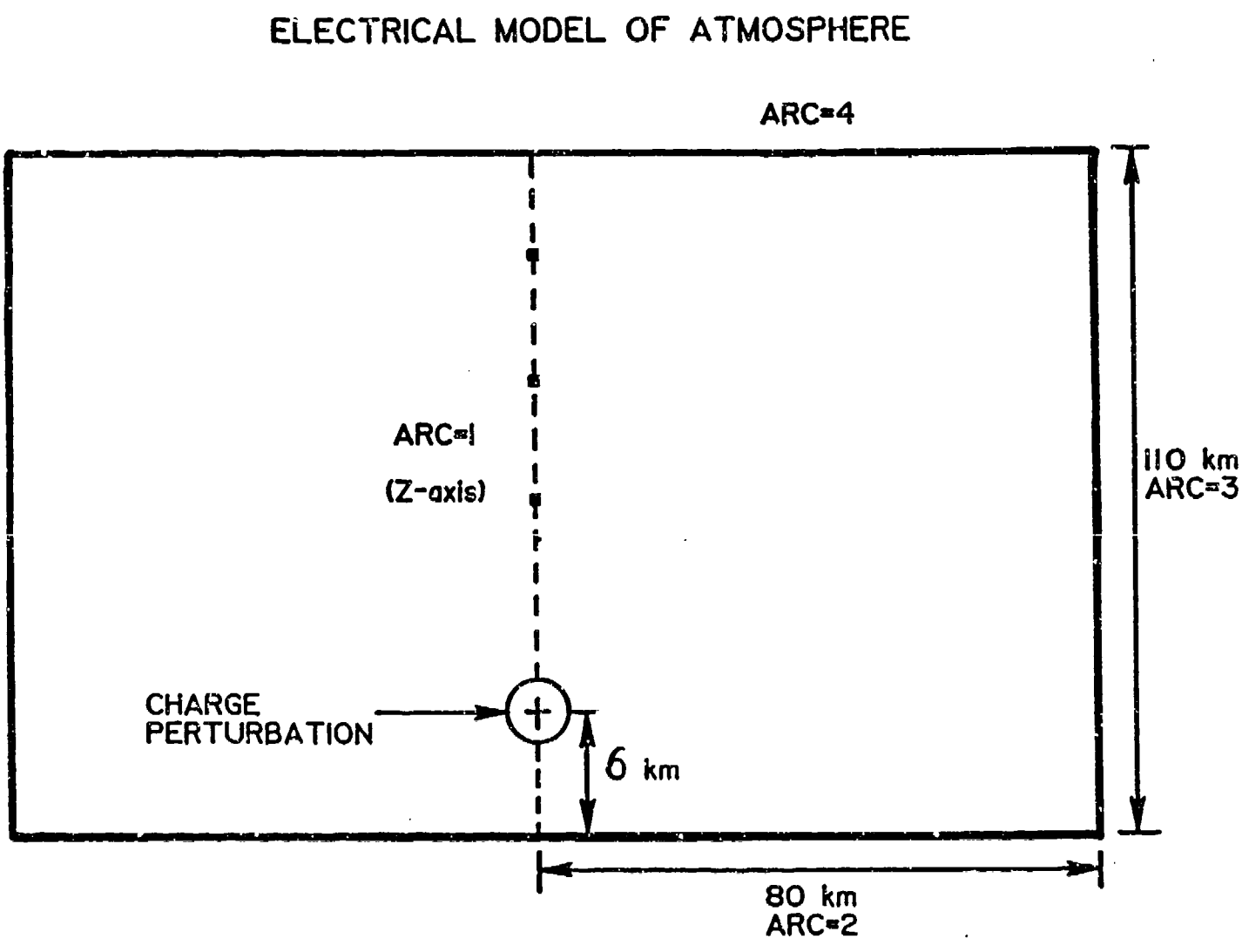


Figure 1 Electrical Model of the Atmosphere.

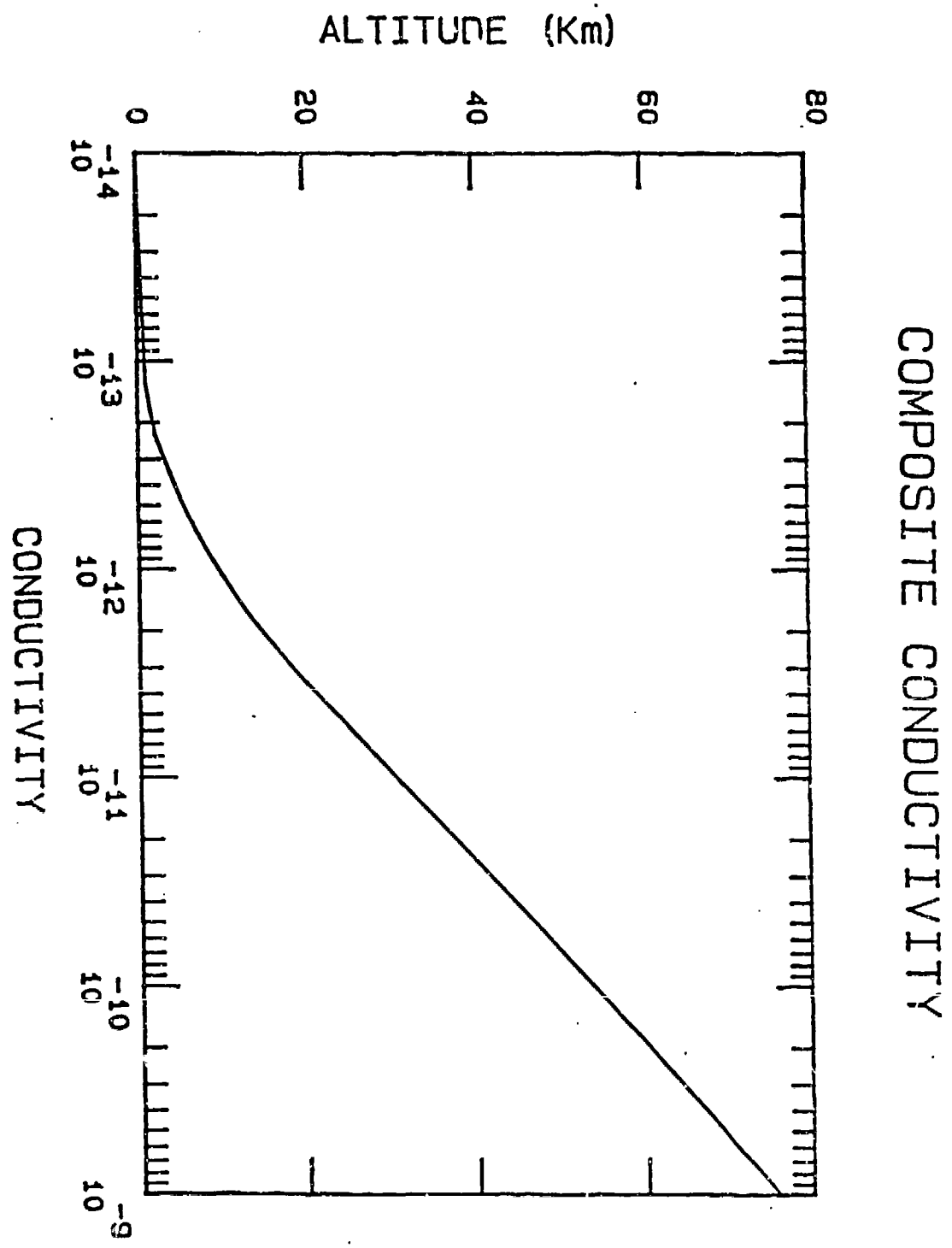


Figure 2 Composite Conductivity Profile Based on Measured Data Obtained August 8, 1981 at Wallops Island, Virginia.

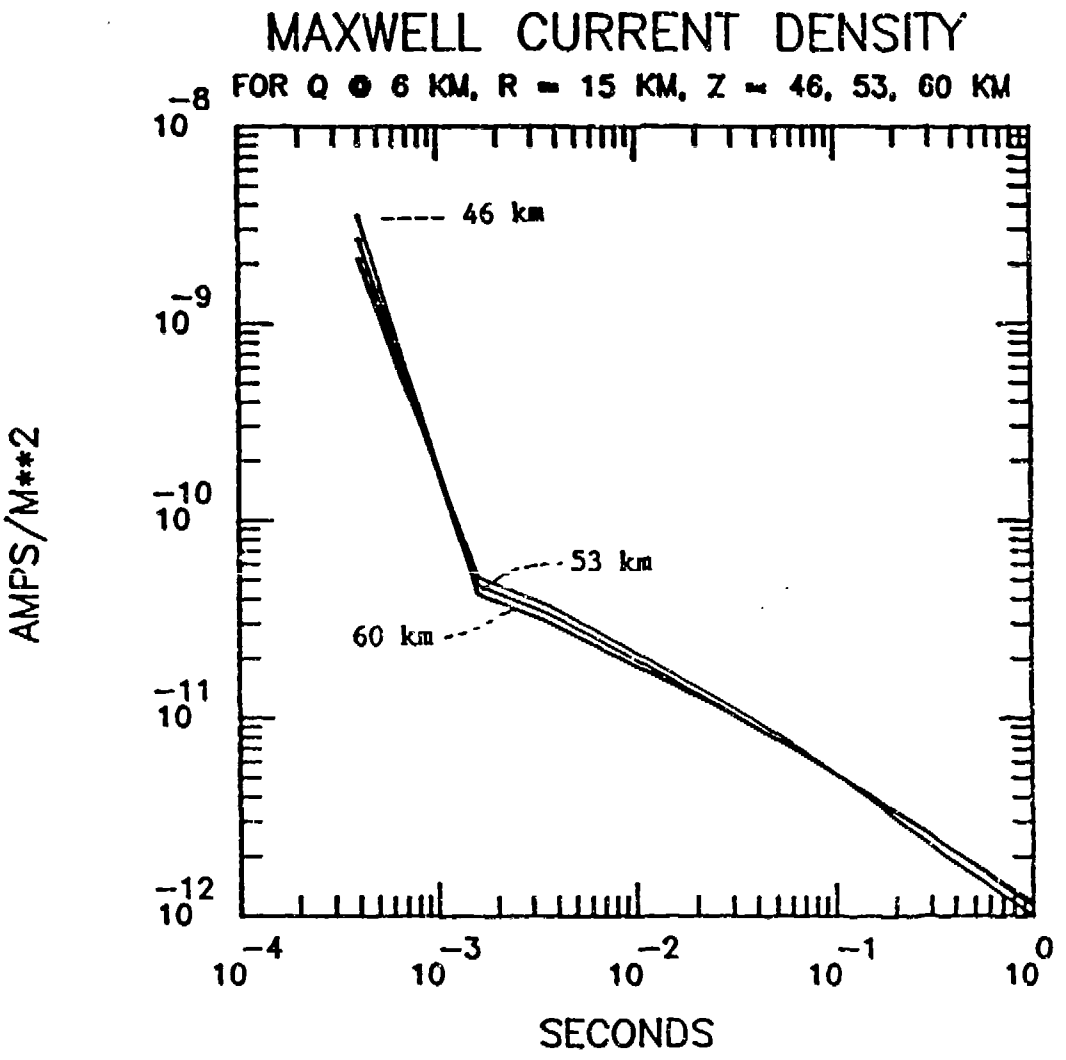


Figure 3 Maxwell Current Density Simulations at a Radial Distance of 15 km for Altitudes of 46, 53, and 60 km.

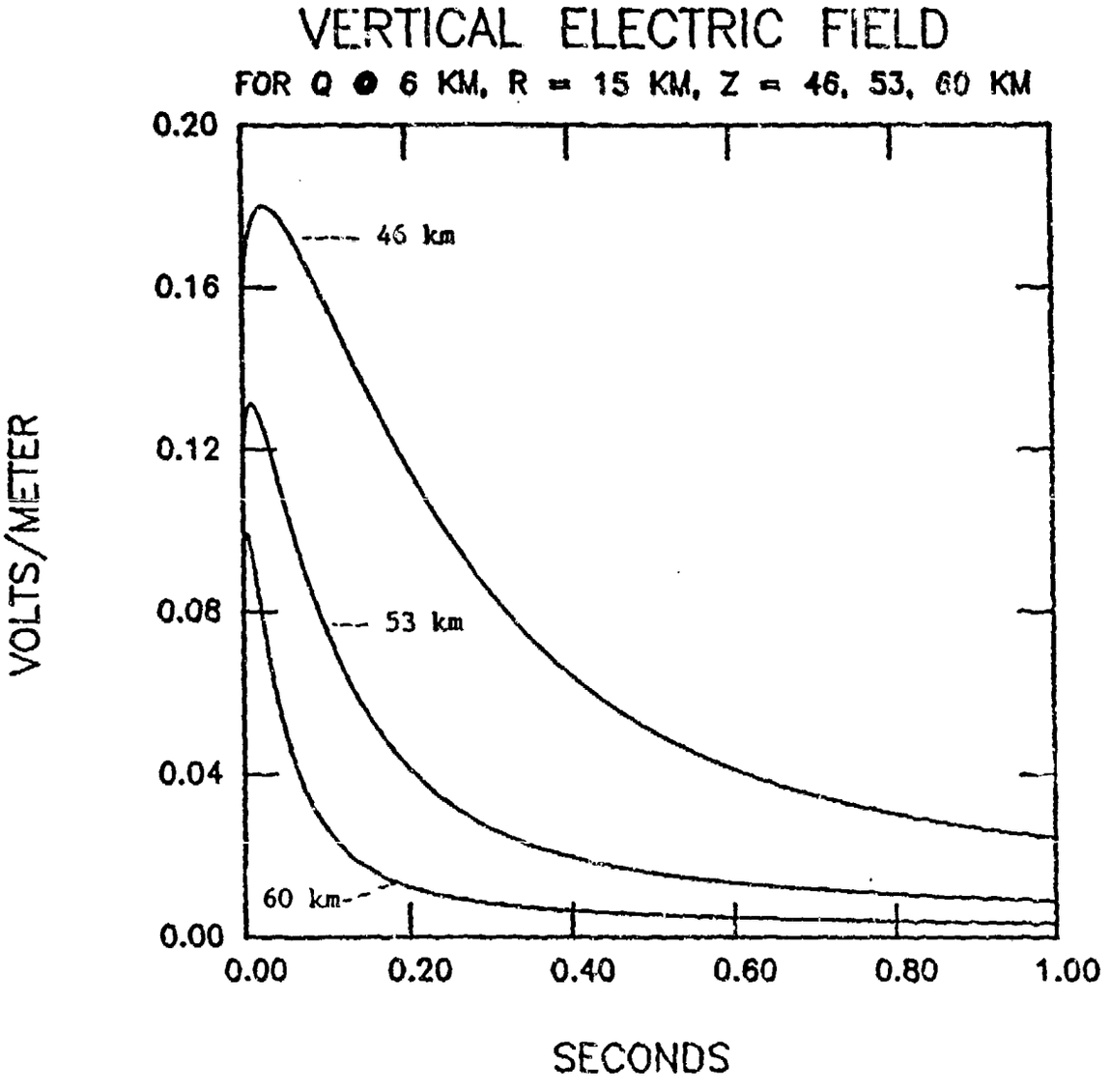


Figure 4 Electric Field Simulations at a Radial Distance of 15 km for Altitudes of 46, 53, and 60 km.

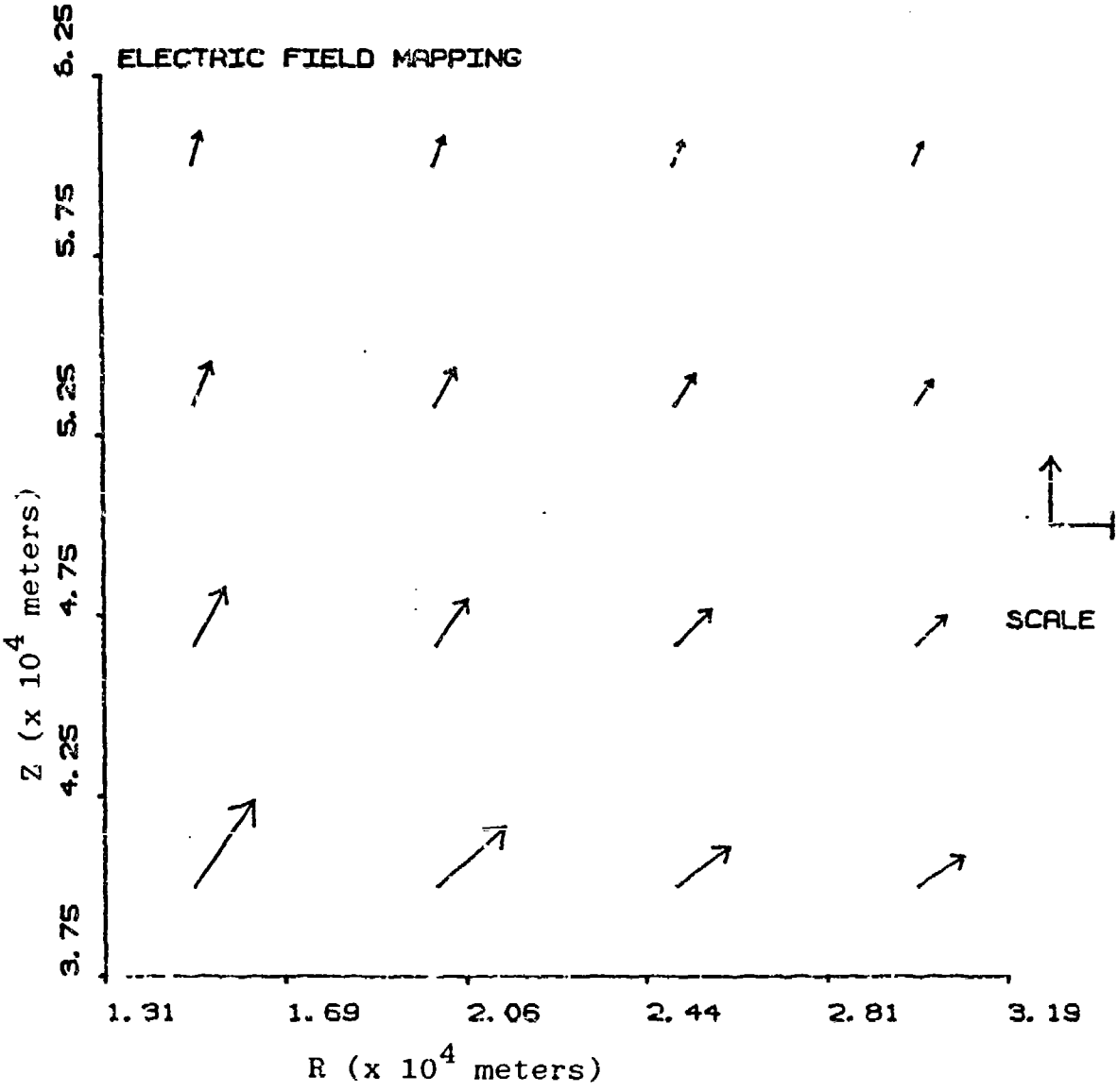


Figure 5 Normalized Simulated Electric Field Mapping for t = 200 milliseconds.

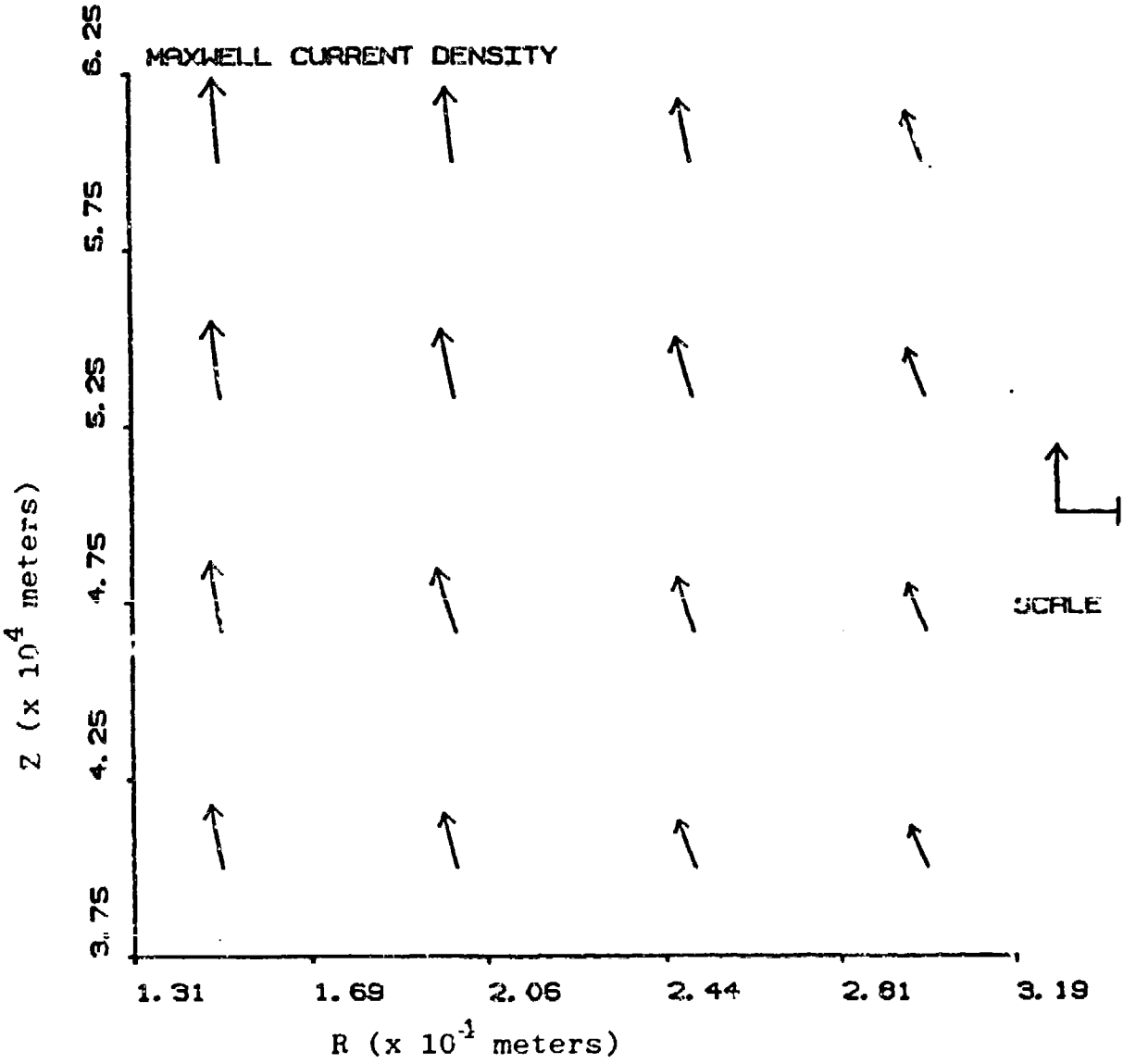


Figure 6 Normalized Simulated Maxwell Current Density Mapping for t = 200 milliseconds.

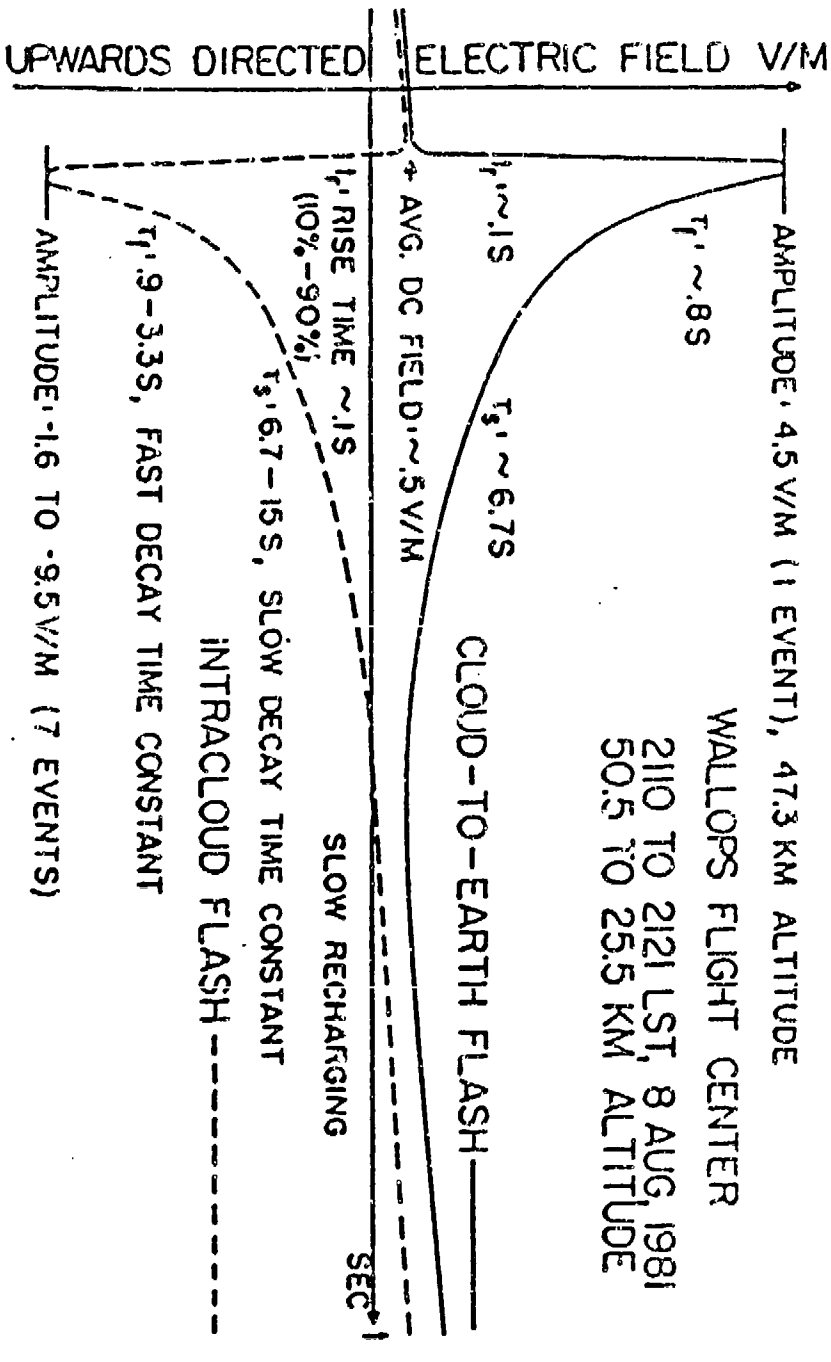


Figure 7 Electric Fields Measured August 8, 1981 by L.C. Hale and C.L. Croskey. Presented at AGU Fall Meeting, San Francisco, California, December, 1979.

TRANSIENT ELECTROMAGNETIC COUPLING TO A CAVITY WITH METALLIC WALLS*

Harold A. Sabbagh
Stephen A. Jenkins
Sabbagh Associates, Inc.
4639 Morningside Drive
Bloomington, IN 47401

I. INTRODUCTION

We are developing a computational model for transient electromagnetic field coupling into a metallic enclosure. The model is based on a finite element technique that uses the Galerkin variant of the method of moments. The expansion (and weighting) functions are piecewise linear, relative to a solid element with eight nodes. The model is fully three-dimensional, and accounts for the presence of a thin, perfectly conducting wire that spans opposite walls of the enclosure.

The finite element model manifests itself in two forms: a vector-matrix equation, and a fully-matrix equation. The former is better suited for explicit time integration, whereas the latter uses an implicit scheme.

Methods of dynamic analysis, including explicit and implicit time integrators, as well as normal modes, are considered, and an algorithm for computing the coupling to the exterior, directly in the time domain, is also included in the model. The exterior coupling algorithm is based on an electromagnetic boundary-integral relation and N-port theory.

This paper will briefly describe the general model, and will then present the results of some numerical experiments with a one-dimensional version of the model.

II. THE FINITE ELEMENT EQUATIONS

In Figure 1 we show a finite element mesh, consisting of rectangular cells. The system ports are shown on the outer surface, and the thin wire is shown as the boundary of several cells. This discretization is convenient for computing the coupling to the exterior world through the ports, and for accounting for the effects of the thin wire.

(a) The Variational Equations (Principle of Virtual Work)

The basic finite element model is derived from the principal of virtual work in electromagnetics, which is simply a variational equation. Start with Maxwell's equations in

* Supported by The Harry Diamond Laboratories under Contract No. DAAL02-87-C-0101

the time domain

$$\begin{aligned} \nabla \times \mathbf{E} &= -\mu_0 \dot{\mathbf{H}} \\ \nabla \times \mathbf{H} &= \epsilon_0 \dot{\mathbf{E}} + \mathbf{J}, \end{aligned} \tag{1}$$

where the dot denotes a time derivative. We can write a weak form of this system (i.e., a "variational form") by multiplying the second equation in (1) by the arbitrary variational function, $\mathbf{s}(\mathbf{r})$, and then integrating over the volume of the interior region. When use is made of the vector identity, $\mathbf{s} \cdot \nabla \times \mathbf{H} = \nabla \cdot (\mathbf{s} \times \mathbf{H}) + \mathbf{H} \cdot \nabla \times \mathbf{s}$, together with Gauss' theorem, we get

$$\oint (\mathbf{s} \times \mathbf{H}) \cdot \mathbf{a}_n dS = \epsilon_0 \frac{d}{dt} \int \mathbf{s} \cdot \mathbf{E} \, dV + \int \mathbf{s} \cdot \mathbf{J} \, dV - \int \mathbf{H} \cdot \nabla \times \mathbf{s} \, dV, \tag{2}$$

where $\mathbf{a}_n$ is the unit outward-pointing normal vector to the surface bounding the interior region. Equation (2) is a statement of the principle of virtual work in electromagnetics. This suggests the following analogy with continuum mechanics; the electric field vector, $\mathbf{E}$, is analogous to the velocity field of the medium, and ϵ_0 is analogous to mass density, so that $\epsilon_0 \dot{\mathbf{E}}$ is analogous to momentum density. The current density, $\mathbf{J}$, is analogous to a body force density, and the magnetic field intensity, $\mathbf{H}$, is analogous to stress. In this analogy, therefore, the first of Maxwell's equations, (1), is simply a stress-strain relation.

Now let $\mathbf{s}$ take on the values $s(x,y,z)\mathbf{a}_x$, $s(x,y,z)\mathbf{a}_y$, $s(x,y,z)\mathbf{a}_z$, sequentially, where $s(x,y,z)$ is a finite element shape function. Note that we use the same shape function for all three components; this is not necessary, but is convenient. Now (2) is equivalent to a vector equation whose components are

$$\begin{aligned} \oint s(\mathbf{a}_x \times \mathbf{H}) \cdot \mathbf{a}_n dS &= \epsilon_0 \frac{d}{dt} \int s E_x dV + \int s J_x dV - \int \mathbf{H} \cdot \nabla \times (s\mathbf{a}_x) dV \\ \oint s(\mathbf{a}_y \times \mathbf{H}) \cdot \mathbf{a}_n dS &= \epsilon_0 \frac{d}{dt} \int s E_y dV + \int s J_y dV - \int \mathbf{H} \cdot \nabla \times (s\mathbf{a}_y) dV \\ \oint s(\mathbf{a}_z \times \mathbf{H}) \cdot \mathbf{a}_n dS &= \epsilon_0 \frac{d}{dt} \int s E_z dV + \int s J_z dV - \int \mathbf{H} \cdot \nabla \times (s\mathbf{a}_z) dV. \end{aligned} \tag{3}$$

The function $s(x,y,z)$ that appears in (3) is called a testing function, in the language of the method of moments. We will shortly expand the unknown fields, $\mathbf{E}$, $\mathbf{H}$, and $\mathbf{J}$ using the same function. When the expansion and testing functions are identical, the method is called Galerkin's method. The method of moments, and Galerkin's variant of the method of moments, have wider applicability than in finite elements. They are often used in discretizing integral equations, as well.

(b) The Vector-Matrix Form of the Equations

In order to continue with the discretization process, we rewrite the volume integrals

in (3) as sums over N_c cells in the grid of Figure 1:

$$
\begin{aligned}
0 &= \sum_{m=1}^{N_c}\left\{-\int_{S_m} s(\mathbf{a}_x \times \mathbf{H})\cdot \mathbf{a}_n dS + \epsilon_0 \frac{d}{dt}\int_{V_m} sE_x dV + \int_{V_m} sJ_x dV - \int_{V_m} \mathbf{H}\cdot\nabla\times(s\mathbf{a}_x)dV\right\}\\
0 &= \sum_{m=1}^{N_c}\left\{-\int_{S_m} s(\mathbf{a}_y \times \mathbf{H})\cdot \mathbf{a}_n dS + \epsilon_0 \frac{d}{dt}\int_{V_m} sE_y dV + \int_{V_m} sJ_y dV - \int_{V_m} \mathbf{H}\cdot\nabla\times(s\mathbf{a}_y)dV\right\}\\
0 &= \sum_{m=1}^{N_c}\left\{-\int_{S_m} s(\mathbf{a}_z \times \mathbf{H})\cdot \mathbf{a}_n dS + \epsilon_0 \frac{d}{dt}\int_{V_m} sE_z dV + \int_{V_m} sJ_z dV - \int_{V_m} \mathbf{H}\cdot\nabla\times(s\mathbf{a}_z)dV\right\}.
\end{aligned}
\tag{4}
$$

The three-dimensional shape function, $s(x,y,z)$, that is to be defined over each element in (4) is called an 8-node isoparametric solid element. In order to learn more about this, refer to Figure 2. The (ξ,η,ζ) coordinate system has its origin at the center of the 8-noded solid element. Let $\mathbf{X}_j$ be the location of the jth node in this element. Then, any other spatial point within the block can be written as

$$
\mathbf{x}(\xi,\eta,\zeta) = \sum_{j=1}^{8} \phi_j(\xi,\eta,\zeta)\mathbf{X}_j, \qquad -1 \le \xi,\eta,\zeta \le 1 \tag{5}
$$

where

$$
\begin{aligned}
\phi_1 &= \frac{1}{8}(1-\xi)(1-\eta)(1-\zeta)\\
\phi_2 &= \frac{1}{8}(1+\xi)(1-\eta)(1-\zeta)\\
\phi_3 &= \frac{1}{8}(1-\xi)(1+\eta)(1-\zeta)\\
\phi_4 &= \frac{1}{8}(1+\xi)(1+\eta)(1-\zeta)\\
\phi_5 &= \frac{1}{8}(1-\xi)(1-\eta)(1+\zeta)\\
\phi_6 &= \frac{1}{8}(1+\xi)(1-\eta)(1+\zeta)\\
\phi_7 &= \frac{1}{8}(1-\xi)(1+\eta)(1+\zeta)\\
\phi_8 &= \frac{1}{8}(1+\xi)(1+\eta)(1+\zeta)
\end{aligned}
\tag{6}
$$

are (trilinear) interpolating functions. Note that $\mathbf{x}(\xi,\eta,\zeta)$ takes on its nodal values, $\mathbf{X}_j$,

at $(\xi,\eta,\zeta) = (\pm 1, \pm 1, \pm 1)$; i.e.,

$$\begin{aligned}
\mathbf{x}(-1,-1,-1) &= \mathbf{X}_1 \\
\mathbf{x}(1,-1,-1) &= \mathbf{X}_2 \\
\mathbf{x}(-1,1,-1) &= \mathbf{X}_3 \\
\mathbf{x}(1,1,-1) &= \mathbf{X}_4 \\
\mathbf{x}(-1,-1,1) &= \mathbf{X}_5 \\
\mathbf{x}(1,-1,1) &= \mathbf{X}_6 \\
\mathbf{x}(-1,1,1) &= \mathbf{X}_7 \\
\mathbf{x}(1,1,1) &= \mathbf{X}_8,
\end{aligned} \tag{7}$$

as indicated in Figure 2.

We expand an arbitrary vector field in the same way within the solid element:

$$\begin{aligned}
\mathbf{v}(x,y,z,t) &= \mathbf{v}(\mathbf{x}(\xi,\eta,\zeta),t) \\
&= \sum_{j=1}^{8} \phi_j(\xi,\eta,\zeta)\mathbf{V}_j(t).
\end{aligned} \tag{8}$$

Because we are using the same parameters $\{\phi_j(\xi,\eta,\zeta)\}$ to expand both the shape of the body, (5), as well as all other vector fields, (8), this is called an isoparametric expansion.

Clearly, the nodal values, $\{\mathbf{V}_j(t)\}$, can be taken as expansion coefficients and the $\{\phi_j\}$ as expansion and testing functions in (4). Thus, in (4) expand the unknown fields as in (8), and let the testing function, s, be $\{\phi_i\}$, $i = 1, ..., 8$. Consider, first, the time-derivative terms in (4)

$$\begin{aligned}
&\epsilon_0 \int_{V_m} \phi_i \sum_{j=1}^{8} \phi_j \dot{E}_{xj} dV \\
&\epsilon_0 \int_{V_m} \phi_i \sum_{j=1}^{8} \phi_j \dot{E}_{yj} dV \\
&\epsilon_0 \int_{V_m} \phi_i \sum_{j=1}^{8} \phi_j \dot{E}_{zj} dV.
\end{aligned} \tag{9}$$

The three sums can be replaced by the vector-matrix product, $\mathbf{N}\dot{\mathbf{e}}$, where

$$\mathbf{N}(\xi,\eta,\zeta) = \begin{bmatrix}
\phi_1 & 0 & 0 & \phi_2 & 0 & 0 & \dots & \phi_8 & 0 & 0 \\
0 & \phi_1 & 0 & 0 & \phi_2 & 0 & \dots & 0 & \phi_8 & 0 \\
0 & 0 & \phi_1 & 0 & 0 & \phi_2 & \dots & 0 & 0 & \phi_8
\end{bmatrix}, \tag{10}$$

and

$$\dot{\mathbf{e}} = \begin{bmatrix} \dot{E}_{x1} \\ \dot{E}_{y1} \\ \dot{E}_{z1} \\ \vdots \\ \dot{E}_{x8} \\ \dot{E}_{y8} \\ \dot{E}_{z8} \end{bmatrix}. \tag{11}$$

Hence, (9) can be written in matrix form as

$$\left[\epsilon_0 \int_{V_m} \mathbf{N}^T \mathbf{N} dV\right] \dot{\mathbf{e}}, \tag{12}$$

where the term within the brackets is the single-cell "mass matrix". Note that it is of order 24×24 (three vector components per node times eight nodes per cell.)

Similarly, the current density term in (4) can be replaced by the matrix-vector product

$$\int_{V_m} \mathbf{N}^T \cdot \mathbf{J} dV, \tag{13}$$

where J is the usual current density vector restricted to the mth element.

Upon expanding the curl operation in the final volume integral in (4), we find that we can rewrite this integral in the form

$$\int_{V_m} \mathbf{B}^T \cdot \mathbf{H}\, dV, \tag{14}$$

where the curl matrix is given by

$$\mathbf{B} = \begin{bmatrix} 0 & -\phi_{1,z} & \phi_{1,y} & \cdots & 0 & -\phi_{8,z} & \phi_{8,y} \\ \phi_{1,z} & 0 & -\phi_{1,x} & \cdots & \phi_{8,x} & 0 & -\phi_{8,x} \\ -\phi_{1,y} & \phi_{1,x} & 0 & \cdots & -\phi_{8,y} & \phi_{8,x} & 0 \end{bmatrix}. \tag{15}$$

H is the usual magnetic field vector restricted to the mth element; the commas denote partial derivatives.

The surface integrals in (4) can be transformed, using the scalar triple-product, into

$$\int_{S_m} s \begin{bmatrix} (\mathbf{H} \times \mathbf{a}_n) \cdot \mathbf{a}_x \\ (\mathbf{H} \times \mathbf{a}_n) \cdot \mathbf{a}_y \\ (\mathbf{H} \times \mathbf{a}_n) \cdot \mathbf{a}_z \end{bmatrix} dS. \tag{16}$$

$\mathbf{H} \times \mathbf{a}_n$ is the tangential magnetic field, $\mathbf{H}_t$, at the surface of the interior system. Upon letting $s = \{\phi_i\}$, $i = 1, \ldots, 8$, as before, then (16) becomes

$$\int_{S_m} \mathbf{N}^T \cdot \mathbf{H}_t dS. \tag{17}$$

Thus, (4) is replaced by the equivalent finite-element form

$$\sum_{m=1}^{N_e}\left\{\left[\epsilon_0\int_{V_m}\mathbf{N}^T\mathbf{N}dV\right]\dot{\mathbf{e}}+\int_{V_m}\mathbf{N}^T\cdot\mathbf{J}dV-\int_{V_m}\mathbf{B}^T\cdot\mathbf{H}\,dV-\int_{S_m}\mathbf{N}^T\cdot\mathbf{H}_t dS\right\}=0, \quad (18)$$

or, in vector-matrix form

$$\mathbf{M}\dot{\mathbf{e}}_g=-\mathbf{i}+\mathbf{h}+\mathbf{h}_t, \quad (19)$$

where M is the global mass matrix, $\mathbf{e}_g$ is the global electric field vector (i.e., the field vector at each nodal point of the entire mesh), i is the global "body-force" vector, that corresponds to the current density term of (13), h is the global "stress-vector" corresponding to (14), and $\mathbf{h}_t$ accounts for the global tangential magnetic field, and corresponds to (17).

Equation (19) is called the "vector-matrix" form of the finite element equations because the mass matrix is the only matrix present, and the forcing-functions are left explicitly as vectors. This is done to facilitate the use of explicit time-integrators. In an explicit approach, matrix methods are not used extensively. Later we will describe a fully-matrix model, in which implicit time-integration is used, together with complete matrix decompositions.

(c) Accounting for the Wire

Along the wire we require that the tangential electric field must vanish for all time. Hence

$$\dot{E}_z(x_w,y_w,z,t)=0, \qquad z_{(-)}\le z\le z_{(+)} \quad (20)$$

where $(z_{(-)},z_{(+)})$ are the bottom and top of the wire, and (x_w,y_w) are the coordinates of the wire in the (x,y)-plane (see Figure 1).

Multiply (20) by an arbitrary variation, $s(z)$, and get

$$\int_{z_{(-)}}^{z_{(+)}}s(z)\dot{E}_z(x_w,y_w,z,t)dz=0. \quad (21)$$

The three-dimensional finite element grid induces a one-dimensional grid along the wire, so that we rewrite (21) as

$$\sum_{m=1}^{N_w}\int_{l_m}s(z)\dot{E}_z(z,t)dz=0, \quad (22)$$

where N_w is the number of segments along the wire.

We define one-dimensional interpolating functions

$$\lambda_1=\frac{1}{2}(1+\xi), \qquad \lambda_2=\frac{1}{2}(1-\xi), \qquad -1\le\xi\le 1, \quad (23)$$

that are derived from (6) by letting $\eta=1$, $\zeta=1$. In the mth cell of the wire, let

$$\begin{aligned} z(\xi)&=z_1\lambda_1(\xi)+z_2\lambda_2(\xi)\\ \dot{E}_z(z(\xi))&=\dot{E}_1\lambda_1(\xi)+\dot{E}_2\lambda_2(\xi), \end{aligned} \quad (24)$$

where (z_1, z_2) and $(\dot{E}_1, \dot{E}_2)$ are the nodal values in the mth cell. Upon substituting (24) into (22), and then letting $s(z) = \{\lambda_1, \lambda_2\}$, sequentially, we get the following matrix version of the constraint equation

$$\sum_{m=1}^{N_w} \left[\int_{l_m} \mathbf{W}^T \mathbf{W} dz \right] \dot{\mathbf{e}}_z(t) = 0, \tag{25}$$

where

$$\mathbf{W} = [\lambda_1 \quad \lambda_2], \qquad \dot{\mathbf{e}}_z = \begin{bmatrix} \dot{E}_{z1} \\ \dot{E}_{z2} \end{bmatrix}. \tag{26}$$

We multiply (25) by a large parameter, p, and add the result to (18) or (19). This introduces a "penalty term" to several elements of the global mass matrix, which, in turn, forces $\dot{E}_z$ to be very small at the nodes on the wire.

The current along the wire can be computed by appealing to Ampere's circuital law, which is the integrated version of the second of Maxwell's equations, (1):

$$\oint \mathbf{H} \cdot d\mathbf{l} = I, \tag{27}$$

where I is the net current, i.e., displacement plus conduction. The closed path that is indicated in (27) lies in the (x, y) plane, which is normal to the wire, and threads the midpoints of those cells that are contiguous to the wire. The line integral is approximated numerically, given the value of H at the midpoint of the appropriate cells. As the path shrinks to the wire, the net enclosed displacement current vanishes.

(d) Diagonal Mass Matrix

In applying an explicit time-integration scheme to (19), we will need to invert the mass matrix at each time step in order to solve for $\dot{\mathbf{e}}(t)$. Thus, it is desirable to have a simple matrix to invert, rather than the consistent mass matrix of (19). We diagonalize the mass matrix simply by summing each row and assigning that value to the diagonal. This is equivalent to assigning the total "mass" of the system to each nodal "point mass". Putting it another way, we say that the "forces" act directly on each point mass.

(e) The Fully-Matrix Form of the Equations

Equation (19) was set up for explicit time-integration, because that method is the most economical for many problems, and we introduced the lumped mass matrix to facilitate the explicit algorithm. Because of the presence of the metal, with its very large conductivity, however, the problem involves two vastly different time scales, one for diffusion through the walls, and the other for propagation within the cavity. Such problems are not easily solved using explicit time-integrators, so in Section III we will introduce an implicit method, specifically, the Newmark scheme. That method, however, or any other implicit method, will require a fully-matrix form of the finite element equations, which will be developed in this section.

We introduce two additional matrices in (19): the damping and stiffness matrices (obviously, we continue to use structural terminology.) In (18) and (19), we have

$$\begin{aligned}\mathbf{i} &= \sum_{m=1}^{N_c} \int_{V_m} \mathbf{N}^T \cdot \mathbf{J} dV \\ &= \sum_{m=1}^{N_c} \int_{V_m} \sigma \mathbf{N}^T \cdot \mathbf{E} dV \\ &= \sum_{m=1}^{N_c} \left[\int_{V_m} \sigma \mathbf{N}^T \mathbf{N} dV \right] \mathbf{e}.\end{aligned} \tag{28}$$

The integral is the single-cell damping matrix, and the global matrix derived from the single-cell matrix is called the global damping matrix, C. Hence,

$$\mathbf{i} = \mathbf{C}\mathbf{e}. \tag{29}$$

We drop the subscript, 'g', from the global vector, e, to simplify notation. Note that C has the same structure as the mass matrix, M. Indeed, if the conductivity were uniform throughout the cavity and walls, then the two matrices would be identical, except for a constant multiplier. Throughout the wall, however, these matrices are identical (except for the constant multiplier).

The third term in (18) has a similar representation

$$\begin{aligned}-\sum_{m=1}^{N_c} \int_{V_m} \mathbf{B}^T \cdot \mathbf{H} dV &= \frac{1}{\mu_0} \sum_{m=1}^{N_c} \int_{V_m} \mathbf{B}^T \cdot (\nabla \times \int_0^t \mathbf{E}(\tau, \tau) d\tau) dV \\ &= \frac{1}{\mu_0} \sum_{m=1}^{N_c} \left[\int_{V_m} \mathbf{B}^T \mathbf{B} dV \right] \int_0^t \mathbf{e}(\tau) d\tau \\ &= \mathbf{K} \int_0^t \mathbf{e}(\tau) d\tau.\end{aligned} \tag{30}$$

K is the stiffness matrix.

Hence, (18) becomes the fully-matrix equation

$$\mathbf{M}\dot{\mathbf{e}} + \mathbf{C}\mathbf{e} + \mathbf{K} \int_0^t \mathbf{e}(\tau) d\tau = \mathbf{F}^{(s)}(t), \tag{31}$$

where the superscript, 's', on the forcing function reminds us that the force is applied to the surface elements, only.

Upon differentiating (31) we get the more familiar looking second-order differential equation

$$\mathbf{M}\ddot{\mathbf{e}} + \mathbf{C}\dot{\mathbf{e}} + \mathbf{K}\mathbf{e} = \dot{\mathbf{F}}^{(s)}. \tag{32}$$

Because M, C, and K are computed only once, at the start of the problem, we can use a more accurate quadrature rule, such as a two-point Gaussian rule, to compute them. Here, M is the consistent, rather than lumped, mass matrix.

III. METHODS OF DYNAMIC ANALYSIS

The finite element model has produced two systems of ordinary differential equations, (II-19)* and (II-32), that must be integrated in order to determine the time-evolution of the electromagnetic field. There are many different time-integrators that could be applied to this task, depending upon the nature of the system, and the information that one hopes to gain from the solution.

In a pure wave-propagation problem, in which there is relatively little dispersion, so that the vector, i, is absent from (II-19) (or the global damping matrix vanishes in (II-32)), (II-19), together with an explicit time-integration scheme would be quite useful. This is due to the fact that explicit schemes require a small time step, commensurate with the smallest cell size in the finite element mesh, to assure stability. Such time steps are reasonable for the short-time response that one is often interested in wave-propagation problems.

In our problem, however, the highly conducting wall filters out much of the high-frequency content that is present in the incident wave, and the model equations now contain a mix of large and small eigenvalues; such equations are said to be 'stiff'. We are no longer interested in only the short-time response, because that response is governed by the high frequencies, which are effectively filtered out. Hence, an explicit integration scheme will no longer be particularly useful because it would require too many time steps to get to the temporal region of interest in the solution. Thus, we consider using an implicit scheme on (II-32).

(a) Explicit Time Integration

The finite element method generated the system of ordinary differential equations (ODE) shown in (II-19). A system such as this was solved in the structural synamics code, DYNA3D [1], by using a standard central- difference formula. An explicit scheme like this is attractive here because of its ease of use and its speed (assuming a reasonable step size can be used). Since we do not have complicated boundary conditions in the time variable, there is no need to use finite elements in the time domain and an explicit finite difference scheme is about the easiest of all schemes to implement. However, the system of ODE's generated by Maxwell's equations, with highly conducting materials present, is extremely 'stiff', and this causes stability problems.

Explicit time integrators were tried extensively with the one dimensional problem that is to be described in Section IV. Central-difference, 2nd-order and 4th-order Runge-Kutta schemes were all tried. All of these schemes required extremely small time steps for stability. Figure 3 shows the numeric solution to the one dimensional problem with spatial dimension 10 cm. The upper and lower wall were 2.5 cm thick, homogeneous in

* This refers to equation (19) of Section II.

the x and y directions, and the 5 nodes were equally spaced in the z direction. The input was a unit step pulse. The graph in the upper right-hand corner shows the y-component of the electric field at the top and bottom nodes of the upper wall. The graph below this shows the y-component of the electrical field at the lower wall, while the graph in the lower left-hand corner shows the response in the center of the cavity (free-space). As can be seen here, even though the scheme is stable for the metallic nodes the free space node shows classic instability. This instability can be eliminated by using even smaller step sizes, but the step size used here is already too small for any hope of using this scheme in a practical way.

Attempts were made to use the consistent mass matrix (not row-summed) to improve performance of these schemes, but without much success. Eventually this whole approach was abandoned. Even though the walls filter out much of the high frequency content of the incident wave, the numerical scheme seems to reintroduce this high frequency through round-off and local truncation errors. There may be a way to improve the stability of these explicit schemes by introducing artificial 'damping' to the free-space elements. This approach has been used in DYNA3D. This could lead to a stable explicit scheme using more reasonable time steps. Also, if we were interested in materials with much lower conductivities, the system would be less stiff and these schemes could be more attractive.

For the present, however, we are forced to turn our attention to implicit schemes, specifically the Newmark method.

(b) The Newmark Implicit Integration Scheme

We will apply the Newmark scheme because it introduces the least trunctation error, is unconditionally stable, and is used in the implicit finite element codes ADINA [2], NIKE2D[3], and NIKE3D[4]. Our discussion follows Bathe and Wilson [2]; see [5], also, for additional information on time integrators in finite element analysis.

The Newmark algorithm starts by expanding the "velocity" and "displacement" vectors at $t + \Delta t$ as:

$$\begin{aligned} \dot{\mathbf{e}}_{t+\Delta t} &= \dot{\mathbf{e}}_t + \left[(1-\delta)\ddot{\mathbf{e}}_t + \delta\ddot{\mathbf{e}}_{t+\Delta t}\right]\Delta t \\ \mathbf{e}_{t+\Delta t} &= \mathbf{e}_t + \dot{\mathbf{e}}_t\Delta t + \left[(1/2-\alpha)\ddot{\mathbf{e}}_t + \alpha\ddot{\mathbf{e}}_{t+\Delta t}\right]\Delta t^2, \end{aligned} \tag{1}$$

where α and δ are parameters that can be chosen to obtain accuracy and stability. The combination $\alpha = 1/4$, $\delta = 1/2$ gives the constant-average-acceleration method, sometimes called the trapezoidal rule; this rule yields the smallest truncation error among all second-order, A-stable, implicit, linear, multistep methods.

Equations (1) are used to solve for $\ddot{\mathbf{e}}_{t+\Delta t}$ and $\dot{\mathbf{e}}_{t+\Delta t}$ in terms of the unknown displacement, $\mathbf{e}_{t+\Delta t}$, and this result is then substituted into the equilibrium equation, (II-32), at time $t + \Delta t$. This produces an equation for $\mathbf{e}_{t+\Delta t}$, in which the stiffness matrix is replaced by an "effective stiffness matrix", and the load is replaced by an "effective load" at time $t + \Delta t$.

The step-by-step application of the Newmark algorithm is summarized in the table [2]:

A. *Initial Calculations*

1. Form stiffness matrix, $\mathbf{K}$, mass matrix, $\mathbf{M}$, and damping matrix, $\mathbf{C}$.
2. Initialize $\mathbf{e}_0$, $\dot{\mathbf{e}}_0$, $\ddot{\mathbf{e}}_0$.
3. Select time step size, Δt, parameters, α, δ, and calculate integration constants:

$$\delta \geq 0.50, \qquad \alpha \geq 0.25(0.5+\delta)^2$$
$$a_0 = \frac{1}{\alpha \Delta t^2}, \qquad a_1 = \frac{\delta}{\alpha \Delta t}, \qquad a_2 = \frac{1}{\alpha \Delta t},$$
$$a_3 = \frac{1}{2\alpha} - 1, \qquad a_4 = \frac{\delta}{\alpha} - 1, \qquad a_5 = \frac{\Delta t}{2}\left(\frac{\delta}{\alpha} - 2\right),$$
$$a_6 = \Delta t(1-\delta), \qquad a_7 = \delta \Delta t.$$

4. Form effective stiffness matrix $\widehat{\mathbf{K}}$: $\widehat{\mathbf{K}} = \mathbf{K} + a_0\mathbf{M} + a_1\mathbf{C}$.
5. Factor $\widehat{\mathbf{K}}$: $\widehat{\mathbf{K}} = \mathbf{L}\mathbf{D}\mathbf{L}^T$.

B. *For Each Time Step:*

1. Calculate effective loads at time $t + \Delta t$:

$$\widehat{\mathbf{F}}^{(s)}_{t+\Delta t} = \mathbf{F}^{(s)}_{t+\Delta t} + \mathbf{M}(a_0\mathbf{e}_t + a_2\dot{\mathbf{e}}_t + a_3\ddot{\mathbf{e}}_t) + \mathbf{C}(a_1\mathbf{e}_t + a_4\dot{\mathbf{e}}_t + a_5\ddot{\mathbf{e}}_t)$$

2. Solve for displacements at time $t + \Delta t$:

$$\mathbf{L}\mathbf{D}\mathbf{L}^T\mathbf{e}_{t+\Delta t} = \widehat{\mathbf{F}}^{(s)}_{t+\Delta t}$$

3. Calculate accelerations and velocities at time $t + \Delta t$:

$$\ddot{\mathbf{e}}_{t+\Delta t} = a_0(\mathbf{e}_{t+\Delta t} - \mathbf{e}_t) - a_2\dot{\mathbf{e}}_t - a_3\ddot{\mathbf{e}}_t$$
$$\dot{\mathbf{e}}_{t+\Delta t} = \dot{\mathbf{e}}_t + a_6\ddot{\mathbf{e}}_t + a_7\ddot{\mathbf{e}}_{t+\Delta t}$$

Note that the effective stiffness matrix is factored once, at the beginning of the problem, and the result is applied to the various right-hand sides (i.e., the effective loads at $t + \Delta t$). Hence, this is a fairly efficient way to solve this problem. The initial value for $\ddot{\mathbf{e}}_0$ can be determined from the differential equation, (II-32); at this point the lumped mass matrix could be useful.

It is very important to observe that if $\widehat{\mathbf{K}}$ is banded, as it will be for finite elements, then $\mathbf{L}$ is also banded, with one-half the bandwidth of $\widehat{\mathbf{K}}$, and $\mathbf{D}$ is diagonal. Therefore, relatively little storage is required to store these factors. The inverse of $\widehat{\mathbf{K}}$, however, is full, so it would not be efficient to compute and store it. This is the reason that we factor $\widehat{\mathbf{K}}$, rather than invert it.

IV. NUMERICAL EXPERIMENTS

We have performed several numerical experiments to confirm the feasibility of our model, and the results will be discussed in this chapter. Because the three-dimensional problem is complicated, with no analytical solution to validate the results, we spent considerable time developing and implementing a one-dimensional model that could be executed using several different approaches. The results of the one-dimensional are thereby validated, and, thus, can serve as an indicator of the correctness of the three-dimensional computations. Of course, the three-dimensional model requires much more computer resources than the one-dimensional model, and, therefore, could only be executed using a very coarse mesh. Even in this case, however, the results have been encouraging, and confirm the feasibility of our approach.

One-Dimensional Model

In Figure 4 we show a one-dimensional sandwich that models the cavity and walls of the actual system. The wire is absent, in order to maintain the one-dimensional simplicity. The purpose of the model is to compute the transient electromagnetic field throughout the sandwich, thereby gaining insight into the expected waveforms in the three-dimensional problem. The infinitely permeable base is used to model a "shadow-zone", which is a zone in which the surface applied magnetic field vanishes. Though we show a plane, TEM wave to be incident onto the structure, we will, in fact, assume that the magnetic field is given on the surface, $x = 0$.

We will solve this problem first using a frequency domain solution that will be inverted using the fast Fourier transform (FFT) algorithm, and then we will use a one-dimensional version of our finite element model.

(a) Frequency Domain (FFT) Solution

Let $\mathbf{E} = E\mathbf{a}_z$, $\mathbf{H} = H\mathbf{a}_y$, and $\partial/\partial y = \partial/\partial z = 0$; then the frequency-domain version of Maxwell's equations becomes

$$\begin{aligned} \frac{dE}{dx} &= j\omega\mu_0 H \\ \frac{dH}{dx} &= j\omega\epsilon_0 E + \sigma E. \end{aligned} \tag{1}$$

In the ith region ($i = 1, 2, 3$) of the sandwich shown in Figure 4, (1) has a solution of the form

$$\begin{aligned} H_i(x) &= A_i e^{k_i x} + B_i e^{-k_i x} \\ E_i(x) &= Z_i(A_i e^{k_i x} - B_i e^{-k_i x}), \end{aligned} \tag{2}$$

where $k_i = j(\omega^2\mu_0\epsilon_0 - j\omega\mu_0\sigma_i)^{1/2}$, is the wavenumber of the ith region, and $Z_i = k_i/(j\omega\epsilon_0 + \sigma_i)$ is the intrinsic wave-impedance of the ith region. A_i and B_i are constants that are to be determined, in the usual way, by forcing continiuity of the two field variables at each interface.

The electric field within the ith region is given by the inverse Fourier transform of $E_i(x,\omega)$

$$\begin{aligned} e_i(x,t) &= \int_{-\infty}^{\infty} E_i(x,\omega)e^{j\omega t}d\omega \\ &= \int_{-\infty}^{\infty} Z_i(\omega)\left(A_i(\omega)e^{k_i(\omega)(x-x_{i-1})} - B_i(\omega)e^{-k_i(\omega)(x-x_{i-1})}\right)e^{j\omega t}d\omega. \end{aligned} \tag{3}$$

The results that are to be shown were computed from (3) using the FFT.

For example, Figure 5 shows the results for the electric field when the parameters of Figure 4 are: $x_3 = 10$ cm, $x_1 = 1$ cm, and $x_2 = 9$ cm. The conductivity of the walls in all the examples of this chapter is $\sigma = 1 \times 10^7$ S/m. The magnetic field at $x = 0$ is taken to be a unit step function.

Curve (a) of Figure 5 is the response at $x = 0.005$ cm, i.e., in the middle of the top wall, whereas (b) is the response in the middle of the cavity, and (c) is the response in the middle of the bottom wall. The effect of shielding is quite clear. The overshoot in the electric field is most pronounced near the step function input magnetic field, whereas the electric field in the bottom layer consists of lower frequencies, only. This is what one would expect for diffusion through a highly conducting medium.

(b) Implicit Time Domain Integration

The Newmark algorithm that we discussed in Section III was applied to the complete system, (II-32), without breaking the problem into sub-regions. Being an implicit scheme, we had systems of linear equations to solve. Since this was a one-dimensional problem the size of the system of equations was not large, so solving this system of equations was not an issue here.

Using $\alpha = 0.25$ and $\delta = 0.5$ (which amounts to the trapezoidal rule) in the Newmark algorithm, we solved the one-dimensional system of equations. The scheme was very stable, allowing step sizes in the neighborhood of 1×10^{-5} seconds.

Using this algorithm, we repeated the same problem that was described in Subsection (a). The one-dimensional mesh had twenty elements, and $\Delta t = 1 \times 10^{-6}$ seconds, with the total time interval being $8\pi \times 10^{-3}$ seconds, as before. The results are shown in Figure 6. Parts (a), (b), and (c) of the figure denote nodal solutions that correspond to the same points as in Figure 5. The good agreement with the FFT results of Figure 5 gives us confidence in applying the Newmark implicit algorithm to this finite element problem.

Three-Dimensional Model

(c) Implicit Time Domain Integration

Once we had a clear understanding of the time scales and solutions to the simplified one-dimensional problem, we were ready to move to the larger three-dimensional setting. Again, the equations described by (II-32) were used. Explicit time integration was not

even explored for the three-dimensional case; only the Newmark implicit scheme was implemented.

Preliminary results in attacking the full three-dimensional problem, including the wire, are encouraging, and further work is to be done in this area, and will be reported later.

V. COUPLING TO THE EXTERNAL REGION

Equations (II-19) and (II-32) show that the cavity is coupled to the external region through the tangential magnetic field, $\mathbf{H}_t$. Hence, we must know $\mathbf{H}_t$ at the external surface of the cavity walls in order to compute the internal response. We will attack this problem by applying an electromagnetic surface integral relation, and then show how this naturally yields an N-port representation of the coupled interior and exterior systems.

This approach seems to be preferable to using a finite element model for the external region, because such a model would require satisfying a boundary condition at infinity, which would complicate matters.

(a) The Space-Time Domain Integral Relation for the External Region

Poggio and Miller [6] derive an electromagnetic boundary-integral relation that is satisfied by the tangential electric and magnetic fields on the surface, S, of a region of space. They then transform the relation into a space-time domain equation:

$$\begin{aligned}\mathbf{H}_t(\mathbf{r},t) - \frac{\mathbf{a}_n}{2\pi} \times \int_{S^*} \left[\frac{\mathbf{H}_t(\mathbf{r}',\tau)}{\rho} + \frac{1}{c}\dot{\mathbf{H}}_t(\mathbf{r}',\tau) \right] \times \frac{\mathbf{a}_\rho}{\rho} dS' \\ = 2\mathbf{H}_t^{(i)}(\mathbf{r},t) + \frac{\mathbf{a}_n}{2\pi} \times \int_{S^*} \left[\frac{\epsilon_0 \dot{\mathbf{E}}_t(\mathbf{r}',\tau)}{\rho} + \frac{\mathbf{a}_\rho}{\rho} \left\{ \frac{\int_0^\tau \nabla'_s \cdot \mathbf{E}_t(\mathbf{r}',\eta) d\eta}{\mu_0 \rho} \right.\right. \\ \left.\left. + \frac{\nabla'_s \cdot \mathbf{E}_t(\mathbf{r}',\tau)}{Z_0} \right\} \right] dS', \end{aligned} \tag{1}$$

where, in our problem, S^* denotes the principal-value integral over the surface of the box, and

$$\mathbf{a}_\rho = \frac{\mathbf{r}-\mathbf{r}'}{|\mathbf{r}-\mathbf{r}'|}, \quad \rho = |\mathbf{r}-\mathbf{r}'|, \quad \tau = t - |\mathbf{r}-\mathbf{r}'|/c, \quad Z_0 = \sqrt{\frac{\mu_0}{\epsilon_0}} = 377\ \Omega. \tag{2}$$

Poggio and Miller [6], and Mittra [7] show how to solve (1) by means of a time stepping procedure, after discretizing the integrals and making use of the principal value concept. The techniques they describe can then form the basis for computing the coupling between the internal (i.e., the walls and cavity) and external regions directly in the time domain. This facilitates coupling the integral relation to the time-domain differential equations of the finite element model.

The idea is described in the next section, but no numerical experiments have yet been performed to validate it.

(b) External Coupling via N-Port Theory

Equations (II-19) and (II-32) indicate that if we know the tangential magnetic field, $\mathbf{H}_t$, over the outer surface of the cavity's walls, then we can compute the global electric field vector, $\mathbf{e}$, throughout the interior system. In particular, we can compute the tangential components of the electric field over the outer surface of the walls. Conversely, (1) shows that once we know the tangential electric field, $\mathbf{E}_t$, over the surface of the walls, then we can compute $\mathbf{H}_t$. Obviously, therefore, the exterior and interior systems are coupled at their common surface.

The surface cells due to the finite-element grid may be thought of as electrical ports through which electric power flows. If there are N such ports, then the interior system behaves as an N-port electric network. If we make the global tangential magnetic field vector, $\mathbf{h}_t$, of (II-19) analogous to an N-dimensional electric current vector, $\{i_n\}$, $n = 1, \ldots, N$, and make the tangential components of the global electric field vector, at the surface cells of the grid, analogous to an N-dimensional electric voltage vector, $\{e_n\}$, $n = 1, \ldots, N$, then the interior system can be replaced by an N-port representation. Here, the current and voltage vectors are the port voltages and currents. Note that the total power delivered to the structure is given by the dot product of the port voltage and current vectors, just as in the actual structure, the total power is given by the dot product of the tangential electric and magnetic field vectors.

An electrical N-port can be characterized by either its impedance matrix, $[Z_s]$, or admittance matrix, $[Y_s]$. These matrices are reciprocals of each other. In the finite-element model of (II-19) and (II-32), the tangential magnetic field is assumed given, from which the electric field is computed. Thus, we are characterizing the structure by its impedance matrix, because we are assuming that the port currents (which are analogous to the tangential magnetic field) are known and that the port voltages (which are analogous to the tangential electric field) are to be computed.

An N-port representation can also be made for the exterior system. In this case, however, we would characterize the exterior system by its radiation admittance matrix, $[Y_r]$, because in (1) we assume that the tangential electric field, $\mathbf{E}_t$, is given, and we must solve for $\mathbf{H}_t$.

In order to obtain an N-port representation of the coupled systems, we return to (1), which we rewrite in the operator form

$$\mathcal{L}_1(\mathbf{H}_t) = 2\mathbf{H}_t^{(i)} + \mathcal{L}_2(\mathbf{E}_t). \tag{3}$$

Upon formally solving (3) for $\mathbf{H}_t$, we get

$$\mathbf{H}_t = \mathcal{L}_1^{-1}(2\mathbf{H}_t^{(i)}) + \mathcal{L}_1^{-1}\mathcal{L}_2(\mathbf{E}_t). \tag{4}$$

We make the definitions $\mathcal{L}_1^{-1}(2\mathbf{H}_t^{(i)}) = \mathbf{I}_0$ and $-\mathcal{L}_1^{-1}\mathcal{L}_2 = \mathcal{Y}_r$, the radiation admittance operator. As before, we let $\mathbf{H}_t$ be analogous to an N-port current vector, and $\mathbf{E}_t$ to an N-port voltage vector, so that (4) becomes $\mathbf{I}_s = \mathbf{I}_0 - \mathbf{I}_r$. The coupled N-port representation of this equation is given in Figure 7.

Note that $\mathbf{I}_0$ is the surface current that flows on a perfect conductor, and has been dealt with in [6] and [7]. Hence, $\mathbf{I}_r$ is the excess "radiation" current that flows if the structure is not a perfect conductor. If the boundary of the structure is a perfect conductor, then $[Y_s]$ short-circuits $[Y_r]$, and $\mathbf{I}_r = 0$.

The algorithm for using the coupled system in the time-domain is as follows: initially, the electric field is zero, so that $\mathbf{I}_r = 0$, and $\mathbf{I}_s = \mathbf{I}_0$. This provides the initial input vector for the finite-element equations.

The tangential electric field at the surface of the structure is computed at the next time step by solving the finite element equations, (II-19) or (II-32), and this field is then substituted into (4), which then provides an update to $\mathbf{H}_t$, which corresponds to $\mathbf{I}_s$. This provides the next input vector for the finite element equations, and the process is repeated.

Clearly, at each time step we must compute a solution to the finite element equations and to the time dependent boundary integral equation. It seems likely that for a structure with metallic walls, we can use the simple physical optics solution that is described in [6]. For walls made of lower-conductivity materials, such as the advanced composite, graphite-epoxy, however, it may be necessary to compute $\mathbf{I}_r$ rigorously.

VI. REFERENCES

[1] John O. Hallquist, *Theoretical Manual for DYNA3D*, Report No. UCID-19401, Lawrence Livermore National Laboratory, March 1983.

[2] K. J. Bathe and E. L. Wilson, *Numerical Methods in Finite Element Analysis*. Englewood Cliffs, New Jersey: Prentice-Hall, Inc., 1976.

[3] J. O. Hallquist, *NIKE2D: A Vectorized, Implicit, Finite Deformation, Finite Element Code for Analyzing the Static and Dynamic Response of 2-D Solids*, Report No. UCID-19677, Lawrence Livermore National Laboratory, February 1983.

[4] J. O. Hallquist, *NIKE3D: An Implicit, Finite-Deformation, Finite Element Code for Analyzing the Static and Dynamic Response of Three-Dimensional Solids*, Report UCID-18822, Rev. 1, Lawrence Livermore National Laboratory, July, 1984.

[5] K. C. Park, "Evaluating Time Integration Methods for Nonlinear Dynamics Analysis", in T. Belytschko, *et al*, eds., *Finite Element Analysis of Transient Nonlinear Structural Behavior*. New York: The American Society of Mechanical Engineers, August 1975, pp. 35-58.

[6] A. J. Poggio and E. K. Miller, "Integral Equation Solutions of Three-dimensional Scattering Problems", in R. Mittra, ed., *Computer Techniques for Electromagnetics*, Chapter 4. Oxford: Pergamon Press, 1973.

[7] R. Mittra, "Integral Equation Methods for Transient Scattering", in L. B. Felsen, ed., *Transient Electromagnetic Fields*, Chapter 2. Berlin: Springer-Verlag, 1976.

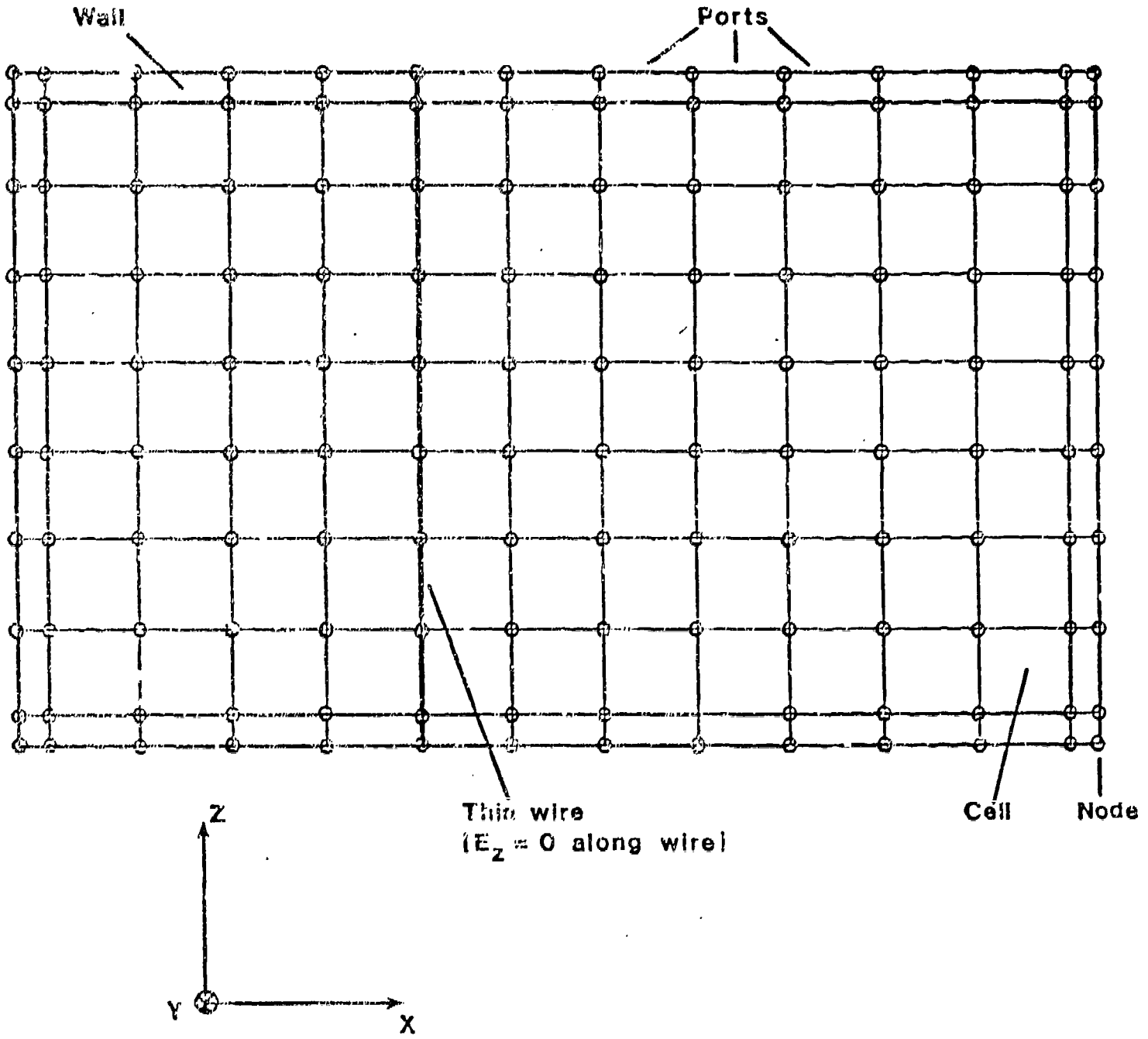


Figure 1. A finite element mesh for the cavity-wall-wire system.

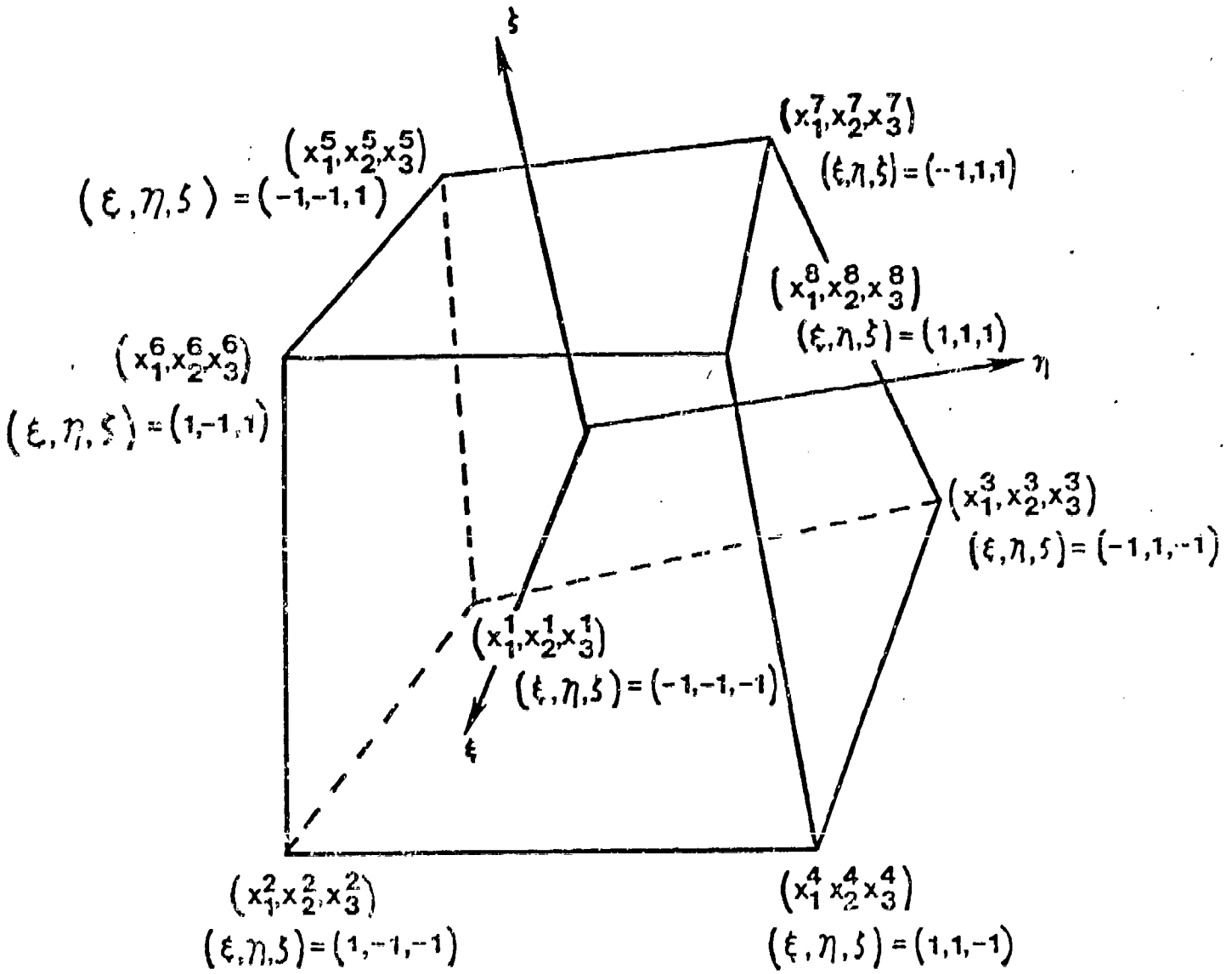


Figure 2. An eight-node solid element.

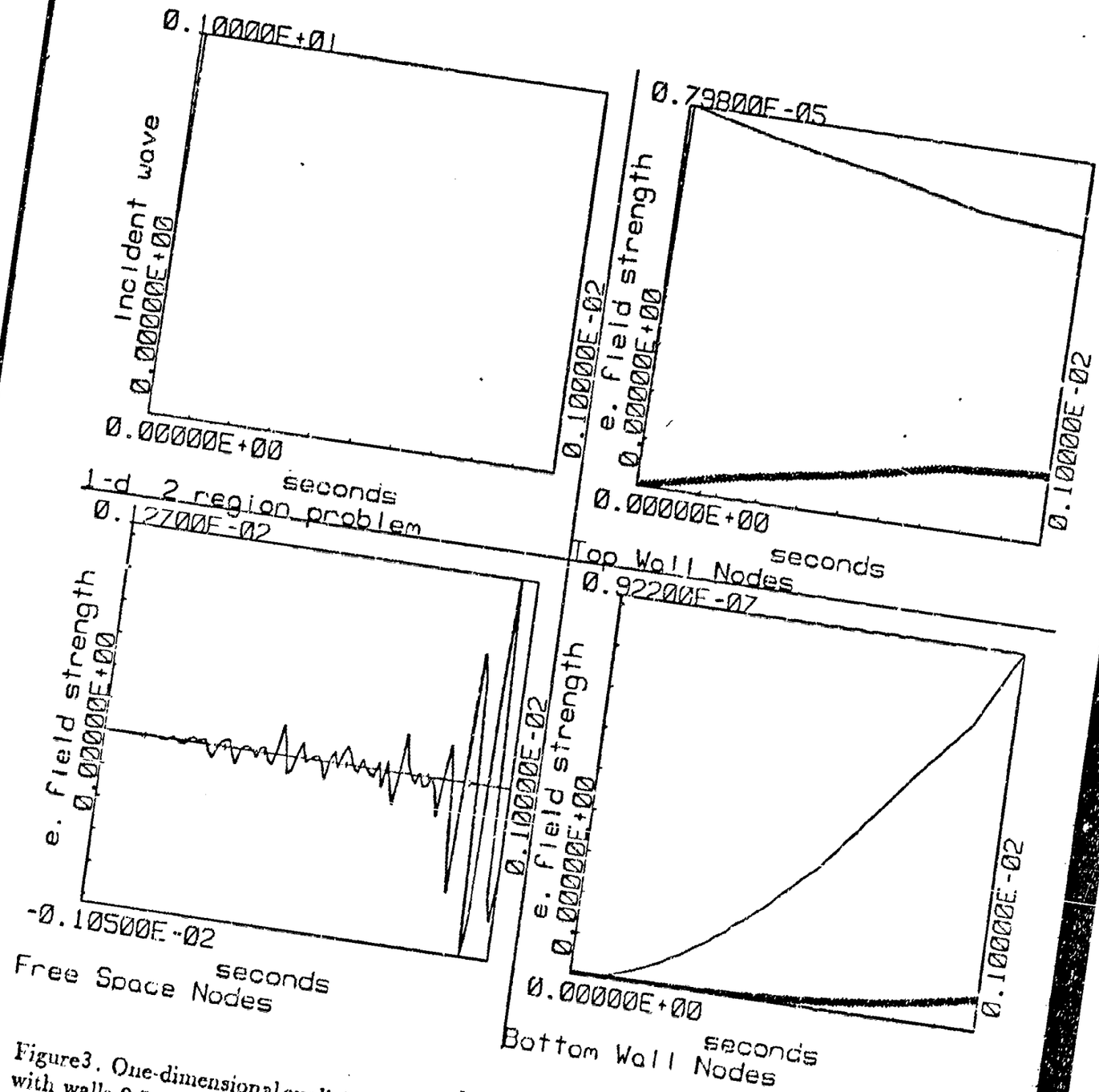


Figure3. One-dimensional explicit time integration. The entire problem mesh is 10cm long, with walls 2.5cm thick, time step 10^{-13} seconds, and four elements. The y-component of the electric field at the five equally spaced nodes are shown. Unit step input.

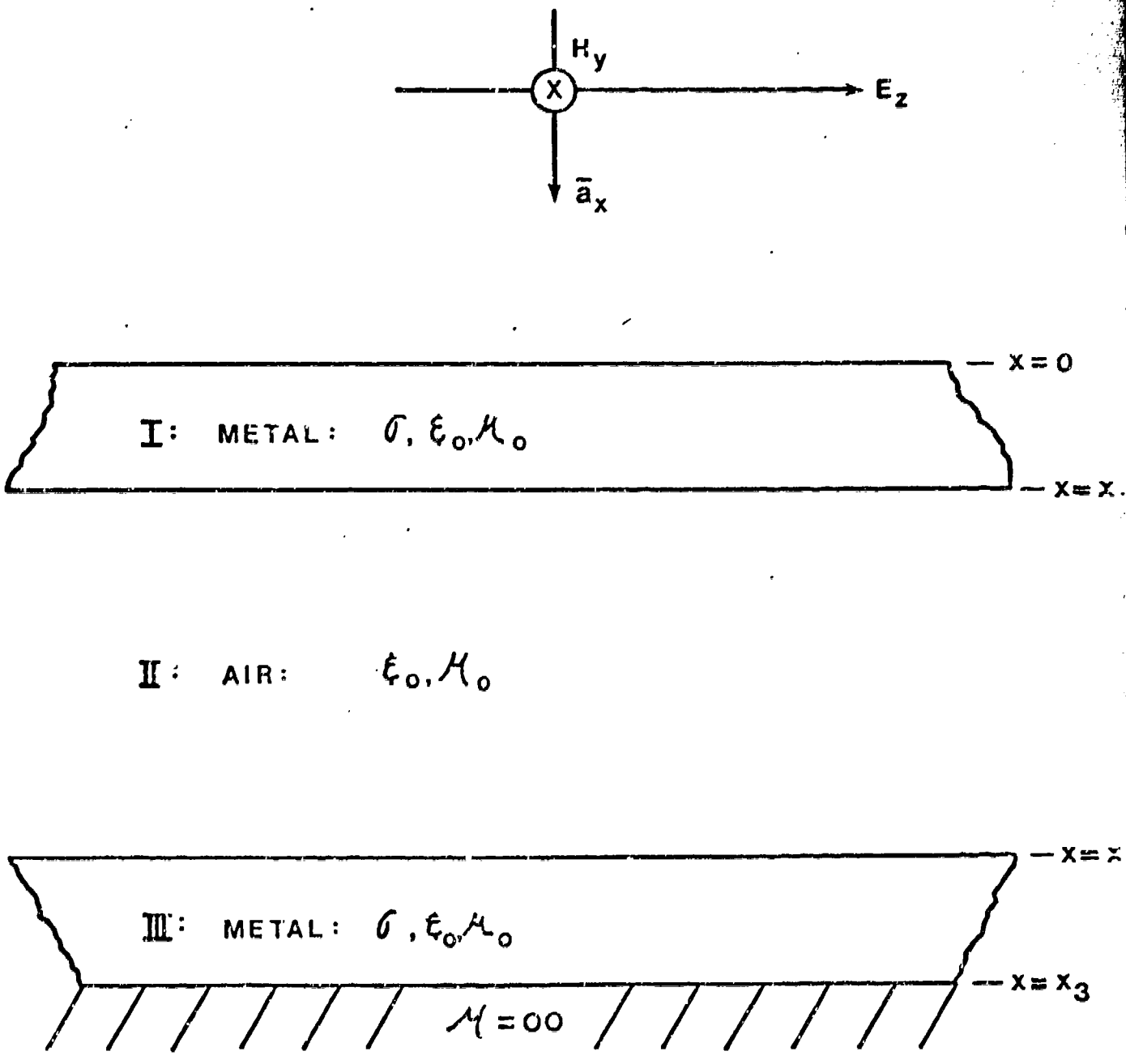


Figure 4. A one-dimensional sandwich that models the cavity and walls of the three-dimensional system. The wire is absent here.

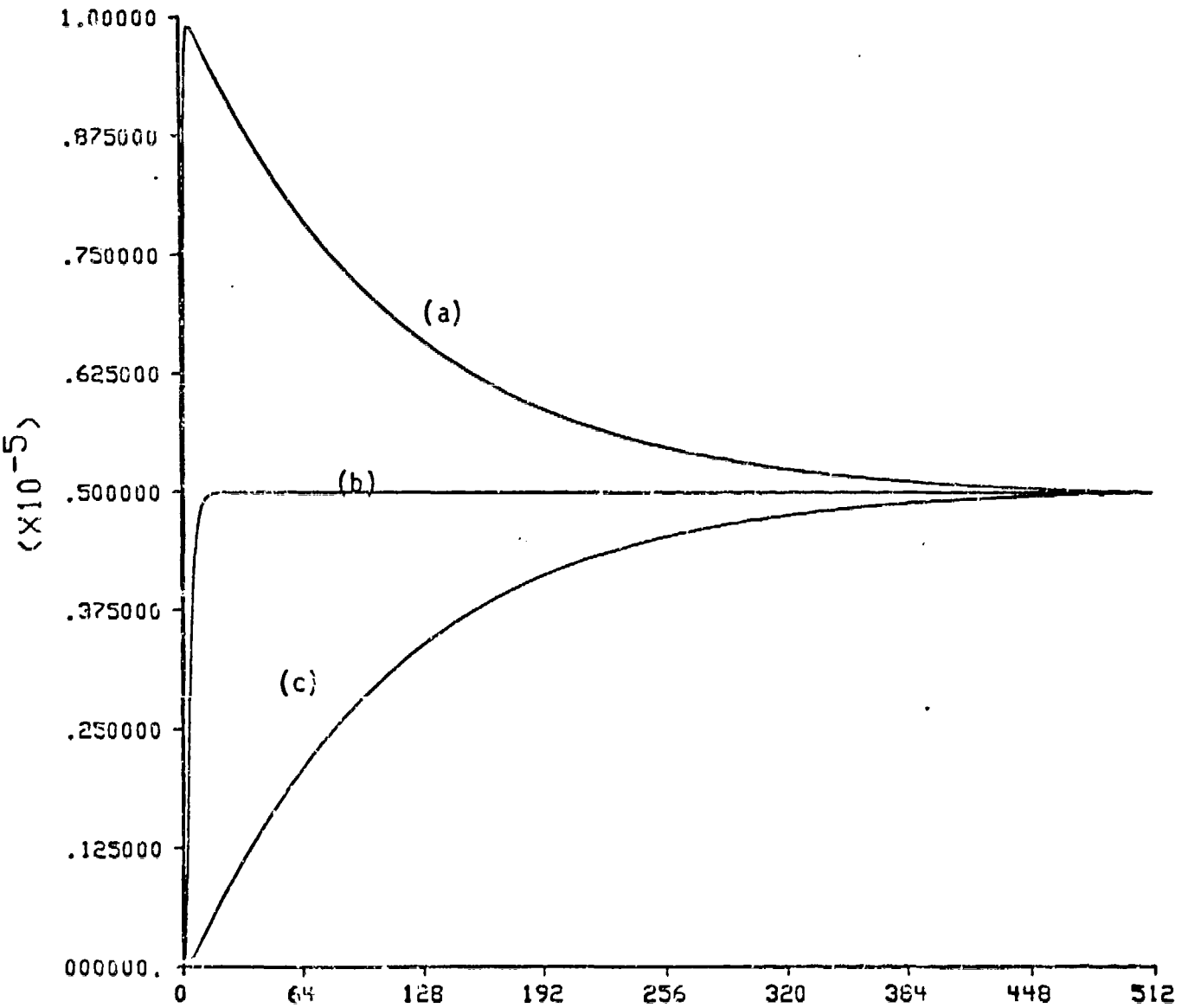


Figure 5. Frequency domain (FFT) solution for electric field in symmetrical one-dimensional sandwich (see Figure 1). A unit step magnetic field is applied to top wall. Total length is 10cm, with total wall thickness of 2cm. (a) field in middle of top wall, (b) field in middle of cavity, and (c) field in middle of bottom wall. Total time interval is $8\pi \times 10^{-3}$ seconds.

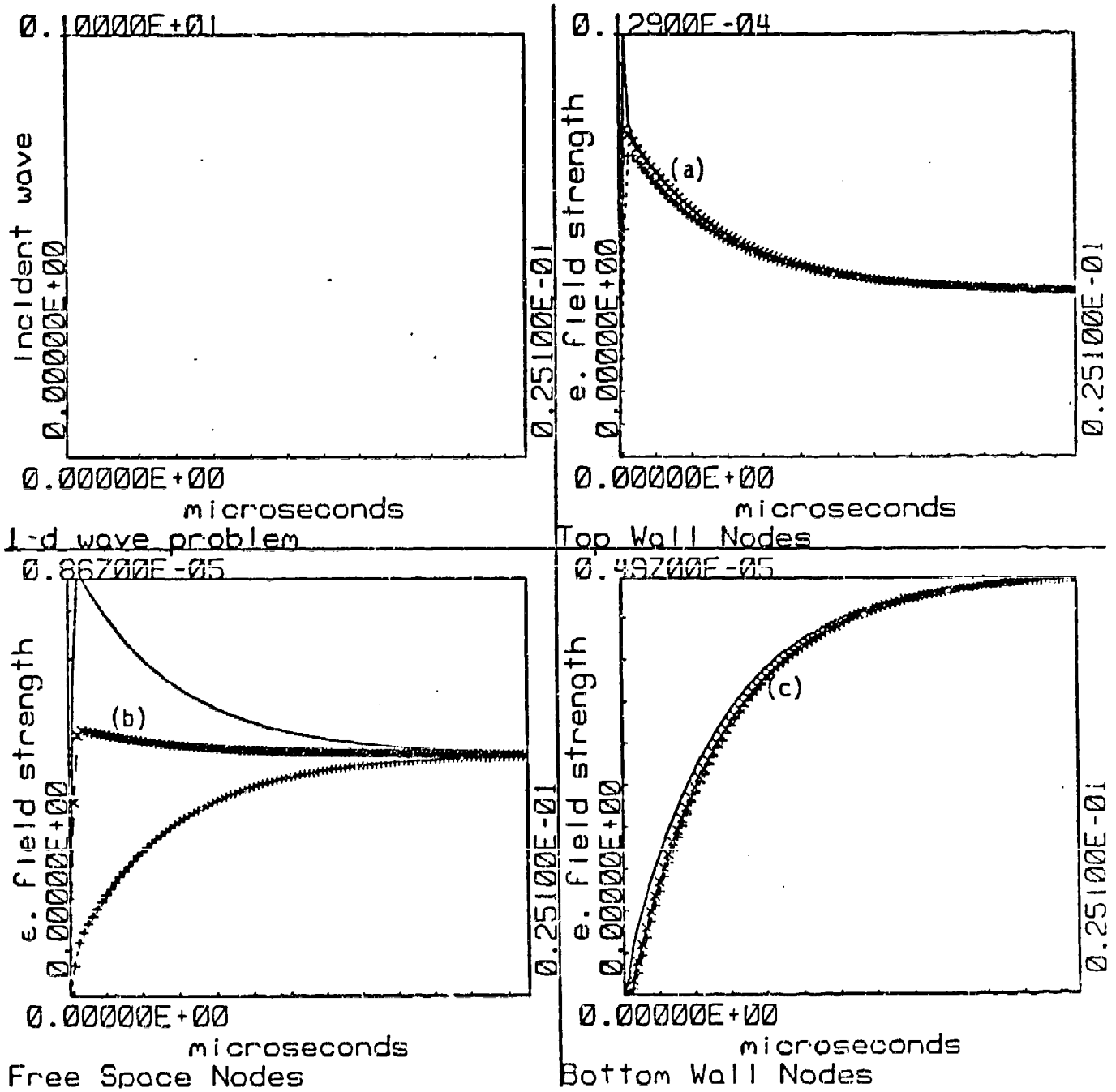


Figure 6. Implicit finite-element solution of same problem as in Figure 7. The mesh has 20 elements, and $\Delta t = 1 \times 10^{-6}$ seconds. The total time interval is the same as in Figure 7. (a), (b), and (c) denote nodal solutions that correspond to the same points as in Figure 7.

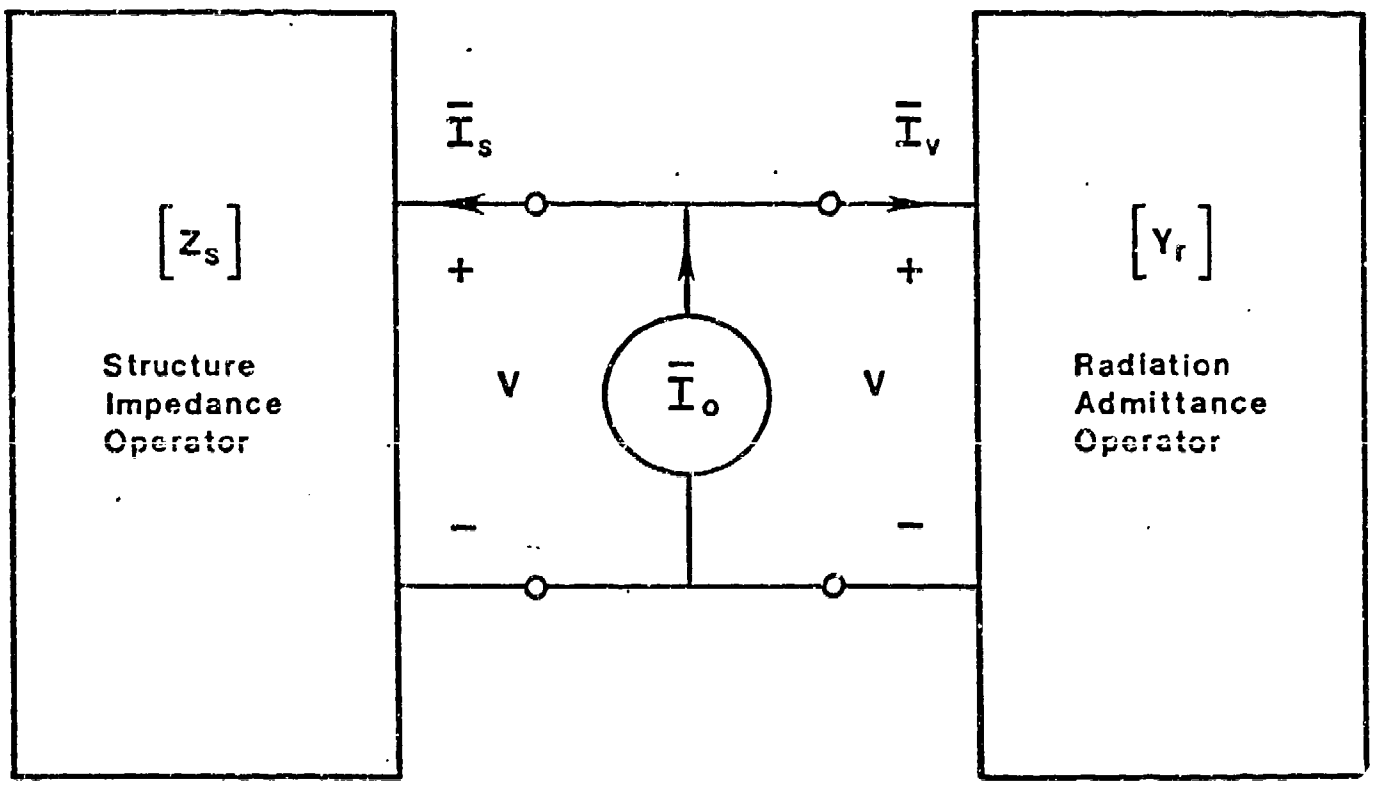


Figure 7. N-port representation of coupled (interior and exterior) systems.

A TIME–DOMAIN DIFFERENTIAL SOLVER FOR ELECTROMAGNETIC SCATTERING PROBLEMS

Vijaya Shankar and William F. Hall
Rockwell International Science Center, Thousand Oaks, CA 91360

Abstract

The objective of this paper is to extend Computational Fluid Dynamics (CFD) based upwind schemes to numerically solve the Maxwell equations for scattering from objects with layered nonmetallic sections. The paper starts with a discussion on the character of the Maxwell equations and shows that they represent a linearly degenerate set of hyperbolic equations. To show the feasibility for applying CFD–based algorithms, first the transverse magnetic (TM) and the transverse electric (TE) wave forms of the Maxwell equations are considered. A finite–volume scheme is developed with appropriate representations for the electric and magnetic fluxes at a cell interface, accounting for variations in material properties in both space and time. This process involves a characteristic subpath integration known as the "Riemann Solver." An explicit Lax–Wendroff upwind scheme which is second–order accurate in both space and time is employed to solve the TM and TE equations. A nonreflecting characteristic based far field condition is applied at the outer computational boundary allowing this boundary to be kept just a few wavelengths from the scattering object. A body–fitted coordinate transformation is introduced to treat arbitrary cross–sectioned bodies with computational grids generated using an elliptic grid solver procedure. For treatment of layered media, a multizonal representation is employed satisfying appropriate zonal boundary conditions in terms of flux conservation. The computational solution extending from the object to a far field boundary located a few wavelengths away constitutes the near field solution. A Green's function based near field–to–far field transformation is employed to obtain the bistatic radar cross section (RCS) information. Results are presented for a number of two–dimensional objects with layered structures for both continuous wave (single frequency–time harmonic) and transient (broadband frequency response) cases. The time–domain solver also provides a unique capability for including nonlinear and time–varying material properties.

A. Introduction

The radar return from complex structures has traditionally been calculated by one of two methods: high–frequency asymptotics, which treats scattering and diffraction as local phenomena; or solution of an integral equation for radiating sources on (or inside) the scattering body, which couples all parts of the body through multiple scattering processes. In this paper, we describe a third alternative, the direct integration of the differential form of Maxwell's equations in time. The time–dependent Maxwell's equations have been applied in other areas of electromagnetics[1], most notably to determine EMP field penetration into shielded cavities[2] and to characterize scattering from thin–wire models of conducting bodies[3].

The time–domain Maxwell's equations represent a more general form than the frequency–domain Helmholtz equations which are usually restricted to solving scattering problems having time harmonic fields, whereas a time domain approach can handle continuous waves (single frequency, harmonic) as well as a single pulse (broadband frequency) transient response. Frequency domain based methods usually provide the RCS response for all angles of incidence at a single frequency, while time–domain based methods provide solutions for many frequencies from a single transient calculation. Also, in a time–domain approach one can consider time varying material properties for treatment of active surfaces. Using spectral methods, the time domain transient solutions can be processed to provide the frequency domain response.

In the present work, it has been our aim to accurately predict the scattering from bodies that include regions with dielectric and magnetic properties significantly different from those of free space. Configurations involving coated inlets, composite radar–absorbing airfoils, and multiple layers of material are typical of many modern aircraft and missiles, and their scattering properties often range over several orders of magnitude as a function of incident and reflected angles.

There are many ways one can numerically solve the time domain Maxwell's equations. The approach to be followed in this paper is to utilize the numerical algorithms that have been proven most successful in integrating the time–dependent equations of fluid dynamics, namely the Euler and the Navier–Stokes equations[4–13]. Computational algorithms to solve these nonlinear equations of fluid dynamics have progressed rapidly over the last 20 years and many of these CFD methods are directly applicable to CEM in solving Maxwell's equations. Some of the attributes of CFD methods that can be effectively employed to design a time–domain differential solver for Maxwell's equations are listed here.

1) The fluid dynamic equations are usually cast in a conservation form (to be described later) conserving mass, momentum, and energy fluxes, thus allowing for numerical capture of flow discontinuities such as shocks and slip surfaces. The Maxwell equations also can be cast in a conservation form. In this particular form, they are naturally structured for numerical simulation of scattering from objects with layered media having discontinuous or gradually varying material properties.

2) Recent development of hyperbolic algorithms[8–13] for solving the time domain Euler equations are based on the characteristic theory of signal propagation and are referred to as the "upwind" schemes. For hyperbolic equations, the upwind based schemes can be constructed to provide the right amount of numerical dissipation to achieve both stability and accuracy of computation. The time domain Maxwell's equations, which are hyperbolic in character (to be shown later), can also benefit from employing such upwind type schemes.

3) For treatment of complex aerospace configuration geometries, CFD methods usually employ a body–fitted coordinate system for easy implementation of boundary conditions. Concepts such as numerical grid generation for a body–fitted system, multizoning[14], adaptive gridding, etc., are well suited for CEM, especially when the scatterer is an aerodynamic object for which the CFD methods are applied. However,

the gridding requirements for a desired field resolution may be different for CEM applications (frequency dependent) from that of CFD needs. Also, CEM problems may involve internal/external layered structures, requiring more involved multizone gridding procedures.

4) There are several proven discretizable procedures in use in CFD for solving the nonlinear fluid dynamic equations. Many discretization concepts such as finite–difference, finite–volume, and finite element schemes[4–12], implicit and explicit time stepping procedures[14], relaxation and approximate factorization techniques[4], etc., are equally applicable to solving the Maxwell equations.

In general, many ideas are in common between CEM and CFD. This is schematically illustrated in Fig. 1. Even the pre– and post–processing graphics packages developed for CFD solutions satisfy the needs of CEM. Thus, our approach is to utilize the numerical algorithms that have proven most successful in integrating the time–dependent equations of fluid dynamics to solve Maxwell's equations.

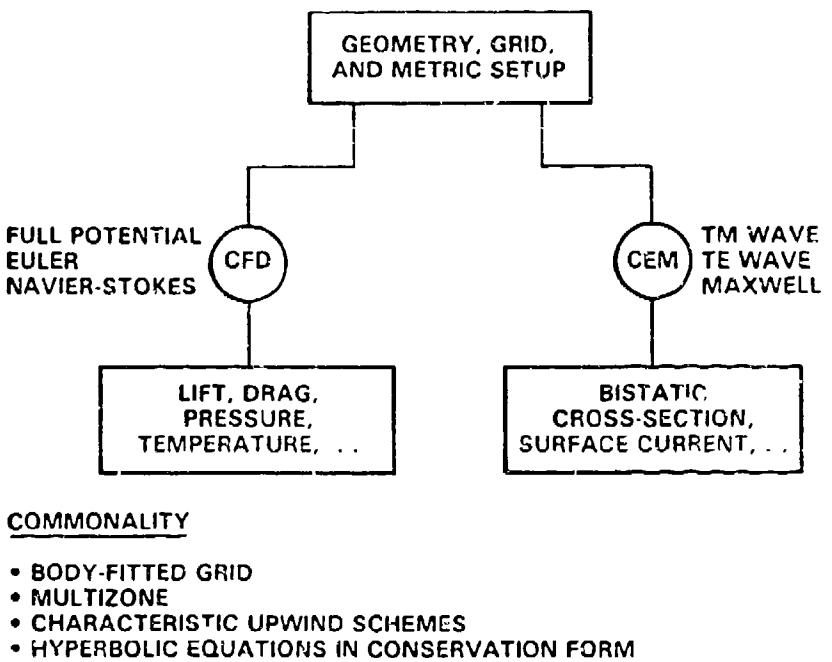


Fig. 1. Commonality between CEM and CFD.

B. Equations in Conservation Form

As mentioned in the Introduction above, many problems in mathematical physics are governed by an appropriate set of partial differential equations. The Navier–Stokes equations in fluid dynamics and the Maxwell equations in electromagnetics are two specific

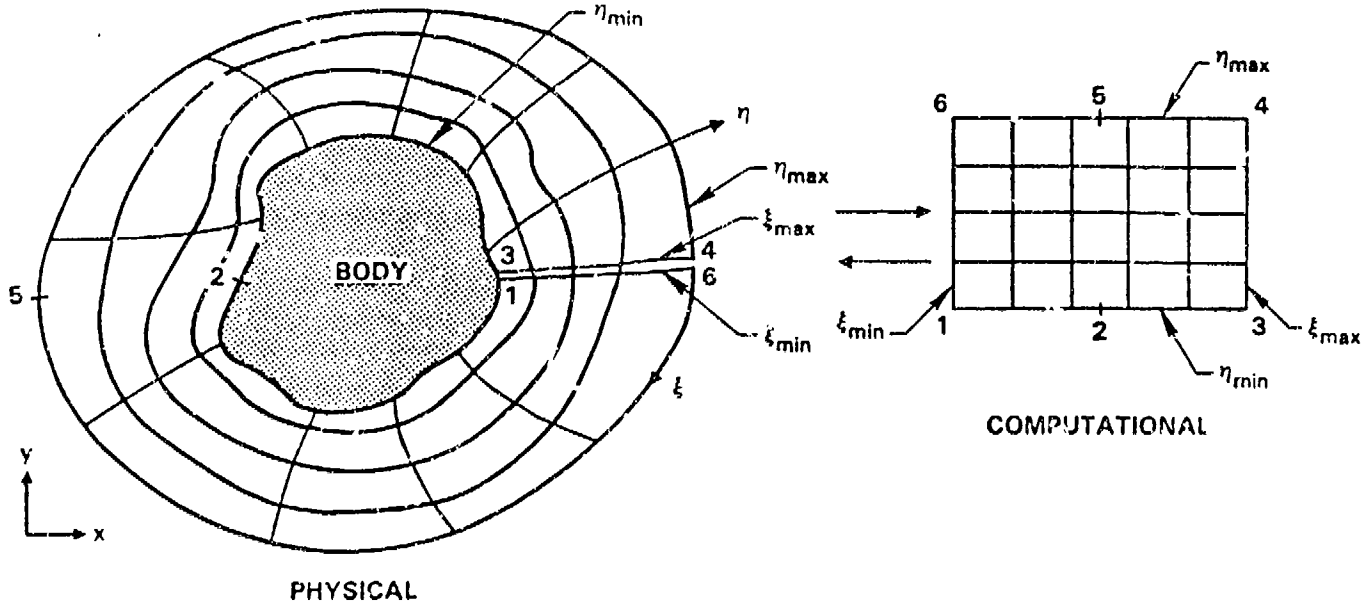


Fig. 2. Schematic of a body–fitted system.

examples. In general, many equations in mathematical physics naturally lend themselves to a conservation form representation given by

$$Q_t + E_x + F_y + G_z = S \tag{1}$$

where the solution vector Q, the source S, and the flux vectors E, F, and G take on different forms depending on the physical problem being modeled. In Eq. (1), the subscripts t, x, y, and z denote partial derivatives. Implementation of Eq. (1) in many realistic problems requires a coordinate transformation to properly represent the physical domain of interest and to aid in the boundary condition treatment.

Under the transformation of coordinates implied by

$$\tau = t\,,\ \xi = \xi(t,x,y,z)\,,\ \eta = \eta(t,x,y,z)\,,\ \zeta = \zeta(t,x,y,z) \quad ,$$

Eq. (1) can be recast in the conservation form given by

$$\overline{Q}_\tau + \overline{E}_\xi + \overline{F}_\eta + \overline{G}_\zeta = \overline{S} \quad , \tag{2}$$

where $\overline{Q} = \frac{Q}{J}$, $\overline{E} = (Q\xi_t + E\xi_x + F\xi_y + G\xi_z)/J$, $\overline{F} = (Q\eta_t + E\eta_x + F\eta_y + G\eta_z)/J$, $\overline{G} = (Q\zeta_t + E\zeta_x + F\zeta_y + G\zeta_z)/J$, and $\overline{S} = \frac{S}{J}$ where, in turn, J is the Jacobian of the transformation

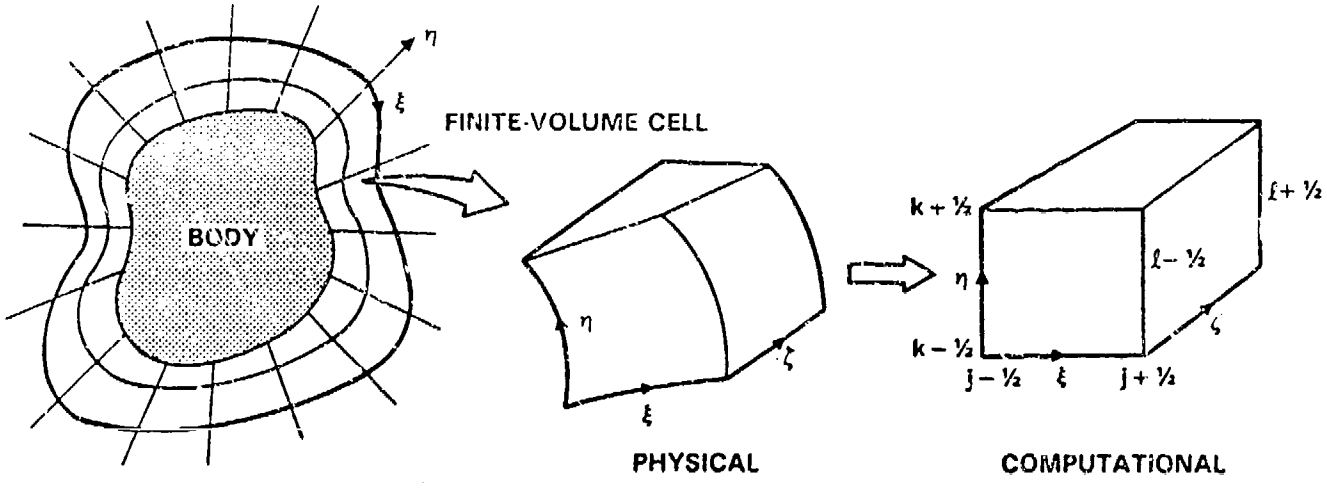
$$J = \partial(\xi,\eta,\zeta)/\partial(x,y,z) \quad .$$

Figure 2 schematically illustrates a body–fitted system in two dimensions.

Associating the subscripts j,k,ℓ with the ξ,η,ζ directions, a numerical approximation to Eq. (2) may be expressed in the semi–discrete conservation law form given by

$$\left(\hat{Q}_{j,k,\ell}\right)_\tau + \left(\hat{E}_{j+1/2,k,\ell} - \hat{E}_{j-1/2,k,\ell}\right) + \left(\hat{F}_{j,k+1/2,\ell} - \hat{F}_{j,k-1/2,\ell}\right) + \left(\hat{G}_{j,k,\ell+1/2} - \hat{G}_{j,k,\ell-1/2}\right) = \hat{S}_{j,k,\ell} \tag{3}$$

where $\hat{E},\hat{F},\hat{G}$ are numerical or representative fluxes at the bounding sides of the cell for which discrete conservation is considered, and $\hat{Q}_{j,k,\ell}$ is the representative conserved quantity (the numerical approximation to $\overline{Q}$) considered conveniently to be the centroidal value. The half–integer subscripts denote cell sides and the integer subscripts the cell itself or its centroid. Figure 3 illustrates the nomenclature associated with a finite–volume cell. The concept of upwinding, to be described subsequently in the paper, will be employed in the evaluation of fluxes at interfaces.



- $j \pm ½$, $k \pm ½$, $\ell \pm ½$ ARE CELL FACES WHERE FLUXES $\hat{E}$, $\hat{F}$ AND $\hat{G}$ ARE EVALUATED
- j,k,ℓ IS CELL CENTROID WHERE $\hat{Q}$ IS DEFINED

Fig. 3. Nomenclature associated with a finite–volume cell.

The objective is to solve Eq. (3) for the dependent vector Q. After incorporation of proper flux representation, the discrete form of Eq. (3) can be written as

$$R(Q) = 0 \quad . \tag{4}$$

If Q is known to lie in the neighborhood of a given state, denoted by Q^*, then the solution to Eq. (4) can be written to first order in $Q - Q^*$ as

$$\frac{\partial R}{\partial Q}(Q - Q^*) = -R(Q^*) \quad , \tag{5}$$

where $\frac{\partial R}{\partial Q}$, in general, is a differential operator. Many numerical algorithmic issues such as implicit methods, explicit methods, relaxation schemes, and approximate factorization procedures, etc., come into play in the modeling of the differential operator $\frac{\partial R}{\partial Q}$. Issues such as higher order accuracy, efficiency, proper upwinding, treatment of discontinuities, etc., come into $\frac{\partial R}{\partial Q}$ as well as in the modeling of the right hand side $R(Q^*)$.

The objective of this paper is to apply CFD–based finite–volume numerical methods developed for solving many nonlinear gasdynamic equations[4–14] to solve the time–dependent Maxwell's equations for electromagnetic scattering problems involving layered material media.

C. Maxwell's Equations

Analysis of electromagnetic scattering from permeable (dielectric and lossy media) and impermeable (metallic) objects is of interest in being able to predict the radar cross section (RCS) of low observable aerospace configurations. The equations that govern the interaction between the electric and magnetic fields are the Maxwell equations. These equations in their vector form are

$$\frac{\partial B}{\partial t} = -\nabla \times \mathcal{E} \tag{6}$$

and

$$\frac{\partial D}{\partial t} = \nabla \times \mathcal{H} - J \quad .$$

The vector quantities $\mathcal{E} = (\mathcal{E}_x, \mathcal{E}_y, \mathcal{E}_z)$ and $\mathcal{H} = (\mathcal{H}_x, \mathcal{H}_y, \mathcal{H}_z)$ are the electric and magnetic field intensities, $D = (D_x, D_y, D_z)$ is the electric displacement, $B = (B_x, B_y, B_z)$ is the magnetic induction, and $J = (J_x, J_y, J_z)$ is the current density. The subscripts x, y, z in the vector representation of $\mathcal{E}$, $\mathcal{H}$, B and D refer to components in respective directions.

In order to apply CFD–based conservation–law form finite–volume methods, Eq. (6) is rewritten in the form of Eq. (1). For isotropic materials, the solution vector Q, and the flux vectors E, F, and G are given by

$$Q = \begin{Bmatrix} B_x \\ B_y \\ B_z \\ D_x \\ D_y \\ D_z \end{Bmatrix} ; E = \begin{Bmatrix} 0 \\ -D_z/\epsilon \\ D_y/\epsilon \\ 0 \\ B_z/\mu \\ -B_y/\mu \end{Bmatrix} ; F = \begin{Bmatrix} D_z/\epsilon \\ 0 \\ -D_x/\epsilon \\ -B_z/\mu \\ 0 \\ B_x/\mu \end{Bmatrix} ; G = \begin{Bmatrix} -D_y/\epsilon \\ D_x/\epsilon \\ 0 \\ B_y/\mu \\ -B_x/\mu \\ 0 \end{Bmatrix} ; S = \begin{Bmatrix} 0 \\ 0 \\ 0 \\ -J_x \\ -J_y \\ -J_z \end{Bmatrix} . \tag{7}$$

The permittivity coefficient ϵ and the permeability coefficient μ are the material properties and satisfy the following relationship, $D = \epsilon\mathcal{E}$, $B = \mu\mathcal{H}$. The current density J is usually represented by $\sigma\mathcal{E}$, where σ is the material electrical conductivity. The objective is to solve Eq. (7) to predict the electromagnetic scattering from objects with layered structure for a given incident field (continuous wave or a pulse). From the time variation of the scattered field, the radar cross section of the scatterer can be obtained.

D. Characteristic Theory for Maxwell's Equations

The application of a finite–volume procedure, Eq. (3), for the Maxwell equations, Eq. (7), requires the evaluation of the various fluxes $\widehat{E}$, $\widehat{F}$, and $\widehat{G}$ at cell interfaces from the solution vector $\widehat{Q}$ known at cell centroids. There are many ways one can represent these fluxes depending on the choice of numerical algorithms, such as central difference schemes and upwind schemes. The choice and construction of a numerical algorithm involves many issues, such as accuracy, efficiency, numerical stability, storage requirements, and treatment of discontinuities in the solution field (shocks in fluid dynamics, discontinuous material properties in electromagnetics), etc. In CFD, upwind based methods that take into account the theory of characteristic signal propagation are widely in use. References 8–13 provide some of the background information on upwind based schemes. The objective of the present work is to adapt the upwind based algorithms of CFD to solve the Maxwell equations.

First, the character of the Maxwell equations is analyzed to aid in the development of a proper upwind scheme for electromagnetic flux representation. This section provides the characteristic theory framework for the one–dimensional Maxwell's equations.

Considering the following conservation form (1–D form of Eq. (7)),

$$\frac{\partial Q}{\partial t} + \frac{\partial E(Q)}{\partial x} = S \tag{8}$$

where

$$Q = \begin{pmatrix} D \\ B \\ e \\ m \end{pmatrix} \quad , \quad E = \begin{pmatrix} -Bm \\ -De \\ 0 \\ 0 \end{pmatrix} \quad , \quad S = \begin{pmatrix} -J \\ 0 \\ \dot{e}(t) \\ \dot{m}(t) \end{pmatrix} \quad ,$$

and the material properties ϵ and μ are represented by $e = \frac{1}{\epsilon}$ and $m = \frac{\lambda}{\mu}$.

The character of Eq. (8) is described by the eigenvalues and the eigenvectors of the Jacobian of E given by $A = \frac{\partial E}{\partial Q}$. The eigenvalues of A are first obtained by solving $|A - \lambda I| = 0$.

$$A = \frac{\partial E}{\partial Q} = \begin{vmatrix} 0 & -m & 0 & -B \\ -e & 0 & -D & 0 \\ 0 & 0 & 0 & 0 \\ 0 & 0 & 0 & 0 \end{vmatrix} . \tag{9}$$

The eigenvalues of A are $\lambda_1 = -\sqrt{me} = -c$, $\lambda_2 = 0$, $\lambda_3 = 0$, and $\lambda_4 = c$. The quantity c represents the speed of light. Since the eigenvalues of A are real, Eq. (8) is hyperbolic.

Now, we construct the numerical flux representation at a cell interface. Referring to Fig. 4 and Eq. (3), the finite-volume treatment requires the evaluation of E at cell faces $j+1/2$ and $j-1/2$, while solving for Q at the cell centroid j. In order to define E at $j+1/2$, first, we define a piecewise smooth, continuous path in phase space, connecting Q_j to Q_{j+1}, made up of four subpaths (equalling the number of eigenvalues for the 1-D Maxwell's equations). Along subpath k, the variation of Q is given by[13]

$$\frac{\partial Q}{\partial s} = r_k\big(Q(s)\big) \tag{10}$$

where r_k is the kth eigenvector corresponding to the kth eigenvalue obtained by solving $(A - \lambda_k I)\, r_k = 0$.

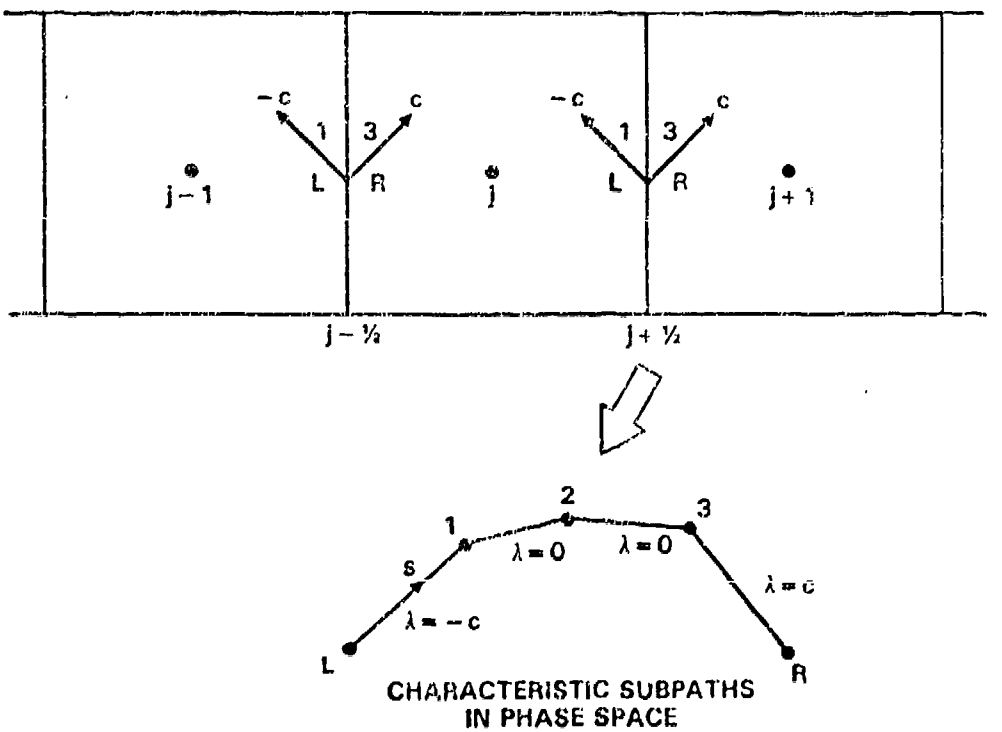


Fig. 4. Numerical flux representation at a cell interface.

Referring to Fig. 4, Eq. (10) defines the solution vector Q at the end of each characteristic subpath marked by 1, 2, and 3. Starting from the left state $Q_L = Q_j$, across the negative characteristics, the solution vector reaches Q_1, then becomes Q_2 and Q_3 across zero eigenvalue fields, and finally reaches the right state $Q_R = Q_{j+1}$ across the positive characteristics.

Performing the integration of Eq. (10) for each characteristic subpath, the interface

electric and magnetic fields are given by

$$
\begin{aligned}
(Bm)_{j+1/2} = (B_1 m_1) &= \frac{(c_{j+1}B_{j+1} + D_{j+1}e_{j+1}) + (c_j B_j - D_j e_j)}{\left(\frac{c_j}{m_j} + \frac{c_{j+1}}{m_{j+1}}\right)} \\
(De)_{j+1/2} = (D_1 e_1) &= \frac{(c_j D_j - B_j m_j) + (c_{j+1}D_{j+1} + B_{j+1}m_{j+1})}{\left(\frac{c_j}{e_j} + \frac{c_{j+1}}{e_{j+1}}\right)}
\end{aligned}
\tag{11}
$$

Use of the characteristic subpath integration approach has resulted in interface flux representation which properly accounts for the variations in material properties ϵ and μ from one cell (j) to the neighboring cell $(j+1)$. Also, the flux forms of Eq. (11) guarantees that the flux fields will remain smooth and continuous across the interface, independent of the level of discontinuity in the material property at a cell interface.

E. Transverse Magnetic (TM) and Transverse Electric (TE) Wave Formulation

The Maxwell equations in three dimensions involve three components of the magnetic field (H_x, H_y, and H_z) and three components of the electric field (E_x, E_y, and E_z), which are coupled. In two dimensions, Maxwell's equations can be decoupled into a transverse magnetic (TM) wave and a transverse electric (TE) wave. The TM wave contains only E_z, H_x, and H_y fields, and the TE wave contains only H_z, E_x, and E_y fields. For algorithm development, the two-dimensional Maxwell's equations in terms of the TM and TE wave framework offer a simplified set of equations without any loss of physics of electromagnetic interaction including material properties.

The TM and TE equations can be written in a unified form following Eq. (7). It takes the form

$$Q_t + E_x + F_y = S \tag{12}$$

where Q is a three element (Q_1, Q_2, Q_3) solution vector, and E and F are three element flux vectors, and S is a source vector containing electric currents.

TM Wave

$$
\left.
\begin{array}{llll}
Q_1 = D_z & E_1 = -Q_3 m & F_1 = Q_2 m & S_1 = -\sigma Q_1 e \\
Q_2 = B_x & E_2 = 0 & F_2 = Q_1 e & S_2 = 0 \\
Q_3 = B_y & E_3 = -Q_1 e & F_3 = 0 & S_3 = 0
\end{array}
\right\} \tag{13}
$$

TE Wave

$$
\left.
\begin{array}{llll}
Q_1 = B_z & E_1 = -Q_3 e & F_1 = Q_2 e & S_1 = 0 \\
Q_2 = -D_x & E_2 = 0 & F_2 = Q_1 m & S_2 = -\sigma Q_2 e \\
Q_3 = -D_y & E_3 = -Q_1 m & F_3 = 0 & S_3 = -\sigma Q_3 e
\end{array}
\right\} \tag{14}
$$

Under a body-fitted coordinate transformation, Eq. (13) takes the form (see Eq. (2))

$$
\begin{array}{llll}
\overline{Q}_1 = \frac{Q_1}{J} & \overline{E}_1 = -m(Q_2 x_\eta + Q_3 y_\eta) & \overline{F}_1 = m(Q_2 x_\xi + Q_3 y_\xi) & \overline{S}_1 = \frac{S_1}{J} \\
\overline{Q}_2 = \frac{Q_2}{J} & \overline{E}_2 = -eQ_1 x_\eta & \overline{F}_2 = eQ_1 x_\xi & \overline{S}_2 = \frac{S_2}{J} \\
\overline{Q}_3 = \frac{Q_3}{J} & \overline{E}_3 = -eQ_1 y_\eta & \overline{F}_3 = eQ_1 y_\xi & \overline{S}_3 = \frac{S_3}{J}
\end{array}
\quad . \tag{15}
$$

The TE equations, Eq. (14), take on similar forms.

It can be verified that the fluxes $\overline{E}_1$ and $\overline{F}_1$ take on the form of surface currents $n \times \mathcal{H}$ or $n \times \mathcal{E}$, depending on whether Eq. (12) is TM or TE.

The characteristics of Eq. (12) are analyzed by considering the Jacobian $\frac{\partial \overline{E}}{\partial Q} = \overline{A}$ and $\frac{\partial \overline{E}}{\partial Q} = \overline{B}$.

$$\overline{A} = \begin{vmatrix} 0 & m\xi_y & -m\xi_x \\ e\xi_y & 0 & 0 \\ -e\xi_x & 0 & 0 \end{vmatrix} \quad , \quad \overline{B} = \begin{vmatrix} 0 & m\eta_y & -m\eta_x \\ e\eta_y & 0 & 0 \\ -e\eta_x & 0 & 0 \end{vmatrix} \tag{16}$$

The eigenvalues of $\overline{A}$ and $\overline{B}$ are given by

$$\left.\begin{array}{ll} \lambda^1_{\overline{A}} = -c\sqrt{\xi_x^2 + \xi_y^2} & \lambda^1_{\overline{B}} = -c\sqrt{\eta_x^2 + \eta_y^2} \\ \lambda^2_{\overline{A}} = 0 & \lambda^2_{\overline{B}} = 0 \\ \lambda^3_{\overline{A}} = c\sqrt{\xi_x^2 + \xi_y^2} & \lambda^3_{\overline{B}} = c\sqrt{\eta_x^2 + \eta_y^2} \end{array}\right\} \quad . \tag{17}$$

Any finite-volume based scheme will require the evaluation of the flux vector $\overline{E}$ (referring to Fig. 5) at the $k + 1/2$ cell interface and $\overline{F}$ at the $j + 1/2$ interface. Using the characteristic subpath integration procedure in the (ξ, τ) plane at $k+1/2$ and in the (η, τ) plane at $j + 1/2$, the following interface relationships are obtained.

At $(k+1/2)$, the left state material properties correspond to cell k $(e^L = e_k, m^L = m_k)$ and the right state corresponds to the $(k + 1)$ cell $(e^R = e_{k+1}, m^R = m_{k+1})$. Also, vector $Q^L = Q_k$ and $Q^R = Q_{k+1}$.

$$(eQ_1)_{k+1/2} = \frac{\left\{(cQ_1)^L - (\overline{Q_2Q_3}m)^L/a_{k+1/2}\right\} + \left\{(cQ_1)^R + (\overline{Q_2Q_3}m)^R/a_{k+1/2}\right\}}{\left(\frac{\xi}{e}\right)^L + \left(\frac{\xi}{e}\right)^R} \tag{18}$$

$$(\overline{Q_2Q_3}m)_{k+1/2} = c^L\left(Q_1^1 - Q_1^L\right)a_{k+1/2} + (\overline{Q_2Q_3}m)^L \tag{19}$$

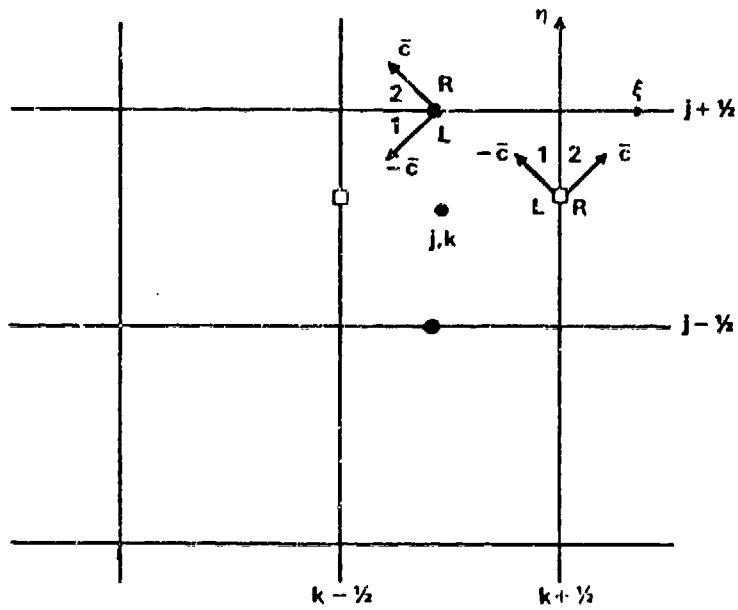
In Eqs. (18) and (19), $a = \sqrt{x_\eta^2 + y_\eta^2}$, $\overline{Q_2Q_3} = (Q_2x_\eta + Q_3y_\eta)$.

At $(j + 1/2)$,

$$(eQ_1)_{j+1/2} = \frac{\left\{(cQ_1)^L + (\widehat{Q_2Q_3}m)^L/b_{j+1/2}\right\} + \left\{(cQ_1)^R - (\widehat{Q_2Q_3}m)^R/b_{j+1/2}\right\}}{\left(\frac{\xi}{e}\right)^L + \left(\frac{\xi}{e}\right)^R}$$

$$\left(\widehat{Q_2Q_3}m\right)_{j+1/2} = -c^L(Q_1^1 - Q_1^L)b_{j+1/2} + (\widehat{Q_2Q_3}m)^L \tag{20}$$

where $\widehat{Q_2Q_3} = (Q_2x_\xi + Q_3y_\xi)$ and $b = \sqrt{x_\xi^2 + y_\xi^2}$. The superscripts L and R refer to left and right states at $(j+1/2)$, denoted in Fig. 5. The quantities $(\overline{Q_2Q_3}m/a)$ and $(\widehat{Q_2Q_3}m/b)$ represent $n \times \mathcal{H}$ for the TM case and $n \times \mathcal{E}$ for the TE case.



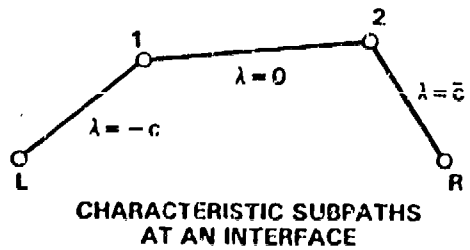


Fig. 5. Characteristics for a two–dimensional finite–volume cell.

F. Boundary Conditions

Perfectly Conducting Scattering Surface

For a perfectly conducting scatterer the boundary condition on the surface is

$$n \times \mathcal{E}^T = 0 \tag{21}$$

where $\mathcal{E}^T$ is the total electric field vector and n is the surface outward normal. For the TM case, the boundary condition Eq. (21) becomes $\mathcal{E}_z^T = 0$, and for the TE case, $x_\xi \mathcal{E}_x^T + y_\xi \mathcal{E}_y^T = 0$.

Nonperfectly Conducting, Isotropic Scatterer

Let $\mathcal{E}_L^T$, $\mathcal{H}_L^T$ be the total field quantities on the left side of the interface, and $\mathcal{E}_R^T$, $\mathcal{H}_R^T$ on the right side. The boundary conditions at the interface then become (see Fig. 6)

$$n \times (\mathcal{E}_L^T - \mathcal{E}_R^T) = 0 \quad , \quad n \times (\mathcal{H}_L^T - \mathcal{H}_R^T) = 0 \quad . \tag{22}$$

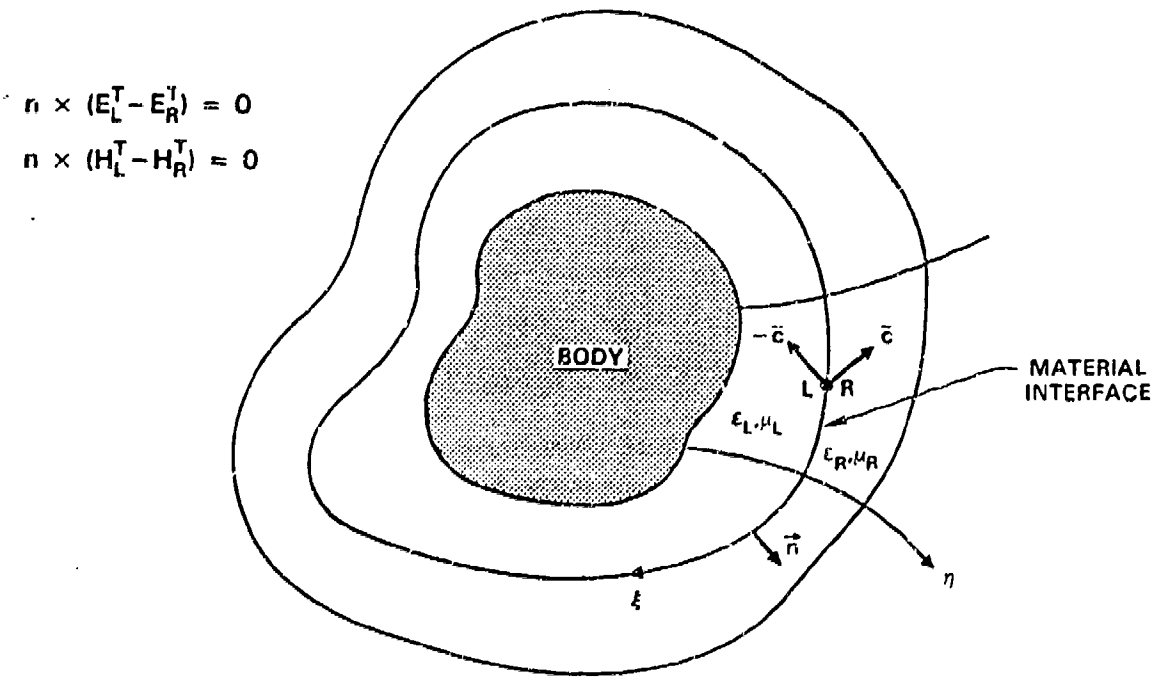


Fig. 6. Boundary conditions at a nonperfectly conducting interface.

The interface flux representations given by Eq. (18) and Eq. (20) strictly satisfy the boundary conditions given by Eq. (22). The boundary conditions at a nonperfectly conducting material interface are also termed as "flux through" boundary conditions.

The key advantage of a finite–volume procedure, Eq. (3), employing interface flux representations, Eqs. (18) and (20), arrived at through use of proper physical theory of characteristic signal propagation is that no special boundary condition treatment is required to enforce conditions given by Eq. (22). However, at a perfectly conducting surface, the boundary conditions $n \times E = 0$ have to be explicitly satisfied through an appropriate procedure.

Besides the boundary conditions at the scatterer surface, one needs to model the boundary condition at the outer boundary representing the far field in the computational setup. The computational domain terminates at some finite distance from the scatterer and the domain is usually referred to as "near field". The proper boundary condition at the outer boundary is that the scattered waves smoothly leave the domain without any reflections from the artificial outer boundary. Characteristic theory principles are employed to satisfy the various boundary conditions. Details will be given in a follow–up paper.

G. Lax–Wendroff Explicit Scheme

A finite–volume procedure applied to Eq. (2) is given by Eq. (3). If $(n + 1)$ is the current time level in which Eq. (3) is satisfied, an implicit scheme would treat all the flux terms at the current level and then employ some form of a flux linearization procedure

to solve for Q implicitly[10-12]. The main advantage of such implicit techniques in CFD is that they allow for large time steps to be taken in modeling the $\overline{Q}_\tau$ term while maintaining numerical stability. However, the problem of electromagnetic scattering deals with Q and flux fields that are highly oscillatory both in time and space. Implicit schemes that preserve the incident and scattered wave profiles without any numerical distortion for large $\Delta\tau$ are yet to be developed. In view of this, explicit type schemes that operate with stability bounds for $\Delta\tau$ governed by spatial resolution (volume of a finite–volume cell), are more attractive. The disadvantage is that when clustered meshes are used in regions of sharp edges and so on, they may restrict the allowable $\Delta\tau$ to very small values requiring a large number of time steps to establish the solution. Some of the criteria in the selection or construction of an explicit scheme are 1) spatial and temporal accuracy, 2) allowable $\Delta\tau$, usually known as the Courant–Friedrichs–Lewy (CFL) condition[14,16,17], 3) storage requirements, and 4) vectorizability of the algorithm.

One of the explicit schemes widely in use is the Lax–Wendroff upwind scheme[16]. Applied to an equation of the form

$$Q_\tau + F_\eta = 0 \quad , \tag{23}$$

the Lax–Wendroff two–step scheme (predictor–corrector) is given by

Predictor

$$\overline{Q^{n+1}} = Q^n - \Delta\tau \left(\widehat{F}^n_{j+1/2} - \widehat{F}^n_{j-1/2} \right) \tag{24}$$

Corrector

$$\begin{aligned} Q^{n+1} = {} & \frac{1}{2} \left\{ Q^n + \overline{Q^{n+1}} - \Delta\tau \left(\widehat{F}^{\overline{n+1}}_{j+1/2} - \widehat{F}^{\overline{n+1}}_{j-1/2} \right) \right\} \\ & - \frac{\Delta\tau}{2} \left[\left\{ (dF)^+_{j-1/2} - (dF)^+_{j-3/2} \right\} - \left\{ (dF)^-_{j+3/2} - (dF)^-_{j+1/2} \right\} \right]^n \end{aligned} \tag{25}$$

The predictor step, Eq. (24), is only first order accurate in time and space. The corrector step makes the scheme second order accurate in time and space. The addition of the square bracketed term in Eq. (25), evaluated at the nth level, makes the scheme second order accurate spatially, while the predictor/corrector two step procedure provides second order time accuracy.

Referring to Fig. 4,

$$\begin{aligned} dF^+_{j-1/2} &= F^R_{j-1/2} - \widehat{F}_{j-1/2} \\ dF^-_{j+1/2} &= \widehat{F}_{j+1/2} - F^L_{j+1/2} \end{aligned} \tag{26}$$

where superscripts R and L refer to right and left states at an interface, and $\widehat{F}$ refers to flux at an interface. In the present method,

$$\begin{aligned} F^L_{j-1/2} &= F\left(Q_j, \text{ metrics at } j - 1/2\right) \\ F^R_{j+1/2} &= F\left(Q_{j+1}, \text{ metrics at } j + 1/2\right) \end{aligned} \tag{27}$$

The Lax–Wendroff scheme being explicit, the allowable $\Delta\tau$ for maintaining numerical stability is bounded by the CFL condition given by

$$\lambda_{\max}\frac{\Delta\tau}{\Delta\eta} \leq 2 \quad , \tag{28}$$

where $\lambda_{\max}$ is the maximum eigenvalue of the Jacobian, $(\partial F/\partial Q)$. The condition given by Eq. (28) is for the one–dimensional equation, Eq. (23). In multidimensions, the value of $\lambda_{\max}$ can be taken to be the sum of λ_s in all directions $(\lambda_{\max} = \max(|\lambda_\xi| + |\lambda_\eta| + |\lambda_\zeta|))$. The maximum eigenvalue usually occurs at a cell that has the least volume.

H. Near Field–to–Far Field Transformation

The finite–volume procedure of this paper which solves the time–dependent Maxwell's equations is applied in a computational domain that extends from the scatterer to some finite distance away, where it is terminated by an outer boundary at which nonreflecting boundary conditions are imposed. The distance of the outer boundary of the computational domain is controlled by the body size and the wavelength of the incident wave, and should be sufficiently far away (several wavelengths) where the numerical implementation of the nonreflecting boundary conditions holds. Even when the computational domain extends to several wavelengths from the scatterer, it still represents only the near field solution. However, the bistatic radar cross section (RCS) computation is based on the intensity of the scattered wave at distances asymptotically approaching infinity, which means the RCS response represents the far field solution. Using a Green's function based asymptotic approach, the far field representation of the scattered wave is obtained from the near field computational solution.

In general, the RCS response is desired in the frequency domain whereas the computational solution of this paper is in the time domain. Of course, the advantage of the time domain approach is that it can accommodate both continuous wave (single frequency, harmonic) and single pulse (multiple frequency, broadband) incident fields. Whether the incident wave is a continuous harmonic wave or a single pulse, the time domain results of electric and magnetic scattered waves are processed using a spectral technique to obtain their response in the frequency domain. Once the near field response is known in the frequency domain, the bistatic RCS response in the far field is computed. For a continuous wave representing a single frequency, the spectral analysis will provide the response at that given frequency, whereas for a pulse case containing many frequencies, the spectral analysis allows one to compute the RCS response for all frequencies contained in the incident pulse from a single time domain transient calculation.

I. Numerical Gridding -- Body–Fitted System

As mentioned in Section B, the Cartesian form of the Maxwell equations are transformed into a body–fitted coordinate system to allow easy implementation of various boundary conditions described in Section F. Only the independent variables x, y, and z are transformed to ξ, η, and ζ and the dependent variables (Q vector in Eqs. (1) and (7)) are left in their Cartesian form.

There are two steps involved in setting up a body–fitted coordinate system: 1) Definition of the geometry, and 2) Construction of the field grid points. As shown in Fig. 2, the objective is to set up the grid in the domain bounded by the body surface (1–2–3) on one side and the outer boundary (4–5–6) on the other. A cut in the domain, 1–6 and 3–4, is created to form a four sided computational domain in two dimensions. In three dimensions, the computational domain will consist of six boundary surfaces. Given the grid point distribution on the computational boundaries (1–2–3 for $\eta_{\min}$, 3–4 for $\zeta_{\max}$, 4–5–6 for $\eta_{\max}$, and 6–1 for $\xi_{\min}$), the interior grid can be constructed in many ways[18], both analytical and numerical. The technique followed in this paper is based on an elliptic grid solver approach[19,20] in which a set of elliptic Poisson's equations is solved numerically to generate the grid in physical space.

$$\begin{aligned} \alpha x_{\xi\xi} - 2\beta x_{\xi\eta} + \gamma x_{\eta\eta} &= -J^2(px_\xi + qx_\eta) \\ \alpha y_{\xi\xi} - 2\beta y_{\xi\eta} + \gamma y_{\eta\eta} &= -J^2(py_\xi + qy_\eta) \end{aligned} \tag{29}$$

where $\alpha = x_\eta^2 + y_\eta^2$, $\beta = x_\xi x_\eta + y_\xi y_\eta$, and $\gamma = x_\xi^2 + y_\xi^2$. The right hand side $p = p(\xi, \eta)$ and $q = q(\xi, \eta)$ are the forcing terms designed to satisfy desired constraints imposed on the nature of the grid, such as specified grid spacings near boundaries and grid intersection angles. J appearing in Eq. (29) is the Jacobian of the transformation. Details on the construction of p and q forcing terms are given in Ref. 19. The objective here is to solve Eq. (29) to obtain the (x, y) values of a grid in the physical space corresponding to a given (ξ, η) point in the computational domain.

In a multizone approach where each structure of the scatterer is gridded separately, the elliptic grid solver given by Eq. (29) will be applied in each zone.

J. Results

Results are presented for both TM and TE two–dimensional cases. In a time domain formulation, the incident wave can be either continuous (harmonic, single frequency) or a single pulse (Gaussian, square, etc.). Of course, for computation of a single pulse transient response, the time domain solver has to be time accurate, and in the present formulation, the Lax–Wendroff explicit scheme is second order accurate both in time and space.

For accuracy, the number of grid points on the scatterer to adequately resolve a wavelength of information is taken to be of the order of 8 to 15. This means, for large bodies (high frequency), the total number of surface grid points to properly resolve the electric and magnetic field distribution can be excessive. However, the present formulation is highly vectorizable and can run efficiently on a supercomputer. If the incident wave is a single pulse containing many frequencies, the number of grid points on the scattering surface must be sufficient to resolve the highest frequency content of the pulse.

A continuous incident wave is represented by (for the TM case)

$$E_z^i = E_0 \cos k(x \cos\theta + y \sin\theta - c_0 t), k = 2\pi/\lambda_0 \quad . \tag{30}$$

The forms for H_x^i and H_y^i are automatically obtained from Maxwell's equation since the incident fields satisfy Maxwell's equations in free space.

$$\begin{aligned} H_x^i &= E_z^i \sin\theta / (\mu_0 c_0) \\ H_y^i &= -E_z^i \cos\theta / (\mu_0 c_0) \end{aligned} \tag{31}$$

where θ is the incident angle. Quantities μ_0, $c_0 = 1/\sqrt{\mu_0 c_0}$ represent free space values usually normalized to 1 ($\epsilon_0 = \mu_0 = c_0 = 1$).

A Gaussian type incident pulse is represented by

$$E_z^i = E_0 e^{-a^2(x\cos\theta + y\sin\theta - c_0 t)^2} \tag{32}$$

where the parameter a controls the width of the Gaussian.

TM Cases

Perfectly Conducting Body in Free Space

For harmonic incident fields, the time domain calculations are carried out until the scattered fields reach a time harmonic steady state (a few wavelengths of calculation). Then the discrete FFTs are employed to obtain the complex field representation in the frequency domain. The bistatic RCS is then computed using a near field–to–far field contour integration.

Figure 7 shows plots of surface currents ($n \times H$) for a square cylinder at two different incident angles and comparisons are made with method of moment (MOM) solutions[21]. The required grid resolution (at least 10 points per wavelength) is maintained only on and near the body surface. The grid is allowed to stretch along the direction leading away from the surface (nonuniform grid between the body surface and the outer boundary).

Figure 8 shows bistatic radar cross section for a circular cylinder and a square cylinder. For accuracy, the contour for RCS evaluation is placed at the centroids of cells neighboring the body surface.

The broadband frequency response from a single transient calculation using a Gaussian–like incident pulse is demonstrated in Fig. 9. The calculation is started when the incident pulse is about to come in contact with the scatterer and is then carried out until the scattered fields completely leave the vicinity of the scattering surface. The transient response is shown in terms of the surface current variation along the body surface in time, which starts as zero at $t = 0$ and gets back to zero at some later time after the transients vanish. This time response is then processed using FFTs to get the field variation in the frequency domain for all frequencies contained in the incident pulse. Then, the bistatic RCS as a function of frequency is computed.

Figure 10 shows results for a perfectly conducting cylinder with a dielectric strip around it. The electric field contours clearly indicate the smoothness of the contours at the interface of free space and dielectric. The characteristic based Riemann solvers employed

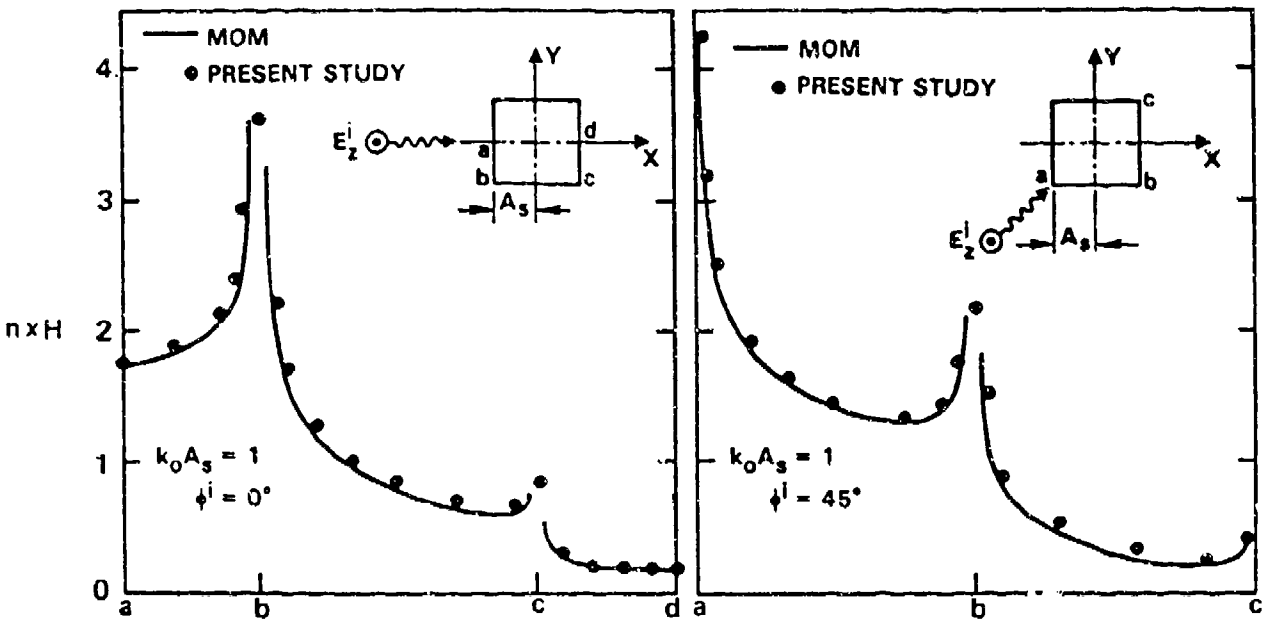


Fig. 7. Surface currents for a perfectly conducting square cylinder.

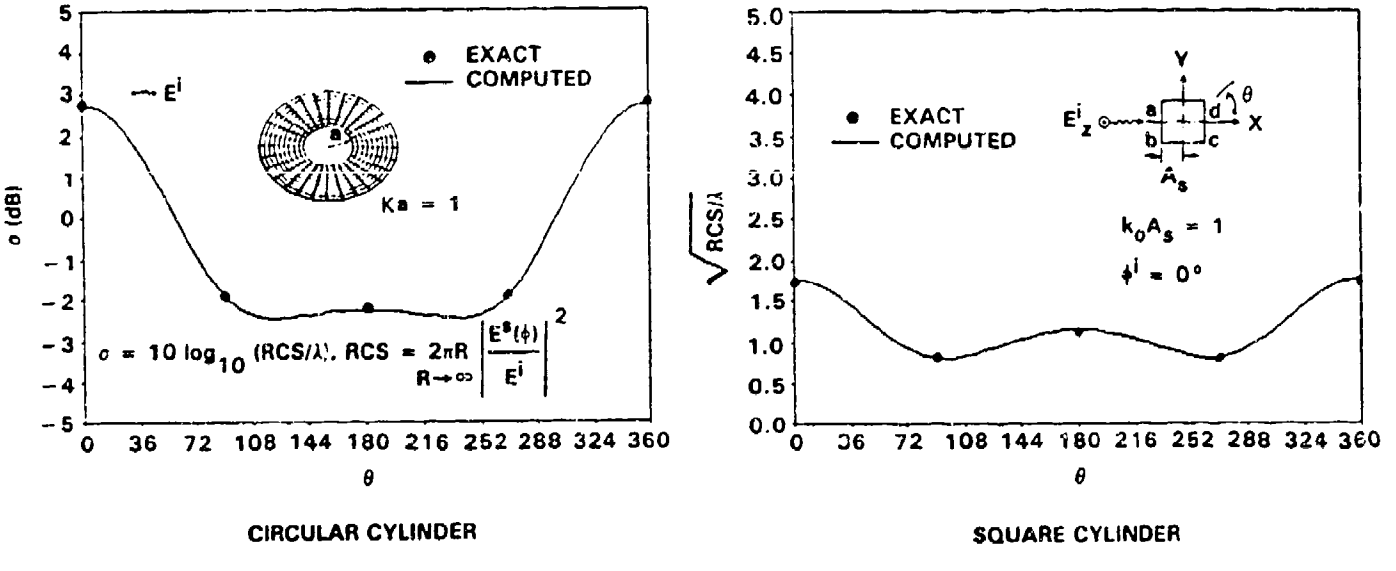


Fig. 8. Two–dimensional RCS calculations.

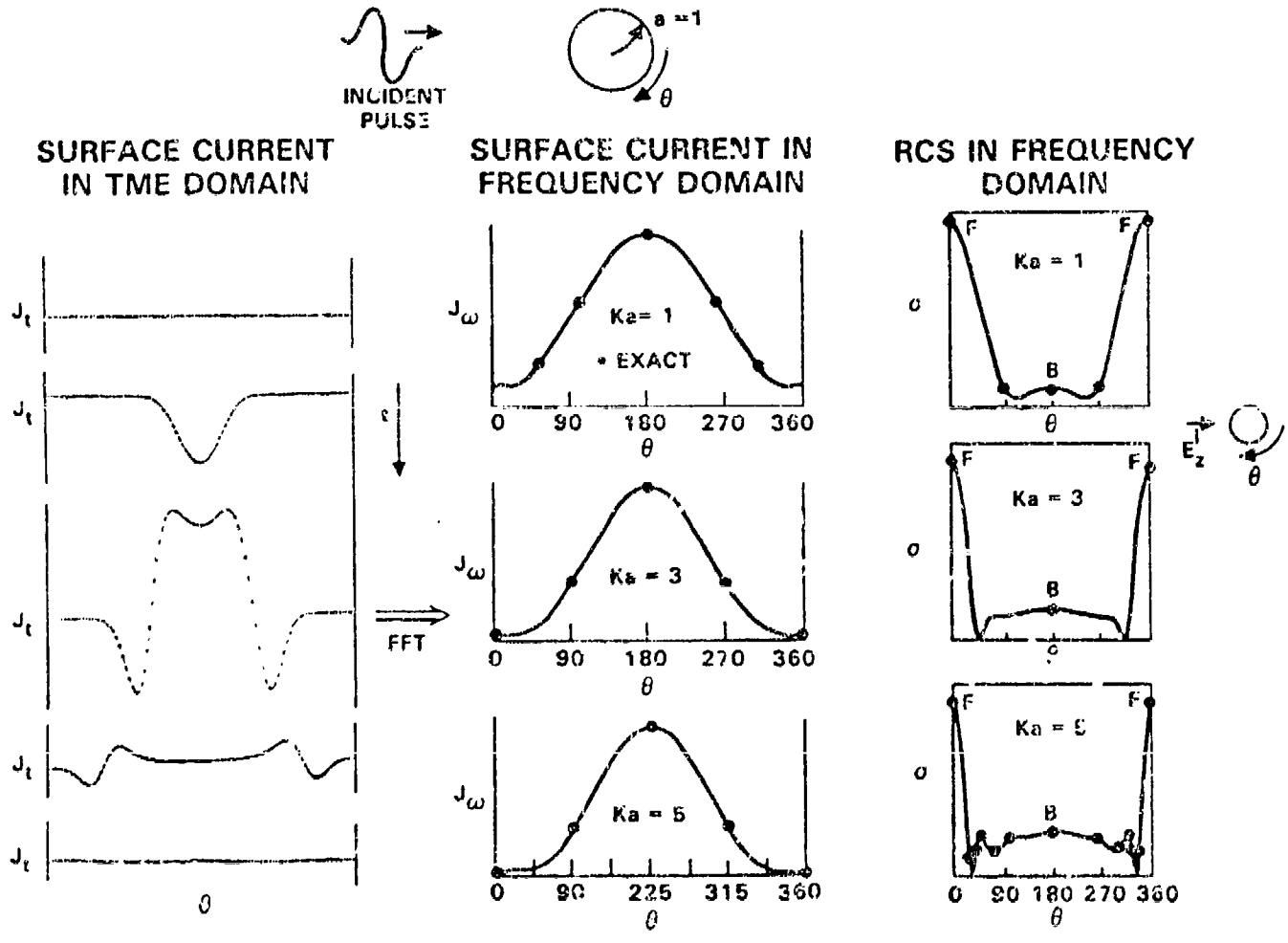


Fig. 9. Transient single pulse calculation.

at a cell interface ensure such continuity and smoothness of electric and magnetic fluxes. The comparisons of bistatic cross section and surface currents with exact solutions are good.

Figure 11 shows a similar dielectric strip calculation with and without loss. The lossy material behavior is modeled in terms of an imaginary component to ϵ. The calculation of Fig. 11 for a body size of $Ka = 10$ used 150 grid points along the body and 30 points away from the body. The smallest grid spacing near the body surface is chosen such that nearly 100 time steps will provide a wavelength of calculation.

Figure 12 shows contours of electric scattered field (E_z^s) at an instant of time for a circular cylinder. The body at the center of the computational domain and the outer boundary are clearly seen. This plot clearly shows that the scattered fields leave the outer boundary smoothly without any noticeable (spurious) reflection. The corresponding total electric field (E_z^T) contours are shown in Fig. 13. The shadow region is clearly seen.

Figure 14 shows the bistatic cross section for the NACA 0012 airfoil at different control surface settings. The airfoil is 10 wavelengths long and corresponds to about 1 GHz incident frequency. The body–fitted gridding for each setting is also shown in the figure.

TE Cases

Figure 15 shows the bistatic RCS for a perfectly conducting cylinder for various ka values. The variation of σ as a function of viewing angle is more pronounced for the TE cases than for the corresponding TM cases. The computational results compare very well with available exact solutions[15].

Figure 16 shows bistatic RCS results for a dielectric cylinder ($\epsilon = 2.56$) of $ka = 1$. This case has a drastic RCS variation in viewing angle. The forward scattering is nearly zero dB whereas around the 100° viewing angle the cross section reduces to -60 dB. The finite–volume calculations based on the present formulation seem to produce very accurate results even for a case having a dynamic range of 60 dB.

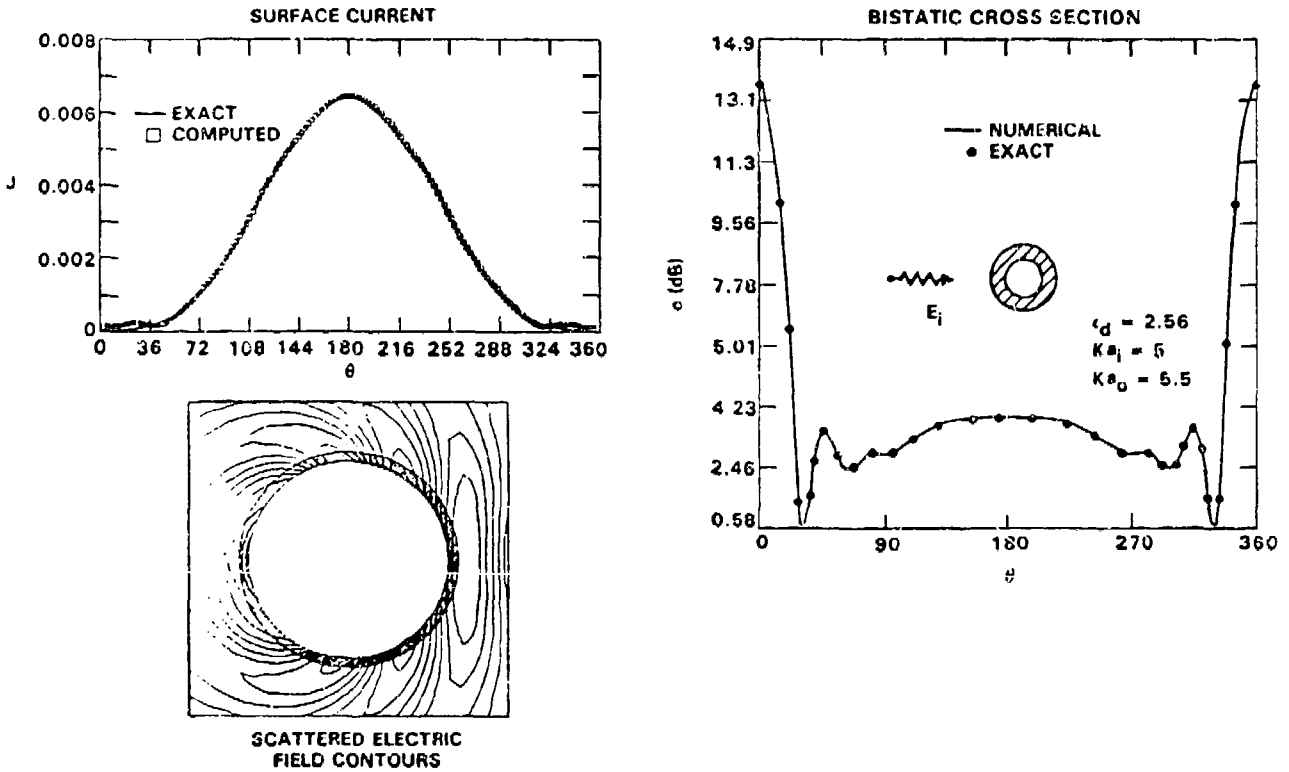


Fig. 10. RCS computation for a conducting cylinder with a dielectric strip.

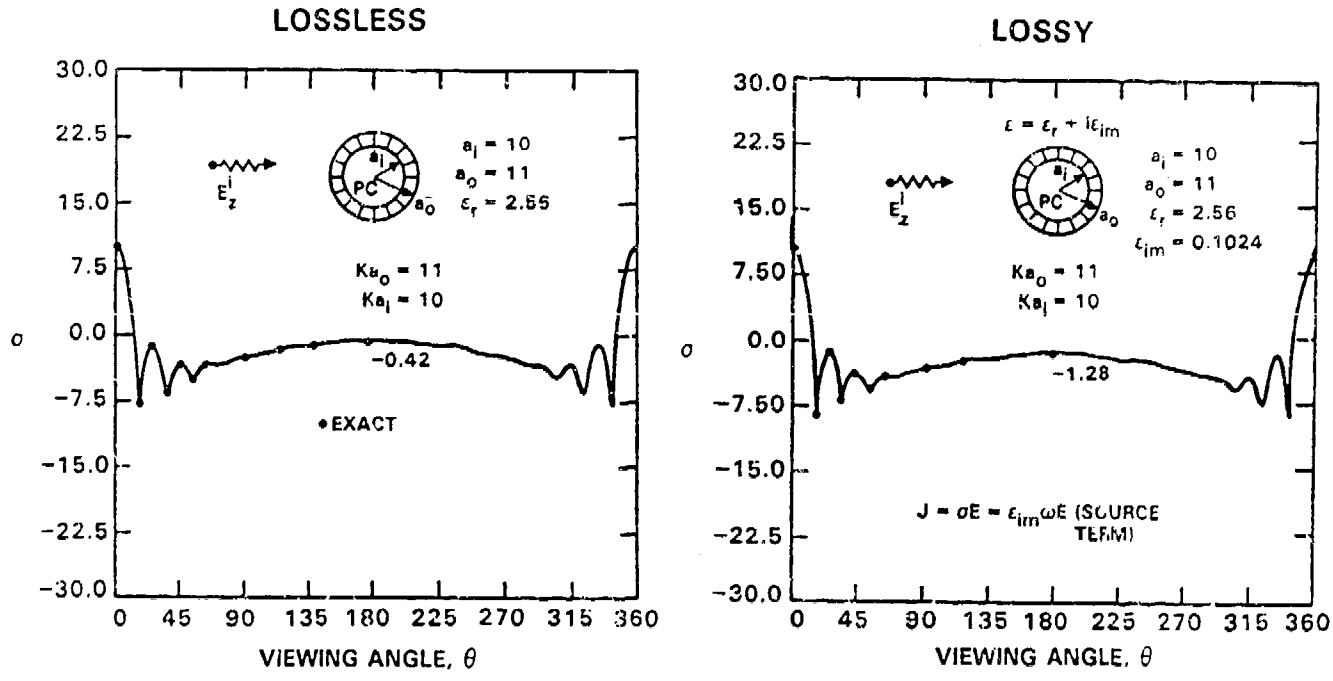


Fig. 11. Effect of lossy coating on RCS.

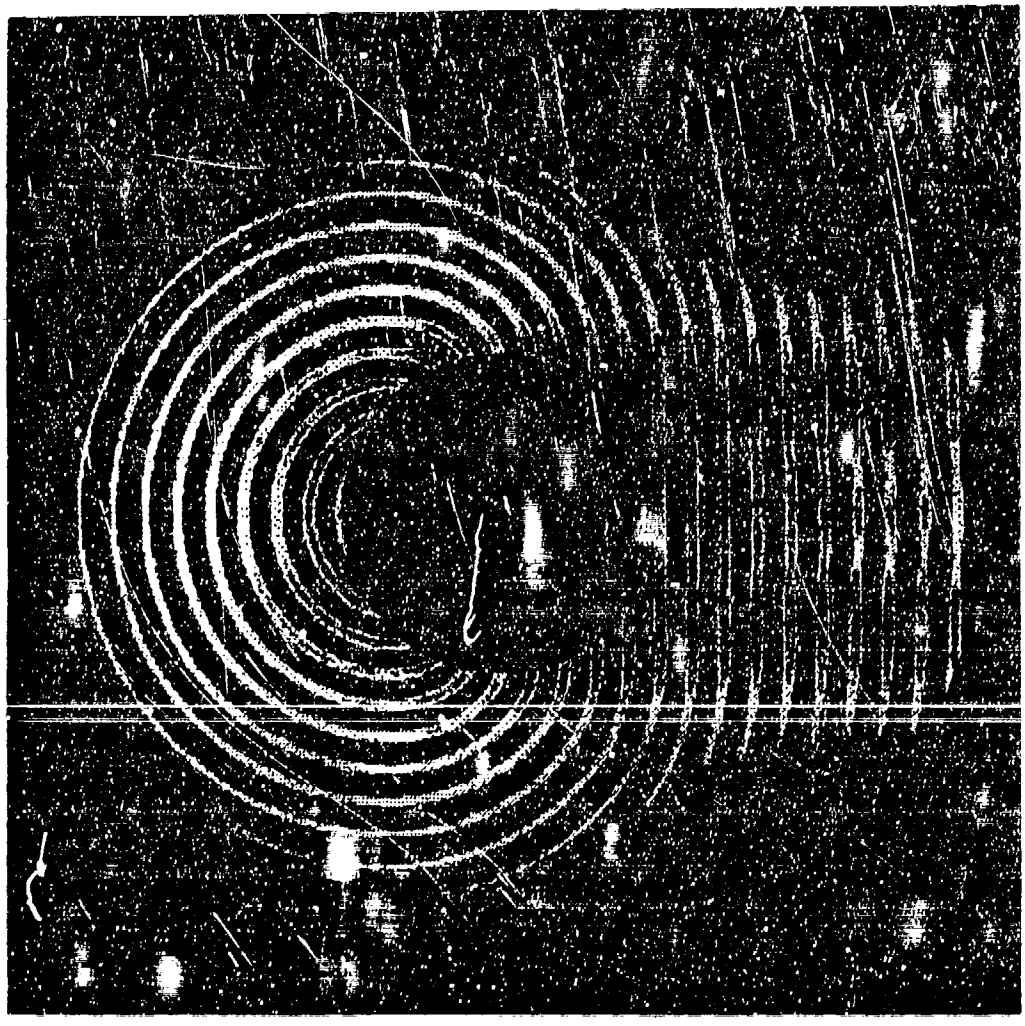


Fig. 12. Scattered electric field contours for a perfectly conducting cylinder.

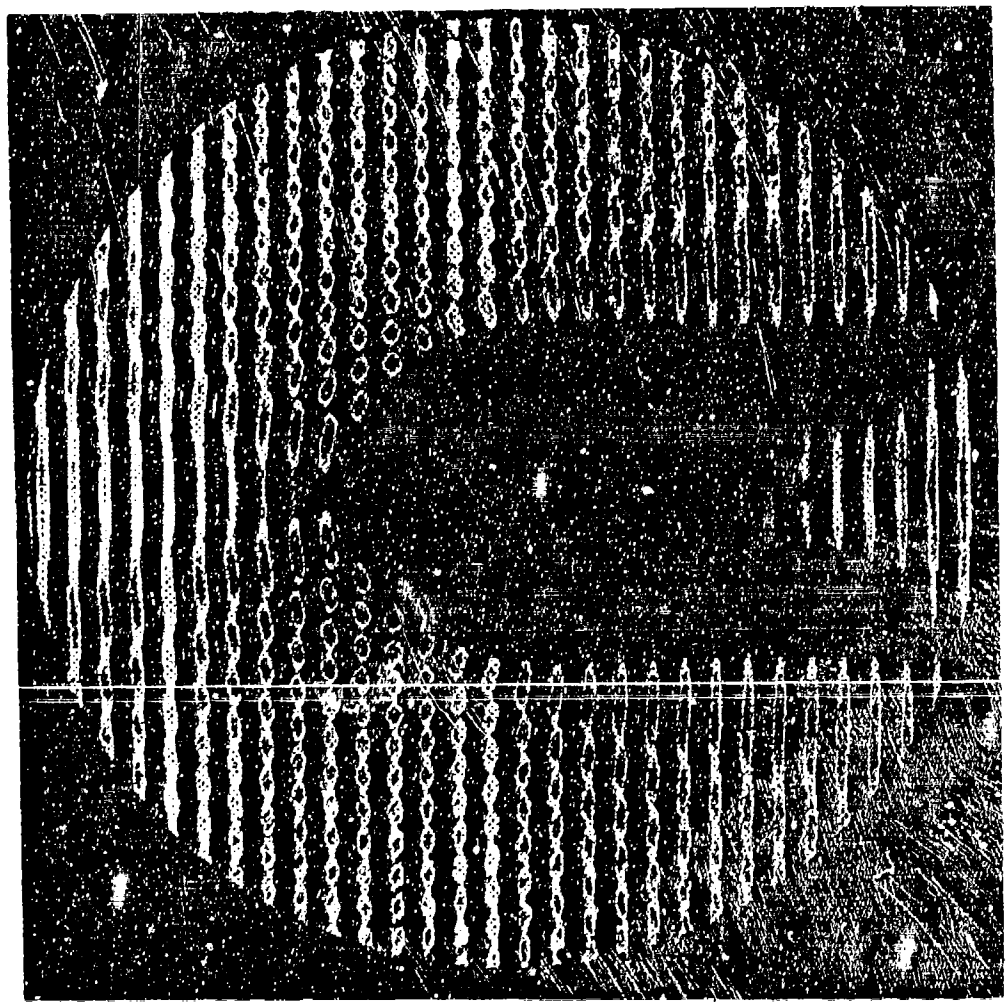


Fig. 13. Total electric field contours for a perfectly conducting cylinder.

SCATTERING FROM NACA0012 AIRFOIL AT 1 GHz

λ = 30 cm, Chord = 300 cm, kc = 62.83

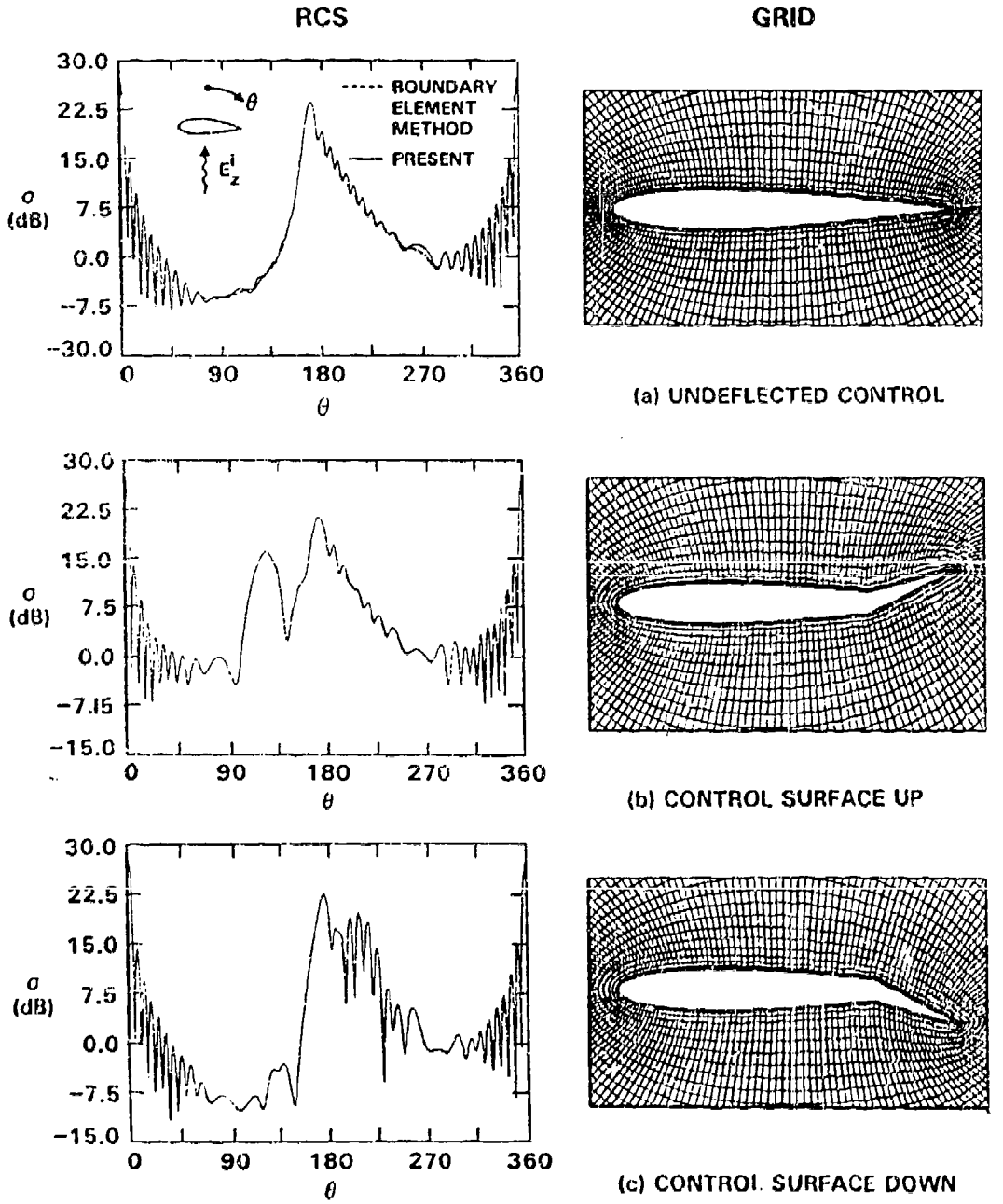


Fig. 14. Scattering from NACA 0012 airfoil.

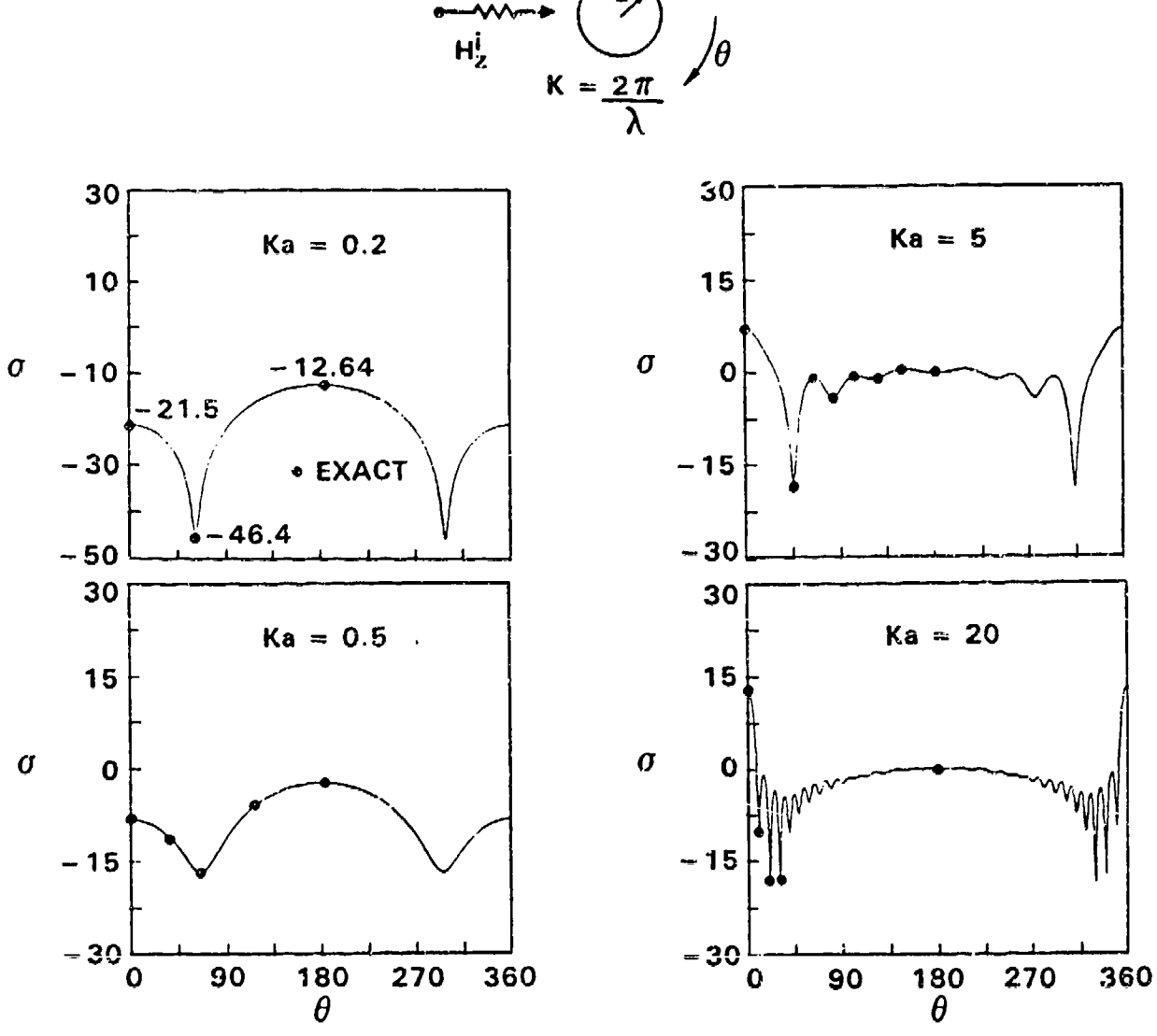


Fig. 15. Two–dimensional TE cases.

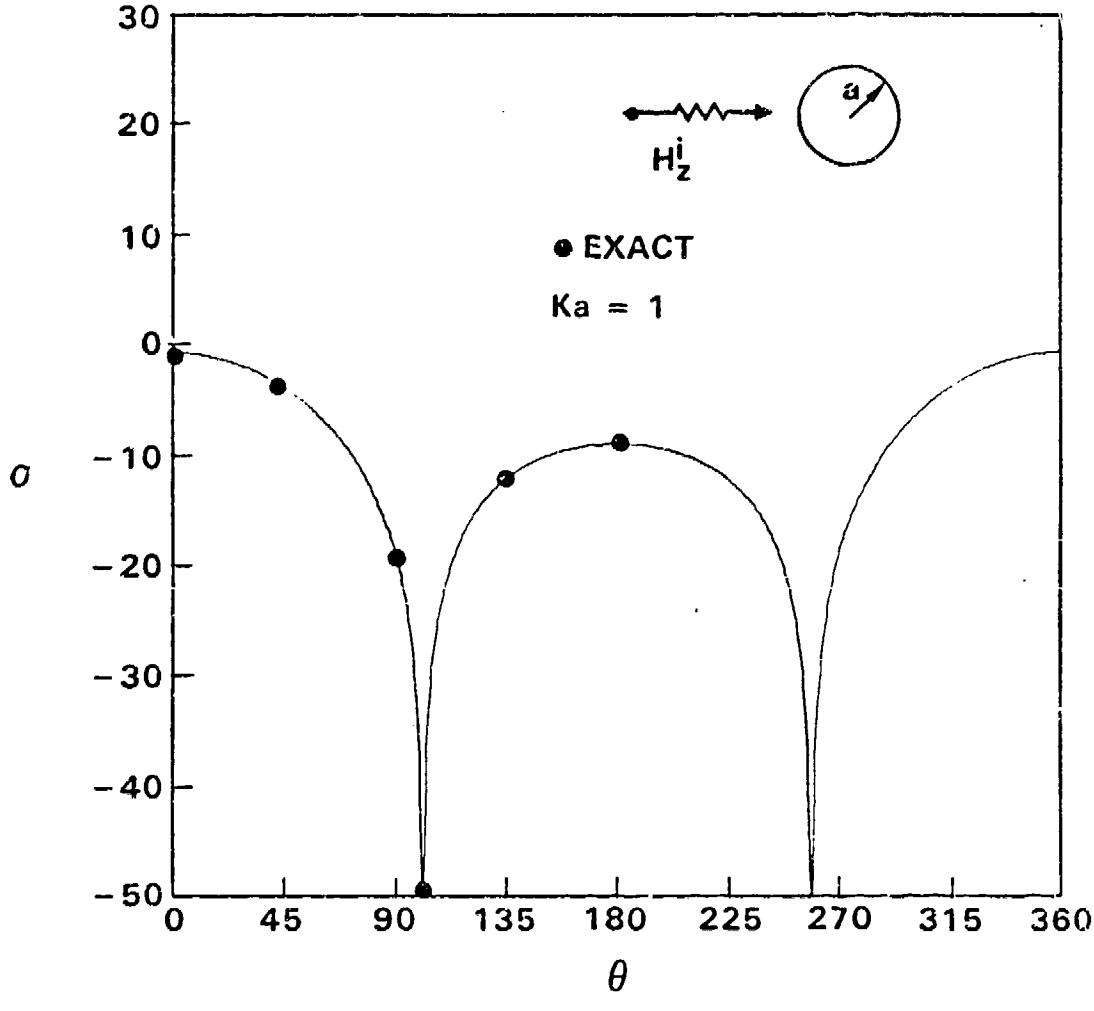


Fig. 16. RCS for a dielectric cylinder - TE wave.

Conclusions

A novel time domain differential solver for Maxwell's equations utilizing proven numerical algorithms of CFD has been developed and applied to solve the two–dimensional transverse magnetic and transverse electric wave equations. Some of the salient features of this approach are

1) Based on physical theory of characteristic signal propagation as it has been implemented in proven CFD methods
2) Treatment of layered media with discontinuous material properties (lossy and lossless)
3) Numerical gridding for arbitrary geometry treatment
4) Near field–to–far field transformation to compute RCS
5) Second order accurate (time and space) upwind Lax–Wendroff explicit scheme
6) Transient and time harmonic computations
7) Application of FFT to derive frequency response from time domain calculation.

Currently work is under way to extend the two–dimensional solver to full three–dimensional Maxwell's equations. Along with the development of a three–dimensional Maxwell's equations solver, work is progressing on many fronts. In the algorithm research arena, implicit type schemes are being looked at to avoid CFL (stability) restrictions placed on Δt by the explicit schemes. Modeling of negative material properties ($\epsilon < 0$) which have significance to plasmas and surface polaritons, treatment of thin sheets (resistive cards, lossy coatings, etc.) through appropriate boundary conditions, incorporation of frequency dependent (time dependent material properties are easily modeled in a time domain based solver) and nonlinear material properties, gridding requirements for large bodies (high frequency), higher order nonreflecting far field outer boundary conditions, computer architecture issues in algorithm design (coarse grain and fine grain parallel processing), etc., are some of the topics of interest.

Acknowledgements

The authors would like to express their sincere appreciation to Dr. Sukumar Chakravarthy and Professor Stanley Osher for many valuable discussions and to Mr. Barna Bihari for his support of computer graphics. The financial support of Rockwell North American Aviation and their continued interest in this development of CFD based methods for CEM are also greatly appreciated.

References

1. K.S. Yee, "Numerical Solution of Initial Boundary Value Problems Involving Maxwell's Equations in Isotropic Media," IEEE Trans. Antennas Propagat. AP–14, 302–307 (1966).
2. A. Taflove and K. Umashankar, "A Hybrid Moment Method/Finite–Difference Time Domain Approach to Electromagnetic Coupling and Aperture Penetration into Complex Geometries," IEEE Trans. Antennas Propagat. AP–30, 617–627 (1982).

3. E.K. Miller, A.J. Poggio, and G.J. Burke, "An Integro–Differential Equation Technique for Time–Domain Analysis of Thin–Wire Structures, Part I–The Numerical Method," J. Comput. Phys. 12, 24 (1973).

4. V. Shankar, S. Chakravarthy, and K.–Y. Szema, "Development and Application of CFD Methods to problems in Computational Science," Workshop on CFD for Aerospace Problems, the University of Tennessee Space Institute, UTSI Publication No. E02–4005–013–88, March 7–11, 1988.

5. V. Shankar, K.–Y. Szema, and S. Osher, "A Conservative Type–Dependent Full Potential Method for the Treatment of Supersonic Flows with Embedded Subsonic Regions," AIAA Paper No. 83–1887; AIAA J. 23 (1), 41–48 (1985).

6. V. Shankar, H. Ide, J. Gorski, and S. Osher, "A Fast, Time–Accurate Unsteady Full Potential Scheme," AIAA Paper No. 85–1512–CP, AIAA 6th Computational Fluid Dynamics Conference, Cincinnati, July 15–17, 1985. Also, AIAA J., Vol. 25, No. 2, February 1987.

7. V. Shankar and H. Ide, "Unsteady Full Potential Computations for Complex Configurations, AIAA Paper No. 87–0110, AIAA 25th Aerospace Sciences Meeting, Reno, January 1987.

8. S.R. Chakravarthy, D.A. Anderson, and M.D. Salas, "The Split–Coefficient Matrix Method for Hyperbolic Systems of Gasdynamic Equations," AIAA Paper No. 80–0268, AIAA 18th Aerospace Sciences Meeting, January 14–16, 1980, Pasadena, California.

9. S.R. Chakravarthy and K.–Y. Szema, "An Euler Solver for Three–Dimensional Supersonic Flows with Subsonic Pockets," AIAA Paper No. 85–1703, presented at the AIAA 18th Fluid Dynamics, Plasmadynamics, and Lasers Conference, Cincinnati, July 16–18, 1985.

10. K.–Y. Szema, S.R. Chakravarthy, and H. Dresser, "Multizone Euler Marching Technique for Flows over Multibody Configurations," AIAA Paper No. 87–0592, January 1987, and AIAA Paper No. 88–0276, January 1988.

11. S.R. Chakravarthy and D.K. Ota, "Numerical Issues in Computing Inviscid Supersonic Flow over Conical Delta Wings," AIAA Paper No. 86–0440, presented at the AIAA 24th Aerospace Sciences Meeting, Reno, January 6–9, 1986.

12. P.L. Roe, "Approximate Riemann Solvers, Parameter Vectors, and Difference Schemes," J. of Computational Physics, Vol. 43, 1981, pp. 357–372.

13. S. Osher and S. Chakravarthy, "High Resolution Schemes and the Entropy Conditions," SIAM Journal of Numerical Analysis, Vol. 21, No. 5, October 1984, pp. 955–984.

14. P. Lax, "Hyperbolic Systems of Conservation Laws and the Mathematical Theory of Shock Waves," SIAM, Philadelphia, 1973.

15. G.T. Ruck, D.E. Barrick, W.D. Stuart, and C.K. Krichbaum, "Radar Cross Section Handbook, Volumes 1 and 2, Plenum Press, New York, 1970.

16. R.F. Warming and R.M. Beam, "Upwind Second–Order Difference Schemes and Applications in Aerodynamic Flows," AIAA J., Vol. 14, No. 9, September 1976.

17. R. Courant, K. Friedrichs, and H. Lewy, "On the Partial Difference Equations of Mathematical Physics," IBM Journal, March 1967, pp. 215–234.

18. J.F. Thompson, F.C. Thames, and C.W. Mastin, "Automatic Numerical Generation of Body–Fitted Curvilinear Coordinate System for Field Containing Any Number of Arbitrary Two–Dimensional Bodies," J. of Computational Physics, Vol. 15, No. 3, July 1974, pp. 299–319.

19. J.L. Steger and R.L. Sorenson, "Automatic Mesh–Point Clustering Near a Boundary in Grid Generation with Elliptic Partial Differential Equations," J. of Computational Physics, Vol. 33, No. 3, December 1979, pp. 405–410.

20. V. Shankar and S. Rudy, "Application of a Two–Dimensional Grid Solver for Three–Dimensional Problems," AIAA J., Vol. 23, No. 3, March 1985.

21. K. Umashankar and A. Taflove, "A Novel Method to Analyze Electromagnetic Scattering of Complex Objects," IEEE Transactions on Electromagnetic Compatibility, Vol. EMC–24, No. 4, November 1982.

ELECTROMAGNETIC ANALYSIS BY THE TRANSMISSION LINE MODELLING (TLM) METHOD

F. J. German, L. S. Riggs, and M. E. Baginski
Electrical Engineering Department
200 Broun Hall
Auburn University, AL 36849-3501

I. INTRODUCTION

The analogy between electromagnetic field quantities and voltages and currents in RLC networks has been known for quite some time [1]. Indeed, actual networks have been built and tested to verify the accuracy of such techniques [2]. In 1971, Johns and Beurle used these principles and the theory of pulse propagation on transmission lines to develop a numerical technique suitable for computer computation for the solution of two dimensional electromagnetic scattering problems [3]. The method, called the transmission line modelling, or matrix, (TLM) method, proved to be a reliable, accurate, and easily formulated numerical procedure for the solution of a wide variety of electromagnetic interaction problems.

II. OVERVIEW OF THE TLM METHOD

The TLM method works by discretizing a given portion of space by inserting into it a mesh of transmission lines. The structure, or structures, of interest are then put into the mesh such that the boundaries intersect the transmission lines. The relationships between voltages and currents on the transmission lines and the electromagnetic fields are then used to obtain all six components of the field at any node. The excitation of the mesh is accomplished by initializing ideal impulses of voltage and current

This work was supported in part by Texas Instruments, Inc., Antenna Dept., McKinney, TX under contract TI-7334277.

which correspond to the fields that are to be excited. Following the initialization, iterations commence and the pulses are followed as they scatter at each node in the mesh according to the scattering matrix for the node. At the boundaries of the scatterers, the pulses are weighted by an appropriate reflection coefficient and then returned to the mesh.

Since the TLM procedure operates on impulses that are injected into the mesh, the solution contains information over a wide band of frequencies. The output, which consists of a series of impulses in time that correspond to each of the field quantities, may be Fourier tranformed to yield steady state, frequency domain information. Alternatively, the impulse response may be convolved with an excitation function to get the time domain response to that excitation. Thus, once the impulse response of a problem has been calculated and saved, the solution for any initial excitation is easily obtained.

After scattering at a node or reflection from a boundary, the impulses take a finite time to travel to the next node or boundary. This gives the TLM model of wave propagation the advantage of being naturally discretized in both time and space. Thus, no approximations need be used and the model can be solved exactly. Errors arise in the TLM method due only to how well the model corresponds to the actual physical situation and not from the solution of that model.

Originally, the scattering matrices for the nodes used in TLM meshes were derived using a lumped element equivalent of the node. Recently, a symmetrical condensed node has been introduced [4] which has many advantages over the previously used expanded and

asymmetrical condensed nodes. The scattering matrix for the symmetrical condensed node is derived by enforcing the Maxwell equations at the center of each transmission line element [5]. Figure 1 shows the expanded and symmetrical condensed TLM nodes. The asymetrical condensed node is obtained by removing the transmission lines linking the individual shunt and series nodes from the expanded node; these link transmission lines are indicated by the arrows in Figure 1(a).

By adding short circuited, open circuited, and matched transmission line stubs to the nodes, materials with arbitrary permittivity, permeability, and conductivity can be modelled. In addition, these stubs allow the use of arbitrarily shaped transmission line elements to be used in the mesh provided the required inductance and capacitance required to model the element can be determined. While in principle, arbitrary elements can be used, most applications to date have been limited to irregularly graded cartesian meshes and cylindrical meshes [6]. Some work has also been done involving the use of meshes which are perturbed to conform to the surface of an arbitrary scatterer at the scatterer surface in a regular cartesian mesh [7].

The symmetrical condensed node is a very significant advance in the TLM technique. Due to the complicated topology of the expanded node mesh, graphic input of problem data has proven to be rather difficult. Also, the field quantities, which are available at the individual shunt and series nodes which make up the expanded node, are separated in space. The introduction of the asymetrical condensed node simplified the problem of graphic data preparation, condensed all six field quantities to one spatial

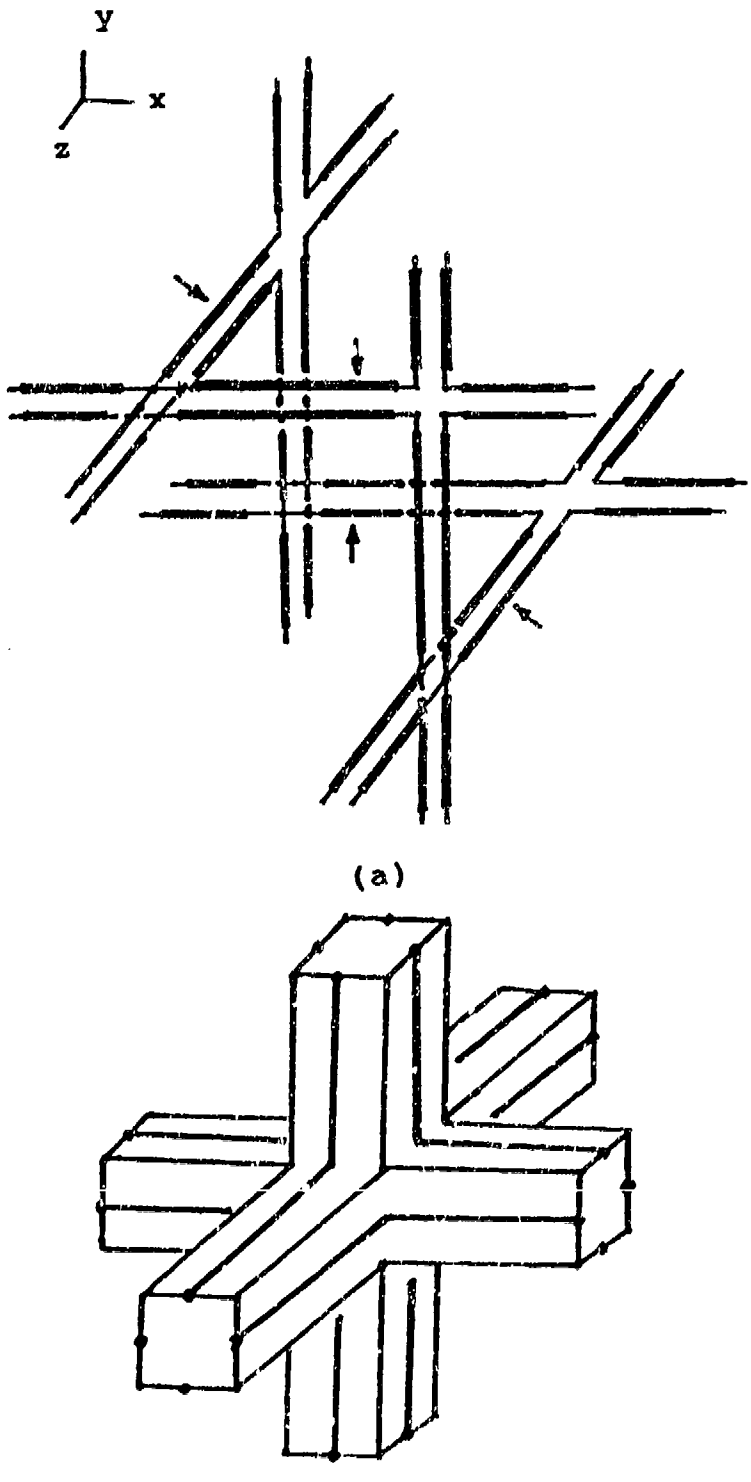


Figure 1. Three dimensional TLM nodes: (a) expanded node and (b) symmetrical condensed node.

point, and also made the nodal scattering calculations simpler and more efficient; however, this node has the disadvantage of being asymmetric and care must be taken when using this version of the TLM algorithm - especially in unbounded field problems. The symmetrical condensed node alleviates the difficulties associated with both the expanded and asymmetric condensed nodes. In addition to allowing easy graphic input of problem data, the scattering calculations are also simpler and computationally more efficient than for any of the previous nodes.

Waves that are propagating on a TLM mesh experience dispersion due to the nature of the transmission line mesh. This dispersion is a function of propagation direction on the mesh and is also affected by the addition of stubs for modelling materials and shapes of elements. Limited theoretical analysis and extensive numerical experimentation indicate that the dispersion characteristics of the symmetrical condensed node mesh are superior to the expanded node and asymmetric condensed node meshes [6]. The effects of the mesh dispersion can be reduced by using a finer mesh. In general, we have found that an area of space which has been discretized to adequately describe the electromagnetic fields requires a mesh that is already fine enough to make the dispersion error negligible. Thus, after specifying the mesh for a specific problem based on the expected field distribution, a cursory check is usually all that is required to verify that mesh dispersion will not have a significant affect on the results.

The development of time domain diakoptics for use in the TLM method has proven to be a very powerful tool for electromagnetic computations [8]. The diakoptic process allows a large problem to

be broken into smaller substructures which are solved separately. The solutions for each substructure are then joined using a connection algorithm to yield the solution to the complete problem. The advantage of diakoptics is that if the geometry of the scatterer changes in one of the substructures then only that single substructure must be re-solved and then connected to the solution for the rest of the problem. The density of the mesh in a substructure can also be made finer than in the others. This allows areas with fine geometrical details to be modelled as substructures with a very fine mesh. Figure 2 shows an example TLM mesh which contains a substructure with a finer mesh than the remaining space. The use of diakoptics permits a tremendous improvement in computational efficiency.

The applications of TLM in the area of electromagnetic analysis and design have been extensive. The three dimensional TLM method has been successfully used to predict the dispersion characteristics of various microstrip integrated circuit structures [9].The method has also been used for the prediction of EMP hazards in aircraft where the induced currents in cable bundles have been calculated [10]. Some preliminary work has also been done in the area of electromagnetic imaging [11] where TLM was used in conjunction with an optimization procedure to reconstruct a two dimensional dielectric target. The electromagnetic interactions of a charge bunch moving at relativistic speeds in a high energy particle accelerator have been predicted with a high degree of accuracy using a TLM model in cylindrical coordinates [12]. Additional areas of applications involve analysis and design of magnetrons and travelling wave

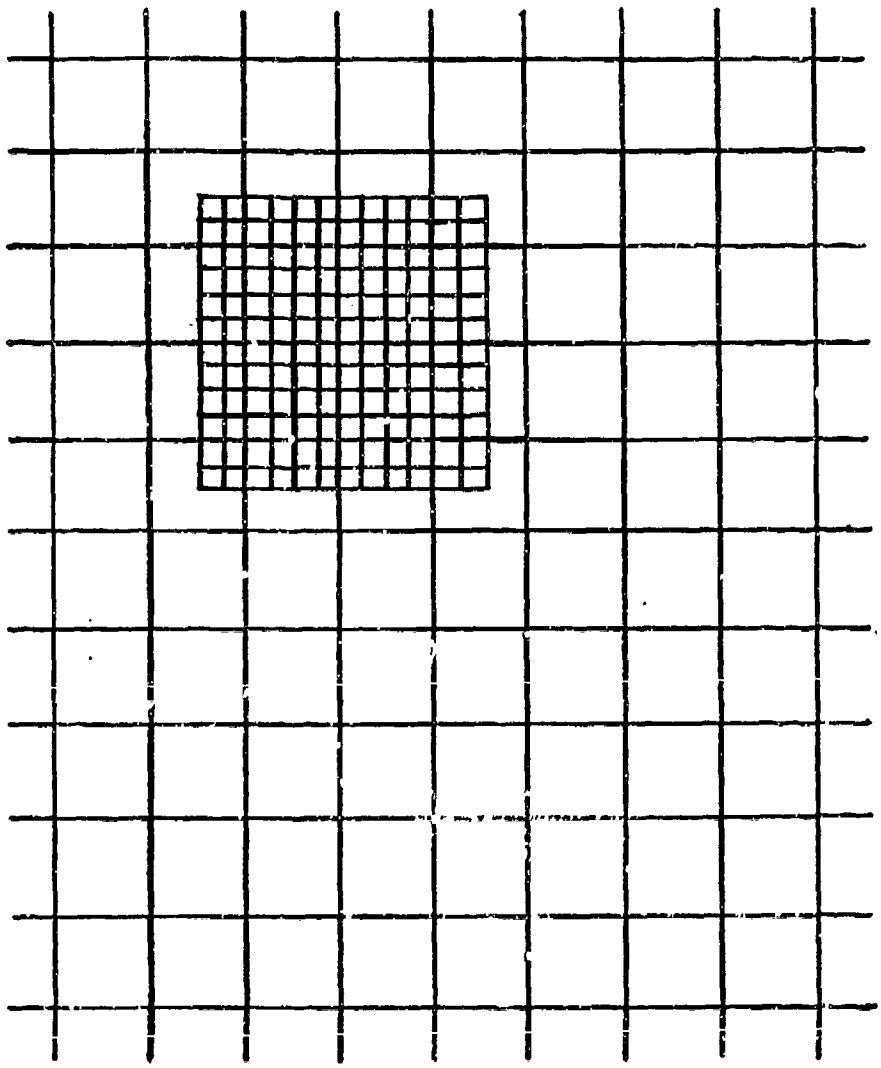


Figure 2. Two dimensional TLM mesh with diakoptic substructure employing a finer mesh.

tubes, prediction of electrostatic discharge (ESD) in LSI circuits, and transient analysis of cross talk in high density VLSI interconnections. In addition to electromagnetic analysis and design, the TLM method has also been applied to the modelling of diffusion [13], and nonlinear networks [14].

III. GTEC: THE THREE DIMENSIONAL TLM COMPUTER CODE

A comprehensive computer program package, GTEC (General TLM Electromagnetics Code), has been developed based on the symmetrical condensed TLM node [15]. The program is organized so that it is user oriented and relatively easy to use. All of the required input data that is necessary to describe the problem is read in from a formatted data file that is assembled by the user; thus, no programming is required for each new problem that is solved.

The problem space is specified by inputting the permittivity, permeability, conductivity, and shape of each transmission line element in the mesh. In addition, the reflection coefficient and location of relective boundaries are specified. After initializing the excitation, iterations based on the TLM algorithm commence. After each iteration (time step), the field components are calculated from the voltage pulses incident on each node and saved at the user specified output points. Since the TLM output consists of a series of impulses in time, further processing is usually required to obtain useful output data. The GTEC package contains both Fourier transform and time domain convolution routines so that both frequency and time domain data are available.

The code also implements stepped impedance boundaries [16]. This type of boundary permits the modelling of waveguiding

structures which are continuous in one coordinate direction to be modelled on a mesh only two nodes in length regardless of the structure's actual physical length in the continuous direction. This drastically reduces computer time and memory requirements - especially when low frequency results are required.

Special versions of the TLM field solver are available that accumulate either the Fourier tranform or time convolution after each iteration at a specified frequency or times. The advantage of this scheme is that the impulse response need not be saved at each time step. While losing some generality, these versions of the field solver require less memory than the usual procedure. The Fourier tranform version is especially useful when steady state time harmonic results are desired.

GTEC has been developed on a VAX 11/780 operating under the VMS version 4.4 operating system and is written in FORTRAN. The program has been written in a modularized fashion in order to maintain maximum versatility. This also allows future additions to the code to be easily added to the total GTEC package. An example of this is the addition of one of the optional field solvers described above. Implementation into GTEC requires only that the new field solver be linked with the rest of the package - no programming or modification to other code segments is required.

A basic skeleton flowchart for the TLM field solver is shown in Figure 3 (the main program driver and the graphics routines are not shown in this figure). Detailed descriptions of the program operations and of all of the subroutines in GTEC are contained in [15].

Present graphics capabilities in GTEC consist of provisions

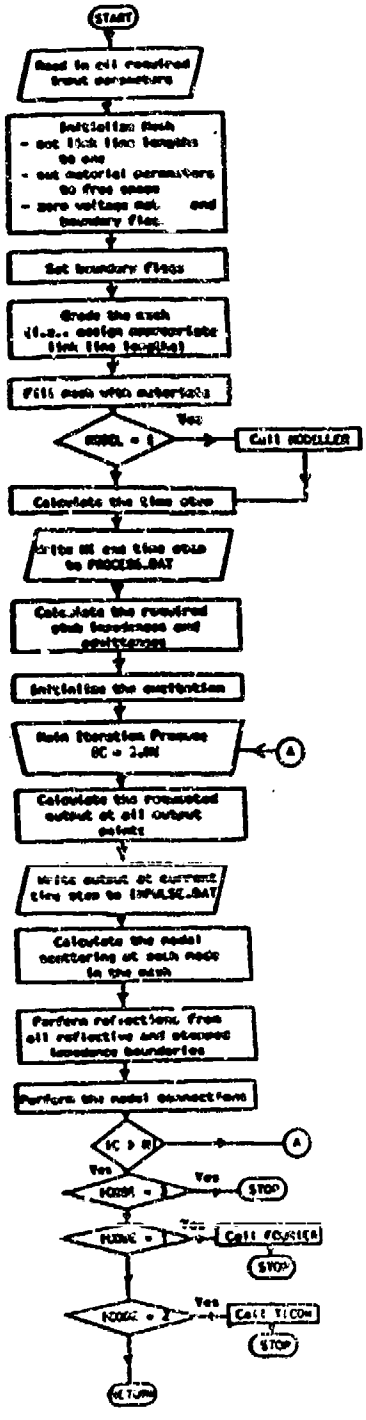


Figure 3. Flow diagram for the TLM field solver.

for plotting the calculated data and for plotting, in three dimensions, the geometry of the structure being investigated. Figure 4 shows the graphic output of an aircraft model that was used to predict the EMP response of the aircraft. The graphic verification of problem geometry is made, if desired, after the input data table has been read in. As an example of a GTEC input table, Figure 5 shows all of the input data required for solving for the surface currents on the aircraft in Figure 4 for an incident EMP pulse; again, reference is made to [15] for a complete description of all input parameters.

Because of the inherent simplicity of the TLM algorithm, GTEC is computationally efficient. For the example aircraft EMP interaction problem described above, the total CPU time required for the TLM solution was approximately 100 minutes on the VAX 11/780 for a 30 x 30 x 30 mesh size and 1 ns of prediction. As seen from the input data of Figure 5, the topological simplicity of the symmetrical condensed node makes data input relatively straight forward.

GTEC has been tested extensively on a wide range of electromagnetic problems. In addition to EMP interaction problems such as the aircraft described above, the code has been used to predict dispersion in many different microstrip integrated circuit structures. We have also used GTEC for the analysis of broadband waveguides, and for predicting cross talk in high density VLSI interconnects. Comparison with other computed data when available has been very good. In addition, preliminary measurements on VLSI interconnects show good agreement with the data predicted using GTEC.

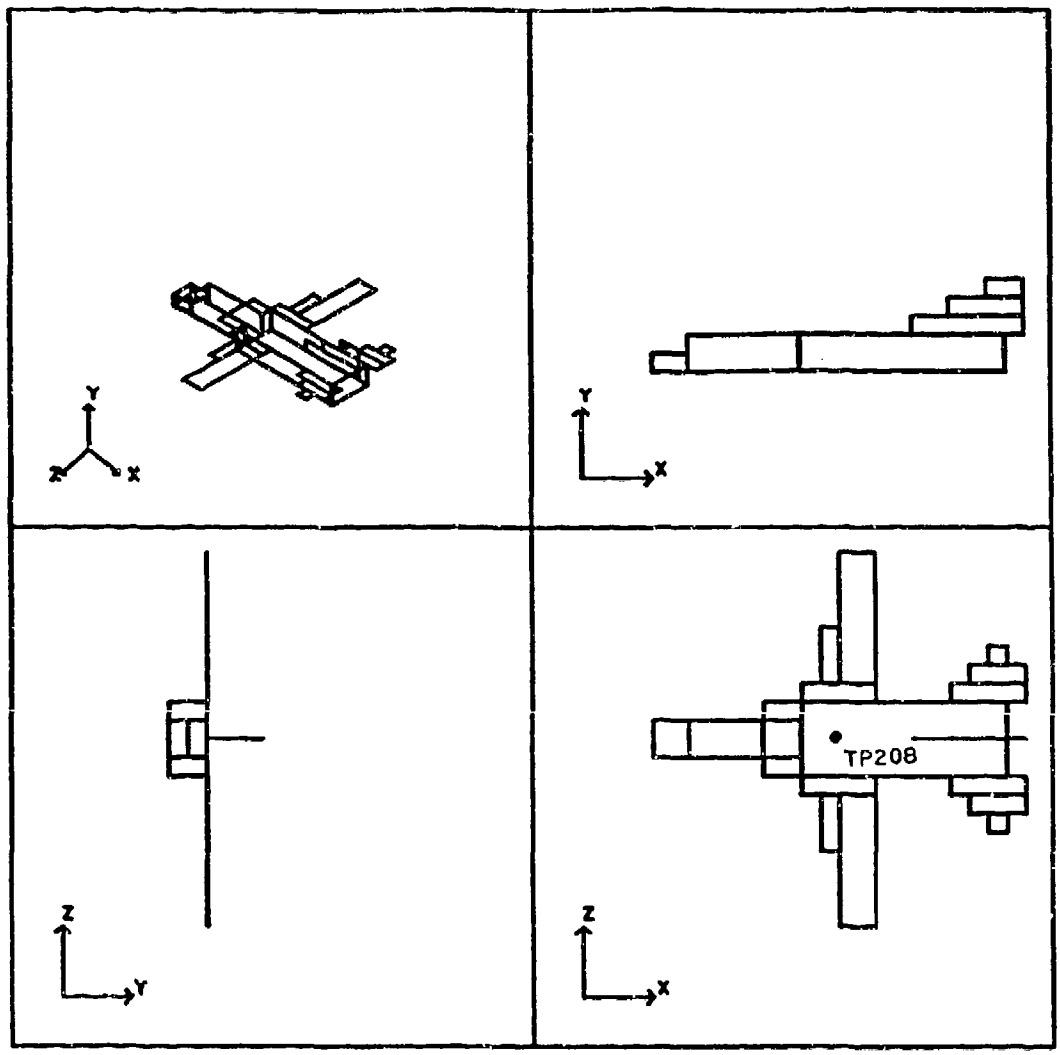


Figure 4. Graphic output for geometry of the aircraft used for EMP analysis by GTEC.

```
  0
  2     2     0     1
EMP RESPONSE OF F-111 AIRCRAFT IN FLIGHT
 30    30    30                                          ! MESH DIMENSIONS
  1    30  2.000000                                     ! X GRADE
  0     0  0.000000
  0     0  0.000000                                     ! Y GRADE
  1    30  2.000000                                     ! Z GRADE
  0     0  0.000000
0.000000  0.000000  0.000000                            ! LOWER BOUNDARIES
  1    30     1    30    30    30     1  0.000000      ! MESH TRUNCATION
 30    30     1    30     1    30     2  0.000000      !   "
  1    30    30    30     1    30     3  0.000000      !   "
 14    17    18    18    13    13     3 -1.000000      ! WINGS                    (1)
 14    17    18    18    18    18     3 -1.000000      !   "                      (2)
 15    15    18    18    10    12     3 -1.000000      !   "                      (3)
 15    15    18    18    19    21     3 -1.000000      !   "                      (4)
 16    17    18    18     6    12     3 -1.000000      !   "                      (5)
 16    17    18    18    19    25     3 -1.000000      !   "                      (6)
 22    25    18    18    13    13     3 -1.000000      ! HORIZONTAL STABILIZERS   (7)
 22    25    18    18    18    18     3 -1.000000      !   "                      (8)
 23    25    18    18    12    12     3 -1.000000      !   "                      (9)
 23    25    18    18    19    19     3 -1.000000      !   "                      (10)
 24    24    18    18    11    11     3 -1.000000      !   "                      (11)
 24    24    18    18    20    20     3 -1.000000      !   "                      (12)
 20    25    19    20    15    15     1 -1.000000      ! VERTICAL STABILIZER      (13)
 22    25    21    22    15    15     1 -1.000000      !   "                      (14)
 24    25    23    24    15    15     1 -1.000000      !   "                      (15)
 13    13    15    18    17    17     2 -1.000000      ! INTAKE COVERS            (16)
 13    13    15    18    14    14     2 -1.000000      !   "                      (17)
 12    24    18    18    14    17     3 -1.000000      ! FUSELAGE - TOP           (18)
  8    11    18    18    15    16     3 -1.000000      !   "                      (19)
  6     7    16    16    15    16     3 -1.000000      !   "                      (20)
  6    13    14    14    15    16     3 -1.000000      ! FUSELAGE - BOTTOM        (21)
 14    24    14    14    14    17     3 -1.000000      !   "                      (22)
  5     5    15    16    15    16     2 -1.000000      ! FUSELAGE - FRONT         (23)
  7     7    17    18    15    16     2 -1.000000      !   "                      (24)
 24    24    15    18    14    17     2 -1.000000      ! FUSELAGE - BACK          (25)
  6     7    15    16    14    14     1 -1.000000      ! FUSELAGE - SIDES         (26)
  6     7    15    16    16    16     1 -1.000000      !   "                      (27)
  8    13    15    18    14    14     1 -1.000000      !   "                      (28)
  8    13    15    18    16    16     1 -1.000000      !   "                      (29)
 14    24    15    18    13    13     1 -1.000000      !   "                      (30)
 14    24    15    18    17    17     1 -1.000000      !   "                      (31)
  0     0     0     0     0     0     0  0.000000
  0     0     0     0     0     0  0.000000  0.000000
  1    30    30    30     1    30     1  1.000000      ! EXCITATION PLANE
  0     0     0     0     0     0     0  0.000000
 16    16     1    19    19     1    15    16     1    ! TEST POINTS
  0     0     0     0     0     0     0     0     0
500                                                     ! NUMBER OF ITERATIONS
```

Figure 5. Formatted input data file for the aircraft EMP interaction problem.

IV. NUMERICAL RESULTS

In this section, two example problems that we have worked with GTEC are presented; the first is the frequency domain analysis of a fin line. Secondly, an exemplary result for the aircraft EMP problem previously described will be given. These two diverse applications of GTEC demonstrate the versatility of the GTEC package.

The geometry used for the dispersion characterization of a fin line is shown in Figure 6. The technique used is to resonate a length of the finline and determine the resonant frequency of the structure via the Fourier tranform of the impulse response. Since the structure is continuous in the z coordinate direction, a stepped impedance boundary has been utilized to reduce computer time and storage requirements. Symmetry in the y direction was also exploited in the calculations. For a cavity length (in the z direction) of 4mm, the GTEC analysis yielded $b/\lambda = 0.23$, while the hybrid two dimensional TLM transverse resonance analysis in [17] yielded $b/\lambda = 0.25$. By changing the cavity length, additional resonances can be determined and from this data the dispersion curve can be plotted.

As an example of a time domain analysis with GTEC, the results for the axial surface current at TP208 on the aircraft of Figure 4 are presented in Figure 7. The excitation function used is given by

$$E_x = E_o[\exp(-t/\tau_f) - \exp(-t/\tau_r)]$$

a = 7.112 mm

b = 3.556 mm

c = 4.0 mm

d = 0.46228 mm

s = 0.254 mm

ϵ_r = 2.22

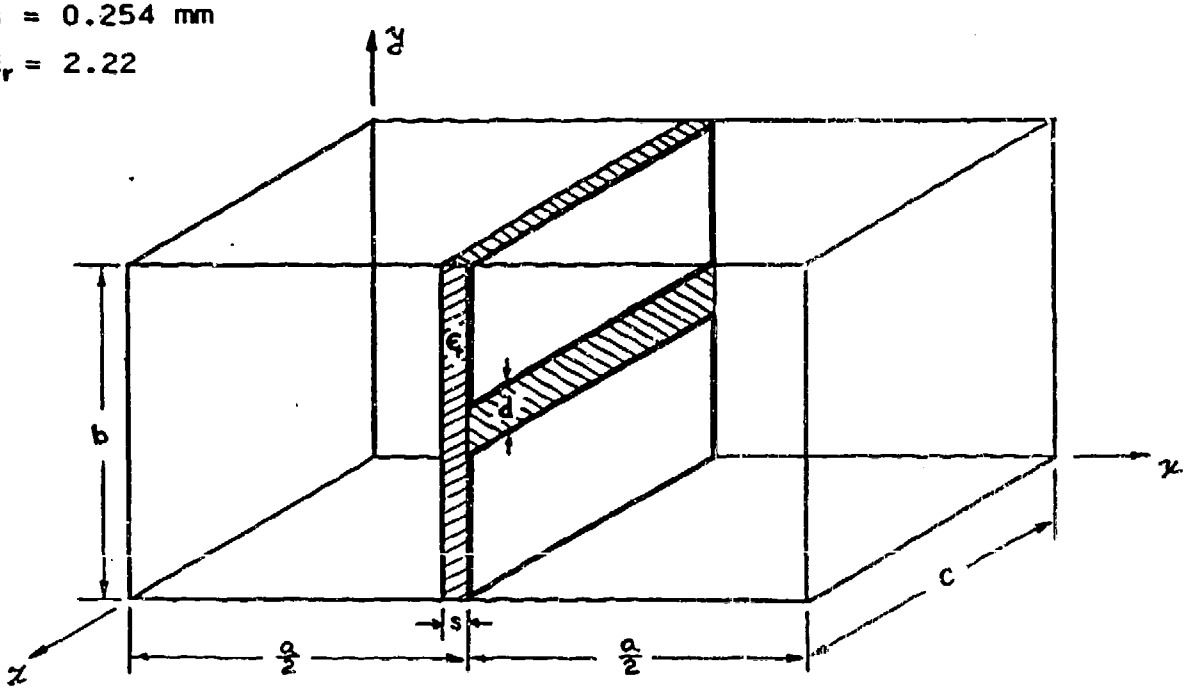


Figure 6. Geometry of fin line cavity used for GTEC analysis.

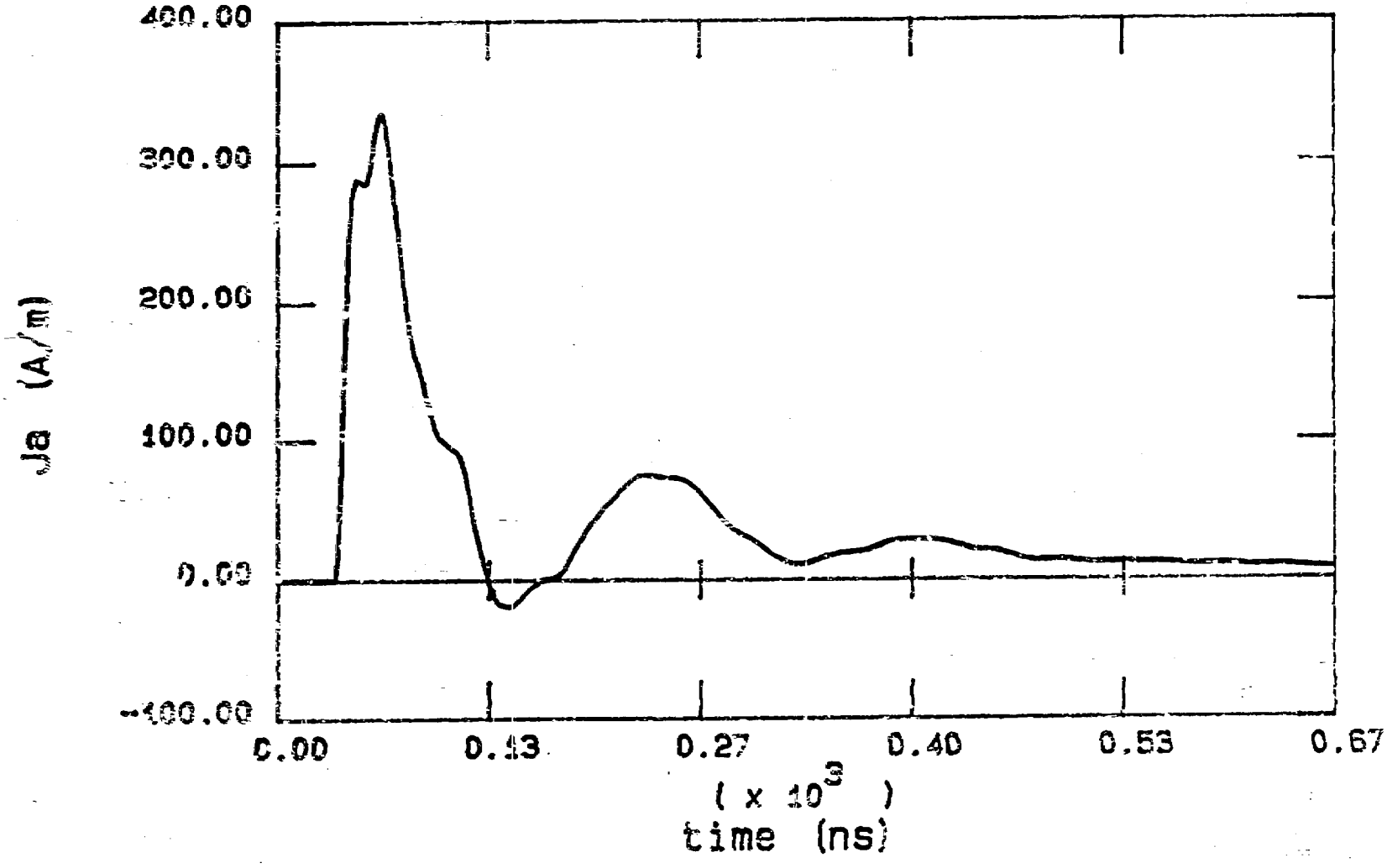


Figure 7. Axial surface current induced on aircraft by incident EMP excitation.

where

$$E_o = 5.97 \times 10^4 \text{ V/m}$$
$$\tau_f = 245 \times 10^{-9} \text{ s}$$
$$\tau_r = 2.85 \times 10^{-9} \text{ s}.$$

The aircraft was assumed to be in flight for these calculations (i.e., no ground plane was modelled). The results are in good agreement with those calculated from other methods as presented in [18].

V. CONCLUSIONS

In its current form, GTEC provides a very powerful electromagnetic problem solving tool. Future developments to the code include the addition of a general time domain diakoptics routine. The incorporation of diakoptics will make the package more efficient for design (synthesis) applications as well as computationally more efficent for the analysis of many problems.

The direct calculation of radiated or scattered fields in the far field region of a scatterer is not pratical with TLM due to the size of the mesh that would be required. For this reason, a near-to-far field tranformation algorithm will be added to the GTEC package.

The addition of an extensive graphics package into the program will eliminate the need for assembling the input data table manually, and also enhance the output of the program. A simple computer aided design (CAD) program is all that will be required to allow the geometry of the problem to be entered graphically on a graphics device and then automatically converted to input data for the TLM solution.

Since the TLM algorithm is quite efficient, implementation on

a PC is very practical and a PC version of GTEC is currently under development. In its final form, the PC GTEC package will incorporate all of the features of the VAX version and also extensive graphic capabilities.

REFERENCES

[1] G. Kron, "Equivalent Circuit of the Field Equations of Maxwell - I," Proc. of the IRE, vol. 32, May 1944, pp. 289-299.

[2] J. Whinnery, C. Concordia, W. Ridgway, and G. Kron, "Network Analyzer Studies of Electromagnetic Cavity Resonators," Proc. of the IRE, vol. 32, June 1944, pp. 360-367.

[3] P. B. Johns and R. L. Beurle, "Numerical Solution of 2-Dimensional Scattering Problems Using a Transmission-line Matrix," Proc. IEE, 1971, vol. 118, no. 9, 1971, pp. 1203-1208.

[4] P. B. Johns, "New Symmetrical Condensed Node for Three-dimensional Solution of Electromagnetic-Wave Problems by TLM," Electron. Lett., 1986, vol. 22, no. 3, pp. 162-164.

[5] P. B Johns, "A Symmetrical Condensed Node for the TLM Method," IEEE Trans. Microwave Theory Tech., 1987, vol. MTT-35, no. 4, pp. 370-377.

[6] R. Allen, A. Mallik, and P. Johns, "Numerical Results for the Symmetrical Condensed TLM Node," IEEE Trans. Microwave Theory Tech., 1987, vol. MTT-35, no. 3, pp. 378-382.

[7] P. B. Johns and G. F. Slater, "Transient Analysis of Waveguides with Curved Boundaries," Electron. Lett., 1973, vol. 9, no. 21, pp. 486-487.

[8] P. B. Johns and K. Akhtarzad, "The use of Time Domain Diakoptics in Time Discrete Models of Fields," Int. J. for Numerical Meth. in Eng., 1981, vol. 17, pp. 1-14.

[9] S. Akhtarzad and P. B. Johns, "Three-Dimensional Transmission-Line Matrix Computer Analysis of Microstrip Resonators," IEEE Trans. Microwave Theory Tech., 1975, vol. MTT-23, no. 12, pp. 990-997.

[10] P. Naylor, C. Christopoulos, and P. B. Johns, "The Use of Transmission-Line Modelling (TLM) in Internal Interaction Problems," Nuclear EMP Meeting, Albuquerque, NM, May 19-23, 1986.

[11] W. N. R. Stevens and P. B. Johns, "Imaging by Numerical Analysis of Wave Scattering in the Time Domain using Transmission-Line Modelling, Signal Processing, and Optimization," IEE Proc., vol. 129, pt. A, no. 3, pp. 190-197.

[12] J. Sarma and P. N. Robson, "Time-Domain Numerical Computations of Electromagnetic Fields in Cylindrical Co-Ordinants Using the Transmission Line Matrix: Evaluation of Radiation Losses from a Charge Bunch Passing Through a Pill-Box Resonator," Nuclear Inst. and Meth., 1979, vol. 159, pp. 529-541.

[13] P. B. Johns, "A Simple Explicit and Unconditionally Stable Numerical Routine for the Solution of the Diffusion Equation," Int. J. for Numerical Meth. in Eng., 1977, vol. 11, pp. 1307-1328.

[14] P. B. Johns and M. O'Brien, "Use of the Transmission-Line Modelling (T.L.M.) Method to Solve Non-linear Lumped Networks," The Radio and Electronic Engineer, 1980, vol. 50, no. 1/2, pp. 59-70.

[15] F. J. German and L. S. Riggs, "GTEC User's Manual," Department of Electrical Engineering, Auburn University, Auburn, AL, October 1987.

[16] J. E. Sitch and P. B. Johns, "Transmission-Line Matrix Analysis of Continuous Waveguiding Structures Using Stepped-Impedance Boundaries," Microwaves, Optics, and Acoustics, 1977, vol. 1, no. 5, pp. 181-184.

[17] Y. -C. Shih and W. J. R. Hoefer, "Dominant and Second-Order Mode Cutoff Frequencies in Fin Lines Calculated with a Two-Dimensinal TLM Program," IEEE Trans. Microwave Theory Tech., vol. MTT-28, no. 12, pp. 1443-1448.

[18] J. Moore and R. Pizer, Moment Methods in Electromagnetics, Research Studies Press, 1984

OBJECT-ORIENTED SCIENTIFIC PROGRAMMING
- A TRANSMISSION LINE CODE EXAMPLE OF 'SMART' ARRAYS -

Daniel F. Higgins
1040 Veronica Springs Road
Santa Barbara, CA 93105
(805) 682-5248

Introduction

Arrays are data structures often used in many types of numerical calculations. In traditional programming of finite-difference models, for example, one usually just defines a set of arrays to represent a discrete version of some function of space or time. Each array holds only numeric values representing the function of interest, while all mathematical relationships between the values are built into equations expressed inside the main program. An alternative to this approach uses ideas recently popularized in newer computer languages - namely the concept of "object oriented programming"[1]. In this case, an array can do more than just store data (i.e. values); an array may also contain the algorithms needed to calculate new values and to do such things as display cell values or graphically plot relationships. One thus thinks of the array as an "object" which contains not only data, but also the instructions on how to process or display the data it contains.

The ideas presented here started out as a time-domain finite-difference model of a transmission line that was implemented using a commercial spreadsheet program[2]. Use of the spreadsheet was very convenient because a one-dimensional array could just be represented as a column in the spreadsheet and graphic output displays are easily generated. It was noted that spreadsheet cells can not only contain some value, but also a mathematical expression that can be used for recalculating the value. This suggested building a "smart array" with similar capabilities, but capable of faster calculational speed than can be obtained with commercial spreadsheets. These "smart arrays" were then used to build a finite-difference code for calculating transmission line transients.

'Smart Arrays'

Consider first the ordinary array as used in traditional programming languages such as FORTRAN. One first has to tell the computer how large the array is, using something like a DIMENSION statement. The computer then reserves an appropriate amount of storage with one 'cell' for every element in the array. Typically, the array name points to the first cell, and subsequent cells are sequentially arranged in memory. One can usually carry out only two operations on each element of an array - namely, putting a value into the cell, or removing a value from the cell. One can think of the cell name combined with an index as referring to a specific location in memory,

and the contents of that memory location (address) is where the cell value is stored. (See Figure 1 below.)

```
DIMENSION AAA (5)
```

Reserves space for a 5 element array
The name 'AAA' is associated with the address of the first element of the array

```
AAA (2) = 2.3
```

Stores the number 2.3 into the 2nd slot of the array

```
XXX = AAA (3)
```

Puts the 3rd element of AAA into the variable XXX

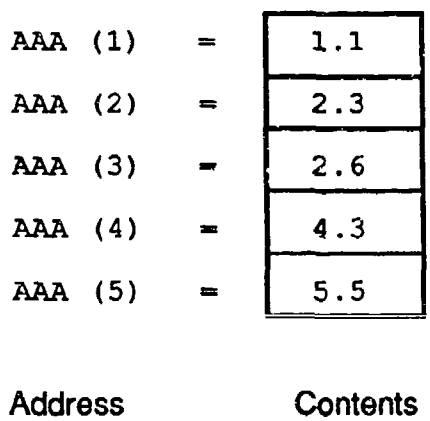


Figure 1 - The Ordinary Array

Now consider the issue of how one might create an array which resembles a column in a spreadshset where each cell can contain a value and some mathematical expression for calculating that value. In addition, other procedures for manipulating array data should also be included as part of the array. The method used in this work is represented in Figure 2, where each element of the array is represented in memory by two cells. One of the cells contains the element value and the other contains a pointer to a some expression or algorithm used to calculate the value. In addition, each array has a pointer to what is called a dispatch table. This table contains a list of actions which might be taken on the array. As indicated, one can not

only save and retrieve the values of individual elements of the array, but also change the array size, change the pointers to the recalculation procedures, and execute the recalculation procedures so that new values are stored in the value cells. Thus, a 'Smart Array' contains not only numerical data, but also all the procedures needed to manipulate and update that data.

```
5 NEW.SVECTOR AAA
```

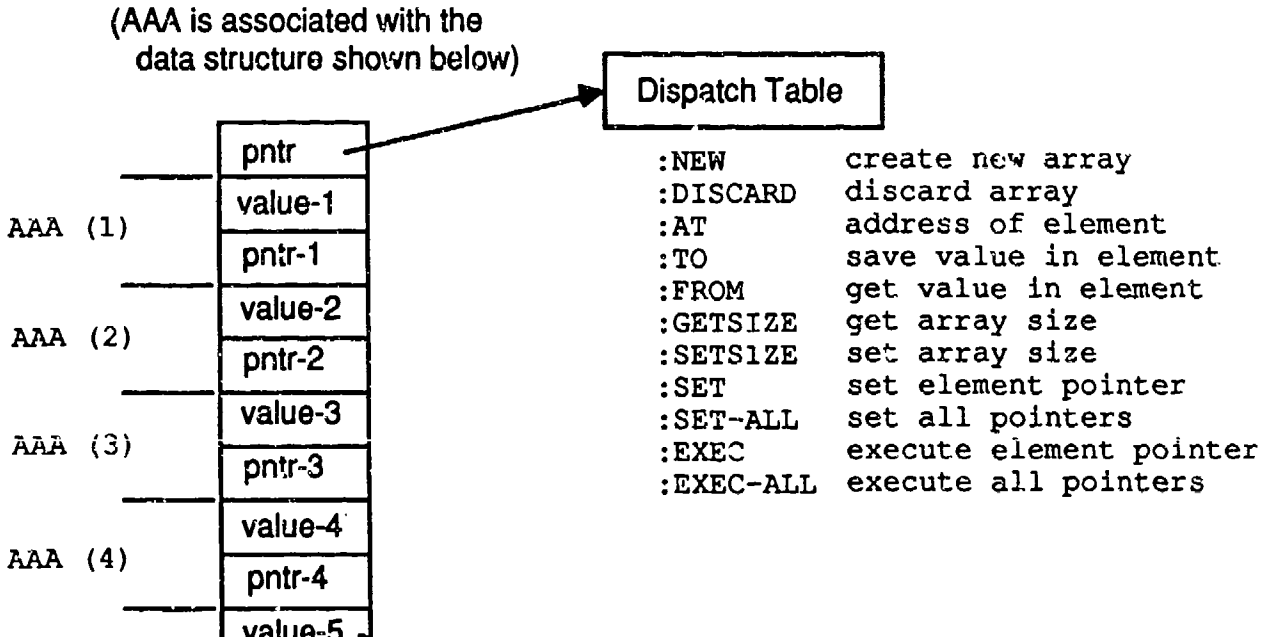


Figure 2 - The 'Smart' Array

One would create a 'smart array' named AAA with 5 elements with the expression

```
5 NEW.SVECTOR AAA
```

(Note that the size of the array (5) precedes the word "NEW.SVECTOR" and the name "AAA". This use of Reverse Polish notation is a feature of the Forth language used to create the 'smart arrays'. Also, one-dimensional arrays are referred to a "Vectors" in the actual implementation.) One would store the value 3.14 into the third element of AAA with the statement

```
3.14  3 AAA :TO
```

while the value of the second element would be retrieved by

```
2 AAA :FROM
```

One could also increase the array size to 10 elements by entering

```
10 AAA :SETSIZE
```

Now assume that some calculational procedure called NEW.VALUE has been defined. A pointer to that procedure is installed in all the cells of the array by the statement

```
TOKEN.FOR NEW.VALUE  AAA :SET-ALL
```

One can then use that newly installed procedure to recalculate new values for the entire array by entering

```
AAA :EXEC-ALL
```

Procedures for individual elements in the array can be set or executed by using `:SET` and `:EXECUTE`.

Note that the procedure in any cell can refer to other cells of the array. As in a spreadsheet, it is convenient to be able to refer to a relative location within the array, rather than an absolute position. Thus, each cell "knows" its own index and one can reference that index using the word CURRENT-INDEX. The preceding cell then has an index of
(CURRENT-INDEX) - 1 and the following cell (CURRENT-INDEX) + 1. It is thus easy to write a single procedure for referencing other cells by relative position.

The smart array obviously requires more memory for a give array size than a conventional array due to the storage of a pointer with each value. (In this implementation, pointers can be as small as 2 bytes, while the floating point value is 4 or 8 bytes long.) However, there is little execution time penalty for storing or retrieving values since addition of the pointer just changes the amount of storage allotted for each cell.

The 'smart arrays' discussed here have been implemented on an Apple Macintosh™ microcomputer using the Forth computer language (specifically, MacForth from Creative Solutions, Inc). Forth is a very powerful language that lets the user build all sorts of extensions and special tools like these 'smart arrays'. Similarly, the Macintosh has a number of capabilities that make studies like this one easy. For example, 'smart arrays' are created and stored in a region of dynamic memory called the "heap", which is part of the Macintosh operating system. Array sizes can thus be manipulated and changed in real time, after a program has been compiled. Array

operations can thus be interactive, rather than depending on values entered before compilation.

With large arrays, one would like an easy method of examining and possibly editing the values of individual elements. This capability has been implemented on the Macintosh by the use of "Smart Windows", one of which is shown in Figure 3. On the left is a scrolling list of array element values. Any value can be selected and edited. The plot on the right shows a graphical plot of array values as a function of index. One can attach any 'smart array' to such a 'smart window' and then quickly examine and edit array values.

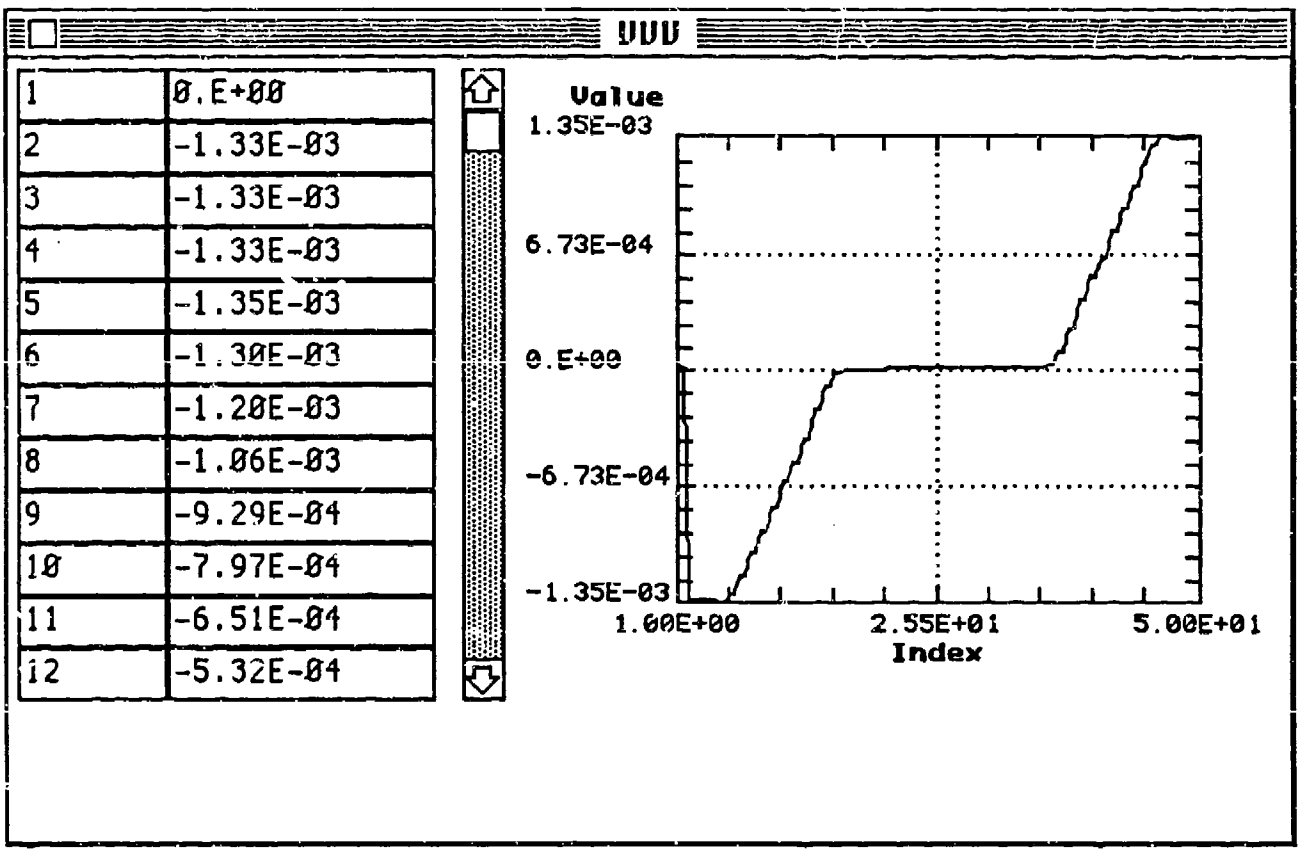


Figure 3 - A 'Smart Window' for the Display and Editing of 'Smart Array' Values

Transmission Line Analysis

Now consider the problem of a time-domain transmission line[3,4]. Such a line is characterized by currents and voltages along the line which are functions of space and time. The current and voltage are determined by the four line parameters, capacitance, inductance, resistance, and conductance per-unit-length, which may also be functions of position and time, the driving voltage source per-unit-length, and the boundary conditions at the ends of the line. The two transmission line equations are

differential equations describing the relationships between these functions.

One method for solving the transmission line differential equations is to form an approximately equivalent set of finite-difference equations where a discrete finite-difference mesh is used to represent space and time. In particular, the spatial mesh can be represented by a number of discrete cells in an array. One can then derive expressions for the values of the current and voltage at a "new" time step in terms of the "old" values. In particular, one can write the new current in terms of the old current at the same location and the old voltage at cells on either side of the cell being considered, with similar expressions available for the "new" voltage. This whole finite-differencing process is summarized in Figures 4-6; this basic method of finite-difference solution is fairly well known[5-8].

Now, one can use 'Smart Arrays' to represent the spatial current and voltage meshes. Each element of the array refers to a particular location. One can then write a procedure corresponding to the equations in Figure 6 which give the new value in terms of the old values. This procedure for calculating the new values is then stored in the pointer cell of each element of the smart array. Each cell of the array then "knows how" to update its own value; for example, values of the voltage array, VVV, for the next time step are obtained by simply executing `VVV :EXEC-ALL` , while a similar expression will update the current array.

In order to keep the calculation quite general, the four line parameters are also implemented as smart arrays. Update procedures would be used if these line parameters were time dependent, or dependent on the current or voltage. (Otherwise, one would not use any update procedure.) A complete time step update thus might look like the following:

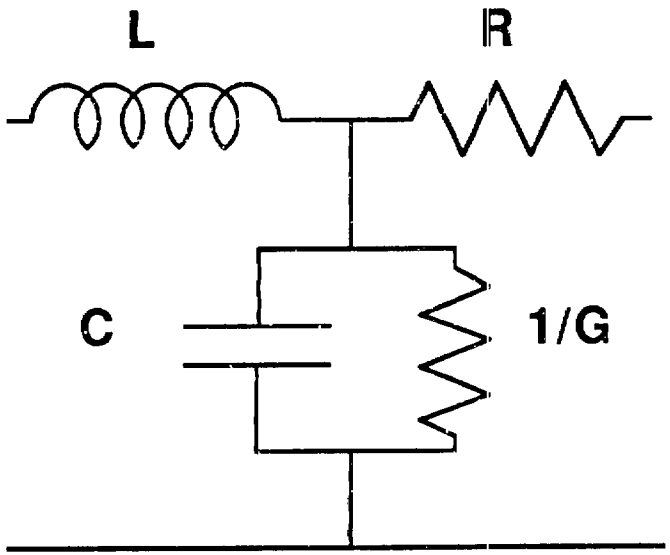
```
TIME = TIME + DT
LL :EXEC-ALL          \ Update the inductance if not constant
...                   \ Update other line parameters
VS :EXEC-ALL          \ Update the voltage source array
VVV :EXEC-ALL         \ Update the voltage array
III :EXEC-ALL         \ Update the current array
```

The time-stepping process is thus effectively isolated from the algorithm used to handle the spatial relationships. One can then assign the current and voltage arrays to "Smart Windows" so that the current and voltage spatial distributions can be displayed as time-stepping moves forward. (Figure 3 shows a voltage array.)

Why Use 'Smart Arrays" ?

The various elements of this approach are really identical with those used in more traditional finite-difference calculations. The difference is in how the elements are arranged and ordered. Data and algorithms are compartmentalized in a different manner with 'smart arrays' which can have certain advantages. For example, with

- The Transmission Line is often used to model various electromagnetic systems
- The Transmission Line is characterized by the four distributed line parameters as well as distributed voltage and current sources and sources/loads at each end
- Analytic solutions for transient excitations limited to a few simple cases
- Electrical Engineers usually taught to think in terms of a circuit model, but more efficient numerical solution techniques may be obtained by starting with the fundamental partial differential equations.



Transmission Line Segment

L = inductance per unit length

R = resistance per unit length

C = capacitance per unit length

G = conductance per unit length

Figure 4 - Transmission Line Models

Differential Equations

$$L\frac{\partial I}{\partial t} + RI + \frac{\partial V}{\partial z} = E_0$$

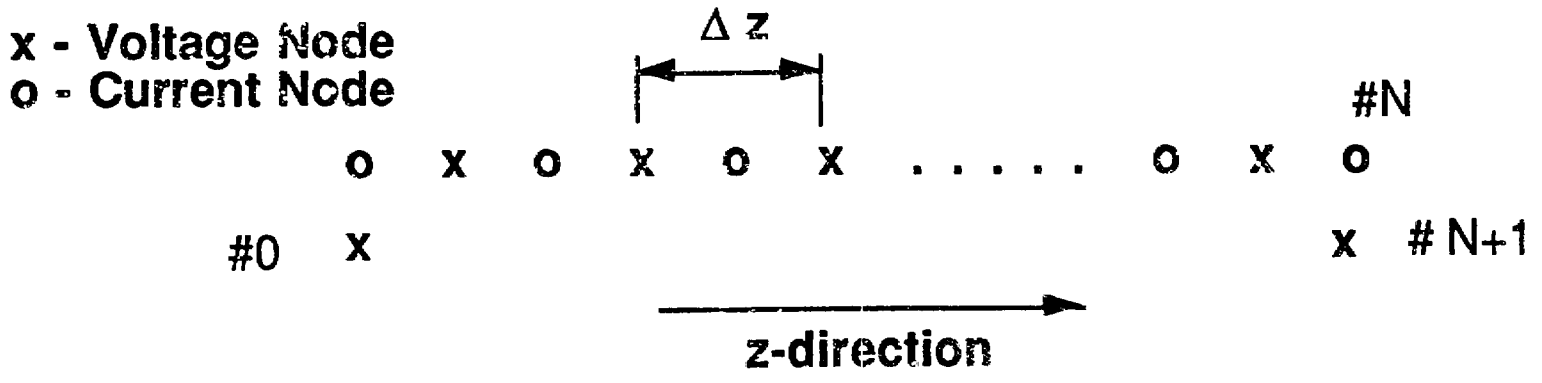
$$C\frac{\partial V}{\partial t} + GV + \frac{\partial I}{\partial z} = 0$$

Equivalent Finite-Difference Equations

$$L\frac{I_k^{n+1} - I_k^n}{\Delta t} + R\,I_k^{n+1} + \frac{V_{k+1/2}^{n+1/2} - V_{k-1/2}^{n+1/2}}{\Delta z} = E_{0\,k}^{n+1/2}$$

$$C\frac{V_{k+1/2}^{n+1/2} - V_{k+1/2}^{n-1/2}}{\Delta t} + G\,V_{k+1/2}^{n+1/2} + \frac{I_{k+1}^n - I_k^n}{\Delta z} = 0$$

Figure 5 - Transmission Line Equations



$$I_k^{n+1} = \frac{E_{0\,k}^{n+1/2}\,\Delta z \;-\; \left(V_{k+1/2}^{n+1/2} - V_{k-1/2}^{n+1/2} \right)}{\left(\frac{L}{\Delta t} + R \right) \Delta z} + \frac{I_k^n}{\left(1 + \frac{R\,\Delta t}{L} \right)}$$

$$V_{k+1/2}^{n+1/2} = \frac{-\left(I_{k+1}^n - I_k^n \right)}{\left(\frac{C}{\Delta t} + G \right) \Delta z} + \frac{V_{k+1/2}^{n-1/2}}{\left(1 + \frac{G\,\Delta t}{C} \right)}$$

Figure 6 - Finite Difference Mesh

'smart arrays' one can experiment with alternative spatial differencing schemes without changing or re-compiling the basic time stepping loop. One simply changes the procedure pointer for the arrays. Or one can change the time dependence of the line parameters after the rest of the code is compiled. Attaching an array to a 'Smart Window' and being able to see the values as the calculation proceeds is also a very useful debugging tool. Programmer-code interaction is thus simplified by the compartmentalization achieved with these techniques.

Another reason for considering these methods is simply that it is a different way of looking at a problem. Adopting a different point-of-view is often very useful in gaining a better understanding of basic mechanisms even though the final numerical results may not be any different than previously achieved with alternative methods.

A basic reason for developing the 'smart arrays' concept is the desire to simplify the scientific programming process. At present, the scientist or engineer spends too much time worrying about the details of his code instead of trying to understand the physical mechanisms being investigated. It was thus hoped that the development of "smarter" computer tools would help alleviate this problem.

References:

1. Brad J. Cox, Object-Oriented Programming - An Evolutionary Approach, Addison-Wesley Publishing Company, Reading, Massachusetts, 1986.

2. Daniel F. Higgins, "Calculating Transmission Line Transients on Personal Computers", 1987 IEEE International Symposium on Electromagnetic Compatibility Symposium Record, Atlanta, GA, August 1987.

3. S. Ramo, J.R. Whinnery, T. Van Duzer, Fields and Waves in Communication Electronics, John Wiley & Sons, New York 1965.

4. E. F. Vance, Coupling to Shielded Cables, John Wiley & Sons, New York, 1978.

5. David Potter, Computational Physics, John Wiley & Sons, London, 1973.

6. W. H. Press, B.P. Flannery, S.A. Teukolsky, W.T. Vetterling, Numerical Recipes, Cambridge University Press, Cambridge, 1986.

7. T.A. Tumolillo, J.P. Wondra, "MEEC-3D: A Computer Code for Self-Consistent Solution of the Maxwell-Lorentz Equations in Three Dimensions", IEEE Trans. on Nuclear Science, Vol NS-24, No. 6, Dec 1977.

8. R. Holland, "THREDE: A Free-Field EMP Coupling and Scattering Code", IEEE Trans. on Nuclear Science, Vol. NS-24, No. 6, Dec 1977.

CALCULATION OF ANTENNA INPUT IMPEDANCE

USING

FINITE DIFFERENCE TIME DOMAIN

K. S. KUNZ AND R. J. LUEBBERS

ELECTRICAL ENGINEERING DEPARTMENT

UNIVERSITY PARK, PA 16802

DEFINITION OF FINITE DIFFERENCE TIME DOMAIN (FDTD) TECHNIQUE AND THE METHOD OF MOMENTS (MOM)

- FDTD based on linearized, central differenced time domain Maxwell curl equations, i.e.,

$$\nabla \times E = -\frac{\partial B}{\partial t} \rightarrow H_x(t_{n+1}) = H_x(t_n) + \frac{\Delta t}{\mu}\left[\frac{\Delta E_y(t_{n+\frac{1}{2}})}{\Delta z} \quad \frac{-\Delta E_z(t_{n+\frac{1}{2}})}{\Delta y}\right]$$

$$H_y(t_{n+1}) = \ldots$$

$$H_z(t_{n+1}) = \ldots$$

$$\nabla \times H = \sigma E + \frac{\partial E}{\partial t} \rightarrow \ldots$$

where at the surface of a metal $E^{scat} = -E^{inc}$

- MOM, as applied here, divides a wire into subsections and obtains a generalized impedance matrix [Z] to describe the electromagnetic interactions between wire subsections, i.e.,

$$[Z]\ [I] = [V]$$

where [I] is a matrix describing the currents on the subsection, [V] the electric field excitation at a single frequency on the same subsections. From a know [Z] and [V], [I] can be found using standard matrix manipulations

CHARACTERISTICS OF THE TWO TECHNIQUES

- FDTD
  - time domain formulation
  - best with volumetric scatterers
  - approximate/engineering code
  - good with lossy dielectrics including anisotropic
  - well suited to interior coupling problems

- MOM
  - frequency domain formulation
  - best with thin wires
  - very accurate
  - complex lossy dielectrics not readily modeled
  - must be used very carefully on interior coupling problems

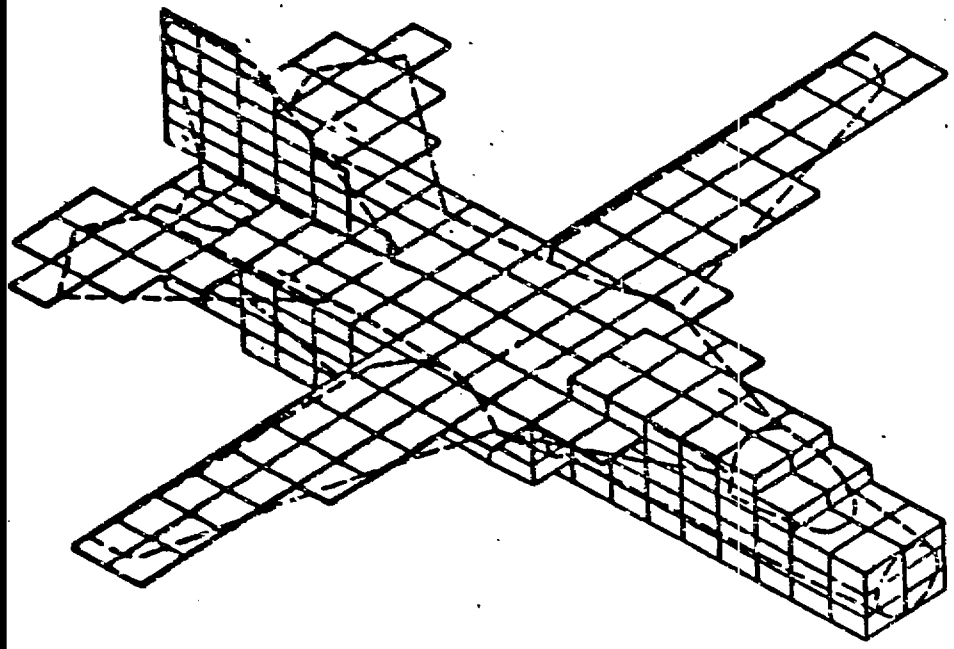


Figure 1. F-111 Finite Difference Model

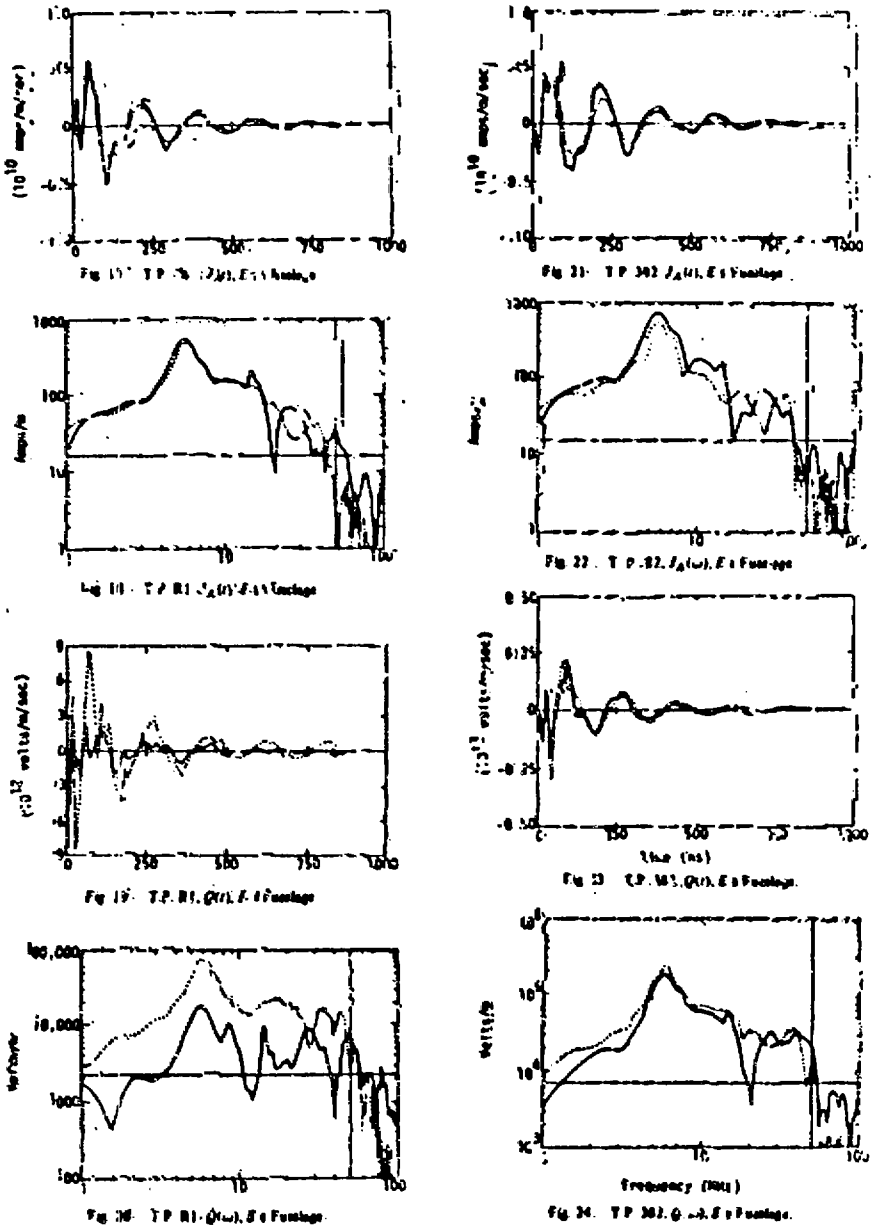


Figure 2. Sample of Predicted vs Measured F-111 Responses

LOSSY DIELECTRIC CAPABILITIES

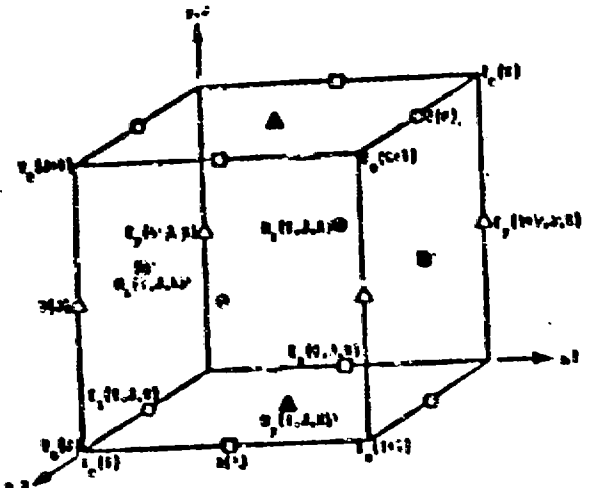


Fig. 1. Convention for imposing the (I, J, K) indices on the (x, y, z) problem space, and location of the six field evaluation points on a typical cell

The lossy-dielectric version of THREDE is based upon

$$\mu \frac{\partial H^s}{\partial t} + \sigma^* H^s = -\nabla \times E^s - \sigma^* H^i - (\mu - \mu_0) \frac{\partial H^i}{\partial t}$$

$$\epsilon \frac{\partial E^s}{\partial t} + \sigma E^s = \nabla \times H^s - \sigma E^i - (\epsilon - \epsilon_0) \frac{\partial E^i}{\partial t} .$$

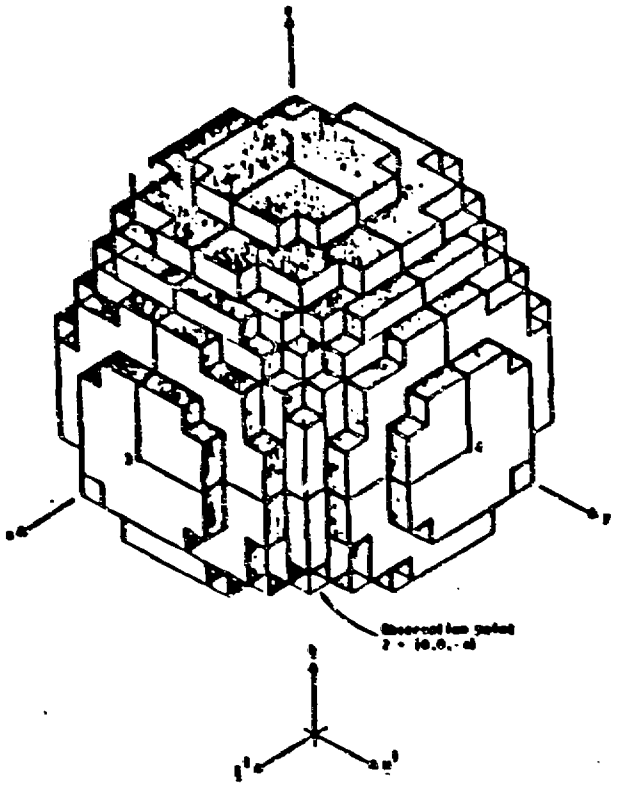


Fig. 2. THREDE model of a dielectric sphere with incident field and observation points indicated. The numbered observation points marked in this figure refer to the observation points cited in Figs. 3-8



Fig. 5. $E_z^s = -E_z^i$ at observation point 2 (pole of illuminated hemisphere) for $\epsilon = 9\epsilon_0$

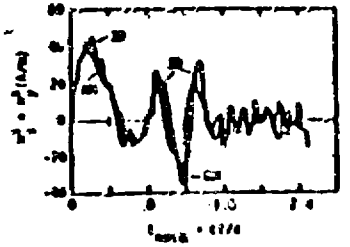


Fig. 6. $H_y^s = +H_y^i$ at observation point 2 for $\epsilon = 9\epsilon_0$

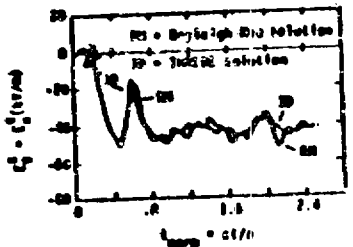


Fig. 3. $E_y^s = +E_y^i$ at observation point 1 (pole of dark hemisphere) for $\epsilon = 9\epsilon_0$

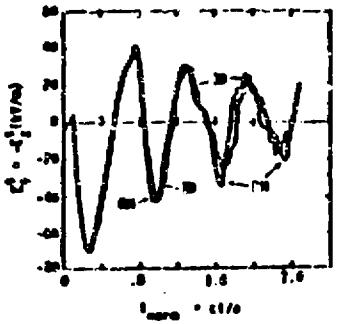


Fig. 7. $E_y^s = -E_y^i$ at observation point 3 for $\epsilon = 9\epsilon_0$

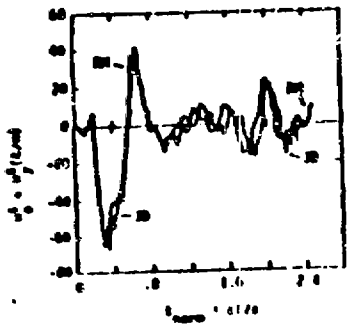


Fig. 4. $H_x^s = +H_x^i$ at observation point 1 for $\epsilon = 9\epsilon_0$

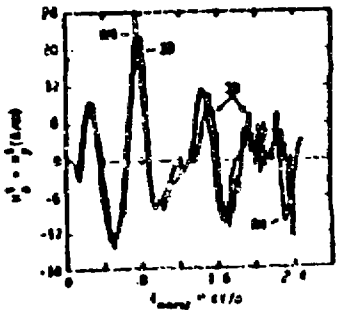


Fig. 8. $H_x^s = +H_x^i$ at observation point 4 for $\epsilon = 9\epsilon_0$

FIGURE 3.

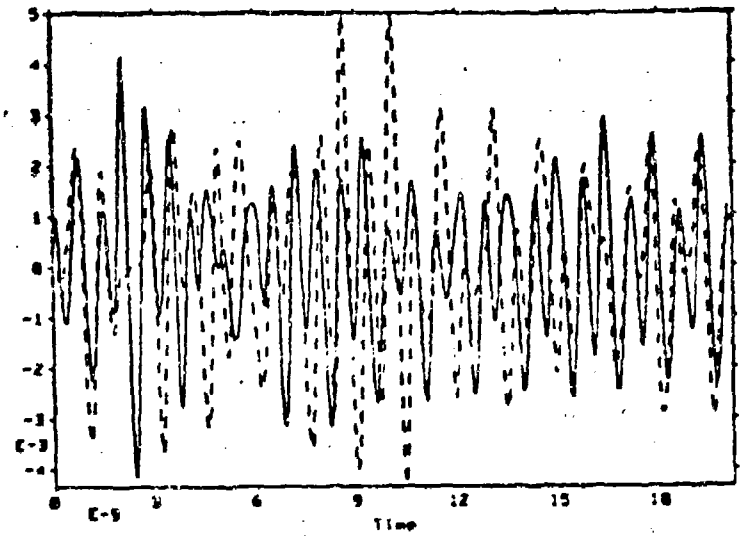


Figure 3-45 Overlay of the Measured Short Circuit Current of a 22.5 cm Wire at Test Point 2 (Solid) versus the Compensated Computed Results (Dashed..

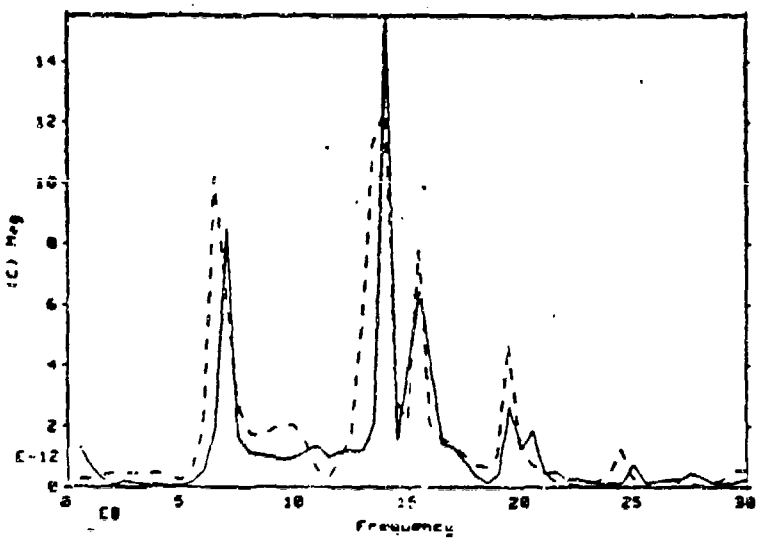


Figure 3-46 Fourier Transform Overlays of the Measured Short Circuit Current of a 22.5 cm Wire at Test Point 2 (Solid) versus the Compensated Computed Results (Dashed).

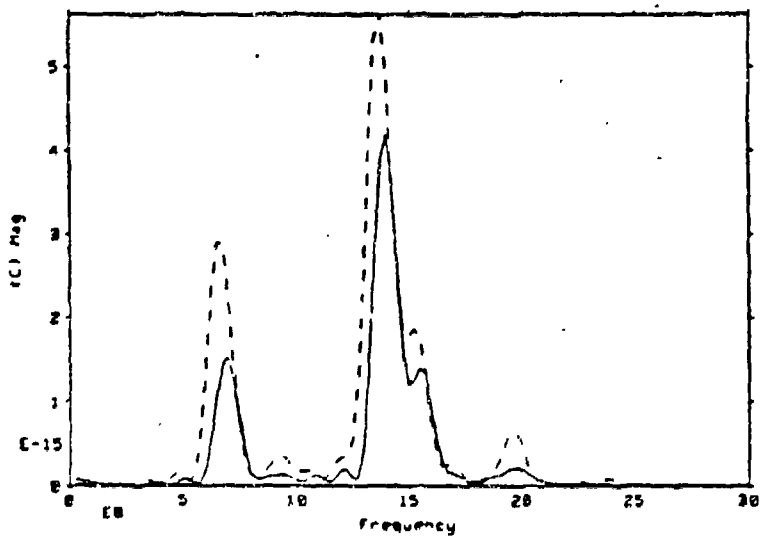


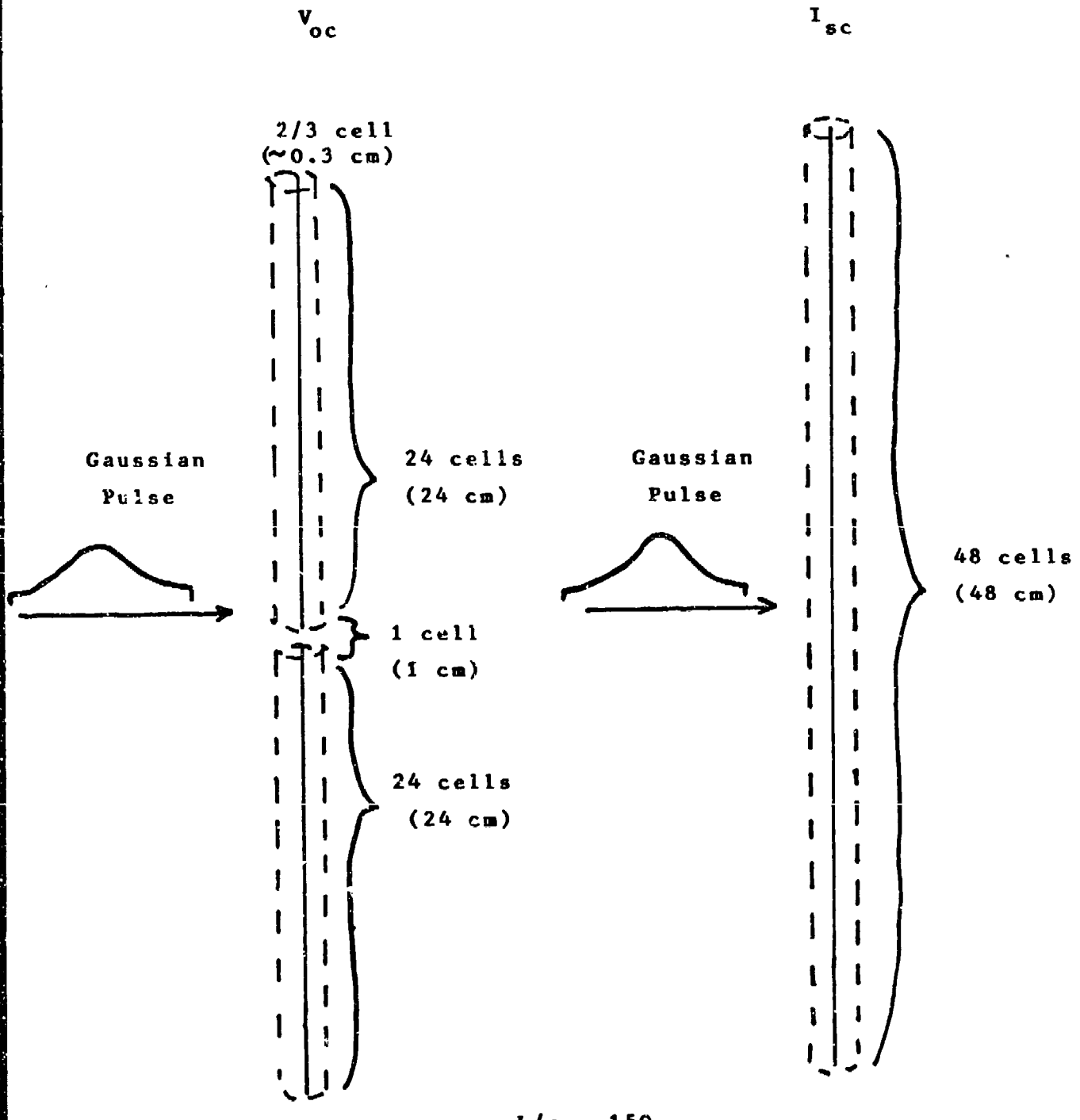
Figure 3-47 Power Spectral Density Overlays of the Measured Short Circuit

NEED FOR VALIDATED THIN WIRE ANTENNA MODELING

- Simple antennas can readily be made complex
  - buried
  - coated
  - enclosed
  - fattened
  - placed over complex shapes/complex materials
- FDTD good for handling above complexities
- Need to know what are the effects of the complexities and what are the limits of FDTD with respect to a simple antenna, i.e.,
  - dynamic range
  - DC limit
  - upper frequency limit
  - fidelity/accuracy
- Can then begin to separate contributions

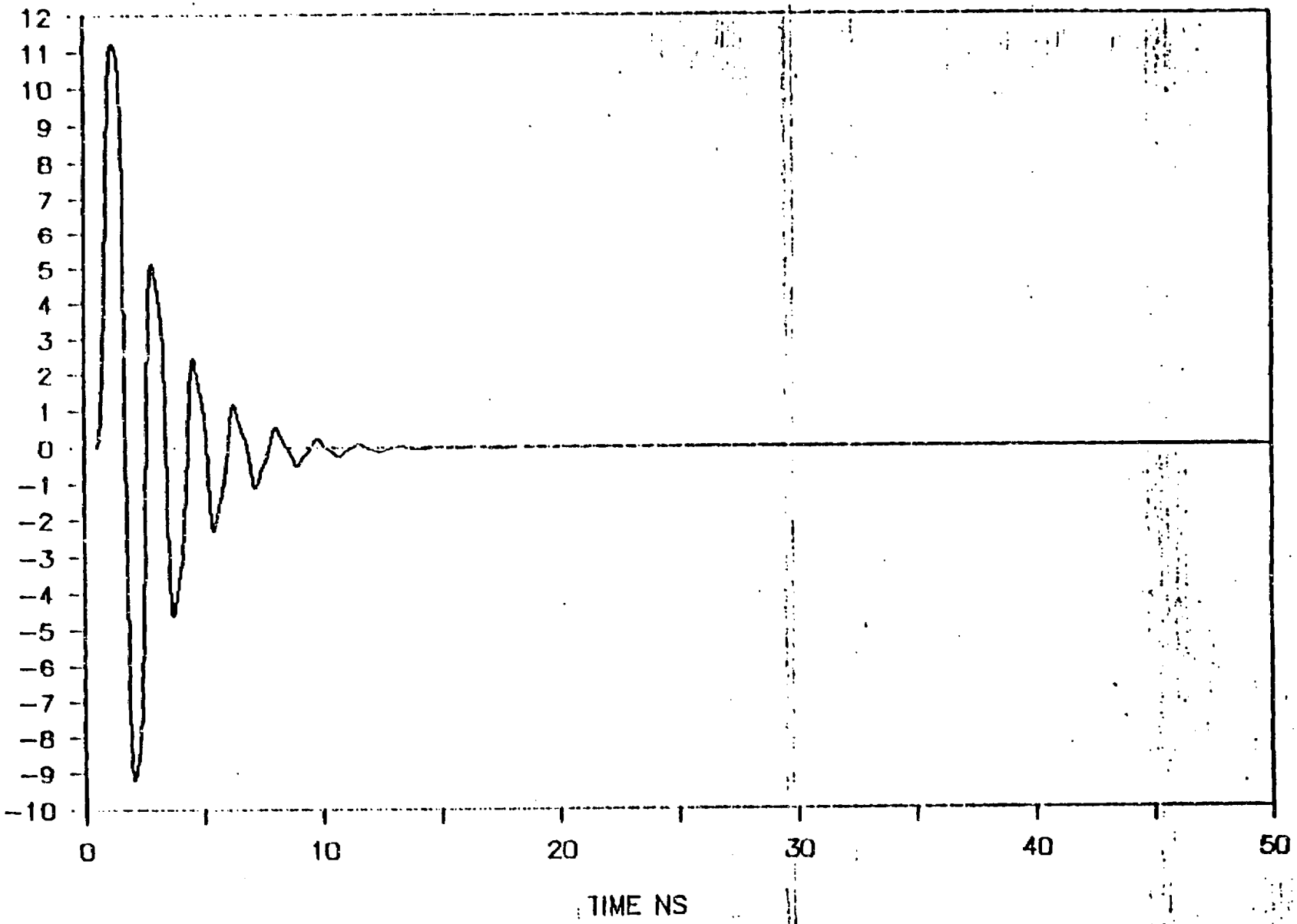
THIN WIRE MODEL

- Dipole Antenna
- Line of $E^{scat} = - E^{inc}$ field components define the arms
- Approximately 2/3 cell thick
- Cells 1 cm high, 0.5 cm x 0.5 cm in cross section
- 24 cell arms
- extra open cell between arms for V_{OC} predictions
  (I_{SC} predictions use continuous 48 cell wire)
- Gaussian excitation - e folds in 16 Δt, truncated at 64 Δt
- Problem space (6 x 64 x 16 cells)
- Total fields used for response calculations

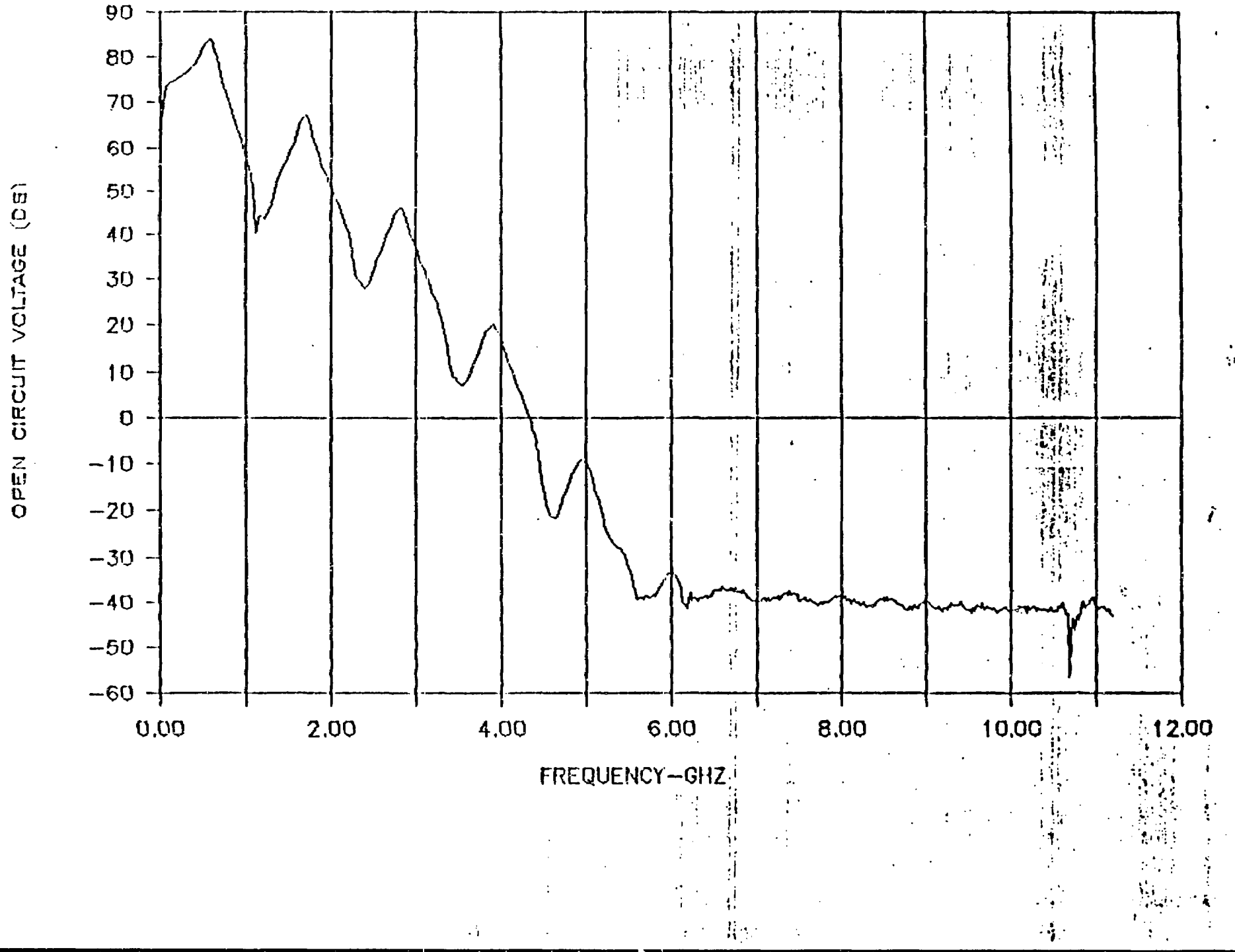

V_{oc}
I_{sc}
2/3 cell
(~0.3 cm)
Gaussian
Pulse
24 cells
(24 cm)
1 cell
(1 cm)
24 cells
(24 cm)
Gaussian
Pulse
48 cells
(48 cm)

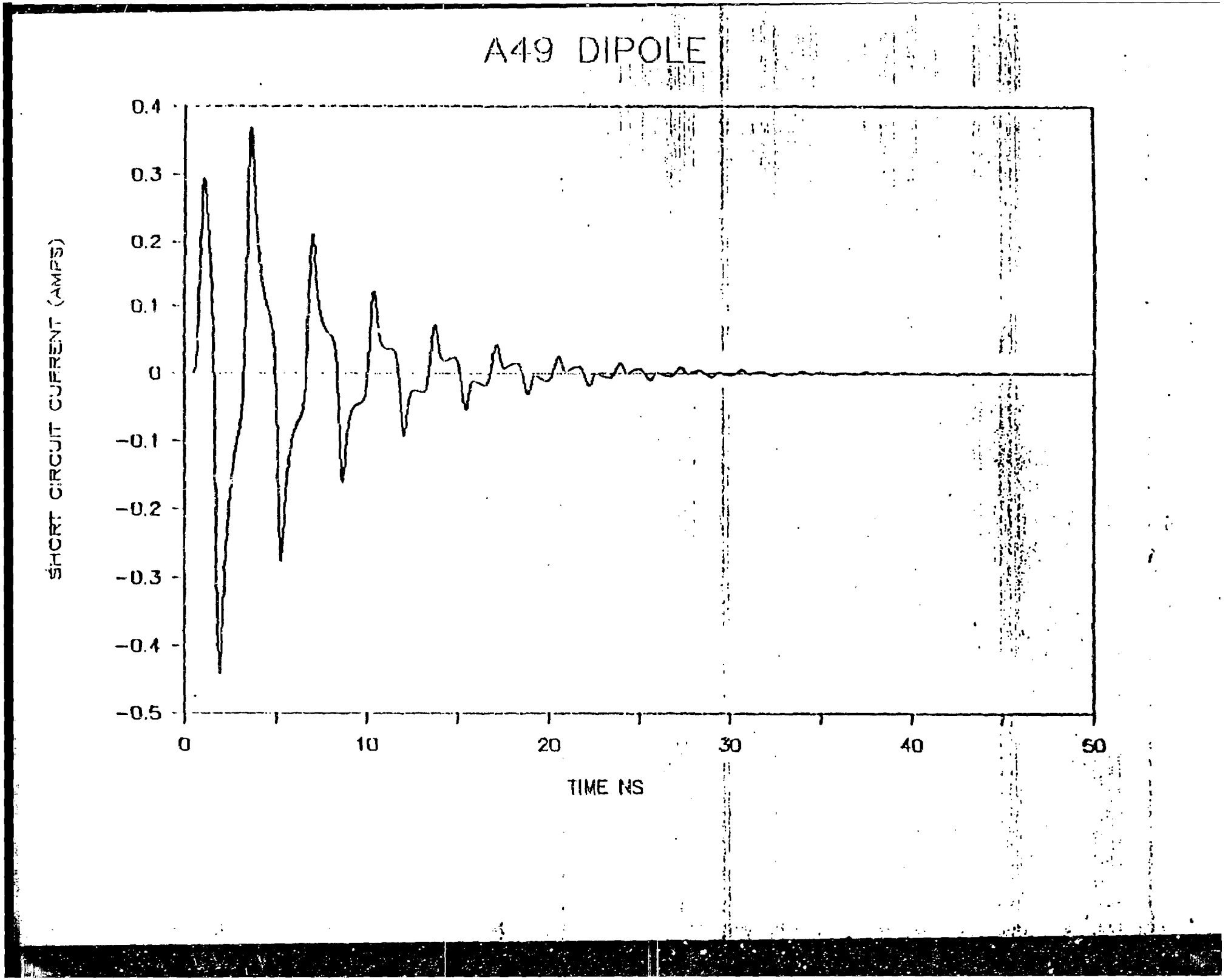
L/a ~ 150

A49 DIPOLE

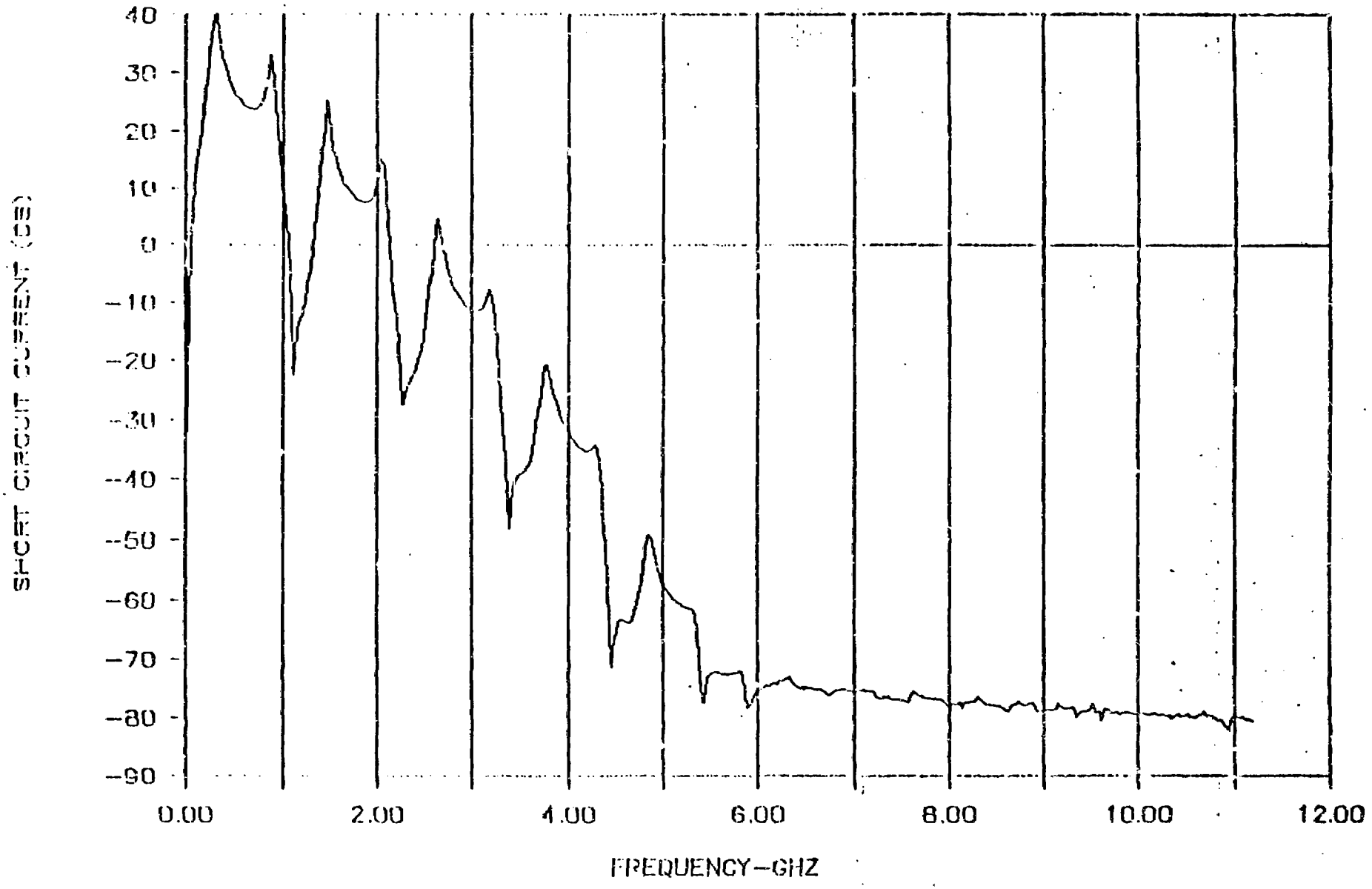

OPEN CIRCUIT VOLTAGE (VOLTS)
(Thousands)
12
11
10
9
8
7
6
5
4
3
2
1
0
−1
−2
−3
−4
−5
−6
−7
−8
−9
−10
0
10
20
30
40
50
TIME NS

A49 DIPOLE

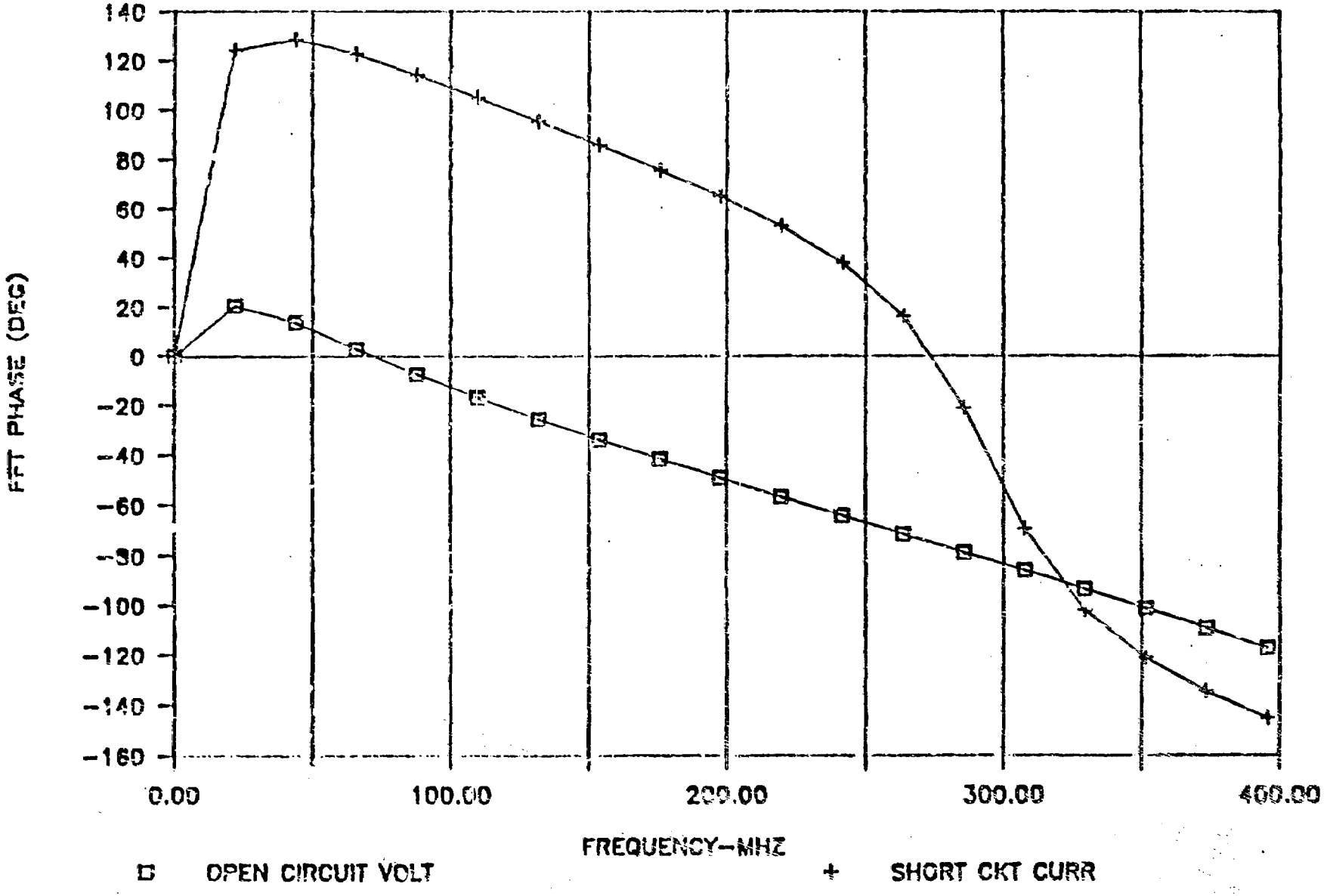

90
80
70
60
50
40
30
20
10
0
-10
-20
-30
-40
-50
-60
OPEN CIRCUIT VOLTAGE (DB)
0.00
2.00
4.00
6.00
8.00
10.00
12.00
FREQUENCY-GHZ


A49 DIPOLE
SHORT CIRCUIT CURRENT (AMPS)
0.4
0.3
0.2
0.1
0
-0.1
-0.2
-0.3
-0.4
-0.5
0
10
20
30
40
50
TIME NS

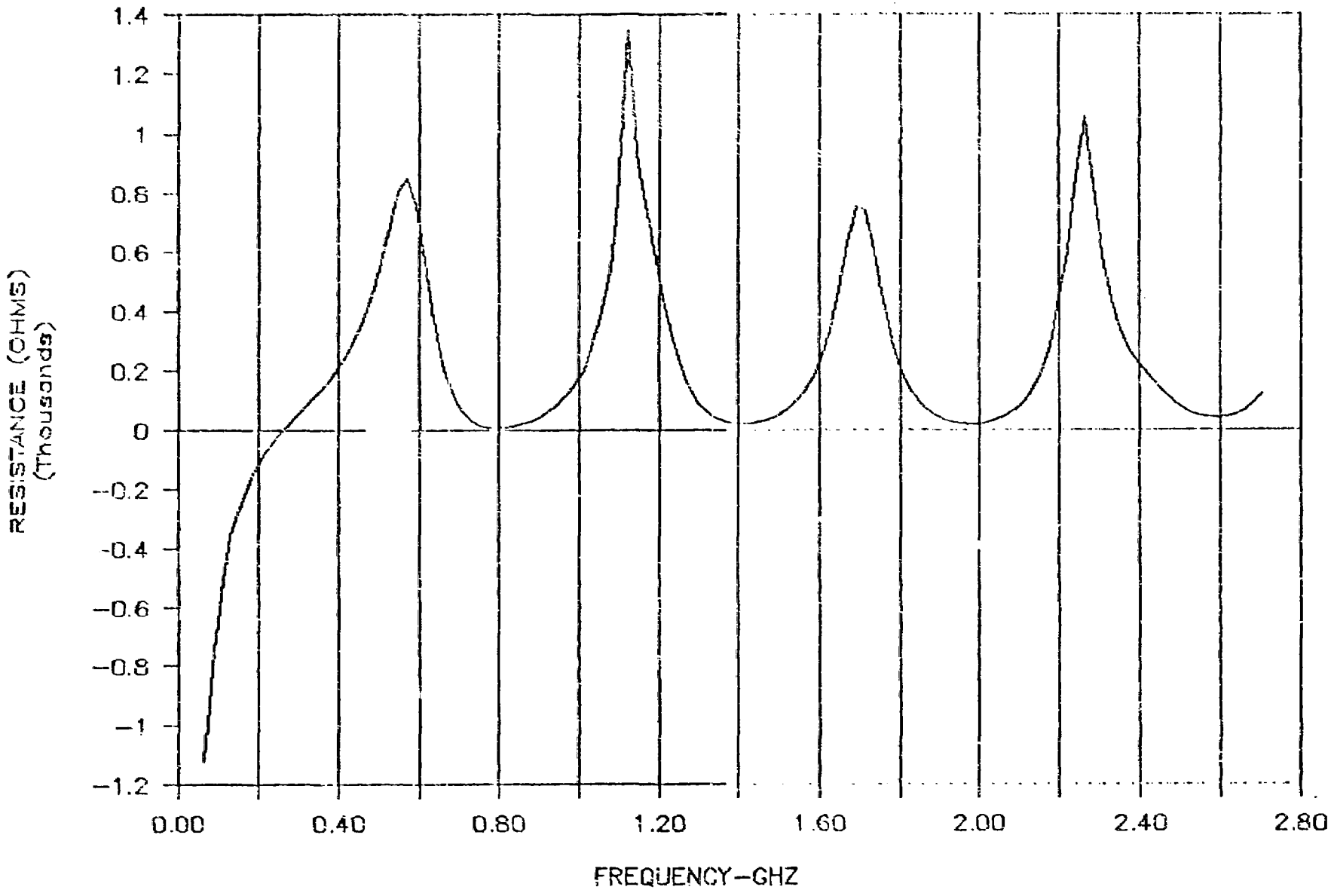
A49 DIPOLE


40
30
20
10
0
-10
-20
-30
-40
-50
-60
-70
-80
-90
SHORT CIRCUIT CURRENT (DB)
0.00
2.00
4.00
6.00
8.00
10.00
12.00
FREQUENCY-GHZ

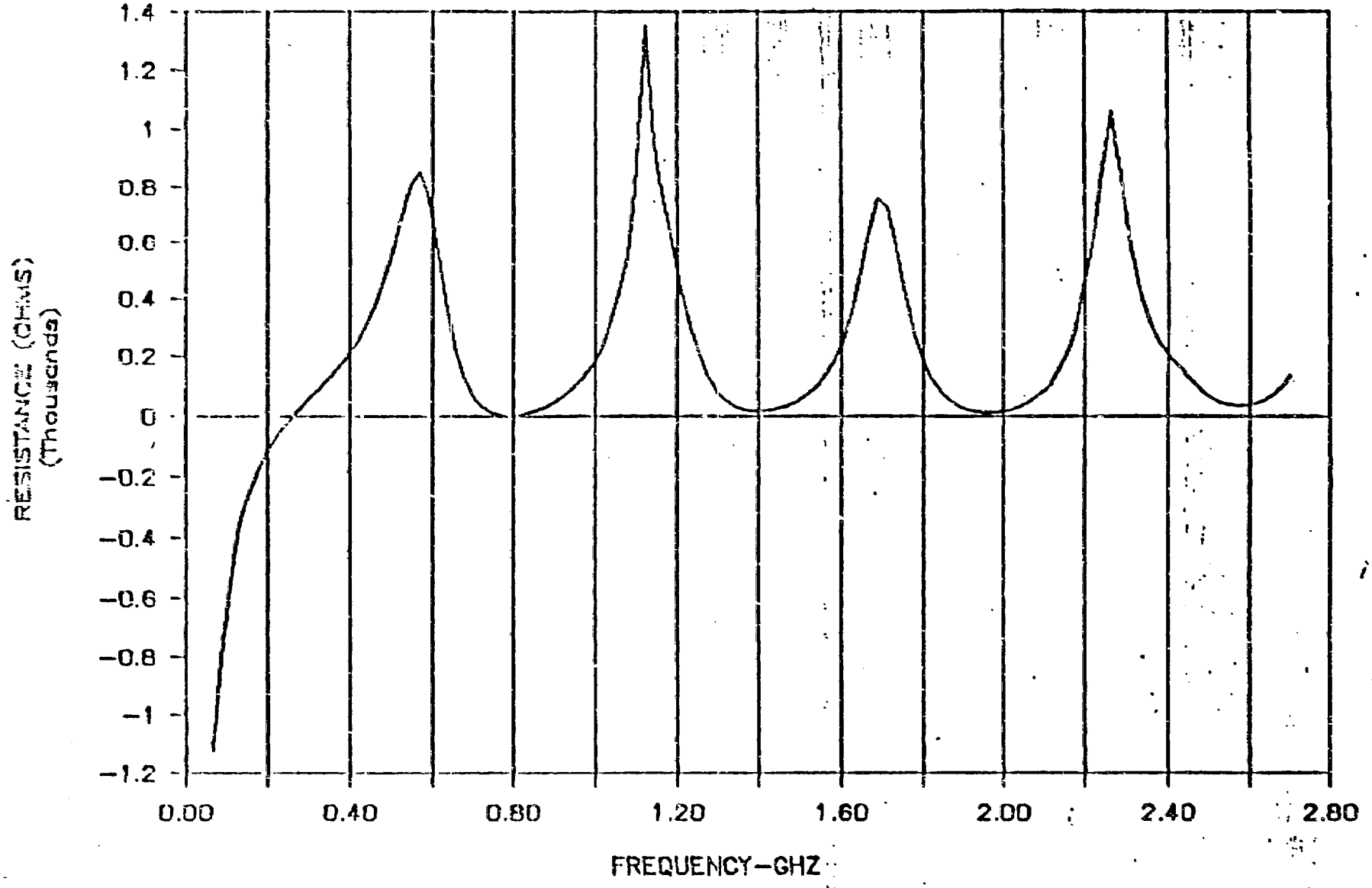
A49 PULSE STARTS T=0



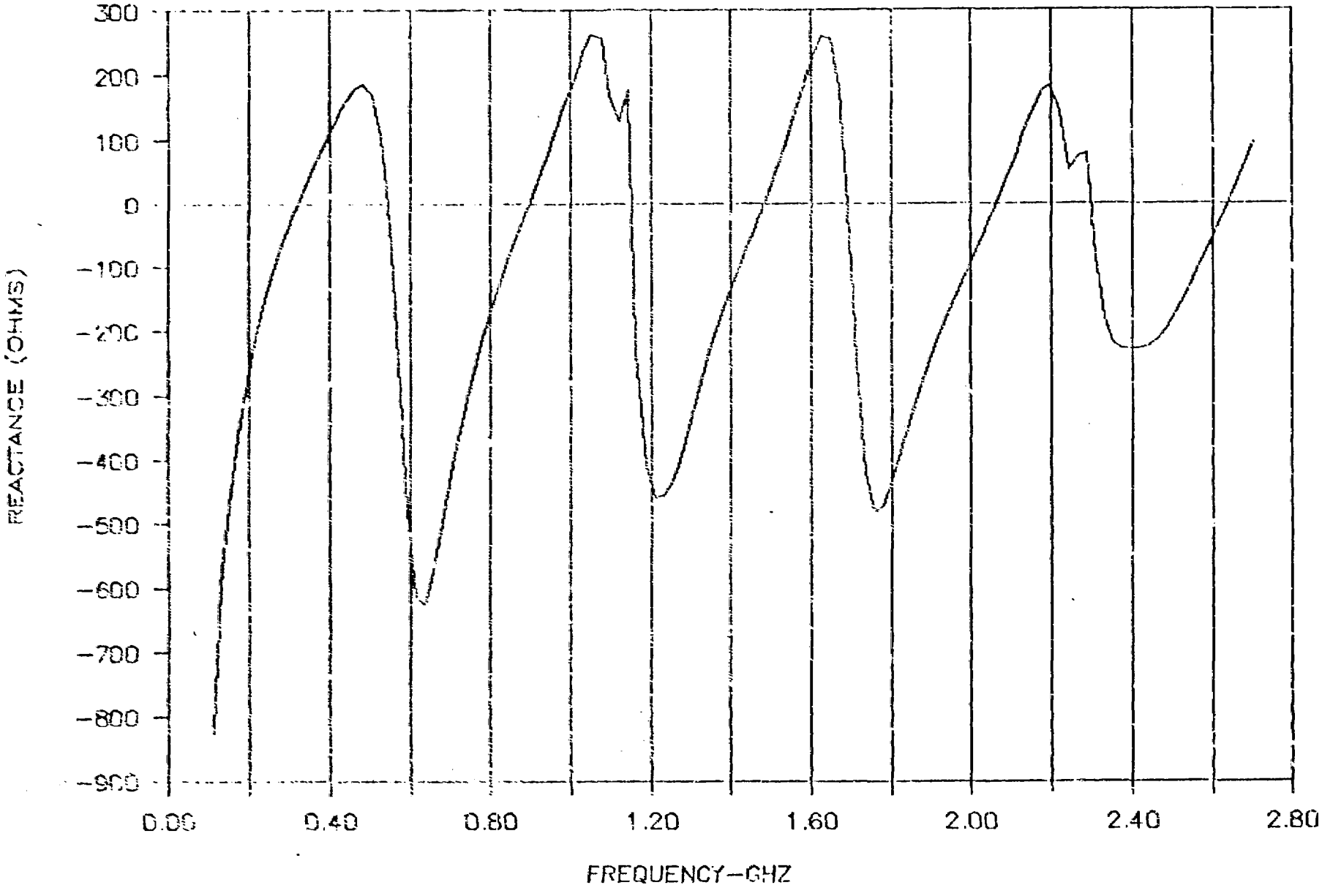
A49 NO SHIFT


RESISTANCE (OHMS)
(Thousands)
1.4
1.2
1
0.8
0.6
0.4
0.2
0
-0.2
-0.4
-0.6
-0.8
-1
-1.2
0.00
0.40
0.80
1.20
1.60
2.00
2.40
2.80
FREQUENCY-GHZ

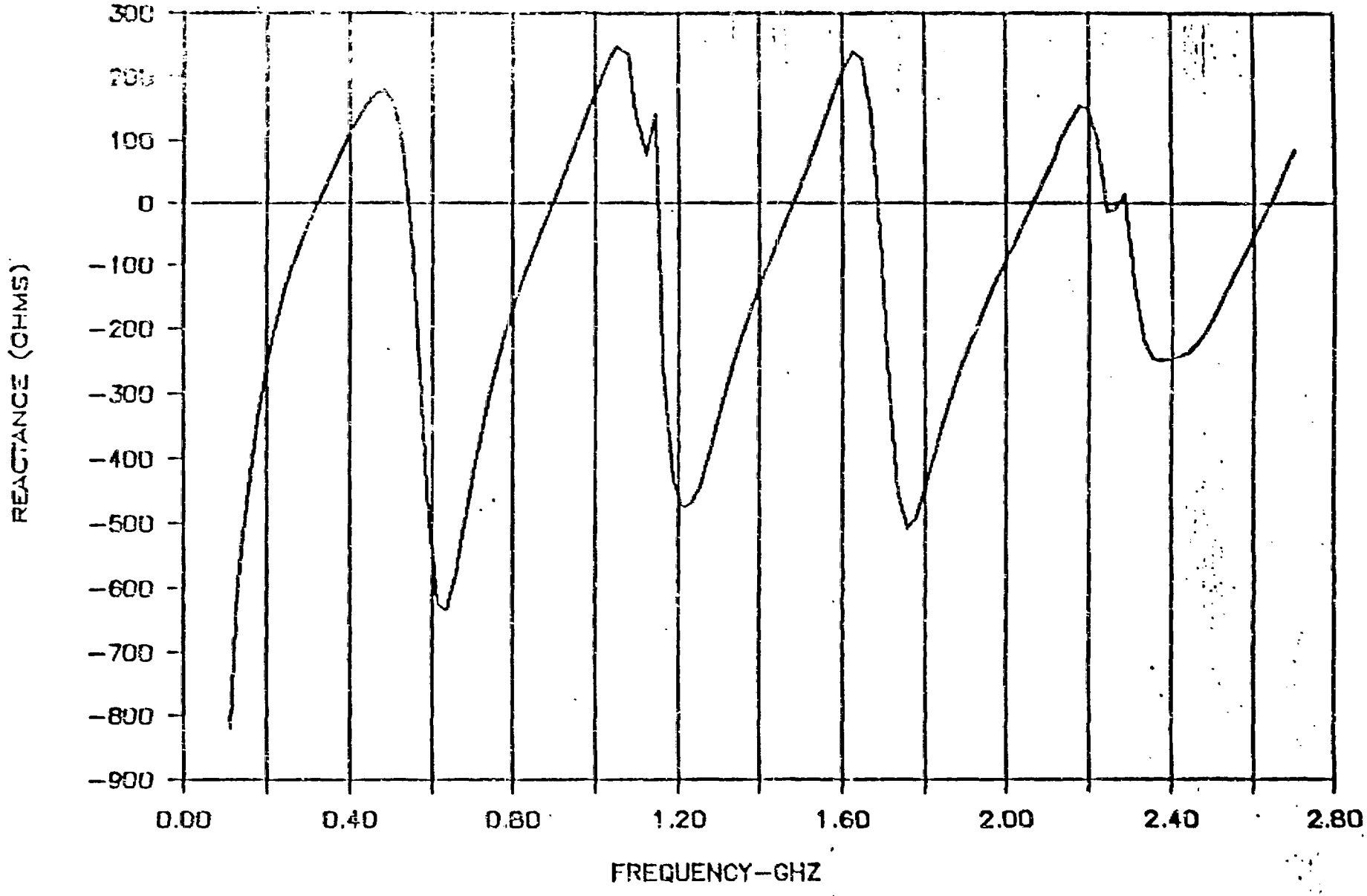
A49 SHIFT + DT/2



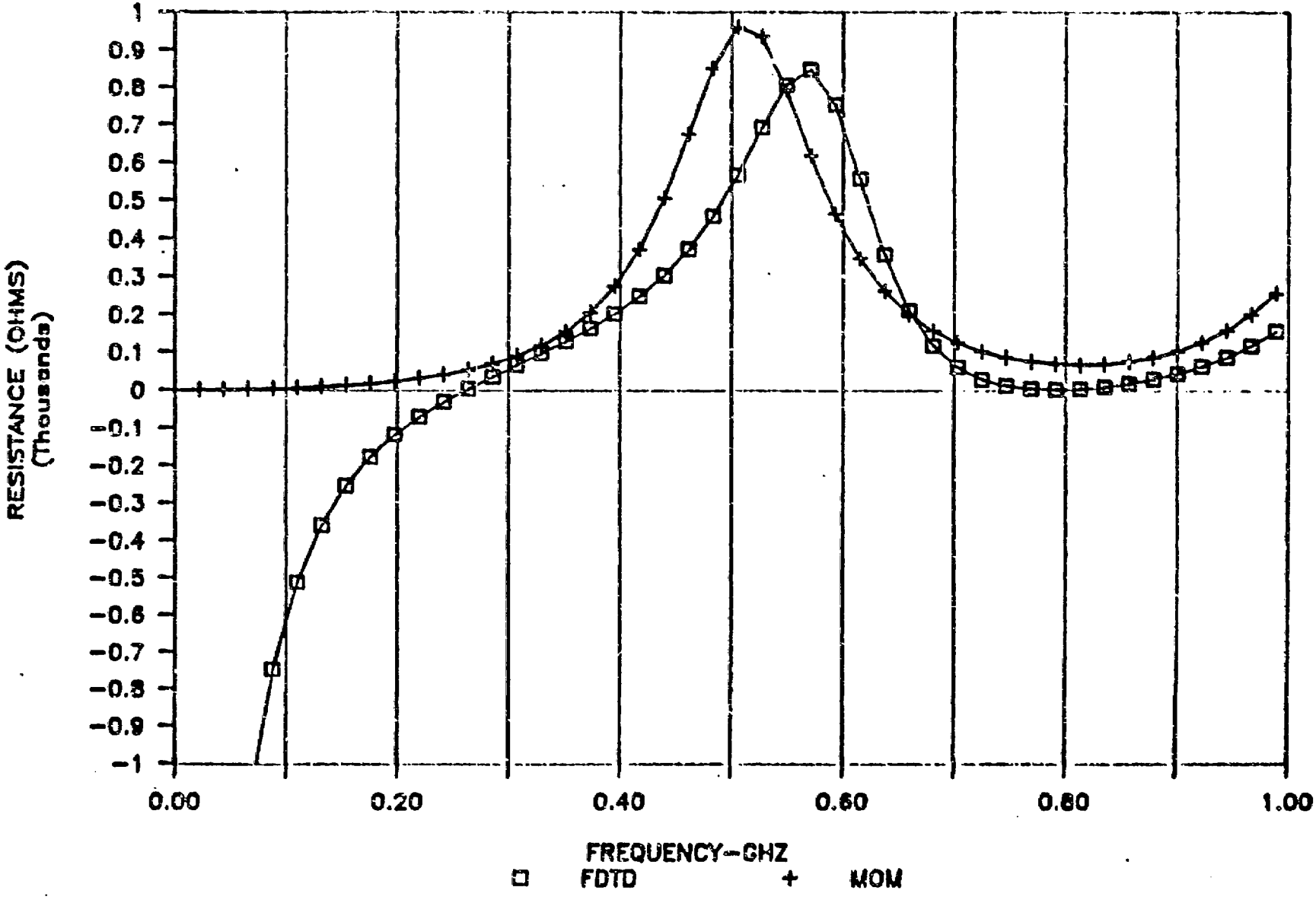
A49 NO SHIFT


300
200
100
0
-100
-200
-300
-400
-500
-600
-700
-800
-900
REACTANCE (OHMS)
0.00
0.40
0.80
1.20
1.60
2.00
2.40
2.80
FREQUENCY—GHZ

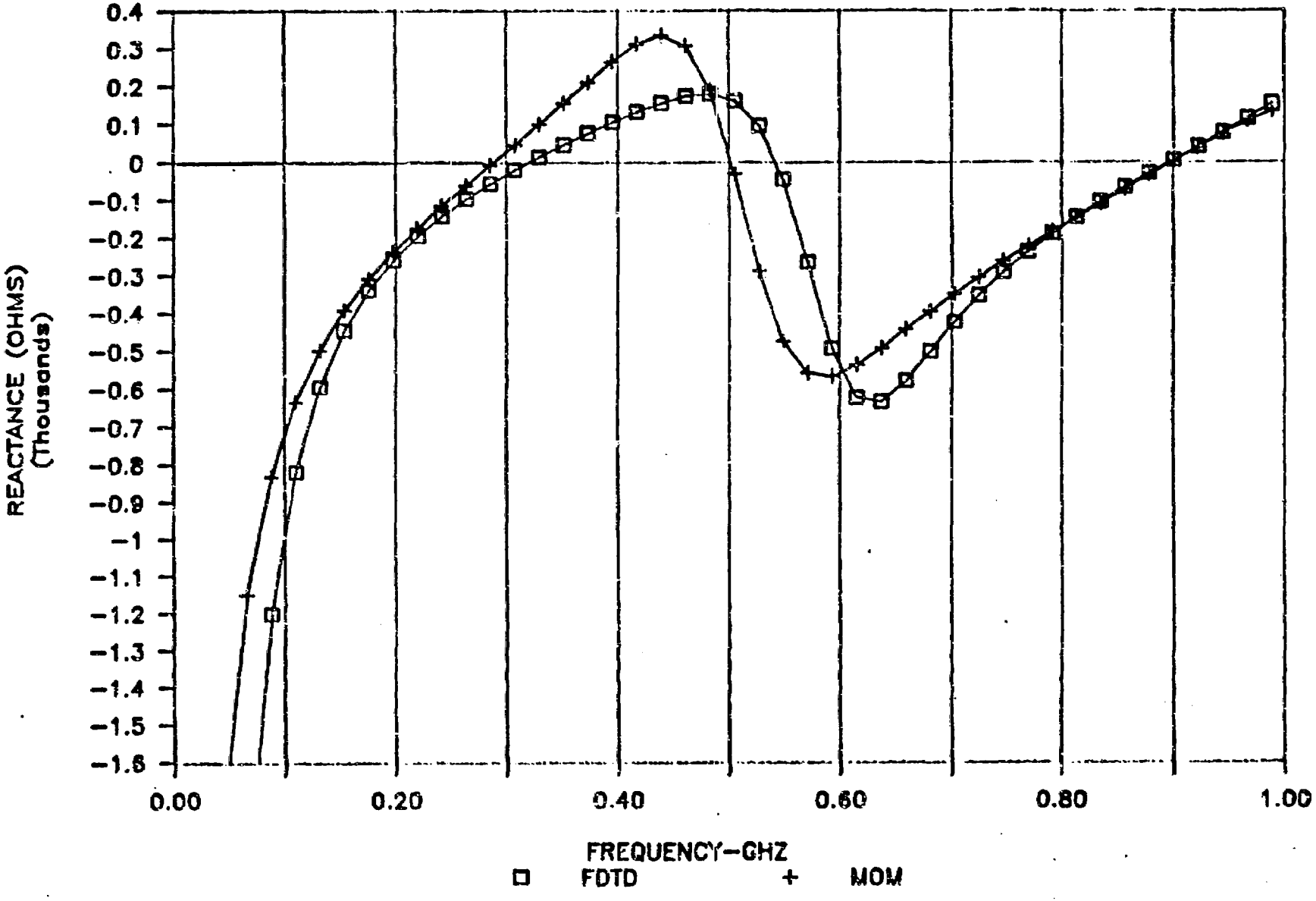
A49 SHIFT + DT/2



A49 MOM VS FDTD



A49 MOM VS FDTD



EVALUATION

- Covers broad frequency range - many resonances
- ~ 120 dB dynamic range
- Resonances match MOM to within ~ 10% in frequency and ~ 10% in amplitude
- Below first resonance, near DC, phase error leads to large non zero resistance error in the admittance -

  Numerous causes studied, no "culprit" yet found

  - wire fatness
  - excitation source
  - (ORBC)

- Usable engineering model
- Need to refine model of error sources

ONE-DIMENSIONAL FINITE DIFFERENCE TIME DOMAIN DEMONSTRATION FOR THE CLASSROOM

R. J. Luebbers and K. S. Kunz
Department of Electrical Engineering
The Pennsylvania State University
University Park, PA 16802

and

K. A. Chamberlin
Department of Electrical and Computer Engineering
University of New Hampshire
Durham, NH 03824

ABSTRACT

At Penn State a graduate level course is offered in computational electromagnetics. This originally included applications of the method of moments and the geometrical theory of diffraction. The approach taken is to require students to write programs "from scratch" to analyze, for example, scattering from a lossy wire or from a circular disk using appropriate techniques. No "canned" programs are utilized in the course.

Recently the course content was expanded to include the finite difference time domain (FDTD) technique. In order to reduce the complexity of the coding, the finite difference equations of the original Yee formulation (K. S. Yee, IEEE AP Trans., 14, 302-307, 1966) were reduced to one dimension. The resulting FDTD code is capable of analyzing propagation through a planar stratified medium of arbitrary permittivity, permeability, and conductivity for normal incidence. This formulation permitted demonstration of the basic elements of the method while greatly reducing the coding effort. The pulse shape, time step size, absorbing boundary conditions, dispersion, precursor energy, etc. could be investigated and displayed in a straightforward way.

The results obtained were transformed to the frequency domain via a Discrete Fourier Transform (DFT), allowing computation of, for example, the complex reflection coefficient vs frequency for a planar stratified material slab. This allowed the students to connect the FDTD results to frequency domain results with which they were already familiar. The one-dimensional FDTD clearly allowed the students to gain insight into the method, perhaps better than if they had to cope with a two- or three-dimensional formulation.

ONE-DIMENSIONAL FDTD FORMULATION

In order to reduce the complexity of programming and displaying FDTD computations we formulate the difference equations in one dimension. If we arbitrarily choose to retain E_y and H_z with propagation in the x direction, and assume "real" ϵ and μ, then Maxwell's equations become

$$\frac{\partial E}{\partial t}y = -\frac{1}{\epsilon}\left(\frac{\partial H}{\partial x}z - \sigma E_y\right) \tag{1}$$

$$\frac{\partial H}{\partial t}z = -\frac{1}{\mu}\frac{\partial E}{\partial x}y \tag{2}$$

Following Yee's notation we let $x = i\cdot\Delta x$, $t = n\cdot\Delta t$, and $F^n(i) = F(i\cdot\Delta x, n\cdot\Delta t)$, where F is any field component. Still following Yee's approach we interleave E_y and H_z in space and time, and specify ϵ, μ, and σ at discrete points (actually layers for our 1-D formulation). After approximating the differential equations as difference equations and simplifying we easily obtain

$$E_y^{n+1}(i) = \left(1 - \frac{\Delta t\sigma(i)}{\epsilon(i)}\right) E_y^n(i) - \frac{\Delta t}{\Delta x\epsilon(i)}\left[H_Z^{n+1/2}(i+1/2) - H_Z^{n+1/2}(i-1/2)\right] \tag{3}$$

$$H_Z^{n+1/2}(i+1/2) = H_Z^{n-1/2}(i+1/2) - \frac{\Delta t}{\Delta x\mu(i+1/2)}\left[E_y^n(i+1) - E_y^n(i)\right] \tag{4}$$

Equations (3) and (4) are readily programmed for solution by iteration of each equation alternately.

One special case which should be considered is high values of conductivity σ. The above difference equations cannot be numerically evaluated for high σ values, yet reflections from, for example, lossy

materials backed by a good conductor are of common interest. In order to avoid this problem good conductors are modeled as perfect conductors by explicitly setting E_y to zero at conductor locations.

The next considerations are the stability and accuracy constraints on Δx and Δt. It must be pointed out that Δx must be much less than the minimum wavelength of interest and the minimum scatterer dimension for good accuracy. For stability, time steps must be small enough so that field values can affect only nearest neighbors during one time step internal. For our 1-D equations an adequate stability criterion is

$$c \cdot \Delta t < \Delta x \tag{5}$$

where c is the speed of light. A safe choice is

$$c \cdot \Delta t = 0.5 \cdot \Delta x \tag{6}$$

and this is used for all of the examples in this paper.

We must also consider excitation of the difference equations. One can discuss different pulse shapes relative to their frequency content. A traditional choice is the Gaussian pulse. If we let Eo be the peak amplitude, x_p be the original location of the peak, and $2 \cdot IP \cdot \Delta x$ be the pulse width to $.001 \cdot Eo$ amplitude, then the Gaussian pulse electric field is given by

$$E_y = Eo \exp\left[-\beta(x - x_p - ct)^2\right] \tag{7}$$

with

$$\beta = \frac{\ln (0.001)}{(IP \cdot \Delta x)^2} = \frac{\ln (0.001)}{(IP \cdot 2 \cdot C \cdot \Delta t)^2} \qquad (8)$$

Writing (7) as a difference equation suitable for exciting a propagating wave, we have, with $x_p = IPC \cdot \Delta x$ locating the initial position of the pulse peak,

$$E_y^o (i) = Eo \exp \left[-\ln (0.001) \cdot \left(\frac{i - IPC}{IP}\right)^2\right] \qquad (9)$$

For propagation in the plus x direction the corresponding magnetic field is given as

$$H_Z^{1/2}(i + 1/2) = \frac{Eo}{Zo} \exp \left[-\ln(0.001) \cdot \left(\frac{i - IPC + 1/4}{IP}\right)^2\right] \qquad (10)$$

where Zo is the impedance of free space.

The final consideration before programming the above equations is absorbing pulses as they are incident at the limits of the problem space. Significant literature exists on FDTD absorbing boundary conditions, but as our problem formulation allows only normal incidence the problem is considerably simplified over 2- and 3-D formulations. An adequate absorbing boundary condition is given by Mur (G. Mur, IEEE EMC Trans., 23, 377-382, 1981) which can be reduced to one dimension. However, due to lack of sufficient time to incorporate general boundary conditions, and due to the simplification of always having normal incidence at the boundary, the pulses incident on the boundary are directly zeroed out as they reach the boundary

(the entire pulse is zeroed at once). It is anticipated that the next time the course is taught more effort will be expended on the absorbing boundary conditions, perhaps illustrating the relative effects of different formulations.

Some examples of the results which can be obtained using the above are illustrated in figures 1-3, which show electric field vs position at different time steps for a 210 picosecond Gaussian pulse incident on a 2.4 cm thick dielectric slab with $\varepsilon_r = 4$ backed by a perfect conductor, with $\Delta x = 0.0015$ m. These computations were done using a personal computer. A demonstration program with menu-driven choices of dielectric slab material and thickness, pulse width, etc., which allowed the user to watch the pulses propagate and interact with planar stratified changes in constitutive parameters was written and provides an excellent means to demonstrate the technique graphically.

Using this program the effects of the frequency content of the Gaussian pulse on the stability of the difference equations can be illustrated. Figure 4 show the effect of reducing the pulse width from the 210 picoseconds used in figures 1-3 to 115 picoseconds. The resulting pulse dispersion is clearly evident and illustrates one of the fundamental limits of the method.

TRANSFORMATION TO FREQUENCY DOMAIN

The effect of frequency content of the Gaussian pulse on pulse dispersion leads naturally to consideration of transforming the time domain results to frequency domain. One can begin by calculating the bandwidths of the 210 and 115 picosecond pulses used previously and

showing that the shorter pulse contains significant energy at frequencies such that the constraint of $\Delta x <<$ "minimum wavelength" is violated, explaining the dispersion of the pulse.

The next step is to actually transform calculation results to the frequency domain. The example which was chosen to illustrate this was determination of the frequency domain reflection coefficient for a pulse incident on a slab using FDTD time domain computations.

We have already seen samples of time domain calculations in figures 1-3. Similar calculations must progress through enough time steps so that the pulse amplitudes have decreased to very low values. The electric field amplitude at the x coordinate just in front of the dielectric vs time is stored. This results in values of total electric field vs time at the surface of the slab. $(E^n_{tot}(i_f))$. We then remove the slab and excite the problem again with free space everywhere, again saving the electric field vs time at the same location as before. This gives us the incident electric field at the front of the slab $(E^n_{inc}(i_f))$ vs time. For each time step the reflected field is given by

$$E^n_{ref}(i_f) = E^n_{tot}(i_f) - E^n_{inc}(i_f) \qquad (11)$$

For our example problems it was found that taking 4096 total time steps was sufficient to determine the total field. The incident field could be determined with just enough time steps to allow the pulse to pass by the position of the slab interface, with zeros used to pad the incident field to 4096 if necessary. Let us denote NTOT as the number

of time steps to determine the total field (4096 for our examples) and NINC as the number of time steps for the incident field (128 was sufficient for this). For the examples shown $\Delta x = 0.0015$ m, $\Delta t = 2.5$ picosecond, the Gaussian pulse width is 180 picoseconds (IP = 18), and all dielectric slabs are 9 (i.e. 30 $\cdot \Delta x$) thick.

The discrete Fourier transform (DFT) is given by

$$e(k\Delta f) = \Delta t \sum_{n=0}^{NT-1} E^n (i_f) \exp\left[-j2\pi nk/NT\right] \qquad (12)$$

After considering the slab thickness relative to the frequency content of the Gaussian pulse it seemed desirable to have results at frequency intervals of approximately 25 MHz. For a power of 2 transform we chose NT as 16,384 resulting in $\Delta f = 1/(NT \cdot \Delta t) = 24.414$ MHz. We further estimated that our maximum frequency of interest would be 10 GHz, so that we were interested in the first 410 frequencies (k = 1,410) of the DFT. Our DFT expressions for the incident and reflected fields became

$$e_{inc}(k\Delta f) = \Delta t \sum_{n=0}^{NINC} E^n_{inc} (i_f) \exp\left[-j2\pi nk/NT\right] \qquad (13)$$

$$e_{ref}(k\Delta f) = \Delta t \sum_{n=0}^{NTOT} E^n_{ref} (i_f) \exp\left[-j2\pi nk/NT\right] \qquad (14)$$

with the frequency domain complex reflection coefficient R(f) given by

$$R(k\Delta f) = \frac{e_{ref}(k\Delta f)}{e_{inc}(k\Delta f)} \qquad (15)$$

The above computations could have been done somewhat faster using an FFT algorithm. But the savings of using the FFT vs the direct computation would be diminished over the usual since we are only interested in 410 values out of 16,384 and since we only have 4096 non-zero terms in our direct summation.

Let us consider some examples of applying the above transforms. First we show in figure 5 the frequency spectrum of our incident Gaussian pulse computed from equation (13). This incident pulse is used for all of the following reflection coefficient computations. Normalizing the reflected to the incident field for computation of the reflection coefficient as indicated in equation (15) simultaneously corrects for the frequency roll-off of the incident pulse while providing the phase reference for the reflection coefficient.

Reflection coefficient computations for several different slab geometries are shown in figures 6-9. Figure 6 is for a slab with ϵ_r = 4, 9 cm thick. Note that the slab has a minimum reflection coefficient (it should be zero) when the slab is a multiple of 1/2 wavelength thick, and a maximum reflection coefficient of 0.6 at odd multiples of 1/4 wavelength in thickness as it should. The accuracy decreases at higher frequencies, perhaps due to the imperfect absorbing boundary conditions.

Figure 7 is for the same 9 cm thick $\epsilon_r = 4$ slab but backed by a perfect conductor. The reflection coefficient magnitude should be exactly 1 for all frequencies, but a periodic error, greatest when the slab is an odd multiple of 1/4 wavelength thick, is evident in the results.

Figure 8 is for the same 9 cm thick $\epsilon_r = 4$ slab backed by a perfect conductor but with a uniform conductivity $\sigma = 1.0$ S/m throughout the slab.

Finally figure 9 has the conductivity linearly increase from 0.01 S/m at the front of the slab to 1.0 S/m at the back of the slab. It would be instructive to provide for the direct frequency domain calculations to compare with these results, and it is hoped that this will be accomplished the next time the course is taught.

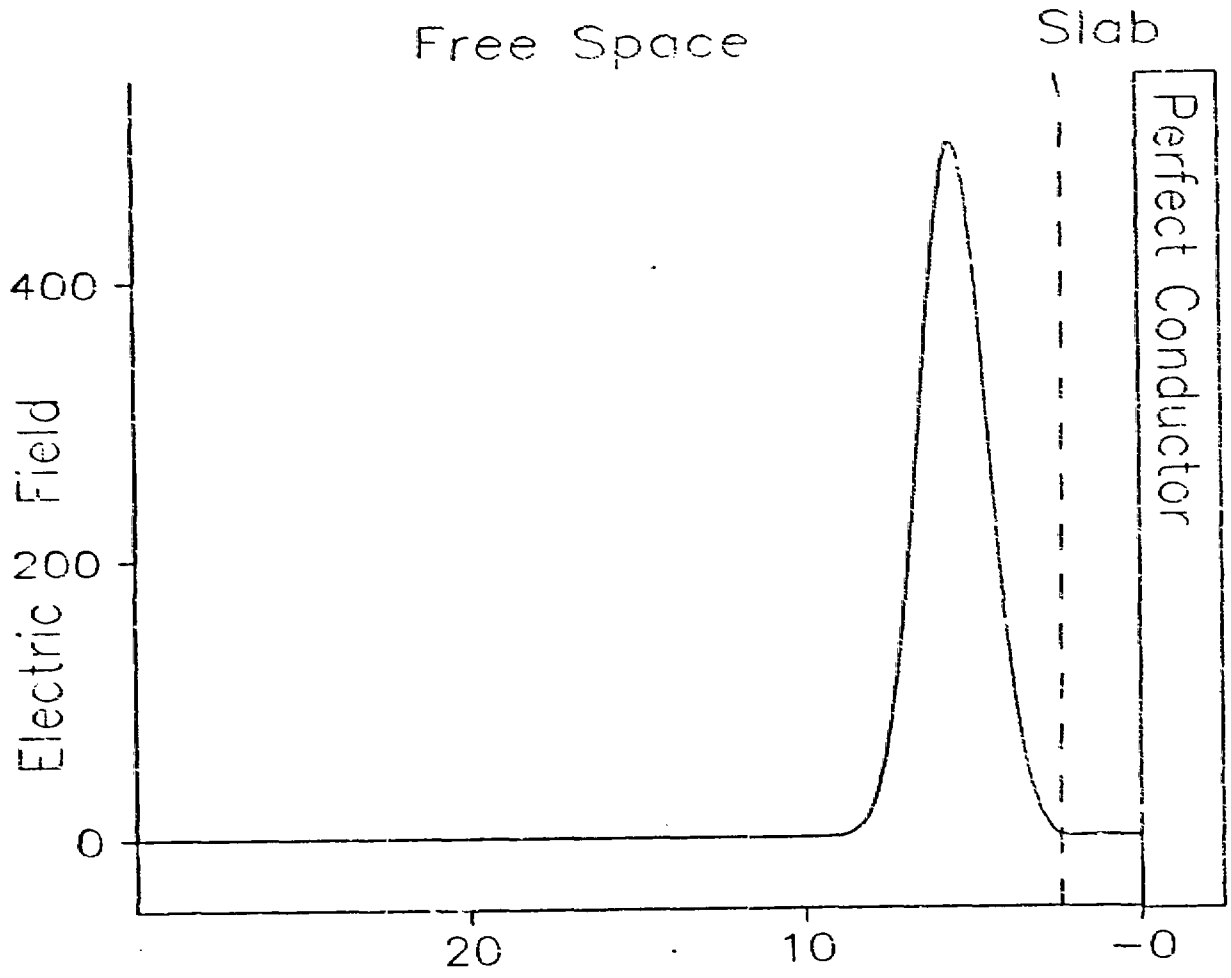


Figure 1. Electric field vs position for Gaussian pulse incident on a dielectric (ε_r = 4) slab backed by a perfect conductor.

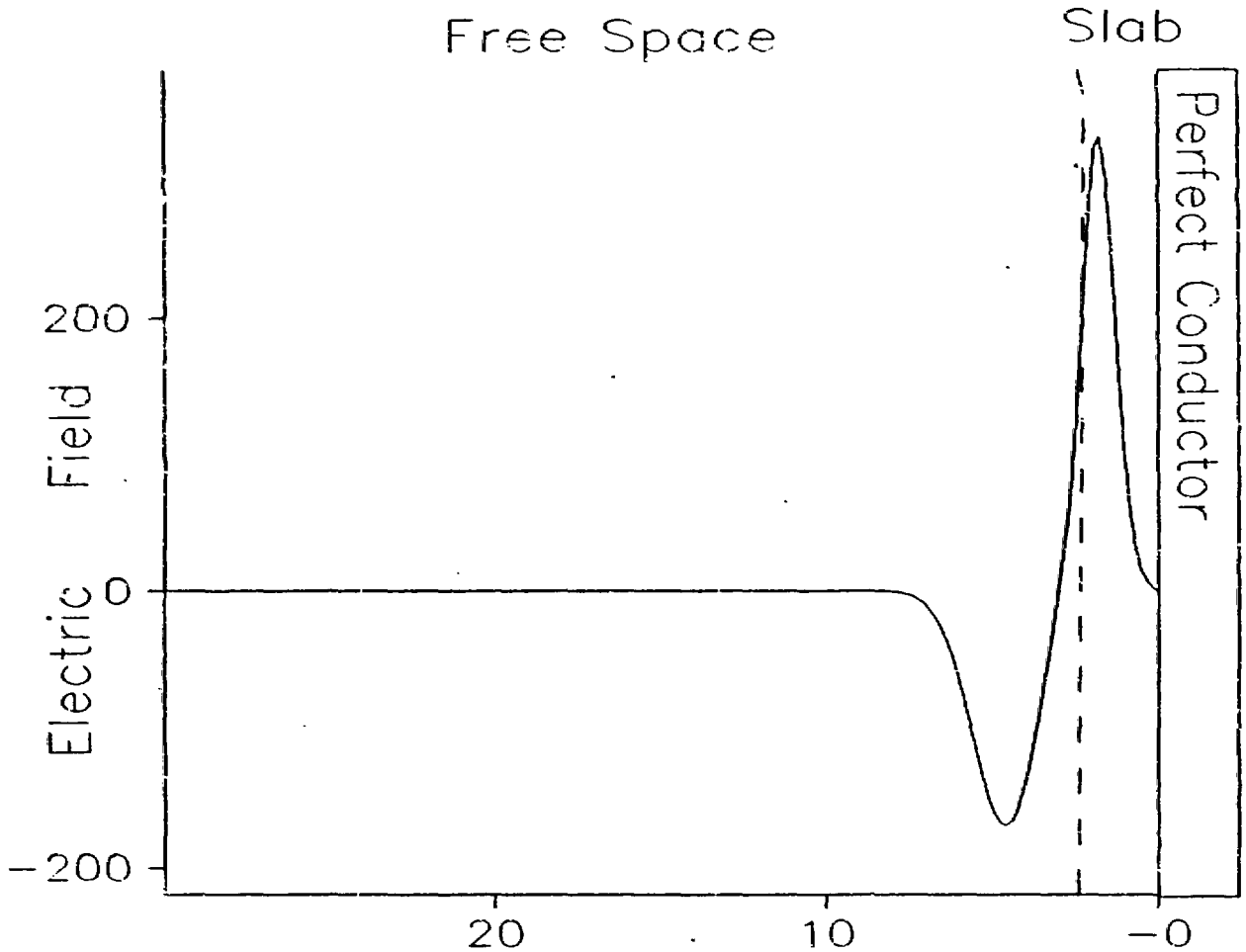


Figure 2. Continuation of figure 1, after partial reflection by dielectric slab.

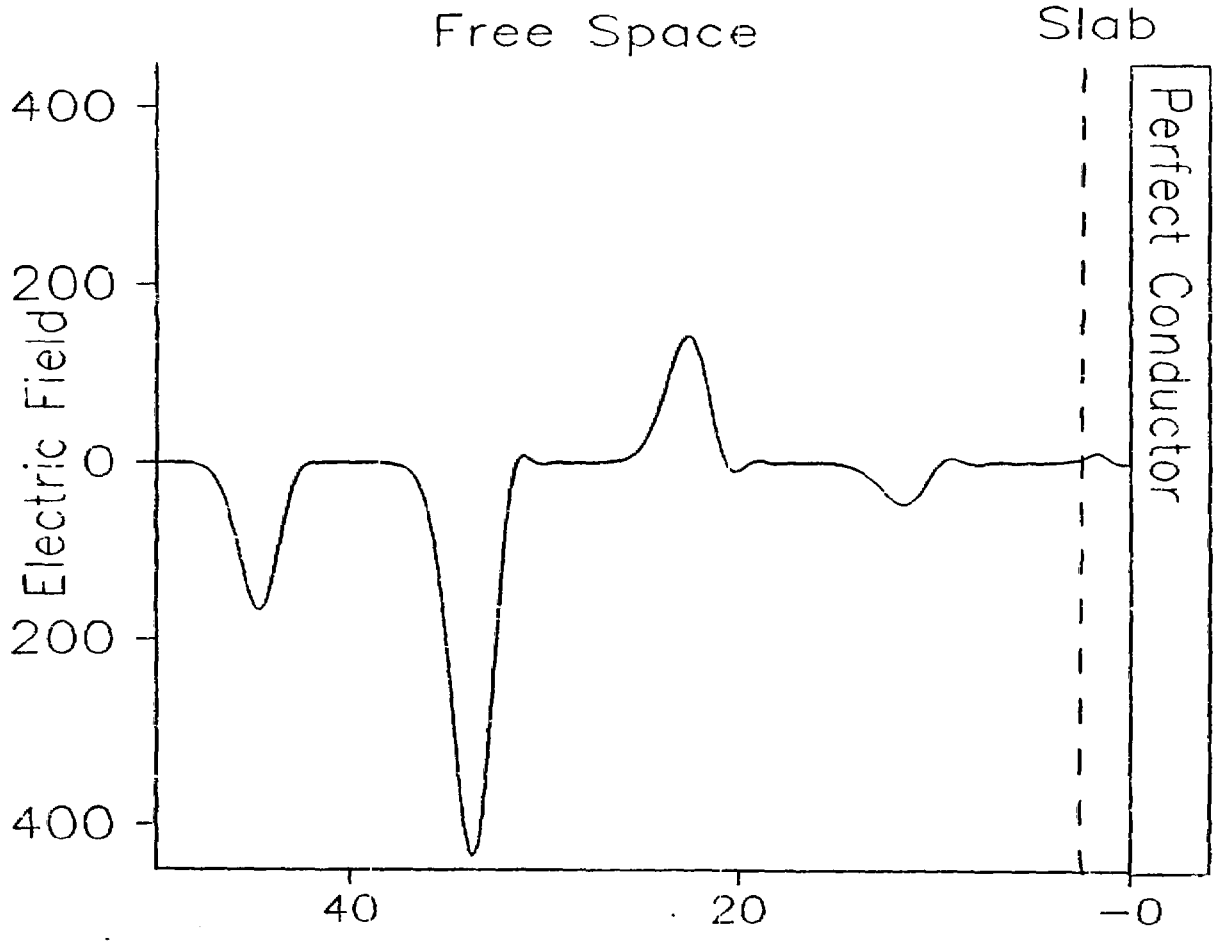


Figure 3. Continuation of figures 1 and 2 after multiple reflections have occurred.

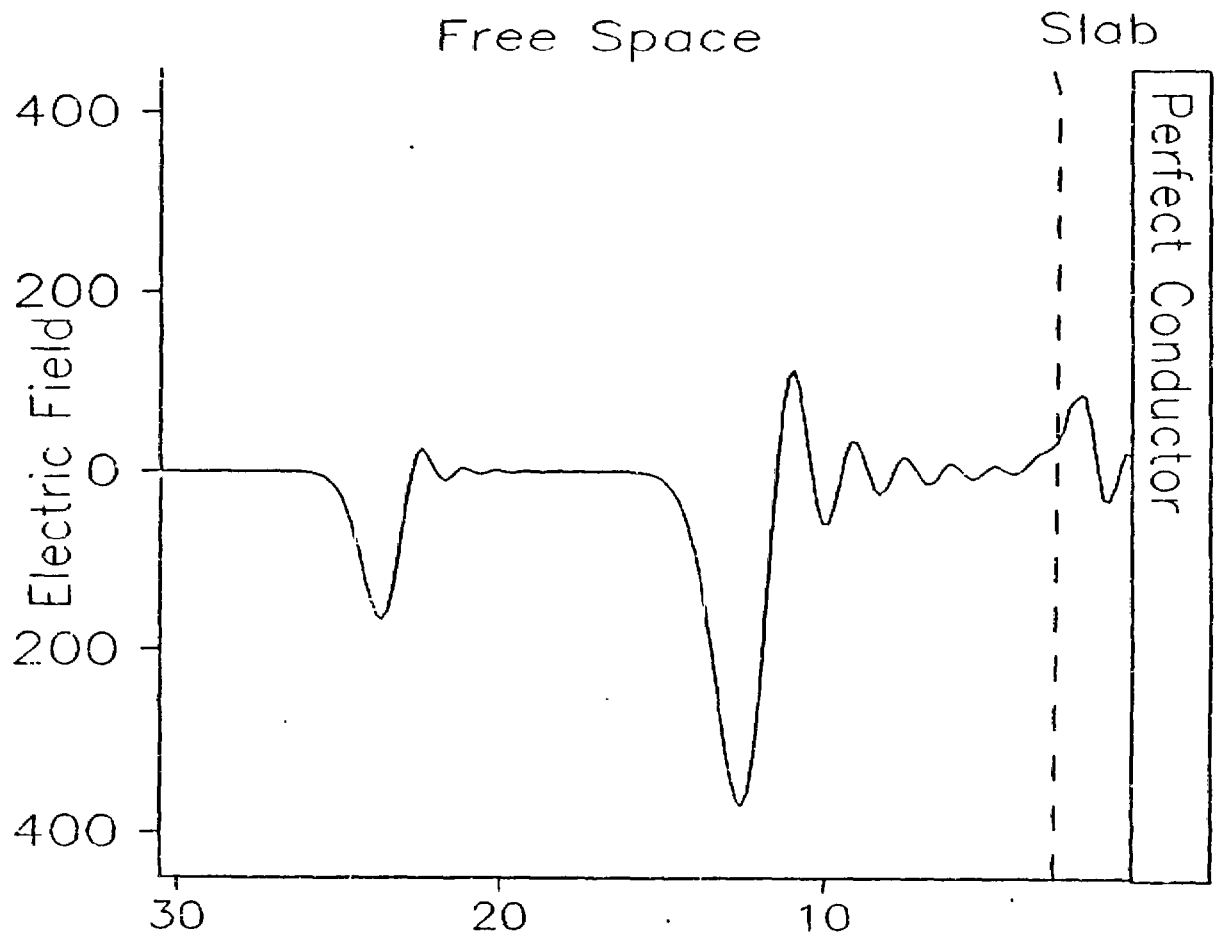


Figure 4. Same geometry as figures 1-3, but with narrower pulse which disperses due to violation of stability conditions.

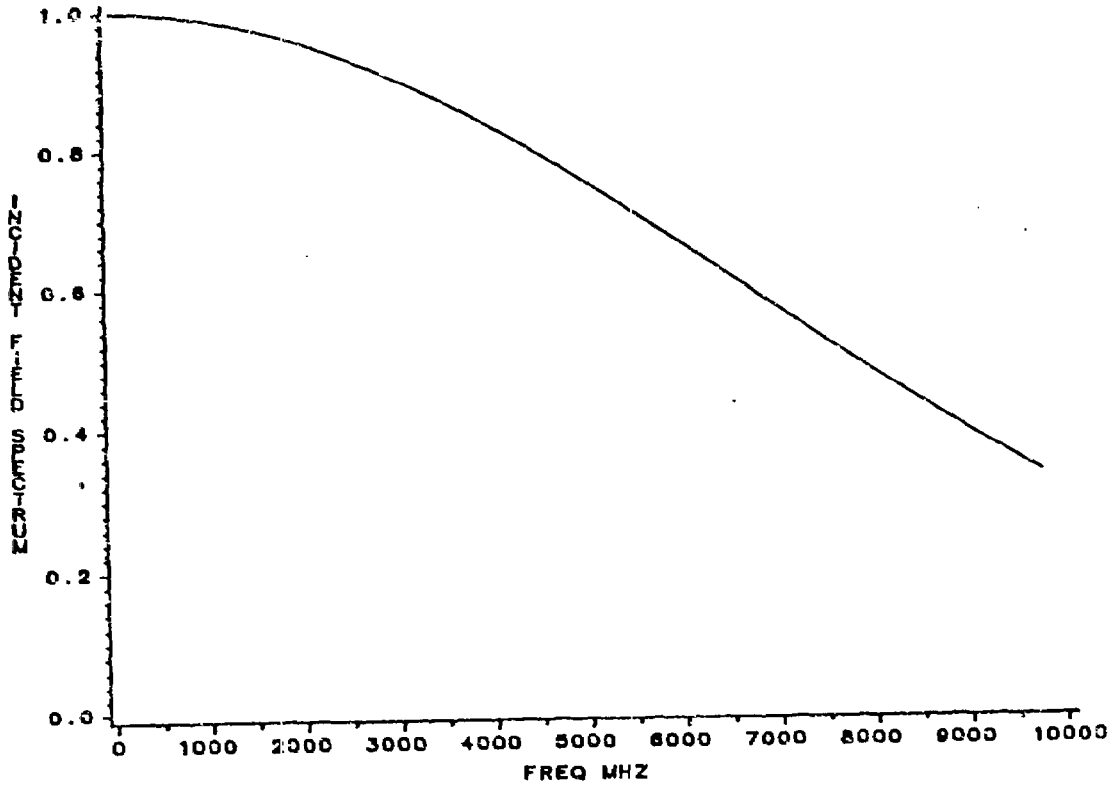


Figure 5. Frequency spectrum of incident Gaussian pulse 180 picoseconds wide.

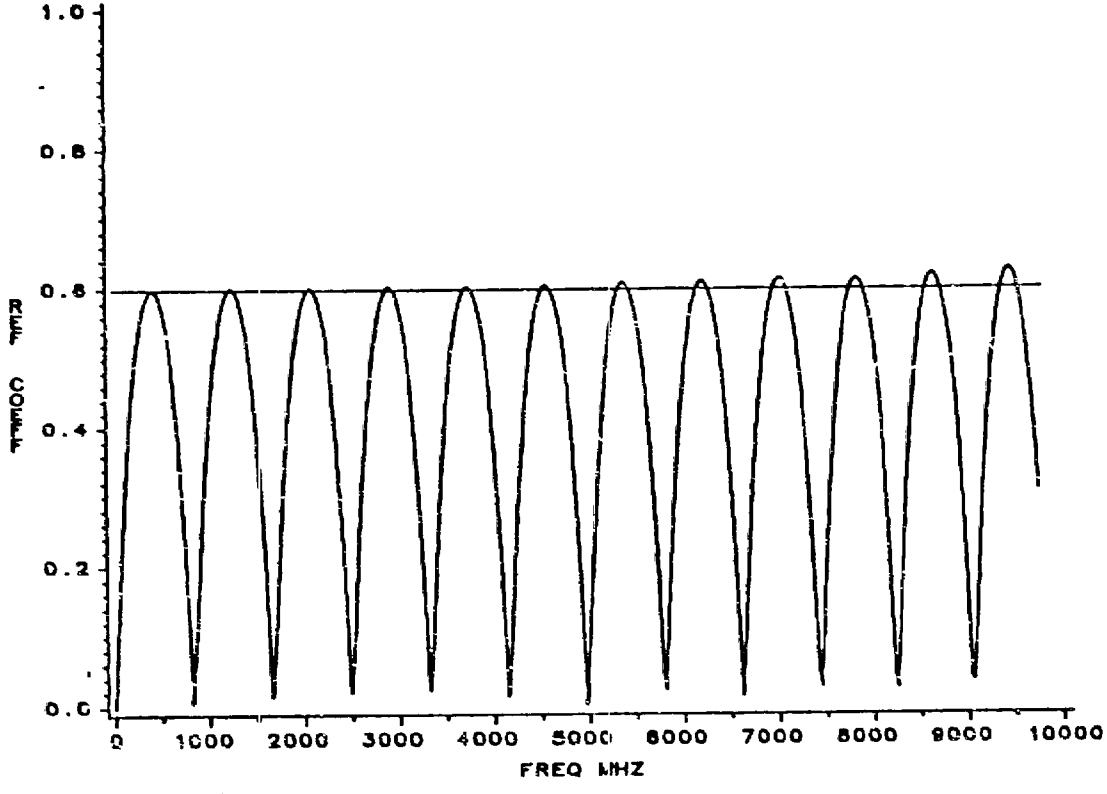


Figure 6. Reflection coefficient magnitude vs frequency for 9 cm thick $\varepsilon_r = 4$ slab computed using one-dimensional FDTD.

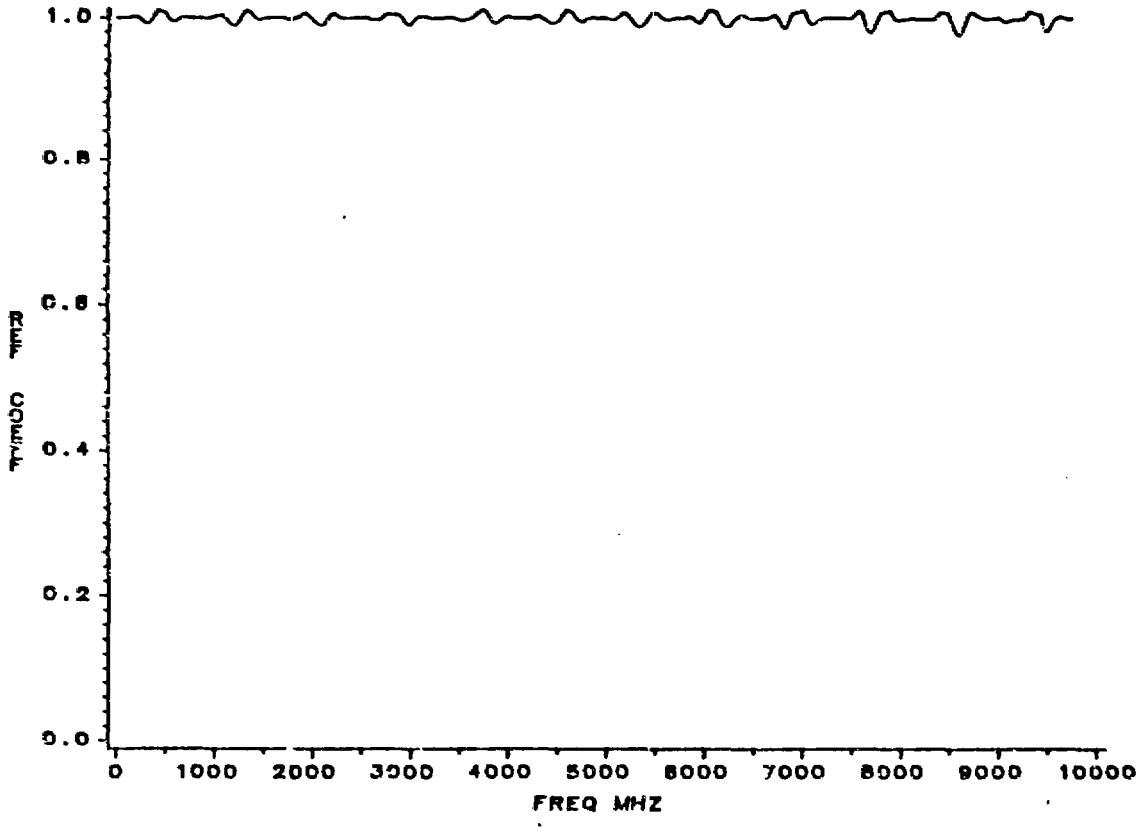


Figure 7. Reflection coefficient magnitude vs frequency for 9 cm thick $\varepsilon_r = 4$ slab backed by a perfect conductor computed using one-dimensional FDTD.

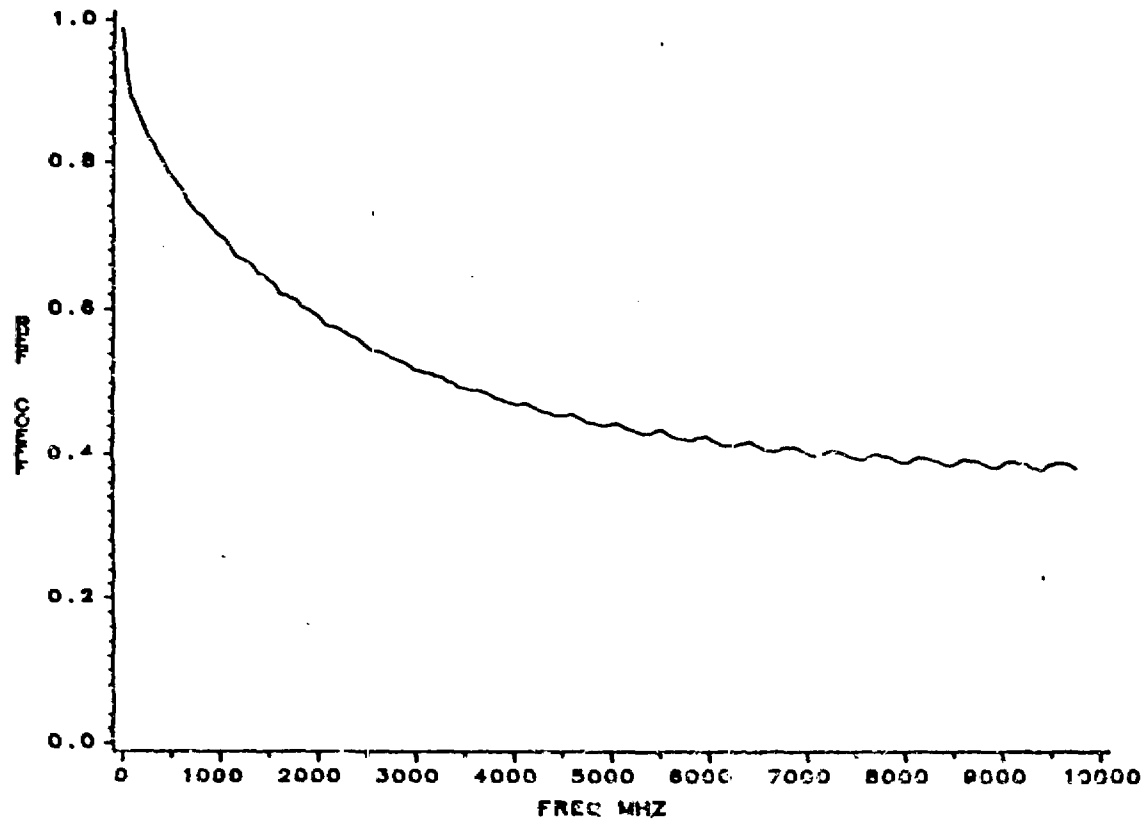


Figure 8. Reflection coefficient magnitude vs frequency for a 9 cm thick $\varepsilon_r = 4$, $\sigma = 1$ S/m slab backed by a perfect conductor computed using one-dimensional FDTD.

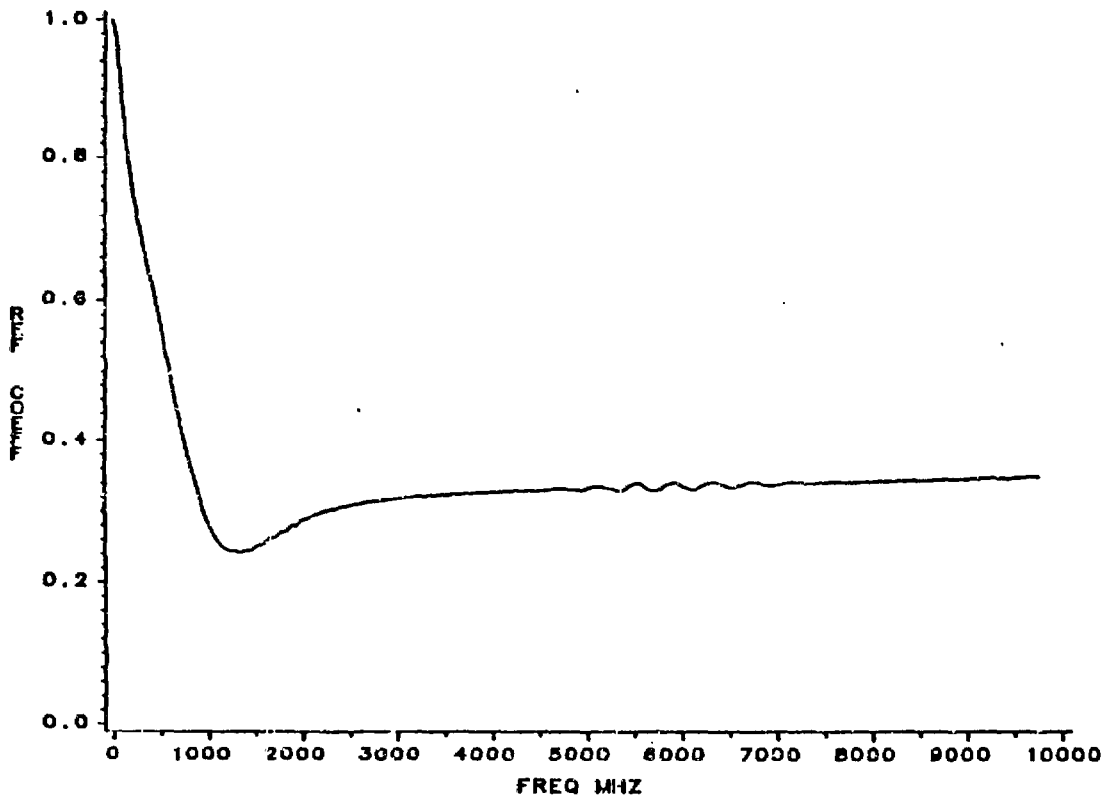


Figure 9. Reflection coefficient magnitude vs frequency for a 9 cm thick slab with $\varepsilon_r = 4$, σ linearly tapered from 0.01 S/m to 1.0 S/m and backed by a perfect conductor computed using one-dimensional FDTD.

A HIGH FREQUENCY REFORMULATION OF THE FDTD ALGORITHM IN GENERALIZED COORDINATES

M.A. Fusco and M.V. Smith
Lockheed R&D Division
3251 Hanover St., Palo Alto, CA 94304-1187
O/92-20, B254E

The Finite Difference-Time Domain algorithm first propounded by Yee (K. Yee, IEEE Trans. Antennas Propagat., AP-14, no.3, 302-307, 1966), and since elaborated on by several authors (A. Taflove and M.E. Brodwin, IEEE Trans. Microwave Theory Tech., MTT-23, 623-630, 1975; K. Umashankar and A. Taflove, IEEE Trans. Electromagn. Compat., EMC-24, no.4, 397-405, 1982; Fusco, to be published) is, in its conventional form, essentially a low to intermediate frequency method. The limitations are imposed by computer resource requirements, and FDTD practitioners have hitherto anticipated advances in computing power to be able to extend the domain of applicability of FDTD methods to higher frequencies. In this paper a procedure is presented which greatly reduces computer resource requirements for a given body size-wavelength ratio. The procedure consists of filling the computational space with the incident radiation (as if the scatterer were not present), then turning the scatterer 'on' and allowing the FDTD algorithm to run its course. Qualitative arguments suffice to show that this leads to the correct solution.

The method applies to arbitrarily shaped conductors and dielectrics in two and three dimensions and can easily reduce CPU times by orders of magnitude. A significant side benefit, resulting in further savings, is that a large class of problems can be solved without having to implement a radiation boundary condition. Results for the two-dimensional case of a TM-polarized plane wave incident on an infinite circular cylinder with $KA \simeq 92$ have been obtained by working in generalized, numerically defined coordinates, which obviates the need to staircase the scatterer. These results have been found to be in excellent agreement with results from a modal expansion code and will be presented herein, along with further findings on curvilinear system implementations.

TABLE OF CONTENTS

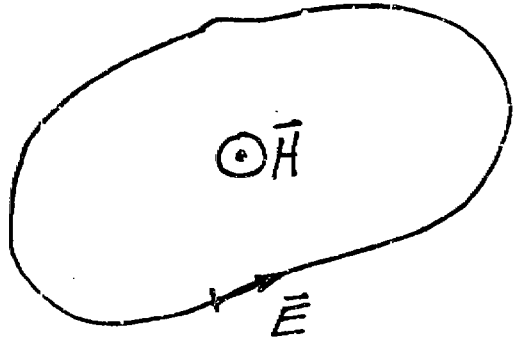
1. Abstract.
2. Maxwell's equations in integral form applied to an arbitrary contour.
3. Discretization of Maxwell's equations.
4. Treatment of scatterers in the FDTD scheme.
5. Simple one-dimensional illustration of radiation boundary condition.
6. Advantages of curvilinear approach.
7. Disadvantages of curvilinear approach.
8. Results for conducting circular cylinder of $KA = 5$ for TE polarization.
9. Results for square conducting cylinder in circular grid - body currents for TM polarization. Results from present work are shown as open circles.
10. Results for square conducting cylinder in circular grid at oblique incidence - body currents for TM polarization. Results from present work are shown as open circles.
11. Placement of field components at singularity for TM polarization.
12. Constraints on the sizes of the space and time increments imposed by the wavelength of the incident radiation.
13. Illustration of variable time stepping.
14. Time dependence of electric field at singularity for TM polarization. Results obtained with singularity processing and variable time stepping with a ratio of five.
15. High frequency initialization.
16. Further description of high frequency approach.
17. Justification for correctness of high frequency approach.
18. Computer loading trade - standard curvilinear vs. high frequency FDTD.
19. High frequency results - bistatic scattering crossection for circular conducting cylinder with $KA = 93$ in TM polarization.
20. Square cylinder embedded in a dense circular grid. $KA = 37$, A=halfside.
21. Bistatic radar crossection for square cylinder in 20. Field incident normally on a face.
22. Near fields for square cylinder. Electric field on illuminated face as a function of time.
23. Near fields for square cylinder. Electric field on dark face as a function of time.
24. Near fields for square cylinder. Tangential magnetic field halfway between scatterer boundary and space boundary.

FDTD APPROACH

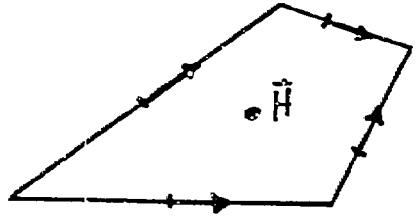
MAXWELL'S EQUATIONS IN INTEGRAL FORM

$$\int \vec{E} \cdot d\vec{l} = -\mu \int \frac{\partial \vec{H}}{\partial t} \cdot \hat{n}\, da$$

$$\int \vec{H} \cdot d\vec{l} = \epsilon \int \frac{\partial \vec{E}}{\partial t} \cdot \hat{n}\, da$$



FDTD DISCRETIZATION



$$\int \vec{E} \cdot d\vec{l} \;\rightarrow\; E_1^n\, dl_1 + E_2^n\, dl_2 + E_3^n\, dl_3 + E_4^n\, dl_4$$

$$\int \frac{\partial \vec{H}}{\partial t} \cdot \hat{n}\, da \;\rightarrow\; \frac{\Delta H_c}{\Delta t}\, da \;\rightarrow\; \frac{1}{\Delta t}\left[H_c^{n+1/2} - H_c^{n-1/2}\right] \Delta a$$

FIELDS MUST BE APPROPRIATELY PLACED ON A COMPUTATIONAL GRID

SCATTERERS

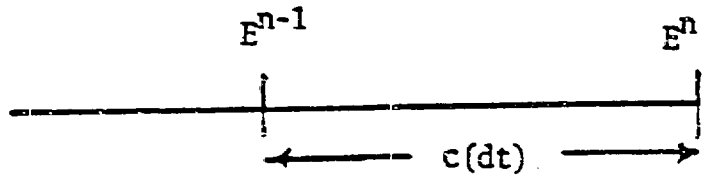
CONDUCTORS - ALL FIELDS ARE ZERO INSIDE. TANGENTIAL E AND NORMAL H ARE ZERO ON THE SURFACE.

DIELECTRICS - BOUNDARY CONDITIONS GENERATED NATURALLY BY ATTACHING THE APPROPRIATE VALUES OF ϵ AND μ AT EACH GRID POINT.

LOSSY DIELECTRICS CAN BE EASILY TREATED BY INTRODUCING A FINITE CONDUCTIVITY AND AN ADDITIONAL TERM IN THE CURL EQUATIONS.

RADIATION BOUNDARY CONDITION

SCATTERED FIELDS AT BOUNDARY OF SPACE MUST HAVE OUTGOING COMPONENTS ONLY. IN ONE DIMENSION THE CONDITION IS TRIVIAL.



IN TWO AND THREE DIMENSIONS APPROXIMATE EXPANSIONS ARE USED. FOR OUR WORK THE FIRST ORDER BAYLISS-TURKEL CONDITION HAS BEEN USED IN CYLINDRICAL COORDINATES AND SPHERICAL COORDINATES RESPECTIVELY.

ADVANTAGES OF CURVILINEAR APPROACH

BODY SHAPE CAN BE FAITHFULLY MODELED -- NO STAIRCASING

LAYERED MEDIA CAN BE REPRESENTED MORE ACCURATELY

NOT RESTRICTED TO ANALYTIC COORDINATE SYSTEMS

CAN ACHIEVE GREATER GENERALITY

DISADVANTAGES OF CURVILINEAR APPROACH

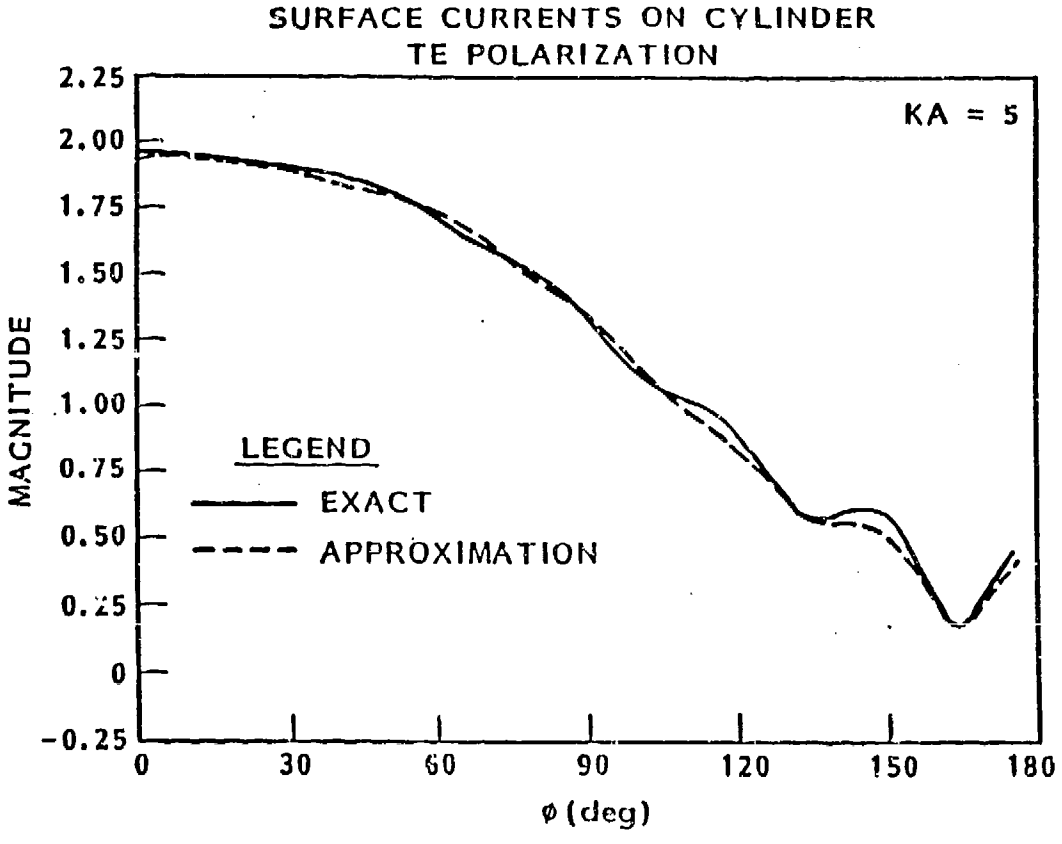
POSSIBLE DISPERSION PROBLEMS

POSSIBLE ANISOTROPY PROBLEMS

DIFFERENTIAL GEOMETRY MUST BE SOLVED
- METRIC TENSOR
- COVARIANT FORMULATION OF EQUATIONS
- COVARIANT-CONTRAVARIANT HOPPING

TIGHTER REQUIREMENTS ON TIME STEP

SINGULARITIES



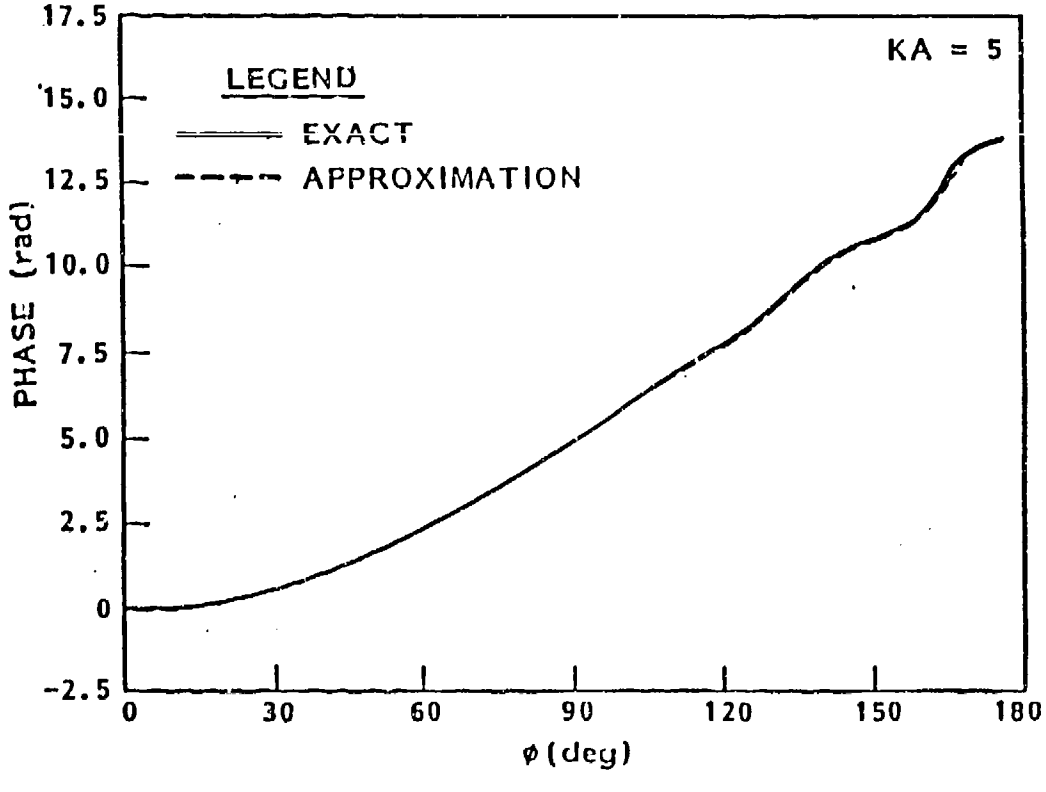
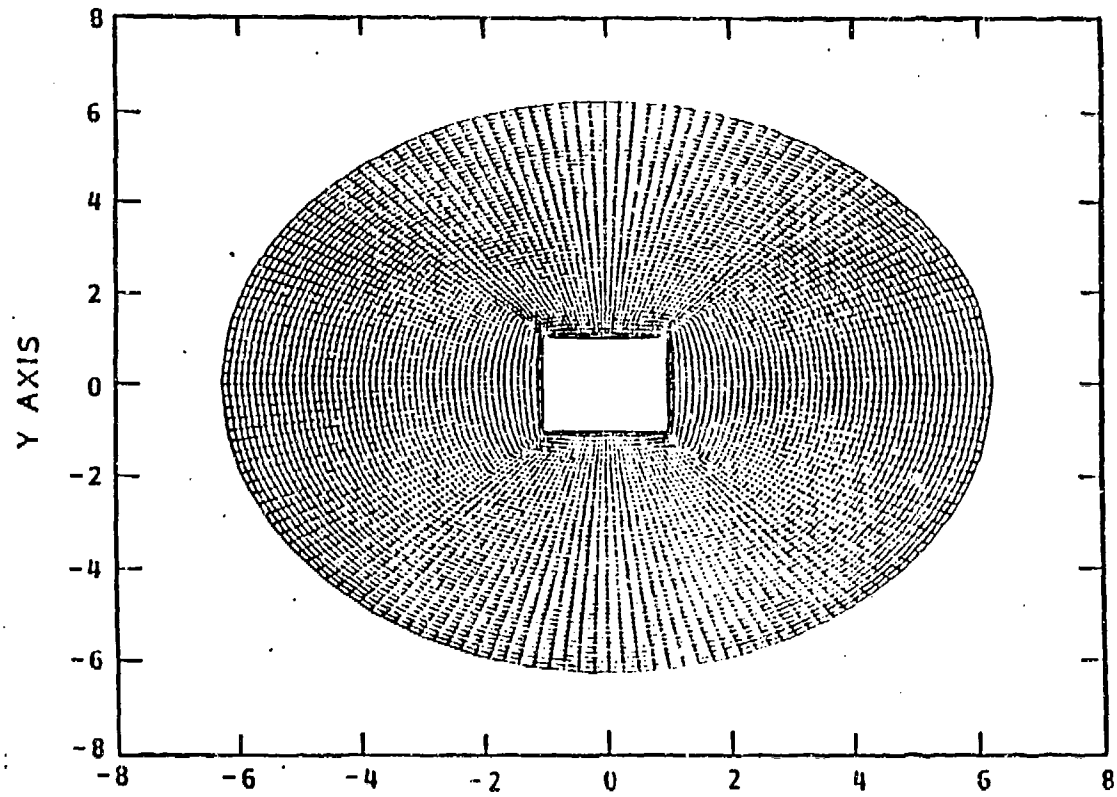


FIGURE 8. CIRCULAR CYLINDER



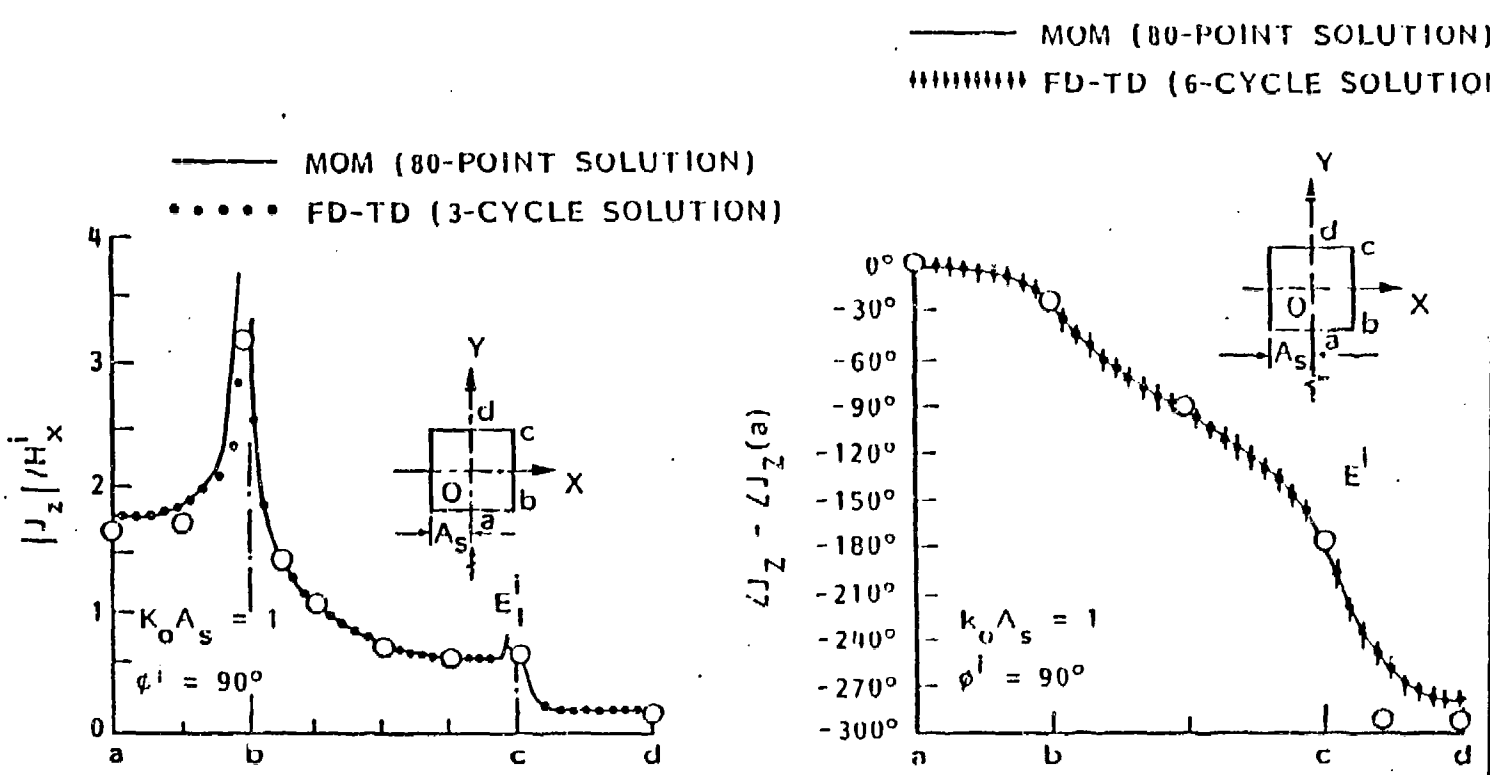


FIGURE 10. SQUARE CYLINDER - NORMAL INCIDENCE

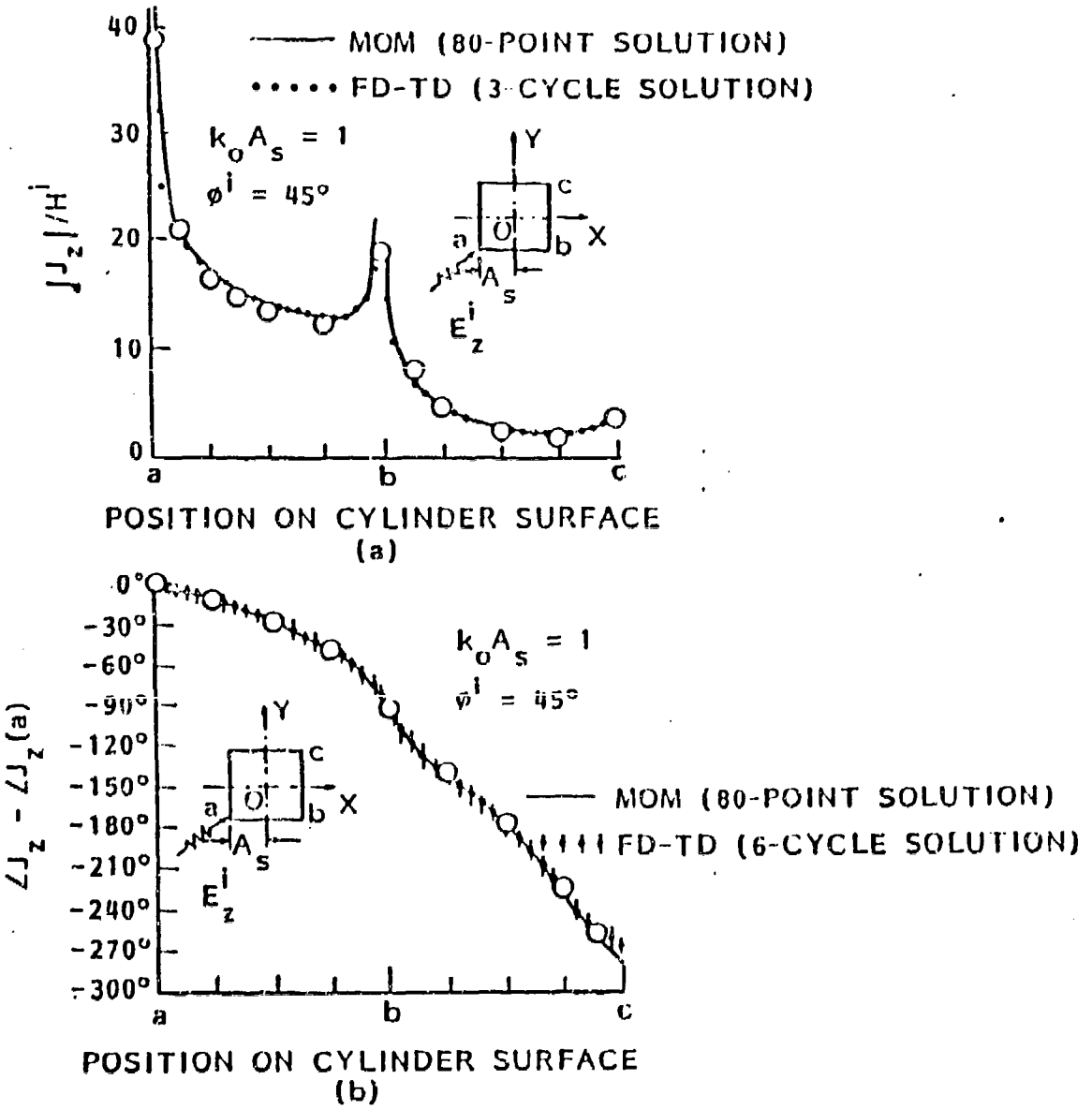
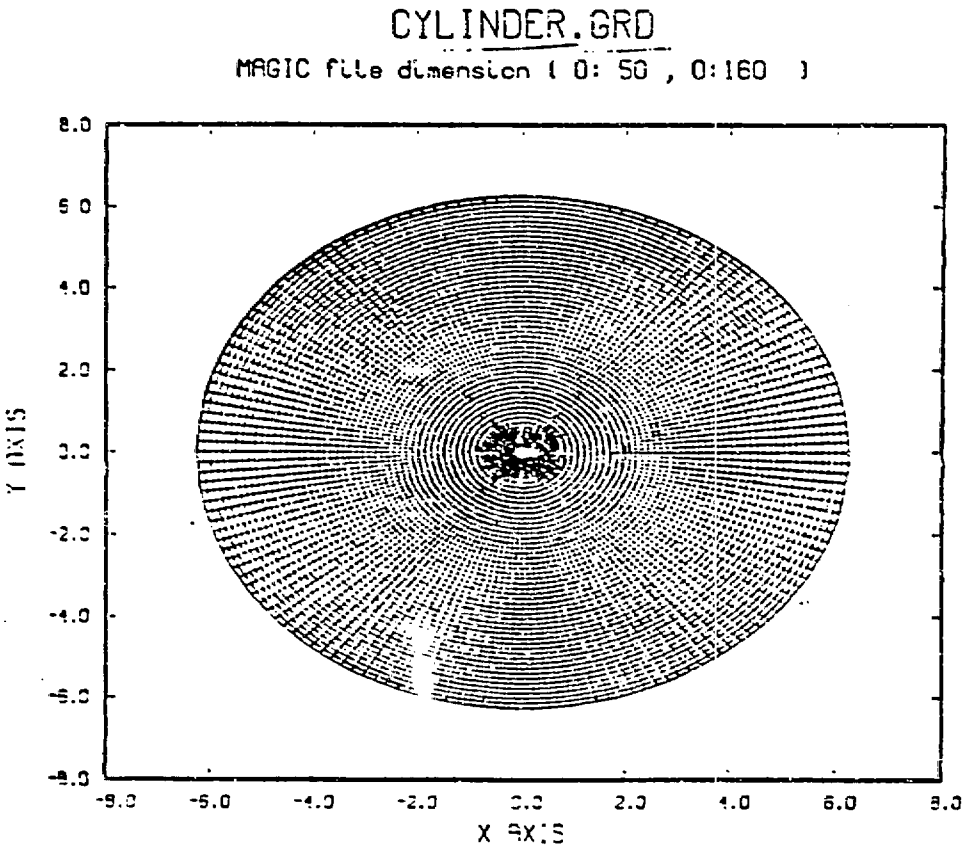


FIGURE 11. SQUARE CYLINDER - OBLIQUE INCIDENCE



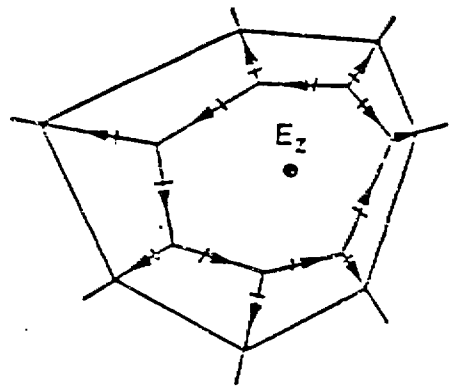


FIGURE 4. FIELDS NEAR SINGULARITY

CONSTRAINTS

COMPUTATIONAL GRID MUST BE SUFFICIENTLY LARGE

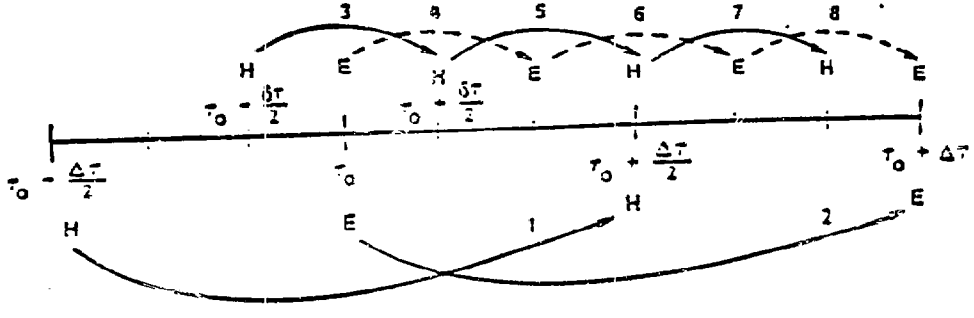
$$\Delta x \leq \lambda/10$$

$$c\Delta t \leq \Delta x$$

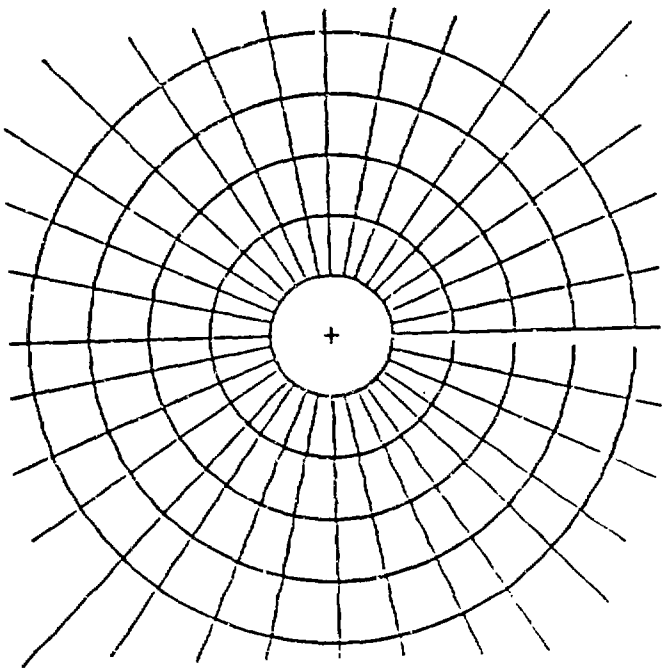
THESE CONSTRAINTS COMBINE WITH COMPUTER RESOURCE CONSIDERATIONS TO PLACE AN UPPER LIMIT ON THE SIZE OF THE SCATTERER. CURRENTLY, SCATTERERS WHOSE DIMENSIONS ARE SEVERAL WAVELENGTHS CAN BE TREATED.

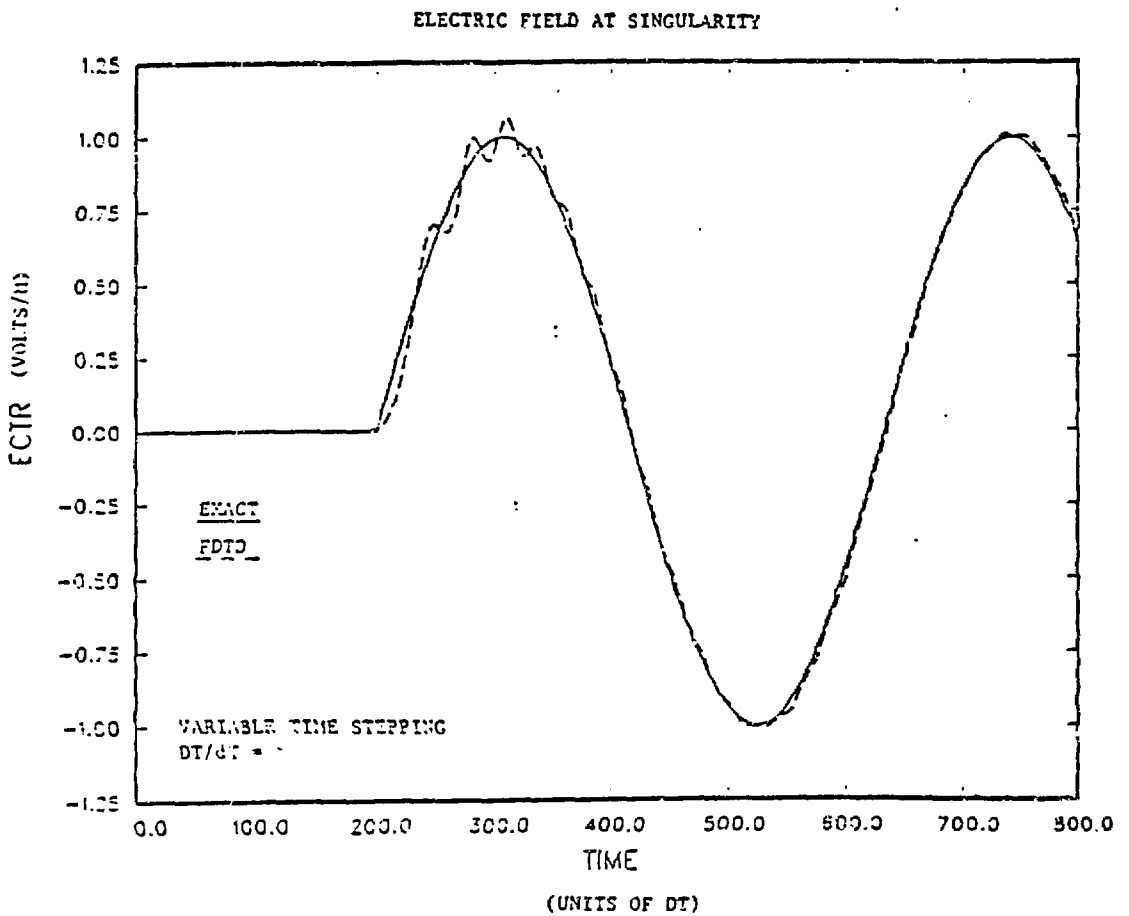
VARIABLE TIME STEPPING

COARSE AND FINE TIME STEPS CAN BE DEFINED IN DIFFERENT REGIONS OF THE GRID. IN EACH REGION THE FDTD ALGORITHM PROCEEDS AS BEFORE; SPECIAL PROCESSING IS REQUIRED ALONG THE 'SEAM'. THIS PROCEDURE HAS BEEN SHOWN TO WORK WITH ESSENTIALLY NO ERROR AND WITH A CONSIDERABLE SAVING IN COMPUTER TIME.



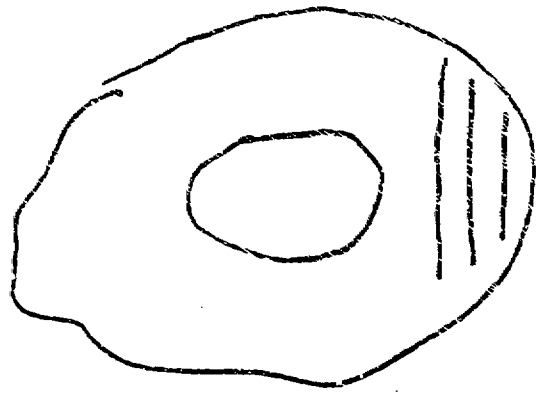
VERIFICATION - SINGULARITY PROCESSING & VARIABLE TIME STEPPING - RATIO = 5



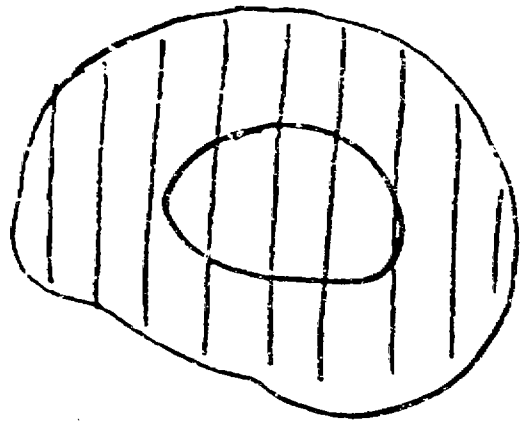


HIGH FREQUENCY FDTD

STANDARD INITIALIZATION



HIGH FREQUENCY INITIALIZATION



TURN ON BODY AT TIME=0

HIGH FREQUENCY FDTD

DISTURBANCE TRAVELS RADIALLY OUTWARD

DROP THE RADIATION BOUNDARY CONDITION

INTEGRATE ON SURFACE HALFWAY TO BOUNDARY

FREQUENCY MUST BE HIGH ENOUGH

RUN TIME MUST BE CAREFULLY SELECTED

HIGH FREQUENCY FDTD

START WITH A SOLUTION TO THE MAXWELL SYSTEM

FDTD ALGORITHM PRODUCES A NEW SOLUTION AT ANY TIME

THE BOUNDARY CONDITIONS ARE ENFORCED

THE SOLUTION IS UNIQUE: IT IS <u>THE</u> SOLUTION!

HIGH FREQUENCY FDTD

CYLINDER WITH A = 1, LAMBDA = .1

CONVENTIONAL: R=2, DR=.01, D(theta)=.005, D(tau)=.005

NI=100, NJ=1200, NTIME=1600

PRODUCT = 1.8E08

THIS RUN WOULD TAKE 50 HOURS ON THE VAX (CPU TIME)

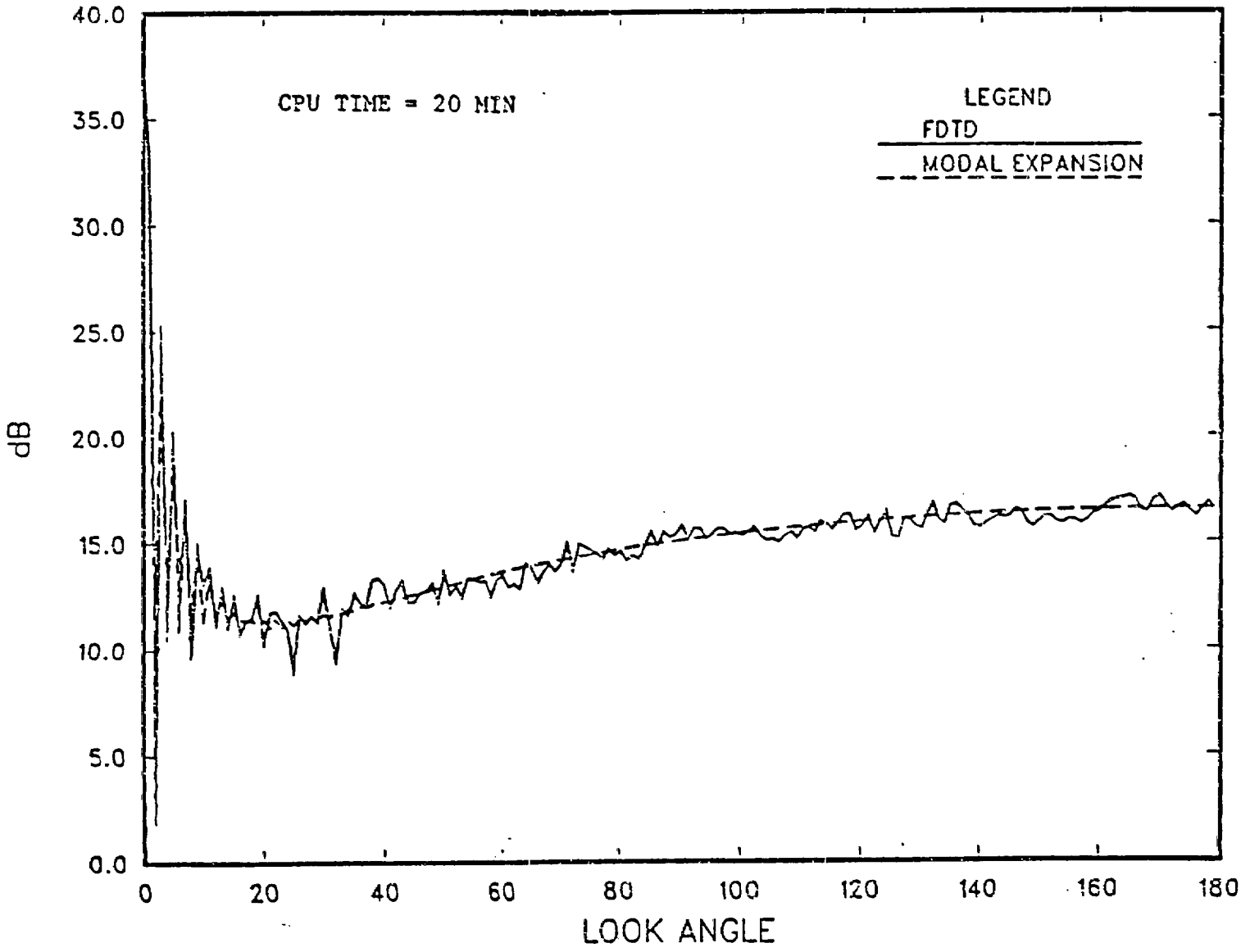
HIGH FREQUENCY: NI=40, NJ=880, NTIME=80

PRODUCT = 2.8E06

LESS THAN HALF HOUR OF VAX CPU TIME

BISTATIC RADAR CROSSECTION

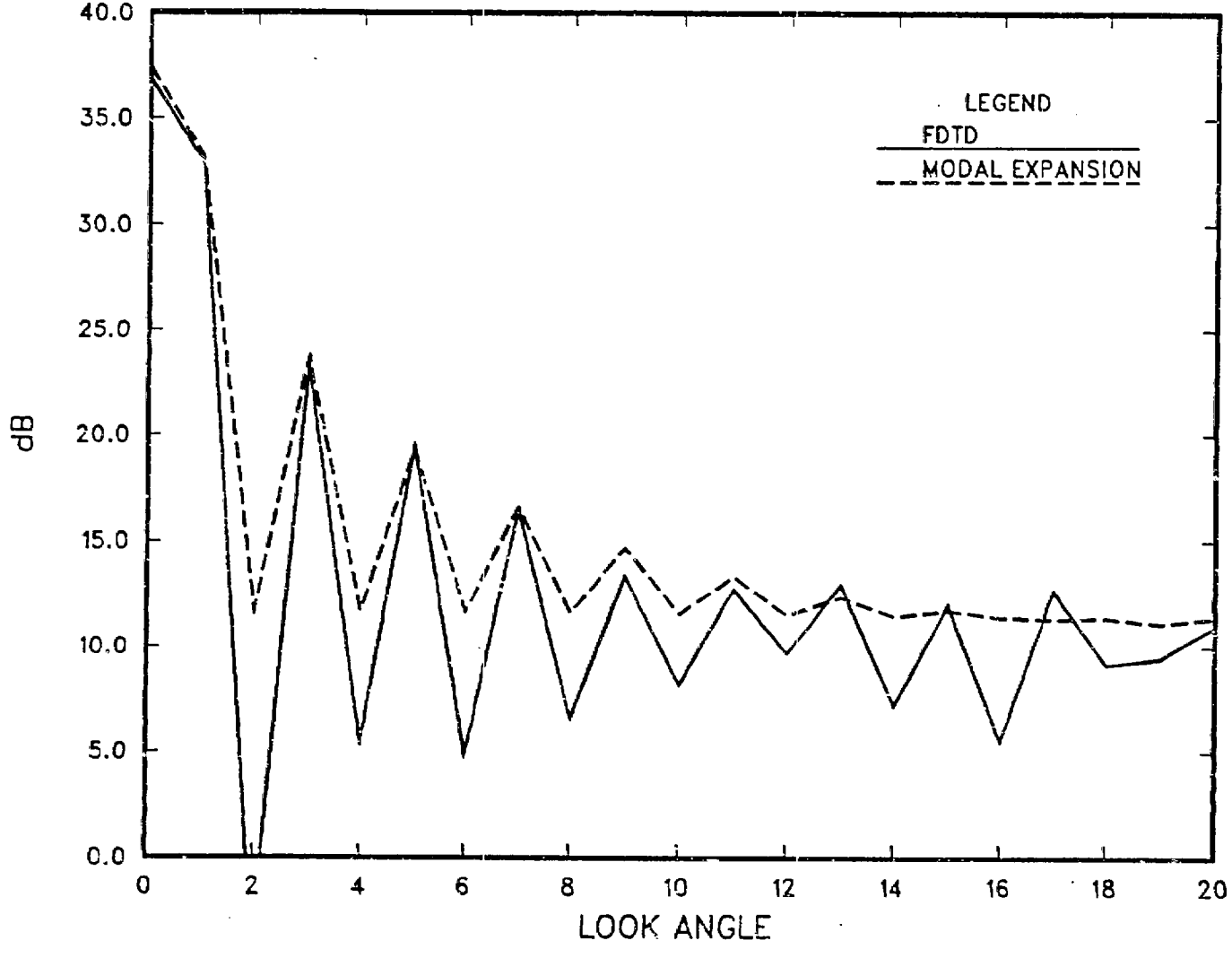
CONDUCTING CYLINDER



FREQUENCY (MHz) = $4.3234 * 10^3$ KA = 90.6403

BISTATIC RADAR CROSSECTION

CONDUCTING CYLINDER



FREQUENCY (MHz) = $4.3234*10^3$ KA = 90.6403

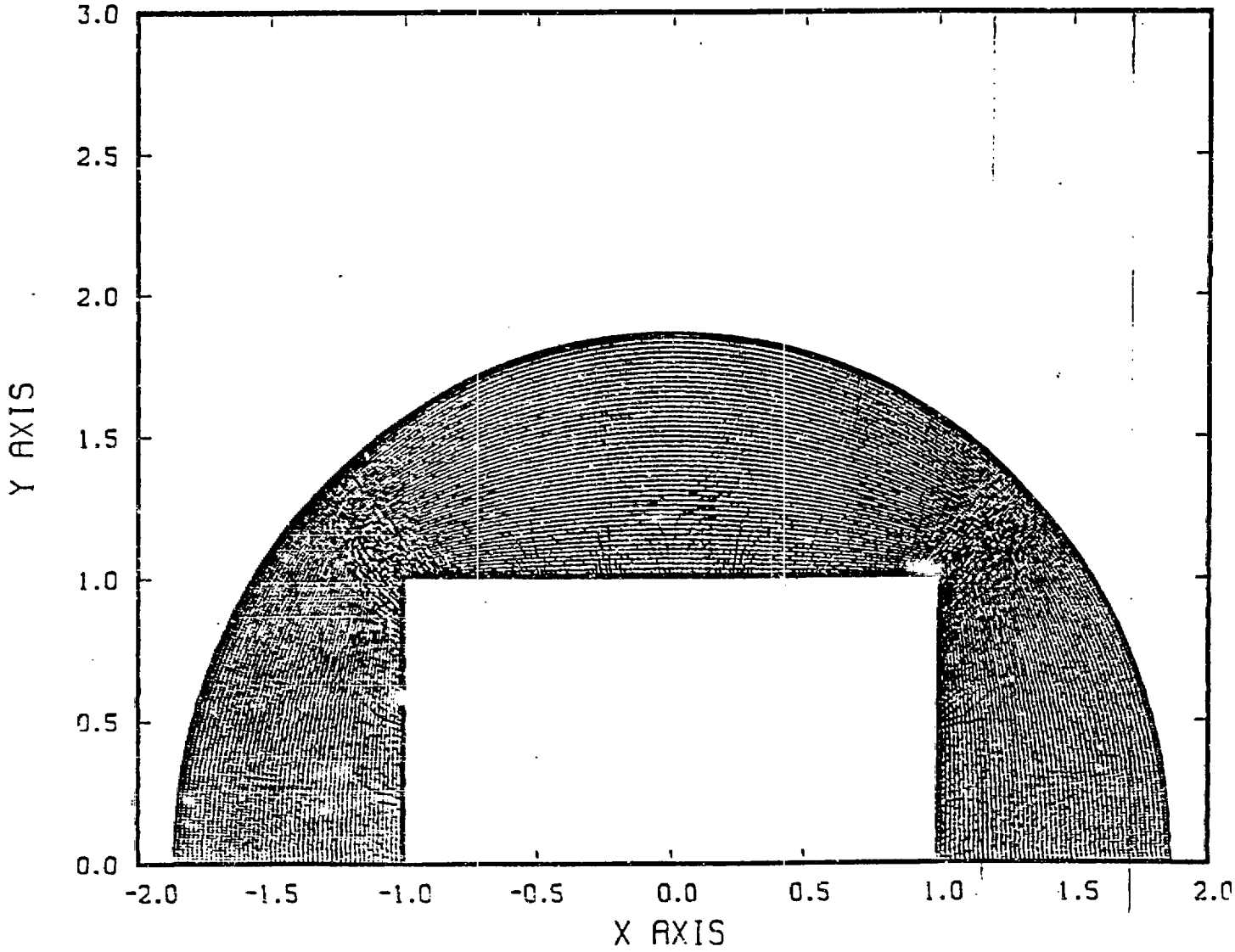
NTIME = 110 IRAD = 15.0000

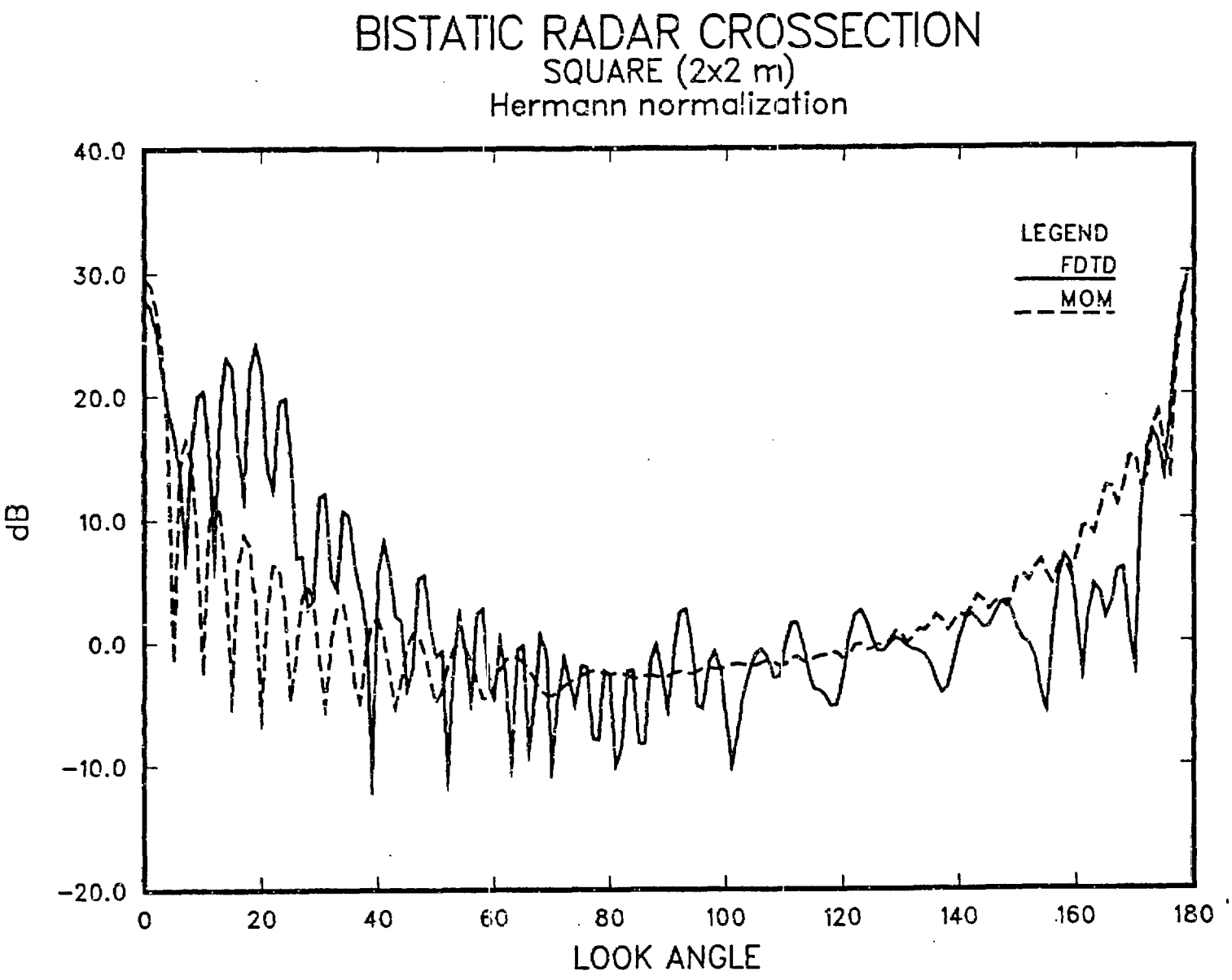
This is only a plot of the grid file

[GORDON.GRIDS]

SQUARE1.GRD

Grid file dimension (0: 50 , 0:1096)



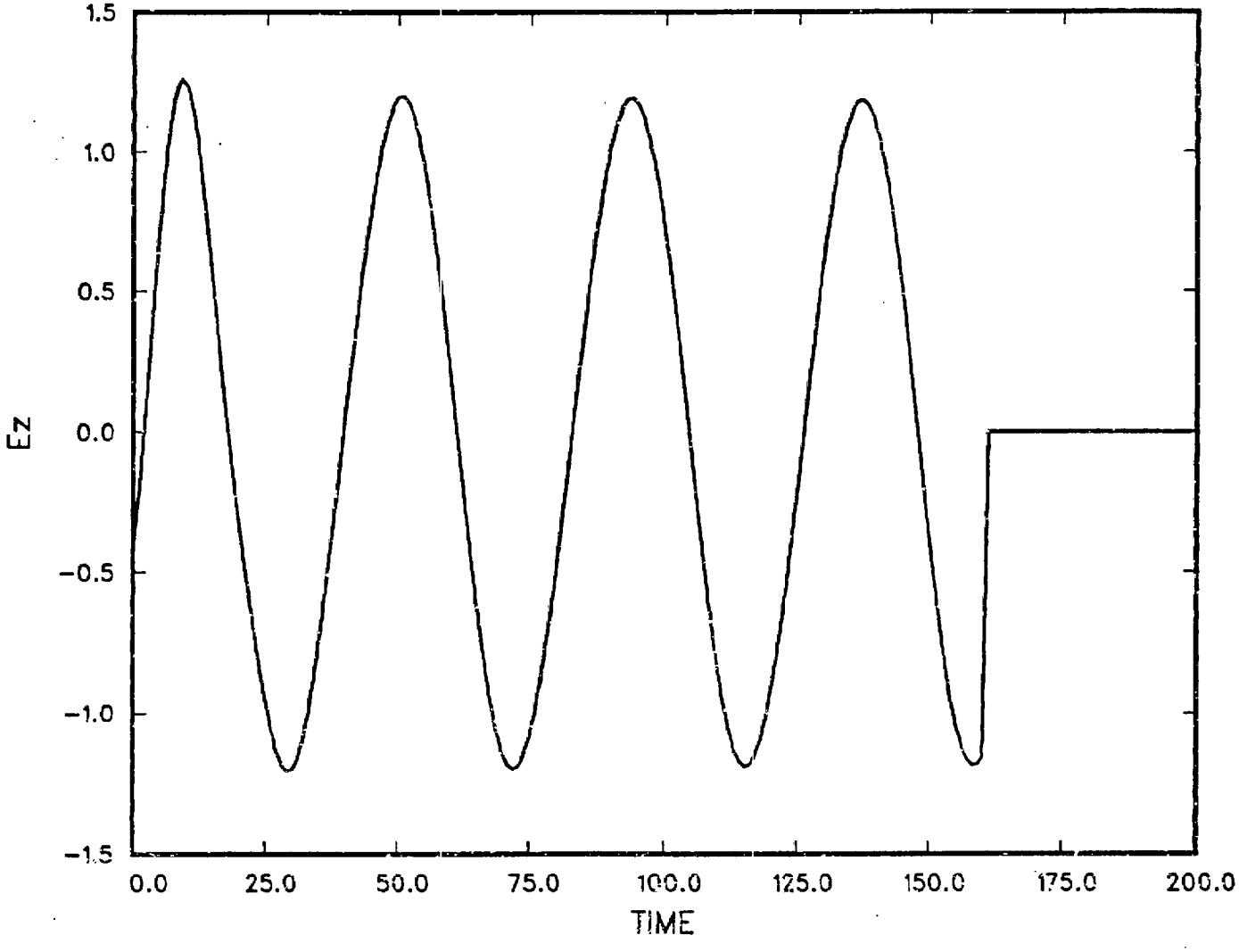


FREQUENCY (MHz) = 1762.94 KA = 36.96 INC. ANGLE = 180.00
NTIME = 160 IRAD = 2.00

PLOT 1 10.27.19 TUES 15 MAR, 1988 JOB-HARRYS , LSMC PALO ALTO LABS DISSPLA 9.0

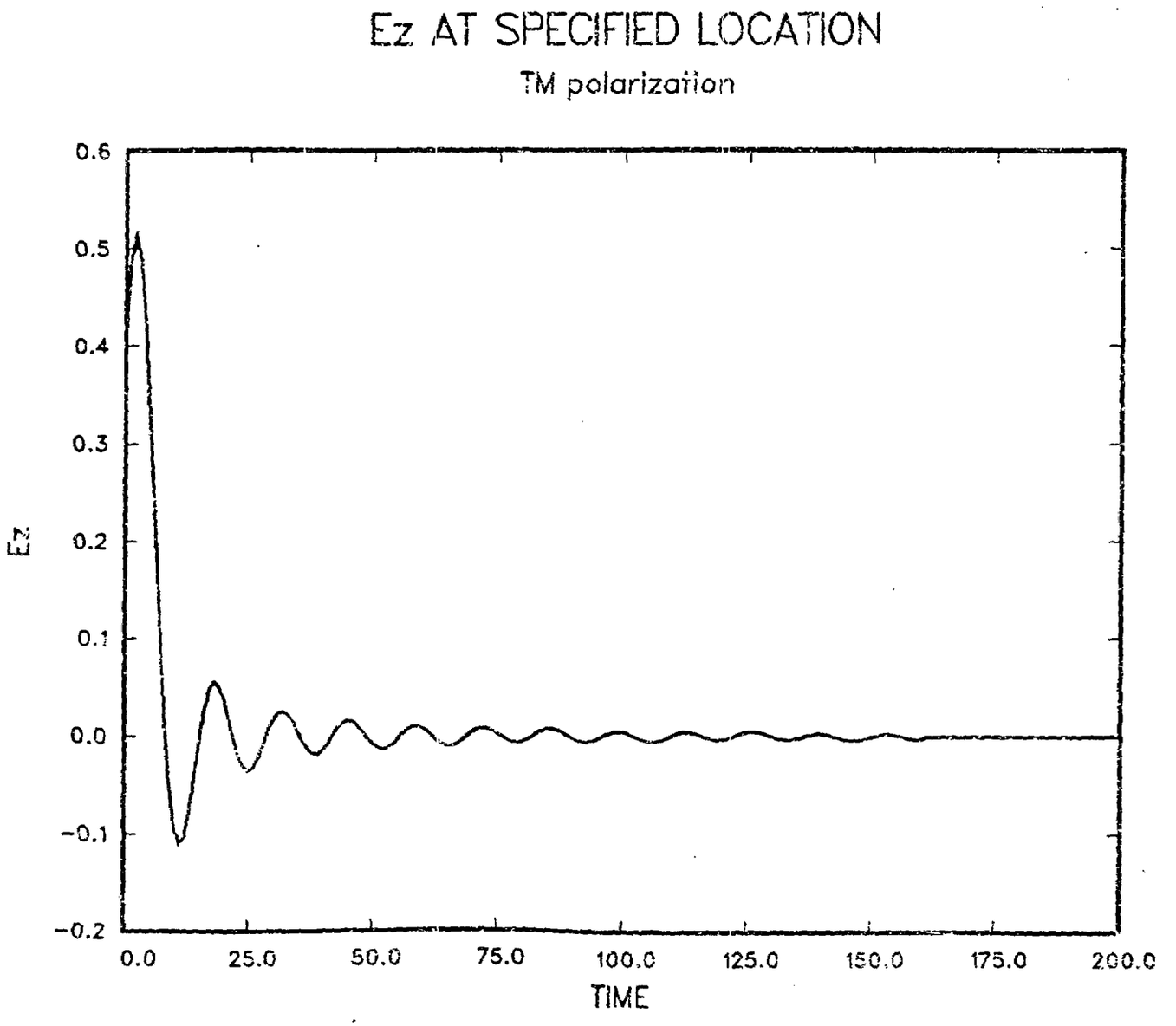
Ez AT SPECIFIED LOCATION

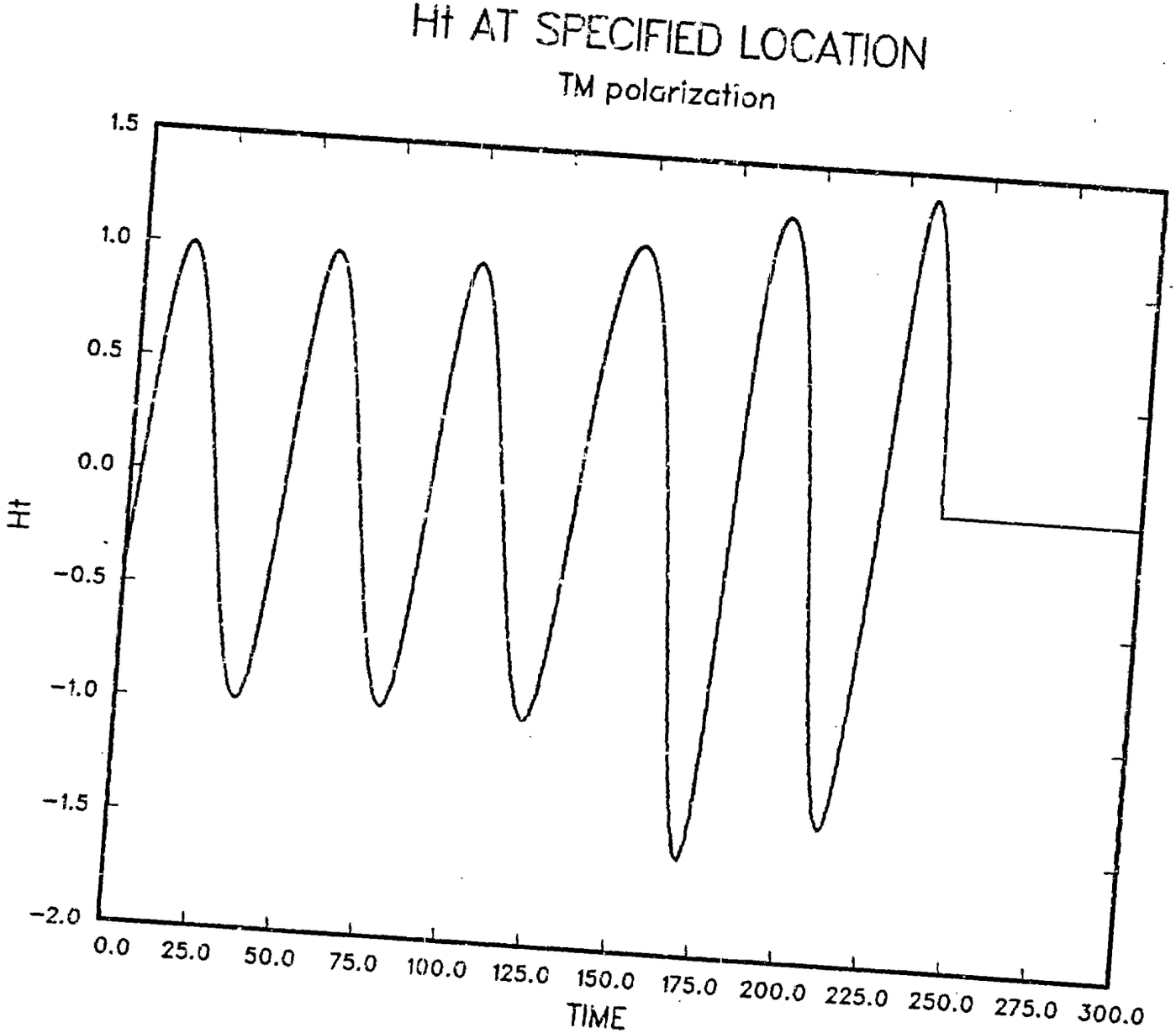
TM polarization



I = 0.000000

I = 0.000000


Ez AT SPECIFIED LOCATION
TM polarization
0.6
0.5
0.4
0.3
0.2
0.1
0.0
-0.1
-0.2
Ez
0.0
25.0
50.0
75.0
100.0
125.0
150.0
175.0
200.0
TIME
I = 0.000000
J = 548.0000



I = 30.00000
J = 0.000000

SESSION II - "COMPUTATIONAL ISSUES"

Moderator: Edgar L. Coffey
Advanced Electromagnetics

"Using Impedance Matrix Frequency Derivatives for Estimating Broadband Transfer Functions"
G. Burke — Lawrence Livermore Lab
E.K. Miller — Rockwell Science Center

"The 7-Digit Precision Environment - A Numerical Challenge"
Ruediger Anders — Applied Electromagnetics Engineering
* Paper was not submitted and is not presented.

"Do We Need Double Precision For EM Applications in the 7-Digit PC and Workstation World?"
Ruediger Anders — Applied Electromagnetics Engineering
* Paper was not submitted and is not presented.

"A Block Elimination Equation Solver for Large Matrices in the 7-Digit Environment"
Ruediger Anders — Applied Electromagnetics Engineering
* Paper was not submitted and is not presented.

"The MAFIA Approach to Solving Maxwell's Equations in Three Dimensions"
R.K. Cooper, M.J. Browman — Los Alamos National Laboratory
T. Weiland — Deutsches Elektronen-Synchrotron

"An Improved Exact Kernel for MININEC"
J.C. Logan and J.W. Rockway — Naval Ocean Systems Center
D. Wilton — University of Houston

"Numerical Integration Schemes in Calculating the Fourier Coefficiencies of the Free-Space Green's Function"
J.C. Peterson — Photon Research Associates Inc.

"Accurate and Efficient Numerical Computation of Sommerfeld Integrals for Layered Media Green's Functions"
B.L. Brim and David C. Chang — University of Colorado

USE OF FREQUENCY-DERIVATIVE INFORMATION TO RECONSTRUCT AN ELECTROMAGNETIC TRANSFER FUNCTION

G. J. Burke, P.O. Box 5504, L-156, Lawrence Livermore National Laboratory, Livermore, CA 94550
E. K. Miller, Rockwell International Science Center, Thousand Oaks, CA 91360

ABSTRACT
A need to determine the electromagnetic response of an object over a specified frequency band is frequently encountered in numerical modeling. This is typically done using many successive evaluations of a moment-method (MM) model over the frequency range of interest, leading to possibly excessive computer time if many frequency samples are required. One way of reducing the number of frequencies at which the MM calculation must be done is by introducing *a priori* knowledge of the expected frequency behavior in the form of a model, a pole series for example. The model could also be based on frequency samples or on frequency derivatives of the response exploiting the fact that these derivatives can be obtained recursively using significantly less time than that needed to develop the initial impedance and admittance matrices. Both of these approaches are discussed here.

I. INTRODUCTION

The electromagnetic response of an antenna, propagation path, or a scatterer is most often needed over a spectrum of frequencies rather than at just one or a few isolated frequency points. This is increasingly the case as the operating bandwidths of systems increase or their transient responses are required.

For various reasons, including the fact that most electromagnetic textbooks and courses continue to emphasize time-harmonic analysis, development of wideband spectral responses or even a short-pulse transient response is most often based on using a set of discrete frequency samples. Unfortunately, the samples used and their spacing in frequency seem to be determined more often by the esthetic appearance of straight-line or other low-order interpolation rather than by exploiting the underlying physics of the phenomenon being modeled. The result can be that many more frequency samples are used than should be necessary from sampling requirements based on information theory, with a consequent but avoidable increase in the cost of the associated computation or measurement.

As an alternative to this interpolatory approach, perhaps best described as curve-fitting , we develop and demonstrate two sampling techniques which incorporate a model of the expected behavior based on electromagnetic physics, which can be called "model-based parameter estimation" (MBPE). An example of this idea, applied in a quite different context, is that of replacing the Sommerfeld integrals which occur in the interface problem by simple analytical approximations whose amplitudes are determined numerically by matching them to accurately computed Sommerfeld integrals [Burke and Miller (1984)]. A more thorough discussion of MBPE applications in electromagnetics is given by Miller (1987).

One MBPE approach uses ordinary discrete frequency samples to develop a functional representation of the sought-for frequency response. The second takes advantage of an evidently previously unused property of the moment-method impedance and admittance matrices to obtain derivatives of the frequency response for much less computational cost than that required to obtain the original response at that same frequency. Each approach utilizes the mathematical property that the frequency response is well approximated by a rational function or ratio of two polynomials (the model) in which the variable is the complex frequency and in which the parameters are the polynomial coefficients. The problem then becomes one of determining numerical values for the unknown coefficients which appear in the rational function by using whatever appropriate data might be available. As we will show, the possibility then also arises of developing a generalized moment-method admittance matrix whose coefficients are themselves functions of complex frequency, leading to further interesting ramifications for obtaining and representing both spectral and temporal responses. The use of both frequency sampling and frequency-derivative sampling is summarized below, followed by representative numerical examples which illustrate application of the latter.

II. MODEL-BASED PARAMETER ESTIMATION

A. A Polynomial Representation

Development of a frequency-sampled MBPE electromagnetic transfer function requires frequency samples of the response which is to be estimated and an appropriate model whose parameters are to be evaluated numerically from those samples. The approach taken here originates from the Singularity-Expansion Method [Baum (1976)] in using a pole series in complex frequency $s = \sigma + j\omega$ having the form

$$F(s) = F_p(s) + F_{np}(s) = \sum_{\alpha=1}^{P} \frac{R_\alpha}{(s - s_\alpha)} + \sum_{\beta=-Q}^{R} C_\beta s^\beta \tag{1}$$

where the polynomial $F_{np}(s)$ accounts for the nonpole (except for possible $s = 0$ poles) portion of $F(s)$, and in $F_p(s)$ the $2P$ parameters R_α and s_α are the residues or amplitudes of the response and the corresponding poles, respectively. We note that the nonpole part of Eq. (1) as used here is assumed to have polynomial terms in complex frequency extending from powers of $-Q$ to $+R$. Also observe that while the number of poles is theoretically infinite, a computationally impractical situation, here we are concerned with developing an approximation to $F(s)$ over a limited frequency band so that the number of poles needed in the model will be relatively small, say 10 or fewer, and problems associated with ill conditioning might be avoided. This presumes that two or more different models might be used to cover a wider frequency band. The difference between models in overlapping frequency intervals could provide an error measure for an adaptive-sampling scheme, as briefly discussed in Section V below.

Upon transforming Eq. (1) into least-common denominator form, we obtain the rational-function counterpart

$$F(s) = N(s)/D(s) \tag{2a}$$

for which a more convenient computational version is obtained by multiplying by $D(s)$ to get

$$F(s)D(s) = N(s) \tag{2b}$$

The numerator and denominator polynomials are given respectively by

$$N(s) = N_0 + N_1 s^1 + N_2 s^2 + \ldots + N_n s^n \tag{3a}$$

and

$$D(s) = [D_0 + D_1 s^1 + D_2 s^2 + \ldots D_d s^P] s^Q \tag{3b}$$

with terms of maximum order given by $n = P + R - 1$ and $d = P + Q$, respectively, in the numerator and denominator. We next discuss how the numerator- and denominator-polynomial coefficients can be computed using frequency sampling or frequency-derivative sampling of the transfer function $F(s)$. For simplicity, we limit our discussion here to the cases where $F_{np}(s) = 0$ for frequency sampling and $F_{np}(s) =$ constant for frequency-derivative sampling, (i.e., $Q = R = C_0 = 0$ and $Q = R = 0$, respectively). We also assume that only the number of samples needed for computing the number of unknown polynomial coefficients is employed, i.e., an overdetermined system is not used.

B. Computing Model Coefficients Using Frequency Samples

The coefficients of Eq. (3) can be found if samples $F_i = F(s=X_i)$, for $i = 0, 1, \ldots, 2P + 1, \ldots$ of the response-function $F(s)$ are available, which for real-frequency sampling means that $X_i = j\omega_i$. Although there seem to be $2P + 1$ unknown coefficients in Eq. (3) as written, at least one of these must be specified independently to obtain an inhomogeneous set of equations, a conclusion that can also be reached by

noting that there are only 2P unknown coefficients represented by R_α and s_α. Furthermore, those 2P complex parameters represent only 2P real unknowns because the poles and residues occur in conjugate pairs, which also means that the numerator- and denominator-polynomial coefficients are real as well. Although any one of the 2P + 1 numerator- and denominator-polynomial coefficients could be specified, this is usually accomplished by setting $D_d = 1$ as is done here.

The resulting procedure may be regarded as a logical extension of Prony's Method which was developed originally for an exponential, rather than a pole, series. For this reason the technique summarized below has been referred to as "Frequency-Domain Prony" [Brittingham, et. al. (1976)], although it is better known as rational-function approximation.

In sampled form, Eq. (2b) is given by

$$F_i D(X_i) = N(X_i);\ i = 0, 1, 2, \ldots, n+d-1=2P-1, \ldots \tag{4}$$

which reduces to the following system of equations [Miller (1987)]

$$\begin{bmatrix} F_0 & X_0F_0 & \cdots & X_0^{P-1}F_0 & -1 & -X_0 & \cdots & -X_0^{P-1} \\ F_1 & X_1F_1 & \cdots & X_1^{P-1}F_1 & -1 & -X_1 & \cdots & -X_1^{P-1} \\ \vdots & \vdots & \vdots & \vdots & \vdots & \vdots & \vdots & \vdots \\ \vdots & \vdots & \vdots & \vdots & \vdots & \vdots & \vdots & \vdots \\ \vdots & \vdots & \cdots & \vdots & \vdots & \vdots & \cdots & \vdots \\ F_{2P-1} & X_{2P-1}F_{2P-1} & \cdots & X_{2P-1}^{P-1}F_{2P-1} & -1 & -X_{2P-1} & \cdots & -X_{2P-1}^{P-1} \end{bmatrix} \begin{bmatrix} D_0 \\ \vdots \\ D_{P-1} \\ N_0 \\ \vdots \\ N_{P-1} \end{bmatrix} = \begin{bmatrix} X_0^P F_0 \\ X_1^P F_1 \\ \vdots \\ \vdots \\ X_{2P-2}^P F_{2P-2} \\ X_{2P-1}^P F_{2P-1} \end{bmatrix} \tag{5}$$

The rational-function approximation to the sampled transfer function is thereby obtained in terms of the frequency-sampled data F_i by solving Eq. (5) for the numerator- and denominator-polynomial coefficients. At this point, the modal calculation has been completed, although as a further step we could also obtain the system poles and zeroes by solving $D(s) = 0 = D(s_\alpha)$ and $N(z) = 0 = N(z_\alpha)$.

C. Computing Model Coefficients Using Frequency-Derivative Samples

The same rational-function model can be used when frequency-derivative samples are employed rather than frequency samples. Starting with Eq. (2) and upon differentiating t times with respect to s and dropping the explicit s dependence, there results the following equations

$$\begin{aligned} &FD = N \\ &FD' + FD' = N' \\ &F''D + 2F'D' + FD'' = N'' \\ &F'''D + 3F''D' + 3F'D'' + FD''' = N''' \\ &\cdot \\ &\cdot \\ &\cdot \\ &F(t)D + t\Gamma(t-1)D(1) + \ldots + C_{t,t-m}F^{(m)}D^{(t-m)} + \ldots + FD^{(t)} = N^{(t)} \end{aligned} \tag{6}$$

where $C_{r,s} = r!/[s!(r-s)!]$ is the binomial coefficient. The system of t+1 equations in Eq. (6) (there are t frequency-derivative samples plus the original frequency sample) provides the information from which the model coefficients can be found if $t \geq n+d+1$. With no loss of generality, Eq. (6) can be simplified by setting $s = 0$ since s can represent the variation in frequency about the point where the frequency-derivative samples are obtained. We then find the following matrix representation for the unknown numerator- and denominator- polynomial coefficients

$$\begin{bmatrix} 1 & 0 & \cdots & 0 & 0 & 0 & \cdots & 0 \\ 0 & 1 & \cdots & \vdots & -F_0 & 0 & \cdots & 0 \\ 0 & 0 & \cdots & 0 & -F_1 & -F_0 & \cdots & 0 \\ 0 & 0 & \cdots & 1 & -F_2 & -F_1 & \vdots & \vdots \\ 0 & 0 & \cdots & 0 & \vdots & -F_2 & \vdots & \vdots \\ \vdots & \vdots & \vdots & \vdots & \vdots & \vdots & \vdots & 0 \\ 0 & 0 & \cdots & 0 & -F_{n+d-1} & -F_{n+d-2} & \cdots & -F_n \end{bmatrix} \begin{bmatrix} N_0 \\ N_1 \\ \vdots \\ N_n \\ D_1 \\ \vdots \\ D_d \end{bmatrix} = \begin{bmatrix} F_0 \\ F_1 \\ F_2 \\ \vdots \\ \vdots \\ \vdots \\ F_{n+d} \end{bmatrix} \tag{7}$$

where the samples are now $F_m = m!F^{(m)}$. As noted above for frequency sampling, at least one coefficient of the two polynomials must be specified to render the system inhomogeneous. We have chosen here to use $D_0 = 1$.

This linear system, solution of which yields the coefficients of the rational-function model for a transfer function based on frequency-derivative samples, is somewhat similar to that presented above for frequency sampling. The approach summarized here is known as Pade approximation [Jones (1979)], although we might regard it as a further generalization of the various extensions of Prony's Method as discussed above and elsewhere [Miller (1987)]. All of these variations of the basic Prony Method have the goal of using computed or measured data to develop a numerical model for some phanomenological response which can be approximated by either a series of exponentials or a series of poles, although as noted above in Eq. (1), some nonpole (or nonexponential) terms can also be included. In the next section, we discuss how the frequency derivatives of the response can be found as a generalization of a moment-method model.

III. COMPUTING FREQUENCY DERIVATIVES IN A MOMENT-METHOD MODEL

A. The Basic Idea

As noted above, the coefficients needed to numerically quantify the pole-series or rational-function model for the transfer function of interest can in principal be obtained from whatever information is available. As an alternative to using only frequency samples, which although a straightforward approach offers no further computational efficiency beyond reducing the number of actual samples required, we now consider using frequency derivatives of the response. The basis for the technique is due to earlier work by one of the authors (Burke) as reported in Miller, et. al. (1970). As we will show, the additional programming complexity that arises in computing frequency derivatives from a moment-method model can be compensated by a further reduction in overall computer time.

On writing the moment-method equations that arise from an integral-equation formulation in matrix form, we have the impedance equation

$$\sum_{j=1}^{N} Z_{i,j} I_j = V_i \tag{8a}$$

where Z, I and V are the usual impedance matrix and the current and voltage vectors, respectively. A solution for the current can then be formally written as an admittance equation

$$I_i = \sum_{j=1}^{N} Y_{i,j} V_j \tag{8b}$$

where the matrix Y is the inverse of Z. We should note however that the approach developed here for the frequency derivatives could be implemented using LU factorization, iteration, or any other solution method.

Now let us differentiate the impedance equation with respect to frequency from which we obtain

$$\sum_{j=1}^{N}(Z_{i,j}I_j' + Z_{i,j}'I_j) = V_i' \tag{9a}$$

where the prime denotes a frequency derivative. A solution of the differentiated impedance equation for the differentiated current can then be written

$$I_i' = \sum_{j=1}^{N} Y_{i,j}\left(V_j' - \sum_{k=1}^{N} Z_{j,k}'I_k\right) \tag{9b}$$

where we observe that while the differentiated impedance matrix appears as part of a modified right-hand-side of the differentiated admittance equation, I' is given in terms of an undifferentiated admittance matrix. Computing the differentiated current thus requires an additional number of computations beyond those needed for solution of the undifferentiated current proportional to N^2 rather than the N^3 that would apply to obtain another frequency sample (assuming that LU decomposition is used rather than iteration).

Continuing this process, we find that the n'th frequency derivative of the current is given by

$$I_i^{(n)} = \sum_{j=1}^{N} Y_{i,j}\left[V_j^{(n)} - \sum_{m=1}^{n} C_{n,m}\left(\sum_{k=1}^{N} Z_{j,k}^{(m)} I_k^{(n-m)}\right)\right] \tag{10}$$

where again $C_{n,k}$ is the binomial coefficient and the superscript in parenthesis indicates differentiation with respect to frequency of the order indicated. This equation is essentially identical in form to Eq. (6), and demonstrates the similarity between the differentiated rational-function and the moment-method models.

It is especially important to observe that information about the n'th frequency derivative of the current continues to require a computer time proportional to N^2. Expressed in another way, each additional frequency derivative of the solution vector for the current can be computed in a number of operations proportional to $A(n,N_{rhs})/N$ where A is a function which depends on the order of the derivative and the number of right-hand sides for which the solution is sought. If the frequency derivatives provide information comparable to that available from the frequency samples themselves, it can be appreciated that there could be a substantial computational advantage to using the solution derivatives in estimating the transfer functions. In the next section, we consider how these computations can be done by modifying the NEC code.

B. An Implementation Using NEC

To implement frequency-derivative interpolation (FDI) as summarized above, the derivatives of the impedance matrix must be evaluated. In a code such as NEC, the fields which comprise the impedance matrix can have two sources of frequency dependence. One of these is due to the frequency dependence of the field expressions themselves, and the other can arise, as in NEC, from the basis and testing functions. NEC employs point sampling, i.e., delta-function testing, which is not frequency dependent but does use the three-term sinusoidal current expansion function

$$I_i(s) = A_i + B_i \sin[k_s(s-s_i)] + C_i \cos[k_s(s-s_i)] \tag{11}$$

where k_s is normally set equal to the medium wavenumber k. This is done because analytical expressions are then available for five of the six field components needed for general problems. But the frequency dependence of the basis function which thereby occurs can greatly complicate implementation of FDI.

In implementing FDI in NEC it was decided to hold k_s constant in the basis functions to simplify the evaluation of derivatives. This step is justified by noting that the basis functions, although constructed from the functions of Eq. (11) which depend on k_s, have the form of B-splines which are insensitive to k_s for small $|k_s\delta|$. In addition, the solution is relatively insensitive to small changes in the shape of the basis functions. Hence, we started with equations for the field of the current components in Eq. (11) for $k_s \neq k$, derived the equations for the derivatives, and then set $k_s = k$. A further simplification was effected by using the VLF version of NEC (NEC3VLF) in which the numerically cancelling fields due to point charges at segment ends are analytically removed from the field equations. With the point-charge fields removed and $k_s \neq k$, the field components for a current of the form

$$I(z') = I_0 \begin{pmatrix} \sin(k_s z') \\ \cos(k_s z') \end{pmatrix} \tag{12a}$$

due to a segment extending from $-\delta$ to δ on the z axis of a cylindrical coordinate system are

$$E_\rho(\rho,z) = -\frac{jmI_0}{4\pi\rho}\left\{\left[k_s(z-z')\begin{pmatrix} \cos k_s z' \\ -\sin k_s z' \end{pmatrix}\frac{e^{-jkR}}{kR} - j\begin{pmatrix} \sin k_s z' \\ \cos k_s z' \end{pmatrix} e^{-jkR}\right]_{-\delta}^{\delta} - \frac{(k^2-k_s^2)}{k}\int_{-\delta}^{\delta} dz'(z-z')\begin{pmatrix} \sin k_s z' \\ \cos k_s z' \end{pmatrix}\frac{e^{-jkR}}{R}\right\} \tag{12b}$$

and

$$E_z(\rho,z) = -\frac{jmI_0}{4\pi}\left\{\left[-k_s\begin{pmatrix} \cos k_s z' \\ -\sin k_s z' \end{pmatrix}\frac{e^{-jkR}}{kR}\right]_{-\delta}^{\delta} + \frac{(k^2-k_s^2)}{k}\int_{-\delta}^{\delta} dz'\begin{pmatrix} \sin k_s z' \\ \cos k_s z' \end{pmatrix}\frac{e^{-jkR}}{R}\right\} \tag{12c}$$

The needed frequency derivatives of the fields are thus obtained by differentiating the above expressions with respect to k and then setting $k_s = k$. Consequently, derivatives of the integrals up to an order one less than the order of the derivative of the field remain when k_s is set equal to k. Considering in addition that E_z due to the constant term in the NEC basis is also needed, there are five integrals to evaluate for each order of differentiation.

The integrals and their derivatives were evaluated by expanding the exponentials and integrating the terms analytically. In this process each derivative shares some terms with the expansion for the previous derivatives. If numerical integration were used, the derivatives would share the exp(-jkR) term which accounts for much of the computation time. Hence, the additional effort is less than proportional to the number of derivatives. The remaining steps in evaluating the derivatives of Eq. (12) with respect to k are straightforward.

IV. SOME REPRESENTATIVE RESULTS

The modified version of NEC described above was applied to three antenna problems as a preliminary test of the frequency-derivative approach. As one of the simpler examples that might be attempted, we chose

a center-excited, straight-wire antenna. A more challenging case is presented by a straight horizontal wire located very near a conducting ground plane, which produces a much sharper resonance. The most difficult problem attempted is that of a forked monopole antenna having arms which are slightly different in length. Results from each case are summarized below.

A. Dipole Antenna In Free Space

Results are presented in Figure 1 for a center-excited dipole antenna modeled with NEC using 21 segments. A Taylor series and rational model were fit to the current and four derivatives ($t = 4$, $n = d = 2$) at a point L/λ_0 which is moved across the first resonance. Directly computed values were obtained at 0.01 intervals in L/λ. The Taylor series result is seen to follow the correct result over a relatively narrow region around the expansion point, while the rational-function model provides a good match over a much wider interval. Of course, the radius of convergence of the Taylor series is limited by the distance to the nearest pole in the complex plane as is evident in the decreased convergence interval as the expansion point moves through the resonance.

Both first and second resonances are shown in Figure 2, with the Taylor series and rational-function models fit at $L/\lambda_0 = 1.0$. Both resonances are recognized in the rational model, but not with high accuracy. Presumably a better result would be obtained with a higher order rational function fit to more derivatives.

B. Horizontal Dipole Antenna Close to a Ground Plane

Results for a horizontal antenna near a perfectly-conducting ground plane are presented in Figure 3. This case was selected to test the frequency-derivative model for a response function having a higher-Q resonance. The solid curve was computed with a sampling interval of 0.001 in L/λ. It can be seen that for a relative bandwidth of about 10^{-3}, the rational function model provides a good match to the actual results even when sampled as far as 250 resonance widths away. The Taylor-series results are not shown here because they are so far from the correct curve.

C. Unequal-Arm Vee-Monopole Antenna

A still more challenging case is presented by a Vee or forked-monopole antenna having arms of unequal length. As shown in Figure 4, this antenna has, in addition to the monopole resonance, a very sharp parasitic resonance due to a differential (transmission-line) current mode in the arms. The parasitic resonance corresponds to a pole very close to the real axis with a small residue, while the monopole resonance has a pole more distant from the real axis with a larger residue. This situation presents a severe challenge to the rational-function model derived from the current and four derivatives. When matched at $L/\lambda_0 = 0.6$ [L is the length of the longer arm with the shorter length (14/15)L with an included angle of 2.6 degrees], the rational-function model matches the monopole resonance with good accuracy. The second resonance is also detected albeit with very poor accuracy. At $L/\lambda_0 = 0.65$, the frequency of the second resonance is determined with reasonable accuracy, but the conductance is still negative. At $L/\lambda_0 = 0.7$, the parasitic resonance is modeled with excellent accuracy, as seen in the detail plot of Figure 5. Accuracy is lost in the monopole resonance, however. The sampling intervals in L/λ_0 for the solid curves were 0.003 for Figure 4 and 0.0005 for Figure 5. Performance of the rational-function model is not as good in this case as in the previous examples, although a very substantial reduction in sampling density can be achieved. We might also observe that the negative conductance and changes in the result with L/λ_0 provide an indication of where an additional sample point is needed.

V. SOME POSSIBLE EXTENSIONS AND APPLICATIONS

Attention so far has focussed on the basic concept of developing an analytical, rational-function form for an electromagnetic transfer function without considering the possible benefits of doing so beyond reducing the overall computer time needed to obtain wideband or transient responses. We discuss briefly below two possible benefits beyond computer-time reduction.

A. An Admittance-Matrix Function

The impedance and admittance matrices that arise in the moment method may be interpreted as

N-port-network approximations to the problem being modeled. When only a single port is excited, as is the case for most antenna applications, then the current vector that results gives the self and mutual admittances for that port. Exciting the other N-1 ports one at a time similarly provides the N(N-1) remaining admittances. Since typical problems rarely require all N^2 admittances, the inverse matrix is usually not computed and the solution is developed by LU decomposition, or iteration. Whatever excitation is used and however the solution is developed, the procedures outlined above can provide a rational-function approximation for the computed response.

A logical generalization of this somewhat limited approach is to represent some, or all, of the admittance-matrix coefficients in rational-function form. This is most easily done by either computing the inverse of the impedance matrix if all N^2 matrix coefficients are desired, or alternatively, computing current vectors caused by a sequence of single-port excitations. Whichever approach is used, we observe that the admittance matrix can be written in the general form

$$\overrightarrow{\overrightarrow{Y}}(s) = \begin{bmatrix} X & \cdots & X & y_{1a}(s) & \cdots & y_{1b}(s) & \cdots \\ X & \cdots & X & y_{2a}(s) & \cdots & y_{2b}(s) & \cdots \\ X & \cdots & X & y_{3a}(s) & \cdots & y_{3b}(s) & \cdots \\ \vdots & \vdots & \vdots & \vdots & \vdots & \vdots & \vdots \\ X & \cdots & X & y_{Na}(s) & \cdots & y_{Nb}(s) & \cdots \end{bmatrix} \tag{14a}$$

where the X's denote the admittances that have not been computed, and the $y_{ij}(s)$ are those whose rational-function forms are modeled. Upon observing that the system poles are analytically the same whatever system observable has been used to obtain them, Eq. (14a) can be rewritten as

$$\overrightarrow{\overrightarrow{Y}}(s) = \frac{1}{D(s)} \begin{bmatrix} X & \cdots & X & n_{1a}(s) & \cdots & n_{1b}(s) & \cdots \\ X & \cdots & X & n_{2a}(s) & \cdots & n_{2b}(s) & \cdots \\ X & \cdots & X & n_{3a}(s) & \cdots & n_{3b}(s) & \cdots \\ \vdots & \vdots & \vdots & \vdots & \vdots & \vdots & \vdots \\ X & \cdots & X & n_{Na}(s) & \cdots & n_{Nb}(s) & \cdots \end{bmatrix} \tag{14b}$$

where 1/D(s) is the common denominator polynomial, and the $n_{ij}(s)$ are the numerator polynomials for each computed admittance. These would usually be found as column vectors since for single-port excitation, solution for the spatial current yields a column of admittances.

The validity of Eq. (14b) derives from the fact that the mode amplitudes in Eq. (1) are the only parts of the pole response which are excitation dependent while the poles themselves are determined solely by the properties of the object for which F(s) has been obtained. We further note, based on Eq. (2b), that if F(s) and D(s) are known, then the corresponding N(s) is obtained from their product. Thus although the response (or its frequency derivatives) must be found for all admittances whose rational-function model is desired, this would not require repeated solution via the matrix equations (5) or (7). Finally, we observe that given part or all of the admittance matrix in the form of Eq. (14b), computing transient responses can be made much more efficient and convenient.

B. Adaptive Frequency Sampling

We mentioned above that application of the MBPE approach is expected to work best when the polynomials are of relatively low order, which means that only a small number of resonances can be spanned by a given model. It therefore follows that two or more separate rational-function models would be needed to cover a frequency interval spanning many object poles. While that may appear to be a disadvantage, it does provide the opportunity of developing an error measure and establishing a strategy for selecting the frequency points to be sampled.

This can be illustrated conceptually by considering two models $M_1(s)$ and $M_2(s)$ developed from samples

$f_1, \ldots, f_5$ and $f_3, \ldots, f_7$ respectively, using a frequency-sampled model. In their region of overlap, i.e., f_3 to f_5, we should expect that some measure of their mismatch, say $\Delta M(s)$, could be used to mutually validate both models. This should also provide an indication about whether more samples are needed in that region [when $\Delta M(s) > E$], or whether the sampling interval should be increased [when $\Delta M(s) < E$], where E is a maximum acceptable error. A similar approach could be employed using the frequency-derivative model. The goal in either case would be to automate selection of the frequencies at which samples of the response or its derivatives are computed or measured while ensuring that the rational-function model which results satisfies some specified error criterion.

VI. CONCLUSIONS

In this paper, we have introduced two main ideas:

1) Use of model-based parameter estimation (MBPE) based on rational-function approximations when obtaining electromagnetic transfer functions to reduce the number of frequencies at which samples are required, and

2) A sampling approach which employs frequency derivatives of the response using a new analytical technique based on differentiating the moment-method impedance equation, and which provides the derivative information in a time proportional to N^2 as contrasted with the N^3 dependency of solving the original problem.

Application of the frequency-derivative approach has been demonstrated for problems having well-defined resonances such as a dipole antenna in free space, and for more challenging problems having much narrower resonances such as a horizontal antenna brought close to a perfectly conducting ground plane and a "forked" monopole whose arms are slightly different in length. It should be clear that MBPE could develop into an important tool for not only increasing the efficiency of model applications, but in yielding more physically useful representations of those models.

VII. REFERENCES

Baum C. E. (1976), "The Singularity Expansion Method", Chapter 3 in *Transient Electromagnetic Fields*, Ed. L. F. Felsen, Springer-Verlag, New York.

Brittingham, J. N., E. K. Miller and J. L. Willows (1980), "Pole Extraction from Real-Frequency Information", Proceedings of the IEEE, 68, pp. 263-273.

Burke, G. J. and E. K. Miller (1984), "Modeling Antennas Near to and Penetrating a Lossy Interface", IEEE Transactions on Antennas and Propagation, AP-32, pp. 1040-1049.

Burke, G. J. (1987), "Enhancements and Limitations of the Code NEC for Modeling Electrically Small Antennas", Lawrence Livermore National Laboratory, UCID-20970, January.

Jones, D. S. (1979), "Methods in Electromagnetic Wave Propagation", Oxford University Press, Engineering Science Series, Oxford, United Kingdom.

Miller, E. K., G. M. Pjerrou, B. J. Maxum, G. J. Burke, S. Gee, D. E. Neely, A. J. Poggio, and A. R. Neureuther (1970), Final Technical Report on the Log-Periodic Scattering Array Program (U), MBAssociates, San Ramon, CA 94583, MB-R-70/105.

Miller, E. K. (1987), "*Model-Based Parameter-Estimation Applications in Electromagnetics*", presented at NATO Advanced Study Institute on Modeling and Measurement in Electromagnetic Analysis and Synthesis Problems, Il Ciocco, Italy, to be published by Sijthoff and Noordhoff.

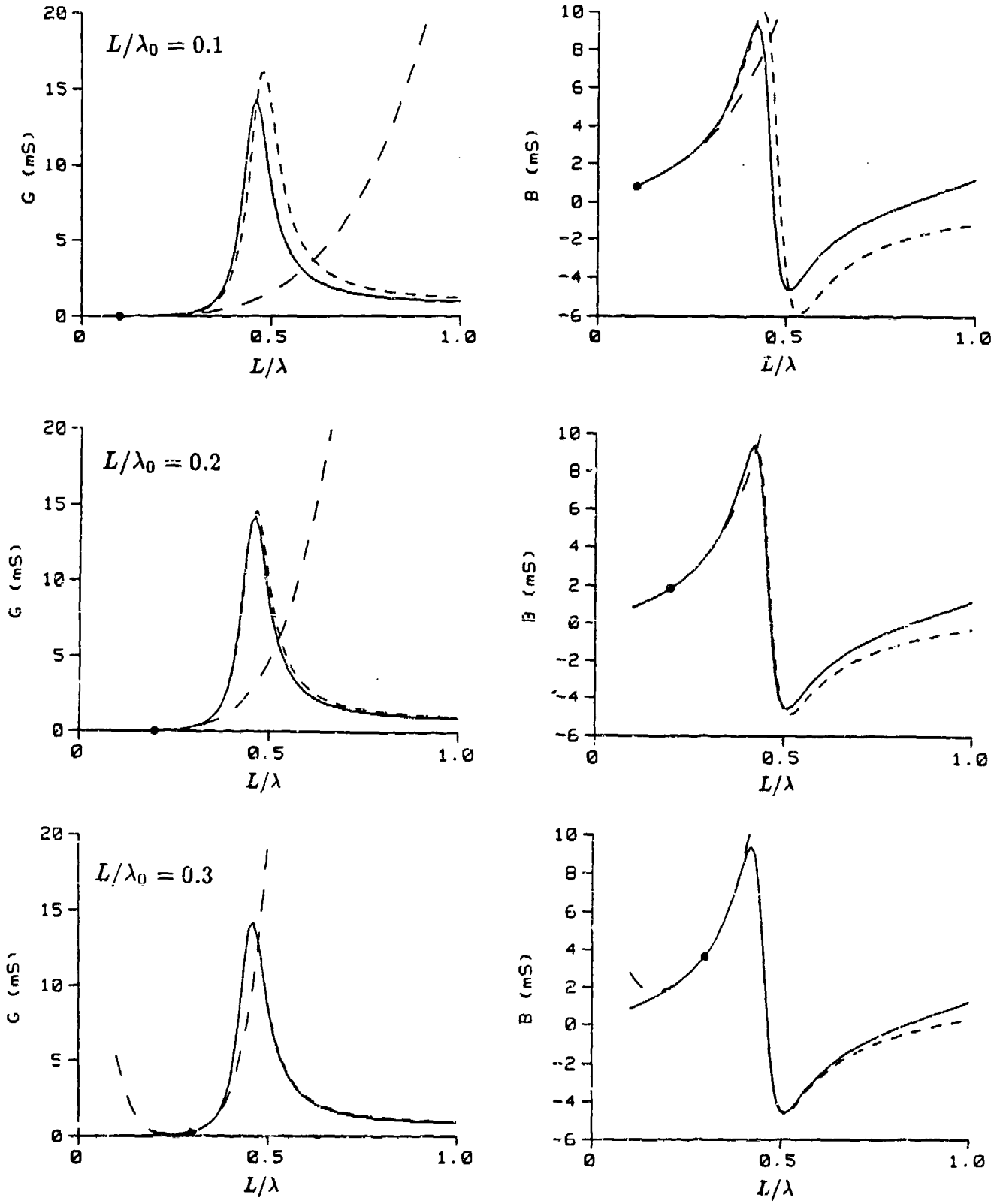


Fig. 1. Input admittance of a dipole antenna with length L and thickness parameter $\Omega = 10$ modeled with 21 segments. Results from a rational function model (- - - - -) and Taylor series (— — —) derived from 4 derivatives at L/λ_0 are compared with directly computed values (————).

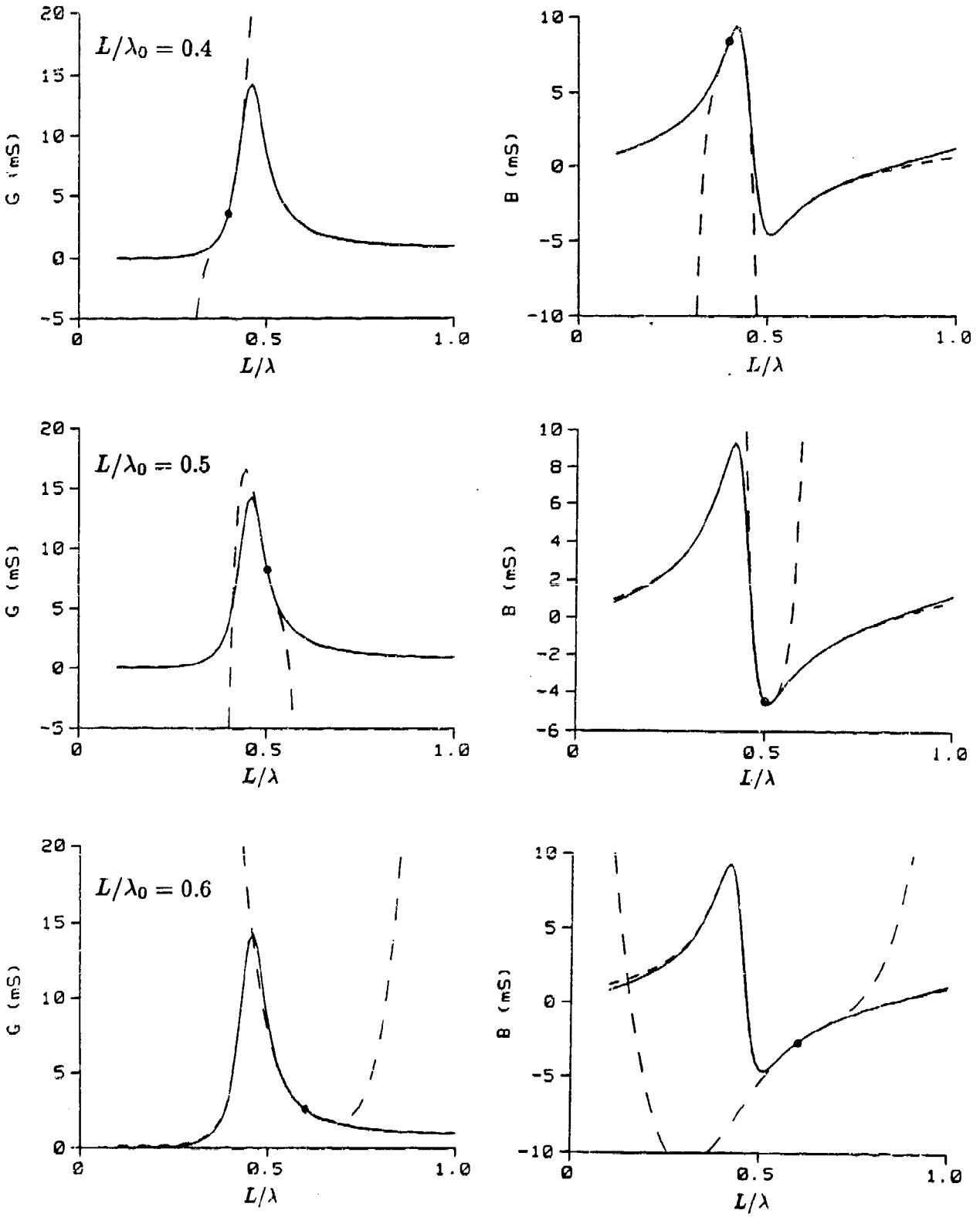

$L/\lambda_0 = 0.4$
G (mS)
B (mS)
L/λ
$L/\lambda_0 = 0.5$
G (mS)
B (mS)
L/λ
$L/\lambda_0 = 0.6$
G (mS)
B (mS)
L/λ

Fig. 1. Cont.

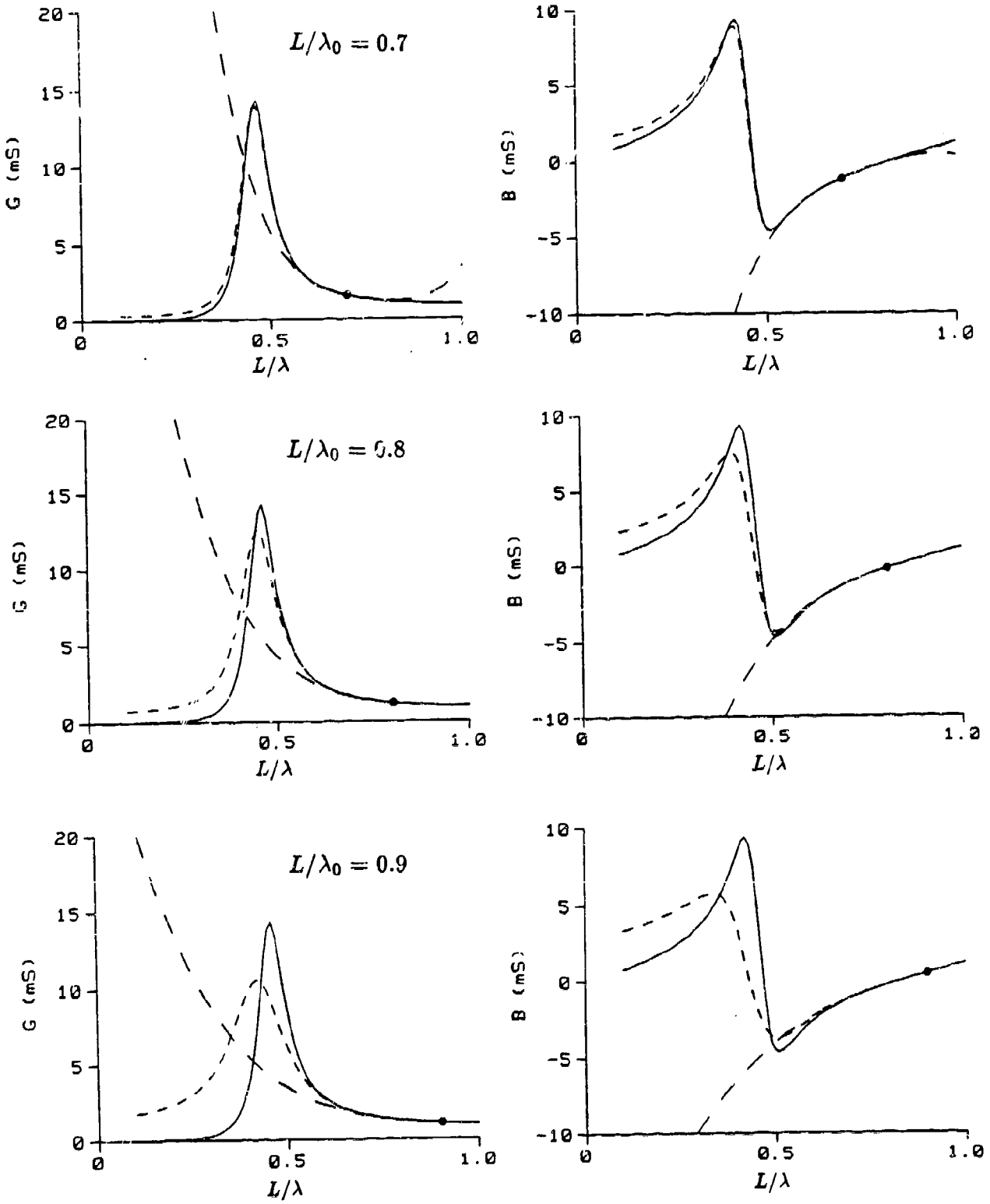

$L/\lambda_0 = 0.7$
$L/\lambda_0 = 0.8$
$L/\lambda_0 = 0.9$
G (mS)
B (mS)
L/λ
0
0.5
1.0
5
10
15
20
-5
-10

Fig. 1. Cont.

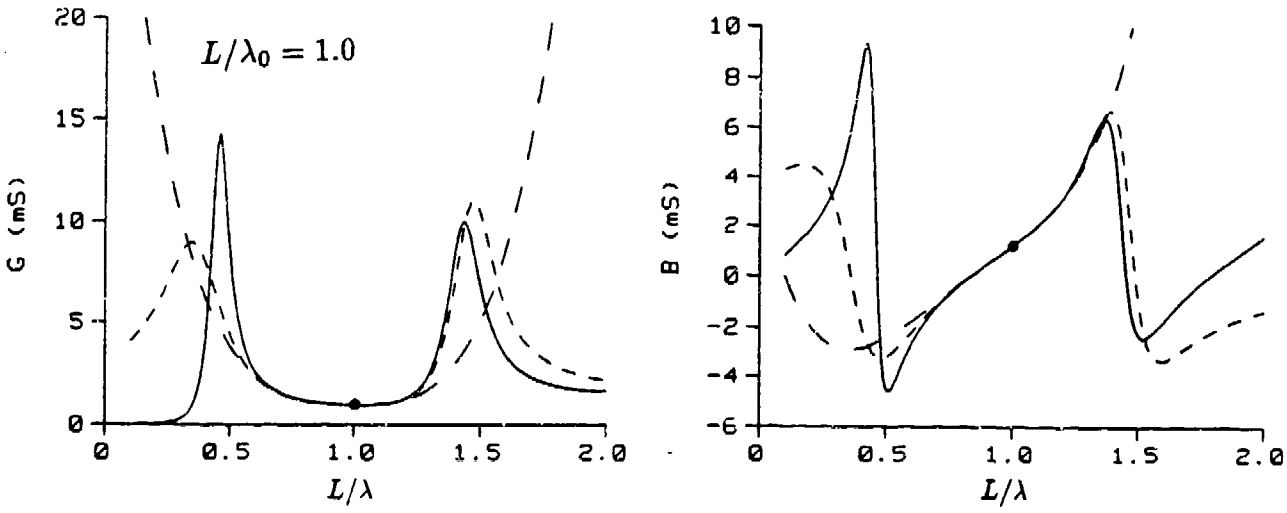


Fig. 2. Input admittance of a dipole antenna as in Fig. 1 showing the first and second resonances of the dipole.

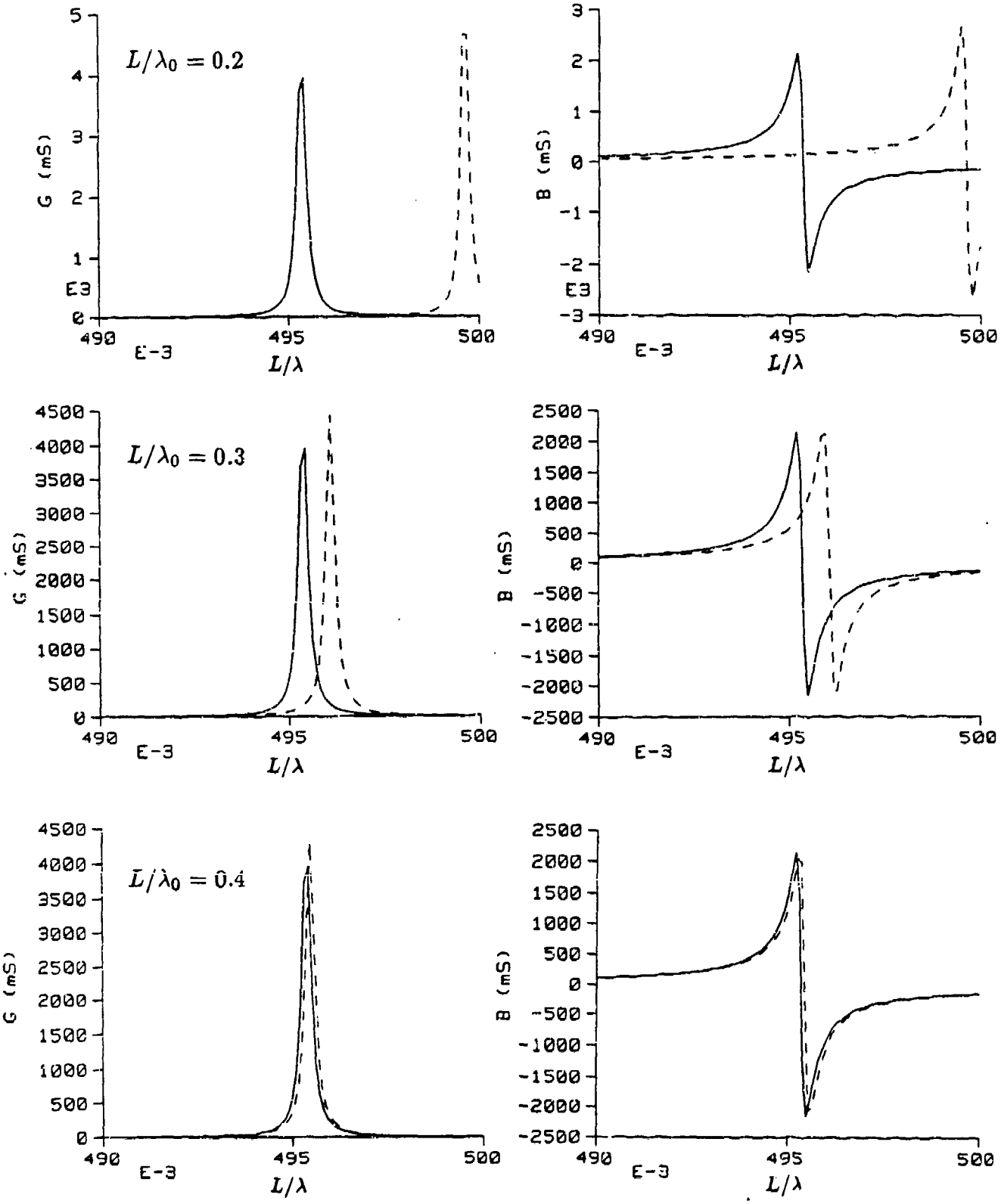


Fig. 3. Input admittance of a dipole antenna with length L and thickness parameter $\Omega = 15$ at height $L/50$ above a perfectly conducting ground. Results from a rational function model (- - - - -) derived from 4 derivatives at L/λ_0 are compared with directly computed values (————).

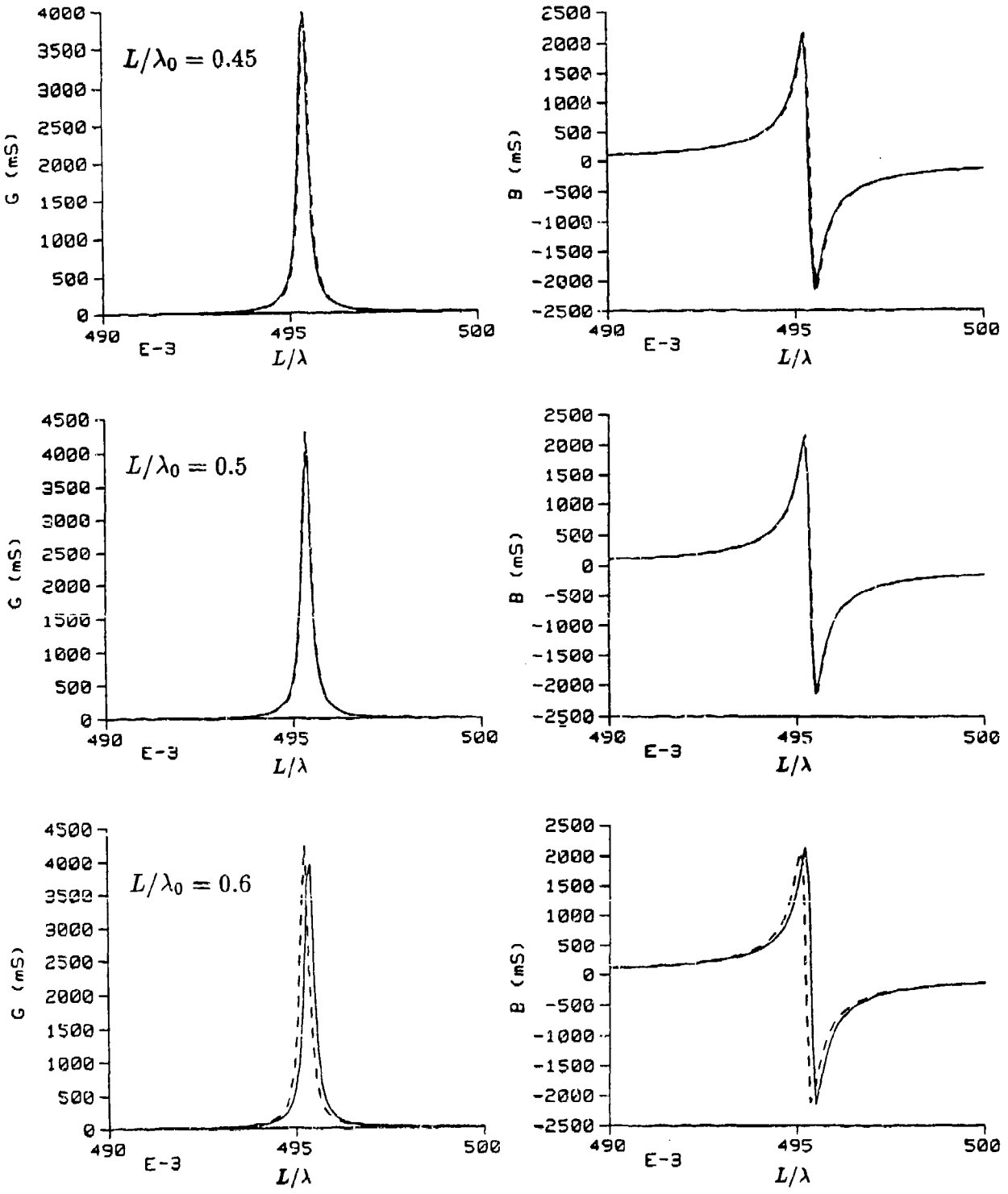


Fig. 3. Cont.

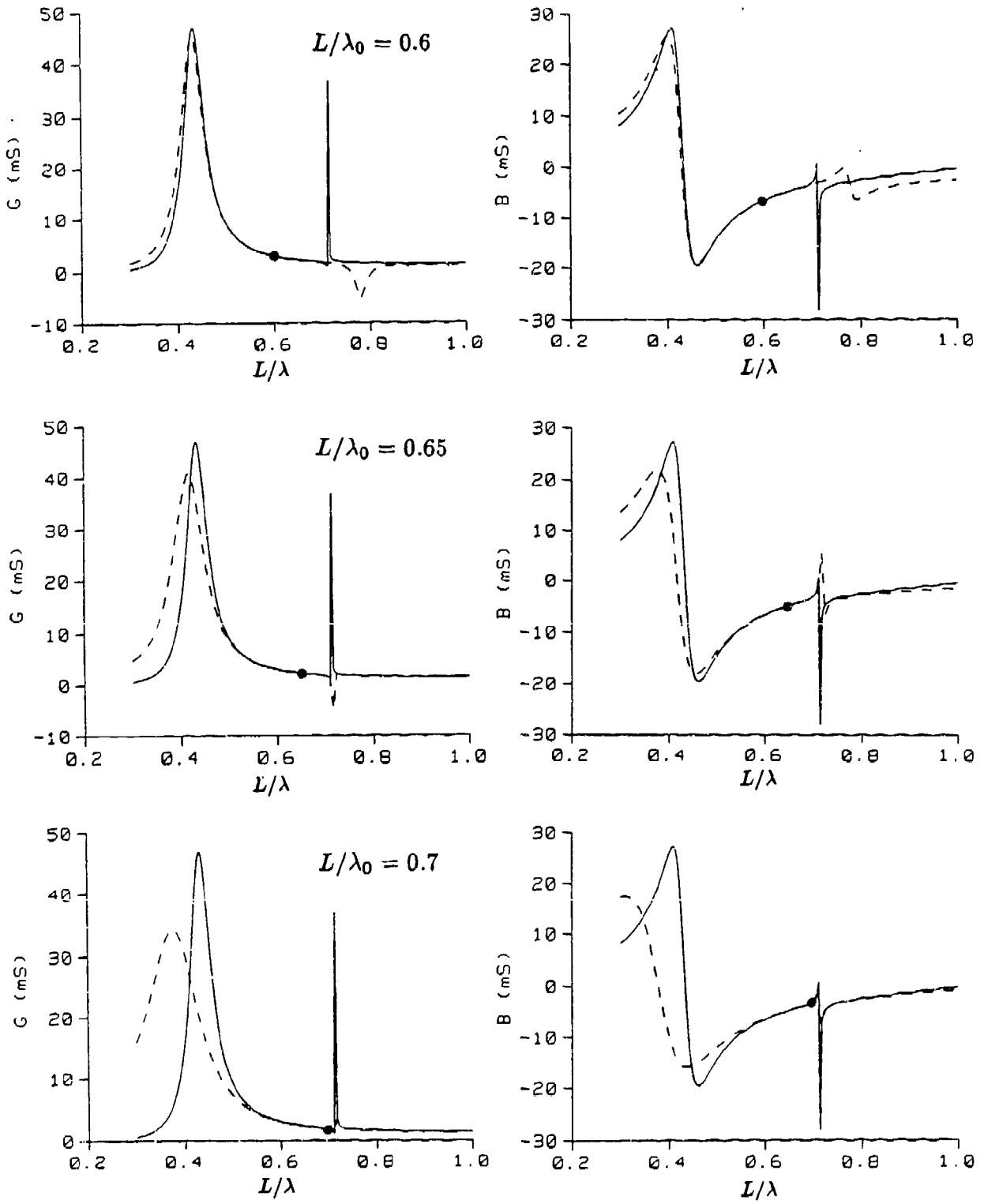


Fig. 4. Input admittance of a forked monopole antenna with legs of length 140 m and 150 m separated by 2.6 degrees. Results from a rational function model (- - - - -) derived from 4 derivatives at L/λ_0 are compared with directly computed values (————).

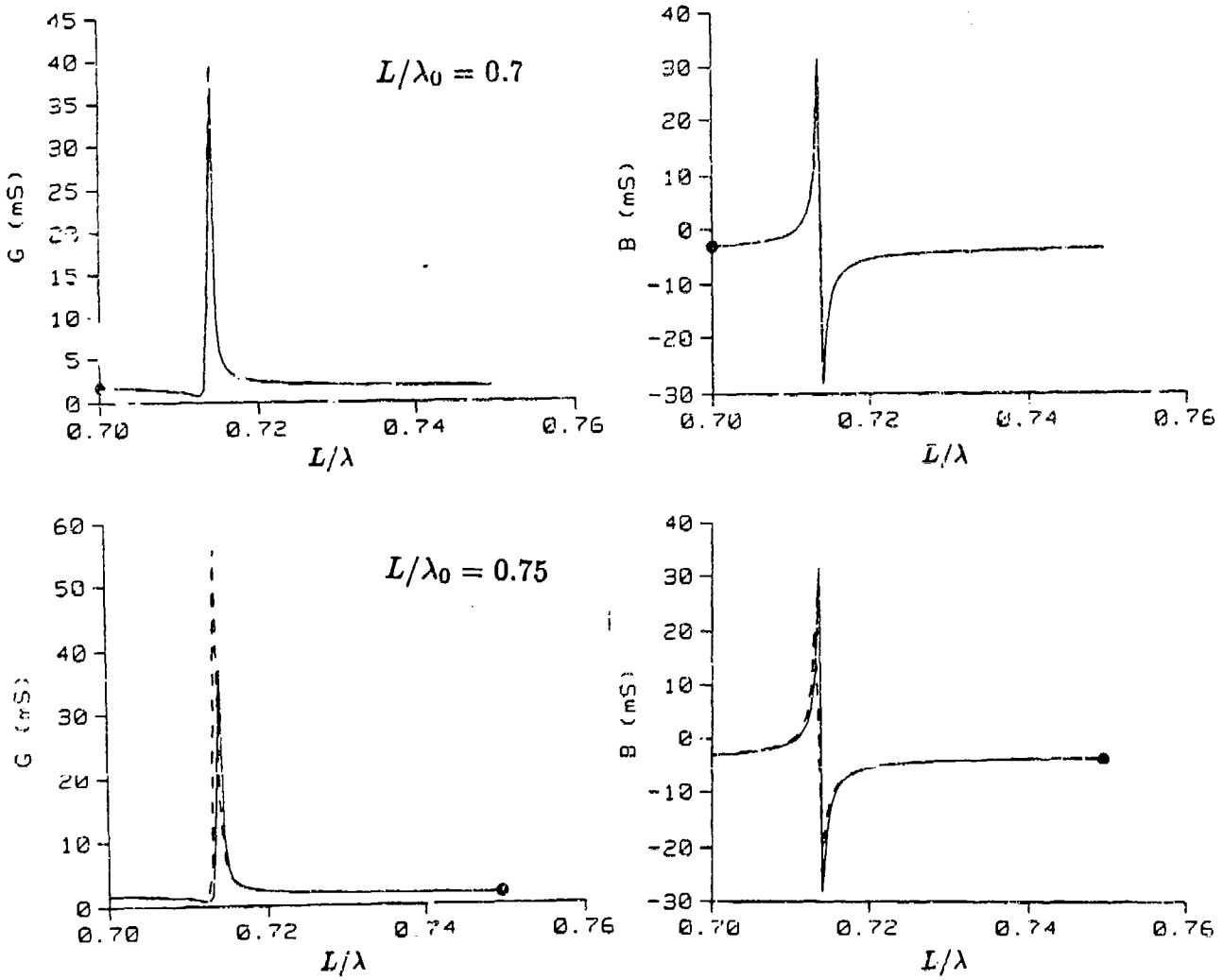


Fig. 5. Input admittance of a forked monopole antenna as in Fig. 4, showing an expanded view of the parasitic resonance.

The MAFIA Approach to Solving Maxwell's Equations in Three Dimensions*

R. K. Cooper and M. J. Browman
Mail Stop H829, Los Alamos National Laboratory
Los Alamos, NM 87545

T. Weiland
Deutsches Elektronen-Synchrotron
Notkestrasse 85, 2000 Hamburg 52, FRG

ABSTRACT

The acronym MAFIA[Klatt, 1986] stands for the solution of Maxwell's equations by the Finite Integration Algorithm and is the name given to a set of codes intended for use in the computer-aided design of three-dimensional magnets, rf structures, and structures in which wake-field effects are important. This paper gives a brief description of the algorithms employed in both the time- and the frequency-domain solvers of the MAFIA collection of codes. Examples of typical accelerator calculations will be presented.

The MAFIA Codes

Figure 1 shows the relationship between the various codes in the MAFIA collection. The individual codes are as follows:

*Work supported by the U. S. Department of Energy, Office of High Energy and Nuclear Physics.

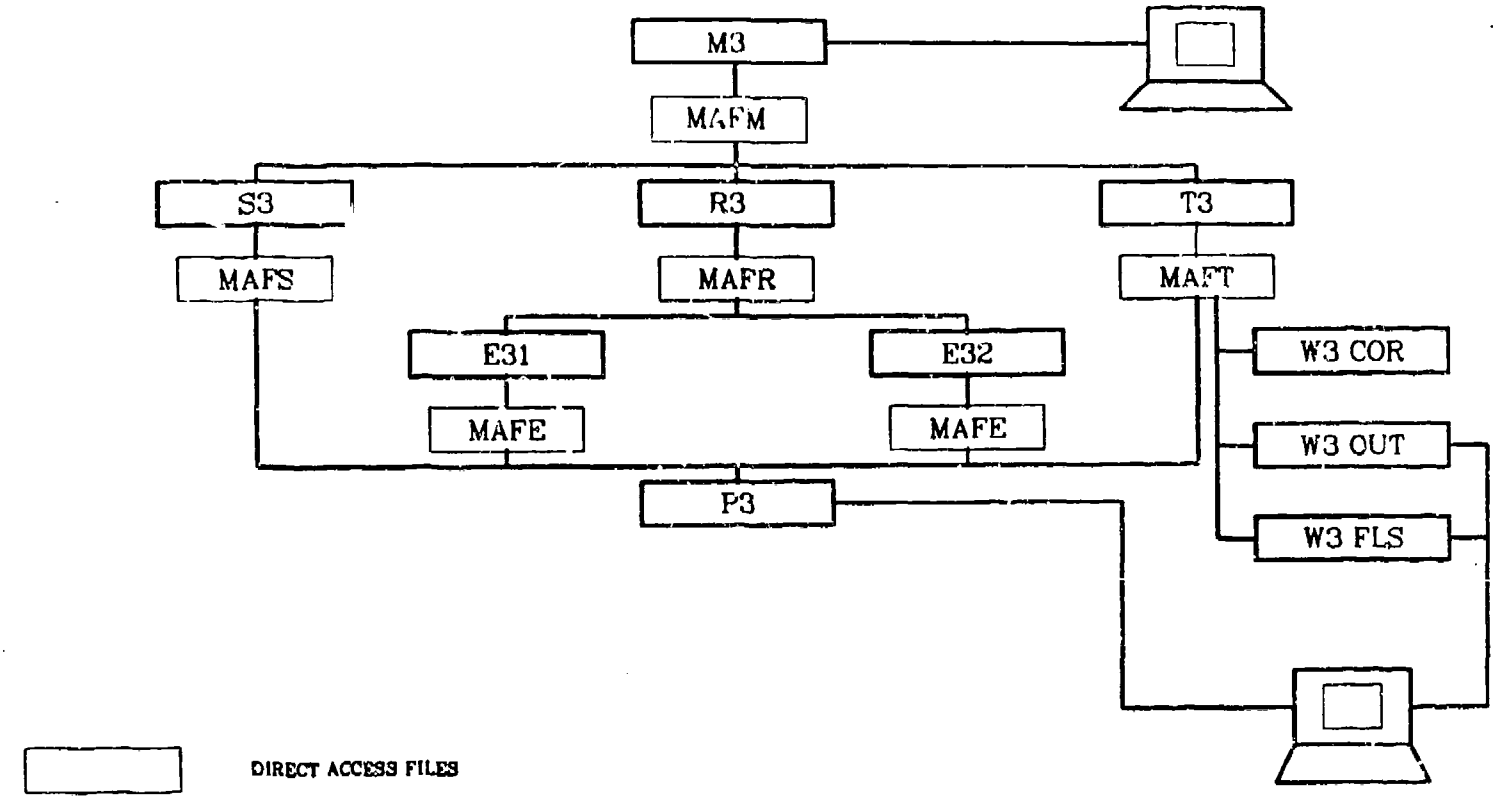


Fig. 1. The MAFIA system with its interrelationships. Depending on the installation, the separate direct access files (e.g., Mafia-M3, Mafia-R3, etc.) may be one single file that is simply extended by consecutive programs.

M3 – the mesh generator used by all the MAFIA codes

S3 – the code that solves electro- and magnetostatic problems

R3 – the code that generates the matrix representation of Maxwell's equations for rf structures; the eigenvalues and eigenvectors of this matrix give the frequencies and electric field components, respectively, of the normal modes of the electromagnetic oscillations of the structure.

E31 and E32 – the codes (only one is used for a given problem) that solve for the eigenvalues and eigenvectors of the matrix generated by R3; E31 is based on a semianalytic procedure[Tückmantel, 1985] and is a modification of an EISPACK[Smith, 1976] routine; E32 uses a multigrid[Steffen, 1985] method.

P3 – the physics postprocessor that calculates the quantities of physical interest, such as shunt impedance, quality factor, deflection integrals, etc.

T3 – the wake-field code

W3COR, W3OUT, W3FLS – postprocessors for T3.

The collection of programs M3, R3, E31 or E32, and P3 are also known as URMEL-3D.

The FIT Method

The Finite Integration Technique[Weiland, 1984, Weiland, 1985] is an algorithm that produces a first-order approximation to Maxwell's equations by replacing the line and surface integrals, appearing in Faraday's law and Ampere's law, by mean field values times path lengths and areas, respectively. Figure 2 shows the basic cell geometry used in this method.

Note that the electric field components are not defined at a single point, but at the midpoints of the sides of the rectangular cells. The magnetic field components are defined in the center of the faces of the cells and, taken together, form a mesh dual to that defined for the electric field. Only continuous components are involved in the assignment of field values to the mesh,

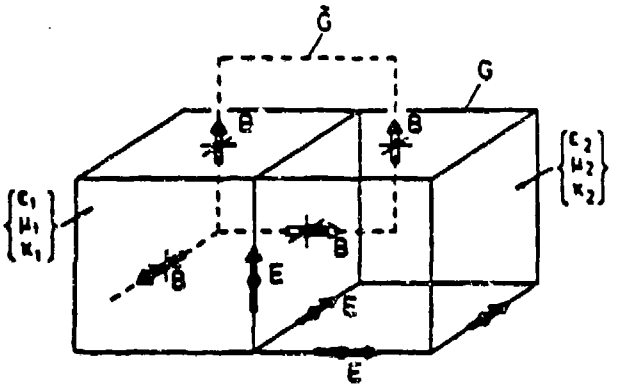


Fig. 2. Geometry and allocation of field components used in the FIT method.

and thus the cells of the mesh may be individually filled with arbitrary permittive and permeable media. Applying the FIT method to a mesh of N nodes, we can write the discrete form of Faraday's law as

$$\mathbf{C}\mathbf{D}_s\mathbf{e} = \mathbf{D}_A\dot{\mathbf{b}},$$

where $\mathbf{e}$ and $\mathbf{b}$ are vectors of length $3N$ that represent the electric field and magnetic induction, respectively; $\mathbf{C}$ is a $3N$ by $3N$ matrix (containing only the values 0, 1, and -1) that corresponds to taking the curl of a field; $\mathbf{D}_s$ is a $3N$ by $3N$ diagonal matrix containing the lengths of the sides of the mesh cells; and $\mathbf{D}_A$ is a $3N$ by $3N$ diagonal matrix containing the areas of the mesh cell surfaces. Similarly, Ampere's law can be written

$$\tilde{\mathbf{C}}\tilde{\mathbf{D}}_s\mathbf{h} = \tilde{\mathbf{D}}_A(\dot{\mathbf{d}} + \mathbf{j}),$$

where the tilde indicates that the matrix corresponds to the dual mesh. When we take the material distribution into account and use a leapfrog integration technique in the time variable, we find the recursive algorithm for the calculation of time-dependent fields:

$$\mathbf{b}^{n+1} = \mathbf{b}^n - \delta t(\mathbf{D}_A^{-1}\mathbf{C}\mathbf{D}_s)\,\mathbf{e}^{n+1/2},$$

$$\mathbf{e}^{n+3/2} = \mathbf{e}^{n+1/2} + \delta t\,(\mathbf{D}_\epsilon^{-1}\tilde{\mathbf{D}}_A^{-1}\tilde{\mathbf{C}}\tilde{\mathbf{D}}_s\mathbf{D}_\mu^{-1})\,\mathbf{b}^{n+1} - \delta t\,\mathbf{D}_\epsilon^{-1}\mathbf{j}^{n+1},$$

where the superscripts refer to the time step ($t_n = n\delta t$), and $\mathbf{D}_\epsilon$ and $\mathbf{D}_\mu$ are diagonal matrices describing the filling of the mesh with permittive and permeable media. These last two equations are solved by T3; given the initial values of the fields, fields at a subsequent time require only two multiplications of a matrix with a vector, per time step.

If we are interested in free oscillations (i.e., undriven oscillations) of the electromagnetic field, we find that combining Faraday's law and Ampere's law yields a linear eigenvalue problem in which the eigenvalues are the squares of the angular frequency of oscillation:

$$(\mathbf{D}_\epsilon^{-1}\tilde{\mathbf{D}}_\mathbf{A}^{-1}\tilde{\mathbf{C}}\tilde{\mathbf{D}}_\mathbf{s}\mathbf{D}_\mu^{-1}\mathbf{D}_\mathbf{A}^{-1}\mathbf{C}\mathbf{D}_\mathbf{s})\,\mathbf{e} = \omega^2\,\mathbf{e}.$$

For the practical solution of this eigenvalue problem, this equation can be transformed into one in which the matrix is symmetric. The program R3 constructs this symmetric matrix, incorporating material distribution and boundary conditions into the process of construction. A more detailed treatment of the application of this method to problems of electromagnetism may be found in[Weiland, 1986].

Sample Structures

Both the time-domain and frequency-domain solvers have been used to study the effects of cavity asymmetries due to a waveguide feed. (See Fig. 3.)

We have also been using the frequency-domain solver to study asymmetries due to the coupling slots in a side-coupled cavity (Figs. 4 and 5) and to understand the jungle gym slow-wave accelerating structure (Fig. 6). This latter work has been accepted for publication in *Particle Accelerators* [Loo, 1988].

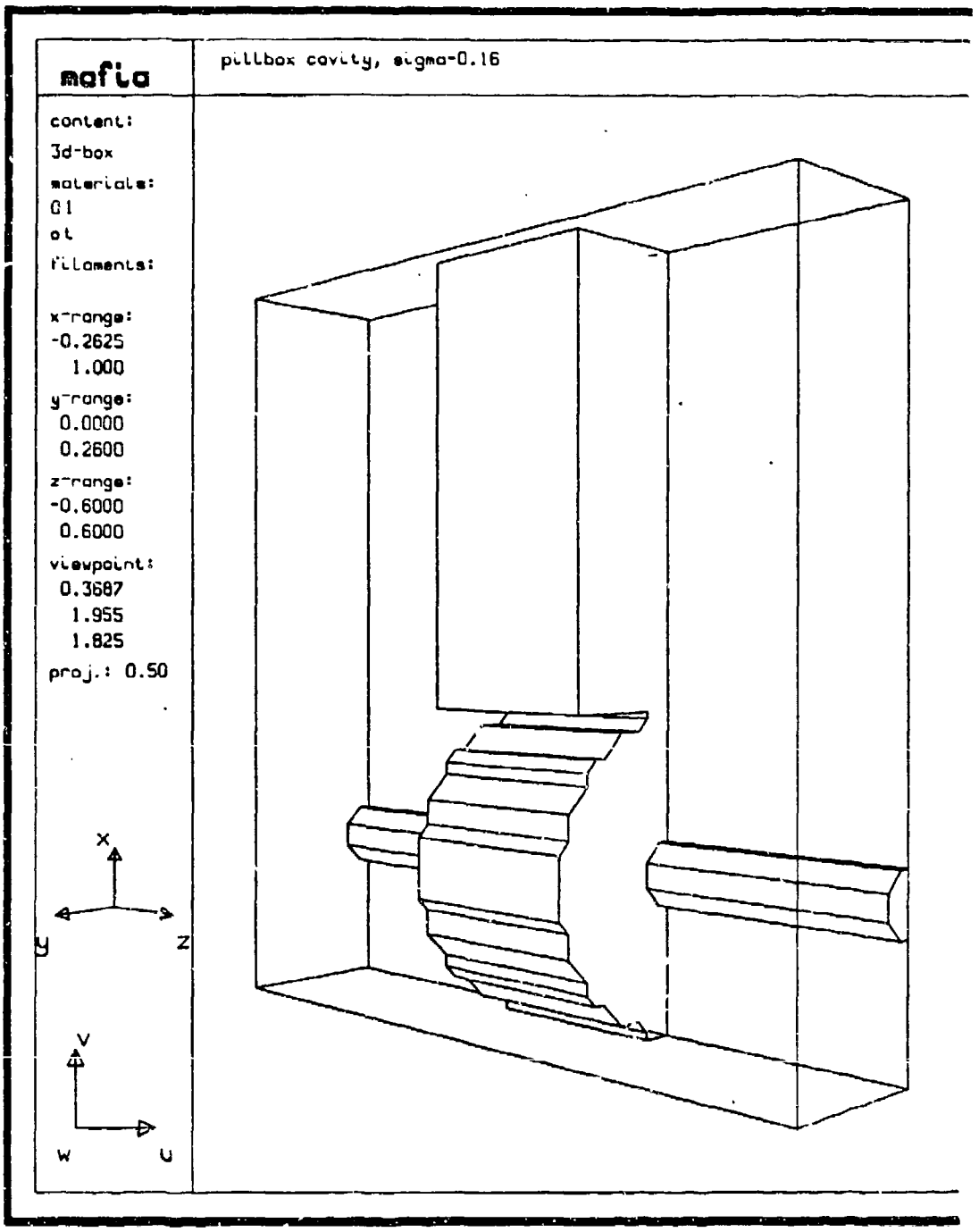


Fig. 3. Cavity used to study the effects of asymmetries due to a waveguide feed.

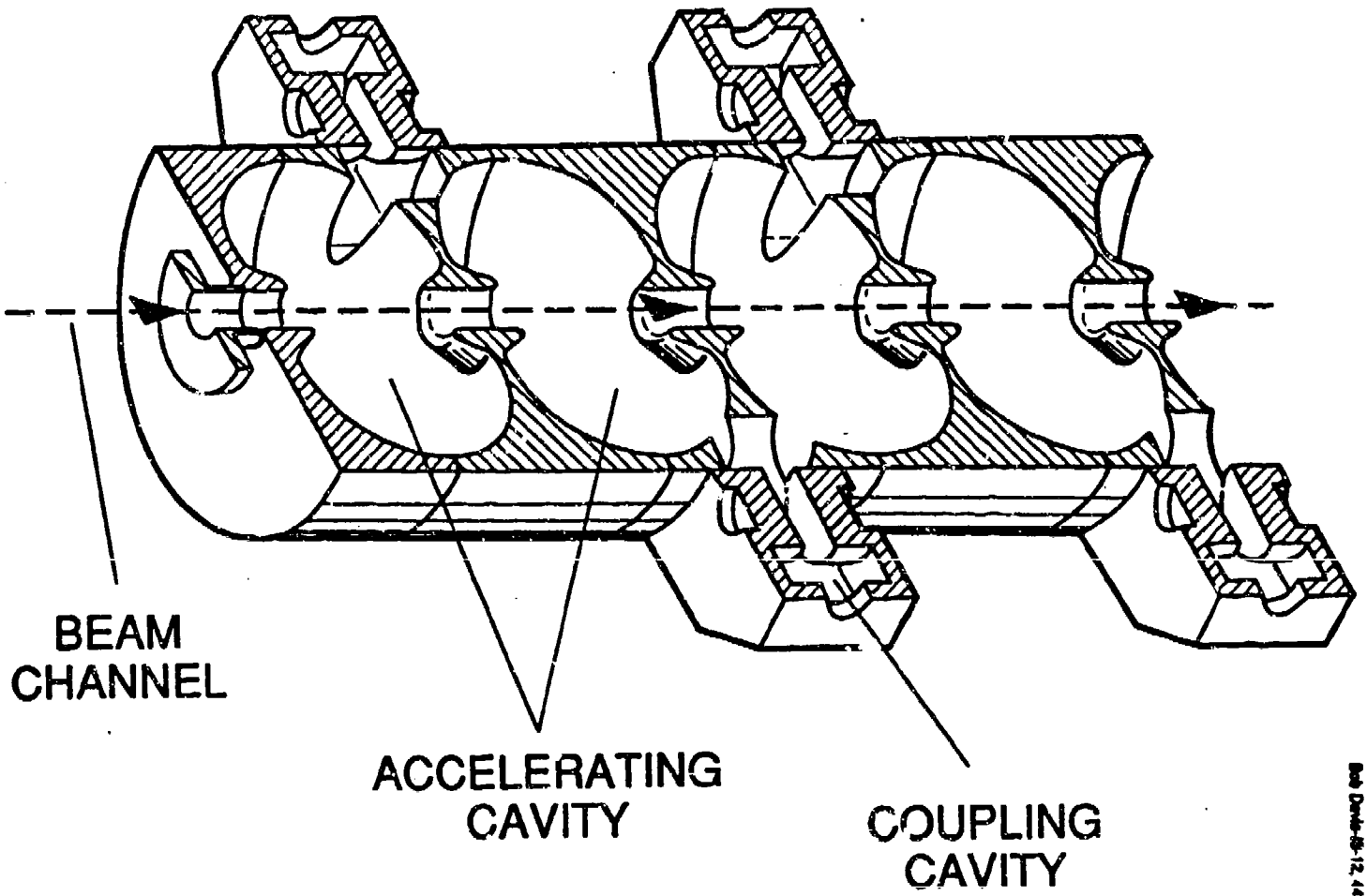


Fig. 4. Drawing of one-half of a side-coupled cavity accelerating structure.

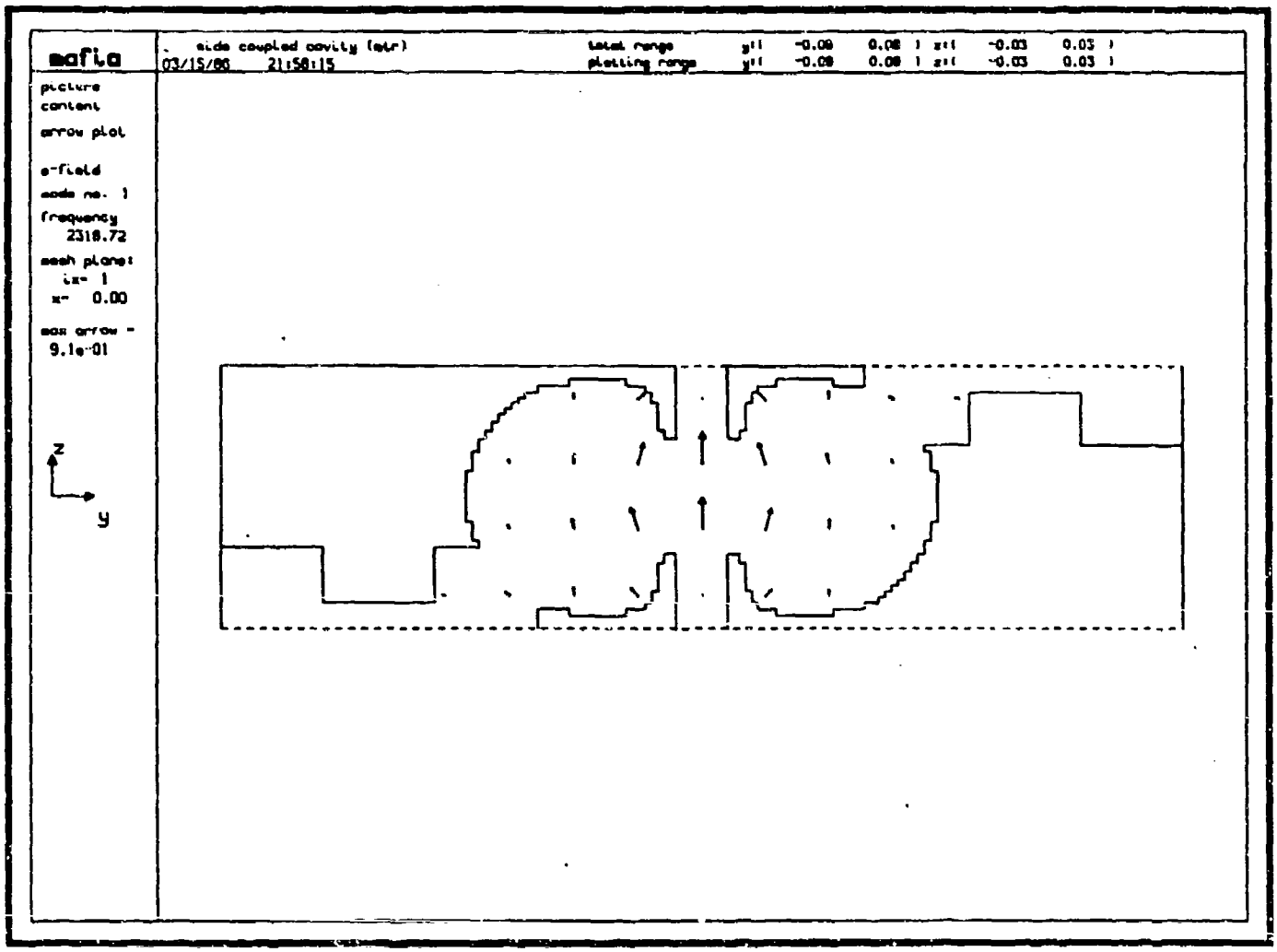


Fig. 5. Computer plot of the electric field in the symmetry plane of a side-coupled cavity.

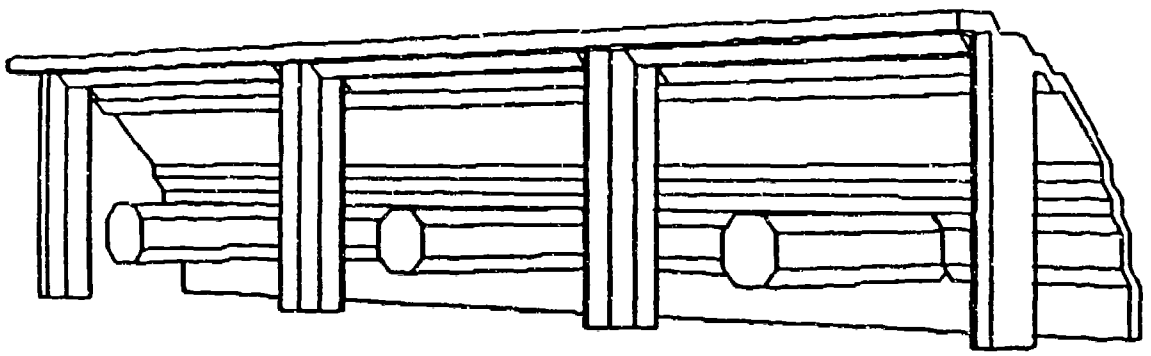


Fig. 6. A computer plot of one-quarter of a three-cell jungle gym acclerating structure.

Availability

The MAFIA codes are written in FORTRAN 77 and currently run on IBM 3081, CRAY, and VAX computers. They are also available to approved users in executable form on the National Magnetic Fusion Energy Center (NMFEC) computers. For more information contact Carol Tull at the NMFEC (phone: 415-422-1556) or Therese Barts at LANL (phone: 505-667-9385).

For those users who want to use the codes at their own installation, there are examples of three graphics interfaces available: DISSPLA on a Los Alamos Cray, PLOT-10 on the DESY IBM 3081, PLOT-10 on the VAX-VMS, and GKS on the DESY IBM 3081. The codes are available without charge to approved nonprofit organizations; for further information contact Thomas Weiland at DESY (Phone: 49-40-8998-3196). Users may not modify nor distribute the codes, and they are asked to be friendly and sometimes patient. Users at other than nonprofit institutions should contact DESY for special contractual arrangements.

Documentation[Cooper, 1987] may be obtained by writing the following address:

Los Alamos Accelerator Code Group
AT-6, Mail Stop H-829
Los Alamos National Laboratory
Los Alamos, NM 87545

The phone number is 505-667-2839.

References

R. K. Cooper, M. T. Menzel, H. K. Stokes, and J. L. Warren, "Code Documentation From the Los Alamos Accelerator Code Group," 1987 Particle Accelerator Conf., Washington DC, March 16-19, 1987, to be published.

R. Klatt, F. Krawczyk, W.-R. Novender, C. Palm, T. Weiland, B. Steffen, T. Barts, M. J. Browman, R. Cooper, C. T. Mottershead, G. Rodenz, S. G. Wipf, "MAFIA—A Three-Dimensional Electromagnetic CAD System for Magnets, RF Structures, and Transient Wake-field Calculations," *1986 Linear Accelerator Conference Proc.*, Stanford Linear Accelerator Center report SLAC-303, 276-278 (1986).

J. Loo, M. J. Browman, K. C. D. Chan, R. K. Cooper, "Numerical Studies of the Jungle Gym Slow-Wave Accelerating Structure," LA-UR-88-19, *Particle Accclerators*, to be published.

B. T. Smith, J. M. Boyle, J. J. Dongarra, B. S. Garbow, Y. Ikebe, V. C. Klema, and C. B. Mole, *Matrix Eigensystem Routines - EISPACK Guide*, (Springer-Verlag, Berlin-Heidelberg-New York, 1976).

B. Steffen, "Incorporation of Multigrid Methods in Accelerator Software," *Proc. Second European Conf. on Multigrids*, Cologne, FRG, October 1985.

J. Tückmantel, Application of SAP in URMEL, CERN/EF/RF 85-4, July 1985.

T. Weiland, "On the Numerical Solution of Maxwell's Equations and Applications in the Field of Accelerator Physics," *Particle Accelerators* **15**, 245-292 and references therein (1984).

T. Weiland, "On the Unique Solution of Maxwellian Eigenvalue Problems in Three Dimensions," *Particle Accelerators* **17**, 227-242 (1985).

T. Weiland, "Numerical Solution of Maxwell's Equation for Static, Resonant and Transient Problems," *URSI Int. Symp. on Electromagnetic Theory*, Akadémiai Kiadó (Budapest, Hungary, August 1986), Part B, 537-542.

AN IMPROVED EXACT KERNEL FOR MININEC

by

J. C. Logan and J. W. Rockway
Naval Ocean Systems Center, San Diego, Ca.

and

D. Wilton
University of Houston, Houston, Tx.

ABSTRACT

The present implementation of MININEC (NOSC TD 938) has a heuristically determined correction to the kernel for closely spaced wires. The approach provides acceptable answers for a wide range of spacing for parallel wires, as shown in TD 938. However, the approach breaks down for connected wires that form an acute included angle. This paper outlines an alternative approach to evaluating the exact kernel and demonstrates that this problem has been corrected.

SUMMARY

The method of moments solution used in MININEC is based on an integral equation relating the incident field to the scalar and vector potentials [1,2,3]:

$$-\bar{E}_{inc}\cdot\hat{s} = -j\omega\bar{A}\cdot\hat{s} - \hat{s}\cdot\nabla\Phi \tag{1}$$

where the scalar and vector potentials are defined in the usual manner as:

$$\Phi = \frac{1}{4\pi\epsilon}\int_s q(s)k(r)ds \tag{2}$$

and

$$\bar{A} = \frac{\mu}{4\pi}\int_s I(s)\hat{s}(s)k(r)ds \tag{3}$$

where the integration is along the length s of the wire and

$$k(r) = \frac{1}{2\pi}\int_{-\pi}^{\pi}\frac{e^{-jkr}}{r}d\phi \tag{4}$$

In MININEC, the charge is removed using a difference relation based on the continuity equation:

$$q(s) = -\frac{1}{j\omega}\frac{dI}{ds} \tag{5}$$

A method of moments Galerkin procedure using pulse expansion functions is used in MININEC to produce a linear set of equations that are expressed in matrix form. Each matrix element associated with the nth current pulse and the Sm observation point on the wire surface involves scalar and potential terms with integrals of the form:

$$\psi_{m,u,v} = \int_{s_u}^{s_v} k(s_m - s')\,ds' \tag{6}$$

where

$$k(s_m - s') = \frac{1}{2\pi}\int_{-\pi}^{\pi} \frac{e^{-jkr_m}}{r_m}\,d\phi \tag{7}$$

and where

$$r_m = \left[(s_m - s')^2 + 4a^2 \sin^2\left(\frac{\phi}{2}\right)\right]^{1/2} \tag{8}$$

Because of the singularity at r=0, the integration in (6) must be carried out with special care. The 1/r term is subtracted from the integrand and then added as a separate term to yield:

$$k(s_m - s') = \frac{1}{2\pi}\int_{-\pi}^{\pi} \frac{e^{-jkr_m} - 1}{r_m}\,d\phi + \frac{1}{2\pi}\int_{-\pi}^{\pi} \frac{d\phi}{r_m} \tag{9}$$

The first integral is evaluated numerically since the singularity has been removed. The second is rewritten as an elliptic integral of the first kind and evaluated following a procedure given by Abramowitz and Stegun [4].

This approach works well for many cases as demonstrated in TD 938. But the difficulty is encountered when the spacing between wires is close to the wire size giving rise to erroneous results. For example, Table 1 gives the impedance given by MININEC(3) for a bent wire antenna for included angles from 2 to 90 degrees. The results for 2 and 10 degrees are suspect.

For the case of two closely spaced wires:

$$R=\sqrt{\left[(s-s')^2+\rho^2+a_s^2-2\rho a_s\cos\phi\right]} \tag{10}$$

as illustrated in Figure 1. As R becomes small, the integrand of (7) although not yet singular, peaks out. The approach is similar to

treating the singularity. The 1/R term is subtracted from the integrand and then added as a separate term:

$$k(s_m-s')=\frac{1}{2\pi}\int_{-\pi}^{\pi}\frac{e^{-jkR}-1}{R}d\phi+\frac{1}{2\pi}\int_{-\pi}^{\pi}\frac{d\phi}{R} \tag{11}$$

The first integral is carried out numerically as before. The second integrand, after some algebra, becomes:

$$\frac{2}{\pi\sqrt{(s-s')^2+(\rho+a_s)^2}}\int_0^{\frac{\pi}{2}}\frac{d\phi}{\sqrt{1-\beta^2\sin^2\frac{\phi}{2}}}=\frac{\beta}{\pi\sqrt{\rho a_s}}F\left(\frac{\pi}{2},\beta\right) \tag{12}$$

where $F\left(\frac{\pi}{2},\beta\right)$ is an elliptical integral of the first kind and

$$\beta^2=\frac{4\rho a_s}{(s-s')^2+(\rho+a_s)^2} \tag{13}$$

and

$$1-\beta^2=\frac{(s-s')^2+(\rho-a_s)^2}{(s-s')^2+(\rho+a_s)^2} \tag{14}$$

When ρ is close in value to a_s and as s approaches s', (12) becomes

$$\frac{\beta}{\pi\sqrt{\rho a_s}}F\left(\frac{\pi}{2},\beta\right)=-\frac{2}{\pi(\rho+a_s)}\ln\left[\sqrt{\frac{1-\beta^2}{4}}\right]=-\frac{2}{\pi(\rho+a_s)}\ln\left[\sqrt{\frac{(s-s')^2+(\rho-a_s)^2}{4(\rho+a_s)}}\right] \tag{15}$$

By substitution, (11) becomes:

$$\psi_{m,u,v}=\int_{s_u}^{s_v}\left[\frac{1}{2\pi}\int_{-\pi}^{\pi}\frac{e^{-jkR}-1}{R}d\phi+\frac{\beta F\left(\frac{\pi}{2},\beta\right)}{\pi\sqrt{\rho a_s}}\right]ds' \tag{16}$$

and finally:

$$\psi_{m,u,v}=\frac{1}{2\pi}\int_{s_u}^{s_v}\int_{-\pi}^{\pi}\frac{e^{-jkR}-1}{R}d\phi ds'+\frac{1}{\pi}\int_{s_u}^{s_v}\left[\frac{\beta}{\sqrt{\rho a_s}}F\left(\frac{\pi}{2},\beta\right)+\frac{2}{\rho+a_s}\ln\sqrt{\frac{(s-s')^2+(\rho-a_s)^2}{4(\rho+a_s)}}\right]ds' \tag{17}$$

$$+\frac{2}{\pi(\rho+a_s)}\left[(s-s')\left(\ln\left[\sqrt{\frac{(s-s')^2+(\rho-a_s)^2}{4(\rho+a_s)}}\right]-1\right)+(\rho-a_s)\tan^{-1}\frac{(s-s')}{(\rho-a_s)}\right]\Bigg|_{s'=s_u}^{s_v}$$

A more detailed discussion of this procedure may be found in [5].

Table 2 shows the impedance given by MININEC with the new exact kernel. The data for included angles of 30 to 90 degrees is the same as Table 1, but the data for 2 and 10 degrees is more reasonable (especially at 2 degrees). The new kernel gives the expected results.

REFERENCES

[1] A.J. Julian, J.C. Logan, J.W. Rockway, "MININEC: A Mini-Numerical Electromagnetics Code", NOSC TD 516, September 1982.

[2] S.T. Li, J.C. Logan, J.W. Rockway, D.W. Tam, Microcomputer Tools for Communications Engineering, Chapter 4, Artech House, Inc., Dedham, MA., 1984.

[3] J.W. Rockway and J.C. Logan, "The New MININEC (Version 3): A Mini-Numerical Electromagnetics Code", NOSC TD 938, September 1986.

[4] M. Abramowitz and I. Stegun, A First Course in Numerical Analysis, McGraw-Hill, New York, 1965.

[5] J.W. Rockway, J.C. Logan, S.T. Li and D.W.S. Tam, The MININEC SYSTEM: Microcomputer Analysis of Wire Antennas, Artech House, Inc., 1988.

TABLE 1. Impedance of a bent wire antenna predicted by MININEC(3).



$l = 2\,m$, $a = .001\,m$
$f = 37.5\,MHz$
$N = 8$ SEG./WIRE

α	IMPEDANCE (OHMS)
90	42.19 -j 16.41
60	21.28 -j 55.89
45	12.33 -j 76.77
30	5.49 -j 96.07
10	0.714 -j 1449.
2	-0.00408 -j 308.9

TABLE 2. Impedance of a bent wire antenna predicted by MININEC with the new kernel.



$l = 2\,m$, $a = .001\,m$
$f = 37.5\,MHz$
$N = 8$ SEG./WIRE

α	IMPEDANCE (OHMS)
90	42.19 -j 16.43
60	21.28 -j 55.88
45	12.33 -j 76.69
30	5.49 -j 96.07
10	0.570 -j 112.33
2	0.0412 -j 146.48

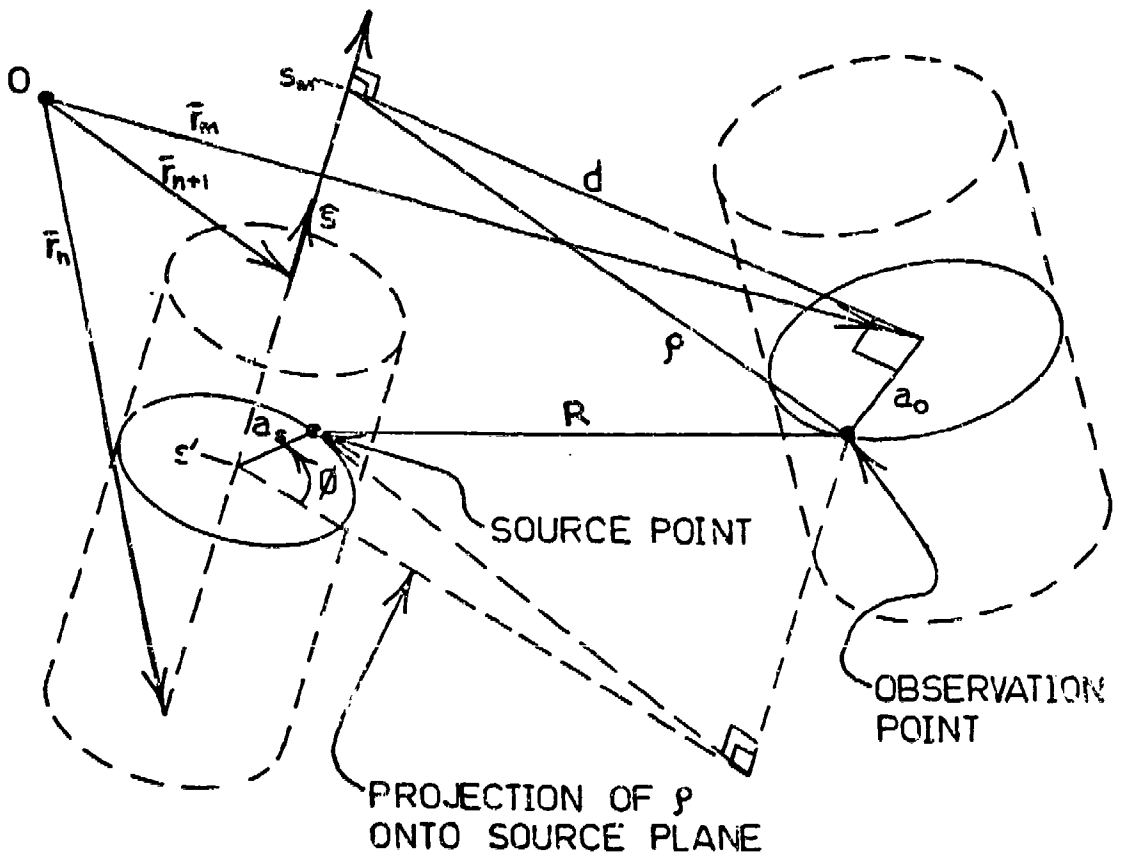


Figure 1. Geometry for observation point near source segment

Numerical Integration Schemes for Calculating the Fourier Coefficients of the Free Space Green's Function

Mr. John C. Peterson
Photon Research Associates, Inc.
3377 N. Torrey Pines Ct. Suite 300
La Jolla, California 92037
Phone: (619) 455-9741
FAX: (619) 455-0658

This paper is a summary of the author's experience with various numerical integration methods for computing the Fourier coefficients of the free space Green's function, an important aspect of body of revolution (BOR) algorithms used for antenna and scattering problems. The algorithms used in popular BOR codes were compared with other methods in use. Issues such as accuracy, robustness, and efficiency were addressed as well as the ease of use and implementation. The suitability of various methods for use on vector computer hardware was also examined in view of the enormous potential for increased efficiency.

When applying moment method techniques to structures with rotational symmetry one takes advantage of the fact that the incident fields and unknown surface currents are periodic functions of the body azimuth angle ϕ. Hence these quantities can be expanded in Fourier series. The Fourier components of the unknown currents can be decoupled, and it is possible to solve for each of them independently. This requires that we determine the coefficients in the Fourier expansion of the free space Green's function. If t denotes the tangential coordinate along the curve which defines the structure geometry, the series expansion is

$$G(t,t',\phi-\phi') = \frac{e^{-jkr}}{r} = \frac{1}{2\pi}\sum_{m=-\infty}^{+\infty} G_m(t,t')\,e^{jm(\phi-\phi')}$$

$$G_m(t,t') = \int_{-\pi}^{+\pi} G(t,t',\alpha)\,e^{-jm\alpha}\,d\alpha$$

where the primed variables correspond to the source, and the unprimed variables correspond to the observer. Several characteristics of the Green's function allow simplifications of the above integral which reduce the computational effort required to compute it. Since the Green's function is an even function about $\alpha = 0$, one only needs to consider the $cos(m\alpha)$ component of $e^{-jm\alpha}$. This also permits a further reduction in effort by computing the integral over the interval $[0,\pi]$ and then multiplying the result by two. This reduces to the following integral

$$G_m(t,t') = 2\int_0^{\pi} G(t,t',\alpha)\,cos(m\alpha)\,d\alpha$$

It is worth stopping for a moment to review the physical significance of the Green's function, and the interpretation of the Fourier integral above. The Green's function represents the field observed at a given point due to an infinitesimal current source somewhere on the surface of the structure. The Fourier integral represents the field observed at a given point with tangential coordinate t due to all the sources with azimuth $\alpha \in [-\pi,+\pi]$ and tangential coordinate t'. When the source and observation points are electrically far away from one another in terms of tangential coordinates, the magnitude of the Green's function is small and the phase will vary slowly. The opposite extreme occurs when the tangential coordinate of the source and observer are the same. Here, the Green's function is singular as the difference in the azimuth of the points goes to zero. If the structure has an electrically large radius, the phase of the Green's function can vary rapidly as a function of the azimuth angles. The integrals associated with coincident observation and source tangential coordinates are usually called the "self-terms".

Accurate calculation of the Fourier integrals is important in the sense that integration errors have an adverse effect on the conditioning of the impedance matrix that must be solved to find the currents. Even

assuming exact calculation of the integrals, the machine precision will eventually place a limit on the electrical size of objects that can be accurately modeled. Beyond a certain electrical size, the condition number of the impedance matrix will be too large to be accurately solved. I have found the estimate of the condition number of the impedance matrix provided by the solution routine CGECO from the SLATEC library quite valuable in cases where the solution accuracy may be in question. It is also helpful in identifying bad conditioning of the impedance matrix due to inaccurate calculation of the Fourier integrals. There is of course slightly more expense associated with the estimation of the matrix condition number.

The singularity of the integrand in the calculation of the self terms can be handled quite nicely by the singularity extraction technique. In this approach, one subtracts the asymptotic behavior at the singularity from the integrand. The resulting quantity is well behaved so that numerical integration can be used, the asymptotic term is then integrated analytically and the result added back in. A complete derivation of the analytical integration can be found in (Simple and Efficient Numerical Techniques for Treating Bodies of Revolution, P. Glisson, D. Wilton, University of Mississippi Technical Report 105, Revised 1982). The analytical integration requires the evaluation of the complete elliptic integral of the first kind $K(sin\phi)$, where ϕ is the modular angle. The elliptic integral can be evaluated quite inexpensively using one of several expansions that can be found in (Handbook of Mathematical Functions, M. Abramowitz, I. Stegun, Dover Publications). The expansions $17 \cdot 3 \cdot 33$ and $17 \cdot 3 \cdot 34$ are quite accurate and only require the evaluation of two polynomials and computation of one logarithm. (A note of caution, I found the notation used by Abramowitz and Stegun to be somewhat confusing, and it is not immediately apparent, but the expansions given are really for $K(sin^2\phi)$). My experience has shown that singularity extraction is well worth this small added expense.

It is worth regressing for a moment to review the characteristic features of desirable numerical integration techniques. Although these are obvious to most of us, it is helpful to keep in mind the characteristics that are most important to us when selecting a method, as there is no one best technique! In brief, a good algorithm should be accurate, robust, efficient, and easy to implement and use. The issue of accuracy usually revolves around the existence of some form of dependable error control. By robust, we mean that the method should have a high probability of providing an answer within desired error bounds. A method which is efficient would be even more ideal if the amount of computational effort involved is fairly predictable in advance. Finally, we would prefer an algorithm which is easy to implement in software, and one that is fairly straight forward to operate from the code user's point of view.

In the popular body of revolution (BOR) codes in general use today, two distinct integration methods are often used. One method is Gauss-Legendre quadrature, often called just Gaussian quadrature, used in the codes written by Harrington and Mautz. The other method in common use is an adaptive technique based on the composite trapezoidal rule. This method is used in most of the codes written by Glisson, and Wilton. Let us briefly review the mechanics of these techniques.

Quadrature methods are those methods which approximate the integral by a weighted sum of the function evaluated at specified abscissa points in the interval of integration. Without any loss of generality we can assume that the interval of integration is $[-1,+1]$. Specifically we would have

$$I(f) = \int_{-1}^{+1} f(x)\,dx$$

$$I(f) \approx A_1 f(\xi_1) + \cdots + A_n f(\xi_n)$$

$$\xi_j \in [-1,+1]\,, \quad j = 1,\cdots,n$$

Almost all familiar numerical integration techniques are in fact quadrature techniques, the composite trapezoidal and Simpson's rule for example. In a certain sense, Gauss-Legendre quadrature is an optimal quadrature technique. Specifically, Gauss-Legendre quadrature will exactly integrate polynomials of maximal degree over all admissible real values for the weights and abscissas. The n point rule will exactly integrate polynomials of degree less than or equal to $2n-1$. At first glance, Gauss quadrature might appear to be somehow unsophisticated. However, if one looks closer at the derivation for the Gauss weights and abscissas, one finds

that the method is beautifully elegant. The abscissa points are the roots of the Legendre polynomial of degree n, which we denote by $P_n(x)$. The weights are given by the following integral

$$A_i = \int_{-1}^{+1} \prod_{j=1,\, i \neq j}^{n} \frac{(x - \xi_j)}{(\xi_i - \xi_j)}\, dx$$

$$P_n(x) = \alpha_n (x - \xi_1) \cdots (x - \xi_n)$$

The Gauss-Legendre abscissas and weights are available from several well known mathematics handbooks, including (Handbook of Mathematical Functions, M. Abramowitz, I. Stegun, Dover Publications).

Gauss-Legendre quadrature is itself very efficient, and it's usage is conducive to a number of additional optimizations to BOR algorithms. When calculating the Fourier integrals required to assemble the impedance matrix we will be evaluating the Green's function at the same angles for all source and observation points. This permits the calculation of the angles α and the quantities $cos(\alpha), sin(\alpha), cos(m\alpha), sin(m\alpha)$ ahead of time and storing them for later use. This represents a sizable time savings on just about any computer. Gauss quadrature is also more compatible with attempts to vectorize the entire matrix assembly calculation. This will be discussed in more detail later on.

As noted above Gaussian quadrature is very accurate for the given number of abscissa points or function evaluations. One problem with quadrature is the absence of some form of simple and dependable error control. The casual user of a body of revolution code is confronted with the question; Just how many of these darn points do I need? The absolute integration error for quadrature rules can be estimated if the behavior of the higher order derivatives of the integrand are known. For the n point Gauss rule the absolute error E_n is given by the following expression

$$E_n = C_n f^{(2n)}(\eta) \;\; , \;\; \eta \in [-1, +1]$$

$$C_n = \frac{1}{(2n)!} \cdot \frac{S_n}{\alpha_n^2}$$

$$S_n = \int_{-1}^{+1} [P_n(x)]^2\, dx$$

$$P_n(x) = \alpha_n (x - \xi_1) \cdots (x - \xi_n)$$

The point η where the derivative is evaluated is some point that will depend on the behavior of $f(x)$. From the above error expression it is easy to see that polynomials of degree $2n - 1$ will be integrated exactly, since the derivative of degree $(2n)$ will vanish everywhere. The multiplicative constant that appears in the error expression can be calculated with a little effort. The constant values were calculated for Gauss-Legendre rules up to the 64 point rule, and can be found tabulated in Appendix I.

We consider a specific example of estimating the absolute integration error. In most practical cases the calculation of the derivatives $f^{(2n)}(x)$ is rather intractable, especially for large n. However the simple trigonometric functions readily lend themselves to repeated differentiation. Consider the function $cos(\mu\phi)$. It is easy to differentiate repeatedly, and it's oscillatory character is not terribly far removed from the behavior of the actual Green's function. Consider the integral

$$I(f) = \int_0^{\pi} cos(\mu\phi)\, d\phi = \int_{-1}^{+1} \frac{\pi}{2} \cdot cos\left(\mu \frac{\pi}{2}(1 + x)\right) dx$$

where a change of variables was used to convert the integration interval to $[-1, +1]$. If we differentiate the integrand of the second integral $2n$ times, we will obtain some constant times the cos function. Even though

we don't know the point η, we know that the absolute value of the cosine function is bounded by unity. Hence we can bound the absolute value of the error by the expression

$$|E_n| < (\frac{\pi}{2})^{2n+1}(\mu)^{2n}$$

Keep in mind that this is the absolute error, and not the relative error. As a specific numeric example consider applying the Gauss-Legendre 32 point rule to the function above with $\mu = 16$. For this example, the error bound is roughly 1×10^{-18}, an impressive error figure for the small amount of computation involved !

The estimation of integration error when using quadrature rules in actual BOR algorithms by use of the above expression is a formidable task. The free space Green's function can be differentiated a few times by someone who is studious, but the calculation of high order derivatives is not really practical. If one keeps the derivation in perspective, a "ball park" estimate for $f^{(2n)}(x)$ is not impossible to arrive at. We consider the worst case of the self-terms, then by using a few approximations we arrive at the following estimate for the absolute error in the coefficients for Fourier mode m when using the n point Gauss-Legendre rule

$$|E_n| < 2C_n(\frac{\pi}{2})^{2n+1}(m + kr_{max})^{2n}$$

where r_{max} is the largest radial dimension of the body being modeled. This estimate is less reliable if singularity extraction is not being used. In that case the derivatives $f^{(2n)}$ are unbounded for self-terms, and error estimates are not theoretically possible. The absence of explicit error control for quadrature methods has made popular the use of certain adaptive methods, and this will be our next topic of discussion.

Integration methods that try to make educated guesses about the behavior of the integrand and adjust accordingly are usually called *adaptive* methods. There are many very reliable adaptive routines available for general application. The SLATEC library contains many well tested routines that are based on adaptive methods, and several of these will be discussed later. We will next discuss an adaptive technique that is used in several popular BOR codes, namely the adaptive trapezoidal rule.

The composite trapezoidal rule is one of the most familiar integration techniques. The integration interval $[a, b]$ is divided into equally spaced intervals of length h. The function $f(x)$ being integrated is approximated in a linear fashion over each interval. If $[a, b]$ is divided into n equal intervals the corresponding trapezoidal rule estimate which we denote by $T_n(f)$ is given by the expression

$$T_n(f) = h[\frac{1}{2}f(x_0) + f(x_1) + \cdots + f(x_{n-1}) + \frac{1}{2}f(x_n)]$$

$$x_i = a + ih$$

$$h = \frac{(b-a)}{n}$$

The basic trapezoidal rule can be made adaptive quite easily. The basic idea is to compute a sequence of estimates $T_1(f), \cdots, T_n(f), T_{2n}(f)$. The sequence is calculated until the absolute value of the difference between successive estimates $|T_{2n}(f) - T_n(f)|$ is less than some desired error tolerance. One advantage of this approach is that by using a nested sequence of function evaluation points, the function evaluations used to compute $T_n(f)$ can also be used to calculate the more accurate estimate $T_{2n}(f)$.

Although the trapezoidal rule is very easy to implement in software, the convergence rate is quite slow compared to other available methods. However, an improvement to this method can be made with some knowledge of the exact nature of the integration error present in the trapezoidal rule. The absolute error for subintervals of length h is given by

$$E_h = \frac{[f'(a) - f'(b)]}{12}h^2 + \mathcal{O}(h^4)$$

Notice that the term that multiplies h^2 does not change as h itself is varied. Hence, if one doubles the number of subintervals, the error is improved by roughly a factor of four. A little algebra shows that the

successive estimates $T_n(f), T_{2n}(f)$ can be used to estimate the h^2 error term and then use it to improve the answer! The resulting rule converges much more rapidly, however it can be adversely affected by arithmetic round off errors. This technique, used to improve the convergence rate of many other numerical methods is known as Richardson extrapolation. The resulting integration technique is called Romberg integration. Most good numerical analysis texts contain programs for Romberg integration, or if you have the IMSL library, you can use the well tested routine DCADRE.

The user should proceed with caution when using any of the above methods derived from the trapezoidal rule when attempting to integrate trigonometric "like" functions. Because the sample points are evenly spaced, these can sometimes coincide with zeros, or extrema of the trig functions. For example, the nested trapezoidal rules will fail when one tries to integrate $sin(m\alpha)$ on the interval $[0, \pi]$ for large even values of m. These methods are not unique in this respect, no method is totally fool proof. It is easy to construct pathological functions for ***any*** specific technique that will completely "fool" the method! Just keep track of the points (x_i, y_i) that your favorite integration routine evaluates your favorite function at. Consider all polynomials of sufficiently high degree which pass through all the chosen (x_i, y_i) points. The given method will produce the same answer when any one of these polynomials is integrated. Thus one can find functions where the integration error is arbitrarily large!

In searching for good integrators for use on the Green's function a number of routines from the SLATEC library were experimented with by the author. The routine GAUS8 was applied to a number of test cases with quite favorable results. GAUS8 is based on the 8 point Gaussian quadrature rule together with subdivision of the integration interval to obtain an error estimate less than the user specified tolerance. The QUADPACK subset of routines of SLATEC contains modules for a very wide variety of general applications, including integrations of singularities! A number of QUADPACK routines based on a little known and very interesting method will be our next topic.

Adaptive rules which use nested sequences of evaluation points enjoy a certain degree of economy not shared by other methods. The Gauss-Legendre rules are such that higher order rules don't share any common evaluation points except for zero in the rules that have an odd number of points. Unknown to most of us, there exist optimal extensions of the ordinary Gauss-Legendre rules where the abscissa points are nested. The Gauss-Kronrod rules are optimal $2n+1$ point extensions of the plain n point Gauss-Legendre rule. The weights in the $2n+1$ point rule are different from those in the n point Gauss-Legendre rule, but this not not significantly impact the economy associated with using the "old" function values. These two nested rules provide the levels of accuracy associated with optimal quadrature rules, together with the availability of comforting error estimates. Note that because we have n predefined abscissa points, the $2n+1$ point Gauss-Kronrod rule will exactly integrate polynomials of degree $3n+1$, making it less accurate than the corresponding Gauss-Legendre rule with the same number of points, but still very accurate. These interesting new methods are already implemented in the QUADPACK package in the SLATEC library. There are several routines which compute the integral using a fixed Gauss-Kronrod rule, and returns an estimate of the error. The rules with 15,21,31,41,51, and 61 points are implemented in modules QK15 , $\cdots$, QK61. These routines appear to be ideal for the user that just wants some feedback on the levels of integration error, and is willing to accept the penalty of recomputing a problem that fails expectations. The predictability of computational effort here is also an enormous advantage in some situations. In addition QUADPACK contains the routines QAG, and QAGE which employ the Gauss-Kronrod rules together with adaptive subdivision of the integration interval to obtain an answer with an error estimate less than some user specified error tolerance. These routines appear best suited to the user that demands accuracy and is prepared to accept some additional computational effort in the cases were it is required. The theory associated with these techniques discussed above, along with interesting additional references can be found in (QUADPACK , A Subroutine Package for Automatic Integration, R. Piessens, E. de Donker-Kapenga, C. Uberhuber, D. Kahaner, Springer-Verlag, 1983).

A comparison of several adaptive solvers can be found in Appendix II. The adaptive trapezoidal rule, Romberg integration, and the SLATEC routines GAUS8 and QK41 were all used to numerically calculate the first few Fourier coefficients of the function $cos(\mu\phi)$. This function was chosen because it's oscillatory character is similar to the free space Green's function, and the coefficients can be computed analytically to

facilitate actual error calculations. The Fourier series which can be found in most handbooks is

$$cos(\mu x) = \frac{2\mu sin(\mu\pi)}{\pi} \cdot \left(\frac{1}{2\mu^2} + \frac{cos(x)}{1^2 - \mu^2} - \frac{cos(2x)}{2^2 - \mu^2} + \frac{cos(3x)}{3^2 - \mu^2} - \cdots \right)$$

where μ cannot be an integer. The tables in Appendix II show the first twenty computed Fourier coefficients for several values of μ. Also shown are the actual absolute errors for each solver, and the number of function evaluations required. The adaptive solvers were given a relative error tolerance of 10^{-4}. Examination of the table clearly demonstrates the more rapid convergence rate of Romberg integration verses the adaptive trapezoidal rule. The errors present in the Romberg results show that the convergence test used by most such solvers cannot always insure that the actual error will be less than the user prescribed tolerance. The error levels obtained from the quadrature based routines demonstrate the superior efficiency of these methods. The qualitative nature of these results is very much in agreement with the author's experience with actual BOR calculations based on these same routines.

With the advent of vector computers such as the **CRAY-XMP** , dramatic improvements in execution times are possible for properly structured algorithms. Execution of vectorized code can be as much as 500 times faster than equivalent scalar code. At this point in time, there appears to be plenty of improvement possible in the vectorization of BOR algorithms. The matrix solution process already vectorizes almost automatically. The matrix assembly process, which accounts for a significant percentage of the total effort, is an area where significant improvement is possible. None of the popular codes in use today are structured such that the impedance matrix assembly calculation will vectorize. Idealy, we would like to vectorize over source and observer pairs. This would mean that the inner DO loops of the code would be over segments, but the popular codes in use today are such that these loops are on the outside. The situation is slightly complicated by the fact that the self terms are treated differently than the other terms, however vectorization is still possible. Although implementation of vectorized adaptive integrators is not impossible, the presence of IF statements in many of the DO loops make the task greatly more complex than vectorizing the simple quadrature rules. It appears that the easiest way to construct a vectorized integration algorithm is to use quadrature based techniques. The Gauss-Kronrod rules in particular seem to be very well suited to this.

In summary we have seen that several improvements in integration methods are possible over methods now in common use. Many accurate and more efficient adaptive techniques are available to the user that demands specific levels of integration accuracy. For the user that demands maximum efficiency, the optimal quadrature rules are unsurpassed. In particular, the relatively unknown Gauss-Kronrod rules can provide efficient and accurate results with error estimates to evaluate the accuracy of integration on specific problems. It is the author's hope that these methods gain recognition in the computational physics community.

Appendix I

Error Constants C_n for Gauss-Legendre Quadrature

$$E_n = C_n \cdot f^{(2n)}(\eta)$$

1	3.33333D-001	33	7.76346D-113
2	7.40741D-003	34	4.26094D-117
3	6.34921D-005	35	2.20591D-121
4	2.87946D-007	36	1.07900D-125
5	8.07929D-010	37	4.99441D-130
6	1.54087D-012	38	2.19091D-134
7	2.12743D-015	39	9.12118D-139
8	2.22477D-018	40	3.60862D-143
9	1.82325D-021	41	1.35846D-147
10	1.20251D-024	42	4.87182D-152
11	6.52056D-028	43	1.66638D-156
12	2.95829D-031	44	5.44211D-161
13	1.13949D-034	45	1.69875D-165
14	3.77297D-038	46	5.07330D-170
15	1.08539D-041	47	1.45100D-174
16	2.73804D-045	48	3.97797D-179
17	6.10607D-049	49	1.04628D-183
18	1.21246D-052	50	2.64239D-188
19	2.15736D-056	51	6.41294D-193
20	3.45947D-060	52	1.49681D-197
21	5.02530D-064	53	3.36240D-202
22	6.64363D-068	54	7.27478D-207
23	8.02750D-072	55	1.51697D-211
24	8.89959D-076	56	3.05077D-216
25	9.08485D-080	57	5.92107D-221
26	8.56732D-084	58	1.10973D-225
27	7.48625D-088	59	2.00965D-230
28	6.07844D-092	60	3.51854D-235
29	4.59789D-096	61	5.95917D-240
30	3.24800D-100	62	9.76849D-245
31	2.14757D-104	63	1.55065D-249
32	1.33190D-108	64	2.38488D-254

Mu= 2.5 Tol= 1.0e-04

m	Analytic Solution	---Adp Trap--- Abs(E)	Nfe	---Romberg---- Abs(E)	Nfe	----GAUS8---- Abs(E)	Nfe	----QK41----- Abs(E)	Nfe
0	0.800000	1.580E-05	513	1.192E-07	33	5.960E-08	56	1.192E-07	41
1	-0.952381	1.574E-05	513	1.252E-06	33	1.788E-07	56	1.192E-07	41
2	2.222222	6.294E-05	257	1.049E-05	33	0.000E+00	56	2.384E-07	41
3	1.818182	1.538E-05	513	2.420E-05	33	1.192E-07	56	2.384E-07	41
4	-0.512821	1.568E-05	513	9.400E-05	33	2.980E-07	56	1.192E-07	41
5	0.266667	3.964E-06	1025	2.384E-06	65	8.941E-08	56	2.980E-07	41
6	-0.168067	3.859E-06	1025	6.288E-06	65	2.533E-07	56	2.980E-08	41
7	0.116959	1.006E-06	2049	5.350E-06	65	1.490E-08	56	5.215E-08	41
8	-0.086580	1.110E-06	2049	9.485E-06	65	6.333E-07	120	1.043E-07	41
9	0.066890	9.984E-07	2049	1.752E-05	65	4.768E-07	120	8.196E-08	41
10	-0.053333	9.462E-07	2049	3.583E-05	65	4.470E-08	120	1.676E-07	41
11	0.043573	1.028E-06	2049	6.530E-05	65	1.416E-07	120	2.831E-07	41
12	-0.036298	9.164E-07	2049	1.764E-04	65	2.757E-07	120	4.843E-08	41
13	0.030722	1.032E-06	2049	2.600E-06	129	1.453E-07	120	8.401E-07	41
14	-0.026350	3.055E-07	4097	4.791E-06	129	2.384E-07	120	3.092E-07	41
15	0.022857	2.664E-07	4097	3.109E-06	129	8.009E-08	120	0.000E+00	41
16	-0.020020	2.477E-07	4097	2.997E-06	129	1.062E-07	184	3.073E-07	41
17	0.017683	2.384E-07	4097	3.671E-06	129	8.233E-07	184	6.277E-07	41
18	-0.015736	2.645E-07	4097	7.469E-06	129	7.674E-07	248	6.761E-07	41
19	0.014094	2.347E-07	4097	4.265E-07	129	3.185E-07	248	6.910E-07	41
20	-0.012698	2.114E-07	4097	3.189E-04	65	2.598E-07	216	7.832E-07	41

Mu= 5.5 Tol= 1.0e-04

n	Analytic Solution	---Adp Trap--- Abs(E)	Nfe	---Romberg--- Abs(E)	Nfe	----GAUS8---- Abs(E)	Nfe	----QK41----- Abs(E)	Nfe
0	-0.363636	8.643E-06	1025	4.834E-05	33	3.874E-07	56	2.980E-08	41
1	0.376068	8.613E-06	1025	1.045E-04	33	3.874E-07	56	5.960E-08	41
2	-0.419048	8.613E-06	1025	2.325E-06	65	8.941E-08	56	8.941E-08	41
3	0.517647	8.762E-06	1025	6.258E-06	65	1.788E-07	56	2.980E-07	41
4	-0.771930	8.523E-06	1025	1.086E-03	33	4.172E-07	56	1.788E-07	41
5	2.095238	3.457E-05	513	1.383E-03	33	4.768E-07	88	2.384E-07	41
6	1.913043	3.433E-05	513	2.077E-03	33	2.384E-07	120	2.384E-07	41
7	-0.586667	8.762E-06	1025	3.308E-05	65	1.788E-07	120	1.192E-07	41
8	0.325926	8.613E-06	1025	7.170E-05	65	1.490E-07	120	5.960E-08	41
9	-0.216749	2.265E-06	2049	1.824E-04	65	2.384E-07	120	7.451E-08	41
10	0.157706	2.086E-06	2049	8.283E-04	65	5.960E-07	120	3.427E-07	41
11	-0.121212	2.190E-06	2049	5.044E-06	129	2.235E-07	120	4.470E-08	41
12	0.096703	2.153E-06	2049	6.154E-04	65	5.960E-08	120	3.576E-07	41
13	-0.079279	2.138E-06	2049	5.413E-04	65	1.714E-07	120	3.502E-07	41
14	0.066365	6.333E-07	4097	5.752E-04	65	4.098E-07	152	4.768E-07	41
15	-0.056483	5.551E-07	4097	4.541E-06	129	1.602E-07	248	1.416E-07	41
16	0.048726	4.768E-07	4097	5.372E-06	129	2.757E-07	248	4.657E-07	41
17	-0.042512	6.184E-07	4097	7.093E-06	129	1.863E-08	216	4.508E-07	41
18	0.037447	5.253E-07	4097	9.865E-06	129	6.333E-08	248	1.118E-08	41
19	-0.033258	5.700E-07	4097	1.396E-05	129	9.052E-07	248	1.032E-06	41
20	0.029750	5.905E-07	4097	2.025E-05	129	5.420E-07	248	1.321E-06	41

Nu= 7.5 Tol= 1.0e-04

m	Analytic Solution	---Adp Trap--- Abs(E)	Nfe	---Romberg---- Abs(E)	Nfe	----GAUS8---- Abs(E)	Nfe	----QK41----- Abs(E)	Nfe
0	-0.266667	2.361E-06	2049	4.798E-06	65	5.960E-08	56	6.557E-07	41
1	0.271493	3.010E-06	2049	6.020E-06	65	1.192E-07	56	5.364E-07	41
2	-0.287081	2.772E-06	2049	5.752E-06	65	4.172E-07	56	1.192E-07	41
3	0.317460	2.950E-06	2049	9.716E-06	65	2.086E-07	120	2.980E-08	41
4	-0.372671	1.174E-05	1025	1.749E-05	65	0.000E+00	120	2.384E-07	41
5	0.480000	1.171E-05	1025	3.359E-05	65	5.066E-07	120	2.682E-07	41
6	-0.740741	1.204E-05	1025	7.141E-05	65	2.384E-07	120	5.960E-08	41
7	2.068965	4.721E-05	513	1.824E-04	65	0.000E+00	120	4.768E-07	41
8	1.935484	4.780E-05	513	8.277E-04	65	1.192E-07	120	1.192E-07	41
9	-0.606061	1.144E-05	1025	1.242E-03	65	5.960E-08	120	1.192E-07	41
10	0.342857	2.831E-06	2049	6.156E-04	65	8.047E-07	120	0.000E+00	41
11	-0.231660	2.891E-06	2049	5.442E-04	65	2.086E-07	120	1.073E-06	41
12	0.170940	2.995E-06	2049	5.681E-04	65	3.874E-07	120	3.129E-07	41
13	-0.133038	2.861E-06	2049	6.435E-04	65	1.788E-07	184	5.960E-07	41
14	0.107335	2.891E-06	2049	7.634E-04	65	7.451E-08	216	2.235E-07	41
15	-0.088889	7.674E-07	4097	9.325E-04	65	2.757E-07	216	9.388E-07	41
16	0.075094	6.706E-07	4097	9.991E-06	129	3.129E-07	248	3.874E-07	41
17	-0.064447	7.227E-07	4097	1.405E-05	129	3.129E-07	248	2.384E-07	41
18	0.056022	7.525E-07	4097	2.004E-05	129	3.390E-07	248	1.047E-06	41
19	-0.049221	6.333E-07	4097	2.873E-05	129	5.215E-08	248	7.637E-07	41
20	0.043636	6.668E-07	4097	4.412E-05	129	2.272E-07	248	1.863E-08	41

ACCURATE AND EFFICIENT NUMERICAL COMPUTATION OF SOMMERFELD INTEGRALS FOR LAYERED MEDIA GREEN'S FUNCTIONS

Bradley L. Brim and David C. Chang
ECE Department - Electromagnetics Laboratory
University of Colorado
Boulder, CO 80309-0425

The name of Sommerfeld has come to be associated with a general class of integral often found in electromagnetics and other fields of applied physics. The form of such integrals may be written as

$$g(r,z) = \int_0^\infty G(\lambda)\, J_\nu(r\lambda)\, \exp(-uz)\, d\lambda \qquad (1)$$

with $u = (\lambda^2 - \kappa^2)^{\frac{1}{2}}$.

The necessity of numerically evaluating such integrals arose in our investigations of a spatial domain moment method-type analysis of microstrip structures. A similar analysis is developed in [3,5] and will not be discussed here in any detail. We are only interested in evaluation of (1) for a single, lossless dielectric layer bounded on alternate sides by free space and a perfect conductor, and for both source and field points on the air/dielectric interface (ie: g(r,0)), see Figure 1. Although this is the case, what is presented here is applicable to more general layered media Green's functions as well. Specifically, we are interested in two functions, $G(\lambda)$, for the parameters $z=0$ and $\nu=0$

$$Gm(\lambda) = \frac{\lambda}{[u_0 + u_1 \mathrm{Ctnh}(\kappa d u_1)]} \qquad Ge(\lambda) = \frac{Gm(\lambda)\,[u_0 + u_1 \mathrm{Tanh}(\kappa d u_1)]}{[\epsilon_1 u_0 + u_1 \mathrm{Tanh}(\kappa d u_1)]} \qquad (2)$$

with $u_0 = (\lambda^2 - \kappa^2)^{\frac{1}{2}}$ and $u_1 = (\lambda^2 - \epsilon_1 \kappa^2)^{\frac{1}{2}}$, for $RE[u_0] \geq 0$ ($\kappa \equiv$ free space wavenumber). On the original, infinite, purely real contour (C_0 in figure 2) the integrand is ill- behaved due to the oscillation of the Bessel function, the presence of a branch point at κ , and possible poles between κ and $\epsilon_1^{\frac{1}{2}}\kappa$ on the λ axis from possible simple zeroes in the denominators of $Gm(\lambda)$ and $Ge(\lambda)$. Our choice of $z=0$ further complicates evaluation using contour C_0, since we do not have exponential decay in the integrand. It is well known that we can consider contours other than C_0, for example: a partially deformed contour (C_1) or a fully deformed contour (C_2) , both shown in figure 2.

Previous authors [1-5] have investigated various techniques that could have been used to compute (1) for these $G(\lambda)$, but we desired a routine that could perform this evaluation to a pre-specified (possibly high) degree of accuracy, and we did not find any one of the techniques presented in these references to suit our needs. Most of these techniques have focused on contours C_0 and C_2 (or its equivalent). Among these techniques are those of ... 1) subtracting from $G(\lambda)$ a term corresponding to the case for $u_1 = u_0$ over the entire contour [3], 2) choosing subintervals of integration in order to form a monotonically decreasing, alternating series that can be truncated with a known error bound [1,2], 3) Filon's (Shank's, Averages) method to accelerate convergence [1,3,5], and 4) various asymptotic methods [1,3,4,5]. We desired to use a single method of evaluation in order to reduce programming time and the ambiguities involved with choosing which of a multiple set of routines to use for each unique set of parameters.

Our routine uniquely applies some of the above mentioned techniques, or ones that are somewhat similar, to obtain highly accurate values for gm(r,0) and ge(r,0) to be used in the numerical characterization of microstrip structures. The values of the radial distance r vary from zero to less than a few free space wavelengths at most, and appropriate techniques must be used accordingly. The first feature of our routine is that we choose to use a method similar to 1) mentioned above, in which we subtract a term

from $G(\lambda)$ corresponding to the well known static portion of g(r,0), done only over certain portions of the chosen contour (a direct and image terms for the "m" case - a direct and weighted image summation terms for the "e" case). We then choose to add back in the image portions of these g(r,0), in effect, subtracting only the singular (r^{-1}) portion of the spatial domain Green's function. Therefore, we define

$$\hat{g}(r,0) = g(r,0) - a/r \qquad (3)$$

with $a = 1/2$ for the "m" case and $a = 1/(\varepsilon_1 + 1)$ for the "e" case.
It is well known that it is advantageous to evaluate g(r,0) using contour C_2 for "large" r, and as many authors have thoroughly investigated the use of contour C_0 and found it difficult to obtain high degrees of pre-specified, known accuracy (even for "small" r) we chose to more thoroughly investigate the use of contour C_2 for all r of interest to us for the function $\hat{g}(r,0)$.

We find that the real axis portion of C_2 is evaluated quite adequately using an adaptive Newton-Cotes routine, and that the possible residue terms (corresponding to the poles of $G(\lambda)$) are also quite easily evaluated, therefore neither numerical procedure will be discussed further here. The imaginary axis portion of (1), using (2), over contour C_2 is of main concern, and the composite integrands (summed for each side of the branch cut) of gm(r,0) and ge(r,0) are shown in figures 3 and 4; for r=0.01, κd=0.10, and ε_1 =9.9. The corresponding integrands of $\hat{g}m(r,0)$ and $\hat{g}e(r,0)$ are shown in figures 5 and 6. From figure 5 one might conclude that method 3) above could be used advantageously, but it turns out to yield little if any improvement. From figure 6 one might conclude that Series methods (ie: 2) above) could use subintervals "folded" about the obvious points of large derivative, but again this yields little if any improvement. The application of method 2) above is an adequate choice, but the creation of a monotonically decreasing, alternating series is more effort than is required. We find that it is more efficient to use fixed sized subintervals while creating an alternating series, which eventually becomes monotonically decreasing, and to increase the number of these subintervals to obtain an adequately small absolute error. The reasoning behind this is that these extra subintegrals are evaluated very quickly with a minimum number of function evaluation, as their absolute error criteria is identical to the earlier subintegrals, but their magnitudes are much less. We find that we can evaluate $\hat{g}m(r,0)$ and $\hat{g}e(r,0)$ to ten or more digits of relative accuracy for all r of interest other than zero using this simple subintegral/series method. The resultant values of $\hat{g}m(r,0)$ and $\hat{g}e(r,0)$ corresponding to figures 3-6 are shown in figures 7 and 8 respectively.

For the necessary case of $\hat{g}(0,0)$ we can choose to use one of three methods (noting that the Bessel function term becomes unity for r=0) ... 1) use contour C_2 for a number of small values of r and then extrapolate to r=0, or 2) use contour C_2 for r=0, or 3) use contour C_0 (or alternately C_1) for r=0. We found it most efficient to use the third method with contour , to avoid the numerical problems that exist on the real axis. To further assist the convergence of this method, asymptotic terms may be subtracted form the integrand, which allows the shortening of the infinite interval by adding the corresponding known analytical truncation terms for some "large" λ. We found through much mathematical manipulation that the derivatives of $\hat{g}m(r,0)$ and $\hat{g}e(r,0)$ wrt. r, for r=0, are expressible analytically in very simple forms, and therefore no further computations are required to obtain their values extremely accurately. The three methods above may be compared to show that the same accuracy may be obtained for $\hat{g}(0,0)$ as for $\hat{g}(r,0)$.

The verification of the accuracy of these computations was carried out in several ways, the first being the comparison of the various techniques mentioned above. Even though all these techniques were not optimized to yield adequate accuracy for our purposes, a few (or possibly several) digits could be compared among them to establish that the proper values were being obtained, then a convergence study could be made on those few methods chosen, and these results compared. Also, the results for the case of an air dielectric (ε_1 =1) are analytically known, and were compared to our routine of final choice when it did not take advantage of this fact. These results are shown in figure 9.

In our analysis of microstrip structures we must repeatedly evaluate $\hat{g}m(r,0)$ and $\hat{g}e(r,0)$. If we were to numerically evaluate the corresponding Sommerfeld integral each time we needed it, we would be foolish, for the functions $\hat{g}m(r,0)$ and $\hat{g}e(r,0)$ are quite smooth wrt. their single parameter r. Therefore, we are able to fit these functions quite accurately using cubic splines. In fact, since their derivatives at r=0 are known analytically, it is advantageous to use a cubic spline fit for known first derivatives at the end points. As seen in figure 10, we can fit the functions quite adequately with a reasonable number of function evaluations.

Finally, it should be mentioned once again that this routine is specialized to z=0 and a unique geometry of a layered media. This, however, does not specialize the routine presented here to the point of not being useful for more general geometries. For example, in any problem (be it layered media or not) the 3-d Green's function will exhibit the same singular behavior (r^{-1}), and similar methods may easily be developed to remove this behavior, allowing a much more efficient computation of g(r,0) for "small" to "moderate" r. Geometry restrictions are easily removed by using a $G(\lambda)$ that corresponds to a different set of dielectric layers, with the corresponding static terms obtained from the asymptotic form of this $G(\lambda)$ for large λ. The lossless dielectric restriction can be removed by making ϵ_1 a complex number, slowing the computations a bit, but quite easily done. If the restriction z=0 is removed, the same routine may be used for r/z "large", but for r/z "moderate" or "small" it will likely be more efficient to use the contour C_0 (or C_1), since significant exponential decay will exist for increasing λ.

References

1. F. Cornille, "Computation of Hankel Transforms", SIAM Review, 14 (2), April 1972, pp. 278-85.

2. D. Bubenik, "A Practical Method for the Numerical Evaluation of Sommerfeld Integrals", IEEE Trans. on Antennas and Propagation", AP-25 (6), November 1977, pp. 904-6.

3. J. Mosig and F. Gardiol, "Analytical and numerical techniques in the Green's function treatment of microstrip antennas and scatterers", IEE Proceedings, Pt. H, 130 (2), March 1983, pp. 175-82.

4. P. Katehi and N. Alexopoulos, "Real axis integration of Sommerfeld integrals with applications to printed circuit antennas", J. Math. Phys., 24 (3), March 1983, pp. 527-33.

5. J. Mosig and F. Gardiol, "A Dynamical Radiation Model for Microstrip Structures", Advances in Electronics and Electron Physics - Vol. 59 (Academic Press), 1982, pp. 139-237.

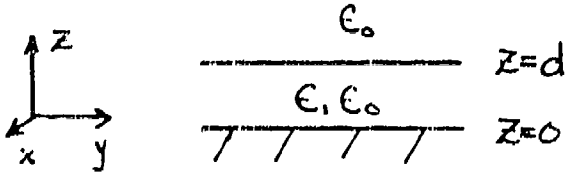


Figure 1 Geometry

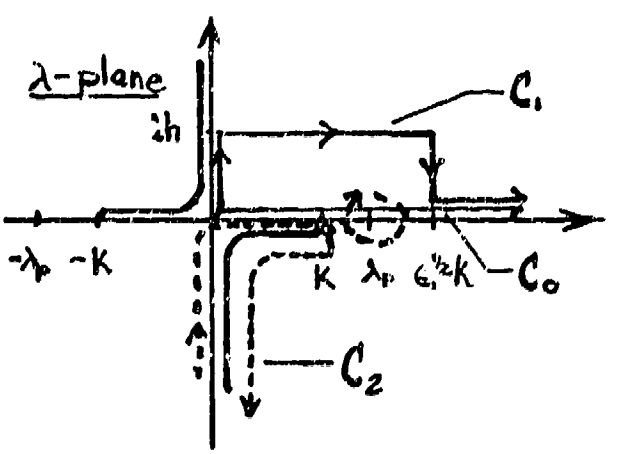


Figure 2 Contours

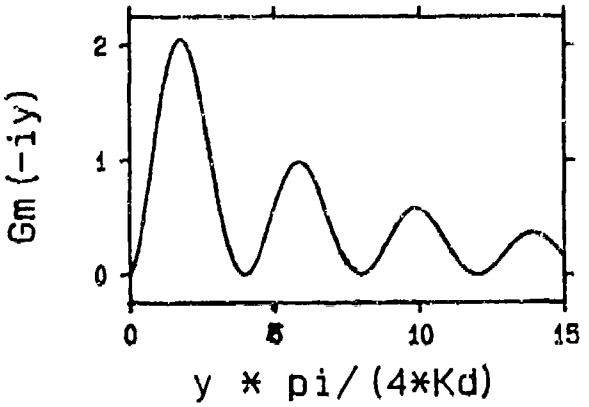


Figure 3 C_2 imaginary axis integrand w/o static term subtracted.

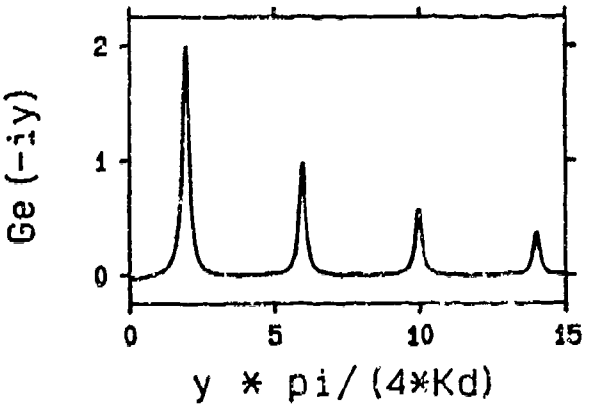


Figure 4 C_2 imaginary axis integrand w/o static term subtracted.

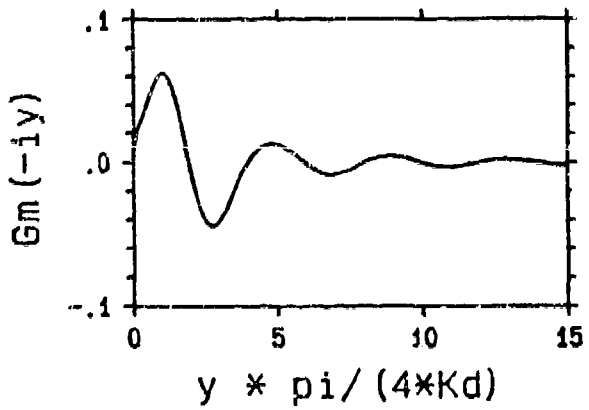


Figure 5 C_2 imaginary axis integrand w/ static term subtracted.

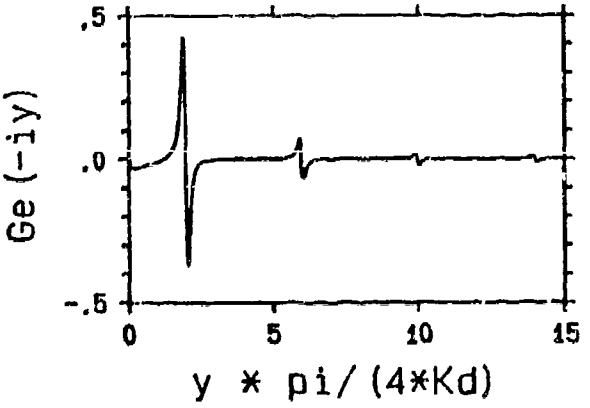


Figure 6 C_2 imaginary axis integrand w/ static term subtracted.

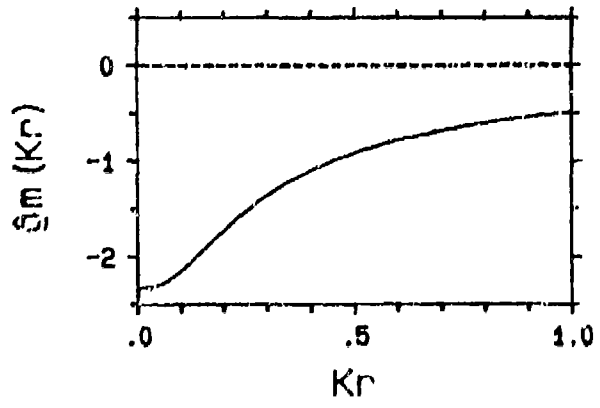


Figure 7 gm(r,0) corresponding to above plots.
(solid/real - broken/imag)

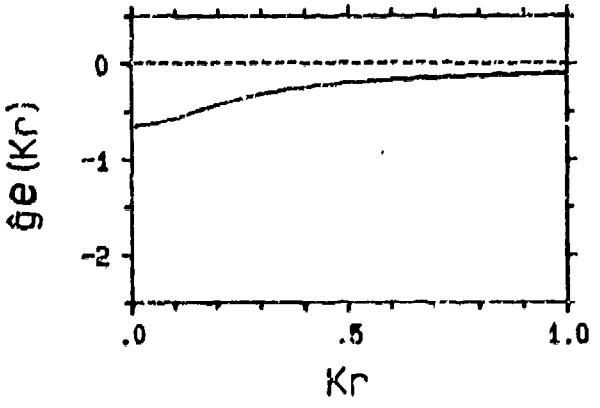


Figure 8 ge(r,0) corresponding to above plots.
(solid/real - broken/imag)

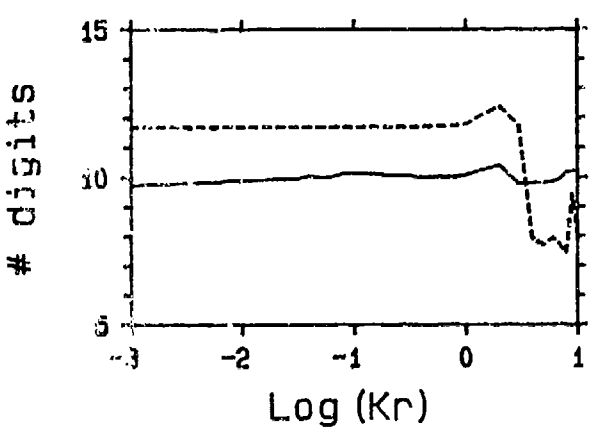


Figure 9 Number of identical digits among $\hat{g}m(r,0)$ for an air dielectric and the exact result. (relACC=10) (solid/real - broken/imag)

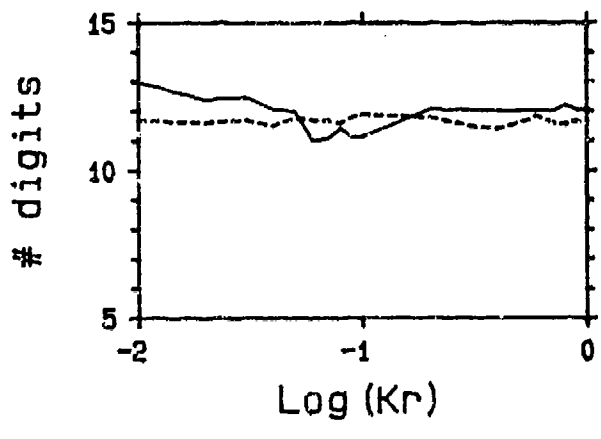


Figure 10 Number of identical digits among computed and curve fit $\hat{g}m(r,0)$. (100 uniformly spaced pts.)

ALGORITHM OUTLINES

Overall Routine

1) Compute $\hat{g}(0,0)$ on contour C_1
2) Analytically evaluate $\hat{g}'(r,0)$ at $r=0$
3) Compute $\hat{g}(r,0)$ at pre-defined points to pre-defined accuracy "relACC"
4) Compute $\hat{g}'(r_{max},0)$ by finite diff.
5) Perform cubic spline fit with known first derivatives at end points

$\hat{g}(0,0)$ Routine

1) Compute integral $(\epsilon_1^{\frac{1}{2}}, \lambda_{max})$ and add analytic truncation terms
2) Define error for below from above
3) Compute integral $(0, ih)$
4) Compute integral $(ih, \epsilon_1^{\frac{1}{2}} + ih)$
5) Compute integral $(\epsilon_1^{\frac{1}{2}} + ih, \epsilon_1^{\frac{1}{2}})$
6) $\hat{g}(0,0)$ = sum of above

$\hat{g}(r,0)$ Routine

1) $E1 = 10^{-(relACC+1)}$
   $E2 = 10^{-(relACC+2)}$
2) $\hat{g}(r,0) = 0$
   $b = 0$
   $n = -1$
3) $n = n+1$
   $a = b$
   $b = (2n+1)\,\pi/(4\kappa d)$
4) Compute subintegral (a,b) on imaginary axis portion of C_2 to error E1
5) $\hat{g}(r,0) = \hat{g}(r,0)$ + subintegral
6) IF |subinterval| > E2, go to 3
7) Compute integral $(0, \kappa)$ on real axis portion of C_2 to error E1
8) Compute possible residue term(s)
9) Add 7) and 8) to $\hat{g}(r,0)$

SESSION III - "SCATTERING"

Moderator: Harold A. Sabbagh
Sabbagh Associates, Inc.

"Numerical Aspects of Scattering by An Impedance Wedge"
Robert T. Brown — Grumman Corporation

"A Lattice Representation for Back Face Removal in Electromagnetic Scattering"
T.K. Pollock — Chirp Technical Services

"Protecting Scattering Computations from Effects of Interior Resonances"
F.X. Canning — Rockwell International Science Center

"Floquet Theory Based Modification to NEC-2 for Analysis of Very Large Periodic Planar Arrays
R.M. Cribb — McDonnell Douglas Astronautics Company
* This paper is not presented here, because the sponsor has not granted approval as of press time.

"Singularity Expansion Method (SEM) Natural Modes as Efficient Entire Domain Expansion Functions in the Analysis of Frequency Selective Surfaces (FSS)"
L.S. Riggs, M.E. Baginski, F.J. German — Auburn University

"Optimal Loading"
B. Tomas and Elizabeth Yip — The Boeing Aerospace Company

"Numerical Difficulties and Software Validation Needs Associated with EFIE Formulations for Dielectric Scatterers"
A.F. Peterson — University of Illinois

"Computation of Frequency-Domain and Time-Domain Scattering from a Cross with the CEMACS and CASSANDRA Codes"
D.E. Thomas and G.R. Salo — BDM Corporation

NUMERICAL ASPECTS OF SCATTERING BY AN IMPEDANCE WEDGE

Robert T. Brown
Corporate Research Center
Grumman Corporation
Bethpage, New York 11714-3580

Abstract

This paper describes some numerically useful mathematical properties of the transcendental function introduced by Maliuzhinets in describing acoustic or electromagnetic scattering by a wedge with two different face impedances. For a given wedge angle the Maliuzhinets function can be written in terms of an infinite integral in the complex plane. The independent variables are thus the wedge angle and a complex variable containing all other parameters in the scattering process, including incidence and scattering angles, polarization, and two complex face impedances expressed as complex Brewster angles. The region of convergence of the integral is an infinite strip in the complex plane with width dependent on the wedge angle. For input variables lying outside the region of convergence there always exist recursion and symmetry relations allowing the desired result to be obtained. When the Maliuzhinets function is examined as a function of a complex variable, it is found that it is analytic everywhere in the infinite strip in which the integral converges. It is in fact a conformal mapping of the infinite strip into a region in the complex plane with the width on the real axis mapped into a finite segment of the real axis, and the point at infinity mapped into a point on the unit circle. Furthermore, for all wedge angles the resultant values on the unit circle fall within the sector $\pi/8 \leq |\text{Arg } z| \leq \pi/4$. These results have important implications in numerical applications, leading to very efficient algorithms for evaluation of the function, especially in terms of the amount of storage required.

The problem of acoustic scattering by a wedge with two different face impedances was solved by Maliuzhinets [1] in terms of a Sommerfeld contour integral. The Maliuzhinets solution is expressed in terms of the complex transendental function $\Psi_\Phi(z)$, where Φ is the exterior wedge half angle, and the complex variable z contains the remaining physical properties describing the scattering process, including angles of incidence and scattering, and the complex surface impedance of each face. The Maliuzhinets function has found widespread application in various treatments of both acoustic and electromagnetic edge diffraction.

Maliuzhinets discussed many of the properties of $\Psi_\Phi(z)$ in his original paper, such as recussion relations, values for particular wedge angles, and two explicit representations, one as a double infinite product, and one as a complex integral. Neither of the two representations given by Maliuzhinets is particularly amenable to numerical evaluation. Later, Zavadskii and Sakharova [2] presented what they called expressions suitable for computing the function $\Psi_\Phi(z)$ on an electronic computer. However, their methods are not all that practical for rapid numerical evaluation, and the numerical tables described in their paper are not readily available. This paper describes the results of an investigation of the numerical properties of the Maliuzhinets function. For the particular case of backscatter it is shown that numerical evaluation of the function can be considerably simplified by making use of some of its mathematical properties.

The geometry of the problem is shown in Fig. 1. The incidence (and scattering, for the case of backscatter) angle is measured from the illuminated face, while the wedge angle is expressed as the external half angle. The Maliuzhinets solution leads to a product of four ratios of the form

$$r_{\pm}(z) = \frac{\Psi_\Phi(z \pm \pi)}{\Psi_\Phi(z)} \qquad (1)$$

for backscatter. In the more general case of bistatic scattering the argument in the numerator depends on the scattering angle, and the denominator is a function of the incidence angle. When expressed as the ratio (1), the integral representation of Zavadskii and Sakharova becomes

$$r_{\pm}(z) = e^{-I_{\pm}(z)} \tag{2}$$

where

$$I_{\pm}(z) = \int_0^{\infty} \frac{\tanh \pi s/2 \sinh s(\pi/2 \pm z)\, ds}{s \sinh 2\Phi s} \tag{3}$$

Written in terms of exponentials, (3) is

$$I_{\pm}(z) = \int_0^{\infty} \frac{Y_{\pm}(z,s)}{X(s)} \frac{ds}{s} \tag{4}$$

where

$$Y_{\pm}(z,s) = \cos ys[(e^{\pi s}-1)e^{\pm xs} + (e^{-\pi s}-1)e^{\mp xs}]$$

$$\pm i \sin ys\,[(e^{\pi s}-1)e^{\pm xs} - (e^{-\pi s}-1)\, e^{\mp xs}] \tag{5}$$

and

$$X(s) = e^{(2\Phi + \pi/2)s}{}_{+}e^{(2\Phi - \pi/2)s}{}_{-}e^{(\pi/2 - 2\Phi)s}{}_{-}e^{-(2\Phi + \pi/2)s} \tag{6}$$

Examination of the explicit form of (4) given by (5) and (6) shows immediately that the integral converges in the open interval

$$|x| < 2\Phi - \pi/2 \tag{7}$$

for all y. The region of convergence is therefore an infinite strip with width given by (7). It is possible to devise a quadrature scheme that is valid everywhere in the strip in which the integral converges. There is one wedge angle, $3\pi/4$, for which a closed form solution for $r_{\pm}$ exists. We have developed a quadrature method that reproduces this exact result to within 5 or 6 significant figures. Yip and Chiavetta have recently discussed this subject in some detail [3].

Considerable reduction in storage required for numerical applications can be achieved by making use of symmetry and recursion relations displayed by the Maliuzhinets function. These are summarized in Figure 2. While the present work was in progress, the symmetry relations permitting numerical evaluation

to be limited to the first quadrant were also noted by Herman, Volakis and Senior [4].

An even more significant reduction in storage requirements is achieved by noting that the Maliuzhinets function is a conformal mapping. The infinite strip containing all information on the scattering process for a given wedge angle is mapped onto a finite region in the complex plane. An example, for a wedge angle of $3\pi/4$, is shown in Fig. 3. Although the complex reflectance of a passive surface must lie within the unit circle, the Fresnel equations relating reflectance and impedance map the unit circle into the right half plane. It would seem therefore that in numerical work it would be necessary to calculate, or have available in storage, values of the wedge function over the entire infinite strip in which the integral representation converges. However, the limiting case as the imaginary part of z becomes infinite, the ratio given by (2), can be shown to approach

$$\lim_{y\to\infty} r_{\pm} = \exp(\mp i\pi^2/8\Phi) \tag{8}$$

so that

$$\lim_{y\to\infty} |r_{\pm}| = 1 \tag{9}$$

The point at infinity is thus mapped onto the unit circle. This important result holds for the ratio of two Maliuzhinets functions describing bistatic as well as monostatic scattering, although in the case of bistatic scattering (8) depends on the difference in incidence and scattering angles as well as the wedge angle.

Since the external wedge half angle is constrained to lie between $\pi/2$ and , the limiting case for backscatter lies on the sector

$$\pi/8 \leq |\text{Arg } z| \leq \pi/4 \tag{10}$$

The particular case in Fig. 3, for a wedge angle of $3\pi/4$, leads to a limiting value of Arg $z = \pm \pi/6$. According to (10), the entire range of possible angles results in mappings not too far from the case shown. Therefore it appears sufficient to store values for only a quite limited number of wedge

angles for interpolation during execution. Also, from examination of Fig. 3 it is apparent that a fairly coarse grid in independent variables can be used; in particular, not very large values of y = Im z have to be considered.

That the mapping is conformal can be shown from the integral representation (2) and (4). The partial derivative of $r_\pm$ are

$$\frac{\partial r_\pm}{\partial x} = - \frac{\partial I}{\partial x} e^{-I_\pm(z)} = - \frac{\partial I}{\partial x} r_\pm \tag{11}$$

and

$$\frac{\partial r_\pm}{\partial y} = - \frac{\partial I}{\partial y} e^{-I_\pm(z)} = - \frac{\partial I}{\partial y} r_\pm \tag{12}$$

The derivatives on the right-hand side of (11) and (12) can be carried out by Leibnitz's rule, so that

$$\frac{\partial I_\pm}{\partial x} = \int_0^\infty \frac{1}{X(s)} \frac{\partial Y_\pm}{\partial x} \frac{ds}{s} \tag{13}$$

and

$$\frac{\partial I_\pm}{\partial x} = \int_0^\infty \frac{1}{X(s)} \frac{\partial Y_\pm}{\partial y} \frac{ds}{s} \tag{14}$$

from which it is easily verified by differentiation of (5) that

$$\mathrm{Re} \frac{\partial r_\pm}{\partial x} = \mathrm{Im} \frac{\partial r_\pm}{\partial y} \tag{15}$$

and

$$\mathrm{Re} \frac{\partial r_\pm}{\partial y} = - \mathrm{Im} \frac{\partial r_\pm}{\partial x} \tag{16}$$

so that the Cauchy-Riemann conditions are satisfied everywhere in the strip in which the integral coverges. Therefore $r_\pm$ is analytic and the transformation is conformal.

Because it is a conformal mapping, the curves of constant x and y generated by the impedance wedge function are orthogonal trajectories. Bilinear interpolation can be expected to be quite accurate except in the

vicinity of the limit as y approaches infinity. Examination of numerical values of the impedance wedge function as y increases for constant x has shown an exponential behavior with a slope of approximately -0.64 as the limit is approached. Figure 4 shows the asymptotic behavior for several fixed values of x. An analytic study [5] of the asymptotic behavior of the function in the neighborhood of the limit shows that for constant x the limit is approached as exp(-2y/3).

This behavior is used as the basis for the linear-exponential interpolation algorithm we have developed for use in the interval between the last y value stored and the limit. The algorithm is show schematically in Fig. 5. The largest y value stored is Y_1. Then for a given X between the two values X_1 and X_2 the quantities $U_0(X,Y_1)$ and $V_0(X,Y_1)$ are obtained by linear interpolation. Finally, the values U(X,Y) and V(X,Y) are obtained by a combination of linear and exponential interpolation, given that the distances S and S_1 are related exponentially as shown, with the constant a equal to 2/3.

An added advantage of the analytic nature of the wedge function is that slopes are easily calculated along with the values of the function, permitting more accurate bicubic interpolation to be used instead of bilinear. The necessity of incorporating this refinement is currently being investigated. In view of the results obtained so far, the addition of bicubic interpolation will probably not be necessary. Figure 6 shows a comparison of values obtained by numerical quadrature of the intergral representation and values obtained from linear-exponential interpolation in the vicinity of the limit for infinite y. The wedge angle is $3\pi/4$, is that the limiting values are $|\mathrm{Re}(r_{\pm})| = \cos 30^{\circ}$ and $|\mathrm{Im}(r_{\pm})| = \sin 30^{\circ}$. Also, for this case exact closed form values are available. The interpolation scheme is seen to yield values that agree with the exact values (and those obtaind by numerical quadrature) to within 0.2 percent in the four outermost examples, and to within 0.1 percent in the cases closer to the limit.

REFERENCES

[1] G. D. Maliuzhinets, "Excitation, Reflection and Emission of Surface Waves from a Wedge with Given Face Impedances," Soviet Physics Doklady 3, 752-755 (1958)

[2] V. Yu. Zavadskii and M. P. Sakharova, "Application of the Special Function $\Psi_\Phi(z)$ in Problems of Wave Diffraction in Wedge Shaped Regions," Soviet Physics, Acoustics, 13, 48-54 (1967)

[3] E. L. Yip and R. J. Chiavetta, "Integration and Interpolation Methods for the Impedance Wedge Transendental Function," RACD-TR-86-234, April 1987

[4] M. I. Herman, J. L. Volakis and T.B.A. Senior, "Analytic Expressions for a Function Occurring in Diffraction Theory."
IEEE Trans. Antennas Propagat., vol. AP-35, pp. 1083-1086, September 1987

[5] M. L. Goodman, to be published.

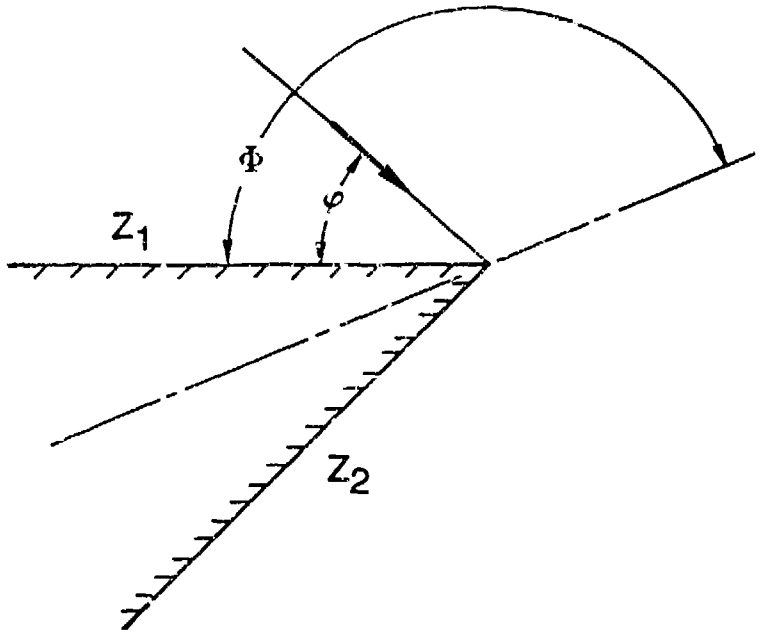
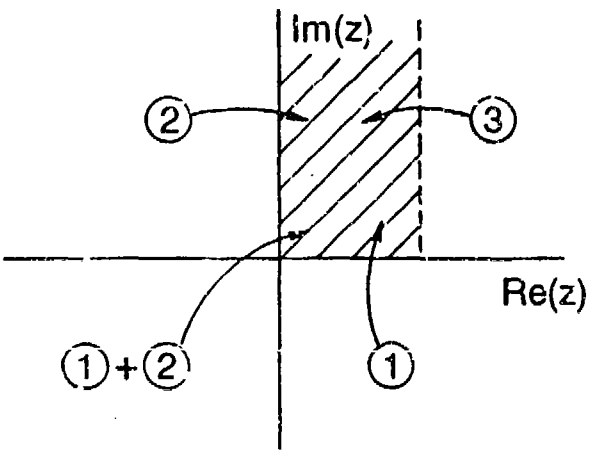


Fig. 1 Geometry of Scattering by an Impedance Wedge



Values needed only in first quadrant because of:

Symmetry Relations:

① $\Psi_\Phi(z^*) = \Psi_\Phi^*(z)$

② $\dfrac{\Psi_\Phi(z-\pi)}{\Psi_\Phi(z)} = \dfrac{\Psi_\Phi(-z+\pi)}{\Psi_\Phi(-z)}$

Recursion Relation:

③ $\Psi_\Phi(z+\pi/2)\,\Psi_\Phi(z-\pi/2) = \Psi_\Phi^2\left(\dfrac{\pi}{2}\right)\cos\dfrac{\pi z}{4\Phi}$

Fig. 2 Storage Reduction Allowed by Symmetry and Recursion Relations

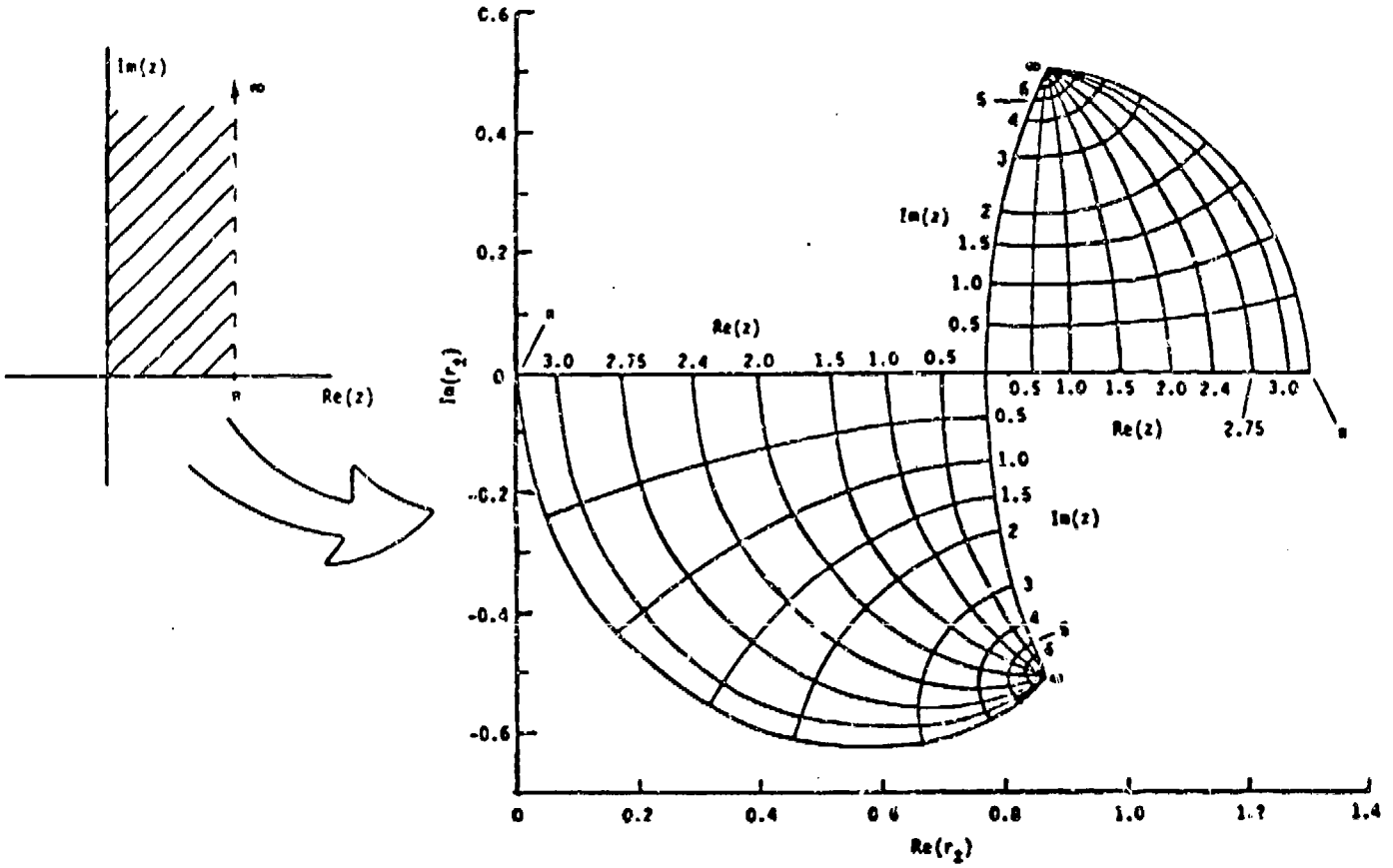


Fig. 3 Impedance Wedge Function as a Conformal Mapping in the Complex Plane

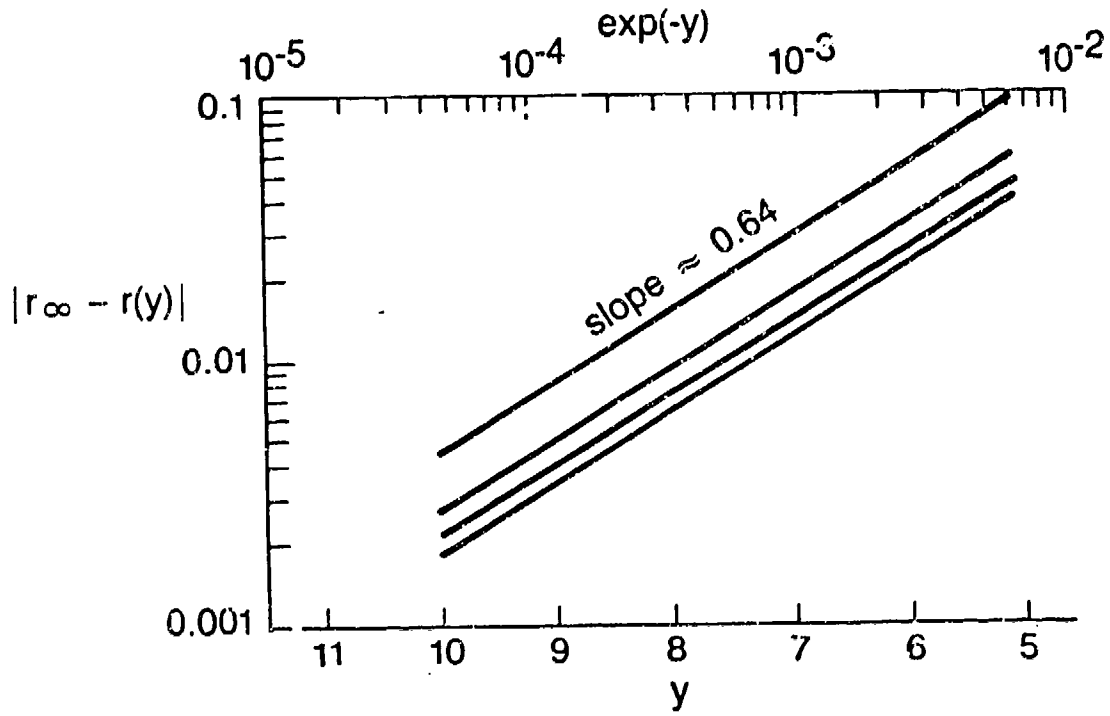


Fig. 4 Asymptotic Behavior of the Impedance Wedge Function

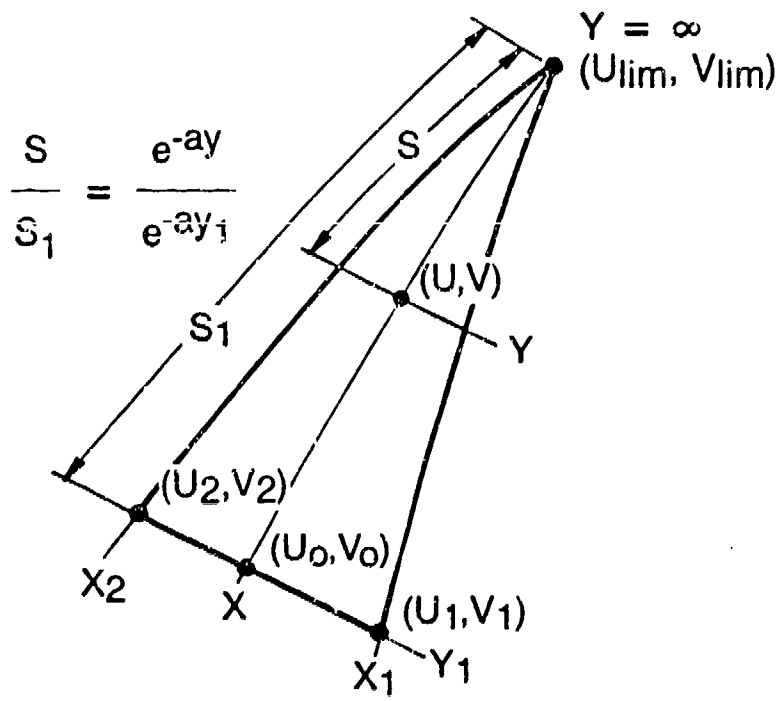


Fig. 5 Linear-Exponential Interpolation Scheme

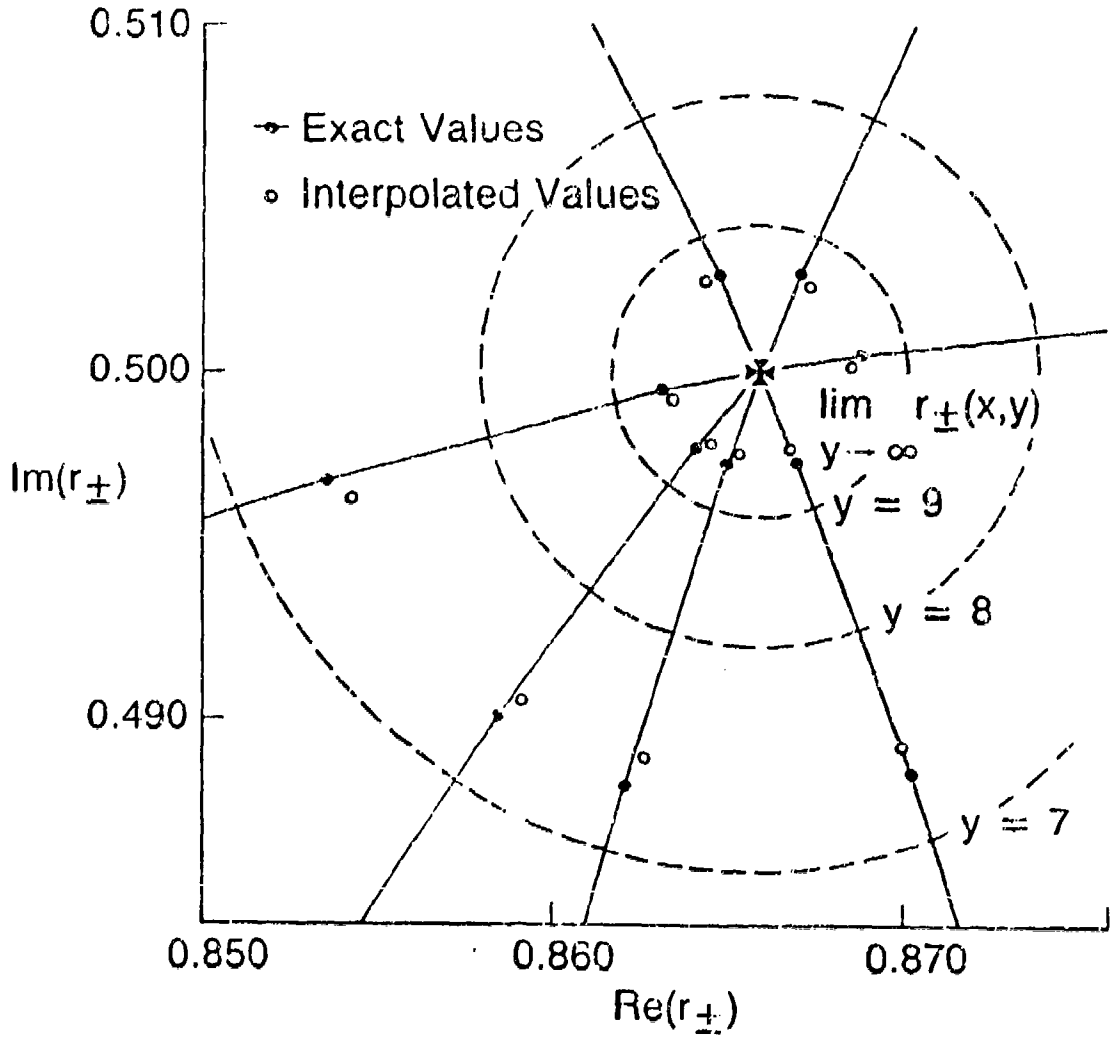


Fig. 6 Comparison of Exact and Interpolated Values of the Wedge Function in the Vicinity of the Limit for Large Y

A LATTICE REPRESENTATION FOR BACK FACE REMOVAL IN ELECTROMAGNETIC SCATTERING

Thomas K. Pollock
Consultant
Chirp Technical Services
505 Camino del Mar
Del Mar, CA 92014-3005
(619) 259-6886

ABSTRACT

A computer program that calculates backscattering including hidden surface removal is described. The scattering geometry is imbedded on a lattice which is oriented towards the frame of reference of the observer. The x and y coordinates of the lattice are mapped to the pixels on the computer console as well as to virtual screen arrays comprising the physical optics (PO) and physical theory of diffraction (PTD) contributions.

By using discrete values for the z direction as well, it is possible to use the FFT algorithm to sum the phase factors due to the propagation delay. Separate virtual screen data are necessary for the physical optics contribution and for the edge current corrections because the components comprising these transformations differ by a wavelength factor. Both three dimensional arrays of virtual screen data are summed in the x and y direction before the FFT is applied.

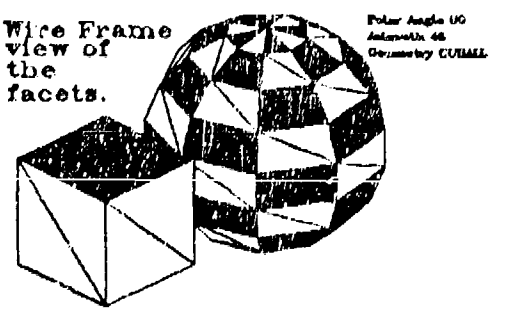
Polygons represent the surface of the scattering object in the lattice. At each monostatic angle the polygons are sorted by depth and written to the lattice. The video graphics library VID calculates the interior points of the polygon, making them available for integration. The code runs on an IBM PC AT or compatible that is equipped with an EGA screen. Separate codes are used to generate and build up the ASCII geometry file.

Introduction

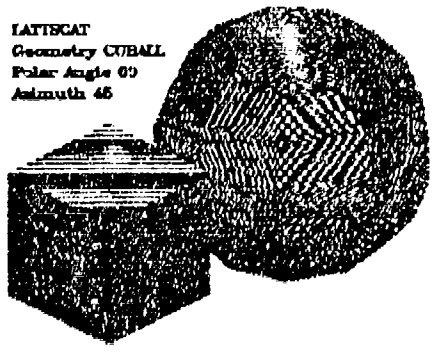
Descriptions follow for an algorithm and an experimental program **LATTSCAT** that calculates hidden surface removal or shadowing and draws a false color image of the object as viewed in the reflectivity calculation with color representing alternatively amplitude or phase. An IBM PC/AT video graphics library **VID.LIB** was recently completed with the additional capability of calculating integrals over surfaces using the same algorithms used to fill polygons imbedded in a three dimensional space. Point drawing subroutines are used both to enable pixels on the video screen, and to fill "pseudo screens" of two dimensional arrays for use in calculations that include hidden surface removal or shadowing. Three dimensional views of the object thus rendered, include a view of the Fresnel regions with the phase displayed as colors on the surface of the scatterer.

Assimilation of Graphical Data

Many relevant questions that must be asked in evaluating the reflectivity of an object, can be answered through the use of a visual tool that displays the way that phase and amplitude combine to form the resultant reflectivity amplitude. A view of the scattering object, based on reflectivity, is presented. The amplitude of a physical optics scatterer is equal to the projected area of the scatterer as viewed in the direction of the monostatic illumination source. When there are many different areas of approximately equal color, the reflectivity



is low. Waves of color representing the actual electromagnetic wave are visible on the object. Intuitive understanding of reflectivity phenomenon is gained by visually experiencing the process. The visual display makes the information tangible.



Motivation for the Program

VID.LIB , is a low level graphics library written for Microsoft FORTRAN which includes hand optimized assembly language subroutines for fast line drawing using Bresenham's algorithm, even faster horizontal line drawing, polygon fill and interfaces to the BIOS and DOS interrupt functions for expanded control of the graphics and system operation of the IBM PC board.

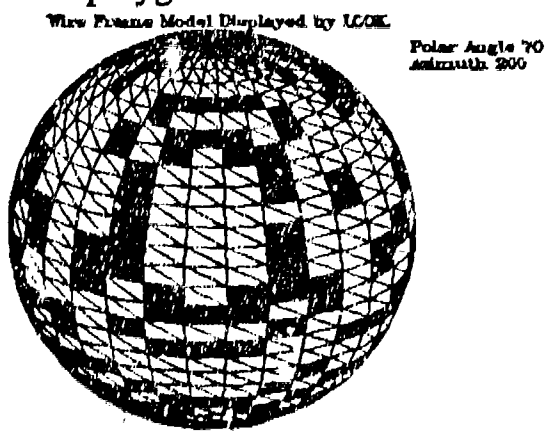
VID.LIB was used to write IBM PC/AT graphics drivers for the higher level **DIG.LIB** graphics library including drivers for CGA and EGA screen modes and arrow key crosshair functions as well as dot matrix printers and plotters.Printing drivers are available for the wide variety of printers that follow the IBM and EPSON printer standards. Supported on these printers are single, double, high speed double, quadruple density modes, single and double density plotter modes which have dot densities of 60, 120, 240, 72 and 144 horizontal dots per inch respectively. Vertical resolution is 72 and 216 dots per inch. The highest density mode supports 240 x 216 dots per inch which amounts to over 4 million dots on the print area.

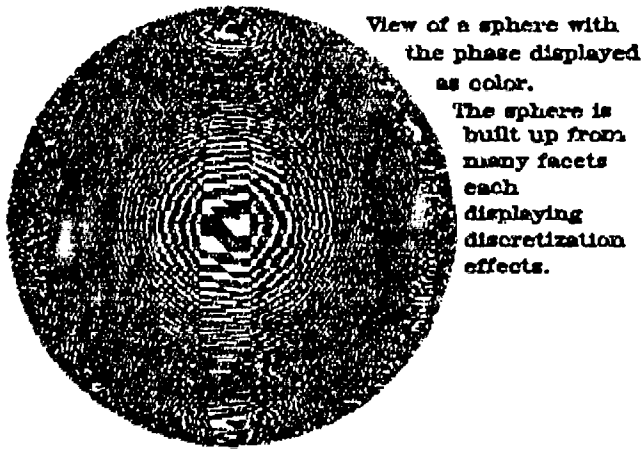
Shadowing and Hidden Surface Removal

Because some objects obscure the view of other objects, the screen drawing process can be considered a multivalued function that takes polygon coordinates from the domain of disk files and maps these coordinates to the I^3 range of (x,y) pixel locations and the pseudo screen. The (also discrete) z coordinate is stored in the two dimensional pseudo screen array. Hidden surface removal amounts to selecting the branch of this multivalued function with the highest z value. In the LATTSCAT program, shadowing is accomplished by comparing the z location of the pixel to be drawn with the z location of any pseudo pixel that has already been drawn into the same x and y location.

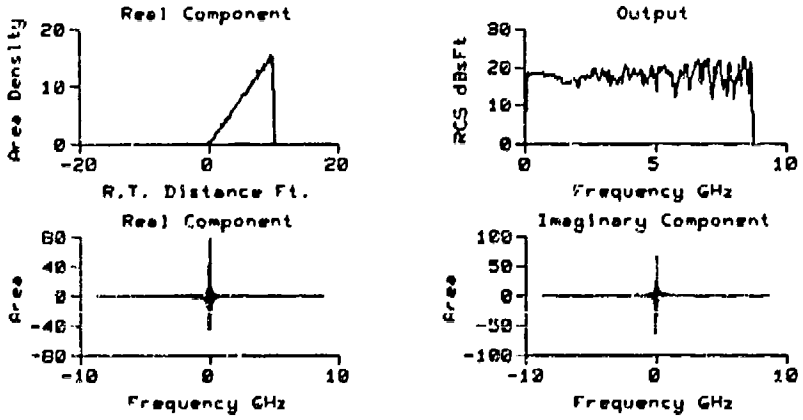
Shadowing effects are often more significant than second order diffraction. Hidden surface removal is also useful for doppler effects because in some cases, the movement causes modulation due to shadowing of background scatterers.

It is ironic that in the very regime where the high frequency approximation becomes accurate, the simulation is inaccurate because of a limitation in the expansion functions used to approximate the geometry. For example, spheres are modeled as multifaceted polyhedrons consisting of a connected collection of polygonal flat plates. At the highest frequencies, each individual flat polygon is evident only when the incident ray is normal to the polygon. The high resolution of the graphics screen should be equivalent to a large number of facets if the sphere were drawn from a high level with each pixel location depth (z value) calculated from the equation for spheres. However, in the current version of LATTSCAT, the spheres are drawn as polygonal facets.





View of a sphere with the phase displayed as color. The sphere is built up from many facets each displaying discretization effects.



LATTSCAT - Fourier Transform

Objectives and Algorithm Description

The primary objective is to add shadowing while maintaining the accuracy of the physical optics and physical theory of diffraction calculations of the reflectivity of a complex 3 dimensional object and to draw the input file geometry. Although the technique applies to edge diffraction as well as physical optics, first consider physical optics only. After the screen and associated data has been calculated, the scattering centers are scaled as necessary by the wavelength and other factors and projected on the z axis by counting the number of pixels that lie a fixed z position and storing the result into a histogram array that includes an entry or index value for each z position. Area as a function of z is the result. Dividing the area in the histogram array by the z step distance gives the area density as a function of z.

For physical optics, no dot specific scaling is necessary. The resulting linear array of complex values is summed with an exp(2ikz) weighting factor to account for the phase shift due to propagational delay. Round trip path length s=2z replaces z in the phase expression, exp(2ikz)=exp(iks).

The concept of area is extended into the complex plane by inclusion of the phase factor so that an area element becomes exp(iks) dA, where dA specifies the area projected on the x, y plane perpendicular to the line of sight of the viewer (the ray of incidence) which is also the area seen on the image drawn on the screen. Summation of the complex area elements results in a total complex area. The absolute value of the complex area is then used in the flat plate formula.

The flat plate formula:

$$\sigma = 4\pi |A|^2 (f/c),$$

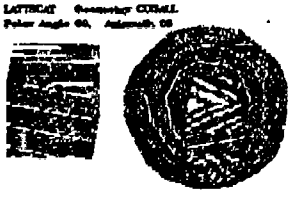
where A is the complex area,
f is the frequency and
c is the speed of light.

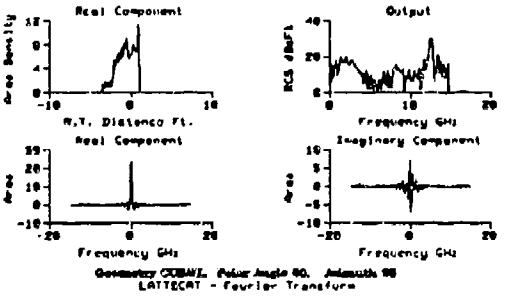
Summation of the area elements is generated by performing a Fast Fourier Transform algorithm on the histogram after it has been centered and zero extended to a 512 value array. Area as a function of frequency is what results from the FFT. These values are scaled using the flat plate formula mentioned above to produce the cross section.

For calculating edge diffraction using Ufimtsev's formulation of the physical theory of diffraction, additional pseudo screen arrays are needed to store the amplitude and z position of the edges. Amplitude must be stored because the amplitude of an individual pixel is not constant as with physical optics. Depth (z position) is also stored in a separate pseudo screen because the frequency dependence differs by a factor of f in the formula analogous to the physical optics (flat plate) formula given above.

Three Dimensional Polygon Filling

Polygon filling is achieved by drawing horizontal lines (the EGA cards on PCs draw horizontal lines the fastest) according to a "pen up", "pen down" routine wherein the line segments that intersect the current row to be filled are sorted so that as the pen moves from left to right across the polygon, the pen is toggled between "up" and "down" whenever a polygon boundary is crossed. When a vertex

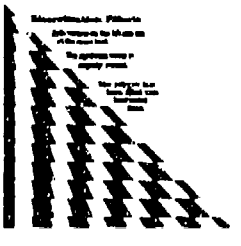




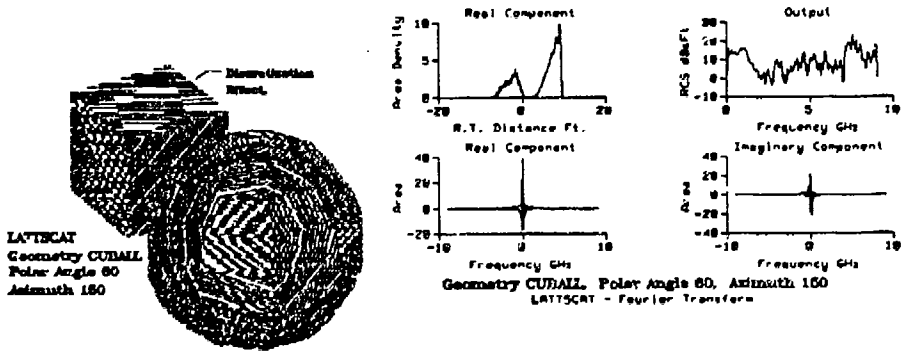
(or a horizontal boundary segment of the polygon) lies on the current row being drawn, additional information must be available to decide if the pen position must toggle. The line drawing routines use the Bresenham algorithm (which does not use multiplication when drawing lines,) both for drawing on the screen and for providing point coordinates to routines that need a series of coordinates to evaluate a summation or integral over a line or polygonal surface that is imbedded in a lattice. Lattice lines can have a left and a right hand side if the total vertical distance is less than the total horizontal distance spanned by the line segment. The extreme case is a horizontal line segment. VID has routines for finding the left and right (or low and high) sides of a lattice line because this type of information is necessary to fill a polygon without counting any polygon point more than once. The line drawing subroutine collection includes three dimensional line capabilities by drawing two dependent lines simultaneously, for example in the x-y plane and in the x-z plane. The final operation of actually drawing the pixel at the various arrays representing the (x,y) location will be undertaken only if the z resulting will be greater than the existing z value at the point (x,y). Otherwise, the point under consideration is shadowed and need not be drawn.

Discretization Effects

Unexpected results can occur when drawing fast lines in this fashion. The figure shows a triangle that is almost perpendicular to the line of incidence. Both left hand vertices are at the same z level whereas the right hand vertex is slightly raised. The endpoints of the horizontal lines used to fill the triangle are determined by line drawing routines for the boundary segments and are have discrete z values. A slower but more accurate process would retain real values for the segment boundaries and thus



always map each (x,y) pair to the z value closest to the polygon surface. This could be done by using a two dimensional polygon fill routine to identify the (x,y) pairs that lie within the projection of the plane and then calculating the z coordinate using an equation for a plane.



Summary

Graphics routines were used to project three dimensional faceted surfaces onto a three dimensional lattice with hidden surface removal. The resulting collection of points was then plotted on the video screen and projected onto the z axis resulting in area density as a function of distance. Fast fourier transformation of the area density function yielded area as a function of frequency. Finally the area was substituted into the flat plate formula for cross section. Edge diffraction is handled similarly. Improvements are planned for geometry handling including higher level specification of shapes like spheres so that faceting will not be necessary. Also changes are planned to eliminate discretization effects that were encountered when filling three dimensional polygons.

PROTECTING SCATTERING COMPUTATIONS FROM EFFECTS OF INTERIOR RESONANCES

Francis X. Canning
Rockwell International Science Center
1049 Camino Dos Rios
Thousand Oaks, CA 91360

It is well known that hollow, closed, conducting bodies can support interior resonances at certain discrete frequencies. This physical fact generally gives rise to numerical problems near these frequencies in computer codes that use the Electric Field Integral Equation (EFIE) to calculate a scattered (external) field. The Magnetic Field Integral Equation (MFIE) is actually invalid at these frequencies, so it will not be considered in this paper.

Due to the simplicity of the EFIE approach and the existence of computer codes utilizing it, it would be useful to have a general method for determining the severity of the numerical problems and for correcting them if necessary. This paper describes such a method, and the very simple modifications necessary to implement it in an existing computer program. Previous work by this author[1,2] showed that, in principle, the correct external field is determined by the EFIE. It was observed that the problems found to date are purely numerical in nature. More importantly, it was also shown that as the frequency of the resonance is approached, the "cavity mode" contributes less and less to the scattered field. This behavior is the opposite of that found in numerical solutions, in which approximations result in the cavity mode generating a strong scattered field. The theoretical work gives a rigorous basis for the simple method that we describe below, which corrects these numerical errors.

The numerical instabilities occur for only a somewhat narrow range of frequencies around the frequency of each resonance. However, as one moves from two to three dimensions and treats larger and larger bodies, the resonances get closer together. Thus, the larger the problem that one is trying to solve, the more likely one is to encounter difficulties.

As a trial case, we examined scattering by a circular conducting cylinder, using the EFIE for the TM polarization. Pulse basis and delta function testing functions were used. We considered frequencies near the resonance at ka = 8.417..., which is degenerate in that the currents of the corresponding modes have azimuthal dependences which may be given as $\cos 2\theta$ and $\sin 2\theta$. Results for 64 and 128 unknowns are shown in the figures.

From Fig. 1, it is clear that the smallest singular value occurs near ka = 8.435 for 64 unknowns and near ka = 8.427 for 128 unknowns. We see that when more unknowns were used, the numerical resonance moved in frequency towards the correct value (ka = 8.417...). These singular values were found by an expensive computational tool, the singular value decomposition. The cost of this tool is several times that of matrix inversion.

We now present a method of calculating the smallest singular value, which has a negligible cost compared to matrix inversion. We also show how to correct the current for numerical errors due to the cavity mode. In the moment method, one solves the matrix equation

$$ZI = V \tag{1}$$

where I is the surface current and V is minus the incident field, evaluated on the surface.

We will use a slightly different notation, and call I_0 the first attempt at a solution, so that

$$I_0 = Z^{-1} V \tag{2}$$

To improve this approximation, I_0, we need to determine whether we are close to a resonance, and if so we also need to determine the cavity mode. Because Z is non-Hermetian, we must deal with its singular values and associated vectors instead of with its eigenvalues and eigenvectors.[1] The singular values of Z are the square roots of the eigenvalues of ZZ^H (which equal those of Z^HZ).

All that is necessary to correct a calculation near a resonant frequency is to calculate the smallest singular value of Z and the appropriate associated mode. This smallest singular value of Z will be the reciprocal of the largest singular value of Z^{-1}, which will be much larger than any others of Z^{-1}. Therefore, an iterative technique called the power method[3] will be very efficient when applied to $Z^{-1}(Z^{-1})^H$.

We apply the power method to find the smallest singular value of Z and its associated cavity mode current to orthogonalize the solution current to the cavity mode current. This generates the formulas:

$$P_1 = Z^{-1}(Z^{-1})^H I_0 \tag{3}$$

$$S_1 = \left[\frac{(I_0, I_0)}{(I_0, P_1)}\right]^{1/2} \tag{4}$$

$$I_1 = I_0 - \frac{(I_0, P_1)}{(P_1, P_1)} P_1 \tag{5}$$

The superscript H denotes Hermetian conjugate. S_1 is an approximation to the smallest singular value of Z, and should be real to the precision of the arithmetic used. P_1 is an approximation to the cavity mode current, and I_1 is the corrected current.

Further accuracy is obtained by iterating, for $\ell = 2,3,\ldots$, according to the rule

$$P_\ell = Z^{-1} (Z^{-1})^H P_{\ell-1} \tag{6}$$

$$S_\ell = \left[\frac{(P_{\ell-1}, P_{\ell-1})}{(P_{\ell-1}, P_\ell)}\right]^{1/2} \tag{7}$$

$$I_\ell = I_0 - \frac{(I_0, P_\ell)}{(P_\ell, P_\ell)} P_\ell \tag{8}$$

It should be noted that this technique is extremely efficient numerically. Only about $4n^2$ floating-point operations are required per iteration. Thus, the cost of this calculation is insignificant compared to matrix inversion.

Figure 1 plots S_1, the estimate after one iteration of the smallest singular value as a function of cylinder radius. One may observe that close to the resonance, i.e., when the singular value really is small, only one iteration is necessary! Far away from the resonance, one does not need to calculate any correction. Calculations were also made of S_2 and S_3. Throughout the region plotted on Fig. 1, the values of S_2 and S_3 agreed with the calculation using the singular value decomposition to better than one part in a thousand.

This discussion provides a simple method for correcting numerical problems. If S_1 is large, do nothing. If S_1 is small, then use I_1 instead of I_0. In the region where S_1 is small, we have calculated I_0, I_1, I_2 and I_3, and the resulting radar cross section at 0° and 180°. They are plotted in Fig. 2 for the 64 unknown case. The radar cross sections for $\ell = 1,2$ and 3 are identical to several decimal places, and are the nearly horizontal lines on the figure. The $\ell = 0$, or uncorrected, radar cross sections give the wildly varying curves.

Clearly, the method we have presented has wide applicability to any internal resonance problem in which the matrix is explicitly inverted. Furthermore, we saw that it is an efficient method, both in terms of execution time and the human effort required to implement it. This correction can easily be added to existing computer programs. One simply makes use of I_0 and Z^{-1} to correct I_0 and replace it by I_1 when necessary. Finally, and possibly most importantly, the corrected currents thus generated allow the calculation of the scattered field to be highly accurate and dependable at all frequencies.

REFERENCES

1. F.X. Canning, "Using the EFIE in the Presence of Cavity Resonances," submitted to IEEE Trans. on Antennas and Propagation.
2. F.X. Canning, "Using the EFIE in the Presence of Cavity Resonances," National Radio Science Meeting, Boulder, CO, January 1988.
3. D.K. Faddeev and V.N. Fadeeva, Computational Methods of Linear Algebra, San Francisco, W.H. Freeman and Co., 1963, Chapter V.

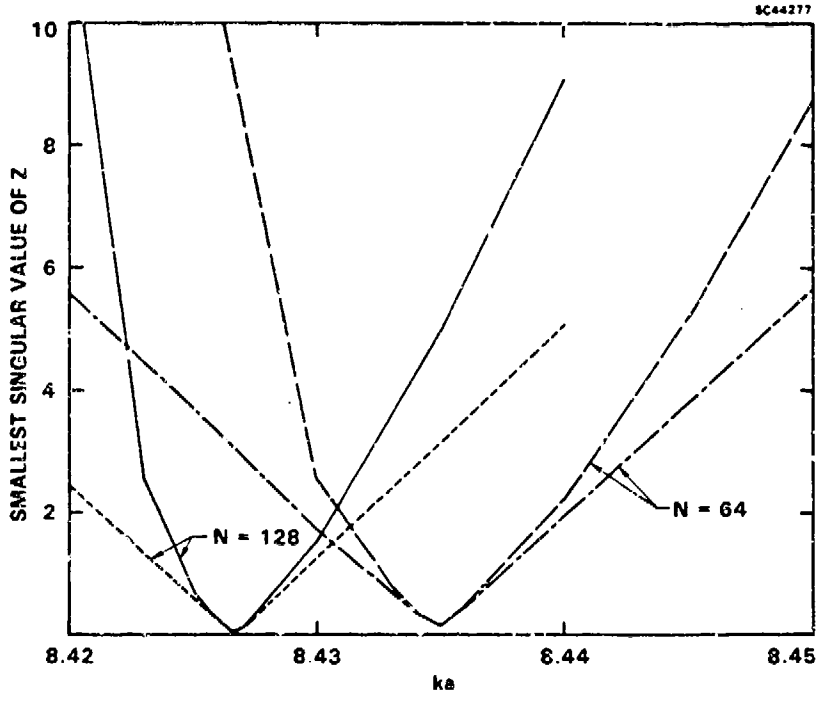


Fig. 1 The smallest singular value of Z as a function of its radius for scattering by a circular conducting cylinder. Results for 64 and 128 unknowns are shown. The short dashed and short-long dashed curves represent both the results of the singular value decomposition, and the results (identical to at least three decimal places) of two or three iterations (ℓ = 2,3) as given by Eq. (7). The solid and long dashed curves represent the results of one iteration, as given by Eq. (4).

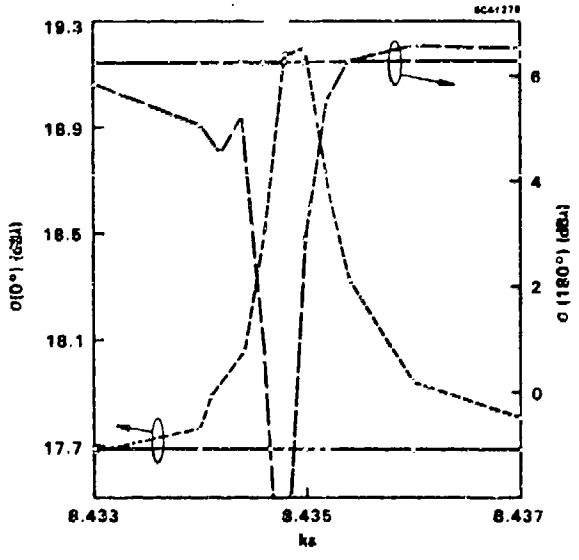


Fig. 2 The radar cross section for backscatter, σ (0°), and for forward scatter, σ (180°), as a function of radius for 64 unknowns and the calculation described in the text. The dashed lines show radar cross sections based on the uncorrected current, I_0. The solid lines show the radar cross sections based on I_1, I_2 or I_3, as all of these results agree to several decimal places.

SINGULARITY EXPANSION METHOD (SEM) NATURAL MODES AS EFFICIENT ENTIRE DOMAIN EXPANSION FUNCTIONS IN THE ANALYSIS OF FREQUENCY SELECTIVE SURFACES

L.S. Riggs, M.E. Baginski, F.J. German
Electrical Engineering Department
200 Broun Hall
Auburn University, Al. 36849-3501

Abstract

In this paper an isolated symmetric penta-arm element is analyzed using the Singularity Expansion Method (SEM) [1]. SEM poles, and modes yield considerable insight into the fundamental scattering characteristics of this element. Is is shown that a simple sinusoidal approximation to the SEM current modes represent a highly efficient entire domain current expansion set when employed in the usual Floquet-Moment Method description of the Penta-arm FSS array.

Introduction

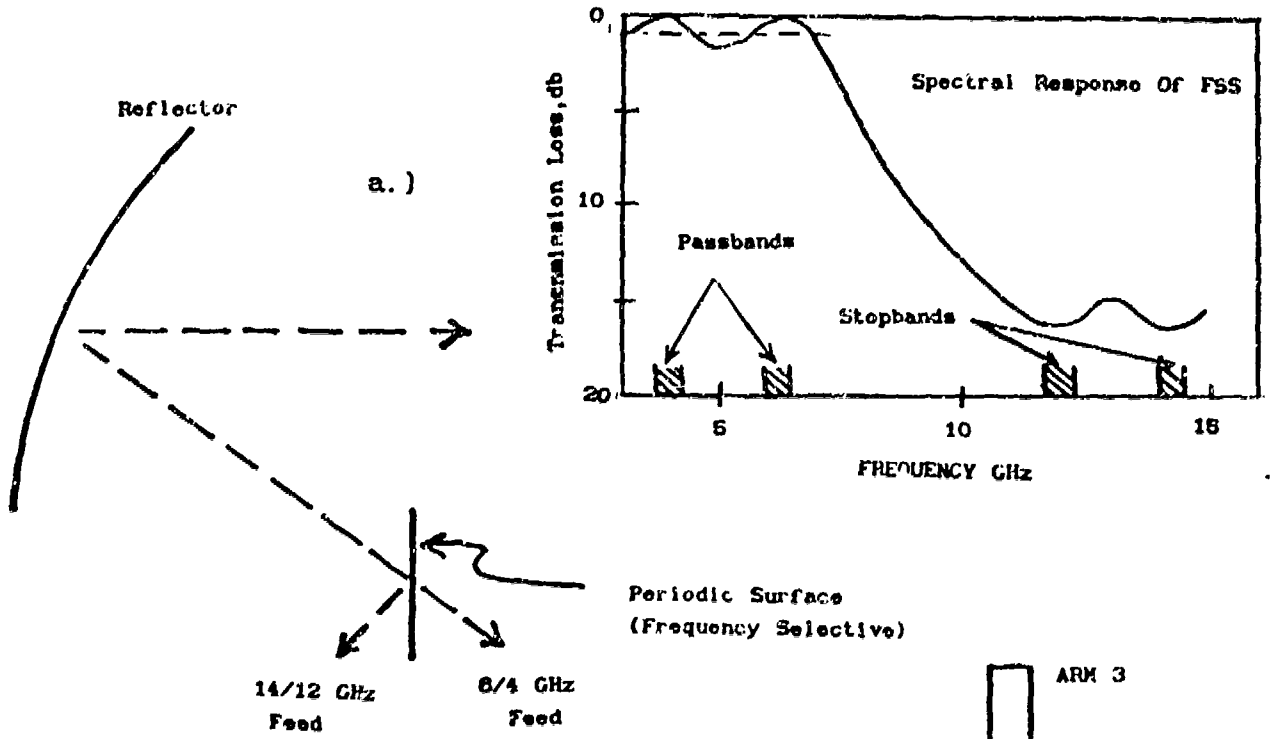
A frequency selective surface (FSS) may be defined as a doubly periodic arrangement of elements on either a planar or conformal surface. The elements can be perforations in a conducting (or resistive) screen or an array of conducting (or resistive) plates backed by a dielectric support. Practical designs often employ several layers of elements sandwiched between multiple dielectric layers.

FSS may be used to combine electromagnetic waves of different frequencies into a single propagating medium (diplexing) or to separate electromagnetic waves of different frequencies from a

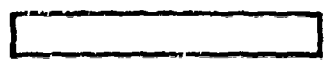
single propagation medium (filtering). As illustrated in Fig.1, a single reflector antenna employing an FSS subreflector can operate at two different frequency bands wherein the diplexing/filtering feature is used in the transmit/receive mode [2]. The Voyager spacecraft employed a shaped FSS subreflector that was transparent at S-band and reflective at X-band (a band-stop to band-pass ratio of 3 to 1) [3].

FSS are often constructed by etching periodic simple metallic elements on thin Kaptan sheets. These thin FSS sheets are then fixed to a low density styrofoam and/or dielectric honeycomb panel to form the finished structure. Commonly used FSS elements are shown in Fig.1 and include the linear dipole, tri-arm, crossed dipole, and Jerusalem-cross. At the resonance frequency of the element the FSS array becomes *completely* reflective so that for band-stop at X-band the tip-to-tip element length would be approximately 1.5 cm (one half wavelength at 10 Ghz). It is generally desirable that the filter characteristics of the FSS be independent of polarization and angle of incidence; therefore, it is important to be able to accurately predict the frequency signature of the array for all variations in the parameters which define the electromagnetic system.

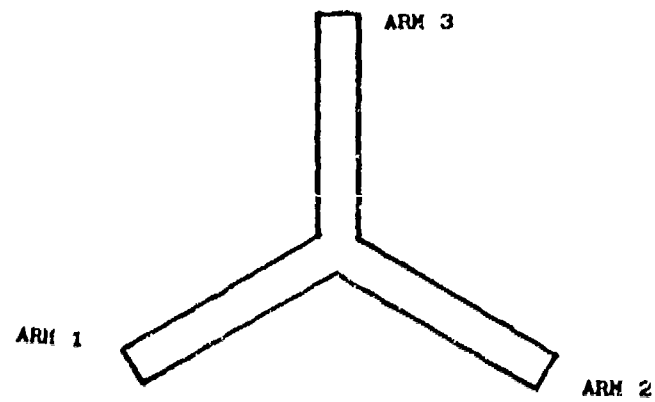
In order to accurately predict the frequency signature of an FSS array an electromagnetic boundary value problem must be solved. A full wave analysis is performed using harmonic matching with fields on either side of the screen expanded in Floquet harmonics. An itergral equation in terms of the current induced on the elements (or fields in the aperature) is constructed by



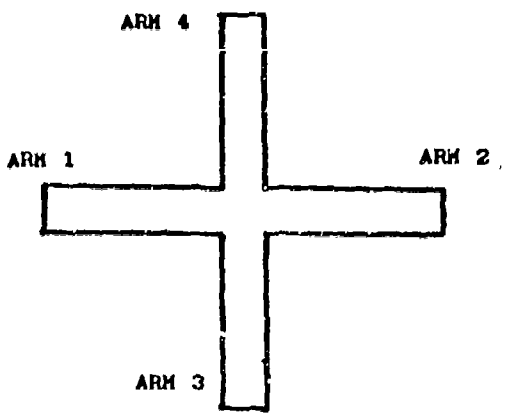
Reflector Antenna System Using
Frequency Selective Screen



Linear Element

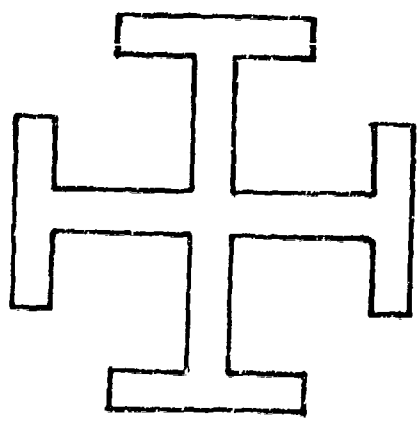


Tri-Arm Element



Crossed Dipole

b.)



Jerusalem-Cross

Fig. 1 a.) Reflector antenna system employing a frequency selective surface and b.) Commonly used frequency selective surface elements

enforcing boundary conditions. Using the method of moments (MOM) [4], the current induced on the elements is computed and the transmission and reflection coefficients determined. The MOM discretization of this integral equation results in impedance elements expressed in terms of doubly infinite series over transverse electric (TE) and transverse magnetic (TM) plane wave modes. Consequently, numerical processing time increases drumatically as the number of expansion functions is increased. Furthermore, as the number of expansion functions increases a greater number of Floquet harmonics must be summed to obtain convergence of the impedance elements. Generally, the number of Floquet harmonics necessary increases with increasing spectral bandwidth of the basis functions involved [5]. For this reason, electrically short, subdomain expansion functions are not as efficient as entire domain expansion functions.

An additional requirement, of course, is that the expansion set chosen span the physical current distribution on the FSS element. It is rather obvious in the case of simple dipole elements without junctions that continuous sinusoidal functions form an efficient entire domain expansion set. However, an efficient physically accurate expansion set is not as easy to select for scattering elements with junctions. Case in point is work by Agrawal and Imbriale [2] who analyzed the crossed dipole FSS array using continuous sinusoidal functions over the perpendicular arms of the cross. Tsao and Mittra [6] later demonstrated that improved results for the crossed dipole array require that Agrawal and Imbriale's expansion set be extended by including current expansion functions which bend at the junction.

The importance of this so-called "junction function" has been identified by several others [7].

In this paper the Singularity Expansion Method (SEM) is used to analyze isolated FSS elements . The SEM factors the transient current response of the element into poles (damped exponentials in time domain), natural current modes, and coupling coefficients. *The SEM natural current modes are used to construct an efficient physically accurate entire domain expansion set for the Floquet-MOM analysis of the FSS array.* Since the SEM analysis of the isolated element is based on a MOM formulation using simple box like expansion and testing functions, no prior knowledge of the physical current distribution is required (except for the usual end and junction conditions). Preprocessing using the SEM also provides important insights into the fundamental scattering properties of the FSS element.

SEM Description of an Isolated FSS Element

Fig. 1b shows the geometry of several commonly used frequency selective surface elements. A MOM matrix equivalent of the electric field integral equation (EFIE) for an isolated FSS element (linear element, tri-arm element, crossed dipole, etc.) may be written, in terms of the complex frequency variable $s=\Omega+j\omega$, as

$$\bar{\bar{Z}}(s)\ \bar{I}(s) = \bar{V}(s) \qquad (1)$$

Pulse expansion and testing functions are used in the MOM formulation and Kirchhoff's current law at an N-arm junction is satisfied by extending current half-pulses for N-1 of the arms

onto the Nth arm. A singularity expansion of the system inverse gives a solution

$$\bar{I}(s) = \sum_{\alpha} \frac{\bar{\bar{R}}_{\alpha}}{s-s_{\alpha}} \bar{V}(s) + \bar{W}_{e}(s) \qquad (2)$$

with the system residue matrix at the αth system pole defined, using Cauchy's residue theorem, as

$$\bar{\bar{R}} = \beta_{\alpha} \bar{M}_{\alpha} \bar{M}_{\alpha}^{t} = \frac{1}{2\pi j} \oint_{c_{\alpha}} \bar{\bar{Z}}^{-1}(s)\, ds \qquad (3)$$

where c_{α} denotes a contour enclosing no poles other than that at $s = s_{\alpha}$, and t denotes the transpose operation. Also, $\bar{W}_{e}(s)$ is an entire function which will henceforth be suppressed. The dyadic nature of the residue matrix in (3) is expressed in terms of a natural current mode vector $\bar{M}_{\alpha}$ and its transpose; β_{α} is simply a convenient proportionality constant so that the current mode's maximum value is real and unity. (Recall that the natural current modes, $\bar{M}_{\alpha}$, form the entire domain expansion set for the FSS array.) Substituting (3) into (2) and writing the excitation vector as $\bar{V}(s) = f(s)\, \bar{A}(s)$ (f(s) is the functional form of the excitation and $\bar{A}(s)$ is a vector whose ith element is the component of the electric vector of a TE or TM impulsive plane wave along the ith segment of the isolated element) yields

$$\bar{I}(s) = f(s) \sum_{\alpha} \frac{\bar{M}_{\alpha}}{s-s_{\alpha}} \eta_{\alpha}(s) \qquad (4)$$

with a coupling coefficient defined as

$$\eta_{\alpha}(s) = \beta_{\alpha} \bar{M}_{\alpha} \bar{A}(s) \qquad (5)$$

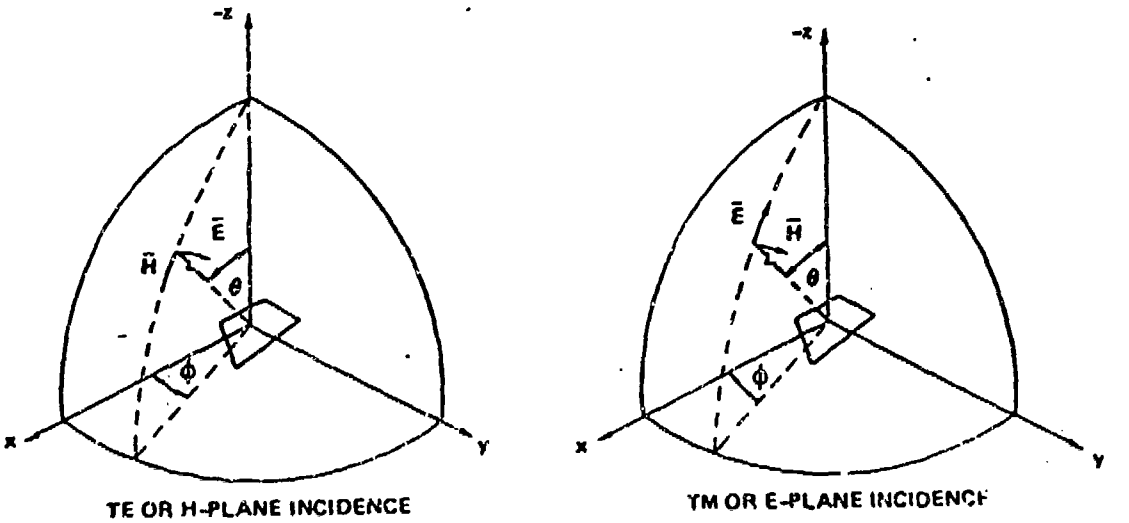
The coupling coefficient determines how much the αth current mode couples into the response.

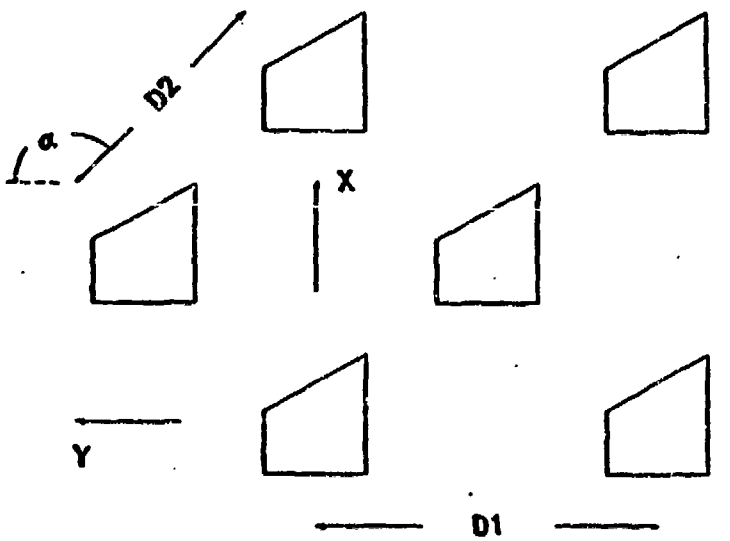
Scattering From A Frequency Selective Surface

In recent years numerous investigators have formulated analyses to predict the reflection and transmission coefficients of FSS, and by now a rather substantial body of literature exists on the subject. Recently, a special issue on FSS was published which contains new results in the field, and articles therein provide an exhaustive list of references [8]. Here, the important steps in the development of the integral equation for the FSS array are summarized without mathematical detail. The reader interested in a more complete development is referred to a paper by Montgomery [9].

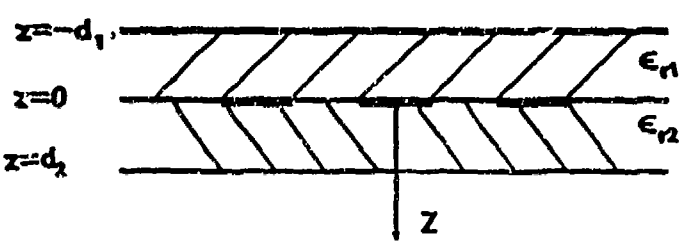
In Fig.2 is shown an infinite FSS array made up of arbitrarily shaped elements mounted between two dielectric sheets. The incident field, defined as the field in the absence of the conducting elements, can be determined by assigning standing waves in the dielectric regions (+z and -z traveling waves with unknown amplitudes), a transmitted (traveling) wave for $z \leq -d_1$ (with unknown amplitude), a reflected wave $z \geq d_2$ (with unknown amplitude), and an incident wave with known amplitude. Application of the boundary conditions (continuous tangential electric and magnetic fields at $z=d_2$, $z=0$, and $z=-d_2$) uniquely defines the incident field in every region in terms of the known incident amplitude.

The next step is to assume that an electric current exists over the perfectly conducting patches located at $z=0$. The electric and magnetic fields radiated by this current are expanded in terms of Floquet harmonics: +z and -z traveling waves in the regions





(a)



(b)

Fig.2 FSS array made up of arbitrarily shaped elements mounted between two dielectric sheets.

$z \geq d_2$ and $z \leq -d_1$ respectively, and standing waves in the regions $-d_1 \leq z \leq 0$ and $0 \leq z \leq d_2$. Again, continuity of the tangential electric and magnetic fields is enforced at $z=-d_1$ and $z=-d_2$. At $z=0$ the tangential electric field must be continuous, but the tangential magnetic field is discontinuous - the change in the magnetic field from $z=0^+$ to $z=0^-$ is exactly equal to the electric current at $z=0$. Lastly, on the conductors at $z=0$, the incident tangential electric field must cancel the tangential electric field radiated by the currents. Applying this final boundary condition and employing the orthogonality of the Floquet modes results in the desired electric field integral equation (EFIE) for the unknown currents induced on the conductors at $z=0$. The MOM can be used to solve for the induced currents, and then it is a simple matter to compute the total reflected and transmitted fields. The total reflected/transmitted field is, of course, the sum of the reflected/transmitted field due to the dielectric slabs (with no conducting elements) and the reflected/transmitted field radiated (in the presence of the dielectric slabs) by the induced currents at $z=0$.

The MOM equation , $\bar{\bar{Z}}\ \bar{I} = \bar{V}$, for the FSS array has some interesting features. Because of the Floquet expansion of the scattered fields , elements of the impedance matrix are represented in terms of a doubly infinite series over TM and TE plane wave modes. More precisely, an element of the matrix $\bar{\bar{Z}}$, say z_{mn}, is represented as an infinite sum of products. One multiplicand is the product of the $(p,q)_{th}$ TE/TM Floquet mode and the nth MOM expansion function integrated over the region occupied by the conducting patch. The other multiplicand is ,as expected,

the product of the conjugate of the $(p,q)_{th}$ TE/TM Floquet mode and the mth MOM expansion function integrated over the same region. As mentioned in the introduction, electrically short (fraction of a wavelength) subdomain expansion functions have larger spectral bandwidths than electrically longer entire domain expansion functions. It is natural to expect that the above mentioned integrals will have significant amplitudes even for relatively high order Floquet modes if electrically short subdomain expansion functions are used. Therefore, to maximize numerical efficiency it is important to use entire domain expansion/testing functions in the MOM description of the FSS array.

Numerical Results

In order to demonstrate the theory, numerical results will be presented for the symmetrical penta-arm element shown in Fig.3. First, the SEM poles and corresponding natural current modes for this element will be presented. These SEM current modes are then used as an efficient physically accurate set of entire domain expansion/testing functions in the Floquet/MOM analysis of the FSS array. Reflection and transmission signatures for the penta-arm FSS array are presented for a variety of excitation conditions.

SEM poles for a simple thin linear element occur in layers roughly parallel to the imaginary axis [10]; and only those poles in the layer nearest the imaginary axis, those with small damping constants, contribute significantly to the response. Poles in the fundamental layer, when multiplied by the tip-to-tip arm length (say 1) and divided by the speed of light, have imaginary parts which occur at approximately $\pi, 2\pi, \ldots,$ corresponding to an element

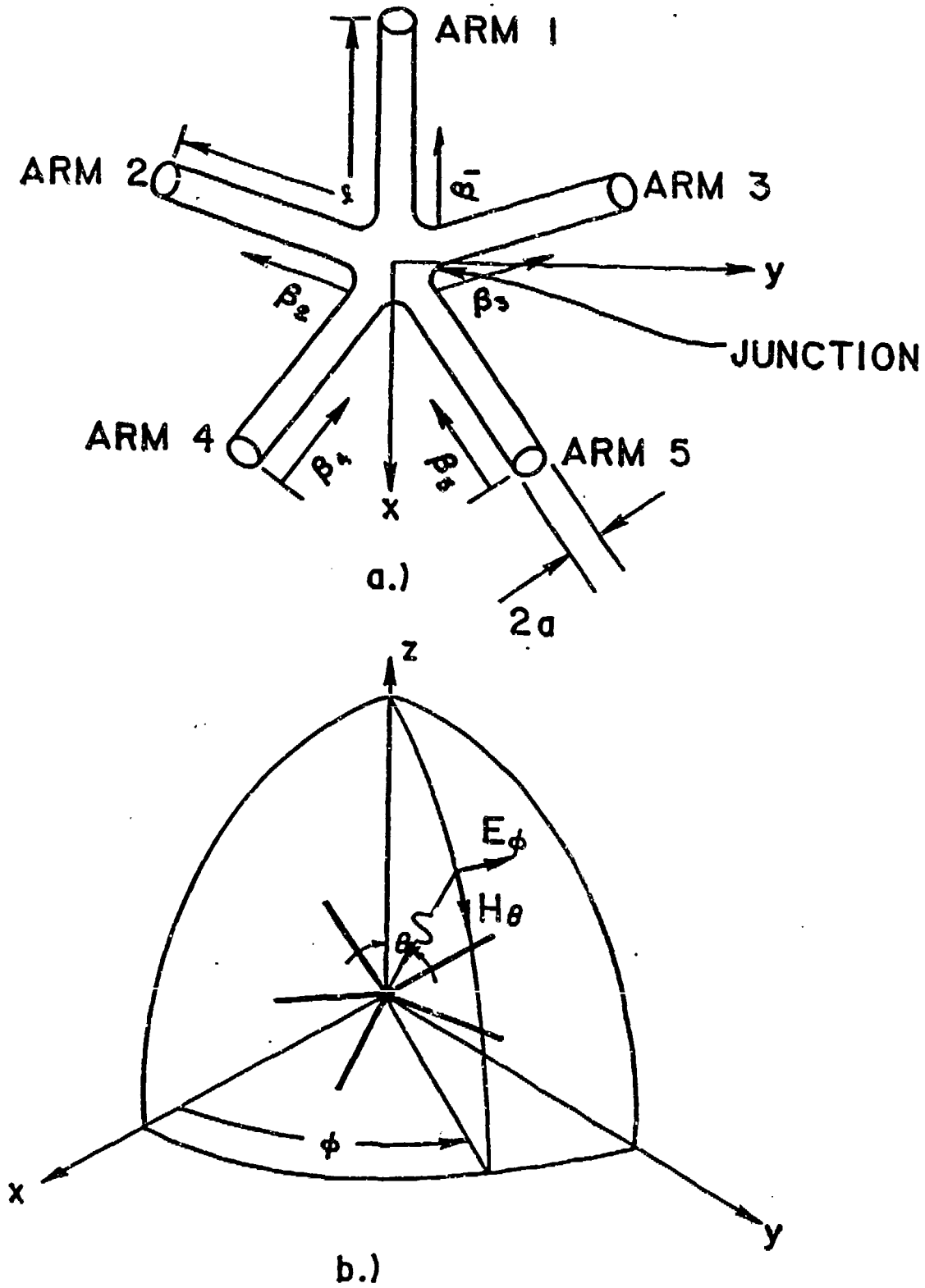


Fig.3 Geometry a.) and excitation configuration b.) for an isolated symmetric penta-arm element.

length of one-half, one, ..wavelengths. As expected, the SEM natural current modes associated with these fundamental layer poles correspond to the resonant current distributions of a dipole driven at its center.

One finds that the tri-arm element (see Fig.1) has a double pole in its first layer fundamental resonance region and that the crossed dipole (see Fig.1) has a double pole and a single pole in its first layer fundamental resonance region. (Actually, it more accurate to view these "double" poles as single order poles with second order degeneracies.) The tri-arm element with its doubly degenerate pole has two distinct current modes; one flows from the tip of arm 1 through the junction to the tip of arm 2 (no current on arm 3), and the other flows from the tips of arms 1 and 2 into the junction and onto arm 3. It is natural to identify the former as an anti-symmetric and latter as a symmetric mode [11]. The doubly-degenerate pole of the cross has one mode that flows from the tip of arm 1 to the tip or arm 2 (no current on arms 3 and 4), and another wherein the current flows from the tip of arm 3 to the tip or arm 4 (no current on arms 1 and 2). The crossed dipole's other fundamental resonance region pole has a mode, the so-called crooked mode [13], which flows from arm 1 to the junction then onto arm 3, and from arm 2 to the junction onto arm 4.

A thin-wire MOM program has been used to extract the SEM parameters of the isolated penta-arm geometry of Fig.3. Poles are located via a numerical search for those complex frequencies which drive the determinant of the system matrix to zero. The corresponding modal current distributions are found from a

numerical adaptation of (3). Fig.4 gives the location of first layer poles for the penta-arm element of Fig.3. The penta-arm element has a pair of "double" poles in its fundamental resonance region. Figs.5-8 show the modal current distributions corresponding to these poles. Current modes shown in Figs. 5 and 6 correspond to the "double" pole farthest from the imaginary axis while those shown in Figs. 7 and 8 correspond to the "double" pole closest to the imaginary axis. Currents shown in Fig. 5 flow from arms 4 and 5 into the junction then onto arms 2,3, and 1. Currents shown in Fig. 6 flow from arm 3 into the junction then onto arm 2, and from arm 5 into the junction onto arm 4. The currents shown in Fig.7 flow from the tips of arms 2 and 3 into the junction and then split and flow onto arms 1,4, and 5. Current flow directions shown in Fig.8 are similar to those of Fig.6 except the current magnitudes and flow directions are reversed.

Now that the SEM modes for the isolated penta-arm element have been identified, the next step is to employ these modes as entire domain testing/expansion functions in the Floquet MOM analysis of the penta-arm FSS array. This is accomplished by using simple sinusoidal approximations to the SEM natural current modes of Figs.5-8. The geometry of the Penta-arm FSS is shown in Fig.9, and all the results given here are for an array with l=6.0mm, w=0.15mm, D1=6.0mm, D2=4.67mm, $\alpha=130^{\circ}$, $d_1=0.0$, $d_2=0.037$mm, and $\varepsilon_{r2}=3.0$. Fig.10 shows the convergence of the TM/TM reflection coefficient (or equivalently the TM impedance elements) for varying numbers of Floquet modes - convergence is essentially reached with 529 Floquet modes. TM/TM and TE/TE reflection and transmission signatures are given in Figs.11 and 12 for various

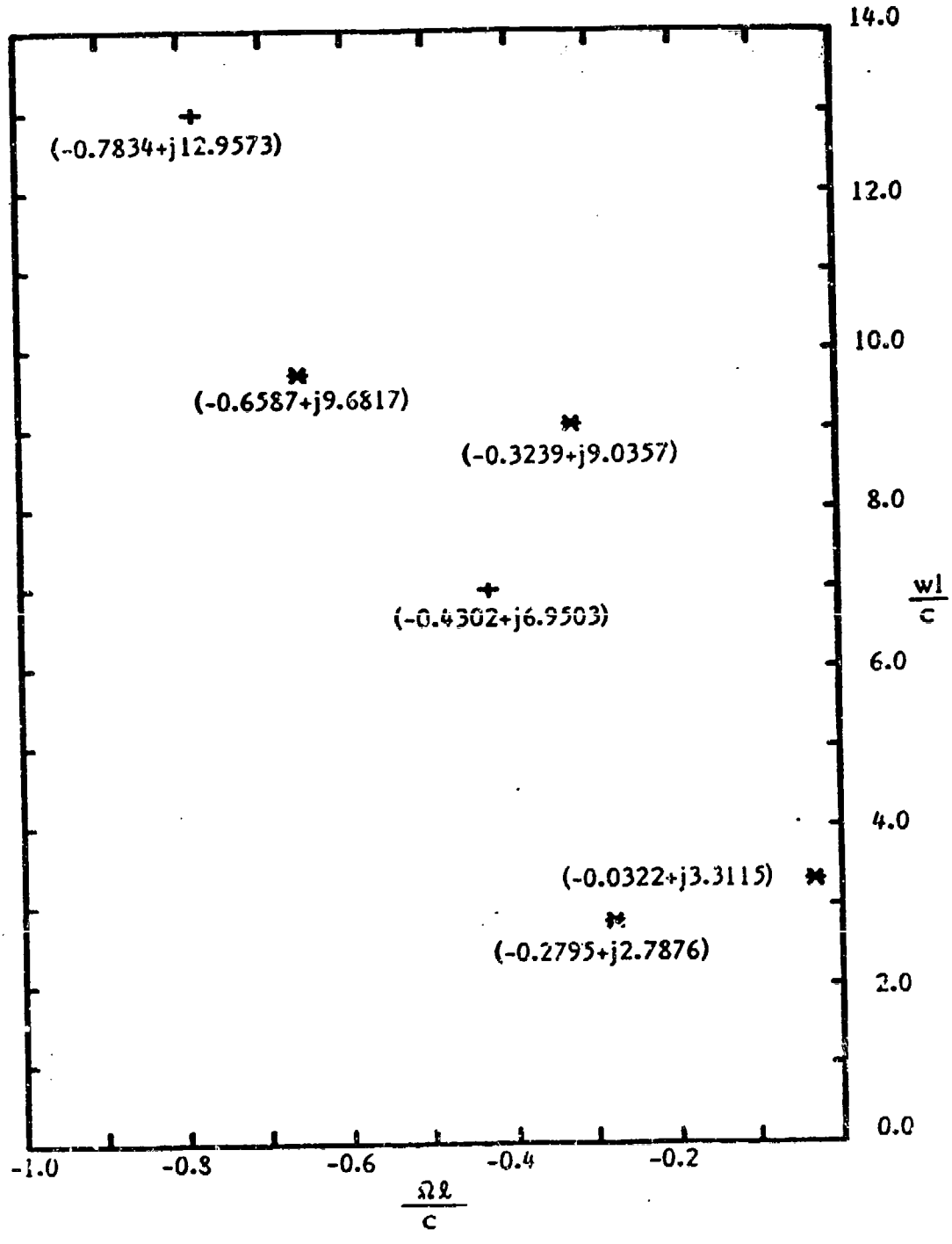


Fig. 4 Location of the first six poles nearest the imaginary axis for the symmetrical penta-arm element with a tip-to-tip arm length-to-radius ratio (l/a) of 200.

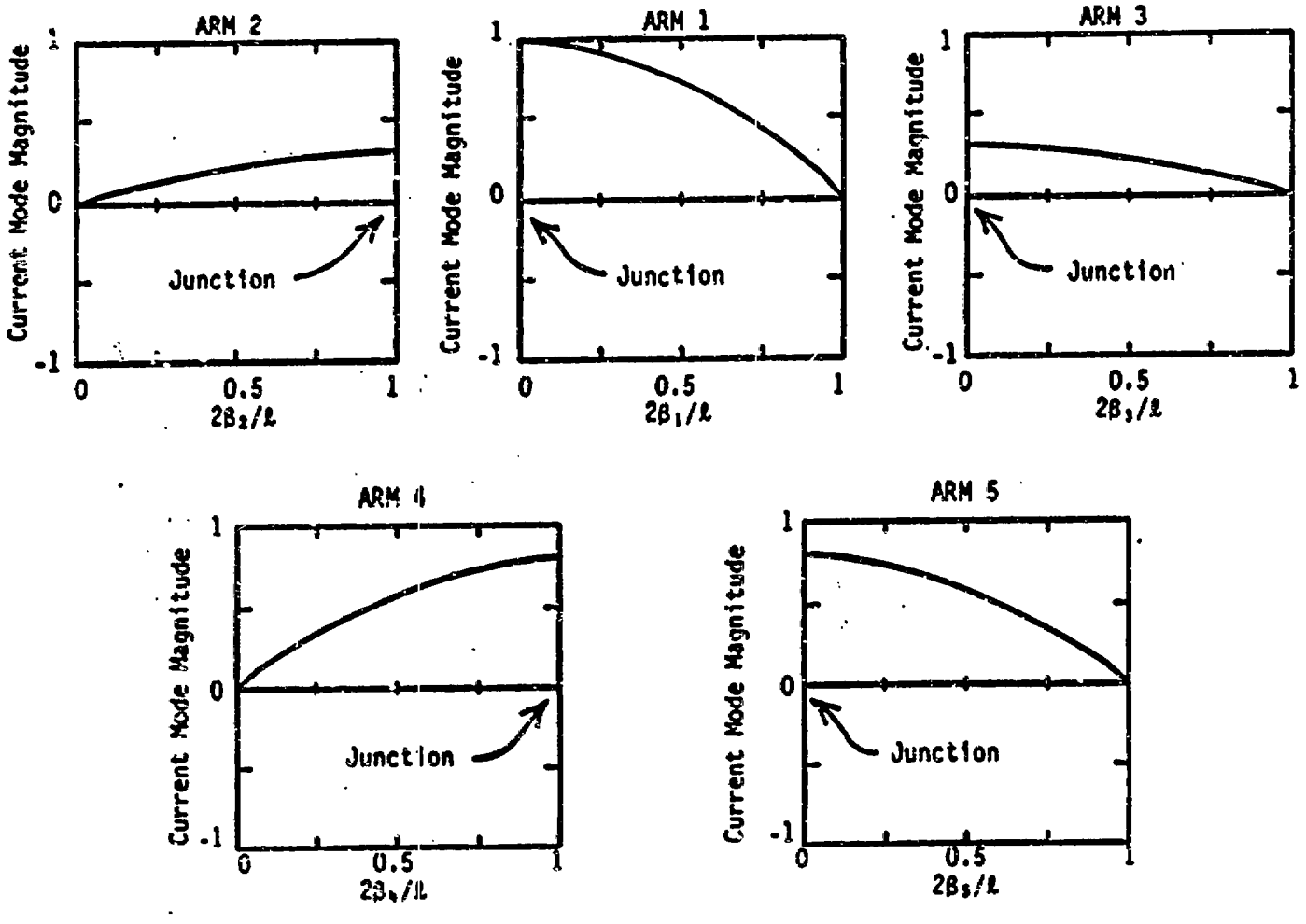


Fig.5 SEM natural current mode for the isolated penta-arm element. This current distribution is associated with the first layer fundamental resonance region pole farthest from the imaginary axis.

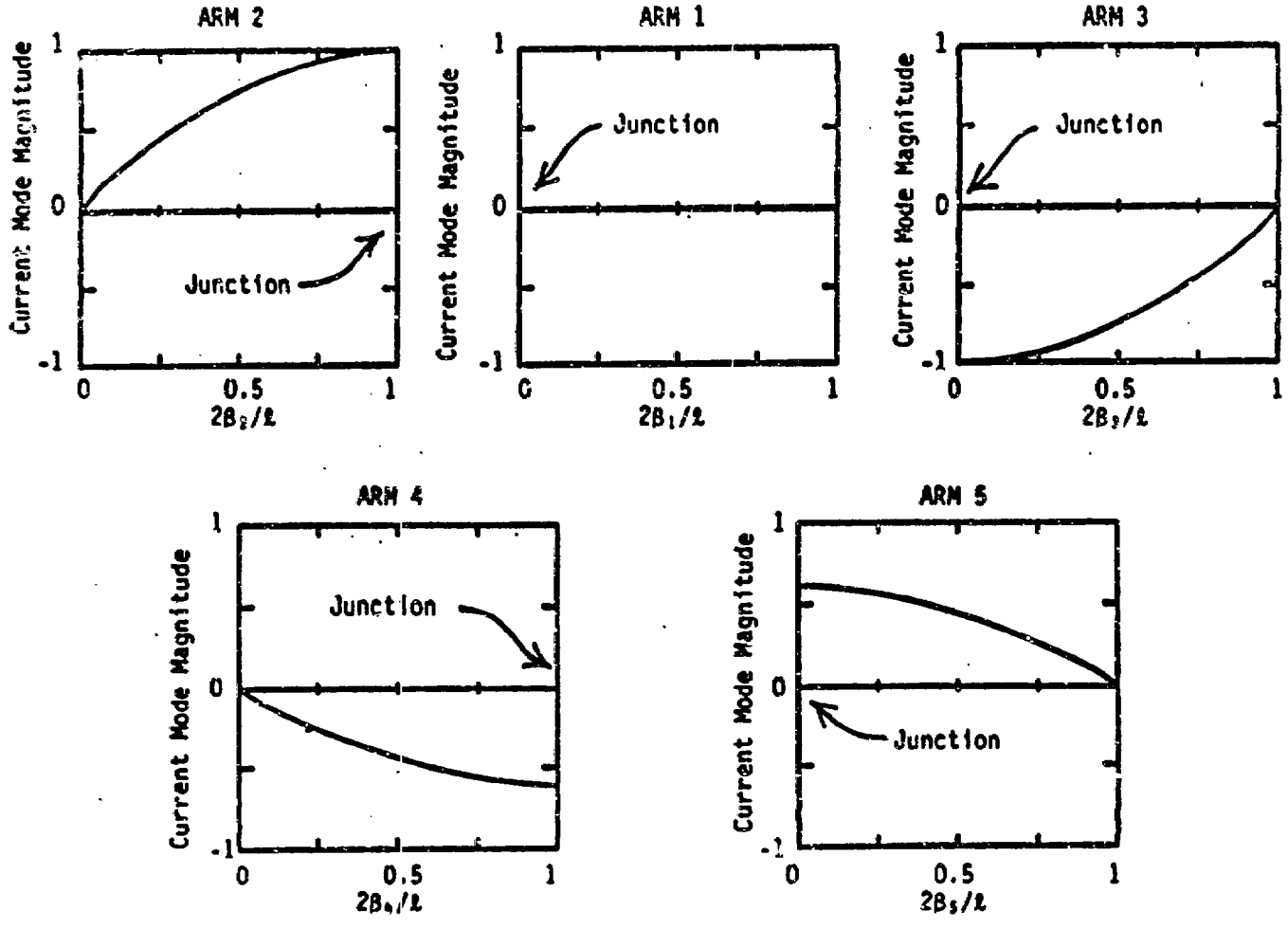


Fig.6 SEM natural current mode for the isolated penta-arm element. This current distribution is associated with the first layer fundamental resonance region pole farthest from the imaginary axis.

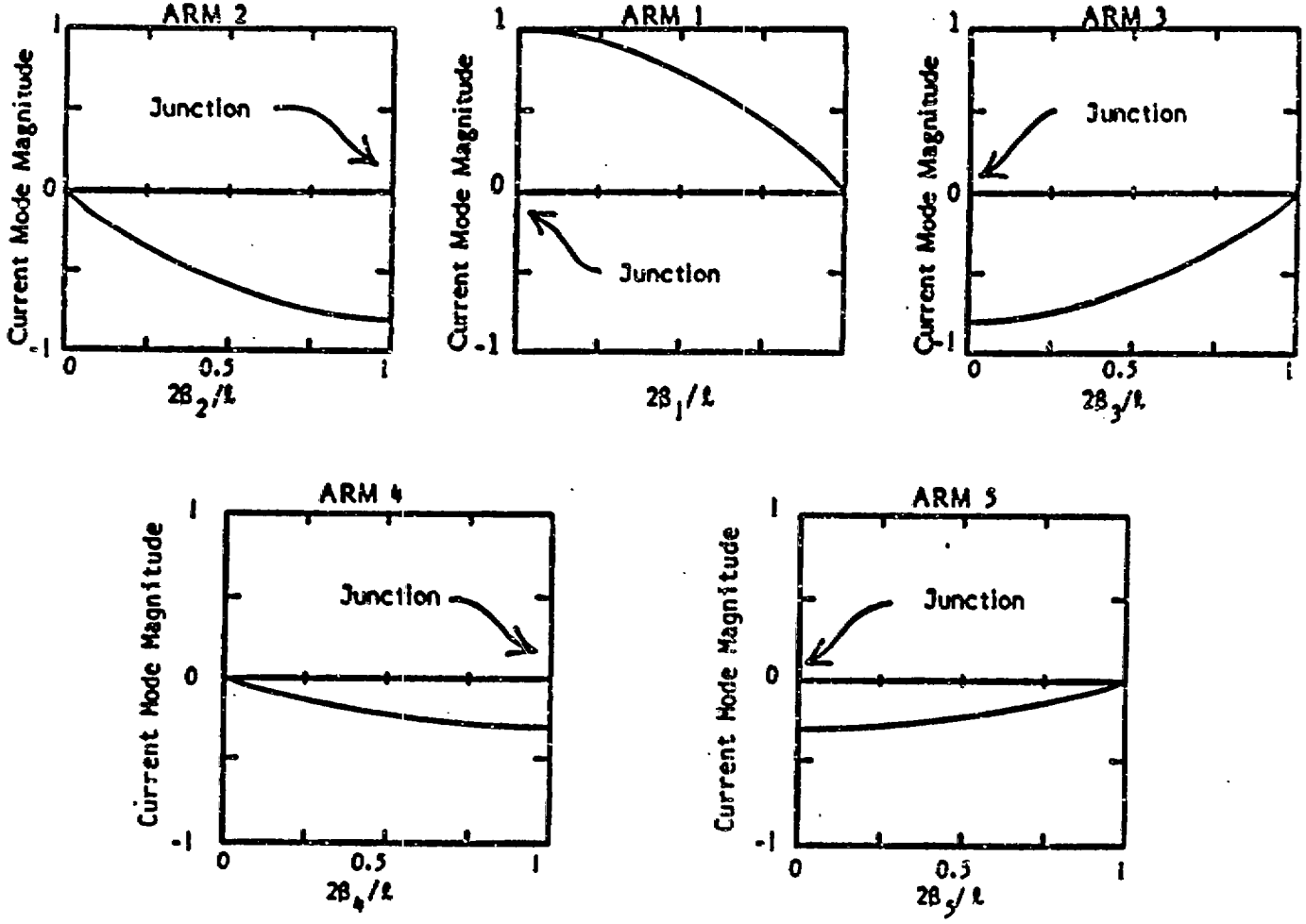


Fig.7 SEM natural current mode for the isolated penta-arm element. This current distribution is associated with the first layer fundamental resonance region pole nearest the imaginary axis.

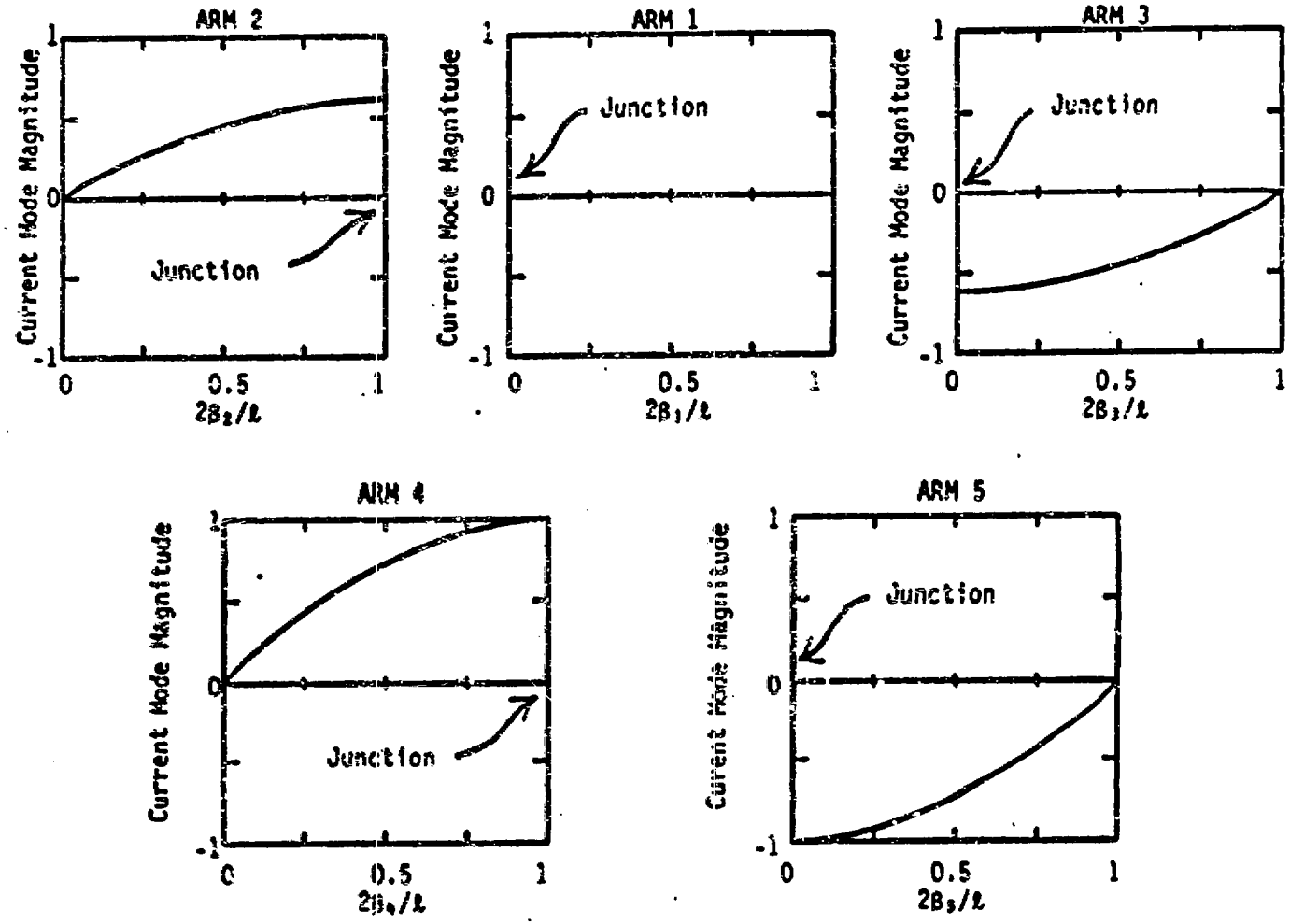
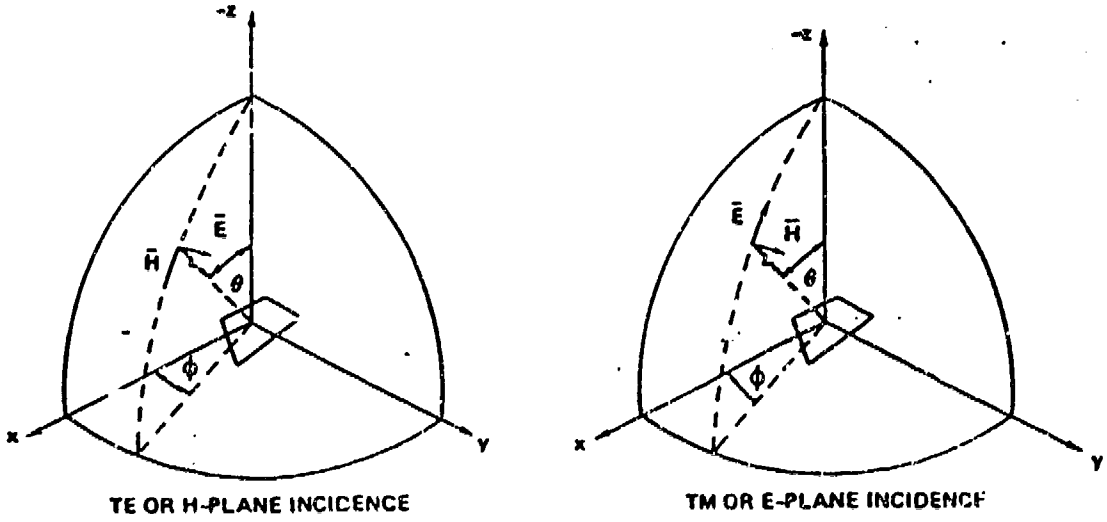
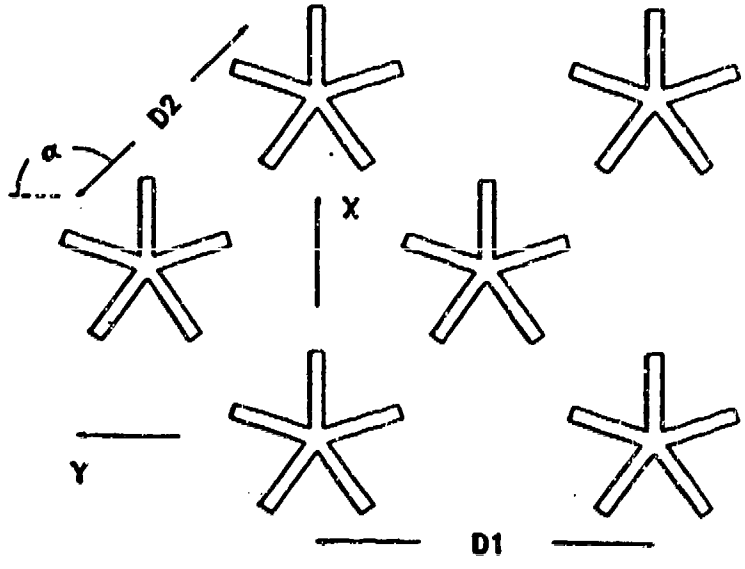


Fig.8 SEM natural current mode for the isolated penta-arm element. This current distribution is associated with the first layer fundamental resonance region pole nearest the imaginary axis.





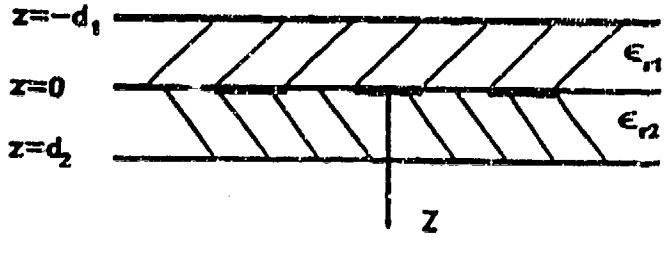


Fig.9 Geometry and excitation definition for the penta-arm frequency selective surface.

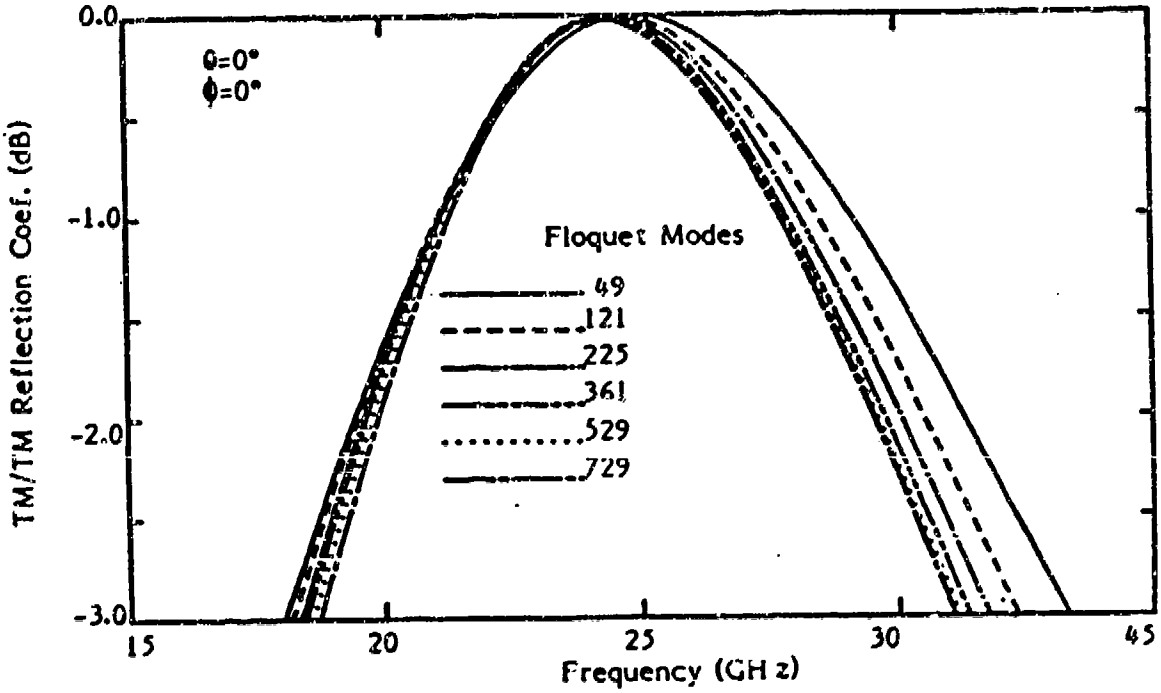
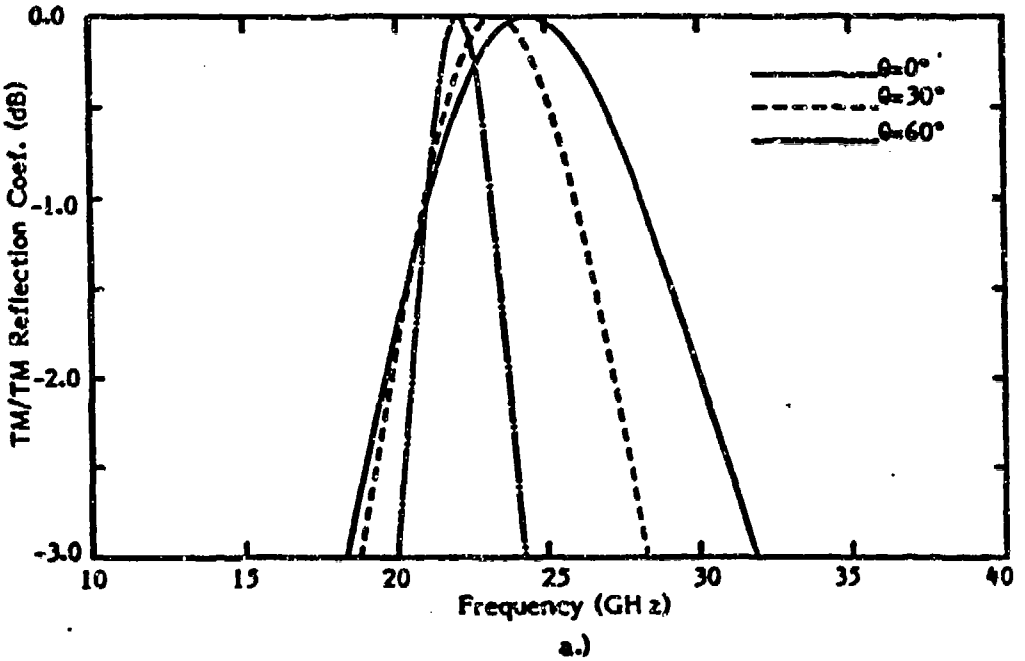


Fig.10 Convergence of the TM reflection coefficient with increasing numbers of Floquet modes for the array geometry of Fig.9 with l=6.0mm, w=0.15mm, D1=6.0mm, D2=4.667mm, $\alpha=130^{\circ}$, $d_1=0$, $\varepsilon_{r2}=3.0$, and $d_2=0.037$mm.



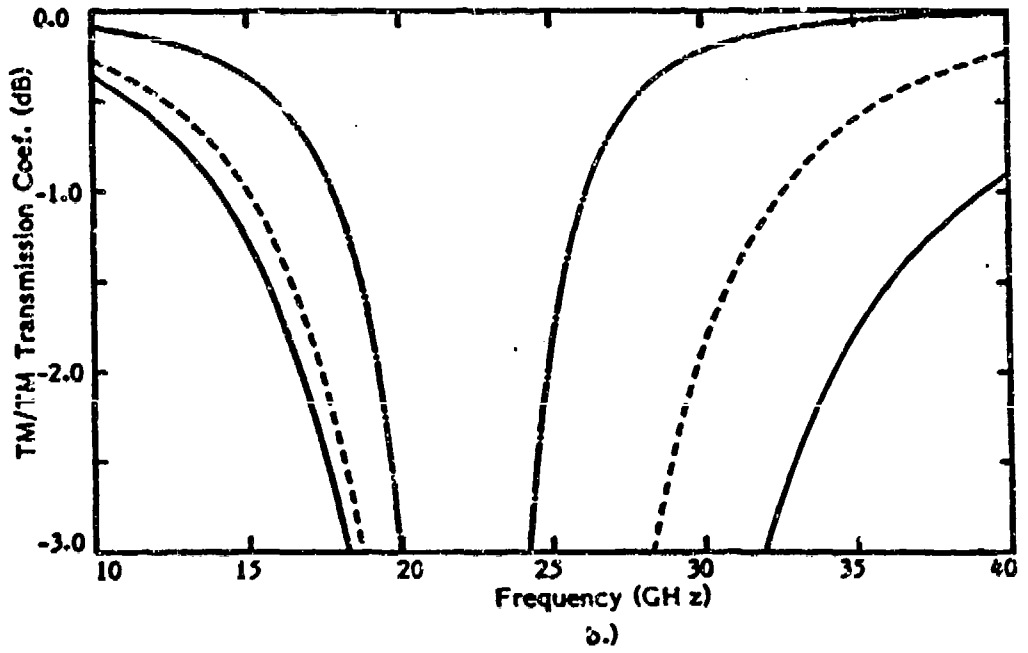
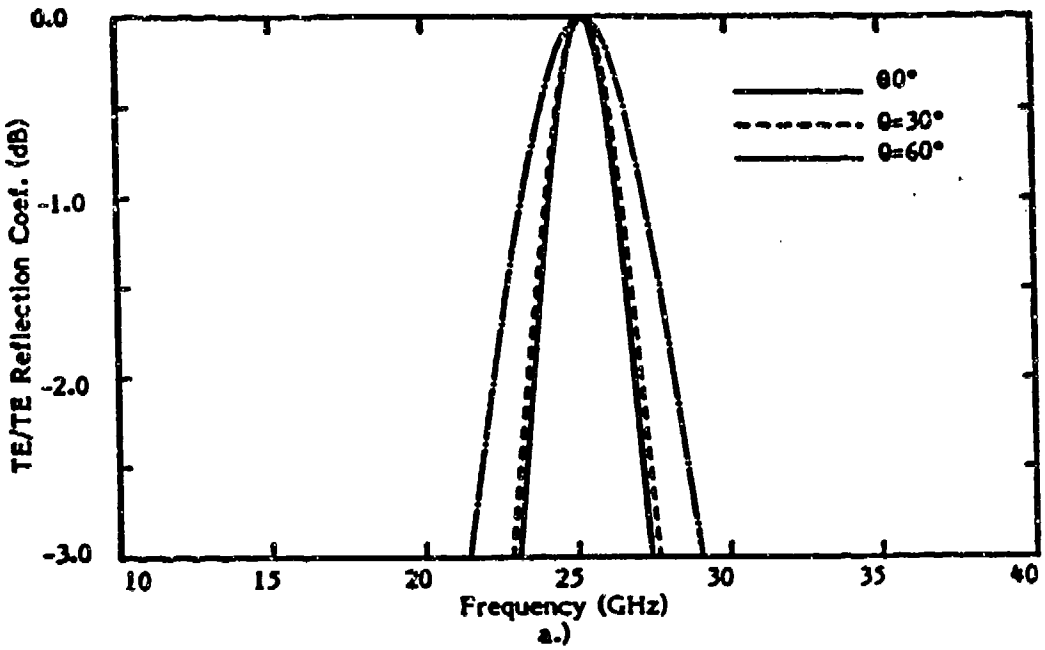


Fig. 11 TM/TM frequency response for the array geometry of Fig. 9 with l=6.0mm, w=0.15mm, D1=6.0mm, D2=4.667mm, $\alpha=130^{\circ}$, $d_1=0$, $d_2=0.037$mm, and $\varepsilon_{r2}=3.0$. a.) TM/TM reflection coefficient, b.) TM/TM transmission coefficient. The plane of incidence is $\phi=0^{\circ}$.



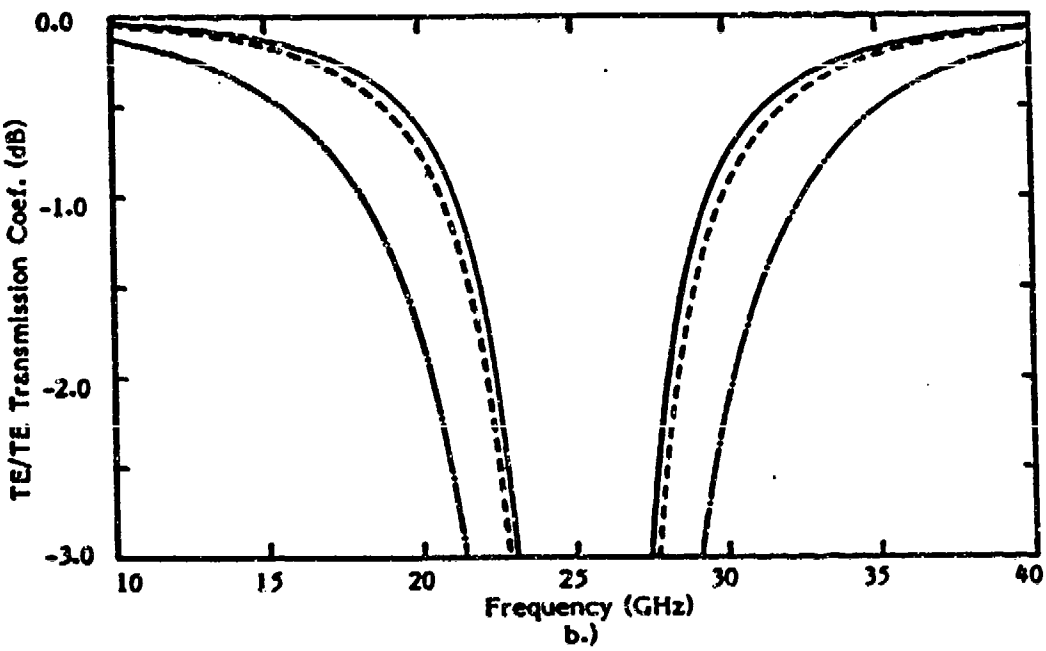


Fig. 12 TE/TE frequency response for the array geometry of Fig. 9 with l=6.0mm, w=0.15mm, D1=6.0mm, D2=4.667mm, $\alpha=130^{\circ}$, $d_1=0$, $d_2=0.037$mm, and $\varepsilon_{r2}=3.0$. a.) TE/TE reflection coefficient, b.) TE/TE transmission coefficient. The plane of incidence is $\phi=0^{\circ}$.

angles of incidence. The TM/TM reflection coefficient resonance point experiences a 2.0 GHz shift as the angle of incidence is varied from $\theta=0^{\circ}$ to $\theta=60^{\circ}$. This shift can be reduced by adjusting the thickness and/or capacitivity of the dielectric sheets which support the array.

In general, the penta-arm FSS array has filter characteristics which are fairly insensitive to polarization and angle of incidence variations. On the other hand, the TM/TM frequency signature of the crossed dipole varies considerably with only slight variations in angles of incidence. (The TE/TE frequency signature of the crossed dipole is quite stable.) A stable frequency signature is also observed for the tri-arm element. It is curious that planar single junction n-arm elements with an odd number of arms seem to have stable responses (e.g. the tri-arm and penta-arm elements) whereas elements with an even number of arms (e.g. the crossed dipole) seem to have polarization sensitive frequency signatures. Further investigation is, of course, required to establish the validity (or lack thereof) of this trend.

Conclusions

In the Floquet-MOM description of scattering from an FSS array, efficient and accurate results depend on the analyst ability to choose a minimum set of expansion functions which result in a physically accurate representation of the current induced on the scattering elements. This paper has demonstrated that for the penta-arm array just such a set can be synthesized from the SEM natural current modes of an isolated penta-arm

element. The MOM-SEM analysis of the isolated element employed simple box like expansion and testing functions which require little or no prior knowledge of the physical current distribution (except for the usual end and junction conditions). Preprocessing using SEM provides important insights into the fundamental scattering properties of the element.

References

[1] C.E. Baum, "On the singularity expansion method for the solution of electromagnetic interaction problems," AFWL Interaction Notes, Note 88, December 1971.

[2] V.D. Agrawal and W.A. Imbraiale, "Design of a dichroic Cassegrain subreflector," IEEE Trans. Antennas Propagat., vol. AP-27, pp. 466-473, July 1979.

[3] Raj Mittra and Vic Galindo-Israel, "Shaped Dual Reflector Synthesis," IEEE Trans. Antennas Propagat. Society Newsletter., vol. 22, No. 4, pp.5-9, August 1980.

[4] R.F. Harrington, Field Computation By Moment Methods, Macmillan, 1968.

[5] S. Contu and R. Tascone, "Scattering from passive arrays in plane stratified regions," Electromagnetics, vol. 5, no. 4, pp. 285-306, 1985.

[6] C.H. Tsao and R. Mittra, "Spectral-domain analysis of frequency selective surfaces comprised of periodic arrays of cross dipoles and Jerusalem crosses," IEEE Trans. Antennas Propagat., vol. AP-32, pp. 478-485, May 1984.

[7] E. L. Pelton and B.A. Munk, "Scattering from periodic arrays of crossed dipoles," IEEE Trans. Antennas Propagat., vol. 5, no. 4, pp. 323-330, May 1979.

[8] Rodolfo S. Zich, Guest Editor, "Special issue on frequency selective surfaces," Electromagnetics, vol. 5, no. 4, 1985.

[9] J.P. Montgomery, "Scattering by an infinite periodic array of thin conductors on a dielectric sheet," IEEE Trans. Antennas Propagat., vol. AP-23, pp. 70-75, January 1975.

[10] F. M. Tesche, "On The Singularity Expansion Method As Applied To Electromagnetic Scattering From Thin Wires," AFWL Sensor and Simulation Notes, Note 177, (May 1973). (Also as F. M. Tesche, "On The Analysis Of Scattering And Antenna Problems Using The Singularity Expansion Technique," IEEE Trans. Antennas Propagat., vol. AP-21,(1973),pp. 52-63.)

[11] C. E. Baum, "Interaction Of Electromagnetic Fields With An Object Which Has An Electromagnetic Symmetry Plane," AFWL Interaction Note, Note 63, (March 1971).

OPTIMAL LOADING

ABSTRACT

Brian Tomas

Elizabeth Yip

The Boeing Aerospace Company

Seattle, WA 98124

The problem of minimizing the scattering cross section of an obstacle by varying the surface impedance can be discreetly approximated as a non-linear optimization problem. This problem can be economically solved by incorporating the Sherman-Morrison-Woodbury (SMW) formula into moment method codes such as NEC.

An appropriate objective function depends on the scattering cross section at the angles and frequencies of interest. Let n be the number of cells in the obstacle and let p be the number of cells with variable impedance; in practice $n >> p$. Then application of the SMW formula results in objective function evaluations requiring an $\bigcirc(np + p^3)$ operation count. In contrast, application of the classical method of moments results in objective function evaluations requiring an $\bigcirc(n^3)$ operation count. Additionally, application of the SMW formula yields objective function gradient evaluations requiring an $\bigcirc(n^2p)$ operation count. Storage savings can also be exploited.

The SMW formulation and required code modifications are explained. Operation counts and efficiency comparisons are examined. Calculations and timing statistics are presented. Calculations are performed using a 2-D code and NEC.

Introduction

We are interested in minimizing the scattering cross section of an obstacle by varying the surface impedance. The discrete approximation to this problem is a nonlinear optimization problem. In the analysis below we consider a single angle and a single frequency; practical applications usually consider a range of angles and frequencies. For simplicity, the case of real-valued impedance is presented in the analysis. The general case is solved by treating the real and imaginary parts as separate variables.

Let μ be the vector of discrete impedances of the cells in the scattering obstacle. Let B be the impedance matrix associated with the obstacle geometry and μ. Then the objective function of the optimization problem is $\sigma = \sigma(\mu)$ where $\sigma = |L(x)|^2$, where L is a linear functional is dependent of μ, and where x solves $Bx = b$ with b the usual excitation vector. In practice the impedance is varying over p cells with $n >> p$, n the total number of cells in the problem. After solving for σ once using the classical method of moments, the Sherman-Morrison-Woodbury (SMW) formula can be applied to economically evaluate $\sigma[i]$ at subsequent values of μ.

Analysis

The SMW formula efficiently solves the system of linear equations $Bx = b$ when $A - B$ consists of a few rows or columns and $A^{-1}b$ is easily computed. Specifically, if $A - B = UV^T$ with U_{nxp} and V_{nxp}, then

$$B^{-1} = A^{-1} + A^{-1}U\left(I - V^T A^{-1} U\right)^{-1} V^T A^{-1}$$

is the SMW formula.

For simplicity, assume below that the cells in the model are ordered so that the only the first p cells have variable impedance, and that these impedances vary independently. The general case can be handled by column pivoting and minor manipulation of indices.

Let A be the impedance matrix associated with an initial impedance μ_0 and let B be the impedance matrix at an updated value of μ. Using the above notation, $A - B = UV^T = U\,[D|0]$ where D is a $p x p$ diagonal matrix and U is independent of μ. This last observation allows U to be overwritten by $A^{-1}U$ at the outset of the problem, then referenced during all subsequent objective function evaluations. Likewise, $A^{-1}b$ can be computed once and stored.

The flow of the optimization calculations and the necessary programming proceeds as follows. Minor modifications to an existing moment method code allow processed geometry, the factored impedance matrix, and pivoting information to be written out for later use in the optimization calculation. At the outset of the optimization calculation, U and b are calculated using subroutines extracted from the existing moment method code, then overwritten with $A^{-1}U$ and $A^{-1}b$. At this stage A^{-1} is no longer needed, so the memory used by A^{-1} can store $A^{-1}U$ if appropriate I/O operations have been used to compute U and $A^{-1}U$ out of core. Next the optimization loop begins with the bulk of the computational expense incurring in the objective function evaluations. Since optimization software is readily available, the main programming effort lies in coding the objective function. The flow of the above calculations is summarized in figure 1.

The details of the operation count for the objective function evaluations appear in figure 2. It can be seen that using the SMW formula results in an $\bigcirc(np + p^3)$ operation count compared with an $\bigcirc(n^3)$ operation count using the classical method of moments.

The utility of derivatives in optimization algorithms is well known. A finite difference approximation to the gradient of σ requires $\bigcirc(np^2)$ operations. The gradient can also be computed in $\bigcirc(np^2)$ operations by applying the SMW formula and observing that required intermediate quantities are already stored for objective function evaluations.

Recall that

$$\sigma = |L(x)|^2 = L(x)\,\overline{L(x)}$$

from which

$$\frac{\partial \sigma}{\partial \mu_k} = L\left(\frac{\partial x}{\partial \mu_k}\right)\overline{L(x)} + L(x)\,\overline{L\left(\frac{\partial x}{\partial \mu_k}\right)}$$

by the linearity of L. The derivatives of x are obtained by implicitly differentiating $Bx = b$:

$$\frac{\partial B}{\partial \mu_k}x + B\frac{\partial x}{\partial \mu_k} = 0$$

$$\frac{\partial x}{\partial \mu_k} = -B^{-1}\left(\frac{\partial B}{\partial \mu_k}x\right)$$

If we write $x = (x_1, \ldots, x_n)^T$ and $U = (U_1, \ldots, U_p)$, then $\frac{\partial B}{\partial \mu_k} = (0, \ldots, U_k, \ldots, 0)$, and so $\frac{\partial B}{\partial \mu_k}x = x_k U_k$. From this it follows that $\frac{\partial x}{\partial \mu_k} = -x_k B^{-1}(U_k)$. Now the SMW formula can be applied to compute $B^{-1}(U_k)$ in $\bigcirc(np)$ operations using the fact that $A^{-1}(U_k)$ is already stored for use in evaluating the objective function. Assuming that $(I - V^T A^{-1} U)^{-1}$ is also already stored, the gradient of σ can be calculated as above in $\bigcirc(np^2)$ operations.

Examples

We first present timing statistics for calculations performed on a VAX 11-785 computer. We consider below a 2-D conducting ogive with a resistive taper. The ogive is viewed edge on, towards the taper, with the electric field vector parallel to the edge. The model contains 75 cells, and the resistive taper contains 3 cells. The resistances are allowed to vary; in the above notation, $n = 75$, and $p = 3$. The optimization was performed over three frequencies. The initial classical method of moments calculation required 20 cpu seconds for all three frequencies. The optimization calculation required 39 cpu seconds to perform a total of 236 objective function evaluations, each over all three frequencies. This

averages to about .165 cpu seconds per iteration, or about a 150 fold improvement over the classical method of moments in this setting.

We now present an example using the NEC2 code. It is well known that impedance loading can be used to control the scattering from dipoles. For example, [2] reports 30 to 40 db reductions in broadside scattering from center loaded dipoles. We consider a pair of parallel dipoles viewed in the plane of the dipoles. The dipoles are 1 meter long, spaced .2 meters apart, and are divided into 6 segments. The center two segments of each dipole are loaded with impedances of $78 + 407j$ and $56 + 487j$. The scattering was optimized over the sector from 0 to 40 degrees using 5 angles at a single frequency, 300 mhz. The result of the loading can be seen in figure 3.

Conclusion

We have shown that the well known technique of impedance loading can be efficiently applied using moment method techniques. The implementation can use subroutines from existing moment method codes and existing optimization software. Unlike earlier techniques [2], a separate analysis is not required for each new geometry.

References

(1) E. Yip, B. Tomas, "Solving Perturbed Problems in a Moment Method Code", 3rd Annual Review of Progress in Applied Computational Electromagnetics, March, 1987.

(2) J.K. Schindler, R.B. Mack, P. Blacksmith, Jr., "The Control of Electromagnetic Scattering by Impedance Loading", Proc. IEEE, vol. 53, pp.993-1004, Aug. 1965

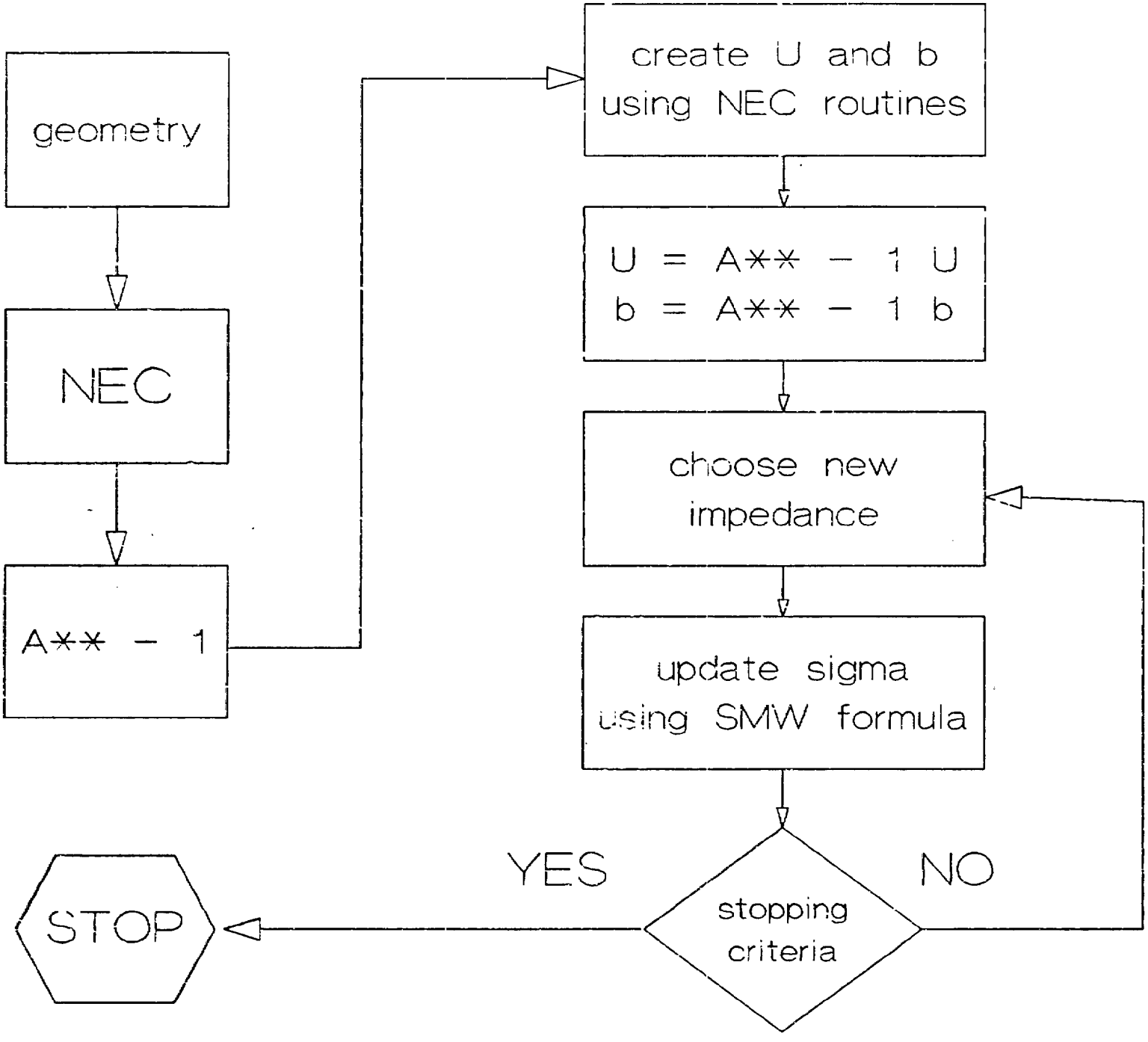


Figure 1. Sample Flowchart Using NEC

Sherman-Morrison-Woodbury Updating:

$$B^{-1}b = A^{-1}b + A^{-1}U(I - V^T A^{-1}U)^{-1}V^T A^{-1}b$$

i)	$I - V^T A^{-1}U$	p^2
ii)	$(I - V^T A^{-1}U)^{-1}$	$p^3/3$
iii)	$k = V^T A^{-1}b$	p
iv)	$w = (I - V^T A^{-1}U)^{-1}k$	p^2
v)	$y = A^{-1}Uw$	np
vi)	$x = y + A^{-1}b$	n

Figure 2. FLOP Counts of Update Calculations:

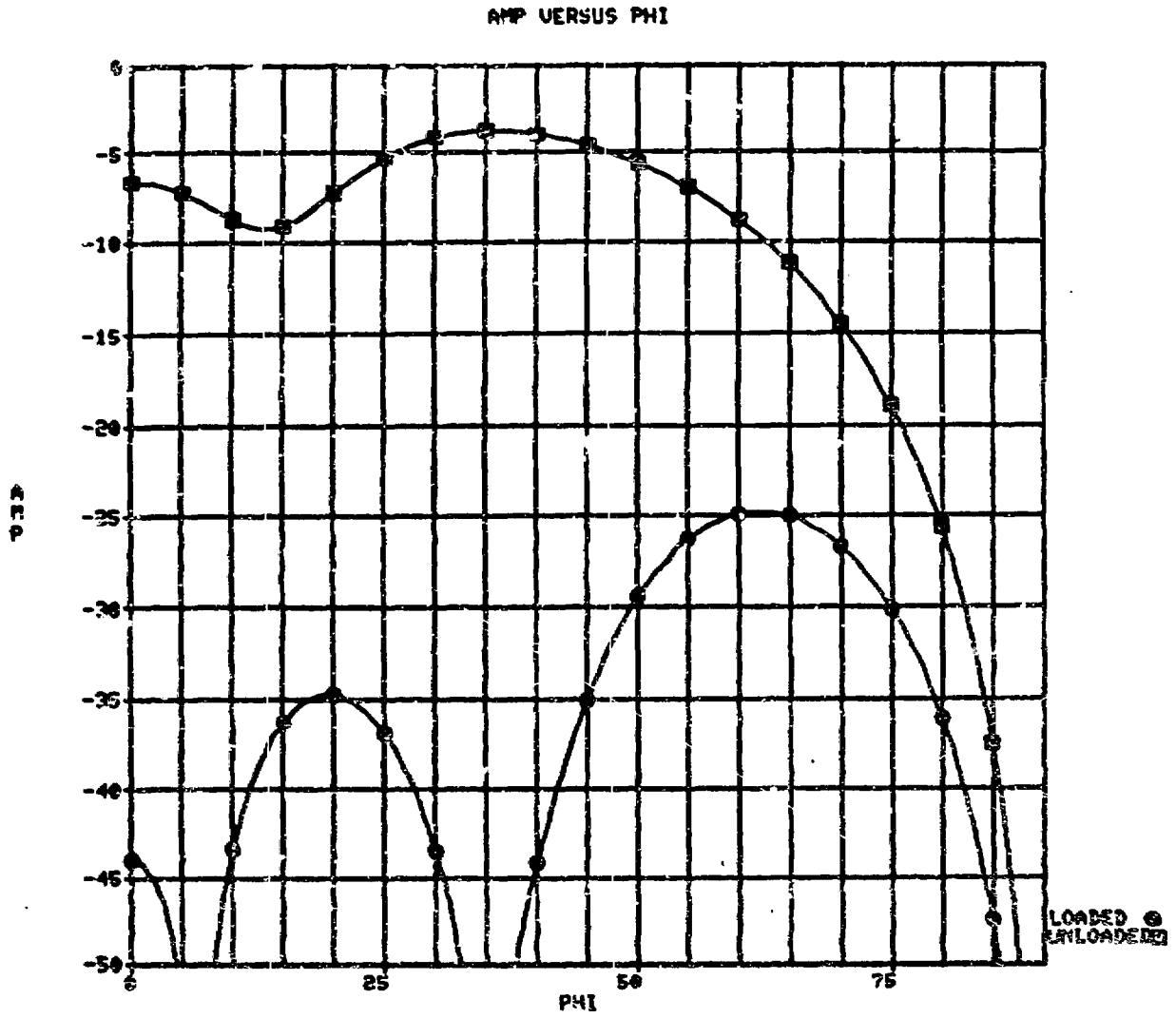


Figure 3. Parallel Dipole Scattering

NUMERICAL DIFFICULTIES AND SOFTWARE VALIDATION NEEDS ASSOCIATED WITH *EFIE* FORMULATIONS FOR DIELECTRIC SCATTERERS

Andrew F. Peterson
Electromagnetic Communication Laboratory
University of Illinois
1406 W. Green St.
Urbana, IL 61801

The development of computational techniques for the analysis of inhomogeneous dielectric bodies began more than two decades ago, with the work of Richmond. Since then, numerous formulations based on integral and differential equations have been proposed. Many of these formulations are based on the electric-field integral equation (EFIE). Throughout the past decade, observed inconsistencies in numerical results produced by some of the EFIE methods led to controversy regarding their accuracy. The lack of consensus evident in the literature is due in part to the absence of systematic validation procedures for computer codes of this type. Adequate validation procedures would identify both software "bugs" and limitations of the mathematical formulation on which the code is based. An important goal of the validation process is to employ a wide range of parameters during testing, because experience suggests that most codes remain robust only over a rather limited range of parameters.

This paper will trace the development of integral equation formulations for scattering from two- and three-dimensional dielectric bodies. Numerical results will be used to illustrate instabilities with some of the EFIE formulations. Numerical difficulties are observed only when surface charge plays a significant role in the scattering mechanism, and thus affect the validity of the two-dimensional EFIE for the TE polarization and the three-dimensional EFIE. After a discussion of validation issues, the paper will consider recent remedies to the numerical difficulties.

INTRODUCTION

Radome design, microwave energy deposition in biological tissues, and radar cross section prediction for complex targets all involve electromagnetic scattering from dielectric bodies. Although numerous techniques have been presented for the electromagnetic analysis of wire structures and other perfectly conducting scatterers, relatively few methods have been developed for the treatment of highly inhomogeneous bodies. The most widely-used procedures suitable for inhomogeneous structures are based on volume discretizations of the electric field integral equation (EFIE). Richmond proposed EFIE formulations for two-dimensional dielectric cylinders based on a pulse basis / point-matching discretization, and square cell models [1-2]. Livesay and Chen presented a similar procedure for treating the three-dimensional case, employing cubical cells or "block" models [3]. Since these original formulations were developed, several techniques employing higher-order basis and testing functions and more sophisticated scatterer models have been proposed. For the low-frequency two-dimensional transverse-electric (TE) case, Hill, Durney and Christensen presented a scheme using linear basis and testing functions with the EFIE in conjunction with polygonal cells [4]. Al-Bundak, Langan and Wilton developed a EFIE formulation employing rooftop basis functions on triangular cells [5-6]. Recently, a magnetic-field integral equation (MFIE) formulation has been developed by Peterson and Klock for the TE case, employing linear basis functions and point matching with triangular cells [7]. For the general three-dimensional case, Schaubert, Glisson and Wilton presented an EFIE formulation employing rooftop basis functions and a tetrahedral cell model [8]. Tsai et al. presented an EFIE formulation using linear basis and testing functions with polyhedral cell shapes [9].

Because of the relative simplicity of the original pulse basis / point-matching EFIE formulations compared to the other approaches, the methods of Richmond [1-2] and Livesay and Chen [3] have been employed by many researchers over the past two decades

for radar scattering work and analyzing power deposition in biological media [10-16]. Unfortunately, observed inconsistencies in the numerical results produced by these simple formulations have contributed to controversy regarding their accuracy [17-21]. Recent investigations into the accuracy of these methods suggest that the difficulties are only observed when surface charge density contributes significantly to the electromagnetic scattering mechanism. In other words, difficulties occur for the three-dimensional and the two-dimensional TE formulations. In addition, numerical instabilities appear to get worse as the relative permittivity of the scatterer becomes large. Borup, Sullivan and Gandhi attribute these difficulties to two factors, the presence of fictitious charge at interfaces between cells and the inadequate modeling of interfaces where charge should occur [21].

It is noteworthy that two decades have passed since the introduction of the original pulse basis / point-matching EFIE formulations for cylinders, and almost 15 years since the analogous formulation for the three dimensional case. Yet, the apparent difficulties have only recently been clearly recognized and their origins identified. One possible explanation for this delay is the lack of systematic validation procedures to test computer codes for electromagnetics problems. The history of the difficulties associated with EFIE formulations for dielectric scatterers suggests several conclusions related to code validation issues.

This paper will discuss the difficulties associated with the EFIE formulations for inhomogeneous dielectric scatterers. Although alternatives to volume integral equation formulations have been developed for treating highly inhomogeneous dielectric scatterers, this paper will not consider time-domain methods, differential equation formulations, "body-of-revolution" formulations, or those approaches that employ iterative algorithms to solve the linear system of equations. Note that all of these alternative procedures can be effective in certain situations and may even be preferable to the integral equation approaches discussed here.

THE ELECTRIC-FIELD INTEGRAL EQUATION

The electric-field integral equation (EFIE) representing a three-dimensional dielectric scattering problem can be written in several forms. If expressed entirely in terms of the magnetic vector potential, the EFIE is

$$\bar{E}^{inc} = \bar{E}^{tot} - \frac{\nabla\nabla\cdot + k^2}{j\omega\varepsilon_0}\bar{A} \tag{1}$$

If expressed in terms of the vector and scalar potentials, the EFIE is

$$\bar{E}^{inc} = \bar{E}^{tot} + j\omega\mu_0\,\bar{A} + \nabla\Phi \tag{2}$$

where

$$\bar{A}(x,y,z) = \iiint \bar{J}(x',y',z')\,\frac{e^{-jkR}}{4\pi R}\,dx'dy'dz' \tag{3}$$

$$\Phi(x,y,z) = \iiint \frac{\rho(x',y',z')}{\varepsilon_0}\,\frac{e^{-jkR}}{4\pi R}\,dx'dy'dz' \tag{4}$$

and

$$R = \sqrt{(x-x')^2 + (y-y')^2 + (z-z')^2} \tag{5}$$

The incident field is the field that would be present in the absence of the scatterer. The typical geometry is shown in Figure 1. Although these forms of the EFIE are analytically

equivalent, they may differ in implementation because of various approximations typically made when constructing a method-of-moments matrix equation [17].

The equivalent polarization current density appearing in Equation (3) is defined

$$\bar{J} = j\omega\varepsilon_0 (\varepsilon_r - 1) \bar{E}^{tot} \tag{6}$$

The charge density appearing in Equation (4) is related to the electric field in the dielectric region by

$$\rho = \varepsilon_0 \varepsilon_r \bar{E}^{tot} \cdot \nabla\left(\frac{1}{\varepsilon_r}\right) \tag{7}$$

Consider the effect of the geometry on the location of charge density. In a homogeneous dielectric scatterer the relative permittivity ε_r is a constant. The gradient in Equation (7) vanishes except on the surface of the scatterer, where it contributes a Dirac delta support to the charge density. Because of this, the integration of Equation (4) will collapse to a surface integral. In a dielectric region that is piecewise homogeneous, charge density is confined to the interfaces between different media. If the scatterer has a continuously varying permittivity profile, there will be a continuous distribution of charge density throughout the volume of the scatterer (as well as a surface layer of charge on any interfaces that may exist).

THE PULSE BASIS / POINT-MATCHING EFIE FORMULATIONS

In the original Richmond formulation for the two-dimensional TE polarization, the internal equivalent current density is expanded in terms of pulse basis functions defined

over cells that are approximately square. It was observed that if the cells were replaced by circular regions, the integrals could be evaluated in closed form [1,2]. The computational efficiency of this approach was appealing, as it circumvented the need for two-dimensional numerical integration. A similar procedure was suggested by Livesay and Chen, who presented closed-form expressions for the diagonal elements of the matrix based on replacing a cubical cell by a sphere of the same volume [3]. They recommended using some form of numerical integration to evaluate the off-diagonal elements. The early formulations [1-3] all employed the form of the EFIE appearing in Equation (1), and thus did not specifically address the treatment of surface charge density.

CELL DENSITIES

The general "rule of thumb" in dealing with integral equation formulations for electromagnetic scattering problems (specifically, when employing subsectional basis and testing functions) is to require the cell sizes in use to fall in the vicinity of 10 cells per wavelength. Translating this into the context of a volume dielectric region, this suggests recommended cell densities of

$$100\,|\epsilon_r|\,\frac{\text{cells}}{\lambda_0^2} \tag{8}$$

for the two-dimensional problem and

$$1000\,|\epsilon_r|^{\frac{3}{2}}\,\frac{\text{cells}}{\lambda_0^3} \tag{9}$$

for the three-dimensional formulation. Note that the wavelength in the dielectric medium is scaled according to the complex permittivity, so that λ_0 represents the free-space wavelength.

It is interesting to examine the recommended cell densities proposed in the literature, and even more interesting to examine the cell densities actually used in a number of applications. Richmond recommended a minimum cell density of

$$88\ |\varepsilon_r|\ \frac{\text{cells}}{\lambda_0^2} \tag{10}$$

with his original pulse basis / point-matching EFIE [2]. Al-Bundak, in connection with a rooftop basis / triangular cell method [5], suggests cell densities of .

$$128\ |\varepsilon_r|\ \frac{\text{cells}}{\lambda_0^2} \tag{11}$$

Both these estimates are in line with the "rule of thumb" mentioned above. However, a paper by Hagmann et al. presents a lower bound of [16]

$$10\ |\varepsilon_r|\ \frac{\text{cells}}{\lambda_0^2} \tag{12}$$

This density seems inadequate to ensure the validity of the numerical solution.

Analogous recommended cell densities are available in the three-dimensional case. In their original paper, Livesay and Chen suggest [3,12]

$$64\ \frac{\text{cells}}{\lambda_0^3} \tag{13}$$

This estimate does not take into account the permittivity of the medium and is obviously inadequate. Schaubert et al. recommend a cell density of [8]

$$500\,|\epsilon_r|^{\frac{3}{2}}\ \frac{\text{cells}}{\lambda_0^3} \tag{14}$$

This is in line with the "rule of thumb" mentioned above. However, Hagmann et al. present a lower bound for the three-dimensional case of [16]

$$17\,|\epsilon_r|^{\frac{3}{2}}\ \frac{\text{cells}}{\lambda_0^3} \tag{15}$$

Although this cell density seems ridiculously low compared to the "rule of thumb," it appears to have been used as a reasonable value by other researchers [15,18].

A survey of the published literature suggests that the cell densities in use are often insufficient. For example, Chen and Guru present results based on [12]

$$18\,|\epsilon_r|^{\frac{3}{2}}\ \frac{\text{cells}}{\lambda_0^3} \tag{16}$$

Massoudi et al. [18] present an example employing a cell density of

$$90\,|\epsilon_r|^{\frac{3}{2}}\ \frac{\text{cells}}{\lambda_0^3} \tag{17}$$

Chen, Livesay, and Guru attempt to model a conductor with the EFIE formulation, employing cell densities of approximately [10]

$$0.0015\,|\varepsilon_r|^{\frac{3}{2}}\,\frac{\text{cells}}{\lambda_0^3} \tag{18}$$

In a different example, they employ

$$15\,|\varepsilon_r|^{\frac{3}{2}}\,\frac{\text{cells}}{\lambda_0^3} \tag{19}$$

In a three-dimensional volume formulation, it is difficult to employ adequate cell densities because of the large required matrix storage. However, these examples suggest that many of the published results based on the EFIE formulations are based on cell densities significantly below that necessary to ensure accurate numerical solutions.

DIFFICULTIES AND REMEDIES

Harrington [17] commented on the TE formulation of Richmond [2], and suggested that pulse basis functions should not be used to discretize the EFIE because they are not in the domain of the operator. In actuality, the true equivalent current may exhibit jump discontinuities at boundaries between different media, and thus a pulse type of discontinuity seems acceptable. However, jump discontinuities in current indicate the presence of surface charge layers, and a pulse expansion will by necessity introduce fictitious charge layers throughout a homogeneous medium. These fictitious charge layers introduce additional error in the fields. For example, Figure 2 illustrates the degree to which the boundary condition

$$E^{tot} = E^{inc} + E^{s} \tag{20}$$

is satisfied throughout the interior of a dielectric cylinder for the TM polarization (using the Richmond formulation [1]). There is no surface charge present in the TM case, and the error in the fields seems reasonable. Figure 3 shows the identical case for the TE polarization. Note the additional error in Equation (20), concentrated at locations of fictitious charge layers.

Although the presence of fictitious charge suggests a problem, it is not always apparent from the numerical solutions. For example, Figure 4 shows the internal E-field in a circular dielectric cylinder for the TE polarization. Good agreement is seen between the numerical solution and the exact analytical result. However, difficulties due to the charge appear to get worse as the relative permittivity becomes greater. Figures 5 and 6 show the E-field magnitude and phase within a circular dielectric cylinder having ε_r=2-j50. Figure 7 shows a similar graph for the case ε_r=75-j300. One explanation for the degrading accuracy is that it is necessary to make the cells smaller to treat media with greater relative permittivity. As the cell size is reduced, fictitious charges seem to play a more dominant role.

Above, we mentioned that the original formulations of Richmond [2] and Livesay and Chen [3] involved replacing the square or cubical cells by circular or spherical cells in order to evaluate the integrals. Hagmann and Levin suggest that this approximation is a source of error, however, and recommend that the integrals for the off-diagonal matrix terms do not employ the replacement of square or cubical cell shapes by circles or spheres [20]. They suggest that the form of the EFIE from Equation (2) be used as an alternative, and that the surface integrations of Equation (4) be carried out over the proper cell boundaries.

For reasons of simplicity, results are often based on models that employ uniform cell sizes throughout the dielectric region. An additional motivation for the use of equal-

size cells arranged along a lattice is the discrete-convolutional nature of the matrix operator, and the ease with which iterative solution algorithms may be employed to significantly reduce the storage requirements due to the Toeplitz symmetries [21-22]. A typical equal-size model of a circular cylinder is shown in Figure 8.

In addition to recommending against the replacement of square cells by circular cells when integrating over the surface charge density, Hagmann and Levin recommend against employing equal-size cells throughout the scatterer. They suggest that significantly better results can be obtained by employing small cells in the region of the boundary or any interfaces [20].

Borup, Sullivan and Gandhi have recently investigated these issues in detail [21]. First, they studied the effect of fictitious charge throughout the interior of a homogeneous TE cylinder modeled with equal-size cells. They reported that eliminating the fictitious charge did not significantly improve the results. In addition, they studied the effect of the boundary model on the accuracy, by replacing square cells along the outer edge with polygonal cells. They reported a significant improvement in accuracy when the boundary shapes were made to conform to the desired scatterer shape, as opposed to the "staircase" approximation required by the equal-size square cell model.

SUMMARY

Volume discretizations of the EFIE employing pulse basis functions and point-matching over square or cubical cells are popular because of their simplicity. However, recent research suggests that these formulations are inadequate unless modified in two ways. First, fictitious charge layers throughout the cylinder should be eliminated. Second, boundaries where charge actually exists must be modeled more accurately than a "staircase" approximation permits.

The drawback to the modified EFIE approach described by Borup et al. [21] is the additional complexity required to model the scatterer and construct the matrix equation. The additional complexity appears to make alternate formulations for dielectric scatterers [4-9] competitive with the pulse basis / point-matching EFIE. Since many of these other approaches employ triangular or polygonal cell shapes, they should be free from the difficulties associated with accurately modeling interfaces between dissimilar media.

CODE VALIDATION ISSUES

From the above discussion, it is apparent that difficulties with specific formulations and computer code implementations can remain undetected or poorly understood for decades. In many cases, "common sense" alone would suggest better ways to validate computer codes from the time of their origination. Unfortunately, for a variety of reasons these ideas have not become routine as of yet.

The first general principle we can conclude from the above is that validation procedures should employ a wide range of parameters. The difficulties with the EFIE formulations discussed above are not apparent unless the complex relative permittivity has a large magnitude. The fact that the accuracy of the pulse basis / point-matching EFIE formulations is dependent on the permittivity is not well-understood suggests that this dependence was never investigated.

A second principle not discussed above but relevant is the idea that it might be very misleading to base validation procedures on volume-averaged parameters. Specifically, quantities such as the Specific absorption rate (SAR) discussed in connection with biological media or the Radar cross section (RCS) are often the desired results of interest, and may be the only results actually studied to any great length during the typical validation

process. However, these parameters often conceal large errors in the primary unknown, i.e., the interior fields or equivalent current density.

Results suggest that the pulse basis / point-matching EFIE formulations are very sensitive to changes in the shape of the scatterer model. This fact does not seem to have been identified until recently, and suggests the following: Validation procedures should seek to identify the sensitivity of an approach to slight changes in modeling parameters.

The discussion concerning the cell densities in use raises some additional points. First, we lack a uniform measure of "accuracy." As a case in point, Richmond described his results as being in "excellent agreement" with exact solutions [2]. Harrington later described the same data as being in "appreciable" error [17]. In addition, it would appear almost essential to report the range of cell densities employed in connection with any numerical result, regardless of the type of problem under consideration. There is also a need for more universal agreement on minimum required cell densities.

REFERENCES

[1] J. H. Richmond, "Scattering from a dielectric cylinder of arbitrary cross section shape," IEEE Trans. Antennas Propagat., vol. AP-13, pp. 334-341, May 1965.

[2] J. H. Richmond, "TE-wave scattering from a dielectric cylinder of arbitrary cross section shape, IEEE Trans. Antennas Propagat., vol. AP-14, pp. 460-464, July 1966.

[3] D. E. Livesay and K. M. Chen, "Electromagnetic fields induced inside arbitrarily shaped biological bodies," IEEE Trans. Microwave Theory Tech., vol. MTT-22, pp. 1273-1280, Dec. 1974.

[4] S. C. Hill, C. H. Durney, and D. A. Christensen, "Numerical calculations of low-frequency TE fields in arbitrarily shaped inhomogeneous lossy dielectric cylinders," Radio Science, vol. 18, pp. 328-336, May 1983.

[5] O. M. Al-Bundak, "Electromagnetic scattering of arbitrarily shaped inhomogeneous cylinders whose cross-sections are modeled by triangular patches," M.S. Thesis, University of Mississippi, University, MS, 1983.

[6] D. K. Langan and D. R. Wilton, "Numerical solution of TE scattering by inhomogeneous two-dimensional composite dielectric / metallic bodies of arbitrary cross section," Abstracts of the 1986 URSI National Radio Science Meeting, Philadelphia, PA, June 1986.

[7] A. F. Peterson and P. W. Klock, "An improved MFIE formulation for TE wave scattering from lossy, inhomogeneous dielectric cylinders," IEEE Trans. Antennas Propagat., vol. AP-36, Jan. 1988 (to appear).

[8] D. H. Schaubert, D. R. Wilton, and A. W. Glisson, "A tetrahedral modeling method for electromagnetic scattering by arbitrarily shaped inhomogeneous dielectric bodies," IEEE Trans. Antennas Propagat., vol. AP-32, pp. 77-85, Jan. 1984.

[9] C. T. Tsai, H. Massoudi, C. H. Durney, M. F. Iskander, "A procedure for calculating fields inside arbitrarily shaped, inhomogeneous dielectric bodies using linear basis functions with the moment method," IEEE Trans. Microwave Theory Tech., vol. MTT-34, pp. 1131-1139, Nov. 1986.

[10] K. M. Chen, D. E. Livesay, and B. S. Guru, "Induced current in and scattered field from a finite cylinder with arbitrary conductivity and permittivity," IEEE Trans. Antennas Propagat., vol. AP-24, pp. 330-336, May 1976.

[11] B. S. Guru and K. M. Chen, "Experimental and theoretical studies on electromagnetic fields induced inside finite biological bodies," IEEE Trans. Microwave Theory Tech., vol. MTT-24, pp. 433-440, July 1976.

[12] K. M. Chen and B. S. Guru, "Internal EM field and absorbed power density in human torsos induced by 1-500 MHz EM waves," IEEE Trans. Microwave Theory Tech., vol. MTT-25, pp. 746-756, Sept. 1977.

[13] M. J. Hagmann, O. P. Gandhi, and C. H. Durney, "Numerical calculations of electromagnetic energy deposition for a realistic model of man," IEEE Trans. Microwave Theory Tech., vol. MTT-27, pp. 804-809, Sept. 1979.

[14] J. F. DeFord, O. P. Gandhi, and M. J. Hagmann, "Moment-method solutions and SAR calculations for inhomogeneous models of man with large numbers of cells," IEEE Trans. Microwave Theory Tech., vol. MTT-31, pp. 848-851, Oct. 1983.

[15] R. J. Spiegel, "A review of numerical models for predicting the energy deposition and resultant thermal response of humans exposed to electromagnetic fields," IEEE Trans. Microwave Theory Tech., vol. MTT-32, pp. 730-746, Aug. 1984.

[16] M. J. Hagmann, O. P. Gandhi, and C. H. Durney, "Upper bound on cell size for moment-method solutions," IEEE Trans. Microwave Theory Tech., vol. MTT-25, pp. 831-832, Oct. 1977.

[17] R. F. Harrington, Field Computation by Moment Methods. Malabar, FL: R. E. Krieger, 1982, p. 59.

[18] H. Massoudi, C. H. Durney, and M. F. Iskander, "Limitations of the cubical block model of man in calculating SAR distributions," IEEE Trans. Microwave Theory Tech., vol. MTT-32, pp. 746-751, Aug. 1984.

[19] M. J. Hagmann, "Comments on 'Limitations of the cubical block model of man in calculating SAR distributions,'" IEEE Trans. Microwave Theory Tech., vol. MTT-33, pp. 347-350, April 1985.

[20] M. J. Hagmann and R. L. Levin, "Criteria for accurate usage of block models," J. Microwave Power, vol. 22, pp. 19-27, Jan. 1987.

[21] D. T. Borup, D. M. Sullivan, and O. P. Gandhi, "Comparison of the FFT conjugate gradient method and the finite-difference time-domain method for the 2-d absorption problem," IEEE Trans. Microwave Theory Tech., vol. MTT-35, pp. 383-395, April 1987.

[22] A. F. Peterson and R. Mittra, "Iterative-based computational methods for electromagnetic scattering from individual or periodic structures," IEEE J. Oceanic Engineering, vol. OE-12, pp. 458-465, April 1987.

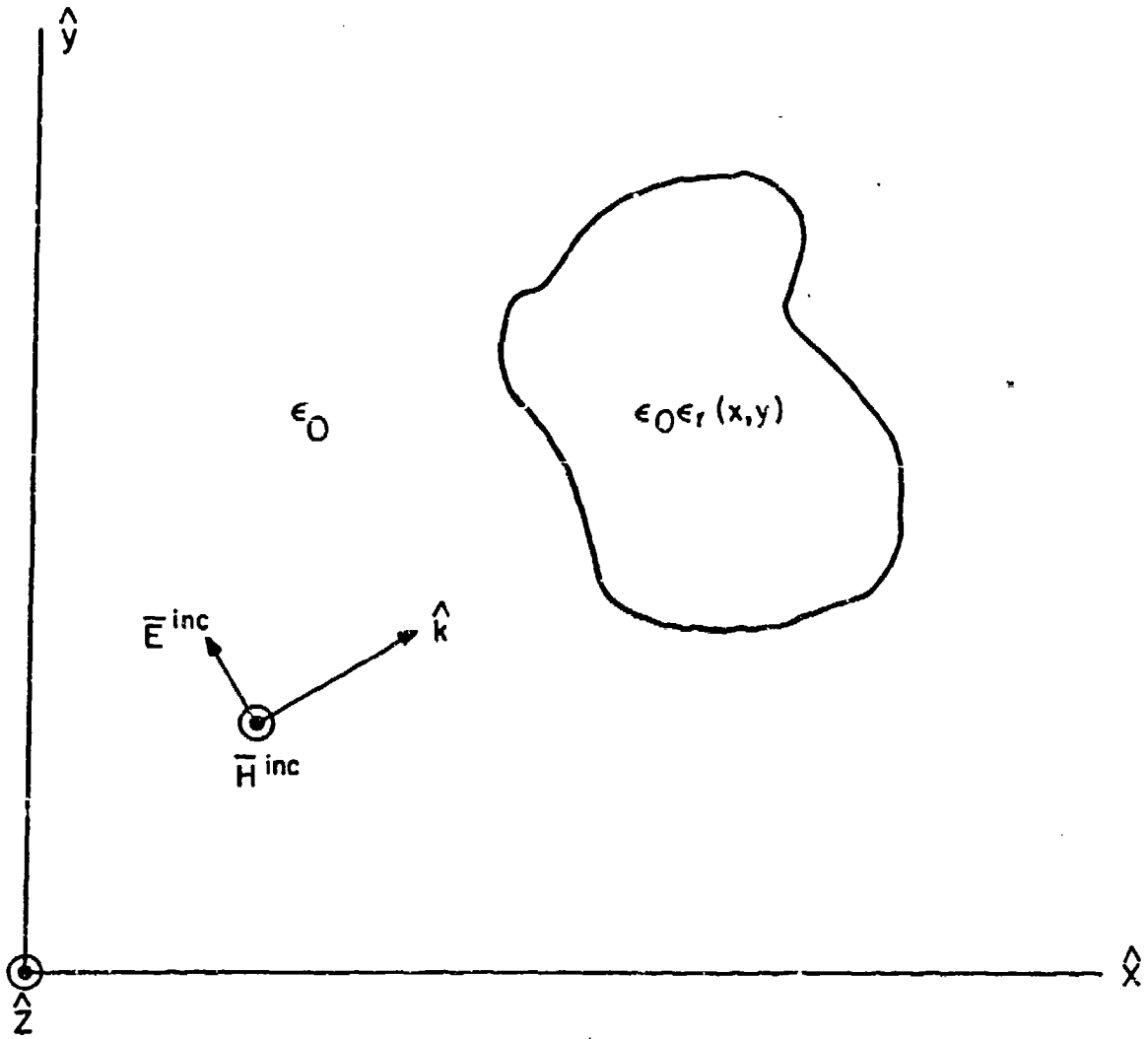


Figure 1. Geometry of the scattering problem.

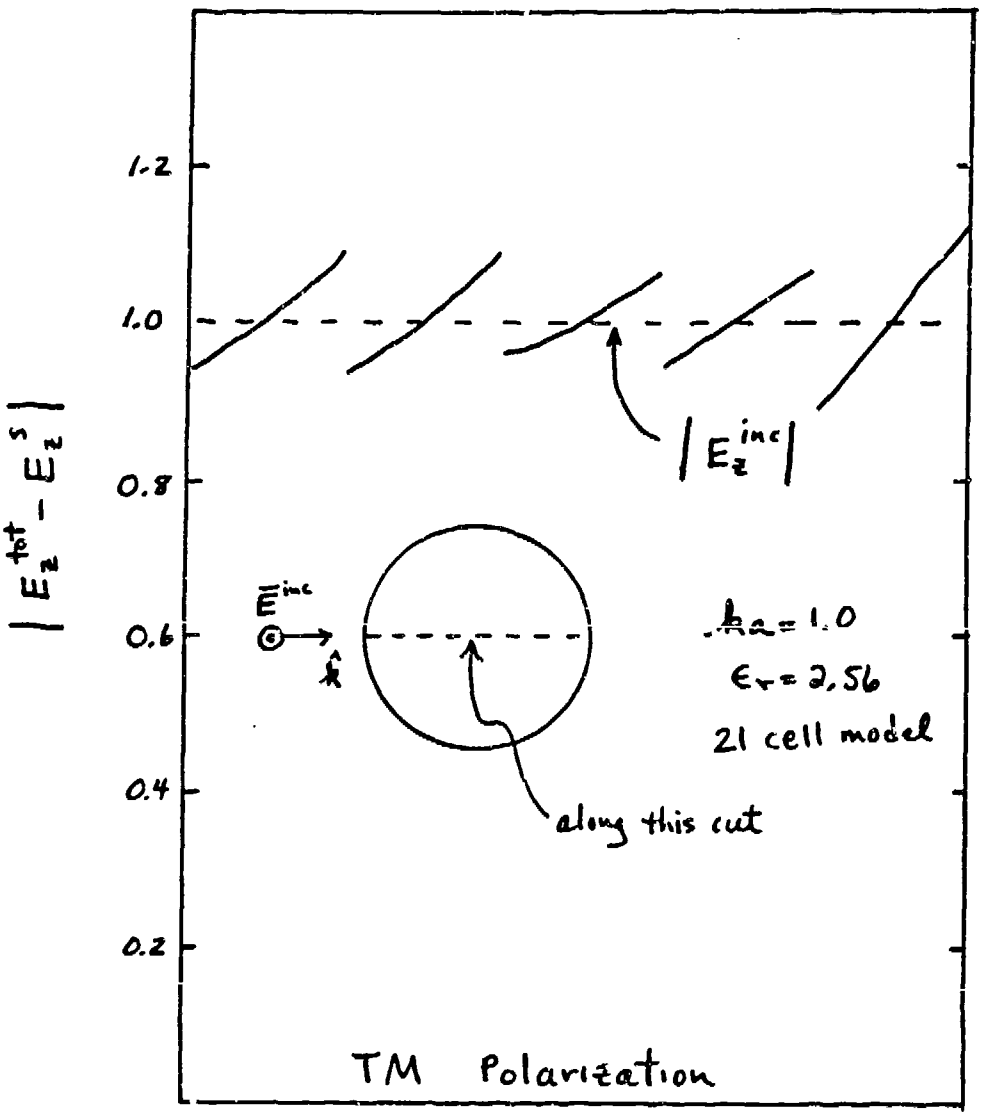


Figure 2. Satisfaction of the boundary condition $E^{tot} = E^{inc} + E^s$ throughout the interior of a dielectric cylinder (TM polarization).

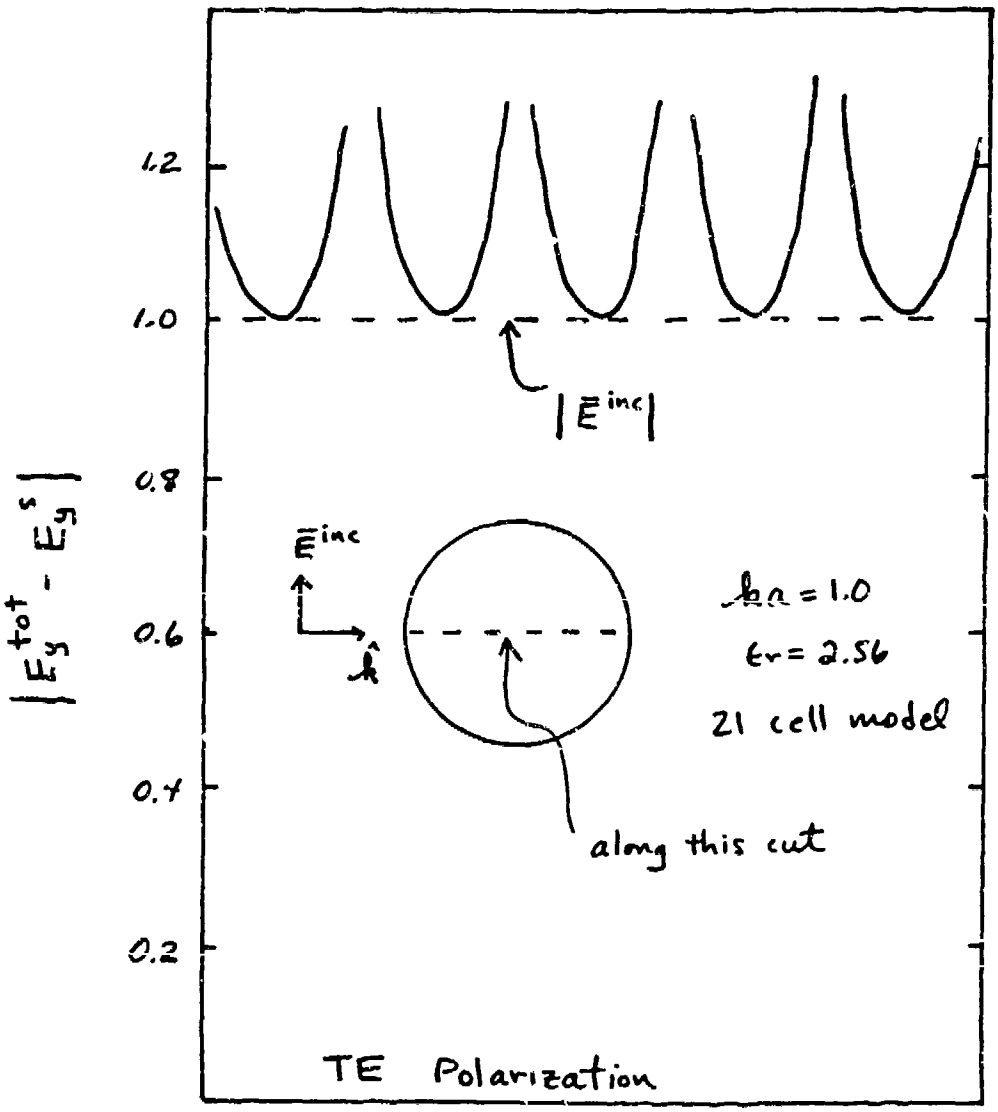


Figure 3. Satisfaction of the boundary condition $E^{tot} = E^{inc} + E^s$ throughout the interior of a dielectric cylinder (TE polarization).

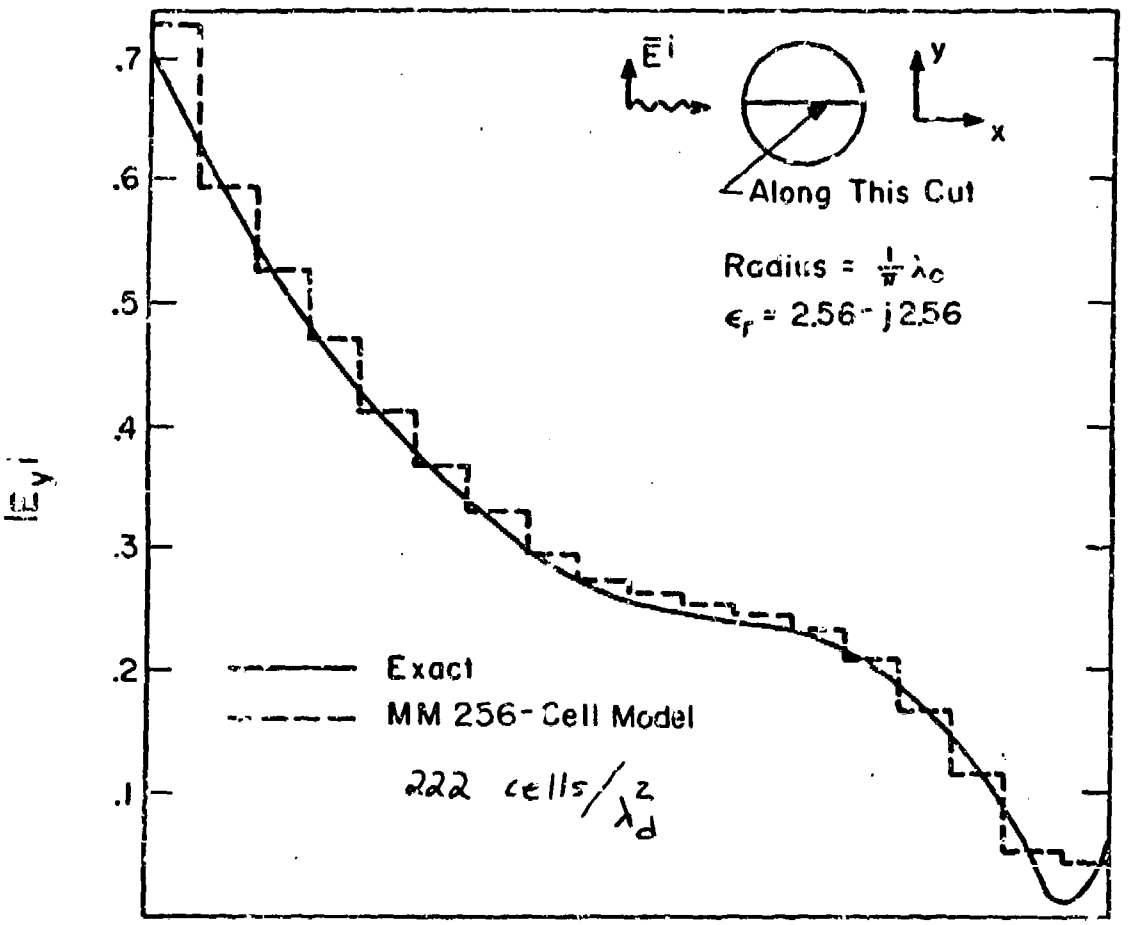


Figure 4. Magnitude of the electric field within a circular cylinder (TE polarization) compared to exact eigenfunction solution, for ϵ_r=2.56-j2.56.

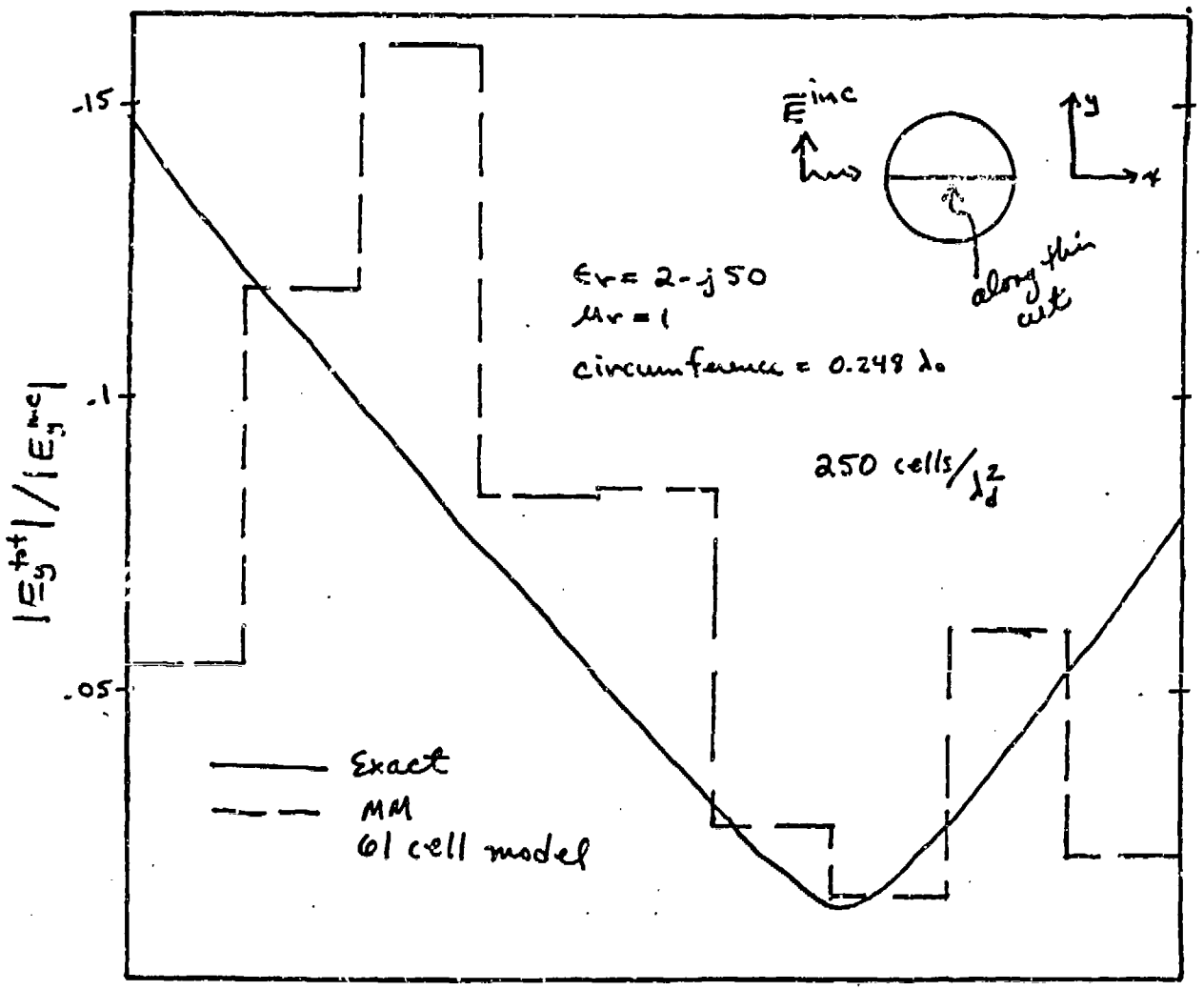


Figure 5. Magnitude of the electric field within a circular cylinder (TE polarization) compared to exact eigenfunction solution, for ϵ_r=2-j50.

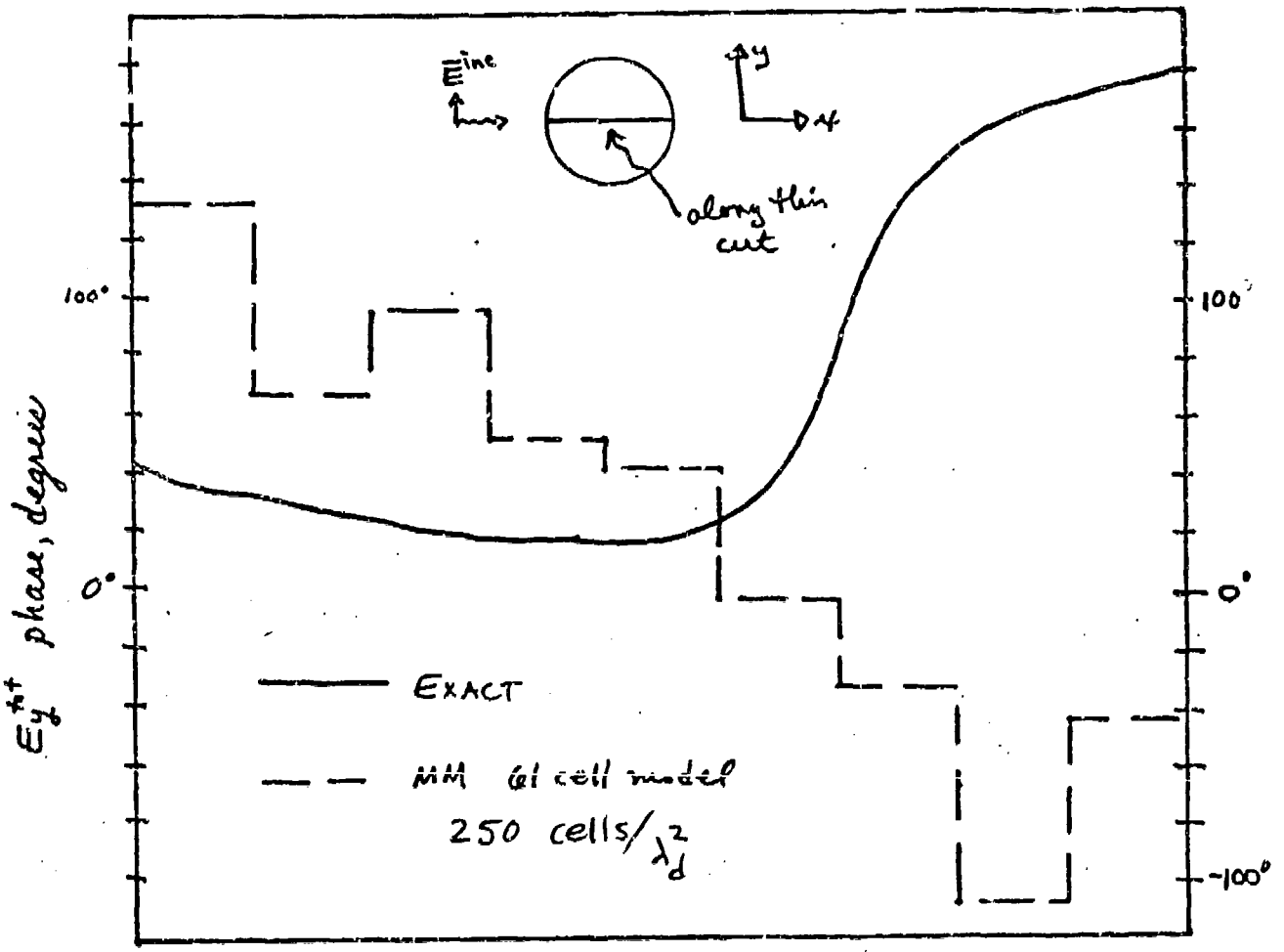


Figure 6. Phase of the electric field within a circular cylinder (TE polarization) compared to exact eigenfunction solution, for $\varepsilon_r = 2 - j50$.

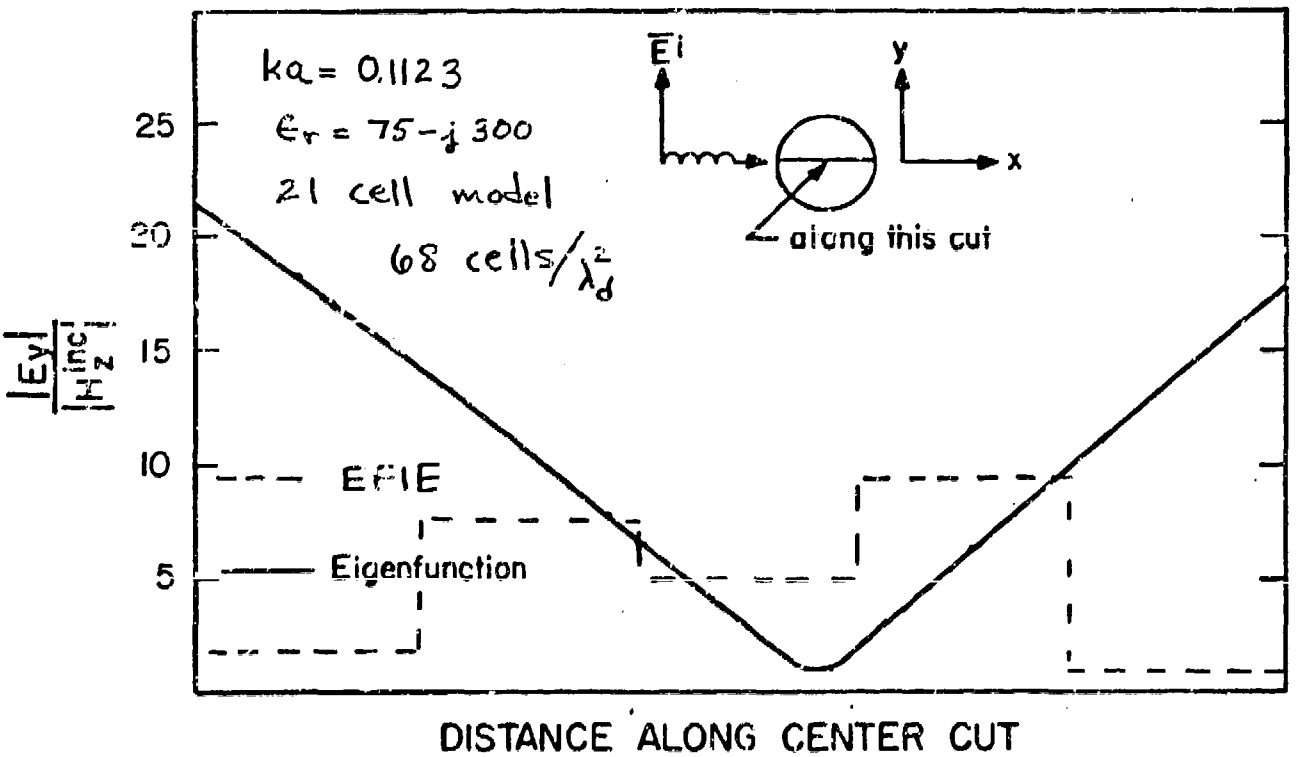


Figure 7. Magnitude of the electric field within a circular cylinder (TE polarization) compared to exact eigenfunction solution, for ϵ_r=75-j300.

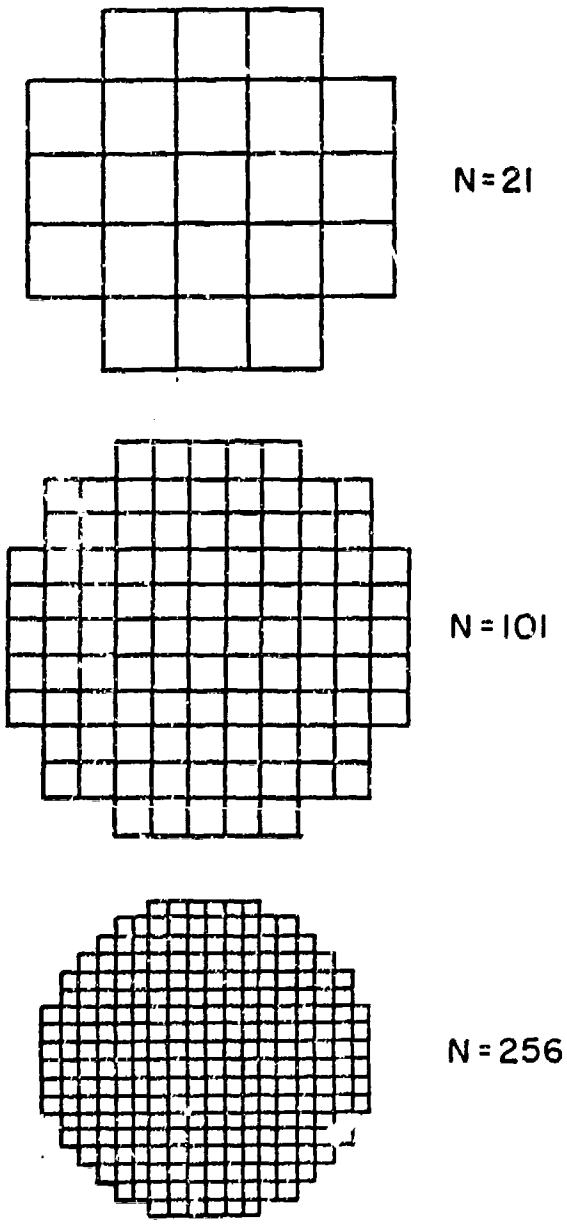


Figure 8. Equal-size square cell models of a circular region.

COMPUTATION OF FREQUENCY-DOMAIN AND TIME-DOMAIN SCATTERING FROM A CROSS WITH THE GEMACS AND CASSANDRA CODES

David E. Thomas and Glen R. Salo
The BDM Corporation
1801 Randolph Road S.E.
Albuquerque, New Mexico 87106

ABSTRACT

Scattering from a crossed-dipole antenna by a vertically-polarized plane wave is analyzed with the GEMACS and CASSANDRA modeling codes. The crossed dipole consists of a three-quarter wavelength vertical cylinder and a half-wavelength horizontal cross-arm; the horizontal arm is located at the half-wave high point, i.e. two-thirds of the way up along the vertical cylinder. The frequency-domain response is modeled with the GEMACS code; the GEMACS Method-Of-Moments solution is obtained with piecewise sine + cosine + constant basis functions, and a collocation testing method. These results are compared to those of other Method-Of-Moments codes and to measured data, as described in the Second Annual Review of Progress in Applied Computational Electromagnetics (R. W. Adler, "A Comparison of Thin-Wire EM Modeling Codes for the Case of Scattering From a Cross", March 1986).

In addition, calculations for the time-domain problem are presented; here, the incident field is modeled as a double exponential waveform. The time-domain results are obtained with CASSANDRA, an admittance-based transmission line code which permits modeling of arbitrary external field drives.

INTRODUCTION

This paper addresses the problem of scattering from a crossed dipole antenna; the antenna and the incident field are pictured in Figure 1. The crossed dipole consists of a three-quarter wavelength vertical cylinder and a half-wavelength horizontal cross-arm, located two-thirds of the way up along the vertical cylinder; the radius of each of the dipole arms is 0.0185185 wavelengths, and the dipole is connected at the bottom to an infinite and perfectly-conducting ground plane. The incident electric field vector is parallel to the vertical arm, and the propagation direction is perpendicular to the plane of the cross. In Reference 1, R. W. Adler has compared the results of 6 thin-wire moment method codes to measured data for this problem; the measurements, obtained by R. W. Burton, are described in Reference 2. In this paper, results for this problem produced by the GEMACS code (General Electromagnetic Model for the Analysis of Complex Systems) are compared to those of References 1 and 2. The crossed dipole problem presents a stringent test of thin-wire codes, especially as regards their treatment of continuity of current and equal charge per unit length at the junction. In addition, a description of the CASSANDRA code solution of the frequency-domain and time-domain problems for the crossed dipole will be discussed. CASSANDRA is an admittance-based transmission line code; the transmission-line network is excited by an arbitrary external field drive.

GEMACS SOLUTION

The GEMACS Method-Of-Moments (MOM) solution is obtained with piecewise sine + cosine + constant basis functions, and a collocation testing method. The MOM routines in GEMACS were derived from the AMP program several years ago, and are described in Reference 3. For this problem, the frequency of 300 MHz was used, so that distances in meters correspond to fractions of a wavelength. Roughly 32 segments per wavelength were used (24 on the vertical arms, and 16 on the horizontal arms).

The GEMACS results for the crossed dipole scatterer are shown in Figures 2,3,4, and 5. For ease of comparison, the plots have been set up to have the same scales which appeared in Reference 1; as in this reference, the plots were adjusted vertically to obtain the best fit with the measurements. The bottom, junction, top, and end of the crossed dipole are labeled B,J,T, and E as shown in the figure. Figure 2 shows the relative current amplitude for the horizontal arm in dB; Figure 3 shows the relative phase in degrees for the horizontal arm. Figure 4 shows the relative current amplitude for the vertical arm, and Figure 5 shows the relative phase for the vertical arm.

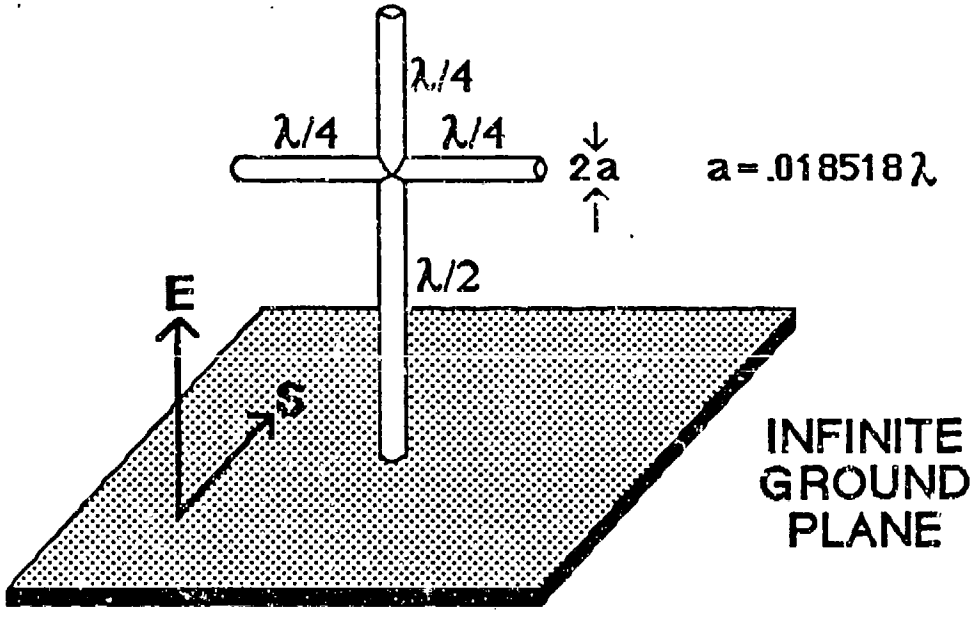


Figure 1. Geometry for the Crossed Dipole Scattering Problem, Showing the Dipole and the Incident Field.

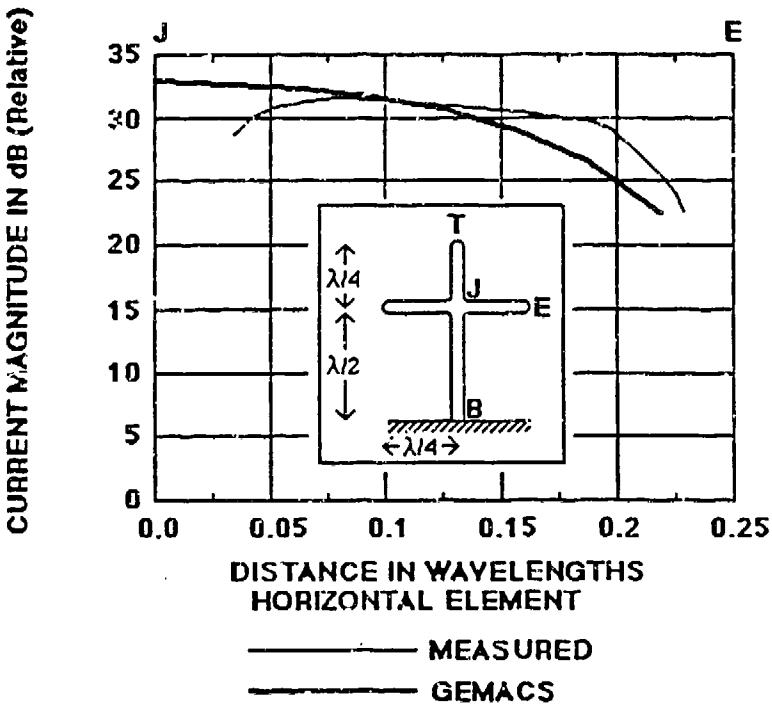


Figure 2. Relative Current Magnitude in dB For the Horizontal Arm of the Crossed Dipole : GEMACS vs. Measured Data

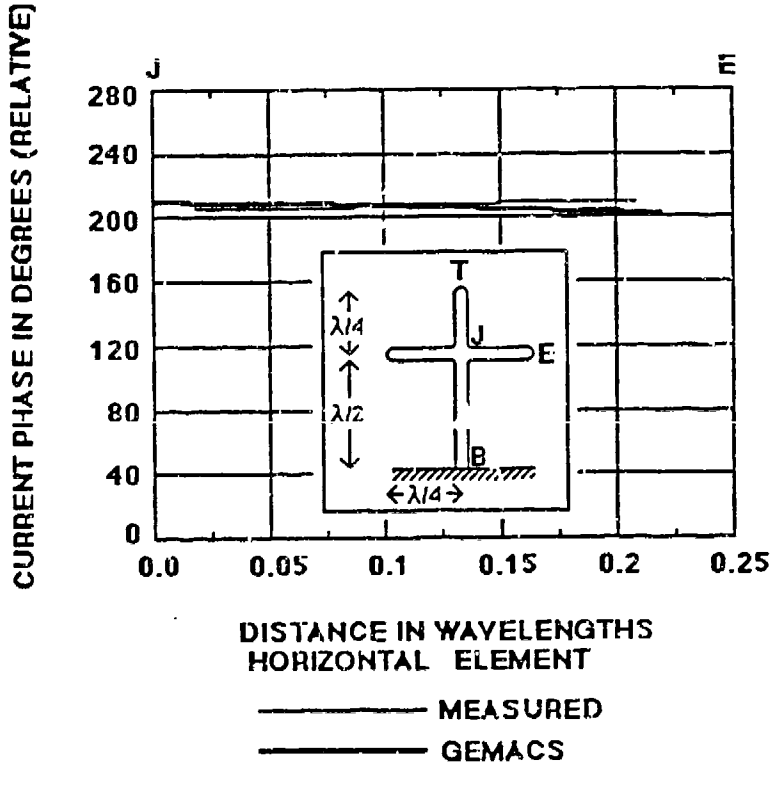


Figure 3. Relative Current Phase in Degrees For the Horizontal Arm of the Crossed Dipole : GEMACS vs. Measured Data

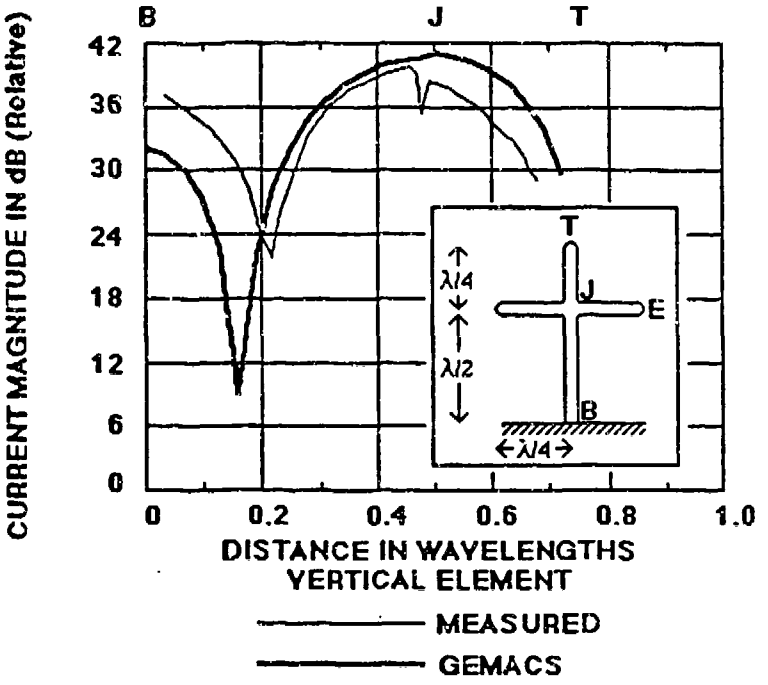


Figure 4. Relative Current Magnitude in dB For the Vertical Arm of the Crossed Dipole : GEMACS vs. Measured Data

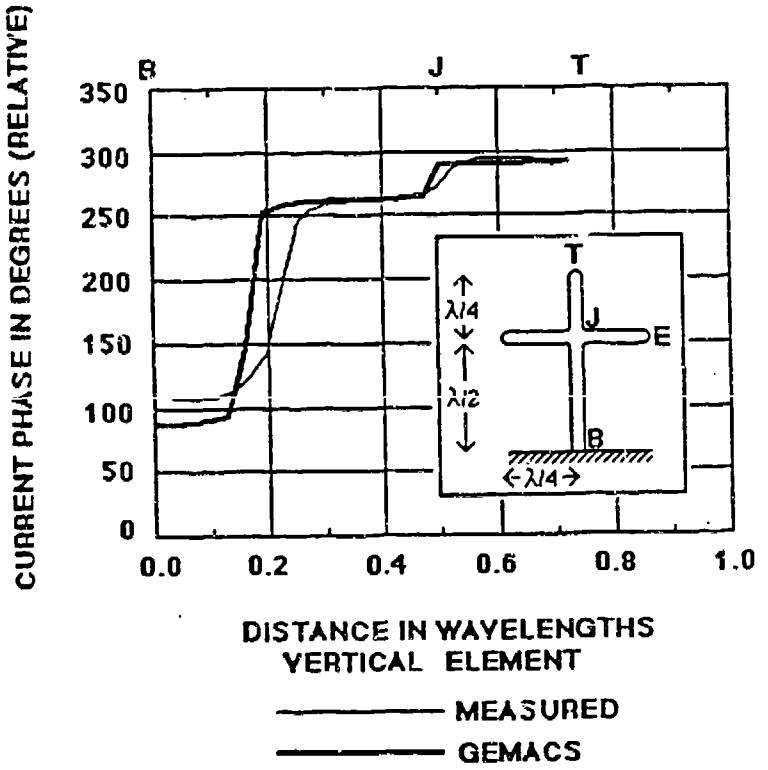


Figure 5. Relative Current Phase in Degrees For the Vertical Arm of the Crossed Dipole : GEMACS vs. Measured Data

Of the 6 moment codes examined in Reference 1 (OSU, Syracuse, MININEC3, TCI, BIGANT, and NEC3) , GEMACS results overall compare most closely to those of the NEC3 and OSU codes. Like NEC3, GEMACS uses a three-term basis function with a collocation testing method. GEMACS did not predict the horizontal arm current magnitude as well as BIGANT, but predicted the horizontal arm phase quite well. The vertical arm current magnitude prediction compared well to those of OSU, NEC3, and MININEC3; none of the seven moment codes predicted the drop in vertical arm current magnitude at the junction. The vertical arm phase prediction was closest to those of OSU, Syracuse, and NEC3, all of which predicted phase ramps at the quarter-wave point and at the junction. The disagreement of the moment code predictions with the measurements are due to the thin-wire approximations of negligible circumferential currents and invariant axial current density along the circumference; for a real junction, rotational symmetry assumptions collapse.

CASSANDRA SOLUTION

CASSANDRA is an admittance-based transmission-line code. It is written in FORTRAN for 8086-based personal computers. The first step in using CASSANDRA to predict scattering from a structure is the development of a transmission-line, or "branch" model, of the structure. An example of a branch model of a 747 airframe is provided in Figure 6(a); the 747 itself appears in Figure 6(b). Each branch is characterized by its length, radius, and its average height above ground (if the ground is present); branches are connected at nodes to form a three-dimensional model of the structure. The user specifies several problem parameters, including the ground conductivity and permittivity; the waveform parameters, elevation, azimuth, and polarization of the incident electromagnetic field; the desired solution points; the frequency range for the solution process; and the desired time range for time-domain outputs. Once the CASSANDRA run starts, the code computes the characteristic impedance and propagation constant for each branch, at all frequencies of interest. In addition, the component of incident electric field parallel to a given branch is integrated over part or all of that branch to develop a source current term, $\mathbf{I}_s$. At each frequency, the matrix equation

$$\mathbf{I}_s = \underline{\mathbf{Y}}\,\mathbf{V}_n$$

is solved for the unknown node voltages $\mathbf{V}_n$, in terms of the computed source currents Is and the known admittance $\underline{\mathbf{Y}}$. Once the node voltages have been determined over all frequencies, the current and voltage at any position along any branch can be found.

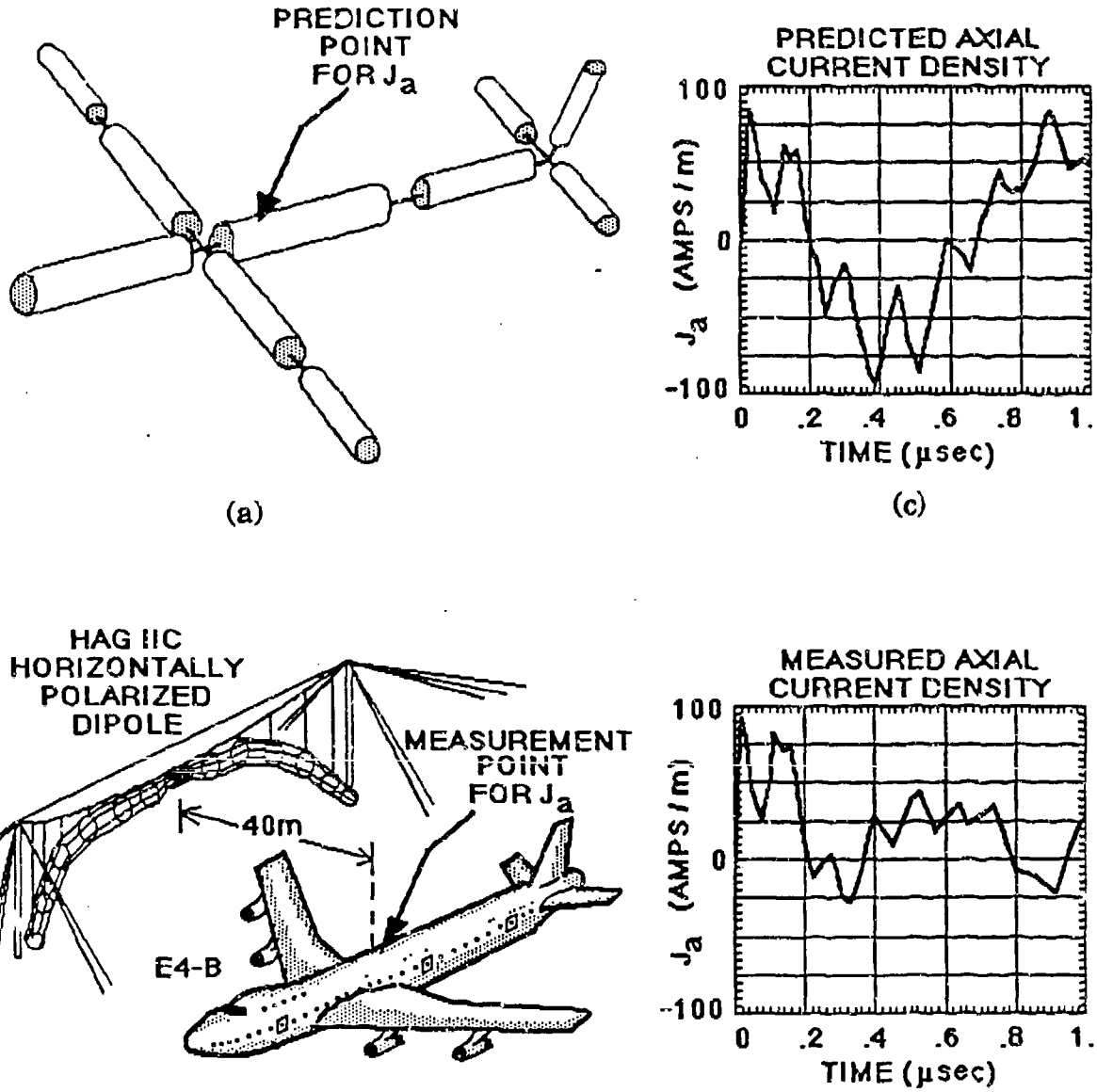


Figure 6. Comparison of CASSANDRA Prediction to Measurement for EMP Scattering from a 747 Airframe : (a) CASSANDRA 10-Branch Model of the 747; (b) 747 / Field Geometry for both the Prediction and a Full Scale Measurement on an E4-B; (c) CASSANDRA Prediction for Axial Surface Current Density on the Fuselage Behind the Wing Root; (d) E4-B Measurement of Axial Surface Current Density on the Fuselage Behind the Wing Root.

The frequency-domain solutions are transformed to the time domain numerically, with a slope-difference Fourier integral transform. Quantities such as axial surface current density, charge density, and normal electric field strength can be determined from the appropriate branch currents and voltages, if desired. A representative CASSANDRA calculation for the axial surface current density at a point on top of the 747 fuselage, just behind the wing root, is shown in Figure 6(c). The incident field is horizontally polarized, and is coming in parallel to the fuselage at an elevation of 35 degrees; the waveform parameters used were obtained from the Bell laboratory characterization of an electromagnetic pulse (EMP) as a double exponential. Figure 6(d) shows a full-scale measurement of the axial surface current density, for the same incident wave/ test point geometrical configuration; this measurement was made on an E4-B aircraft at the Horizontally Polarized Dipole (HPD) facility at Kirtland Air Force Base in Albuquerque, New Mexico. The computed axial surface current density is found by dividing the CASSANDRA net branch current by the given branch's circumference. Although the measured current density decays faster than the CASSANDRA prediction, the amplitude and wave shape for measured and the predicted waveforms are in generally good agreement.

CASSANDRA was used to examine the original crossed dipole problem of Figure 1. A 4-branch model was used; the combined length of the 2 vertical arms was 0.75 meter (3/4 λ at 300 MHz), and each horizontal arm was 0.25 m (λ/4 at 300 MHz). CASSANDRA was run in "continuous-wave" mode (excitation independent of frequency) for several points along the horizontal arm, and the results for each point at 300 MHz were tabulated and plotted; the result appears in Figure 7, along with Burton's measurements. CASSANDRA predicts the horizontal arm current magnitude fairly well, except at the end (E), where the prediction falls short by about 12 dB. As with the moment codes, CASSANDRA uses the assumptions of nonexistent circumferential currents and constant axial currents along the circumference. The relative current magnitude along the vertical arms was also examined : the result appears in Figure 8. The CASSANDRA predictions compare reasonably well to the measurements between the bottom of the dipole and the quarter-wave point, fall about 9 dB too low between the quarter-wave point and the junction, and are about 6 dB too high between the junction and the top of the dipole. The discrepancies between CASSANDRA and measurement for vertical arm currents are most likely due to the difficulty of defining a characteristic impedance for transmission lines which are perpendicular (rather than parallel) to the ground plane.

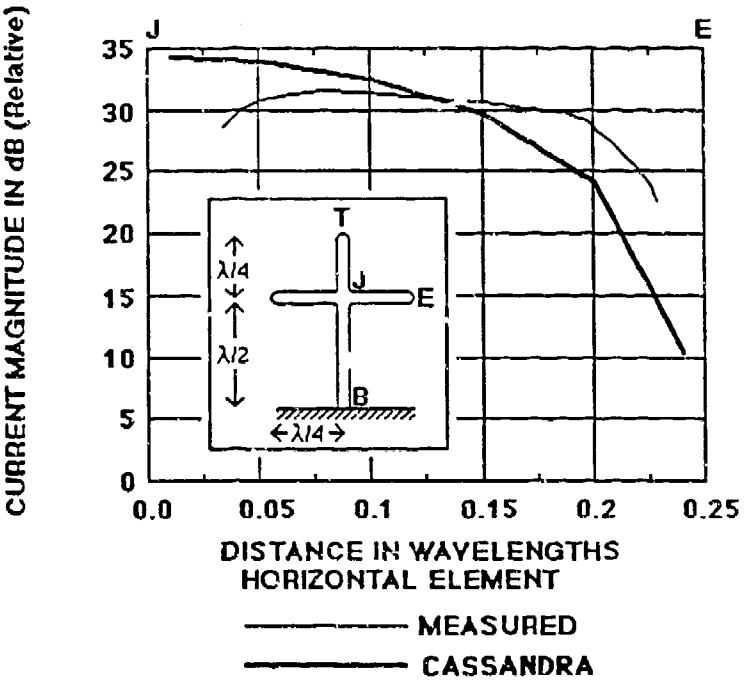


Figure 7. Relative Current Magnitude in dB For the Horizontal Arm of the Crossed Dipole : CASSANDRA vs. Measured Data

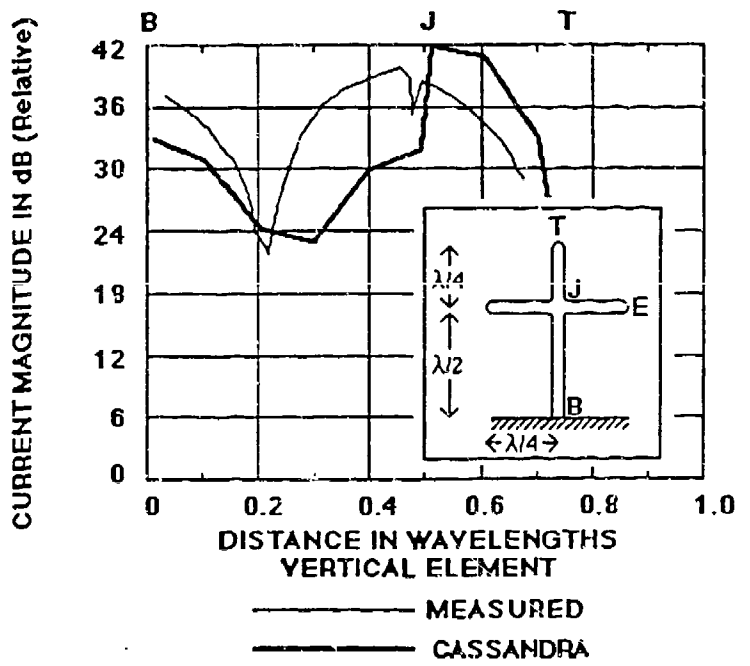


Figure 8. Relative Current Magnitude in dB For the Vertical Arm of the Crossed Dipole : CASSANDRA vs. Measured Data

Normally, CASSANDRA produces the current magnitude at a single point on a branch, over a wide range of frequencies. One such calculation is presented in Figure 9; the point in question is located just 0.01 meter above the crossed dipole's junction, on the vertical arm. For this figure, unit excitation was used at each frequency (continuous-wave mode). The resonance at 300 MHz is obvious; however, a significant resonance can be observed at 75 MHz as well. The 75 MHz resonance occurs because the horizontal arms effectively add to the antenna's length, making it look like a quarter-wave monopole over ground at this frequency (a $\lambda/4$ monopole at 75 MHz is about 1.0 meters long, while the vertical length of the crossed dipole is 0.75 meters).

The crossed dipole problem was run again, this time using the double-exponential Bell laboratory EMP waveform, given in the time domain as E(t) = 52.5e3 [(exp(-4.0e6*t) - exp(-4.76e8*t)] . Frequency-domain results for the point 0.01 meter above the junction, on the vertical arm, are shown in Figure 10; here, the high-frequency roll-off of the EMP waveform serves to emphasize the effect of the 75 MHz resonance over the 300 MHz resonance. The time-domain solution for the same point was obtained with a numerical Fourier integral transform, and is displayed in Figure 11; the response is dominated almost entirely by the 75-Mhz ring.

CONCLUSION

Solutions of problems concerning scattering from crossed dipole antennas with the GEMACS and CASSANDRA codes have been discussed. Like the other moment-method codes examined in Reference 1, GEMACS predictions have difficulty with current and charge at the junction of the crossed dipole. Results from the CASSANDRA admittance-based transmission-line code were compared to measured data for problems involving both the crossed dipole and a 747 aircraft.

REFERENCES

1. R. W. Adler, "A Comparison of Thin-Wire EM Modeling Codes for the Case of Scattering From a Cross," Second Annual Review of Progress in Applied Computational Electromagnetics, March 1986.

2. R. W. Burton and R. W. P. King, "Measured Current and Charges on Thin Crossed Antenna in a Plane Wave Field," IEEE Transactions on Antennas and Propagation, VOL. AP-23, No. 5, Sept. 1975, pp. 657-664.

3. E. L. Coffey, D. L. Kadlec, General Electromagnetic Model for the Analysis of Complex Systems (GEMACS) - Version 4 Engineering Manual. RADC-TR-87-68, Vol. II, Rome Air Development Center, New York, May 1987.

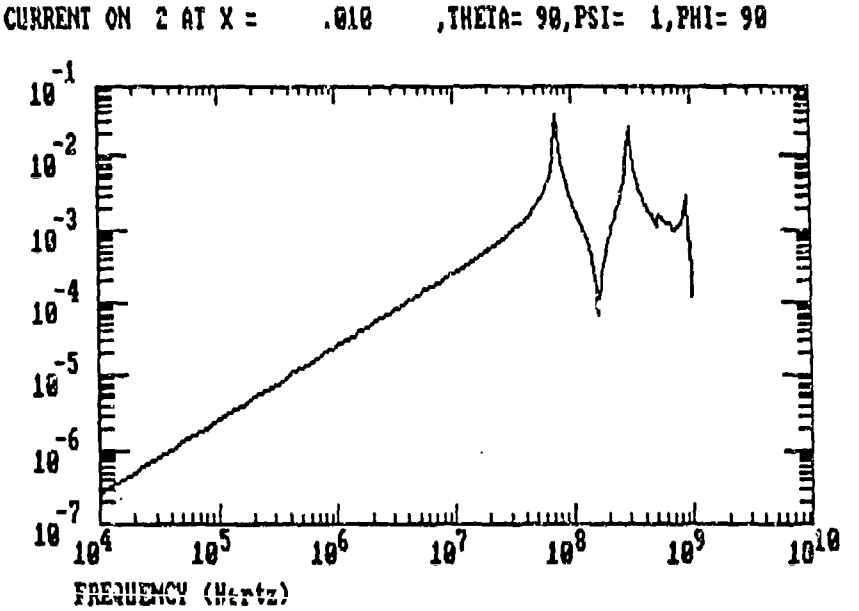


Figure 9. CASSANDRA Frequency-Domain Solution for Net Axial Current at a Point 0.01 Meters Above the Junction of the Crossed Dipole, On the Vertical Arm: Continuous-Wave Mode Excitation (Independent of Frequency).

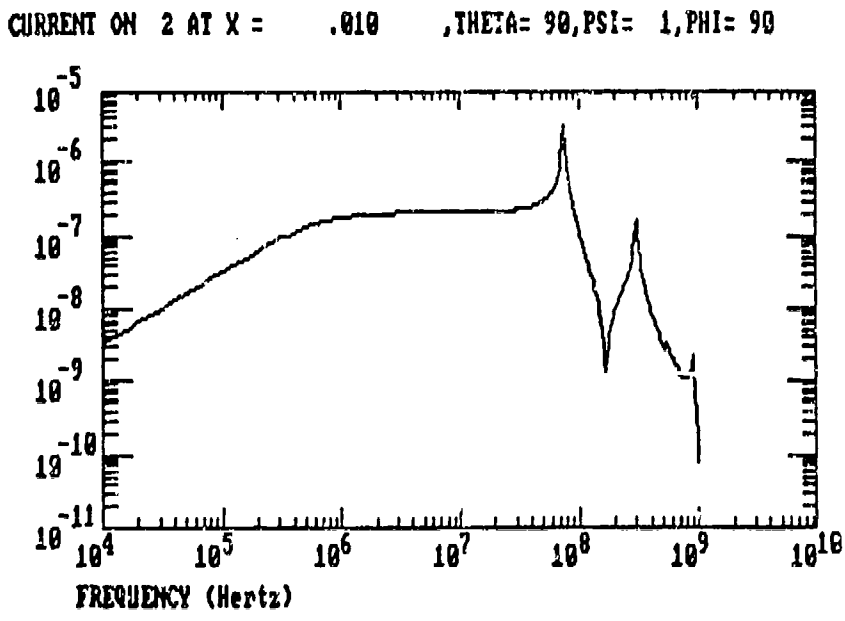


Figure 10. CASSANDRA Frequency-Domain Solution for Net Axial Current at a Point 0.01 Meters Above the Junction of the Crossed Dipole, On the Vertical Arm: Bell Lab EMP Waveform Excitation.

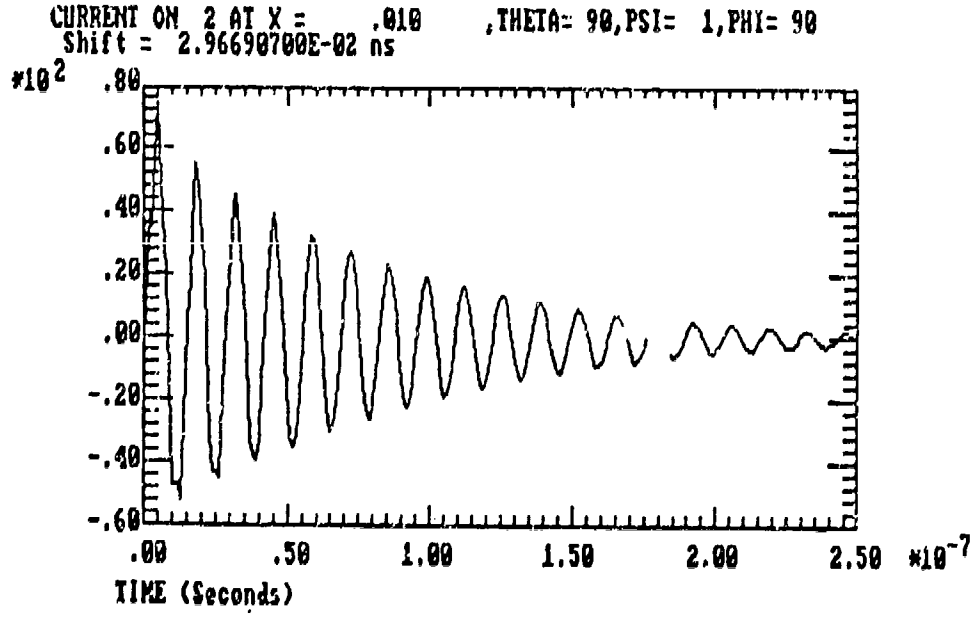


Figure 11. CASSANDRA Time-Domain Solution for Net Axial Current at a Point 0.01 Meters Above the Junction of the Crossed Dipole, On the Vertical Arm: Bell Lab EMP Waveform Excitation.

SESSION IV - "INPUT-OUTPUT ISSUES"

Moderator: Ruediger Anders
Applied Electromagnetics Engineering

"An EM Language Translator and Macro Processor"
E.L. Coffey — Advanced Electromagnetics
A. Lockyer — Northrop Corporation

"Graphical Aids for Users of GEMACS (GAUGE)"
A. Lockyer, P. Tulyathan — Northrop Corporation
K.R. Siarkiewicz — Rome Air Development Center

"Graphics Programming for Electromagnetic Modeling"
G. Upshaw, M. J. Grage — Northrop Corporation
K.R. Siarkiewicz — Rome Air Development Center

"MATHPLOT - A Modeling Tool for Scientists and Engineers"*
D.F. Higgins — Consultant

"PC Program for Plotting the Vector Fields"
D. Kajfez and J.A. Gerald — University of Mississippi

"Scientific Visualization in Computational Electromagnetics"
S. Lamont — San Diego Supercomputer Center

* Paper was not submitted and is not published.

An EM Language Translator and Macro Processor

Edgar L. Coffey
Advanced Electromagnetics
5617 Palomino Dr. NW
Albuquerque, New Mexico 87120

Allen Lockyer
Pravit Tulyathan
Northrop Corporation
Hawthorne, California 90250

Introduction

Much of the effort in making electromagnetic models of physical structures is spent in the mechanics of describing the geometry to the EM computer program. In addition, many times it is desirable to use more than one program in analyzing the problem electromagnetically. Yet, the popular EM computer programs (BSC, GEMACS, NEC) have similar though distinctly different geometry languages and capabilities. To use all three codes to model the same structure many times would require that three different geometry descriptions be developed.

The purpose of this paper is to describe a language translator program which will automatically re-write a user's input geometry language (be it in BSC, GEMACS, or NEC) into one of the other languages. For example, a set of "GW" NEC wire commands can be converted into equivalent GEMACS "RA" and "WR" commands. Likewise, the BSC GTD geometry elements (plates, cylinders, end caps) can be converted into GEMACS "PL", "CY", and "EC" elements. A side benefit of using the translator is that other EM languages can take advantage of the PC-based GEMACS Graphics package (GAUGE) [1], described elsewhere in this volume.

A second capability of this program is an embedded macro language command set. Geometry elements or operations which are too complex for most computer programs (e.g., generating a spiral geometry) can be performed by using a set of macro language commands for loops, branching, calls to subordinate routines, and arithmetic operations.

Description of the Translator Package

The EM Language Translator (ELT) is a single FORTRAN program composed of 59 FORTRAN and one assembly language subroutines. It is hosted on an IBM Personal Computer (or compatible) with at least 512K and DOS 2.1 or greater. A color monitor enhances the program but is not necessary.

The user interface to the ELT is a single split screen, which is displayed when the translator is run. The top two thirds of the screen (blue on color monitors) is the user input area (or "panel"). In this window the user enters input and output files, input and output languages, and several optional processing directives. The lower third of the screen (black on color monitors) is a window which displays the input statements as they are processed and the output statements as they are generated. Figure 1 shows how the translator screen might appear when the ELT is executed. The responses are in upper case in the figure, though on the screen they are highlighted in a distinct color.

This work was sponsored by Rome Air Development Center, RADC/RBCT, Griffiss Air Force Base, NY under contract F30602-87-C-0110 to Northrop Corporation, Aircraft Division, Hawthorne, California. The software described in this paper is available through RADC/RBCT (Kenneth R. Siarkiewicz), Griffiss AFB, NY 13441-5700.

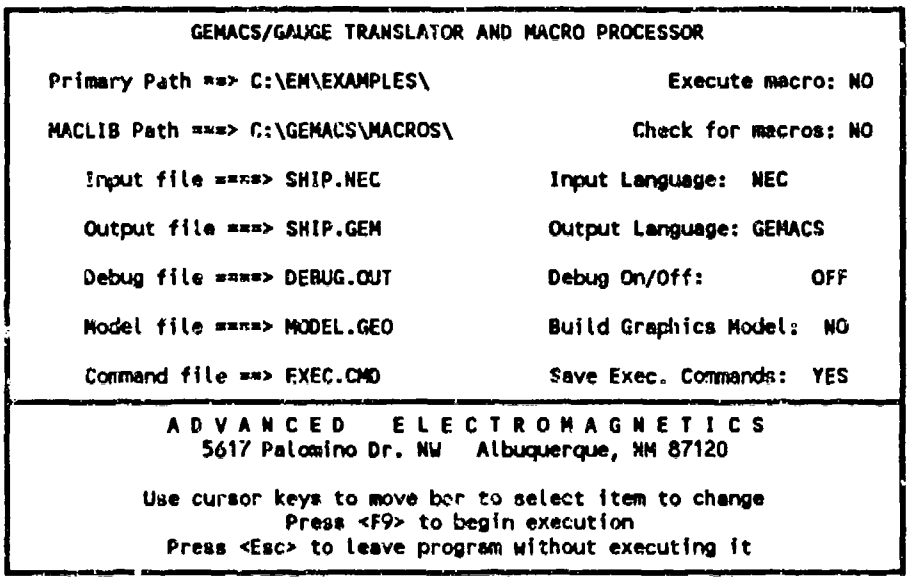


Figure 1. Initial Translator Input Screen.

The screen in figure 1 shows that the input file is C:\EM\EXAMPLES\SHIP.NEC, and the input language is NEC. The output file is C:\EM\EXAMPLES\SHIP.GEM, and the output language is GEMACS. The translation process is started by pressing the <F9> key. The NEC geometry commands in SHIP.NEC are read by the ELT, processed by the program, and output into SHIP.GEM in GEMACS format.

For now we will ignore the "Execute macro" and "Check for macros" fields as they will be discussed below. The "Debug file" and "Debug On/Off" fields enable debug printouts onto a peripheral file. These are useful in finding problems when a particularly complex structure does not translate correctly. The "Model file" and "Build Graphics Model" fields generate a point and polygon based database which can be read by graphics programs other than GAUGE. The "Command file" and "Save Exec. Commands" fields permit comments and other non-geometry commands to be temporarily saved during language translation, then placed back into the output file in the same places from which they were extracted.

A NEC to GEMACS Example

One of the inhibiting factors in upgrading computer programs is the regeneration of input data in the new program's format. With the ELT, this task is made trivial. Consider the simple NEC geometry model of a square shown below. There is one wire composed of one segment for each leg of the loop.

```
CM NEC GEOMETRY MODEL OF A SQUARE LOOP
CE DEMONSTRATION ONLY (DO NOT EXECUTE)
GW 1  1  0   0.  0.  1.  0.  0.  0.01
GW 2  1  1.  0.  0.  1.  1.  0.  0.01
GW 3  1  1.  1.  0.  0.  1.  0.  0.01
GW 4  1  0.  1.  0.  0.  0.  0.  0.01
GE
```

Notice that the NEC deck has a true free-field input format. Such an input cannot be read by NEC (so don't try to execute it "as is"), but the ELT doesn't care about the format of the input. Fields can be separated by blanks, commas, or both. When the

NEC deck shown above is run through the ELT, the following GEMACS deck is generated.

```
$  NEC GEOMETRY MODEL OF A SQUARE LOOP
$  DEMONSTRATION ONLY (DO NOT EXECUTE)
KA      .01[illegible].0
PT 10001    0.0000000E+00   0.0000000E+00   0.0000000E+00  0
PT 10002    1.0000000E+00   0.0000000E+00   0.0000000E+00  0
CP  10001   10002 1      1  1
PT 10003    1.0000000E+00   1.0000000E+00   0.0000000E+00  0
CP  10002   10003 1      2  1
PT 10004    0.0000000E+00   1.0000000E+00   0.0000000E+00  0
CP  10003   10004 1      3  1
CP  10004   10001 1      4  1
END
```

The NEC comments (CM, CE) have been turned into GEMACS comments ($). While GEMACS has a "WR" command syntactically equivalent to the NEC "GW" command, the translator chose another wire generation format. Points are defined by the "PT" commands, then segments are generated between two points by the connect point (CP) commands [2]. Point numbers are automatically generated in this example, beginning with point 10001.

A BSC to GEMACS Example

The geometry description for a simple aircraft (example 20 of [3]) has been extracted from a BSC input deck and is shown below.

```
CM:     BSC EXAMPLE 20, PAGE 7-112.
CM:     POLARIZATION HH,ROLL ANGLE 0.
CE:     THIS IS THE GEOMETRY PORTION OF THE DECK ONLY ONLY!
UN:
3
CG:   THE BODY OF THE PLANE
0.,0.,0.
90.,0.,0.,0.
6.,6.
-42.,90.,42.,90.
PG:   RIGHT REAR STABILIZER
4,0
-42.,-6.,0.
-48.,-20.5,0.
-44.,-20.5,0
-24.,-6.,0.
PG:   LEFT REAR STABILIZER
4,0
-42.,6.,0.
-24.,6.,0.
-44.,20.5,0.
-48.,20.5,0.
PG:   VERTICAL STABILIZER
4,0
-42.0,0.,6.
-48.0,0.,20.5
-44.0,0.,20.5
-24.0,0.,6.
PG:   LEFT WING
4,0
3.,6.,0.
-25.,36.,0.
-12.,36.,0.
40.,6.,0.
PG:   RIGHT WING
4,0
3.,-6.,0.
-25.,-36.,0.
-12.,-36.,0.
40.,-6.,0.
```

The aircraft itself is shown in figure 2. The GEMACS output of the ELT follows the BSC input deck quite closely. The BSC UN: (units) command corresponds to GEMACS' SC command. The BSC CG: (cylinder geometry) generates a GEMACS coordinate system (CS) in which are located a GEMACS cylinder (CY) and two end caps (EC). Each BSC PG: (plate geometry) command generates GEMACS points (PT) for the plate corners and plate (PL) for the surface itself. The ELT output is shown below.

```
$     BSC EXAMPLE 20, PAGE 7-112.
$     POLARIZATION HH,ROLL ANGLE 0.
$     THIS IS THE GEOMETRY PORTION OF THE DECK ONLY ONLY!
$
$   THE BODY OF THE PLANE
CS    10001       .0000       .0000       .0000       .0000     90.0000       .0000
CY      1   1.5240000E-01   1.5240000E-01   2.1336000E+00  10001
EC      1     1   0.0000000E+00   0.0000000E+00
EC      2    -1   1.8000000E+02   0.0000000E+00
$   RIGHT REAR STABILIZER
PT 10001  -1.0668000E+00  -1.5240000E-01   0.0000000E+00  0
PT 10002  -1.2192000E+00  -5.2070000E-01   0.0000000E+00  0
PT 10003  -1.1176000E+00  -5.2070000E-01   0.0000000E+00  0
PT 10004  -6.0960000E-01  -1.5240000E-01   0.0000000E+00  0
PL      1     4 10001 10002 10003 10004     0
$   LEFT REAR STABILIZER
PT 10005  -1.0668000E+00   1.5240000E-01   0.0000000E+00  0
PT 10006  -6.0960000E-01   1.5240000E-01   0.0000000E+00  0
PT 10007  -1.1176000E+00   5.2070000E-01   0.0000000E+00  0
PT 10008  -1.2192000E+00   5.2070000E-01   0.0000000E+00  0
PL      2     4 10005 10006 10007 10008     0
$   VERTICAL STABILIZER
PT 10009  -1.0668000E+00   0.0000000E+00   1.5240000E-01  0
PT 10010  -1.2192000E+00   0.0000000E+00   5.2070000E-01  0
PT 10011  -1.1176000E+00   0.0000000E+00   5.2070000E-01  0
PT 10012  -6.0960000E-01   0.0000000E+00   1.5240000E-01  0
PL      3     4 10009 10010 10011 10012     0
$   LEFT WING
PT 10013   7.6200000E-02   1.5240000E-01   0.0000000E+00  0
PT 10014  -6.3500000E-01   9.1440000E-01   0.0000000E+00  0
PT 10015  -3.0480000E-01   9.1440000E-01   0.0000000E+00  0
PT 10016   1.0160000E+00   1.5240000E-01   0.0000000E+00  0
PL      4     4 10013 10014 10015 10016     0
$   RIGHT WING
PT 10017   7.6200000E-02  -1.5240000E-01   0.0000000E+00  0
PT 10018  -6.3500000E-01  -9.1440000E-01   0.0000000E+00  0
PT 10019  -3.0480000E-01  -9.1440000E-01   0.0000000E+00  0
PT 10020   1.0160000E+00  -1.5240000E-01   0.0000000E+00  0
PL      5     4 10017 10018 10019 10020     0
END
```

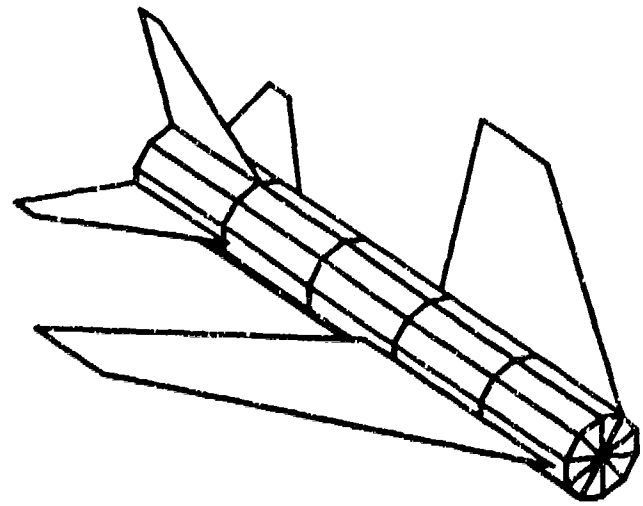


Figure 2. Simple Aircraft from BSC Example 20.

A Mixed Language Example

It is also possible to intermix GEMACS, BSC, and NEC input languages to achieve a hybrid model. For example, there is no GEMACS equivalent to the NEC GA (wire arc) geometry command. So, a mostly GEMACS deck could be supplemented by one or more GA commands from NEC (as well as other NEC or BSC commands) and still produce a valid GEMACS output deck. The ELT performs mixed language input processing when the "Input Language:" field is set to MIXED.

In addition, the BSC and NEC languages do not have as many CAD-like geometry commands as does GEMACS. Hence, a mostly NEC deck, for example, can be supplemented with GEMACS defined element (DF) commands, etc.

```
DF NECGEO
   GW ...
   GW ...
    .
    .
    .
DE
RF  DF NECGEO  Y Z  1   (Reflect NECGEO through the xz- and xy- planes)
```

(Define NECGEO element with NEC geometry elements)

The Macro Language Processor

The GEMACS, BSC, and NEC codes have a fixed set of "hardwired" geometry commands from which a user can select to describe his structure. The geometry command repertoire for all three is extensive, and quite complex structures can be described with a minimal number of commands. Yet, as would be true with any command set, there are structures which do not lend themselves to GEMACS, BSC, or NEC. For example, the wires which comprise a simple spiral antenna must each be entered individually with one WR (GEMACS) or GW (NEC) command per straight wire segment. This not only yields hundreds of GEMACS commands for a simple antenna, but the coordinates of each wire must be calculated by hand and entered explicitly on the commands.

The Macro Language Processor (MLP) can alleviate the tedium of calculating data by hand, entering repetitious blocks of data, and re-entering frequently used descriptions of structures or parts of structures. The MLP allows GEMACS, BSC, NEC, and many other EM codes to have predefined and stored parametric geometry models in plain English text without having to write new FORTRAN and modify the host code for each new model the user may wish to conceive.

The MLP is built upon GEMACS (or any other language's) geometry commands, replaceable macro parameters (like FORTRAN variables), a set of MLP commands for conditional execution, looping, and calling subordinate macros (like FORTRAN subroutine calls), and an arithmetic statement processor which can be used to evaluate expressions for parameter assignment, loop indices, and conditional execution switches.

Replaceable parameters are FORTRAN-like variables composed of up to 18 characters (A-Z, 0-9, and underscore _) the first of which must be alphabetic. They are used in GEMACS, BSC, or NEC geometry commands so that the parameter itself is replaced by its value (calculated elsewhere in the macro definition). For example, suppose the parameter NSEGS had been set to 10. Then the statement

```
WR  0.  0.  0.  0.  0.  1.0  &NSEGS  1  1
```

would be output as

```
WR 0. 0. 0. 0. 0. 1.0 10 1 1
```

The ampersand (&) precedes the parameter to be replaced to distinguish it from a geometry keyword.

MLP arithmetic operations are used to manipulate the replaceable parameters. The MLP has a FORTRAN-like syntax processor that will interpret valid FORTRAN assignment and mathematical statements, evaluate them, and assign their results to a replaceable parameter. To distinguish these statements from the EM language geometry statements, each arithmetic statement begins with an ampersand (&). An example to calculate the hypotenuse of a right triangle is shown below. The statements with (!) are macro comments and are neither printed nor executed.

```
!
!  Compute the hypotenuse HYPO of a right triangle with sides
!  SIDE1 and SIDE2
&SIDE1 = 3.0
&SIDE2 = 4.0
&HYPO = SQRT(SIDE1**2+SIDE2**2)  !Or, the '^' could be used for '**'
$ RESULTS:  HYPO = &HYPO
```

The first three lines are MLP comments and are not printed to the output file. The next two lines assign 3.0 and 4.0 to SIDE1 and SIDE2 respectively. Note that the replaceable parameters (and MLP commands) must use upper case letters, though MLP and GEMACS comments may have lower case letters as well.

The hypotenuse is computed in the next statement. A number of FORTRAN functions are available in the MLP, as discussed in a later section. The parameters SIDE1, SIDE2, and HYPO are available for use on GEMACS commands, such as the GEMACS comment in line 7.

Neither the MLP comments nor the MLP commands (with the & as first character) are printed to the output file. The sole output from the seven-line macro model above is a single line.

```
$ RESULTS:  HYPO = 5.0000000E+00
```

There are presently twelve (12) MLP keywords which may be used to define eight distinct MLP commands.

&DEBUG	Turn on/off debug printing
&CALL	Call a subordinate macro definition
&MACRO	Begin a macro definition
&MEND	End a macro definition
&LOOP	Begin a loop/label block
&LABEL	End a loop/label block
&IF-&THEN	Begin if/then/else/endif block
&ELSE	Optional alternative in if/then/else/endif
&ENDIF	End an if/then/else/endif block
&INPUT	Prompt user for input
&OUTPUT	Display output to user
&JUMP	Jump (relative)

Explanation of each command is beyond the scope of this paper, but full descriptions may be found in [4].

An Example Macro: The Spiral Antenna

The spiral antenna can be modeled well by GEMACS or NEC, but its input must be generated by hand if unaided by the MLP. Below is a MLP description of a spiral antenna, complete with user-input parameters. Its output (when processed by the MLP) is a set of GEMACS geometry commands that will produce a MOM wire segment model of the antenna described by the user's input parameters. The spiral macro is invoked by answering "YES" to the "Execute macro:" field of the ELT input window.

```
&MACRO  NTPI NTOT IR NSEG RAD HEIGHT
!
! This macro generates a two-arm Archimedean spiral antenna
! centered at the origin and in the (x,y)-plane.
!
! There is an option of generating a "spiral-cone" antenna by
! entering a positive entry for HEIGHT
!
!    Input Parameters:
!
!       NTPI   =  Number of turns per inch
!       NTOT   =  Total number of turns in the spiral (one arm)
!       IR     =  Spiral Inner radius (inches)
!       NSEG   =  Number of GEMACS Wire Segments per turn
!       RAD    =  Radius of the wires modeling the spiral
!       HEIGHT =  If positive, the total height of the antenna
!
!
&DATE = '11-13-87'
&PI = 3.141592
&TOTSEG = NSEG*NTOT
&DZ = 0.
&IF (HEIGHT .GT. 0.) &THEN
   &DZ = HEIGHT/TOTSEG     ! Indent for clarity, not required.
&ENDIF
&DRIVE1 = 1
&DRIVE2 = 2 + TOTSEG
&DIAM = NTOT/NTPI*2
&RHOO = 1/(2*PI*NTPI)
!
! Limits on phi-angles
!
&PHIMIN = PI/2+IR/RHOO
&PHIMAX = 2*PI*NTOT+PHIMIN
&DPHI = 2.*PI/NSEG
!
!  Coordinates for feed wire segment
!
&RHOMIN = RHOO*PHIMIN
&XMIN = RHOMIN*COS(PHIMIN)
&YMIN = RHOMIN*SIN(PHIMIN)
!
! Compute longest segment to determine highest operating frequency
!
&RHOMAX = RHOO*PHIMAX
&XMAX = RHOMAX * COS(PHIMAX)
&YMAX = RHOMAX * SIN(PHIMAX)
&PHINXT = PHIMAX - DPHI
&RHONXT = RHOO*PHINXT
&XNXT = RHONXT * COS(PHINXT)
&YNXT = RHONXT * SIN(PHINXT)
&LENGTH = SQRT((XMAX-XNXT)**2 + (YMAX-YNXT)**2 + DZ**2)
&LAMBDA = 10 * LENGTH / 39.37
&FRQMAX = 300./LAMBDA
$
$-----------------------------------------------------------------------
&IF (HEIGHT .LE. 0.) &THEN
$  GEOMETRY FOR AN ARCHIMEDEAN SPIRAL ANTENNA
&ELSE
$  GEOMETRY FOR A SPIRAL-CONE ANTENNA
```

(Listing Continued on Next Page)

```
&ENDIF
$
$  GENERATED ON: &DATE
$
$
$  TURNS PER INCH:   &NTPI
$  TOTAL TURNS:      &NTOT
$  INNER RADIUS(In): &IR
$  SEGS PER TURN:    &NSEG
$  WIRE RADIUS(In):  &RAD
$  TOTAL DIAMETER:   &DIAM
&IF (HEIGHT .GT. 0.)  &THEN
$  ANT HEIGHT (In):  &HEIGHT
&ENDIF
$
$  MAX SEG LENGTH(In):   &LENGTH
$  FREQ. LIMIT(MHZ):     &FRQMAX  FOR LAMBDA/10 MODELING
$
$
$  THE ANTENNA SHOULD BE DRIVEN WITH +0.5 VOLTS ON SEGMENT &DRIVE1
$                                AND -0.5 VOLTS ON SEGMENT &DRIVE2
$-------------------------------------------------------------------------
$
SC IN    $UNITS PRESUMED TO BE INCHES IN INPUT DATA
RA &RAD
$ DRIVE SEGMENT# &DRIVE1
WR &XMIN &YMIN 0.  0. 0. 0. 1  1  1
&PHI = PHIMIN - DPHI
!
!  Loop over the total number of segments in one arm, with COUNT as
!  the loop counter.
!
&COUNT = 0
&Z2 = 0.
&LOOP TOTSEG
&Z1 = Z2
&Z2 = Z1 + DZ
!
!  Print out a GEMACS comment every 10 wires so that the user can keep
!  track of the segment numbers easily.
!
&IF (COUNT/10*10 .EQ. COUNT) &THEN
   &COUNT1 = COUNT + 2
   &COUNT2 = COUNT + 11
   &IF (COUNT2 .GT. TOTSEG+1) &THEN   !The last block of wires may not
      &COUNT2 = TOTSEG + 1            !have a full 10 segments.
   &ENDIF
$
$ BELOW ARE SEGMENTS &COUNT1 TO &COUNT2
$
&ENDIF
!
! Negative end point quantities
!
&PHI = PHI + DPHI      !The angle (radians)
&RHO = RHOO*PHI        !The radius (inches)
&XN = RHO*COS(PHI)     !X-coordinate
&YN = RHO*SIN(PHI)     !Y-coordinate
!
! Positive end point quantities
!
&PHIP = PHI + DPHI     !The angle (radians)
&RHOP = RHOO*PHIP      !The radius (inches)
&XP = RHOP*COS(PHIP)   !X-coordinate
&YP = RHOP*SIN(PHIP)   !Y-coordinate
!
&IF (HEIGHT .GT. 0.) &THEN
WR &XN &YN &Z1 &XP &YP &Z2 1 1 1
&ELSE
WR &XN &YN 0. &XP &YP 0.  1 1 1
```

(Listing Continues on Next Page)

```
&ENDIF
!
&COUNT = COUNT + 1
&LABEL
!
! End of looping...Now make the other arm by using the RZ command
!
&TOT1 = DRIVE2
&TOT2 = 2*(1+TOTSEG)
$
$  ROTATE ARM ONE TO GENERATE ARM TWO
$
$  SEGMENTS &TOT1 TO &TOT2
$
RZ TG 1 1  180.
END
&MEND
```

This macro deck is quite extensive because it performs a lot of error checking and gives a lot of extra output. The first part of the macro's output is shown below. Notice the frequency limit in the header comments and the automatic calculation of drive segments.

```
$
$-----------------------------------------------------------------
$  GEOMETRY FOR AN ARCHIMEDEAN SPIRAL ANTENNA
$
$  GENERATED ON: 11-13-87
$
$
$  TURNS PER INCH:    3.0000000E+00
$  TOTAL TURNS:      15
$  INNER RADIUS(In):  5.0000000E-01
$  SEGS PER TURN:    10
$  WIRE RADIUS(In):   1.0000000E-02
$  TOTAL DIAMETER:    1.0000000E+01
$
$  MAX SEG LENGTH(In):    3.4405370E+00
$  FREQ. LIMIT(MHZ):      3.4328940E+02  FOR LAMBDA/10 MODELING
$
$
$  THE ANTENNA SHOULD BE DRIVEN WITH +0.5 VOLTS ON SEGMENT 1
$                               AND -0.5 VOLTS ON SEGMENT 152
$-----------------------------------------------------------------
$
$UNITS PRESUMED TO BE INCHES IN INPUT DATA
RA     .010
$ DRIVE SEGMENT# 1
PT 10001  -6.0818920E-08  -1.4816670E-02   0.0000000E+00  0
PT 10002   0.0000000E+00   0.0000000E+00   0.0000000E+00  0
CP  10001  10002 1  1  1 0
$
$ BELOW ARE SEGMENTS 2 TO 11
$
PT 10003   9.2066410E-03  -1.2671930E-02   0.0000000E+00  0
CP  10001  10003 1  1  1 0
PT 10004   1.5701930E-02  -5.1019120E-03   0.0000000E+00  0
CP  10003  10004 1  1  1 0
PT 10005   1.6507190E-02   5.3634660E-03   0.0000000E+00  0
CP  10004  10005 1  1  1 0
PT 10006   1.0699680E-02   1.4726790E-02   0.0000000E+00  0
CP  10005  10006 1  1  1 0
PT 10007   3.5390260E-08   1.9050000E-02   0.0000000E+00  0
CP  10006  10007 1  1  1 0
PT 10008  -1.1694950E-02   1.6096770E-02   0.0000000E+00  0
CP  10007  10008 1  1  1 0
PT 10009  -1.9728080E-02   6.4100720E-03   0.0000000E+00  0
CP  10008  10009 1  1  1 0
PT 10010  -2.0533320E-02  -6.6716560E-03   0.0000000E+00  0
CP  10009  10010 1  1  1 0
```

(Listing Continues on Next Page)

```
PT 10011  -1.3187960E-02  -1.8151640E-02   0.0000000E+00  0
CP  10010  10011 1  1  1 0
PT 10012  -1.3969840E-08  -2.3283340E-02   0.0000000E+00  0
CP  10011  10012 1  1  1 0
$
$ BELOW ARE SEGMENTS 12 TO 21
$
PT 10013   1.4183260E-02  -1.9521590E-02   0.0000000E+00  0
CP  10012  10013 1  1  1 0
PT 10014   2.3754230E-02  -7.7182200E-03   0.0000000E+00  0
CP  10013  10014 1  1  1 0
(etc.)
```

Summary

The EM Language Translator and Macro Processor described in this paper have the potential for vastly multiplying the effectiveness of the EM engineer as he uses several of the more popular EM computer codes. No more does he have to meticulously translate by hand the geometry descriptions from one language to another language. Moreover, he may mix his languages in order to achieve even more effectiveness.

The Macro Language Processor can be used with *any* geometry description to produce structure data that would be unthought of with just a computer code's geometry processor. In addition, the MLP can also be used with a code's execution commands to produce an "expert system" which can guide the user into the correct modeling methods and command selections for a particular application.

References

1. A. J. Lockyer, P. Tulyathan, and G. Upshaw, *Graphical Aids for Users of GEMACS (GAUGE)*, appearing elsewhere in this volume.

2. E. L. Coffey and D. L. Kadlec, *General Electromagnetic Model for the Analysis of Complex Systems (GEMACS)*, Volumes I-III (Version 4), Rome Air Development Center Technical Report RADC-TR-87-68, May 1987.

3. R. J. Marhefka and W. D. Burnside, *Numerical Electromagnetic Code (NEC) - Basic Scattering Code*, Part I: User's Manual, Technical Report 712242-14, December 1982, The Ohio State University ElectroScience Laboratory, Columbus; prepared under contract N00123-79-C-1459 for Naval Regional Contracting Office.

4. A. J. Lockyer, P. Tulyathan, and G. Upshaw, *Graphical Aids for Users of GEMACS (GAUGE)*, User Manual, Northrop Corporation, prepared for Rome Air Development Center under contract F30602-87-C-0110, January 1988. *(to be published as an RADC Technical Report)*

GRAPHICAL AIDS FOR USERS OF GEMACS (GAUGE)

Allen Lockyer and Pravit Tulyathan

Aircraft Division, Dept. 3564/83
Northrop Corporation
Hawthorne, California 90250

Kenneth R. Siarkiewicz
Rome Air Development Center (RBCT)
Griffiss AFB, New York 13441

ABSTRACT

A new, user-friendly, IBM PC based graphical interface for GEMACS and other electromagnetic codes is described. GAUGE enables users to perform pre- and post-processing of electromagnetic models and data. Interactive graphics and CAD features are tailored dircectly towards electromagnetic modeling.

Features of the GAUGE graphical processor are illustrated by discussion of specific electromagnetic examples modeled by GEMACS and NEC. The examples discussed are *bistatic scattering from a cube*, electromagnetic coupling for an *AIM-7 illuminator*, MOM and GTD hybridization modeling for a *spiral antenna*, and the *near field* of an antenna located on a shipboard platform. The pre-processor graphical features illustrated include: view (zoom, view angle, color, etc.), show/no show, rotate/translate, interactive picks, rejects, merging models, and saving all or part of a model. Post-processor features discussed are: the display of computed observables by color coding elements, contours on structure, two dimensional plots, cut and paste, hard copy to dot matrix printer, HP pen plotter and a HP laserjet printer.

INTRODUCTION

GEMACS (*General Electromagnetic Model for the Analysis of Complex Systems*), although comprehensive in its ability to solve a wide range of electromagnetic problems, needed an I/O graphical interface to support the current version (4.0) and for future growth (version 5.0). Until now, a user had to interface his own graphics package with the GEMACS code for construction of model geometry or to display computed results. To avoid this difficulty a graphical interface entitled "Graphical Aids for Users of GEMACS" (GAUGE)[†] has been designed based on universally available hardware - the IBM PC. The software developed is user-friendly and should encourage further use of the GEMACS code among the government, its contractors, and to the electromagnetic community at large.

GAUGE interfaces with GEMACS by external file manipulation leaving the parent code unchanged, and is flexible enough to interface with other electromagnetic codes

† This work was performed by Northrop Corporation sponsored by RADC/RBCT under contract F30602-87-C-0110.

including NEC (*Numerical Electromagnetic Code*), BSC (*Basic Scattering Code*). MISCAT and NASTRAN. GAUGE consists of 350 subroutines and 39,000 (approx) lines of code programmed in Microsoft Fortran 4.0 and uses IBM PC assembly language. Details of the programming design are described elsewhere[1].

GAUGE can be implemented on IBM PCs, or compatibles, and supports both Enhanced Graphics Adapter (EGA) and Color Graphics Adapter (CGA) monitor options. The minimum required hardware is an IBM PC with tow floppy diskette drives, 640K of memory and the CGA monitor. For performance, an IBM AT with a hard disk, an 80287 numerical coprocessor, and an EGA card is recommended.

Functionally, GAUGE consists of three individual parts: a graphical processor which performs all the pre- and post-processing of GEMACS derived data, a macro-processor[2] to enable more complex geometry structures to be defined and stored in a macro library, and translators which change the data format of the parent program for suitable processing[3].

Much of the design philosophy for the GAUGE program was developed at Northrop as part of an on-going IR&D research activity entitled *"User-friendly Electromagnetic Workstation"*, and has been previously published [4]. This paper will show how the techniques embodied in the GAUGE graphical processor are applied to four specific electromagnetic modeling examples. The examples discussed are 1) bistatic scattering from a cube, 2) electromagetic coupling between AIM-7 missile and illuminator, 3) MOM/GTD hybridization modeling for a spiral antenna, and 4) the induced skin current from near field shipborne antennas computed by NEC. The first example discussed, though simpler electromagnetically, will be covered in more detail than subsequent examples to introduce the reader to the GAUGE graphical processor menu structure.

The graphical features illustrated in relation to these electromagnetic examples are: view (zoom, view angle, color etc.) rotate/translate, interactive picks, rejects, merging models, saving all or part of a model, color coding elements, contours on structure, two dimensional plots, electronic cut and paste, and hardcopy to a pen plotter or HP laserjet printer.

BISTATIC SCATTERING from a CUBE

For this first simple example, the steps in solving a GEMACS problem using the GAUGE graphical processor will be described in some detail. Suppose we wish to compute the far field scattering at 300 MHz from a simple cube with dimensions 0.1 x 0.1 x 0.1m from a plane wave source with a vertically polarized E-field located at THETA=90 PHI=0, and the observation is from PHI=0 to PHI=180, and THETA=90. We wish to find the current and field distribution at both 300 MHz and 9 GHz.

GEMACS can be used to solve this problem using the MOM solution technique at 300 MHz and the GTD method at 9 GHz. Formerly, we would have used the GEMACS command language to formulate this problem and its rather rudimentary tabular output to view the results. But now the model can be easily constructed with the pre-processor option of GAUGE, the model integrity once built can be viewed and modified if

necessary, while the post-processor can be used to display the GEMACS computed results. Figures 1.A and 1.B show the extent of the graphical processor menu tree and will not be discussed in detail here. It is possible, however, even for the casual reader, to see the relationship between the GAUGE main menu and the first tier of sub-menus which are outlined in bold.

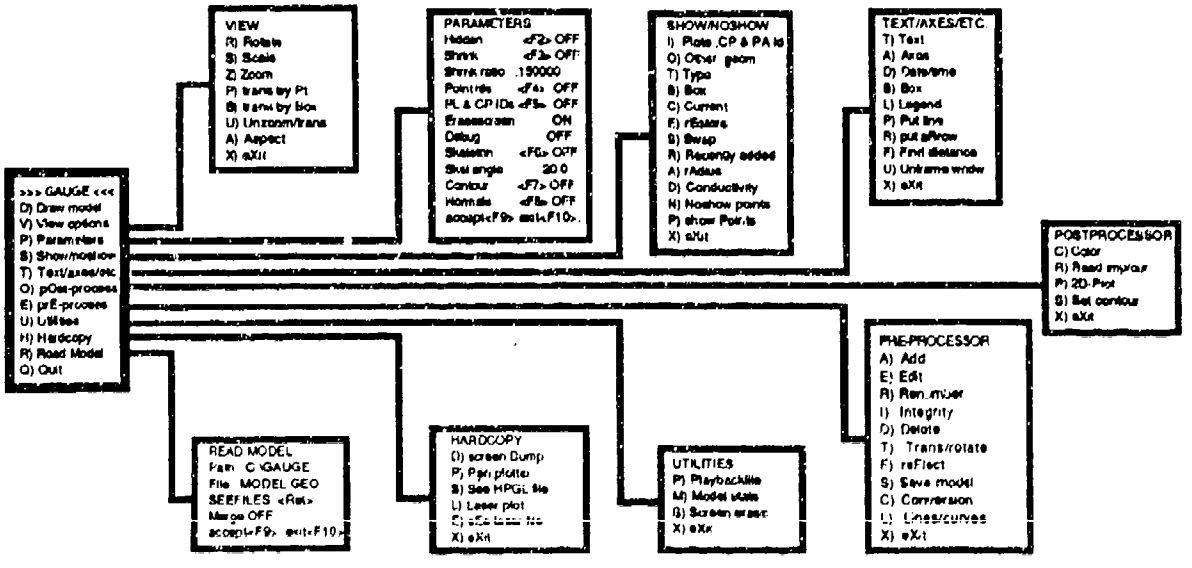


FIGURE 1.A Graphical Processor Tree (First Level)

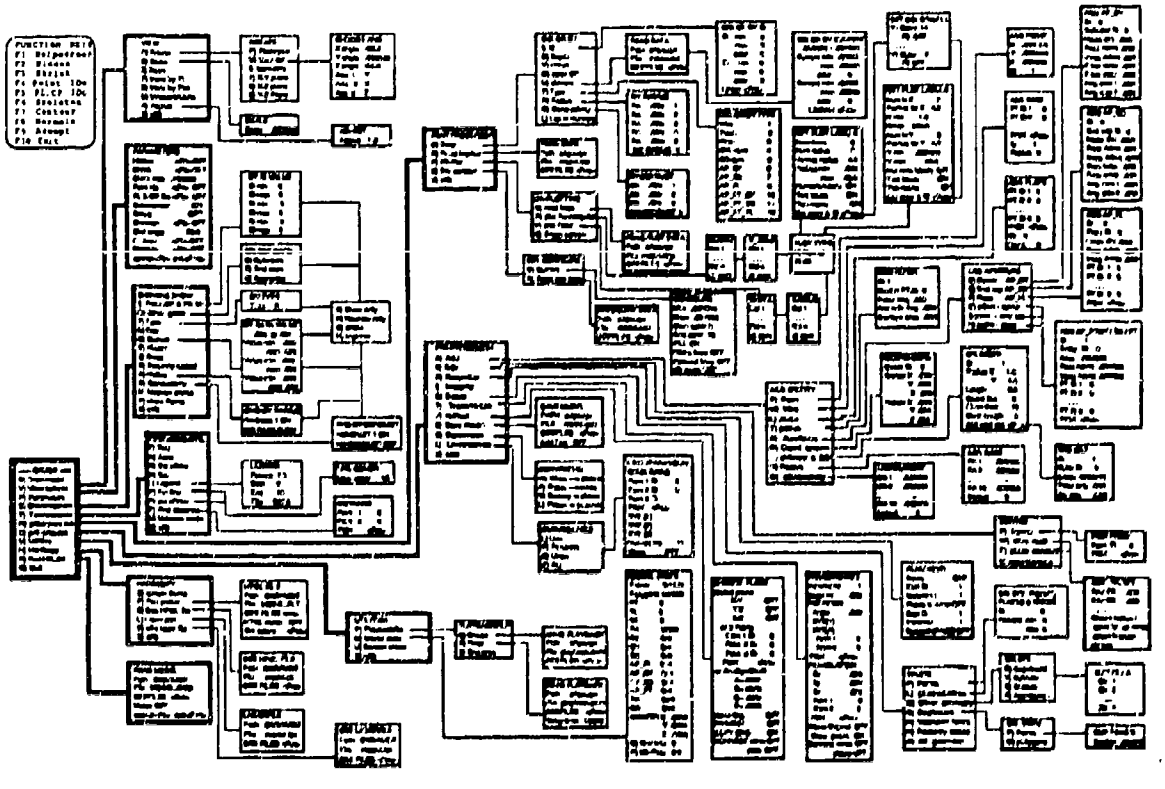


FIGURE 1.B Graphical Processor Tree (Extensive)

Construction with the GAUGE Pre-processor Options

The first task is to provide four points defining the base of the cube: (-.05, -.05,-.05), (0.05,-0.05,-.05), (.05,.05,-.05), (-.05,.05,-.05). These points are provided through the use of the pre-processor's *add points* menu. The *point ID* starts at "1" and automatically increments by unity. Upon exiting the menu, four points are drawn on the screen.

Rather than specify each separate corner point to build the wire grid model, it is quicker to make a plate and then use the pre-processor's powerful translate features to construct the cube. This can be accomplished in two easy steps in the *Translate/rotate* option of the pre-processor function by using the *add plates* and *connect Plates* sub-options.

The final step in constructing the cube is to check the plate normals. Normals may be turned ON in the *parameter* menu, as may plate ID values. When the model is re-drawn, it is clear that plate ID 1 has a normal pointing towards the interior of the cube. From the *edit plate normals* menu in the pre-processor we can specify plate ID 1. When the model is re-drawn all the normals will be correct as shown in Figure 2. The cube can then be retained in a file specified in the pre-processor *save model* menu, assigned the file name "cubeplat.geo" and used as a GTD plate geometry model for GEMACS.

Cubeplat.geo shown with IDs and normals

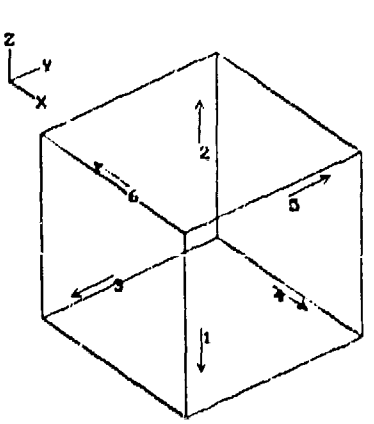


Figure 2

The next objective is to build a wire frame model of the cube to use in the GEMACS MOM modeling solution process. This is an easy task - accomplished in one step from the pre-processor *plates ==> wires conversion* menu. When the model is re-drawn (with shrink plot ON) the plates and wires can clearly be distinguished not only by their shapes but also by the different colors used to display plates and wires. The plates are now unnecessary and should be deleted. One way to delete the plates is to go to the *show/noshow* menu and specify *show by type*. Wires are selected by specifying type 1 and *show only*. When the model is re-drawn, only the wires will be displayed. The plates are then deleted from the pre-processor *delete noshow items* menu. Nothing changes in the display of the model, but the *model stats* sub-menu under *utilities* shows that there are only 12 wires (CP) in the model.

At this point the wire ID values should be checked, the wires were created when the plates were still in the model and so have ID values that were automatically incremented. Turning *plate&CP&PA ID* ON in the *parameter* menu shows that the wire IDs start at 7. The wires are renumbered in the pre-processor *renumber* menu by turning *plates&CP&PA* ON and not changing the default start ID and increment. When the model is re-drawn, see Figure 3, the ID values start at 1. This wire frame model may be retained in the pre-processor *save model* menu under the filename "cubewire.geo".

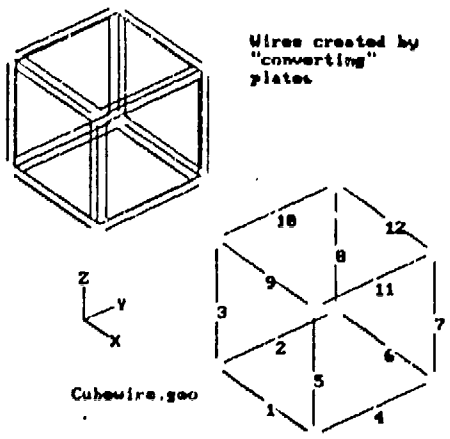


Figure 3

After creating the two geometry files, the GEMACS command language would have to be added to the geometry description to complete the required GEMACS input deck used to process the results for the wire grid MOM model at 300 MHz and GTD model at 9 GHz. This is explained in greater detail in [2] Section B. However, for information purposes, the GEMACS command deck for running the MOM example for this problem is shown in Figure 4.

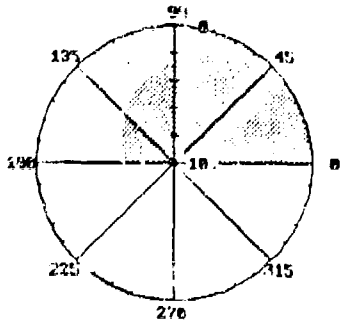
```
      $
      $  GEMACS COMMANDS TO CALCULATE BISCATTERING FROM A CUBE
      $  AT 300 MHZ BY METHOD OF MOMENTS.
      $
      NUMFIL=17
      TITLE "WIRE GRID OF A CUBE"
      FRQ=300.
      SETINT MOM
      GMDATA=CUBE
      ZGEN GMDATA=CUBE ZMATRX=ZIJ                                  GEMACS
      $RC=ESRC(CUBE) SW=-1.,0. THETA=90. PHI=0.                    COMMAND
      SOLVE ZIJ*I=SRC                                              STREAM
      PRINT I                                                      ADDED
      FFLD1=EFIELD(CUBE) T1=90. P1=0. DP=1. P2=180.                TO GEOMETRY
      PRINT FFLD1                                                  FILE
      END OF COMMANDS                                              COMPLETES
$                                                                  GEMACS
$  GEMACS GEOMETRY WIRE GRID REPRESENTATION OF CUBE                INPUT DECK
$
RA  .10000E-02
PT      1     -.5000E-01     -.5000E-01     -.5000E-01
PT      2      .5000E-01     -.5000E-01     -.5000E-01
PT      3      .5000E-01      .5000E-01     -.5000E-01
PT      4     -.5000E-01      .5000E-01     -.5000E-01
PT      5     -.5000E-01     -.5000E-01      .5000E-01
PT      6      .5000E-01     -.5000E-01      .5000E-01
PT      7      .5000E-01      .5000E-01      .5000E-01
PT      8     -.5000E-01      .5000E-01      .5000E-01
CP      1      2      1      1      1
CP      1      4      1      2      1
CP      1      5      1      3      1                             GEOMETRY
CP      2      3      1      4      1                             COMMANDS
CP      2      6      1      5      1                             CREATED
CP      3      4      1      6      1                             BY THE
CP      3      7      1      7      1                             PREPROCESSOR
CP      4      8      1      8      1                             AND STORED
CP      5      6      1      9      1                             IN
CP      5      8      1     10      1                             CUBEWIRE.GEM
CP      6      7      1     11      1
CP      7      8      1     12      1
 END
```

FIGURE 4 GEMACS Command Deck

Model Display and Plotting with the GAUGE Post-processor Option

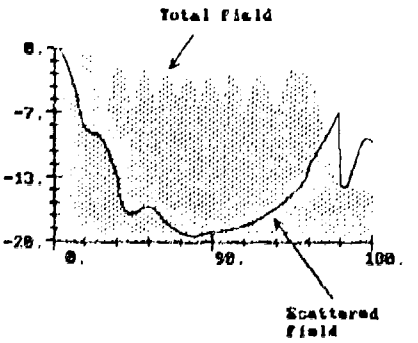
The GAUGE graphical processor can be used to examine the results of the GEMACS run. Assume that the fields and currents computed by GEMACS are in a suitable data format for further processing by the post-processor ([2] Section B) and stored in "cubewire.cr1". Current can be mapped onto the wireframe model and displayed by color. The *color by current* menu in the post-processor option maps the current density to the geometry structure. The results are not shown (monochrome paper) but display the highest current along the wires parallel to the Z-axis as would be expected. The global axes and a legend showing the correspondence of current to color values can also be added using the *text/axes/etc.* menu option.

An E-field pattern is displayed by choosing *2-D plots* under the post-processor menu, then *read plot data* and specifying the file "cubewire.ef1" which was created by the GEMACS output translator. Of the eight columns of data available, the only data to be used in the polar plot are the "PHI" values (angle) and the "E-THETA" values for the radii. A dB plot is chosen and the minimum radius value is set to -10. The *set color&fill* menu is used to set the color to pink (12) and fill turned ON. A box outlining the size of the plot is moved and sized on screen and, then, the polar plot is drawn as illustrated in Figure 5.



Far field polar plot using the output file "cubewire.ef1".

FIGURE 5. Polar Plot



Rectangular plot showing the data files "cubeplat.ef1", and "cubplot.ef1".

FIGURE 6. Rectangular Plot

The results of the GTD run are displayed by again choosing *2-D plot* and reading the plot data file "cubeplat.ef1". *Rectangular plot* is chosen, showing the total E-field from the source and the scattered field from the cube. The X-axis (horizontal) is "PHI", and the Y-axis is "E-THETA". A dB plot is chosen and the formats for X and Y are set. *Set color&fill* is used to set the color to green (4) and fill turned OFF. A box then appears on screen and is moved and sized. When return is pressed, the rectangular plot is then shown as illustrated in Figure 6.

AIM-7 ILLUMINATOR

Our next example shows some of the graphical features used to model the AIM-7 illuminator. A previous publication [5] showed how Northrop's 3-D mainframe CAD package (NCAD) could be used to generate or display sophisticated aircraft geometry

Figure 9 shows a cavity-backed spiral constructed using the GAUGE graphical processor's pre-processor function to build the GTD portion of the geometry with plates, and the macro-processor for the MOM spiral portion. Figure 10 shows the far field pattern with text to annotate the plot.

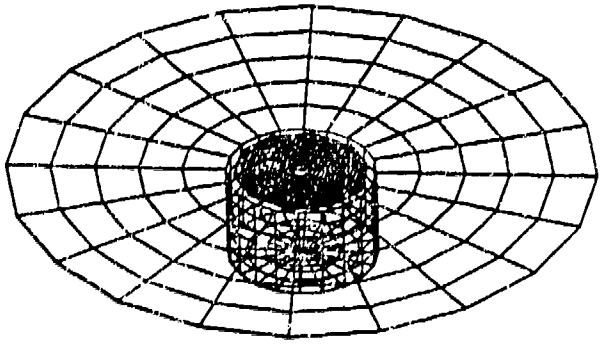


FIGURE 9 Cavity-backed Spiral

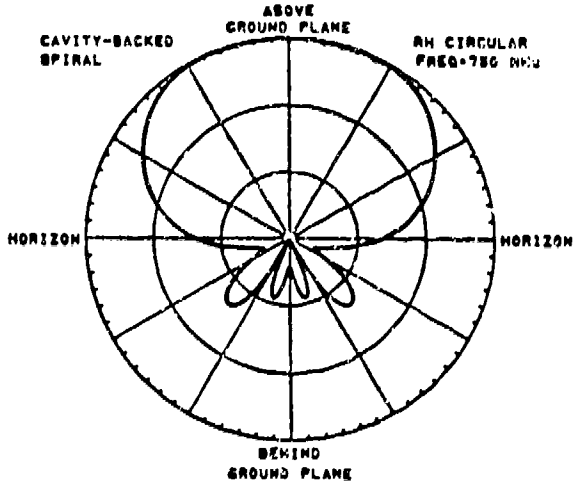


FIGURE 10 Far Field Pattern

ANTENNA NEAR FIELD DISTRIBUTION on SHIPBORNE PLATFORM

The final example demonstrates the capability of GAUGE to accept and process NEC data. GAUGE has been designed with sufficient flexibility to interact with other electromagnetic codes and can interpret NEC geometry commands. The graphical processor cannot interact directly with NEC, but (as in the case for GEMACS data) needs to go through a translator [6]. Details of this are explained in ([2], section D.1).

Figure 11 shows a NEC MOM geometry model of a ship displayed by the GAUGE graphical processor. The *zoom* feature of the pre-processor function, combined with the ability to change the view angle, uncovered a number of duplicate wires which were subsequently removed by the *delete points* menu. After performing all the model integrity checks in the graphical processor, an antenna radiation problem was run using a mainframe version of NEC; and the results were saved in an external file.

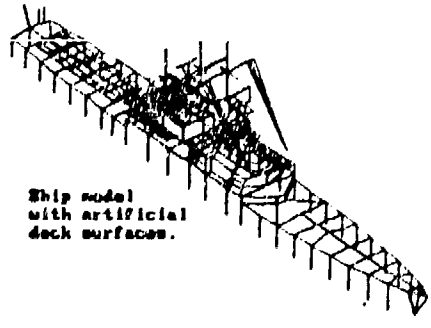


Figure 11

Since the antennas are modeled with a different wire radius, they can be identified by the post-processor option to select wires by *radius* value which, in conjuntion with the very powerful *show/no show* option, can be used to identify the antenna locations. This is illustrated by Figure 12.

models, which could be reduced from a MOM representation to a simplified GTD form by interactive picks. The same methodology can be used with the GAUGE graphical processor at the PC level without incurring the expense and complexity of a sophisticated mainframe refresh tube or software support.

Figure 7 illustrates the polar antenna patterns for roll and yaw plane cuts of the AIM-7 illuminator transmit antenna located in the fairing of the vertical stabilizer. The GAUGE post-processor features illustrated here include not only *model view*, *polar plotting*, and *textual annotation*, but the ability to associate related computed observables (plots, model, etc) in one screen by *Electronic Cut & Paste*. *Hard copy* to an HP laserjet is also illustrated since the figures are photocopies of the actual plots created by the GAUGE graphical processor.

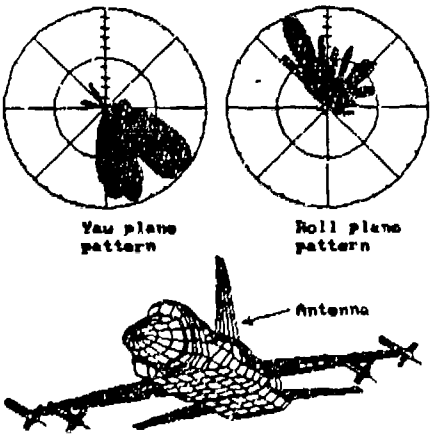


Figure 7

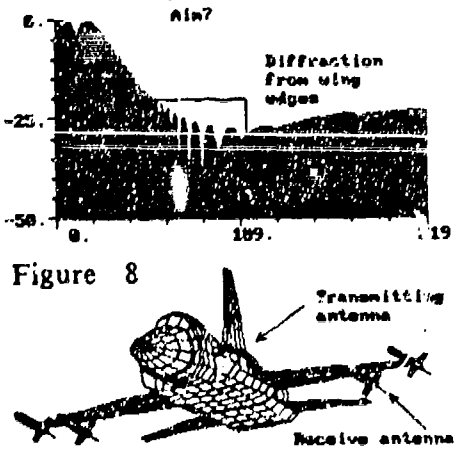


Figure 8

Figure 8 shows the electromagnetic coupling between the transmit and receive antennas mounted on the missile located on the outboard pylon. The upper plot shows the expected diminishing of antenna-to-antenna coupling (dB) with distance after the missile is fired. The figure illustrates the post-processor *linear plotting* capability and the ability to draw a box to encapsulate areas such as the wing diffraction portion of the plot.

MOM MODELING of a CAVITY-BACKED SPIRAL

An application of the GEMACS MOM solution technique to compute the far field antenna pattern of a cavity-backed spiral is described in [6] *GEMACS Source Book*. Antenna input impedance, current distribution and field patterns can all be computed by a GEMACS hybrid run, when the geometry has been defined. The crux of the problem is to construct the center archimedean spiral portion of the antenna. This would be a formidable undertaking if constructed manually by the modeling technique offered in the standard GEMACS program.

GAUGE, however, offers a powerful macro modeling feature [3] separate from the graphical processor, which alleviates the tedium of calculating data by hand, and re-entering frequently used descriptions of structures or parts of structures. A Macro-Library capability in GAUGE allows a GEMACS or GAUGE user to define and store parametric geometry models in plain English text without having to write new FORTRAN and modify GEMACS or GAUGE. This is also described in ([2] Section Dj).

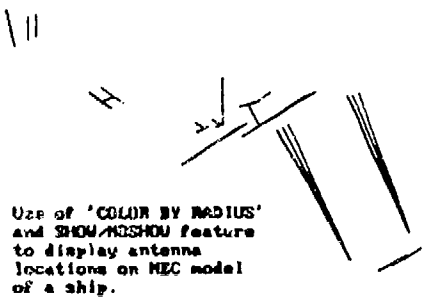


FIGURE 12 Antenna Locations

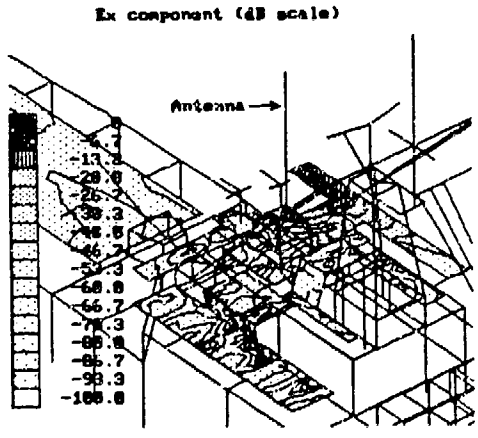


FIGURE 13 Current Contours

Figure 13 illustrates yet another powerful feature of the GAUGE Output translator, the ability to map data onto the geometry and look at its distribution. This was performed for the distribution of E-Field component across the ship's deck due to near field antenna excitation. This is particularly useful for locating "hot spots" and critical areas on the ship's deck where sensitive equipment should not be placed. Figure 13 further illustrates the graphical processor's *zoom* capability, and the *grey-scale* shading feature, useful for assigning different grades of shadow for specific ranges of mapped current as an alternative to color.

CONCLUSIONS

The lessons learned during the IR&D research activity *User-Friendly Electromagnetic Workstation* program [4] made it possible to code a versatile graphical interface, GAUGE, in a short six month period. The GAUGE design interfaces a powerful set of features, based on the IBM PC, to the parent GEMACS code. GAUGE can be interfaced with other codes by writing a suitable translator as has been proven with NEC, BSC, MISCAT and NASTRAN. All of the software is public domain and can be obtained from RADC/RBCT, Griffiss AFB, New York 13441-5700, through the government representative Mr. K. R. Siarkiewicz, at (315) 330-2465.

REFERENCES

1. Upshaw, G., Grage, M., Siarkiewicz, K. R., "Graphics Programming for Electromagnetic Modeling," Northrop Corporation, presented at the Fourth Annual Review of Progress in Applied Computational Electromagnetics at the Naval Postgraduate School, Monterey, CA, March 1988.

2. Lockyer, A. J., Tulyathan, P., Upshaw, G., Grage, M., "Graphics Aids for Users of GEMACS (GAUGE) Users Guide," Northrop Corporation, sponsored by Rome Air Development Center, under Contract F30602-87-C-0110, January 1988.

3. Coffey, E. L., Lockyer, A., J., Siarkiewicz, K. R., "An EM Language Translator and Macro Processor," Advanced Electromagnetics, presented at the Fourth Annual Review of Progress in Applied Computational Electromagnetics at the Naval Postgraduate School, Monterey, CA, March 1988.

4. Lockyer, A. J. and Tulyathan, P., "PC Electromagnetic Workstation Good NEWS for ACES' NEEDS," Northrop Corporation, presented at the Third Annual Review of Progress in Applied Computational Electromagnetics at the Naval Postgraduate School, Monterey, CA, March 1987

5. Nelson, W. S., Tulyathan, P., Wehling M. L., "Application of Computer-Aided Design to Electromagnetic Modeling," Northrop Corporation, presented at the Second Annual Review of Progress in Applied Computational Electromagnetics at the Naval Postgraduate School, Monterey, CA, March 1986

6. Coffey, E. L., Kadlec, D., "GEMACS Source Book", Advanced Electromagnetics, sponsored by Rome Air Development Center, under Contract F30602-86-C-0015

GRAPHICS PROGRAMMING FOR ELECTROMAGNETIC MODELING

Garth Upshaw and Michael J. Grage

Aircraft Division, Dept. 3564/83
Northrop Corporation
Hawthorne, California 90250

Kenneth R. Siarkiewicz
Rome Air Development Center (RBCT)
Griffiss AFB, New York 13441

ABSTRACT

A new, IBM PC based, graphical interface for GEMACS and other electromagnetic codes is described. GAUGE enables users to perform pre- and post-processing of electromagnetic models and data. Interactive graphics and CAD features are tailored directly towards electromagnetic modeling. The discussion emphasizes the design philosophy during *programming* the GAUGE graphical interface software, and highlights *database design, language choice, menus, drivers, utilities, hardcopy and hidden line compromise*, and *documentation* as key items adopted by the approach.

INTRODUCTION

A new, user-friendly, graphical interface termed GAUGE (*Graphical Aids for Users of GEMACS*)[1,2] has been developed for use with GEMACS (*General Electromagnetic Model for the Analysis of Complex Systems*)[3] and other electromagnetic codes. The GAUGE software has been written for installation on the IBM PC and is programmed in Microsoft Fortran 4.0 and IBM PC assembly language.

GAUGE resides at the PC level and interacts with mainframe-implemented versions of GEMACS by external file manipulation. The graphical interface helps an engineer build, view, and store geometry for electromagnetic models, and conveniently displays GEMACS processed results in a variety of different ways. GAUGE was programmed specifically for GEMACS to support all version 4.0 electromagnetic solution techniques including MOM, GTD, FD and hybrid formulations†, and wires, patches, plates, cylinders, end caps and apertures for building complex shapes. Enough flexibility was programmed into GAUGE for it to "stand alone" or interface with other electromagnetic codes. The rich set of graphics features developed on this program [1,2] can already be interfaced (to a degree) to NEC (*Numerical Electromagnetic Code*, BSC (*Basic Scattering Code)*, and MISCAT.

The programming of the GAUGE graphical interface was performed in a six-month period. The programming described was accomplished by Northrop Corporation and sponsored by RADC/RBCT under contract F30602-87-C-0110. During that period, over 350 subroutines and 39,000 lines were coded.

† Method of Moments (MOM), Geometrical Theory of Diffraction (GTD), Finite Difference (FD) are different electromagnetic solution techniques which can be hybridized in GEMACS.

The success of the contract depended on programming GAUGE quickly and choosing a very specific approach to the program design. Some key attributes of this approach are discussed herein and include *database design, language choice, utilities, hardcopy and hidden surface*, and *documentation* with emphasis throughout on the programming design rationale.

GAUGE DESCRIPTION

GAUGE, illustrated in Figure 1, is not executed in a single program step. The complete GAUGE ensemble consists functionally of four program modules: a graphics processor, input translators and output translators, and a macro-processor. The translators are used to convert between the EM-derived database format used by GEMACS and the database adopted by the GAUGE graphics processor, which are different (as explained later). Details of the macro processor, which enables more complex geometries to be defined, the translators, and how GAUGE interfaces with GEMACS, can be found in References [1,2,4].

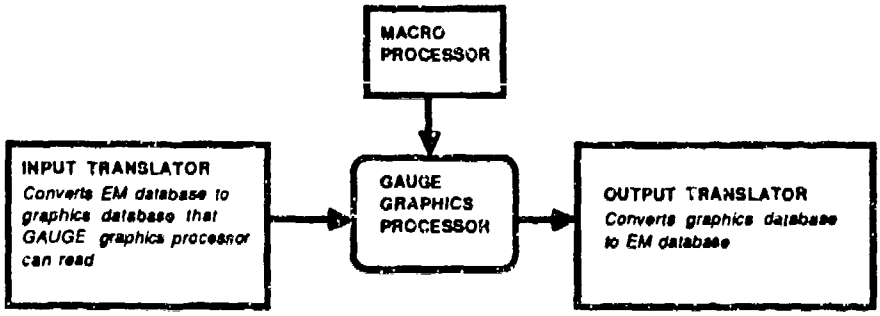


Figure 1. GAUGE Modules and Interface

The focal point of the interface design is the graphics processor comprising more than 70% of the total program code, whose role is to provide a wealth of graphics features for the pre and postprocessing of GEMACS derived data. The graphical features are not discussed in detail but include: *create wires, patches, plates, cylinders, end caps, apertures, rotate/translate, projection onto plane, reflection through plane, use of arrow keys for geometry construction, 3-D rotations, zooms, translations, scaling, show noshow options, shrink plots, skeleton plots, hidden surface plots, ID labeling, and polar and cartesian field pattern plotting.*

GAUGE can be implemented on IBM PCs or compatibles and supports both Enhanced Graphics Adapter (EGA) and Color Graphics Adapter (CGA) monitor options. The minimum required hardware is an IBM PC with two floppy diskette drives, 640K of memory, and the CGA monitor. For performance, an IBM AT with a hard disk, an 80287 numerical coprocessor, and an EGA card is recommended.

PROGRAMMING DESIGN APPROACH

Background and Restrictions

Many of the concepts used in designing GAUGE were derived from a parent IR&D program at Northrop entitled *"User-friendly Electromagnetic Workstation"*, where the design objective is to develop a graphical interface for *many* codes sharing a common data base. A PC-based graphics package termed PCNEWS (*PC - Northrop Electromagnetic Workstation*) was developed[5], but the coding requirements were entirely different. PCNEWS[6] is coded in the "C" programming language and uses an inexpensive commercial graphics package (Metagraphics) as the interface driver to the IBM graphics card monitor. The restrictions placed on the GAUGE software design required all software to be coded in Microsoft FORTRAN and no commercial software to be used.

Despite these restrictions, the programming design goal was to achieve a user-friendly, portable, modular graphical interface that would be easy for engineers to use and flexible enough to interface a variety of EM codes (other than GEMACS). From the many important considerations used to achieve this goal key items discussed are data base design, menu structure, basic algorithms and utilities, onscreen help, and documentation.

Database Design

The database format is the most critical element of the graphical processor design. It enables a large repertoire of graphical features to be coded and used to display EM models in an efficient, flexible manner giving the graphical processor considerable generality.

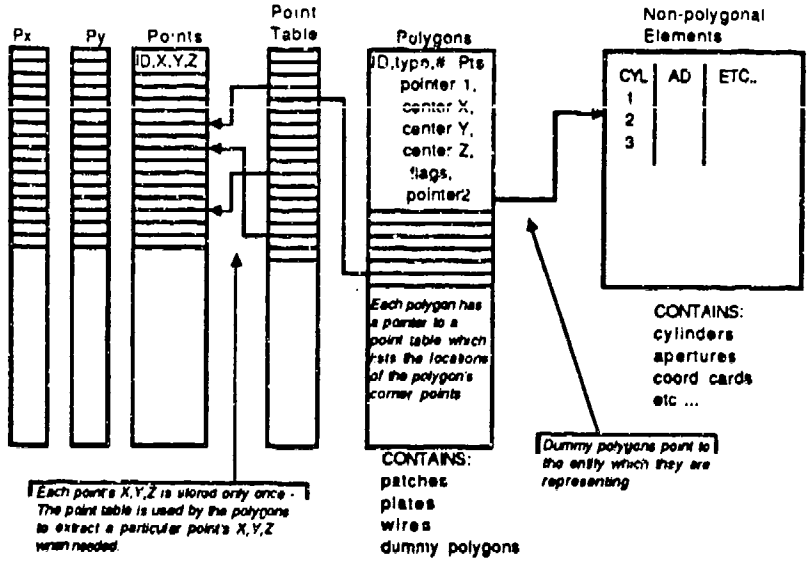


Figure 2. Graphics Data Base Arrays

Careful examination of the GEMACS database revealed that it was not suitable, or optimized, for the display of graphics. For example, a cylinder must be converted to points and polygons before display. Similar shortcomings were found with other electromagnetic codes (NEC, BSC, etc.) while considering how to make the software versatile.

It was thus decided to choose points and polygons for the new data base format for simplicity and efficient display of GEMACS data. Figure 2 illustrates how data are stored in the graphical processor database in a series of arrays. There are point arrays and tables and a large polygon table containing all the wire, plate, patch and polygon, information for GEMACS, and another table for nonpolygonal elements for GEMACS cylinders, apertures, coord cards etc.. GEMACS geometric entities that are not points or polygons (e.g. cylinders) are kept in separate arrays; however, for display purposes, dummy points and polygons of these entities are generated and also stored in the point and polygon tables.

This data base arrangement was adopted for simplicity and speed. Plotting routines merely have to cycle through the point and polygon tables when displaying information. The trade-off is simplicity and speed versus memory allocation. The generated lists of dummy polygons can be large but are drawn efficiently. The number of points and polygons is limited by memory allocation to 1500 each, which is sufficient for most modeling purposes. Figure 3 shows a GEMACS MOM wire grid model of an F-20 plotted near the data base limits.

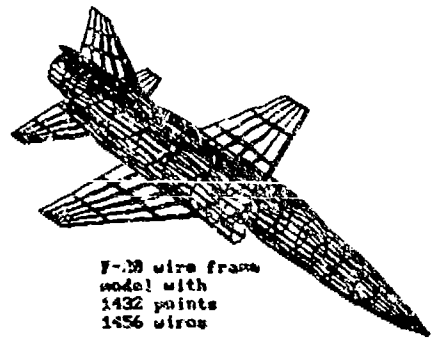


Fig. 3 Wire grid model at Database Limits

3-D Considerations

A method had to be devised to visually represent three-dimensional objects formulated by MOM and GTD electromagnetic modeling of cylinders or 3-D aircraft geometries on the two-dimensional screen.

The geometry data-base depends on points and how they are connected. Every polygon refers to the stored point arrays for its corners. For model viewing on the screen each point's world coordinates needs to be converted to screen coordinates representing the screen pixels. This process is accomplished in three main steps indicated in Figure 4. First, a view orientation specified by the user is used to create a four by four rotation matrix. Next, the rotated and projected coordinates (P_x, P_y) for each point are generated using the rotation matrix. Finally, the rotated and projected coordinates are scaled and shifted to the exact screen pixel locations.

Storing P_x, P_y (the rotated projected coordinates) allows great flexibility in model display. The model can be redrawn easily with little recomputation as long as the view orientation does not change.

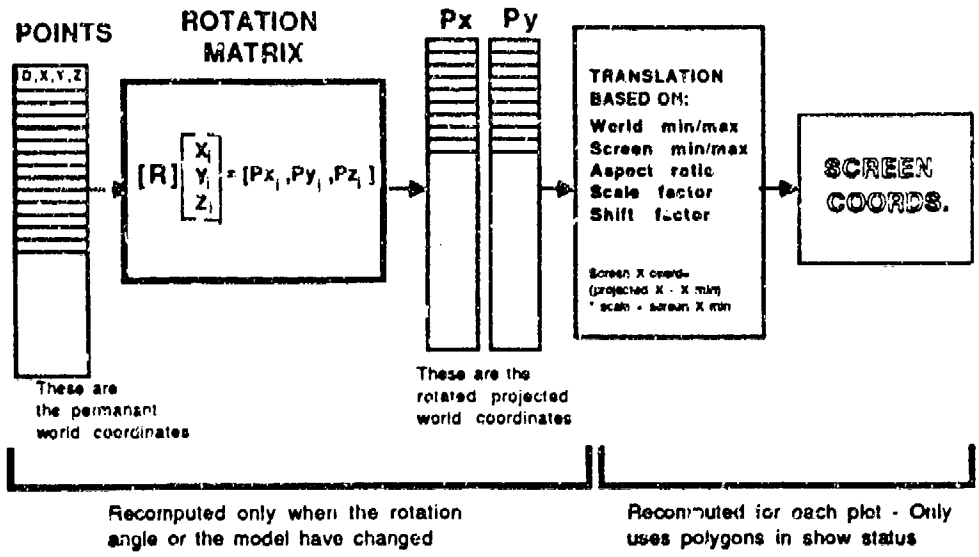


Figure 4. World-Coordinates to Screen-Coordinates Conversion

Polygonal Representation of 3-D Objects

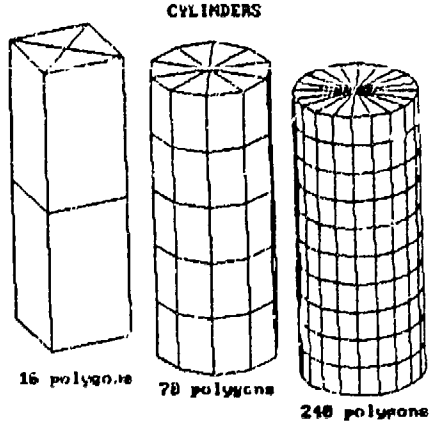


Fig. 5 Polygonal Faceting of Cylinder

As described earlier, the strict mathematical representation of a 3-D object cannot be represented exactly on a flat screen. Cylinders used in GEMACS GTD modeling, for example, are represented as faceted polygons for display purposes. Predictably, cylinders displayed with more faceting look closer to the real thing than coarsely faceted representations, but there is a trade-off between computer memory requirements and display time. The smooth-looking screen image of multifaceted cylinders must also be traded with complexity, particularly when modeling GEMACS' cylinders with end caps and multiple apertures. Figure 5 shows several representations of cylinders with different degrees of faceting.

Language Choice

The "C" programming language would have been (and still is) the preferred choice for this interface design, for its high-level and low-level language flexibility, its built-in library utilities, and its recursive nature; nevertheless, a program design requirement was to provide software to the government that could easily be modified when distributed to the current GEMACS user community, who are predominantly well versed in FORTRAN. This need caters to the potential customer who may wish to customize or modify the delivered GAUGE software package to individual requirements.

For similar reasons, it was also required that software design should not include any commercial software such as the Metagraphic's MetaWINDOWS[7] graphics toolkit that had been customized for development work on PCNEWS[5,6]. The restrictions here involve legal implications as well as third party dependency.

The majority of the software for the graphical processor consists of 239 subroutines coded in Microsoft FORTRAN; the remaining part comprises 22 subroutines

The *graphic drivers* and *utility routines* were design factors instrumental in progressing the skeleton design toward more established code.

Graphic Drivers

The timely design of the assembly language graphics drivers presented a formidable problem that had to be quickly resolved, since the FORTRAN graphics software routines could not be tested without the drivers "in place". An interim solution to this difficulty was provided by the Metagraphics' Metawindow routines already developed for PCNEWS and described elsewhere[5,6]. This solution permitted graphics subroutine software to be developed and tested while the assembly language drivers were being coded. The Metagraphics interface used for bit mapping and screen operations was completely replaced by assembly language routines in the final software.

Typical assembly language routines coded include: *drawdot*, *drawpolygon*, *fillpolygon*, and *drawmessage*. Details of these routines with subroutine descriptive data can be found in Reference [1], Section F. Complete program listings are provided with the program source code.

Utility Subroutines

A library of utility subroutines was formed early in the software design phase. These utility subroutines greatly simplified the coding performed downstream and enabled the program to be accomplished within the tight schedule requirements.

Preeminent among routines developed for this purpose were the *menu utilities*. Implementing menus as utility programs early in the design phase standardized the menu appearance and prevented much duplication of code. Another important group of modular utility routines is contained in the *graphics module*. These routines were designed not only to facilitate programming as the software progressed but also serve to make the GAUGE graphical processor *portable*. The rest of the program *only* calls the FORTRAN routines in the *graphics module*, which call the appropriate assembly language routines. This isolates the rest of the code from dependencies on a particular graphics card or machine.

Another useful utility developed during the software development task was the *getfile* routine. This is used in any module for I/O to an external file providing extra features which cannot be accomplished by simple FORTRAN "open" and "close" statements. For example the *path* and *seefiles* option enables users to search any desired subdirectory for a user-specified extension.

HARDCOPY AND HIDDEN LINE COMPROMISE

There are difficulties posed by providing "true" *hidden line*[8] capabilities for hardcopy devices driven from personal computers. The problem is associated with the PC's restricted processing power (as compared to mainframes) to compute multiple intersections required by true hidden line algorithms[9].

The graphical processor provides hidden line capability with the *painter's algorithm* which is used to display models with their hidden lines removed on the PC video monitor. This technique uses a raster screen's ability to color fill polygons by overpainting the screen. The polygons are sorted and drawn in order from background to foreground; thus, closer polygons will "hide" portions of the model behind them.

written in IBM assembly language for the graphic drivers. The graphic drivers, discussed elsewhere, are used for bit mapping and screen operations interfacing with IBM's Extended Graphics Adapter (EGA), and Color Graphics Adapter (CGA) options for the screen monitor.

Menus, Drivers, and Utilities

The software design strategy adopted in the original phases of the program focused on developing a working skeleton outline that could initially read and perform very basic functions required by the final software. For example, the skeleton could read geometry files, view the screen model, and store model information in output files. The menu structure and appearance, were determined during the infancy of the design process even though a great majority of the menus originally acted only as "place holders". Gradually, these menus were finalized as the software design evolved. Figure 6 shows some typical menus used in the initial skeleton design, while Figure 7 shows the menu tree of the graphical processor.

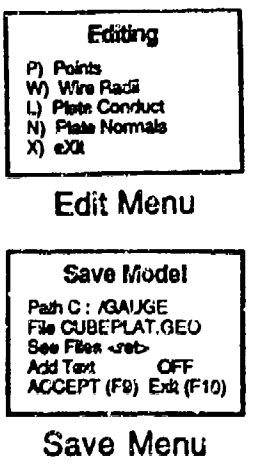


Fig. 6 Typical Menus

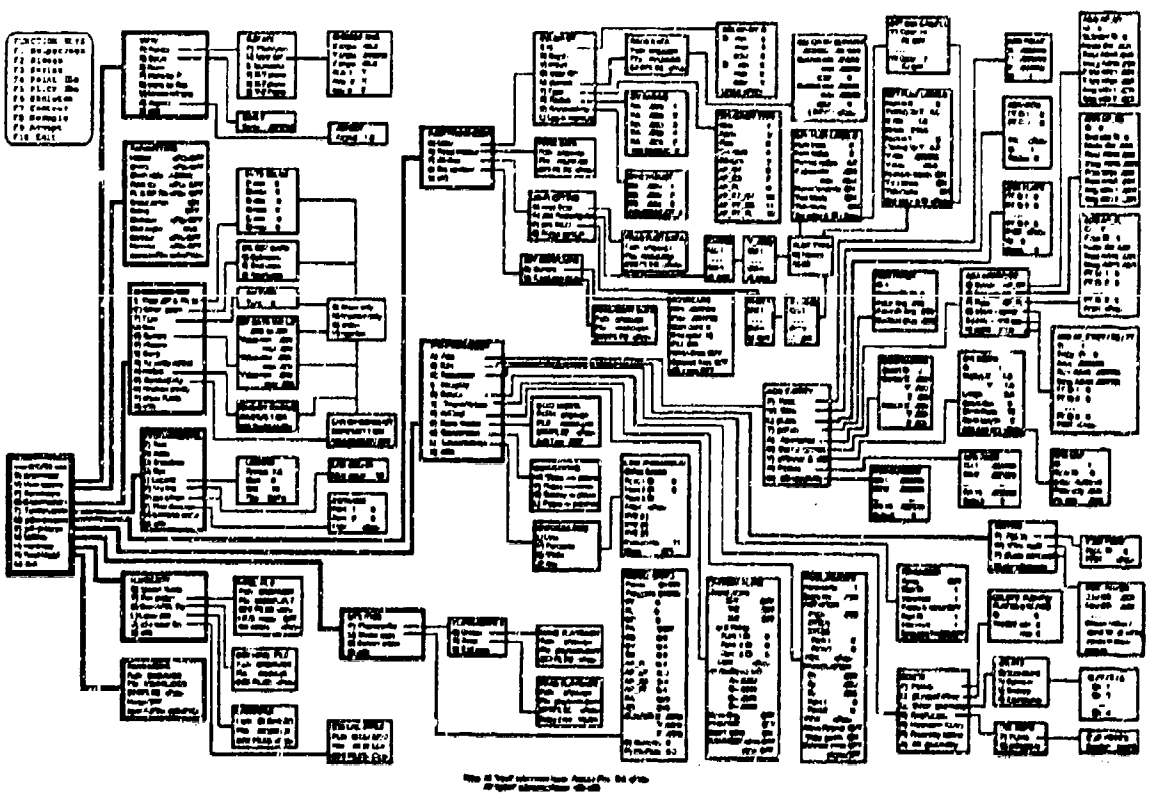


FIGURE 7. Menu Tree for Graphical Processor

This is illustrated in Figure 8 by comparing the original cluttered image with the resulting solid-looking profile. For screen viewing, the hidden line removal can be removed quickly and efficiently, and the screen can be dumped to a laser printer for high-quality hardcopy, or a dot matrix printer for draft-quality copies (see Figure 9).

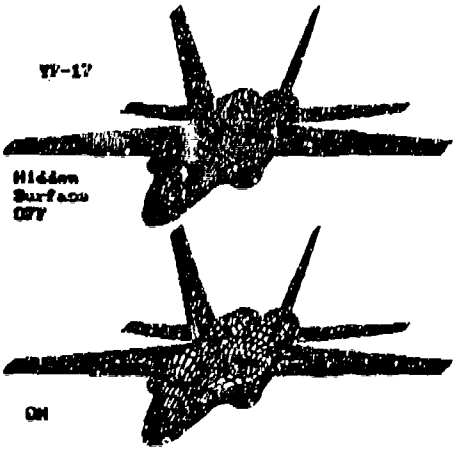


FIGURE 8. Hidden Line Removal



FIGURE 9. Draft Quality Print

The painters algorithm approach has been incorporated into the graphical processor design for hidden-line applications because the method is easy, quick, and flexible, and is not CPU intensive. But the real utility for this particular design is the flexibility of the technique. Hidden surface can be combined with other graphic features including *shrink*, *skeleton*, and *contouring*[1,5,6] to produce very powerful graphics for the post- and pre-processing of GEMACS data, including current mapping to structure. Figure 10 illustrates hidden surface, hidden surface together with the shrink option, hidden surface with skeleton, and finally hidden surface plus skeleton and contour fill features all combined.

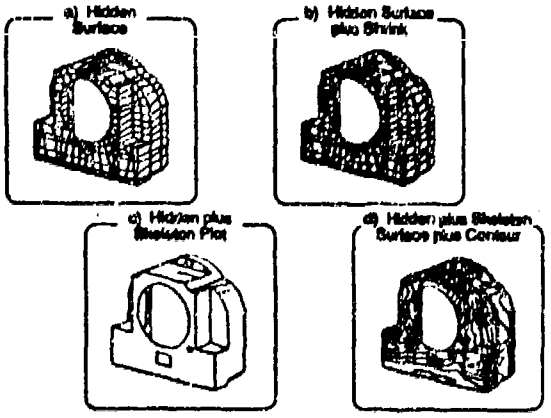


FIGURE 10. Hidden Surface Flexibility

The disadvantage of the painter's algorithm method is that it lacks some precision i.e. it is about 95% accurate, and it cannot draw models to non-bit mapped devices such as pen plotters. An alternative approach not currently supported by the graphical processor is to compare each of the polygonal faces to the remaining faces, or portions of faces that are not visible, and then draw only the visible lines. This method has not been installed in the current version of GAUGE but should be incorporated in a future upgraded version.

DOCUMENTATION

An exposition of the programming approach described in this paper must be addressed since it played an important role in the development of the software. Comments were provided liberally throughout the code to explain special or unusual features. Other programmers were the target audience. As each subroutine was coded, a header block defining its purpose and I/O variables was written (see Reference 1 Sections F,G,H). This proved useful for reference purposes during the software development phase.

A valuable feature which proved helpful during software testing, and for personnel unfamiliar with the software interface, was the incorporation of an on-line screen help facility that is readily available by pressing the *<F1>* function key from any menu. Twenty-two lines of text are used to convey guidelines for novice users. This is illustrated in Figure 11. Each menu contains a cross reference to more detailed descriptions contained in the program users guide (Reference 1. Section C).

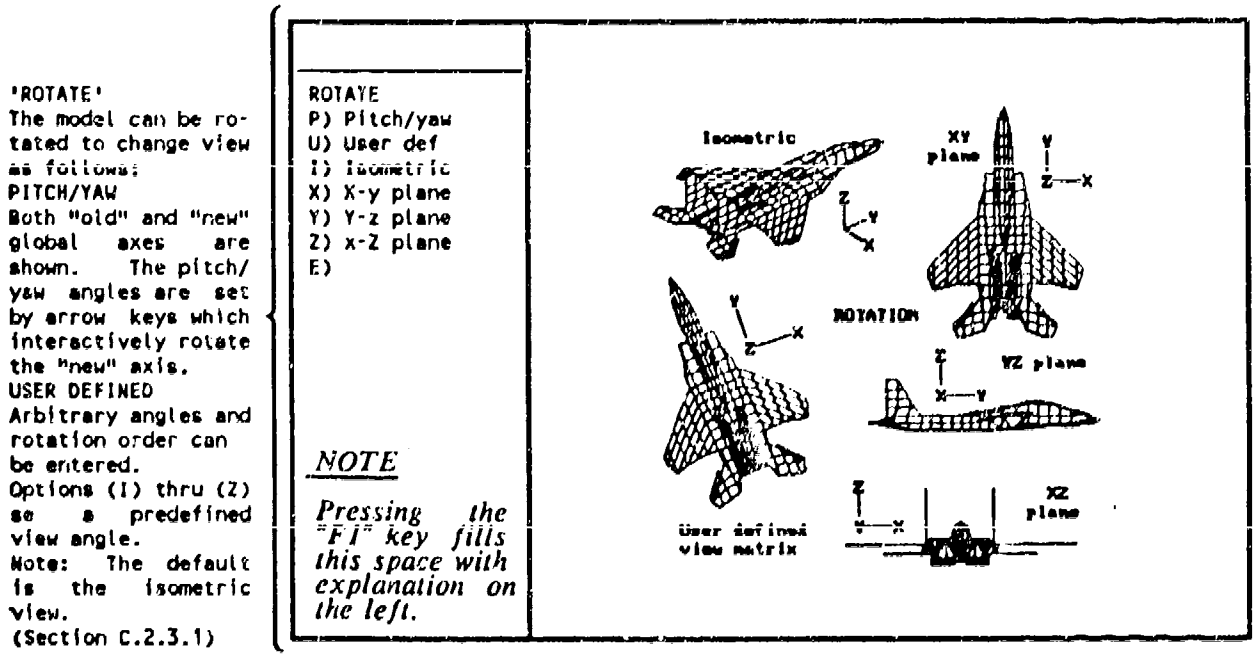


Figure 11. GAUGE On-line Help Feature

A further feature facilitating documentation was the *playback feature*. This is yet another helpful utility which enables keystrokes for a particular sequence of events to be recorded, stored in permanent file, and played back for viewing or demonstration purposes.

Since the GEMACS code does many things and is quite extensive (over 120,000 lines of FORTRAN), GAUGE is also large. The Users Manual therefore provides desriptions of each of the GAUGE program modules and their interaction with GEMACS. Information in the final report is presented in a progressive manner to avoid overwhelming the reader all at once. The documentation begins with a short introductory first section [1] and follows with a "Getting Started" section to provide an opportunity for a user to gain a quick appreciation of the graphics software capabilities without having to read the entire document first. The macro processor section and more detailed subsequent sections are intended for experienced GEMACS users.

CONCLUSIONS

Full justice to the entire set of software design considerations used in programming GAUGE cannot easily be given in a short paper of this nature, but hopefully the key items have been addressed. Experienced and novice GEMACS users are encouraged to obtain the software, which is public domain and available from RADC/RBCT, Griffiss AFB, New York 13441-5700, through the government representative Mr. K. R. Siarkiewicz, at (315) 330-2465.

REFERENCES

1. Lockyer, A. J., Tulyathan, P., Upshaw, G., Grage, M., "Graphics Aids for User's of GEMACS (GAUGE) Users Guide," Northrop Corporation, sponsored by Rome Air Development Center, under Contract F30602-87-C-0110, January 1988.

2. Lockyer, A. J. and Tulyathan, P., Siarkiewicz, K. R., "Graphics Aids for Users of GEMACS," Northrop Corporation, presented at the Fourth Annual Review of Progress in Applied Computational Electromagnetics at the Naval Postgraduate School, Monterey, CA, March 1988

3. Kadlec, D .L. and Coffey, E. L., "General Electromagnetic Model for the Analysis of Complex Systems (GEMACS), User Manual (Version 4)," The BDM Corporation, RADC-TR-87-68, Volumes I, II, and III, May 1987.

4. Coffey, E. L., Lockyer, A., J., Siarkiewicz, K. R., "An EM Language Translator and Macro Processor," Advanced Electromagnetics, presented at the Fourth Annual Review of Progress in Applied Computational Electromagnetics at the Naval Postgraduate School, Monterey, CA, March 1988.

5. Lockyer, A. J., "User-Friendly Electromagnetic Workstation," IR&D program Technical Brochure, Northrop Corporation, April, 1987

6. Lockyer, A. J. and Tulyathan, P., "PC Electromagnetic Workstation Good NEWS for ACES' NEEDS," Northrop Corporation, presented at the Third Annual Review of Progress in Applied Computational Electromagnetics at the Naval Postgraduate School, Monterey, CA, March 1987

7. METAGRAPHICS Software Corporation, distributor of MetaWINDOW graphics toolkit, 4575 Scotts Valley Drive, CA 95066.

8. Newell, M. E., Newell, R. G., and Sancha, T. C., "A Solution to the Hidden Surface Problem," Compcon Spring 1979, 8th IEEE Computer Society International Conference.

9. Sutherland, I. E., Sproul, R. F., Schumacker, R. A., "A Characteristic of Ten Hidden-Surface Algorithms," Compcon Spring 1979, 8th IEEE Computer Society International Conference.

MathPlot - A Modeling Tool for Scientists and Engineers

by

Daniel F. Higgins
Consultant
1040 Veronica Springs Road
Santa Barbara, CA 93105
(805) 682-5248

Introduction

Mathematics is the fundamental language used by scientists and engineers to describe and analyze physical phenomena. In fact, much of the basic training received by the scientist or engineer is designed to teach him or her how to understand and use this language of mathematics. This use of mathematics to express fundamental physical laws is not some historical accident; instead, it is based on the fact that mathematical expressions can be used to capture vast amounts of information in a very compact and succinct forms.

The scientist or engineer typically works with many types of mathematical expressions which are often combined to create a "model" of the phenomena under investigation. This model will depend on the expressions used and the values of parameters inserted in the expressions. Building a model or studying its performance often involves trying to understand the interrelationships between equations and the effects of parameter variations. One method for understanding such relationships is to characterize functional 'mappings' which relate input values to output values, and a method for displaying such functions is the xy-plot where y is plotted as a function of x.

MathPlot is a microcomputer program designed to help the scientist or engineer to build such mathematical models and to help in understanding the relationships by providing the capability for interactive graphical displays of various types of xy-plots. MathPlot is designed to run on the Apple Macintosh™ computer; it incorporates a number of the user-interface features built into that computer such as buttons, windows, and menus. The MathPlot program is written in MacForth (from Creative Solutions) and is basically a specialized set of extensions to the Forth computer language.

MathPlot lets the user create a mathematical model by typing some set of expressions describing the basic parameters and functions which characterize the phenomena of interest. The functions can then be plotted on linear or logarithmic scales and the parameters varied by simply selecting a parameter and changing its value by 'clicking' a button or typing a number. Parameters are stored in a linked list so that whenever one parameter is changed, any other parameter which depends on it is

also updated to reflect the new value. New functions can be overlayed on previously plotted functions or the same function can be replotted with a new parameter value. This whole process is designed to be easily implemented so that the scientist or engineer can concentrate on the equations in his/her model rather than the mechanics of the computer program.

MathPlot is in some ways similar to a spreadsheet program. The primary idea used in a spreadsheet, however, is some table of numbers. That table can depend on equations or be plotted in a graph, but the tables of numbers themselves are the primary focus of spreadsheet operation. (This is not too surprising, since spreadsheets were designed for financial planning where numbers (i.e. dollars) are the primary focus.) In MathPlot, however, the mathematical expression is the primary item and the user does not need to worry about building some table of numbers to see a plot of a function. (The program does build such a table, but it is invisible to the user.)

Program Description

MathPlot functions are divided into three areas, each of which has its own window on the screen. These windows are: (1) the command window; (2) the editor window; and (3) the plot window. The command window is simply used for entering interactive commands. The edit window is a standard text editor (with all the usual Macintosh select, cut, and paste features) which is used to create descriptions of the models being created. The plot window lets the user create a variety of plots and easily do parameter studies and compare functions.

Building Models

Models are created in the editor window using two types of expressions called VARs and FUNCTIONs. A VAR is a combination of what might ordinarily be called constants, variables, and mathematical expressions. VARs are best thought of as objects which have a name, an associated value, and perhaps a defining expression. Some examples are:

```
VAR 2PI = 2 * PI ;                    \ VAR used as a constant
VAR XXX ;  3.0 TO XXX                 \ VAR used as a variable
VAR ZZZ = 2PI * XXX / SQRT ( 3 ) ;
                                      \ VAR with an expression
```

Note that VARs are created by starting with the word "VAR" followed by the name of the VAR, an optional defining expression or constant value, and terminated by a semicolon. Spaces are used as required delimiters around names and operators. [The expression "`3.0 TO XXX`" puts the value 3.0 into the VAR XXX.]

VARs are similar to cells in a spreadsheet in that VARs are linked in a linear list as they are created. When the value of any one VAR is changed, the values of all VARs further down the list are automatically recalculated. For example,

```
VAR XXX ;    2 TO XXX      \ XXX now has the value 2
VAR YYY = 2 * XXX ;        \ YYY = 4
VAR ZZZ = 2 * YYY ;        \ ZZZ = 8
3 TO XXX                   \ YYY is now 6; ZZZ = 12
```

Recalculation occurs only when a new value is stored into a VAR using <number> TO <Var-Name>. This feature allows one to build a model which contains a number of small pieces in the form of VARs, and then go into the model at any level and change parameter values and see the results automatically.

The second major building block for models is a FUNCTION. A FUNCTION is a named operator which 'maps' one or more input values into one or more output values. A number of predefined functions are built-in, including SIN, COS, TAN, ARCSIN, ARCCOS, ARCTAN, EXP, LN, LOG, ^, SQRT, SINH, COSH, TAHN, ARCSINH, ARCCOSH, ARCTANH. (The four operators +, - , *, and / can also be thought of as functions; complex number versions of these operators are also included.) In addition, the user can create user-defined FUNCTIONs by combining previously defined FUNCTIONs and VARs. For example, one might define POWER as

```
FUNCTION POWER ( X N ) = X ^ N END
```

A FUNCTION can have any number of input variable and any number of output variables. Of course, a FUNCTION with one input variable and one output result is particularly useful since it can be displayed as an XY-plot.

A table of x-y pairs of numerical data can also be used to define a numerical FUNCTION. This avoids the need to create some sort of analytic curve fit to numerical information. One can simple read the data from an ASCII text file and thus create a named FUNCTION which can be used just like any analytic function.

FUNCTIONs and VARs, once defined, can then be used in any subsequent definitions of new FUNCTIONs and VARs. A simple example of how one would define the difference of exponentials in terms of FUNCTIONs and VARs is shown below:

$$E_{DE} = E_P k_0 \left(e^{-\beta t} - e^{-\alpha t} \right)$$ **Difference of Exponentials**

```
VAR ALPHA ;     4.76E8 TO ALPHA
VAR BETA ;      4E6 TO BETA
VAR EP ;        1E4 TO EP

VAR K0 = 1.0E / ( ( ALPHA / BETA - 1.0E ) *
  ( BETA / ALPHA ) ^ ( 1.0E / ( 1.0E - BETA / ALPHA ) ) ) ;
```

```
FUNCTION F1  ( X ) = ( EXP  ( -1.0E * BETA * X )
                   - EXP  ( -1.0E * ALPHA * X ) ) END

FUNCTION E_DE  ( T ) = K0 * EP * F1  ( T ) END
```

The Plot Window

The Plot Window is reproduced in Figure 1. As is indicated, it consists of the Plot Area, the Value Box, the VAR List, the FUNCTION List, and the PLOT and OVERLAY Buttons. The Plot Area is, of course, where plots are actually drawn. Linear or log scales can be chosen using the PARAMETERS menu, and minimum and maximum values of the scales can be set by the user. The curve to be plotted is chosen from the Function List by 'pointing' with the mouse to the FUNCTION name of interest and 'clicking' the mouse button. The FUNCTION List contains all the currently defined FUNCTIONs; the list will scroll using the scroll bar on the right if more functions have been defined than can fit in the box. Once a FUNCTION name is selected (i.e. hilighted in black), that FUNCTION can be plotted on a new graph by 'pressing' the PLOT button below the FUNCTION List, or it can be overlayed on the existing plot with the OVERLAY button.

Similarly, names of all the current VARs are shown in the VAR List box. When a VAR is selected by pointing with the mouse and clicking, the value of that VAR appears in the VALUE Box directly above the VAR List. The value of the selected VAR can then be changed by clicking in the VALUE Box and then entering a new number. [The number in the VALUE Box can also be changed by factors of 2 by clicking the up or down arrows directly to the right of the box.] Note that whenever a new value is entered into the VALUE Box, all VARs below the currently selected VAR are automatically updated. It is thus very easy to do a parameter variation study by simply plotting a FUNCTION, selecting the VAR parameter of interest, changing its value, and then pressing the OVERLAY button. That is how the series of curves shown in Figure 1 were generated.

Another example showing the use of the PLOT Window is shown in Figure 2. This figure shows how several different FUNCTIONs can be compared using different types of scales. The PARAMETERS menu and the dialog box for setting graph parameters are also illustrated.

An Example of a MathPlot Model

As an example of the kind of models one can build with MathPlot, consider the issue of the currents induced on a cylinder by an incident electromagnetic

transient. One first describes the incident EM waveform using a difference of exponentials. Parameters include the peak value, rise time, and decay time of the waveform, as indicated in the equations below and shown graphically in Figure 3.

"Double Exponential" Incident Waveform

$$E_{inc} = E_p k_0 \left(e^{-\beta t} - e^{-\alpha t} \right)$$

where

$$k_0 = \frac{\alpha + \beta}{\alpha} \left[\frac{\alpha}{\beta} \right] \left(\frac{\beta}{\alpha + \beta} \right)$$

The step-function response of a cylinder is then represented by the expressions below (also shown in Figure 4), where the resonant frequency and decay time of the fundamental mode depend on the cylinder dimensions. [For those interested, the formulas given here are curve fits to numerical data from a finite-difference calculation.]

Step-Function Cylinder Currents

$$I_{STEP} = I_0 \exp(-at) \sin(2\pi f_n t) \cos\left(\frac{\pi z}{2h} \right)$$

where

$$I_0 = 4.3 \frac{4 h \varepsilon_0}{\Omega Z_0}$$

$$\Omega = 2 \ln \left(\frac{2h}{a_r} \right)$$

$$a = \frac{c}{h} \left[\frac{0.460}{\Omega - 3.446} \right]$$

$$f_n = \frac{c}{4h} \left[1 - \frac{0.500}{\Omega - 3.446} \right]$$

Now, these step-function response formulas can be convolved with the expressions for the incident field to give the expressions for the cylinder current for a double exponential incident pulse. In this case, one can obtain an analytic formula for the axial current on the cylinder, but the expressions (shown below) are complicated and it is far from obvious how a change in incident field risetime or cylinder length would change the final current.

Cylinder Currents for a Double Exponential Incident Pulse

$$I_{DE} = I_0 \cos\left(\frac{\pi z}{2h}\right) \left\{ k_1 e^{-at} \sin(2\pi f_n t) \right.$$

$$\left. -(D_\beta - D_\alpha) e^{-at} \cos(2\pi f_n t) + D_\beta e^{-\beta t} - D_\alpha e^{-\alpha t} \right\}$$

where

$$D_\alpha = [-\alpha 2\pi f_n] / [(\alpha - a)^2 + (2\pi f_n)^2]$$

$$D_\beta = [-\beta 2\pi f_n] / [(\beta - a)^2 + (2\pi f_n)^2]$$

$$k_1 = D_\beta(\beta - a)/(2\pi f_n) - D_\alpha(\alpha - a)/(2\pi f_n)$$

With MathPlot, however, it is relatively easy to see how parameter variations change the response functions. Some examples are shown in Figure 4. The plot window on the left shows the set of curves generated by changing the risetime variable ALPHA by factors of 4, while the plot window on the right shows the corresponding effect on the axial current on the cylinder. Such parameter variation studies take only a few minutes to carry out once the model has been created and entered into the program.

Summary

MathPlot is an experiment in trying to develop a specialized computer language and graphics system which lets the scientist or engineer concentrate on building mathematical models rather than getting too involved in the details of computer programming. The program is still "under construction" with many desirable features not yet implemented (e.g. a 3-D or contouring plotting package to display functions of two input variables). Even in its present state, however, it has been quite useful for examining the how parameters affect the various functions in fairly simple sets of equations.

Anyone interested in obtaining a copy of the MathPlot program should contact the author.

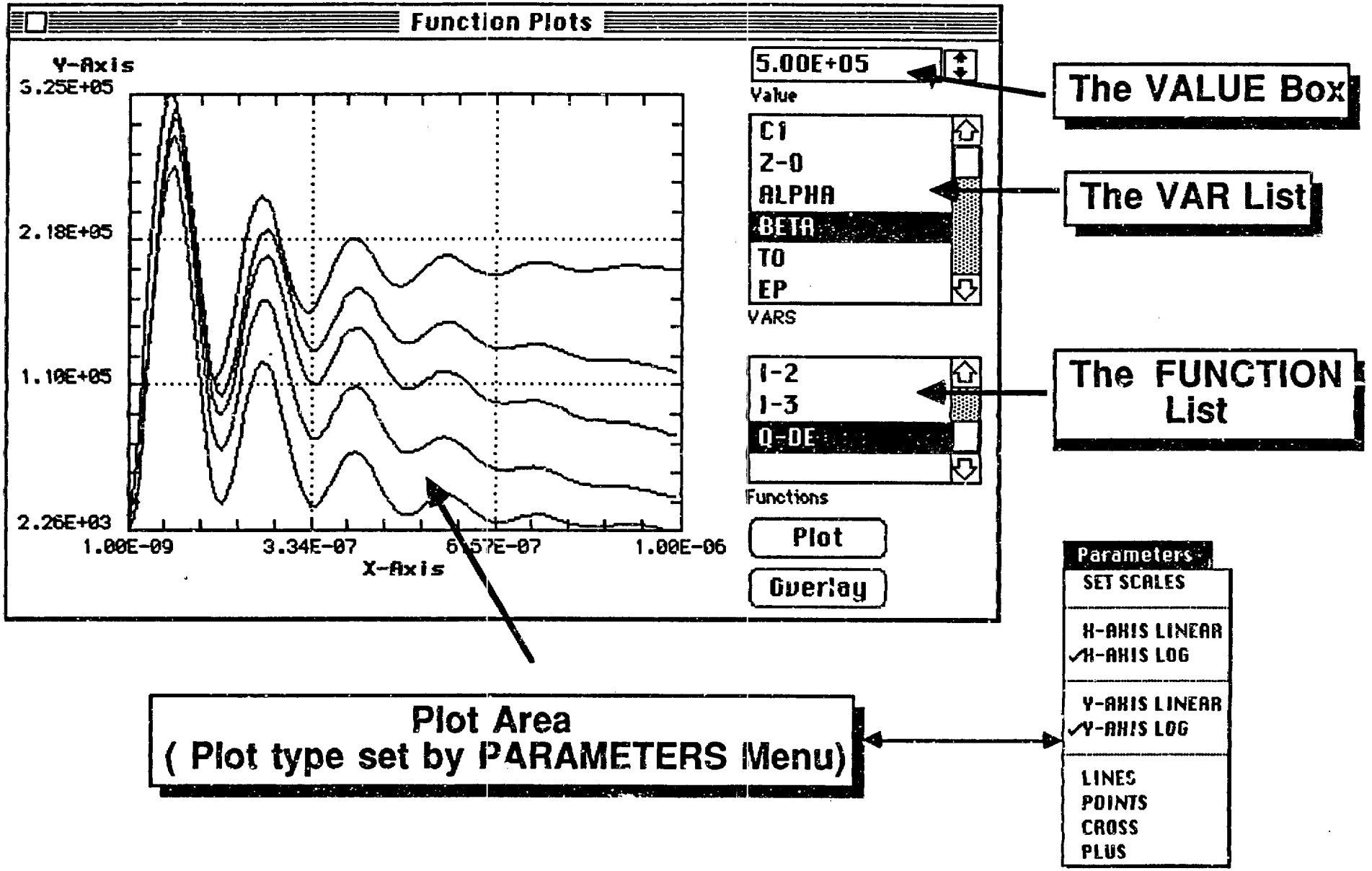
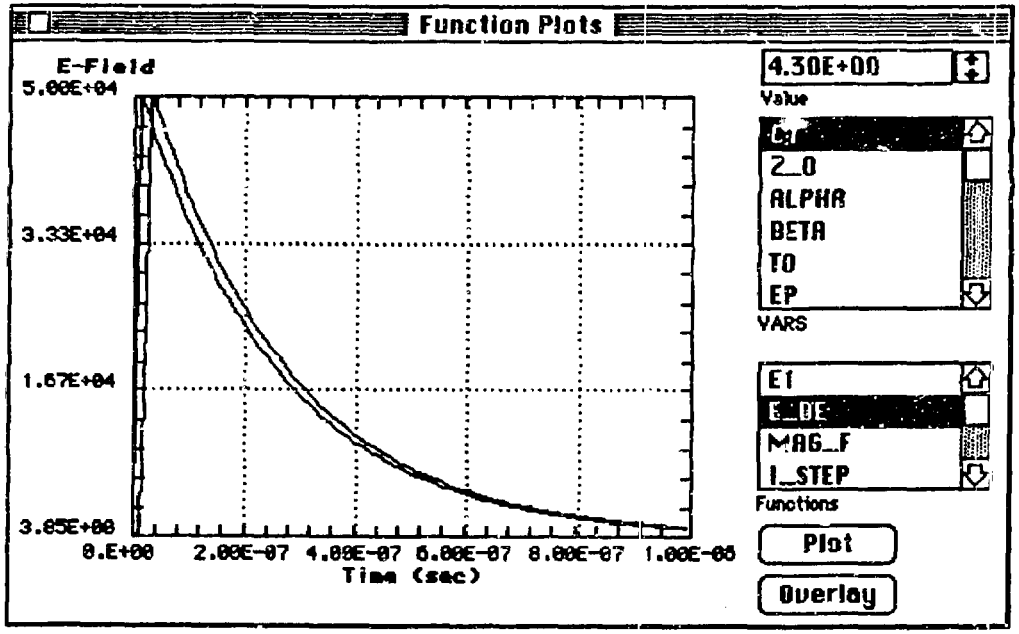

Function Plots
Y-Axis
3.25E+05
2.18E+05
1.10E+05
2.26E+03
1.00E-09
3.34E-07
1.00E-06
X-Axis
5.00E+05
Value
C1
Z-0
ALPHA
BETA
TO
EP
VARS
I-2
I-3
Q-DE
Functions
Plot
Overlay
The VALUE Box
The VAR List
The FUNCTION List
Plot Area
(Plot type set by PARAMETERS Menu)
Parameters
SET SCALES
X-AXIS LINEAR
✓X-AXIS LOG
Y-AXIS LINEAR
✓Y-AXIS LOG
LINES
POINTS
CROSS
PLUS

Figure 1



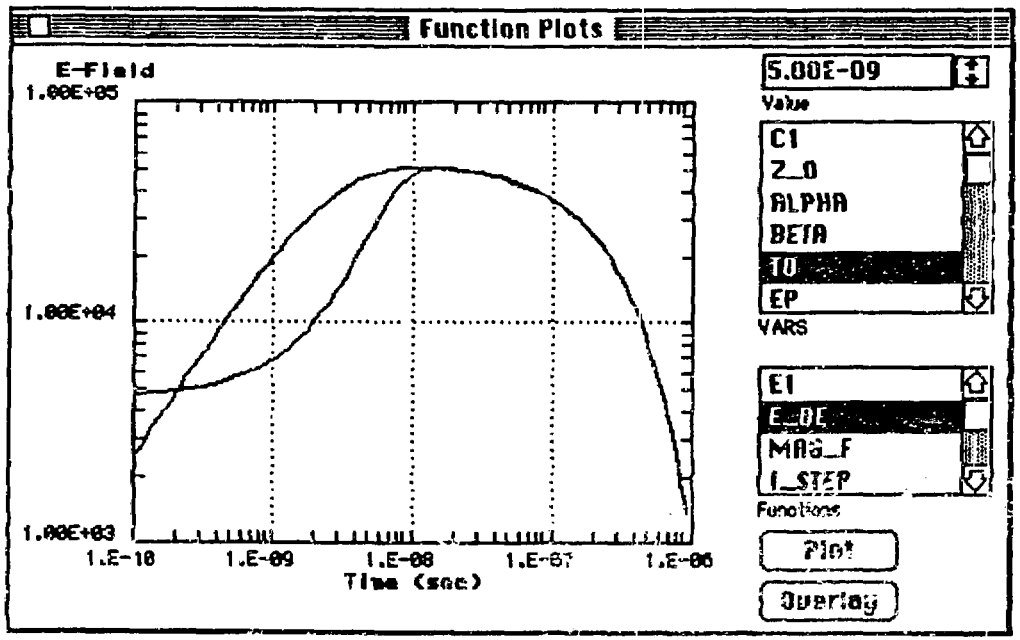
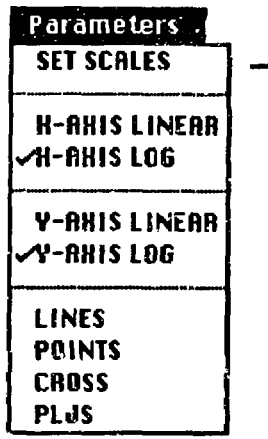
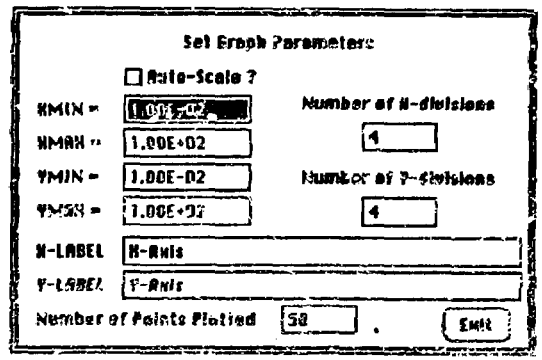


Figure 2

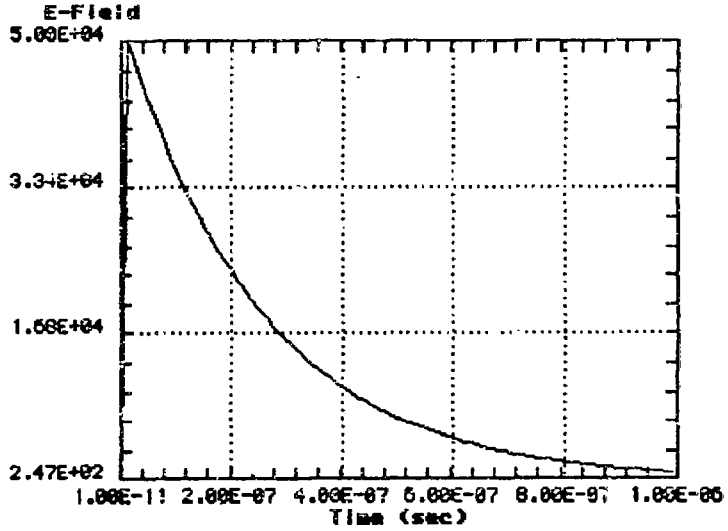
$$E_{DE} = E_p k_0 \left(e^{-\beta t} - e^{-\alpha t} \right)$$

$$E_{EOE} = \frac{k E_0 \exp\left[\alpha (t - t_0)\right]}{1 + \exp\left[(\alpha + \beta)(t - t_0)\right]}$$





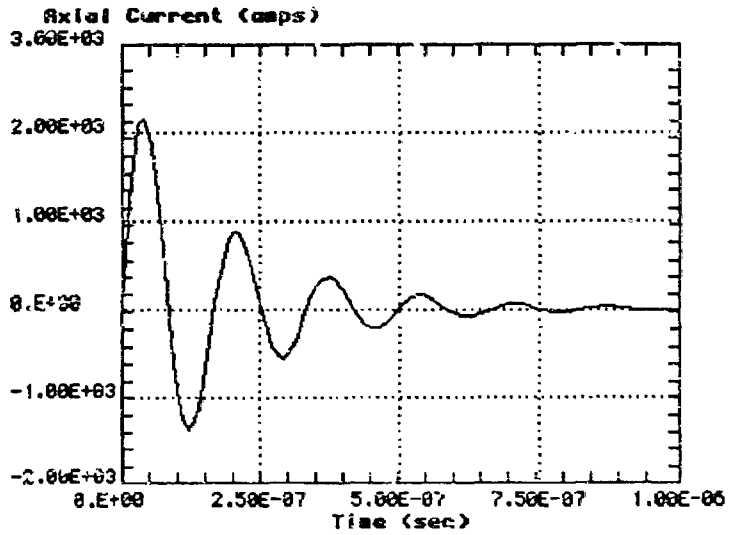
Incident Field

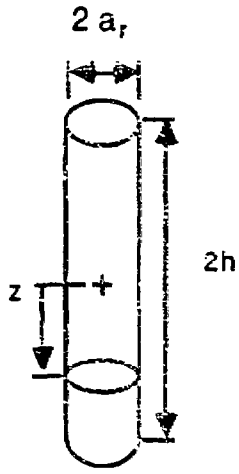


$$E_{inc} = E_p k_0 \left(e^{-\beta t} - e^{-\alpha t} \right)$$

where $$k_0 = \frac{\alpha + \beta}{\alpha} \left[\frac{\alpha}{\beta} \right]^{\left(\frac{\beta}{\alpha + \beta} \right)}$$

Step Function Response Current on a Cylinder





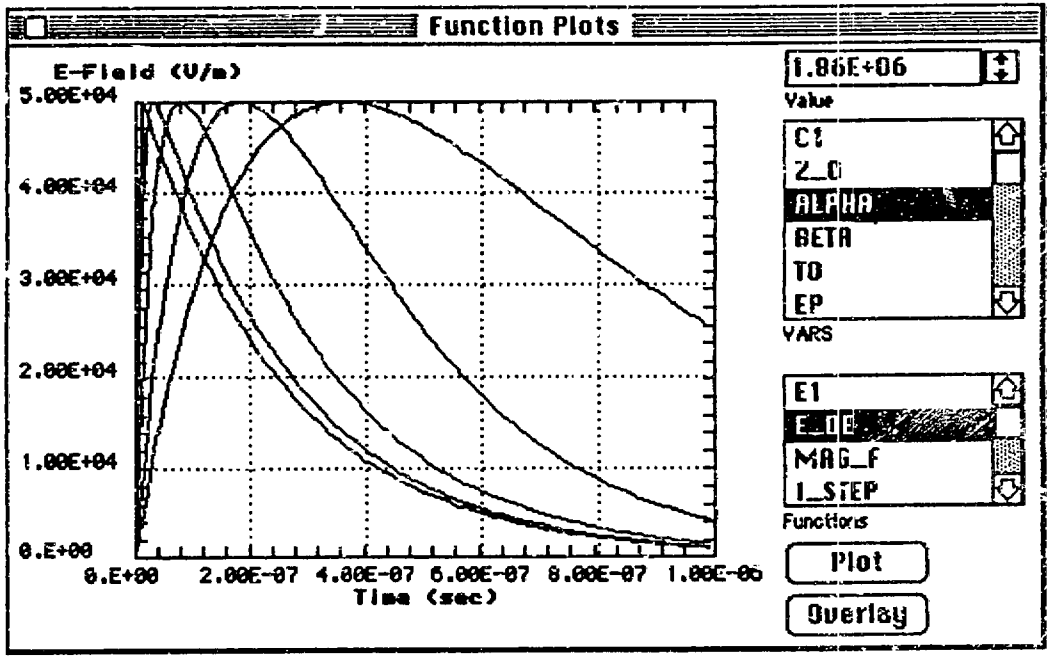
$$I_{STEP} = I_0 \exp(-at) \sin(2\pi f_n t) \cos\left(\frac{\pi z}{2h}\right)$$

where

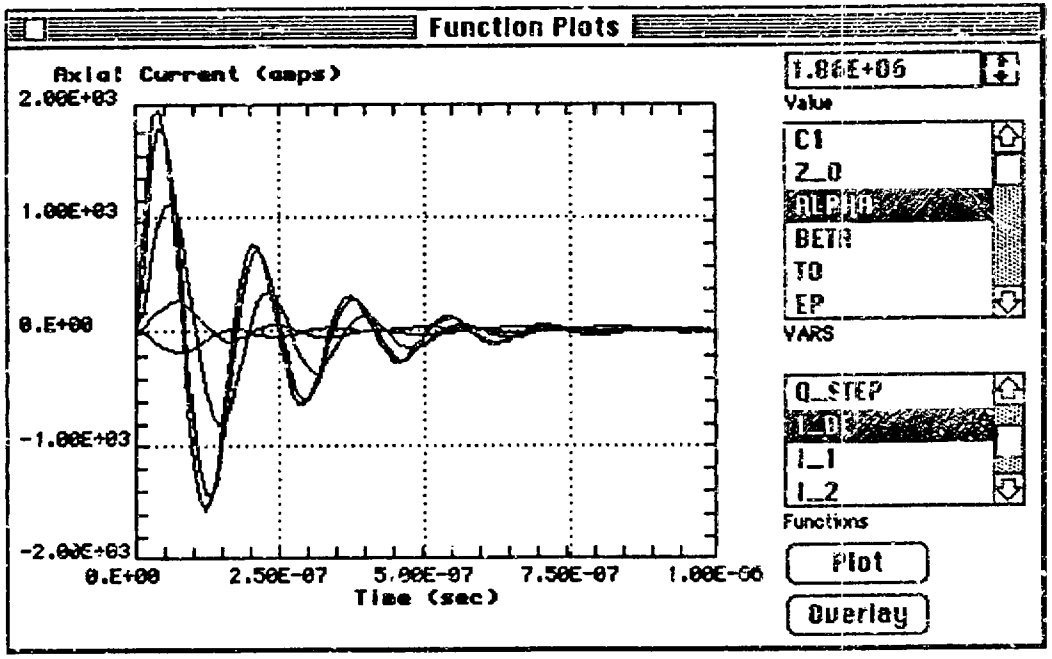
$$I_0 = 4.3 \frac{4 h \varepsilon_0}{\Omega Z_0} \qquad a = \frac{c}{h} \left[\frac{0.460}{\Omega - 3.446} \right]$$

$$\Omega = 2 \ln \left[\frac{2h}{a_r} \right] \qquad f_n = \frac{c}{4h} \left[1 - \frac{0.500}{\Omega - 3.446} \right]$$

Figure 3



Effect of Risetime Variation on Incident Field Waveform



Effect of Risetime Variation on Axial Cylinder Current

$$I_{DE} = I_0 \cos\left(\frac{\pi z}{2h}\right) \left\{ k_1 e^{-at} \sin(2\pi f_n t) - (D_\beta - D_\alpha) e^{-at} \cos(2\pi f_n t) + D_\beta e^{-\beta t} - D_\alpha e^{-\alpha t} \right\}$$

$$D_\alpha = [-\alpha 2\pi f_n] / [(\alpha - a)^2 + (2\pi f_n)^2]$$

$$D_\beta = [-\beta 2\pi f_n] / [(\beta - a)^2 + (2\pi f_n)^2]$$

$$k_1 = D_\beta(\beta - a)/(2\pi f_n) - D_\alpha(\alpha - a)/(2\pi f_n)$$

Figure 4

PC PROGRAM FOR PLOTTING THE VECTOR FIELDS

Darko Kajfez,
Department of Electrical Engineering
U. of Mississippi, University, MS 38677

and

James A. Gerald
Department of Electrical Engineering
Syracuse U., Syracuse, NY 13210

Abstract

The operation of the program VMAP is described, which displays and plots the vector field data in an interactive manner. Any vector field, such as electric, magnetic, current density, etc., specified at the number of equidistant points, can be mapped in terms of smooth field lines. Even a small number of input data points can produce a realistic appearance of the interpolated field lines.

Introduction

Plotting of scalar fields is accomplished with the so-called "contour plot" programs [1], which are commercially available. This paper describes a PC based program for plotting the vector fields. The program constructs the field lines for general vector fields, irrespective of the fact whether the field in question can be described in terms of the scalar potential or not.

The principle of operation has been described in [2, 3]. Basically, the procedure consists of incrementing the field line in small steps, which is reminiscent of a second-order Runge-Kutta solution of the differential equation. The approach utilized here is to separate the program for the numerical solution of the vector field values from the program which generates the field plots. The field evaluation program is required to create a file of vector field components at a set of equidistant points. This computation is usually performed on a mainframe computer, although in some simple cases these data may also be generated by a personal computer.

The convenience of the program VMAP is that the operations which require an interactive mode (like selecting the position and density of field lines, drawing the outlines, etc.) are performed on a PC, which is under the total control of the user. The results of each command are instantly displayed on the screen, or plotted on an x-y plotter.

Input data files

Program VMAP has been developed for the DOS of IBM PC or compatibles. In order to increase the speed of execution, the program is compiled in Turbo Basic [4]. The input data must be stored on a diskette. Each point in the equidistant grid must contain the horizontal and the vertical component of the vector field in question. The first data line specifies the size of the illustration, the number of horizontal and vertical divisions, the position of singular points (if any exist), and it also specifies whether there will be any comments at the end of the file.

When the program is executed, the data files are normalized to the largest field amplitude, and stored in an integer array, allowing up to 100 by 100 data points.

As an example, consider the electric field of the TE_{11} mode in the square waveguide, with sides 1 m by 1 m. The data file for a grid of 4 by 4 points is given in Table. 1.

TABLE 1
Electric field of the TE_{11} mode

```
4          4                1                1                0                0
0                    0
0                   -.86603
0                   -.86603
0                    0
 .86603              0
 .43301             -.43301
-.43301             -.43301
-.86603              0
 .86603              0
 .43301              .43301
-.43301              .43301
-.86603              0
 0                   0
 0                   .86603
 0                   .86603
 0                   0
```

The first line specifies that there are 4 rows and 4 columns of data points, the total size of the illustration is 1 by 1 (arbitrary units), there are no singularities and no comments. Afterwards, we have 16 lines containing the horizontal and the vertical components of the vector field to be plotted. They are entered starting with the left lower corner of the illustration.

Interactive display

The user selects the mode of operation with the menu shown in Fig. 1. The first step is to read the data from the diskette. As a next step in

creating the field plot, the user selects the F3 key, which enables the selection of "flux intercept lines" [3]. The interactive display will appear, which is shown in Fig. 2. In this display, the input data are graphically displayed in the form of arrows. This gives the user a feeling of the shape of the field, so that he can decide where to put the intercept lines.

In this example, one places the first intercept line along one of the waveguide walls. For instance, the user may select the left-hand wall as the first intercept line. This is done conveniently by moving the red dot with the cursor keys, and pressing <s> for start and <f> for finish. If the cursor steps are too large or too small, they may be changed by using the keys <i> for increase or <d> for decrease.

After selecting the intercept line, the user presses <g> for graphing. The program reacts by asking for the desired number of field lines which should be crossing this intercept line. Figure 3 shows the electric field lines constructed from the data shown in Table 1, by requesting 4 field lines crossing the intercept line. It is seen that only one half of the field pattern is obtained in this way. To map all the electric field lines of this mode, another flux intercept line must be placed along the right-hand waveguide wall. Up to 20 additional flux intercept lines may be accommodated by the program.

Hard copy

The resolution of the ordinary PC graphics monitor is only 200 pixels in the vertical direction, which allows only a crude display of the vector fields. However, the program VMAP is designed to drive an x-y plotter, which has a resolution of 0.025 mm (HP 7475A or equivalent). Thus, the quality of the final copy of the field depends only on the step size of constructing the field lines, and on the state of the plotting pen.

The standard step size is 1/80 of the diagonal of the total illustration, or 1/3 of the grid size, whichever is smaller. This step size is selected as a compromise between the speed of plotting and the quality of the field lines obtained in this way. The user may increase or decrease the step size through the menu commands. He can also plot the illustration over the entire page of the paper, or select the margins so that the illustration falls on a particlar portion of the paper.

Figure 4 shows the TE_{11} electric field pattern plotted by an x-y plotter, constructed by using the data from Table 1. The field lines are remarkably smooth, considering that the entire area of the illustration is described by only 16 data points.

When the x-y plotter is not available, or when the plotter is available but the pens are all dried out, a hard copy of a lesser quality can be made on a dot matrix printer. Figure 5 is a plot of the TE_{01} mode magnetic field in the circular cylindrical cavity, obtained by the PrtSc command on a dot matrix printer. The left-hand border of the figure is the axis of rotation, so that only one half of the total cavity cross section is visible.

Availability

VMAP will work on IBM PC, XT, AT or compatibles, with 256 k or more storage. The mathematical coprocessor is desirable for the speed of execution, but not required. The color monitor is convenient, but the monochromatic monitor will also work. The x-y plotter may be HP7470 or HP7475A, or compatible.

To obtain a copy of the diskette with the compiled version of VMAP, please include a check for $25 and write a letter on the stationery of your institution or company to:

Department of Electrical Engineering
University of Mississippi
University, MS 38677

References

[1] SAS/ Graph User's Guide, SAS Institute Inc., Cary, NC, 1981, p. 43.

[2] D. Kajfez and T. Ward, "Plotting of two-dimensional vector fields with computer," Technical Report, U. of Mississippi, NTIS accession No. PB86-196318, April 1986

[3] D. Kajfez and J. A. Gerald, "Plotting vector fields with a personal computer," IEEE Trans. Microwave Theory Tech., vol. MTT-35, pp. 1069-1072, November 1987.

[4] Turbo Basic Owner's Handbook, Borland International, Scotts Valley, CA, 1987.

Two-dimensional Vector Fields

F1: Read data from disk.	F2: Plot preview.
F3: Select intercept lines.	F4: Graph field lines.
F5: Plot field lines.	F6: Change step size.
F7:	F8: Change default settings.
F9: Save default settings.	F10: Exit program.

The current step size is 100.00% of standard.

Fig. 1 Main menu

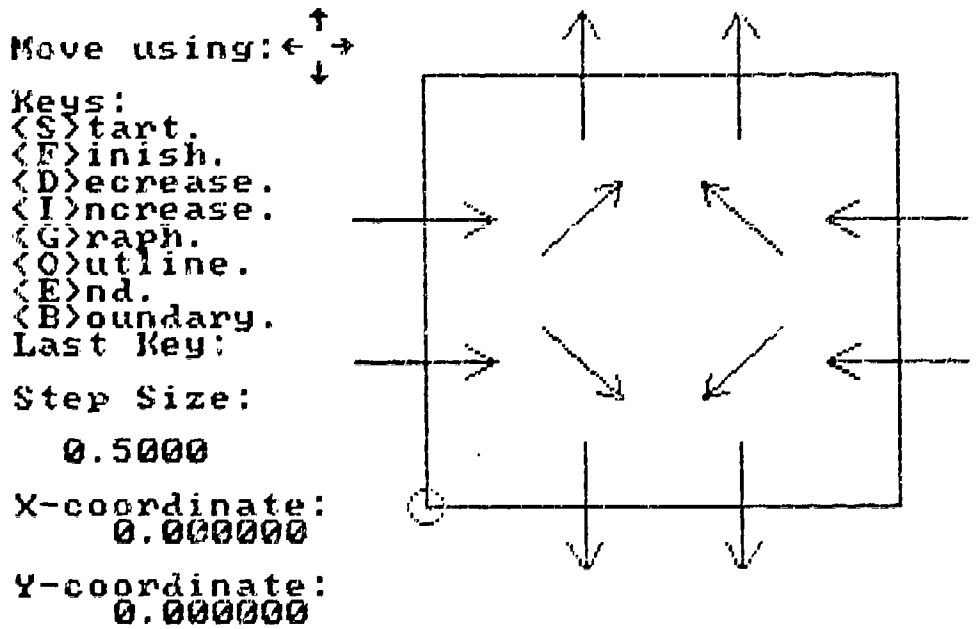


Fig. 2 Interactive display of TE_{11} mode in a square waveguide

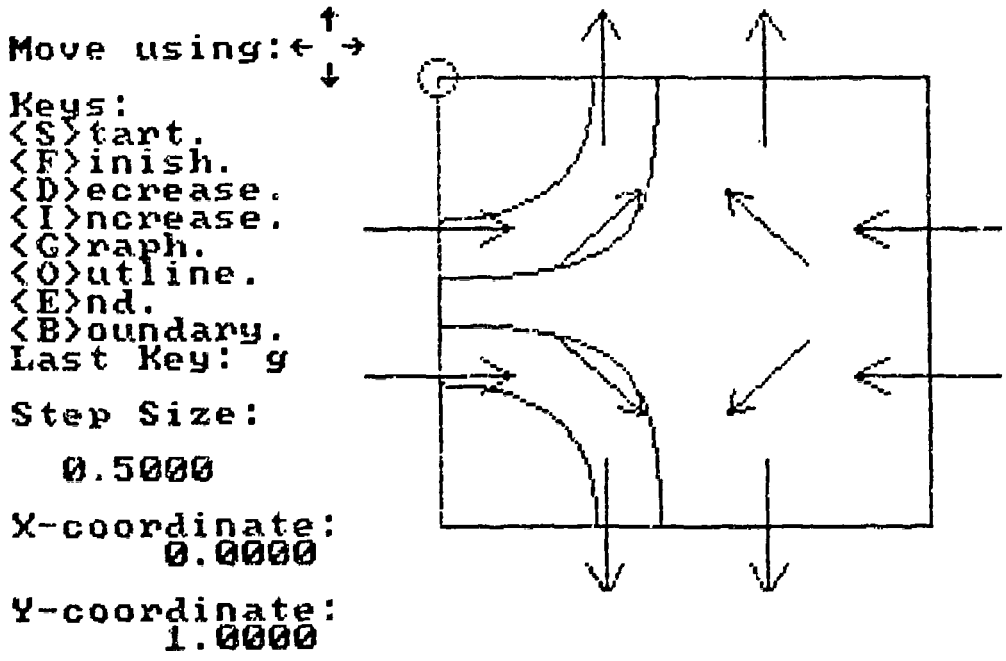


Fig. 3 Interactive display, after "graphing" four field lines

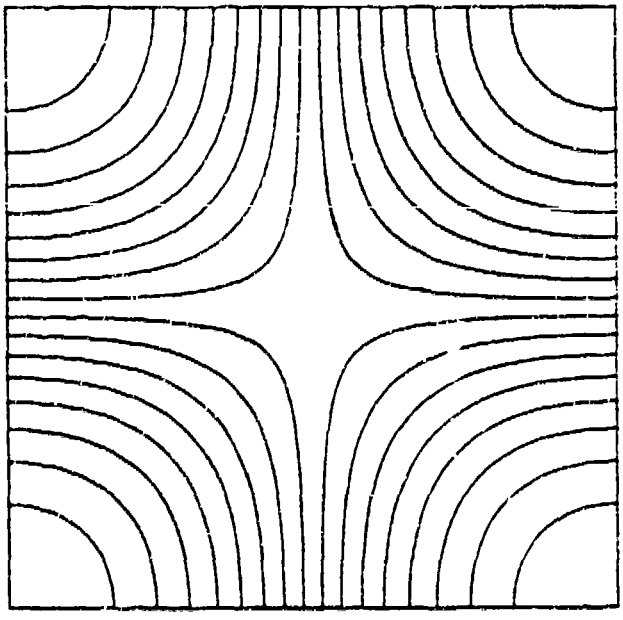


Fig. 4 TE_{11} mode in a square waveguide, electric field lines using an x-y plotter

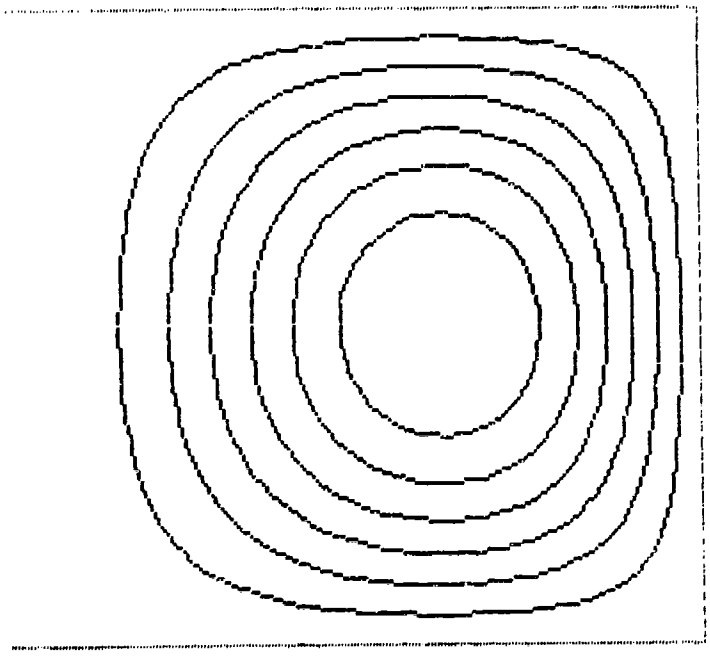


Fig. 5 TE_{01} mode in circular cylindrical cavity, magnetic field lines using dot matrix printer

SESSION V - "GEMACS"

Moderator: David E. Thomas
The BDM Corporation

"GEMACS – The Present and the Future"
K.R. Siarkiewicz Rome Air Development Center

"A GEMACS Source Book"
E.L. Coffey Advanced Electromagnetics
K.R. Siarkiewicz Rome Air Development Center

"Solution of Multi-Region, Aperture-Coupled Problems with GEMACS 4.0"
E.L. Coffey Advanced Electromagnetics
K.R. Siarkiewicz Rome Air Development Center

"Application of GEMACS-IV for Small Aperture Coupling"
R.J. Balestri Booz Allen & Hamilton, Inc.

"GEMACS on a Personal Computer"
E.L. Coffey Advanced Electromagnetics

GEMACS – The Present and the Future

Kenneth R. Siarkiewicz
Rome Air Development Center
Griffiss AFB, NY 13441-5700

The General Electromagnetic Model for the Analysis of Complex Systems (GEMACS) is a general-purpose computerized electromagnetic fields analysis tool in wide use throughout the Air Force and its contractor community. It has evolved from simply providing an estimate of the electromagnetic coupling between pairs of antennas to being capable of system analysis, including consideration of both the interior and exterior regions of a structure, coupling the two by modeling the arbitrary apertures in the structure skin.

The computer program has gone through three major modifications since it was first released in 1977, as shown in figure 1. It can be seen from the figure that GEMACS has generally taken advantage of existing technology and its computer implementation, at times incorporating whole sections of existing computer programs that had been previously developed under government contract. The generally unique features include the Banded Matrix Iteration (BMI) technique to speed up the solution of the matrix equation, the overhead structure including the file handling and input language processing schemes, the use of Kron's finite difference diakoptic method and Householder's method of modified matrices in the development of the finite difference (frequency domain) formulation, and the hybridization scheme that connects the MOM, GTD, and FD formulations. It should also be noted that the computer program is highly transportable, being written in ANSI standard FORTRAN (1977), with all system-dependent routines, such as date and time and elapsed processor time, all clearly identified for installation ease.

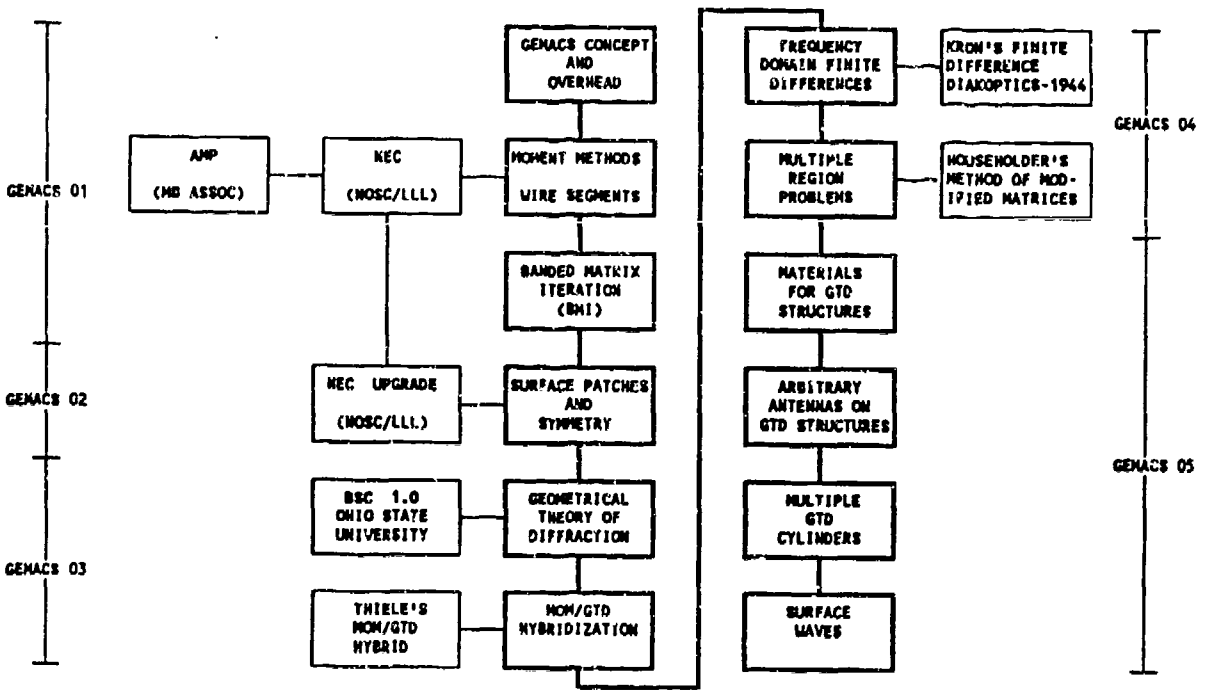


Figure 1. Development of the GEMACS Computer Program.

GEMACS exists in the form that it does for a number of philosophical reasons decided upon in 1972. It was determined that the primary users of this tool would be government contractors, rather than a limited number of government agencies. This decision required high transportability. It also required a more cumbersome overhead structure to accommodate the installation of the program on an arbitrary host machine. The growth and diffusion of this computer program attest to the robustness of its original design.

In addition, since it would be required to solve a wide range of geometries in an equally wide range of scenarios, and do so across a broad range of frequencies from HF to microwave, the program would need to incorporate more than one computational electromagnetic field analysis technique. This required that a high degree of flexibility be designed into the overhead structure to allow the data to flow in the proper format among the various formulations incorporated within the code.

It is the success in achieving the original design goals that has enabled GEMACS to grow in capability and expand its sphere of analyzable problem types and observables.

At the present time there are several generic problem types to which GEMACS has been put. These include antenna analysis (both in isolation and in the presence of a given environment), coupling between pairs of antennas collocated on a complex platform, the susceptibility and vulnerability of weapons systems when subjected to a given electromagnetic environment, the effect of dielectrics as opposed to metal on the shielding and performance of a given system in the presence of electromagnetic irradiation, the electromagnetic scattering (both monostatic and bistatic) of a structure, and the characterization of measurement setups designed to quantify electromagnetic phenomena associated with a given structure.

Figure 2 shows the various antenna types and the GEMACS solution techniques that could be used when these antennas are studied in a free space environment. The parameters of interest that could be computed include bandwidth, center frequency, directivity, ellipticity, efficiency, gain, input impedance, patterns (both near and far field), and polarization. Many of these observables are not automatically calculated and output by GEMACS, but the computer program does provide the needed data to perform the off-line calculation of the quantity.

These basic antenna types can also be modeled *in situ* in order to determine their operational characteristics in the presence of a complex conducting obstacle. It is here that the power of the hybrid methodology comes to the fore. It is generally true that the radiating or receiving element is small compared to a wavelength (resonant at best) and the platform is large compared to a wavelength. In this situation the user of GEMACS can model the antenna using MOM elements and the platform using GTD elements. A typical example of this would be the analysis of a blade antenna located on the surface of a B-52 aircraft.

The initial application of GEMACS at RADC was the determination of the electromagnetic compatibility (EMC) posture of a subset of a given system. The primary goal is to calculate the amount of electromagnetic coupling that exists between pairs of antennas on a structure, and determine whether or not excessive interference is present at the terminals of the victim antenna. This has been easily extended to an analysis in which more than one transmitting antenna is present and the effect of all radiators on one receptor is the issue. GEMACS does directly provide a measure of the power delivered to a specified load connected to an antenna. One further extension of this concept

would be to calculate the open circuit voltage and short circuit current and then off-line calculate the power delivered to any arbitrary load.

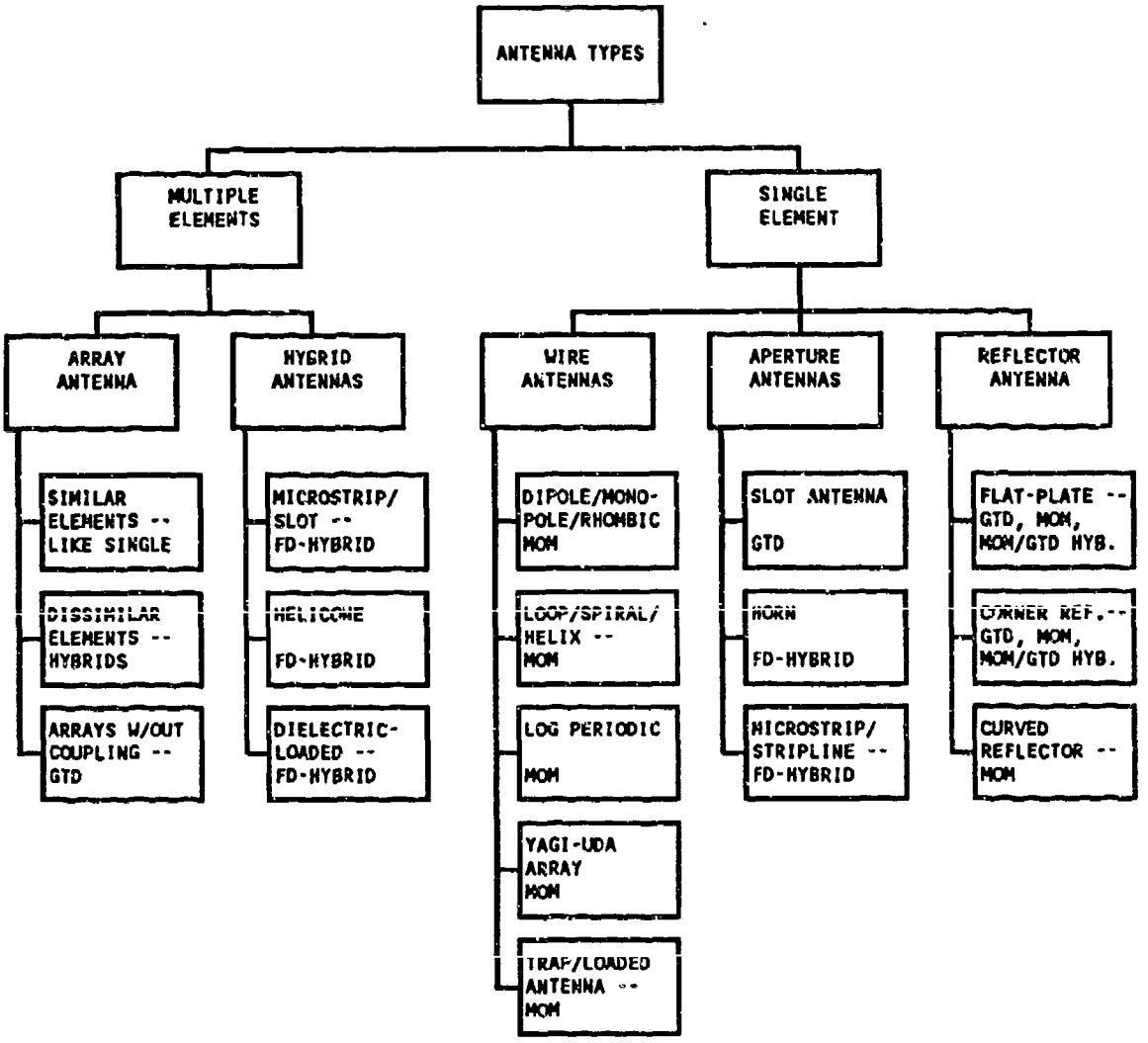


Figure 2. Antenna Types and GEMACS Solution Techniques.

Several other applications flow from these basic uses to which GEMACS was applied. Many of the antennas that can be analyzed include reflectors or top hats or some other focusing device. These can be considered to be scatterers of the incident energy from the source element. Thus, GEMACS is capable of determining the electromagnetic scattering from any structure that can be properly modeled. The electric field data output by GEMACS can be used in off-line calculations to analyze the monostatic and bistatic radar cross section of the structure. Moreover, since GEMACS is capable of near-field as well as far-field calculations, it can be used in the correlation of far-field calculations from near-field data. Compact ranges can thus be "calibrated" to provide a measure of the error introduced by the measurement environment. More will be said about this later.

Since the calculation of the scattered energy using MOM presupposes knowledge of the current distribution on the surface of the structure, the analyst can find the location of "hot" spots on the platform. Knowledge of these areas can provide information to the design and system engineers such that they will avoid placing apertures and antennas for sensitive receivers in such areas.

The ability to calculate scattered energy enables an analyst to also model test facilities and measurement setups and their equipment to determine extraneous sources of electromagnetic energy which can color the results of the measurement program. The predicted magnitude can be used to "calibrate" open antenna test ranges, mounting platforms in anechoic chambers, compact range environments, and radar cross section measurement ranges.

Of particular importance in the use of the last type of facility is the determination of the "glint," the apparent instantaneous angular displacement of the RCS center of a target from the actual position of that target. Since this results from the variation in phase of radar signal scattered by separate scattering sources on a target, and since the target consists not only of the object of interest but the mounting structure and the physical environment as well, the output from a GEMACS analysis of the measurement setup with the object in place can be useful to eliminate "spikes" and other spurious data from the patterns obtained by the measurement.

Alternate methods to reduce the scattering from an object can be studied now that GEMACS can take into account the conductivity and permittivity of the material of which the object is constructed. Although this is a brute-force calculation in the sense that the interior region FD formulation is used to study a portion of the external problem and thus is not the most efficient way to approach the problem, at least the user does have a tool with which the problem can be approached and studied.

Finally, with the addition of the FD formulation the user of GEMACS can now evaluate interior responses to external electromagnetic stimuli. That is, given a specific set of incident electromagnetic waves one can calculate as a total interior/exterior problem space the current induced in any wires and cables inside the structure. This has application to the study of high power microwave (HPM) phenomena,to the determination of the susceptibility and vulnerability of the system to any electromagnetic threat, and to the analysis of the effectiveness of proposed fixes for the elimination of unintentional ports of entry on the vehicle. Since this capability allows one to calculate the electromagnetic fields set up within the structure, a system designer can locate wires and equipments in regions of low electromagnetic field intensity, thereby designing in an assurance that the system as a whole will have a minimum susceptibility level.

These and other applications are described in detail in a soon to be distributed RADC technical report entitled *GEMACS Source Book*, developed under contract by Advanced Electromagnetics in Albuquerque, NM. This is a rather extensive document that covers a broad range of topics associated with the area of computational electromagnetics, including both the theoretical aspects of the MOM, GTD, and, FD formulations, as well as the hybridization schemes tying these techniques together. Many examples are described, set up, and have their results shown. While the document itself uses GEMACS as the base computer code, it does have much usefulness for anyone versed in electromagnetics, but recently introduced to the field of computer-aided electromagnetic fields analysis. A summary of the report's contents is shown in figure 3.

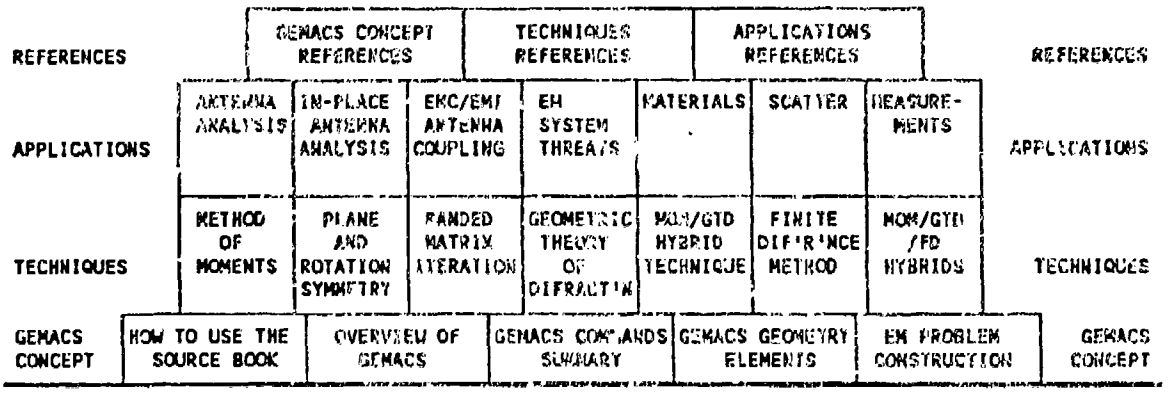


Figure 3. The Four Layers of the GEMACS Source Book.

As powerful as it now is, there are numerous areas in which GEMACS could be improved. The GTD formulation as implemented in the code is one of those areas. This formulation is based on the work accomplished by Ohio State University (OSU) in 1978-80 and implemented in their first version of the Basic Scattering Code (BSC-I). There are several deficiencies that are being addressed in a current RADC contract with Advanced Electromagnetics. These are shown in figure 4. First, the modeling elements (plates, cylinders, and end caps) are all assumed to be perfectly conducting. The new version of GEMACS will allow the user the opportunity to arbitrarily locate on an element arbitrarily shaped patches of material with arbitrary values of conductivity and permittivity. More than one such patch may be located on the same element and such patches may also share a common boundary.

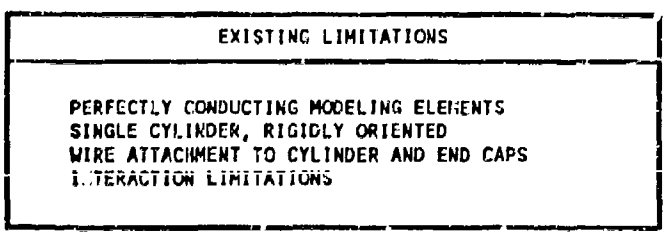


Figure 4. Limitations Existing in GEMACS 4.0.

Secondly, at the present time only one cylinder and its two end caps are available with which the user can model the structure. Furthermore, the cylinder must be entered in its own coordinate system and may be aligned only along the z-axis of that system. This seriously limits the flexibility of the user in being able to input the data to model the structure. The present work will allow for ten cylinders and twenty end caps (limits set by array sizes and therefore also variable). The cylinders will be able to be located arbitrarily in any previously defined coordinate system and will not need to be in any preconceived geometrical relationship with each other. It may even be possible for the cylinders to intersect each other in almost any manner.

Third, while the geometry routines of the present version of GEMACS do allow the user to attach a wire to the cylinder, the physics are not implemented to assure continuity of current between the wire and the cylinder at the point at which the wire is attached.

GEMACS now treats that end of the wire as if it were unconnected to anything (a free space condition). The present work will implement the physics to provide a path of current flow into the cylinder. There may be a limitation on this, requiring large radii of curvature for good engineering approximation. However, this may not be a serious situation since one assumes that one is working with an electrically large object when one is using the GTD analysis technique.

Finally, the existing version of GEMACS hosts a very limited set of interactions among the various modeling elements. These include the usual repertoire of reflection and diffraction from single surfaces and edges along with a number of double interactions (i.e., reflection/diffraction, diffraction/reflection, reflection/reflection). A summary of what is available and what is planned for inclusion in a future release of GEMACS is shown in figures 5, 6, and 7.

FIRST INTERACTION	SECOND INTERACTION		
	PLATE REFLECTION	PLATE EDGE DIFFRACTION	MATERIAL EDGE DIFFRACTION
PLATE REFLECTION	●	●	○
PLATE EDGE DIFFRACTION	●	○	○
MATERIAL EDGE DIFFRACTION	○	○	○

● VERSION 4
○ VERSION 5

Figure 5. Second Order Plate GTD Interactions for GEMACS 5.

FIRST INTERACTION	SECOND INTERACTION		
	PLATE REFLECTION	PLATE EDGE DIFFRACTION	MATERIAL EDGE DIFFRACTION
CYLINDER REFLECTION	●	●	○
END CAP REFLECTION	●	●	○
CYLINDER CREEPING WAVE	●	●	○
END CAP RIM DIFFRACTION	○	○	○
CYLINDER MATERIAL EDGE DIFFRACTION	○	○	○
END CAP MATERIAL EDGE DIFFRACTION	○	○	○

● VERSION 4
○ VERSION 5

Figure 6. Second Order Plate-Cylinder GTD Interactions for GEMACS 5.

Work has progressed well in achieving the objectives of the contract. One highly significant feature from the standpoint of implementation of theory in computer code is

the fact that even though nearly 70 interactions will be available for analysis, the amount of computer program lines will in all likelihood be reduced from the present amount. This is due to the fact that an iterative step process will be used to calculate the field at a point due to a source at an arbitrary point. Starting with the source point and magnitude, first calculate the propagation loss to an interaction point. Then calculate the interaction loss at that point. This is followed by the calculation of the next propagation loss to the second interaction point, the second interaction loss, and the final propagation loss to the field point from the second interaction point. This is an alternative to the present method of determining the path from source to field point and then calculating the total path loss in one subroutine specifically addressing the combination of phenomena associated with that overall path. It also follows that one could continue to concatenate other interaction points and propagation paths to any level that the user would want, recognizing the law of diminishing returns (calculation time vs. relative magnitude of higher level interaction sets).

FIRST INTERACTION	SECOND INTERACTION					
	CYLINDER REFLECTION	END CAP REFLECTION	CYLINDER CREEPING WAVE	END CAP RIM DIFFRACTION	CYLINDER MATERIAL EDGE DIFFRACTION	END CAP MATERIAL EDGE DIFFRACTION
CYLINDER REFLECTION	○	○	○	○	○	○
END CAP REFLECTION	○	○	○	○	○	○
CYLINDER CREEPING WAVE	○	○	○	○	○	○
END CAP RIM DIFFRACTION	○	○	○	○	○	○
CYLINDER MATERIAL EDGE DIFFRACTION	○	○	○	○	○	○
END CAP MATERIAL EDGE DIFFRACTION	○	○	○	○	○	○

● VERSION 4 ○ VERSION 5

Figure 7. Cylinder-Cylinder GTD Interactions for GEMACS 5.

Secondly, it has been determined with a fair degree of certainty that all of the theory to accomplish the objectives of the contract is available. The varying number of physics and geometry modeling assumptions make it uncertain at this time just what the accuracy and applicability of the upgraded computer program will be. For example, patches of lossy dielectrics will be defined by stepped values of relative dielectric constant rather than smooth curves. Also, layered dielectrics will be represented by equivalent constituent parameters, which in turn will affect the surface wave calculations.

At the present time the design document for the code development and integration is under review. Subroutine hierarchy trees, common block structures, data flow and availability are being considered in great detail to assure the smooth and complete integration of new FORTRAN with that already in place. Code development,

integration, and preliminary testing are expected to be completed by September 1989. Further testing and final documentation preparation will necessitate that the fielding date for what promises to be version 5 of GEMACS occur in the second quarter of calendar year 1990.

The newest addition to the GEMACS arsenal is a set of graphical aids to support the electromagnetics analyst. The Graphical Aids for the User of GEMACS (GAUGE) is a PC-based computer program that eases geometry data input to GEMACS and output data formatting. It is written in Microsoft FORTRAN (version 4.01) and PC assembly language for screen and keyboard drivers. There is no propriety software within the computer program, and it is anticipated that the transportability of the software will be as great as that for the GEMACS code itself. Features of GAUGE include:

- o Screen drivers for EGA and CGA
- o Pen plotter HPGL hardcopy support
- o In-line documentation of the source code
- o Extensive hardcopy documentation
- o Automatic generation of GEMACS geometry input deck
- o Augmented by input translator
  - Full compatibility with existing geometry decks
  - Conversion of NEC decks to GEMACS format
  - Conversion of BSC decks to GEMACS format
  - Mixed language capability
- o Multi-color palette for data screen or hardcopy
- o Menu driven
- o On-line HELP screens

Minimum system requirements are an IBM PC or compatible with two floppy drives, 640K of memory and a CGA monitor. For best performance, an IBM AT or compatible with a hard disk, 640K of RAM, an 80287 numerical coprocessor, and an EGA card is recommended. The code itself is transferred via 10 floppy disks in source language, as well as executables for both EGA and CGA cards. Greater detail regarding capabilities and coding for computational electromagnetics on a PC are given in "Graphical Aids for the Users of GEMACS (GAUGE)" by Allen Lockyer and Pravit Tulyathan, "Graphics Programming for Electromagnetic Modeling" by Garth Upshaw and Michael J. Grage, and "An EM Language Translator and Macro Processor" by Edgar Coffey and Allen Lockyer, all of which are found elsewhere in these symposium proceedings.

While on the subject of computer programs and the PC machines, it should be noted that GEMACS itself is available on floppy disks for the IBM-AT compatibles. Furthermore, this is a full version of GEMACS 4.0 with capabilities equaling those that are available for the mainframe computers, including both the interior and exterior analysis features. The advantages of having GEMACS on a PC are numerous, among which are quick turn-around times for small concept studies, greater ease and opportunity for executing classified studies, and ease of modification and update. Further detail can be found in a companion paper "GEMACS on a Personal Computer" by Edgar Coffey.

As is apparent from these developments, GEMACS is a continually growing analysis system. New features are being added to increase its usability and versatility, as well as provide a capability for studying finer details with more precision. Other tools, such as the Source Book and GAUGE, make approaching and using GEMACS easier than has ever been available for any computational electromagnetic fields analysis tool.

A GEMACS Source Book

Edgar L. Coffey
Advanced Electromagnetics
5617 Palomino Dr. NW
Albuquerque, New Mexico 87120

Kenneth R. Siarkiewicz
Rome Air Development Center
RADC/RBCT
Griffiss Air Force Base, NY 13441

Introduction

A *Source Book* for the GEMACS (*General Electromagnetic Model for the Analysis of Complex Systems*) computer code has been written to aid the user of GEMACS in areas which require electromagnetic analysis, design, and measurement. Over 800 pages long, its purpose is to aid in the transfer of "lessons learned" in the use of GEMACS to solve practical problems, a tool to help you use GEMACS better. It is definitely not a treatise on theoretical electromagnetics or fundamental numerical techniques, though there is material on these subjects. The greater bulk of material concerns "what" GEMACS' capabilities are, "how" those capabilities can be tapped to solve practical problems, and a little of "why" GEMACS does some things the way it does. Though some of the material is very specific to GEMACS (e.g., multi-region aperture coupling), many of the concepts and ideas will be useful to users of other computer programs.

This paper delves into the contents of the *Source Book*, including applications and examples, by discussing its concept, layout, and the solution of some of the examples contained in it. It is hoped that readers will be encouraged to submit their own contributions to the authors and that the *Source Book* can serve as a vehicle for interchanging EM modeling ideas and "lessons learned."

Source Book EM Concepts

The first major section of the *Source Book* is devoted to a description of the GEMACS execution and geometry commands, GEMACS concepts and the thought processes one might go through in setting up a typical electromagnetic problem with GEMACS. Figure 1 shows a communications hut with roof-mounted antennas for which eight (8) different electromagnetic problems have been formulated.

1. Antenna Design and Performance
2. Antenna Siting
3. Antenna-to-Antenna Coupling
4. Intrasystem Interference
5. Radiation Hazard
6. Emissions from Structure
7. Vulnerability to Electromagnetic Threats
8. Interior Coupling

For each problem category, the major electromagnetic issues are identified and possible solution approaches discussed. Then, a skeleton outline of a GEMACS input to solve the problem is given. Each command line is cross referenced to a *Source Book* section which more fully explains the command syntax and function.

This work was sponsored by Rome Air Development Center, RADC/RBCT, Griffiss Air Force Base, NY under contract F30602-86-C-0015.

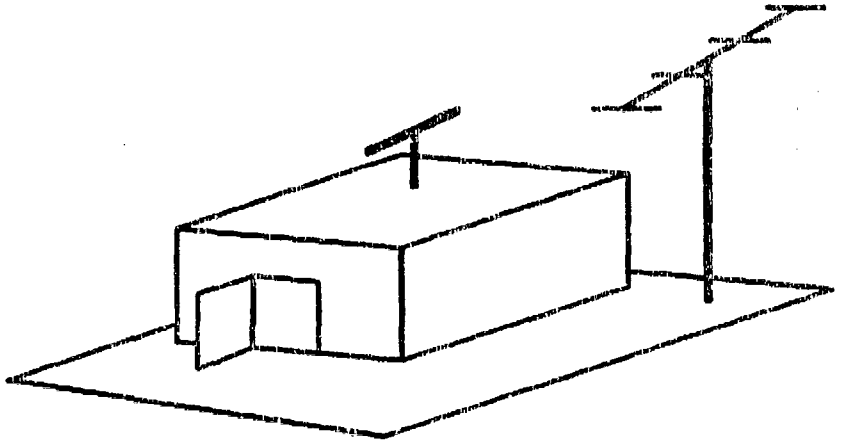


Figure 1. Communications Hut with Roof-Mounted Antennas.

Later in the section, the concepts discussed for the eight example problems are distilled into a discussion of their common attributes. These include (1) problem topology, (2) structure and environment (both exterior and interior regions), (3) the interface of multiple regions at apertures, and (4) structure modeling guidelines. All subjects have been cross referenced into the various sections of the *Source Book* in which the concepts are more thoroughly discussed and have been illustrated with other examples. The section ends with a discussion of selecting a well-suited solution method from among the seven major solution approaches offered by GEMACS.

1. Method of Moments (MOM) with Wires, Patches, or Both
2. Method of Moments Combined with Plane or Rotational Symmetry
3. Method of Moments Combined with Banded Matrix Iteration (BMI)
4. Geometrical Theory of Diffraction (GTD)§
5. A MOM/GTD Hybrid Method
6. Finite Differences (FD) in the Frequency Domain
7. FD hybrids with MOM and GTD

Other subsections of the EM Concepts section deal with hosting GEMACS on a computer and descriptions of all the GEMACS execution and geometry commands. The subsection on hosting GEMACS gives information regarding GEMACS' structure into six (6) modules, GEMACS' peripheral file system, and some ideas on how to interface GEMACS with other computer programs (*e.g.*, a CAD/CAM graphics system). The subsections on execution and geometry commands discuss the "ins and outs" of using the commands, though information in the *GEMACS User Manual* is not repeated here. For instance, it is shown how to loop over frequency in both linear and logarithmic steps, the function and use of user-defined symbolic names, and how to change the physics interactions midway through a problem to achieve great time savings.

Source Book Techniques

The *Source Book* material has been divided into concepts, techniques, applications, and reference material, with the vast bulk of material dealing with techniques and applications. There are seven techniques implemented in GEMACS, each of which is discussed in the *Source Book*:

§The uniform theory of diffraction is included in this category even though the "GTD" designation is used throughout the paper.

- o Method of Moments (wires, patches, hybrids) (MOM)
- o Plane and Rotational Symmetry
- o Banded Matrix Iteration
- o Geometrical Theory of Diffraction (GTD/UTD)
- o A MOM/GTD Hybrid Technique
- o Frequency-Domain Finite Differences (FD)
- o Hybrids of MOM/GTD and FD for Aperture Coupling Problems

The overall purpose of each chapter in the Techniques section is to give the reader a better understanding of the basic solution techniques in GEMACS version 4. The theory of each method is discussed, not by page after page of complex equations, but in terms of concepts with which a practicing engineer would be familiar. Emphasis is placed on transferring the "theoretical" knowledge into an understanding of how to implement a particular solution technique with GEMACS execution commands and how to construct a geometry model of the structure for that solution method. Most chapters have at least one worked problem showing the GEMACS input deck and the actual output listings generated by the GEMACS modules.

These chapters also attempt to introduce "thought provoking" ideas which a reader can develop more fully on his own. For example, when one thinks of modeling a surface with a thin-wire mesh, inevitably one draws a surface with square or rectangular meshes. However, it is shown that a triangularly shaped mesh (figure 2) yields the same density of coverage with a 13% savings in the number of wire segments. This could yield a matrix fill time savings of 28% (i.e., $1.13^2 = 1.28$) and a matrix solution time savings of 44% (i.e., $1.13^3 = 1.44$).

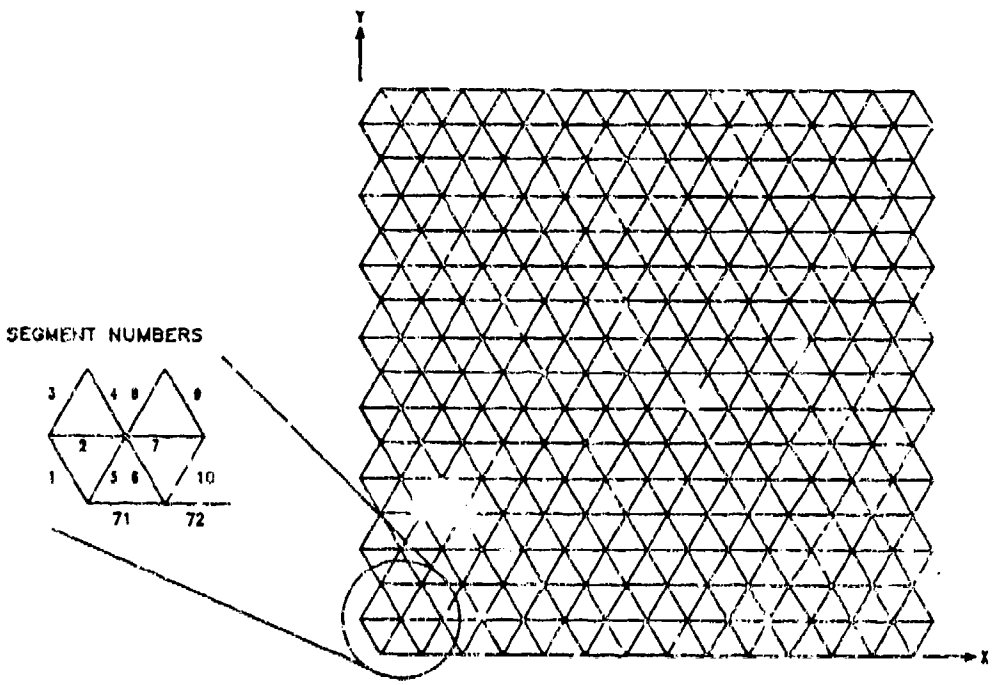


Figure 2. Triangular Thin-Wire Mesh Generated by GEMACS.

As an example of how the *Source Book* covers a particular technique, consider the topic of Plane and Rotational Symmetry. First the plane and rotational symmetry concepts are described in terms of everyday phenomena, followed by a discussion of the advantages

and disadvantages of using symmetry with GEMACS. Then, the reader is walked through the concepts which he must consider if he desires to utilize symmetry. Finally, three complete examples using plane or rotational symmetry are described and solved with GEMACS.

The results of the examples are used to drive home the important concepts of the section. For instance, the savings in computer time that can be achieved with various orders of symmetry is illustrated by running a symmetric cylinder problem with several degrees of symmetry. Results such as those shown in figure 3 make clear that symmetry can give great time savings up to the point that the overhead in utilizing symmetry overtakes the time saved in the physics and mathematics.

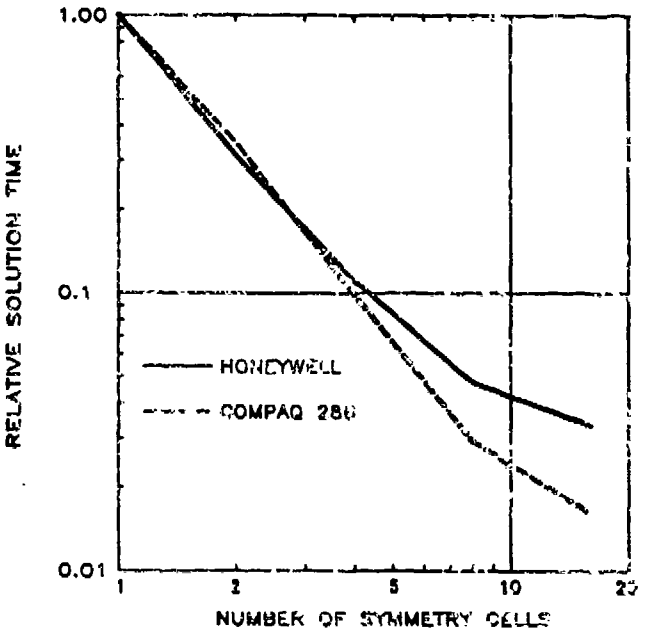


Figure 3. Time Savings Achieved Using Rotational Symmetry with a MOM Cylinder.

Source Book Applications

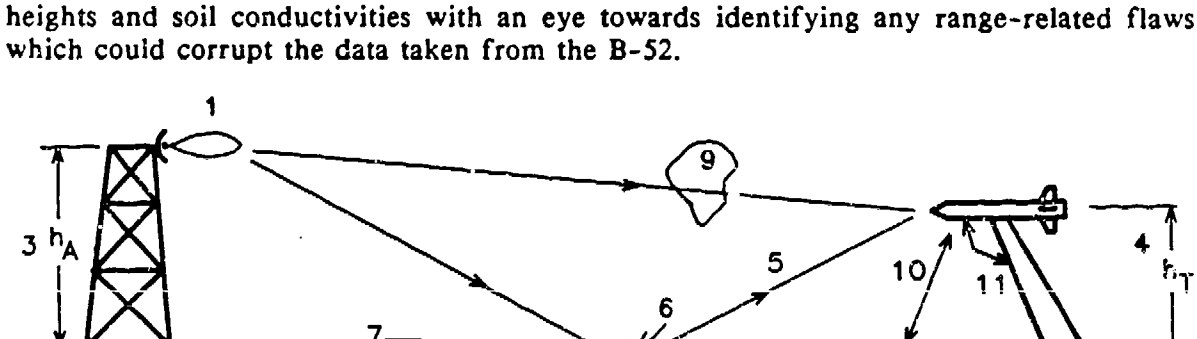
Seven applications topics were chosen for inclusion in the initial release of the *Source Book*. It is hoped that as the *Source Book* becomes used by the EM community others will contribute new topics and augment the present ones listed below.

- o Antenna Analysis
- o In-Place Antenna Analysis (Antennas on Structures)
- o EMC/EMI Antenna-to-Antenna Coupling
- o EM System Threats (e.g., Aperture Coupling)
- o EM Problems with Materials
- o EM Scatter
- o Characterization of Measurements

The *Source Book* application chapters focus on the issues, techniques, and solution methods of a particular topic area. For instance, the antenna analysis chapter defines the standard antenna parameters (*e.g.*, impedance, gain, efficiency) and relates them to GEMACS outputs (*e.g.*, currents, power input, peak field strength). Alternate solution approaches are given when feasible, such as the four different methods of modeling a cavity-backed spiral antenna. Numerous examples are given in each chapter, including GEMACS inputs and results.

Unusual and unique approaches to problems are pointed out, too. For instance, the GEMACS checkpoint/restart feature is used to find the effects of a parabolic dish feed type and placement on dish field patterns for several feeds with just one MOM interaction matrix for the patch model of the dish surface. This represented a 60:1 time savings on the second and subsequent simulations. The interaction matrix is computed and factored for the first feed type and position, then stored in the GEMACS checkpoint file. Subsequent feed types and positions are studied by first restarting GEMACS using the previously generated checkpoint file. This reads back into the problem the factored interaction matrix. A new excitation is defined and back substituted to generate new dish currents.

To illustrate the content of a *Source Book* application area, consider the Characterization of Measurements application topic. This *Source Book* chapter discusses the principal issues on an outdoor electromagnetic measurement range (figure 4) and how most of them can be modeled with GEMACS. For instance, figure 5 shows a B-52 aircraft on a turntable at the RADC/Stockbridge range. This scenario was studied with GEMACS to see how the Stockbridge results compared to free space predictions for various turntable heights and soil conductivities with an eye towards identifying any range-related flaws which could corrupt the data taken from the B-52.



1. ANTENNA PATTERN AND GAIN
2. RANGE LENGTH
3. ANTENNA HEIGHT
4. TARGET HEIGHT
5. REFLECTED RAY(S)
6. DIFFUSE SCATTER
7. GROUND PLANE SURFACE PROFILE
8. GROUND CONSTITUTIVE PARAMETERS
9. ATMOSPHERIC ANOMALIES
10. TARGET–TO–GROUND COUPLING
11. TARGET–TO–SUPPORT COUPLING

Figure 4. Outdoor Test Configuration Showing Principal Sources of Measurement Error.

Not all range examples need be as complex to illustrate an important point. One of the most revealing range examples in the chapter is a clutter fence placement study. Clutter fences are used to break up ground reflections on ranges where target and antenna heights are insufficient to keep ground clutter to a minimum. However, the price paid for having no ground reflection is that rays will diffract from the edges of the clutter fences (figure 6), creating some standing waves in the working volume. The GEMACS study in the chapter shows how one could efficiently simulate various fence positions and orientations to achieve the "best" field taper in the working volume. In the particular example given in the *Source Book* the SWR in the working volume was reduced from greater than 12 dB (no clutter fences) to less than 1.3 dB (with 3 fences 60 m apart and tilted 60° up from horizontal).

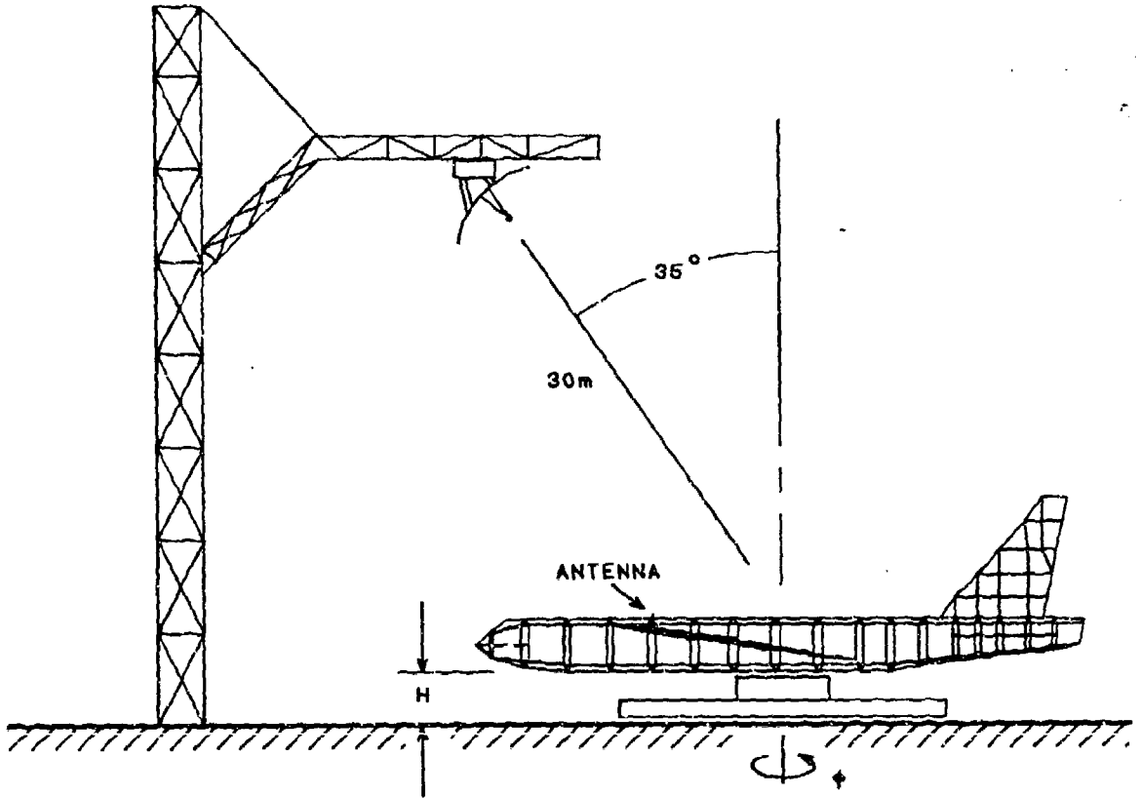


Figure 5. Schematic View of RADC/Stockbridge B-52 Range.

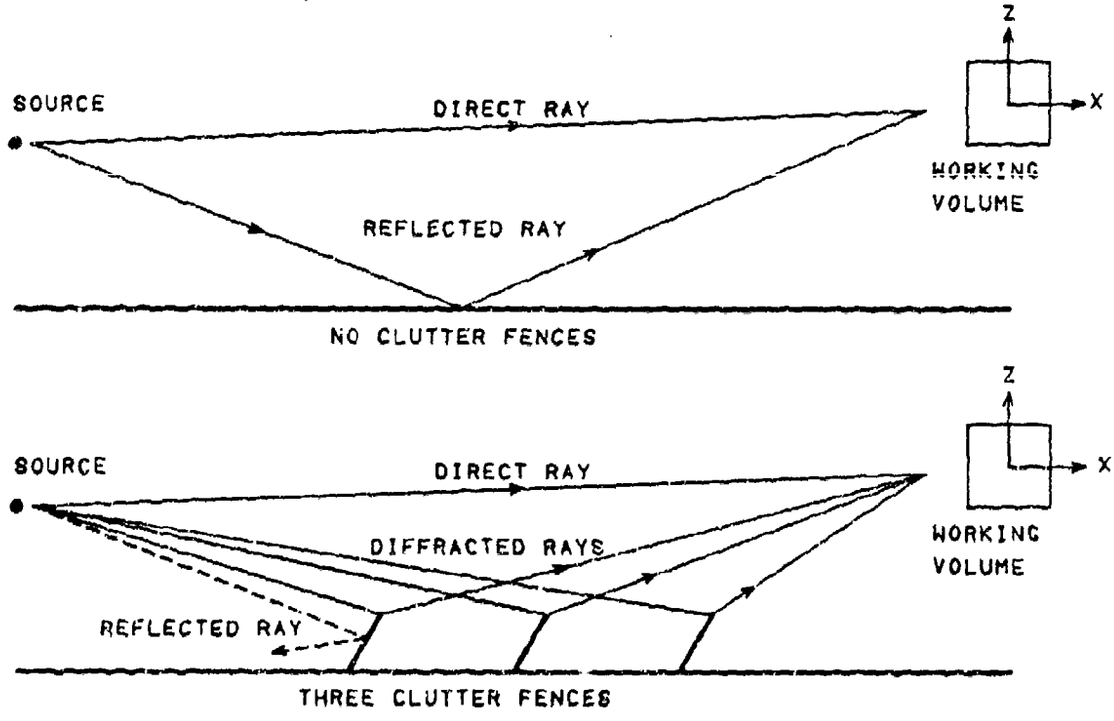


Figure 6. Placement of Clutter Fences to Break Up Specular Ground Scatter.

Source Book Appendixes

The *Source Book* contains appendixes of (1) cross reference topics and (2) customizing GEMACS for a particular computer. Over 180 EM topic areas are cross referenced into nearly 2,000 *Source Book* sections so that the reader may find all discussions on a particular topic by referring to this appendix. Cross references are also liberally sprinkled throughout the *Source Book* so that the reader can immediately find additional information on a topic about which he is reading.

The second *Source Book* appendix shows how the GEMACS program can be customized to any host computer system by changing its array sizes. This is not merely a "big is better" discussion but an approach for optimizing the use of available computer resources for the types of problems a particular user is most likely to encounter. For example, MOM-only problems run more efficiently the more that storage can be allocated to the matrix factor process (GEMACS SOLVE command). But GTD-only problems do not generate an interaction matrix, thus freeing storage for more geometry elements (plates, cylinder, end caps). This appendix shows the user the effects of changing the array sizes on all GEMACS solution techniques and gives clear instructions as to exactly what changes are required for a particular situation.

Solution of Multi-Region, Aperture-Coupled Problems with GEMACS 4.0

Edgar L. Coffey
Advanced Electromagnetics
5617 Palomino Dr. NW
Albuquerque, New Mexico 87120

Kenneth R. Siarkiewicz
Rome Air Development Center
RADC/RBCT
Griffiss Air Force Base, NY 13441

Introduction

Many of the important electromagnetic (EM) analyses which must be performed on today's complex military systems involve the calculation of coupling through breaks in a structure's outer "skin" onto cables and equipment inside the structure. Computations are also frequently performed on the radiation of internal signals which "leak" out through these same breaks in the structure surface. In either case the coupling mechanisms need to be evaluated.

The popular electromagnetic techniques in use today (MOM, GTD, FD, *etc.*) have difficulty working an exterior/interior problem. MOM and GTD are well-suited for fields analysis external to closed surfaces because they utilize the integral form of Maxwell's equations. Finite differences, by virtue of its differential equation form, is better suited for interior or cavity fields analysis. But neither category of physics works particularly well outside its region of applicability.

A multiple region hybrid solution capability has been implemented in version 4.0 of GEMACS in order to attack problems such as these. A complex structure is divided into a number of separate regions (*e.g.*, an exterior and several interior regions). Areas between adjacent regions which permit the flow of EM energy are called "apertures," and may be thought of as "holes" in otherwise solid, perfectly conducting surfaces. Basis functions are defined within the apertures, and each problem region is worked *separately* from the others, with its aperture basis functions as unknowns. Since the regions have been separated, the exterior can be worked with MOM or GTD, while the interior(s) may be worked with FD. This method has been given the name "FD Hybrid."

This paper describes the physics and mathematics of working multiple region aperture-coupled problems. Two examples will be used to illustrate the technique: (1) rectangular aperture in an infinite screen and (2) waveguide opening onto a finite ground plane.

Overview of the Theory

The foundation for the FD-hybrid method is the ability to divide an electromagnetic problem into several regions so that different numerical techniques can be used on different parts of the structure. Perhaps MOM and GTD could be used in the exterior and FD (or finite elements) in the interior. There may be more than one interior region, as shown in figure 1.

This work was sponsored by Rome Air Development Center, RADC/RBCT, Griffiss Air Force Base, NY under contracts F30602-83-C-0183 and F30602-86-C-0015.

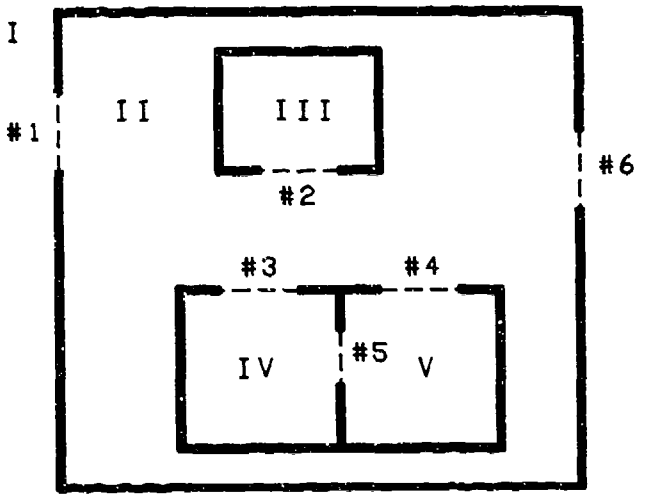


Figure 1. Aperture Coupling Among Five Problem Regions.

A region can be thought of as a volume almost completely enclosed by an opaque boundary, with at most a few "holes" cut into the boundary surface. These holes are called apertures, and it is only through the apertures that electromagnetic energy can penetrate into a region.

The basic theory of the FD-hybrid method comes from Mautz and Harrington [1]. Basis functions of magnetic current are defined in each aperture area (figure 2). These functions then interact with the structure from which an interaction matrix§ can be computed using standard MOM or MOM/GTD techniques. Likewise, sources in a region will impinge on the aperture basis functions and create a MOM-like excitation vector.

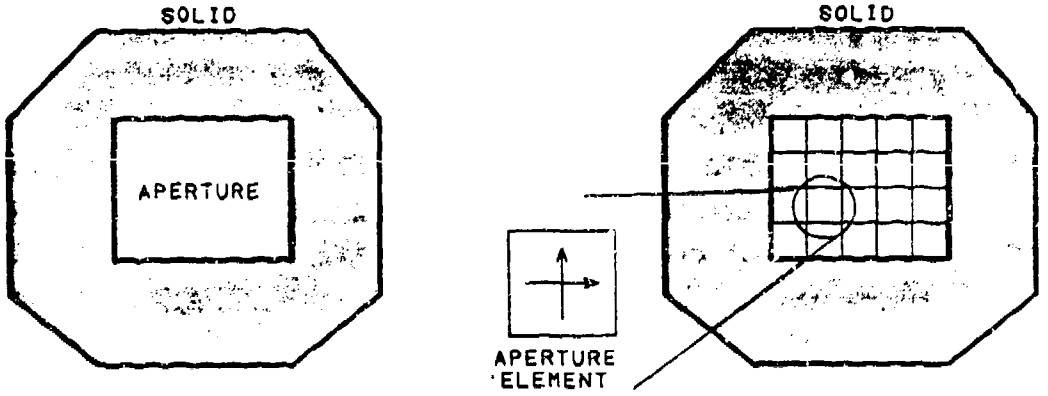


Figure 2. Division of Aperture Into Basis Functions.

Mautz and Harrington compute interaction matrices on either side of the aperture, add them together, and solve the resulting set of simultaneous equations for the magnetic surface current (hence, electric field) in the aperture. Once the aperture field is known, the fields anywhere on either side of the aperture can be found.

§The units of an aperture-to-aperture matrix element is admittance, hence the term "interaction" matrix instead of "impedance" matrix. The matrix symbol [Z] will be retained, however.

This approach is straightforward to implement for simple problems involving only a single aperture and no other MOM elements, but it is cumbersome to use for the general case such as the one shown in figure 1. A more general formulation becomes mathematically tedious (beyond the scope of this paper to present) but yields an elegant numerical implementation. Details on the mathematics may be found in [2] and [3].

Perhaps the clearest way to explain the general formulation is by analogy with network theory. The interaction matrix and excitation vector for the physics in each problem region can be thought of as a network interaction matrix [Z] and excitation vector [V].§ In figure 3 the left-hand network represents region *A*, while the right-hand network represents region *B*. [Z] and [V] for each region are computed with the networks disconnected (*e.g.*, not coupled). The common network nodes, in the center of the figure, represent the aperture field voltage equivalent $[V_{AP}]$. The electric current flowing into the region *A* network is $[I_{total}]_A$, and the current flowing into the region *B* network is $[I_{total}]_B$, the negative of $[I_{total}]_A$. The currents represent the aperture magnetic field in the analogy. The network nodes not joined together represent non-aperture unknowns in both regions (*e.g.*, wires, patches).

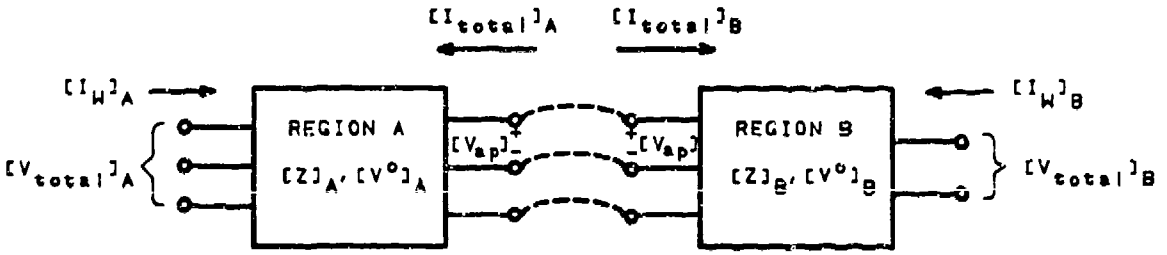


Figure 3. Network Connection Analog to the Aperture Problem.

The problem in figure 3 is solved for $[V_{AP}]$ and $[I_{total}]$ in each region. Once these quantities have been determined, they can be used as "stiff" sources to drive a particular region. This lets the adjoining region(s) be ignored, as the "stiff" sources mask out their effects. Hence, to find wire currents, cavity fields, etc. in regions *A* and *B*, the network analogy in figure 4 can be used.

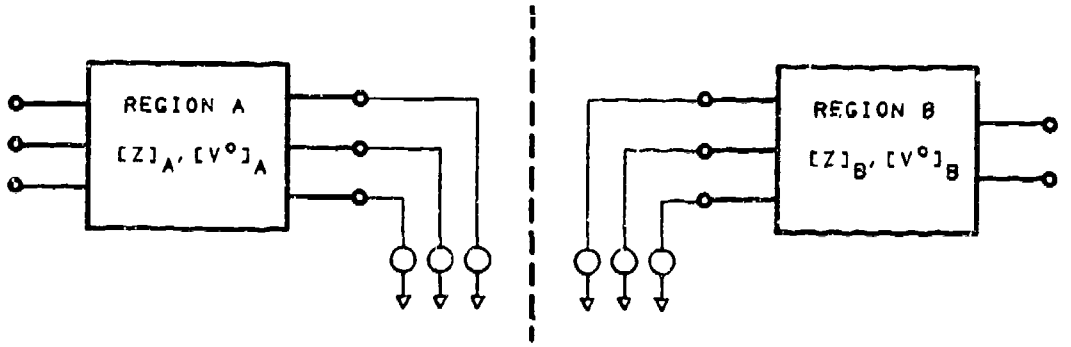


Figure 4. Replacement of Aperture Unknowns with "Stiff" Sources.

By following the network analog, the solution approach becomes obvious.

§Note that while the symbols [Z] and [V] imply units of ohms and volts, the actual units of [Z] and [V] can be just about anything.

1. Disconnect networks *A* and *B* by shorting the common terminals.
2. Find [Z] and [V] for each of the disconnected networks.
3. Enforce known boundary conditions at the nodes not associated with apertures.
4. Reduce [Z] and [V] for each region to just the common nodes.
5. Connect the common nodes together and solve for voltage and current at the interface.
6. Use the interface voltages and currents as "stiff" sources to again disconnect the regions.
7. Solve for observables of interest in the disconnected regions.

This approach is not limited to just one aperture between two regions or to a classical layered topology. It allows a layered topology to any depth, multiple apertures on any and all boundaries, etc., as shown in figure 1. In addition, any region can have other unknowns (wire and patch currents) as manifested by the unconnected nodes in figure 3. Finally, the method is not dependent on how the physics of the individual regions are transformed into a numerical equivalent. The only constraint is that there must be field points analogous to the connected nodes in figure 3. Hence, we are free to pose cavity problems with finite differences, finite elements, unimoment method, etc. while at the same time work the exterior problem with MOM or MOM/GTD.

Implementation in GEMACS

The solution approach described above has been implemented into GEMACS version 4.0 by using existing execution commands for generating physics quantities, adding a new CONECT command to join together multiple regions, and using existing execution commands to factor and solve the matrices generated by the simultaneous equations.

What lets us implement so powerful a method with so few changes to GEMACS is the introduction of the aperture basis function (following the approach of [1]). Apertures are short-circuit modeling elements (*cf.* open-circuit wire segments), so the problem regions are disconnected automatically (step 1 above).

Apertures can be thought of as holes cut into an otherwise solid surface. Hence, the structure model for a multiple region problem can be built as follows. For each region of the problem:

- Build what would be a solid enclosing boundary (were there no apertures) from GTD geometry elements. This boundary may be multiply connected (*e.g.*, a cavity within a cavity.
- Add conducting and dielectric obstacles within the boundary using modified GTD geometry elements.
- Model cables, hydraulics, etc. with MOM wire elements.
- Cut out the aperture "hole" by adding aperture elements to the boundary where the hole should be cut.

GEMACS reads and processes geometry data into a form readable by the physics tasks with the GMDATA command. For an FD-hybrid problem there will be as many GMDATA commands as there are multiple regions. Among other things GMDATA sorts the basis function unknowns so that wire segments appear first in the [Z] matrix, then patches, and finally aperture elements. By sorting the geometry with GMDATA, GEMACS can easily distinguish between the connected and unconnected nodes in figure 3.

The physics for each region is cast into numerical form (step 2) with a number of GEMACS commands. The numerical technique to be used in a particular region is selected with the SETINT command. The interaction matrix is generated by the ZGEN command. Excitations can be voltage sources (VSRC command) or field sources (ESRC command), and near and far fields may be requested with the EFIELD command. Physics commands for a particular region are grouped together in the GEMACS input stream, as shown below.

```
SETINT MOM GTD                    $SELECT MOM AND GTD PHYSICS
GMDATA=OUTER                      $READ AND PROCESS GEOMETRY DATA
ZGEN GMDATA=OUTER ZMATRX=ZIJ      $GENERATE [Z]
SRC=VSRC(OUTER) V=1.,0. SEGS=47 $GENERATE [V]
EPLANE = EFIELD(OUTER) P1=90. T1=0. DT=1. T2=180. $FIELD PATTERN
HPLANE = EFIELD(OUTER) T1=90. P1=0. DP=1. P2=180. $FIELD PATTERN
```

Steps 3-5 in the last section are all executed with a single GEMACS command: CONECT. The CONECT command tells GEMACS which apertures in which problem regions are to be joined together. Suppose apertures 1, 2, and 3 in region OUTER correspond to apertures 11, 12, and 13 in region INNER. Then the CONECT command to join apertures 1-3 to apertures 11-13 would be

```
CONECT OUTER(AP 1-3) TO INNER(AP 11-13)
```

and would appear in the GEMACS input stream after all the physics commands. What CONECT does is to fill in the unknown excitations in [V] for each region so that the problems can again be disconnected (step 6). The mathematical foundation of the connection process is not the solution of simultaneous equations but Householder's method of modified matrices. Details of the mathematics may be found in [2].

Once the regions have all been connected together and aperture excitations determined, any remaining observables may be found (step 7) by using one of the GEMACS solution commands (BMI or SOLVE). For example, currents in region OUTER may be found with

```
SOLVE Z*J * I = SRC
PRINT I
```

Example 1: Aperture in an Infinite Screen

Just about the simplest two-region problem that can be imagined is that of a simple slot cut into an infinite conducting sheet (figure 5). It is this problem that Mautz and Harrington use to illustrate their technique [1]. The slot is 0.05λ x 0.5λ and is modeled by nine (9) aperture elements. Since each aperture element has two tangential components of magnetic current, a total of 18 unknowns are generated in each region.

Region I is the half space $z < 0$, while region II is the half space $z > 0$ and contains the plane wave source. The geometry data for each region are identical, as listed below. Note that the "infinite" screen is modeled by a very large (200m x 200m) GTD plate.

```
$-------------------------------------------------
$  GEOMETRY DATA FOR REGION I  (Z < 0)            -
$-------------------------------------------------
PL 1 4  -100.  -100.  0.
*        100.  -100.  0.
*        100.   100.  0.
*       -100.   100.  0.
PT  1  -0.20  0.  0.
XL PT 1 8 0.05  0.  0.
AP 1 PT 0.0025   0. 0.  PL 1  9   1 2 3 4 5 6 7 8 9
END
```

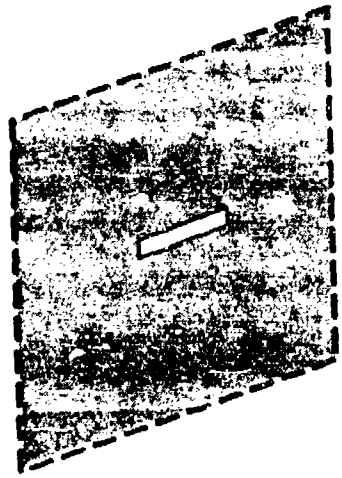


Figure 5. Slot in an Infinite Sheet.

The physics commands for the two regions are different, however. Region II contains the source, which models a pseudo-plane wave as a spherical wave far from the aperture. The incident field is 1 V/m. In addition, scattered fields are requested in the principal planes. The physics commands are shown below and correspond to the outline given earlier. Note that the plate reflection (PR) GTD interaction is selected with SETINT to turn off the diffractions from the plate edges, giving the effects of a true infinite screen. The excitation of region I (SRC1) is not required by the physics (no sources are in region I) but permits problem solution in that region if desired. A dummy source (zero excitation) has been inserted in the commands for that purpose.

```
$
$-------------------------------------------------
$  REGION I                                      -
$-------------------------------------------------
$
SETINT  MOM PR ES  $PR IS USED TO SIMULATE "INFINITE" GROUND PLANE
GMDATA=GEOM1
ZGEN GMDATA=GEOM1 ZMATRX=Z1MAT
SRC1=VSRC(GEOM1) V=0.,0. SEGS=1
$
$-------------------------------------------------
$  REGION II                                     -
$-------------------------------------------------
$
SETINT  MOM PR ES  $PR IS USED TO SIMULATE "INFINITE" GROUND PLANE
GMDATA=GEOM2
ZGEN GMDATA=GEOM2 ZMATRX=Z2MAT
SRC2=ESRC(GEOM2) SW=1000.,0. R=1000. THETA=0.1 PHI=90.
```

The above commands generate all data required before reconnecting the two regions together. Once the problem has been connected (with CONECT), the observables in a region may be found separately from the other regions. In the listing below, region I has been reconnected with region II, and then region II is solved for the aperture fields (symbol I2). Of course, the same fields would be obtained by solving region I instead.

```
$
$-------------------------------------------------
$  CONNECT THE REGIONS TOGETHER AND SOLVE REGION II   -
$-------------------------------------------------
CONECT GEOM1 (AP=1) TO GEOM2 (AP=1)
SOLVE Z2MAT*I2=SRC2
PRINT I2
```

The computed aperture fields (I2) are plotted in figure 6 along with predictions from [1] using different basis functions and solution methods. The field patterns from GEMACS and reference [1] are identical and are shown in figure 7.

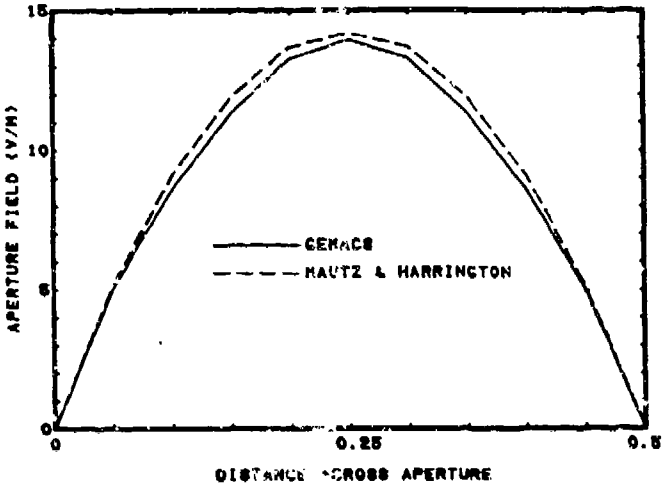


Figure 6. Aperture Fields for the Problem of Figure 5.

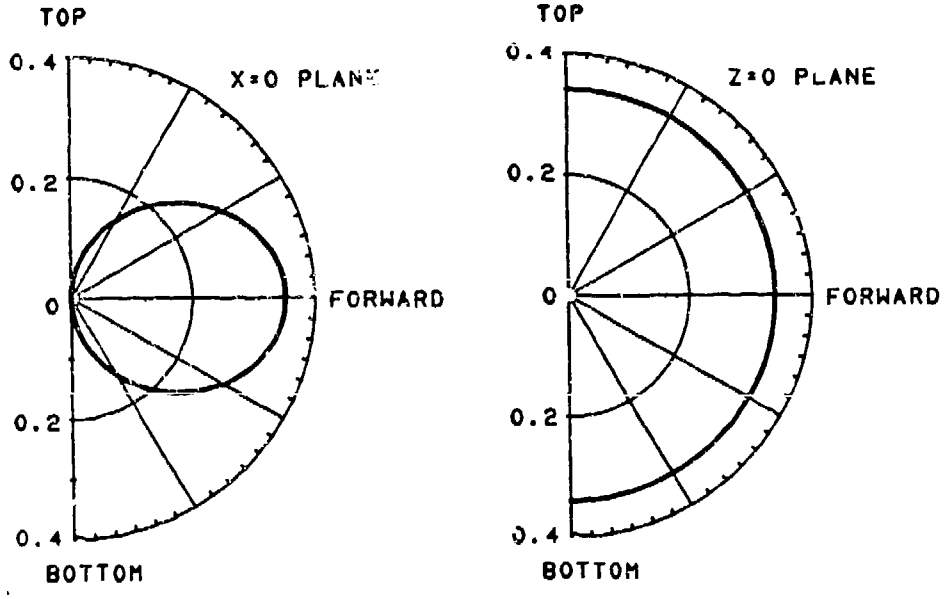


Figure 7. Transmitted Field Pattern of Figure 5.

Example 2: Waveguide Opening onto a Finite Ground Plane

A more interesting example is the structure shown in figure 8. A section of WR-90 waveguide forms a cavity which opens up onto a finite ground plane. It is excited by a probe very close to the back wall of the cavity. In this case, different solution methods must be used to find the fields in the opening, fields in the cavity, and far-field pattern of the waveguide-plate combination. However, all these observables may be found in just one GEMACS execution.

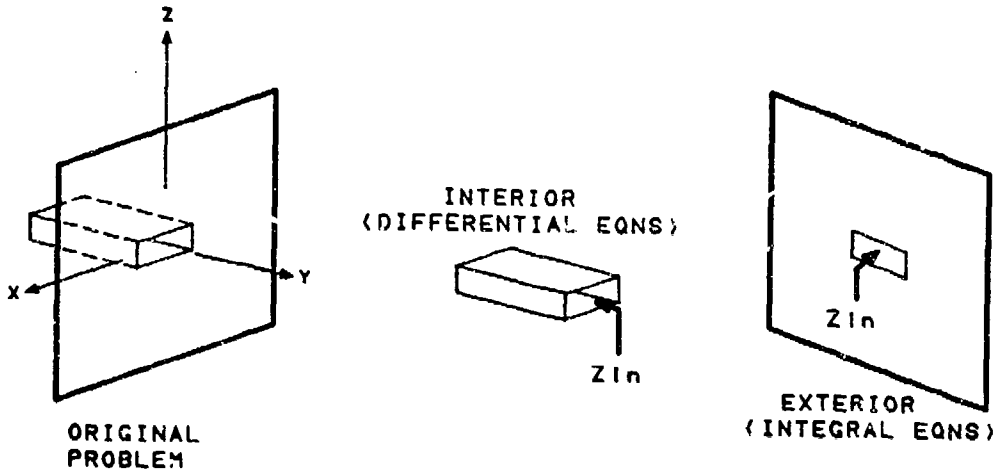


Figure 8. Waveguide Opening onto Finite Ground Plane.

Let region I be the interior of the cavity. As such it is formulated using finite difference physics. Its geometry model is shown below and is nothing more than a box made from six GTD plates, one of which has an aperture opening cut into it. This aperture has been modeled with six aperture elements, yielding a total of 12 unknowns per region. The GRID command tells the FD physics to subdivide the cavity interior into a uniform grid of 0.01563 x 0.02186 x 0.0547 meters. The x-dimension has been more finely subdivided than the $\lambda/10$ criterion requires so that higher order modes (introduced by the placement of the probe) can be adequately supported. The z-dimension is the entire height of the cavity. Other runs with finer z-axis subdivisions took much more computer time but yielded little difference in results, indicating that the z-dimension field taper is nearly uniform. The COND command places a conductivity of $\sigma = 5.7 \times 10^8$ mhos/m on the cavity boundary.

```
$-----------------------------------------------------------------
$   GEOMETRY DESCRIPTION FOR REGION I (CAVITY)                   -
$   THIS HAS BEEN TAKEN FROM THE GEMACS ENGR MAN (P. 174.1)      -
$-----------------------------------------------------------------
GRID  0.01563 0.02186  0.0547
COND 5.7E8
PT  1  0.  0.  0.
PT  2  0.1094 0.  0.
PT  3  0.1094 0.  0.0547
PT  4  0.  0.  0.0547
PT  5  0.  0.21883 0.
PT  6  0.1094  0.21883  0.
PT  7  0.1094  0.21883  0.0547
PT  8  0.  0.21883  0.0547
$
PL  1  4  1  2  3  4  1   $ BACK WALL
PL  2  4  2  6  7  3  1   $ SIDE WALL
PL  3  4  8  7  6  5  1   $ FRONT WALL (CONTAINS APERTURE)
PL  4  4  5  1  4  8  1   $ SIDE WALL
PL  5  4  7  8  4  3  1   $ TOP WALL
PL  6  4  5  6  2  1  1   $ BOTTOM WALL
$
PT 10  0.01563  0.21883  0.02735
XL  PT  10  5  0.015630  0.  0.  $PTS 11-15
AP  1  PT  2.44253E-4  0.  0.  PL  3  6  10 11 12 13 14 15
END
```

The exterior geometry model is identical to the interior's model except that the GRID and COND commands have been removed and that the corners of plate 3 have been extended to make a 60 x 60 cm ground plane.

The GEMACS execution commands are shown below and are similar to those for the slot problem. The major difference is that now two different physics techniques are required, as manifested by the different SETINT commands for the two regions. Now region I requires an FD solution, while region II uses MOM (for the aperture basis functions) and GTD (for the plates). Like the slot problem, a dummy drive (DRV) has been defined for the exterior. The zero excitation vector (DRV) creates a valid GEMACS symbol which is used in the SOLVE command for region II. Since the excitation is zero, the physics are unaffected by it.

```
$
$-------------------------------------------------------------
TITLE "OPEN-ENDED WAVEGUIDE OPENING ONTO A FINITE GROUND PLANE"
$-------------------------------------------------------------
NUMFIL=27
TIME = 40.          $ESTIMATE FOR IBM PC-AT
FRQ = 2000.         $SET FREQUENCY TO 2 GHZ
$
$-------------------------------------------------------------
$   SET UP GEOMETRY AND PHYSICS FOR REGION I (CAVITY)          -
$-------------------------------------------------------------
$
SETINT FD
GMDATA = CAVITY
$  SET SOURCE AT (0.0547, 0.0054747, 0.02735) METERS
SRC = ESRC(CAVITY) DW=1.,0.  R=0.0614 THETA=63.55 PHI=5.71
ZGEN GMDATA=CAVITY ZMATRX=ZIJMAT
CAVFLD=EFIELD(CAVITY) Z1=0.0274 X1=0.1094 Y1=0.DY=0.02186
*                     Y2=0.2188   $ CAVITY FIELDS
$
$-------------------------------------------------------------
$   SET UP GEOMETRY AND PHYSICS FOR REGION II (EXTERIOR)       -
$-------------------------------------------------------------
$
SETINT MOM PL SI
GMDATA = OUTSID
ZGEN GMDATA=OUTSID ZMATRX=ZOUT
DRV = VSRC(OUTSID) V=0.,0.  SEGS=1
YAWFLD=EFIELD(OUTSID) T1=90. P1=0. DP=1. P2=360.   $FIELD PATTERNS
PITFLD=EFIELD(OUTSID) P1=90. P2=270. T1=0. DT=1. T2=180.
PURGE ZSHD
$
$-------------------------------------------------------------
$   CONNECT THE REGIONS TOGETHER                               -
$-------------------------------------------------------------
$
CONECT CAVITY (AP 1)  TO  OUTSID (AP 1)
$
$-------------------------------------------------------------
$   SOLVE REGION I PROBLEM                                     -
$-------------------------------------------------------------
$
SOLVE ZIJMAT*I1 = SRC
PURGE ZIJLWR,ZIJUPR
$
$-------------------------------------------------------------
$   SOLVE REGION II PROBLEM                                    -
$-------------------------------------------------------------
$
SOLVE ZOUT*I2=DRV
PURGE ZLWR,ZUPR
PRINT I2            $APERTURE FIELDS
END
```

The fields in the aperture look essentially like figure 6 and are not shown. The cavity field pattern is shown in figure 9 and is taken down the center of the waveguide from the back wall (near the probe) to the front wall (at the aperture). Note that GEMACS has computed a number of higher order modes in order to reproduce the spike near the probe.

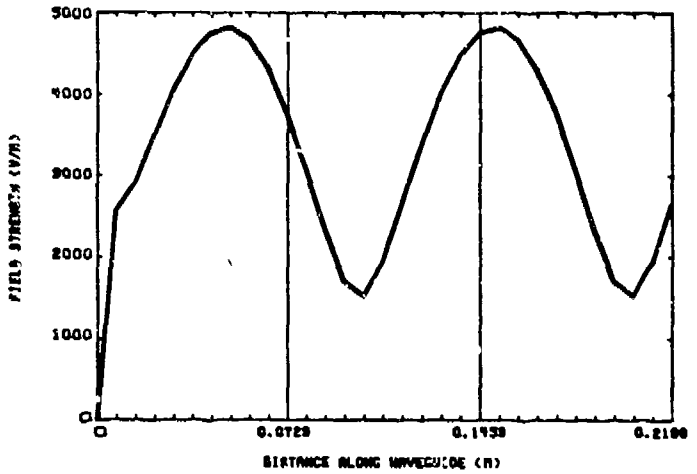


Figure 9. Cavity Fields of Figure 8.

The principal plane far-field patterns are shown in figure 10. These follow the same shape as the patterns from the slot (figure 7) except for the ripple and back lobes caused by diffractions from the plate edges.

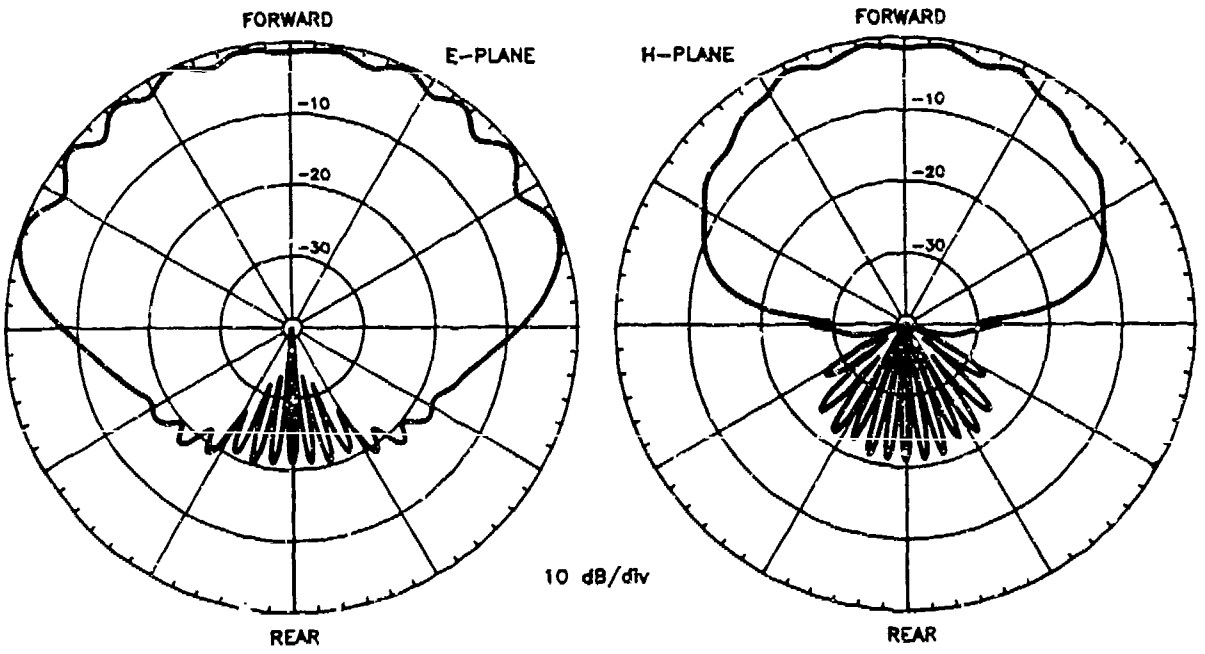


Figure 10. Principal Plane Patterns of Structure in Figure 8.

Summary

An overview of how GEMACS version 4.0 solves multiple region, aperture-coupled problems with the FD-hybrid method has been presented. Theoretical details have been omitted in favor of a conceptual discussion as the theory can be found in the literature [1-3]. The two examples in the paper show the fundamentals of using the technique, though the implementation of FD-hybrid in GEMACS has far more power than can be shown in a single paper.

References

1. J. R. Mautz, R. F. Harrington, and D. T. Auckland, *Electromagnetic Coupling Through Apertures*, RADC Technical Report, RADC-TR-81-380, January 1982.

2. E. L. Coffey and D. L. Kadlec, *General Electromagnetic Model for the Analysis of Complex Systems (GEMACS)*, Version 4 Engineering Manual, RADC Technical Report, RADC-TR-87-68, AD B113530, May 1987.

3. E. L. Coffey, N. W. Coffey, and D. L. Kadlec, *GEMACS Source Book*, Volumes I and II, Advanced Electromagnetics Report AE88R001, for Rome Air Development Center under contract F30602-86-C-0015, February 1988. *(to be published as an RADC technical report)*

APPLICATION ON OF GEMACS-IV FOR SMALL APERTURE COUPLING

R.J. Balestri
Booz Allen & Hamilton, Inc.
East West Towers
4330 East West Highway
Bethesda, MD 20814

INTRODUCTION

The recent release of GEMACS-IV with the incorporation of aperture models should be of great utility in modeling coupling of electromagnetic energy to the interior of structures. This paper will explore the effect of the selection of the number of aperture points and their location on the current induced on a wire located behind an infinite ground screen with an electrically small aperture. Comparison with results obtained by Butler [1] and Lin and Curtis [2]. Both of these works deal with electrically small apertures and the Lin and Curtis paper presents measured data. As will be demonstrated, GEMACS-IV is quite sensitive to the number of point chosen to represent the aperture as well as the excitation employed to drive the aperture. At this time, no modelling guidelines can be developed to aid the user in correctly modeling small apertures although large aperture results compare favorably with [3] which is the formalism implemented in GEMACS-IV.

MODELING APPROACH

GEMACS-IV models apertures using the method of moments formalism [3] to provide the exterior to interior coupling in support of the frequency domain finite difference solution process to solve for interior coupling. These apertures are associated with the plate and cylinder GTD model elements. When apertures are placed on plates, they are associated with the side of the plate for which the normal is defined. Thus a small aperture in an infinite ground screen is constructed by placing the aperture on the positive side of a plate using one of the GEMACS-IV AP geometry commands. The solution is then obtained using only the GTD and MOM processes. The FD process is not used since there is not a closed volume representing the back side of

---

1 Butler and Umashankar, IEE PROCEEDINGS, vol. 127, pt. H, pp. 161-169, June 1980

2 Lin and Curtis, IEEE TRANSACTIONS ON ANTENNAS AND PROPAGATION, vol. AP-24, NO. 2, MARCH 1976

3 Mautz, Harrington and Auckland, ELECTROMAGNETIC COUPLING THROUGH APERTURES, RADC-TR-81-380, JANUARY 1982

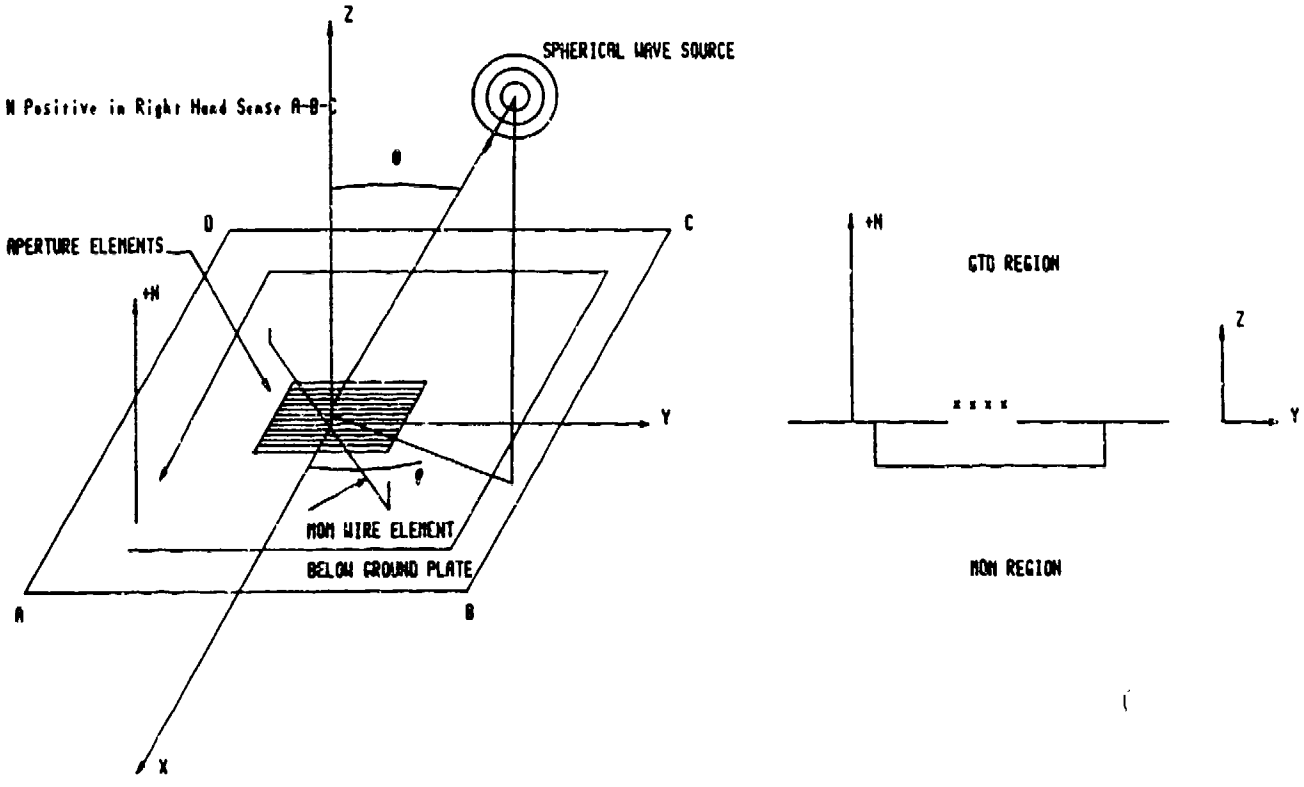


Figure 1 - GEMACS-IV Geometry Regions for Apertures in an Infinite Screen

the plate. This approach is presented in figure 1 where the wire to be coupled to is located on the back side of the plate and the source is on the positive or front side of the plate and illuminates the aperture. While this investigation was limited to a single wire, the objects on the "back" side of the plate could be any MOM developed structure. The two regions are joined by using the CONECT command. Only the aperture elements on the GTD side of the plate are driven by the spherical wave source. Continuity of the field components is performed by the CONECT command.

Since GEMACS-IV models apertures using pulse basis functions, the rule of thumb would dictate using 10 sample points per wavelength, however, since these apertures are extremely small, this rule leads to a single point aperture. In this work, several models were used to determine the sensitivity of the computed results to the number of points in the aperture. The results will be presented in the next two sections for the data presented in references [1] and [2] respectively.

COMPARISON WITH BETHE SMALL HOLE THEORY

Butler's work is based on Bethe small hole theory. His geometry is depicted in figure 2. Figure 3 corresponds to figure 6 of [1], however curves b and c in [1] are mislabelled and have been corrected here. It is worth noting that the results as depicted in figure 3 are normalized to wavelength leading one to believe that, with proper scaling, the results should be identical for any wavelength for which the theory is valid. Figure 4 presents the GEMACS-IV results for a frequency of 300 MHz and all configurations of figure 2. The agreement is excellent using a single point to represent the aperture on a plate.

Figure 5 presents the results for configuration (a) of figure 3 for frequencies of 100, 300, and 1000 MHz. All elements have been scaled to the wavelength. The results bring into question the validity of the scaling presented in [1], however, the agreement found at 300 MHz was obtained by trial and error in the first place. There is not sufficient information to determine if the data in [1] was actually computed with a wavelength of unity, however, if this is so, GEMACS-IV is readily adaptable to small apertures coupling using this modeling technique.

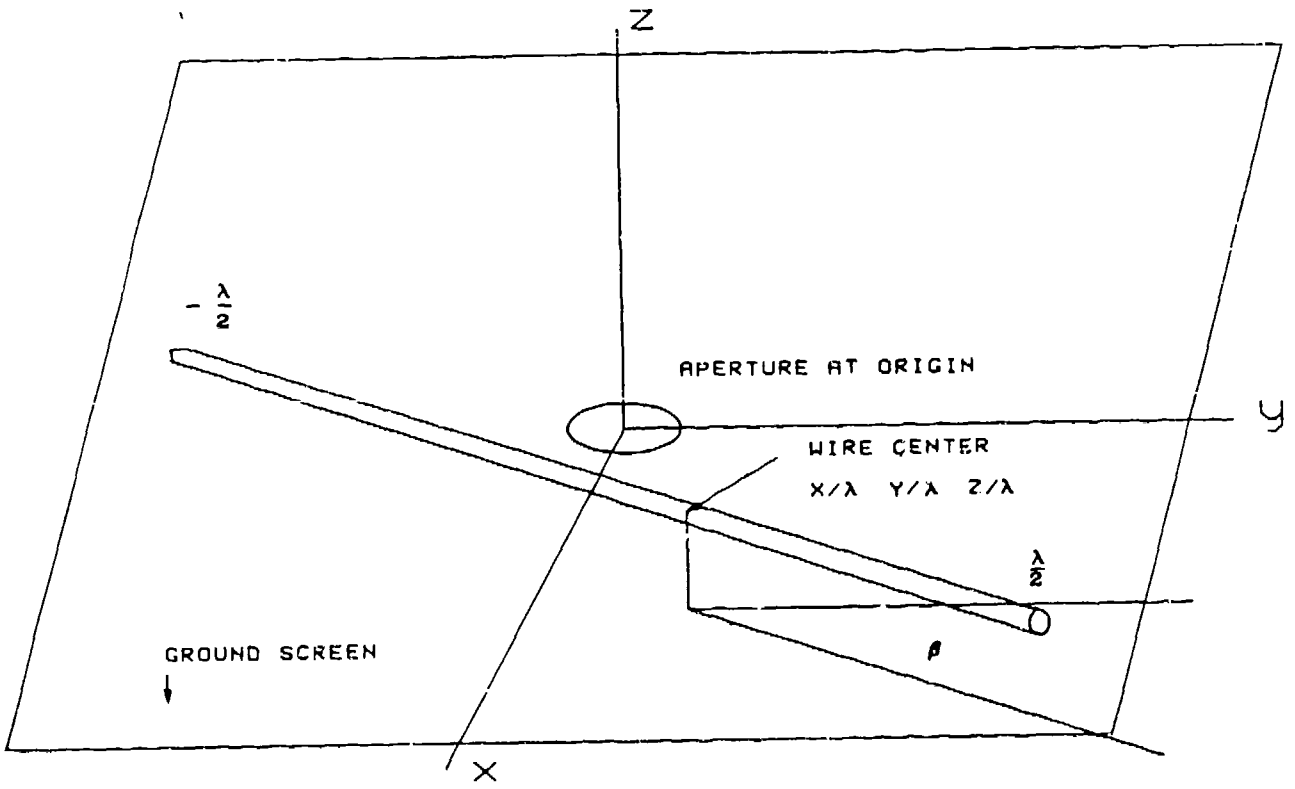


Figure 2 - Small Hole Theory Geometry [2]

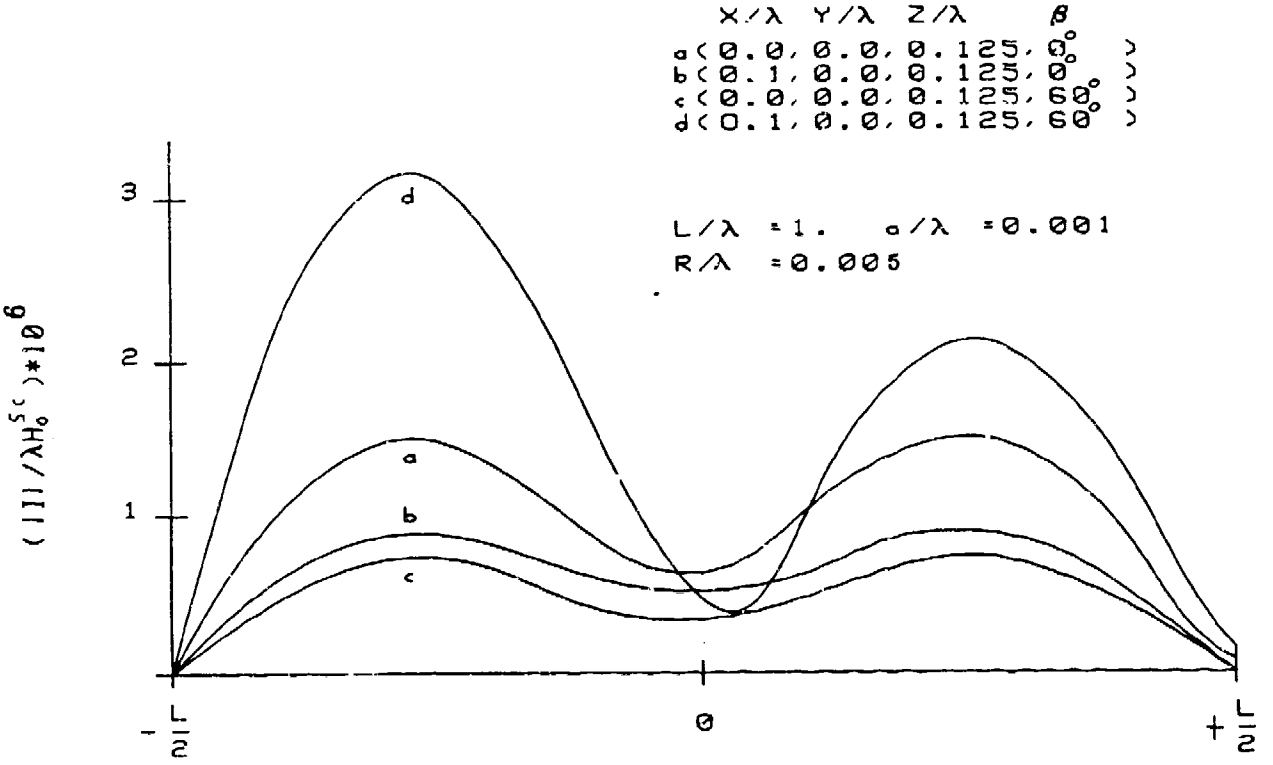


Figure 3 - Small Hole Coupling Results

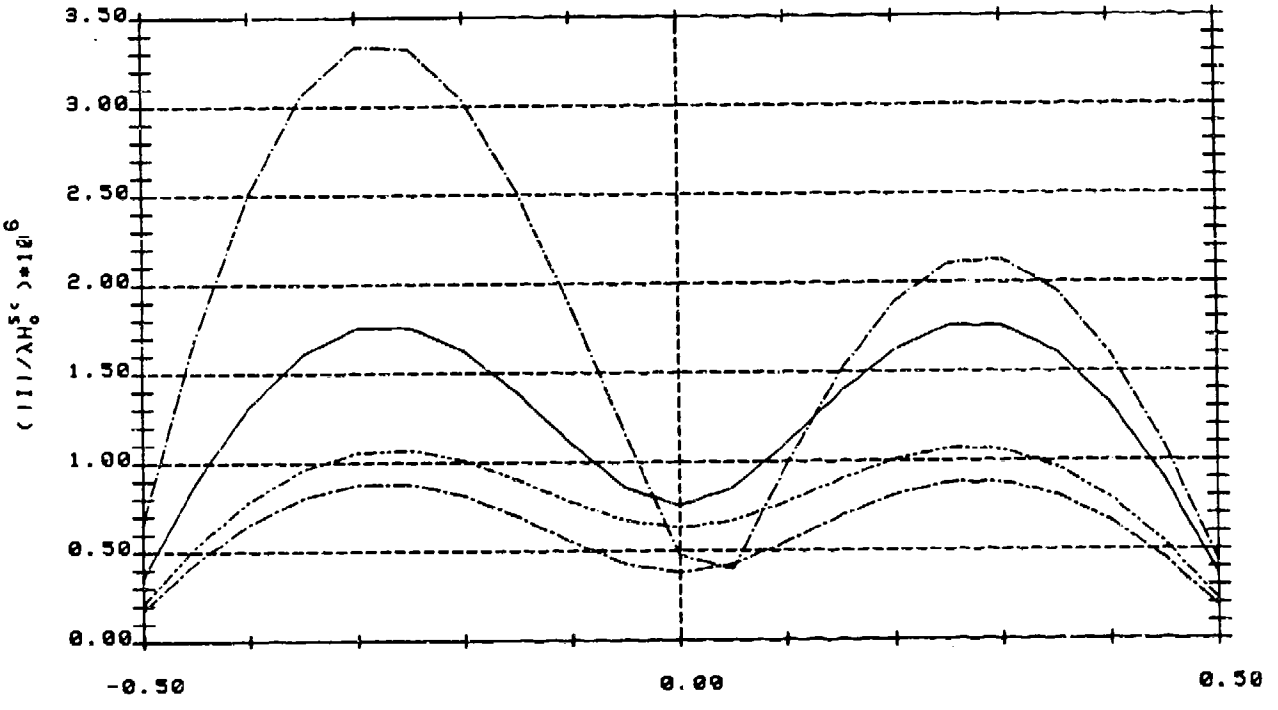


Figure 4 - GEMACS-IV Results for Geometry of Figure 2 at 300 MHz

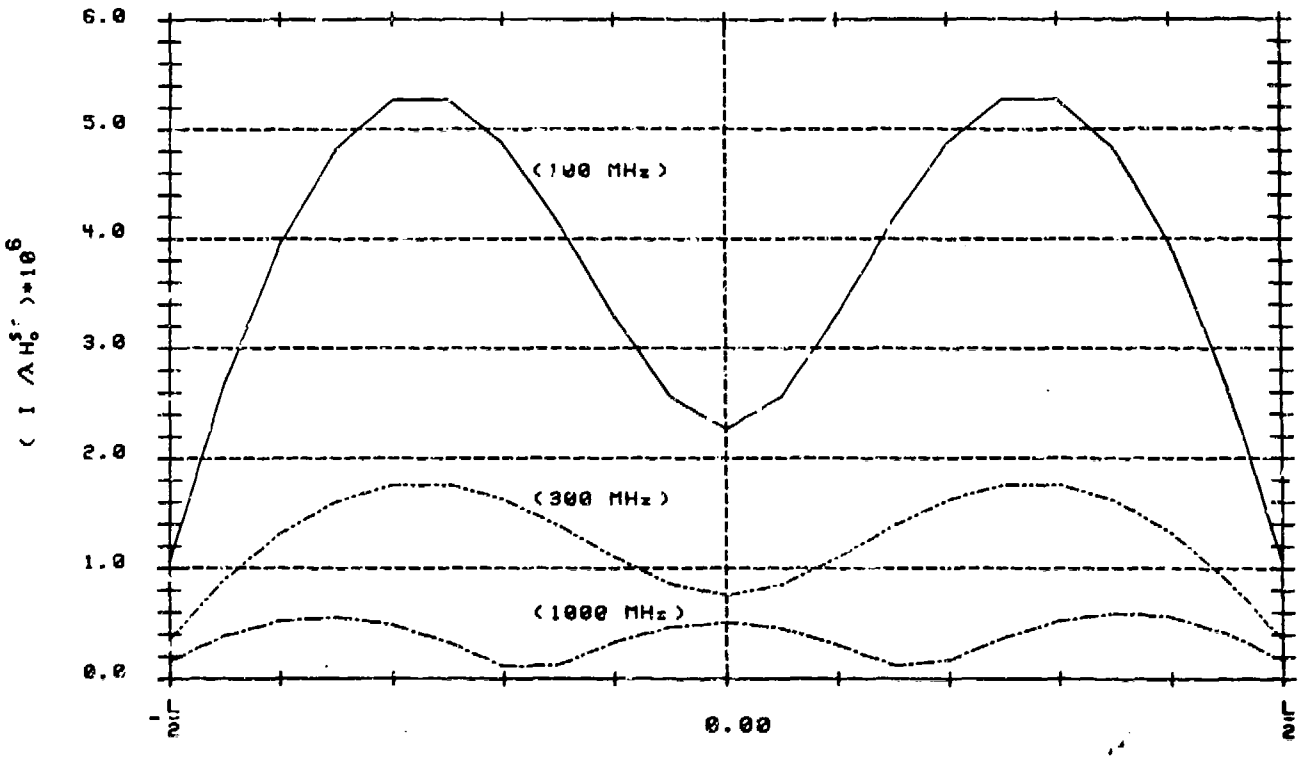


Figure 5 - GEMACS-IV Results for Figure 2(a) at 100,300, and 1000 MHz

COMPARISON WITH MEASUREMENT AND BABINET PRINCIPLE MODEL

The model of Lin and Curtis [2] was based upon using Babinet's principle with the aperture currents computed using a pulse expansion function. In [2], the grid used to represent the aperture appears to have been represented using 49 basis points, however the exact model is not presented.

Figure 6 illustrates the geometry of the problem and the results obtained using Babinet's principle and a transmission line model to obtain the open circuit voltage are presented in figure 7. Figure 8 presents the GEMACS-IV results for 3 aperture models containing 16, 4 and 1 point. As can be seen, the number of aperture elements greatly influences the results with the 16 point model being in close agreement with the results of [2]. It is worth noting that the aperture half wavelength circumference corresponds to 82 MHz which is the resonant frequency observed in both models whereas the measurement of figure 7 indicates an observed resonance closer to 70 MHz. The details of the cavity containing the aperture are not available and these influences may be appreciable.

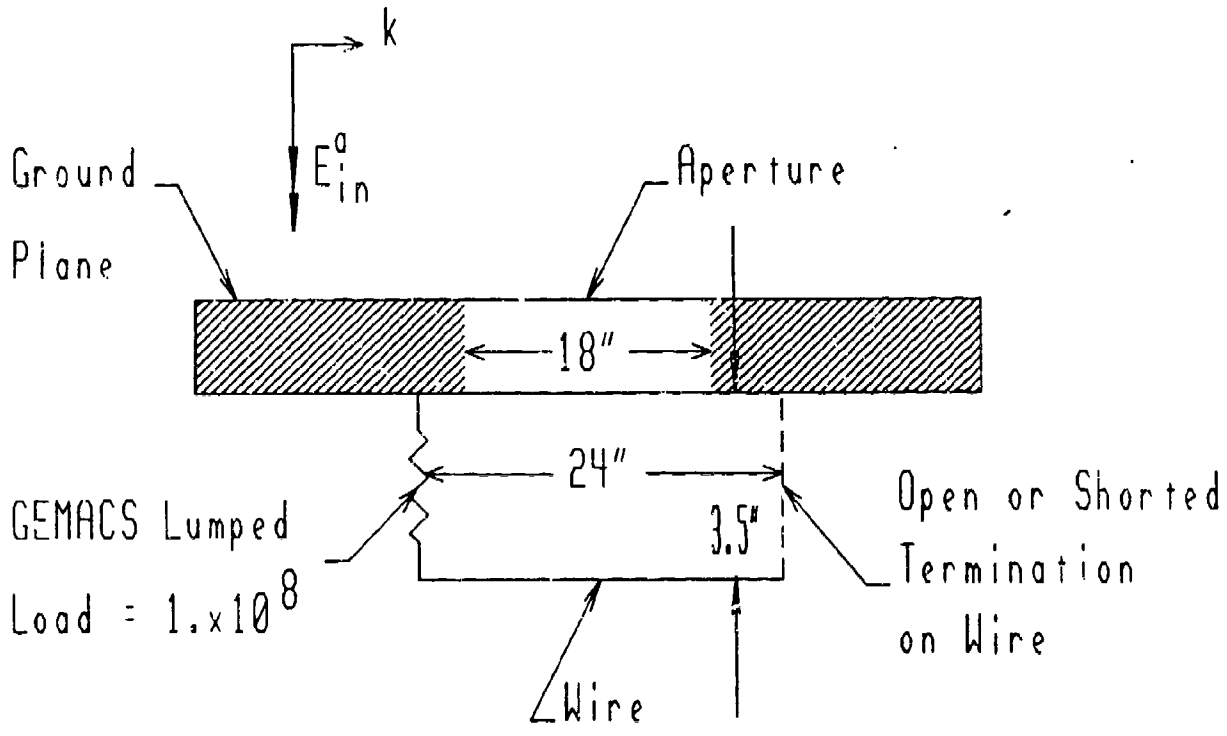


Figure 6 - Reference[1] Geometry and GEMACS-IV Model

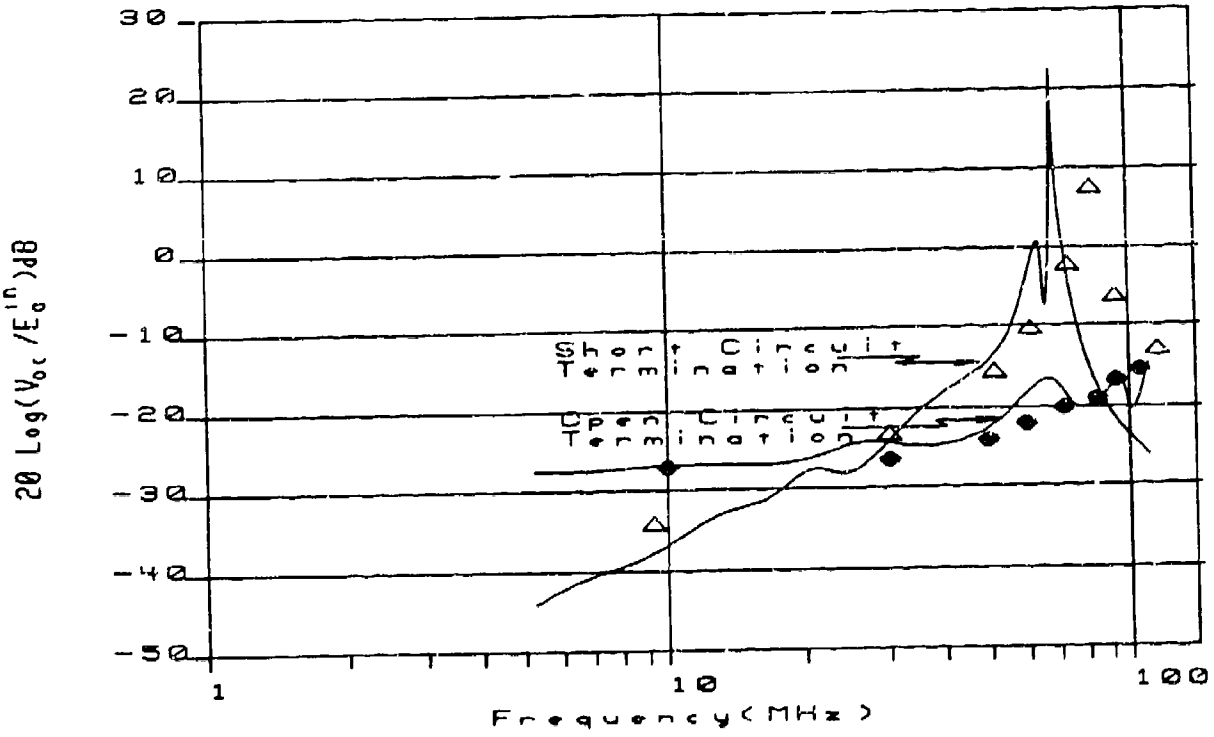


Figure 7 - Open Circuit Voltage for Open and Sort Termination from [2]

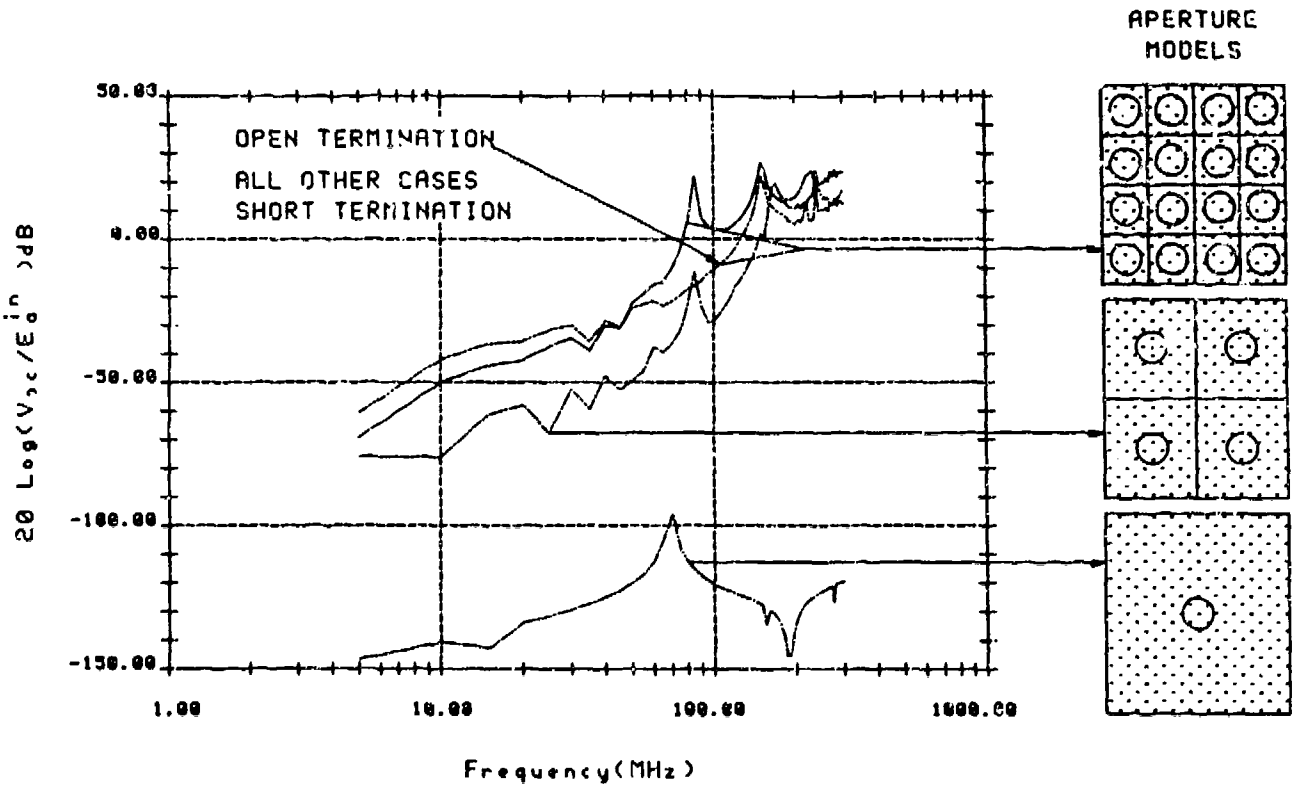


Figure 8 - GEMACS-IV Results for Three Aperture Models for [2]

While the model of [2] satisfied the boundary conditions on the aperture edge as well as in the aperture, GEMACS-IV actually displaces the boundary condition points off of the aperture edge. Since the dominant frequency observed corresponds to the perimeter of the aperture, it seems wise to consider this as the controlling model guideline. In the 16 point aperture model of figure 8, the sampling of the perimeter corresponds to an upper frequency of approximately 200 MHz at 10 samples per wavelength. That the results are in good agreement with [2] is then not surprising since they also effectively used method of moments with pulse expansion functions.

CONCLUSIONS

It appears that when standard MoM rules of thumb modelling guidelines are used, GEMACS-IV can be used to represent electrically small apertures in infinite ground screens. For extremely small apertures such as those of [1], a single point aperture model is sufficient, while for the moderate size aperture of [2], the aperture perimeter is the major modeling consideration. From the experience gained in the preparation of this paper, it can be stated that <u>over/under sampling the aperture will result in extreme variation in results</u> as depicted in figure 8. This is partly due to numerical precision since the MoM interaction elements are on the order of 10^{4} while aperture interaction elements are on the order of 10^{-6}. It should be re-

emphasized that no finite differencing was required due to the association of apertures with the positive side of GTD plate elements. Hence, when cavity effects are not important or first order approximations are sufficient, GEMACS-IV has a new and unique method of combining the GTD and MOM modules to obtain solutions for structures illuminated via apertures.

GEMACS on a Personal Computer

by

Edgar L. Coffey
Advanced Electromagnetics
5617 Palomino Dr. NW
Albuquerque, New Mexico 87120

Most electromagnetic computer programs until recently have required host machines of mainframe or super-mini size. The large number of complex computations needed to generate and solve a method of moments interaction matrix or a geometrical theory of diffraction ray tracing set forced the user to the largest computer available to him. This was not necessarily an ideal solution, since mainframe computers must support a large number of users in order for them to be cost effective. A typical electromagnetic analyst using GEMACS, BSC, or NEC might only be able to run two or three problems per day in this shared environment.

The power and speed of the present generation of personal computers now makes it possible (and even desirable) to host large electromagnetic codes on machines readily available to most engineers. We have converted a number of supposedly "mainframe" programs to personal computers without having to sacrifice *any* of the original capabilities of those programs, thus creating an electromagnetic engineering work station at modest cost. We have found in addition that for all but the largest EM problems the PC-based work station gives better turnaround than larger mainframe or super-mini computer systems, primarily because the PC is a single-user machine.

The purpose of this paper is to show how RADC's GEMACS (*General Electromagnetic Model for the Analysis of Complex Systems*) computer program has been successfully installed on 80286- and 80386-based personal computers (PCs) [1]. The GEMACS code was selected for the paper because it is by far the largest and most complex of the popular general-purpose electromagnetic programs, having over 100,000 lines of code. It also has most of the same capabilities and physics of the NEC and BSC computer programs, as well as many features not contained in any other code.

Whether or not the reader is interested in GEMACS *per se*, he will find the information given in this paper to be a useful guide in configuring and converting other large electromagnetic codes for his particular installation.

Vital Statistics

GEMACS for the PC is composed of eight (8) FORTRAN programs (or "modules") which execute sequentially, as opposed to six (6) programs for the mainframe version. Each program executes a portion of the physics, mathematics, or input/output, as shown in the following table. In the mainframe version, GEMGTD1, GEMGTD2, and GEMGTD3 are combined into a single GEMGTD.EXE program.

This work was sponsored in part by Rome Air Development Center, RADC/RBCT, Griffiss Air Force Base, NY under contracts F30602-86-C-0015 and F30602-86-C-0186.

GEMACS MODEL NAMES, FORTRAN PROGRAMS, AND FUNCTIONS

MODULE NAME	FORTRAN NAME	FUNCTIONS
INPUT	GEMINP.EXE	PERFORM COMMAND LANGUAGE SYNTAX AND GRAMMAR CHECKS. CHECK FOR EXISTENCE OF DATA SETS. PROCESS GEOMETRY COMMANDS AND CHECK FOR SYNTAX AND MODELING ERRORS. CHECK FOR DATA SET CONSISTENCY. CHECK MULTIPLE REGION GEOMETRY INTERFACES.
FD	GEMFFD.EXE	PERFORM ALL FINITE DIFFERENCE (FREQUENCY DOMAIN) CALCULATIONS ON INTERIOR (CAVITY) GEOMETRIES. GENERATE APERTURE INTERFACES FOR INTERIOR PORTIONS OF MULTIPLE REGION PROBLEMS.
GTD1	GEMGTD1.EXE	PERFORM ALL GTD RAY TRACING AMONG PLATE GEOMETRY ELEMENTS. GENERATE THE GTD PORTION (PLATES ONLY) OF THE PHYSICS DATA FOR MOM/GTD AND MULTIPLE REGION HYBRID PROBLEMS.
GTD2	GEMGTD2.EXE	PERFORM ALL GTD RAY TRACING AMONG CYLINDER AND END CAP GEOMETRY ELEMENTS. GENERATE THE GTD PORTION (CYLINDER AND END CAPS ONLY) OF THE PHYSICS DATA FOR MOM/GTD AND MULTIPLE REGION HYBRID PROBLEMS.
GTD3	GEMGTD3.EXE	PERFORM ALL GTD RAY TRACING BETWEEN PLATES AND CYLINDER/END CAP ELEMENTS. GENERATE THE GTD PORTION (PLATE-CYL ONLY) OF THE PHYSICS DATA FOR MOM/GTD AND MULTIPLE REGION HYBRID PROBLEMS.
MOM	GEMMOM.EXE	PERFORM ALL METHOD OF MOMENTS INTERACTIONS WITH WIRES AND PATCHES. GENERATE LOADS AND EXCITATIONS FOR MOM OBJECTS. GENERATE THE MOM PORTION OF THE PHYSICS DATA FOR MOM/GTD AND MULTIPLE REGION HYBRID PROBLEMS.
SOLN	GEMSOL.EXE	PERFORM ALL MATHEMATICS AND SOLUTION PROCESSES IN GEMACS. IMPLEMENTS MATRIX BANDING AND BANDED MATRIX ITERATION. DOES LU-DECOMPOSITION AND BACK SUBSTITUTION ON FULL AND BANDED MATRICES. JOINS MULTIPLE REGIONS TOGETHER AT APERTURES. ALLOWS ALL DATA TO BE MODIFIED BY USER PRIOR TO PROBLEM SOLUTION. PURGES UNWANTED/UNNEEDED DATA SETS.
OUTPUT	GEMOUT.EXE	COMBINE SCATTERED AND INCIDENT FIELD DATA AND PRINT OUT ALL REQUESTED FIELD PATTERNS. PRINT ANY AND ALL GEMACS DATA TO TO PRINTER OR WRITE DATA TO A PERIPHERAL FILE.

It is convenient to break up the eight modules into eleven (11) sets of subroutines. There is one set for each module plus additional sets for common blocks, subroutines used by the GTD1, GTD2, and GTD3 modules, and subroutines used by several modules. The statistics on each set are given below.

Hardware and Software Requirements

The only unavoidable hardware requirement for GEMACS on a PC is having a minimum of 640K of RAM memory installed, and the only unavoidable software requirement is having the DOS operation system version 2.x or 3.x. Practical considerations dictate several more requirements. However, GEMACS has been run on computers as small as an IBM PCjr (with 640K). And this is *not* a "miniature" version, but rather the same code that you may be using on a mainframe. Of course, running a mainframe code on a PCjr takes a lot of time!

STORAGE REQUIREMENTS FOR GEMACS ON A PC

MODULE NAME	NUMBER OF ROUTINES	SOURCE SIZE	OBJECT SIZE	EXECUTABLE SIZE
INPUT	59	456K	520K	499K
FD	42	380K	412K	559K
GTD	65	464K	692K	----
GTD1	5	72K	80K	432K
GTD2	5	64K	84K	454K
GTD3	5	64K	68K	518K
MOM	26	196K	288K	372K
SOLN	18	160K	172K	544K
OUTPUT	5	52K	48K	261K
COMSUBS	64	372K	376K	----
COMMONS	104	416K	----	----
TOTALS	398	2,696K	2,740K	3,639K

A more practical set of hardware requirements is:

- o 80286 or 80386 CPU
- o 80287 or 80387 Math Coprocessor *highly* recommended
- o 640K RAM memory (Operating system plus 580K for GEMACS)
- o Hard disk drive with 8+ Megabytes storage available to GEMACS

The two configurations in use at Advanced Electromagnetics are (1) a COMPAQ 286 (80286 machine) with 80287 math coprocessor, 640K RAM, and 30 Megabyte hard disk and (2) a COMPAQ 386 (80386 machine) with 80387 math coprocessor, 640K RAM, and 130 Megabyte hard disk. Additional RAM memory (extended memory) has been installed on both machines and is used for a disk cache and/or RAM disk (see below).

The software used by Advanced Electromagnetics for GEMACS is:

- o Microsoft DOS 2.1 or greater (3.x recommended)
- o Microsoft Optimizing FORTRAN Compiler Version 4.01
- o Microsoft Macro Assembler (Any Version)
- o Microsoft Linker (comes with FORTRAN compiler)
- o Word Processor which reads/writes ASCII text files

Microsoft FORTRAN 4.01 is listed because it is the latest version. GEMACS has also been compiled with versions 3.31 and 4.0 of Microsoft's compilers, as well as Ryan-McFarland and Lahey FORTRAN compilers. However, beware of a number of bugs in Microsoft's FORTRAN 4.0 when performing operations with complex numbers (especially the CMPLX function).

Code Conversion to the PC

As GEMACS is written in ANSI FORTRAN 77, its conversion to a personal computer was straightforward, though time consuming. First, all subroutines and common blocks were put into separate files for easier text editing and modifications. Common blocks are now accessed by the individual subroutines via $INCLUDE: statements. The subroutines are combined together again to make the GEMACS modules at link time. This one step accounted for 90% of the code conversion time.

The second conversion step was to write assembly language interface routines between Microsoft FORTRAN and the operating system, since Microsoft FORTRAN did not originally have function calls for time of day, CPU time, etc. Four (4) simple assembly language programs were written so that GEMACS could operate under DOS:

DATE	Calendar date in mm/dd/yy format
ITICK	Elapsed CPU time in timer ticks (1/18th sec)
MAXFIL	Overcome DOS file limit (see below)
TIME	Time of day in hh:mm:ss format

These routines are self-explanatory with the exception of MAXFIL. MAXFIL was written because of a DOS limitation on the number of files which can be open at one time. DOS restricts the user (arbitrarily) to a maximum of 20 open units, regardless of how large a number is placed on the FILES= command in the CONFIG.SYS file. DOS takes three of the 20 for itself, leaving only 17 for GEMACS (or any other program). Many GEMACS problems can be run with just 17 peripheral files, but the multiple region (interior/exterior) coupling problems and some complex exterior region MOM problems require many more files.

MAXFIL overcomes the DOS limit by setting aside its own storage for up to 255 open files. Hence, the new open file limit is imposed by the FILES= command in CONFIG.SYS or by the compiler itself. For example, the "C" language compiler imposes no restrictions, and all 255 files can be open. Some FORTRAN compilers allow all 255 files, but the Microsoft FORTRAN compiler only allows 27 files. Subtracting three files for DOS leaves 24 files for GEMACS. This is enough to work a four region interior/exterior problem on the PC.

The third GEMACS conversion was to make GEMACS' file system compatible with DOS. This change was not strictly required, but not to have made the conversion would have invited much extra effort in executing the code.

GEMACS uses the NUMFIL command [2] to tell GEMACS how many peripheral files are available to the program. On the PC file names are generated for all peripheral files using the format FOR*nnn*.DAT for files whose unit number *nnn* is less than or equal to NUMFIL and the format FOR*nnn*.USR for files whose unit number is greater than NUMFIL. The FOR*nnn*.DAT files are automatically closed and deleted (except for the checkpoint file [2]) when a module terminates.

One file conversion feature that is not ANSI standard is the use of the BINARY file structure (rather than UNFORMATTED) and the BLOCKSIZE= parameter in the OPEN statements. For compilers that don't support these extensions of the ANSI standard, change BINARY to UNFORMATTED and omit the BLOCKSIZE= field on the OPEN statements.

The final conversion step was to divide the single mainframe GTD module into three PC GTD modules: GTD1, GTD2, and GTD3. The real purpose of dividing up GTD was to allow for future growth in GEMACS version 5. However, it was fortunate that GTD had been divided with the release of DOS 3.2. some 20K larger than DOS 3.1. A single GTD module which worked fine with DOS 3.1 won't fit into memory with DOS 3.2.

It is possible to change GEMACS' array sizes to optimize the code for a particular machine or problem type [3]. But this step has not been performed on the PC version.

To Cache or Not to Cache

A number of software programs have been touted as greatly speeding up the performance of a hard disk by 2:1 or better. The programs basically set up a portion of memory to be used as a large disk I/O buffer with the idea that once data are in memory the disk doesn't need to be accessed every time the data need to be read. Such a system is called a "disk cache."

Since GEMACS is so I/O intensive, the use of such a program sounds attractive. And for small problems, a disk cache will provide minor improvements (*ca.* 10%) in performance. Yet a disk cache does not lend itself to the GEMACS I/O file structure. All GEMACS data sets are unformatted, sequential files. Since GEMACS is set up to access these files sequentially, the disk cache buffer will not normally contain the file data desired. The savings from those few times that a "hit" is made are lost in the overhead of running the cache in the first place. For very large problems (*ca.* 500 unknowns or more), the cache has created a performance penalty! Hence, it is strongly recommended that a disk cache not be used.

Advantages of a RAM Disk

A RAM disk is a section of computer random access memory (RAM) set up to emulate a disk drive. The obvious advantage of a RAM disk over a hardware disk is that the RAM disk operates at the speed of memory while the speed of a physical disk is limited by its hardware. The RAM disk's disadvantage is that it is electronic: the data disappear when the power is turned off. In addition, the size of a RAM disk is limited by available RAM memory.

We have found that an 80286 or 80386 computer with extended memory (memory beyond 1 Megabyte) configured with a RAM disk in extended memory can give performance increases of 1.5:1 in the MOM module (matrix fill) and over 5:1 in the SOLN module (matrix factor and back substitution) for large problems. The best speedup figures are obtained with the 80386 chip since the RAM disk routines are written for a 32-bit data path (as opposed to 16 bits for the 80286) and the 80386 can be operated in its "virtual 8086" mode.

We highly recommend the use of a RAM disk for all GEMACS problems. A 1.5 Megabyte RAM disk can handle up to a 200 unknown problem (including interaction matrix, factored matrix, scratch files, and the checkpoint file). For larger problems, more extended memory is needed or the RAM disk concept must be abandoned in favor of the standard hard disk.

Running GEMACS on a PC

To run the GEMACS program on a PC, an input file containing physics, mathematics, and geometry commands is generated with an ASCII-output word processor. Most all PC-based word processors have an ASCII output mode, though that mode may not be the default (*e.g.*, WordStar, pfs: First Choice). The input file should be given the extension .GEM to indicate that it is a GEMACS input deck.

The eight GEMACS modules are then executed in the order listed in the first table. However, if the physics of a particular module is not needed, that module may be eliminated from the list in order to save a few seconds of execution time. For example,

a MOM-only problem (*e.g.*, a dipole antenna in free space) would only require the INPUT, MOM, SOLN, and perhaps OUTPUT modules.

The output of each GEMACS module is a printer image (132 column) ASCII file. It is suggested that the extension for the GEMACS outputs correspond to the name of the module generating the output, such as .MOM for the output from the MOM module. The primary file name would be the same as the file name of the .GEM input deck. Hence, with an input deck named DIPOLE.GEM, a MOM-only execution would generate DIPOLE.INP (from the INPUT module), DIPOLE.MOM (from the MOM module), DIPOLE.SOL (from the SOLN module), and DIPOLE.OUT (from the OUTPUT module).

To facilitate the automatic execution of GEMACS, a batch file named GEMACS.BAT is included with the PC version of GEMACS. GEMACS.BAT executes a list of GEMACS modules given by the user for a particular input deck. After executing each module, all scratch files are eliminated, and the module's results are renamed using the convention described above. The format of GEMACS.BAT is

GEMACS *input-file-name list-of-modules-to-be-run*

where the *input-file-name* is the file (without .GEM extension) containing the input data (*e.g.*, DIPOLE for DIPOLE.GEM). The *list-of-modules-to-be-run* is a list of the GEMACS programs to be executed in the order listed. The first three letters ("GEM") of each program name are omitted, as well as the .EXE extension. Hence, to run the INPUT module (GEMINP.EXE), specify only INP and not GEMINP.

Suppose the commands and geometry of a MOM-only dipole antenna have been stored in DIPOLE.GEM. Then, GEMACS can be invoked by typing

GEMACS DIPOLE INP MOM SOL OUT <Enter>

The INPUT, MOM, SOLN, and OUTPUT modules will be run in sequence, generating four output files named DIPOLE.INP, DIPOLE.MOM, DIPOLE.SOL, and DIPOLE.OUT which contain the results of each GEMACS program.

In addition to the standard printer (unit 6) FORTRAN outputs, the user can specify that status messages be displayed on the computer screen by using the undocumented DISPLA command. These messages are helpful to the user by letting him know how the execution is progressing through each module. The DISPLA command should almost always be one of the first executable commands in the input file. Its format is

DISPLA ON/OFF LU=*unit*

where DISPLA is the computer screen message keyword and *unit* is the logical unit number to which the messages are to be written (default=0, the screen). To invoke status messages throughout the GEMACS execution, enter

DISPLA ON LU=0

as one of the first executable commands.

An Example Run with PC GEMACS

Below is a listing of the file DIPOLE.GEM. It contains commands to perform a MOM-only execution on a simple dipole antenna centered at the origin and directed along the z-axis. In GEMACS the execution commands (to generate excitations, fields, etc.) come first and are terminated by the END command. The geometry commands follow the execution commands, and they, too, are terminated with END. More information on the execution and geometry commands may be found in [2].

```
$
$  DIPOLE EXAMPLE FOR THE PC VERSION OF GEMACS
$  WRITTEN BY: E. L. COFFEY
$  DATE:       16 FEB 88
$
$  REQUIRES:  INPUT, MOM, SOLN, AND OUTPUT MODULES
$-------------------------------------------------------
$
DISPLA ON LU=0                    $TURN ON SCREEN MESSAGES
NUMFIL=17                         $ALLOCATE 17 PERIPHERAL FILES
FRQ=300.                          $SET FREQUENCY (MHZ)
TIME = 1.                         $SET EXECUTION TIME LIMIT (MINUTES)
SETINT MOM                        $SELECT MOM PHYSICS
GMDATA=DIPOLE                     $READ AND PROCESS GEOMETRY
ZGEN GMDATA=DIPOLE ZMATRX=ZIJ     $GENERATE MOM INTERACTION MATRIX
SRC=VSRC(DIPOLE) V=1.,0. SEGS=6 $EXCITE CENTER OF DIPOLE WITH 1 VOLT
SOLVE ZIJ*I=SRC                   $FACTOR AND BACK SUBSTITUTE TO FIND CURRENTS
PRINT I                           $PRINT CURRENTS
FLD = EFIELD(DIPOLE) P1=0. T1=0. DT=2. T2=180.  $COMPUTE FIELDS
END OF COMMANDS
$
$  GEOMETRY FOR A SIMPLE RESONANT DIPOLE ANTENNA
$
RA 0.001   $RADIUS OF 0.001 M
WR  0.  0.  -0.2375  0.  0.  0.2375  11  1  1  $WIRE WITH 11 SEGMENTS
END OF GEOMETRY
```

Execute this problem with GEMACS on the PC by typing

GEMACS DIPOLE INP MOM SOL OUT

When execution is complete, the DOS prompt returns to the screen, and the file contents can be printed or examined with an ASCII-based word processor. Here is a summary of what the files contain:

RESULTS OF THE DIPOLE.GEM SIMULATION

MODULE	FILE NAME	CONTENTS
INPUT	DIPOLE.INP	LIST OF COMMANDS GEOMETRY DESCRIPTION
MOM	DIPOLE.MOM	STATUS MESSAGES FOR MOM PHYSICS CALCULATIONS
SOLN	DIPOLE.SOL	SOLUTION PROCESS MESSAGES INPUT IMPEDANCE INPUT POWER
OUTPUT	DIPOLE.OUT	DIPOLE WIRE CURRENTS DIPOLE FIELD PATTERNS

The GEMACS output files are in standard line printer image format with up to 132 columns of text per line. Hence, when printing, use a wide carriage printer or compressed type on a standard carriage printer to avoid "line wrap."

Performance Statistics

The table below shows a sample of GEMACS' performance on PCs compared with a number of larger systems. In general, the file I/O on PC systems is terribly slow when compared to mainframe machines. Hence, computationally intense problems with little I/O compare favorably with mainframes, while I/O bound problems on the PC perform much, much slower than their mainframe counterparts. Note however that the timing statistics for the PCs include both CPU and I/O time (essentially wall clock time) while the mainframes have only the CPU time listed. By including I/O time in the mainframe statistics, the performance ratios will become better.

EXECUTION TIME (SECONDS) OF GEMACS PROBLEMS ON VARIOUS COMPUTERS

PROBLEM	COMPAQ 286	COMPAQ 386	VAX 11/785	IBM 3084
SPIRAL ANTENNA	7,340	1,400	1,774	167
20 ELEMENT ARRAY	782	197	298	42
SPHERE (224 PATCHES)	399	58	71	10
MONOPOLE/FINITE GROUND PLANE	703	78	84	23
THREE REGION EXT/INT COUPLING	24,736	6,959	N/A	844

Limitations Imposed by the PC

Perhaps the first PC limitation on GEMACS which comes to mind is that of inferior CPU performance. Naturally, a PC-based system is going to be several times slower than a mainframe system. But this is not a "hard fence" limit since the PC can be run several times longer if necessary.

The second limitation which comes to mind is that of core storage. A PC operating under DOS is limited to 640K of which about 40K is consumed by the operating system, device drivers, etc., leaving only 600K for GEMACS. Mainframes have many times this amount of storage available. But GEMACS' file system lets users work problems many times the size of available memory. For example, the PC version of GEMACS will solve problems with up to 1,375 unknowns with the arrays dimensioned to fit within 559K, though 1,375 complex unknowns will generate an interaction matrix of about 15 Megabytes.

The true "hard fence" which GEMACS faces on a PC is the lack of hard disk storage space. For every version of DOS through DOS 3.3, the maximum hard disk device size has been 32 Megabytes, though a large physical drive could be partitioned into several 32 Megabyte drives. But by the time the interaction matrix, LU-decomposed matrix, scratch files, and checkpoint files are all considered, 32 Megabytes translates into an 800 unknown problem. Banding and banded matrix iteration [2,3] can increase this to a 2,000 unknown problem.

Code Availability

The GEMACS software and documentation are subject to the Arms Export Control Act (Title 22, U.S.C., Sec 2751 *et seq.*) or Executive Order 12470. Requests for the code and/or documentation should be referred to RADC/RBCT (K. R. Siarkiewicz), Griffiss

Air Force Base, New York, 13441-5700, telephone (315) 330-2465 (commercial) or 587-2465 (Autovon).

The PC version of GEMACS is maintained and supported by Advanced Electromagnetics. Requests for the PC version should also be directed to RADC in order to comply with the Export Control Laws. Upon receipt of approved paperwork from RADC, Advanced Electromagnetics can distribute the PC version of GEMACS to you.

Summary

Is GEMACS on a PC for you? Before deciding against it, consider the true cost and true turnaround time for a mainframe computer. Execution time rates may be fairly reasonable, but add to them I/O, page fault, and disk storage charges and the true cost of an hour of VAX 11/780 CPU time may be $500.00. Just 16 hours at $500/hr will pay for the 80386 PC system described above.

A study of turnaround time on the time-shared Honeywell 6180 mainframe at RADC showed that 16 simple GEMACS problems could be batched through the system in one day, assuming that one problem had finished prior to submitting the next one. On the 80386 PC system, we run the same 16 problems in a single hour!

References

1. E. L. Coffey, *Installation Instructions for PC GEMACS 4.0*, Advanced Electromagnetics Report AE87R002, December 1987.

2. E. L. Coffey and D. L. Kadlec, *General Electromagnetic Model for the Analysis of Complex Systems (GEMACS)*, Volumes I-III (Version 4), Rome Air Development Center Technical Report RADC-TR-87-68, May 1987.

3. E. L. Coffey, N. W. Coffey, and D. L. Kadlec, *GEMACS Source Book*, Volumes I and II, Advanced Electromagnetics Report AE88R001, for Rome Air Development Center under contract F30602-86-C-0015, February 1988. (*to be published as an RADC technical report*)

SESSION VI - "ANTENNA ANALYSIS"

Moderator: Robert Bevensee
Lawrence Livermore National Laboratory

"The Design of Antenna Matching Networks Using a Microcomputer"
S.T. Li and D.W.S. Tam — Naval Ocean Systems Center

"Numerical Methods Used for Analysis of a Transmitting Biconical Antenna"
V. Badii, K. Tomiyama, D. Grimes — Pennsylvania State University

"Design Program for Microstrip Antennas with a Dielectric Cover"
R. Bancroft — Martin Marietta Astronautics Group

"Efficient Computation of the Far Field of Offset Dual Reflector Antennas with Offset Feeds"
J.S. Hoover and L.Q. Bowers — Martin Marietta Astronautics

"Development and Validation of a New Version of the NEC-BSC"
R.J. Marhefka — Ohio State University

"Prediction and Measurement of Transverse Wave Impedance in the Vicinity of Electrically Small radiating Structures"
M.E.G. Upton and A.C. Marvin — University of York

"The Analysis of Two Inverted F-Antenna Structures on a Box Using NEC Wire Model"
M. Somersalo — Technical Research Centre of Finland

"Synthesis Techniques for Circular Arrays"
K.J. Moeller and V.P. Cable — California Microwave, Inc.

"Moment Method Analysis of Large Finite Phased Arrays"
H.K. Schuman and G.A. Bright — Atlantic Research Services Corporation
S. Barbour — Grumman Aerospace Corp.

"Application of the Network Approach to Electromagnetic Solutions Involving Apertures on a Body of Revolution"
J.R. Rogers — Atlantic Aerospace Electronics Corporation

THE DESIGN OF ANTENNA MATCHING NETWORKS USING A MICROCOMPUTER

S. T. Li and D. W. S. Tam
Naval Ocean Systems Center, Code 822
271 Catalina Blvd.
San Diego, California 92152-5000

1.0 INTRODUCTION

In a communication system, one of the primary concerns is maximum efficiency in signal transmission and reception. For maximum power transfer there must be an impedance match between the antenna and transmitter (or receiver). A basic problem is to design a coupling network between a given source and a given load so that the transfer of power from the source to the load is maximized over a given frequency band of interest. The device used to perform this impedance matching is called an antenna matching network.

The number of pieces of equipment requiring an antenna connection in some applications may exceed the number of acceptable locations available for antennas. One solution is the use of broadband antennas that have a low VSWR (voltage standing-wave ratio) over the operating band. Broadband antennas are used in conjunction with multicouplers (filters with multiple inputs) to provide a sufficient number of antenna connections.

Despite the aid of Smith Charts, the traditional design of an antenna matching network by engineering experience and manual calculation means is an extremely time-consuming task. This report is intended to relieve the engineer of the tedious numerical calculations involved in the network design.

Antenna Matching (ANTMAT), an interactive BASIC language computer program to aid in the design of a matching network for a broadband antenna, has been developed. (S. T. Li and D. W. S. Tam, NOSC TD 1148, September 1987).

An optimization algorithm finds the value of the components that minimize the input reflection coefficients. At first, the ANTMAT program uses the optimization algorithm with an exponential weighting function for the determination of a list of network candidates from which a matching network topology is selected. After a topology (either a pi network or a T network) is specified, the optimization algorithm with other weighting functions finds the values of the components that minimize the input reflection coefficients.

2.0 AN OPTIMIZATION ALGORITHM

2.1 THE MINIMIZATION OF VSWR

The objective of designing a broadband matching network is to minimize VSWR over the operating frequency band. VSWR is defined as:

$$VSWR = \frac{1 + |\Gamma|}{1 - |\Gamma|} \qquad (1)$$

where Γ is the voltage reflection coefficient.

Figure 1 shows an antenna with matching network.

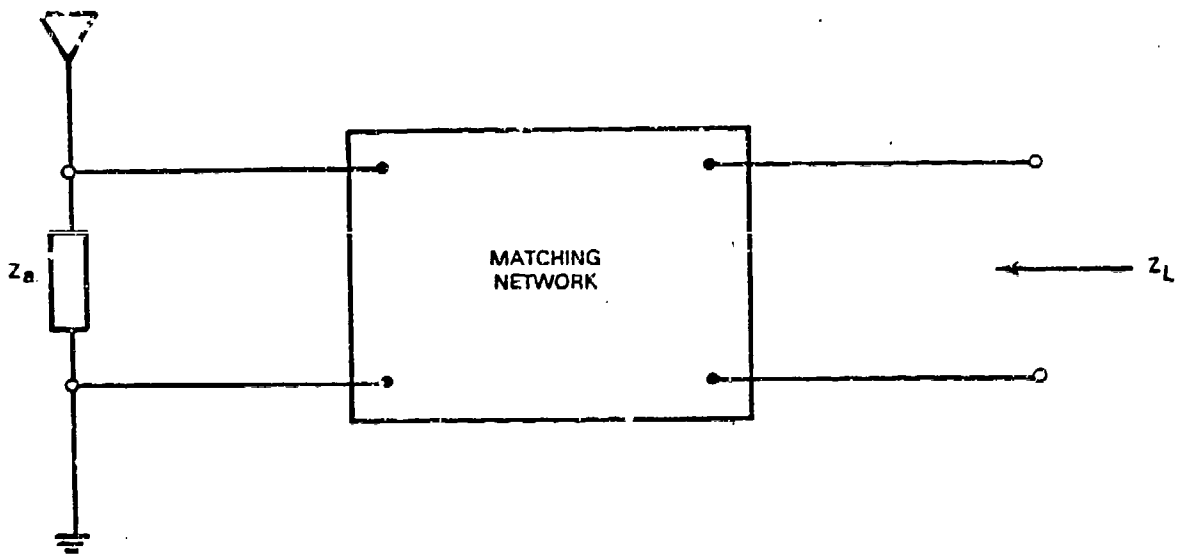


Figure 1. Antenna with matching network.

Z_a is the antenna impedance. Z_L is the impedance at the matching-network terminal. Z_o is the characteristic impedance, which is 50 ohms for the Navy shipboard application. The voltage reflection coefficient can be expressed

as:

$$\Gamma = \frac{Z_L - Z_0}{Z_L + Z_0} \qquad (2)$$

Consider a frequency band consisting of N frequencies, f_i, i = 1, 2, ..., N. The impedance at the matching-network terminal at each frequency f_i is Z_{L_i}. The reflection coefficient at each frequency is then:

$$\Gamma_i = \frac{Z_{L_i} - 50}{Z_{L_i} + 50} \qquad \text{where } i = 1, 2, 3, \ldots, N \qquad (3)$$

A minimum VSWR in the specified frequency range can be obtained by minimizing:

$$f(p_1, p_2, p_3) = \sum_{i=1}^{N} |\Gamma_i|^2, \qquad (4)$$

where p_1, p_2, and p_3 are component values of a desired matching network which consists of three branches.

The desired matching network is a lossless two-port network, which can be realized as either a pi network or a T network as shown in Figures 2 and 3, respectively. The pi (or T) network has three branches. There are six possible types of elements (L, C, L-C parallel, L-C series, short-series, and open-parallel) for each branch of the pi (or T) network, except as limited by the following rules:

1. L-C parallel should not be used for a series branch.
2. L-C series should not be used for a parallel branch.
3. Short-series should not be used for a parallel branch.
4. Open-parallel should not be used for a series branch.

Figure 4 shows the six possible types of elements. Each type of element may have two components, one component, or zero components. For examples, an L-C parallel element consists of two components, but a short-series element has no circuit component.

Since $f(p_1, p_2, p_3)$ is a continuous and differentiable function, it can be minimized by any method of optimization. The method of Steepest Descent is used here.

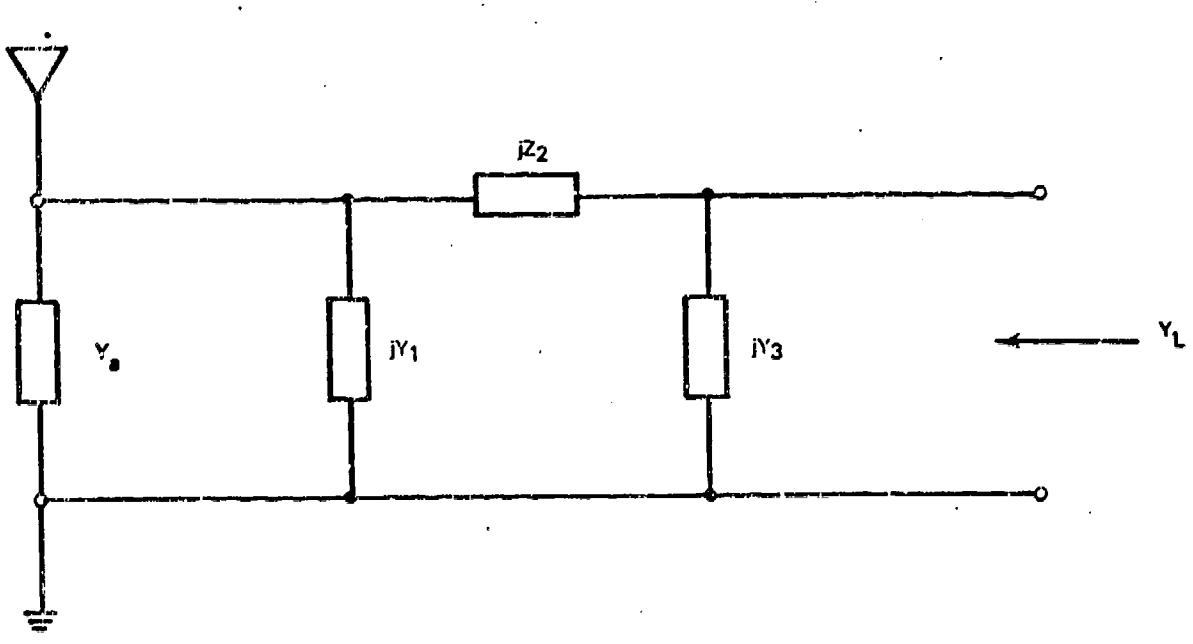


Figure 2. Antenna with π matching network.

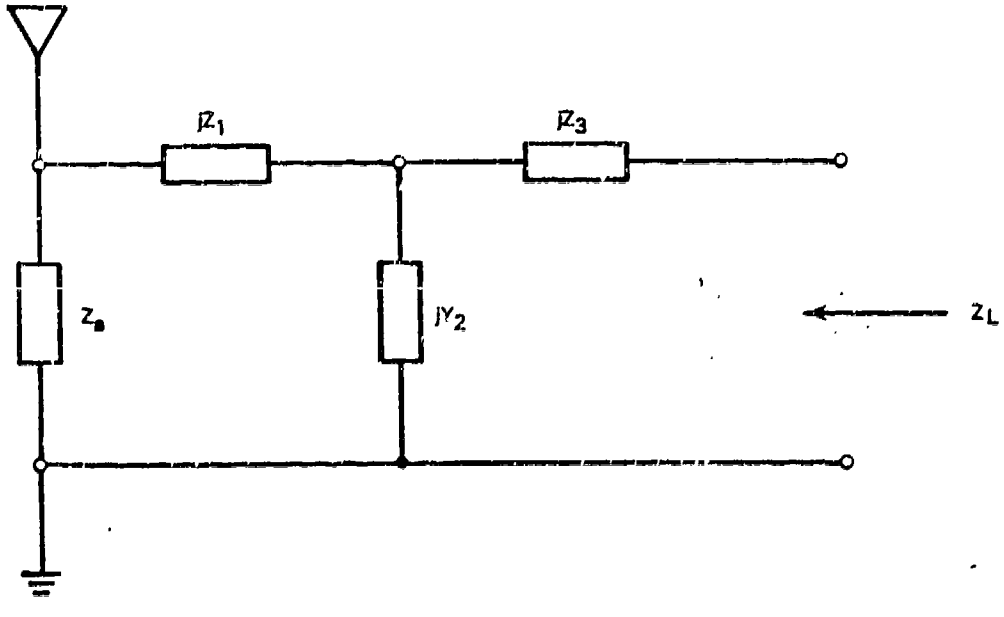
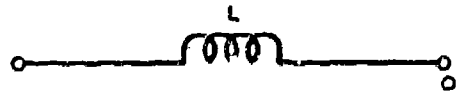
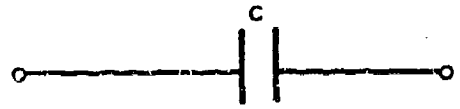


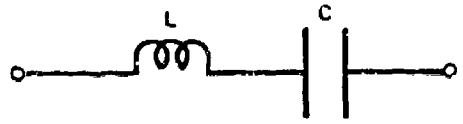
Figure 3. Antenna with T matching network.



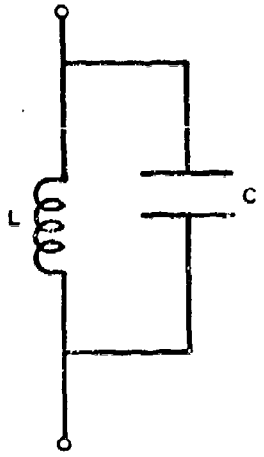
L element



C element



L and C in series (LCS)



L and C in parallel (LCP)



Short-Series





Open-parallel

Figure 4. Six possible types of elements in a branch.

2.2 WEIGHTED OPTIMIZATION FUNCTION

As an alternative, $\sum_{i=1}^{N} |\Gamma_i|^2$ can be replaced by a weighted optimization function, which is

$$f = \sum_{i=1}^{N} W_i |\Gamma_i|^2 \quad , \tag{5}$$

where W_i is a weighting factor that can either be chosen by the user or calculated by the program. The use of weights allows the user to put more emphasis in the matching over certain portions of the frequency range. The weights can be chosen by the user or calculated by the program. There are four options available to the user for selecting weights:

1. Exponential weighting function.
2. Around-the-average weighting function.
3. User input weights on selected frequencies.
4. Weight is 1 on all frequency points.

In the first option, the weighting factor is assumed to be in proportion to some exponent of the VSWR. The values of the exponent must be greater than one which may be specified by the user. If the user does not specify an exponent value, an exponent of 1.02 is used in the program. The larger the exponent is, the more weight is put on the impedance point which has a high VSWR. It will pull this impedance point into the definition circle on the Smith Chart quickly. However, it may push another impedance point which has a low VSWR outside the definition circle. The weighting factor is calculated by the following expression:

$$W_i = \begin{cases} 1 & , \text{ if } VSWR_i \leq v \\ (VSWR_i)^e & , \text{ if } VSWR_i > v \end{cases} \tag{6}$$

where W_i = new weighting factor

$VSWR_i$ = current VSWR value

$v = 1.0$, if user does not input any value

$e = 1.02$, if user does not input any value

The exponential weighting function option with an exponent of 1.02 is used in the determination of network topology procedure.

The second option is intended to bring each VSWR to a narrow region around its average value. This option is used when the average VSWR value is less than the required VSWR value (say 3:1). A weighting factor is assigned to each frequency point when its VSWR is greater than the average VSWR value in accordance with the following calculations:

$$W_i = \begin{cases} LI \cdot \text{Maximum}\,(W_c, W_{old}), & \text{if } VSWR_i > AVSWR \\ W_{old}, & \text{if } VSWR_i \le AVSWR \end{cases} \quad (7)$$

where

W_i = new weighting factor

W_c = CONST $\cdot$ ($VSWR_i$ - AVSWR) + 1

CONST = First multiplier for average weighting

= 2, if user does not input any value

$VSWR_i$ = Current VSWR value

AVSWR = Average VSWR value

W_{old} = Current weighting factor

LI = Second multiplier for average weighting

= 1, if user does not input any value. However, if $W_{old} = 1$, then LI must be 1.

$$\text{Maximum}\,(W_c, W_{old}) = \begin{cases} W_c, & \text{if } W_c > W_{old} \\ W_{old}, & \text{if } W_c \le W_{old} \end{cases}$$

The third option gives user a chance to change weighting factor at any selected frequency. This option allows the user to put more emphasis in certain selected frequencies according to the user's engineering judgment.

The last option sets the weighting factor to 1 on all frequency points.

2.3 Practical Range of Component Values

In general, for the HF frequency band (2-30 MHz), inductors should be in

the range of 0.25 μH to 12 μH. Capacitors usually should be in range of 50 pF to 2500 pF. Initial component values, as well as the final design component values, should remain within these practical ranges. The establishment of practical ranges is based on physical size considerations.

3.0 AN ANTENNA MATCHING PROGRAM

3.1 OVERVIEW OF THE ANTMAT PROGRAM

The ANTMAT program is based on the optimization algorithm described in section 2 to aid in design of a matching network for a broadband antenna. It is written by using Microsoft's BASIC language. The ANTMAT is a function-driven program. That is, the user is given a menu of the various functions that the program can perform. From this menu, the user selects the function or sequencing of functions that allows him to carry out the desired operation. The menu of the various functions are:

1. Read antenna impedance file.
2. Determine network candidates.
3. Optimize selected network.
4. Adjust component value manually.
5. List network candidates.
6. Digitize impedance plot from tablet.
7. Exit.

Because it is of a function-oriented nature, ANTMAT is driven by a main routine (called "menu driver") that waits for a command entered via the function key, processes this command, returns to the menu driver, and continues in this manner until the exit function is chosen.

3.2 DETERMINE NETWORK CANDIDATES

This section discusses the determination of a list of network candidates from which a network topology and initial component values are obtained by using the ANTMAT program. The network topology is either a pi network or a T network. A network should consist of as few

components as possible to minimize losses. The fewer the components in a given design, the more efficient will be the resulting network. The number of network components ranges from one component to six components. This is because:

1. There are three branches in either a pi network or a T network (see Figures 2 and 3).

2. There are six possible types of elements in a branch. Each element may consist of zero components (such as short-series element and open-parallel element), or one component (such as L element and C element), or two components (such as LCS element and LCP element) as depicted in Figure 4.

The ANTMAT program inquires as to the number of network components. The program will investigate all possible networks which have the specified number of network components. For each of these possible networks, ANTMAT uses the optimization algorithm described in section 2 to find the component values that minimize the input reflection coefficient. The initial component values used for the optimization are 6.125 μH for inductors and 1275 pF for capacitors, which are the middle points within the practical range of component values. The number of iterations for the optimization process is set between 30 and 60 for speeding up the process. However, the user can override these preset values. The exponential weighting function option with an exponent of 1.02 is used in this determination of network topology procedure. The program then calculates impedance and VSWR with matching network at each frequency. For each and every possible network with the specified number of network components, the ANTMAT calculates the mean (m) and standard deviation (σ) of VSWR and ranks these possible networks according to the following ranking factor (RF):

$$RF = m + 3\sigma \quad . \tag{8}$$

The network with the lowest value of RF is ranked as the first choice among the network candidates. A network with a negative component value will not be considered as a candidate. A network with a component value outside the practical range is ranked as a candidate with caution (a question mark is

shown). The ranked network candidates can be saved in a data file which can be recalled by using the "list network candidates" command. Usually a few top ranked networks will be selected for further consideration. The network topology and the component values which are obtained by using this "determine network candidates" command will be considered as inputs to execute the next "optimize selected network" command.

3.3 OPTIMIZE THE SELECTED NETWORK

Upon the completion of "determine network candidates" command, there exists a list of network candidates with initial component values available to the user. The user will select a network from the list for further optimization. The same optimization algorithm described in section 2 will be used. However, a weighting function which is different from the exponential weighting function can be employed. These weighting functions are discussed in section 2.2. Usually at this stage of the design, the around-the-average weighting function will be used. The number of iterations for the optimization process is increased from between 30 and 60 to between 100 and 200.

When the optimization algorithm finds new network component values for a specified weighting function, the user should decide whether these component values are acceptable and are to be saved in a disk file for future use. If the component values are not acceptable, the user should return to menu driver and select an appropriate command to continue the design of a matching network.

4.0 SUMMARY

An interactive BASIC language computer program to aid in design of a matching network for a broadband antenna has been described. The ANTMAT program provides a computer-aided design tool for determining network topology element values of the networks. It improves the speed and accuracy of the

broadband matching network design procedure. An optimzation algorithm finds the values of the elements that minimize the input reflection coefficient. At first, the optimization algorithm with an exponential weighting function is employed for determining a list of network candidates (either a pi network or a T network) from which a network topology is selected. After a topology is specified, the optimization algorithm with other weighting functions is used for finding optimum element values.

Design Program for Microstrip Antennas with a Dielectric Cover

Randy Bancroft
P.O. Box 179 Mail Stop H8080
Martin Marietta Astronautics Group
Denver, Colorado 80201

Microstrip Antennas are often designed with a dielectric cover (radome) to protect the microstrip element from the environment and to increase power handling capability.

A program to design covered microstrip antennas has been written using equations presented in [1] and [2] (in Microsoft FORTRAN on a PC). The program variables are defined in Figure 1.

d= Cover thickness
H= Substrate Thickness
L= Patch length
W=Patch width
Er = Dielectric constant

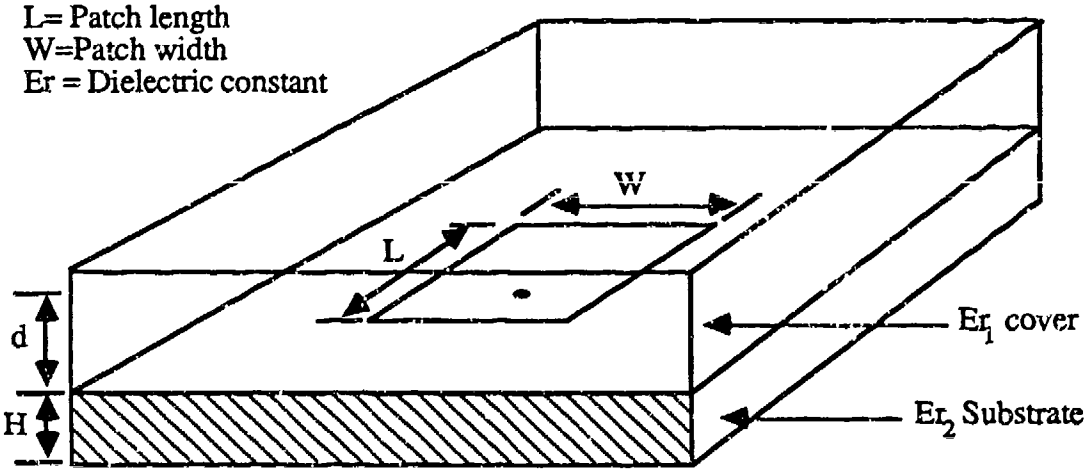


Figure 1

Approximate closed form equations for the case where the cover is air are readily available[2] and presented below:

(1) $L=(c/(2*Fr*\sqrt{Ee})-2*\Delta l$

(2) $\Delta l=0.412*H*((Ee+0.3)*(W/H-0.2674))/((Ee-0.258)*(W/H+0.8))$

(3) $Ee=(Er+1)/2+(Er-1)/(2*\sqrt{(12*H/W)})$

Where: c=Speed of light
Fr=Patch resonant frequency
Ee=Effective dielectric constant of patch with no dielectric cover
Δl=Capacitive cutback factor
Er=Substrate dielectric constant

The percentage change in resonant frequency of the covered to uncovered case is presented in [2], equations (4) and (5) below:

(4) $\Delta Fr/Fr=(\sqrt{Ee}-\sqrt{Eeo})/\sqrt{Ee}$

If $Ee=Eeo+\Delta Ee$ and $\Delta Ee <= 0.1\ Eeo$, then (5) is more accurate

(5) $\Delta Fr/Fr=(\Delta Ee/Eeo)/(2*(1+1/2*\Delta Ee/Eeo))$

Where: ΔFr=Change in resonant frequency
Eeo=Effective dielectric constant of antenna without radome and substrate
Ee=Effective dielectric constant of antenna with radome and substrate

The effective dielectric constant of the radome covered antenna may be found from [1] as:

(6) $Ee=Cd/Co$

$$(7)\quad \frac{1}{C}=\frac{1}{4\pi Eo}\int_0^{\infty}\frac{\left(1.6\frac{\mathrm{Sin}(\frac{\beta W}{2H})}{(\frac{\beta w}{2H})}+\frac{2.4}{(\frac{\beta w}{2H})^2}\left\{\mathrm{Cos}(\frac{\beta w}{2H})-\frac{2\,\mathrm{Sin}(\frac{\beta W}{2H})}{(\frac{\beta w}{2H})}+\frac{\mathrm{Sin}^2(\frac{\beta W}{4H})}{(\frac{\beta w}{4H})^2}\right\}\right)^2}{\left[Er1\frac{Er1\,\mathrm{TanH}(\frac{\beta d}{H})+1}{Er1+\mathrm{TanH}(\frac{\beta d}{H})}+Er2\,\mathrm{CotH}(\beta)\right]\beta}\,d\beta$$

Where: Cd=Line capacitance with dielectric present

Co=Line capacitance without dielectric present

Eo=Permittivity of free space

The characteristic impedance of the line is given by:

(8) $Zo=1/(Co*c)$

(9) $Z=Zo/\sqrt{Ee}$

Where: Zo=Line impedance without dielectric

Z=Line impedance with dielectric

The integral presented in equation (7) was approximated using a 96-point Gaussian quadrature [3] equation (10) below:

$$(10)\quad \int_a^{\infty} f(x)\,dx \approx 2\sum_{i=1}^{96} \frac{Wi}{(1+Zi)^2}\, f\left(\frac{2}{1+Zi} + a - 1\right)$$

Where: Wi=Gaussian weights
+/- Zi=Gaussian abscissas

This approximation was compared to the results of [1] and [2] with good agreement. A further comparison of equations (3) and (6) was undertaken. It was discovered that for values of $1 \le W/H \le 15$ and $1 \le Er < 10$, equation (3) was within 1% of (6) for the uncovered case. The computer program uses (6) in place of (3) for the open patch in (1) and (2).

Equation (11) predicts the resonant frequency of the open patch and when multiplied by equation (4) or (5) produces a value of ΔFr for the covered case. The integration in (7) is independent of the patch length and therefore the effective dielectric constants used in (4) and (5) are also independent of patch length.

(11) $Fr = c/(2*(L+2*\Delta l)*\sqrt{Eeo})$

Equation (12) is an expression which may be written in terms of patch length only. Equation (11) may be substituted into (12) to obtain (13)

(12) $Fr*(1-\Delta Fr/Fr)-Df=0$

Where: Df=Design Frequency

(13) $L=((1-\Delta Fr/Fr)*c)/(2*\sqrt{Eeo}*Df)-2\Delta l$

Equation (4) or (5) may be substituted into (13) to produce

(14) $L=((1-Var)*c)/(2*\sqrt{Eeo}*Df)-2\Delta l$

Where: $Var=\Delta Fr/Fr$ as defined in (4) and (5)

The dielectric covered microstrip patch length may now be obtained from Equation (14).

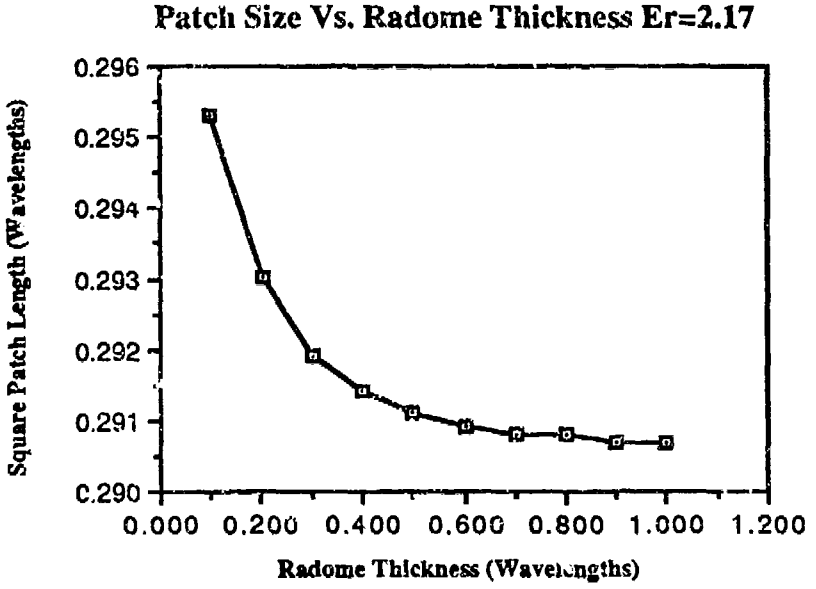


Figure 2a
H=0.05 lambda

Figure 2a presents a plot of patch length vs. radome thickness for the special case of Er1=Er2=2.17 (all graph values are in free space wavelengths). The graph indicates that the patch length approches an asymptotic value. This result is consistent with Ee approaching Er as the radome thickness becomes infinite. This patch length value remains essentially unchanged beyond a one-half wavelength thick radome. The total patch size change is 1.56%.

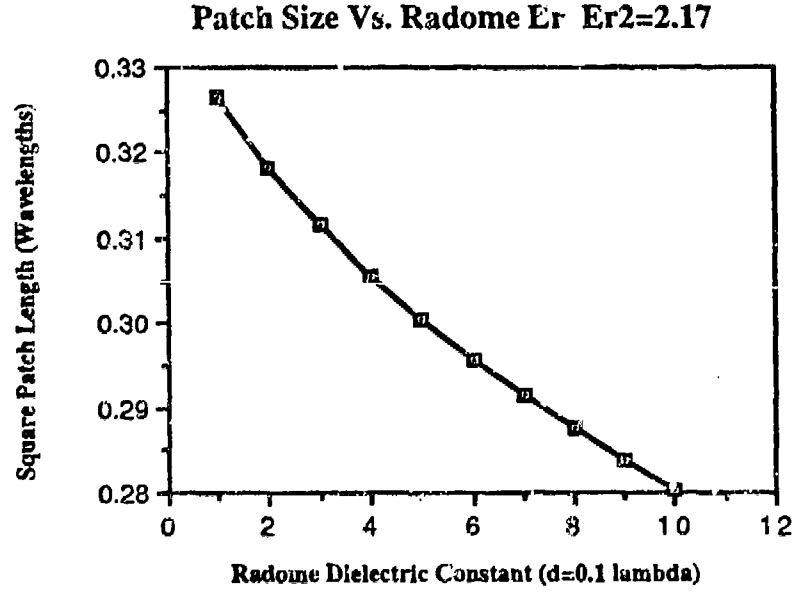


Figure 2b
H=0.025 lambda

Figure 2b shows the relationship between patch size and radome dielectric constant with the radome thickness held constant at one-tenth wavelength. This range of dielectric constants produces about a 14% patch size change.

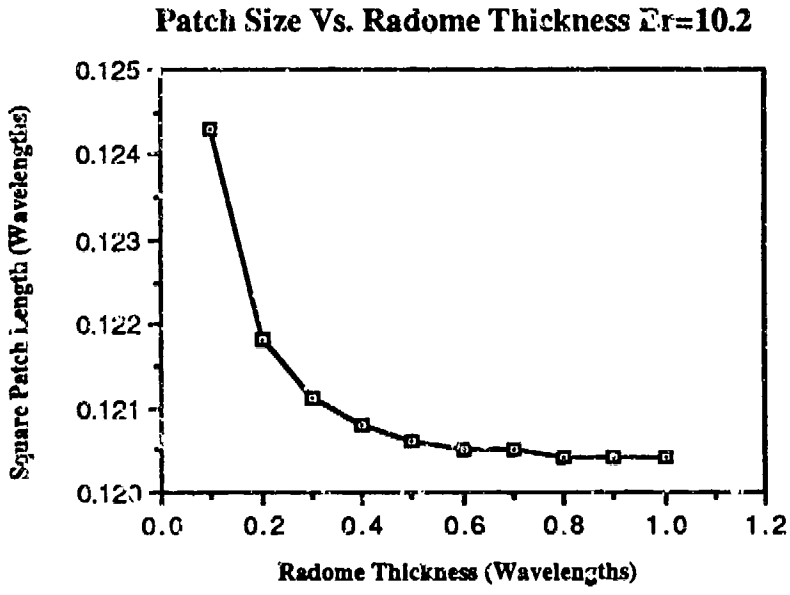


Figure 3a
H=0.05 lambda

Figure 3a again presents a plot of patch length vs. radome thickness; this time for Er1=Er2=10.2. Note that beyond one-half wavelength the patch length change is again negligible as was the case in Figure 2a. The total length change is 3.14% in this case.

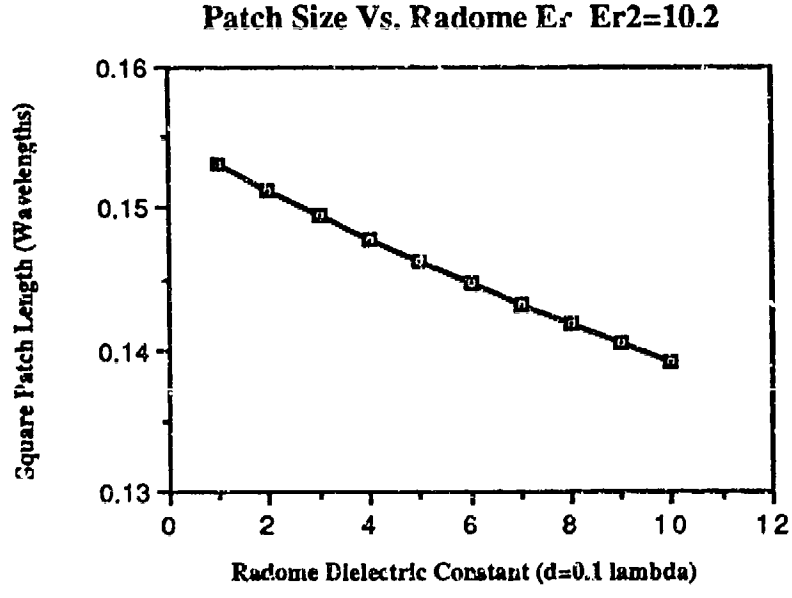


Figure 3b
H=0.025 lambda

Figure 3b is the same as Figure 2b with a substrate dielectric constant of 10.2. The patch length is less affected by this range of radome dielectric constants than that shown in Figure 2b, as expected. For this case the total change is 9.14% vs. 14% for Figure 2b.

Experimental Results:

The experimental results in [6] correlate very well with predicted theoretical values. However, experimental verification of the predicted dimensions of radomed microstrip antennas has been less than successful for this author. Below are the results for a pair of antennas constructed using 3M CUCLAD 233 microwave substrate (Er1=Er2=2.33 H=0.062" D=0.052"). Impedance and return loss were measured using an HP 8510 automatic network analyzer.

Patch 1 W=0.9575" L=0.9502" +/- 0.001"

Patch 2 W=0.9516" L=0.9521" +/- 0.001"

	No Radome Resonant Frequency (GHz)		Radome Resonant Frequency (GHz)		Frequency change %	
	Predicted	Measured	Predicted	Measured	Predicted	Measured
Patch 1	3.958	3.83	3.896	3.63	1.56%	5.22%
Patch 2	3.951	3.82	3.889	3.60	1.56%	5.75%

The uncovered antenna resonant frequency predictions are too high by about 1.5%. The predicted percentage change from the open to radomed case may be seen to be 1.56% vs. approximately 5% experimental.

Antennas fabricated for the SICBM program at Martin Marietta have mirrored this discrepancy between theory and experiment. The difference in experimental results beween [6] and the author's results are not readily explainable. Reference [6] presents two sets of data for the same prototype antenna. Upon more careful examination, it appeared that the data matched theory well only when the patch area alone was covered. Experimental data in a second table gave measured values of percentage change in frequency with the antenna completly covered with dielectric. The predicted theoretical values were not included for comparison. This author generated the predictions and noticed that, for 10 significant data points, the mean difference between theory and experiment was 2.03. Other data not published here, also showed the factor of two change. A factor of two was placed into equation (14) due to these empirical considerations and is rewritten as (15).

$$(15)\quad L=((1-2*Var)*c)/(2*\sqrt{Eeo}*Df)-2\Delta l$$

Equation (15) is used in the author's computer program. The experimental data consulted indicates that (15) should be accurate within 3.0% for $2.1<Er2<2.55$, $2.1<Er1<10.5$ and $d/H<2.0$. The new predictions vs. the measured data are in the table below. The delta is close to the accuracy expected for most open patch formulas.

	$2\Delta Fr/Fr$	measured	
Patch #1	3.17%	5.22%	Δ = 2.04%
Patch #2	3.18%	5.75%	Δ = 2.56%

A further examination will be undertaken in the future to determine if a theoretical basis exists for the factor of two introduced in (15).

The program calculates S:1 VSWR bandwidth using a formulation presented in [4]. This treatment argues that the bandwidth of a 1/4 wave patch is approximately 80% of the bandwidth of a 1/2 wave patch. This difference is attributed to the fact that the radiation Q for a single radiating edge is different from that of two edges because of mutual coupling effects. The patch radiation efficiency is calculated from [5], while the directivity is from [2] as are the impedance and edge resistance calculations. The bandwidth and gain calculations agree well with experiment but tend to be slightly low. Feed point impedance calculations also agree very well. The measured return loss and input impedance for patch 1 are -25.63 dB and 45.77 -j5.09 ohms respectively for the open patch. When the radome was attached it became -22.92 dB and 55.93 +j4.10 ohms respectively. Patch 2 showed similar results.

Conclusion:

A Fortran program has been presented which predicts dimensions for a rectangular microstrip patch antenna within 1.5% without a radome and 3.0% with. The program designs quarter or half wavelength square or rectangular patches and predicts the location of a probe feed when provided with a desired real input impedance. It provides bandwith and gain information of use to the microstrip antenna designer.

References:

[1] "Analysis of a Microstrip Covered with a Lossy Dielectric" Bhal & Stuchly IEEE Trans. MTT Pg. 104-109 February 1980

[2] "Microstrip Antennas" Bahl & Bhartia Artech House 1980

[3] "Gaussian Quadrature" HP41C High Level Math Solutions

[4] "Microstrip Antenna Theory and Design" J.R. James, P.S. Hall C. Wood UK:IEE/Peter Peregrinus Ltd. 1981

[5] "Microstrip Antenna Performance is Determined by Substrate Constraints" Microwave System News August 1982 Pg 73-84

[6] "Design of Microstrip Antennas Covered with a Dielectric Layer" Bahl, Bhartia and Stuchly IEEE Trans. AP Vol. AP-30 No.2 March 1982 pg. 314-318

EFFICIENT COMPUTATION OF THE FAR FIELD OF DUAL OFFSET REFLECTOR ANTENNAS WITH OFFSET FEEDS

John S. Hoover Larry Q. Bowers
Martin Marietta Astronautics Group
Denver, Colorado 80201

I. INTRODUCTION

An efficient method of computing the far field of dual offset reflector antennas with offset feeds has been developed and validated by measurement in the Martin Marietta Near Field Test Facility. The method relies on the use of Geometrical Optics to evaluate the vector field in the aperture of the reflector on a grid of equally spaced points. Once the aperture fields have been computed, two-dimensional discrete Fourier Transform techniques are used to rapidly compute the far field radiation patterns and contours for both the co- and cross-polarized components. Modified algorithms are also used to compute principal plane far fields directly from the aperture field data. A modified form of the Cooley-Tukey FFT algorithm allows densely spaced far field data computation over a specified angular range, making no unnecessary intermediate calculations.

The method differs from that described in [1] in three ways. Dual reflector surfaces are analyzed by modification and extension of the reflection point location algorithm. Secondly, reflector surface errors (usually derived from accurate mechanical measurements) can be accounted for in the computations allowing a quantitative evaluation of the effects of surface error on the beam-steered far field pattern. Finally, the reflected field divergence is obtained directly from the gradient computations associated with the numerical location of reflection points on the dual reflector surfaces, thus minimizing the computer time required for evaluation of the aperture field.

The analytical techniques and algorithms associated with this method (as well as some important considerations) are discussed in detail below.

Comparison of computations and meaurements of a 20 foot diameter cassegrain antenna (operating at 13.6 GHz) not only demonstrate validity of the modeling techniques, but also show that much insight into beam-steered dual reflector design and optimization can be gained.

II. EVALUATION OF THE APERTURE FIELD

Figure 1 illustrates the geometry of the offset dual reflector antenna as well as the aperture plane. The aperture plane is positioned perpendicular to the axis of the paraboloid, a fixed distance (in the Z-dimension) from the vertex of the parent paraboloid. Rays emanating from the feed strike the aperture plane at various points depending on the reflection points on the dual reflector surfaces.

In order to evaluate the Geometrical Optics vector reflected field at each of the aperture grid points, the asociated reflection points on the reflector surfaces must be determined. For electrically large apertures, this can be a formidable task since there is no "closed form" solution for arbitrary aperture and feed point locations. In one form or another, a numerical algorithm is required to determine the reflection points by successive iteration.

In [1], this is accomplished by numerical minimization of the distance function between feed and aperture points along the reflected ray path. The technique described here makes use of an error function defined in aperture plane coordinates and numerically drives the error to zero resulting in a solution for the reflection points for a desired aperture point. Referring to Figure 1, the process is initiated with the choice of a ray direction from the feed, R. This vector is then stepped (minutely) in the ϕ and θ directions to produce R_ϕ and R_θ. R, R_ϕ and R_θ are then traced to the aperture to determine the corresponding aperture point locations. If the error function is defined as the distance (in aperture plane coordinates) between the desired aperture point and the "ray-traced" aperture point, then the zero of this function should correspond to the value of R which satisfies the law of reflection. The gradients of the error function can be written as:

$$\frac{\delta a_x}{\delta \theta} \qquad \frac{\delta a_x}{\delta \phi} \qquad \frac{\delta a_y}{\delta \theta} \qquad \frac{\delta a_y}{\delta \phi}$$

and are easily evaluated numerically. From these quantities, a new value of R is determined, and the process is repeated until the error is insignificant. This algorithm is extremely efficient in that it is not computationally intensive, and convergence is typically achieved in 1 to 3 iterations.

Once the reflection points associated with an aperture grid point have been determined, the Geometrical Optics vector reflected field can be computed. As given by Kouyoumjian [2], the reflected field is:

$$\mathbf{E}_r = \mathbf{E}_i(Q_r) \cdot \overline{\overline{R}} \cdot A(s) \exp(-jks)$$

$$\mathbf{E}_i(Q_r) = \frac{Eo \exp(-jks')}{s'}$$

$$\overline{\overline{R}} = \begin{vmatrix} 1 & 0 \\ 0 & -1 \end{vmatrix}$$

$$A(s) = \sqrt{\frac{\rho_1^r \rho_2^r}{(\rho_1^r + s)(\rho_2^r + s)}}$$

$E_i(Q_R)$ is the vector incident field at the point of reflection resolved into the components which permit the use of the reflection dyad, R. A(s) is the divergence coefficient which describes the divergence of the wavefront as it reflects from Q_R and radiates outward. As such, the quantities ρ_1^r and ρ_2^r are the principle radii of curvature of the reflected wavefront evaluated at the reflection point, Q_R.

For a single reflection (with spherical wave incidence) the evaluation of the divergence coefficient is a relatively simple matter. Multiple reflections from doubly curved surfaces, however, make this computation difficult and time consuming since the reflected wavefront radii of curvature are functions of the incident wavefront radii of curvature, the radii of curvature of the surface, and the principle directions of the surface

and incident wavefront. For these reasons, a simpler formulation for the divergence coefficient is used:

$$\vec{A}(s) \propto \det \begin{vmatrix} \frac{\delta a_x}{\delta \theta} & \frac{\delta a_y}{\delta \theta} \\ \frac{\delta a_x}{\delta \phi} \cos(\theta) & \frac{\delta a_y}{\delta \phi} \cos(\theta) \end{vmatrix}$$

In this way, the divergence of the wavefront from feed to aperture point is accounted for and conservation of power in a "ray tube" is satisfied. With reference to Figure 1, it can also be seen that these computations are the same as those performed in the gradient calculations associated with the reflection point location algorithm. This allows for an extremely efficient evaluation of the vector field in the aperture of the dual reflector antenna.

III. EVALUATION OF THE FAR FIELD

Once the vector reflected field has been evaluated in the aperture plane, the data must be integrated to obtain the far field. Conventional aperture integration techniques can be employed, however, they are usually computationally intensive for even moderately sized apertures. Fast Fourier Transform (FFT) techniques are ideal since they are not computationally intensive and can be employed to compute the complete spatial pattern (in the forward hemisphere) or principal plane far field patterns.

The transformation techniques used to produce far field data from near field measurements in the Martin Marietta Near Field Facility are essentially the same as those used in the modeling method described here. In the test facility, near fields are measured on an equally spaced grid of aperture points on a plane parallel to the radiating aperture. As described above, the analytical model computes the near field along a similarly positioned sample lattice. The antenna far field radiation patterns are then computed in the same manner. Differences between far field measurements and those predicted by theory are traced to near field disagreement and usually indicate the source of error in the model.

The far field is related to the near field by

$$A(k_x,k_y) = \sum_{i=1}^{M} \sum_{j=1}^{N} E(x_i,y_j) \exp(-i(x_i k_x + y_j k_y)) \qquad (1)$$

The far field argument, (kx,ky) is in wave number, actually the Cartesian unit vector components scaled by the propagation constant. The far field location is represented by the unit vector u, in the same coordinate system as the near field. The three components of u are

$$u = u_x x + u_y y + u_z z \tag{2}$$

The wave number far field argument is

$$k = (2\pi/\lambda)u \tag{3}$$

Principal plane cuts are more efficiently determined by rewriting (1) as

$$A(k_x,k_y) = \sum_{i=1}^{M} \left[\sum_{j=1}^{N} E(x_i,y_j)\ \exp(-jy_jk_y) \right] \exp(-jx_ik_x) \tag{4}$$

This form is convenient because each of the rows of the two dimensional near field matrix may first be collapsed to a single value, represented by the inner summation. The outer summation is then performed on the resulting column vector for each far field value desired. For principal plane pattern calculations, far less arithmetic operations are required than would be necessary for a two dimensional FFT [3].

Directivity is computed from both the analytical and measured near field from

$$D = (4\pi/\lambda^2)\ (\Delta x)^2\ (\Delta y)^2\ A(k_x,k_y) \tag{5}$$

where delta x and delta y are the near field sample spacings in x and y. The maximum directivity of the far field pattern is the value of (5) for which A(kx,ky) is maximized.

IV. CONSIDERATIONS

In reality, most reflector surfaces show some degree of deviation from the ideal analytic curves and can be expected to alter the far field pattern with respect to that one would predict for a perfect surface. The

analytical method decribed here lends itself well to the study of these effects. If the surface deviations are much less than a wavelength (as they are for most functional high gain antennas), then the phase of the aperture field can be modified appropriately based on a knowledge of the local surface deviation. If the aperture plane is placed close to the antenna, the effects on the divergence of the wavefront can be ignored, and the amplitude of the field can be computed as described above.

Dual reflector antennas, in many cases, exhibit significant aperture blockage due to the subreflector and strut supports. This can be accounted for in this method by shadowing the aperture and assuming the field to be zero in those regions of the aperture where the rays are blocked by reflector structures. Again, this works well when the aperture plane is located as close to the reflector as possible.

Computer time computational requirements are an important part of the evaluation of techniques and methods such as that described here. If a 20 foot diameter aperture is analyzed at 13.6 GHz using a 512 x 512 aperture point array, the number of aperture points is 262,144. If the grid spacing is chosen to be three quarters of a wavelength, then two dimensional FFT processing will produce valid far field data out to 45° off boresight of the antenna (this also corresponds to the alias free range). The computer time required to compute this far field is approximately one CPU hour on a DEC VAX 11/780 computer system. Considering the fact that the antenna is 275 wavelengths in diameter and that far field data in a 90° cone about boresight is produced, this computer time benchmark clearly shows that this method is extremely quick and efficient.

IV. COMPUTED AND MEASURED RESULTS

Figure 2 shows the geometry of the antenna used to validate the pattern prediction method. The 20 foot diameter reflector was measured at 12.0, 13.6, and 15.2 GHz. The feed was mounted on a fixture allowing all three dimensions of translation and one angle of rotation. The subreflector support also allowed these independent variable positioning alternatives. These fixtures were designed to provide accurate focusing capability of the antenna and accurate steering of the beam using both feed and subreflector movement.

Surface deviations of this reflector are large enough to significantly modify the far field radiation pattern. The surface was measured mechanically and the measurements incorporated into the model as described above. Figure 3 illustrates the mechanical fixture used to measure the deviation of the reflector. Dial guages were mounted to a parabolic reference template with focal length equal to that of the reflector. The template was aligned so that it rotated about the axis of the parabola. Surface deviation was measured along 16 radial locations every 7.5 degrees of template rotation and are shown in contour and format in Figure 4. Far field patterns for a perfect reflector surface are compared to those with the measured reflector surface in Figures 5(a) and 5(b) at 13.6 GHz. The measured pattern of this antenna is shown in Figure 6(b). The surface is seen to significantly modify the sidelobe structure and decreases the peak directvity by 0.73 dB. Subsequent predictions of pattern performance all incorporate this mechanical reflector surface deviation measurement.

The antenna was focused using near field measurements almost exclusively. Before measurements were begun, the analytical model was used to explore imperfections in the near fields caused by misalignment of the feed and/or subreflector to gain insight into the effects of these misalignments. Computations associated with translation and rotation of the feed and subreflector from their nominal positions showed that each misalignment possibility uniquely perturbs the near field. These perturbations could be recognized in a single near field cut across the aperture. Each iteration of adjustment consisted of measuring and displaying near fields along a single pass of the probe through the center of the aperture, and moving feed components based on the interpretation of this measurement. The usual lengthy mechanical alignment procedure was, thus, avoided.

Focused far field measurements at 13.6 GHz are shown in Figure 6(a) and the associated model prediction in Figure 6(b). Directivity and beamwidth measurements and predictions for 12.0, 13.6, and 15.2 GHz are shown in Table 1. The agreement between measurement and computations is very good. Deviations in the sidelobe areas are due to an inadequate representation of the surface errors in the model. The agreement in the sidelobe regions could be improved if more densely spaced surface measurements were incorporated in the model.

High performance beam steering by movement of the feed horn requires the phase center of the feed to be positioned along an optimal surface, and the feed to be tilted at an optimum angle. The computer model (described here) was used to find the positions and tilt angles of the feed horn for which directivity was maximized for each desired angle of beam steering before the measurements were conducted. Figures 7(a) and 7(b) show the measurement and prediction of the steered plane patterns for beam steer angles of from 0 to 4.5 degrees, representing 18 beamwidths of steering. Figures 8(a) and 8(b) show the measurement and prediction of the sidelobe structure for the extremely steered cased. Figure 9 shows the measured and predicted beam steering loss for these cases. As can be seen, the agreement between measurement and computations is extremely good.

Beam steering may also be performed by moving the subreflector. Optimal positions and tilt angles of the subreflector were determined using the model before measurements were conducted, then demonstrated with measurement. Figures 10(a) and 10(b) show the measured and predicted steered plane performance of subreflector tilt for angles up to 2 degrees, or 8 beamwidths of steering at 13.6 GHz. Again, the agreement between measurement and computations is very good.

V. CONCLUSIONS

An efficient method of computing the far field of dual offset reflector antennas with offset feeds has been described in detail. Comparison of results with measurements conducted in the Martin Marietta Near Field Antenna Test Facility clearly demonstrate the validity of the method and suggest some improvements which could enhance the capability to predict the far out sidelobe region of the pattern. Although they have not been discussed, many of the design problems and issues associated with this class of antennas can be addressed and studied using the techniques described here. The versatility and speed of these techniques allows the antenna designer to vary a wide range of parameters in a short period of time in the process of developing the best possible antenna system design for a given set of requirements.

In conclusion, several significant enhancements to the model should be noted. First, a more appropriate method of incorporating reflector surface deviations should be implemented when these deviations are significant. The method should account for the incident angle (with respect to the local surface normal) of the ray field when these angles become large. Secondly, measured co- and cross-polarized feed patterns in amplitude and phase should be used wherever possible so long as these patterns are accurate. Lastly, the edge diffracted field (and slope diffracted field) of the subreflector [2] associated with the incident field from the feed should be evaluated at the surface of the main reflector and subsequently computed in the aperture plane when the subreflector edge illumination is significant.

VI. REFERENCES

[1] L. Q. Bowers, J. S. Hoover, "Efficient Computation of the Far Field of Offset Reflector Antennas with Offset Feeds," Proceedings of the Second Annual Review of Progress in Applied Computational Electromagnetics, 1986.

[2] R. G. Kouyoumjian, P. H. Pathak, "A Uniform Geometrical Theory of Diffraction for an Edge in a Perfectly Conducting Surface," Proceedings of IEEE, Vol. 62, pp. 1448-1461, November 1974.

[3] E. Brigham, The Fast Fourier Transform, Prentiss Hall, Inc., 1974.

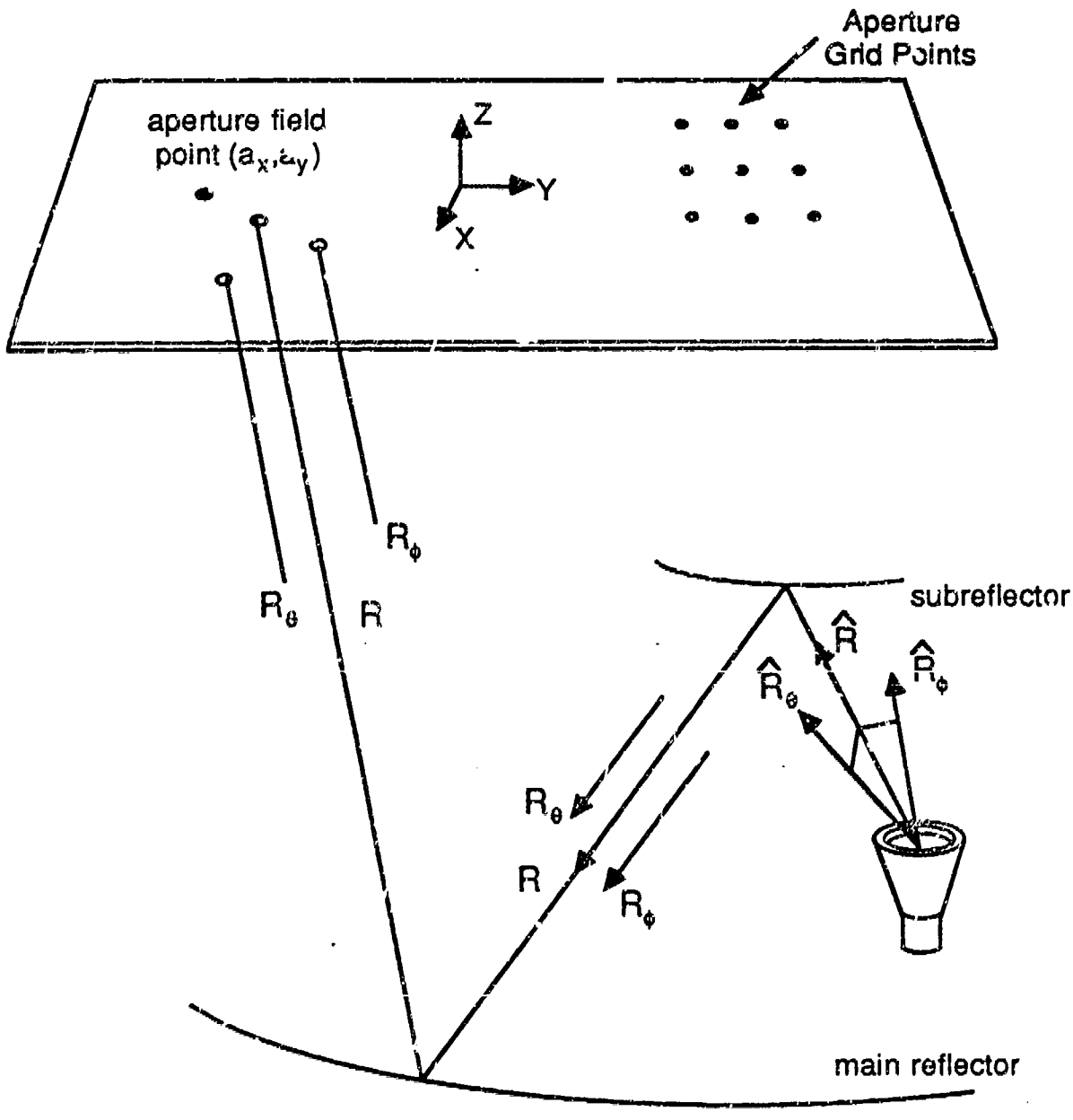


Figure 1 Dual Reflector and Aperture Geometry

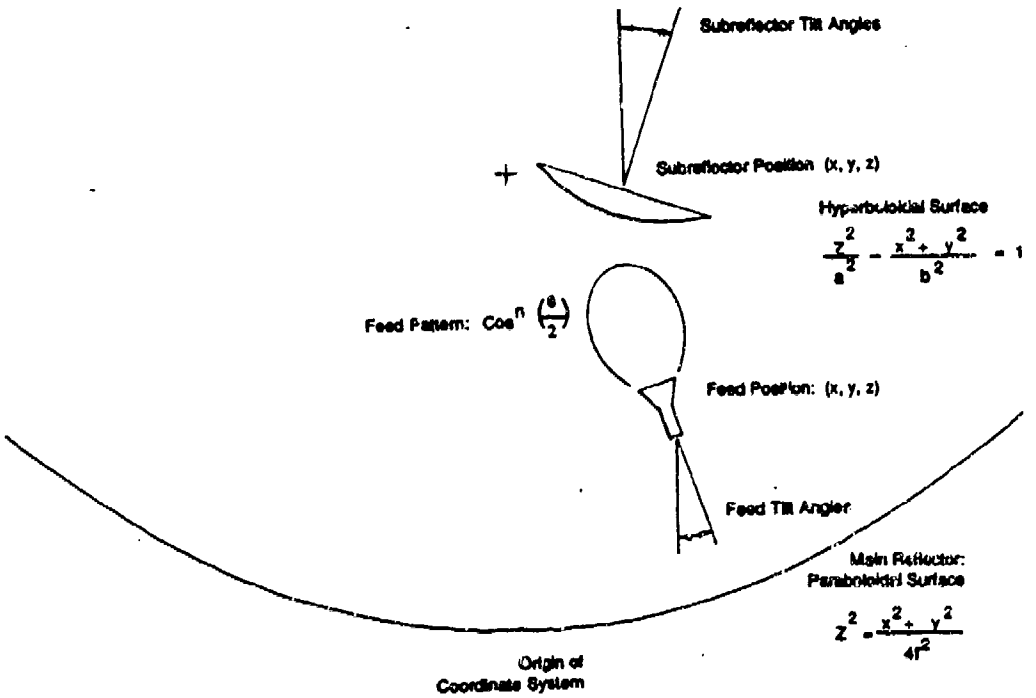


Figure 2 Antenna Model Geometry Specification

Table of values for measured antenna

Subreflector surface	a = 15.2059
	b = 17.9173
Subreflector diameter	D = 33.0
Main reflector surface	f = 72.0
Main reflector diameter	D = 240.0
Feed pattern :	12.0 GHz : n = 40.0
	13.6 GHz : n = 52.0
	15.2 GHz : n = 64.0

Nominal feed position (x,y,z) = (0,0,25.0)

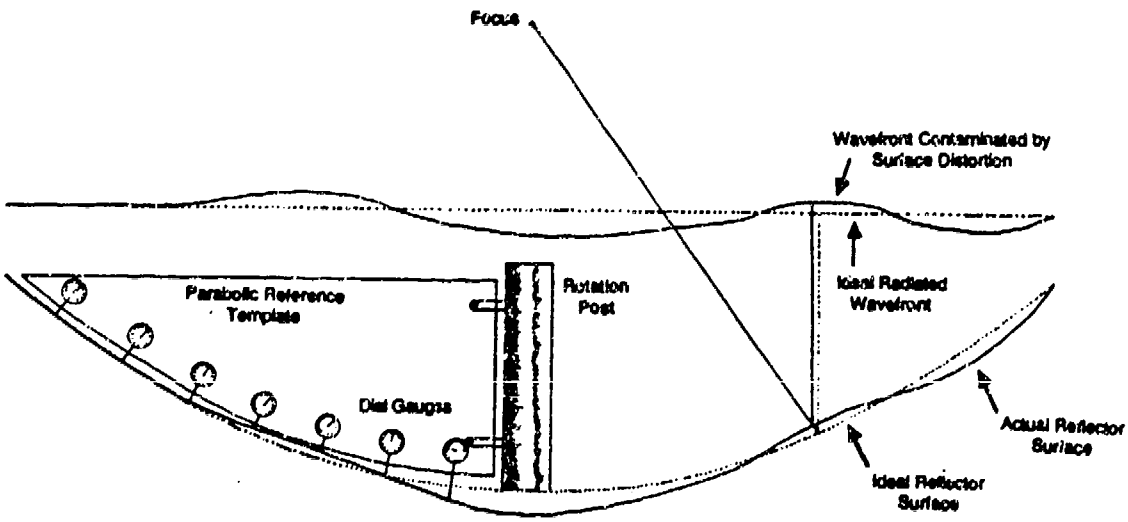


Figure 3 Mechanical Reflector Surface Measurement

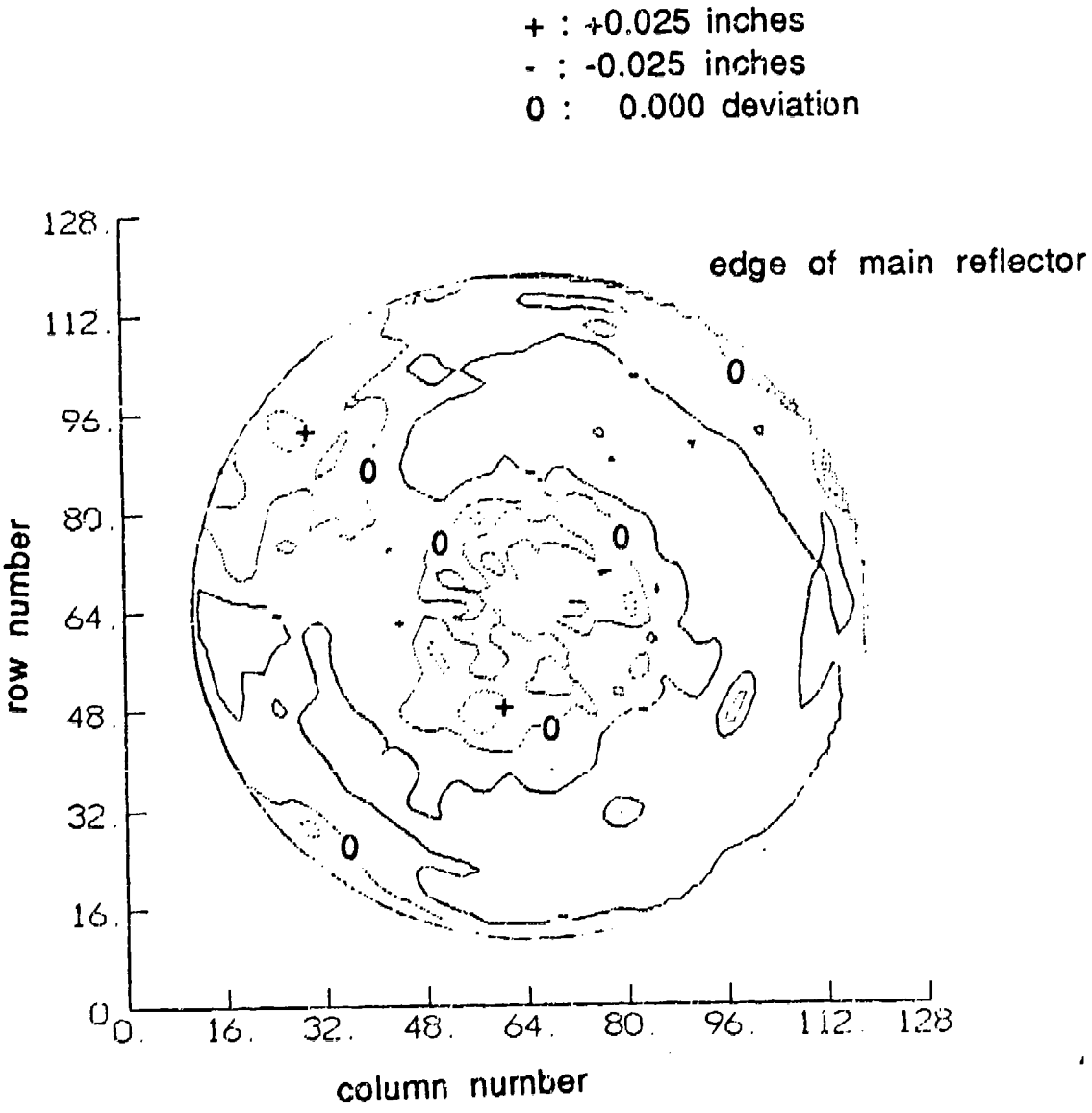


Figure 4 Mechanically Measured Reflector Surface Deviation

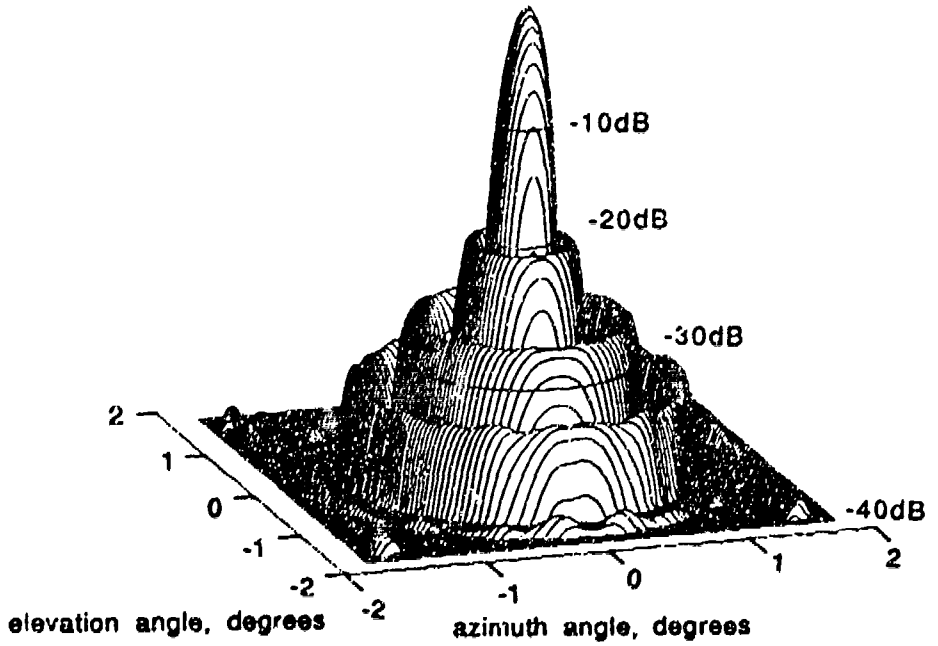


Figure 5(a) Predicted Far Field Pattern for Ideal Surface

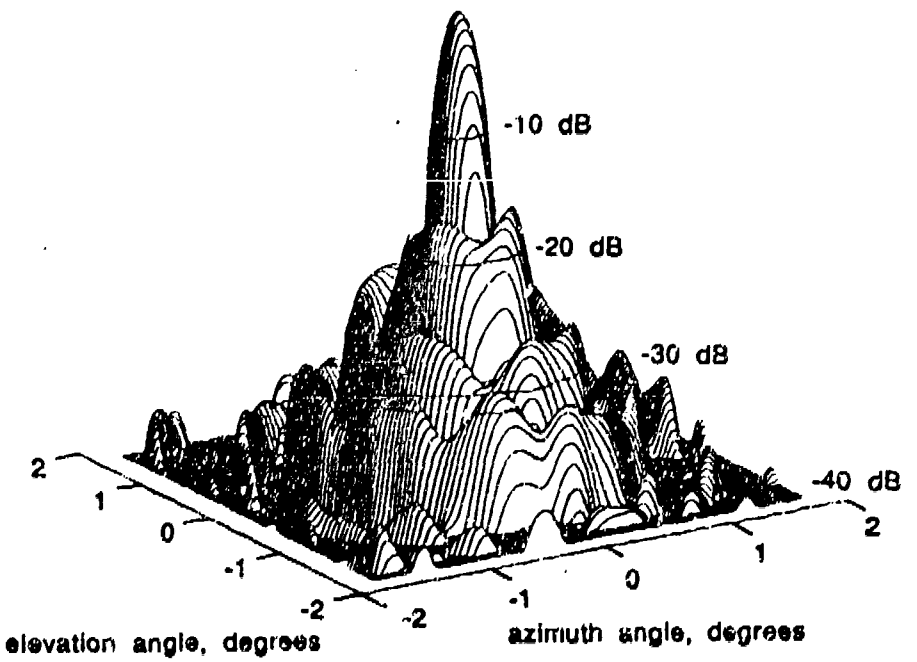


Figure 5(b) Predicted Far Field Pattern Including Effect of Surface Deviations

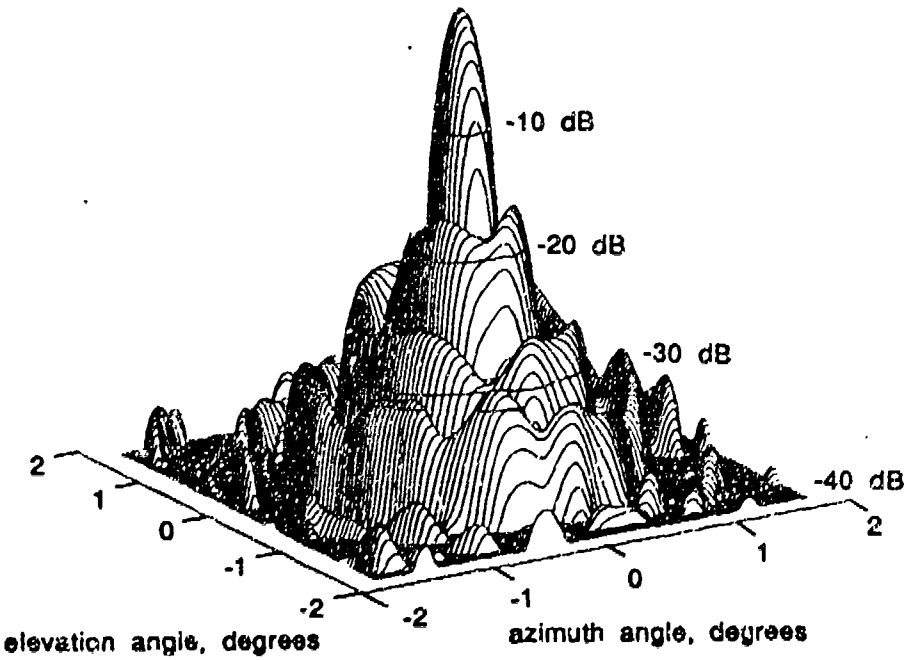


Figure 6(a) Predicted Far Field Pattern Including Effect of Surface Deviations

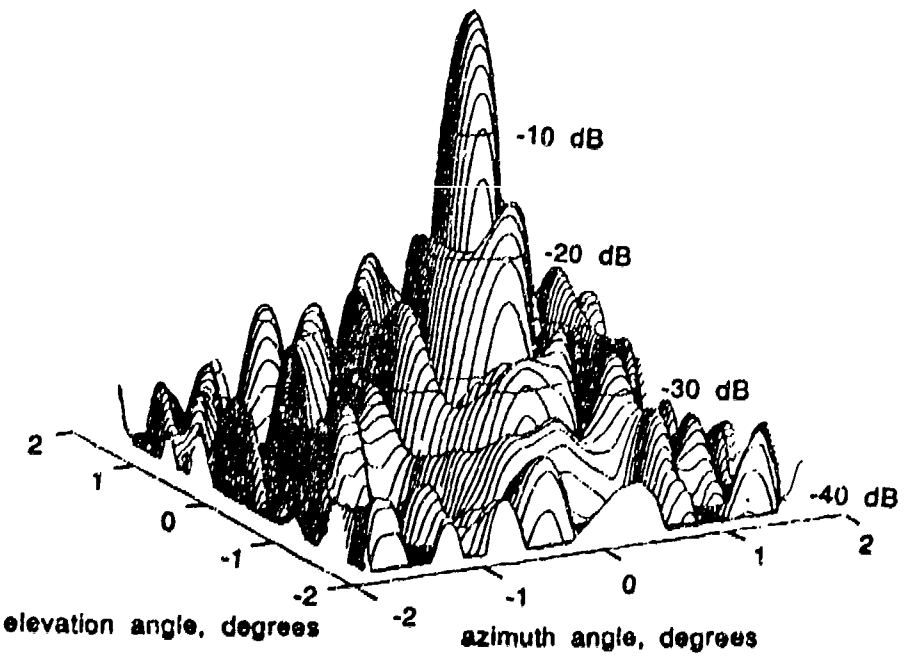


Figure 6(b) Measured Far Field Pattern

Table 1 Directivity and Beamwidth Comparisons

Frequency GHz	Measured Directivity dBi	Measured Beamwidth Degrees	Predicted Directivity dBi	Predicted Beamwidth Degrees
12.0	55.51	0.255	55.39	0.265
13.6	56.99	0.230	56.85	0.237
15.2	57.83	0.210	57.90	0.215

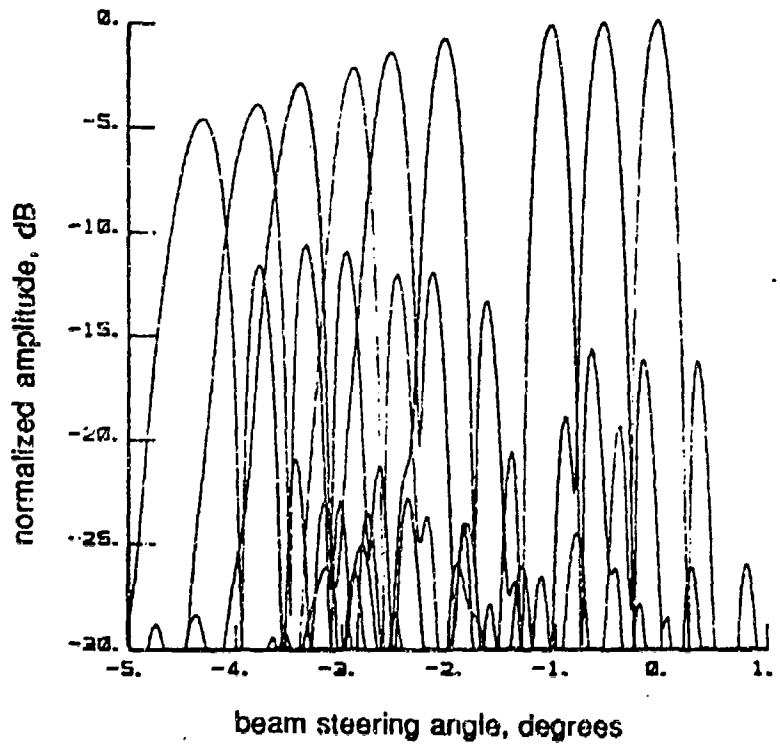


Figure 7(a) Measured Far Field -Beam Steering with Feed Movement

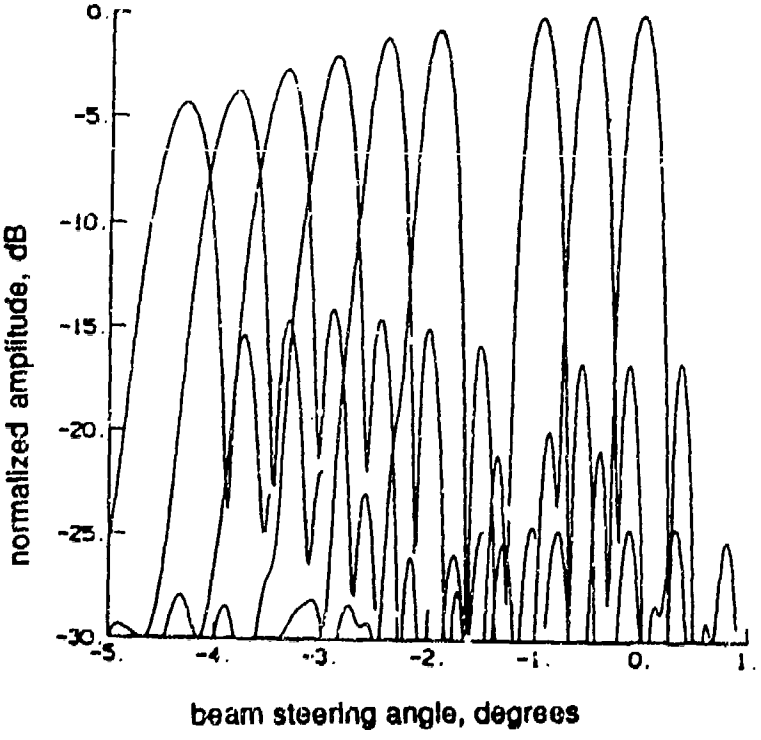


Figure 7(b) Predicted Far Field -Beam Steering with Feed Movement

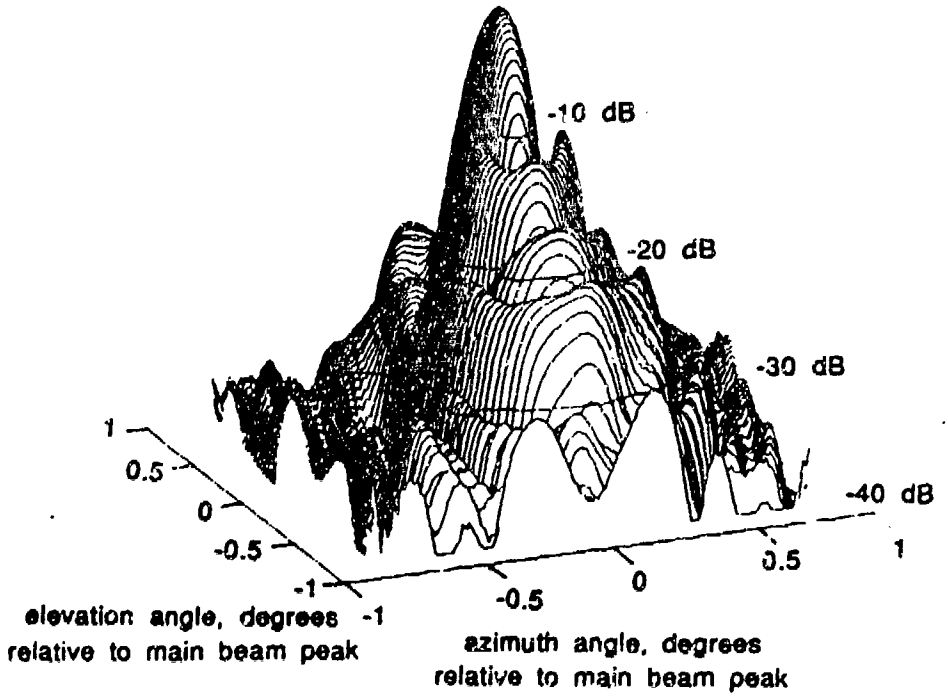


Figure 8(a) Predicted Far Field Pattern Showing Sidelobe Structure for Extremely Steered Case

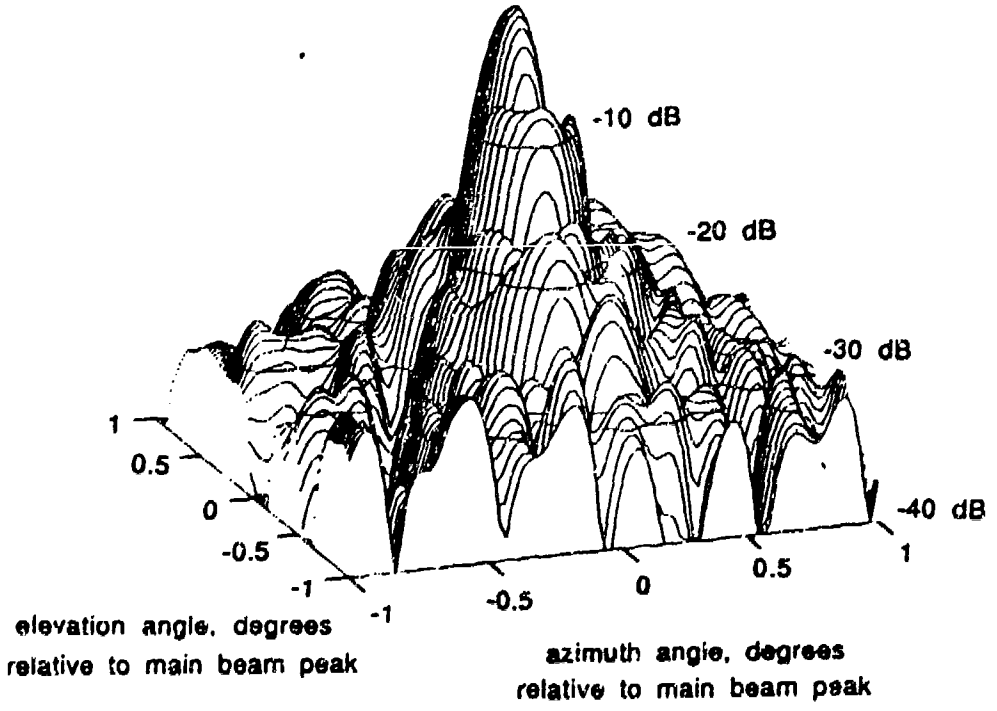


Figure 8(b) Measured Far Field Pattern Showing Sidelobe Structure for Extremely Steered Case

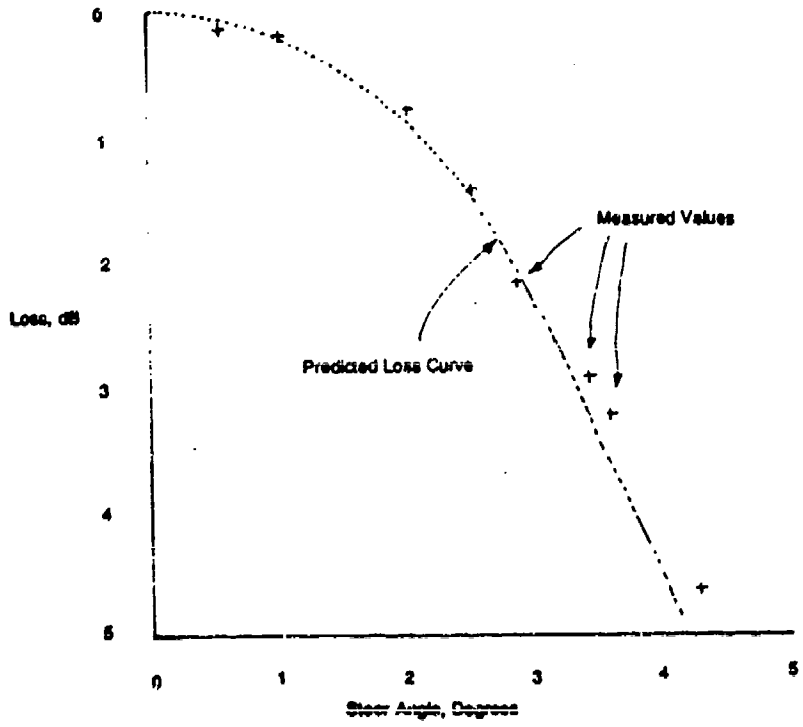


Figure 9 Comparison of Predicted and Measured Beam Steering Loss (Feed Movement)

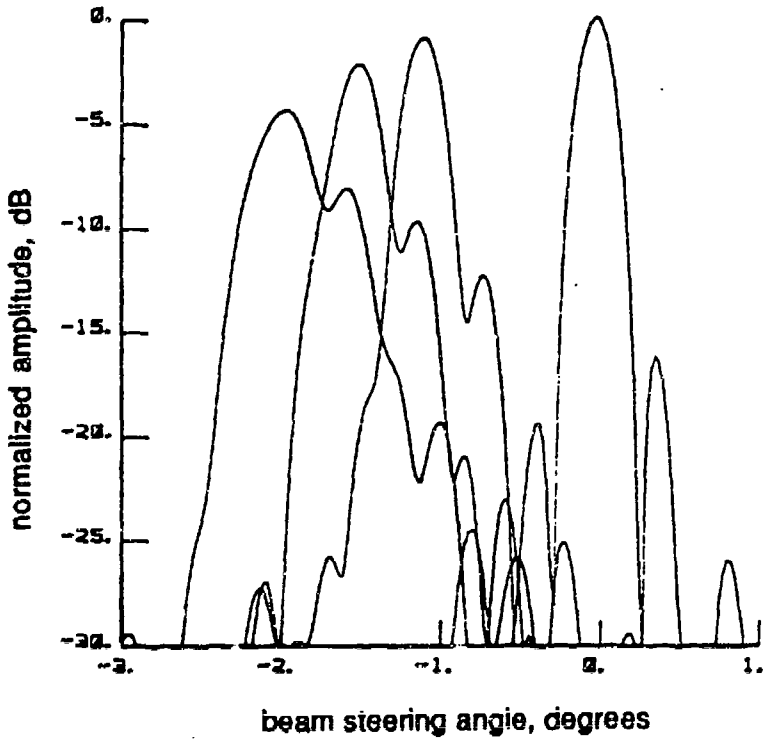


Figure 10(a) Measured Far Field Patterns -Beam Steering with Subreflector Tilt

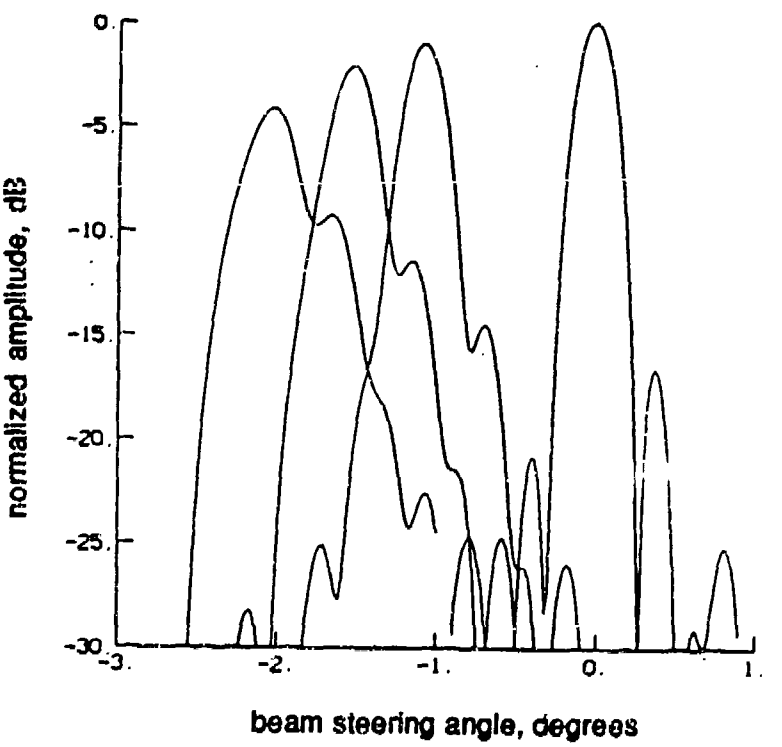


Figure 10(b) Predicted Far Field Patterns -Beam Steering with Subreflector Tilt

DEVELOPMENT AND VALIDATION OF A NEW VERSION OF THE NEC-BSC

R. J. Marhefka
The Ohio State University
ElectroScience Laboratory
1320 Kinnear Road
Columbus, Ohio 43212

The NEC - Basic Scattering Code is a user oriented computer code based on the Uniform Geometrical Theory of Diffraction (UTD). It can be used to model complex scattering structures with multiple flat plates and finite elliptic cylinders. The new version under development also allows the use of multiple sectioned cone frustums and finite composite ellipsoids. A brief discussion of the new capabilities of this version will be given. Some of the experiences in developing a code which is approaching 20,000 lines in length will be presented.

Validation of the code is one of the central issues that needs to be addressed before a new version can released. Not only does the new features that were added to the code need to be checked, but also so does previous capabilities need to be re-validated. This becomes more and more difficult as the number of applications for a code increases. The developer can strive for a structured environment whereby changes can be made without effecting the rest of the code, but can this be insured? Experience has shown that a code should be sent to at least a few knowledgeable but separate users to exercise the code. This can help find bugs, since a different user may set up the same problem in a slightly different way and can try various other applications.

Validation of a result can obviously be made by checking the code against alternative codes or measurements. Of particular concern to a UTD code, however, is when discrepancies arise in the comparison to what can they be attributed. Is it a coding bug, theory limitation, or lack of an important UTD term? A challenging problem is to construct test problems that will answer whether an individual UTD term is correct or not. This is very difficult because alternative methods normally give the total result only. Self consistency checks is one way of addressing this problem.

Validation of the input geometry and the code's understanding of the geometry is also an issue. Graphics is one way of helping the user validate the input set. Just drawing a pretty picture, however, is not enough. Experience has shown that drawing a picture using the same geometry algorithms that the EM code uses helps find more bugs. These and other issues of validation of UTD codes will be discussed.

DEVELOPMENT AND VALIDATION OF A NEW VERSION OF THE NEC-BSC

R. J. Marhefka
The Ohio State University
ElectroScience Laboratory
1320 Kinnear Road
Columbus, Ohio 43212

1 Introduction

The NEC - Basic Scattering Code is a user oriented computer code based on the Uniform Geometrical Theory of Diffraction (UTD). It can be used to model complex scattering structures with multiple flat plates and finite elliptic cylinders [1,2]. The new version under development [3] also allows the use of multiple sectioned cone frustums and finite composite ellipsoids [4,5]. A brief discussion of the new capabilities of this version will be given. It adds to many of the details given in a previous discussion of its immediate predecessor [6].

Some of the experiences in developing a code which is approaching 20,000 lines in length will also be presented. In addition, how some of the validation issues from the code developers point of view will be addressed. Two graphics codes which are helpful tools for developing and validating the code are discussed. The first is for plotting the geometry, the second is for pattern plots.

2 NEC-BSC V3.1 Capabilities

As reported last year [6], the NEC-BSC scattering code is in the process of being improved. The changes previously discussed were centered on improving the structure of the code and the addition of many useful user oriented features. Since then improvements in modeling capabilities have taken place. In particular, a multi-sectioned elliptic cone frustum and a composite finite ellipsoid capability have added. At the time of this talk, this version of the code is going through a validation and documentation process.

An overall summary of the new version of the code is outlined here.

- User oriented command word based input structure.
- Pattern calculations.
  - Near zone source fixed or moving.
  - Far zone observer.
  - Near zone observer.
- Single or multiple frequencies.
- Antenna to antenna spacial coupling calculations.
  - Near zone receiver fixed or moving.
- Efficient representation of antennas.
  - Infinitesimal Green's function representation.
  - Six built in antenna types.
  - Linear interpolation of table look up data.
  - Method of Moments code or Reflector Code interface.
- Multiple sided flat plates.
  - Separated or joined.
  - Infinite ground plane.
  - Limited dielectric plate capability.
- Curved surfaces.
  - Multiple elliptic cylinders.
  - Multiple sectioned cone frustums.
  - Composite finite ellipsoids.
- UTD single and multiple interactions included.
  - Second order plate terms not including double diffraction.
  - First order curved surface terms only.
  - Presently no plate - cylinder interactions.

In addition to the above features, algorithm development is continuing in a few other areas as given below.

- Under Development
  - Double diffracted fields.
  - Third order interaction terms.
    - triple reflected fields
    - reflected-reflected-diffracted fields
    - reflected-diffracted-reflected fields
    - diffracted-reflected-reflected fields
  - Specular dielectric for curved surfaces.

Possible future improvements in the code are being explored as theoretical topics at the present time.

- Potential Future Developments
  - Super ellipsoids.
  - Composite shaped curved surfaces.
  - Creeping waves for all curved surfaces.
  - Improved dielectric treatment with surfaces waves.

As an example of the new cone frustum capabilities, the geometry in Figure 1 is used. This is from Example 20 of Version 2 of the NEC-BSC's user's manual. The wings are not included here. The source and receiver were 864 inches away from the object. It should be noted that Version 2 did not have the cone present. The measured and calculated results at 10 Ghz for horizontal polarizations are compared in Figure 2.

3 Development Issues

As a developer of a user oriented computer code, questions are often asked concerning the applicability of the code for a particular application. In general, it difficult to give a specific answer without information about the specific problem. The applicability of a code like the NEC-BSC, however, can be best explained by looking at three areas. They are its modeling capabilities, numerical limitations, and theoretical considerations. These areas are not the final say as to the validity of the code for a particular application, but they provide a useful starting point. Ultimately the code should be tried and validated on each problem's own merit.

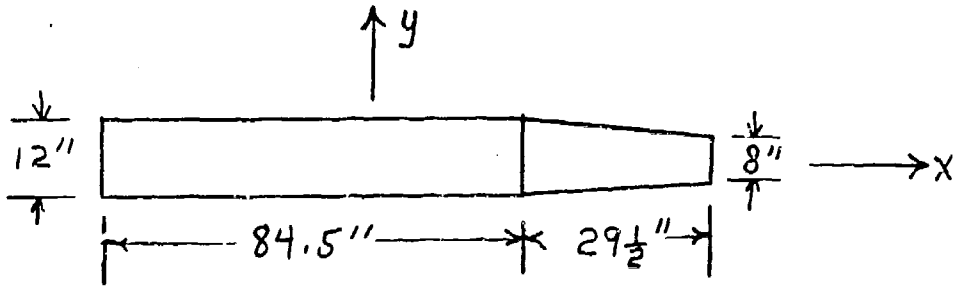


Figure 1: Cone cylinder geometry.

3.1 Modeling Capabilities

Codes such as the NEC-BSC are generally designed around a few given application's needs. Not all possible needs can be anticipated as the development proceeds. The given implementation of the code results from many trade-offs such as computer size, speed, etc. Generally, the UTD codes like the NEC-BSC have started out by including fundamental building blocks such as plates and cylinders. These units were deemed to be basic enough to help a wide class of applications especially for antenna pattern prediction.

As broader scattering issues have needed to be addressed, it has been necessary to increase the curved surface modeling capabilities. In any event, whether the present class of surfaces meets the exact needs of a particular applications it has been generally found that good cause and effect engineering answers can still be obtained. This increases the need to understand and validate the conclusions that are reach in each situation.

3.2 Numerical Limitations

Computer codes must be designed to work on computer which have finite precision. These leads to possible loss of accuracy or unpredictable result from computer to computer and implementation of a particular application. Many examples have arisen in the use of the NEC-BSC where the size or distance of a particular geometry has caused terms to be included in unsymmetric or inconsistent ways. The code has been developed to anticipate these problems but many of the fixes turn out to be conflicting with other applications unforseen at the time. Solutions

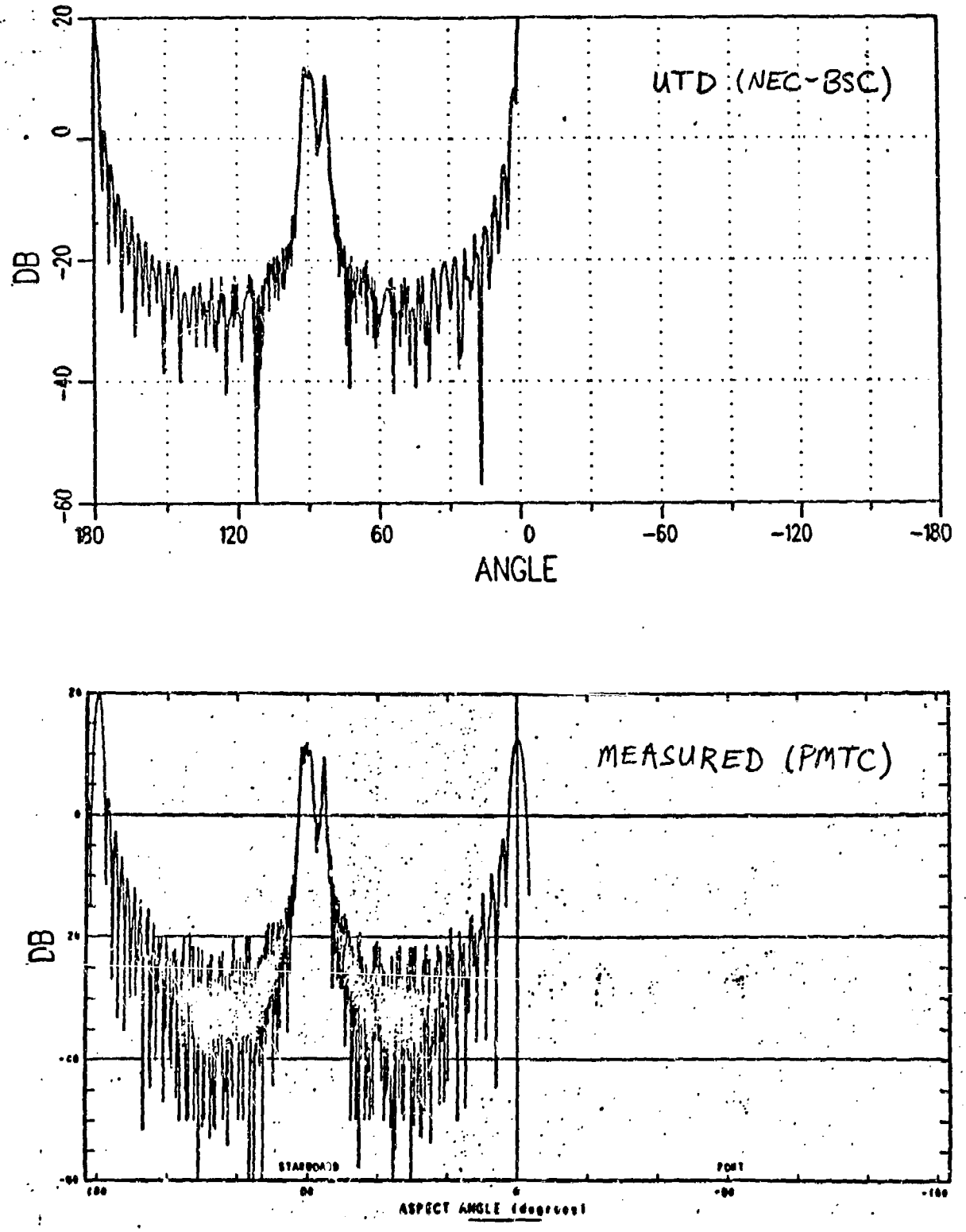


Figure 2: Comparison of calculated (top) and measured (bottom) pattern from a cone - cylinder geometry.

such as doing the problem in a different coordinate system sometimes fixes the problem. In others, using smaller ranges will help and still give a reasonable result.

Logic to take care of special cases has also been included in the code. It has been found, however, that the small number problems associated with these decision processes can be a cause for error. One possible fix that works many times is to change the small number bound that exist in a common block in the NEC-BSC. This often makes inconsistent results consist, since the logic branch decisions are made at a higher level. A better means of desensitizing codes to these types of problems needs to be sought.

3.3 Theoretical Considerations

Many of the modeling decisions and numerical fixes above center around avoiding limitations in the present diffraction coefficients. On going work is being done to make the diffraction coefficients as uniform as possible. The fewer logic decisions made, the less chance for error. UTD has the nice feature that the validity of a code is not completely destroyed by a small limitation in the diffraction coefficient. In general, the results obtained may be corrected over the majority of a pattern and discontinuous over only a small region.

The number of terms implemented also impact on the level of validity of a solution. This is usually determined by the application. As the number of terms are added to a code such as the NEC-BSC, it is important to note that the time require to do the calculations will increase. Intelligent way to pick the optimum terms for a given application is being sought. It should be noted that if terms are left out, UTD gives a gauge of its accuracy by the largeness of the discontinuities that result.

4 Coding Issues

One of the biggest issues on developing a code is vriting it in a way that avoids transportability problems. The NEC-BSC is being written on a VAX 8550 at present using standard Fortran 77. It has also been run on a number of different machines. Different compilers seem to still find different problems even though nominally Fortran 77 is used. One example is that the VAX "/OPTIMIZE" feature sometimes causes erroneous results to occur. These problems are not easily found and

removed, especially on another persons computer if they can't be duplicated on the developers computer. Desensitizing the code to numerical problems for consistent results and providing good dynamic range is difficult from machine to machine. Finding good ways to write the code to avoid these problems needs to be continuously pursued. Little help is found in the literature.

In order to improve development time, validation, and maintance of a code it has been attempted to write the new version of the code in a more structured manner. How well can a code adhere to structured coding over repeated improvement phases is a good question. Large codes tend to have more than one person working on them. Many times even small deviations from predetermine conventions lead to bugs that are hard to detect. Code development would seem to follow more Inside-Out than Top-Down practices.

A question that is often asked of the NEC-BSC is will it fit on a small machine? The answer is that it will fit on machines whose compilers will address large sizes. The codes arrays can easily be adjusted to smaller size, however, The code is still large in terms of the number of statements. Overlay techniques can be used to compute the various terms separately and then added later.

5 GKS Graphical Codes

With the new versions of the NEC-BSC, two graphics codes are being prepared. They are based on the Graphic Kernal System (GKS) ANSII standard. The first draws the geometry based on the input command word data set and the second plots the output in polar or rectangular form.

The NEC-BSC Draws Code reads the same input set as the EM code to draw the geometry. This gives a good visual aid to ensure that the input set is correct. In addition to simply reading the input geometry and outputting a drawing, it uses most of the same geometry routines for joining plates and organizing the data. It also uses the same shadowing subroutines as the EM code. This has been found to be very helpful in validating the EM code. Bugs have been found in certain geometrical situations that were not found previously by looking at the resultant patterns. This suggest that codes that aid the user in inputting the code alone do not give the full picture for code validation. An example output for a aircraft model is given in Figure 3.

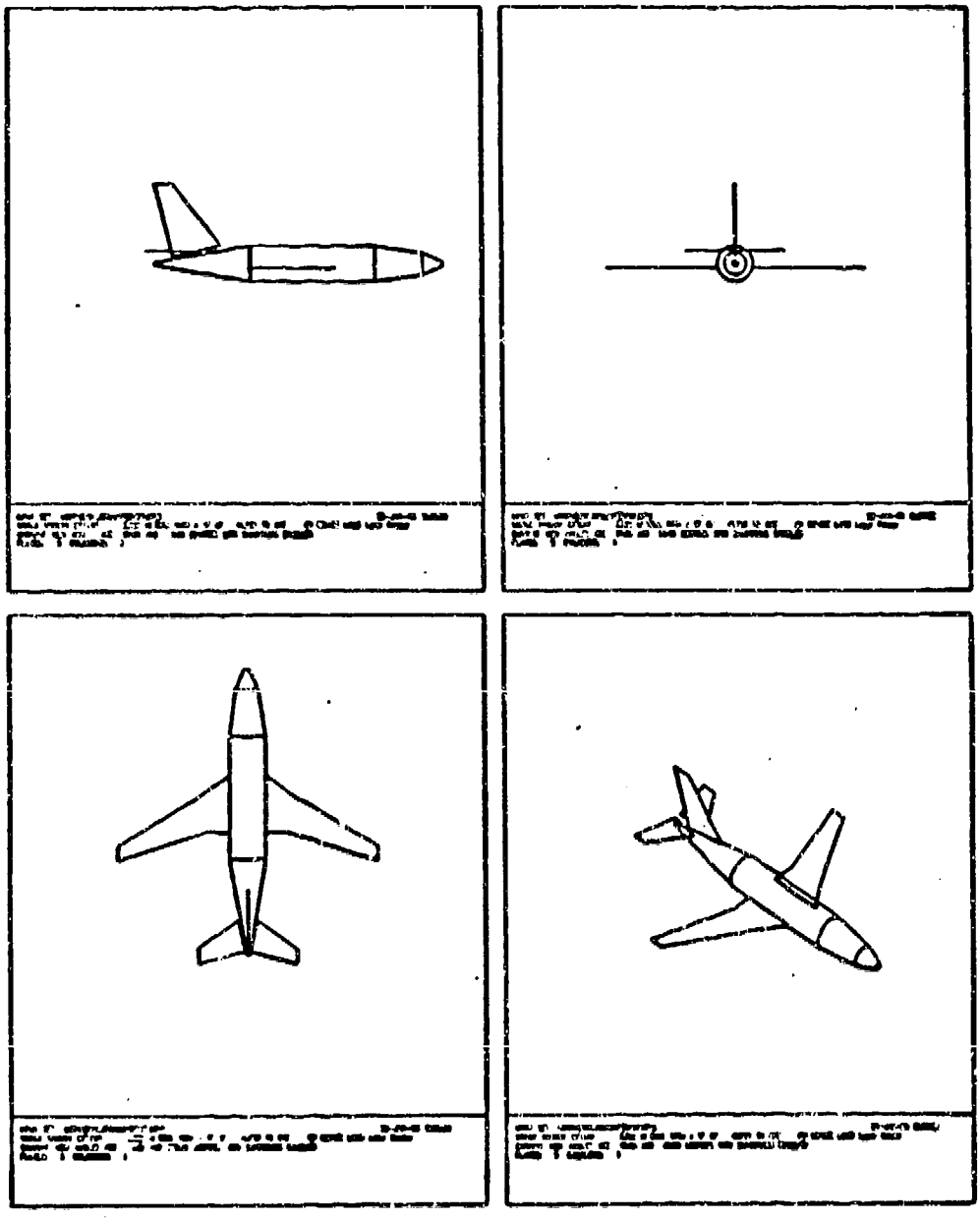


Figure 3: Example output from NEC-BSC Draws Code.

The second graphical aid being developed is a NEC-BSC Pattern Plot Code. It uses output from the NEC-BSC to draw rectangular or polar plots of the various polarizations of the fields, power values, or coupling depending on how the particular run was configured. It will also allow the user to plot individual cuts of volumetrical obtained data from the code. It will plot based on the prespecified size and normalization or allow for changes at plot time.

References

[1] R. J. Marhefka and W. D. Burnside, "Numerical Electromagnetic Code - Basic Scattering Code, NEC - BSC (Version 2), Part I: User's Manual," Technical Report 712242-14, December 1982, The Ohio State University ElectroScience Laboratory, Department of Electrical Engineering; prepared under Contract No. N00123-79-C-1469 for Naval Regional Contracting Office.

[2] R. J. Marhefka, "Numerical Electromagnetic Code - Basic Scattering Code, NEC - BSC (Version 2), Part II: Code Manual," Technical Report 712242-15, December 1982, The Ohio State University ElectroScience Laboratory, Department of Electrical Engineering; prepared under Contract No. N00123-79-C-1469 for Naval Regional Contracting Office.

[3] R. J. Marhefka and J. W. Silvestro, "Numerical Electromagnetic Code - Basic Scattering Code, NEC - BSC (Version 3), User's Manual," to be published, The Ohio State University ElectroScience Laboratory, Department of Electrical Engineering; under preparation for Contract No. N60530-85-C-0249 for Naval Weapons Center.

[4] R. J. Marhefka and J. H. Choi, "Bistatic Scattering Analysis of an Ellipsoid," Applied Computational Electromagnetics Society, 3rd Annual Review Conference Proceedings, Monterey, California, March 24–26, 1987.

[5] J. H. Choi and R. J. Marhefka, "Bistatic Scattering Analysis of an Ellipsoid," Technical Report 717674-2, November 1986, The Ohio State University ElectroScience Laboratory, Department of Electrical Engineering; prepared under Contract No. N60530-85-C-0249 for Naval Weapons Center.

[6] R. J. Marhefka and J. W. Silvestro, "Recent Updates to the NEC-BSC," Applied Computational Electromagnetics Society, 3rd Annual Review Conference Proceedings, Monterey, California, March 24–26, 1987.

PREDICTION AND MEASUREMENT OF TRANSVERSE WAVE IMPEDANCE IN THE VICINITY OF ELECTRICALLY SMALL RADIATING STRUCTURES

M E G Upton and A C Marvin
Department of Electronics
University of York
Heslington
YORK. YO1 5DD
United Kingdom

INTRODUCTION

The work in this paper forms part of a study of the detailed field structure in the induction-field region around radiating sources. The variation of transverse wave impedance is of particular interest as this conveys information about both electric and magnetic fields. In addition, the efficiency of an electromagnetic shield is directly related to the incident wave impedance and it may therefore be possible to produce an optimum shielding configuration for a given wave impedance distribution. The eventual aim of our work is to investigate this possibility.

In some situations it may not be possible to reconfigure the shield and the radiating source may need to be adjusted. In this paper we consider a small, resistively loaded, vertical loop above a ground plane. The aim is to assess the effect of varying the load resistance upon the wave impedance distribution in the plane of the ground. It is known (ref[1]) that an electrically small loop radiates a low impedance wave in the induction-field. When loading is introduced, however, the current distribution around the loop is modified and an element of electric dipole (high impedance) radiation is present. A high impedance wave is proportionally easier to screen.

Note that the following results consider the transverse wave impedance which is defined as the ratio of the electric and magnetic field components perpendicular to the radial vector from the radiating source. This enables a much simpler practical

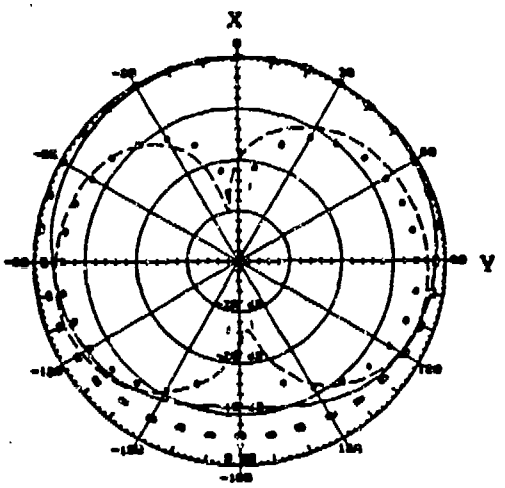


Fig. 2a: X-Y-cut

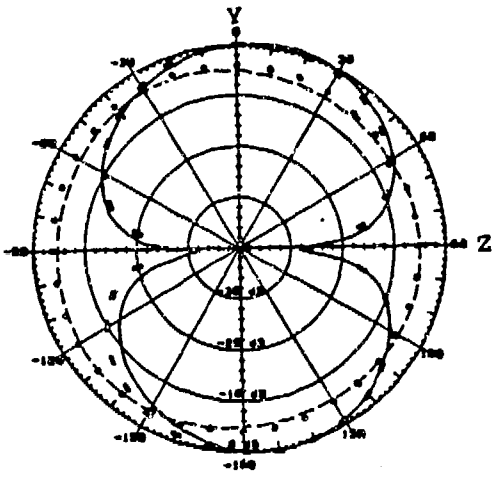


Fig. 2b: Y-Z-cut

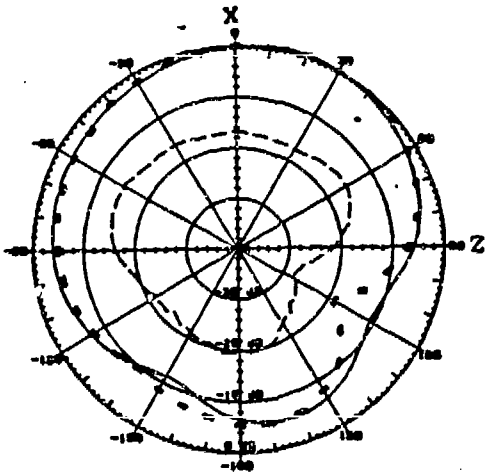


Fig. 2c: X-Z-cut

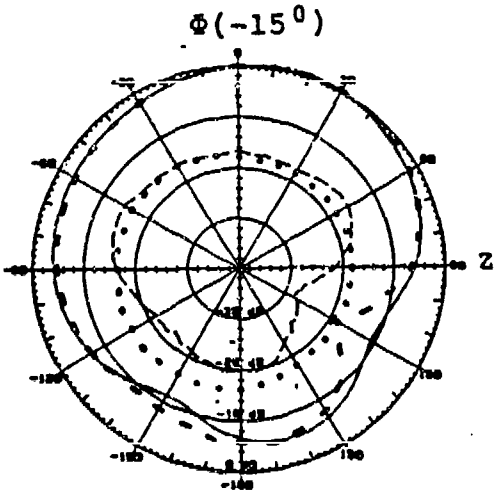
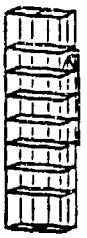


Fig. 2d: $\Phi(-15^0)$-Z-cut

vert. pol., calculated
vert. pol., measured
hor. pol., calculated
hor. pol., measured



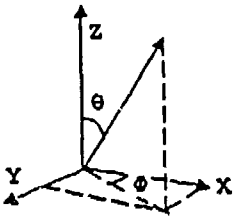


Fig. 2: Radiation patterns of the LIFA-structure.
a) X-Y-cut, b) Y-Z-cut, c) X-Z-cut,
d) $\Phi(-15^0)$-Z-cut

measurement system to be used. The generalized wave impedance also includes the radial components of electric and magnetic field, which only exist in the induction field.

RADIATING LOOP GEOMETRY AND THE NEC3 MODEL

The geometry of the radiating source is a 4cm square wire loop mounted on a BNC connector (fig.1), which was chosen for the ease of practical construction and simplicity of the NEC3 model. The loop is made of 1mm diameter wire and is mounted vertically upon a 3m by 1.5m aluminium ground plane. The wave impedance sensor consists of discrete electric and magnetic field sensors situated 50cm from the radiating loop and 8cm apart (to minimise the coupling between the sensors). In order to vary the effective distance between source and sensor, the frequency of excitation of the loop is scanned from 10MHz to 400MHz which corresponds to a wavelength variation from $\lambda/60$ to $2\lambda/3$. Furthermore, the effective size of the loop varies from $\lambda/750$ to $4\lambda/75$.

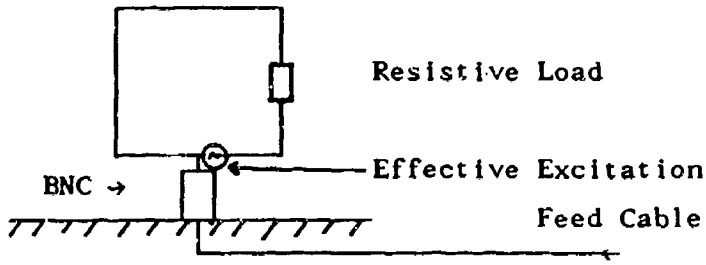


Fig.1 Configuration of Practical Radiating Loop

In NEC3 this situation is modelled using 5 segments per side, except the side of the loop with the voltage source which has 6 segments. Thus the shortest segment is $\lambda/4500$ at 10MHz which goes beyond the accuracy limits of NEC, but gives reasonable results for this simple structure if double precision arithmetic is used. The 8cm separation of the sensors is significant compared with the 50cm source-sensor separation and this is modelled as $\pm 4.5^{\circ}$ offsets from the main axis for the field calculations.

Data is generated for a 180° scan in the plane of the ground and the response is sampled every 10° (the limit of practical accuracy) at a height of 5mm above the ground. A full 360° scan is unnecessary as the wave impedance distribution is symmetrical about the plane of the loop. The results are plotted as a three dimensional surface where the frequency and angle are used to define 'r' and 'θ' in a cylindrical polar coordinate system and the wave imepdance at that point defines the height 'z'. Logarithmic scales are used on both the frequency and the wave impedance axes.

SIMULATION AND PRACTICAL RESULTS

Figs 2–6 show the wave impedance responses produced by load resistances of 0,40,98,219 and 469Ω respectively. In each case, fig.2(a) gives the distribution predicted by NEC3 and fig.2(b) gives the practical distribution, and so on.

The unloaded loop distribution (fig.2) shows the expected (ref[1]) response, rising from a low impedance wave (typically 30Ω) and becoming asymptotic to 377Ω as frequency is increased. In addition, there is good qualitative agreement between the two responses except in the 70° area of the response. This discrepancy arises because the large changes in wave impedance occuring in the 70° region make the results very sensitive to accurate angle measurement, which is not possible with the present practical test set-up. It is interesting to note that the response is not isotropic in the test plane, as would be expected from the equations given in [1]. Although the loop is electrically small, its size is significant when compared with the 50cm source-sensor separation and this causes variation of the response with angle.

The addition of a 40Ω load in the loop (fig.3) modifies the distribution significantly. At low frequencies a high impedance (typically 800Ω) 'ridge' is present in the 70° response and, in the practical case, a trough in the wave impedance also occurs in the 70° response. Less noticeably, the peak in the 90°-180° responses is reduced. Again there is

good agreement between the two responses except in the sensitive 70° area.

As load resistance is increased to 98Ω (fig.4), the trough in the 70° response can be seen to have developed in both distributions, though it is more pronounced in the practical case. Away from the 70° region, the responses can be seen to be flattening out, with the low frequency wave impedance portions starting around 100Ω.

A further increase in load to 219Ω (fig.5) causes a sharp trough in wave impedance to develop in the distribution, which drops as low as 20Ω. This is present on the NEC response at 70° and the practical response at 60°. Although this anomaly can be attributed to inaccurate practical angle measurement and the coarse angle sampling missing the true depth of the null, part of the discrepancy must be attributed to inaccuracies in the NEC model. The majority of the practical distribution is approximately flat, though this is less evident in the NEC distribution.

Finally, fig.6 considers the loop loaded with 469Ω. Again a 10° discrepancy exists between the practical and NEC distributions for the position of the null. Furthermore, the 0–40° section of the practical distribution consists of much deeper troughs than the NEC distribution. The tendency of a highly loaded loop to act like an electric dipole can be seen from this last response if it is compared with the distribution of a monopole above a ground plane (fig.7).

CONCLUSIONS

The results in this paper demonstrate that NEC3 can be used for very good qualitative assessment of induction-field wave impedance distributions. The majority of the discrepancies between the practical and NEC3 distributions occur as the result of inaccuracies in angle measurement in the practical test set up. Further improvements in the practical measurement technique should enable a more quantitative analysis of the

NEC3 predictions.

The tendency of a loaded loop to act like an electric dipole as load is increased has been demonstrated. A trough that occurs in the low resistance distributions (40Ω and 98Ω) on the 70° response, deepens and moves towards the 0° axis as load is increased. Also the low frequency portion of the distribution increases in wave impedance as laod increases. This suggests that improvements in shielding effectiveness may be possible if loop loading is modified. Conversely, the sharp null in the wave imepdance may need to be avoided as this would cause a drop in the shielding effectiveness.

REFERENCES

1. KEISER B. 'Principles of Electromagnetic Compatibility: Third Edition', Artech House, 1987, pp28-31.

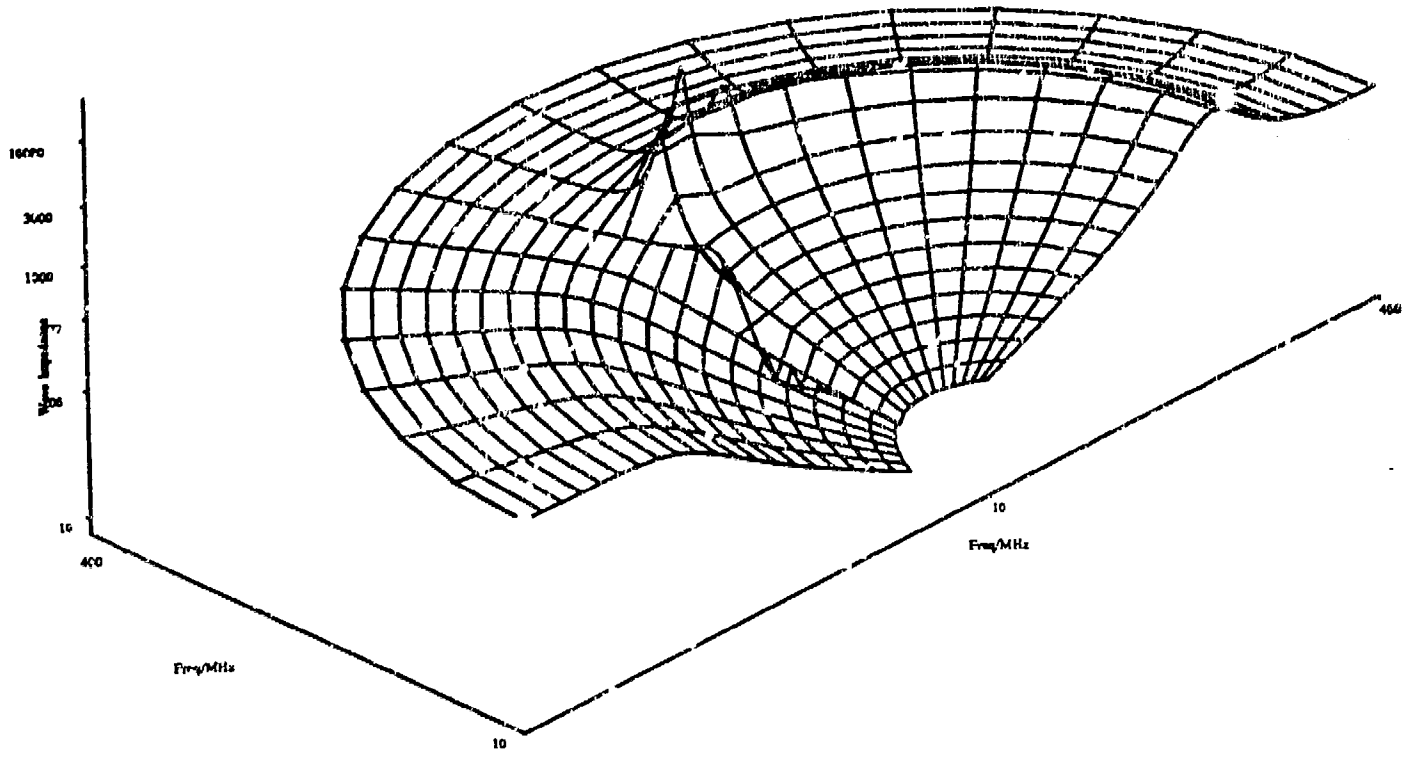


Fig.2(a) Wave Impedance Distribution of Unloaded Loop from NEC3.

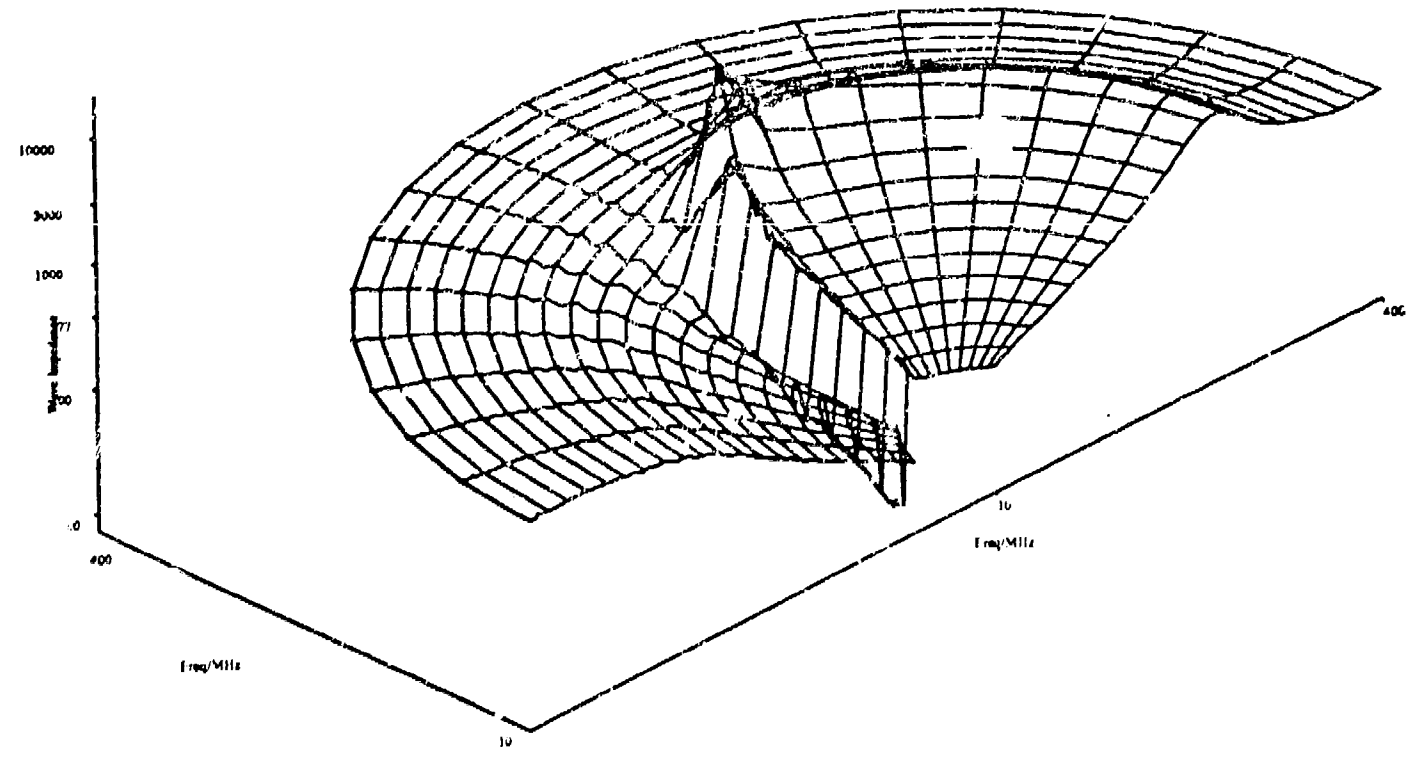


Fig.2(b) Wave Impedance Distribution of Unloaded Loop: Practical Results.

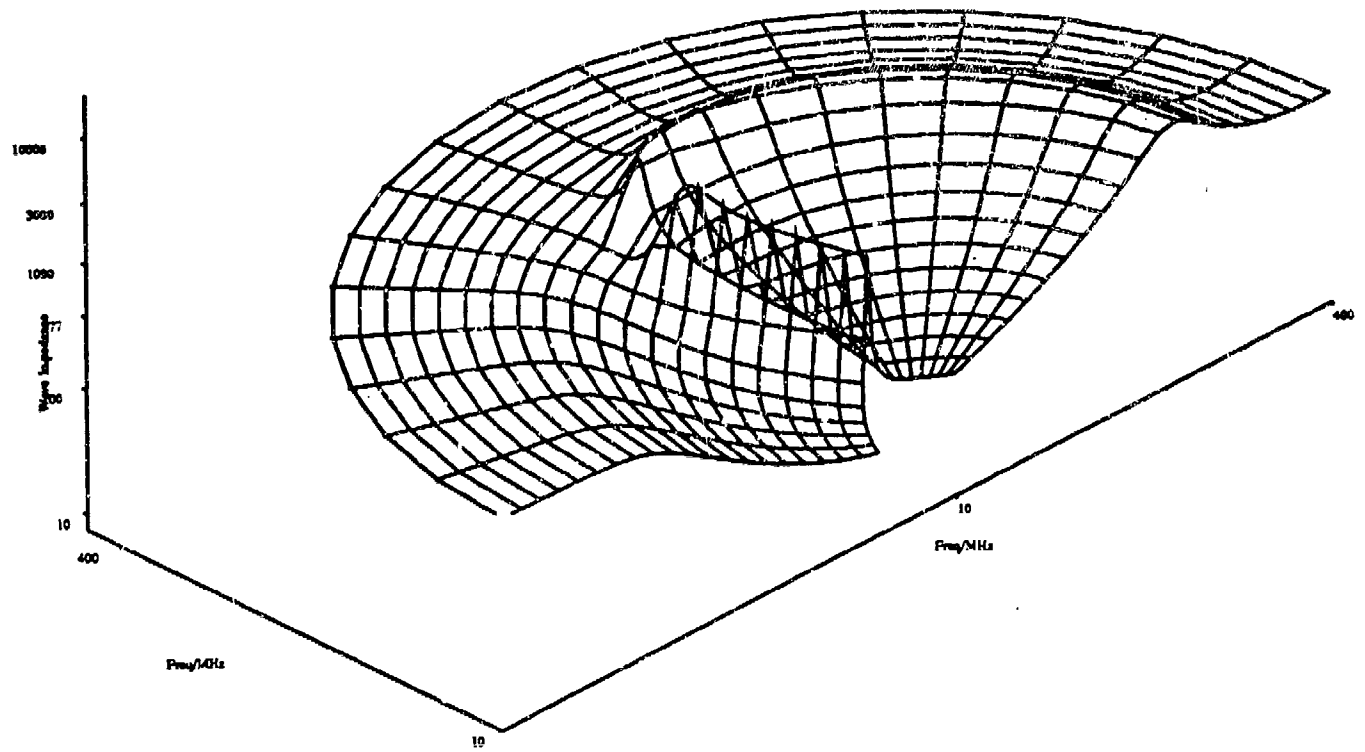


Fig.3(a) Wave Impedance Distribution of Loop Loaded with 40Ω from NEC3.

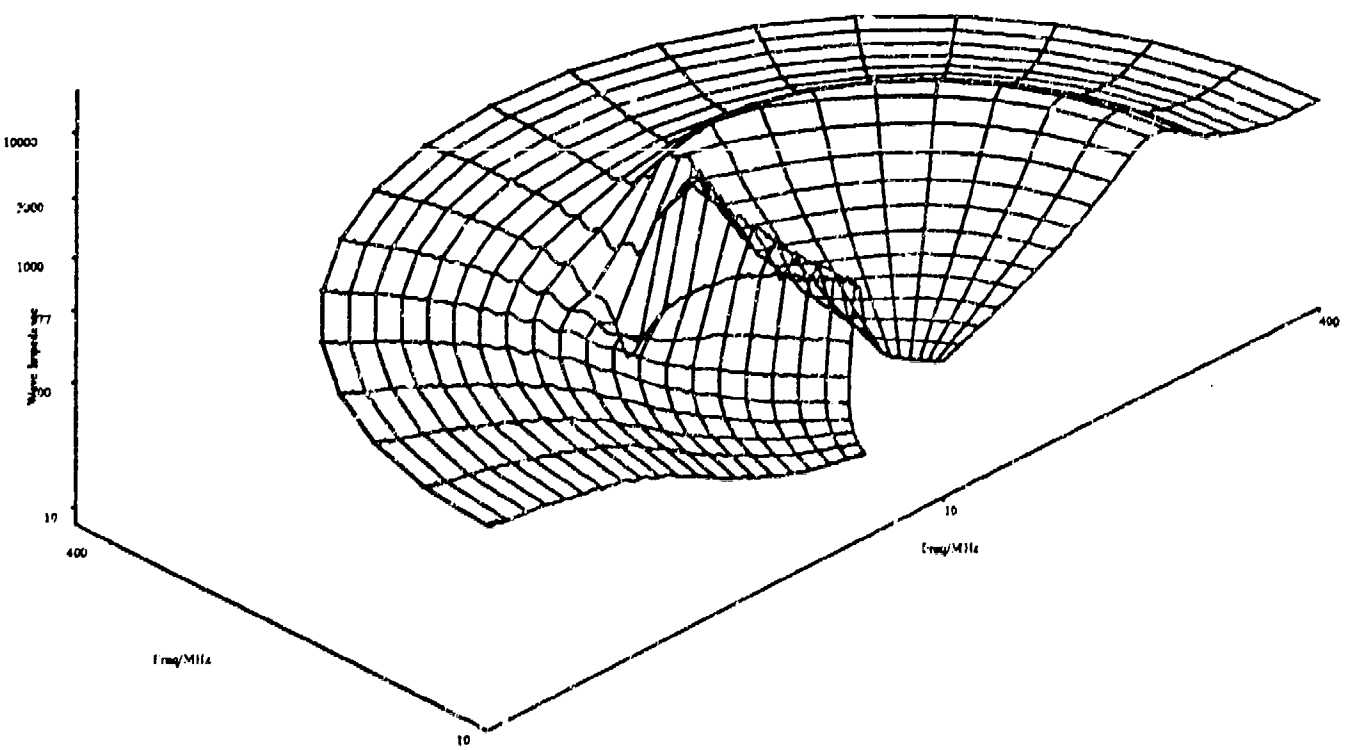


Fig.3(b) Wave Impedance Distribution of Loop Loaded with 40Ω: Practical Results.

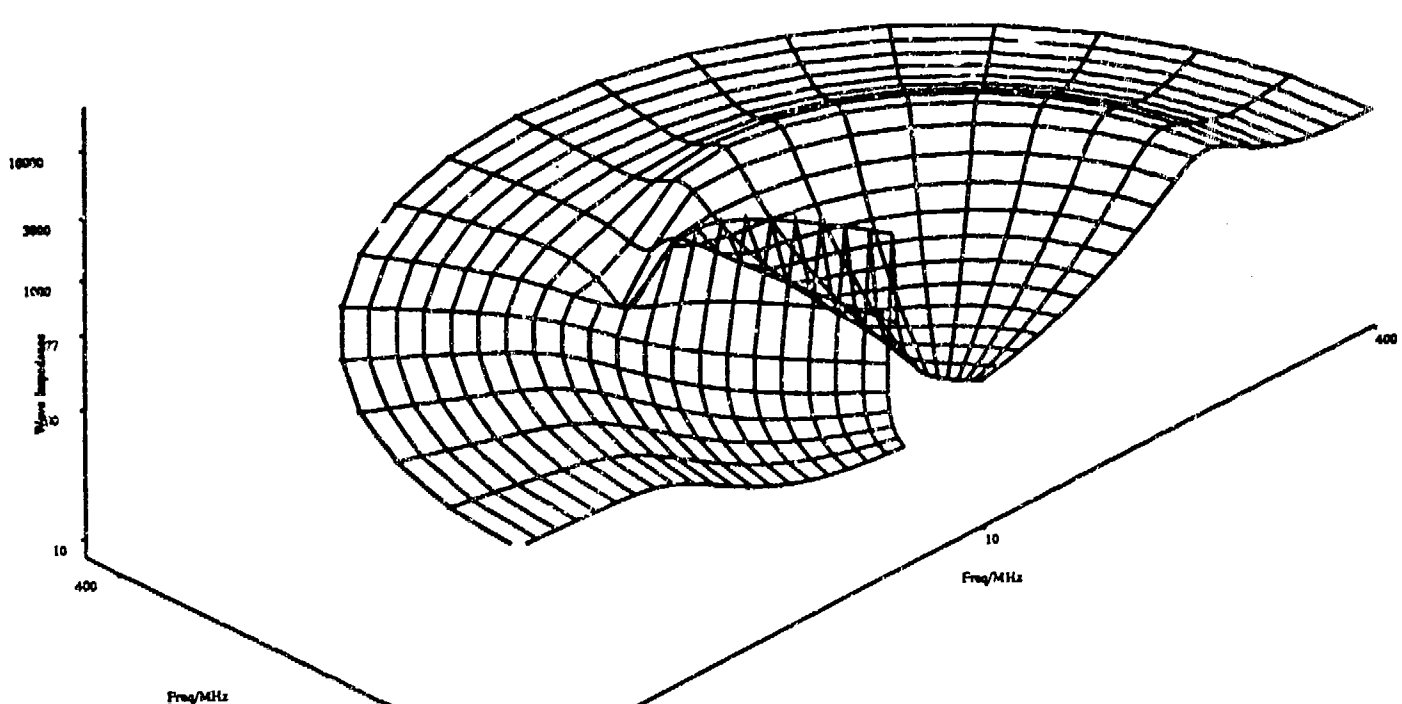


Fig.4(a) Wave Impedance Distribution of Loop Loaded with 98Ω from NEC3.

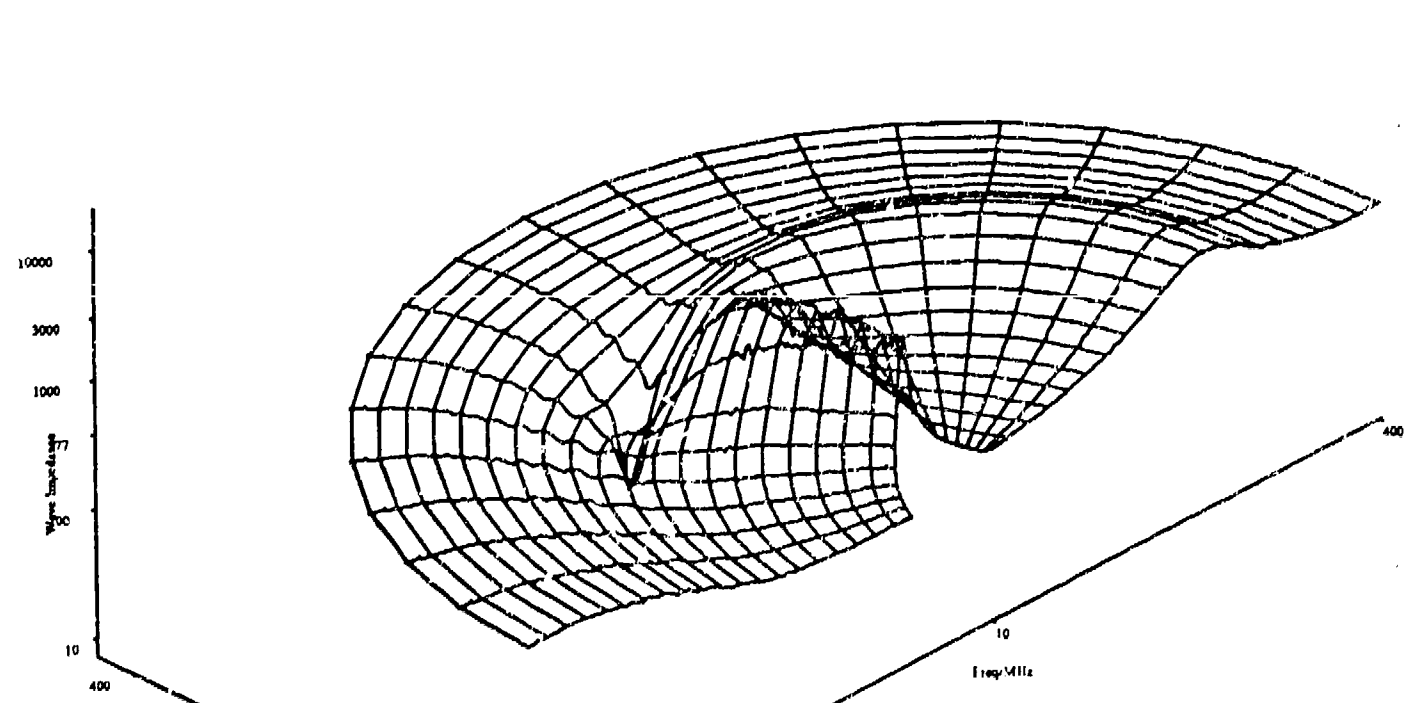


Fig.4(b) Wave Impedance Distribution of Loop Loaded with 98Ω: Practical Results.

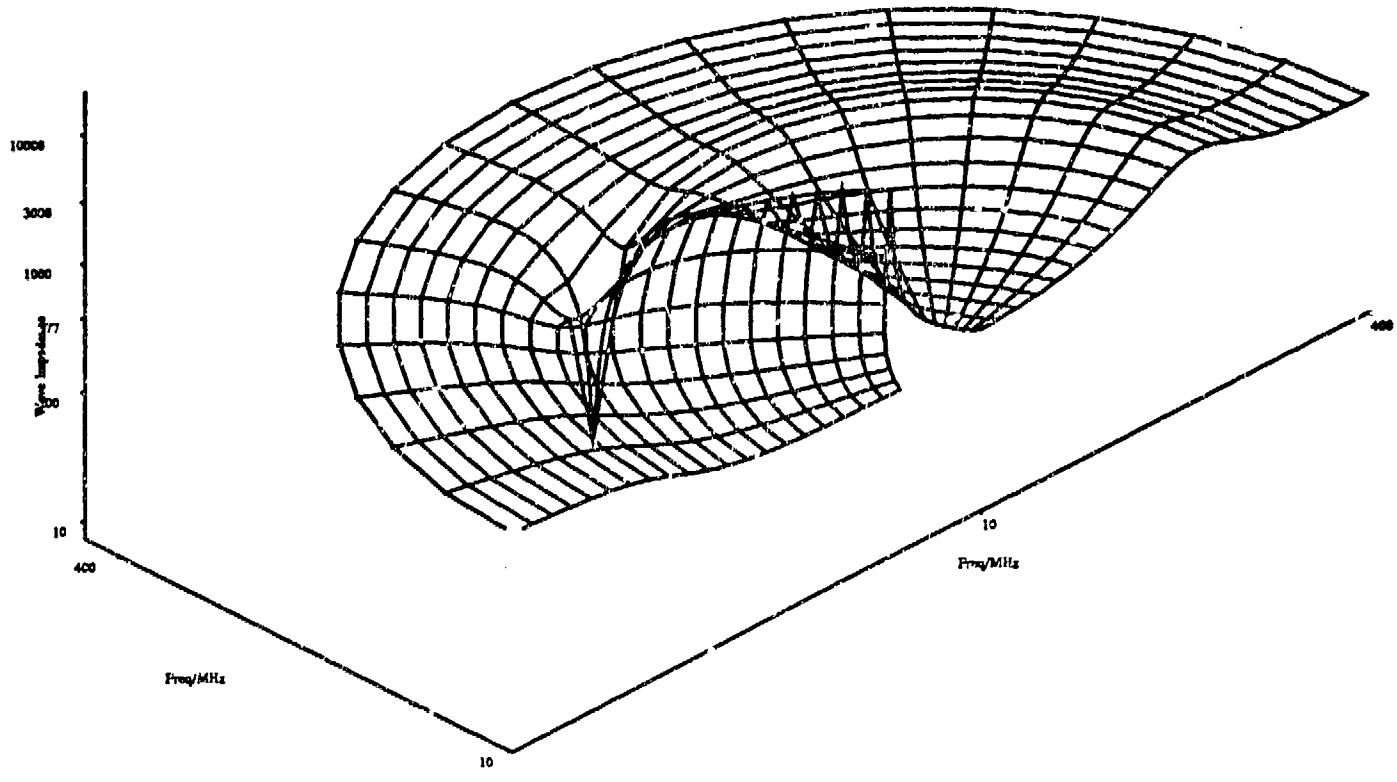


Fig.5(a) Wave Impedance Distribution of Loop Loaded with 219Ω from NEC3.

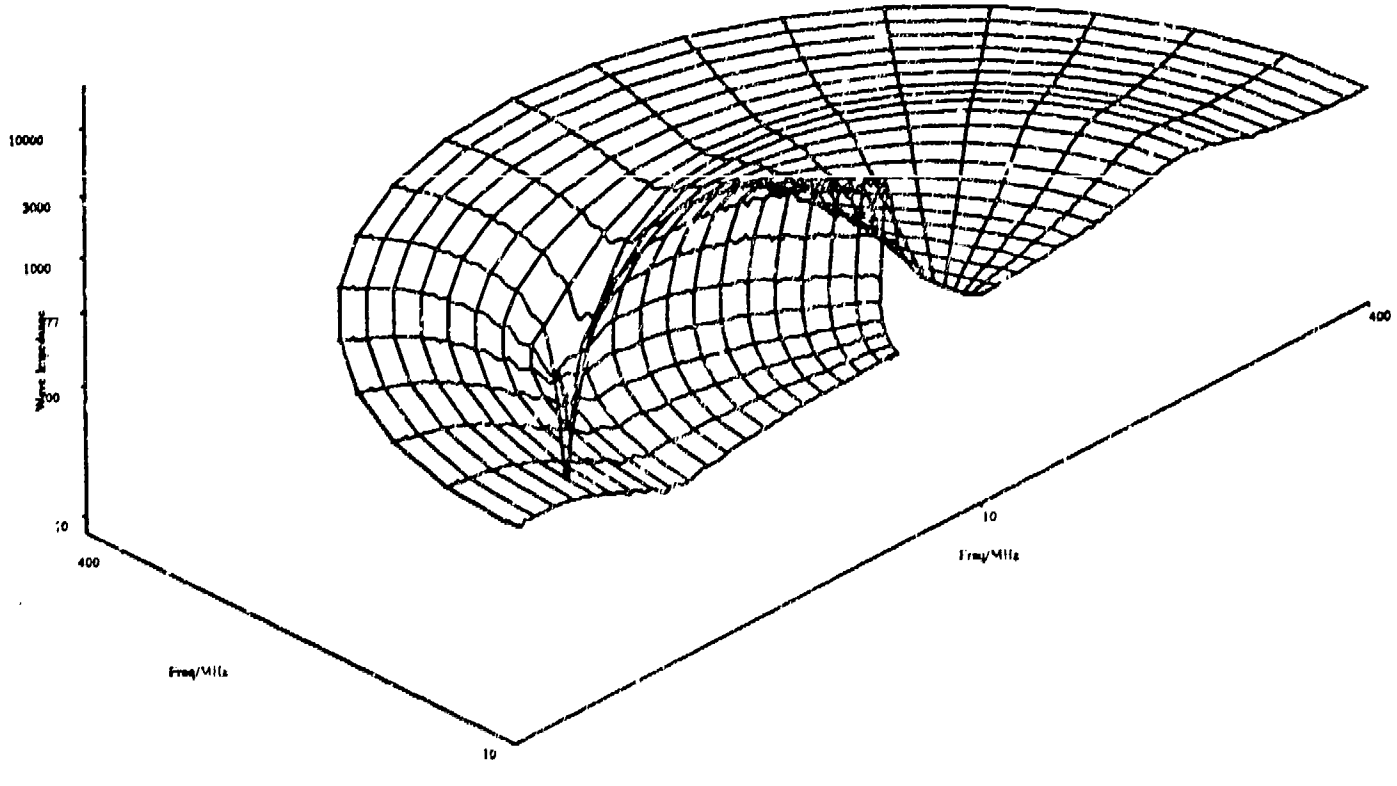


Fig.5(b) Wave Impedance Distribution of Loop Loaded with 219Ω: Practical Results.

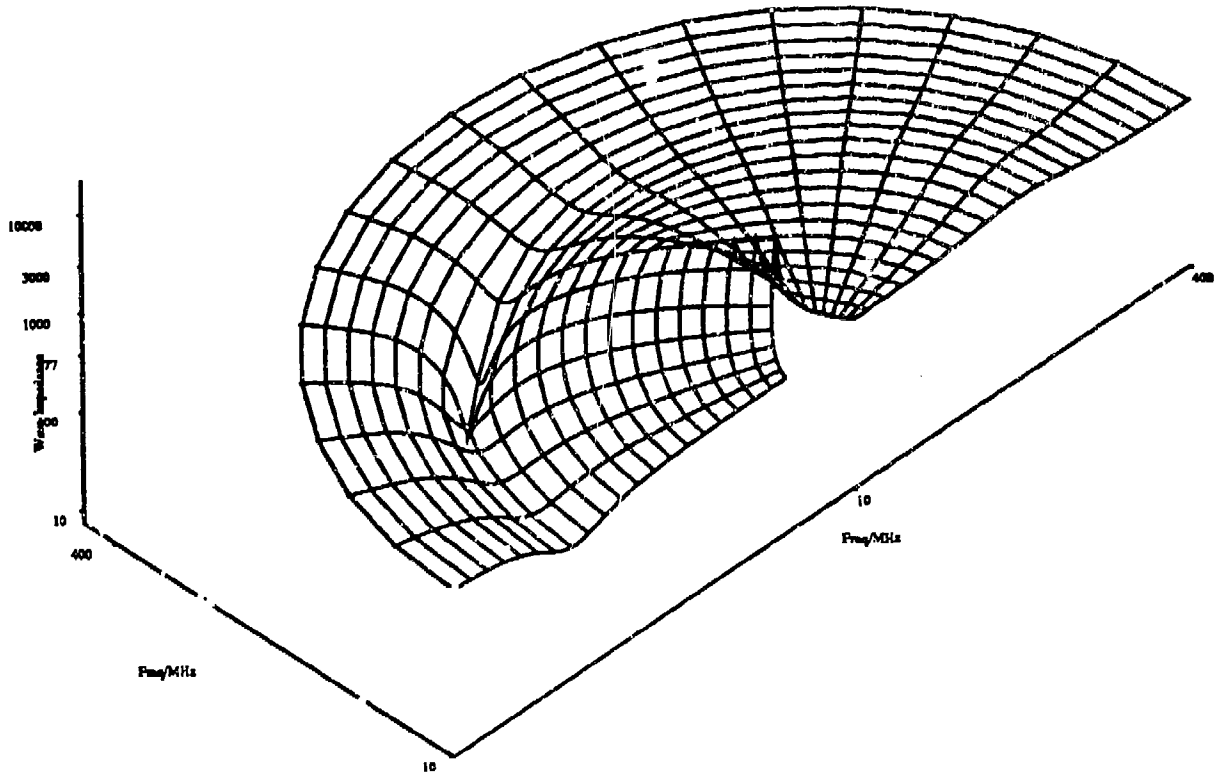


Fig.6(a) Wave Impedance Distribution of Loop Loaded with 469Ω from NEC3.

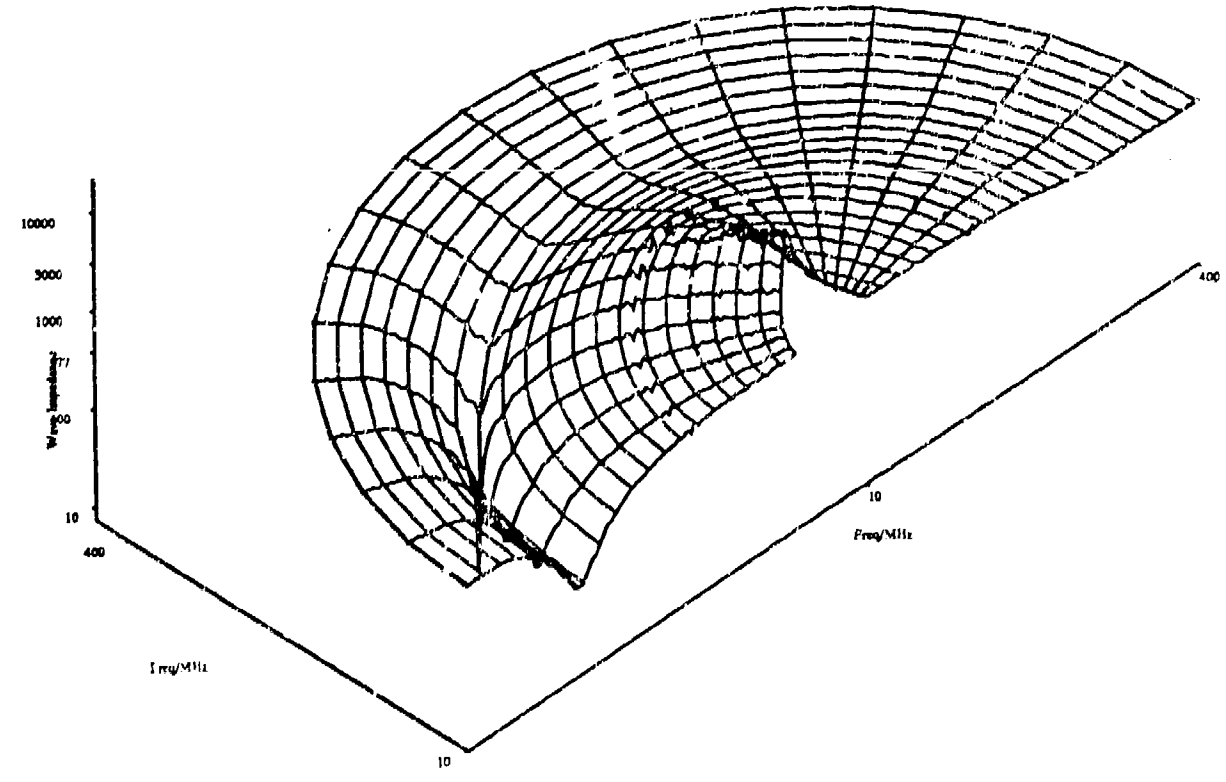


Fig.6(b) Wave Impedance Distribution of Loop Loaded with 469Ω: Practical Results

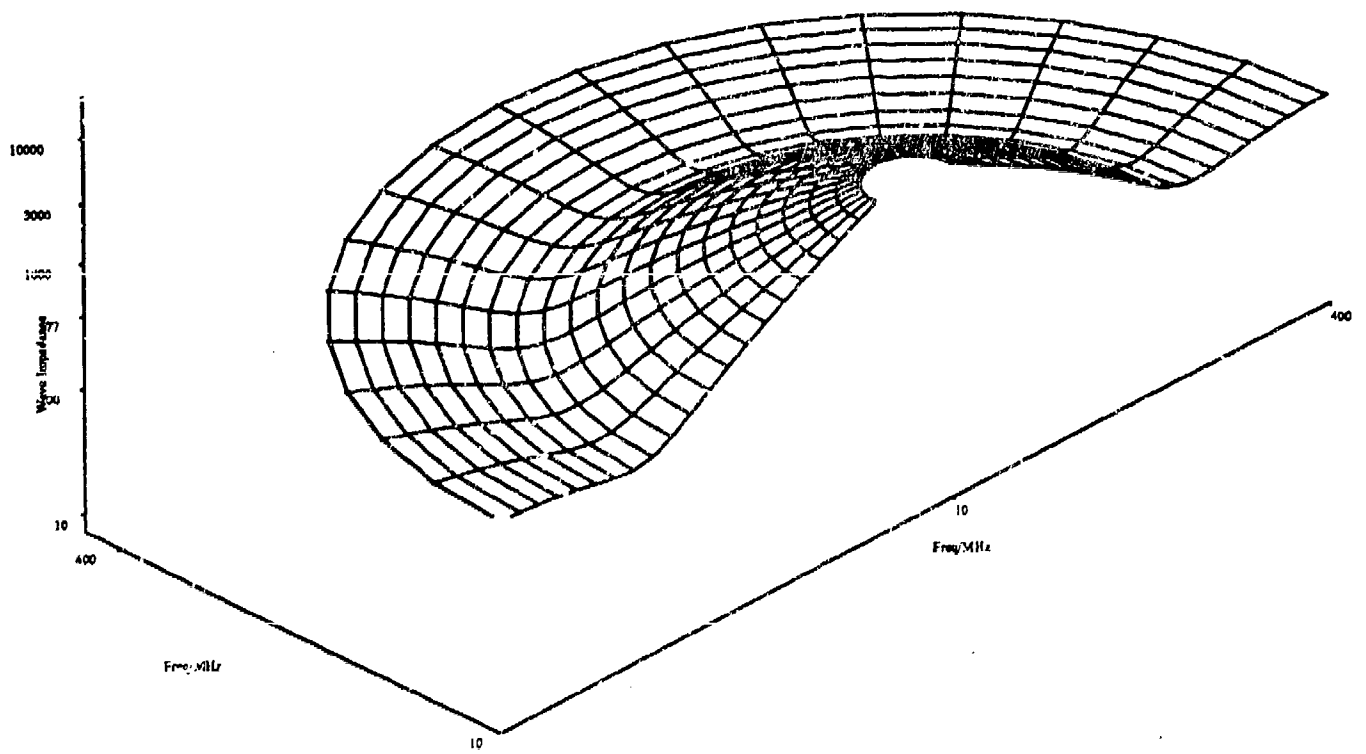


Fig.7 Wave Impedance Distribution of Monopole from NEC3

THE ANALYSIS OF TWO INVERTED F-ANTENNA STRUCTURES ON A BOX USING NEC WIRE MODEL

M. Somersalo
Technical Research Centre of Finland
Telecommunications Laboratory
Otakaari 7 B, SF-02150 Espoo, Finland

ABSTRACT

NEC has been used to analyse two antenna structures, the first being LIFA-type (Linear Inverted F-Antenna), the other a pair of PIFA:s (Planar Inverted F-Antenna) on a box. Using NEC the radiation patterns of the structures in three orthogonal planes are calculated. The bandwidths are determined through the Q-factor obtained from the calculated input impedance curve. Comparison between NEC results and measured data has been made.

1. MODELLING THE STRUCTURES

A wire model has been used to analyse two types of inverted F-antennas (IFAs) mounted on a box. The structures are shown in fig. 1. The antenna in fig. 1a is a wire antenna called LIFA (linear IFA) whereas the antennas in fig 1b are patch-type and called PIFAs (planar IFAs).

The box of the LIFA (LIFA-box) was modelled using 124 wire segments and the antenna was divided into 5+2 segments. The PIFA-box was modelled using 112 segments and the patches using 18+3 segments.

The mutual coupling between the two PIFAs and the box was strong. Experimentally it was observed that slight changes in the width of the shorting section (modelled as two wire segments) and the position of the feed affected greatly the antenna characteristics. This gave only small hopes for a very accurate modelling of the PIFA-structure.

The radii of the wires have been chosen to be equal with the radius of the feeding probe i.e. 0.0015λ. Doubling the radius seemed to have little effect on the calculations.

2. RADIATION PATTERNS

2.1 LIFA-STRUCTURE

The radiation patterns in three orthogonal planes were calculated using applied E-field voltage source excitation (EX0). The current slope discontinuity voltage source (EX5) gave similar shape for the patterns, but the gain level was 1.4 dB less (in boresight).

The analysed and measured radiation patterns are shown in fig. 2a-d. The data is scaled to make the vertical polarisation curves to touch the 0dB ring of the polar chart at 0 degrees. In some directions the difference between analysed and measured patterns is quite considerable. Most of the error, however, can be explained by measurement inaccuracies. This is seen comparing the gain levels at the plane intersections and keeping in mind the structural symmetry about X-Z-plane. As a whole it may be concluded that the used wire model is accurate enough to describe the radiation patterns of the LIFA-structure.

It took 279 seconds CPU-time to calculate the patterns using NEC2S in a VAX 11/750 computer. Using NEC2D 820 seconds CPU time was required, but the difference between the results was marginal.

2.2 PIFA-STRUCTURE

Only the X-Y-plane radiation patterns of the PIFA-structure are reproduced in fig. 3. The patterns are drawn with dBi scaling the outer ring of the chart being the 0dBi level.

At first, the calculations were made by a model without the dashed wire segments of fig. 1b. Comparing the analysed and measured field components, the difference was seen to be most striking between the axial ratios. Adding the dashed segments to the model had the effect of moving the gain levels towards the measured ones as is seen from fig. 3a.

Fig. 3b and c show the cases where the SMA-connector of the parasitic antenna is shorted or open. The model doesn't take the connector in account, its effect to the patterns, however, is considerable.

Fig. 3d shows the case where both PIFA:s are feeded in equal amplitude and phase. The measured patterns are quite far from the symmetry expected along X- and Y-axes. The figure also supports the conclusion that the measured patterns made with more care would be more similar to the analysed ones.

In the case, where the antennas were fed in equal amplitude but with phase difference, NEC didn't give sensible results. The input impedances of the antennas as well as the radiated power were far from being equal. No improvement of the results was obtained when the feeding was made through transmission lines.

As a whole it may be concluded that NEC can give reasonable information of the two-PIFAs-on-a-box-type structures. To avoid severe errors NEC should be used with much care.

3. INPUT IMPEDANCE

3.1 LIFA-STRUCTURE

The measured impedance curve on the Smith chart was a circle and the equivalent circuit of the antenna structure was therefore a simple resonant circuit as shown in fig. 4. To find the four unknowns it is enough to know the impedance (only) at four frequencys.

The impedance was calculated by NEC at eight points for the EX0 and EX5 excitations. The frequency deviation compared to the measured one, the Q-value and the 10dB bandwidths of the equivalent circuits are collected to table 1.

The measured bandwidth (return loss >10dB) is 2/3 of the calculated one. As seen from fig. 5, NEC impedance circles are smaller in size than the

measured ones. The smaller the circle the shorter the distance of the feed from the shorting segment.

Table 1. Equivalent circuit data of the LIFA-structure.

	$\frac{\lvert frm-fr \rvert}{frm}$	Q	BW
measured	-	32	2.2 %
NEC EX0	0.6 %	21	3.3 %
NEC EX5	2.4 %	22	3.3 %

fr= calc. res. freq.
frm= meas. res. freq.

3.2 PIFA-STRUCTURE

The interaction between the two antennas and the box deteriorates the impedance circle on the Smith chart. The equivalent circuit for the antenna would now consist of three resonators with mutual couplings. Of course a section of the impedance curve may still be characterized by a single resonator.

The measured and calculated curves for the cases of feeding PIFA A and PIFAs A and B are shown in fig. 6a and b. From figure 6a it is seen that the NEC-curve has a resonance around the measured resonance, too. Now the bandwidth and resonant frequency should be calculated in the vicinity of this frequency, not from the "circle" in fig. 6a, as it represents a different resonance. The bandwidths obtained from the more well behavig case of fig. 6b were within a few per cent the same for measured- and NEC- curves.

The calculations above were made with the wire model of fig. 1b the dashed wires excluded. The impedance curve is more affected by the density of the wire grid than the radiation patterns, but even the model used gave acceptable results for the bandwidth and the resonant frequency. The accuracy in general was, however, not as good as in the case of a LIFA on a box

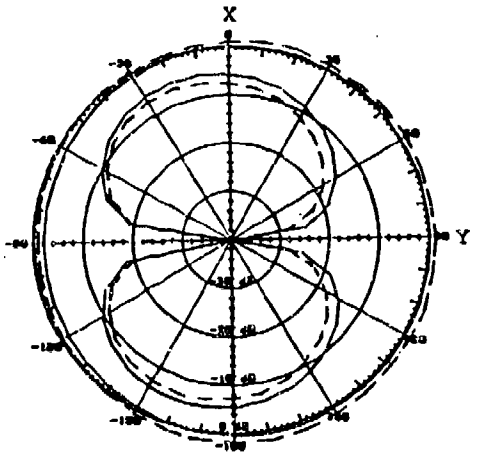


Fig. 3a: Calculated X-Y-patt. of fig. 1b. with (——) and without (- -) dash. segm. PIFA A fed.

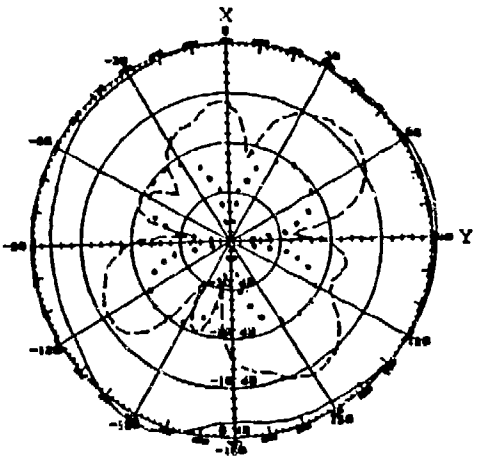


Fig. 3d: X-Y-cut, PIFAs A+B fed in phase.

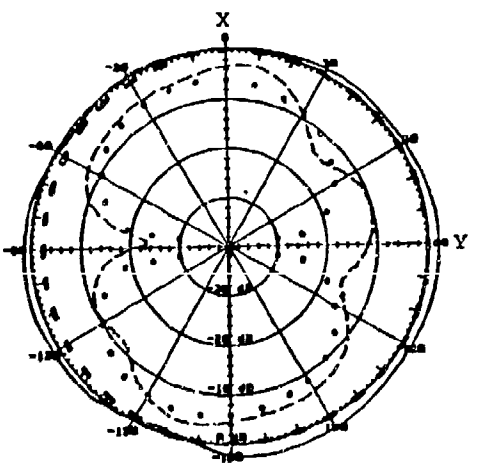


Fig. 3b: X-Y-cut PIFA A fed, PIFA B open.

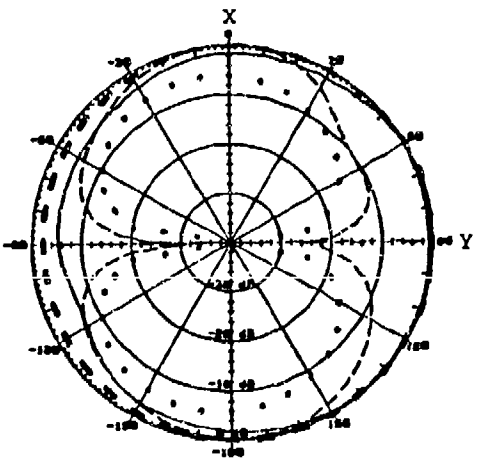


Fig. 3c: X-Y-cut PIFA A fed, PIFA B shorted.

▬ ▬ ▬ vert. pol. calculated
——— vert. pol., measured
• • • hor. pol., calculated
- - - hor. pol., measured

(fig. 3b,c,d)

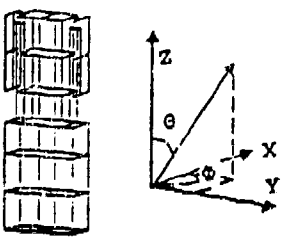


Fig. 3 : X-Y-cut radiation patterns of PIFA-struct.

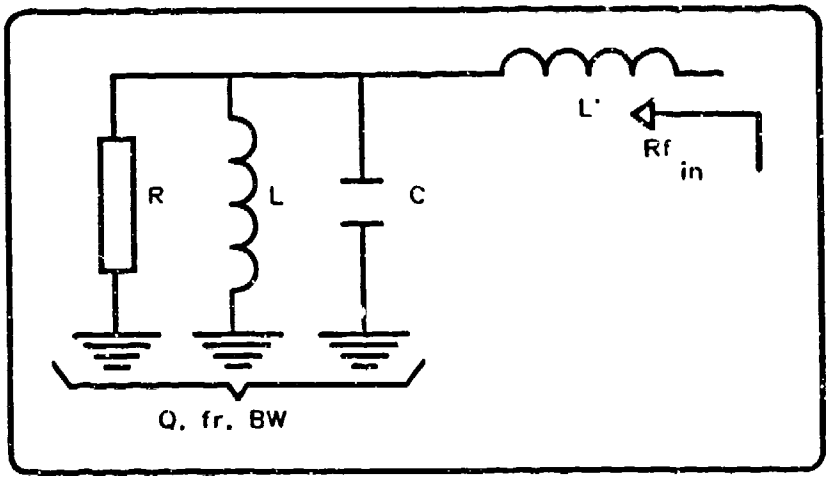


Fig 4. Equiv. circuit of a one resonance antenna.

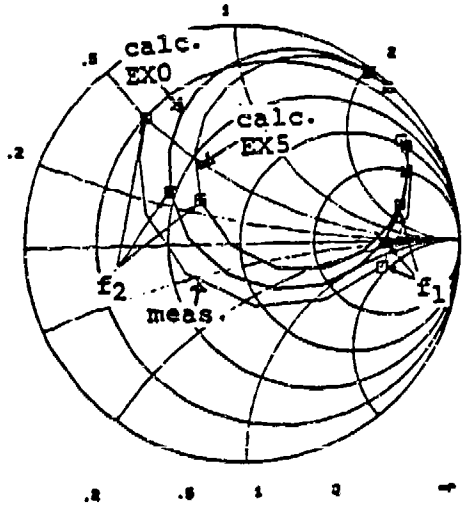


Fig. 5: Input impedance of LIFA.

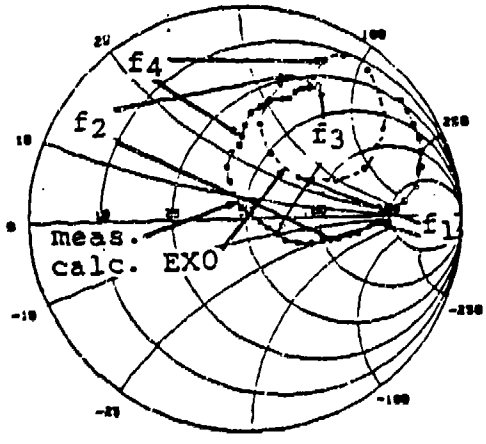


Fig. 6a: Input impedance of PIFA A

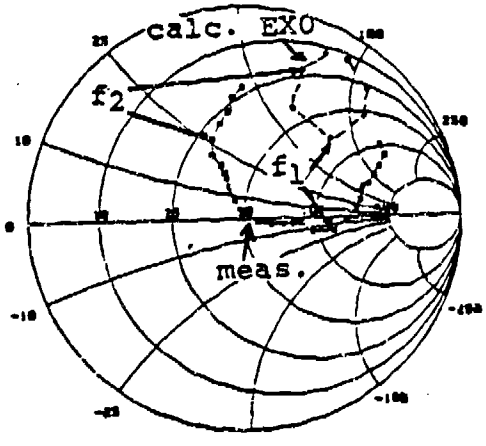


Fig 6b: Input impedance of PIFAs A+B

On the Analysis and Synthesis of Circular Arrays

Karl J. Moeller and Vaughn P. Cable

ABSTRACT

The characteristics of an open, circular array of antenna elements in free space have been investigated. With the main beam in the plane of the array (endfire), calculated antenna patterns reveal an elliptical beam cross-section, broad in the vertical plane, with high near-in sidelobes. A Taylor-like amplitude distribution was found to reduce the near-in sidelobe levels in the horizontal plane without significantly degrading the vertical plane pattern. Also, mutual coupling effects were found to be significant.

INTRODUCTION

The circular array constitutes a special class of planar array with the ability to electronically scan an endfire main beam through 360° in the plane of the array. This ability has made circular arrays attractive for applications in radio direction finding and surveillance radar [1].

The directive endfire pattern produced by the properly phased elements of a circular array is similar to the pattern produced by a linear array of length equal to the circle diameter. Due to the symmetry of the placement of the elements in a circular array, the endfire pattern may be scanned by commutating the current excitations around the array. As is the case for linear arrays, amplitude tapers can be used to lower the near-in sidelobes of the directive pattern. Synthesis of such patterns is considerably more challenging for circular arrays, however, since the mutual coupling between the elements of a circular array can be quite severe.

The objective of this work was to determine a practical means for synthesizing an endfire pattern with reduced near-in sidelobes for a circular array of mutually coupled dipoles. The usual approach to array synthesis is to treat the array (linear or otherwise) as a set of uncoupled elements with no interactions between elements. In this case, only the array factor is involved in the synthesis procedure and the overall directivity of the array is determined by imposing the element pattern as a multiplicative factor. This separatability of the array and element patterns is usually referred to as pattern factorization.

In practice, however, this last step is often an oversimplification which does not accurately predict the outcome of the synthesis procedure. One reason, of course, is

---

K. Moeller is with California Microwave, Inc., Woodland Hills, CA 91303

Dr. Cable, formerly with California Microwave, is with Lockheed Aeronautical Systems Company, Valencia, CA 91355

that the mutual coupling between elements affects the distributions of current on the individual elements differently. Hence, the elements and their respective patterns cannot all be assumed to be identical and pattern factorization does not hold. Another effect which might cause this same discrepancy is interaction with other objects not normally considered to be part of the antenna array; e.g., finite ground plane effects. The results reported here consider the array to be located in free space and only element to element mutual coupling effects are studied.

BEAMSHAPE AT ENDFIRE (UNCOUPLED CASE)

Consider an array of N elements arranged on a circle of radius a in the xy plane, as shown in Figure 1.

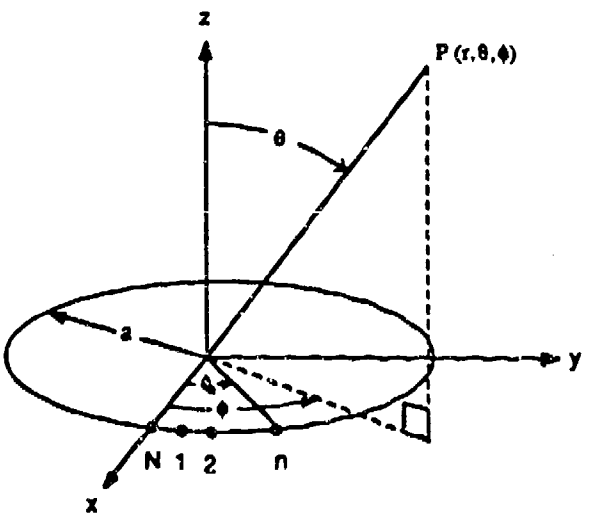


Figure 1. - A circular array

The far-field array factor for arbitrarily positioned, isotropically radiating elements [2] is given by

$$E(\theta, \phi) = \sum_{n=1}^{N} I_n e^{jk(x_n \sin\theta\cos\phi + y_n \sin\theta\sin\phi + z_n \cos\theta)} \tag{1}$$

where I_n is the complex total current and (x_n, y_n, z_n) are the coordinates of the n^{th} radiator. Since all elements of the circular array lie in the xy plane,

$$E(\theta, \phi) = \sum_{n=1}^{N} I_n e^{jk \sin\theta(x_n \cos\phi + y_n \sin\phi)} \tag{2}$$

Let ϕ_n denote the location of the n^{th} element on the circle, then

$$E(\theta, \phi) = \sum_{n=1}^{N} I_n e^{jk\sin\theta(a\cos\phi_n\cos\phi + a\sin\phi_n\sin\phi)} \tag{3a}$$

$$= \sum_{n=1}^{N} I_n e^{jka\sin\theta\cos(\phi-\phi_n)} \tag{3b}$$

If $|I_n|$ denotes the magnitude, and α_n the (relative) phase of the current of the n^{th} radiator, then

$$E(\theta, \phi) = \sum_{n=1}^{N} |I_n| e^{j\alpha_n} e^{jka\sin\theta\cos(\phi-\phi_n)} \tag{4}$$

For uniform spacing of the elements on the circle, $\phi_n = \frac{2\pi n}{N}$.

A beam maximum is obtained when the elements are phased to add together in a single direction. This condition is called *cophasal excitation* and is obtained when

$$\alpha_n = -ka\sin\theta_0\cos(\phi_0-\phi_n) \tag{5}$$

where (θ_0, ϕ_0) is the position of the beam maximum.

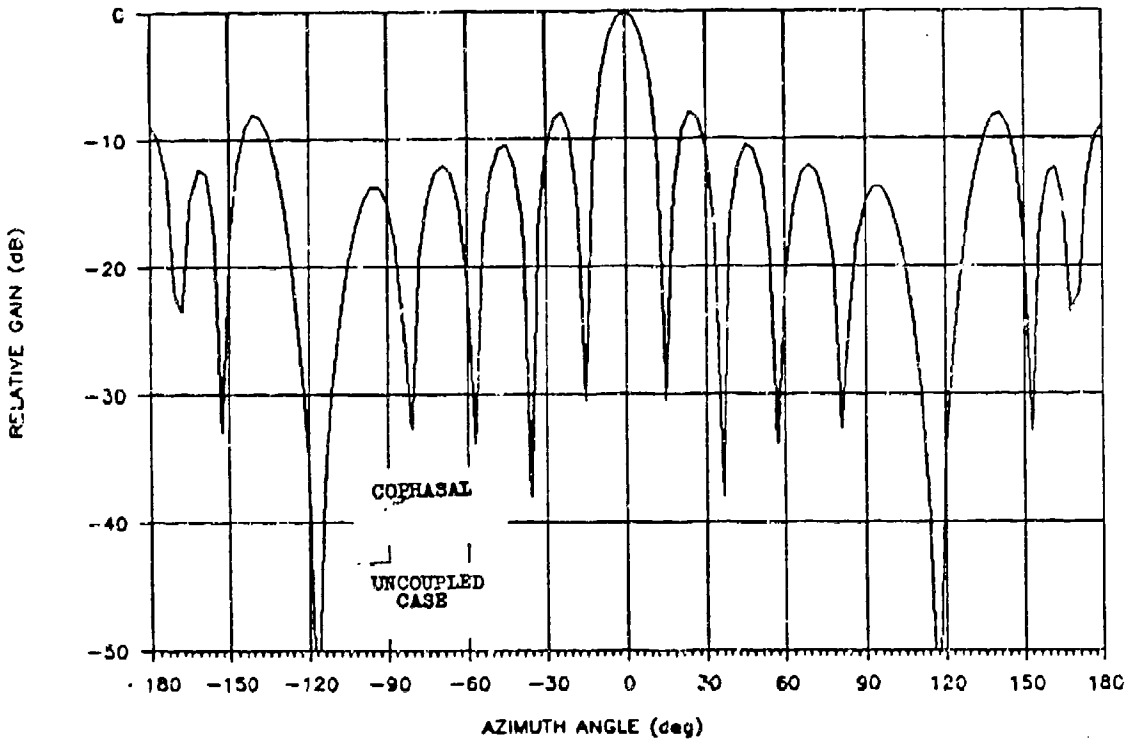
We examine first the characteristics of a uniform amplitude, ($|I_n| = |I|$) cophasal circular array. Uncoupled power pattern plots for an 18 element circular array of z-directed elementary dipoles with $\lambda/2$ interelement spacing are shown in figure 2. Equation (5) is used to design the beam maximum to point in the direction of the x axis, ($\theta_0 = 90°$, $\phi_0 = 0°$). These patterns, which neglect the effects of element interactions, can be generated by multiplying the array factor, given in equation (4), by the element factor (pattern of an elementary dipole).

The horizontal pattern, which lies in the plane of the array elements, has high near-in sidelobes (-8 dB) and a beamwidth slightly narrower than that obtainable from a linear array of length equal to the circle diameter. A region of back-radiation approximately 120° wide is present in the direction of the negative x axis. Over this region the cophasal excitation falls apart and the elements add in a random manner.

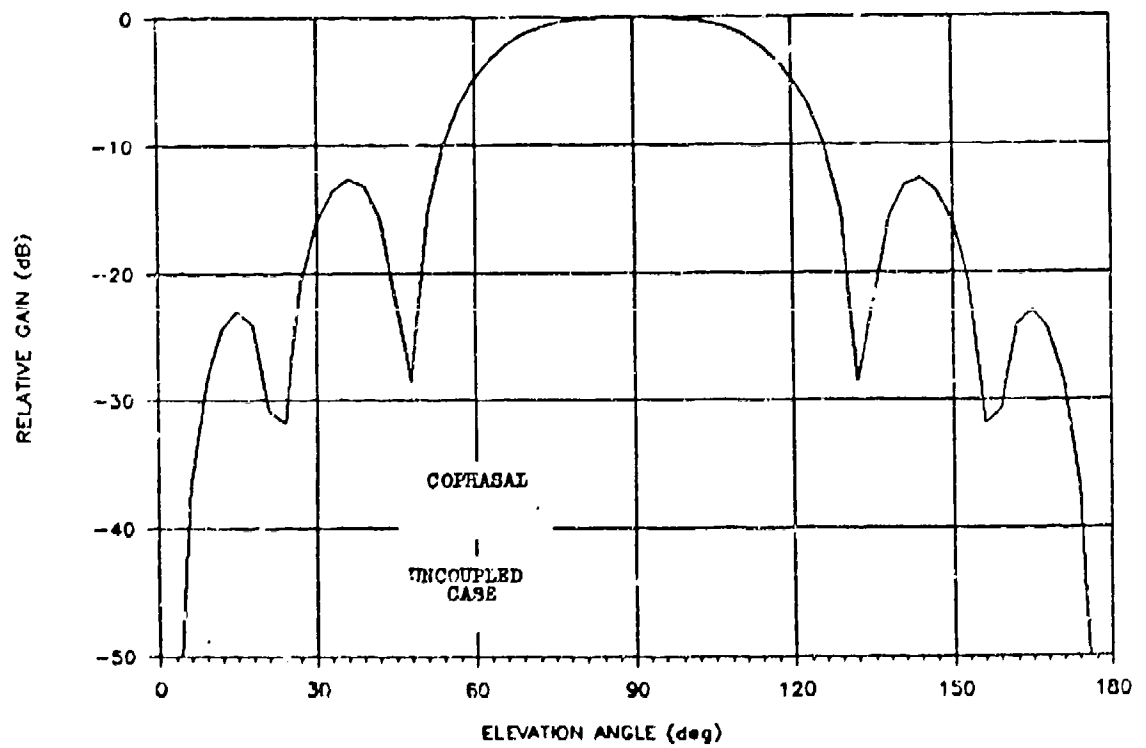
The vertical pattern has a wide beamwidth with near-in sidelobes of approximately the same height as those in the horizontal pattern. The circular array therefore provides a convenient fan beam for rotation through 360 °. Examination of the power pattern in additional planes through the main beam reveals that the beamwidth varies elliptically from the vertical to horizontal planes.

BEAMSHAPE AT ENDFIRE (COUPLED CASE)

In order to determine the behavior of the array when the effects of the array factor and element mutual coupling are combined, the circular array of Figure 1 was modeled using the Ohio State thin wire codes of Richmond, [3]. Half-wave thin-wire dipoles were located at each of the array element positions.



(a) Phi cut (azimuthal pattern), $|E(90°, \phi)|^2$



(b) Theta cut (elevation pattern), $|E(\theta, 0°)|^2$

Fig. 2 - Power patterns for a uniform amplitude, cophasal circular array ($\theta_0 = 90°, \phi_0 = 0°$) when element interactions are neglected.

Figure 3 shows the coupled case power pattern plots for the 18 element circular array and excitation described in the previous section. The overall pattern in the azimuthal plane is considerably changed from the uncoupled case shown in Figure 2. The main beam is slightly broadened and near-in sidelobes appear approximately 13 dB down from the main lobe.

CIRCULAR ARRAYS WITH TAPERED AMPLITUDES

When viewed from endfire, the circular array appears as a linear aperture with a higher concentration of elements at the ends of the aperture than at the center. This results in a reduced beamwidth and higher sidelobes in the azimuthal plane of the endfire pattern than that which would be obtained from a linear array (of equispaced elements) of length equal to the circle diameter.

The sidelobes of a linear array can be reduced by tapering the amplitude of the current excitations from a maximum at the central element to a minimum at the elements at the array ends. Similarly, an amplitude taper symmetrically applied to the front and back halves of a circular array will reduce the near-in sidelobes in horizontal plane of the endfire pattern.

The procedure used here consisted of spatially sampling two amplitude tapers from linear array theory; full cosine on a pedestal and a Taylor type distribution. Sampling locations were determined by projecting the element positions of the circular array onto the array diameter which lies perpendicular to the direction of the main beam. Each taper was then applied to this non-uniform linear array geometry and sampled at the projected element positions. This results in a symmetric distribution over the two halves of the circular array bisected by the array diameter.

The results for a cosine on a pedestal amplitude taper for the uncoupled and coupled cases appear in Figures 4 and 5, respectively. A general expression for this distribution can be found in Silver [4]. The particular form used for these results is given by

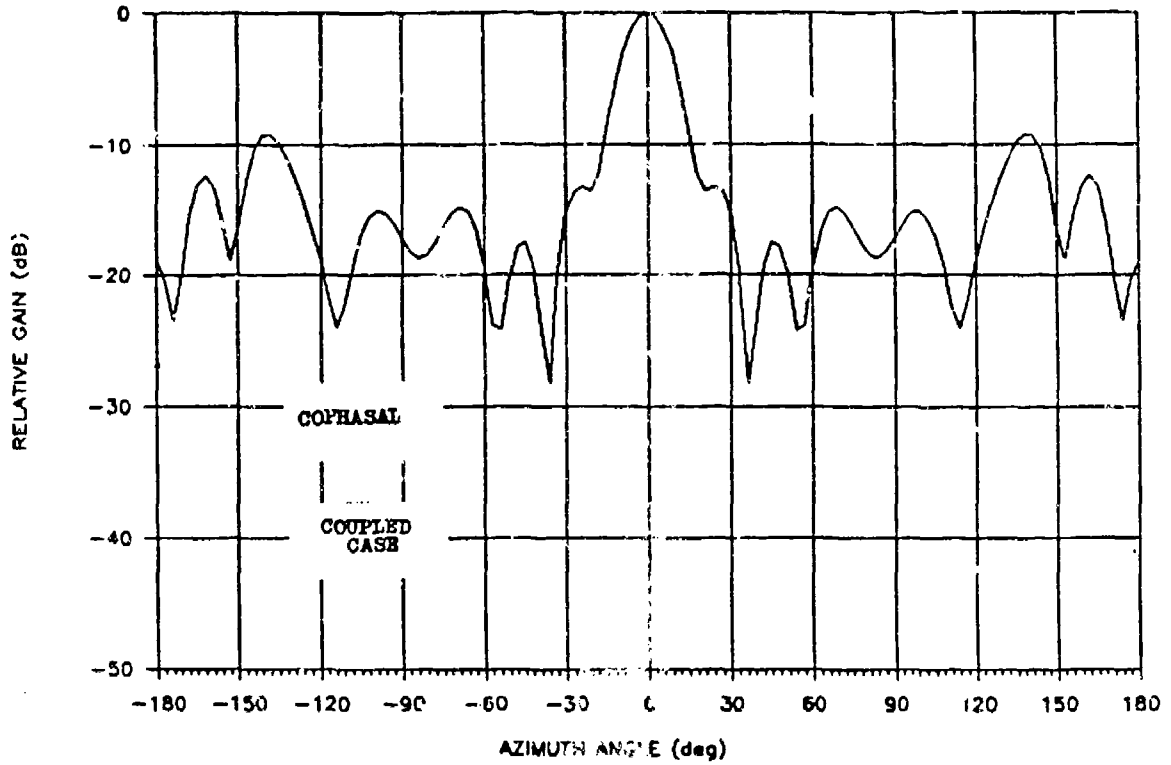
$$f(y) = 1 - .25\left[1 - \cos\left(\frac{2\pi y}{d}\right)\right] \tag{6}$$

where y is the linear aperture dimension variable (the variable of the array diameter onto which elements are projected) and d is the array diameter. Again, the coupled case calculations show sidelobes approximately 7 dB below those predicted from uncoupled calculations. Also, the main beam is broadened in the coupled case.

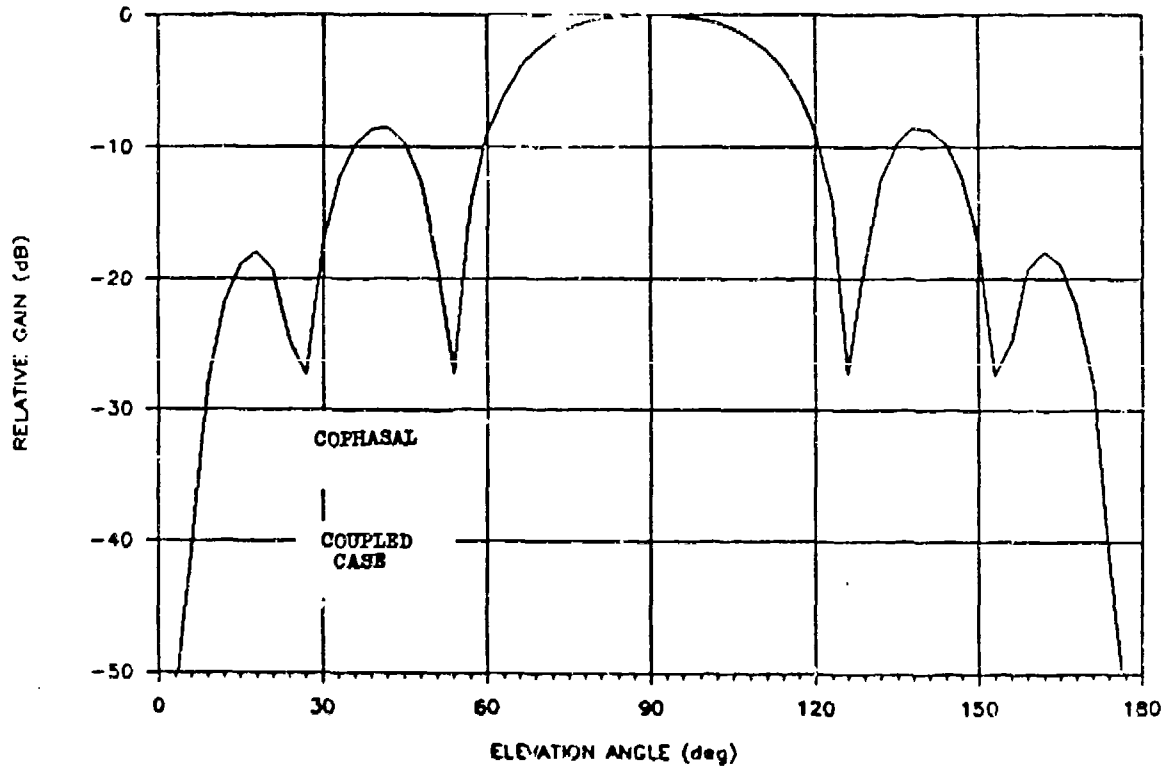
The uncoupled and coupled cases for the Taylor type distribution are presented in Figures 6 and 7, respectively. A general expression for this type of distribution is given in Collin and Zucker [5]. The form used here is

$$f(y) = \frac{I_0\left(\frac{kdc}{2}\sqrt{1-\left(\frac{2y}{d}\right)^2}\right)}{a} \tag{7}$$

where I_0 is the modified Bessel function of order 0, k is the wave number, d is the



(a) Phi cut (azimuthal pattern), $|E(90°, \phi)|^2$



(b) Theta cut (elevation pattern), $|E(\theta, 0°)|^2$

Fig. 3 - Power patterns for a uniform amplitude, cophasal circular array ($\theta_0 = 90°, \phi_0 = 0°$) when the effects of element interactions are accounted for.

diameter of the array, y is the linear aperture dimension variable, and c satisfies

$$\frac{1}{R} = \frac{(2dc)}{[3\lambda \sinh(\frac{kdc}{2})]} \tag{8}$$

where R is the desired main beam to sidelobe ratio and λ is the wavelength of the excitation. For the results presented here, $R = 10^4$. The data presented shows that, of all the distributions tested, the Taylor type distribution appears to have the lowest overall sidelobe level in the azimuthal plane for the coupled case.

CONCLUSION

An investigation of the radiation characteristics of a circular array of half-wavelength dipoles has been presented. An examination of a uniform amplitude, cophasal array has revealed an endfire pattern with an elliptical main beam cross-section and high near-in sidelobes. Sidelobes in the azimuthal plane of the endfire pattern can be controlled through the use of amplitude distributions derived from linear array theory.

Pattern calculations presented here have shown that the effects of element-to-element mutual coupling are dramatic for circular arrays. Idealized pattern synthesis techniques which neglect the effects of element interactions are not adequate for this type of array. Further work is in progress to develop a practical synthesis procedure which accounts for these effects.

REFERENCES

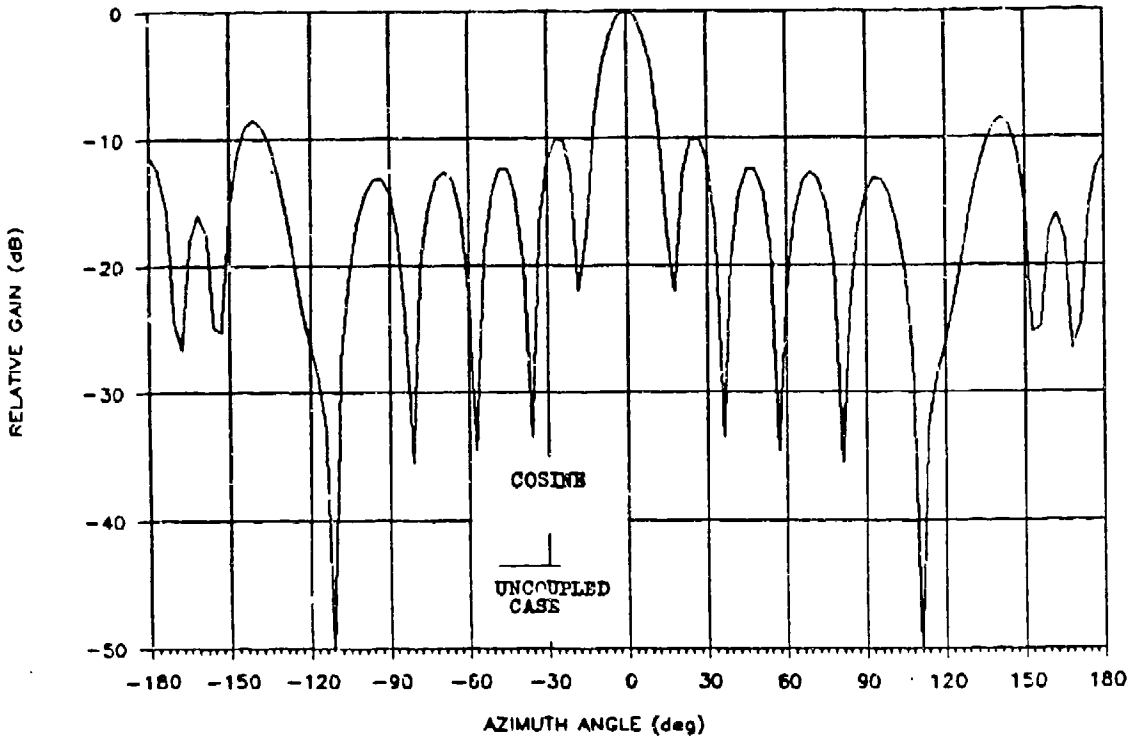
1. A. W. Rudge, K. Milne, A. D. Olver and P. Knight, *The Handbook of Antenna Design, Volume 2*, (Exeter, England: Short Run Press Ltd., 1983), Chapter 12

2. R. S. Elliott, *Antenna Theory and Design*, (Englewood Cliffs, New Jersey: Prentice-Hall, Inc., 1981), Section 4.2

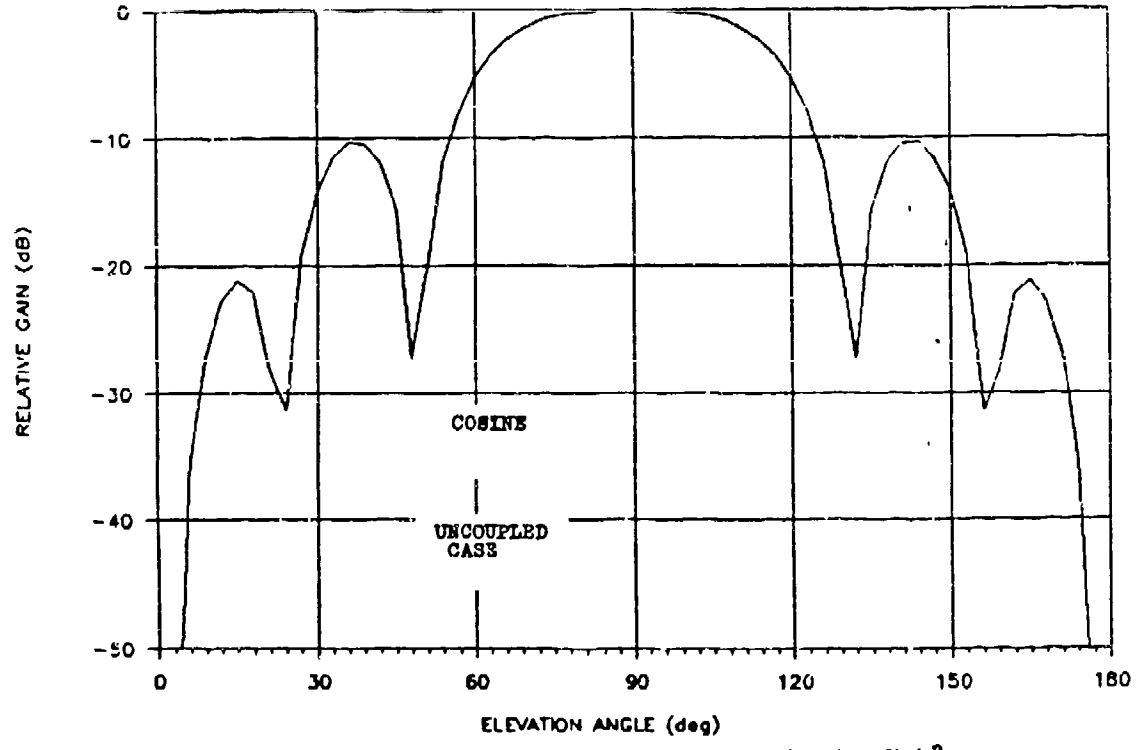
3. J. H. Richmond, *Computer Program for Thin-Wire Structures in Homogeneous Conducting Medium*, Technical Report 2902-12, (ElectroScience Laboratory, Ohio State University, 1973)

4. S. Silver, *Microwave Antenna Theory and Design*, (New York, New York: Dover Publications, 1965)

5. R. E. Collin and F. J. Zucker, *Antenna Theory, Part 1*, (New York, New York: McGraw-Hill, 1969)

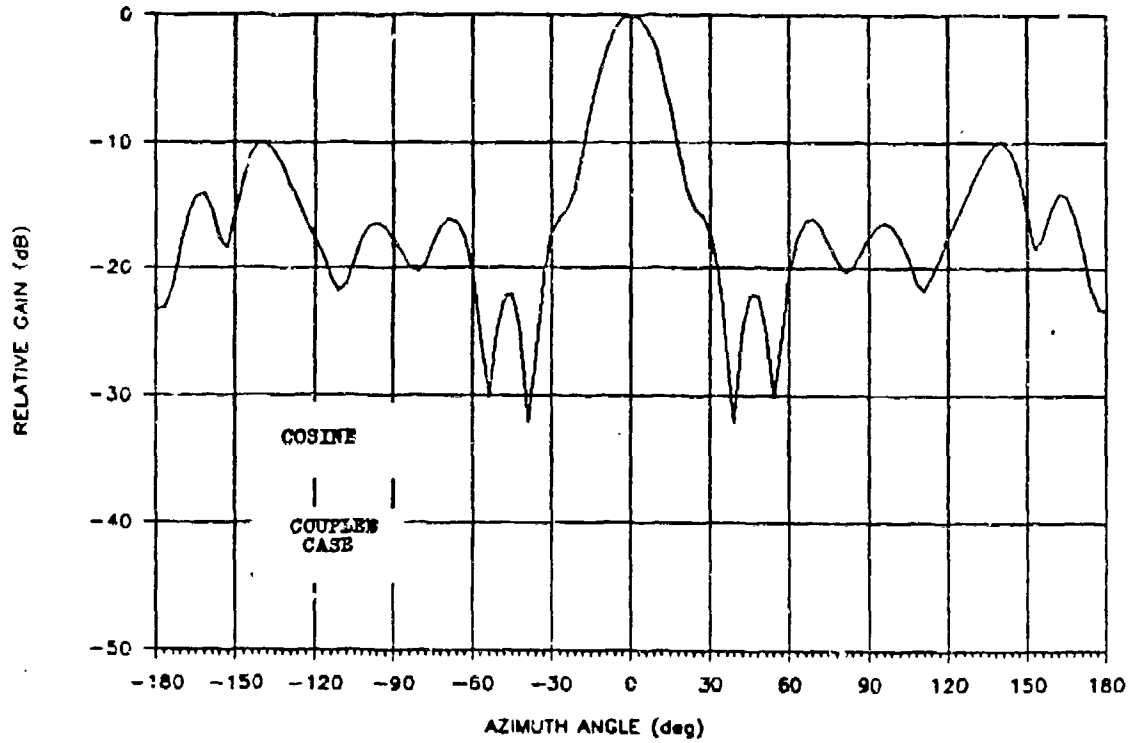


(a) Phi cut (azimuthal pattern), $|E(90^\circ, \phi)|^2$

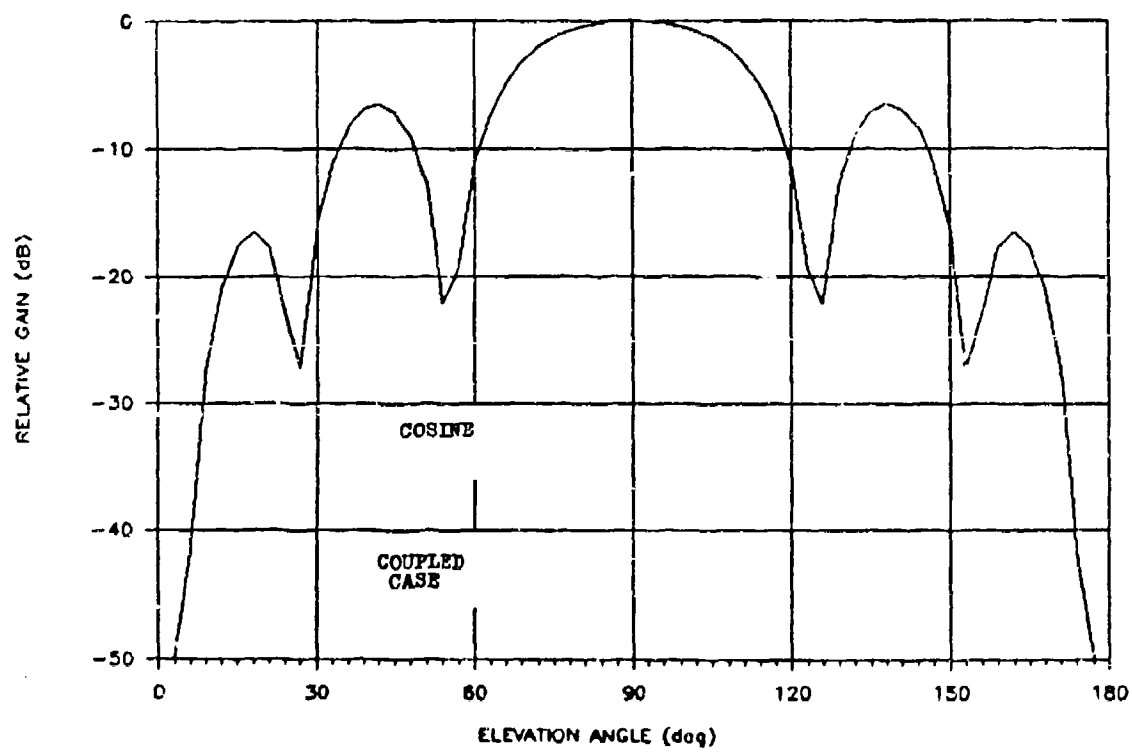


(b) Theta cut (elevation pattern), $|E(\theta, 0^\circ)|^2$

Fig. 4 - Power patterns for a cophasal circular array ($\theta_0 = 90^\circ$, $\phi_0 = 0^\circ$) with a "cosine-on-a-pedestal" amplitude taper, uncoupled case.

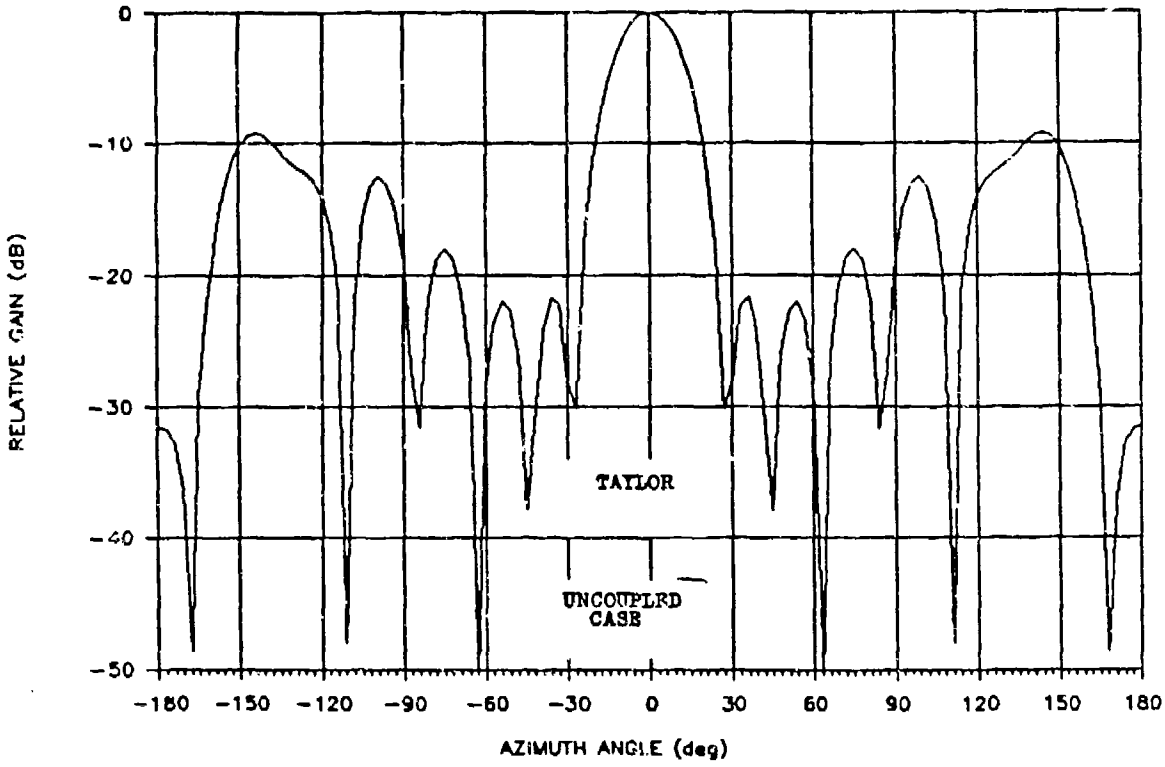


(a) Phi cut (azimuthal pattern), $|E(90°, \phi)|^2$

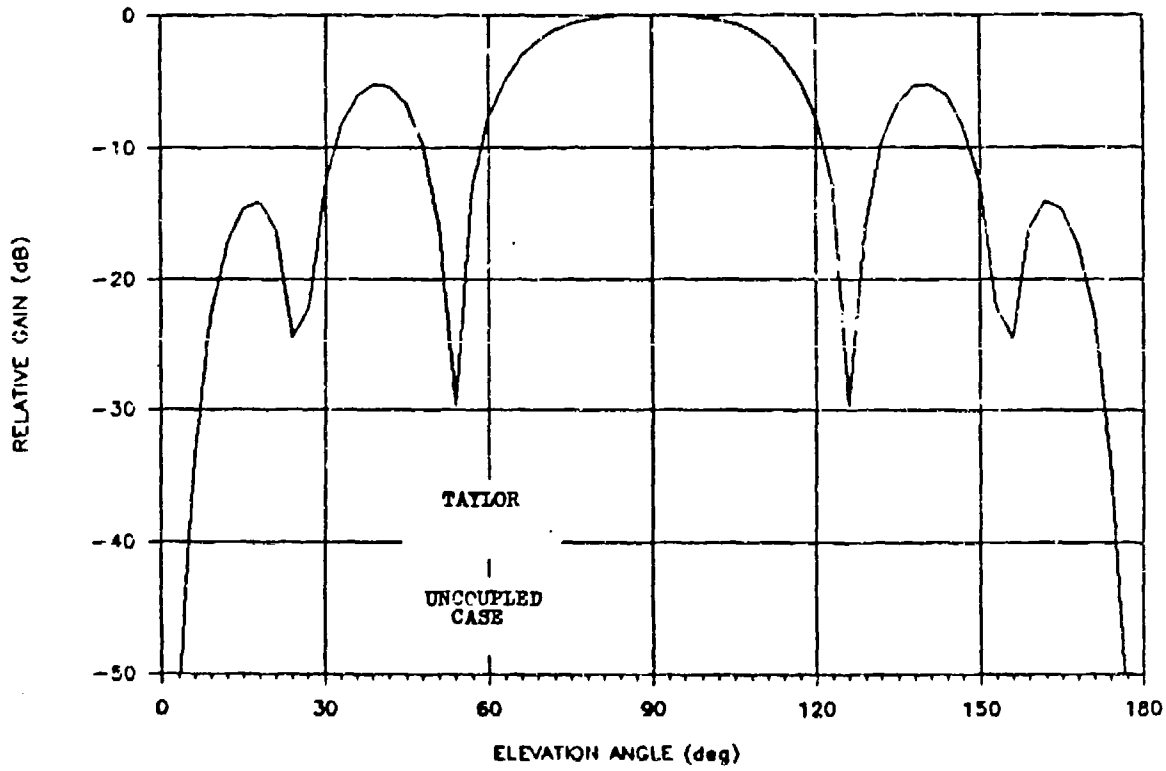


(b) Theta cut (elevation pattern), $|E(\theta, 0°)|^2$

Fig. 5 - Power patterns for a cophasal circular array ($\theta_0 = 90°, \phi_0 = 0°$) with a "cosine-on-a-pedestal" amplitude taper, coupled case.

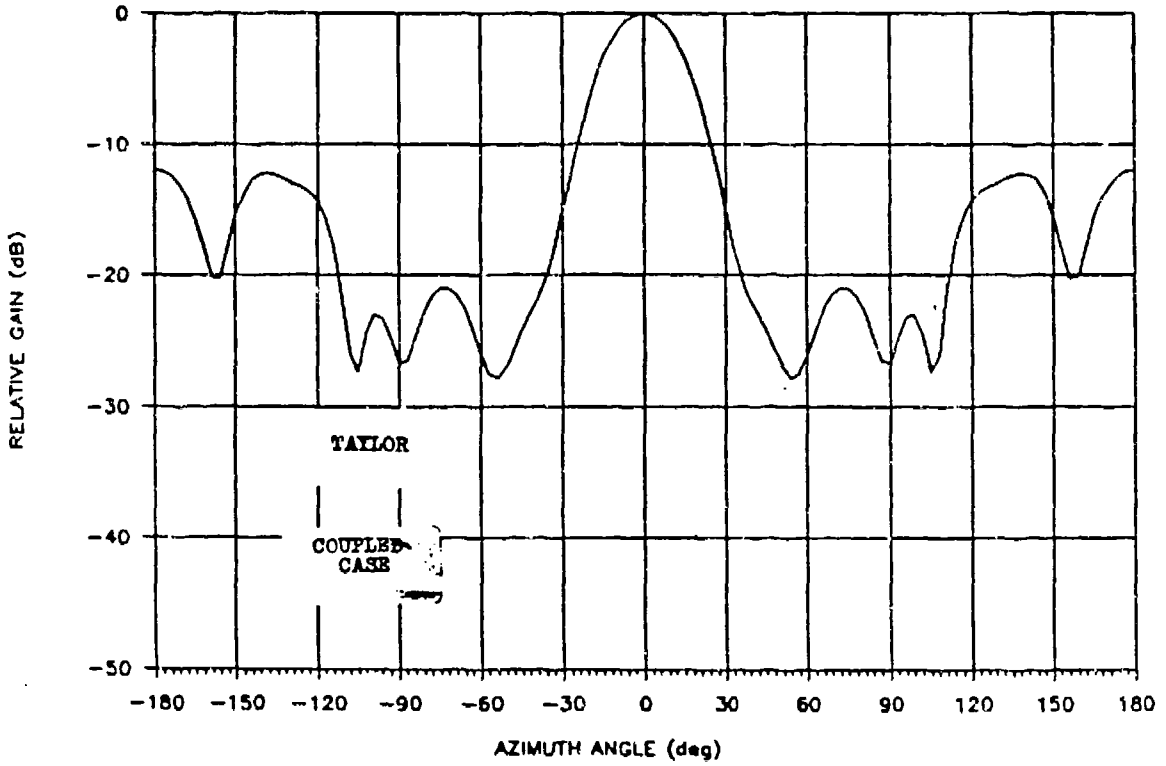


(a) Phi cut (azimuthal pattern), $|E(90°, \phi)|^2$

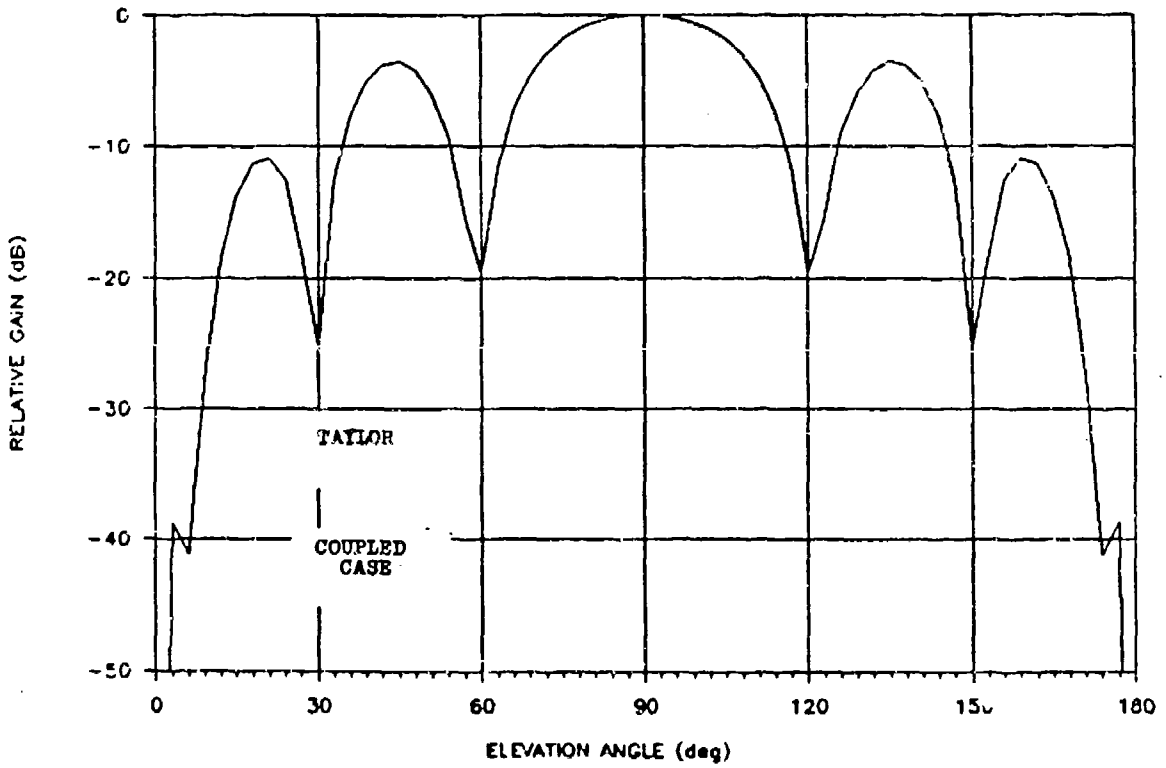


(b) Theta cut (elevation pattern), $|E(\theta, 0°)|^2$

Fig. 6 - Power patterns for a cophasal circular array ($\theta_0 = 90°, \phi_0 = 0°$) with a Taylor-type amplitude distribution, uncoupled case.



(a) Phi cut (azimuthal pattern), $|E(90°, \phi)|^2$



(b) Theta cut (elevation pattern), $|E(\theta, 0°)|^2$

Fig. 7 - Power patterns for a cophasal circular array ($\theta_0 = 90°, \phi_0 = 0°$) with a Taylor-type amplitude distribution, coupled case.

MOMENT METHOD ANALYSES OF LARGE FINITE PHASED ARRAYS

H.K. Schuman and G.A. Bright
Atlantic Research Services Corporation
1721 Black River Blvd.
Rome, NY 13440

S. Barbour
Grumman Aerospace Corporation
South Oyster Bay Rd.
Bethpage, L.I., NY 11714

1. Introduction

Large planar phased array antennas frequently are included in modern radar system concepts because of their high directive gains and rapidly redirectable beams. Because such arrays are expensive to build and difficult to test, it is important to have analysis tools available for accurately predicting the performance of candidate radiating elements. Active impedances, current distributions, and radiation patterns are of interest.

The Numerical Electromagnetic Code (NEC) (Reference 1) is one such tool. The basis of NEC is a finite conducting body moment method that can be applied to analyzing a finite array of arbitrarily excited thin conductor radiators. A limitation with NEC, however, is that as the sizes of the arrays increase, in excess of 50 radiators or so, reasonable computer memories and computational times are quickly exceeded.

The plane wave expansion moment method (Reference 2) on the other hand, can be applied efficiently to obtain the active impedances, current distributions and active element patterns of infinite planar arrays. All radiators must be identical, progressively phased, and uniformly spaced. Even large arrays, however, are not infinite and many radiators of such arrays reside near array edges or other discontinuities in array periodicity.

An alternative method, the Higher Approximation Analysis, has been developed that combines plane wave expansion and finite antenna moment methods in an iterative procedure that is both reasonably efficient for large arrays and accurate in so far as modeling edge effects and other discontinuities. The Higher Approximation Analysis is briefly described here and several examples of its application are given. The method has been implemented into a computer program that applies to phased array lenses as well as to constrained feed arrays. The radiating elements can be thin conductor types ("dipole-like") or microstrip patch types.

2. Higher Approximation Analysis

In the Higher Approximation Analysis, an initial solution is determined by imposing infinite array conditions and solving for the current distributions on all the array radiating elements. This solution is referred to as the "first approximation solution" or "Level 1 solution." An element near an irregularity such as the array edge, a failed phase shifter module, or a discontinuity in lattice periodicity then is identified as a candidate for recomputation of current. The resulting current is referred to as a "Level 2 solution." The current, and associated port voltages and impedances, is determined by a finite array moment method. The candidate element only, referred to as the "considered element," is subsectioned in accordance with standard moment method procedure. The element is "excited" by the existing excitation (the incident illumination in the phased array lens case or the port voltage in the constrained feed array case) and by the first approximation currents on neighboring elements. The order of the moment method matrix equation that results is small, equal to the number of current expansion functions on a single radiating element.

The "neighboring elements" are chosen to fall within a circular border. The enclosed area is called the "region of influence." The radius of the region of influence (r_d) is determined by observing convergence of current, or port impedance, on the considered element as r_d is increased. Large values of r_d are associated with increased computer processing (run) time. Problems analyzed to date indicate that an $r_d \approx 3\lambda$ yields accuracy to within a few percent.

The procedure continues by computing the Level 2 approximation currents on other elements near the irregularities in a similar manner. Once a sufficient number of elements are upgraded to Level 2 approximations, the next higher level approximation could be determined on a designated ("considered") element. The procedure would be identical with that for Level 2, with the exception that the exciting currents on neighboring elements (those within the region of influence) now would be the Level 2 currents as opposed to the Level 1 currents.

The procedure would continue until a satisfactory number of higher approximations (levels) are obtained on elements near irregularities. The minimum number of levels, as well as the radius of influence, must be determined by numerical experiment.

SUMMARY

Two inverted F-antenna structures has been analysed using wire models with NEC. Reasonably good results has been obtained for the LIFA-on-a-box-case (fig. 1a) even though the calculated bandwidth was 30% too wide. The difference between the measured and analysed data was more obvious in the more complex case of two PIFAs on a box (fig 1b). NEC proved yet to be a potential tool for this sort of antenna design as the calculated shape of the patterns and the bandwidth are comparable with the measured ones. As the wire model may still be improved (and more attention may be paid to antenna measurements) better results are to be expected.

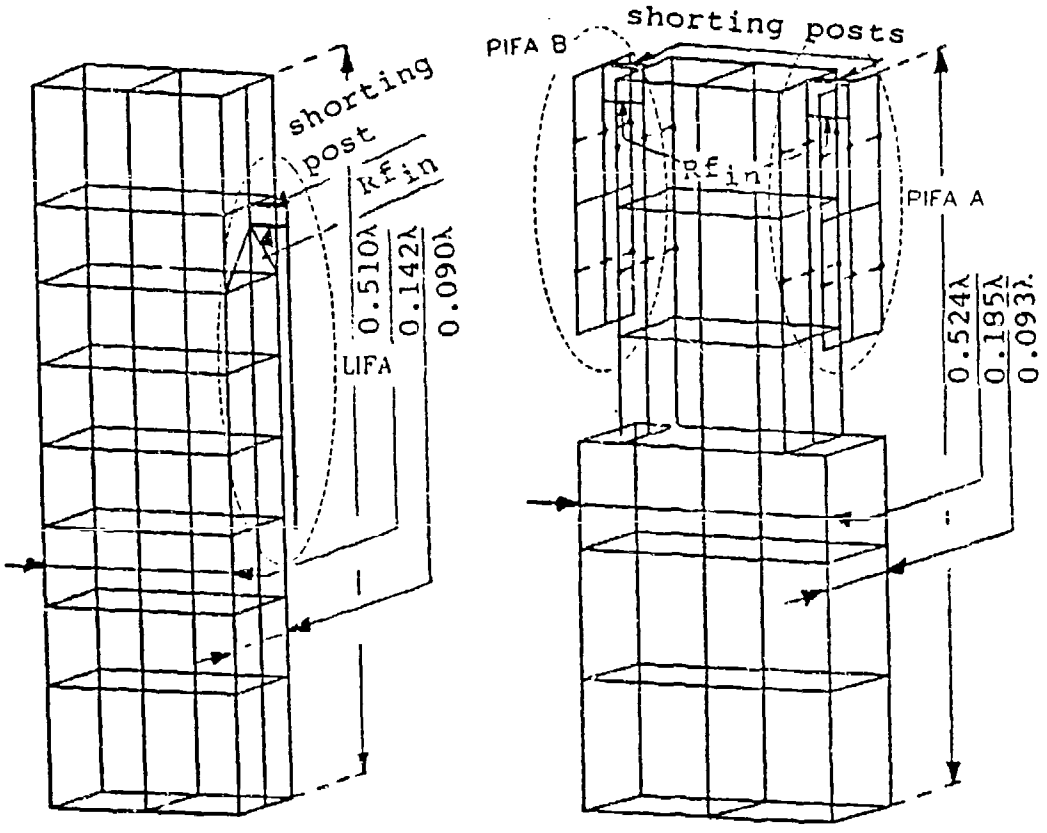


Fig. 1a: LIFA on a box b: Two PIFAs on a box

Figure 1 shows the relationship between a considered element and the radius of influence for a circular aperture array. Details including relevant equations can be found in Section 3.3 of Reference 3.

3. Implementation

The higher approximation analysis has been implemented with consideration given to high computational efficiency and ease of user interface. The structure of the implementation is illustrated, by example, in Figure 2. The user identifies a considered element, a radius of influence, and a level of approximation. The illustration pertains to a considered element near the edge of a circular array and a Level 5 approximation. The computer automatically schedules Level 4 current approximations on all elements within the region of influence. To obtain the Level 4 currents, Level 3 current approximations on all elements within the regions of influence of the elements of which Level 4 currents are required are scheduled, and so on, until Level 1 current approximations are called upon. All computed levels of current approximations on all elements are saved to minimize the subsequent computation of either higher levels of approximation on the same considered element or any level of approximation on another considered element. Thus, whereas substantial run time may be expended in the Level 5 computation of a considered element in the beginning of an analysis, much less run time would be expended for a subsequent nearby considered element. Because of such structuring, the run time for an N_1 level analysis on all the elements in a N_e element array can be shown to be approximately proportional to $N_1 \cdot N_e \cdot r_d^2$. Of course, typically only a relatively few elements need undergo a higher approximation analysis.

4. Validation

An equilateral lattice array of dipole radiating elements $\lambda/4$ above a ground plane is shown in Figure 3. The dipole lengths are $.5\lambda$ and radii are $.001\lambda$. The 37 element array was analyzed by both NEC and the Higher Approximation Analysis (HAA). The active impedances of each element in a quadrant of the array when excited for broadside beam direction are shown in Figures 4 (NEC) and 5 (HAA). Corresponding full array E- and H-plane radiation patterns are shown in Figures 6 (NEC) and 7 (HAA). The element active impedances and radiation patterns are in good agreement. The agreement between NEC and HAA for the array scanned to 60° in the E-plane (Figures 8 and 9) and in the H-plane (Figures 10 and 11) also is good.

5. Discussion

The higher approximation analysis method described here for analyzing phased array antennas has only begun to be applied to problems of interest. Guidelines for selecting minimum regions of influence, minimum number of approximation levels, and minimum number of considered elements must await extensive application of the method. It presently is being used to (1) determine the minimum number of outer rings of terminated elements that would ensure that all excited elements exhibit nearly the same element gain patterns, (2) evaluate the mutual coupling effects of subarraying whereby to each phase shifter is assigned a group of radiating elements, and (3) characterize the disturbance to neighboring radiators resulting from a failed phase shifter module. For example, the active impedances of elements in the 37 element array of Figure 3 when the center element phase shifter module is open circuited and short circuited are shown in Figure 12. These results can be compared with those of Figure 4.

The implementation of the method includes modeling that applies to a wide variety of microstrip patch arrays as well as to the thin conductor ("dipole-like") arrays examplified here.

6. References

1. G.J. Burke and A.J. Pogio, "Numerical Electromagnetics Code (NEC) - Method of Moments," NOSC TD 116, Naval Ocean Systems Center, San Diego, CA, Vols. 1 and 2, January 1981.

2. H.K. Schuman, D.R. Pflug, and L.D. Thompson, "Infinite Planar Arrays of Arbitrarily Bent Thin Wire Radiators," IEEE Trans. Ants. Propg., Vol. AP-32, No. 4, pp 364-377, April 1984.

3. H. Schuman, D. Pflug, and L. Thompson, "Space-Based Array System Simulation and Validation," First Technical Report, Rome Air Development Center, Griffiss AFB, NY, June 1980.

GEOMETRY OF HIGHER APPROXIMATION ANALYSIS

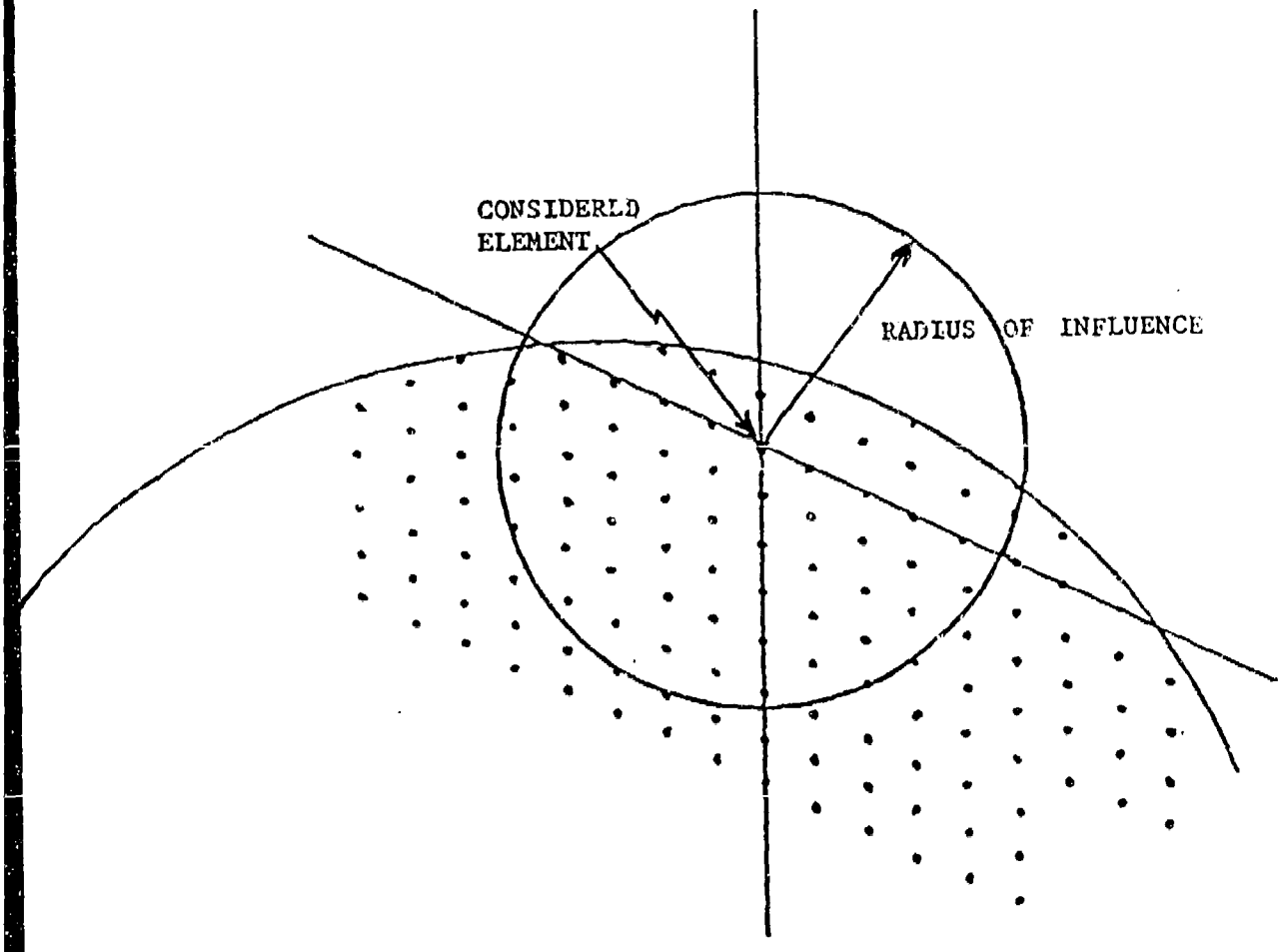


Figure 1.

EDGE ELEMENT SOLUTION APPROACH
USING A RADIUS OF INFLUENCE ITERATION

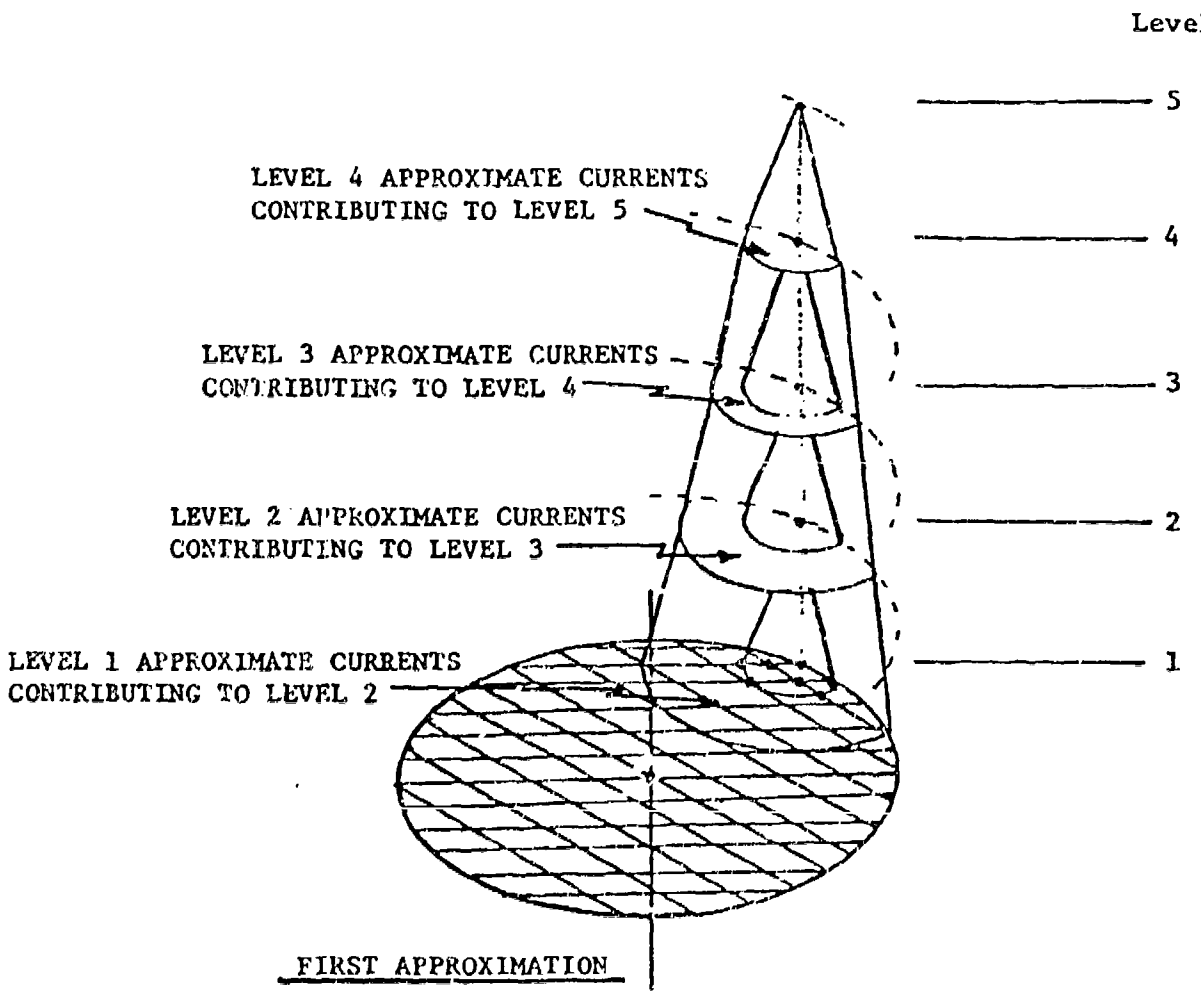


Figure 2.

HIGHER APPROXIMATION ANALYSIS VALIDATION CASE
37 ELEMENT SIMPLE DIPOLE ARRAY

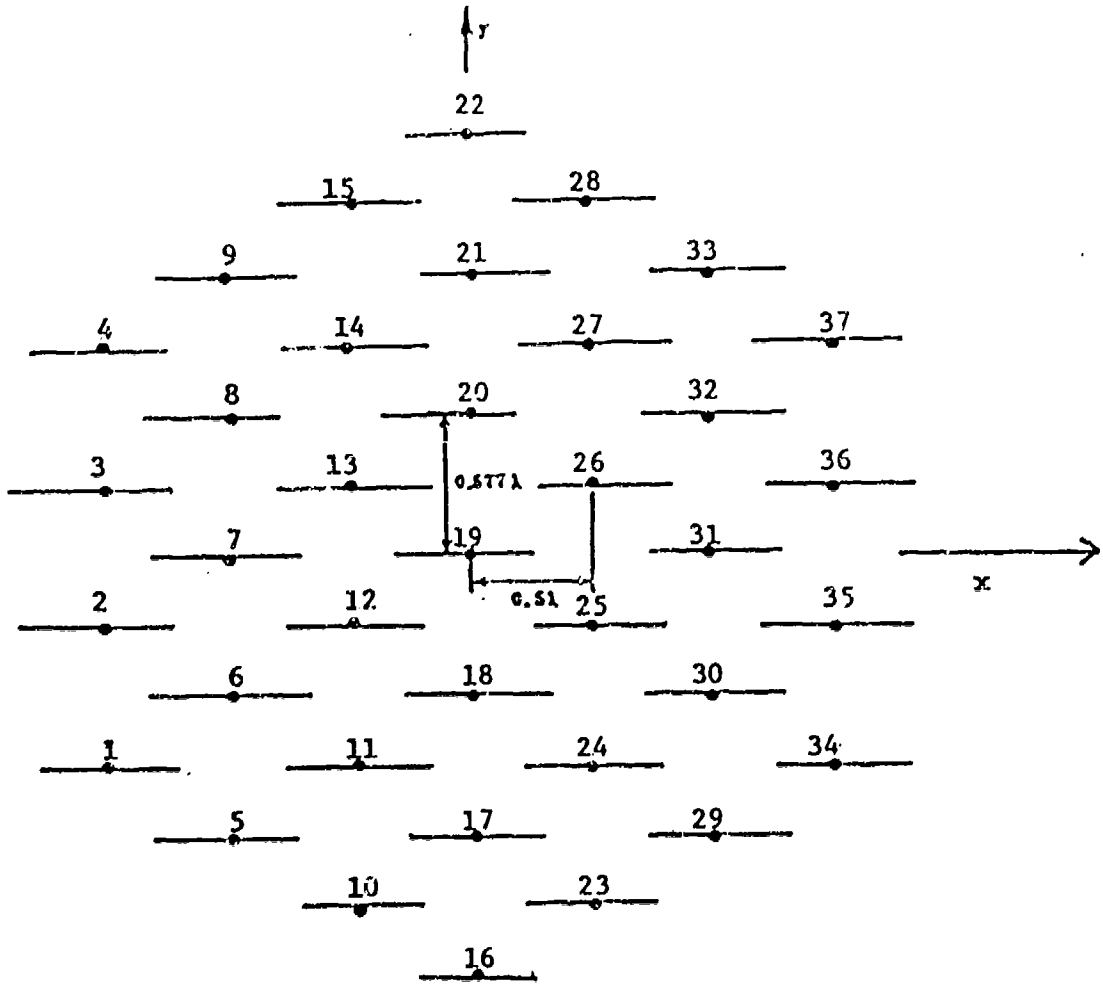
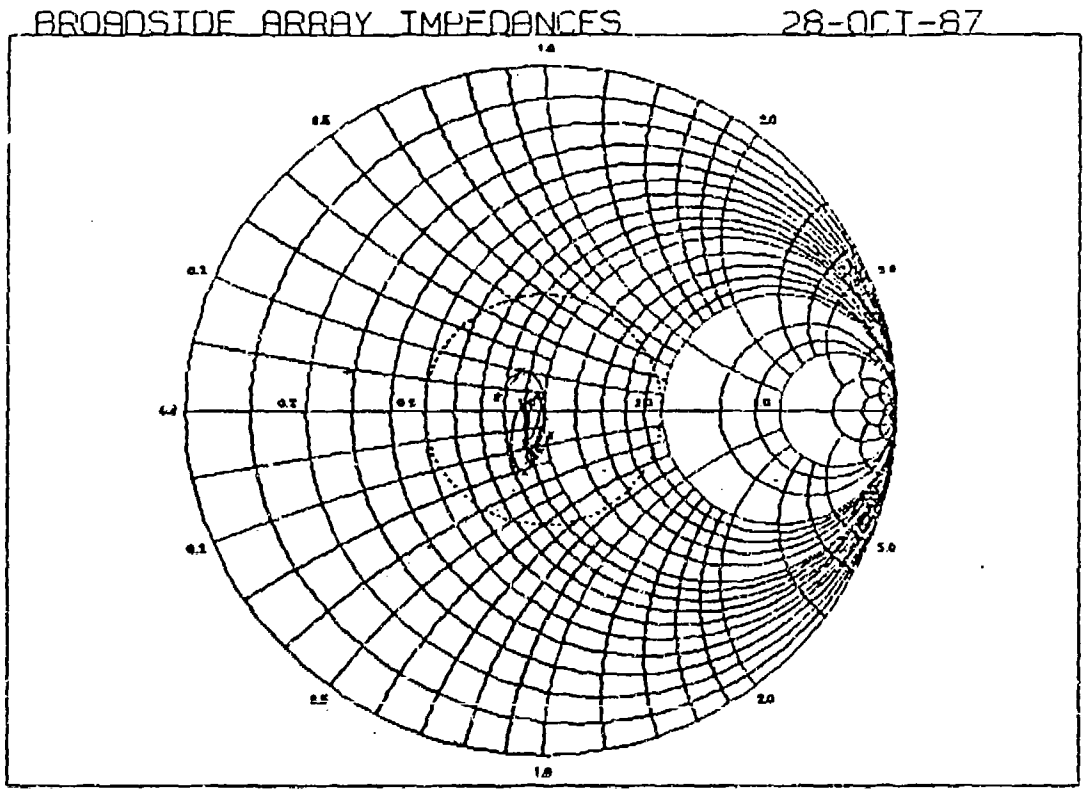


Figure 3.

NUMERICAL ELECTROMAGNETICS CODE
BROADSIDE SCAN
37 ELEMENT IMPEDANCE SET



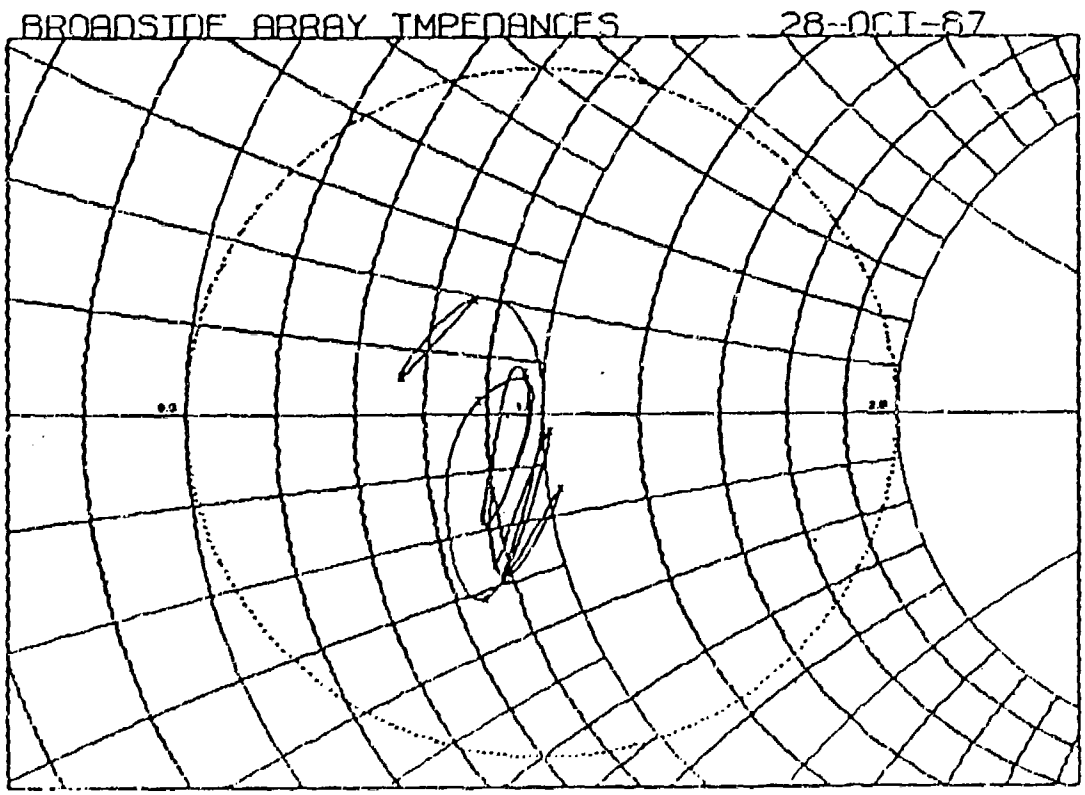
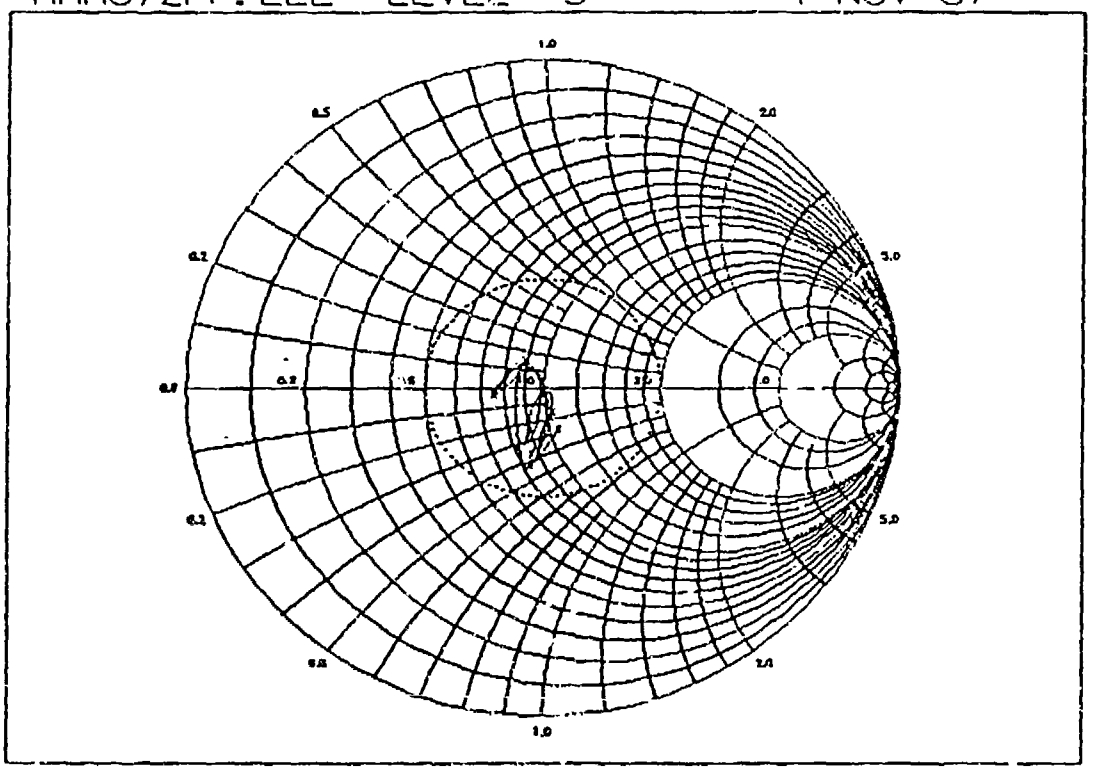


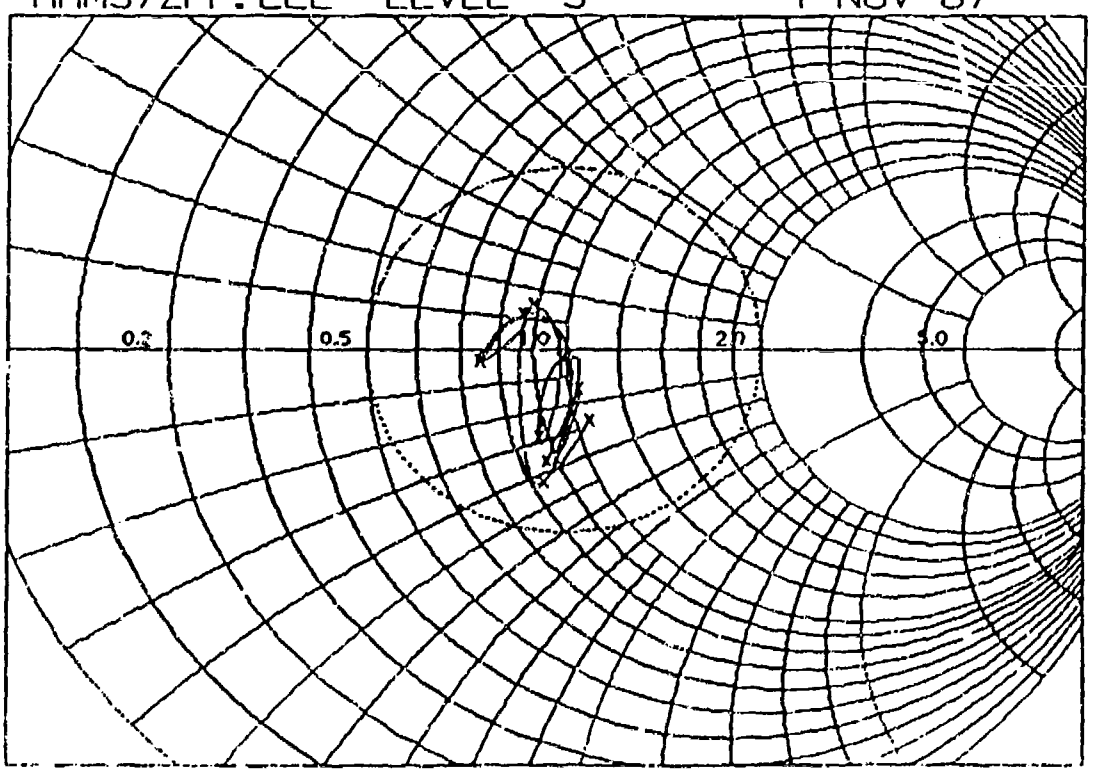
Figure 4

HIGHER APPROXIMATION ANALYSIS
BROADSIDE SCAN, INFINITE ARRAY START
37 ELEMENT IMPEDANCE SET

HAM37ZFP.ELE LEVEL 5 4-NOV-87



HAM37ZFP.ELE LEVEL 5 4-NOV-87



NUMERICAL ELECTROMAGNETICS CODE
37 ELEMENT BROADSIDE PATTERN

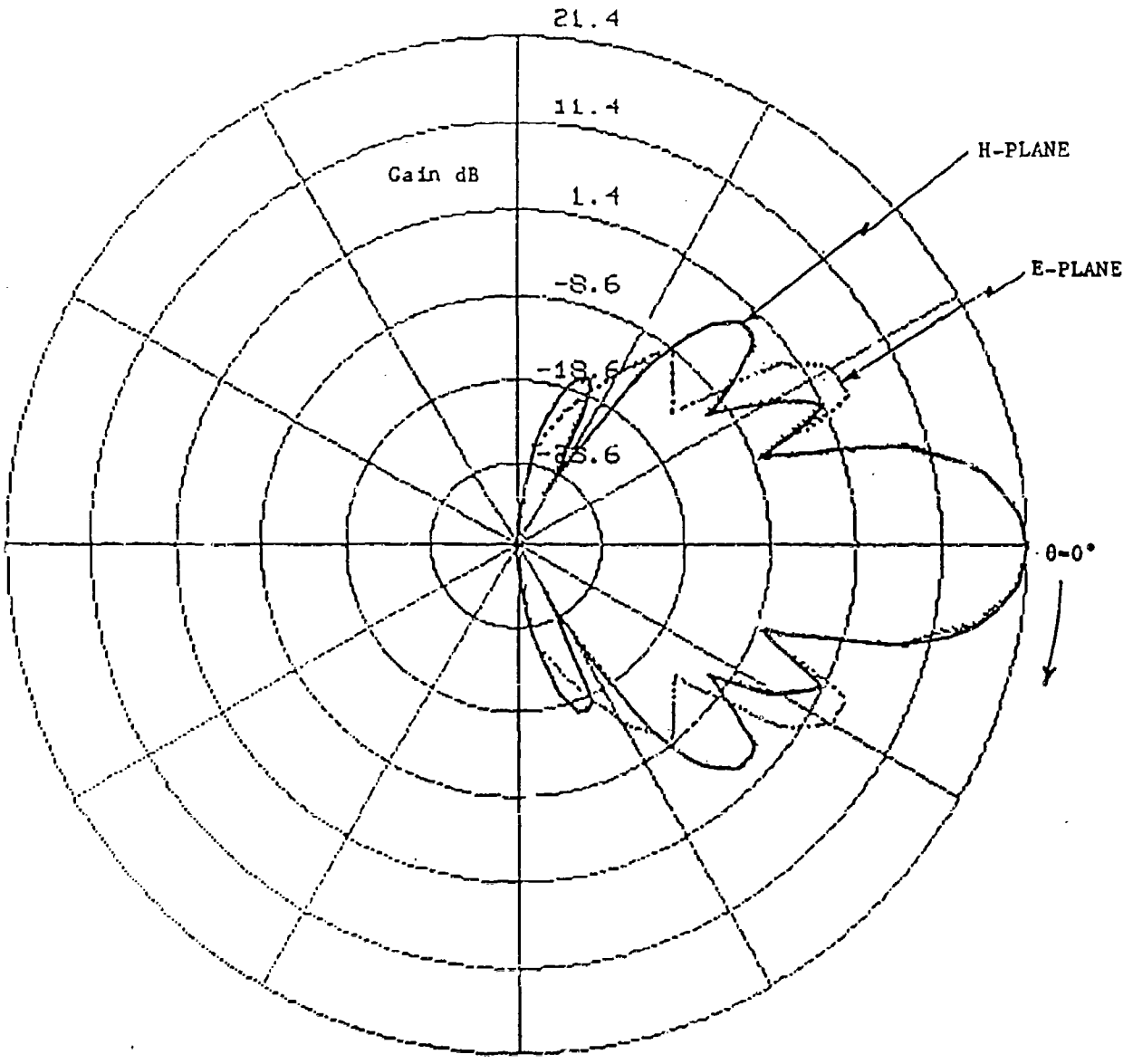


Figure 6.

HIGHER APPROXIMATION ANALYSIS
37 ELEMENT BROADSIDE PATTERN

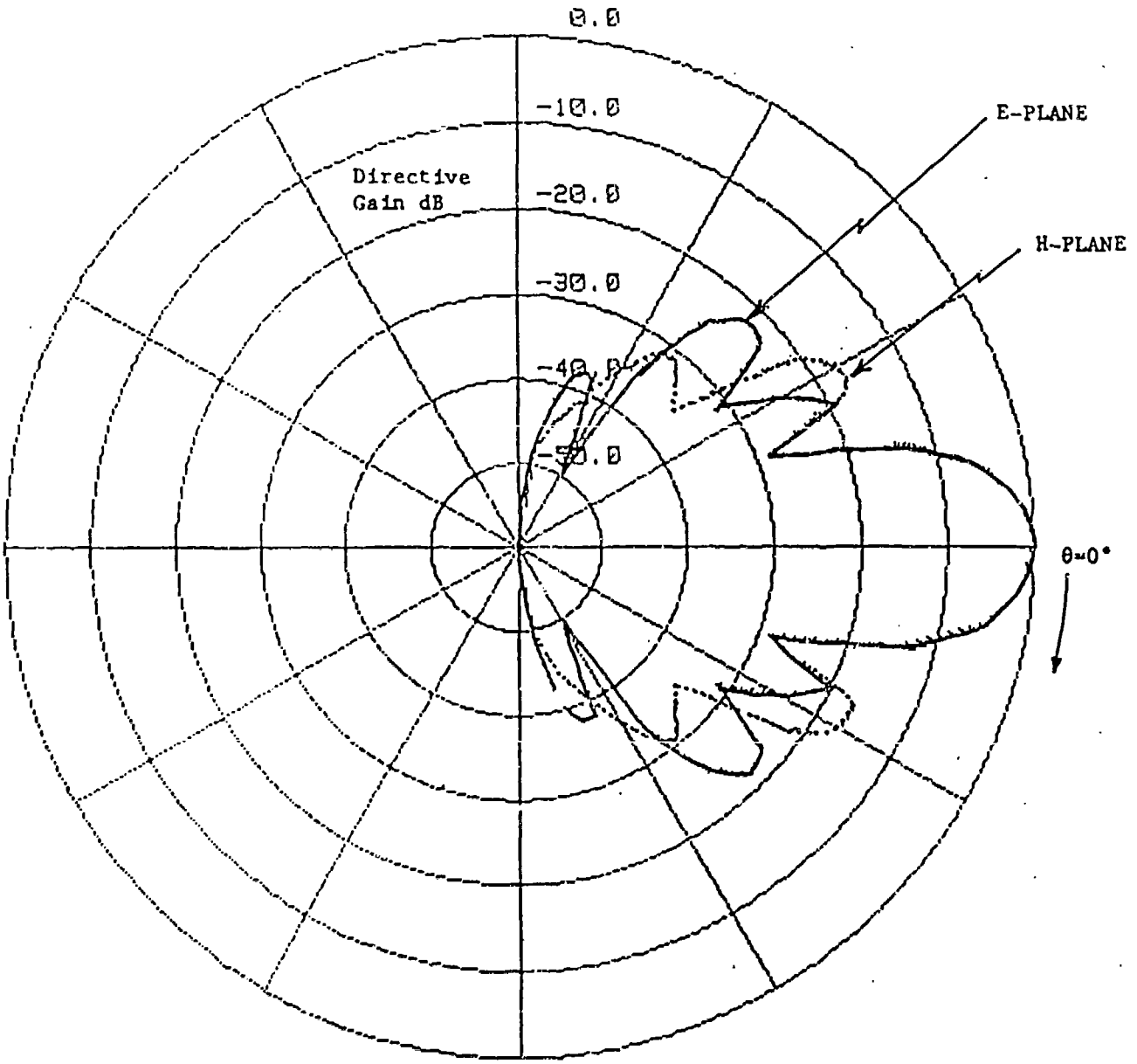
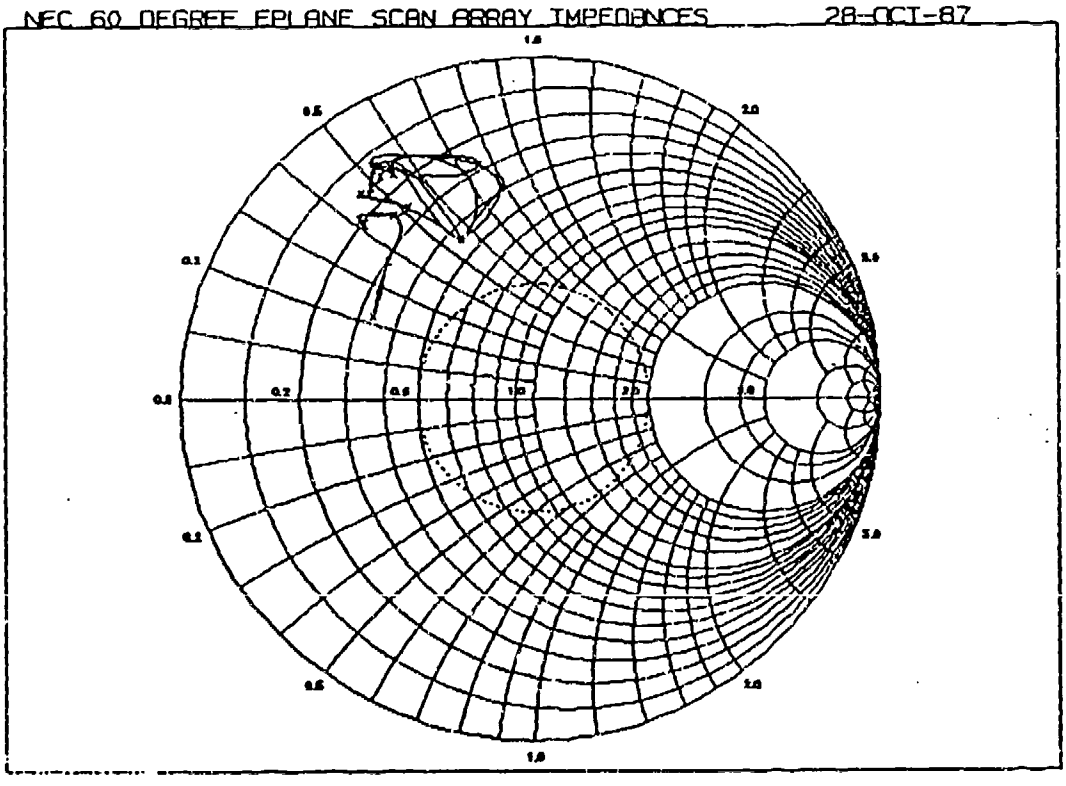


Figure 7.

NUMERICAL ELECTROMAGNETICS CODE
60 DEGREE E-PLANE SCAN
37 ELEMENT IMPEDANCE SET



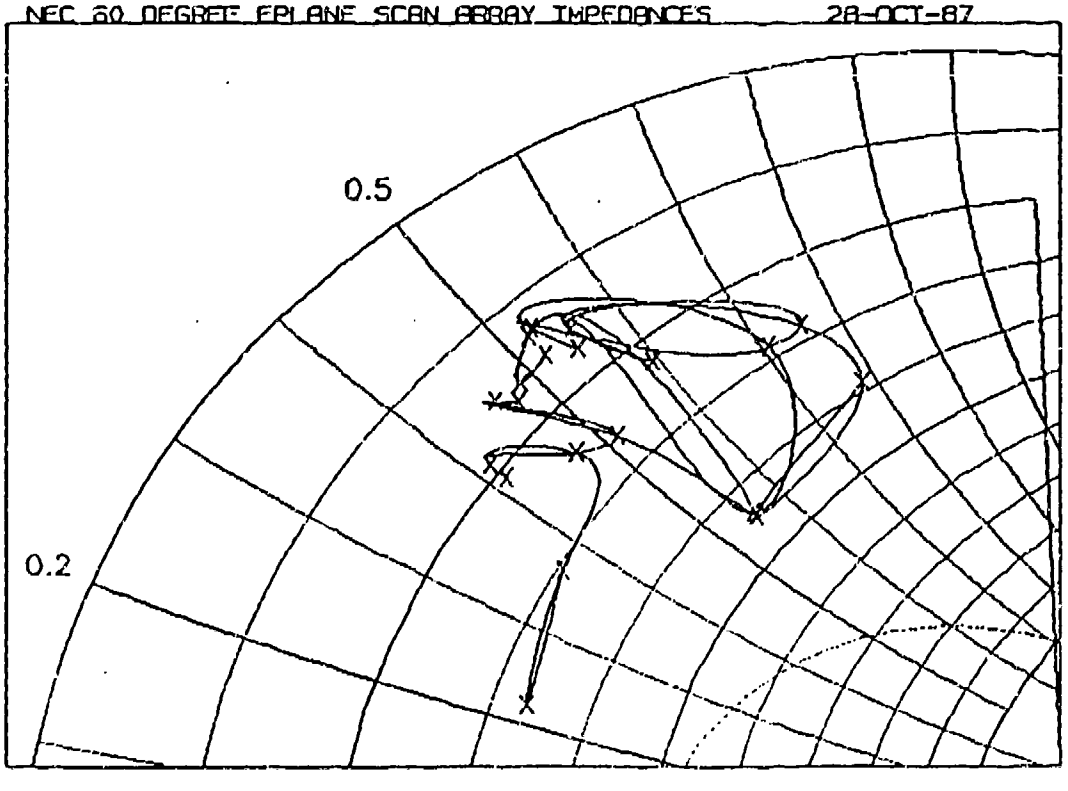
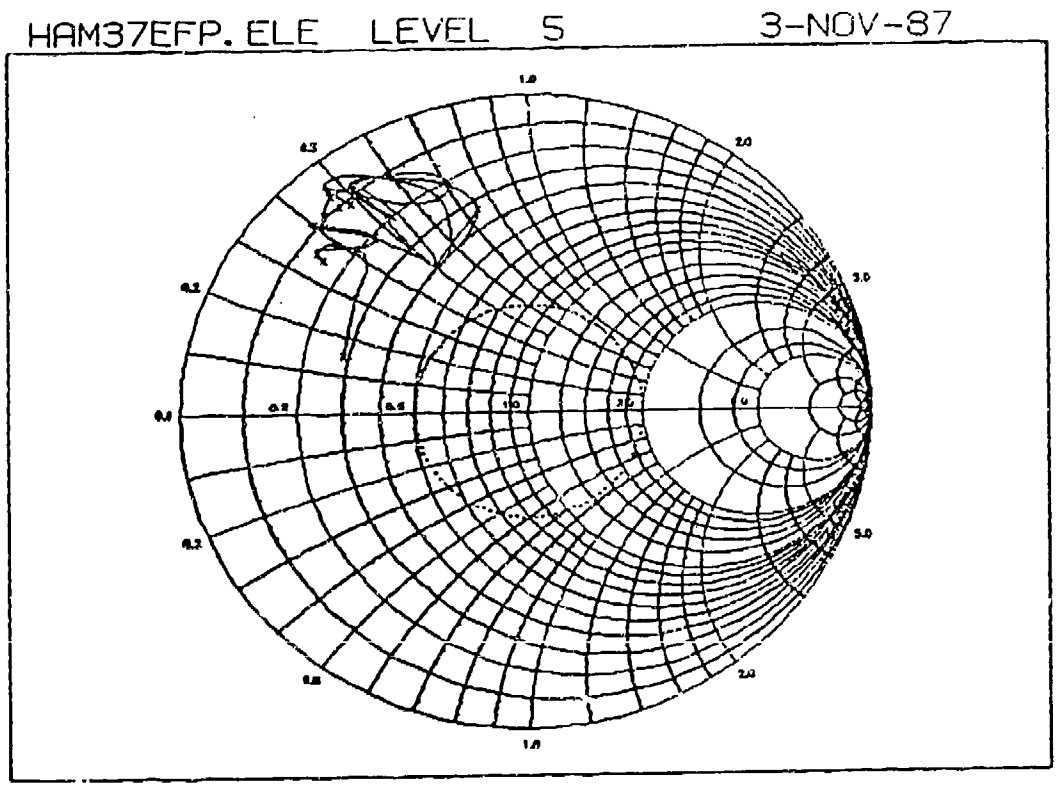


Figure 8

HIGHER APPROXIMATION ANALYSIS
E-PLANE SCAN, INFINITE ARRAY START
37 ELEMENT IMPEDANCE SET



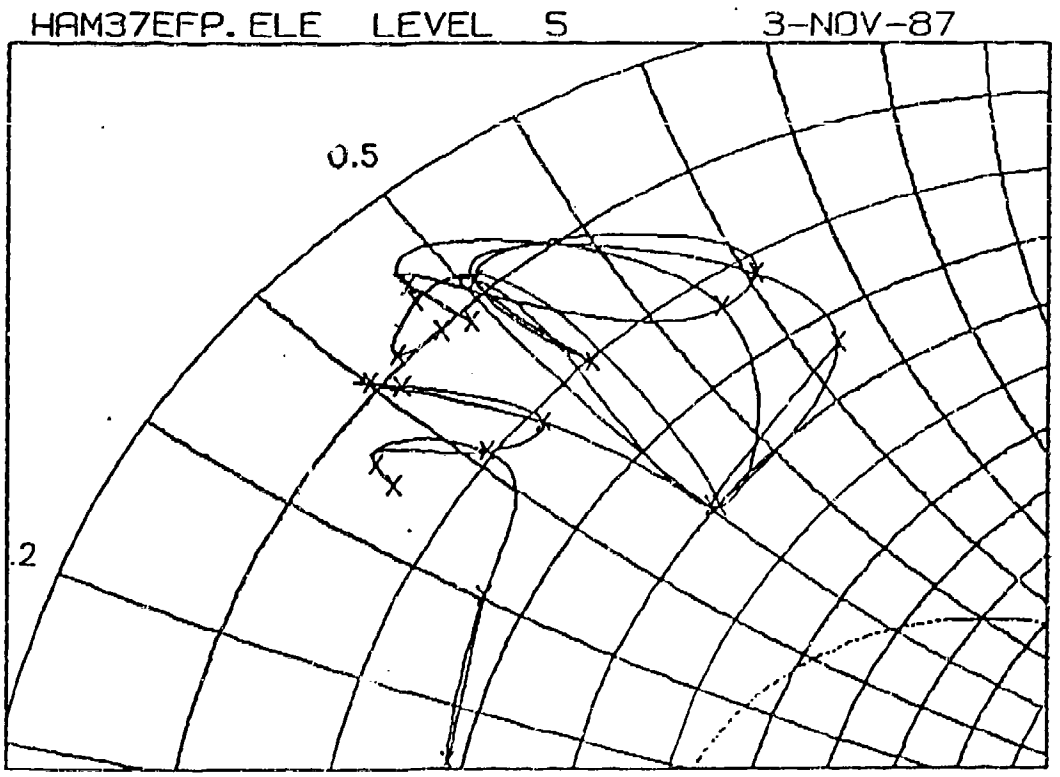
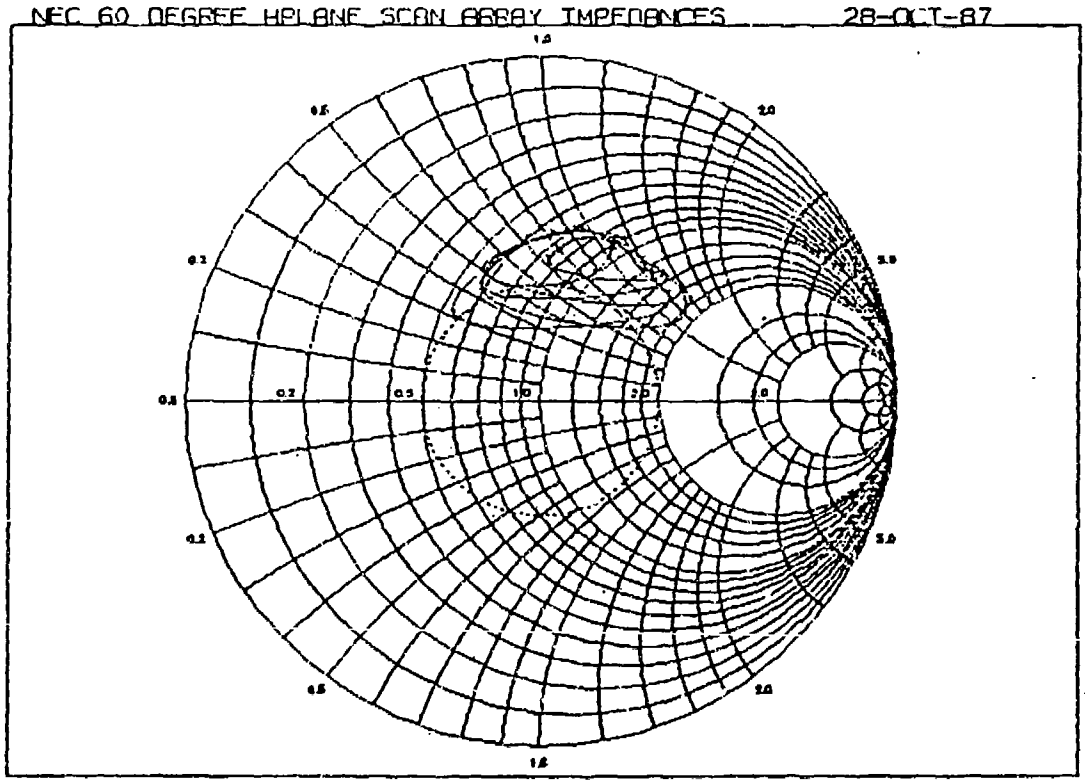


Figure 9.

NUMERICAL ELECTROMAGNETICS CODE
60 DEGREE H-PLANE SCAN
37 ELEMENT IMPEDANCE SET



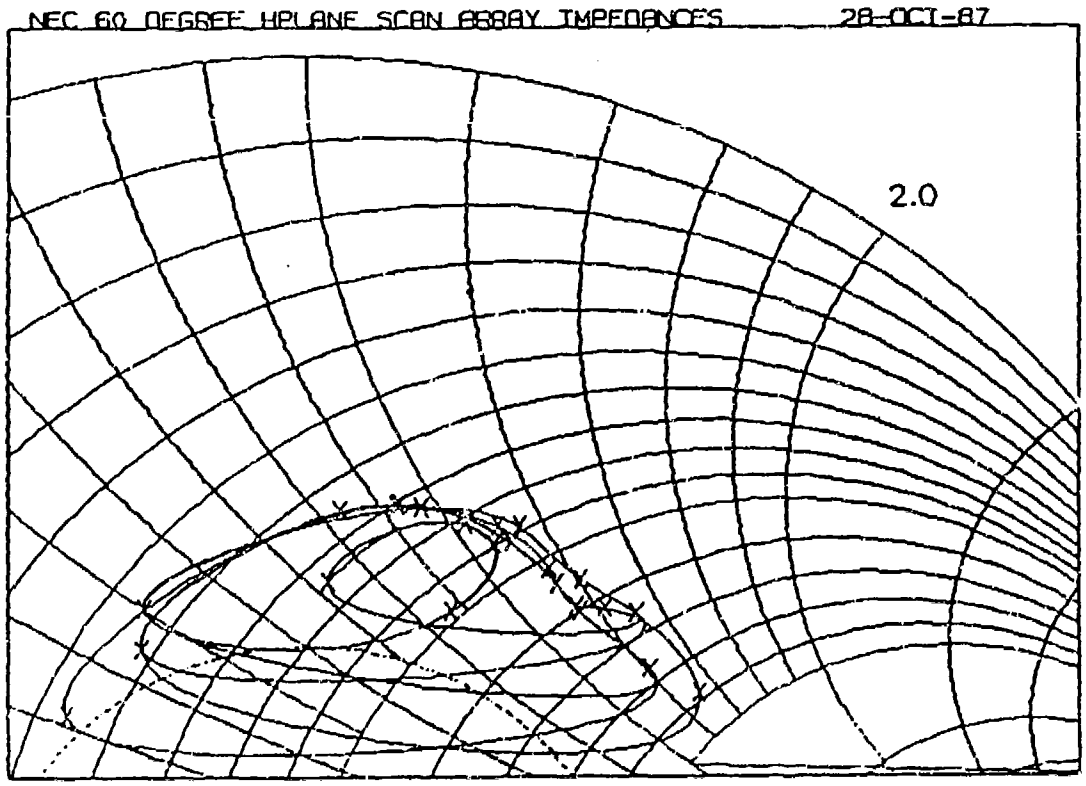
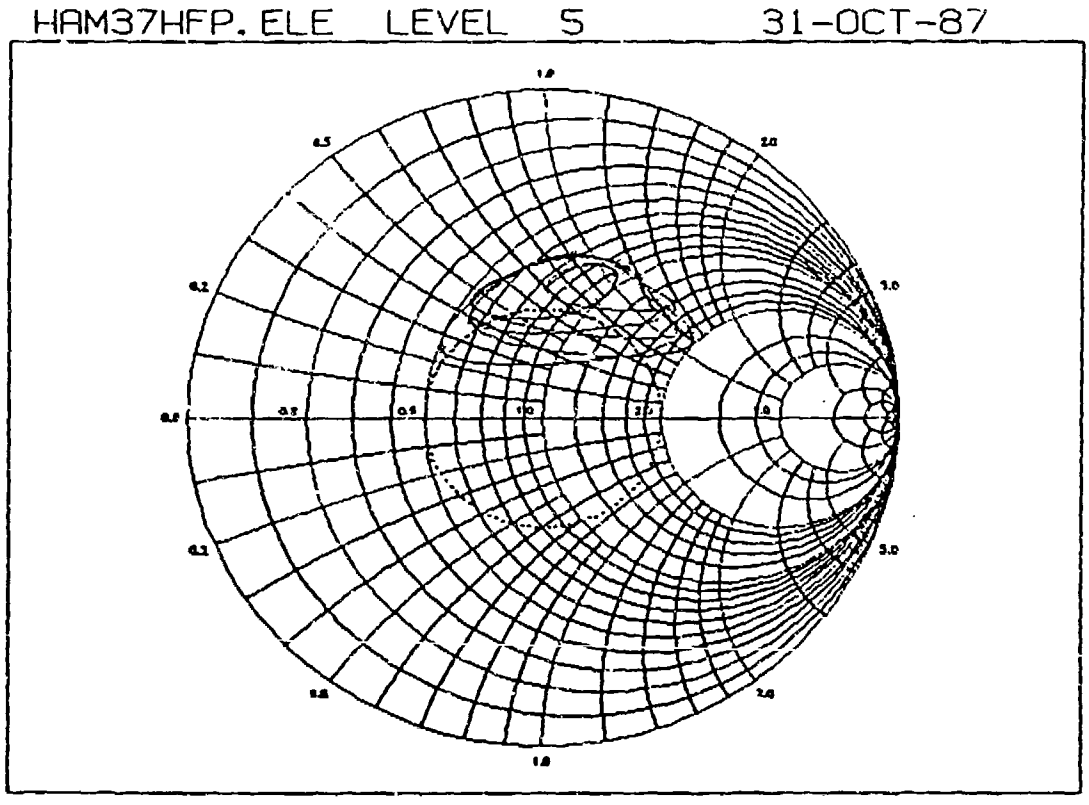


Figure 10.

HIGHER APPROXIMATION ANALYSIS
H-PLANE SCAN, INFINITE ARRAY START
37 ELEMENT IMPEDANCE SET



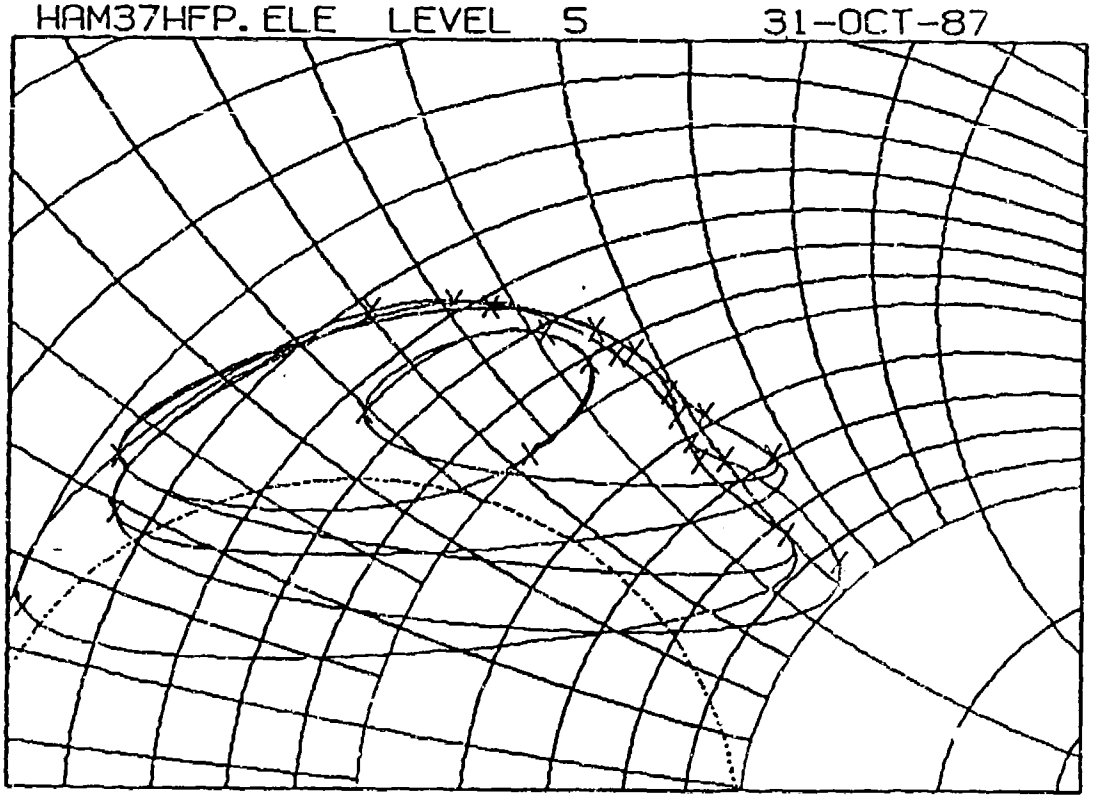
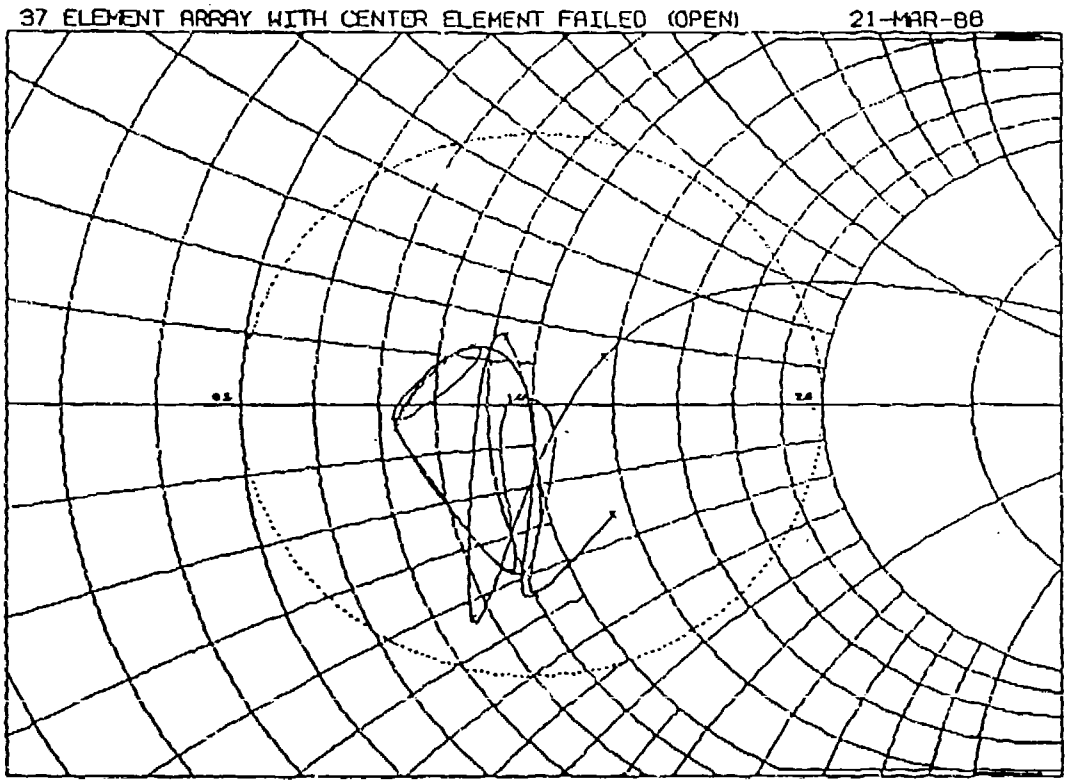


Figure 11.

HIGHER APPROXIMATION ANALYSIS
OF
FAILED ELEMENTS



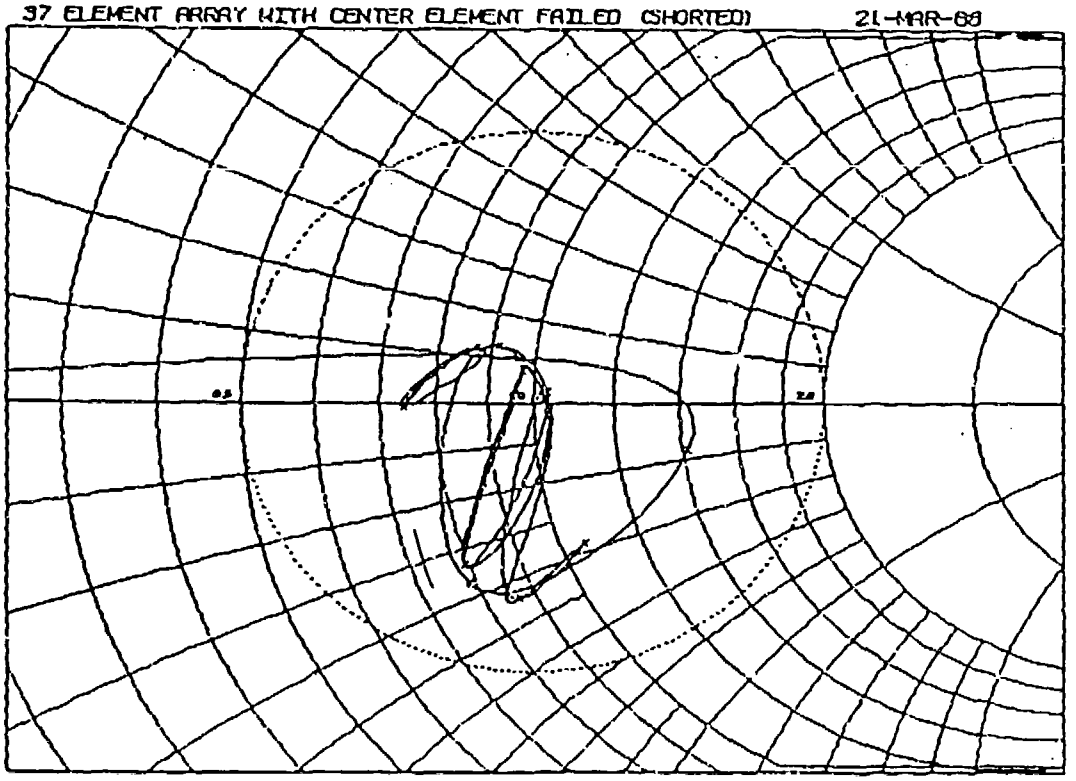


Figure 12.

Application of the Network Approach to Electromagnetic Solutions Involving Apertures on a Body of Revolution

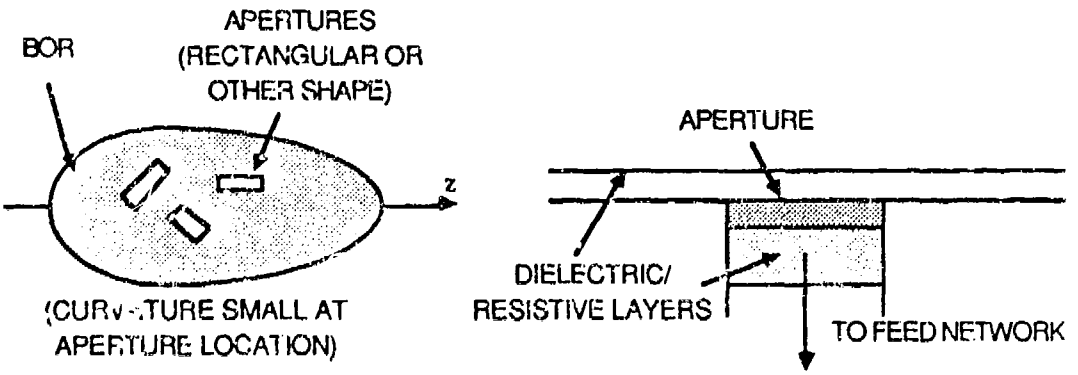
Dr. James R. Rogers

Atlantic Aerospace Electronics Corporation
6404 Ivy Lane, Suite 300
Greenbelt, Maryland 20770-1406

1.0 Introduction

The network approach to solving aperture electromagnetic problems (Harrington and Mautz, IEEE Trans. AP, Nov. 1976) is a powerful way of formulating the solution of a complex problem into a set of simpler, connected problems. The technique is particularly useful when parameters of a small part of the problem are to be changed repeatedly (as in a design process) while those of a larger part of the problem remain constant. Because of its systematic approach to constructing solutions, the network approach is ideal for translating formulations into a modular computer code.

Using the network approach, we are currently developing a computer program to model waveguide-fed aperture antennas on a general body of revolution (BOR). This general problem toward which we are working is depicted below:



While our current implementation is much less general than above, we have more

general modules already developed which can be incorporated after fully checking the basic network program.

Our basic objectives in developing this computer program are to:

1. rigorously model small apertures on a large, complex body-of-revolution, so that various dielectric and installation effects can be examined,

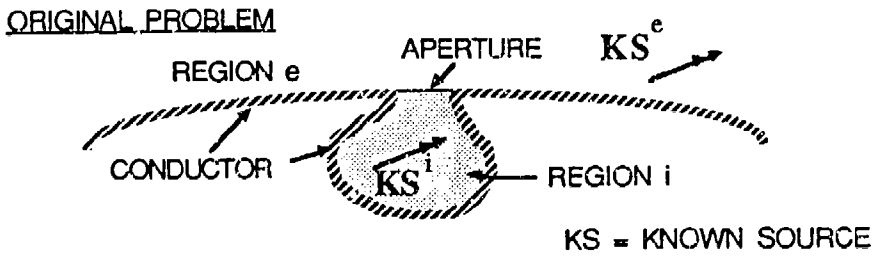
2. structure the analysis so that the aperture and interior parts of the problem can be changed repeatedly while the large exterior part of the problem remains constant

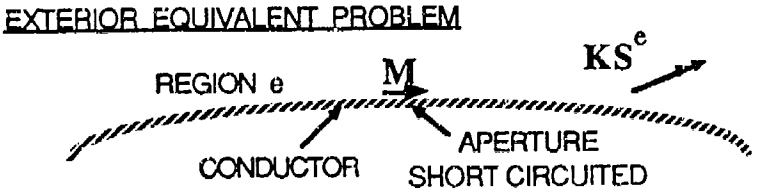
3. create a modular program so that parts of the problem (such as the exterior or interior geometry, aperture shape, etc) can be changed easily

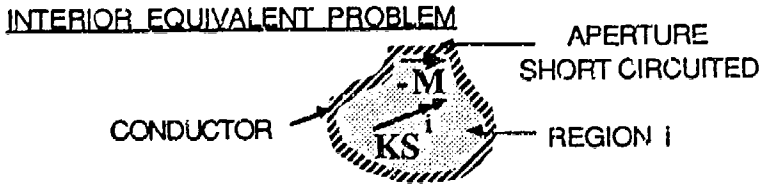
The remaining sections of this paper will outline the network formulation, describe the current program implementation and give an example of electromagnetic solutions for a rectangular waveguide-fed aperture on a finite conducting cylinder.

2.0 Formulation

The network approach makes use of the equivalence principle (Harrington, Time Harmonic Electromagnetic Fields, McGraw-Hill, 1961). Depicted on the next page is an illustration of an original problem consisting of two regions connected by an aperture; and two coupled problems that are equivalent to the original problem. This equivalent formulation, which I will call the "short-circuit" formulation casts the problem into finding unknown equivalent magnetic currents, **M** on the aperture. This is different from the more usual application of the equivalence principle where the problem is to find both equivalent electric, **J**, and magnetic currents on all surfaces. The solution of the short-circuit formulation can be thought of as containing implicitly the electric equivalent currents, rather than explicitly.







The choice of $\mathbf{M}$ in the exterior equivalent problem and $-\mathbf{M}$ in the interior equivalent problem ensure that continuity of tangential electric field is satisfied across the aperture. The remaining boundary condition leads to an operator equation for the unknown magnetic current source:

BOUNDARY CONDITION

$$\mathbf{H}^{e}_{tan\ total} = \mathbf{H}^{i}_{tan\ total} \qquad \begin{matrix} e = \text{exterior} \\ i = \text{interior} \end{matrix}$$

OPERATOR EQUATION

$$\mathbf{H}^{e}_{tan}(\mathbf{M}) + \mathbf{H}^{i}_{tan}(\mathbf{M}) = -\mathbf{H}^{e}_{tan}(\mathbf{KS}^{e}) + \mathbf{H}^{i}_{tan}(\mathbf{KS}^{i})$$

To obtain an approximation for $\mathbf{M}$, we use the method of moments:

- EXPANSION FOR M: $\mathbf{M} = \sum_{j=1}^{N} V_j \mathbf{m}_j$
- TESTING FUNCTIONS: $\mathbf{W} = (\mathbf{m}_i)^* \qquad i = 1, \ldots N$
- INNER PRODUCT: $< \mathbf{W} , \mathbf{A} > = \int_S \mathbf{W} \cdot \mathbf{A} \, ds$

WHERE :

V -- UNKNOWN SCALAR COEFFICIENTS
m-- KNOWN MAGNETIC CURRENT BASIS FUNCTIONS

Upon substituting the expansion for **M** into the operator equation and testing the equation with the N testing functions, we obtain a matrix equation for the unknown coefficients of our expansion for **M**:

$$[Y^e + Y^j] [V] = - [I^{sc,e}] + [I^{sc,i}]$$

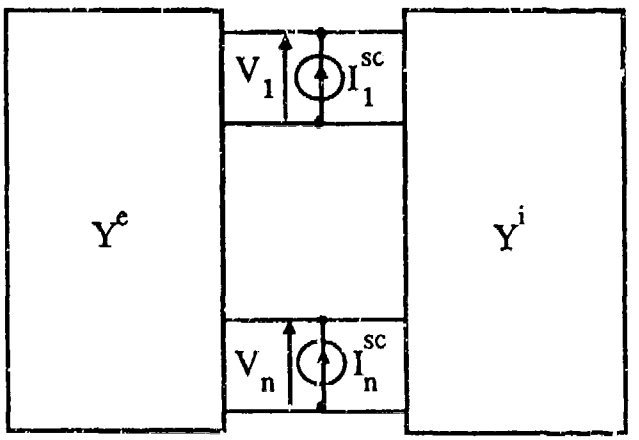
WHERE:

$$Y_{ij}^p = < \mathbf{m}_i^* , \mathbf{H}_{tan}^p(\mathbf{m}_j) >$$
$$I_i^{sc,p} = < \mathbf{m}_i^* , \mathbf{H}_{tan}^p(KS^p) >$$

(p denotes region e or i)

The Y's are the admittance matrix elements (due to the magnetic current basis functions radiating into the region with the conducting boundary present) and the I^{sc}'s are the short circuit excitation elements (due to the known source radiating into the region with the conducting boundary present). Both of these are given by solution of a boundary value problem appropriate to the particular region. Once the matrix and vector elements are calculated, then we can solve the system of equations for the coefficients V. Although I have written the right hand side as adding the interior and exterior excitation vectors, usually, the system of equations is solved for the V's using the excitation vectors one at a time (i.e., either the interior or exterior excitation vectors are zero).

The matrix equation has the following network interpretation:



$V_1, \ldots, V_n$ UNKNOWN VOLTAGES

$I_1^{sc}, \ldots I_n^{sc}$ KNOWN SHORT-CIRCUIT CURRENT GENERATORS

Shown is an exterior network connected to an interior network through a series of ports. Each port has associated with it an unknown voltage which corresponds to a magnetic current basis function.

3.0 Initial Geometry for Program Implementation

We currently have developed the computer program using:

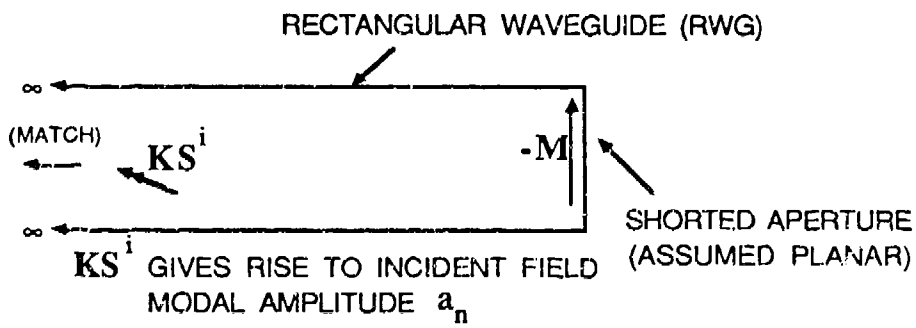
1. a rectangular aperture

2. a simple rectangular waveguide interior region (same cross sectional shape as the aperture), matched looking into the feed

3. a conducting BOR exterior region

The aperture basis functions are **z** x the transverse E-field functions of a rectangular waveguide mode. Usually, we only have one aperture basis function, namely that relating to the dominant waveguide mode. However, the program generality allows for an arbitrary number of basis functions.

The interior equivalent problem is thus:



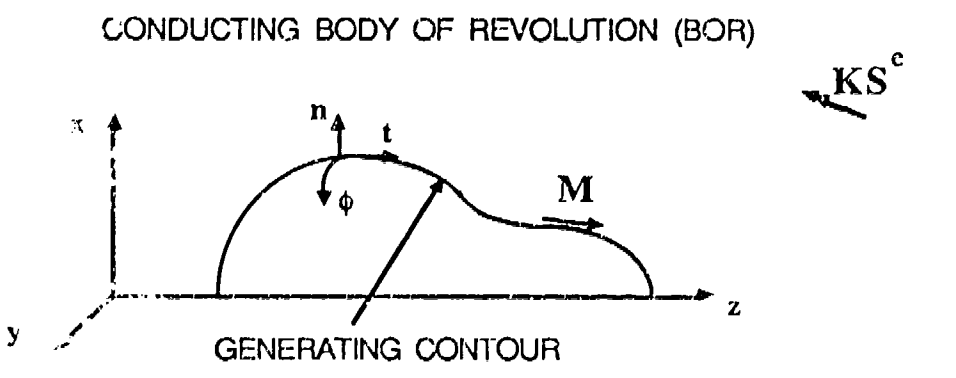
$$Y^{i}_{nm} = Y^{wg}_{n}\,\delta_{nm}$$

$$I^{sc,i}_{n} = 2\,a_{n}$$

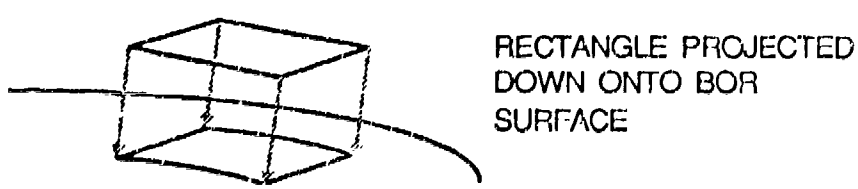
Y^{wg}_{n} = MODAL WAVE ADMITTANCE

We assume that the short circuit termination of the interior region is planar, which restricts the generality of the program to rectangular apertures on surfaces of small curvature. Using waveguide modal analysis and our choice for the magnetic current basis functions, the boundary value problem for this interior region is trivial.

The exterior equivalent problem is depicted below:



ASSUMPTION: CURVATURE SMALL NEAR APERTURE



We represent the rectangular aperture on the surface of the BOR by defining a planar aperture and projecting down onto the surface of the BOR normally.

As in the interior problem, we have two sources in the exterior problem: M and the known sources (at infinity) which give rise to an incident planewave. Each of these sources, radiating in the presence of the conducting BOR represents an exterior scattering problem. As described previously, we must solve the boundary value problem appropriate to the exterior region to obtain the admittance and excitation elements. Here, it is desirable to use solutions for BORs that have already been obtained in the literature: such as those by Mautz and Harrington (AEU,32,157,1978) and Mitschang and Putnam (IEEE Trans. AP-32,797,1984). These codes solve the exterior scattering problem by an application of the equivalence principle to obtain the solution in terms of equivalent electric current density, **J**. The typical expansion for **J** is in terms of unknown Fourier coefficients, I_n (not to be confused with the short-circuit excitation vectors) with the basis functions along the contour of the BOR being overlapping triangles functions:

$$\mathbf{J} = \sum_n \sum_k (I^t_{nk}\, t + I^{\phi}_{nk}\, \phi)\, f_k(t)\, e^{jn\phi}$$

For our aperture problem, the exterior admittance and excitation elements are given by the formulas on the next page. In these formulas, the elements I' essentially relate the magnetic current basis functions to the BOR basis functions.

Thus, we are solving a BOR method-of-moments problem simply to obtain the exterior elements of our aperture method-of-moments problem. If it sounds like alot of work -- it is!

ADMITTANCE ELEMENTS:

$$Y_{ij}^{e} = -\sum_{n} [P_n^i]^{*T} [N] [I_n^{m_j}]$$

$[I_n^{m_j}]$ DUE TO MAGNETIC CURRENT BASIS FUNCTION j

SHORT CIRCUIT EXCITATION ELEMENTS:

$$I_i^{sc,e} = -\sum_{n} [P_n^i]^{*T} [N] [I_n^{pw}]$$

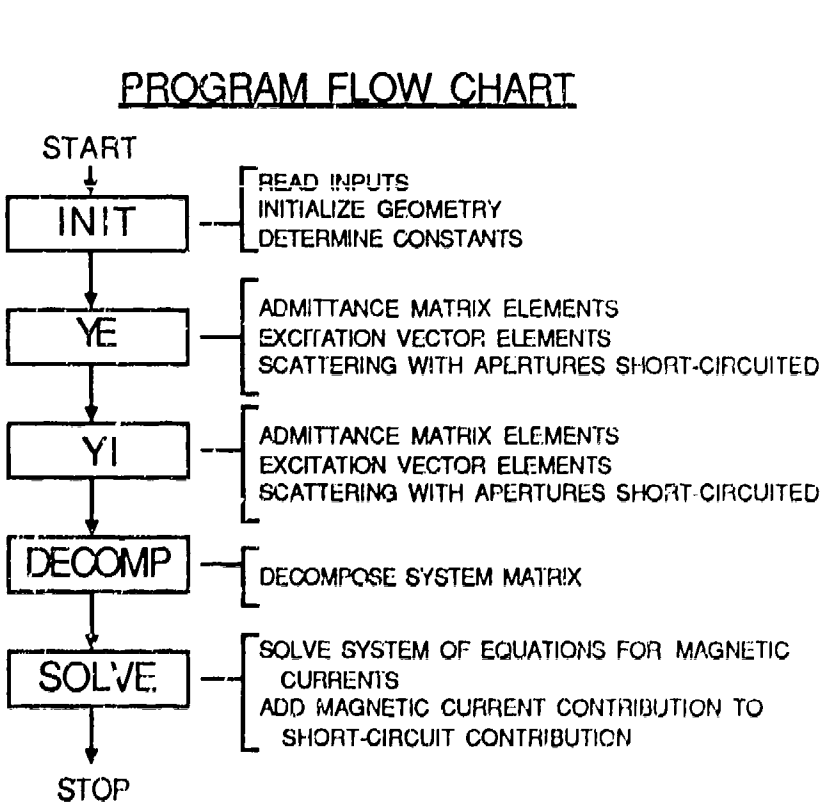
$[I_n^{pw}]$ DUE TO INCIDENT PLANEWAVE AT CERTAIN ANGLE

WHERE: $(P_n^i)_k^p = < f_k(t)\, e^{-jn\phi}\, \mathbf{p}\, ,\, \mathbf{m}_i >$

T = TRANSPOSE
* = COMPLEX CONJUGATE
n = FOURIER MODE INDEX

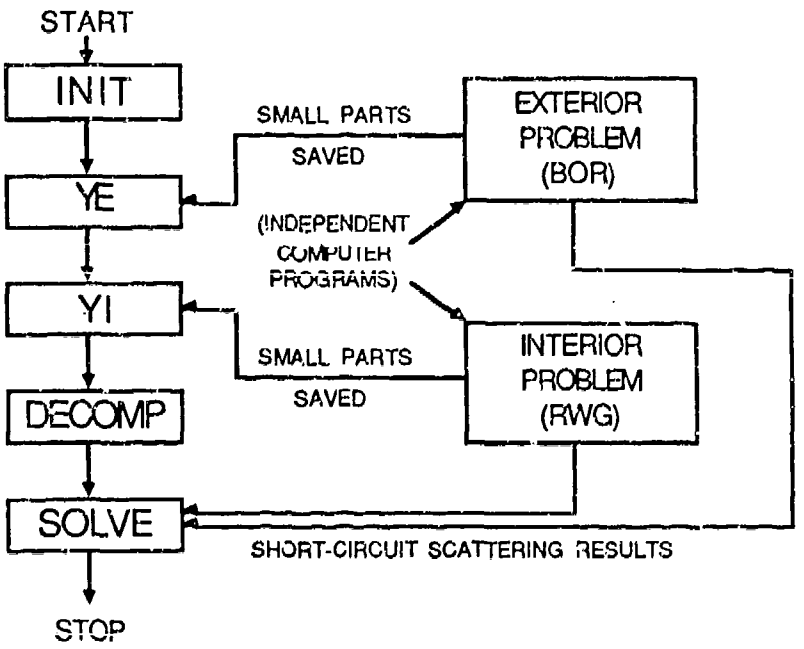
Given the exterior and interior regions as previously described, we have implemented a computer program which solves the system matrix equstions for either exterior or interior excitations. A flow chart of this program is illustrated below:

PROGRAM FLOW CHART



The main part of the calculations are in the blocks YE and YI, each of which calculate admittance matrix elements, excitation matrix elements and the short-circuit scattering matrix elements (apertures shorted) appropriate for each region. As implemented, the minimum storage allocation required is dominated by the system admittance matrix, Y, and the normalized BOR matrices Z_n and Y_n, all of which must be stored in core simultaneously.

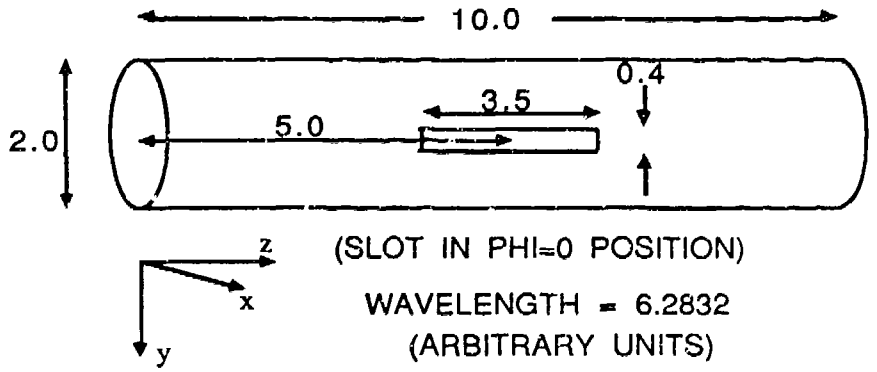
A possibly better organization of the program is illustrated in the flow chart below.



Here, the exterior and interior equivalent problems are solved by independent programs which save only the short-circuit scattering results and those parts of the matrices needed to calculate the admittance and excitation elements. For many situations of multiple small apertures on a large BOR, these parts that are needed to be saved are far smaller than total core storage required in performing the exterior (or interior) calculations, especially if the region is particulary complex with multiple dielectric layers, etc. Thus it may make sense to break up the network computer program into a series of independent programs, with a separate program to make the connection.

4.0 Example

The computer program is currently being used for some preliminary calculations which appear promising. An example is for a waveguide-fed aperture on a conducting cylinder, illustrated below.



APERTURE BASIS FUNCTION: TE10 MODE FIELD FUNCTION

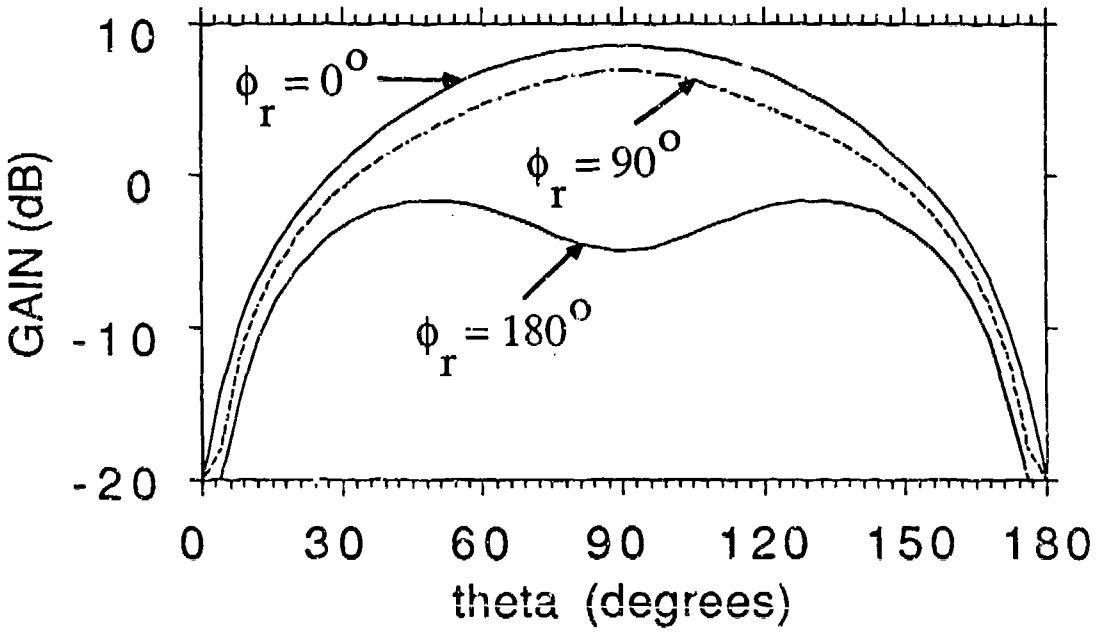


Some of the results for both interior and exterior excitations are shown in the figure on the next page. For the exterior radiation calculations (internal excitation) three different phi-planes for the gain pattern are shown. For the exterior scattering, only the phi-phi polarization pattern in the phi=0 plane is shown. The plot displays the short-circuited-aperture results, the magnetic current (aperture) contribution and the coherent total.

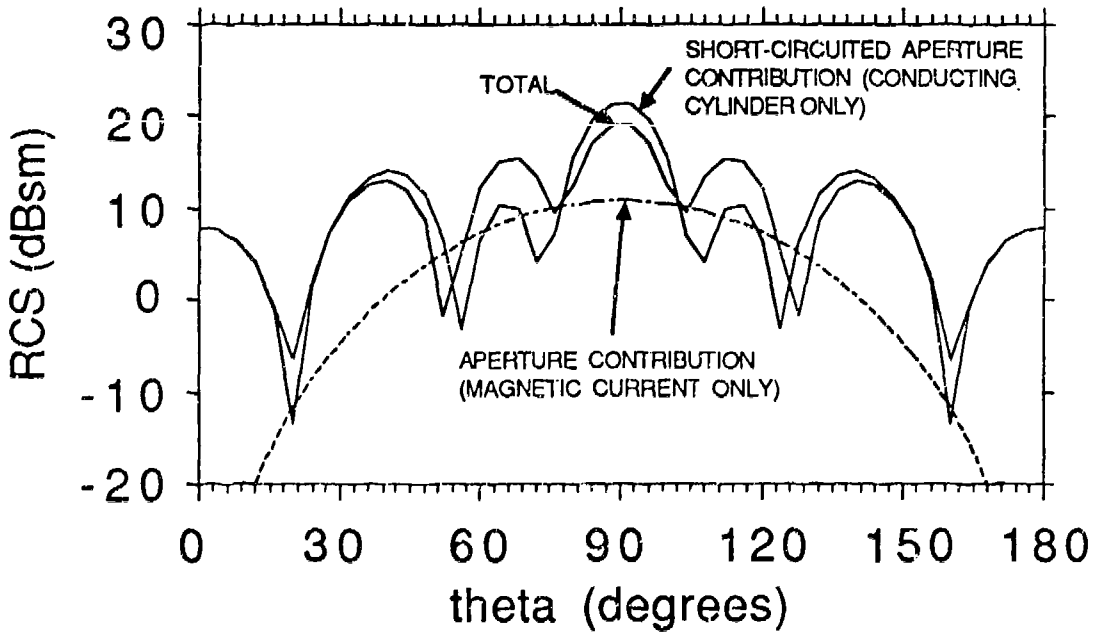
5.0 Conclusions

The network approach as described by Harrington appears to be a very useful way to construct electromagnetic solutions to problems involving small apertures on large complex bodies. Also, the approach is very useful for combining different types of analyses into electromagnetic solutions; e.g., series solutions in one region and method of moments solutions in another. We have implemented a very modular computer program for waveguide-fed apertures on a conducting body of revolution BOR. The usefulness of the computer program appears to be when design issues require that a small part of the problem (such as the aperture or dielectric parameters of the waveguide) is to be varied repeatedly

EXTERIOR RADIATION PATTERN
INTERNAL WAVEGUIDE MODE EXCITATION



EXTERIOR SCATTERING PATTERN
EXTERIOR PLANEWAVE EXCITATION



while a large part of the problem (such as the exterior region) remains constant. Initial results appear promising, but the accuracy of the implementation is yet to be tested.

Our analysis and computer program is structured so as to be able to incorporate more general waveguide and exterior regions for which we have existing computer codes, devloped in-house. These include traveling-wave fed, thick slots with multilayered dielectrics as the interior region and multilayered dielectric/resitive shell and impedance BORs for the exterior region. After fully developing the network computer program, we plan to incorporate these more general modules.

SESSION VII - "CAVITIES INTERACTIONS AND TRANSMISSION"

Moderator: Dawson Coblin
Lockheed Missiles and Space Company

"FITPAK - A Finite Integration Technique Package For Numerical Solution of Interior Electromagnetic Boundary Value Problems"
J. Lebaric — Rose-Hulman Institute of Technology
D. Kajfez — University of Mississippi
* Paper was not submitted and is not presented.

"A Computational Model for Electromagnetic Interactions with Advanced Composites"
H.A. Sabbagh, T.M. Roberts, J.C. Treece, L.D. Sabbagh — Sabbagh Associates Inc.

"A Computational Model of Eddy-Current Probes Over a Stratified Composite Workpiece"
H.A. Sabbagh, L.D. Sabbagh, J.R. Bowler — Sabbagh Associates Inc.

"Comparison of Soil Models with Frequency-Dependent Constitutive Parameters"
J.W. Williams and G.D. Rensner — Science Applications International Corp.

"MULTINEC - A MININEC Modification For Analysis of Multiconductor Transmission Lines"
J.E. Lebaric, J.A. Allred, T.M. Cantrell, C. Pfeifer and D.W. Yergeau — Rose-Hulman Institute of Technology
* Paper was not submitted and is not presented.

"Analysis of Large Parallel-Plate EMP Simulators Using the Numerical Electromagnetics Code (NEC)"
S. Gedney and R. Mittra — University of Illinois

A COMPUTATIONAL MODEL FOR ELECTROMAGNETIC INTERACTIONS WITH ADVANCED COMPOSITES[1]

L. David Sabbagh
Thomas M. Roberts
Denis J. Radecki
Jeffrey C. Treece
Harold A. Sabbagh

Sabbagh Associates, Inc.
4639 Morningside Drive
Bloomington, IN 47401

I. INTRODUCTION

In a previous paper (H. A. Sabbagh, *et al, 2nd Annual ACES Conference Proceedings*, March 18-20, 1986), [1], we presented a model for computing electromagnetic interactions with advanced composites, specifically graphite-epoxy. That model, which was developed for use in eddy-current nondestructive evaluation (NDE), has now been extended to include the effects of lay-ups of arbitrary order, i.e., in which the principal axes of each layer may be rotated from layer-to-layer. In addition, an equivalent 'bulk model' has been developed, in which the multi-layer composite slab is replaced by a single layer with an effective single-layer conductivity tensor.

In this paper we will describe the extended model, and discuss its validation using experimental eddy-current data.

II. COMPUTING A NUMERICAL GREEN'S FUNCTION FOR A HALFSPACE

In this section, we develop a computational method for generating the Green's function for a halfspace. The approach we use is based on our need to generalize to workpieces of finite extent in the z-direction and to multi-layered anisotropically-conducting media.

Using the results in [1] for S_{14}, S_{24}, S_{32}, and S_{31} and the eigenvalues $\pm\lambda_1$ and $\pm\lambda_3$, we make the following definitions:

$$\begin{array}{llll} \alpha_1 = S_{14}/\lambda_1, & \alpha_{10} = S_{140}/\lambda_0, & \alpha_2 = S_{24}/\lambda_1, & \alpha_{20} = S_{240}/\lambda_0, \\ \gamma_1 = S_{32}/\lambda_3, & \gamma_{10} = S_{320}/\lambda_0, & \gamma_2 = S_{31}/\lambda_3, & \gamma_{20} = S_{310}/\lambda_0. \end{array} \tag{1}$$

Using the expressions in (1), the eigenvectors in the medium are:

$$\bar{v}_1 = \begin{pmatrix} \alpha_1 \\ \alpha_2 \\ 0 \\ 1 \end{pmatrix}, \quad \bar{v}_2 = \begin{pmatrix} -\alpha_1 \\ -\alpha_2 \\ 0 \\ 1 \end{pmatrix}, \quad \bar{v}_3 = \begin{pmatrix} 0 \\ 1 \\ \gamma_1 \\ -\gamma_2 \end{pmatrix}, \quad \bar{v}_4 = \begin{pmatrix} 0 \\ 1 \\ -\gamma_1 \\ \gamma_2 \end{pmatrix}, \tag{2}$$

while the eigenvectors in free space are :

[1]Supported by The Naval Surface Weapons Center (White Oak Labs) under Contract No. N60921-86-C-0172, and The Naval Air Systems Command under Contract No. N00019-86-C-0219, both with Sabbagh Associates.

$$\bar{v}_{10} = \begin{pmatrix} \alpha_{10} \\ \alpha_{20} \\ 0 \\ 1 \end{pmatrix}, \quad \bar{v}_{20} = \begin{pmatrix} -\alpha_{10} \\ -\alpha_{20} \\ 0 \\ 1 \end{pmatrix}, \quad \bar{v}_{30} = \begin{pmatrix} 0 \\ 1 \\ \gamma_{10} \\ -\gamma_{20} \end{pmatrix}, \quad \bar{v}_{40} = \begin{pmatrix} 0 \\ 1 \\ -\gamma_{10} \\ \gamma_{20} \end{pmatrix}. \tag{3}$$

In the present development, there are three regions; Region A is above the source, Region B is between the source and the halfspace and Region C is in the halfspace. If we assume the source is at $z' > 0$ and the halfspace is located at $z = 0$, then the Green's function becomes,

$$\tilde{G}(z,z') = \begin{cases} a\bar{v}_{20}e^{-\lambda_0(z-z')} + b\bar{v}_{40}e^{-\lambda_0(z-z')}, & z' < z \\ c\bar{v}_{10}e^{\lambda_0(z-z')} + d\bar{v}_{20}e^{-\lambda_0(z-z')} \\ \quad + e\bar{v}_{30}e^{\lambda_0(z-z')} + f\bar{v}_{40}e^{-\lambda_0(z-z')}, & 0 < z < z' \\ c'\bar{v}_1e^{\lambda_1 z} + e'\bar{v}_3e^{\lambda_3 z} & z < 0 \end{cases} \tag{4}$$

The eight unknowns a, b, c, d, e, f, c', e' in each column vector are computed with the aid of four boundary conditions at the halfspace-air boundary and four boundary conditions at the location of the source. Thus, singly Green's matrices can be computed by solving 8×8 systems of equations. However, by carefully examining the conditions at the source, we see that the c and e are computed from the source values and that a is a function of d while b is a function of f. Hence, we can reduce the computation to solving an 4×4 system for d, f, c', e'.

The two tables below give the expressions for a, b, c, e in terms of their values and functional relationships with d and f.

Magnetic Sources

coefficient	x–directed	y–directed	z–directed
c	0	$-1/2\alpha_{10}$	$(\gamma_{20}k_x + \gamma_{10}k_y)/2\omega\mu_0\gamma_{10}$
a	d	$d - 1/2\alpha_{10}$	$d - (\gamma_{20}k_x + \gamma_{10}k_y)/2\omega\mu_0\gamma_{10}$
e	$1/2$	$\alpha_{20}/2\alpha_{10}$	$k_x/2\omega\mu_0\gamma_{10}$
b	$f - 1/2$	$f - \alpha_{20}/2\alpha_{10}$	$f + k_x/2\omega\mu_0\gamma_{10}$

Electric Sources

coefficient	x–directed	y–directed	z–directed
c	$1/2$	$-\gamma_{20}/2\gamma_{10}$	$-k_x/2\alpha_{10}\omega k_{33}$
a	$d - 1/2$	$d + \gamma_{20}/2\gamma_{10}$	$d - k_x/2\alpha_{10}\omega k_{33}$
e	0	$-1/2\gamma_{10}$	$-(\alpha_{10}k_y - \alpha_{20}k_x)/2\omega\alpha_{10}k_{33}$
b	f	$f - 1/2\gamma_{10}$	$f + (\alpha_{10}k_y - \alpha_{20}k_x)/2\omega\alpha_{10}k_{33}$

The actual 4 × 4 system that we solve is

$$SX = Y, \tag{5}$$

with

$$\begin{aligned} S &= \left(\bar{v}_{20},\ \bar{v}_{40},\ -\bar{v}_1,\ -\bar{v}_3 \right) \\ X &= \left(\tilde{d},\ \ ,\ \ ,\ e' \right)^T \\ Y &= \left(-\bar{v}_{10}c - \bar{v}_{30}e\right) e^{-\lambda_0 z'} \\ \tilde{d} &= de^{\lambda_0 z'},\ \ \tilde{f} = fe^{\lambda_0 z'} \end{aligned} \tag{6}$$

Note that the right hand side, Y, is a function of the source type, magnetic or electric, and the direction of the source, x–, y–, or z–.

The solution of (5) gives $\tilde{d}$ $(\rightarrow d)$, $\tilde{f}$ $(\rightarrow f)$, c', and e'. From d and f, we can find a and b thus giving all coefficients in (4).

If all we desire is the reflection coefficients, which are $de^{2\lambda_0 z'}$ and $fe^{2\lambda_0 z'}$, then we solve the system

$$\left(\bar{v}_{20},\ \bar{v}_{40},\ -\bar{v}_1,\ -\bar{v}_3 \right) \begin{pmatrix} x_1 \\ x_2 \\ x_3 \\ x_4 \end{pmatrix} = -\bar{v}_{10}c - \bar{v}_{30}e \tag{7}$$

for x_1 and x_2.

III. COMPUTING A GREEN'S FUNCTION FOR A FINITE WORKPIECE

In this section, we extend our method to workpieces of finite extent in the z-direction. The expressions (1), (2) and (3) are still valid but (4) changes due to an extra region, Region D which is below the workpiece. We assume that the workpiece thickness is z_w and that it satisfies $-z_w < z < 0$.

The Green's function now becomes:

$$\tilde{G}(z,z') = \begin{cases} a\bar{v}_{20}e^{-\lambda_0(z-z')} + b\bar{v}_{40}e^{-\lambda_0(z-z')}, & z' < z \\ c\bar{v}_{10}e^{\lambda_0(z-z')} + d\bar{v}_{20}e^{-\lambda_0(z-z')} \\ \quad + e\bar{v}_{30}e^{\lambda_0(z-z')} + f\bar{v}_{40}e^{-\lambda_0(z-z')}, & 0 < z < z' \\ c'\bar{v}_1e^{\lambda_1 z} + d'\bar{v}_2e^{-\lambda_1 z} + e'\bar{v}_3e^{\lambda_3 z} + f'\bar{v}_4e^{-\lambda_3 z}, & -z_w < z < 0 \\ g\bar{v}_{10}e^{\lambda_0(z+z_w)} + h\bar{v}_{30}e^{\lambda_0(z+z_w)}. & z < -z_w \end{cases} \tag{8}$$

Again using the boundary conditions and the conditions at the source, we can find the unknowns by solving an 8 × 8 system of equations for $d, f, c', e', d', f', g, h$ and then use the table for Magnetic Sources or Electric Sources to find c, a, e, b. The actual 8 × 8 system that we solve is

$$SX = Y, \tag{9}$$

where

$$\mathcal{S} = \begin{pmatrix} R_1 & -S & 0_{4\times 2} \\ 0_{4\times 2} & SE_{13} & -R_2 \end{pmatrix} \tag{10}$$

and

$$\begin{aligned} R_1 &= \begin{pmatrix} \bar{v}_{20}, & \bar{v}_{40} \end{pmatrix} \\ R_2 &= \begin{pmatrix} \bar{v}_{10}, & \bar{v}_{30} \end{pmatrix} \\ S &= \begin{pmatrix} \bar{v}_1, & \bar{v}_3, & \bar{v}_2, & \bar{v}_4 \end{pmatrix} \\ E_{13} &= \begin{pmatrix} e^{-\lambda_1 z_w} & 0 & 0 & 0 \\ 0 & e^{-\lambda_3 z_w} & 0 & 0 \\ 0 & 0 & e^{\lambda_1 z_w} & 0 \\ 0 & 0 & 0 & e^{\lambda_3 z_w} \end{pmatrix} \\ X &= \begin{pmatrix} \tilde{d}, & \tilde{f}, & c', & e', & d', & f', & g, & h \end{pmatrix}^T \\ Y &= \begin{pmatrix} -\bar{v}_{10}c - \bar{v}_{30}e \\ 0_{4\times 1} \end{pmatrix} e^{-\lambda_0 z'} \end{aligned} \tag{11}$$

Again, if all we desire is the reflection coefficients, then solve the above equation for the first two unknowns with $e^{-\lambda_0 z'}$ omitted from Y.

The equation (9) is ill-conditioned as it is defined, hence we must do some scaling in order to get meaningful results. Examination of $\mathcal{S}$ shows that column 5 is multiplied by $e^{\lambda_1 z_w}$ and column 6 by $e^{\lambda_3 z_w}$. If we divide these columns by the exponential factors, $\mathcal{S}$ is better conditioned which allows us to solve for X. This, of course, means that the 5^{th} and 6^{th} positions in the solution must be 'unscaled' which is accomplished by dividing these positions by $e^{\lambda_1 z_w}$ and $e^{\lambda_3 z_w}$, respectively.

IV. COMPUTING A GREEN'S FUNCTION FOR A LAYERED WORKPIECE

In this section, we extend our method to workpieces of finite extent in the z-direction that are layered. Again there are four regions; however Region C is now divided into, say 10, subregions which are defined as follows:

Layer 1:	$z_1 < z < z_0 = 0$
Layer 2:	$z_2 < z < z_1$
$\vdots$	$\vdots$
Layer 10:	$-z_w = z_{10} < z < z_9$

The Green's function now becomes:

$$\tilde{G}(z,z') = \begin{cases} a\bar{v}_{20}e^{-\lambda_0(z-z')} + b\bar{v}_{40}e^{-\lambda_0(z-z')}, & z' < z \\ c\bar{v}_{10}e^{\lambda_0(z-z')} + d\bar{v}_{20}e^{-\lambda_0(z-z')} & \\ \quad + e\bar{v}_{30}e^{\lambda_0(z-z')} + f\bar{v}_{40}e^{-\lambda_0(z-z')}, & 0 < z < z' \\ c^{(i)}\bar{v}_1^{(i)}e^{\lambda_1(z-z_{i-1})} + d^{(i)}\bar{v}_2^{(i)}e^{-\lambda_1(z-z_{i-1})} & \\ \quad + e^{(i)}\bar{v}_3^{(i)}e^{\lambda_2(z-z_{i-1})} + f^{(i)}\bar{v}_4^{(i)}e^{-\lambda_2(z-z_{i-1})}, & z_i < z < z_{i-1}, i = 1,\ldots,10 \\ g\bar{v}_{10}e^{\lambda_0(z+z_w)} + h\bar{v}_{30}e^{\lambda_0(z+z_w)} & z < -z_w \end{cases} \tag{12}$$

Again using the boundary conditions and the conditions at the source, we can find the unknowns by solving (in the case of 10 layers) a 44×44 system of equations for d, f, $c^{(1)}$, $e^{(1)}$, $d^{(1)}$, $f^{(1)}$, $\ldots$, $c^{(10)}$, $e^{(10)}$, $d^{(10)}$, $f^{(10)}$, g, h and then use the table for Magnetic Sources or Electric Sources to find c, a, e, b. In general, if there are n_l layers, then the system to solve is $(4n_l + 4) \times (4n_l + 4)$. The form of this system is:

$$SX = Y, \tag{13}$$

where

$$S = \begin{pmatrix} R_1 & -S^{(1)} & 0_{4\times4} & 0_{4\times4} & \cdots & 0_{4\times4} & 0_{4\times4} & 0_{4\times2} \\ 0_{4\times2} & S^{(1)}E^{(1)} & -S^{(2)} & 0_{4\times4} & \cdots & 0_{4\times4} & 0_{4\times4} & 0_{4\times2} \\ 0_{4\times2} & 0_{4\times4} & S^{(2)}E^{(2)} & -S^{(3)} & \cdots & 0_{4\times4} & 0_{4\times4} & 0_{4\times2} \\ \vdots & \vdots & \vdots & \vdots & \ddots & -S^{(9)} & 0_{4\times4} & 0_{4\times2} \\ 0_{4\times2} & 0_{4\times4} & 0_{4\times4} & 0_{4\times4} & \cdots & S^{(9)}E^{(9)} & -S^{(10)} & 0_{4\times2} \\ 0_{4\times2} & 0_{4\times4} & 0_{4\times4} & 0_{4\times4} & \cdots & 0_{4\times4} & S^{(10)}E^{(10)} & -R_2 \end{pmatrix} \tag{14}$$

with the terms not previously defined being

$$\begin{aligned} S^{(i)} &= \begin{pmatrix} \bar{v}_1^{(i)}, & \bar{v}_3^{(i)}, & \bar{v}_2^{(i)}, & \bar{v}_4^{(i)} \end{pmatrix} \\ E^{(i)} &= \begin{pmatrix} e^{\lambda_1 h_i} & 0 & 0 & 0 \\ 0 & e^{\lambda_2 h_i} & 0 & 0 \\ 0 & 0 & e^{-\lambda_1 h_i} & 0 \\ 0 & 0 & 0 & e^{-\lambda_2 h_i} \end{pmatrix} \\ h_i &= z_i - z_{i-1}, \\ X &= (\tilde{d}, \tilde{f}, c^{(1)}, e^{(1)}, d^{(1)}, f^{(1)}, \ldots, \\ &\quad c^{(10)}, e^{(10)}, d^{(10)}, f^{(10)}, g, h)^T \\ Y &= \begin{pmatrix} -\bar{v}_{10}c - \bar{v}_{30}e \\ 0_{40\times1} \end{pmatrix} e^{-\lambda_0 z'} \end{aligned} \tag{15}$$

Again, if all we desire is the reflection coefficients, then solve the above equation for the first two unknowns with $e^{-\lambda_0 z'}$ omitted from Y.

As before, equation (13) is ill-conditioned as it is defined. The columns of S that contain the factors $e^{-\lambda_1 h_i}$ and $e^{-\lambda_2 h_i}$ (remember, $h_i < 0$) are the ones that need to be scaled and this

is done by dividing these columns by the exponential factors. Again, we must be sure that the corresponding positions in the solution vector are 'unscaled' to give the correct solution.

Careful examination of $\mathcal{E}$ shows that it is a banded matrix with its upper bandwidth $m_u = 5$, its lower bandwidth $m_l = 5$ and its (total) $m = m_u + m_l + 1 = 11$. We used subroutines **zgbco** and **zgbsl** from **LINPACK** to solve the system.

Up to this point, we have assumed that all layers are oriented in the same direction with respect to a global coordinate system. Let us now suppose that each layer can be rotated. Since eigenvalues are unchanged aud eigenvectors are merely transformed by the rotation, it is straight forward to set up the equations in this situation. The rotation matrix in this case is

$$\mathcal{T}(\theta) = \begin{pmatrix} \mathcal{R}(\theta) & 0_{2\times 2} \\ 0_{2\times 2} & \mathcal{R}(\theta) \end{pmatrix}$$

where

$$\mathcal{R}(\theta) = \begin{pmatrix} \cos(\theta) & \sin(\theta) \\ -\sin(\theta) & \cos(\theta) \end{pmatrix}$$

If we let θ_i be the angle of rotation of the i^{th} layer with respect to the global system, then the eigenvectors for this layer become

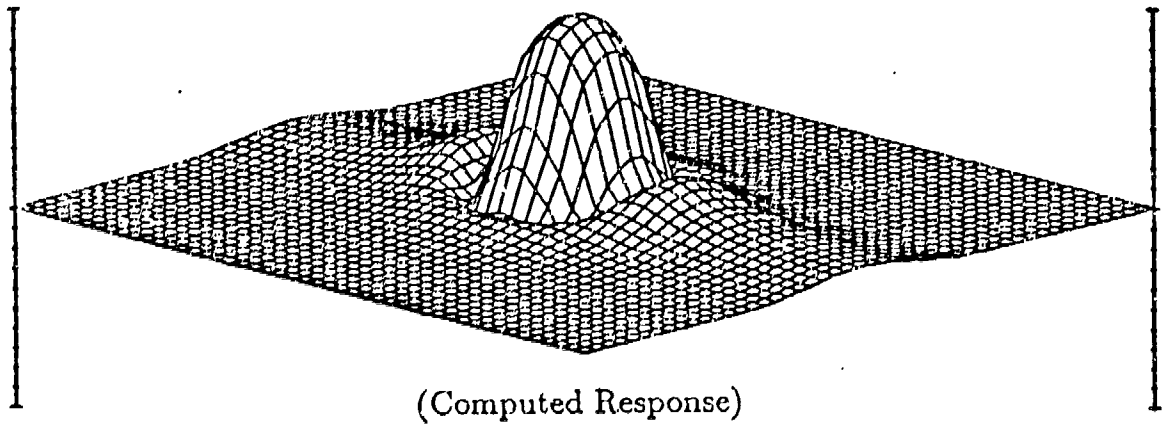
$$v_1^{(i)'} = \mathcal{T}(\theta_i)v_1^{(i)}, \quad v_2^{(i)'} = \mathcal{T}(\theta_i)v_2^{(i)}, \quad v_3^{(i)'} = \mathcal{T}(\theta_i)v_3^{(i)}, \quad v_4^{(i)'} = \mathcal{T}(\theta_i)v_4^{(i)}. \tag{16}$$

and the only change in (13) is the definition of $S^{(i)}$ which becomes,

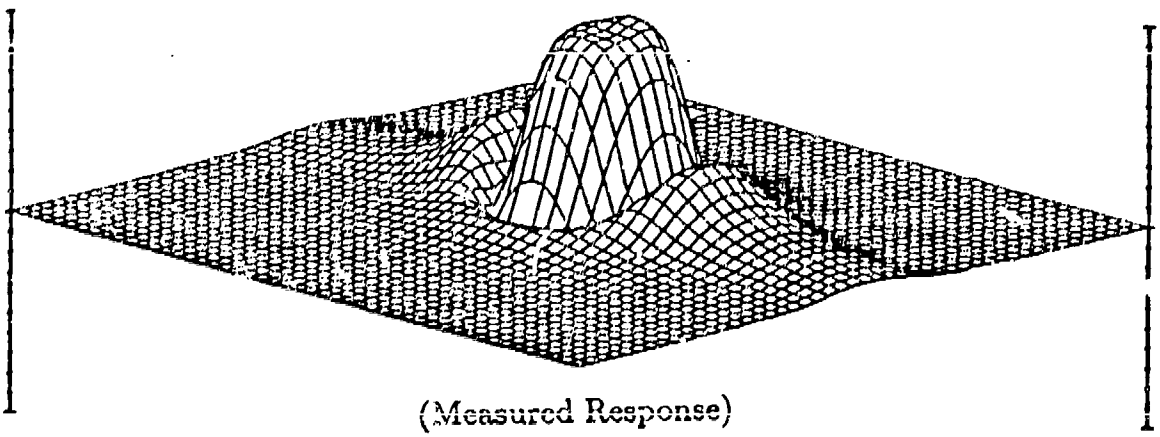
$$\begin{aligned} S^{(i)'} &= \left(v_1^{(i)'}, \; v_3^{(i)'}, \; v_2^{(i)'}, \; v_4^{(i)'} \right) \\ &= \left(\mathcal{T}v_1^{(i)}, \; \mathcal{T}v_3^{(i)}, \; \mathcal{T}v_2^{(i)}, \; \mathcal{T}v_4^{(i)} \right) \end{aligned} \tag{17}$$

This is a general model for the computation of the Green's function and the computation of reflection coefficients that has been implemented into our computer codes. In our model, we have assumed that the conductivities of each layer are the same. However, the generalization to a model where each layer has its own unique conductivities could be easily accomplished by computing the eigenvalues and eigenvectors of each layer in its own 'local' coordinate system and then proceeding with the rotation stage above.

We are constantly attempting to validate our computer models in several ways, one of those ways is comparing computed values with measured values. The figure below shows such a comparison. The workpiece consisted of 18 layers, the first eight at 0°, the ninth and tenth at 90°, and 11–18 at 0°. The results show very good correlation and give us confidence in the model.



(Computed Response)



(Measured Response)

Figure 1. EMF induced into a probe coil due to a circular current loop above a graphite-epoxy workpiece, which consists of eighteen unidirectional layers in a $[0\ 0\ 0\ 0\ 0\ 0\ 0\ 0\ 90]_S$ lay-up. Neither the conductivities of any layer, nor the conductivity of the bulk workpiece, were known. The peak computed value is 3.5V, and the peak measured value is 4.4V.

V. A BULK MODEL

Part 1: Theory

One alternative to modeling layers individually is to model them in bulk with an equivalent single-layer slab. The bulk model is acceptable when wavelengths are larger than a cycle of plys: a condition satisfied in our laboratory by the workpieces and radiative frequencies we use. (Many graphite epoxy layups are built from repeated cycles, with each identical cycle consisting of a few plys of various orientations. The cycle $[+22.5°, -22.5°]$ describes a layup of plys, each with unidirectional fibers, whose orientations alternate between $+22.5°$ and $-22.5°$.) It is computationally more efficient to use the bulk model, rather than the multilayer model, whenever the thin-cycle approximation is satisfied.

The most general conductivity matrix for stratified conductors is

$$\overline{J} = \overline{\overline{\sigma}} \cdot \overline{E}, \qquad \overline{\overline{\sigma}} = \begin{pmatrix} \sigma_{xx} & \sigma_{xy} & 0 \\ \sigma_{yx} & \sigma_{yy} & 0 \\ 0 & 0 & \sigma_{zz} \end{pmatrix}, \tag{5.1}$$

where z is the axis of stratification. A short derivation (see our NSWC Phase 2 Fifth Quarterly Report, Appendix B, pp.18-19) shows that rotating x and y coordinates by an angle θ changes the conductivity matrix as follows:

$$\overline{\overline{\sigma}}'(\theta) = \begin{pmatrix} [c^2\sigma_{xx} + cs(\sigma_{xy} + \sigma_{yx}) + s^2\sigma_{yy}] & [c^2\sigma_{xy} + cs(\sigma_{yy} - \sigma_{xx}) - s^2\sigma_{yx}] & 0 \\ [c^2\sigma_{yx} + cs(\sigma_{yy} - \sigma_{xx}) - s^2\sigma_{xy}] & [c^2\sigma_{yy} - cs(\sigma_{xy} + \sigma_{yx}) + s^2\sigma_{xx}] & 0 \\ 0 & 0 & \sigma_{zz} \end{pmatrix}, \tag{5.2}$$

$c = \cos\theta, \ s = \sin\theta.$

Two examples: a $[+22.5°, -22.5°]$-layup of identical plys is represented by a matrix $\overline{\overline{\sigma}} = \frac{1}{2}[\overline{\overline{\sigma}}'(+22.5°) + \overline{\overline{\sigma}}'(-22.5°)]$; a $[0°, +30°, -45°, -45°]$-layup of identical plys is represented by $\overline{\overline{\sigma}} = \frac{1}{4}[\overline{\overline{\sigma}}'(0°) + \overline{\overline{\sigma}}'(+30°) + 2\overline{\overline{\sigma}}'(-45°)]$.

It is easy to show (see *ibid.*, pp.19-21 and our NSWC Phase 2 Sixth Quarterly Report, Appendix C, pp.1,2) that if the slab is an energy absorber (as opposed to source) then $\sigma_{xy} = \sigma_{yx}$. Given that the matrix in (5.1) is symmetric, it is easy to show that rotation by an angle ϕ—such that $\tan 2\phi = 2\sigma_{xy}/(\sigma_{xx} - \sigma_{yy})$—leads to a diagonal conductivity matrix

$$\overline{\overline{\sigma}}'(\phi) = \begin{pmatrix} \sigma_x & 0 & 0 \\ 0 & \sigma_y & 0 \\ 0 & 0 & \sigma_z \end{pmatrix} \tag{5.3}$$

with nonnegative elements $\sigma_x, \sigma_y, \sigma_z$. The angle ϕ defines a principal coordinate system.

It is for conceptual simplicity that we showed general layered conductors have diagonal conductivity matrices, up to rotations. In our bulk model, however, it is just as easy to use conductivities (5.1) as it is to use (5.3); we treat the more general case.

We will not repeat here the details of the eigenmode technique developed in our NSWC Phase 1 Final Report. We will show only how to compute eigenmodes. In our eigenmode technique, a four-component eigenvector v_λ and its eigenvalue λ represent a travelling wave according to the

code $(\tilde{E}_x, \tilde{E}_y, \tilde{H}_x, \tilde{H}_y)^T = \bar{v}_\lambda e^{\lambda z + i\omega t}$, where tilde denotes Fourier transformation with respect to x and y; each conductor has four such eigenmodes. There is a method for selecting the linear combination of eigenmodes that represents radiation due to a point current in the presence of a slab—the linear combination defines a so-called Green's matrix. The field due to a distributed current is the integral, evaluated over point sources in the distribution, of the field due to point sources. Thus, eigenmodes are at the heart of field computation for arbitrary currents in the presence of anisotropic conductors.

Fourier analysis yields a matrix $\overline{\overline{S}}$

$$\overline{\overline{S}} = \begin{pmatrix} 0 & 0 & -a & -b \\ 0 & 0 & -c & -d \\ -\alpha & -\beta & 0 & 0 \\ -\gamma & -\delta & 0 & 0 \end{pmatrix}$$

$$-a = \frac{-ik_x k_y}{\omega \varepsilon_z}, \qquad -b = -i\mu_0\omega + i\frac{k_x^2}{\omega\varepsilon_z},$$
$$-c = i\mu_0\omega - i\frac{k_y^2}{\omega\varepsilon_z}, \qquad -d = i\frac{k_x k_y}{\omega\varepsilon_z},$$
$$-\alpha = i\omega\varepsilon_{yx} + i\frac{k_x k_y}{\mu_0\omega}, \qquad -\beta = i\omega\varepsilon_y - i\frac{k_x^2}{\mu_0\omega},$$
$$-\gamma = -i\omega\varepsilon_x + i\frac{k_y^2}{\mu_0\omega}, \qquad -\delta = -i\omega\varepsilon_{xy} - i\frac{k_x k_y}{\mu_0\omega},$$

$$\varepsilon_x = \varepsilon_0 - i\frac{\sigma_{xx}}{\omega},\ \varepsilon_y = \varepsilon_0 - i\frac{\sigma_{yy}}{\omega}\ \varepsilon_{xy} = \varepsilon_0 - i\frac{\sigma_{xy}}{\omega};\ \varepsilon_{yx} = \varepsilon_0 - i\frac{\sigma_{yx}}{\omega},\ \text{and}\ \varepsilon_z = \varepsilon_0 - i\frac{\sigma_{zz}}{\omega} \qquad (5.4)$$

whose eigenvectors and eigenvalues lead to eigenmodes. An elementary derivation (see our NSWC Phase 2 Fifth Quarterly Report, Appendix B, pp. 22,23) shows that the four eigenvalues $(\pm\lambda_1, \pm\lambda_3)$ of $\overline{\overline{S}}$ may be computed in just a few steps:

$$\Delta_a = \det\begin{pmatrix} a & b \\ c & d \end{pmatrix},\ \Delta_\alpha = \det\begin{pmatrix} \alpha & \beta \\ \gamma & \delta \end{pmatrix},\ \text{and}\ \Sigma = a\alpha + b\gamma + c\beta + d\delta.$$
$$r_1 = \frac{1}{2}\left(\Sigma + \sqrt{\Sigma^2 - 4\Delta_a\Delta_\alpha}\right)\ \text{and}\ r_2 = \frac{1}{2}\left(\Sigma - \sqrt{\Sigma^2 - 4\Delta_a\Delta_\alpha}\right). \qquad (5.5)$$
$$\text{If } |r_1| > |r_2| \text{ then } j = 1; \text{ otherwise } j = 2.$$
$$\pm\lambda_1 = \pm\sqrt{r_j}\ \text{and}\ \pm\lambda_3 = \pm\sqrt{\frac{\Delta_a\Delta_\alpha}{r_j}}.$$

There is an algorithm for computing explicitly the eigenvectors of $\overline{\overline{S}}$. (See our NSWC Phase 2 Fifth Quarterly Report, Appendix B, pp.24,25.) The eigenvector algorithm is as elementary and as straightforward as the eigenvalue algorithm.

Part 2: Partial Verification

The bulk model can be used to predict fields due to an arbitrary current in the presence of an anisotropic slab, provided the conductivity of the slab is known. Sabbagh Associates owns anisotropic workpieces (±22.5° layups of graphite epoxy) but has no "tried and true" means of

measuring nondestructively their anisotropic conductivities. We used the bulk model to infer the conductivity of workpieces and thereby verified indirectly the validity of the bulk model.

In the laboratory, a 1MHz alternating current loop was placed above a graphite epoxy workpiece and a pickup coil scanned over loop and slab. The resulting measurements are plotted in Figure B1 (left). Theoretical computations were performed for the laboratory setup (including physical parameters such as radius and position of current and pickup coils, and the thickness of the workpiece) for theoretical $\pm 22.5°$ layups of various total conductivities. The bulk conductivity that best reconstructed the experimental data had $\sigma_x = 6000\frac{S}{m}$ and $\sigma_y = 1000\frac{S}{m}$; the theoretical reconstruction is in Figure B1 (right). (The reconstruction is insensitive to σ_z in the range from $1\frac{S}{m}$ through at least $1000\frac{S}{m}$.) The inferred conductivity corresponds to a $\pm 22.5°$ layup of unidirectional plys that each has conductivity $\sigma_x = 7000\frac{S}{m}$ and $\sigma_y = 0\frac{S}{m}$; $\sigma_y = 0$ is reasonable for our workpieces because high resin denisty between fiber tows affects the transverse conductivity as resistors in series, zeroing the bulk transverse conductivity. The short-cycle bulk approximation is satisfied because the computed 1MHz wavelengths ($2\pi/\mathrm{Im}\lambda_1$ =10cm and $2\pi/\mathrm{Im}\lambda_3$ =4cm) are much longer than the $\approx$.02cm cycle length.

Figure B1 represents a partial verification of the bulk model because it shows that the model can reconstruct experimental data, with the aid of some parameter fitting. The result of parameter fitting is a conductivity inference that yields conductivities in the right "ballpark" for graphite epoxy. The verification in Figure B1 is not total because we have not compared conductivities inferred from eddy-current measurements to tried and true conductivity measurements.

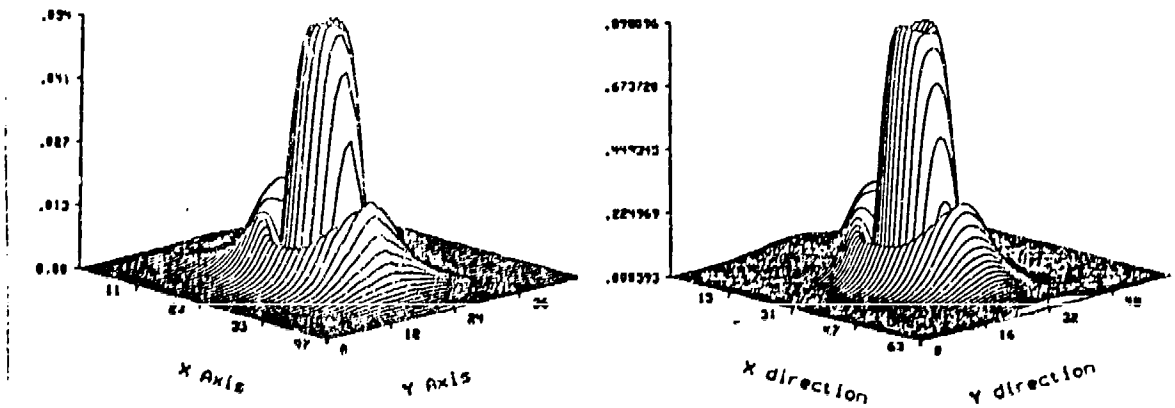


Figure B1. Magnitude of EMF at 1MHz for a $\pm 22.5°$ layup. The experimental data (left) is in units of A/D counts. The theoretical reconstruction (right) is in units of volts and assumes a 1A current in the circular exciting loop.

A COMPUTATIONAL MODEL OF EDDY-CURRENT PROBES OVER A STRATIFIED COMPOSITE WORKPIECE*

John R. Bowler
Harold A. Sabbagh
L. David Sabbagh
Sabbagh Associates, Inc.
4639 Morningside Drive
Bloomington, IN 47401

Introduction

The design of eddy-current probe coils is important in the quantitative nondestructive evaluation (NDE) of advanced composite materials, such as graphite-epoxy. Much of the present state of the art in the design of such probes is empirical, or based on elementary circuit-theoretic models. These models do not yield as much information as a designer needs, even when the workpiece is a 'classical material', such as stainless steel. In the presence of the newer composite materials, the problem becomes exacerbated because a large proportion of these are anisotropic, and many of the conventional design rules-of-thumb become useless.

We are developing a computer code that will allow the designer of probes to compute fields within a multi-layer composite workpiece, and to determine such important probe parameters as impedance and coupling. The model will be fully three-dimensional and will include the effects of ferrite cores and shielding. It is based on a volume integral equation that is solved iteratively using conjugate gradients and FFT techniques. Problems with 12,000 unknowns are being routinely solved on the Alliant FX/1 minisupercomputer, in reasonable times. In this paper we will briefly outline the electromagnetic, computational and graphics aspects of the model and code. In addition, we will describe the first validation steps, which involve code-comparison and convergence-of-solution criteria.

Ferrite-Core Probe Model

(a) Integral Equation for the Magnetisation

In our previous work[1-4], we have developed a model of a ferrite-core probe over a planar stratified workpiece as illustrated in Figure 1. In this model, which was developed for NDE, the field computations require the known currents in the coils and the unknown 'Amperian currents' due to the magnetization of the ferrite core. Hence, we include a magnetic current source, $\mathbf{J}_m = -j\omega\mu_0\mathbf{M}$ to account for the presence of the ferrite. With two distinct current source types and the surface of the workpiece in the plane $z = 0$, the magnetic field has the form

$$\mathbf{H}(\mathbf{r}) = \int_{coil+core} [\mathbf{G}^{(me)}(\mathbf{r}|\mathbf{r}') \cdot \mathbf{J}_e(\mathbf{r}') + \mathbf{G}^{(mm)}(\mathbf{r}|\mathbf{r}') \cdot \mathbf{J}_m(\mathbf{r}')]d\mathbf{r}', \qquad (1)$$

$\mathbf{J}_e$ being the coil current. The first superscript on the Green's tensors, $\mathbf{G}^{(me)}$ and $\mathbf{G}^{(mm)}$, indicates the type of field (m for magnetic and e for electric) and the second the nature of the source current. These tensors depend partly on the structure and material properties of the workpiece since such factors will determine the reflected field. In fact all the relevant effects of the workpiece are embodied in a set of reflection coefficients contained in the above Green's functions. In the most general case we have encoded, a laminated composite material is modeled as a multi-layered anisotropic slab structure and the reflection coefficients computed accordingly. Simpler structures can also be accomodated; for example by putting the reflection coefficients to zero, we compute the magnetisation of the core in free space.

The first term under the integral in (1) is the incident magnetic field, $\mathbf{H}^{(i)}$, produced by the prescribed electric currents in the coil. $\mathbf{H}^{(i)}$ is given independently of the ferrite core and is therefore independent of $\mathbf{M}$ or $\mathbf{J}_m$. Hence, assuming a nonconducting core,

$$\mathbf{H}(\mathbf{r}) = \mathbf{H}^{(i)}(\mathbf{r}) + \int_{core} \mathbf{G}^{(mm)}(\mathbf{r}|\mathbf{r}') \cdot \mathbf{J}_m(\mathbf{r}')d\mathbf{r}'. \tag{2}$$

Our aim is to define a volume integral equation for computing the core magnetisation, preferably in such a way that a numerical solution may be found even in cases where the ferrite permeability is infinite. In most practical situations the relative permeabilty of the ferrite used in eddy-current probes is fairly large, typically in the range 200 to 2000, and it is useful to get infinite permeability solution for comparison. To derive the desired equation, we put $\mathbf{H}(\mathbf{r}) = \mathbf{B}(\mathbf{r})/\mu_0 - \mathbf{M}(\mathbf{r})$, so that (2) becomes

$$\begin{aligned} \frac{\mathbf{B}^{(i)}(\mathbf{r})}{\mu_0} &= \frac{\mathbf{B}(\mathbf{r})}{\mu_0} - \mathbf{M}(\mathbf{r}) + j\omega\mu_0 \int_{core} \mathbf{G}^{(mm)}(\mathbf{r}|\mathbf{r}') \cdot \mathbf{M}(\mathbf{r}')d\mathbf{r}' \\ &= \frac{\mathbf{B}(\mathbf{r})}{\mu_0} + j\omega\mu_0 \int_{core} \left[\mathbf{G}^{(mm)}(\mathbf{r}|\mathbf{r}') - \frac{\delta(\mathbf{r}-\mathbf{r}')}{j\omega\mu_0}\mathbf{I}\right] \cdot \mathbf{M}(\mathbf{r}')d\mathbf{r}'. \end{aligned} \tag{3}$$

$\mathbf{I}$ being the unit tensor. Then multiplying (3) by $\nu = (1 - \mu_0/\mu)$, and using the fact that $\mathbf{M} = (\mathbf{B}/\mu_0)(1 - \mu_0/\mu)$, gives

$$\mathbf{M}^{(i)}(\mathbf{r}) = \mathbf{M}(\mathbf{r}) + j\omega\mu_0\nu(\mathbf{r}) \int_{core} \left[\mathbf{G}^{(mm)}(\mathbf{r}|\mathbf{r}') - \frac{\delta(\mathbf{r}-\mathbf{r}')}{j\omega\mu_0}\mathbf{I}\right] \cdot \mathbf{M}(\mathbf{r}')d\mathbf{r}'. \tag{4}$$

This is the basic integral equation for the magnetization vector. Its solution is the starting point for determining the fields and driving-point impedance of the ferrite core.

The Green's function can be written in the form of a two-dimensional Fourier transform,

$$\mathbf{G}^{(mm)}(x-x', y-y', z, z') = \iint_{-\infty}^{\infty} \tilde{\mathbf{G}}^{(mm)}(k_x, k_y; z, z')e^{-j[k_x(x-x')+k_y(y-y')]}dk_x dk_y, \tag{5}$$

When this is substituted into (4) the integrals over x' and y' become Fourier transforms and the resulting integral equation for the magnetisation becomes:

$$\begin{aligned} &\mathbf{M}^{(i)}(\mathbf{r}) = \mathbf{M}(\mathbf{r}) + \\ &j\omega\mu_0\nu(\mathbf{r}) \int dz' \iint_{-\infty}^{\infty} \left[\tilde{\mathbf{G}}^{(mm)}(k_x, k_y; z, z') - \frac{\delta(z-z')}{j\omega\mu_0}\right] \cdot \widetilde{\mathbf{M}}(k_x, k_y; z')e^{-j(k_x x + k_y y)}dk_x dk_y \end{aligned} \tag{6}$$

Note that ν vanishes for a core region with the free space permeability and is equal to 1.0 when the permeability is infinite.

The Green's function consists of two parts, a free-space part, which ignores the presence of the slab and a part which transforms the source into the reflected field. The free-space part, in turn, consists of two parts, $\tilde{\mathbf{G}}_{(0)}^{(mm)}$, and a 'depolarization' term, $\tilde{\mathbf{G}}_{(d)}^{(mm)}$. $\tilde{\mathbf{G}}_{(0)}^{(mm)}$ is given by

$$\tilde{\mathbf{G}}_{(0)}^{(mm)}(k_x,k_y;z,z') = j\omega\epsilon_0 \begin{bmatrix} 1-k_x^2/k_0^2 & -k_xk_y/k_0^2 & \pm jk_x\lambda_0/k_0^2 \\ -k_xk_y/k_0^2 & 1-k_y^2/k_0^2 & \pm jk_y\lambda_0/k_0^2 \\ \pm jk_x\lambda_0/k_0^2 & \pm jk_y\lambda_0/k_0^2 & 1+\lambda_0^2/k_0^2 \end{bmatrix} \frac{e^{-\lambda_0|z-z'|}}{2\lambda_0}, \tag{7}$$

where the $(+)$ sign goes with $z > z'$, $(-)$ with $z < z'$, and $\lambda_0 = (k_x^2 + k_y^2 - k_0^2)^{1/2}$. The depolarization term is given by

$$\tilde{\mathbf{G}}_{(d)}^{(mm)}(k_x,k_y;z,z') = -j\frac{\delta(z-z')}{\omega\mu_0}\mathbf{a}_z\mathbf{a}_z. \tag{8}$$

The reflected Green's function is defined in terms of reflection coefficients R_{xx}, R_{xy} etc., whose values depend upon the nature of the slab and are independent of the location of the source and field points. Thus, the reflected Green's function has the general structure

$$\tilde{\mathbf{G}}_{(r)}^{(mm)}(k_x,k_y;z,z') = \begin{bmatrix} R_{xx} & R_{xy} & R_{xz} \\ R_{yx} & R_{yy} & R_{yz} \\ R_{zx} & R_{zy} & R_{zz} \end{bmatrix} e^{-\lambda_0(z+z')}, \tag{9}$$

The $x-x'$, and $y-y'$ dependence of the complete Green's tensor $\mathbf{G}^{(mm)}$, implies than the source integation, equation (4), is a convolution in x and y. In addition, the free space Green's tensor has a $z-z'$ dependence while the reflection Green's term has a $z+z'$ dependence. Therefore (4) contains the sum of a convolution and a correlation in z. In designing a numerical algorithm for computing M from a discrete version of (4), we have taken full advantage of this convolutional/correlational structure.

(b) Discretization of the Integral Equation by Taking Moments

The discretization of the integral equation (4) is done by subdividing the region of space occupied by the core into N_z layers, each of depth δ_z and then expanding the magnetisation vector and the permeabilty function ν using pulse functions. Thus

$$\mathbf{M}(x,y,z) = \sum_{l=0}^{N_x}\sum_{m=0}^{N_y}\sum_{j=0}^{N_z} \mathbf{I}_{lmj} P_l(\frac{x}{\delta_x}) P_m(\frac{y}{\delta_y}) P_j(\frac{z-z_0}{\delta_z}). \tag{10}$$

and

$$\nu(x,y,z) = \sum_{l=0}^{N_x}\sum_{m=0}^{N_y}\sum_{j=0}^{N_z} \nu_{lmj} P_l(\frac{x}{\delta_x}) P_m(\frac{y}{\delta_y}) P_j(\frac{z-z_0}{\delta_z}), \tag{11}$$

where z_0 is the perpendicular distance from the workpiece to the bottom of the source grid and the pulse functions satisfy

$$P_k(s) = \begin{cases} 1, & \text{if } k \le s < k+1.0; \\ 0, & \text{otherwise.} \end{cases} \tag{12}$$

We are going to use Galerkin's variant of the method of moments to complete the discretization. In Galerkin's method, we 'test' the integral equation (4) with the same pulse functions that we used to expand the unknown, M, in (7). That is, we form moments of (4) by multiplying (6) by $P_l(\frac{x}{\delta_x})P_m(\frac{y}{\delta_y})P_j(\frac{z-z_0}{\delta_z})$ with M given by (7), and then integrating with respect to x, y and z over each cell. This yields a linear system for $\mathbf{I}_{lmj}$:

$$\mathbf{I}^{(i)}_{lmj} = \delta_x \mathbf{I}_{lmj} + \nu_{lmj} \sum_{J=0}^{N_z} \sum_{L=0}^{N_x} \sum_{M=0}^{N_y} \mathrm{G}_{j,J,l-L,m-M} \cdot \mathbf{I}_{LMJ}, \tag{13}$$

where

$$\begin{aligned} \mathrm{G}_{j,J,l-L,m-M} &= j\omega\mu_0\delta_x\delta_y/4\pi^2 \iint_{-\infty}^{\infty} e^{-j[k_x\delta_x(l-L)+k_y\delta_y(m-M)]} \tilde{\tilde{\Gamma}}^{(mm)}_{jJ}(k_x, k_y) \\ &\quad \left(\frac{\sin(k_x\delta_x/2)}{k_x\delta_x/2}\right)^2 \left(\frac{\sin(k_y\delta_y/2)}{k_y\delta_y/2}\right)^2 dk_x dk_y \end{aligned} \tag{14}$$

$\tilde{\tilde{\Gamma}}^{(mm)}_{jJ}$ is defined by letting $z_j = z_0 + j\delta_z$; $j = 1, N_z$, as

$$\tilde{\tilde{\Gamma}}^{(mm)}_{kj}(k_x, k_y) = \int_{z_{k-1}}^{z_k} dz \int_{z_{j-1}}^{z_j} dz' \left[\tilde{\mathrm{G}}^{(mm)}(k_x, k_y; z, z') - \frac{\delta(z-z')}{j\omega\mu_0}\mathrm{I}\right]. \tag{15}$$

(13) is the equation we use to calculate moments of the ferrite core magnetisation. As well as being of Toeplitz form in (l, L) and (m, M), the matrix of coefficients decomposes into two matrices, one of which has the Toeplitz form in (j, J) and the other has a Hankel form in (j, J). This structure, which is a direct consequence of the convolutional/correlational nature of the basic integral equation, allows us to use the fast Fourier transform for computing the result of multiplying an arbitrary vector by the matrix. It is important that this operation is carried out efficiently since it is used repeatedly in the conjugate gradient procedure.

Validation and Results

Validation checks on the package have been done by self consistancy testing, by comparing results with data computed directly from available analytical expressions and by comparing field calculations with data obtained independently using a finite-element code designed for solving two-dimensional electromagnetic field problems[6]. Agreement with the two-dimensional finite-element code is important since it validates a crucial part of the package that determines the magnetisation of ferromagnetic materials.

To give an example of an external validation, the electric field was determined for an axially symmetric ferrite-cored probe (core radius $0.25mm$, core length $10mm$, coil O/D $0.45mm$, coil I/D $0.25mm$ and axial coil length $0.5mm$). The probe, shown in Figure 2, is based on a design for turbine disc inspection at $1MHz$ on components of conductivity $0.82 \times 10^6 Sm^{-1}$ and has a core of negligible conductivity whose relative permeability is 200. The azimuthal electric field was computed using both a two-dimensional finite-element code[6] and our volume integral method. Figures 3 and 4 compare the real and imaginary parts of the field at the surface of the test piece for the two calculations showing good agreement between the results.

Experimentally it has been shown that cup-cored probes (figure 5) provide very good coupling with the workpiece and are well suited for testing composite materials such as graphite-epoxy.

Figure 6 shows the azimuthal electric field at the surface of an isotropic testpiece for zero lift-off, showing that the field is mainly confined within the probe region. An assessment of the coupling can be found from the normalized impedance characteristic and therefore it is important that impedance calculations are included in the model. A normalized impedance diagram for the cup-core probe at various lift-off values is shown in figure 7. These results were computed for the cup core probe above an isotropic half-space of conductivity $20,000 Sm^{-1}$.

Conclusion

A comprehensive computer code for research and design studies in electromagnetic NDE is now at an advanced stage of development. It has the capability of predicting the impedance characteristics of fully three-dimensional eddy-current probes in the presence of metals, semiconductors and advanced composites, as well as finding the electric and magnetic field. By using a combination of the conjugate gradient method applied to a matrix and FFT techniques, we have arrived at an algorithm that is both efficient in CPU time and has modest storage requirements. Pre- and post-processors are currently being developed to make the pakage available to the general user.

Acknowledgement

This work is supported by The Naval Surface Weapons Center (White Oak Labs) under Contract No. N60921-86-C-0172 with Sabbagh Associates.

References

1. Harold A. Sabbagh *A Model of Eddy-Current Probes with Ferrite Cores,* IEEE Transactions on Magnetics, Vol. Mag-23, No. 3, May 1987.

2. Harold A. Sabbagh, Thomas M. Roberts, *A Model for Eddy-Current Interactions with Advanced Composites,* Review of Progress in Quantitative Nondestructive Evaluation 5B, D. O. Thompson and D. E. Chimenti, Eds., (Plenum Press, New York, 1986), pp. 1105-1111.

3. Harold A. Sabbagh, L. David Sabbagh, Thomas M. Roberts, *An Eddy-Current Model and Algorithm for Three-Dimensional Nondestructive Evaluation of Advanced Composites.* Part 1: The Model; Part 2: *The Algorithm,* submitted for publication to IEEE Transactions on Magnetics.

4. H. A. Sabbagh, L. D. Sabbagh and J. R. Bowler, *A Model of Eddy-Current Probes Above a Composite Workpiece,* Review of Progress in Quantitative Nondestructive Evaluation, Vol.7, D.O.Thompson and D.E.Chimenti, Eds. (in press).

5. J. R. Bowler, *Eddy-Current Probe Interaction with Subsurface Cracks,* Review of Progress in Quantitative Nondestructive Evaluation, Vol. 6A, D.O.Thompson and D.E.Chimenti, Eds. (Plenum, New York, 1987) p185-191.

6. A. G. A. Armstrong and C. S. Biddlecombe, *The P.E2D package for transient eddy-current analysis* IEEE, VolMag-18, No.2, 411-415 (1982).

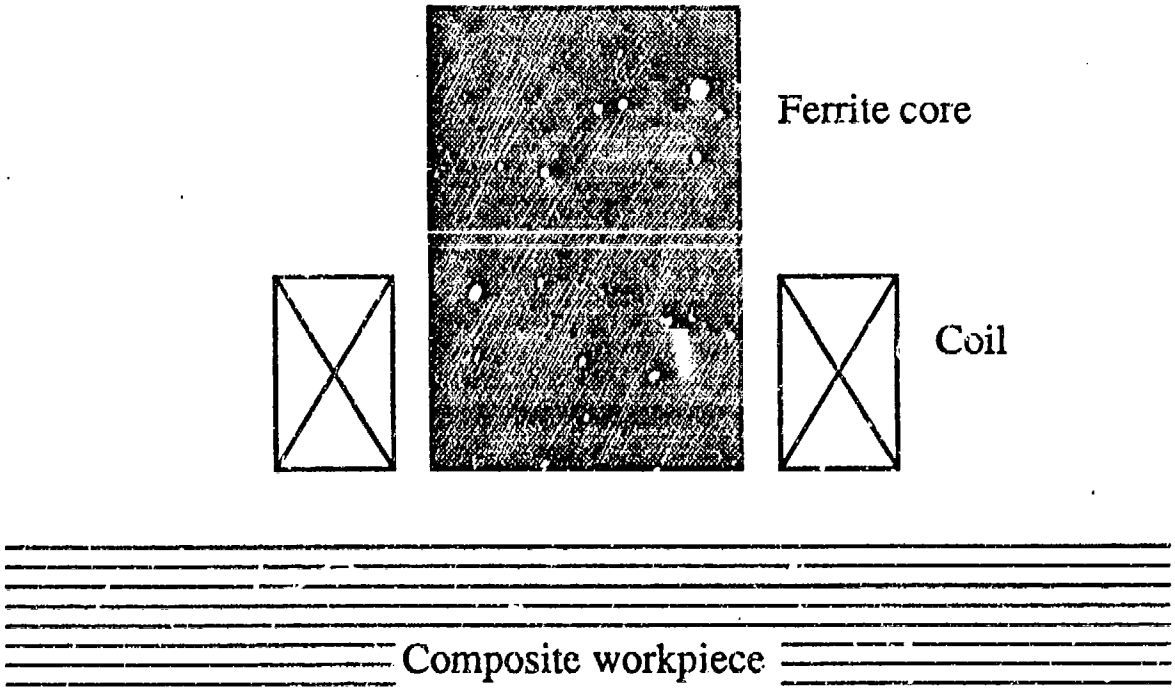


Figure 1. A ferrite core eddy-current probe over a stratified anisotropic workpiece.



Figure 2. High resolution eddy-current probe. Core length $10mm$, diameter $0.5mm$, coil O/D $0.9mm$, I/D $0.5mm$, axial length or coil $0.5mm$.

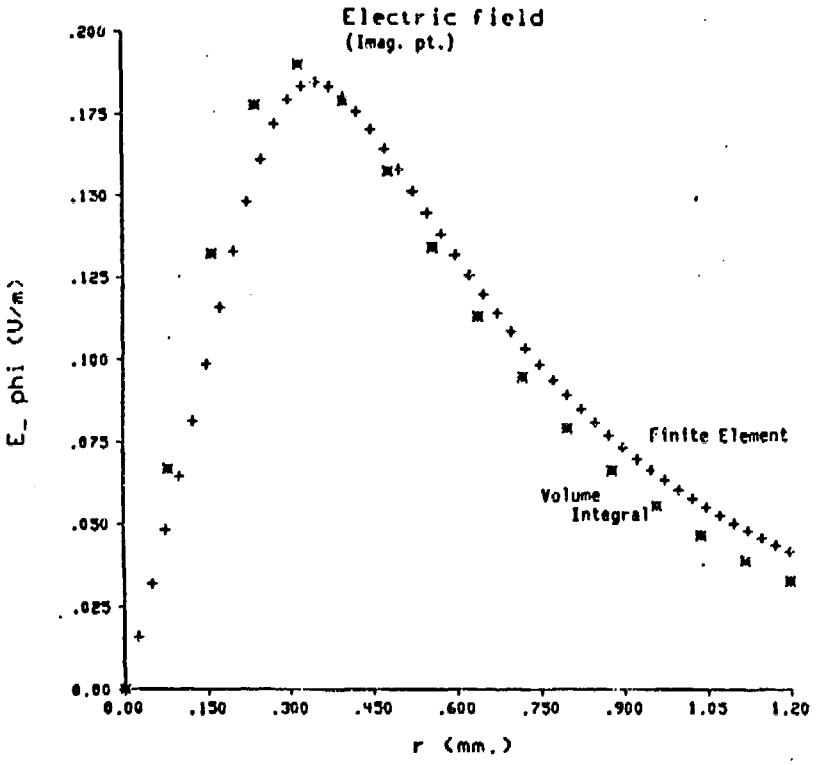


Figure 3. Radial variation of the azimuthal electric field, E_ϕ, at the surface of a homogeneous half-space conductor for the probe shown in fig.2. Comparison of volume integral and finite element results: imaginary part.

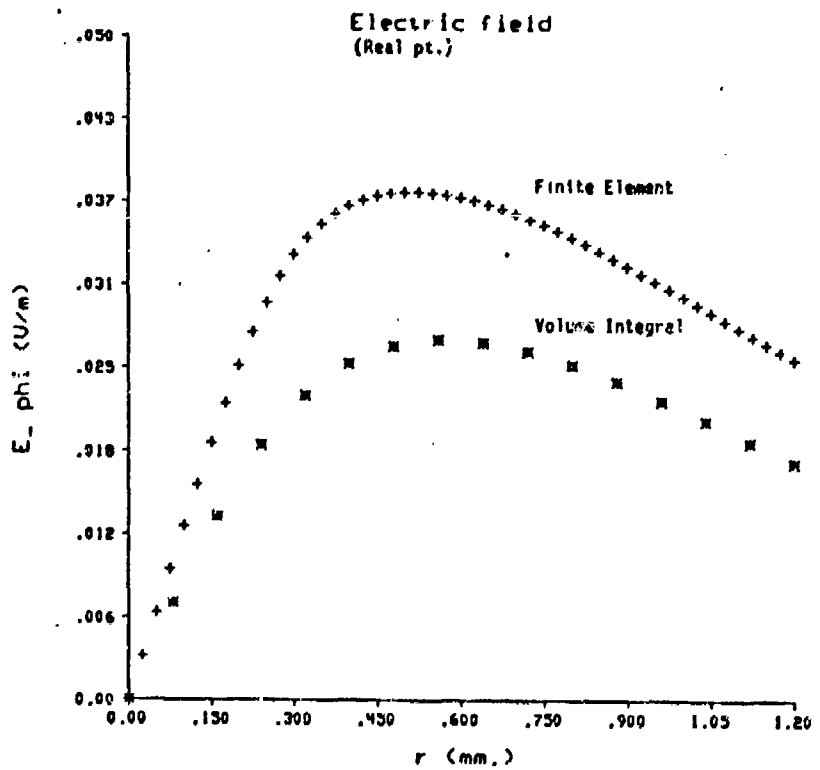


Figure 4. Radial variation of the azimuthal electric field, E_ϕ, at the surface of a homogeneous half-space conductor for the probe shown in fig.2. Comparison of volume integral and finite element results: real part.

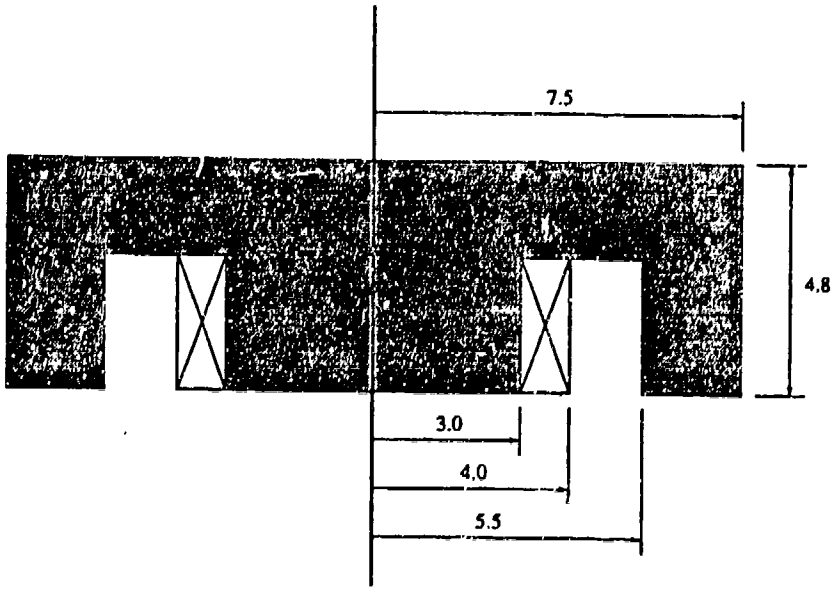


Figure 5. Cup core eddy-current probe of a type suitable for the inspection of graphite-epoxy. Dimensions are in *mm*. Typical operating frequency, $1MHz$.

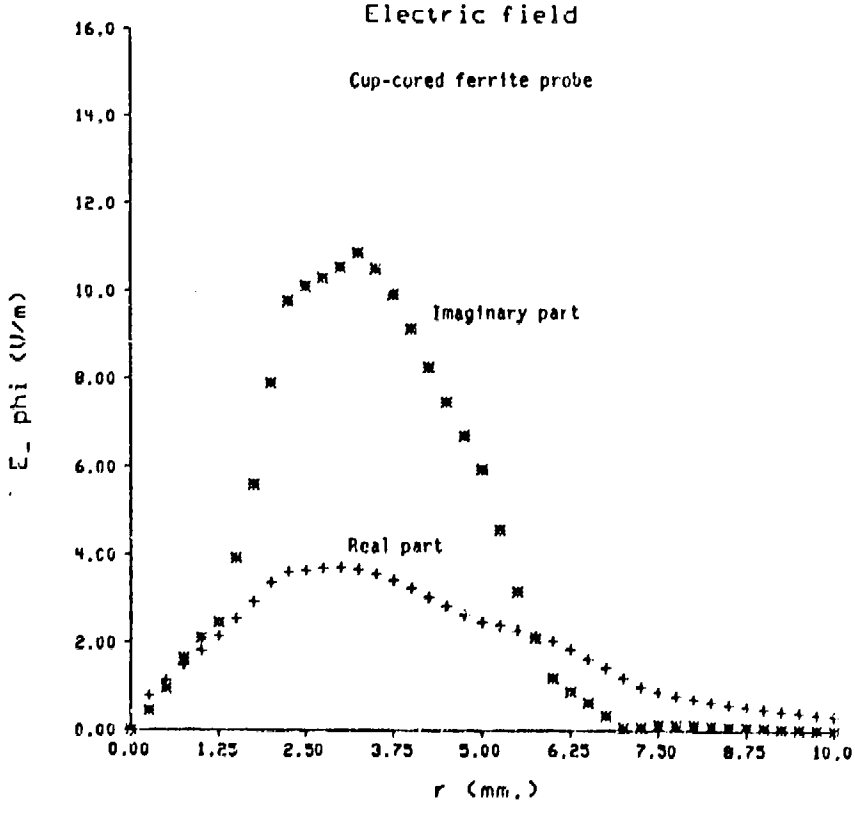


Figure 6. Radial variation of the azimuthal electric field, E_ϕ, at the surface of a homogeneous half-space conductor for the cup core probe shown in fig.5.

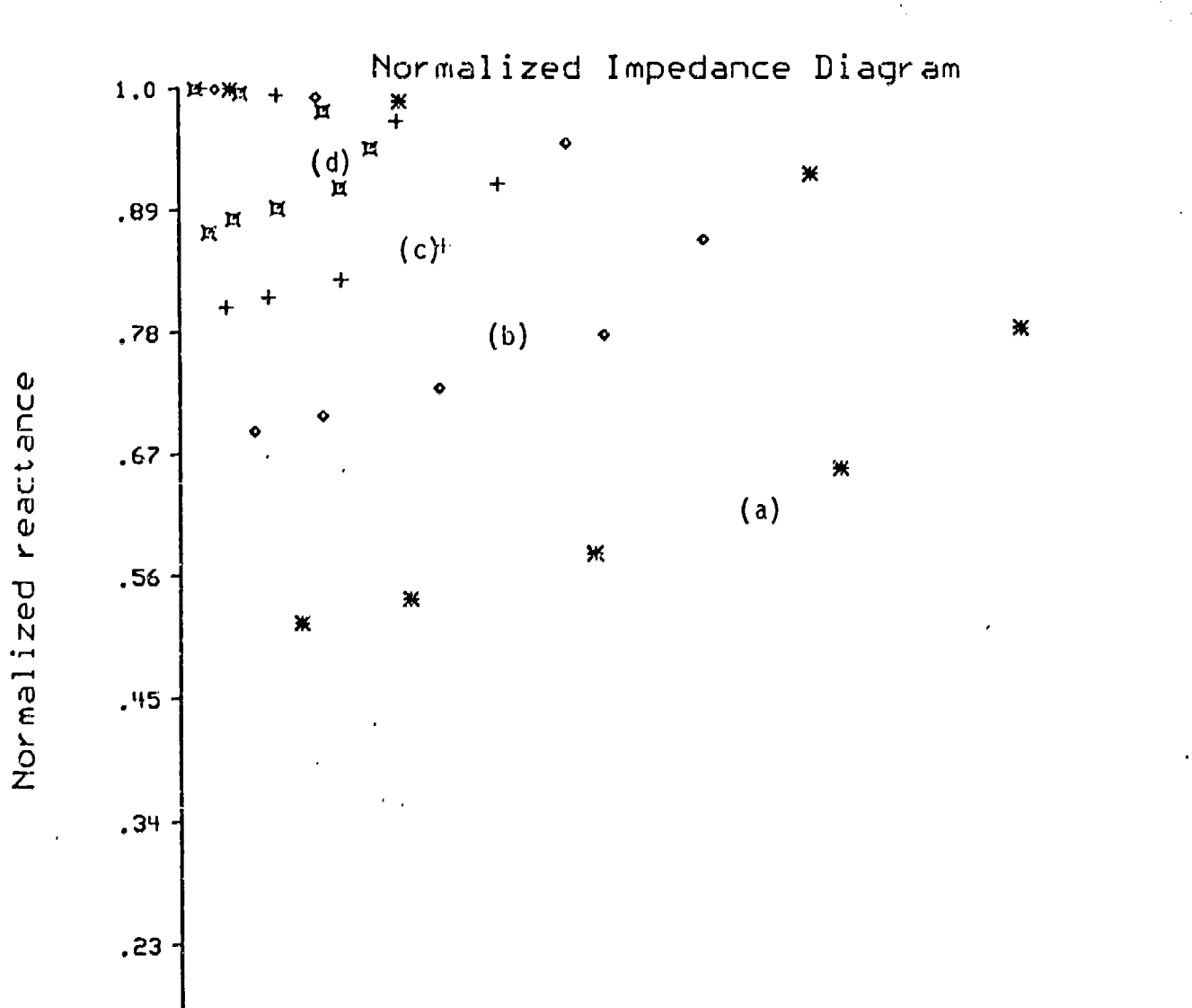


Figure 7. Normalised impedance characteristic for a cup core probe (fig.5) above an isotropic workpiece of conductivity $20,000 Sm^{-1}$ for lift-off values (a) zero (b) $0.6mm$ (c) $1.2mm$ (d) $1.8mm$.

COMPARISON OF SOIL MODELS WITH FREQUENCY–DEPENDENT CONSTITUTIVE PARAMETERS

JOHN W. WILLIAMS AND GARY D. RENSNER
SCIENCE APPLICATIONS INTERNATIONAL CORPORATION
2109 AIR PARK ROAD S.E.
ALBUQUERQUE, NEW MEXICO 87106
505/247–3737

Abstract

This paper examines soil models which are useful for calculations of responses of long, aerial wires to plane wave excitation. Electrical characteristics of non–magnetic soils are compared for soil models with frequency–dependent and frequency–independent constitutive parameters σ_{soil} and ϵ_{soil}. Responses of aerial wires are presented for plane wave excitation with risetimes ranging from 0.1 ns to 10.0 ns.

Introduction

It has long been known that soil conductivity and dielectric constant are frequency–dependent[1,2]. Early measurements by Scott[3] were used to formulate a soil model whose frequency–dependent constitutive parameters are calculated solely from volumetric water content[2]. By extrapolation of the experimental data, the resulting soil model can be used over a wide frequency band from a few Hertz to about 30 GHz. However, since this model ignores potentially important variables such as soil composition and temperature, it is necessarily limited in applicability. For example, later measurements of soil conductivity and dielectric constant for samples obtained near Albuquerque, NM were not in agreement with the earlier data[4]. As will be discussed below, there is also a lack of agreement between soil models presented in the first two references.

Electrical properties of soil have also been an important concern for geophysical applications [5,6]. Soil models for the 1 GHz to 20 GHz band have been formulated by several authors based upon soil temperature, composition, and volumetric water content.

Semi-empirical models show good agreement with experimental data at microwave frequencies[5]. However, these models are limited to a relatively narrow band of microwave frequencies. Very detailed analytical models based upon dielectric mixing have also been employed for the microwave region[6,7]. These analytical models require detailed specification of soil composition and macroscopic structure. Unfortunately, these detailed models contain adjustable parameters, such as dispersed and crevice water fraction, that allow considerable variation in results.

Thus, while there has been considerable study of the electrical properties of soil, there are not many frequency-dependent models that provide ready tools for calculation over a reasonably wide bandwidth. In the sections below we discuss the various soil models available for calculation of plane wave response for a long metal wire above soil. Then calculations of wire response in the frequency domain are transformed to the time domain using the Fourier integral transform.

Soil Models

Soil models suitable for calculations at radio or microwave frequencies range from very simple models, which assume constant constitutive parameters, to extremely detailed models in which frequency-dependent soil constitutive parameters are functions of soil moisture content, temperature, and composition.

One of the more convenient soil models for calculations is the "Universal" model which is based on some early experimental data in the 100 Hz to 1 Mhz band[2,3]. This model is particularly convenient for calculations with non-magnetic soils because it provides frequency-dependent constitutive parameters over a wide frequency band. Since this soil model is discussed in reference 2 in detail, we will summarize the essential features here.

The "Universal" soil model assumes that a unit volume of soil can be electromagnetically modeled as network of resistors and capacitors. Experimental data available at the time the model was formulated[3] indicated that values of the equivalent capacitors remain fixed with respect to soil water content, while the equivalent resistances increase with increasing water content. Using the fact that measured values of the soil dielectric constant for various water contents tend to overlay when shifted in frequency, Longmire and Smith[2] were able to formulate a wideband soil model which gave good

agreement with the available experimental data. In essence, this model gives:

$$\epsilon_{soil}^{(r)} = \epsilon_{\infty} + \epsilon[f/f_n(P)] \tag{1}$$

$$\sigma_{soil} = \sigma_o(P) + \sigma\,[f/f_n\,(P)] \tag{2}$$

where f/f_n denotes scaled frequencies, P represents the volumetric percentage of water, and index n is determined from available experimental data. By extrapolation of the experimental data, Longmire and Smith obtained a 13 parameter model for water–dependent soils. Figure 1 shows the loss tangent as a function of soil water content at various frequencies calculated with the "Universal" soil model. Below about 100 kHz, this soil model is dominated by electrical soil conductivity for all but the driest soils. On the other hand, above 100 MHz the model indicates that all but the wettest soils are dominated by dielectric properties. Since we will examine soil interactions with plane waves having risetimes from 0.1 ns to 10 ns, both ends of the frequency band are of interest.

It should be noted that not all measurements of soil constitutive parameters are in accordance with the "Universal" soil model. Later measurements by Mallon,[4] et al., are quantitatively at odds with the model, and furthermore do not allow the frequency scaling which provided extrapolation of the Scotts' experimental data[3]. As another example, we have attempted to match generic soil models of reference 1 (see Figure 2). In this case we attempted to reconcile the "Universal" model and generic model by minimizing $|\sigma_{universal} - \sigma_{generic}|$, where the generic soil model is characterized by [1]:

$$y = Bx^M \qquad 2\ \text{MHz} \leq x \leq 30\text{MHz}, \tag{3}$$

where x denotes the frequency, y represents soil dielectric constant or conductivity, and constants B and M are different for each generic soil type. Although several schemes for matching the two models in the 2 MHz to 30 MHz bands were attempted, the agreement is not very good. As indicated in Figure 2, one would anticipate very poor agreement over a wide frequency band. Table 1 summarizes the values of the "Universal" soil model used to represent the various soil generic types. Column 1 lists the generic soil type, while the percentage of water content used to model the generic soil type is given in Column 2. Average values of soil conductivity and relative dielectric constant in the frequency band

from 1 KHz to 1 GHz are listed in the third column. In the sections below, we will compare responses of aerial wires over the soil types listed in Table 1.

Excitation and Wire Models

Figure 3 shows the configuration for a conducting wire located a distance h above a conducting soil. Elevation angle Ψ is the complement of the angle of incidence. We assume that the conducting wire is illuminated by a vertically–polarized plane wave. For convenience, we selected the time–dependence of the incident field as:

$$E_{inc}(t) = 1/2\,\{1 + \sin[\omega_r(t - \tau_r)]\} \qquad t_s < t \leq t_s + t_r \qquad (4)$$

$$= 1 \qquad t_s + t_r < t \leq t_s + t_r + T \qquad (5)$$

$$= 1/2\,\{1 + \sin[\omega_f(t - \tau_f)]\}$$

$$t_s + t_r + T < t \leq t_s + t_r + T + t_f \qquad (6)$$

$$= 0 \qquad \text{elsewhere} \qquad (7)$$

where $\omega_r = \pi/t_r$, $\omega_f = \pi/t_f$, $\tau_r = t_s + t_r/2$, and $\tau_f = t_s + t_r/2 + T$. This waveform is causal, smooth, and time–limited. In the applications below, we assume that the incident electric field is described by this time–dependence with $T = 0$ and $t_f = 1000\ t_r$. Figure 4 shows a comparison of the sum of sinusoids with a commonly used double exponential pulse having 10 ns risetime and (roughly) 1000 ns falltime.

The response of long wires above soil has received considerable attention in the past because of the practical importance of electromagnetic surges in communication and power systems[8–11]. In order to facilitate inclusion of frequency–dependent constitutive parameters for the soil, we adopt the scattering model developed in reference 8 for an aerial wire of outer radius "b" above a conducting soil:

$$I(\omega) = jE_{inc}(\omega)\, e^{-jk_o z\cos\psi}\,(1 - R_v e^{-j2k_o h\sin\psi})/C \qquad , \qquad (8)$$

where

$$C = \frac{\pi}{2} k_o\, b\, Z_{bb}\, H_1^{(2)}(k_o b \sin\psi) + \frac{j\omega\mu_o}{4} \sin\psi\, H_o^{(2)}(k_o b \sin\psi) \qquad (9)$$

and R_v is the reflection coefficient for vertical polarization:

$$R_v = \frac{\sin\psi - \xi}{\sin\psi + \xi} \qquad (10)$$

with

$$\xi = (\eta_{soil}/\eta_o)[1-(k_o \cos\psi/k_{soil})^2]^{1/2} \qquad (11)$$

Here k_o denotes the free space wave number, ω/c, and η represents the intrinsic impedance of the medium,

$$\eta^2 = j\omega\mu/(\sigma + j\omega\epsilon) \quad , \qquad (12)$$

and

$$k^2 = j\omega\mu\,(\sigma + j\omega\epsilon) \quad . \qquad (13)$$

We use $H_\nu^{(2)}(x)$ to denote Hankel functions of the second kind of order ν and argument x. Surface impedance Z_{bb} is given to a good approximation by:[12]

$$Z_{bb} = [\eta_{wire}/(2\pi b)]\,[\coth(k_{wire}\, t) + (\frac{\pi}{2\, k_{wire}})\,(\frac{3}{a} + \frac{1}{b})] \quad , \qquad (14)$$

where "t" represents the thickness of the cable shield, and "a" denotes the inner radius of the outer shield ($t = b - a$).

In the sections below, we are primarily concerned with near–grazing incidence. Recall that for the case of vertical polarization, if the angle of elevation, ψ, is less than the Brewster angle, then the reflected wave is in–phase with the incident wave. However, for conductive media, the Brewster angle is frequency–dependent. As illustrated in Figure 5, at low frequencies soils act as good electrical conductors ($\sigma_{soil} >> \omega\epsilon_{soil}$). The reflection coefficient is nearly real with magnitude with 1. As the frequency increases, the reflection coefficient can become purely imaginary. As the frequency is further increased, or the elevation angle is decreased, the reflection coefficient again approaches one in magnitude with phase near 180^o. As indicated in Equation 8, this means that the reflected wave adds constructively with the incident wave. An example of this constructive interference is shown in Figure 6 for the driest soil indicated in Table 1.

In the event that the surface impedance of the wire vanishes, Equation 8 for the current reduces to:

$$I(\omega) = \frac{4E_{inc}\,\bar{e}^{jk_0 z\cos\psi}}{\omega\ \mu_0 \sin\ \psi\ H_0^{(2)}(k_0 b\sin\psi)}(1 - R_v\,\bar{e}^{j2k_0 h\sin\psi}) \qquad (15)$$

As illustrated in Figure 7, inclusion of finite wire conductivity is necessary to avoid a singularity in the expression for current as ω approaches zero.

Results

In order to compare the various soil models, calculations of currents on aerial wires above soil were performed with both frequency–dependent and frequency--independent constitutive parameters. Figures 8 and 9 show the impulse response ($E_{inc} = 1$) calculated from equation 8 for water–dependent models in Table 1 and some commonly used values for the constitutive parameters. Comparing results in the two figures, the calculated impulse responses are similar in shape for both models. As one would anticipate from Figure 2, volumetric water contents in excess of about 30% correspond to soils with frequency–independent conductivity above 10^{-2} S/m. Similarly, a frequency–independent conductivity below 10^{-4} S/m is required to closely match frequency–dependent soils characterized by volumetric water content below about 1%. Figure 10 displays a comparison of two soil models at normal and near–grazing incidence. At frequencies above about 10 MHz, the two soil models yield about the same results. At the higher frequencies, the impulse response calculated with the average soil conductivity (see Table 1) exceeds the corresponding response calculated with the frequency–dependent constitutive parameters. This is to be expected since the average soil conductivity is less than the high frequency value. The opposite is true at low frequencies, so that the impulse response calculated with P = 5.5% water content exceeds that obtained from the model with constant constitutive parameters obtained by averaging over the frequency band from 1 KHz to 1 GHz..

Variations of the impulse response with angle of elevation are illustrated in Figure 11. As indicated in equation 8 and 9, the magnitude of the impulse response is limited by the DC resistance of the wire as frequency vanishes. The first term on the right side of equation 9 also limits the wire response to finite values as the elevation angle vanishes. As

indicated in Figure 12, the impulse response eventually decreases from maximum values near $\psi = 1^{o}$ as the elevation angle approaches zero.

As a final example of impulse response in the frequency–domain, Figure 12 shows the impulse response calculated for a long steel wire above a water–dependent soil. Due to the relatively high surface impedance of the steel wire in comparison with copper wire, the impulse response is significantly less than that obtained for copper wire. As indicated in the figure, the impulse response is nearly in direct proportion to the wire radius.

Figures 13 through 15 show wire responses in the time–domain for incident fields with risetimes, t_r, of 0.1 ns, 1.0 ns, and 10.0 ns, respectively Referring to equations 4 through 7, for all calculations the parameter T was zero and $t_f = 1000\ t_r$. Finite values for start time, t_s, were used to insure integrity of the Fourier integral transforms which were used to obtain wire currents in the time domain from inversion of Equation 8. Comparing results in Figures 13 through 15, the disparity in currents calculated with the two soil models increases with increasing values for risetime. This trend is in general agreement with frequency domain responses discussed above where it was shown that the disparity in impulse responses increased with decreasing frequency.

Also note that results calculated with frequency–independent and frequency–dependent soil parameters are in better agreement as the volumetric water content increases. This is illustrated in Figure 16 for the case of normal incidence. The reason for this is that the frequency–independent portion of soil conductivity, σ_o (P) in equation 2, eventually becomes the dominant contribution to soil conductivity as P increases.

Conclusion

This paper has examined plane wave responses of aerial wires above various soil models. The "Universal" soil model was used to characterize soils with frequency–dependent constitutive parameters. This soil model assumes that soil conductivity and dielectric constant depend solely on volumetric water content, and hence do not provide a good estimate of constitutive parameters when variation soil composition or temperature become important. Nevertheless, it provides a useful computational tool over a wide frequency band without requiring a detailed description of soil structure and composition.

It was found that for very wet soils, variations in the constitutive parameters with frequency can reasonably be ignored in calculations of the response of aerial wires. Soils characterized by volumetric water content less than a few percent are now likely to require a frequency dependent model for accurate calculations. The disparity in results between frequency–dependent and frequency–independent soil models were shown to decrease with increasing risetime for the incident plane wave.

References

1. George H. Hagn, "HF Ground and Vegetation Constants, "3rd Annual Meeting of the Applied Computational Electromagnetic Society, Monterey, CA, March 1987.

2 Conrad L. Longmire and Ken S. Smith, "A Universal Impedance for Soils," DNA 3788T, October 1975.

3. J.H. Scott, "Electrical and Magnetic Properties of Rock and Soils", EMP Theoretical Notes, AFWL EMP 2–1, April 1971.

4. C. Mallon, et al., "Low–Field Electrical Characteristics of Soil," AFWL Theoretical Note 315, January 1981.

5. Myron C. Dobson, et al., "Microwave Dielectric Behavior of Wet Soil – Part I: Empirical Models and Experimental Observations, "IEEE Trans. Geosci. Remote Sensing, GE–23, pp. 25–34, January 1985.

6. Myron C. Dobson, et al., "Microwave Dielectric Behavior of Wet Soil Part II: Dielectric Mixing Models, "IEEE Trans. Geosci. Remote Sensing, GE–23, pp. 35–46, January 1985.

7. Darold Wobschall, "A Theory of the Complex Dielectric Permittivity of Soil Containing Water: The Semidisperse Model," IEEE Trans. Geosci. Electron., GE–15, pp 49–58, January 1977.

8. C.P. Bates and G.T Hawley," A Model for Currents and Voltages Induced Within Long Transmission Cables by an Electromagnetic Wave, "IEEE Trans. Electromagnetic Compat., EMC–13, PG 18–31, November 1971

9. H.P. Neff, Jr. and D.A. Reed, "Multiple Parallel Wires above a Finitely Conducting Plane Earth in the Presence of a Plane Wave (EMP), "Interaction Note 441, July 1984.

10. Kenneth C. Chen, "Time Harmonic Solutions for a Long Horizontal Wire over the ground with Grazing Incidence, "Interaction Note 447, October 1984.

11. Kenneth C. Chen, "EMP–Induced, Time–Domain Grazing Solution for an Infinite Wire over the Ground, "Interaction Note 448, May 1985.

12. S.A. Schelkunoff, "The Electromagnetic Theory of Coaxial Transmission Lines and Cylindrical Shields," Bell Syst. Tech. J., 13 pp. 532–579, October 1934.

TABLE 1. Summa y of Soil Constitutive Parameters

Generic Soil Type[1]	Percent Water Content	Average soil conductivity and Relative Dielectric Constant
Mountain, Rock Steep Hills	0.2	3.9×10^{-3} S/m, 15.2
Medium Hills, Forestation	5.5	2.2×10^{-2} S/m, 152.1
Rich Agricultrual Land	29.2	8.7×10^{-2} S/m, 899.1
Marsh	56.5	1.8×10^{-1} S/m, 2002.0

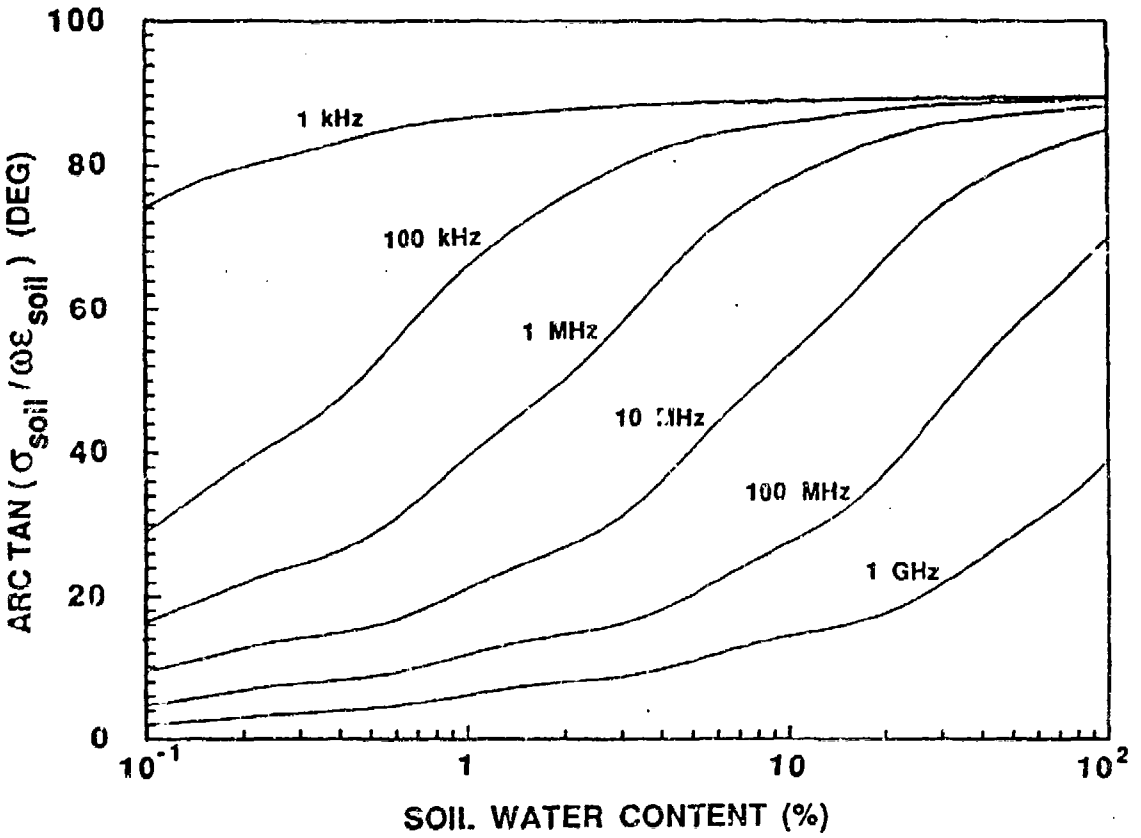


Figure 1. Loss Tangent as a Function of Water Content

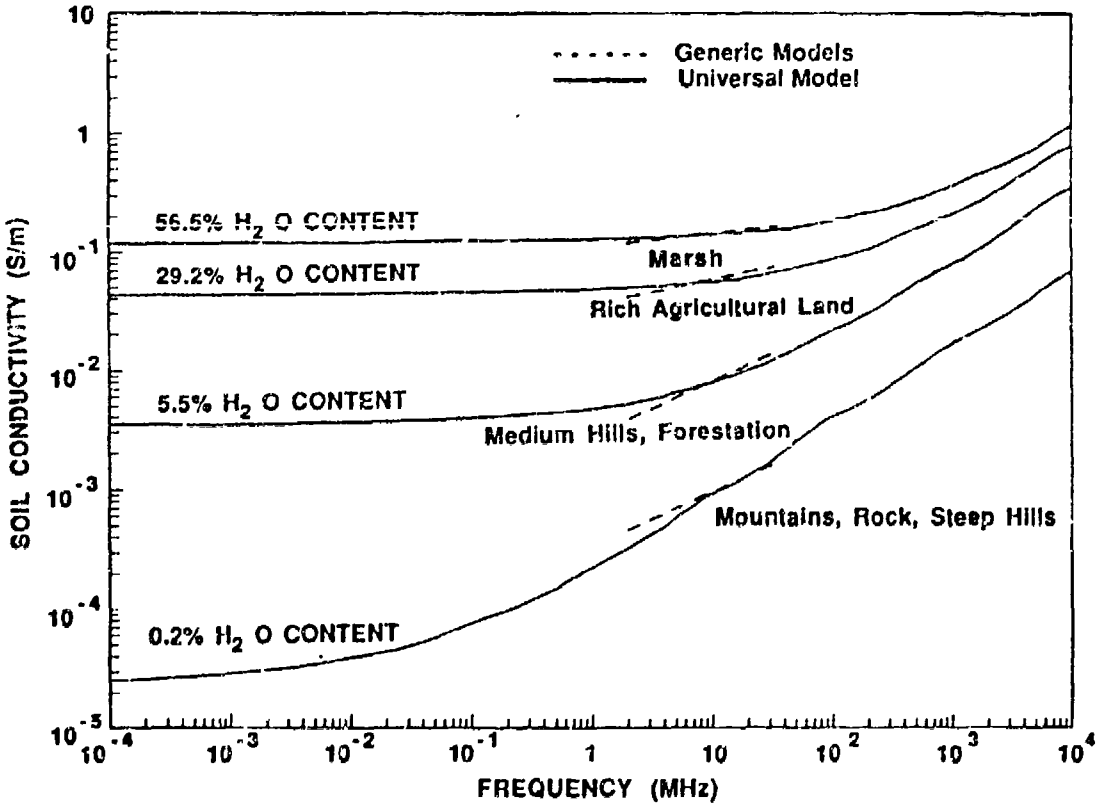


Figure 2. Soil Conductivity as a Function of Frequency

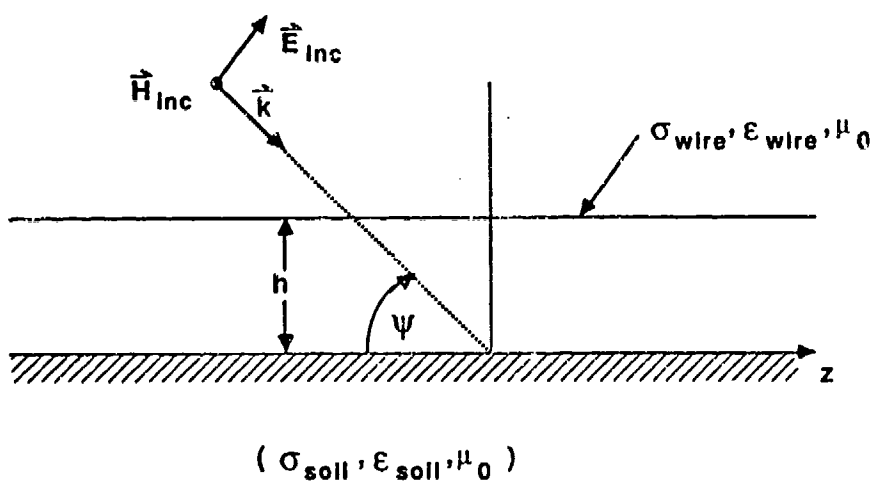


Figure 3. Configuration for a Long Wire above Soil

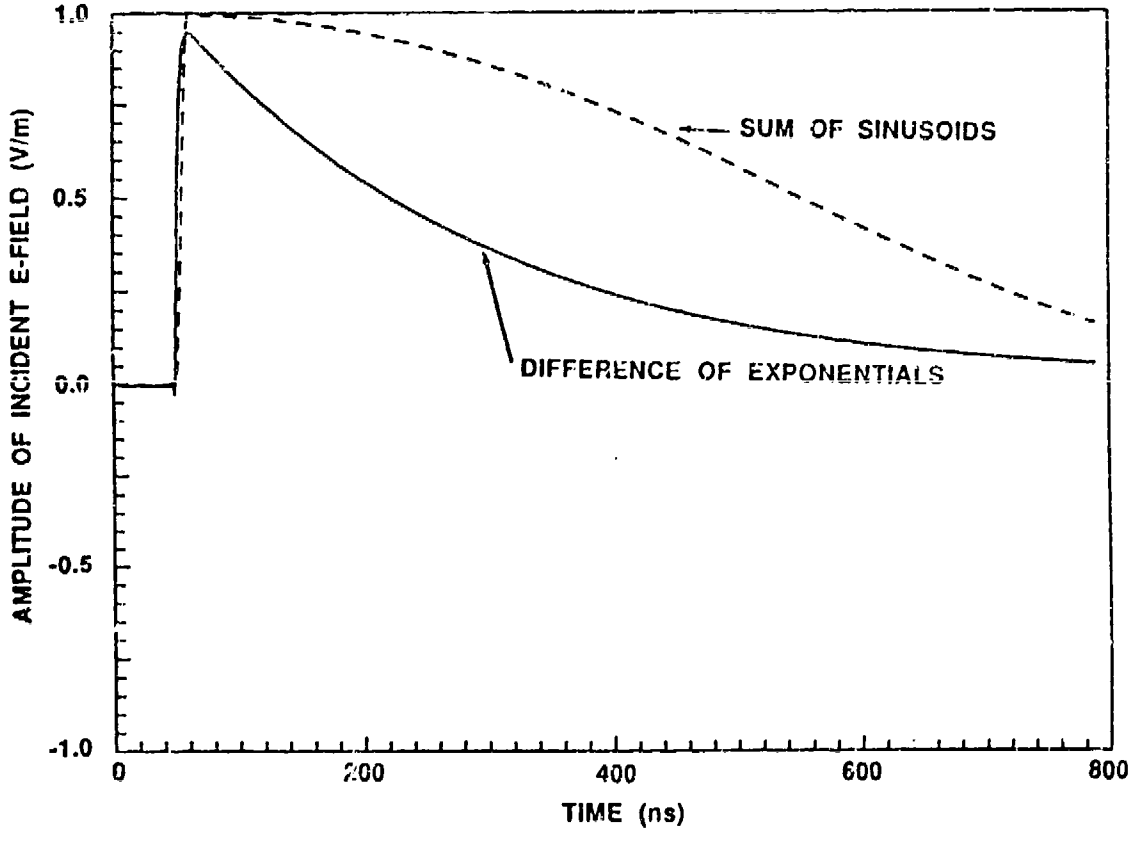


Figure 4. Comparison of Excitations

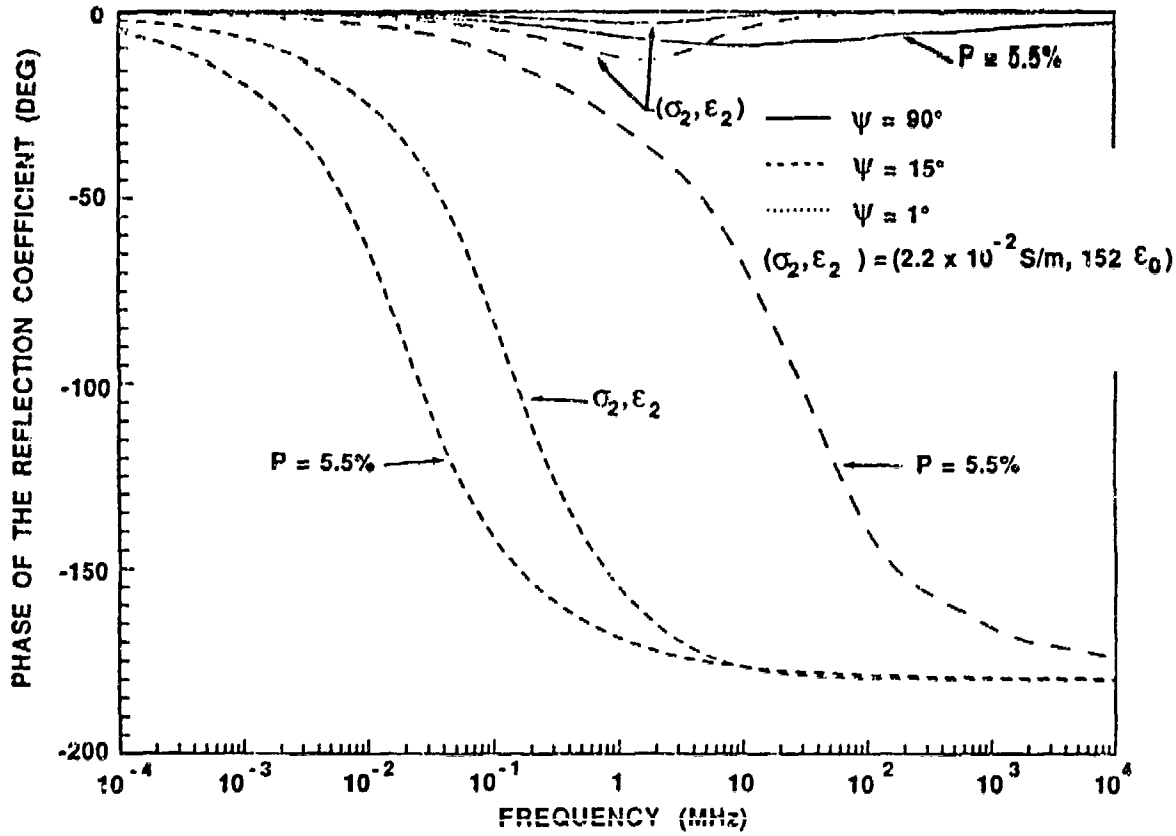


Figure 5. Phase of the Reflection Coefficient for Two Soil Models

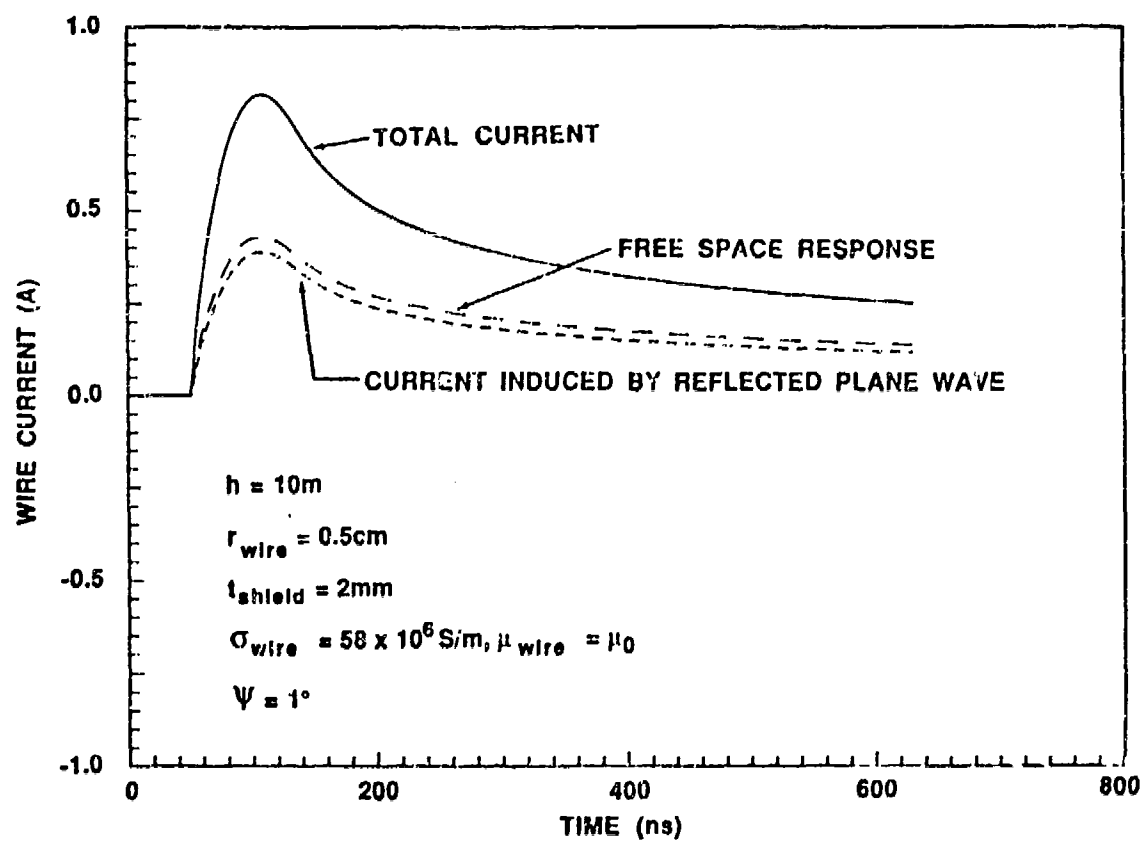


Figure 6. Current Induced on a Wire above Soil Characterized by 0.2% Water Content

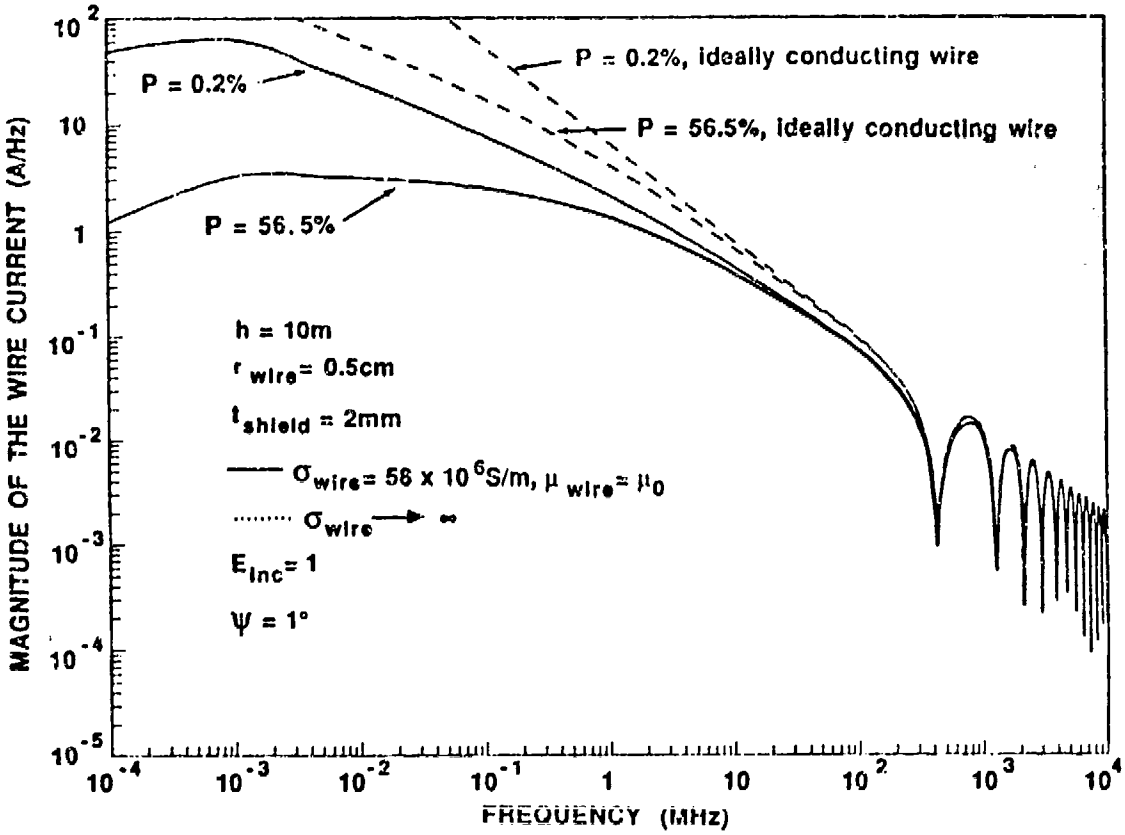


Figure 7. Impulse Resource Calculated for Long Wires with Finite and Infinite Electrical Conductivity

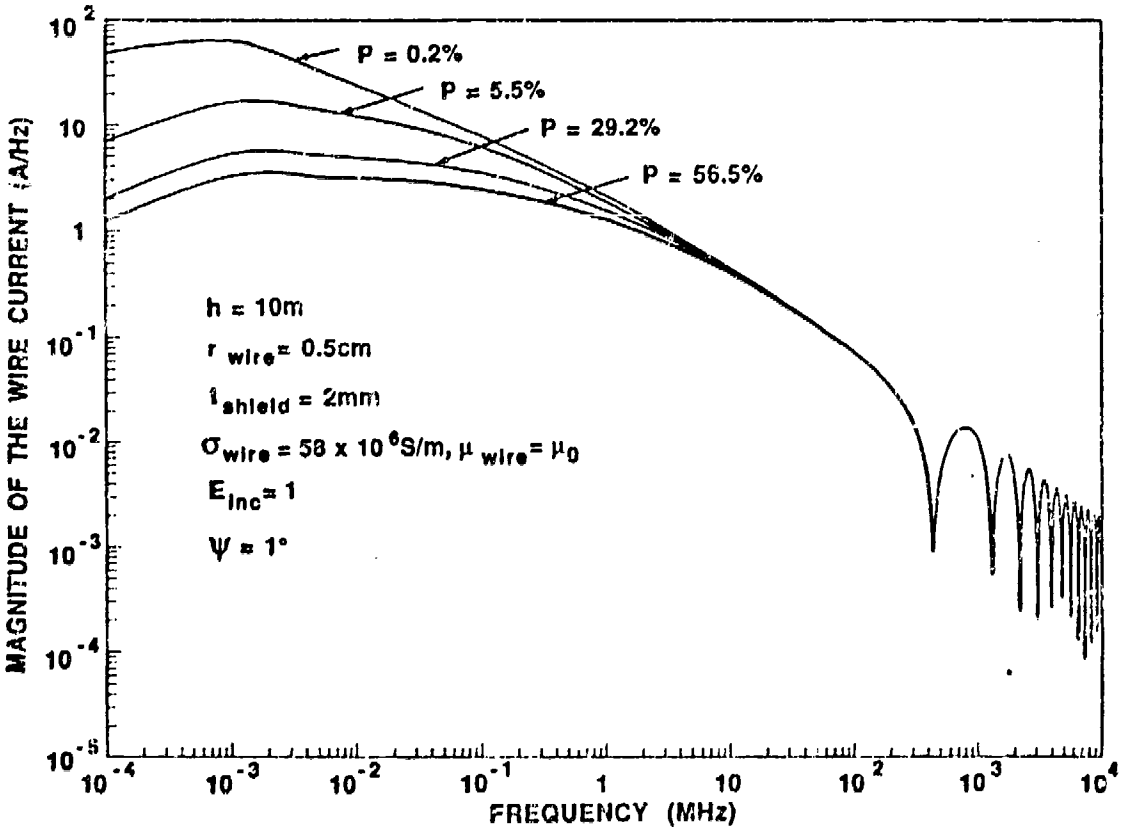


Figure 8. Magnitude of the Impulse Response Calculated for Soils Shown in Table 1 at Near Grazing Incidence

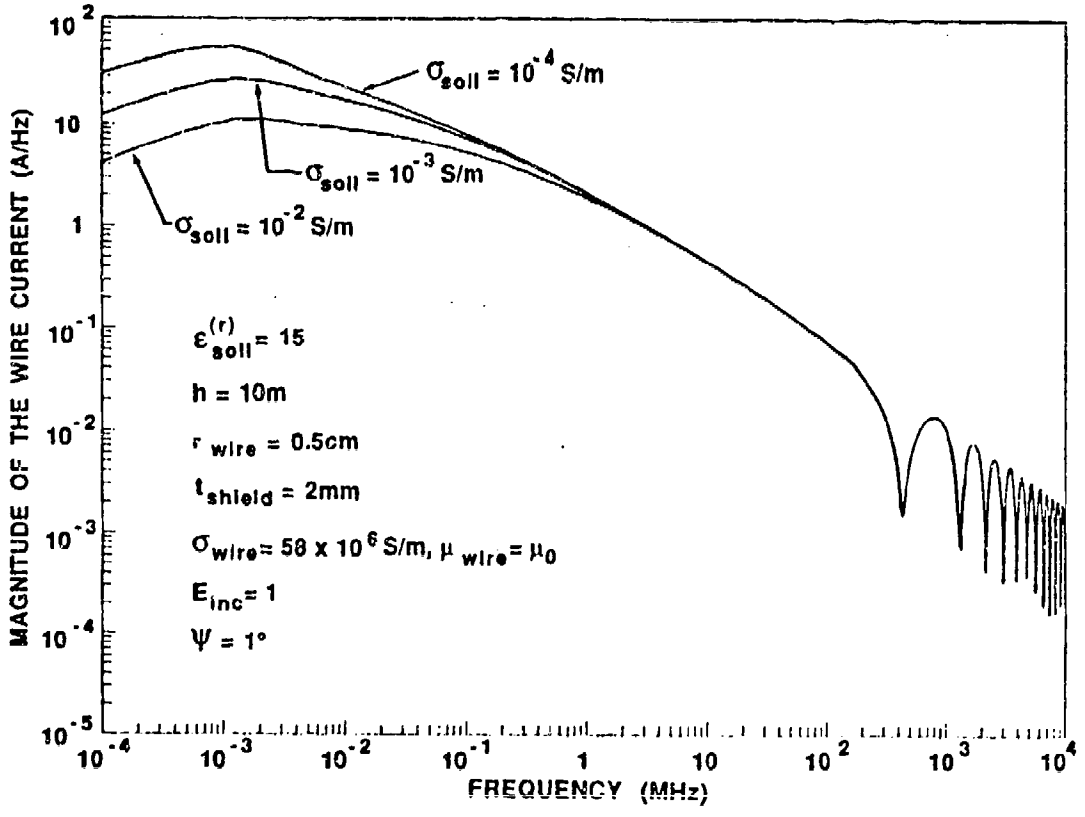


Figure 9. Magnitude of the Impulse Response Calculated for some Commonly Used Soil Models

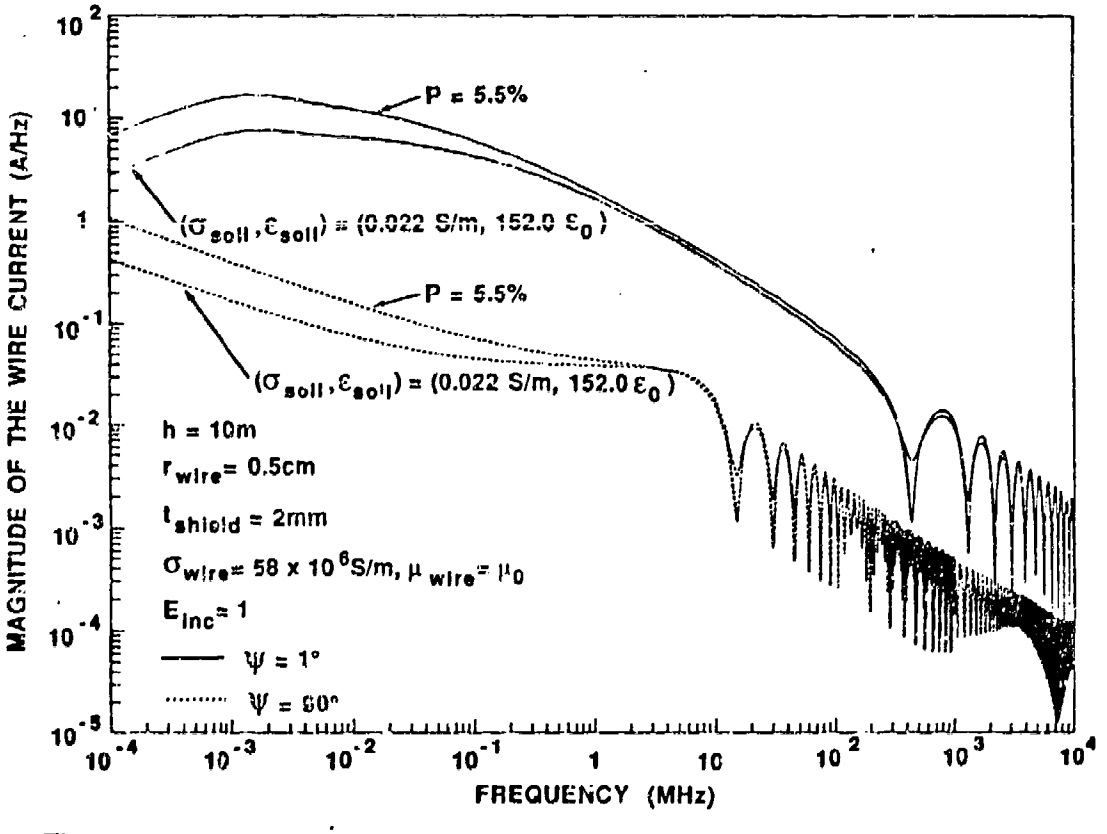


Figure 10. Magnitude of the Impulse Response Calculated for Two Soil Models at Normal and Near-Grazing Incidence

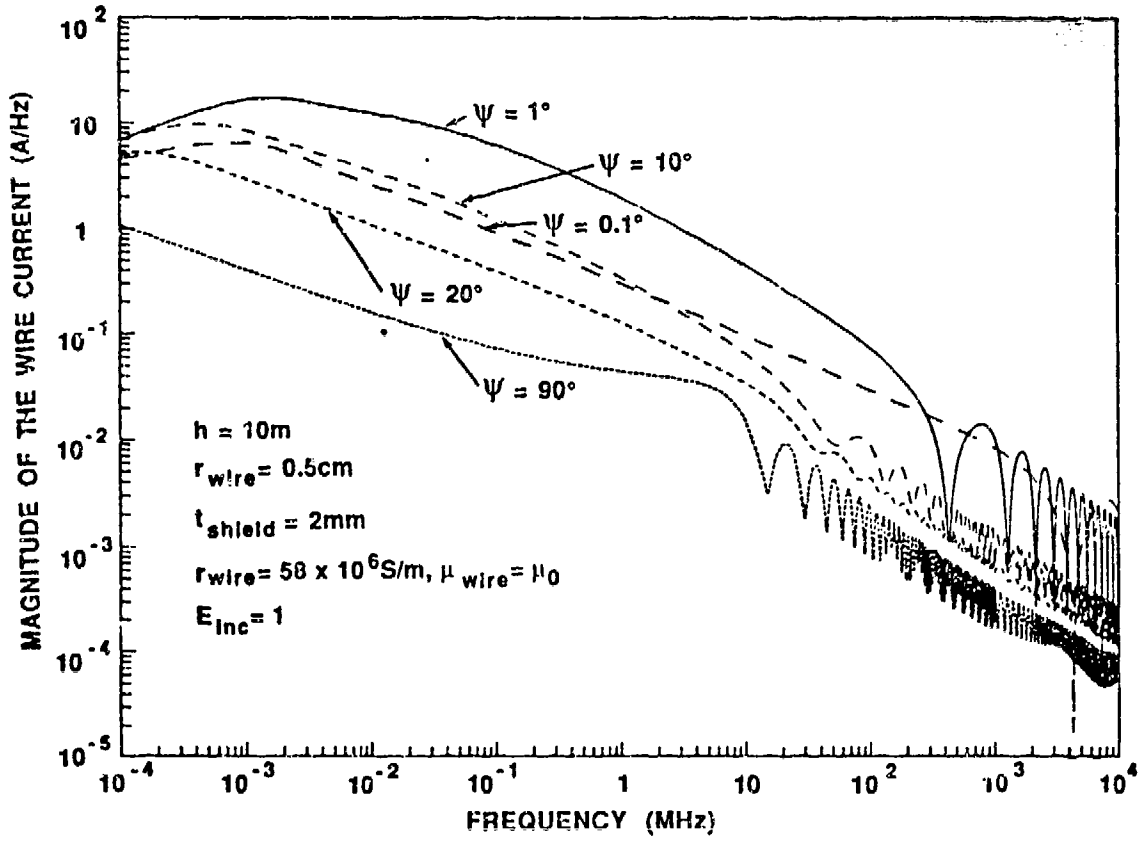


Figure 11. Magnitude of the Impulse Response Calculated for a Wire Above Soil with P=5.5% at Various Angles of Elevation

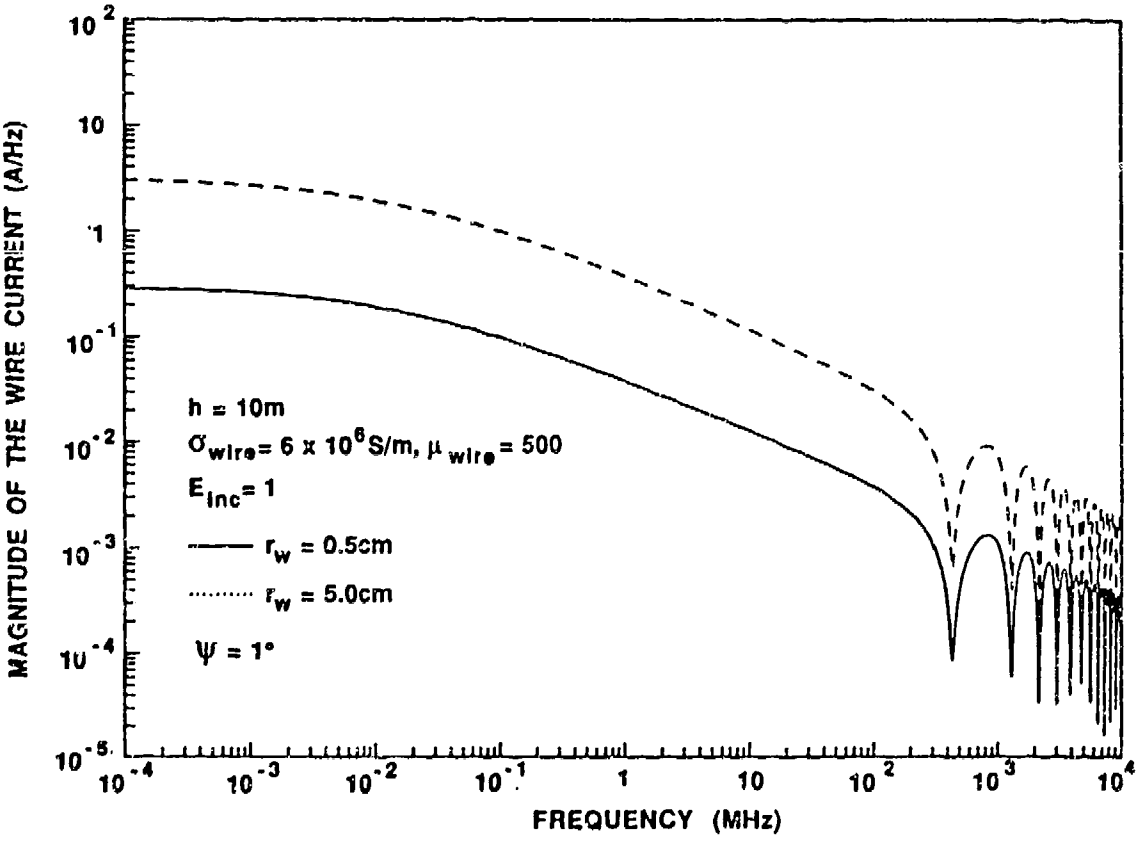


Figure 12. Magnitude of the Impulse Response Calculated for a Steel Wire above Soil with 5.5% Volumetric Water Content

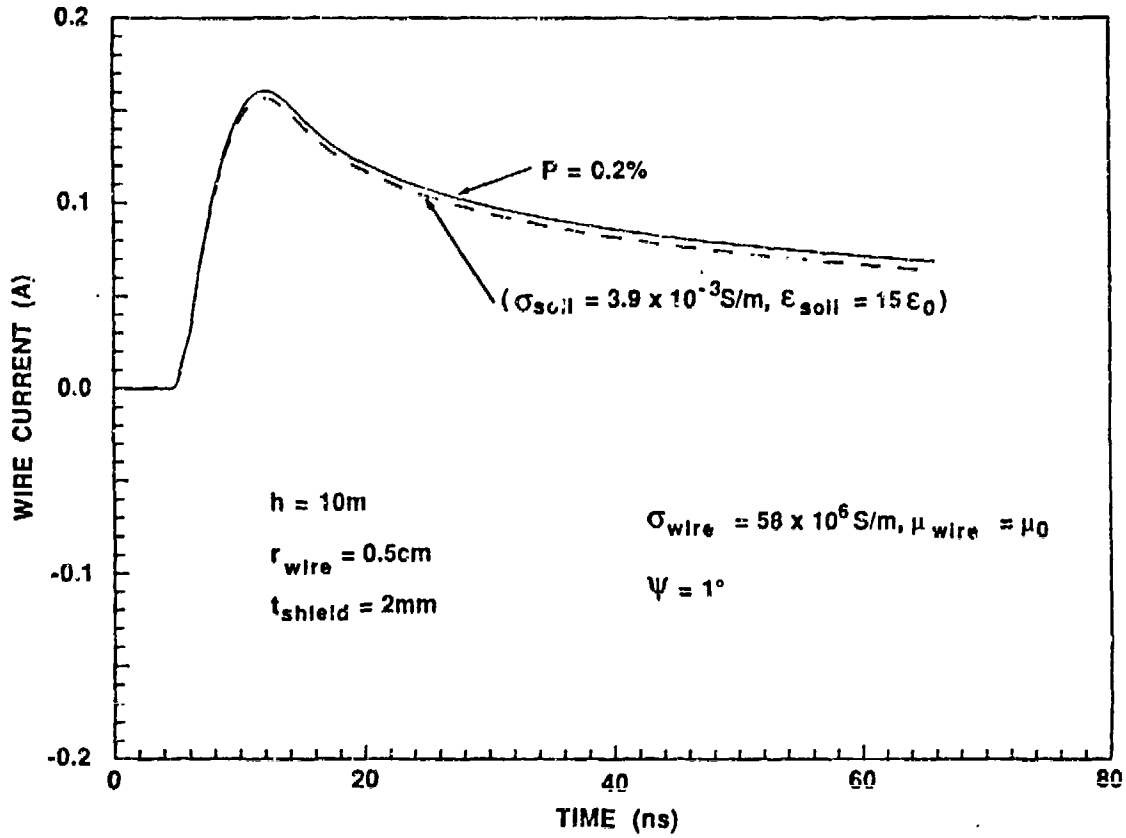


Figure 13. Wire Current Induced by Plan Wave Excitation with 0.1 ns Risetime

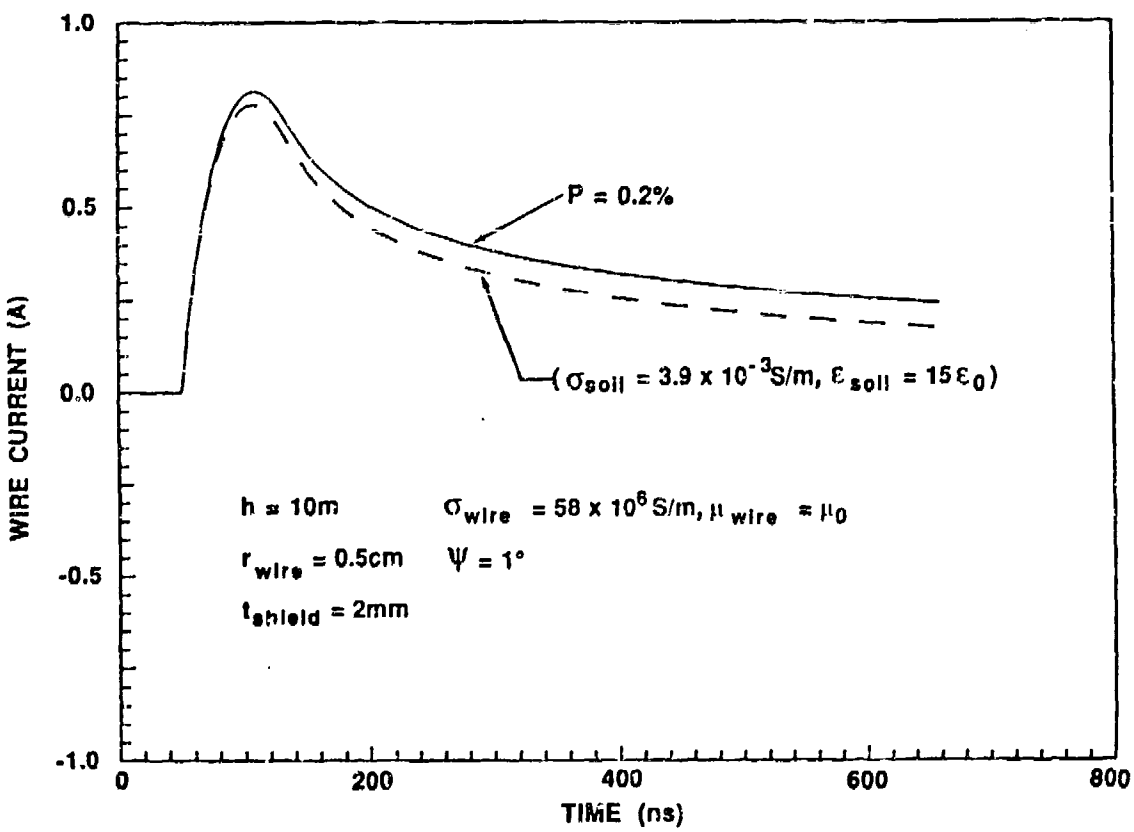


Figure 14. Wire Current Induced by Plane Wave Excitations with 1.0 ns Risetime

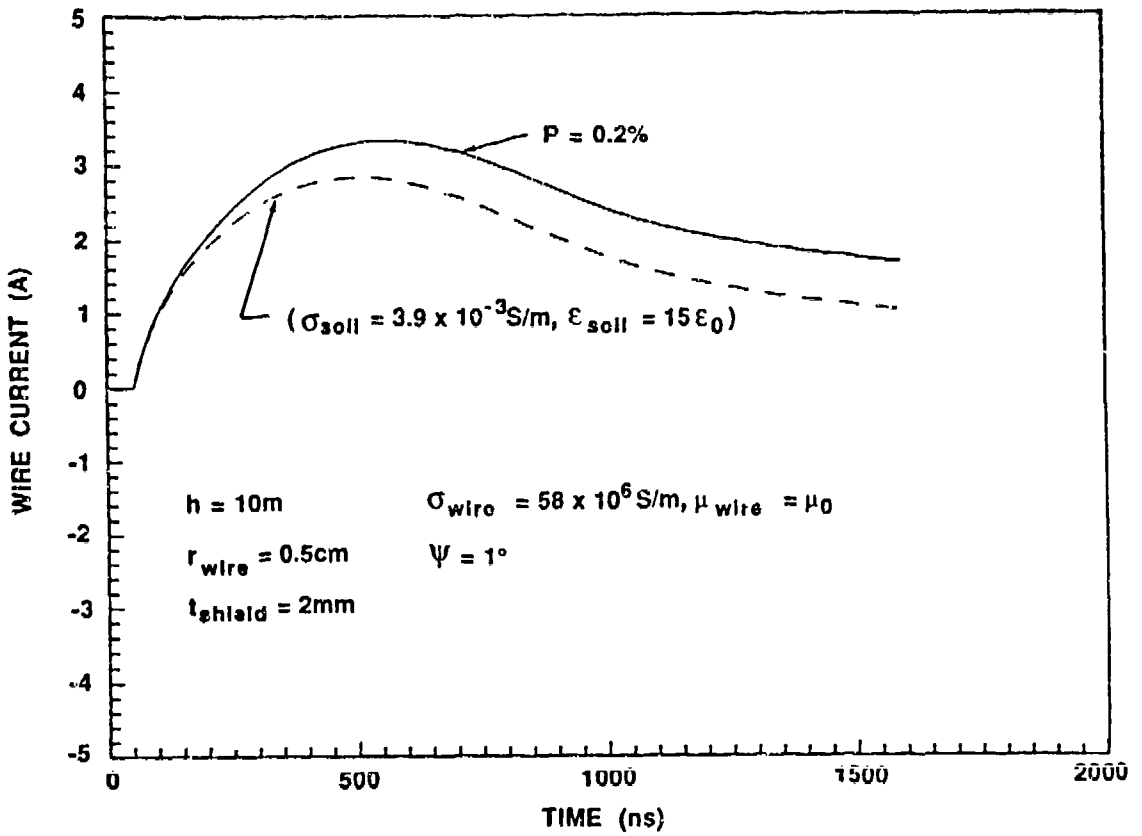


Figure 15. Wire Currents Induced by Plane Wave Excitations with 10.0 ns Risetime

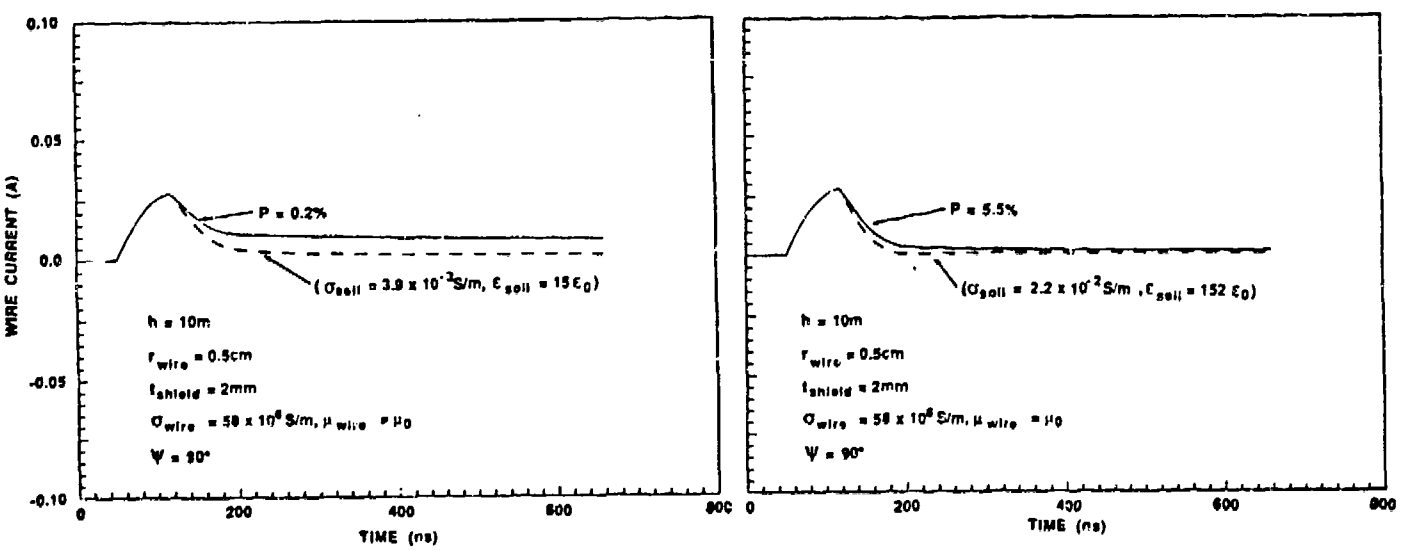


Figure 16. Wire Currents Calculated for Two Soil Models and Plane Wave Excitation with 1.0 ns Risetime

NEAR FIELD ANALYSIS OF LARGE PARALLEL-PLATE EMP SIMULATORS USING NEC

Stephen Gedney and Raj Mittra
Electromagnetic Communication Laboratory
University of Illinois
Urbana, Illinois 61801

INTRODUCTION

The Electromagnetic Pulse (EMP) produced by a high-altitude nuclear burst presents a severe threat to electronic systems due to its extreme characteristics. In order to test the vulnerability of large systems, such as airplanes, missiles, or satellites, they must be subjected to a simulated EMP environment, characterized by a highly peaked transient pulse with a planar wavefront that uniformly illuminates the test object. One type of simulator that has been used to approximate the EMP environment is the Large Parallel-Plate Bounded-Wave Simulator. The parallel-plate bounded-wave simulator is a guided wave simulator which has the properties of a transmission line and supports a single TEM mode at sufficiently low frequencies. Ideally, it has a uniform characteristic impedance that is independent of frequency and when terminated by a matched impedance provides a pure traveling wave.

Parallel-plate bounded-wave EMP simulators consist of finite-width parallel-plate waveguides, which are excited by a wave launcher and terminated by a wave receptor. Typically, conical tapered waveguides are matched to the parallel-plate region in order to excite and terminate a plane wave in the parallel-plate region. This geometry is illustrated in Figure 1. The apex of the wave launcher is excited by a transient source which has a rise time, on the order of 1-5 nanoseconds, that is significantly smaller than the transit time of the waveguide, and a fall time on the order of 1 microsecond. In theoretical computations, the pulse is usually represented as a double exponential waveform and has broadband characteristics.

In this paper, the characteristics of the simulator and the field distribution within its central region are to be determined. The simulator is an open waveguide structure and its complete field representation is a superposition of discrete and continuous modes. At very low frequencies, where the plate separation is much less than one-half of a wavelength, only the TEM modes of the discrete spectrum will propagate

along the waveguide and the field distribution is easily computed using a quasi-static analysis [1]. However, in practice, the plate separation will be quite large in order to accommodate large test objects. Under a transient pulse excitation, there will be significant energy distributed throughout a very broad band, extending into the high-frequency region. As a result, higher-order TE and TM modes will propagate along the waveguide, in the high-frequency region, and the open simulator will act as a radiator no longer supporting purely guided modes.

There has been much work done on computing the field distribution within the simulator by modal analysis [2-5]. These works offer excellent physical and theoretical interpretation of the parallel-plate bounded-wave EMP simulator by considering ideal situations. Through such analysis, the explanation of notches in the magnetic fields has been determined [6], optimum loads have been designed, and other standards in design have been developed [7]. However, these works have been restricted to infinite and semi-infinite empty waveguides. When designing an EMP simulator, the engineer has much more to consider than the transmission line properties of the simulator itself. A test object, placed within the parallel-plate region, can greatly perturb the simulator fields and the relative amplitude of the modes may greatly differ from those calculated in the empty working volume. Therefore, one cannot treat the calculated fields of the empty working volume as the incident field that establishes the charge and current density on the test object throughout the entire bandwidth of operation. This so-called "simulator-obstacle" interaction can be analyzed analytically for certain geometries only [8], such as an infinite cylinder in a parallel-plate waveguide.

In this paper, the Numerical Electromagnetics Code (NEC) is shown to be a valid tool for performing a dynamic field analysis of the parallel-plate bounded-wave simulator in the frequency domain. Initially, the development of the wire mesh approximation is presented and the computed characteristics of an asymmetric parallel-plate EMP simulator is given as an example. Finally, the problem of simulator-obstacle interaction is presented with the use of NEC.

DEVELOPING THE PROBLEM

The parallel-plate EMP simulator is characterized as a transmission-line type of simulator which, in this paper, will be treated as a thin-wire scattering problem. The conducting surfaces of the simulator will

be approximated by a thin-wire mesh model, and the incident field will be an applied voltage source distributed across the source gap region. In this section, the thin-wire model of the simulator is discussed.

NEC is used in this paper to analyze the thin-wire scattering problem (a complete analysis of the NEC-2 code is provided in [10]). NEC is particularly useful in this application since it provides the capability of modeling multiple-wire junctions. The unknown electric current distributed over the wire mesh is expanded into subdomain basis functions defined by a three term spline function, in which two terms are eliminated by enforcing charge and current continuity across each multiple wire junctions, and the third by satisfying the surface boundary condition on the tangential E-field by point matching the Electric Field Integral Equation (EFIE).

A preliminary study of the plane-wave scattering from a finite-dimensional conducting plate, modeled by a thin-wire mesh, has verified that the NEC code provides a valid approximation to such a scattering geometry [9]. In order to minimize the number of unknowns as well as best approximate the surface currents, a rectangular mesh was used to model the plate, with segment lengths no greater than a tenth of a wavelength. Furthermore, the area of the mesh openings was kept constant. This model provided a good approximation of the edge singularities. The conducting surface of the EMP simulator was modeled in the same manner, with the inclusion of an edge wire, and continuous wires along the longitudinal direction. A sample geometry is illustrated in Figure 2.

NEC has been used to wire-model conducting surfaces for a large number of problems in which the principal area of interest was the far field. In the EMP simulator problem, however, one is interested in the near field characteristics, viz., the field distribution in the central region of the simulator. NEC enforces Kirchoff's current law across each multiple wire junction to satisfy total current continuity. However, the discontinuity in the vector currents, at a wire bend or at a wire junction of more than two wires, leads to non-physical singularities in the near field which could produce errors in the results. It was found through numerical solution that the singularities are negligible when sampling the electric-field at distances of at least $\lambda/12$ from the wire mesh [9].

An accurate source model is extremely important to establish the proper excitation of the transmission-line type of EMP simulator. It must be distributed across the source gap region, as well as excite the dominant TEM mode. Similarly, the load model is important to properly terminate the

waveguide, minimizing reflections due to model limitations. The Applied E-Field (AEF) source was used distributing a constant E-field over the source region. The wire model used is illustrated in Figure 3. Figure 4 illustrates the surface scattered E-field computed along the source wire segment for a 1-volt excitation. The amplitude, as expected, is constant and has a phase of -180^{o}. There is a noticeable singularity in the pulse due to the sharp wire bend of the model, however, it was found that the error due to this singularity in the fields in the central region of the simulator is negligible. Figure 5 illustrates the thin wire approximation of the load model used. Ideally, it is desirable to place a resistive sheet across the load gap, terminating the fields. However, purely resistive loads were distributed along the thin wires to establish the termination.

The source and load models of the parallel-pate simulator were developed through the analysis of the transmission-line type rhombic EMP simulator. The models described above provided an excellent approximation of the desired distributed source and load and reproduced both the theoretical and experimental results reported by Shen and King [11,12]. It should be noted that error was encountered in the characteristic impedance of the simulator, computed with the use of NEC, when the source and load gap heights were on the order of one-quarter of a wavelength. This was due to the phase shift in the current inherent to the model limitations. Despite the error in the matched impedance value, the simulator fields and the conductor currents compared extremely well under matched conditions [9].

NUMERICAL RESULTS

The simulator to be analyzed is that of an asymmetrical, parallel-plate simulator, with conical tapered end sections. The dimension is same as the ACHATES simulator, designed by the Air Force Weapons Laboratory [13]. The ACHATES simulator was chosen for its unique characteristics which will subsequently enable the results to be easily interpreted.

The ACHATES simulator has a height to width ratio of

$$\frac{h}{a} = 1.2335 .$$

This aspect ratio is chosen such that the simulator has a quasi-static characteristic impedance of 100 Ω. Furthermore, it can be shown that a one-volt excitation across the source gap will produce a field of one-volt per meter at the center of the ground plane (at x = 0). The length of the conical tapered end sections

is chosen such that the simulator has an operating "bandwidth" of 450 MHz. This bandwidth is determined by a time dispersion that results from the matching of a quasi-spherical wavefront, supported by the conical tapered end sections, into a planer wavefront of the parallel-plate region. When the maximum dispersion distance, defined by the maximum lag along the curve of constant phase, becomes on the order of a quarter wavelength, energy is coupled into higher order modes significantly distorting the fields. The frequency associated with this wavelength defines the upper cutoff, or bandwidth, of the simulator. The dimensions of the simulator are illustrated in Figure 6.

The E-field distribution has been computed in the central parallel-plate region, often referred to as the working volume, due to a one-volt excitation. In each case presented, the simulator was terminated in its characteristic impedance, which was defined as the resistive load that minimized the current standing standing wave ratio, and maximized the amount of power dissipated by the load. Two examples will be illustrated: 1) 75 MHz, which has a computed characteristic impedance of 120Ω, 2) 125 MHz, which has a characteristic impedance of 95Ω. Figures 7 and 8 illustrate the vertical E-field (E_z) computed along the longitudinal-direction. The fields are quite uniform and have a linear progressive phase shift throughout the working volume along the longitudinal direction. It should also be noted that there is very little change in phase along the vertical direction since the propagating waves have planar equiphase fronts. As expected through the design of ACHATES, a one-volt excitation produces a one-volt per meter vertical E-field at the ground plane and at x=0. Some deviation is due to the existence of non-TEM modes, as well as some limitations of the approximate simulator model.

Figure 9 illustrates the vertical E-field as a function of the vertical direction due to a 125 MHz excitation. The fields are quite uniform throughout the height of the simulator. However, it is apparent that there is error in the computed field close to the thin-wire mesh. The error is due to both the wire mesh approximation of the conducting surface, as well as the singularities of the current discontinuities at the wire junctions. Figure 10 illustrates the longitudinal field (E_y) in the x=0 plane which is representative of the propagating TM field. The longitudinal field is on the order of a magnitude smaller than the vertical E-field. E_y becomes more significant in the higher-frequency regions which can be explained as follows: A "quasi-spherical" wavefront propagates from the wave launching conical tapered section into the parallel-plate region. Along the ground plane, the incident E-field is purely TEM. However, due to the

mismatch the TM mode becomes more significant along the vertical direction above the ground plane. At higher frequencies, the trailing edge of the spherical wavefront will become comparable to a wavelength and significant TM modes are generated. Furthermore, it is noted that E_y tends to be a minimum at y=0 and increases again as y progresses due to the mismatch with the terminating conical end section.

SIMULATOR-OBSTACLE INTERACTION

The purpose of an EMP simulator is to simulate the conditions of a test object being illuminated by the electromagnetic pulse produced by a nuclear explosion. The currents induced on the object and the fields coupled within, due to various defects, are then measured in order to determine its vulnerability. The electric field within the central region of the parallel-plate simulator closely approximates the plane-wave pulse environment desired, with some deviations as expressed in the previous section. However, when a test object is placed within the simulator, the desired environment will be distorted due to mutual coupling. Therefore, an understanding of the interaction between the simulator and the test object is quite important.

Once a test object is placed within the central region of the simulator, the fields will be a superposition of both the incident field and a perturbed field, which will introduce coupled energy into undesirable modes. Not only will this distort the pulse environment, but the characteristics of the simulator can change, i.e., the simulator may no longer be matched. If the test object is small compared to the dimensions of the parallel-plate region, then there will be very little change in the simulator characteristics. However, when the dimensions of the test object become comparable to half the height of the parallel-plate above the ground plane, the amount of coupling can be quite significant. This problem can be studied with the use of the NEC code by introducing a test object, modeled as a wire mesh, in the working volume of the simulator. With the introduction of the test object, the perturbation of the simulator characteristics can be observed.

For the purposes of this paper, we will present the problem of placing a cube, with a side dimension of one-half of the simulator height, within the parallel-plate region. This is illustrated in Figure 11.

Figure 12 illustrates the vertical E-field computed along the ground plane for the case of an empty working volume, as well as in the presence of the conducting cube for a 100 MHz excitation. In the presence of the obstacle, the fields within the simulator are a superposition of the incident field, the scattered field and the fields multiply-scattered between the object and the simulator.

Figures 13 and 14 illustrate the edge currents of the simulator for the case of the empty working volume and in the presence of the cube, respectively. Comparing the two figures, it is observed that indeed there is a perturbation of the surface currents, thus distorting the desired environment. Measuring the input impedance of the simulator under both conditions [9], it is found that under matched conditions, the input impedance of the simulator with an empty working volume is $97.04+j\,14.68\ \Omega$, whereas with the cube in the working volume the input impedance was $76.64+j\,17.03\ \Omega$. Furthermore, due to coupling the simulator is no longer matched by the 120 Ω load and subsequent reflections are encountered by the termination.

COMPUTATIONAL CONSIDERATIONS

The NEC-2 code was rewritten and compiled in double precision Microsoft Fortran, and the computations presented in this paper were performed using an AT&T PC6300 desktop microcomputer or a compatible DOS machine. The program itself requires 450 kbytes of RAM to load, and approximately 6 Mbytes free on a hard disk for out of core solutions with up to 600 unknowns (problems with over 800 unknowns have been solved on the PC). Table 1 lists the computation times required to fill and factor the moment matrix for the ACHATES simulator with a 450 MHz bandwidth. It should be noted that the computations include one plane of symmetry about the x-axis, which reduces the computation time by a factor of $N^2/4$. One obvious limitation of the use of the NEC code is that as the frequency becomes larger, the number of unknowns increase as $1/\lambda^2$. Therefore, in the high-frequency region, where the wavelength is quite small compared to the simulator dimensions, the total number of unknowns becomes extremely large.

CONCLUSIONS

In this paper it has been shown that the Numerical Electromagnetics Code can be used to develop the characteristics of a parallel-plate bounded wave EMP simulator using a thin-wire mesh approximation of the conducting surfaces. The fields computed within an asymmetric, parallel-plate simulator operating in its mid-frequency range were presented, and the simulator characteristics were developed. Furthermore, NEC has been shown to be a useful tool in analyzing the more complex problem of simulator-obstacle interaction. With the use of the NEC code, more complicated configurations may be studied as well, and using the model described herein, useful results may be obtained.

REFERENCES

[1] Carl E. Baum, "Impedance and field distributions for parallel plate transmission line simulators," Sensor and Simulation Note 21, Air Force Weapons Laboratory, Kirtland AFB, NM, 6 June 1966.

[2] T. Itoh and R. Mittra, "Analysis of modes in a finite width parallel-plate waveguide," Sensor and Simulation Note 208, Air Force Weapons Laboratory, Kirtland AFB, NM, January 1975.

[3] A. M. Rushdi, R. C. Menendez, R. Mittra and S.W. Lee, "Leaky modes in parallel plate EMP simulators," *IEEE Transactions on Electromagnetic Compatibility*, vol. EMC-20, pp. 443-451, August 1978.

[4] C-H. Tsao, E. Yung and R. Mittra, "The source excitation of a finite-width parallel-plate waveguide," Sensor and Simulation Note 255, Air Force Weapons Laboratory, Kirtland AFB, NM, February 1979.

[5] J. Lam, "Excitation of the parallel-plate section of a bounded-wave EMP simulator by a conical transmission line," Sensor and Simulation Note 263, Air Force Weapons Laboratory, NM, 31 May 1979.

[6] R. W. P. King and D. J. Blejer, "The electromagnetic field in an EMP simulator at high frequency," *IEEE Transactions on Electromagnetic Compatibility*, vol. EMC-21, pp. 263-269, August 1979.

[7] D. V. Giri, T. K. Liu, F. M. Tesche and R. W. P. King, "Parallel-plate transmission line type of EMP simulators: A systematic review and recommendations," Sensor and Simulation Note 261, Air Force Weapons Laboratory, Kirtland AFB, NM, 1 April 1980.

[8] R. W. Latham, "Interaction between a cylindrical test body and a parallel-plate simulator," Sensor and Simulation Note 55, Air Force Weapons Laboratory, NM, May 1978

[9] phen D. Gedney, "A dynamic analysis of the parallel-plate EMP simulator using a wire mesh approximation and the Numerical Electromagnetics Code", USA-CERL Technical Manuscript M-87/15, U.S. Army Corp of Engineers CERL, Champaign, IL, September 1987.

[10] G. J. Burke and A. J. Poggio, "Numerical Electromagnetics Code (NEC) - method of moments," Naval Ocean Systems Center Technical Document 116,volumes I and II, Lawrence Livermore Laboratory, January 1981.

[11] H. M. Shen and R. W. P. King, "The rhombic EMP simulator," *IEEE Transactions on Electromagnetic Compatibility*, vol. EMC-24, pp. 255-265, May 1982.

[12] H. M. Shen and R. W. P. King, "Experimental investigation of the rhombic EMP simulator: Comparison with theory and parallel-plate simulator," *IEEE Transactions on Electromagnetic Compatibility*, vol. EMC-24, pp. 349-355, August 1982.

[13] K. Chen, Capt G. Michaelidis, Carl Baum and D. V. Giri, "ACHATES design," ACHATES Memo no. 1, Air Force Weapons Laboratory, Kirtland AFB, NM, 5 November 1976.

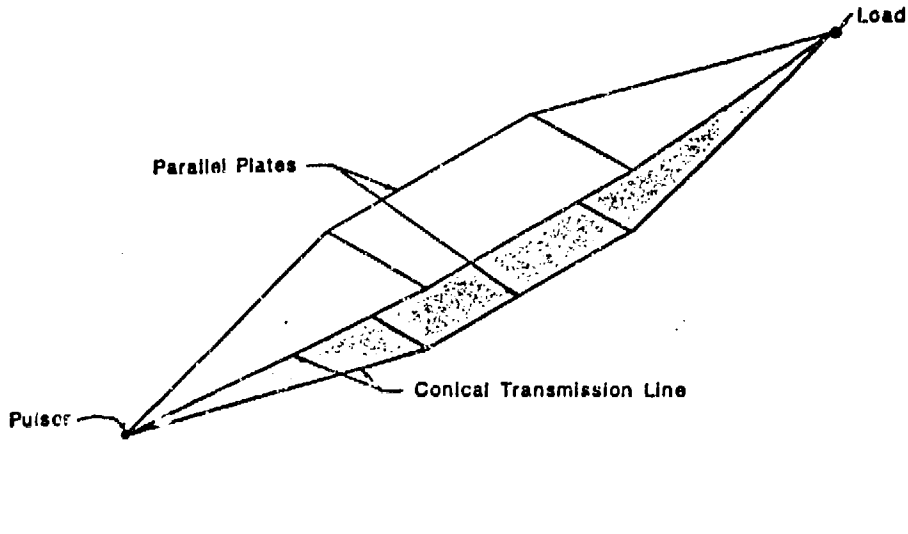


Figure 1. Symmetric parallel-plate bounded wave EMP simulator.

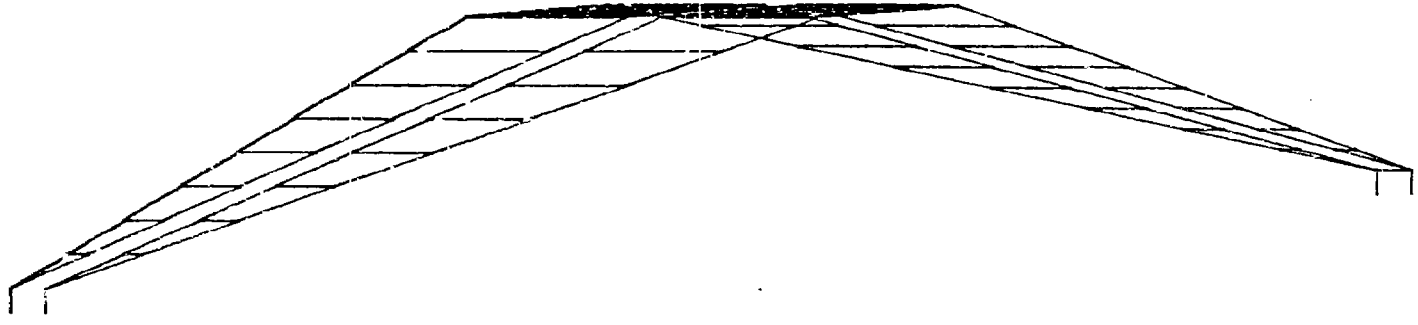


Figure 2. Wire mesh approximation of the conducting surface of the asymmetric parallel-plate EMP simulator.

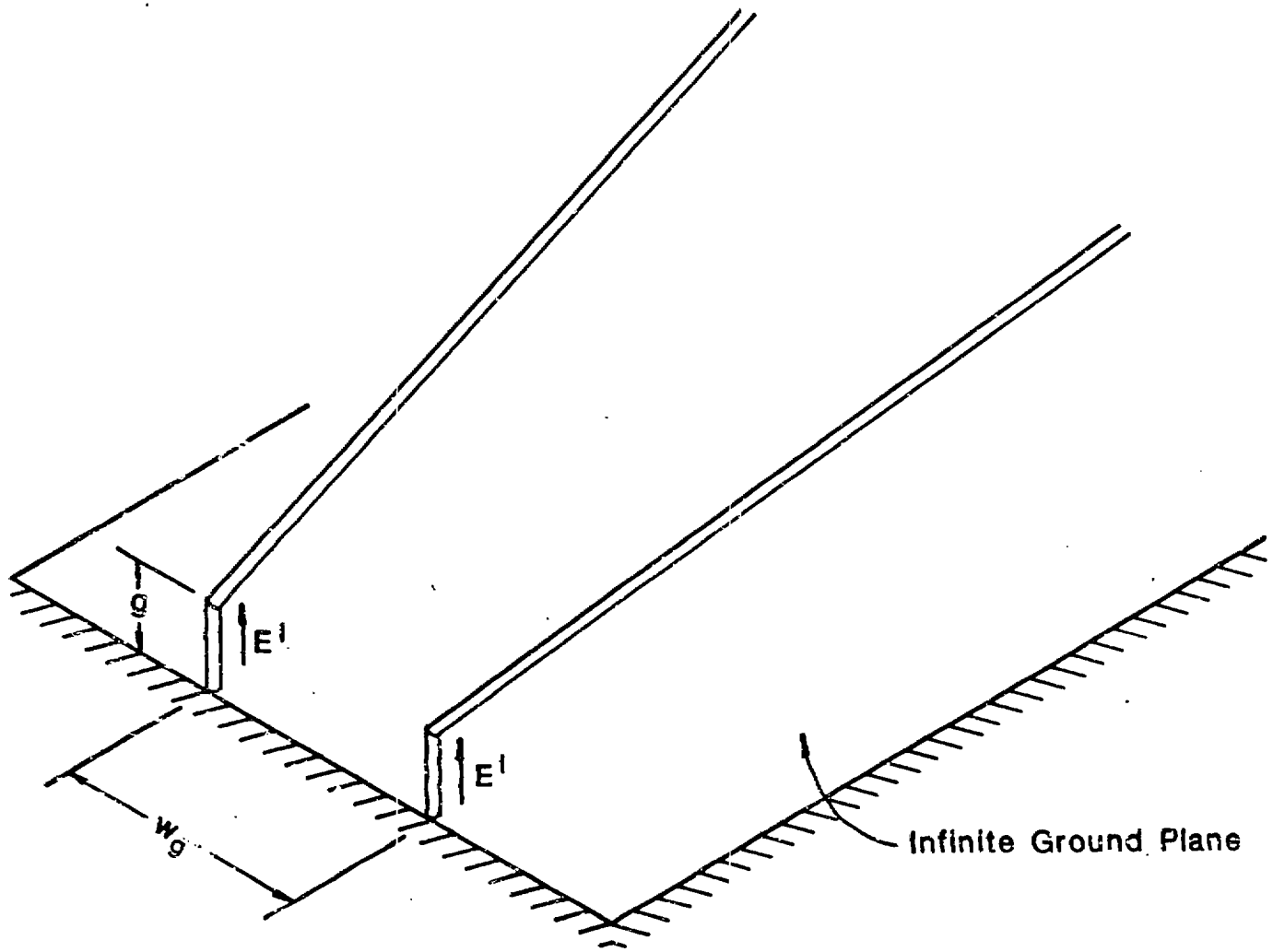
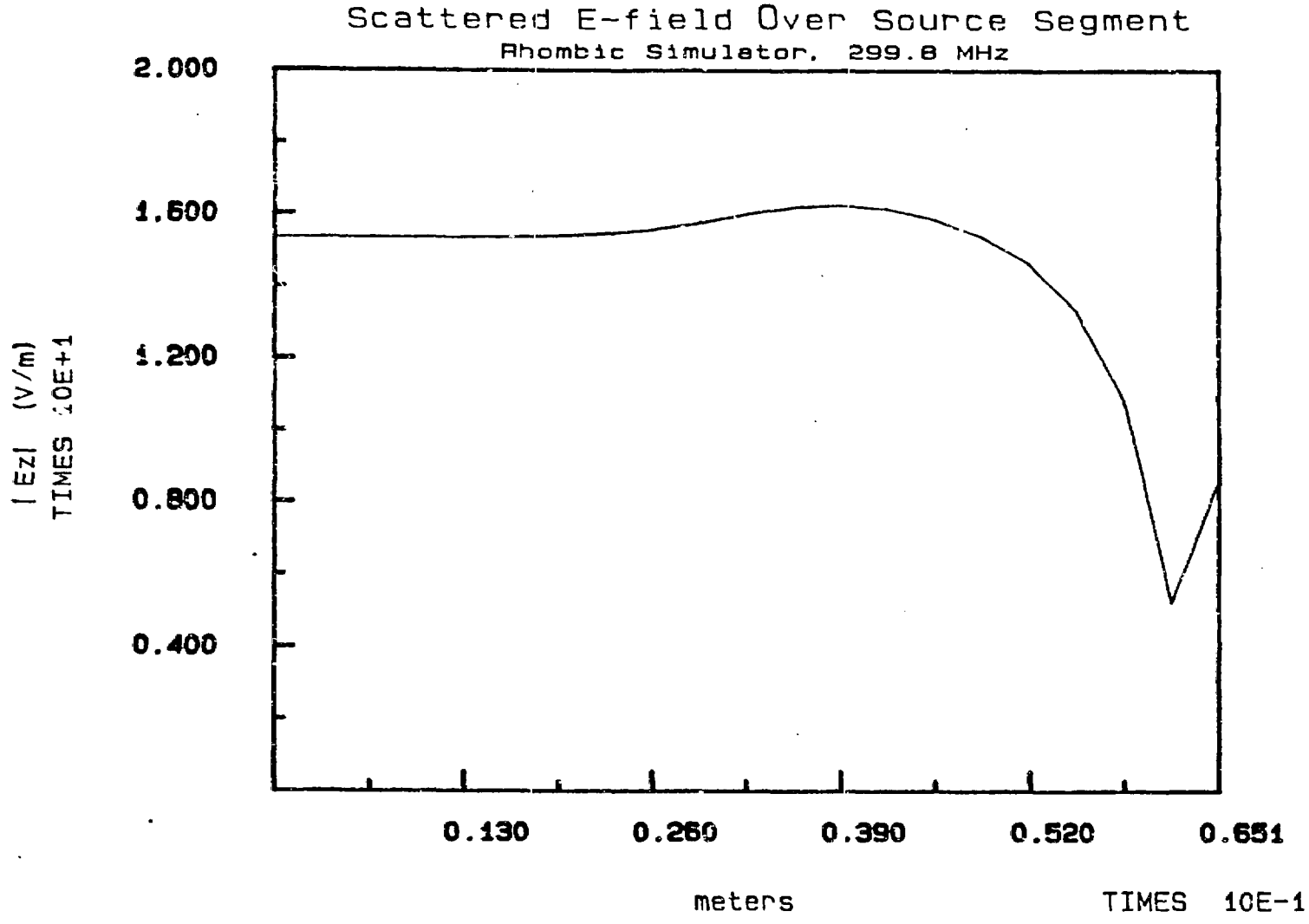


Figure 3. Thin-wire model of the source gap region of the rhombic EMP simulator.



Magnitude of axial E-field.

Figure 4 . Scattered axial E-field due to an AEF on the surface of the source segment.

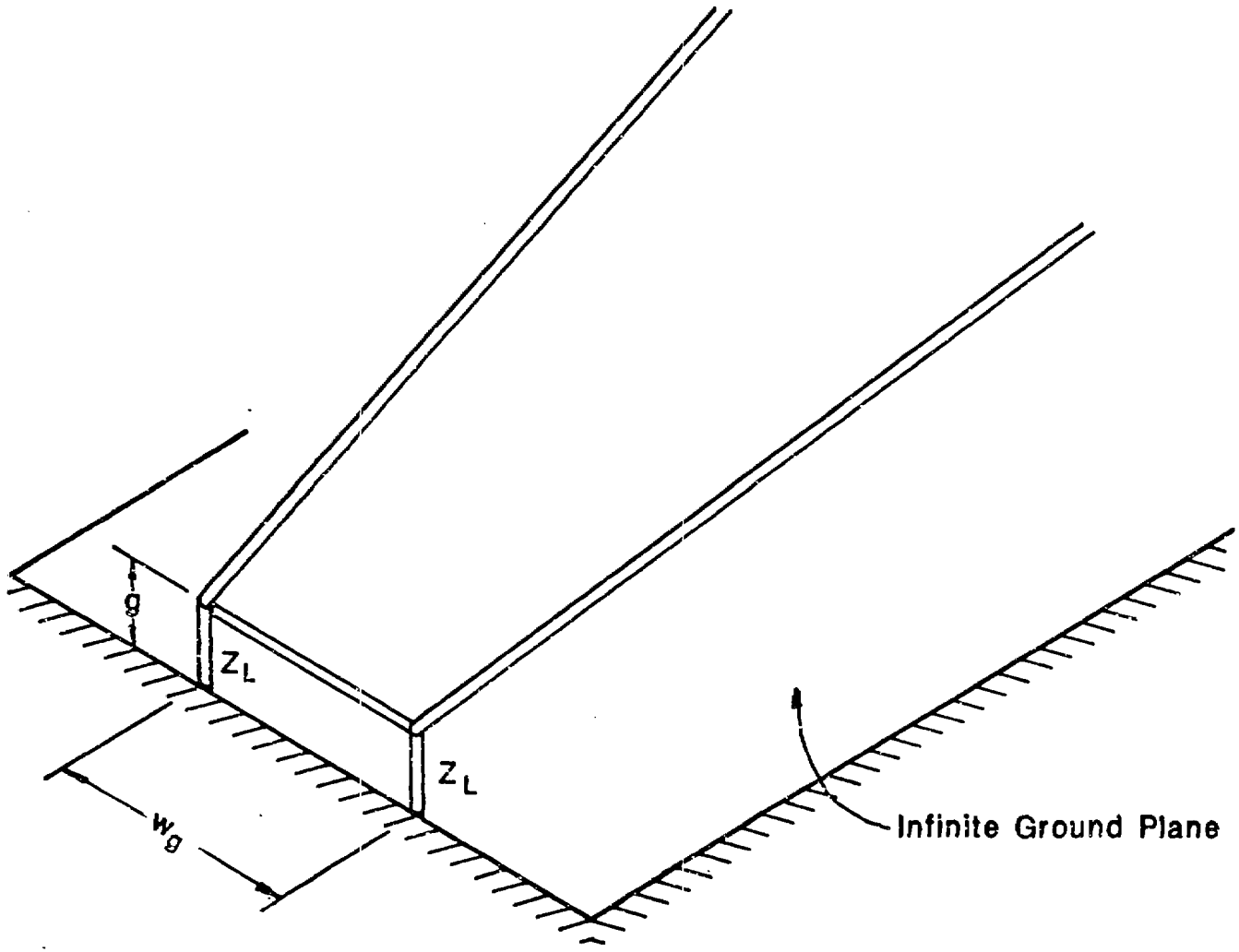
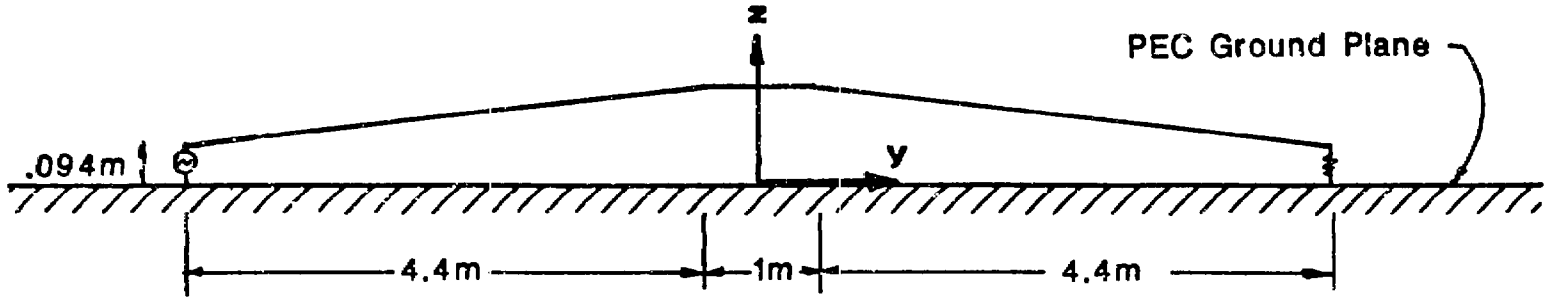
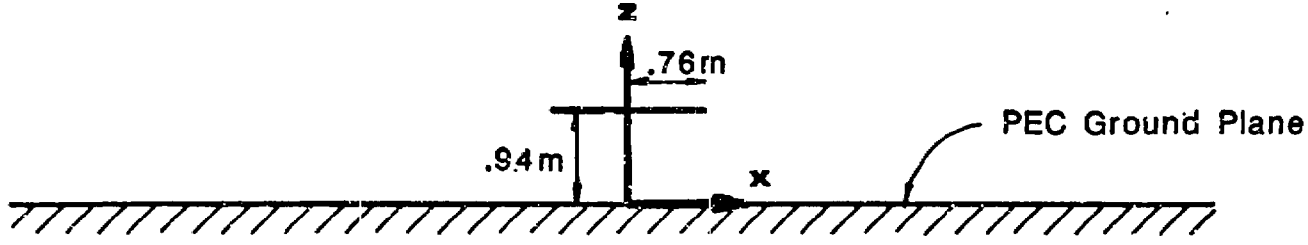


Figure 5. Thin-wire model of the terminating load gap region of the rhombic EMP simulator.

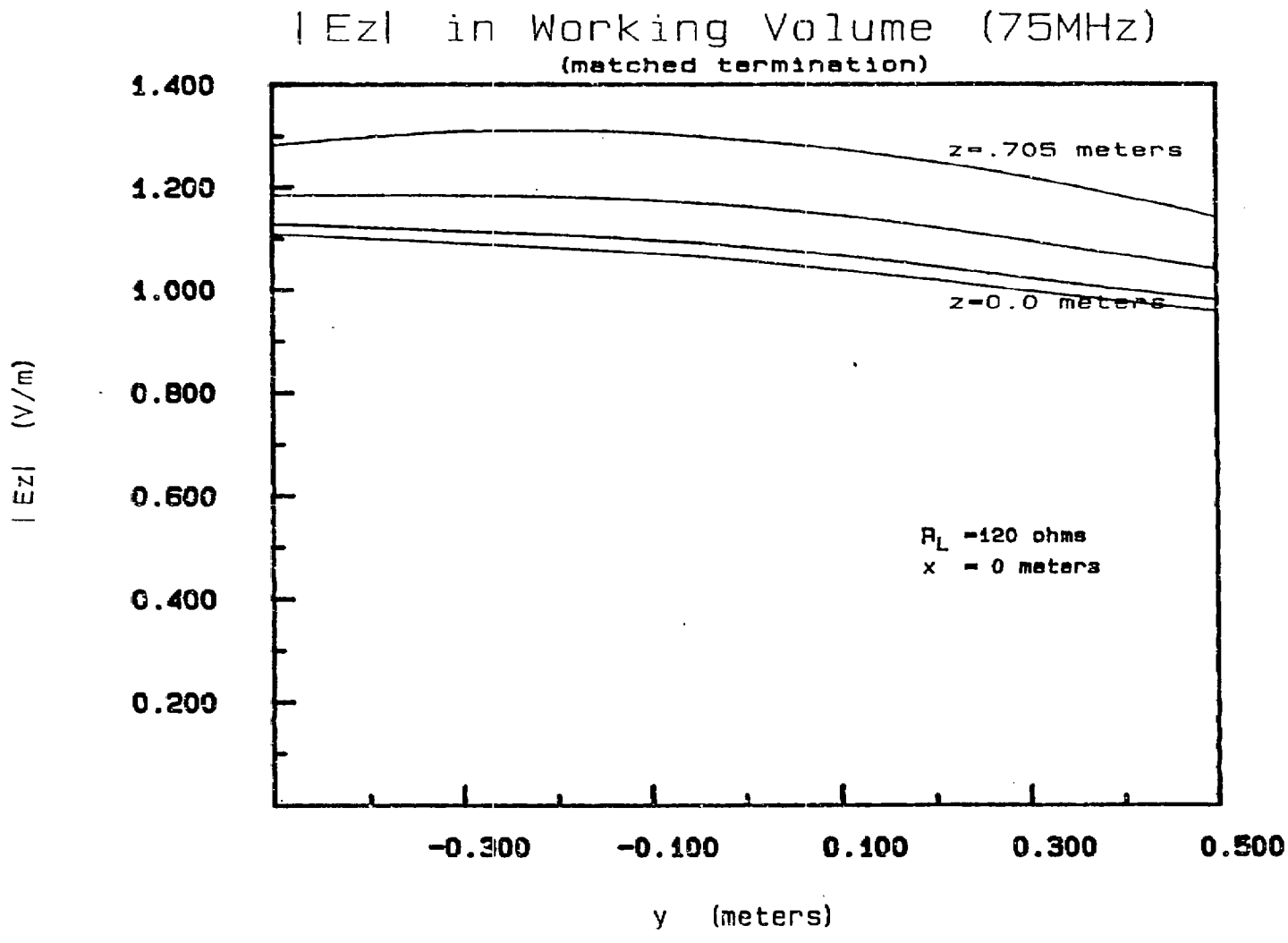


(a) Side view.



(b) Cross section; inside of parallel-plate region.

Figure 6. Dimensions of the ACHATES asymmetric parallel-plate bounded wave EMP simulator with a 450 MHz bandwidth.



(a) Magnitude of E_z.

Figure 7. Vertical E-field computed along the longitudinal direction in the parallel-plate region of the 450 MHz bandwidth ACHATES EMP simulator due to a unit amplitude, 75 MHz excitation.

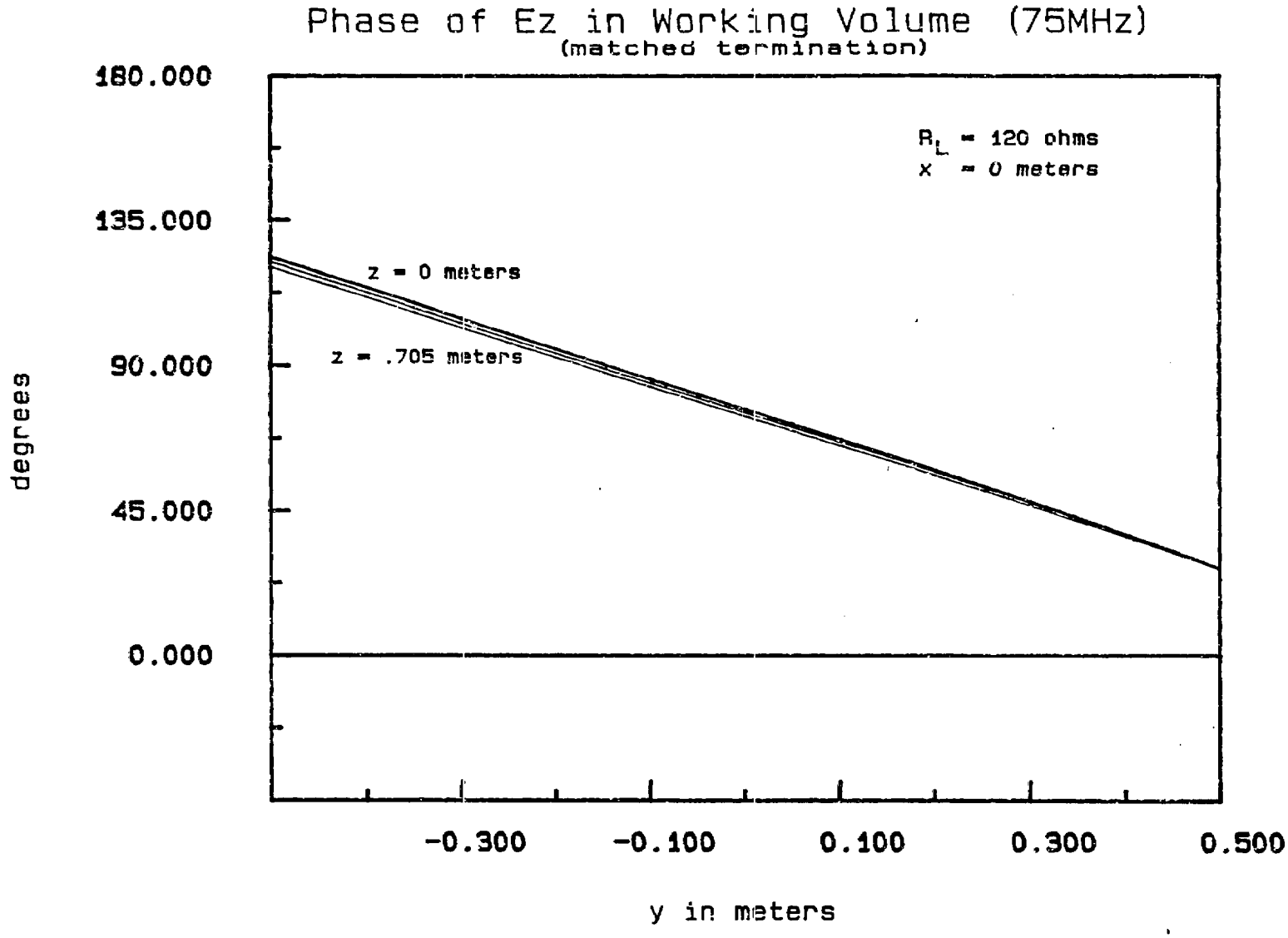
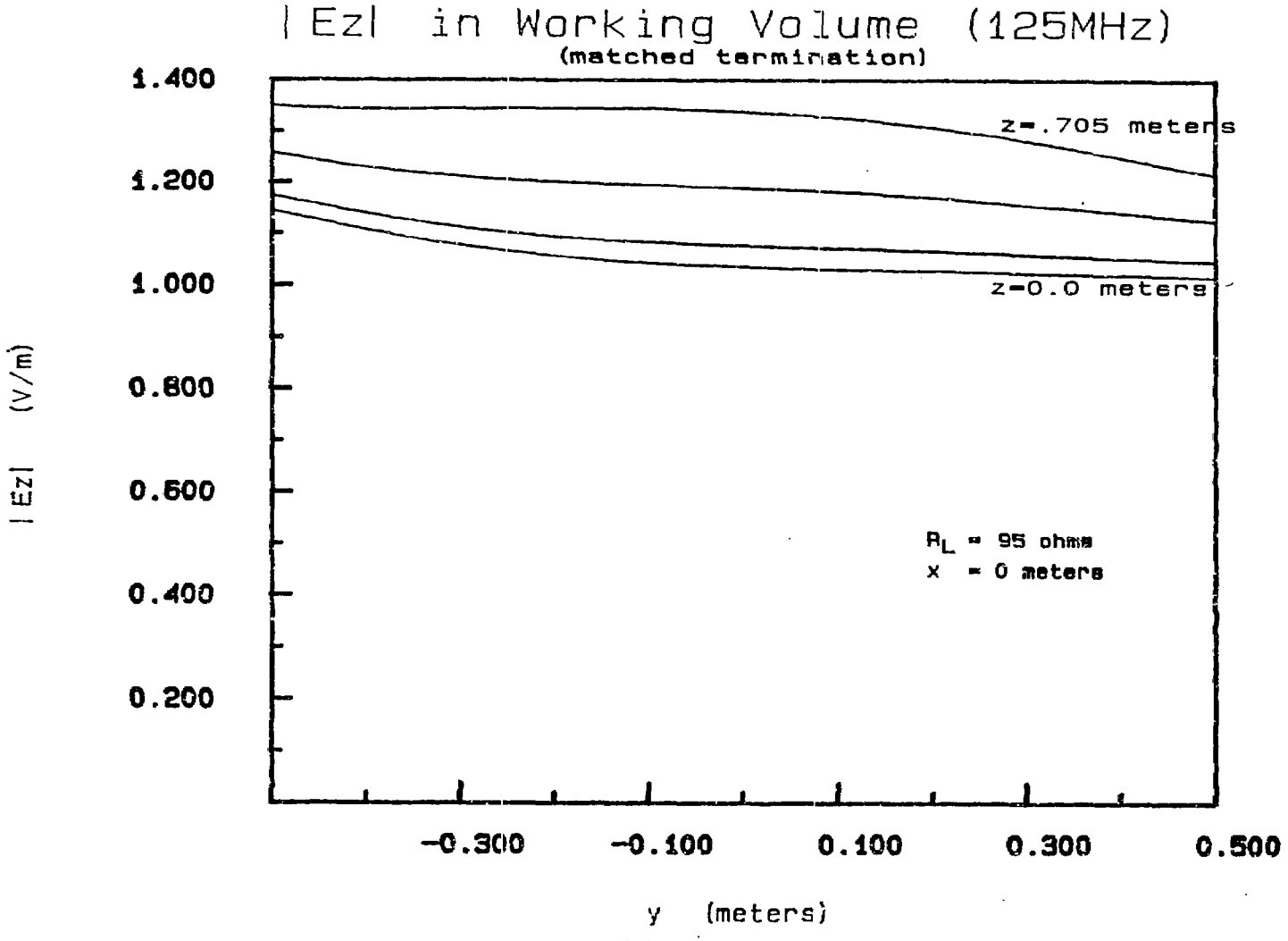


Figure 7 .(b) Phase of E_z.



(a) Magnitude of E_z.

Figure 8 . Vertical E-field computed along the longitudinal direction in the parallel-plate region of the 450 MHz bandwidth ACHATES EMP simulator due to a unit amplitude, 125 MHz excitation.

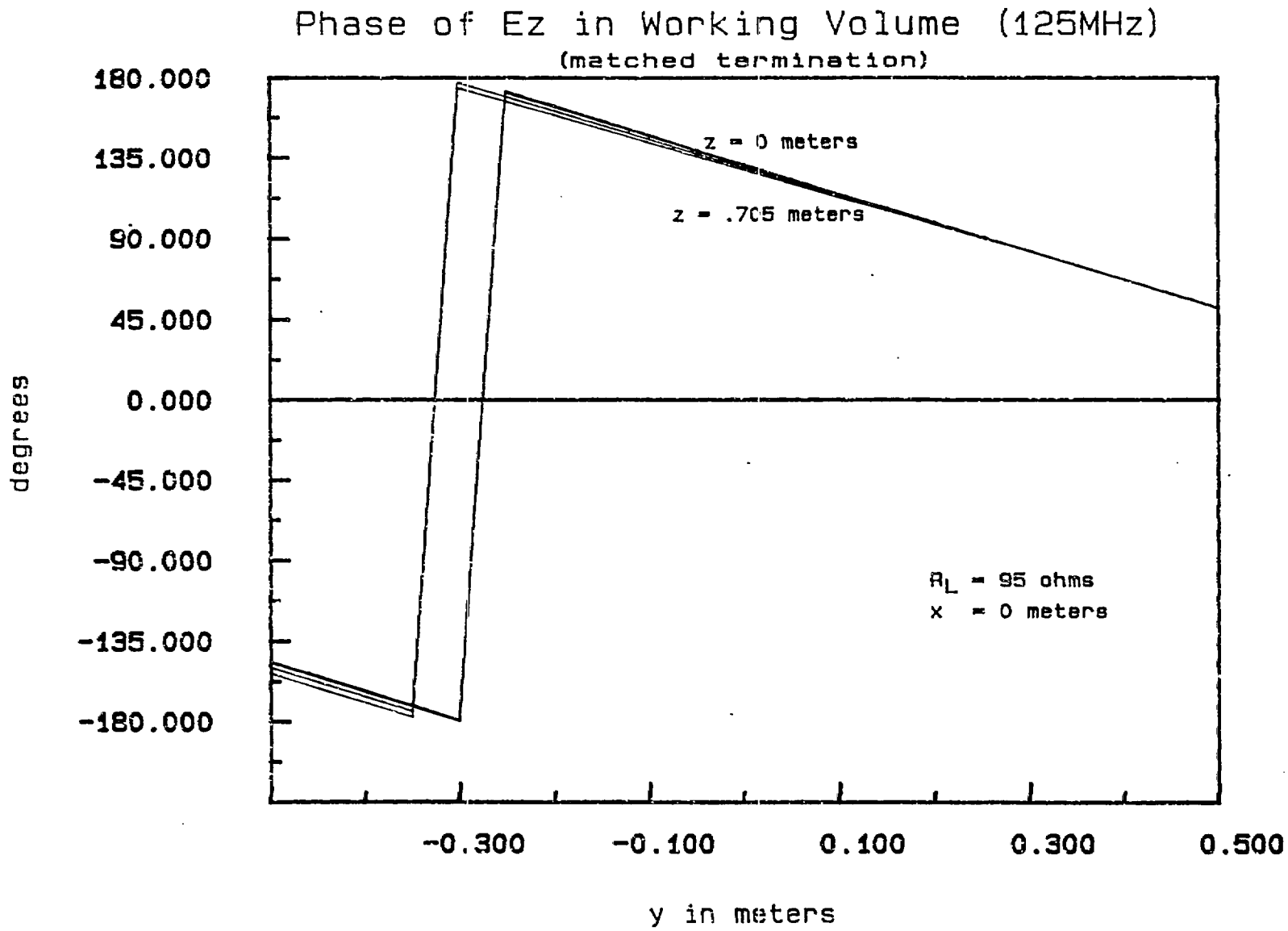


Figure 8 . (b) Phase of E_z .

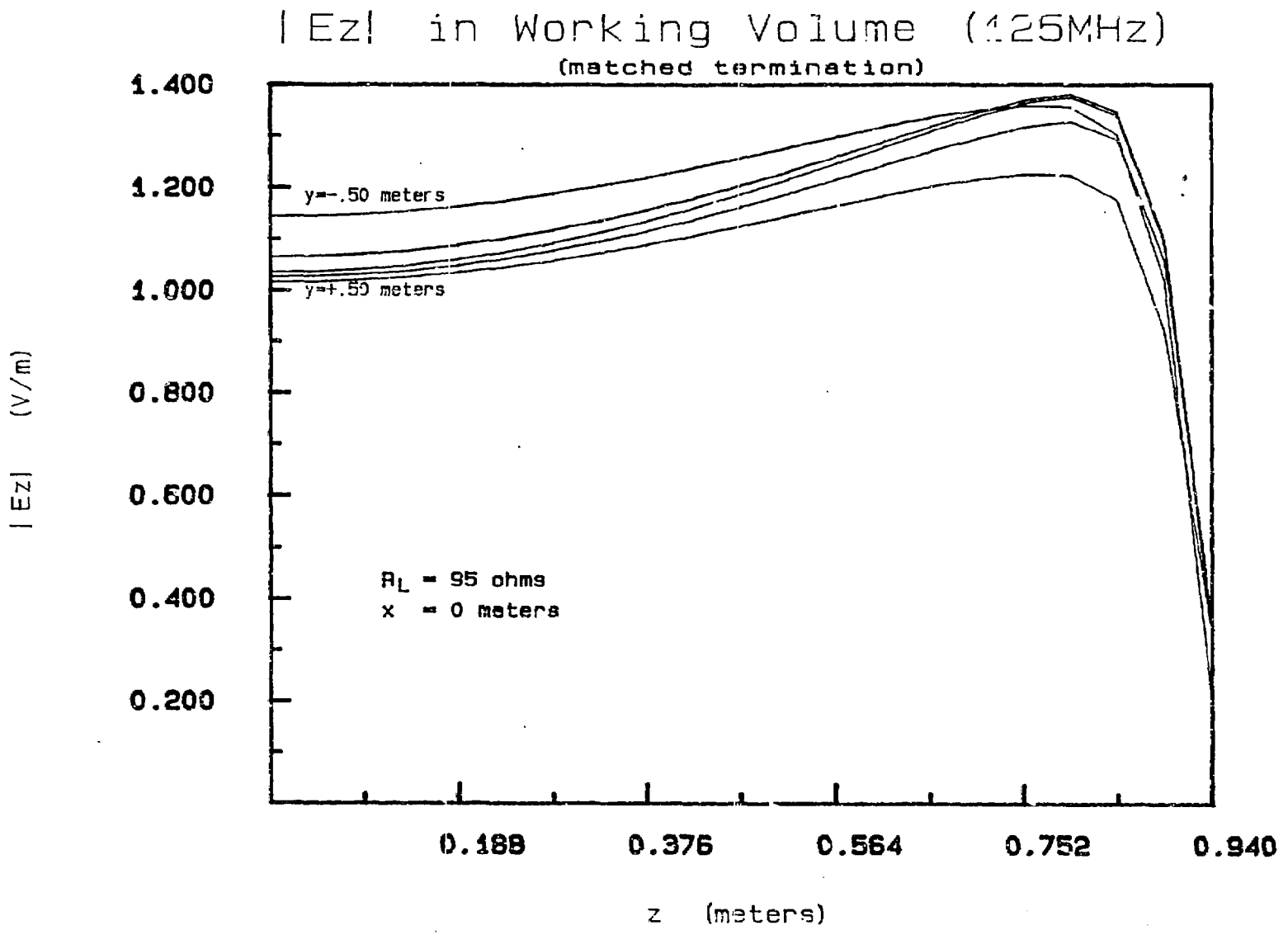


Figure 9. Magnitude of the vertical E-field computed along the vertical direction at various longitudinal positions due to a unit amplitude, 125 MHz excitation.

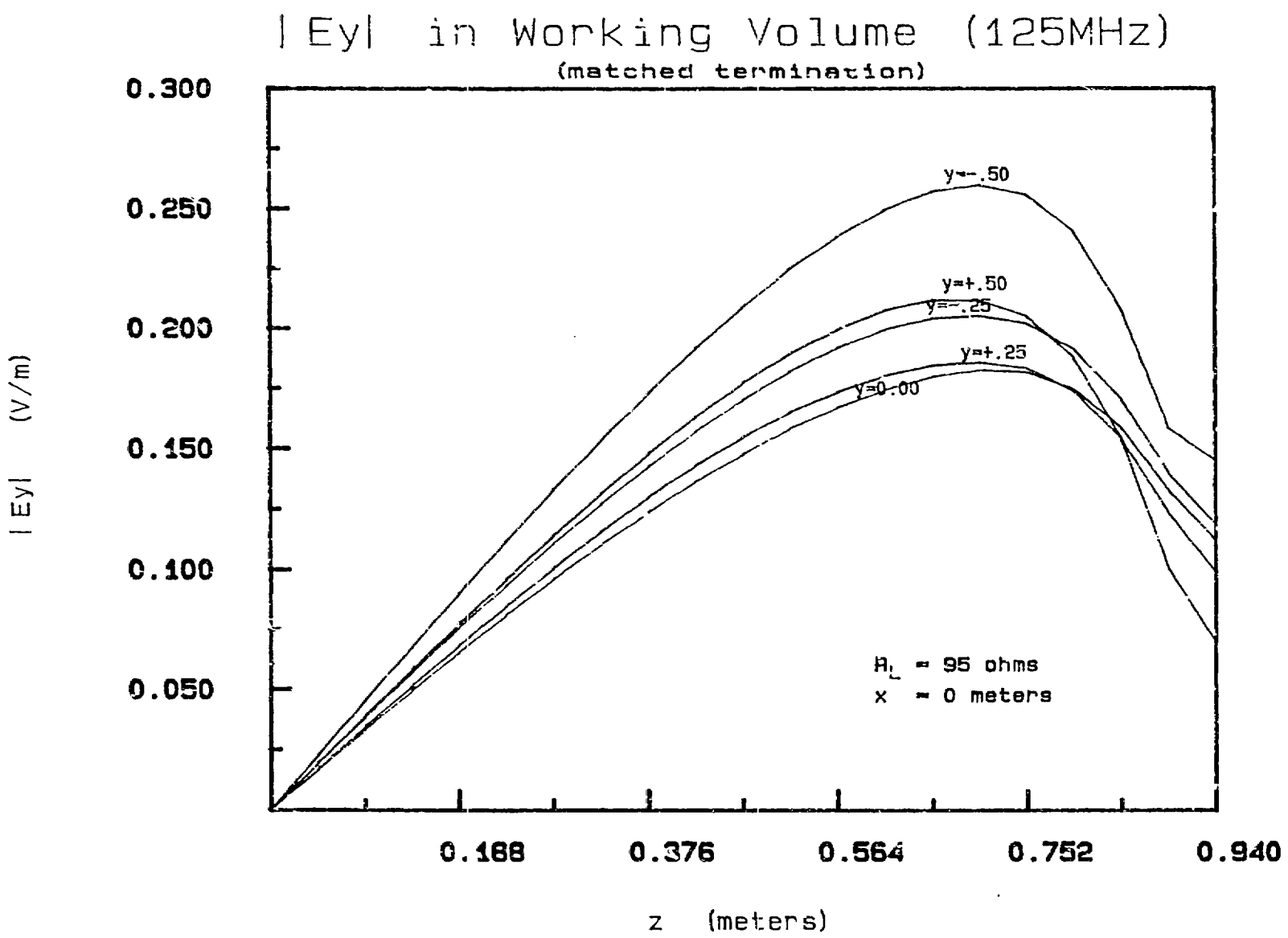


Figure 10 . Magnitude of the longitudinal E-field computed along the vertical direction at various longitudinal positions due to a unit amplitude, 125 MHz excitation.

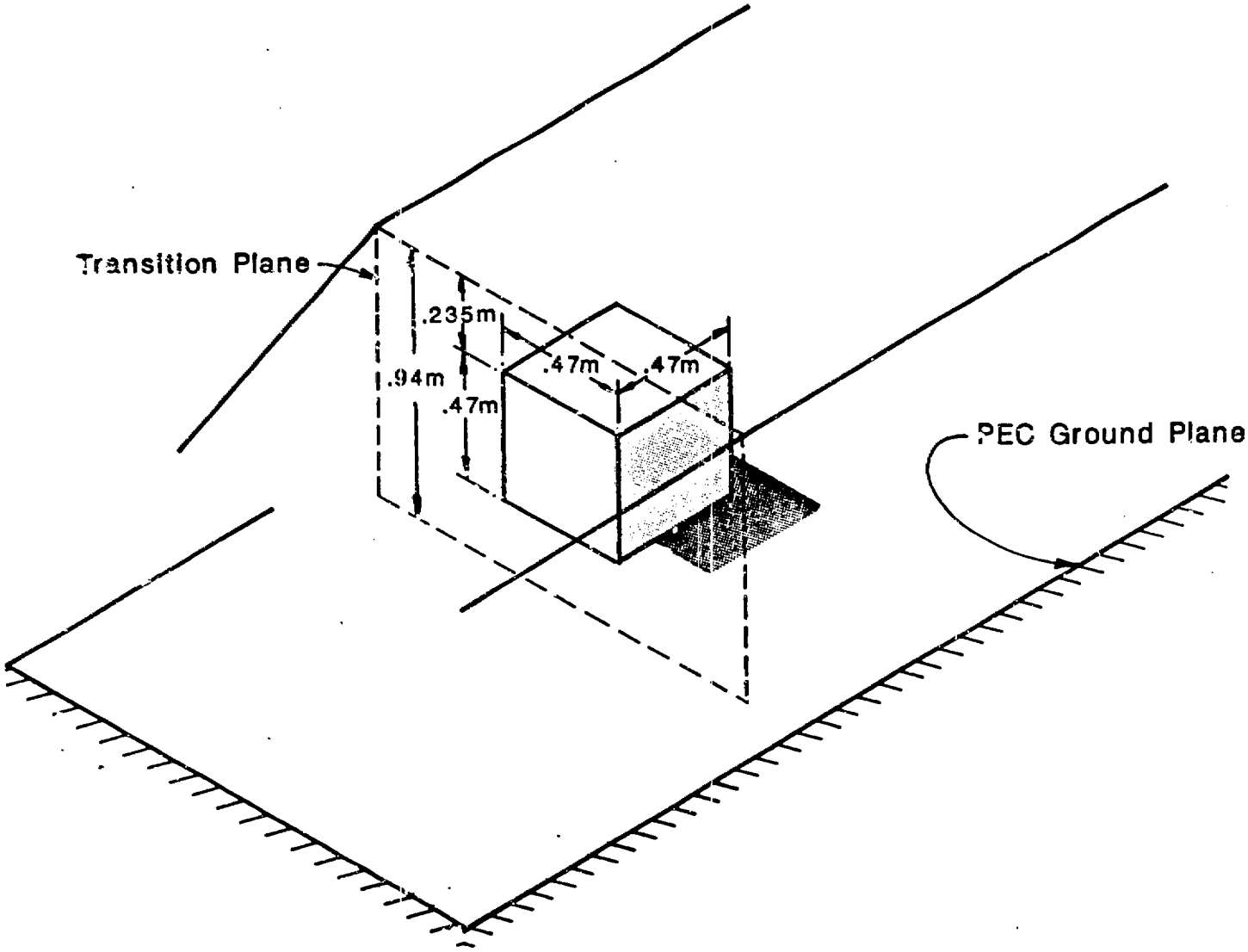
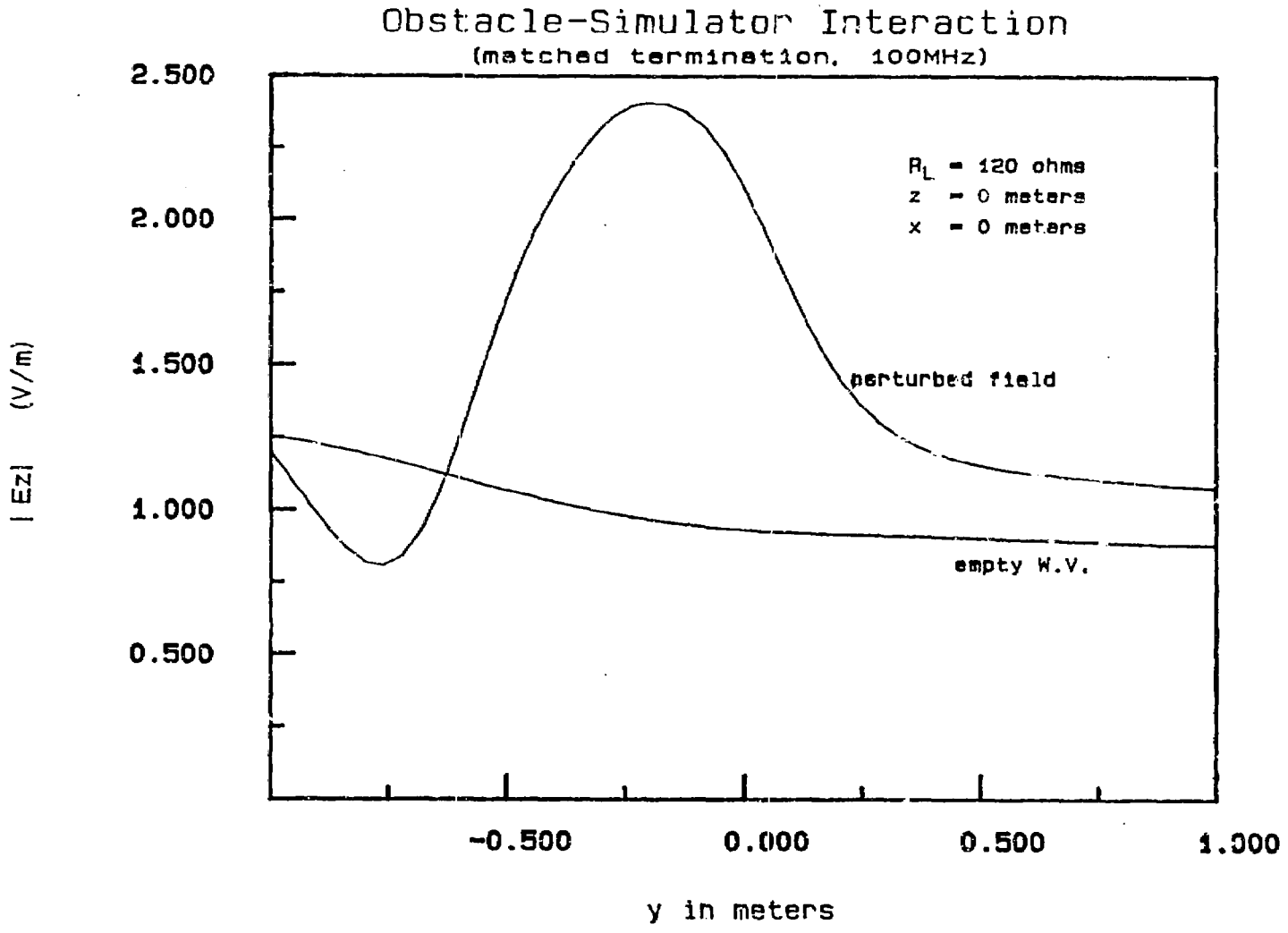
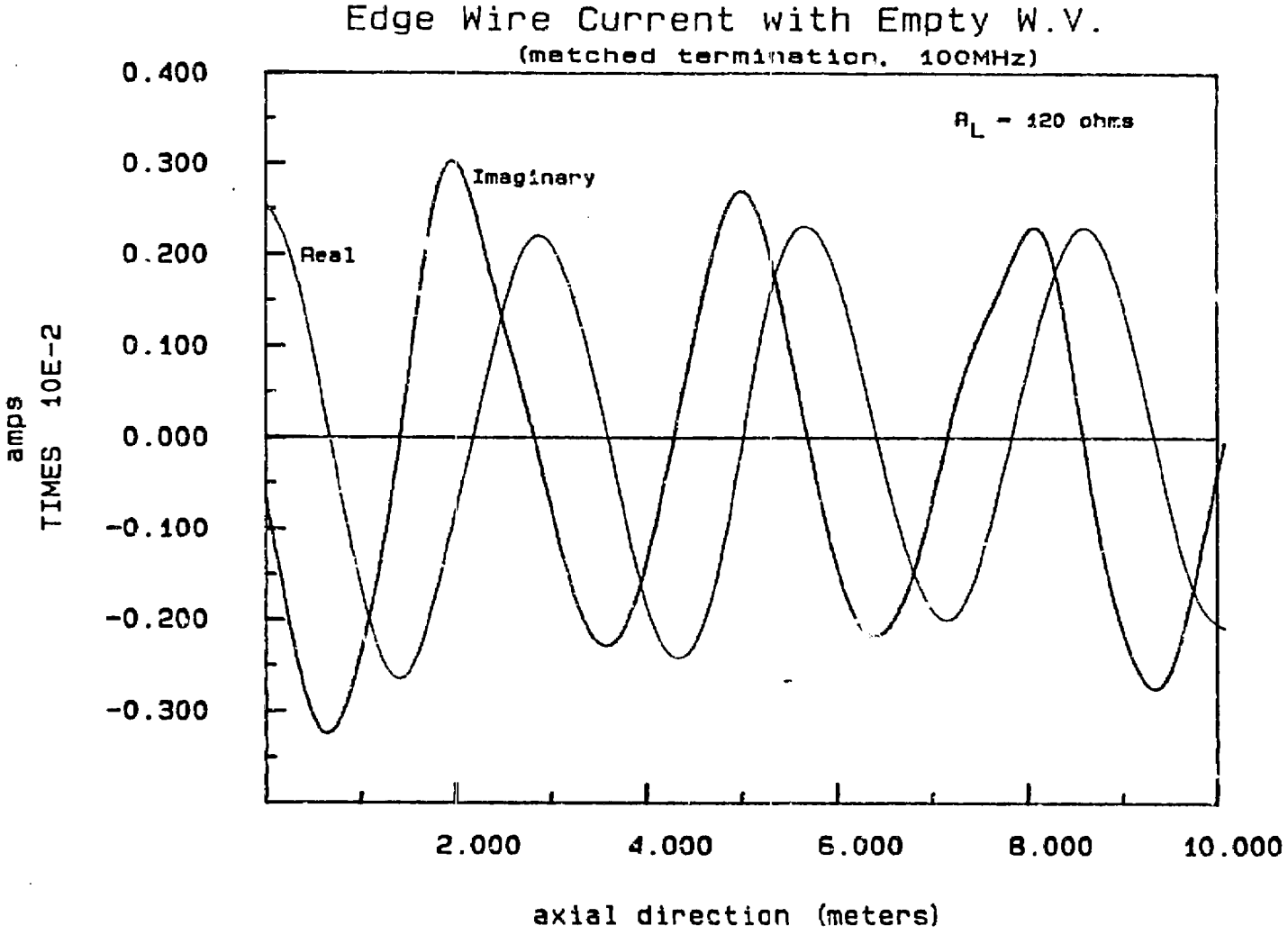


Figure 11. Cubic obstacle placed in the working volume, with the front face lying in the transition plane and placed symmetrically in the vertical and horizontal directions with respect to the parallel-plate.



Magnitude of E_z.

Figure 12. Vertical E-field computed along the ground plane of the 450 MHz bandwidth ACHATES EMP simulator. Comparison of fields in the empty working volume, with the perturbed fields in the presence of the obstacle.



Empty working volume.

Figure 13 . Edge wire currents produced by a 100 MHz excitation.

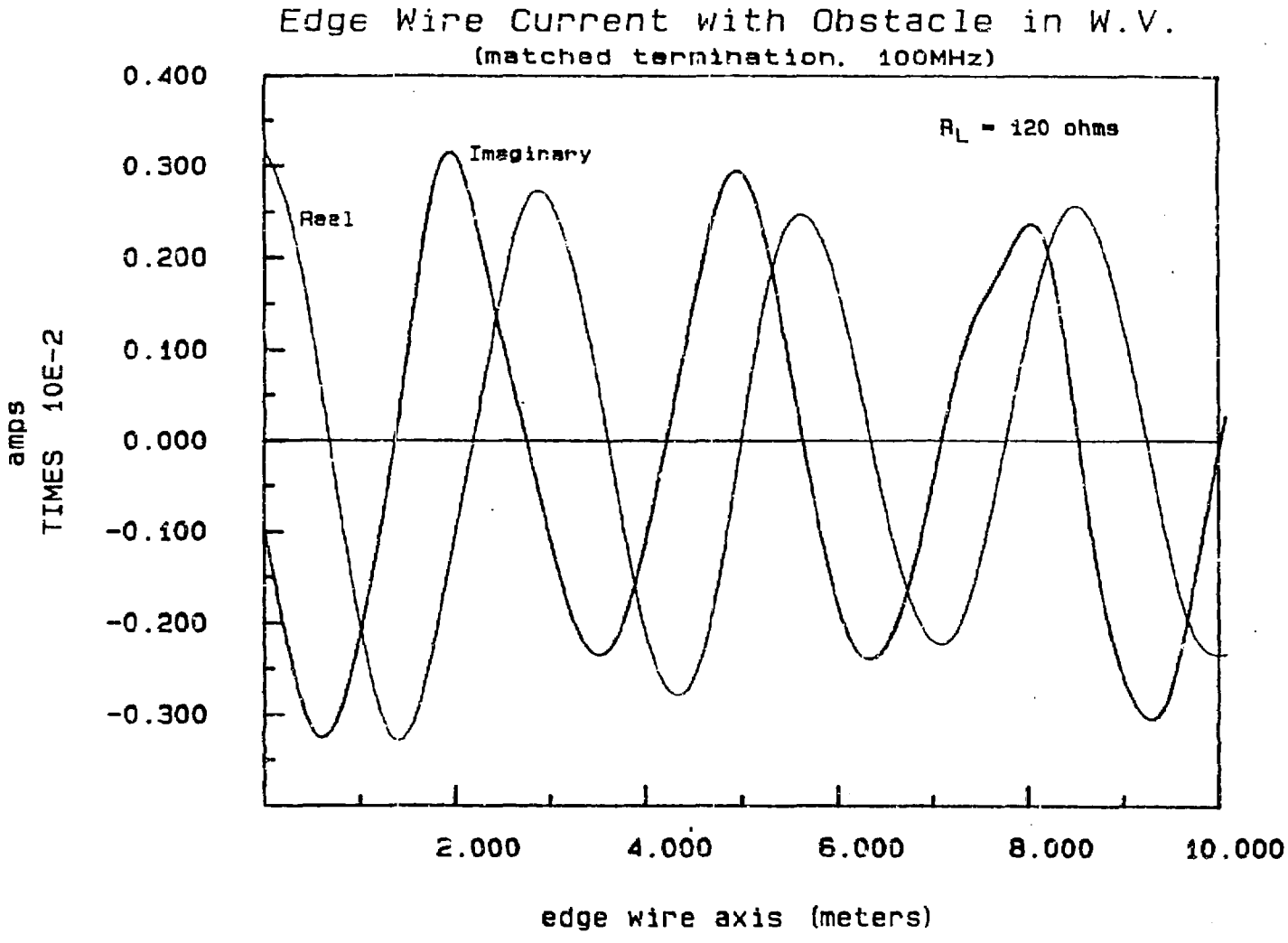


Figure 14 . Cubic obstacle in the working volume.

TABLE I COMPUTATIONAL CHARACTERISTICS OF NEC

(run on an AT&T PC6300 microcomputer)

Frequency (*MHz*)	*No.of Segments*	*MatrixFill* (*sec*)	*Factorization* (*sec*)
75	220	2,595.	1,003.
100	320	5,485.	3,095.
125	466	11,597.	12,059.

SESSION VIII - "ANTENNAS NEAR GROUND"

Moderator: George H. Hagn
SRI International

"Relationships Between Base Drives and Fields In Broadcast Medium Wave Directional Antennas"
J.B. Hatfield — Hatfield & Dawson Consulting Engineers, Inc.

"HF Ground Constant Measurements at the Lawrence Livermore National Laboratory (LLNL) Field Site"
G. Hagn — SRI International

"Experimental Antenna Measurements for the Validation of the Numerical Electromagnetics Code (NEC)"
J.K. Breakall and A.M. Christman — Lawrence Livermore National Laboratory

"NEC Modeling of HF Monopole Antennas with Elevated Radials"
A. Christman and R. Radcliff — Ohio University

Field Tests of HF Monopole Antennas with Elevated Radials"
A. Christman and R. Radcliff — Ohio University
J.K. Breakall — Lawrence Livermore National Laboratory

"A Simplified Model of the Terminated, Sloping Long-Wire (AFW0NXX) Antenna"
B. Campbell and W. Stuart — IIT Research Institute

RELATIONSHIPS BETWEEN BASE DRIVES AND FIELDS IN BROADCAST MEDIUM WAVE DIRECTIONAL ANTENNAS

James B. Hatfield

Hatfield & Dawson, Consulting Engineers, Inc.

4226 6th Avenue N.W.

Seattle, Washington 98107

Abstract

FCC specifications for the patterns of AM standard broadcast medium wave directional antennas include constants known as the "field parameters". The field parameters for each tower in an AM directional array are the ratios of the magnitudes and time phases, relative to an arbitrary reference, of the electric field component of the radiation that results from the summation of the current moments in that particular element of the directional array.

The field parameters and voltage drive parameters are not the same. The correct base drive voltages for method of moments programs can be found by inverting a matrix that is formed using the field parameters and antenna current moment summations for the various array elements. These voltages, when used as base drives for AM antenna modeling with the NEC program, produce horizontal plane antenna patterns that have the same shape as FCC patterns.

The inverse of this procedure involves loading the drive segments with resistances so that the base currents are proportional to the drive voltages. The field parameters are then found by ratioing the summations of the current moments for the array elements. These techniques can also be used to de-tune re-radiating objects.

The electrical parameters that are officially listed by the FCC for the purpose of specifying pattern shape for AM standard broadcast directional antennas are called "field parameters". One of the radiators is chosen as the reference tower and the parameters of the other radiators are specified relative to that tower. The field parameters are the relative ratios and phases of the magnitudes of the electric field components of the electromagnetic waves leaving the towers along the horizontal plane.

Section 73.150(b)(5) of the "Rules" requires submission of the relative field ratios and phases of the array when an application is made to the FCC for a permit to construct an AM directional antenna. The mathematical expressions used to generate the pattern size and shape (see Appendix) are functions of the relative field ratios and antenna current phases. The implicit assumption that is made here is that the phases of the antenna loop currents are identical to the field phases. The list of equations used by the Commission that are shown in the appendix of this report contains an expression that relates loop currents to field ratios:

$$Ii = \frac{KFi}{(C2)\ (1-\cos Gi)}$$

This equation says that the loop current and the field ratio of a given tower in a directional array are proportional to each other.

The conclusion to be drawn from the above observations is that it is assumed in the "Rules and Regulations" of the FCC that the relative ratio and phase of the loop current (current at the current maxima) is the same as field ratio and phase for a given tower in an AM directional array. The expectation by the Commission that the antenna current parameters should be identical to the field parameters is also implied by Section 73.151(a)(2)iii of the FCC "Rules" which requires that if the design field parameters and the monitored antenna current parameters of the adjusted array are different "... a full explanation of the reasons for these differences shall be given."

Station licenses list parameters that must be maintained during station operation to demonstrate that the pattern of the radiated fields is within specified limits. These "antenna parameters" are the ratios and phases of the

antenna currents monitored at a specific location on the towers. The antenna current is monitored at the point of maximum current or at the base of the tower. These operating antenna parameters are, in practice, carefully distinguished from the field parameters. Only the field parameters (along with other necessary electrical and physical parameters ((element spacings, heights and orientations)) that are necessary for proper description of the array) are used for international notifications and calculations of interference.

It has been standard practice in the past to build and adjust AM directional arrays under the assumption that the field parameters and the antenna parameters are synonymous. It was thought that this was a particularly safe assumption for uniform cross section guyed towers whose height was in the vicinity of a quarter of a wave length.

When one looks at the antenna parameters and the field parameters from a moment method perspective their differences become apparent. The radiated electric field from a tower is proportional to the summation of the current moments of that tower. The magnitude and phase of the current in each tower varies from segment to segment in such a fashion that there is not a fixed relationship between the field parameters for that tower and the antenna parameters given by the current at any fixed point on the tower. While the antenna and field parameters may be similar for towers 90 degrees and shorter they diverge sharply with increasing tower height and are obviously different for unequal height towers and towers of radically different cross section.

The conclusion to be drawn from these considerations is that the current sources used to drive AM directional antennas must usually have relative magnitudes and phases that are different from the relative field magnitudes and phases given by FCC records if the correct pattern is to be achieved.

Four terminal network theory can be used to relate the driving voltages and fields of the towers in an AM directional array. In this way the voltage drives that are necessary to achieve the correct pattern can be found for a given set of field parameters. The resulting voltage drives are used for method of moments modeling and the necessary antenna current parameters are found in the antenna current output provided by the program.

A method used at the Harris corporation for a number of years and discussed in "Modelling A Standard Broadcast Directional Array With The Numerical Electromagnetics Code,"[1] involves determining the constants of a matrix through the use of a program like NEC. The equations forming the two tower matrix are:

E1 = T11 V1 + T12 V2
E2 = T21 V1 + T22 V2

The "E" variables are the field parameters, the "V" variables are the base voltage drives while the "T" variables in each column are the current moment summations for the towers resulting from driving the towers one at a time with one volt and with the undriven tower shorted. Once the "per unit" current moment summations are known through repeated runs of the NEC, or some other program, the matrix can be inverted to find the voltages for any given set of field parameters.

R. Adler has been loading the drive segments with large resistances when he models AM arrays. This gives equivalent current sources for NEC voltage drives that are scaled to antenna current parameters. When the array is modeled in this fashon the field parameters can be found by summing the current moments for each tower. The voltage drives for the unloaded array can then be found by applying the matrix inversion technique to the resulting field parameters after the "per unit" current moment summations are determined.

It is thus possible to use a method of moments program like NEC or MININEC and find field parameters from antenna current parameters or antenna current parameters from field parameters. We use a version of MININEC III that has a few lines of code added to sum the current moments and to calculate the relative field parameters.

Re-radiating utility towers can be de-tuned by modeling them as a part of the AM array. The "per unit" current moment summations are found for the array elements and for the towers to be de-tuned, and the matrix inversion procedure is used to find base voltage drives. The normal array field parameters are used in the matrix while very small field

[1]By C.W. Trueman, published in IEEE Transactions on Broadcasting, Vol. 34, No. 1, March 1988.

ratios are used for the towers that are to be de-tuned. A NEC run using the resulting base drives yields the base impedances for the array and for the re-radiating towers. Conjugate reactance loading from the base of the re-radiating tower to ground will minimize pattern distortion effects. For towers close to the array the resistive component of the base impedance could be a large positive number. In this case the re-radiating tower would have to be actively driven to completely de-tune it. Passive loading is usually sufficient for minimizing pattern distortion.

SESSION VIII - "ANTENNAS NEAR GROUND"

Moderator: George H. Hagn
SRI International

"Relationships Between Base Drives and Fields in Broadcast Medium Wave Directional Antennas"
J.B. Hatfield — Hatfield & Dawson Consulting Engineers, Inc.

"HF Ground Constant Measurements at the Lawrence Livermore National Laboratory (LLNL) Field Site"
G. Hagn — SRI International

"Experimental Antenna Measurements for the Validation of the Numerical Electromagnetics Code (NEC)"
J.K. Breakall and A.M. Christman — Lawrence Livermore National Laboratory

"NEC Modeling of HF Monopole Antennas with Elevated Radials"
A. Christman and R. Radcliff — Ohio University

Field Tests of HF Monopole Antennas with Elevated Radials"
A. Christman and R. Radcliff — Ohio University
J.K. Breakall — Lawrence Livermore National Laboratory

"A Simplified Model of the Terminated, Sloping Long-Wire (AFWONXX) Antenna"
B. Campbell and W. Stuart — IIT Research Institute

RELATIONSHIPS BETWEEN BASE DRIVES AND FIELDS IN BROADCAST MEDIUM WAVE DIRECTIONAL ANTENNAS

James B. Hatfield

Hatfield & Dawson, Consulting Engineers, Inc.

4226 6th Avenue N.W.

Seattle, Washington 98107

Abstract

FCC specifications for the patterns of AM standard broadcast medium wave directional antennas include constants known as the "field parameters". The field parameters for each tower in an AM directional array are the ratios of the magnitudes and time phases, relative to an arbitrary reference, of the electric field component of the radiation that results from the summation of the current moments in that particular element of the directional array.

The field parameters and voltage drive parameters are not the same. The correct base drive voltages for method of moments programs can be found by inverting a matrix that is formed using the field parameters and antenna current moment summations for the various array elements. These voltages, when used as base drives for AM antenna modeling with the NEC program, produce horizontal plane antenna patterns that have the same shape as FCC patterns.

The inverse of this procedure involves loading the drive segments with resistances so that the base currents are proportional to the drive voltages. The field parameters are then found by ratioing the summations of the current moments for the array elements. These techniques can also be used to de-tune re-radiating objects.

The electrical parameters that are officially listed by the FCC for the purpose of specifying pattern shape for AM standard broadcast directional antennas are called "field parameters". One of the radiators is chosen as the reference tower and the parameters of the other radiators are specified relative to that tower. The field parameters are the relative ratios and phases of the magnitudes of the electric field components of the electromagnetic waves leaving the towers along the horizontal plane.

Section 73.150(b)(5) of the "Rules" requires submission of the relative field ratios and phases of the array when an application is made to the FCC for a permit to construct an AM directional antenna. The mathematical expressions used to generate the pattern size and shape (see Appendix) are functions of the relative field ratios and antenna current phases. The implicit assumption that is made here is that the phases of the antenna loop currents are identical to the field phases. The list of equations used by the Commission that are shown in the appendix of this report contains an expression that relates loop currents to field ratios:

$$Ii = \frac{KFi}{(C2)\ (1 \cos Gi)}$$

This equation says that the loop current and the field ratio of a given tower in a directional array are proportional to each other.

The conclusion to be drawn from the above observations is that it is assumed in the "Rules and Regulations" of the FCC that the relative ratio and phase of the loop current (current at the current maxima) is the same as field ratio and phase for a given tower in an AM directional array. The expectation by the Commission that the antenna current parameters should be identical to the field parameters is also implied by Section 73.151(a)(2)iii of the FCC "Rules" which requires that if the design field parameters and the monitored antenna current parameters of the adjusted array are different "... a full explanation of the reasons for these differences shall be given."

Station licenses list parameters that must be maintained during station operation to demonstrate that the pattern of the radiated fields is within specified limits. These "antenna parameters" are the ratios and phases of the

antenna currents monitored at a specific location on the towers. The antenna current is monitored at the point of maximum current or at the base of the tower. These operating antenna parameters are, in practice, carefully distinguished from the field parameters. Only the field parameters (along with other necessary electrical and physical parameters ((element spacings, heights and orientations)) that are necessary for proper description of the array) are used for international notifications and calculations of interference.

It has been standard practice in the past to build and adjust AM directional arrays under the assumption that the field parameters and the antenna parameters are synonymous. It was thought that this was a particularly safe assumption for uniform cross section guyed towers whose height was in the vicinity of a quarter of a wave length.

When one looks at the antenna parameters and the field parameters from a moment method perspective their differences become apparent. The radiated electric field from a tower is proportional to the summation of the current moments of that tower. The magnitude and phase of the current in each tower varies from segment to segment in such a fashion that there is not a fixed relationship between the field parameters for that tower and the antenna parameters given by the current at any fixed point on the tower. While the antenna and field parameters may be similar for towers 90 degrees and shorter they diverge sharply with increasing tower height and are obviously different for unequal height towers and towers of radically different cross section.

The conclusion to be drawn from these considerations is that the current sources used to drive AM directional antennas must usually have relative magnitudes and phases that are different from the relative field magnitudes and phases given by FCC records if the correct pattern is to be achieved.

Four terminal network theory can be used to relate the driving voltages and fields of the towers in an AM directional array. In this way the voltage drives that are necessary to achieve the correct pattern can be found for a given set of field parameters. The resulting voltage drives are used for method of moments modeling and the necessary antenna current parameters are found in the antenna current output provided by the program.

A method used at the Harris corporation for a number of years and discussed in "Modelling A Standard Broadcast Directional Array With The Numerical Electromagnetics Code,"[1] involves determining the constants of a matrix through the use of a program like NEC. The equations forming the two tower matrix are:

E1 = T11 V1 + T12 V2
E2 = T21 V1 + T22 V2

The "E" variables are the field parameters, the "V" variables are the base voltage drives while the "T" variables in each column are the current moment summations for the towers resulting from driving the towers one at a time with one volt and with the undriven tower shorted. Once the "per unit" current moment summations are known through repeated runs of the NEC, or some other program, the matrix can be inverted to find the voltages for any given set of field parameters.

R. Adler has been loading the drive segments with large resistances when he models AM arrays. This gives equivalent current sources for NEC voltage drives that are scaled to antenna current parameters. When the array is modeled in this fashon the field parameters can be found by summing the current moments for each tower. The voltage drives for the unloaded array can then be found by applying the matrix inversion technique to the resulting field parameters after the "per unit" current moment summations are determined.

It is thus possible to use a method of moments program like NEC or MININEC and find field parameters from antenna current parameters or antenna current parameters from field parameters. We use a version of MININEC III that has a few lines of code added to sum the current moments and to calculate the relative field parameters.

Re-radiating utility towers can be de-tuned by modeling them as a part of the AM array. The "per unit" current moment summations are found for the array elements and for the towers to be de-tuned, and the matrix inversion procedure is used to find base voltage drives. The normal array field parameters are used in the matrix while very small field

[1]By C.W. Trueman, published in IEEE Transactions on Broadcasting, Vol. 34, No. 1, March 1988.

ratios are used for the towers that are to be de-tuned. A NEC run using the resulting base drives yields the base impedances for the array and for the re-radiating towers. Conjugate reactance loading from the base of the re-radiating tower to ground will minimize pattern distortion effects. For towers close to the array the resistive component of the base impedance could be a large positive number. In this case the re-radiating tower would have to be actively driven to completely de-tune it. Passive loading is usually sufficient for minimizing pattern distortion.

HF GROUND CONSTANT MEASUREMENTS AT THE LAWRENCE LIVERMORE NATIONAL LABORATORY (LLNL) FIELD SITE

By

George H. Hagn
Information Sciences and Technology Center
SRI International
1611 North Kent Street
Arlington, Virginia 22209

ABSTRACT

The SRI International open-wire-line (OWL) kit was used 3-5 July 1987 to measure the HF ground constants at the Lawrence Livermore National Laboratory (LLNL) field site in Livermore, CA. Data were acquired at 11 locations about 250 ft west of the LLNL facility fence in the vicinity where a longwire and broadband dipole were erected in August 1987 for making impedance measurements for the purpose of validating the Numerical Electromagnetics Code (NEC). An additional location was measured to the north of the antenna site where field strength data were to be taken. Several samples were taken at most locations. Best estimates of the conductivity, relative permittivity (relative dielectric constant), dissipation factor and skin depth were computed as the median values versus frequency for 2 through 30 MHz. Data were acquired at 1-MHz intervals from 2 MHz through 8 MHz, and the interval was increased to 2 MHz from 8 MHz to 30 MHz. The maximum and minimum values were also determined as bounds on the conductivity and relative permittivity values for use in parameter sensitivity analyses. The conductivity values for the relatively dry, densely packed light brown clay fell between those typical of pastoral land and rich agricultural land at about 4×10^{-2} S/m. The relative permittivity values exhibited more variation with frequency. At the low end of the HF band, the relative permittivity values exceeded those of a non-flooded rice paddy (e.g., about 150 at 2 MHz); whereas, at the high end of the band, the relative permittivity approximated values typical of rich agricultural land (about 17 at 30 MHz). The skin depth varied from about 2 m at 2 MHz to 0.7 m at 30 MHz. The dissipation factor was about 1.5, so the soil acted almost as a semiconductor rather than as a lossy conductor or a lossy dielectric. Both the relative dielectric constant and conductivity are important in modeling antennas and propagation over the ground at the LLNL site. Data from nearby wells indicated that the water table was at least 20 m below the surface. Therefore, a one-layer slab model adequately described the ground at this site for HF down to the skin depth.

1. INTRODUCTION

The Lawrence Livermore National Laboratory (LLNL) has developed a method-of-moments model, the Numerical Electromagnetics Code (NEC),[1-3] for modeling antenna characteristics over real ground. The model requires the specification of the wire geometry and the electrical characteristics of the ground over which the antenna is installed. The most recent version, NEC-3,[3] which handles wires that penetrate the earth's surface, has had only limited validation with field measurements. The antenna measurement possibilities include:

- Input impedance;
- Directivity pattern shape;
- Absolute gain; and,
- Ground-wave field strength versus distance from the antenna.

During a previous group of studies, the first three quantities were modeled with NEC-3 and measured in the HF band by SRI International (SRI) for a 7.5-ft vertical monopole with sixteen 40-ft radials buried 7 inches at several sites with different soils.[4-6] The NEC model predictions compared favorably with the measurements when measured ground conductivity and permittivity (i.e., relative dielectric constant) values were used.[7] These values of "ground constants" were obtained using the SRI open-wire-line (OWL) kit designed for this purpose.[8-10]

The LLNL has planned additional NEC validation work at their field site near Livermore, CA, using a broadband dipole and a sloping long-wire.[11] Input impedance and ground-wave field strength values will be measured in the HF band (2-30 MHz). SRI was asked to measure the ground constants in the HF band at the LLNL site for use by LLNL in this validation effort.[12] This paper describes the SRI measurements and presents the ground constants results. The NEC validation results are presented in Ref. 11.

2. DESCRIPTION OF EQUIPMENT

The SRI open-wire line (OWL) ground constants kit consists of a set of 0.5-inch diameter aluminum probes of various lengths from 3 inches to 36 inches, a probe adapter, an HP 4193A Vector Impedance Meter, an HP85B computer, and appropriate software. The kit is powered from generators, and a metered variac is used to maintain the correct voltage at the instrumentation when a long power cord is used. A power-line filter with spike suppression is sometimes used. The kit is shown schematically in Figure 2.1, and it is shown in use at Livermore in Figure 2.2.

The SRI OWL kit semiautomatically measures the soil conductivity and relative permittivity vs frequency in the band 0.5 to 110 MHz. The frequency spacing for measurements between 0.5 and 2 MHz is 0.5 MHz, from 2 MHz to 8 MHz the spacing is 1 MHz, and from 8 to 30 MHz the spacing is 2 MHz. A 4-MHz spacing is used from 30 MHz to 110 MHz.

3. SAMPLING STRATEGY AND MEASUREMENT SITE AND LOCATION DESCRIPTIONS

3.1 Sampling Strategy

The general sampling strategy evolved from consideration of the following:

- Sampling Locations:
  - Proposed antenna locations;
  - Proposed field strength measurement location;
  - Land accessability;
  - Possibility of small-scale lateral inhomogeneities;
  - Availability of water well data; and,
  - Surface vegetation differences.
- Sample Depths:
  - The need for observing variations (if any) in soil electrical properties with depth; and,
  - The depth to which it was possible to penetrate the soil and retrieve the probes.

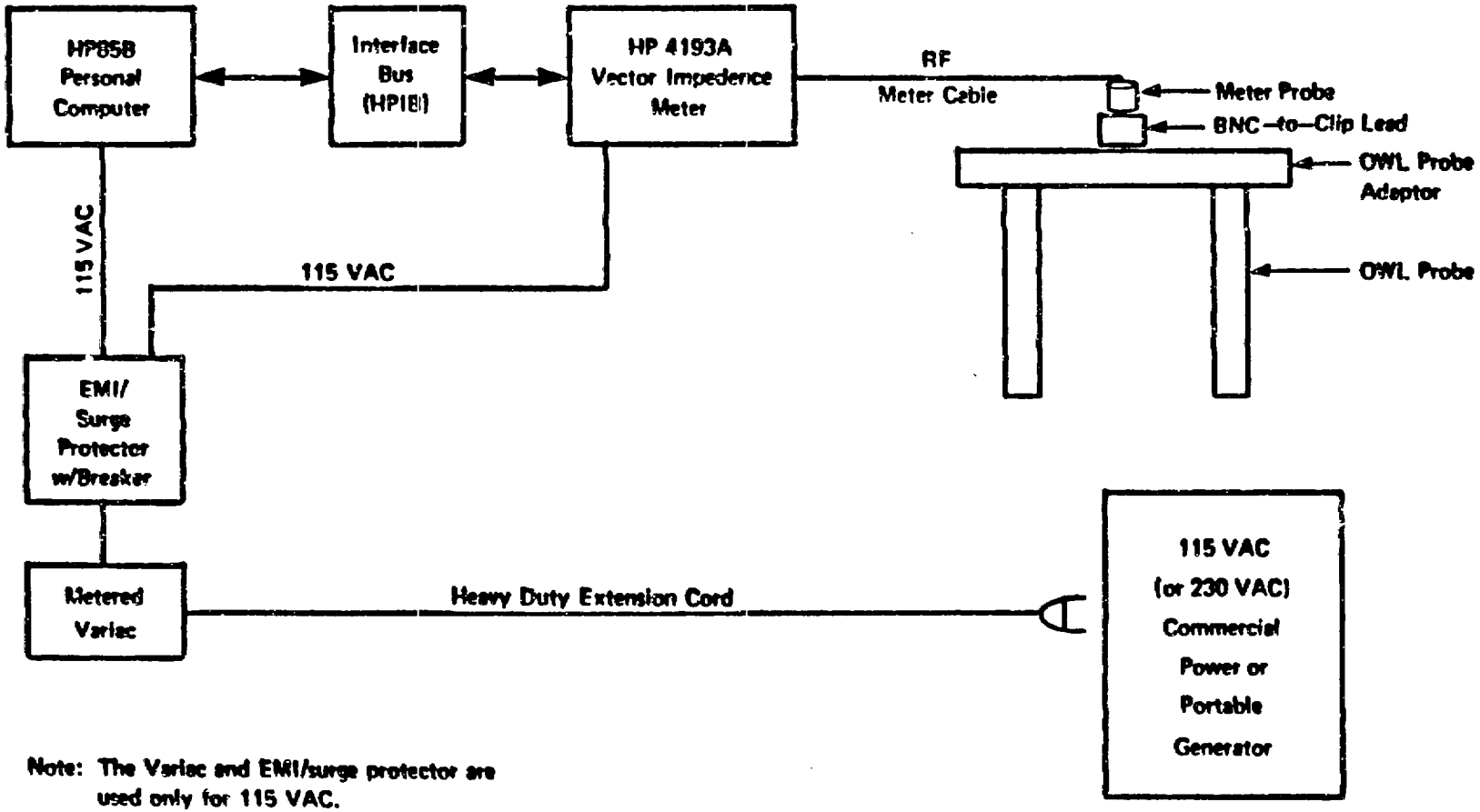


Figure 2-1 BLOCK DIAGRAM OF THE SRI OWL KIT FOR MEASURING RF GROUND CONSTANTS



a) Probe Insertion



b) Data Acquisition

Figure 2.2 SRI OWL KIT IN USE AT LIVERMORE

- Selection of Test Frequencies:
  - Band in which the test antennas operate; and,
  - Added frequencies to mitigate possible interference and facilitate interpolation.
- Choice of Measurement Day:
  - Antenna setup schedule;
  - Personnel availability; and,
  - Suitable weather conditions.

Mr. Al Christman of Ohio University selected the proposed antenna locations and the radial for the field strength measurements. Some land was not available for field strength measurements due to use by livestock. Several water wells had been drilled for test purposes,[13] and one location was selected to be near a well. At a given general location, several sample points usually were identified within about 1 m of each other to check for small-scale variations. Differences (if any) that might relate to changes in surface vegetation were also a consideration.

Probe lengths up to 36 inches were used; however, it was not possible to get the longest probes into the ground (or back out of the ground) at every location.

The basic test frequencies were in the HF band (defined for the OWL measurements as 2-30 MHz). As previously noted, these data were taken at a 1-MHz interval from 2-8 MHz and at 2-MHz intervals from 8 MHz to 30 MHz. This provided enough samples on different frequencies so that data taken on interference- contaminated frequencies (if any) could be discarded without impacting the ability to estimate the ground constant values versus frequency.

The measurement day was a possible variable. Data were taken on three consecutive days (3-5 July 1987) in order to sample all the locations selected. No locations were repeated on different days at this site due to the extreme difficulty in getting the probes into and out of the ground.

There was no rain during the test period, and it had not rained for some weeks before. Therefore, no significant change in ground constant values with measurement day was expected.

At a given location (an area within a radius of several meters of the stake marking the location), samples were taken at several sample points within about 1 m of each other in order to check the small-scale variations. The 3-inch probe spacing was used, and this approximates a 300-ohm line. An alphanumeric coding system was used to identify the location number, probe configuration, and sample number at that location. For example, L1P3S2 indicates Location 1, a probe spacing of 3 inches and Sample 2. Two identical OWL kits were used at most of the locations, and the data from Kit 1 was assigned odd sample numbers and Kit 2 was assigned even sample numbers.

3.2 General Site Description

The LLNL Livermore, CA test site was located to the west of the scientific compound about 250 feet from the outer security fence. The land is quite flat, and it is covered with dry grass about 1-2 feet high (see Figure 3.1). Occasional green thistles are present and a few small leafless bushes about 3-4 feet high were the tallest vegetation on the site. The soil was a light brown clay containing occasional small rocks.

3.3 Specific Measurement Locations

Twelve measurement locations were selected (see Figure 3.2). Locations 1, 2 and 3 represent the feedpoint, center and termination point where the longwire antenna was erected. Locations 4, 5, 6 and 7 are 25 ft away from the longwire, 75 ft from its center, and Locations 8, 9, 10 and 11 are 75 ft from the longwire at 25 ft from its center. Locations 4 through 11 are symmetrically located around Location 2 to document the area where the broadband dipole was erected. Location 12 was along the line of the longwire beyond Location 3 at the end of the lab fence. It was selected to be along a radial where the field strength data would be taken.

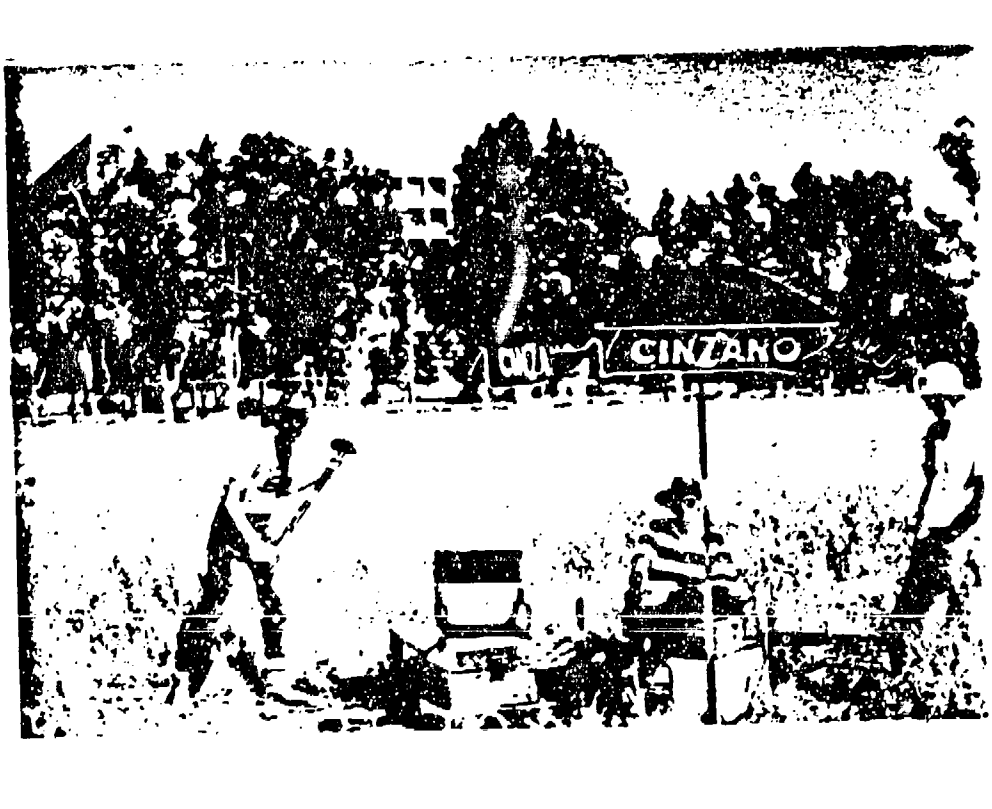


Figure 3.1 PHOTO OF LLNL FIELD SITE

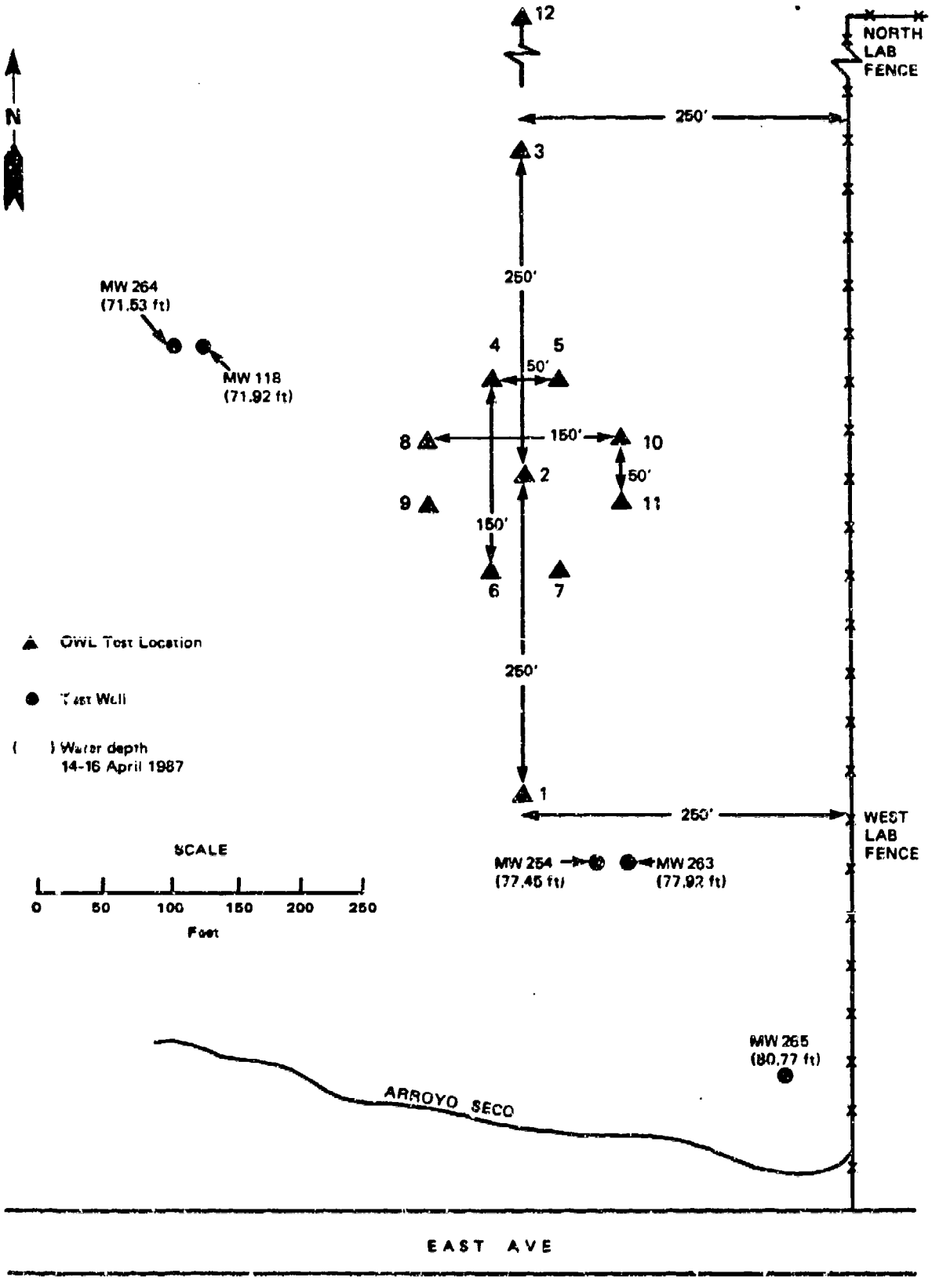


Figure 3.2 LOCATIONS OF OWL MEASUREMENTS AND TEST WELLS AT LIVERMORE SITE

All of the locations appeared very similar to the eye. The 0.5-inch steel rod used to create the hole for the aluminum OWL probe was very difficult to drive into the dry ground using a sledge hammer (see Figure 3.3). Frequently the pointed steel rod would only penetrate less than 1 inch per hit, although it was somewhat easier to drive at Locations 1 (beside a road near the well), 4 and 8.

There was a band about 10 yards wide with no vegetation at Location 5. The ground at this site was very hard, and 3 driving rods were broken trying to drive into it. At the other locations, it was necessary to clear the vegetation prior to making the holes for the probes (see Figure 3.4 taken at Location 12). The vegetation at Location 8 consisted of dried grasses 1-2 ft high, and several 3- to 4-ft bushes (the tallest at the site) were nearby. Several green thistles about 3 ft high were near Location 12, and they were the only green vegetation at the entire site (exclusive of trees along the security fence).

4. SOIL DESCRIPTION

The soil was highly compacted light brown clay with some occasional small (1-2 inch) smooth rocks. The surface moisture content, temperature and pH were measured at each location. These results are summarized in Table 4.1. Surface soil samples were taken at Locations 1, 2 and 3 for use in estimating soil moisture content by measuring the percent of change in weight before and after heating, but the ground was so hard that it was not practical with only a pick and shovel to take samples at different depths except at Location 1 (where additional samples were taken at 1 ft and 2 ft). Regretably, these soil samples were lost when the sample pans melted in the microwave oven. It was observed that the samples were successively more moist as the sample depth increased. The sealed pan for the sample taken at 2 ft had condensation on the inside several days later. Therefore, it is assumed that there was a gradient of moisture content which increased with depth.



Figure 3.3 DRIVING STEEL AT LIVERMORE



Figure 3.4 CLEARING THE VEGETATION AT LOCATION 12
(With Supervision from Advisors)

TABLE 4.1

Summary of Soil Measurements at LLNL Site

Location Number	M.C.*	Temp. (°C)	pH	Comments
1	1	24.5	7.0	Soil less compacted
2	1	23.0	6.9	Soil very compacted
3	1	22.0	6.9	
4	1	28.5	7.0	Soil less compacted
5	1	27.0	7.0	Soil very compacted
6	1	28.0	7.0	
7	1	28.5	7.0	
8	1	28.0	7.0	Soil less compacted
9	1	28.0	7.0	
10	1	30.0	7.0	
11	1	27.5	7.0	
12	1	24.0	7.0	Soil very compacted

* M.C. = Moisture Content (on a scale from 1 = dry to 8 = wet)

The water table can cause a very significant change in effective ground constants if it occurs closer to the surface than a skin depth at the radio frequency of interest. Fortunately, the LLNL site has been recently surveyed using the test wells shown in Figure 3.2.[13] The water table was between 71 and 81 feet below the surface at the test site. The water depth, measured on 14-16 April 1987, is given in parentheses beside each test well shown on the map of ground constant measurement locations (Figure 3.2).

5. DATA REDUCTION AND ANALYSIS

5.1 Data Reduction

Data were taken at 12 locations. The number of samples per location ranged from one to four. Thirty-one samples were taken in all, but two were discarded due to excessive separation of the soil from the probes near

the surface or the inability to get the probes completely into the ground (see Table 5.1). OWL probe lengths up to 36 inches were used at 8 locations, and lengths up to 24 inches were used at 4 locations due to the difficulty in probe insertion and extraction. The data were recorded on thermal printer paper and on magnetic cassettes using the HP 85B. Figure 5.1 is an example of the raw data for the 3- and 6-inch probe lengths, and Figure 5.2 shows the reduced data for these samples.

TABLE 5.1

Summary of Data Samples

Location Number	Number of Samples	Longest Probe (Inches)
1	4	36
2	4	36
3	2	36
4	1	24
5	2	36
6	4	36
7	3	36
8	1	24
9	1	24
10	2	36
11	2	24
12	3	36

There was a considerable spread in the measured results for a given frequency, so a statistical data reduction was required.

5.2 Data Analysis

Three types of estimates of the ground constants versus frequency are required for subsequent use by LLNL in the NEC validation:

- Estimate for sloping longwire;
- Estimate for broadband dipole; and,
- Estimate for field strength.

SITE NAME	LIV
LOCATION NUMBER	5
SAMPLE NUMBER	1
DATE	07-05-87
TIME (HOURS)	16.30
OPERATOR'S ID	GHH
PROBE CONFIG NO.	3
PROBE KIT NUMBER	1

3 INCH PROBES IN GROUND

FREQ.	/Z/	θ	Er	SD
2.0	1856	-48.7	45	7.32
3.0	1431	-50.8	37	5.59
4.0	1197	-49.9	34	4.15
5.0	1073	-52.3	28	3.83
6.0	934	-51.7	28	3.11
7.0	871	-51.0	26	2.63
8	781	-52.4	24	2.45
10	759	-39.0	33	.97
12	731	-62.2	14	2.76
14	620	-60.0	15	2.09
16	525	-62.7	14	2.19
18	475	-60.2	14	1.72
20	449	-61.0	13	1.63
22	400	-59.6	14	1.39
24	375	-56.7	14	1.09
26	364	-53.3	15	.83
28	352	-51.9	16	.71
30	369	-49.4	16	.55

6 INCH PROBES IN GROUND

FREQ.	/Z/	θ	Er	SD
2.0	783	-48.1	55	7.26
3.0	585	-47.4	48	5.00
4.0	493	-42.2	48	3.19
5.0	467	-42.2	40	2.73
6.0	404	-40.6	41	2.15
7.0	410	-38.7	36	1.80
8	355	-36.6	39	1.43
10	471	-46.6	18	2.06
12	360	-51.4	18	2.09
14	308	-53.6	17	1.99
16	256	-57.0	16	2.04
18	232	-50.8	18	1.42
20	212	-51.3	17	1.34
22	200	-46.7	17	1.03
24	199	-43.5	18	.84
26	203	-42.6	16	.76
28	210	-41.8	15	.69
30	218	-46.8	12	.83

Figure 5.1 EXAMPLE OF RAW DATA

LIV

LOCATION # 5
SAMPLE # 1
PROBE CONFIGURATION 3 in.
PROBE LENGTH 3 in.

FREQ	Er	COND.	D.F.	S.D.
2	45	5.39E-003	1.08	7.32
3	37	6.36E-003	1.04	5.59
4	34	8.28E-003	1.11	4.15
5	28	8.11E-003	1.04	3.83
6	28	9.95E-003	1.08	3.11
7	26	1.15E-002	1.15	2.63
8	24	1.19E-002	1.16	2.45
10	33	4.17E-002	2.26	.97
12	14	7.64E-003	.84	2.76
14	15	1.06E-002	.92	2.09
16	14	9.53E-003	.79	2.19
18	14	1.24E-002	.89	1.72
20	13	1.27E-002	.87	1.63
22	14	1.53E-002	.92	1.39
24	14	2.05E-002	1.07	1.09
26	15	2.68E-002	1.29	.83
28	16	3.43E-002	1.41	.71
30	16	4.73E-002	1.80	.55

LIV

LOCATION # 5
SAMPLE # 1
PROBE CONFIGURATION 3 in.
PROBE LENGTH 6 in.

FREQ.	Er	COND.	D.F.	S.D.
2	55	5.90E-003	.97	7.26
3	48	8.11E-003	1.01	5.00
4	40	1.31E-002	1.23	3.18
5	40	1.40E-002	1.26	2.73
6	41	1.82E-002	1.34	2.15
7	36	2.10E-002	1.49	1.80
8	39	2.78E-002	1.61	1.43
10	18	1.25E-002	1.23	2.06
12	18	1.18E-002	.99	2.09
14	17	1.19E-002	.90	1.99
16	16	1.12E-002	.77	2.04
18	18	1.72E-002	.97	1.42
20	17	1.70E-002	.95	1.34
22	17	2.41E-002	1.13	1.03
24	18	3.05E-002	1.30	.84
26	16	3.29E-002	1.39	.76
28	15	3.54E-002	1.51	.69
30	12	2.50E-002	1.29	.83

Figure 5.2 EXAMPLE OF REDUCED DATA

The estimate for the sloping longwire was made by computing the median values for each frequency from Locations 1 through 7. The estimate for the broadband dipole was obtained by computing the comparable median values from Locations 2 and 4 through 11. The estimate for the field strength was obtained by computing the site median values using data from all 12 locations. For each of these types of estimates, the appropriate data (taken as a set) were used to perform the following steps:

- Compute the median values of conductivity and relative dielectric constant for each measurement frequency used;
- Compute median dissipation factor and skin depth using the median relative dielectric constant and conductivity; and,
- Tabulate and plot the results vs frequency.

6. DISCUSSION OF RESULTS

6.1 Results

The results for Locations 1-7, pertinent to the longwire, are given in Table 6.1. The upper and lower bounds (i.e., the maximum and minimum observed values) are given for the conductivity and relative dielectric constant. The median conductivity was approximately 4×10^{-2} S/m across the band; whereas, the median relative dielectric constant decreased from 182 at 2 MHz to 17 at 30 MHz. The upper and lower bounds were separated by about one order of magnitude for the conductivity and about half that separation was typical for the relative dielectric constant. The dissipation factor was about 1.5 and the skin depth varied from about 1.5 m at 2 MHz down to about 0.7 m at 30 MHz.

Comparable data were obtained for the area where the broadband dipole is to be erected (Locations 2, 4-11). These data are summarized in Table 6.2 for the conductivity and relative dielectric constant. The overall site median values (Locations 1-12) for these same parameters are tabulated in Table 6.3.

TABLE 6.1

Summary of Data for Longwire Antenna
(Locations 1 through 7)

Frequency (MHz)	Best Estimate		Lower Bound		Upper Bound	
	ϵ_r	σ (S/m)	ϵ_r	σ (S/m)	ϵ_r	σ (S/m)
2	182	4.72 X 10-2	82	1.16 X 10-2	455	1.56 X 10^{-1}
3	141	7.10 X 10-2	71	2.15 X 10-2	371	2.04 X 10-1
4	92	6.09 X 10-2	73	2.55 X 10-2	328	2.73 X 10^{-1}
5	71	3.93 X 10-2	52	2.10 X 10-2	301	3.36 X 10^{-1}
6	71	4.98 X 10-2	49	2.51 X 10-2	293	4.35 X 10^{-1}
7	62	5.45 X 10-2	38	2.62 X 10-2	217	3.06 X 10^{-1}
8	51	5.00 X 10-2	22	2.67 X 10-2	213	3.68 X 10^{-1}
10	46	5.18 X 10-2	28	2.01 X 10-2	78	1.12 X 10^{-1}
12	39	4.32 X 10-2	19	1.56 X 10-2	58	8.38 X 10-2
14	31	3.67 X 10-2	19	1.59 X 10-2	54	9.59 X 10-2
16	30	3.54 X 10-2	19	1.87 X 10-2	52	1.04 X 10^{-1}
18	24	3.09 X 10-2	17	1.91 X 10-2	46	8.83 X 10-2
20	23	3.11 X 10-2	16	2.08 X 10-2	44	9.32 X 10-2
22	22	3.80 X 10-2	14	1.03 X 10-2	28	5.55 X 10-2
24	20	3.91 X 10-2	12	1.53 X 10-2	31	6.80 X 10-2
26	20	4.48 X 10-2	10	1.32 X 10-2	27	6.43 X 10-2
28	18	4.45 X 10-2	10	1.22 X 10-2	26	6.98 X 10-2
30	17	4.33 X 10-2	9	1.26 X 10-2	24	7.23 X 10-2

TABLE 6.2

Summary of Data Broadband Dipole
(Locations 2, 4 through 11)

Frequency (MHz)	Best Estimate		Lower Bound		Upper Bound	
	ϵ_r	σ (S/m)	ϵ_r	σ (S/m)	ϵ_r	σ (S/m)
2	137	2.72 X 10-2	54	1.16 X 10-2	314	9.22×10^{-2}
3	112	3.52 X 10-2	49	1.00 X 10-2	230	1.10×10^{-1}
4	87	3.73 X 10-2	45	1.17 X 10-2	266	2.14×10^{-1}
5	71	3.93 X 10-2	42	1.78 X 10-2	189	1.63×10^{-1}
6	63	3.49 X 10-2	33	1.01 X 10-2	205	2.73×10^{-1}
7	57	4.46 X 10-2	28	1.27 X 10-2	153	2.36×10^{-1}
8	48	3.70 X 10-2	22	1.47 X 10-2	150	2.48×10^{-1}
10	45	4.66 X 10-2	22	1.18 X 10-2	78	1.12×10^{-1}
12	39	4.37 X 10-2	19	1.46 X 10-2	58	8.38 X 10-2
14	32	4.24 X 10-2	19	1.81 X 10-2	54	9.59 X 10-2
16	32	4.55 X 10-2	19	1.87 X 10-2	52	1.04×10^{-1}
18	23	2.99 X 10-2	17	1.91 X 10-2	46	8.83 X 10-2
20	22	3.11 X 10-2	16	2.08 X 10-2	44	9.32 X 10-2
22	20	3.41 X 10-2	10	1.01 X 10-2	28	5.55 X 10-2
24	22	4.80 X 10-2	11	1.40 X 10-2	31	7.09 X 10-2
26	20	5.05 X 10-2	10	1.28 X 10-2	27	6.53 X 10-2
28	18	4.26 X 10-2	9	1.22 X 10-2	26	6.98 X 10-2
30	17	3.80 X 10-2	9	1.26 X 10-2	24	6.67 X 10-2

TABLE 6.3

Summary of Data for Field Strength Tests
(Locations 1 through 12)

Frequency (MHz)	Best Estimate		Lower Bound		Upper Bound	
	ε_r	σ (S/m)	ε_r	σ (S/m)	ε_r	σ (S/m)
2	153	3.55 X 10-2	54	6.37 X 10^{-3}	455	1.56 X 10^{-1}
3	129	4.18 X 10-2	49	1.00 X 10-2	371	2.04 X 10^{-1}
4	109	4.74 X 10-2	45	1.17 X 10-2	328	2.73 X 10^{-1}
5	77	3.82 X 10-2	42	1.78 X 10-2	301	3.36 X 10^{-1}
6	60	3.41 X 10-2	33	1.01 X 10-2	293	4.35 X 10^{-1}
7	56	4.43 X 10-2	28	1.27 X 10-2	217	3.06 X 10^{-1}
8	48	3.91 X 10-2	22	1.47 X 10-2	213	3.68 X 10^{-1}
10	45	4.34 X 10-2	22	1.18 X 10-2	78	1.12 X 10^{-1}
12	39	4.35 X 10-2	19	1.46 X 10-2	58	8.38 X 10-2
14	32	4.10 X 10-2	19	1.59 X 10-2	54	9.59 X 10-2
16	29	3.34 X 10-2	19	1.87 X 10-2	52	1.04 X 10^{-1}
18	23	3.03 X 10-2	17	1.91 X 10-2	46	8.83 X 10-2
20	23	3.07 X 10-2	16	2.08 X 10-2	44	9.32 X 10-2
22	21	3.59 X 10-2	10	1.01 X 10-2	28	5.55 X 10-2
24	22	4.14 X 10-2	11	1.40 X 10-2	31	7.09 X 10-2
26	20	4.61 X 10-2	10	1.28 X 10-2	27	6.53 X 10-2
28	18	4.36 X 10-2	9	1.22 X 10-2	26	6.98 X 10-2
30	17	3.96 X 10-2	9	1.26 X 10-2	24	7.23 X 10-2

6.2 Horizontal Homogeneity

There are two scales of horizontal homogeneity to consider: variations among samples taken on a given frequency with the probes inserted within about 1 m of each other at a given location, and variations with location across the entire antenna field. The small-scale variations seemed rather large (see the bounds given in Appendix A of Ref. 12 for the data on a given frequency at each location), but the small-scale variation seemed to decrease with increasing measurement frequency. The median values for each location showed relatively little variation (for this type of data) across the entire antenna field (with a few minor exceptions), as discussed below.

The median data were quite similar for the three groupings. This is to be expected because the data sets were not mutually exclusive. The horizontal (lateral) homogeneity across the entire site can be considered by focussing on a few selected frequencies. Table 6.4 summarizes the conductivity and relative dielectric constants data for 7, 14 and 30 MHz.

TABLE 6.4

Summary of Median Data for 7, 14 and 30 MHz

Location No.	7 MHz		14 MHz		30 MHz	
	ϵ_r	σ(S/m)	ϵ_r	σ(S/m)	ϵ_r	σ(S/m)
1	55	4.35×10^{-2}	23	1.86×10^{-2}	16	4.12×10^{-2}
2	62	5.77×10^{-2}	32	4.31×10^{-2}	17	4.33×10^{-2}
3	63	5.56×10^{-2}	41	5.45×10^{-2}	21	5.56×10^{-2}
4	54	4.00×10^{-2}	31	3.61×10^{-2}	12	2.42×10^{-2}
5	67	5.45×10^{-2}	39	4.84×10^{-2}	22	5.48×10^{-2}
6	50	3.38×10^{-2}	29	2.77×10^{-2}	16	3.18×10^{-2}
7	66	5.91×10^{-2}	31	3.67×10^{-2}	21	5.54×10^{-2}
8	54	4.46×10^{-2}	31	3.96×10^{-2}	14	3.59×10^{-2}
9	41	2.10×10^{-2}	33	4.24×10^{-2}	11	2.07×10^{-2}
10	59	5.02×10^{-2}	37	4.91×10^{-2}	16	3.80×10^{-2}
11	57	4.40×10^{-2}	34	4.24×10^{-2}	21	5.57×10^{-2}
12	37	1.99×10^{-2}	22	1.80×10^{-2}	17	3.62×10^{-2}

These frequencies are approximately octavely related across the HF band. At 7 MHz, the location median values are very similar except at Locations 9 and 12. At each of these locations there was some difficulty with the soil breaking away from the top of the probe holes as the holes were being made. This added air may have caused the OWL kit readings to be biased to the low side. The data reduction equations assume that the soil is touching the rods for their full length. The suspicion that the air holes caused reduced readings was verified by using the same set of probe holes twice. The second readings, taken in the enlarged holes (with more air), gave lower values. The problem caused by the dry brittle soil was not unique to these two locations, but it was more pronounced there. Excluding these two locations, the conductivity values varied between 3.38×10^{-2} S/m and 5.91×10^{-2} S/m, and the relative dielectric constant values varied between 50 and 67. At 14 MHz, the data from Locations 1 and 12 were low relative to the other locations. Excluding these two locations, the conductivity values varied from 2.77×10^{-2} S/m to 5.45×10^{-2} S/m, and the relative dielectric constant values varied from 29 to 41. At 30 MHz, the data at Locations 4 and 9 were lower for both the conductivity and relative dielectric constant. At Location 9, the problem of air around the probes was probably responsible for the values being lower. At Location 4, the surface soil (pertinent to the 9-inch probes used to obtain the data at 30 MHz) was much less compacted, and this resulted in the lower values. As noted in Table 4.1, the soil was less compacted at Locations 1, 4 and 8. The Location 8 data for all three frequencies seems to be very similar to the data from the other locations even though the steel rods were somewhat easier to drive at this location.

The conclusion is that the site is relatively horizontally homogeneous from a statistical standpoint--with the possible exception of Locations 9 and 12.

6.3 Vertical Homogeneity

As mentioned in Section 3, there was a vertical gradient of moisture content with the soil getting more moist with increasing depth down to 2 or 3 ft. The water table was at 71 to 81 feet below the surface. Therefore,

it was not a factor since the skin depth was only about 3 to 6 feet. Next, the variation of the relative dielectric constant (most closely correlated with volumetric moisture content)[14] with depth at the same location is considered by comparing the results obtained for several probe lengths on the same frequency at Location 2.

The relative dielectric constant data for Location 2 are given in Table 6.5 for the seven probe lengths for the following frequencies: 2, 4, 7, 14 and 30 MHz. These data show that there is a variation of relative

TABLE 6.5

Examples of Variation of Relative Dielectric Constant with Depth for Selected Samples and Frequencies at Location 2

Loc. No.	Sample No.	Freq. (MHz)	Probe Length (inches) 3	6	5	12	18	24	36
2	1	2	32	59	59	84	138	95	141
2	1	4	24	45	45	74	99	85	i.d.*
2	1	7	23	63	47	65	53	55	i.d.
2	1	14	12	15	17	22	30	39	i.d.
2	1	30	16?	17	12	17	i.d.	i.d.	i.d.
2	2	2	20	37	45	128	212	266	197
2	2	4	16	28	35	73	114	176	169
2	2	7	14	25	24	40	71	94	i.d.
2	2	14	11	13	16	27	54	i.d.	i.d.
2	2	30	10	9	11	20	i.d.	i.d.	i.d.
2	3	2	22	97	72	100	63	76	89
2	3	4	17	64	74	126?	68	81	i.d.
2	3	7	16	80	76	101	36	38	i.d.
2	3	14	10	18	18	22	18	19	i.d.
2	3	30	16?	16	12	15	18	i.d.	i.d.
2	4	2	25	29	65	51	104	92	250
2	4	4	18	22	41	41	54	79	i.d.
2	4	7	15	20	32	35	34	62	i.d.
2	4	14	11	12	16	17	26	45	i.d.
2	4	30	13?	10	10	11	i.d.	i.d.	i.d.

* i.d. = invalid data; ? = questionable data.

dielectric constant with probe depth for a given frequency that generally increases with increasing probe depth up to 18 or 24 inches, except at 30 MHz where little real variation is apparent. All four samples were obtained within 2 meters of each other; Samples 1 and 3 (Kit 1) and Samples 2 and 4 (Kit 2) were within 1 meter of each other for a given kit. The conclusion is that the moisture content and the resulting ground constants varied considerably over relatively short distances, and that it would be necessary to sample several times at a given location and use some measure of central tendency (e.g., the median) to describe the soil as it would be seen by a passing radio wave with a wavelength in the medium which is larger than the scale of variation being observed.

6.4 Comparison of Livermore Data with Generic Curves and Data from Other Sites

In 1980, the author developed some "generic curves" for the ground constants vs frequency, and they were first published in 1982.[15] These curves provide estimates of the ground constants for different terrain categories of the types described in handbooks.[16,17] These curves for the HF band for conductivity, relative dielectric constant, dissipation factor and skin depth, are reproduced here (from Ref. 5) as Figures 6.1 through 6.4, respectively. Also shown on these curves are data taken at other sites as presented and discussed in Ref. 18. The Livermore median values for all 12 locations are shown on Figures 6.1 through 6.4 to facilitate the comparison. The closest fit for the Livermore data to the generic curves is with rich agricultural land. The Livermore data are almost identical to the results obtained earlier by SRI on a farm near Delta, UT, where again rich agricultural land seemed an apt description.[4,5]

A useful parameter for NEC modeling is the wavelength in the soil at the radio frequency of interest. This parameter is needed in order to determine the number of segments needed for NEC-3 for the wire which has penetrated the air-ground interface. A set of generic curves for this parameter were developed recently by Hagn.[19] using the equations in Table 6 of Ref. 18 or Table 1 of Ref. 19. The curves of wavelength in the soil

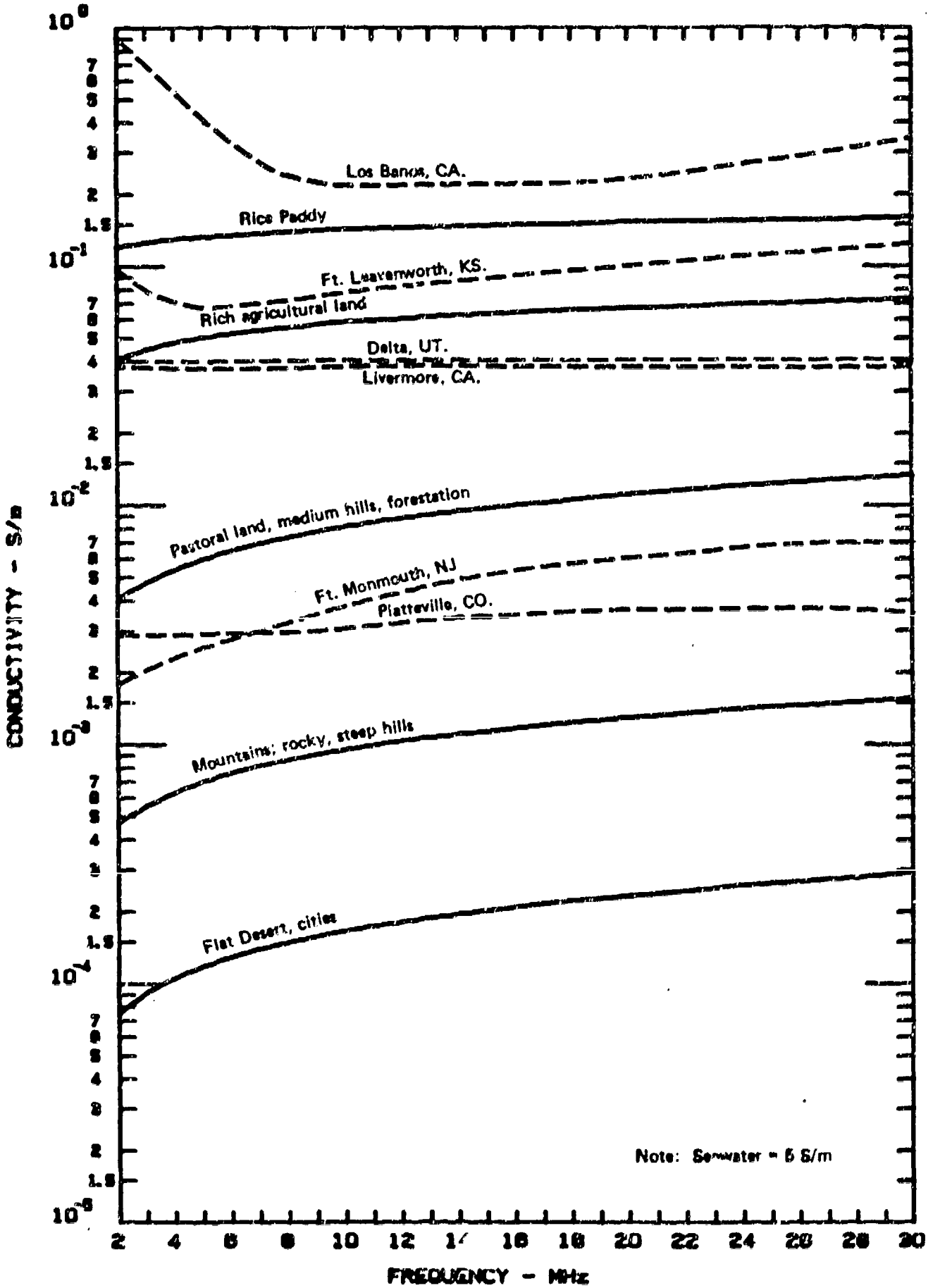


Figure 6.1 EFFECTIVE GROUND CONDUCTIVITY FOR SIX ANTENNA TEST FIELD SITES VS SRI GENERIC CURVES FOR SELECTED TERRAIN CATAGORIES

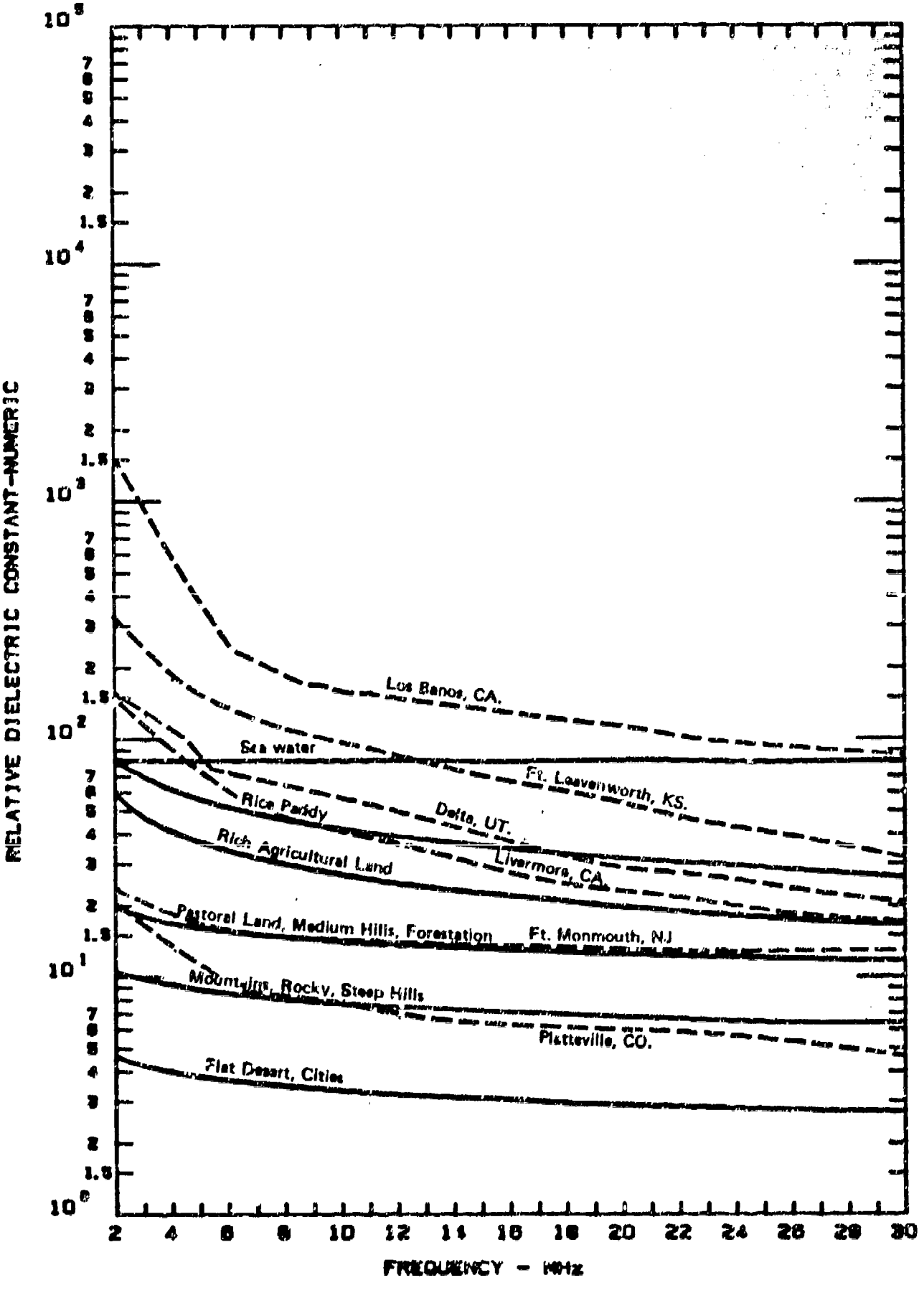


Figure 6.2 EFFECTIVE RELATIVE DIELECTRIC CONSTANT FOR SIX ANTENNA TEST FIELD SITES VS SRI GENERIC CURVES FOR SELECTED TERRAIN CATAGORIES

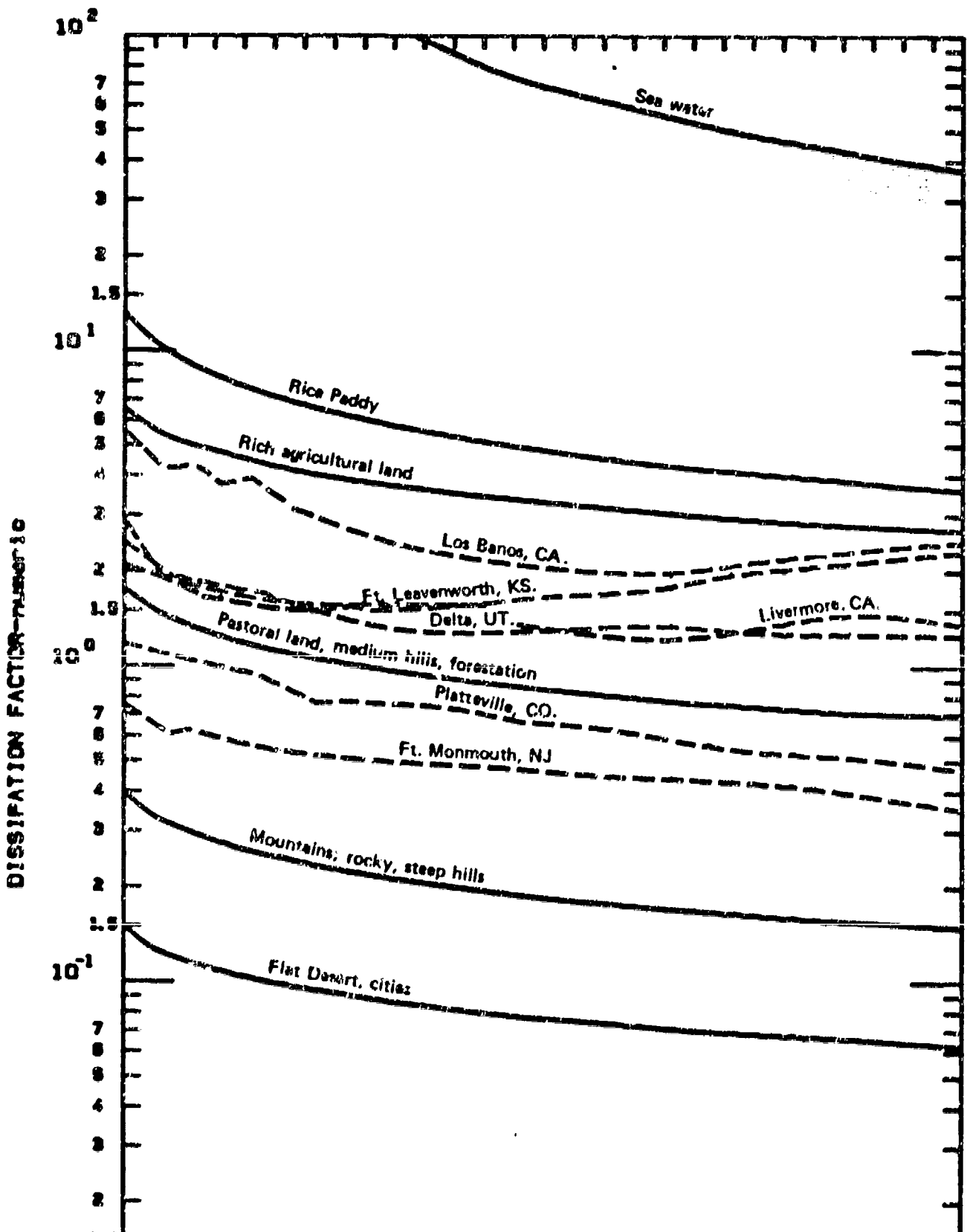


Figure 6.3 EFFECTIVE GROUND DISSIPATION FACTOR FOR SIX ANTENNA TEST FIELD SITES VS SRI GENERIC CURVES FOR SELECTED TERRAIN CATAGORIES

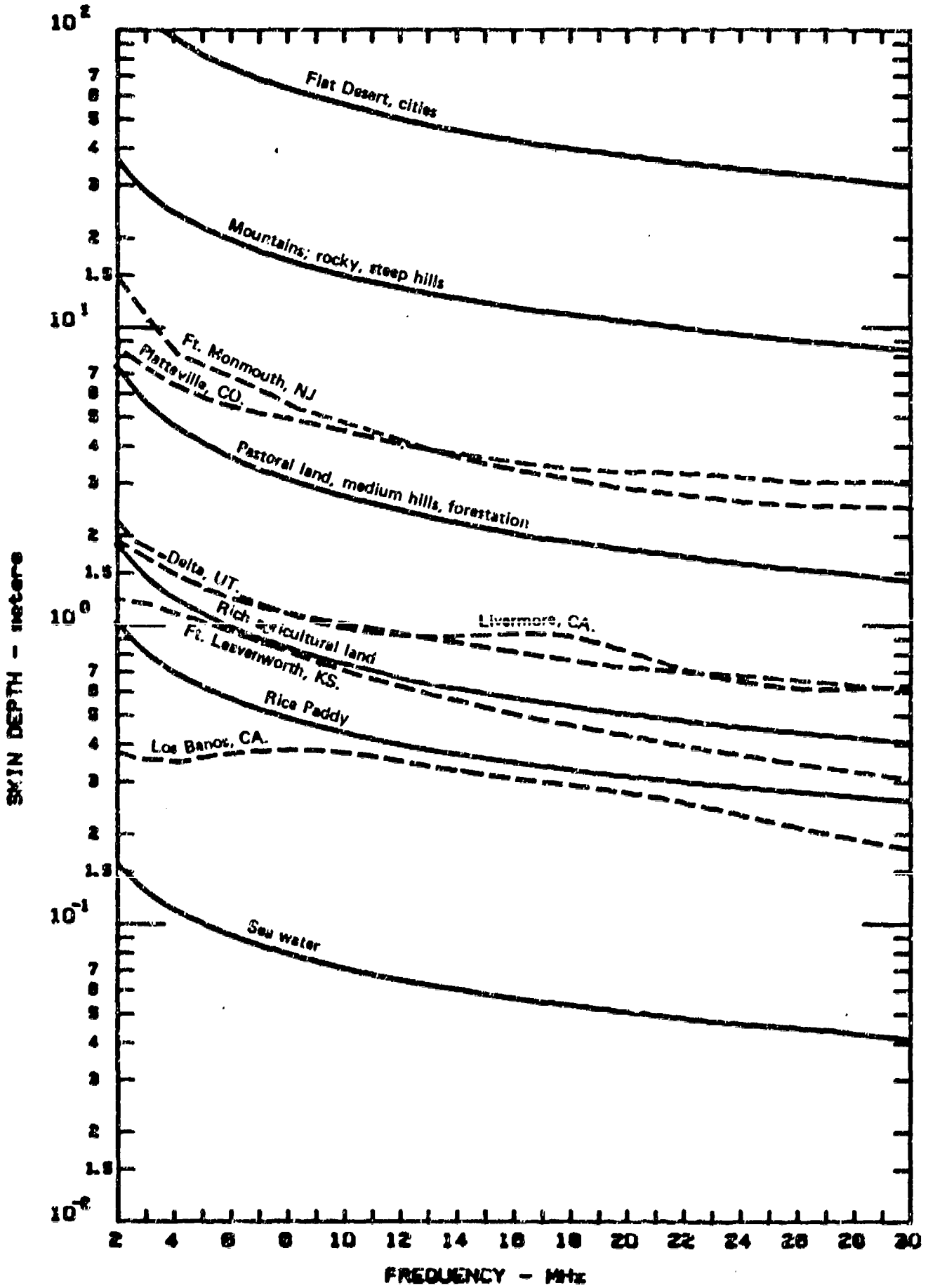


Figure 6.4 EFFECTIVE SKIN DEPTH FOR SIX ANTENNA TEST FIELD SITES VS SRI GENERIC CURVES FOR SELECTED TERRAIN CATAGORIES

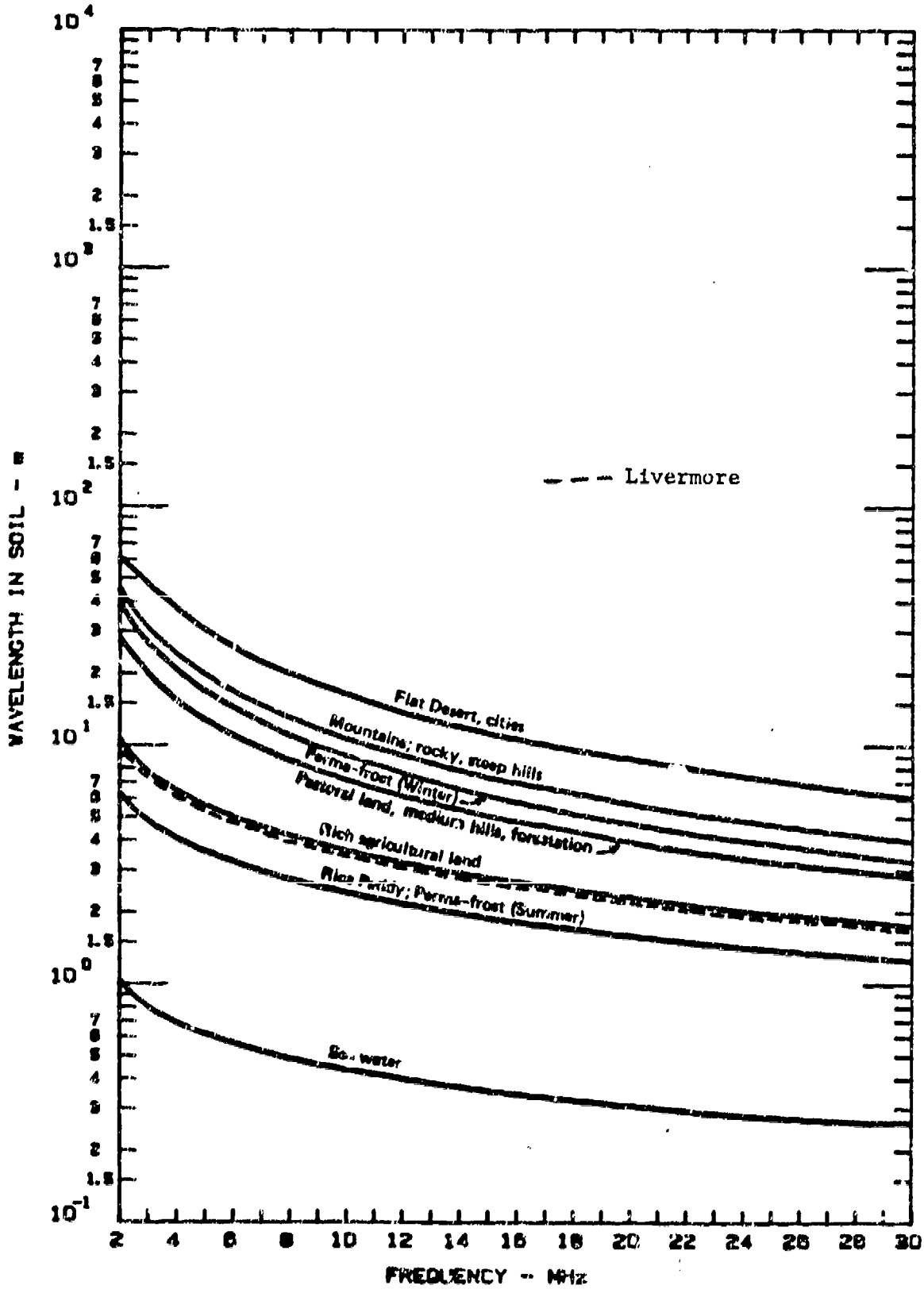


Figure 6.5 LIVERMORE DATA AND SLC GENERIC CURVES OF WAVELENGTH IN SOIL VS FREQUENCY FOR SELECTED TERRAIN CATEGORIES

(or sea water) vs frequency are plotted in Figure 6.5. The data from the Livermore site are plotted for comparison.

6.5 Accuracy Considerations

Accuracy checks with the HP 4193A on a 52.0-ohm dummy load, as measured at DC with a Micronta Model 2-211 two-jewel meter, provided values less than 0.6 ohm different across the HF band on the measurement frequencies. The phase angle difference was never more than 1.9 degrees, and it was 1 degree or less for frequencies below 16 MHz. The frequency accuracy is ± 0.01 percent. The HP 4193A features built-in test equipment (BITE), and the front-panel display flashes "PASS" or a "NOT READY" light comes on. This ensures that the instrument is operating properly prior to data acquisition.

The resulting accuracy of measurement of the ground constants is better than 25 percent.

7. CONCLUSIONS AND RECOMMENDATIONS

7.1 Conclusions

The following conclusions were reached:

- The ground constants data were particularly difficult to obtain at Livermore due to the hardness (and brittle nature) of the soil at this site.
- There was a significant variation of the data for a given frequency at a given location and between locations, and this necessitated a statistical analysis to obtain best estimates of the ground constants at the Livermore site suitable for use in NEC validation.
- These small-scale variations could have been caused by localized variations in moisture content or by differing amounts of air around the probes (biasing the reading to be too low), or by both effects.
- The data from selected locations required grouping

together to obtain the sample set for the two antennas (longwire and broadband dipole) and for the field strength test.

- The location median values of the conductivity and relative dielectric constant were reasonably consistent across the antenna field.

- The spreads between the bounds about the median formed by the maximum and minimum observed values were about an order of magnitude for the conductivity and about half that for the relative dielectric constant. These are typical of the spreads observed at other locations where there was less of a problem with air around the probes.

- The effective skin depth is less than about 2 meters in the HF band at Livermore, and it decreases to about 0.7 m at 30 MHz. Therefore, the water table (which is over 20 m down) has no significant effect on HF antennas or propagation at this site.

- The ground at the Livermore site behaves as a lossy conductor in the HF band with an effective dissipation factor that is relatively constant with frequency at about 1.5.

- The conductivity also is relatively constant in the HF band at about 4×10^{-2} S/m; whereas, the relative dielectric constant decreases with increasing frequency from about 150 at 2 MHz to about 17 at 30 MHz.

- The SRI OWL kit, adapted from the approach of Kirkscether,[20] is an effective tool for estimating effective ground constant values for the HF band when appropriate sampling techniques are used and when appropriate statistical processing of the valid data is performed.

7.2 Recommendations

The following recommendations are offered:

- The median values of conductivity and relative dielectric constant given in Tables 6.1 through 6.3 should be used to estimate (by interpolation) the values for the NEC validation computations for the longwire and broadband dipole input impedance and the field strength vs distance.

- A parameter sensitivity analysis should be performed using the bounds given in Tables 6.1 through 6.3 of Ref. 11 as input values for NEC. Priority should be given to the upper bounds due to the problem with air around the top of the probes at some locations which probably biased those values low.

- The vertical electric field strength data vs distance from the longwire should be fit using an SRI program or the NEC while varying the ground constants. Any ground constant estimates obtained through such curve fitting should be compared with the data from the OWL kit.

- The moisture content vs depth should be measured and correlated with the relative dielectric constant data vs probe length of the type given in Table 6.5. The soil samples for this comparison should be taken from the same volume sampled by the OWL kit (a cylinder approximately twice the probe spacing and as deep as the probes) to check the small-scale variations in relative dielectric constant and to determine if they are caused by highly localized moisture content variations or by different amounts of air around the probes near the top of the holes. It may be necessary to carefully drill the holes for the probes and to use a core drill for the soil samples.

ACKNOWLEDGMENTS

The author is pleased to acknowledge the assistance of the following individuals during data acquisition: Al Christman, Jim Breakall, Dick Adler and Warren Averill. It took the combined efforts of this group, working with the author, to extract the data (and OWL probes) from the very hard ground at the LLNL site. The author also appreciated the loan of electronic and other equipment by LLNL so that two OWL kits could be run in parallel to acquire twice the amount of data originally envisioned. Cheryl Hagn assisted with data reduction and computed the sample medians. The author is grateful to all of these individuals for their help. The author and LLNL also appreciate the encouragement and support of Ward Nair, Janet McDonald and Lee Corrington of USAISEIC, Ft. Huachuca, AZ, who provided the funds for the NEC validation. Any errors of commission or omission are those of the author alone.

DISCLAIMER

The findings in this report are not to be construed as an official Department of Energy or Department of Defense position unless so designated by other authorized documents. Citation of trade names in this report does not constitute an official endorsement or approval of the use of such commercial items by SRI International or by the Lawrence Livermore National Laboratory, or by the USAISEIC.

REFERENCES

1. G.J. Burke and A.J. Poggio, "Numerical Electromagnetics Code (NEC) -- Method of Moments," NOSC Technical Document 116, Volume 1, Contract M1PR-N0095376MP, Lawrence Livermore Laboratory, Livermore, CA, January 1981.

2. J.K. Breakall, G.J. Burke and E.K. Miller, "The Numerical Electromagnetics Code (NEC)," Proceedings of the 6th Symposium and Technical Exhibition on Electromagnetic Compatibility, pp. 301-308, Zurich, March 1985.

3. G.J. Burke, "Numerical Electromagnetics Code - User's Guide Supplement for NEC-3 for Modelling Buried Wires," Lawrence Livermore Laboratory, Livermore, CA, October 1983.

4. L.O. Harnish, G.H. Hagn and J.H. Faulconer, "Advanced Development Model Tactical HF Antenna Kits and Related Field Tests," Quarterly Technical Status Report: 2 December 1984 - 21 March 1985, Contract DAAB07-84-C-K545, SRI Project 7439, SRI International, Arlington, VA, 21 March 1985.

5. L.O. Harnish, G.H. Hagn and J.H. Faulconer, "Advanced Development Model Tactical HF Antenna Kits and Related Field Tests," Quarterly Technical Status Report: 22 March - 21 June 1985, Contract DAAB07-84-C-K545, SRI Project 7439, SRI International, Arlington, VA, 21 March 1985.

6. L.O. Harnish, G.H. Hagn and M. Lee, "Full-Scale Measurements of the Boresight Elevation-Plane Directivity Pattern and Gain of an HF Beverage Antenna Array," Final Report, Contract P.O. NB2149, SRI Project 2624, SRI International, Arlington, VA, 15 December 1986.

7. L.O. Harnish, M. Lee and G.H. Hagn, "Comparison of Measured and NEC-Calculated Characteristics of a Vertical Monopole with Buried Ground Radials," Proceedings of the 3rd Annual Review of Progress in Applied Computational Electromagnetics, Monterey, CA, March 1987.

8. W.E. Goldstein, H.W. Parker and G.H. Hagn, "Three Techniques for Measurement for Ground Constants in the Presence of Vegetation," Special Technical Report 30, Contract DA-36-039 AMC-00040(E), SRI Project 4240, Stanford Research Institute, Menlo Park, CA, March 1967. AD 672 496.

9. G.H. Hagn and J.C. Gaddie, "Medium and High Frequency (MF and HF) Ground Electrical Parameters Measured during 1982 at Seven Locations in the United States with the SRI OWL Probe Kit," Presented to URSI Com. A., National Radio Science Meeting, Boulder, CO, Abstract, p. 78, 11-14 January 1984.

REFERENCES
(Concluded)

10. G.H. Hagn and L.O. Harnish, "Measurement Techniques for HF Tactical Antennas," Proceedings of the DARPA-AFCEA-IEEE conference on Tactical Communications: The Next Generation, Fort Wayne, Indiana, 22-24 April 1986.

11. J.K. Breakall and A.M. Christman, "Experimental Antenna Measurements for the Validation of the Numerical Electromagnetics Code (NEC), Proceedings of the 4th Annual Review of Progress in Applied Computational Electromagnetics, Monterey, CA, March 1988.

12. G.H. Hagn, "HF Ground Constant Measurements at the Lawrence Livermore National Laboratory (LLNL) Field Site," Letter Report, Purchase Order No. 214 7603, SRI Project 3942, SRI International, Arlington, VA, August 1987.

13. C.P. Webster-Scholten, M.D. Dresen, W.A. McConachie, R.O. Devany, D.S. Thompson and D.N. Homan, "LLNL Ground Water Project," Report No. UCAR-10160-87-5, Environmental Protection Investigations and Corrections Series, Lawrence Livermore National Laboratory, Livermore, CA, 15 March - 15 April, 1987.

14. R.W.P. King, S. Smith, M. Owens and T.T. Wu, Antennas in Matter, The MIT Press, Cambridge, MA, 1981.

15. G.H. Hagn, B.M. Sifford and R.A. Shepherd, "The SRICOM Probabilistic Model of Communication System Performance -- A Users Manual for Engineers, Applications Programmers, and System Programmers," Final Report, Contract NT-81-RC-16011, SRI Project 3603, SRI International, Arlington, VA, May 1982.

16. F.E. Terman, Radio Engineer's Handbook, McGraw Hill Book Company, Inc., New York, p. 709, 1943.

17. ITT, Reference Data for Radio Engineers, Howard W. Sams and Company, Inc., 7th Edition, New York, 1985.

18. G.H. Hagn, "Ground Constants at High Frequencies (HF)," Proceedings of the 3rd Annual Review of Progress in Applied Computational Electromagnetics, Monterey, CA, March 1987.

19. G.H. Hagn, "HF Ground Constant Measurements at the Lawrence Livermore National Laboratory (LLNL) Field Site," Proceedings of the Fourth Annual Review of Progress in Applied Computational Electromagnetics, Monterey, CA, 22-24 March 1988.

20. E.J. Kirkscether, "Ground Constant Measurements Using a Section of Balanced Two-Wire Transmission Line," IEEE Trans. Ant. and Prop., Vol. AP-8, No. 3, pp. 307-312, May 1960.

EXPERIMENTAL ANTENNA MEASUREMENTS FOR THE VALIDATION OF THE NUMERICAL ELECTROMAGNETICS CODE (NEC)*

by
J. K. Breakall and A. M. Christman
Engineering Research Division
Lawrence Livermore National Laboratory
Livermore, CA.

ABSTRACT - There has been a need for the last ten years to test thoroughly several of the modeling features of the Numerical Electromagnetics Code (NEC), a state of the art antenna analysis computer program based on the method of moments integral equation solution technique, which was developed at the Lawrence Livermore National Laboratory (LLNL). This paper will describe the efforts and results of a project which was initiated and completed in 1987 to carry out such tests. Experimental measurements of several types of antennas in the field at Livermore have been made over the band of frequencies from 2-30 MHz, including input impedance, radiated field strength, and current distributions, which have been used to compare with computed results using models of the antennas with NEC. The antennas have been chosen to test a host of options and features that are used in NEC and especially the close ground interactions of these structures. To achieve the highest accuracy, a significant effort was made to measure the ground parameters in the field where the antennas were located. The data obtained from all measurements will be discussed and compared to the corresponding NEC results for validation of the code.

1. INTRODUCTION

The Lawrence Livermore National Laboratory (LLNL) was tasked with conducting a series of antenna measurements in the fields at Livermore and providing results of these and computer modeling of the antennas to the United States Army Information Systems Engineering and Integration Center (USAISEIC), Ft. Huachuca, Arizona. There has been a need to thoroughly test several of the modeling features and options of the most recent version of the Numerical Electromagnetics Code (NEC-3), but it was not until now that the effort was initiated. NEC-3 is a state-of-the-art antenna analysis computer program which was developed at LLNL [1,2] This latest version of the Numerical Electromagnetics Code, NEC-3, which can treat finitely-conducting earth and allow buried and penetrating objects below and across the interface, was used in this work. Previous versions of NEC only allowed objects above the interface and have been extensively validated with both experiment and comparisons with other analytical methods and results.

Several weaknesses of the NEC-3 code have been reported by others outside of LLNL. The measurements carried out in this project on the antennas tested will quan-

* Work performed under the auspices of the U. S. Department of Energy by the Lawrence Livermore National Laboratory under Contract W-7405-Eng-48 and the U.S. Army Information Systems Engineering and Integration Center, Ft. Huachuca, Arizona with order number ISEIC-M-04-87.

tify any inaccuracies that might exist to a degree that is the best that can currently be achieved. This data will therefore form a benchmark for NEC-3 and other codes for problems of similar type and construction.

To achieve the required accuracy and confidence, a significant effort was made to measure the ground constants, conductivity, σ, and the dielectric constant, ϵ, in the fields just west of LLNL in early July, 1987. Since no rain fell throughout the measurement period, the ground stayed dry, and the ground parameters remained unchanged.

This paper will describe the experimental and computational task plan for validating NEC-3 on some specific antenna configurations. A detailed discussion of all measurements and computations will be given on both the full scale antennas in the field and the scaled model versions in the anechoic chamber facilities at LLNL. Finally, results of this work will be provided and discussed with the implications for future antenna modeling.

2. NEC VALIDATION AND MEASUREMENTS TASK PLAN

After discussions at a meeting at Ft. Huachuca in June, 1987, a plan was formulated for carrying out measurements of two types of antennas in the field at Livermore. It was decided that measurements would be made over the band of frequencies of 2-30 MHz of input impedance, radiated field strength, and current distributions which would be used to compare with computed results using models of the antennas with NEC. The antennas have been chosen to test a host of options and features that are used in NEC and especially the close ground interactions of these structures.

The Army at Ft. Huachuca provided additional funding to also have the ground measurements of our site characterized by G. Hagn (SRI) using his Open Wire Line (OWL) technique [3,4]. We carried out these measurements over the holiday weekend of July 3, 4, and 5 with the help of J. Breakall, A. Christman, R. Adler, and W. Averill assisting G. Hagn. Many long hours of hard labor were spent in this effort mostly due to the extremely hard cement-like ground found in our test field just outside the LLNL fence boundaries. When completed Sunday night, we had made some 3000 to 4000 independent measurements of σ and ϵ at 12 different test sites with about 3 probe locations at each site and 7 different probe lengths over 18 different frequencies from 2-30 MHz. G. Hagn provided a statistical summary characterization of the values found so we can use this data to test our NEC models [5].

The plan was formulated to have the Air Force (Scott AFB, Ill.) arrive and set up the first antenna the last week of July, 1987, and measurements were completed during that week. The Air National Guard (Hayward, Ca.) arrived the following week and set up the 2nd antenna and measurements were completed during that week. The NEC modeling was performed during the rest of the month of August and September, 1987. The scale model of one of the antennas was constructed and tested the following month in the anechoic chamber facilities at LLNL. Work then continued with the data reduction and processing of results into the final report. We predict that this work will provide some extremely useful information for validating the NEC code and evaluating

the importance of good ground parameter determination.

3. MODELING THE ANTENNAS

Figure 3.1 is a computer-generated drawing of the NEC model for the Bent Bow dipole antenna. The three-dimensional right-handed Cartesian co-ordinate system shown in the Figure 3.1 was used throughout the modeling process. The origin of the co-ordinate system is located at ground level directly beneath the apex of the antenna. The spherical co-ordinate system is also used (R,θ,ϕ), with θ being measured from the positive z-axis and ϕ measured in the x-y plane from the positive x-axis toward the positive y-axis. This drawing includes the mast and/or coaxial transmission line. The coax does not touch the antenna at its apex, but is separated by a distance of 4 inches (to simulate the electrical isolation provided by the balun). The short horizontal section of wire immediately above the top end of the coaxial transmission line represents the feed-point, which will be discussed in more detail later. The wire used throughout is # 18 gauge finite conductivity copper wire. The antenna is supported by an aluminum mast and ground rod. The antenna is fed through a Palomar 9:1 balun at the top of the mast.

Because the Bent Bow antenna has quite a few degrees of symmetry, considerable savings in CPU time can be achieved by taking advantage of certain features built into NEC. The use of two planes (Y-Z, X-Z) of symmetry and the Numerical Green's Function (NGF) in NEC has been used.

The other antenna is a simple Sloping Longwire which is 500 feet in length. The computer-generated drawing of the model of this antenna for use in NEC is shown in Figure 3.2. The end is terminated with a 600 Ω resistor into a 1.5 foot ground rod. The feeder wire slopes from the apex to one side and is connected to a TMC 12:1 balun. The other terminal of the balun is connected to a 1.5 foot ground rod. Finite conducting steel wire is used throughout with a radius of .00055 meters. The antenna is supported by a 35 foot aluminum mast and 1.5 foot ground rod.

Tapering has been used on both antennas to reduce the number of segments and to ensure accuracy in critical regions. Models were constructed and guidelines followed for all frequencies from 2 to 30 MHz.

4. GROUND CONSTANTS MEASUREMENTS

G. Hagn of SRI, International was tasked to come to our field site and make measurements of conductivity, σ, and dielectric constant, ϵ, in July, 1987. Mr. Hagn has made similar measurements all over the world and has a very good system and technique. The system called the Open Wire Line (OWL) technique uses an electrically short two-wire transmission line which has the equivalent circuit of a low-loss capacitor. Measurement of the capacitance and dissipation factor (the ratio of conduction to displacement current) is made with a HP 4193A vector impedance bridge in air and ground to determine σ and ϵ.

The location of the measurement site is shown in Figure 4.1 for the OWL and all antenna measurements. Test wells are also shown in this figure for some other work

being carried out by LLNL for testing ground water, etc. Many more measurements were made in the vicinity of where the antennas were positioned since it is the local near-field region which primarily determines the input impedance and current distributions. Test points were also selected so that the Bent Bow antenna could be measured in two basic configurations, endfire and broadside. This antenna takes up a space of about 150 by 50 feet as shown. Other test points were selected along the radial line of propagation for field strength measurements.

Photographs of the site and measurement process are shown in Figures 4.2 to 4.9. The median conductivity and relative dielectric constant versus frequency are shown in Figures 4.10 and 4.11. Effective ground conductivity and relative dielectric constant for six different antenna test field sites including Livermore are compared with some SRI generic curves for selected terrain categories in Figures 4.12 and 4.13. It is interesting to notice that the Livermore site has almost exactly the same ground constants as that of the Delta, Utah site. For more detailed information on these measurements and description of the technique please refer to the SRI report mentioned above.

5. FIELD STRENGTH MEASUREMENTS

Field strength measurements were made from both of the antennas at distances of 500, 750, and 4648 feet north of the center of the Bent Bow dipole antenna for both the endfire and broadside configurations. The far field criterion for this antenna is as follows:

At 2 MHz,

$$\frac{2D^2}{\lambda} = 91.5 feet$$

At 30 Mhz,

$$\frac{2D^2}{\lambda} = 1372 feet$$

where D is the largest dimension of the antenna.

Therefore, the field test point locations are both in the near and far fields at some of the frequencies.

For the Longwire antenna the field strengths were measured at distances of 500, 750, and 4648 feet north of the center of the antenna. This corresponds to distances of 746.7, 996.7, and 4895 feet north of the feedpoint of the Longwire.

At 2 MHz,

$$\frac{2D^2}{\lambda} = 1016 feet$$

At 30 MHz,

$$\frac{2D^2}{\lambda} = 15,244 feet$$

The field strength location test points are likewise in both the near and far field regions at some frequencies.

For measuring absolute field strength a Rhode & Schwarz ESH-2 Calibrated Receiver was used which had digital frequency readout. This equipment is supplied with both an active Rod antenna (monopole on fold-out ground radials) and an active Loop antenna that is mounted on a tripod. Calibration is done automatically between the antennas and the receiver and electric field strength can be read in dB referenced to 1 μVolt per meter (dBμV/m). Error is specified to be less than 2 dB. We used the Loop to measure one component of the magnetic field and the Rod to measure one component of the electric field.

The field strength was measured with the Bent Bow antenna in two configurations, endfire and broadside. Endfire corresponds to the sloping wires from the feedpoint to the ground pointing in-line to the field strength test locations. Broadside corresponds to the dipole being rotated 90 degrees from Endfire and the sloping wires are then perpendicular to the direction pointing to the test locations. The Bent Bow antenna is fed through 29.31 meters of 50 Ω coaxial cable and a Palomar 9:1 balun at the antenna terminals.

The field strength of the Sloping Longwire was measured in just one configuration with the test point locations being located in a line in the sloping direction of the longwire (endfire). The antenna was fed through 30.25 meters of 50 Ω coax and a TMC 12:1 balun. The feeder wire is connected to one terminal of the balun and the other terminal is grounded by connection to a 1.5 foot ground rod.

The field strength measuring antennas were oriented as follows. The Rod was always mounted on fold-out radials and was positioned on the ground for all cases. It therefore was used to measure the vertical component of the electric field. The plane of the Loop was oriented normal to the radius vector for the broadside dipole configuration. This corresponds to measuring the radial component of the magnetic field and indicates that power is being lost into the lossy ground. The plane of the Loop was oriented parallel to the radius vector for the endfire dipole and longwire configurations. This corresponds to measuring the horizontal component of the magnetic field which is transverse to the direction of propagation for the appropriate radially outward wave.

The corresponding NEC components of both the electric and magnetic fields have been computed and compared directly with the measured values. These results will be shown later in this report. The Rhode & Schwarz receiver only gives the absolute electric field strength (E-field, Volts/meter). When using the Loop sensor antenna, the Rhode & Schwarz manual states that the E-field is determined by multiplying the magnetic field measured by the impedance of free space, $\eta_o = 377\ \Omega$. This may or may not be correct in practice due to surface impedance effects near the ground. Since NEC can give the magnetic field directly from computations, one is really interested

in knowing the measured magnetic field for direct comparison. The magnetic field can thus be determined by simply taking the measured E-field value with the loop and dividing by 377 or subtracting 51.527 dB from the measured dB (μV/m).

Electric field strength measurements were also made with another piece of equipment at our access, an Electro-Metrics (EMC) R-70B portable hand held receiver. This instrument is battery operated and is quite small in size and uses a collapsable whip sensor antenna. This receiver was used sitting on the radials which are used for the Rod antenna, sitting alone on the ground, and hand held at a height of 1 meter above the ground. These positions were chosen to determine the sensitivity of placement and make comparisons with the Rhode & Schwarz results. The results from the Electro-Metrics unit had to be corrected for individual calibration of the receiver and antenna factor of the antenna. This information is supplied with the equipment as calibrated at the factory.

A representative E-field strength result as measured with the Rhode & Schwarz instrumentation for the Longwire antenna is shown in Figure 5.1 (750 feet). The corresponding NEC computed result is shown on the same plot for comparison. Likewise, a result is shown in Figure 5.2 for the endfire orientation of the Bent Bow dipole. The measured results shown in the above figures are all with the active Rod sensor antenna. The H-field strength results as measured with the active Loop antenna are similarly shown in Figure 5.3 for the Longwire antenna and Figure 5.4 for the Bent Bow dipole.

The above field strength results have all been normalized to a power of 15 watts at the terminals of the antenna. This was done by measuring the actual input power to the coaxial cable line at the transmitter end using the digital wattmeter. This input power is simply the forward power minus the reflected power at the transmitter end of the line. The power actually at the antenna terminals is less than this input power because of losses in the coaxial cable and the balun. A loss factor was measured in the laboratory of this combination of coaxial cable and the balun by using a directional bridge and corresponding power meters driven by a RF generator source. By measuring accurately the load power, P_{load}, and the input power, P_{in}, the loss factor is then:

$$Loss factor = \frac{P_{load}}{P_{in}}$$

The field strength normalized to 15 watts is:

$$FS(dB\mu V/m) = 10Log(\frac{15}{P_{input} Loss factor}) + FS_{measured}$$

Also, all field strengths have been normalized to be RMS values.

6. CURRENT PROBE MEASUREMENTS

Current was measured at 6 locations on the Bent Bow dipole using a Tektronix oscilloscope and RF current probe which is a magnetic field sensing loop with a conversion factor of 2 milliamp per milliVolt of deflection on the scope. The positions of the locations are given in Table 8.1. For the Longwire the current was measured at

the junction of the sloping end of the longwire and the termination resistor junction. Current was also measured at the midpoint of the longwire, 250 feet from the termination resistor, and 7.5 feet above ground level. The currents have been normalized in a similar fashion as with the field strengths and are shown in Figure 6.1 for the Bent Bow dipole and Figur 6.2 for the Longwire.

7. IMPEDANCE RESULTS

Input impedance at the transmitter end of the coaxial feed cable was measured for the Bent Bow dipole antenna in both the broadside and endfire orientations and for the Longwire in the endfire orientation. Both orientations of the Bent Bow dipole antenna were measured to see if any differences could be observed which if found would indicate extremely non-homogeneous ground or something in the environment coupling and interfering with the antenna. The same HP vector impedance bridge was used for both antennas as used in the ground constant measurements. The impedance measured therefore included the effects of the balun and coaxial cable as well as that of the antenna under test. The NEC results which were determined at the antenna terminals therefore had to be transformed through the balun and the coaxial cable using proper relationships for each frequency of measurement used. The balun ratio used was 9:1 and 12:1 for the Bent Bow dipole antenna and the Longwire, respectively. For a coaxial transmission line the input impedance at the transmitter end, Z_{in}, is

$$Z_{in} = Z_0 \frac{(Z_{ant} + jZ_0 tan\beta l)}{(Z_0 + jZ_{ant} tan\beta l)}$$

where

$$\beta = \frac{2\pi}{\lambda}$$

and

$$Z_0 = 50\Omega$$

The above transformations were tested with the actual coaxial cables and baluns used in the field with a test resistor of measured value with the impedance bridge in the laboratory. The coaxial cable line length had to be converted to electrical length by measuring the velocity of propagation on the line. The results are shown in Figures 7.1 (Real part of impedance) and 7.2 (Imaginary part of impedance) for the coaxial cable and balun used with the Bent Bow dipole. These figures show the impedance measured at the transmitter end of the cable with a resistor connected on the other end of the balun (the terminals where the antenna would be connected) as compared to the input impedance computed from the measured impedance of the resistor with the appropriate transformations applied for the balun and the transmission line. Similar results were obtained for the coaxial cable and balun used with the Longwire antenna.

The input impedance results for the Bent Bow antenna are shown in Figures 7.3 and 7.4. The Longwire input impedance results are shown in Figures 7.5 and 7.6.

8. SCALE MODEL RESULTS

The Lawrence Livermore National Laboratory has an anechoic (free space) chamber which covers the frequency range from 1 GHz to 18 GHz. A positioner is installed which allows pattern measurements in any plane of interest. This equipment has been supplied by Scientific Atlanta. A full HP 8510 vector network analyzer covering the frequency range from 45 MHz to 18 GHz has also been installed with appropriate frequency synthesizers and test sets to measure both magnitude and phase over the range of frequencies mentioned above. The lower limit of the chamber is set from the size of the absorbers used and that of the chamber itself. The actual upper limit of the chamber is specified as 40 GHz but the network analyzer can presently only go to 18 GHz. All of the equipment is controlled by a Digital Equipment Corporation (DEC) LSI-11 computer. Data taking is also accomplished with this computer and data can then be transferred to other larger computers for reduction and analysis.

A scale model of the Bent Bow dipole antenna was constructed from measurements taken from the full scale computer model and built so that patterns could be taken at the lower frequency end of the anechoic chamber. This was done to construct a model of practical size, otherwise, it would have been too small to work with. The final scaling chosen worked out as follows:

1.0068 GHz corresponds to 15.102 MHz full scale

1.5326 GHz corresponds to 22.989 MHz full scale

1.9933 GHz corresponds to 29.900 MHz full scale

The scaling factor is 66.67 for actual full size to that of the scale model. A photograph is shown in Figure 8.1.

Since a balun of miniature size is not readily available at this frequency range, another method of feeding the dipole was developed. A parallel 50Ω transmission line was constructed out of miniature hardline coaxial cable and the center conductors of the cable were connected to each side of the dipole appropriately. A perfect ground plane was constructed as a platform and the twin coaxial cable was fed through the ground plane to the other side. A balun was then installed at this position where it would not interfere with the antenna due to the shielding effect of the large ground plane. The balun was then connected to the positioner rotary joint through flexible coaxial cable. Since only relative patterns were desired, effects of impedance mismatch, etc. could be ignored.

Elevation angles were selected at appropriate intervals of the positioner and the placement of a temporary transmitting horn and NEC models of this antenna were run over a perfect ground plane for corresponding patterns. The NEC modeling was carefully chosen to correspond with all dimensions of the physical scale model and the actual full size model. Some results are shown in Figures 8.2 to 8.4.

9. RESULTS AND DISCUSSION

9.1 FIELD STRENGTH RESULTS

The Longwire E-field results for the three test points as measured with the Rhode & Schwarz Rod antenna are within about 3 to 10 dB with the NEC computed results from 2 to 6 MHz. The measured results are generally higher than NEC. From 6 to 16 MHz the two closest test points to the antenna are in almost exact agreement and the farthest test point is within about 3 dB. From 16 to 30 MHz the two closest test points are within 3 dB and the farthest test point is within about 7 dB. The NEC results are higher than the measured values in this upper end of the frequency band. The curves are very flat except for the low frequency end of the range.

The Bent Bow dipole E-field results in the endfire orientation measured with the Rod antenna are within a maximum of 20 dB of the NEC results in the 2 to 6 MHz range with NEC being mostly higher. From 6 to 30 MHz the results are within about 3 to 7 dB of each other with NEC being higher at the closest and farthest distance. The structure of the curves is the same for both results.

The Bent Bow dipole E-field results for the broadside orientation are generally in good agreement in structure and absolute level. The maximum deviation is about 2 to 10 dB with most of the range within 3 dB. The broadside orientation is about 30 dB less in signal strength than the endfire configuration as expected for this polarization component.

The Longwire H-field results as measured with the Rhode & Schwarz Loop antenna are very close to the E-field results discussed above except for a shift in the dB value related to the impedance of free space, 377 Ω. There is also a couple of dB more disagreement between the results with the measurements being even less than the NEC computed magnetic fields as compared to results for the E-field.

The Bent Bow dipole H-field results for the endfire orientation is in good agreement with the corresponding E-field results. The same trends are noted with the lower range of frequencies from 2 to 6 MHz being closer to the computed results.

The Bent Bow dipole H-field results for the broadside orientation is in good agreement with the NEC computed results except for the middle test location where values are in disagreement of as much as 20 dB. Also the shapes of the curves are not the same as for the corresponding E-field results for both NEC and the measurements and are therefore not related by a factor of 377.

The Longwire E-field results as measured with the EMC unit in all three positions, on radials, on ground, and handheld, are all in good agreement with NEC results within 3 to 7 dB. The handheld results are in less agreement than either of the two ground mounted positions.

The Bent Bow E-fields results for the EMC unit in all three positions is in good agreement with NEC results within about 3 to 7 dB as with the Longwire. All results using the EMC are in agreement with the Rhode & Schwarz measurements within about 3 to 5 dB.

As can be seen the field strength results are in good agreement (less than 3 dB) in some frequency ranges and poor in other ranges, especially at lower frequencies. There seems to be little difference between using either the Rod or the Loop antenna except for the broadside case of the Bent Bow dipole where other components of the fields exist not in direct relationship. The EMC unit seems to perform well except for its limited frequency range only up to 7 MHz. It is not known why the results are poor at some frequencies and good at others. The sensitivity of the ground constants may offer some explanation and more work should be done to study the ground parameter variation on NEC results. Other explanations could be from errors with the measuring equipment or problems with the NEC models of the antennas. Results can be generally said to be within 3 to 7 dB for all measurements as compared to NEC and quite better at some specific frequencies.

9.2 CURRENT PROBE RESULTS

The Bent Bow dipole current probe results are in excellent agreement with NEC for all of the test points located on the wires parallel to the ground except at the lowest frequencies where some differences can be noticed. Both the shape of the curves and the absolute values of the current are in good agreement on these specific wires. The results on the sloping wires are not in as good of agreement as the ground wires. The results on these wires are in disagreement by a factor of 2 to 3 at most frequencies. This corresponds to values of between 6 to 10 dB. These results state the fact that the current distributions can be appreciably different without affecting the field strengths greatly because of the integral averaging effect of the field from the current.

The Longwire current probe results were measured in just two test point locations on the wire. The results for test point 1, at the resistor termination end, are in good agreement with NEC within about a factor of 2 or less. For the test point at the midpoint of the Longwire the agreement is not as good. Disagreements of factors as high as 8 or more occur at some frequencies and an average factor of 3 to 6 is seen. Again it can be said that the integral effect of this current is most important and not the exact absolute values of the distribution for determining field strength.

9.3 IMPEDANCE RESULTS

The tests of the impedance transformations of the coaxial cables and the baluns using a resistor of measured value in the laboratory are in excellent agreement. Results are within about 5 to 10 Ω for the Bent Bow balun with the greatest differences at the higher frequencies which can be expected. The Longwire results are somewhat worse being within about 10 to 20 Ω which may be due to the larger size of the TMC balun and the resulting distributed reactance effects with connections, etc.

The actual field impedance measurements on the Bent Bow dipole are in good agreement with NEC except at the lower frequency range between 2 to 6 MHz. The results are essentially the same for both the broadside and endfire configurations which is a good sign of a clean site free from interfering objects. The shapes of the curves are tracked well and the variation is greater than the differences noted in the resistor

tests. The impedance is primarily resistive in nature and around a value of 50 Ω.

The Longwire results are also in good agreement and it is seen that this antenna has less structure in the impedance curve. Also the reactive part of the impedance is very small and the resistive part is very close to 50 Ω.

9.4 SCALE MODEL RESULTS

Results for the pattern measurements made on the scale model of the Bent Bow dipole antenna are in good agreement with NEC computed patterns at 15.102 MHz for elevation angles above 33.29°. Below this elevation angle results are very similar in sidelobe structure but noticeable differences are detected. The main beam from measurements is wider than those predicted by NEC and the first sidelobes are much reduced or nonexistent. The other sidelobes are clearly there but amplitude differences of between 5 to 10 dB are seen.

The results for patterns at 22.989 MHz are also seen to be in good agreement for elevation angles above 33.29° except for some small differences (1 to 2 dB) at the highest angle measured, 75.25°. At and below this angle of 33.29° the results are in generally good agreement within 3 to 5 dB except for a noticeable widening of the main beam as compared with NEC results.

Results for the highest frequency at 29.900 MHz are in good agreement (3 to 5 dB) for angles below 54.17° even at the lowest elevation angle of 2.80°. The patterns at and above 54.17° are noticeably different in shape, especially at 64.61°. They are qualitatively in agreement and differences as high as 15 dB are noted.

It is not known exactly why some of these results are different. Some possibilities are that this antenna is very sensitive to slight changes in orientations since the ground wires are so close to the perfectly conducting ground plane. Also there probably are some diffraction effects not taken into account from the edge of our circular ground plane platform. The transmit antenna is fairly close to our model and may be contributing some near field effects which are not taken into account, also. In general, the results are of good quality and demonstrate the capability of measurements with our system and the validity of the NEC computations.

10. CONCLUSIONS AND RECOMMENDATIONS

This work has demonstrated the capabilities of performing full scale antenna measurements in the field and achieving comparable results to those of numerical computations using NEC-3. It has been shown that one must measure and determine the ground constants of the field site to insure meaningful calculations and comparisons. The field strength measuring equipment must be well calibrated and one must insure that the equipment is responding correctly to the desired components present of the electric and/or magnetic fields. The proper transformations must be applied to all impedance measurements to quantify the effects of items such as baluns, coaxial cable transmission lines, etc. When scale models are used, one must insure that the scaling adheres as closely as possible to the actual full scale antenna including things such as wire radius, feed arrangements, etc. Diffraction and other effects must be quantified if

extreme accuracy is desired.

Several suggestions are offered to be considered for future work:

1. Perform more work with measuring and validating the ground constants of different sites since measurements of this type really become statistical in nature.
2. Explore and compare other techniques of measuring the ground constants to provide added confidence and ease of making measurements.
3. Perform a parameter variation study with NEC-3 on the antennas investigated in this work to quantify the effect of varying the ground constants on the parameters measured.
4. Investigate the sensitivity and accuracy of field strength measuring equipment in a controlled laboratory environment.
5. Perform other experiments on antennas with known difficulties such as the stepped radius problem, VLF effects, loop antennas, wire grids, buried antennas, etc. to provide useful guidelines for further modeling and validity of results.
6. Investigate sky wave effects on antennas from measurements to provide useful information on both antenna codes and propagation codes.
7. Determine what is important in scale modeling and use this method to provide further validation of codes on difficult to construct and measure full scale antennas.

We hope that this work will provide much incentive and feasibility for more future efforts to be carried out on both full scale and scale model antennas for the further validation of present and new Numerical Electromagnetic Codes.

REFERENCES

[1] G. J. Burke and A. J. Poggio, "Numerical Electromagnetics Code (NEC) - Method of Moments," Lawrence Livermore Technical Report, UCID-18834, Jan. 1980.

[2] G. J. Burke, "Numerical Electromagnetics Code - Method of Moments, User's Guide Supplement for NEC-3 for Modeling Buried Wires," Lawrence Livermore Technical Report, UCID-19918, Oct. 1983.

[3] G. H. Hagn and J. C. Gaddie, "Medium and High Frequency (MF and HF) Ground Electrical Parameters Measured during 1982 at Seven Locations in the United States with the SRI OWL Probe Kit," Presented to URSI Com. A., National Radio Science Meeting, Boulder, CO, Abstract, p. 78, Jan. 11-14, 1984.

[4] G. H. Hagn, "Ground Constants at High Frequencies (HF)," Proceedings of the 3rd Annual Review of Progress in Applied Computational Electromagnetics, Monterey, CA, March 1987.

[5] G. H. Hagn, "HF Ground Constant Measurements at the Lawrence Livermore National Laboratory (LLNL) Field Site," SRI Letter Report, SRI Project 3945, August, 1987.

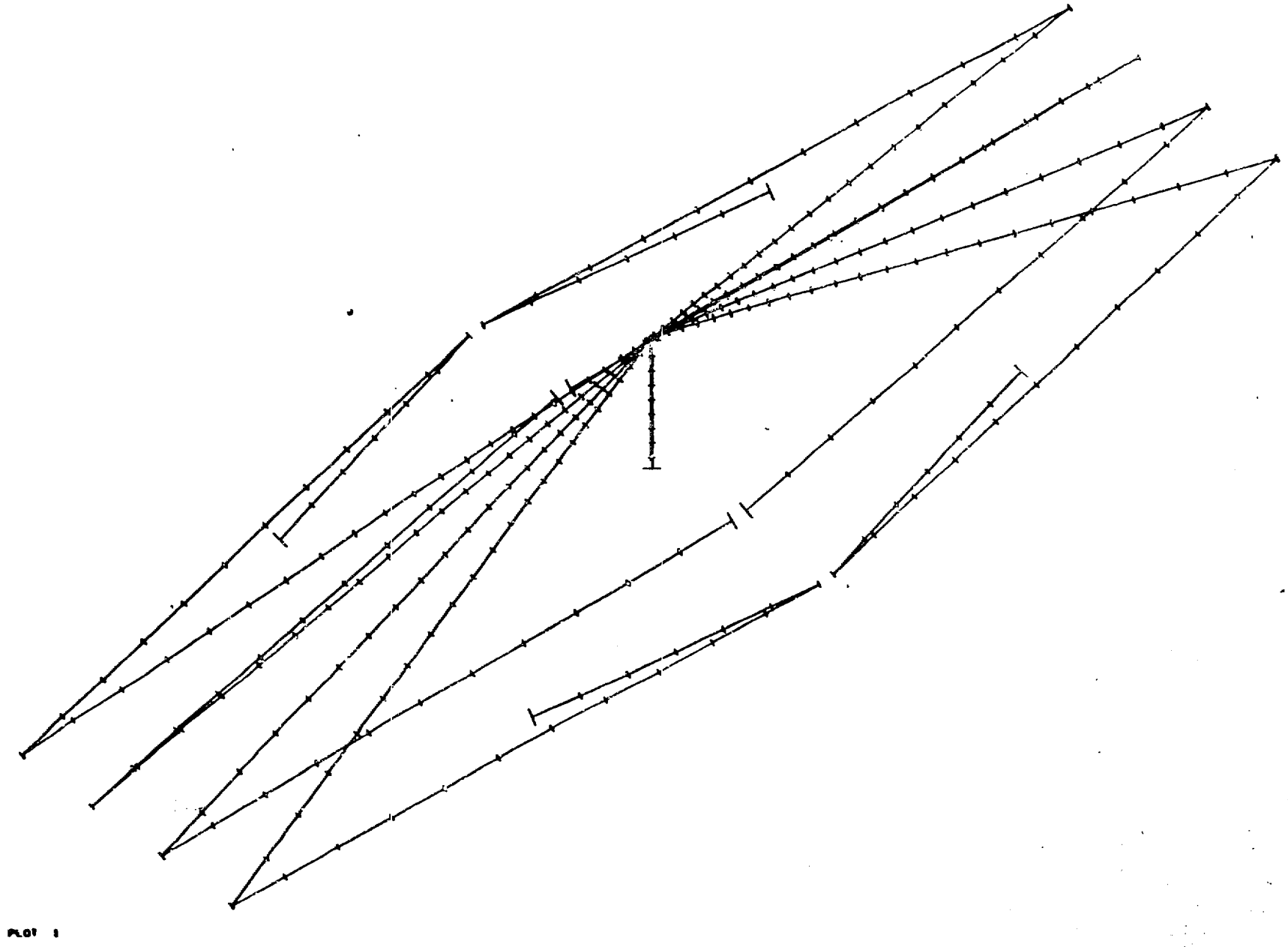


Figure 3.1 NEC Model for the Bent Bow Dipole Antenna.

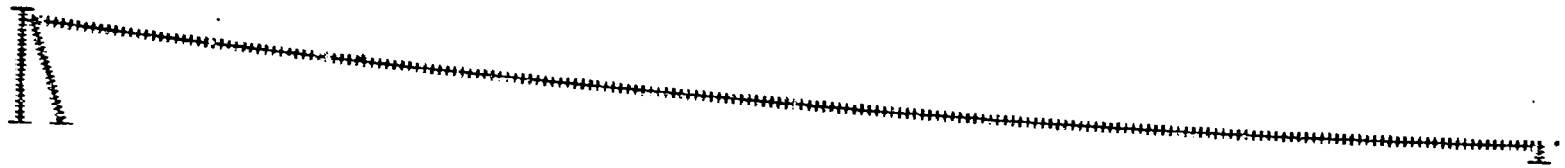


Figure 3.2 NEC Model for the Sloping Longwire Antenna.

PLOT 1

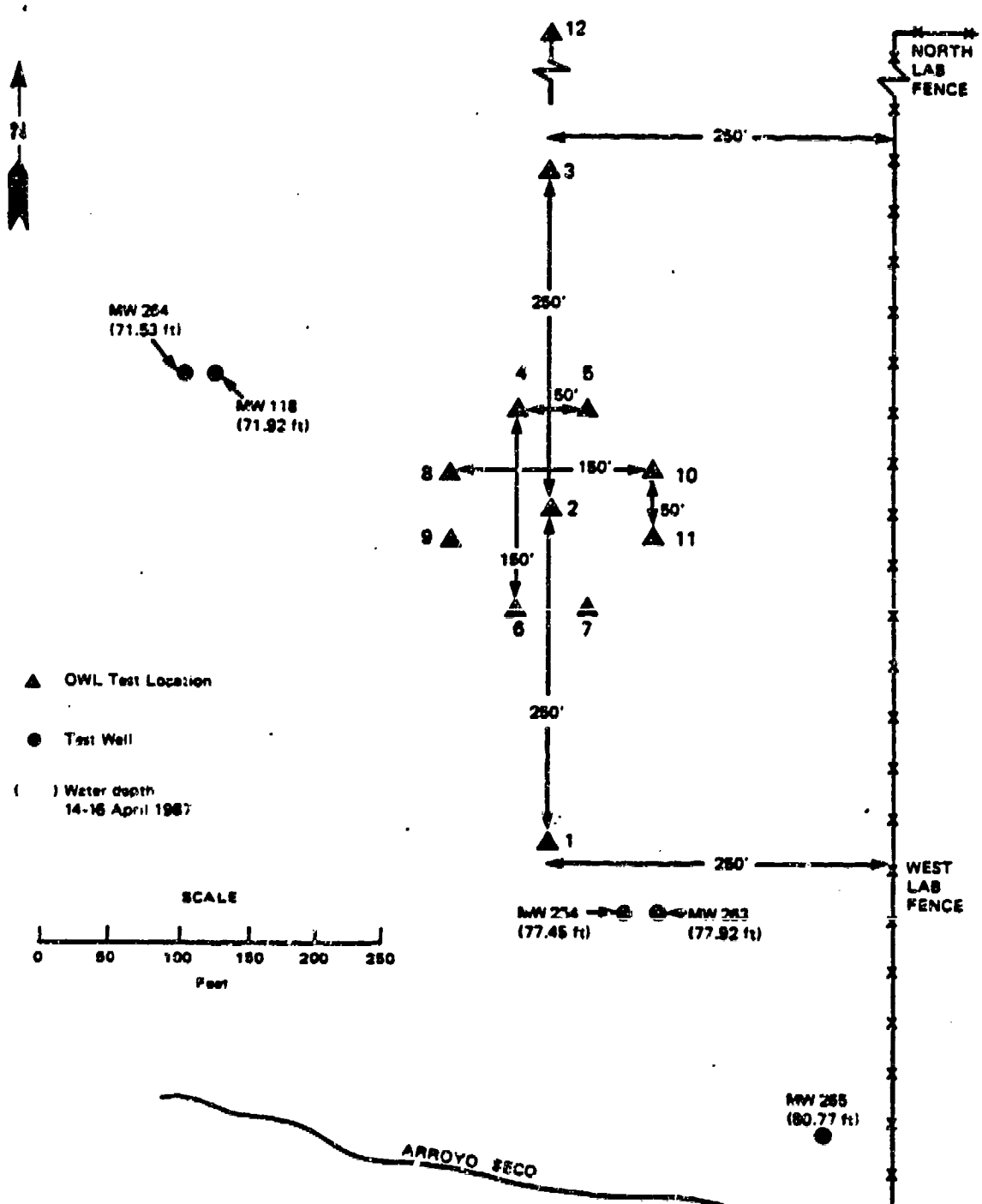


Figure 4.1 At Livermore Site.

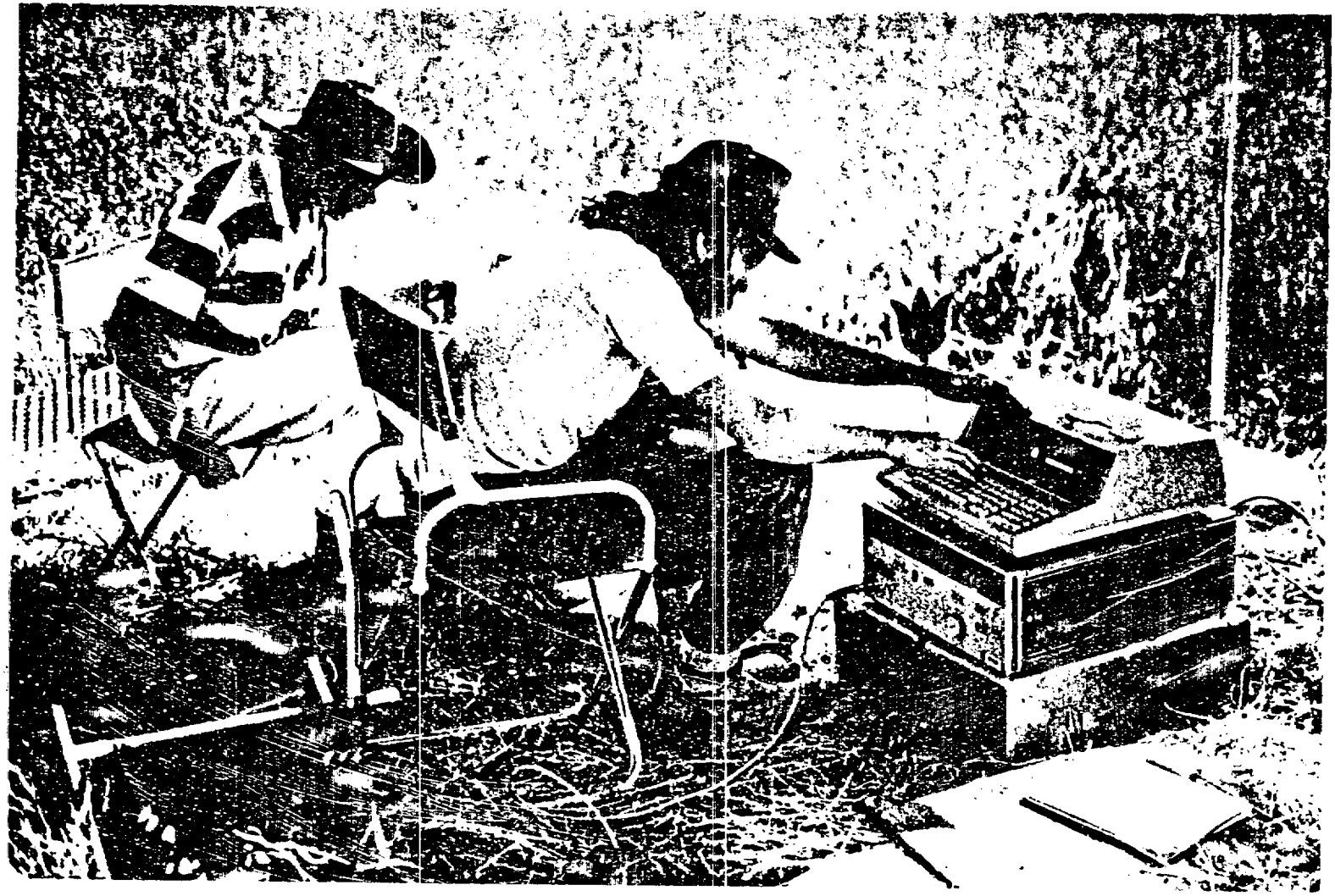


Figure 4.2 SRI OWL Kit in use at Livermore, Data Acquisition. Shown here are J. K. Breakall and A. M. Christman.

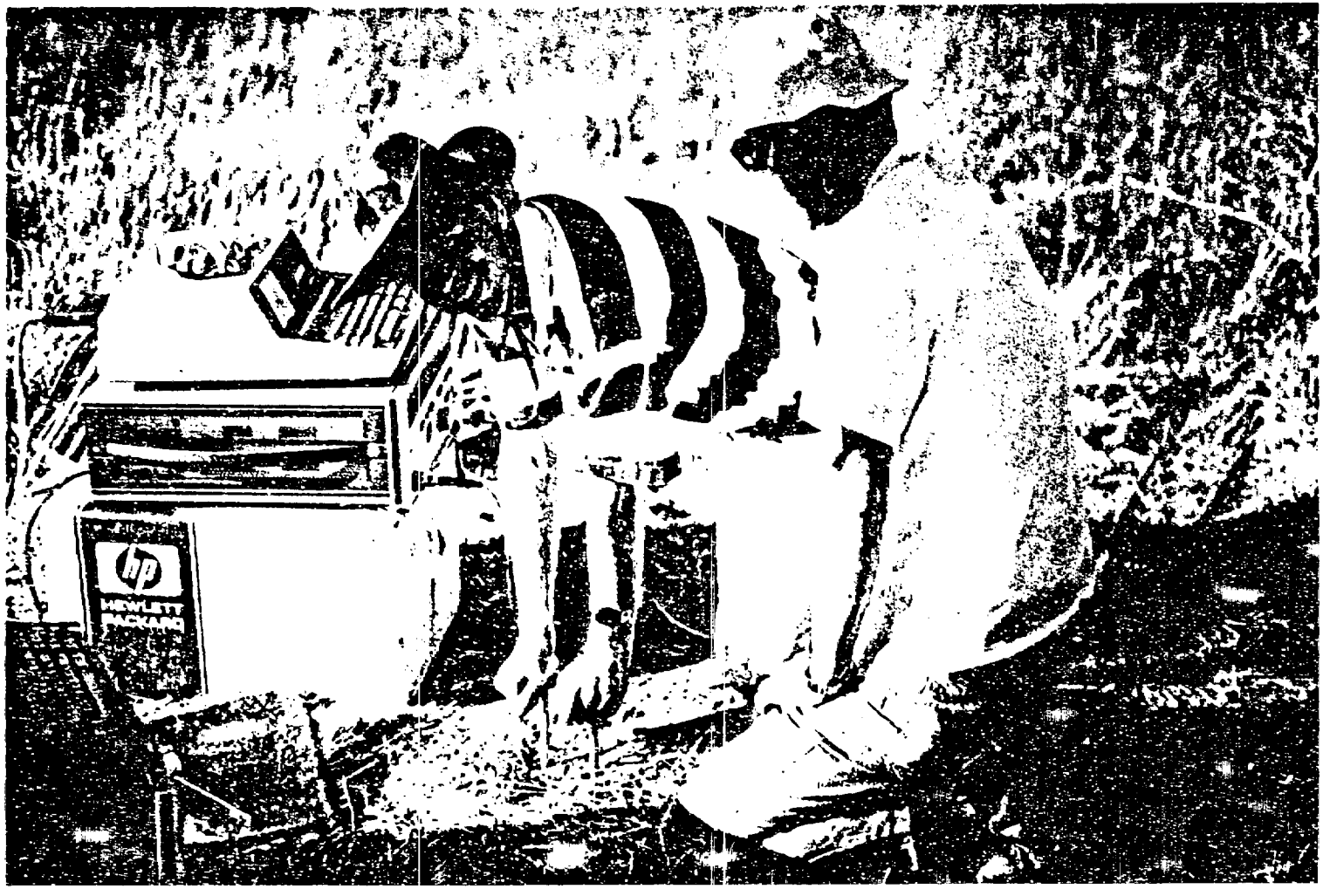


Figure 4.3 SRI OWL Kit in use at Livermore, Probe Insertion. Shown here are J. K. Breakall and R. W. Adler.



Figure 4.4 Photo of LLNL Field Site. Shown are A. M. Christman, J. K. Breakall, and R. W. Adler.



Figure 4.5 Driving Steel at Livermore. Shown are J. K. Breakall and A. M. Christman.



Figure 4.6 Clearing the Vegetation at Location 12. Shown here is A. M. Christman with Supervision from Advisors J. K. Breakall and R. W. Adler.



Figure 4.7 Members of Ground Constant Measurements Team. Shown are G. H. Hogn, J. K. Breakall, and A. M. Christman.

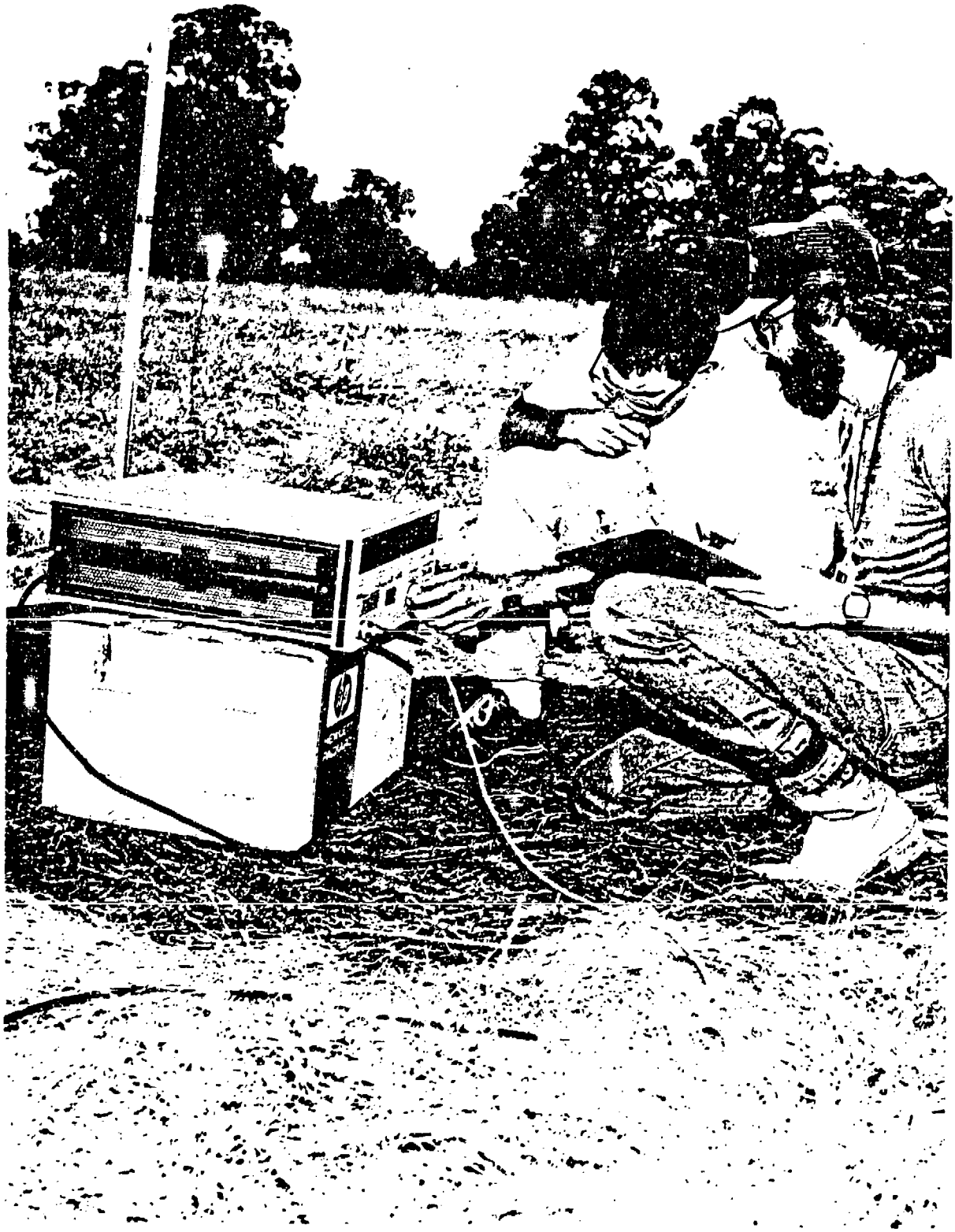


Figure 4.8 Measuring Antenna Input Impedance. Shown here are M. Millett and A. M. Christman.

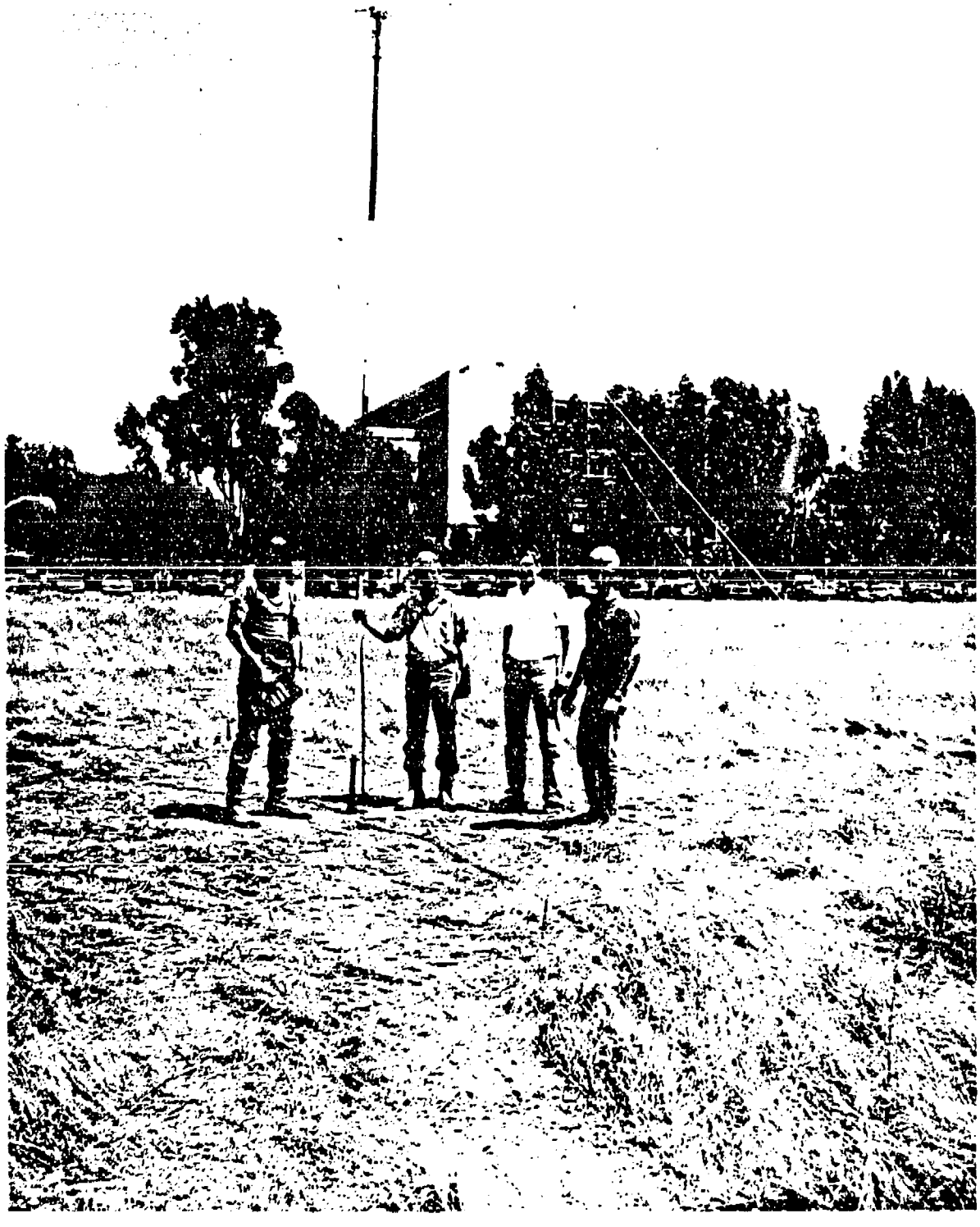


Figure 4.9 The Bent-Bow Broadbond Dipole Antenna at Livermore. Shown are A. M. Christman, J. K. Breakall, M. Millett, and A. Cole.

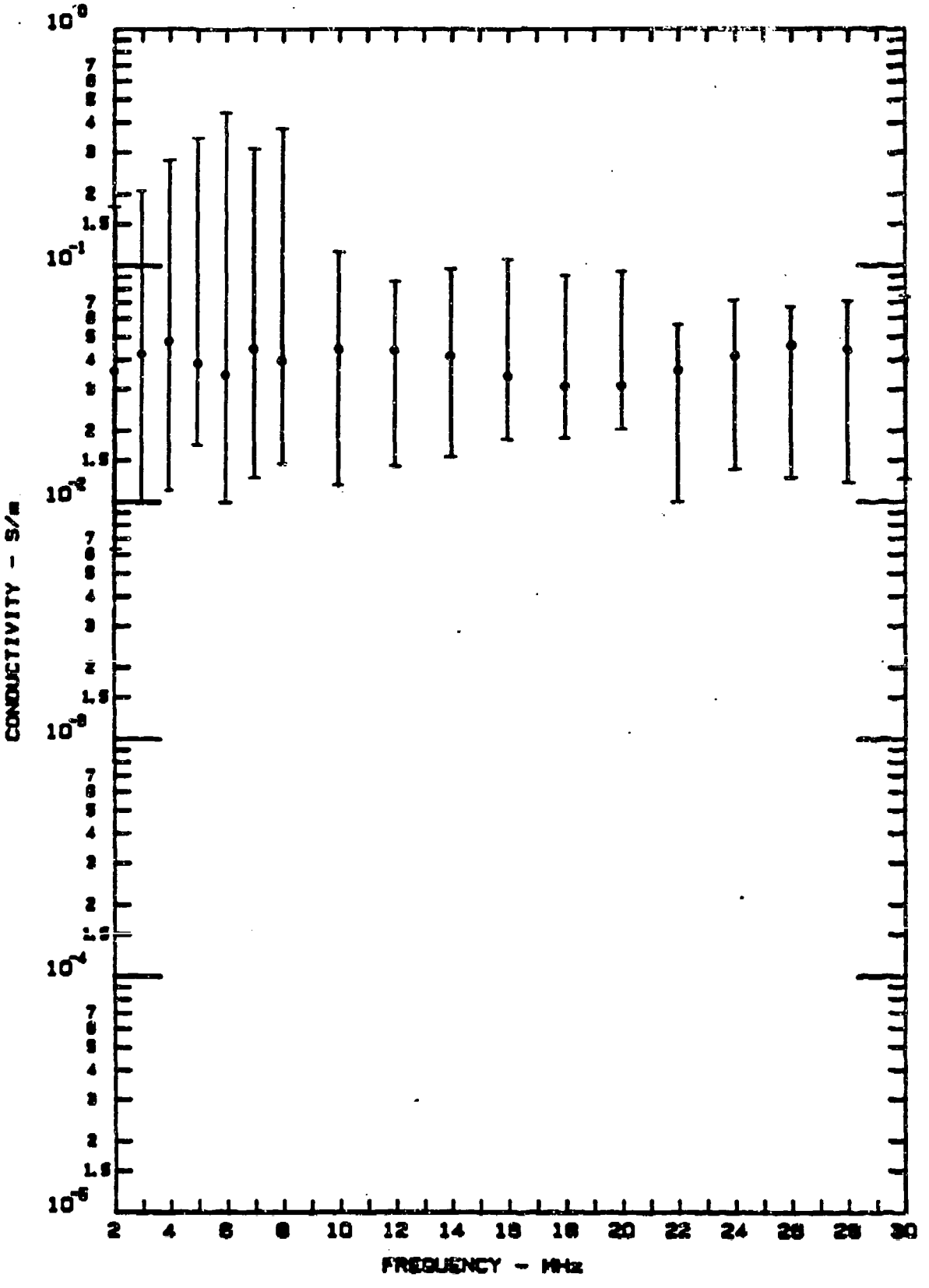


Figure 4.10 Median Conductivity vs Frequency for Locations 1-12 (Field Strength).

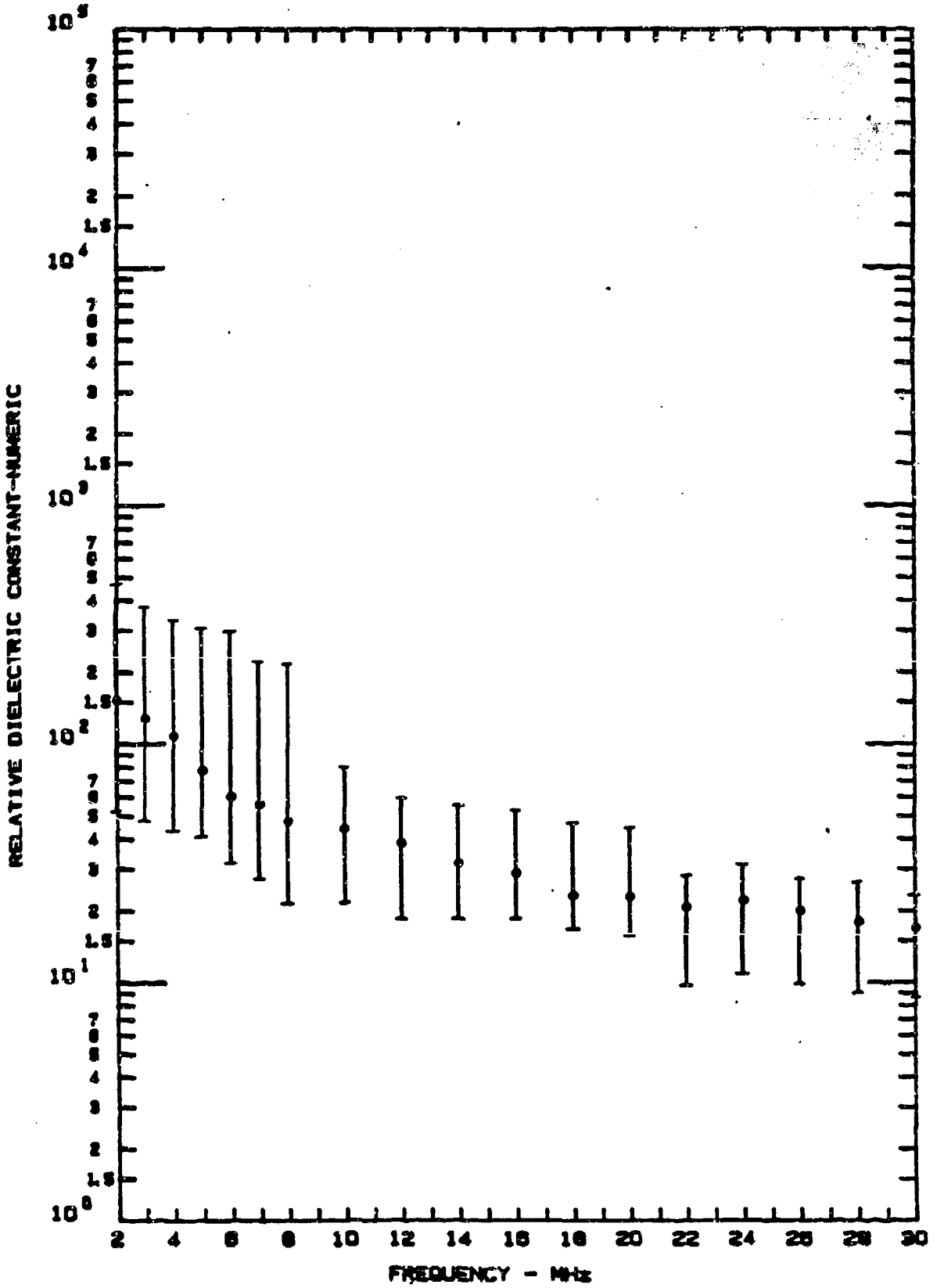


Figure 4.11 Median Relative Dielectric Constant vs Frequency for Locations 1-12 (Field Strength)

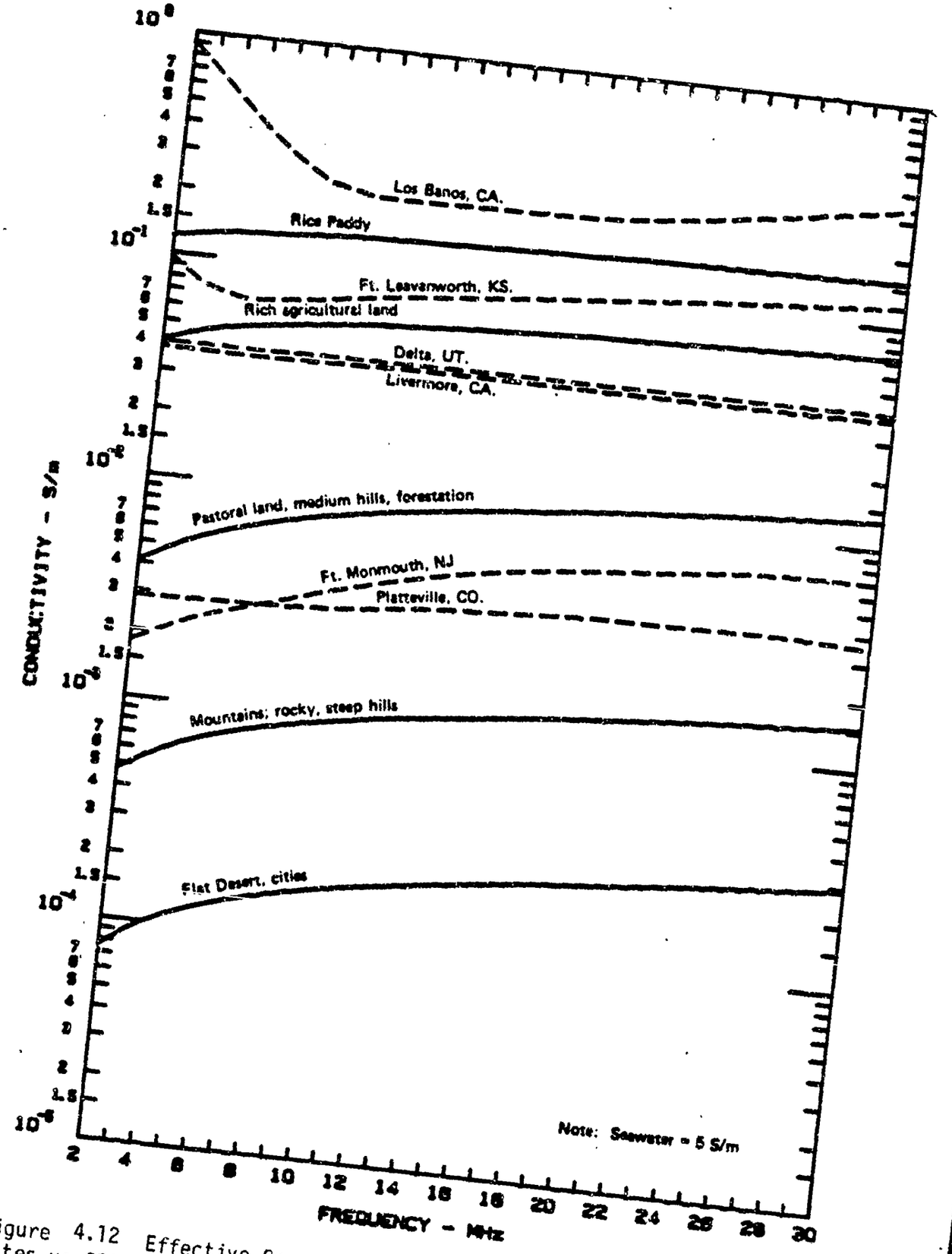


Figure 4.12 Effective Ground Conductivity for Six Antenna Test Field Sites vs SRI Generic Curves for Selected Terrain Categories.

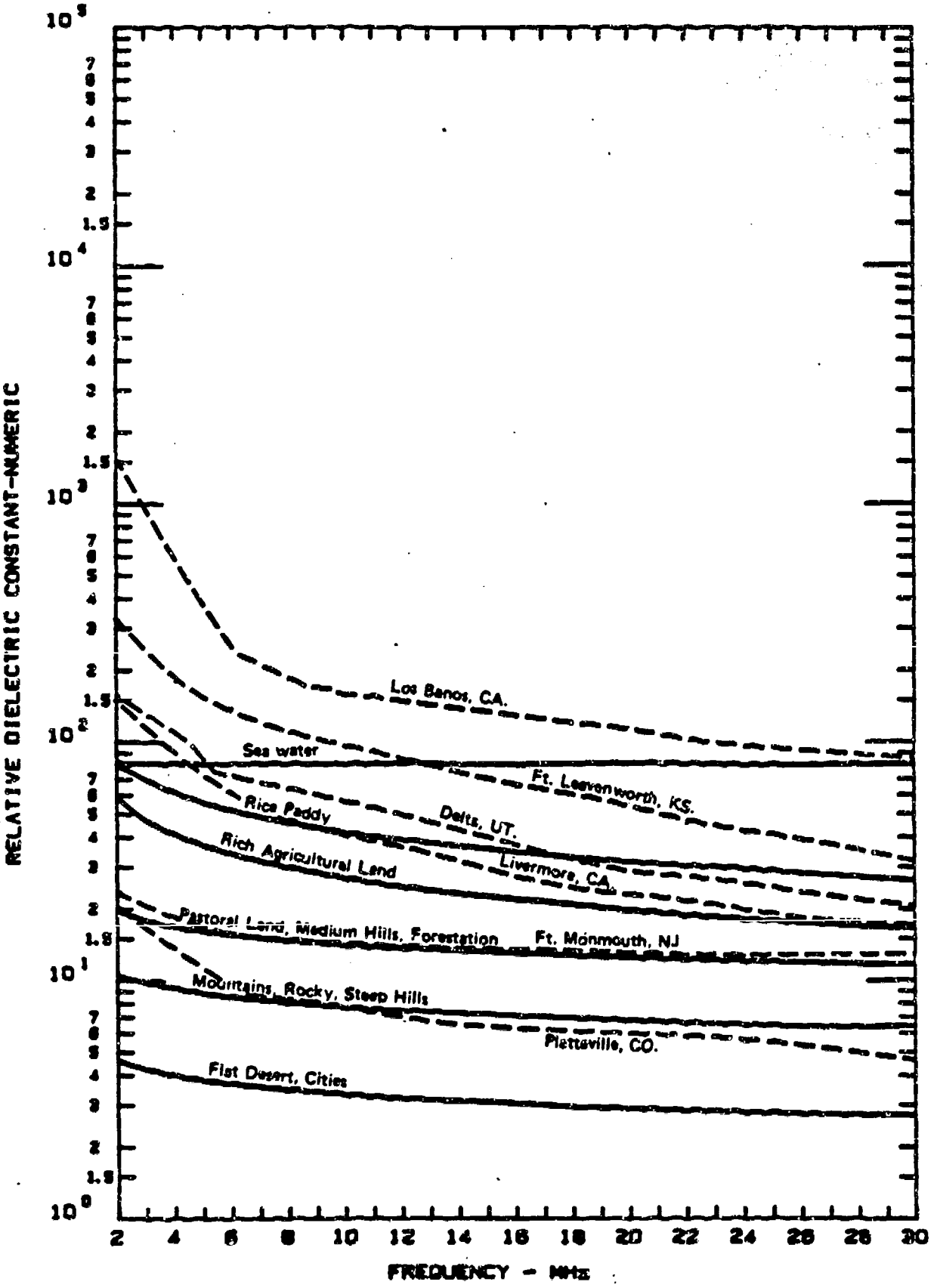


Figure 4.13 Effective Relative Dielectric Constant for Six Antenna Test Field Sites vs SRI Generic Curves for Selected Terrain Categories.

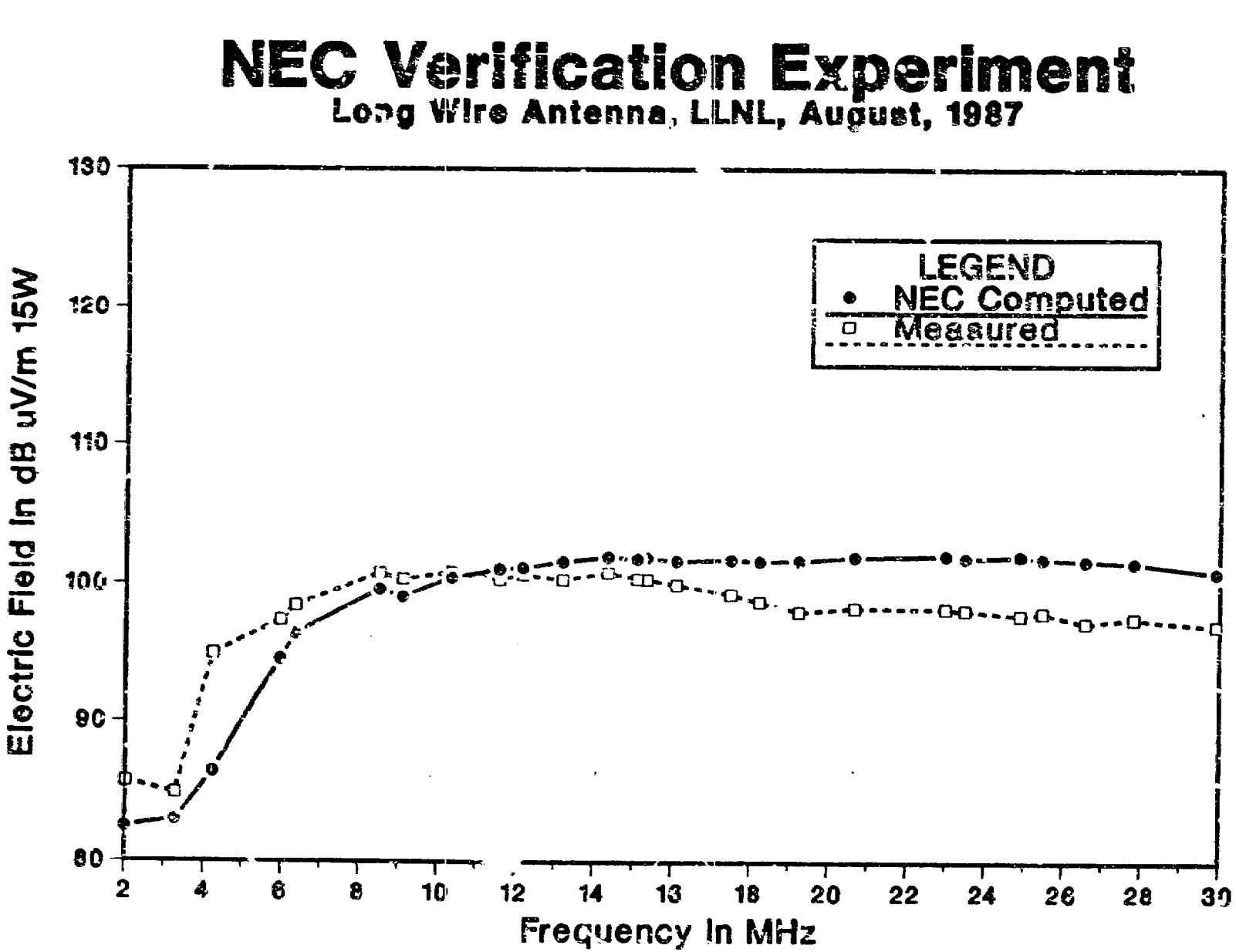


Figure 5.1 Electric Field Strength Results for the Sloping Longwire Antenna (Endfire) at the 750 Foot Test Point Location.

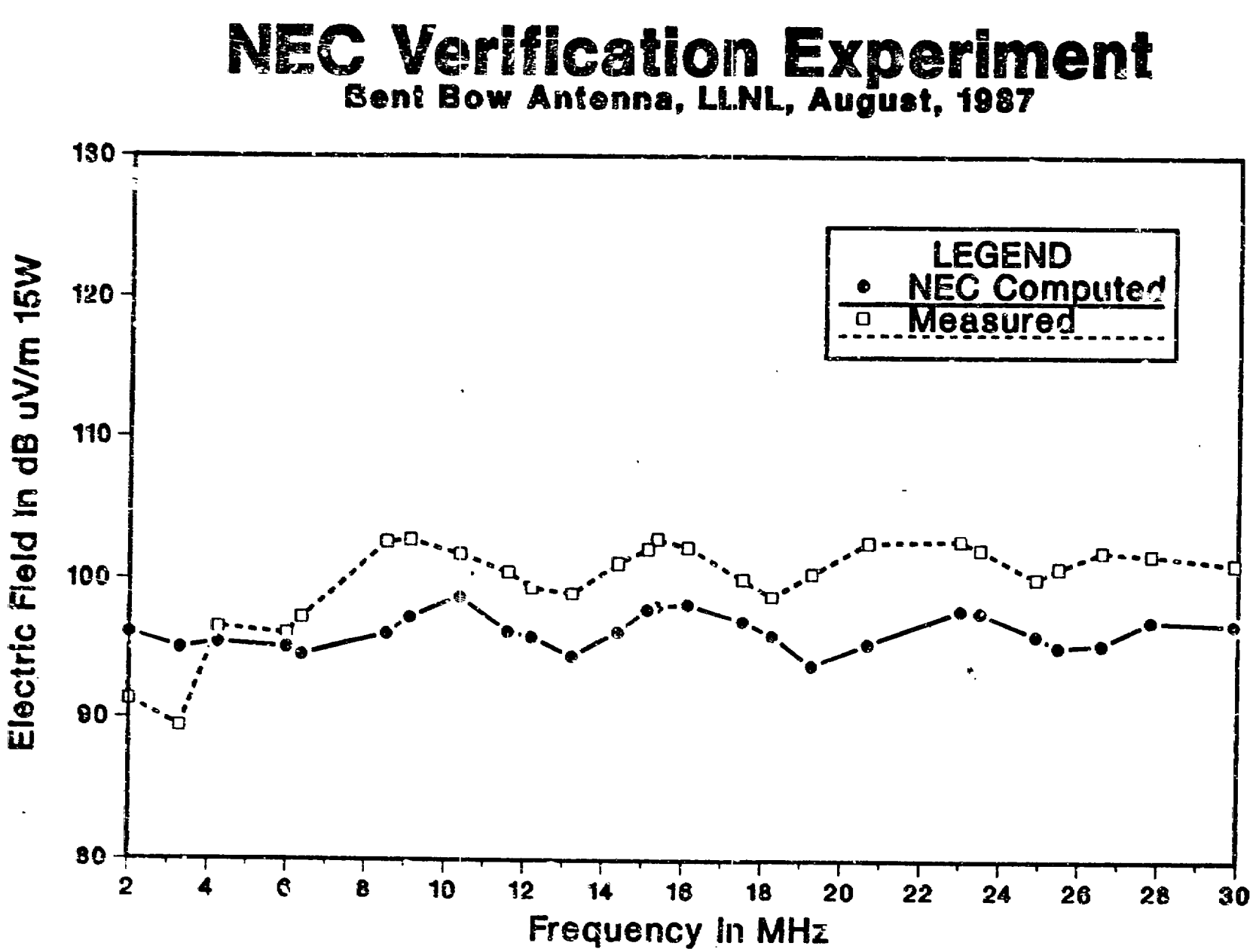


Figure 5.2 Electric Field Strength Results for the Bent Bow Antenna (Endfire) at the 750 Foot Test Point Location.

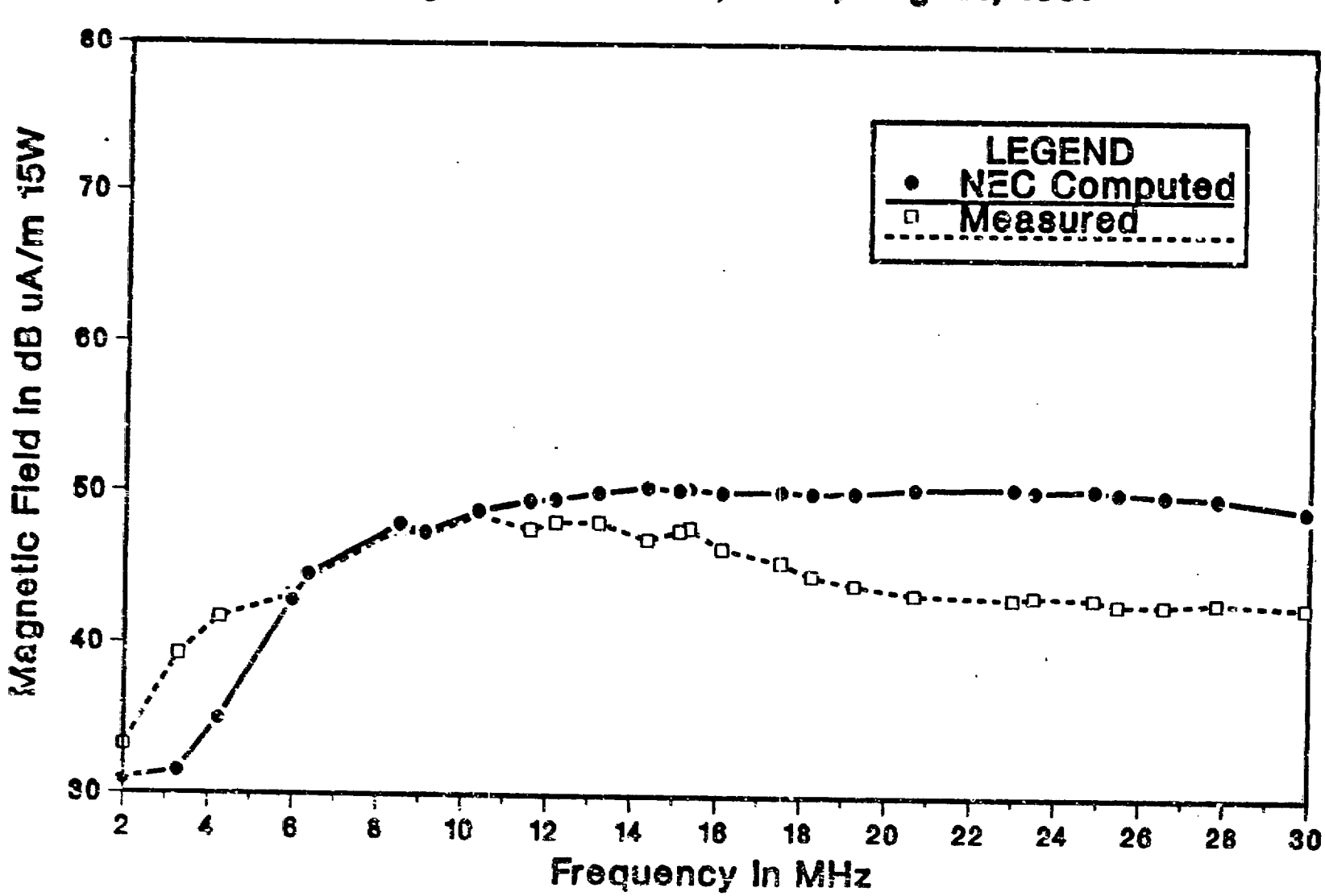


Figure 5.3 Magnetic Field Strength Results for the Sloping Longwire Antenna (Endfire) at the 750 Foot Test Point Location.

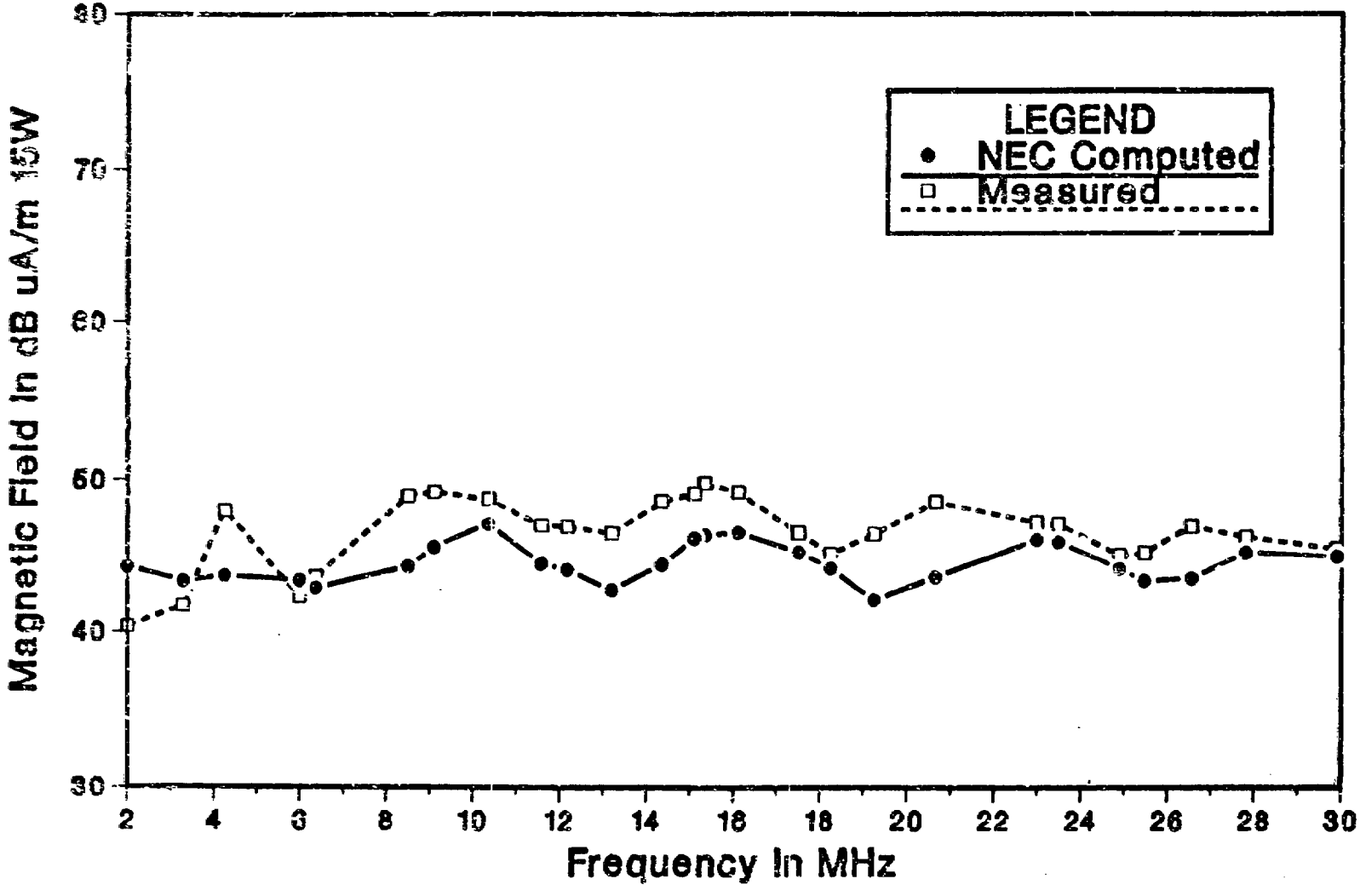


Figure 5.4 Magnetic Field Strength Results for the Bent Bow Antenna (Endfire) at the 750 Foot Test Point Location.

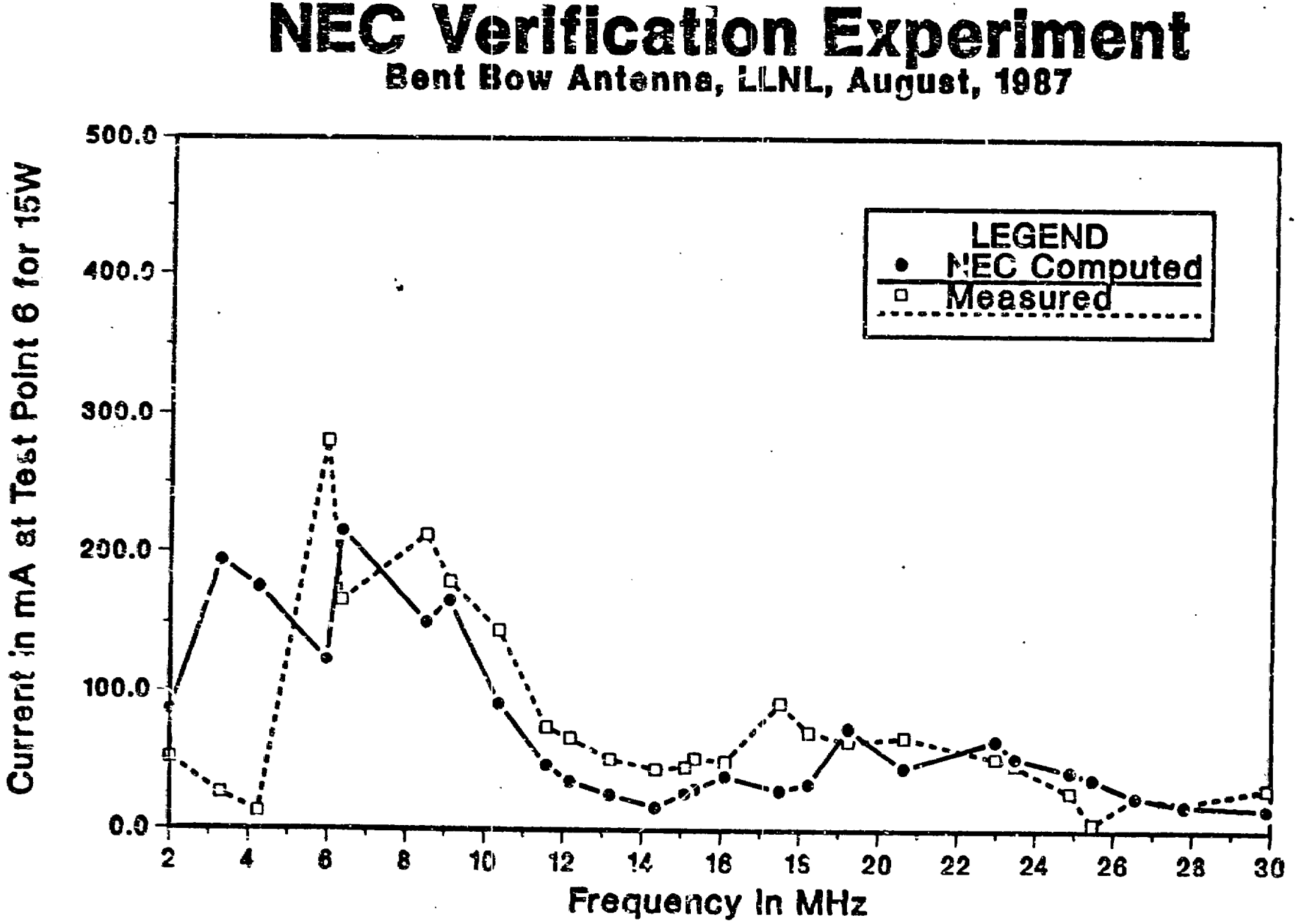


Figure 6.1 Current Results for the Bent Bow Antenna (Endfire) at Wire Location 6.

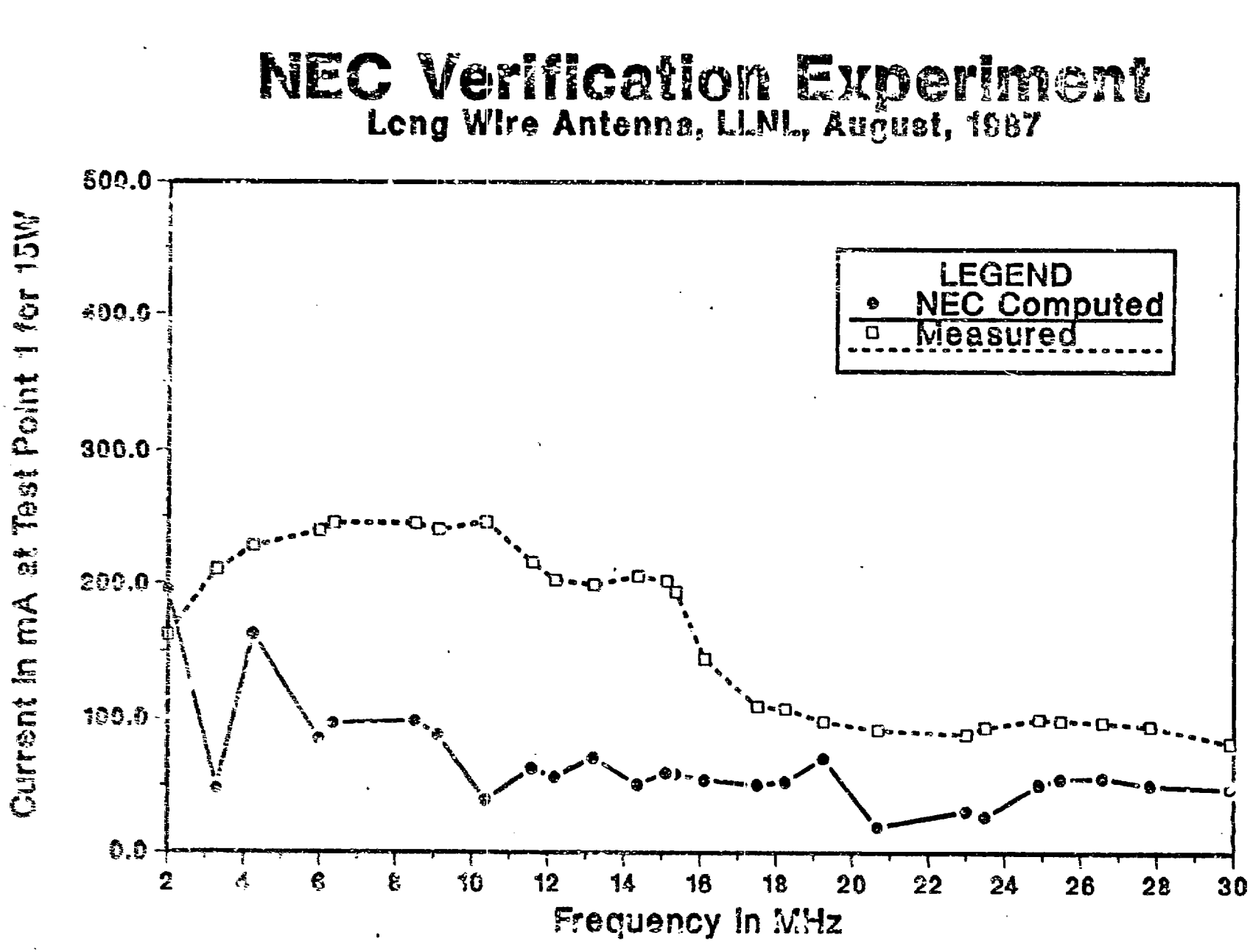


Figure 6.2 Current Results for the Sloping Longwire Antenna (Endfire) at Wire Location 1.

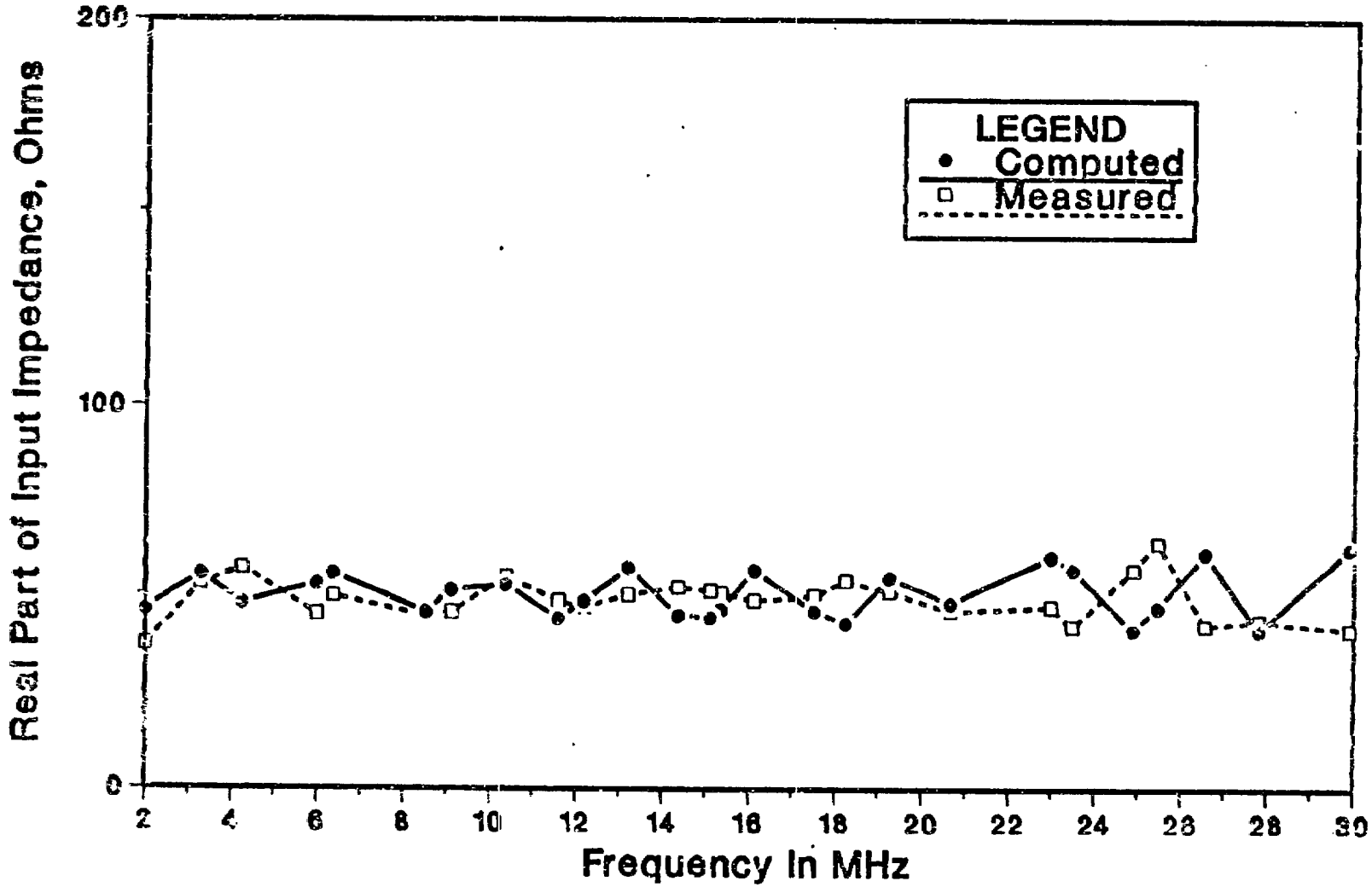


Figure 7.1 Resistor Load Test Results for the Bent Bow Antenna, Real Part of Input Impedance.

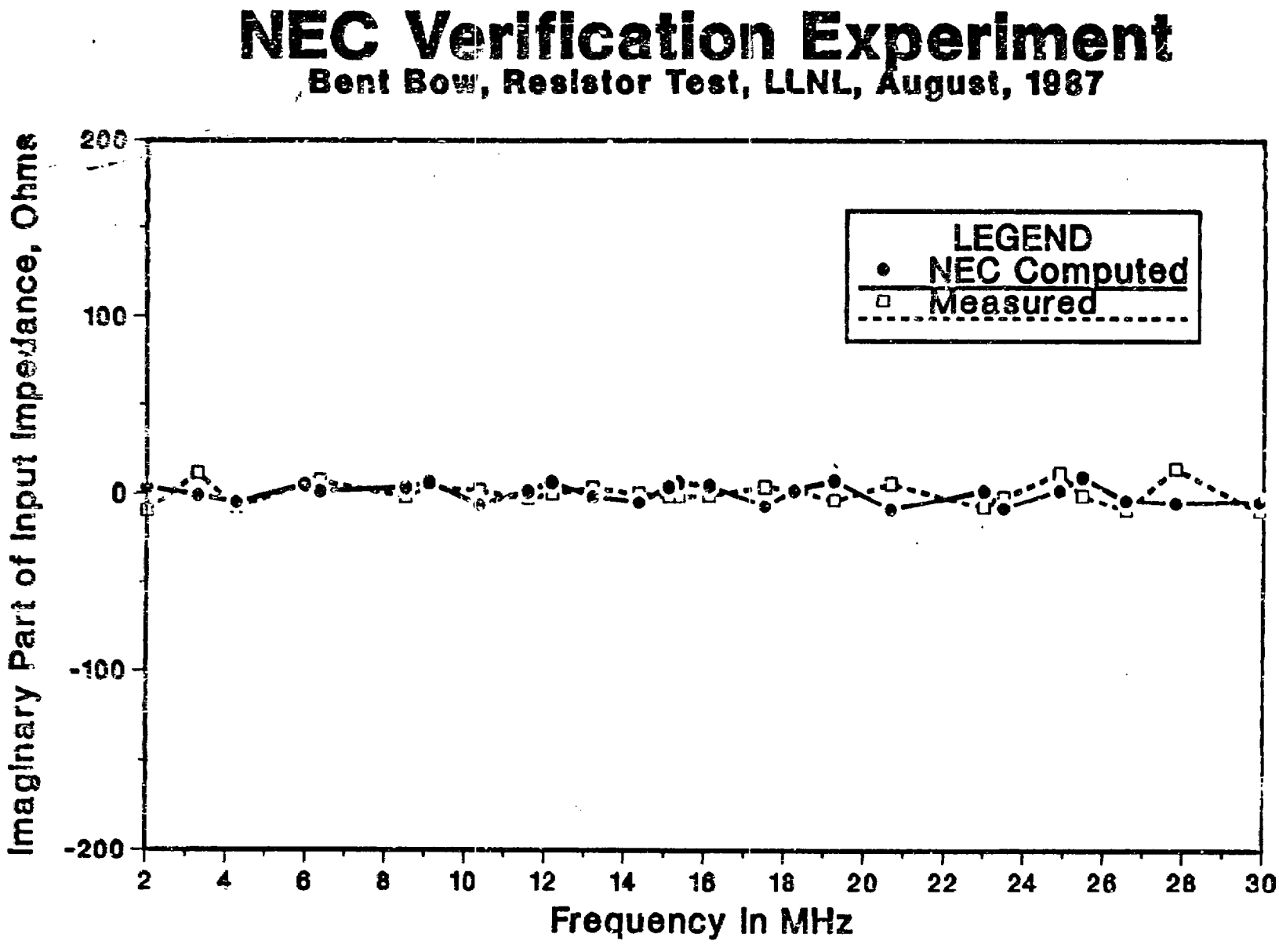


Figure 7.2 Resistor Load Test Results for the Bent Bow Antenna, Imaginary Part of Input Impedance.

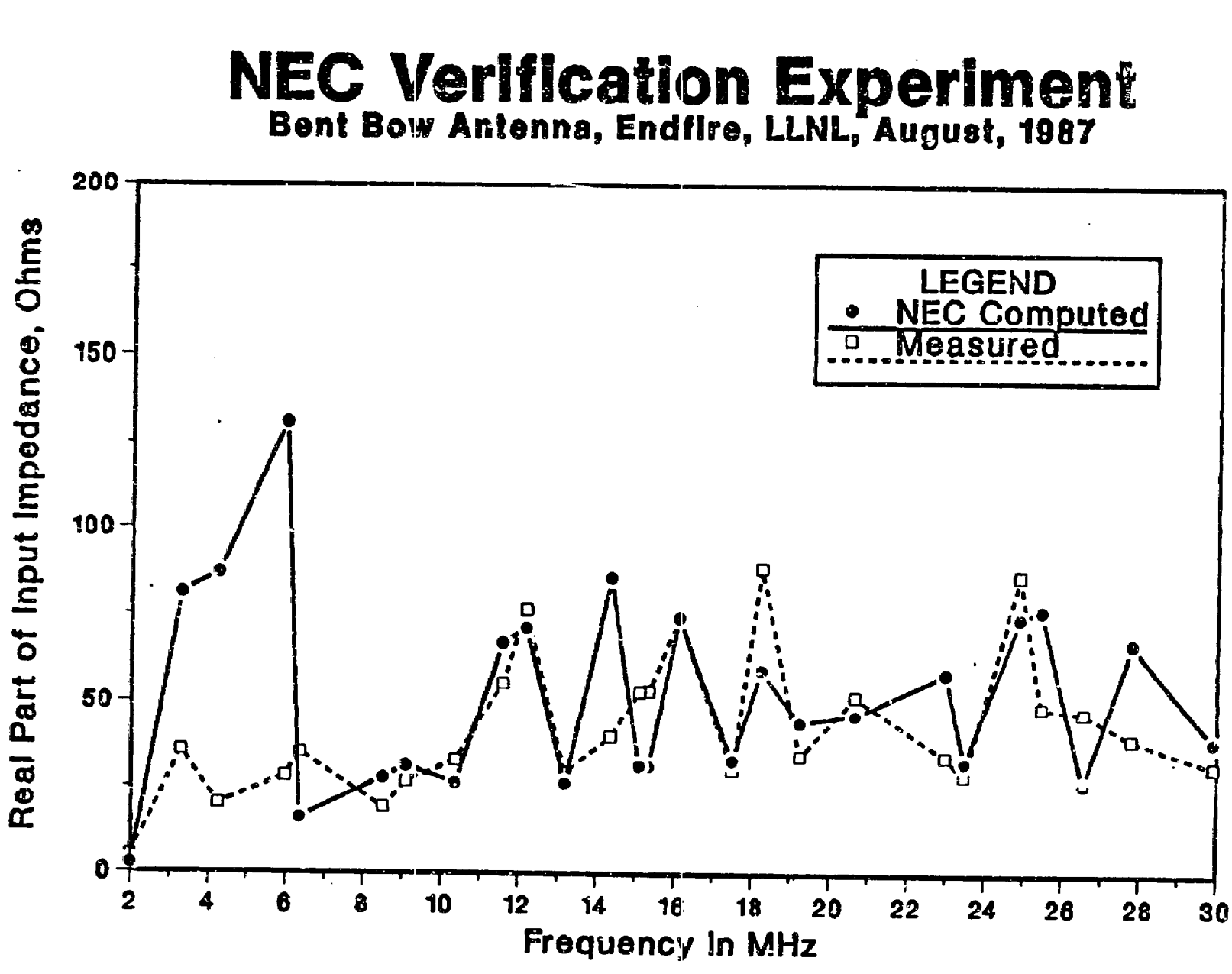


Figure 7.3 Input Impedance Results for the Bent Bow Antenna (Endfire), Real Part of Input Impedance.

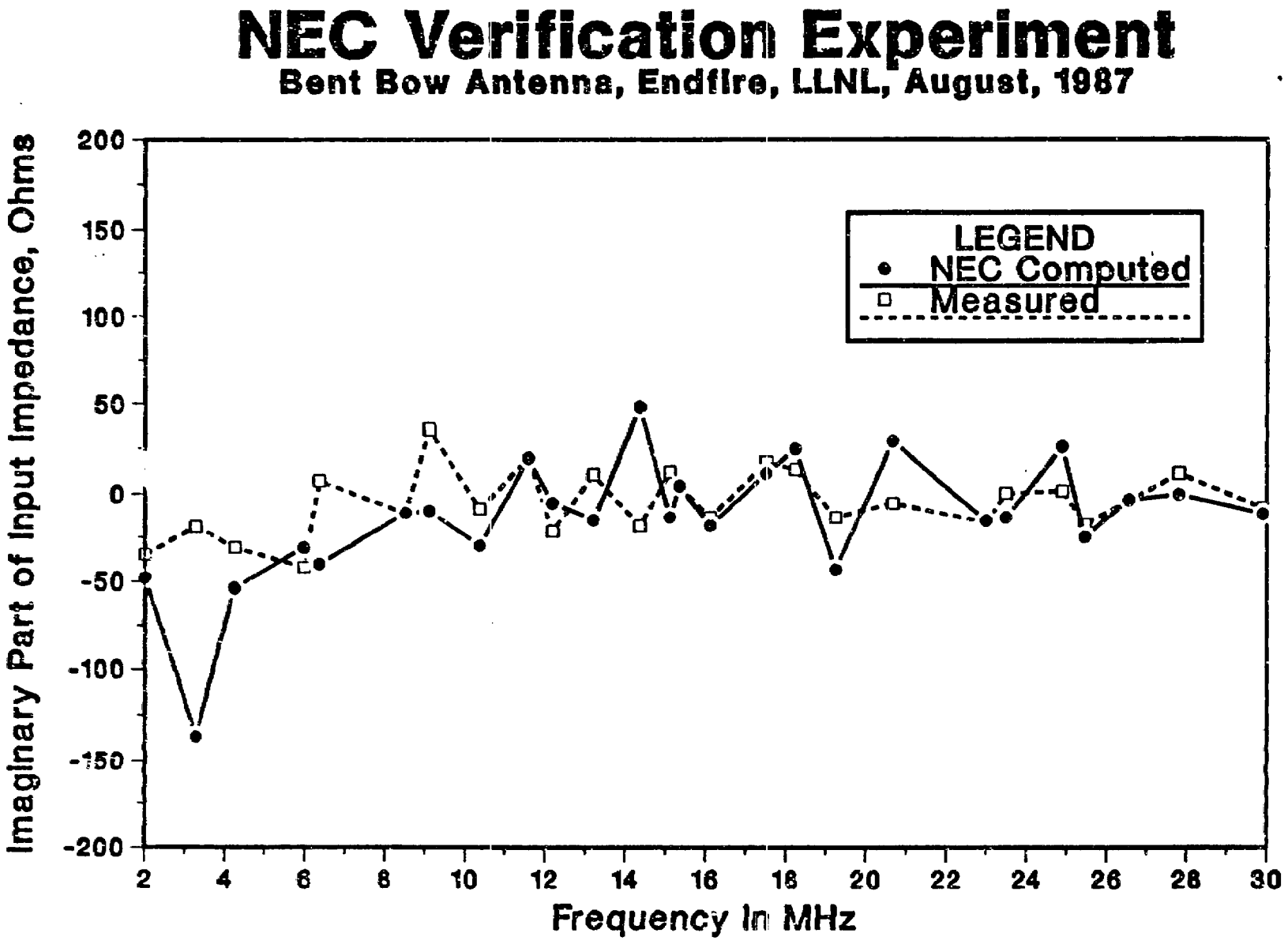


Figure 7.4 Input Impedance Results for the Bent Bow Antenna (Endfire), Imaginary Part of Input Impedance.

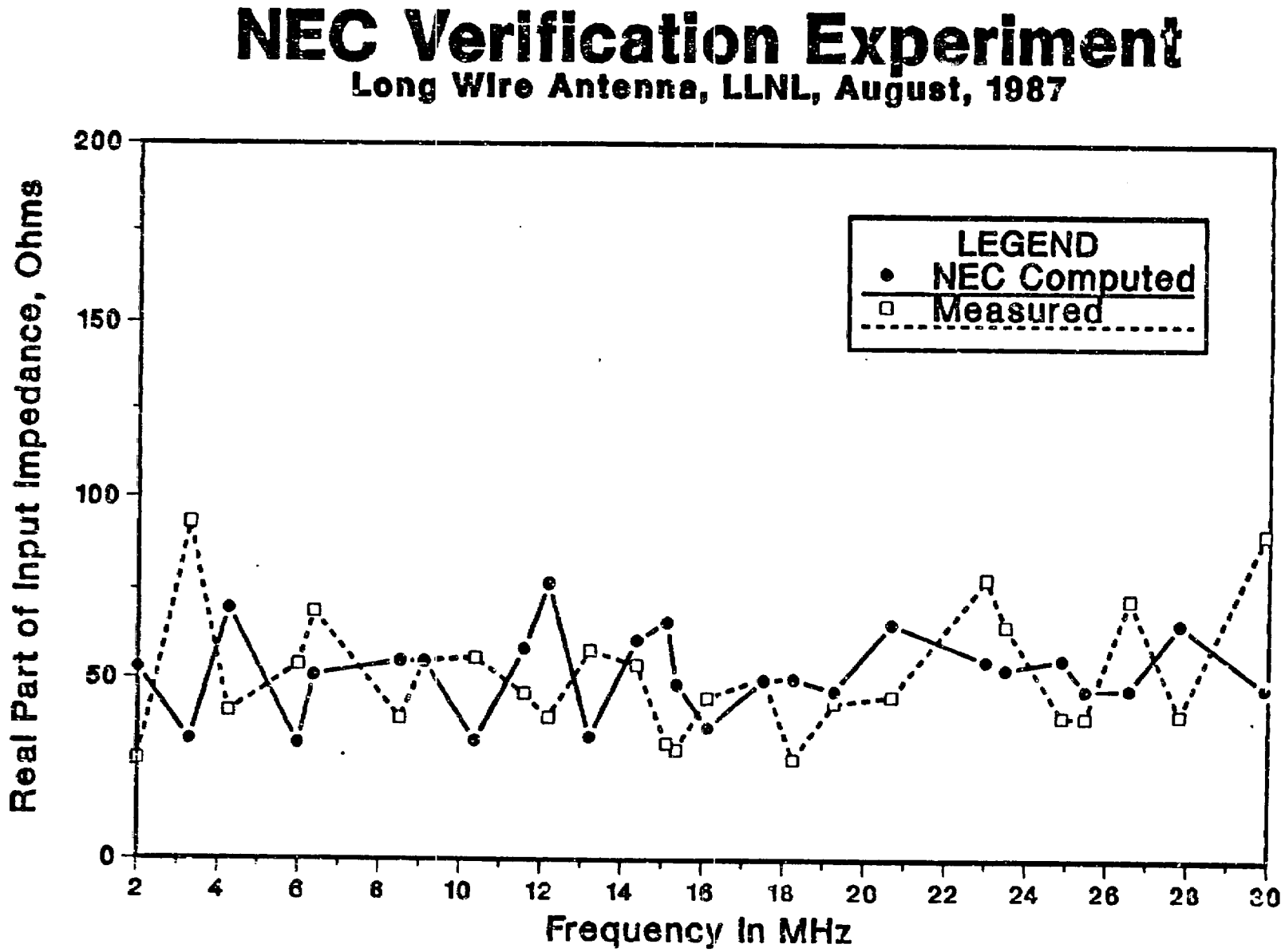


Figure 7.5 Input Impedance Results for the Sloping Longwire Antenna (Endfire), Real Part of Input Impedance.

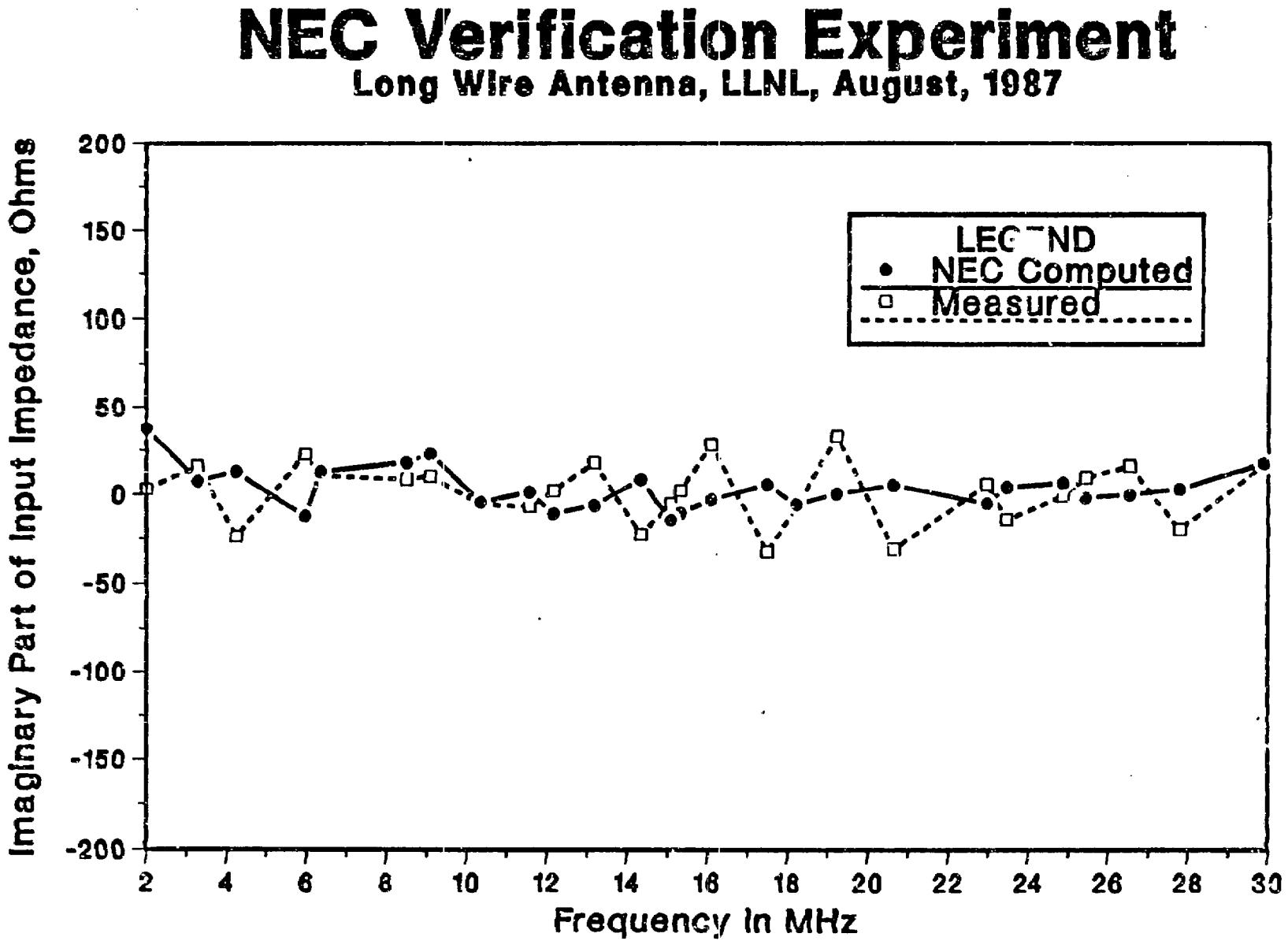


Figure 7.6 Input Impedance Results for the Sloping Longwire Antenna (Endfire), Imaginary Part of Input Impedance.

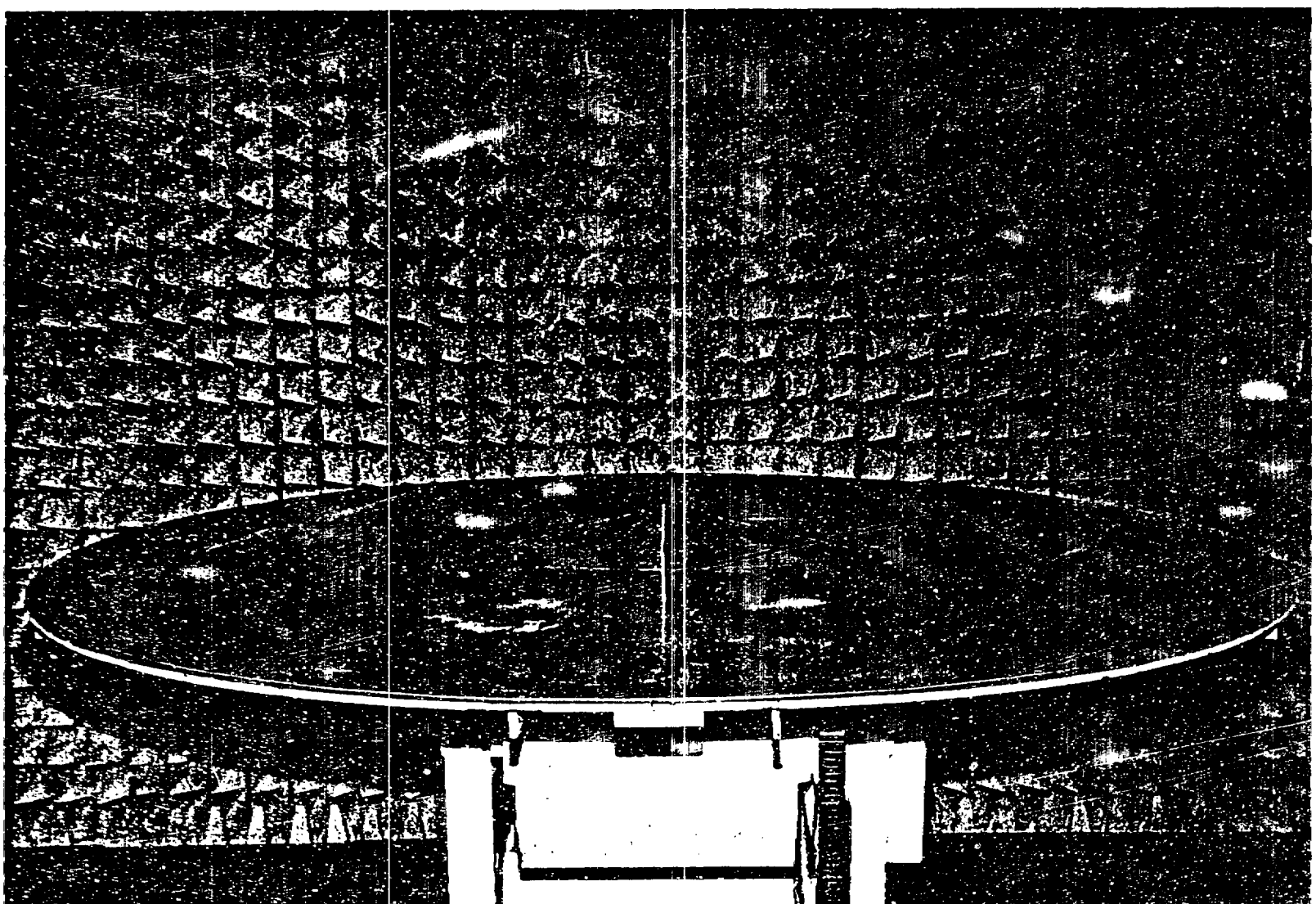


Figure 8.1 Scale Model of Bent-Bow Dipole Antenna Mounted on Ground Plane in LLNL Anechoic Chamber.

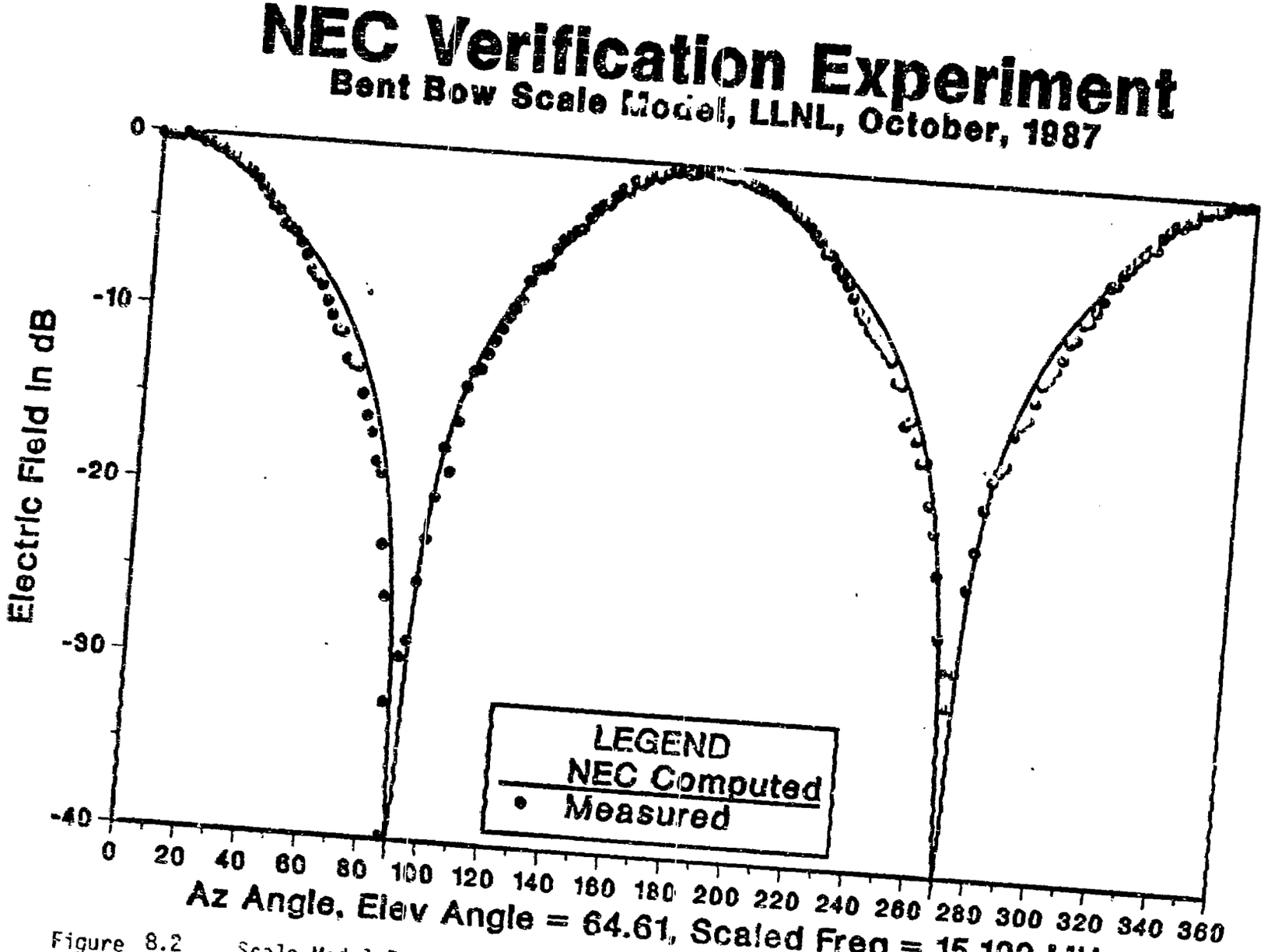


Figure 8.2 Scale Model Pattern Measurements for an Elevation Angle of 64.61° at a Frequency of 15.102 MHz.

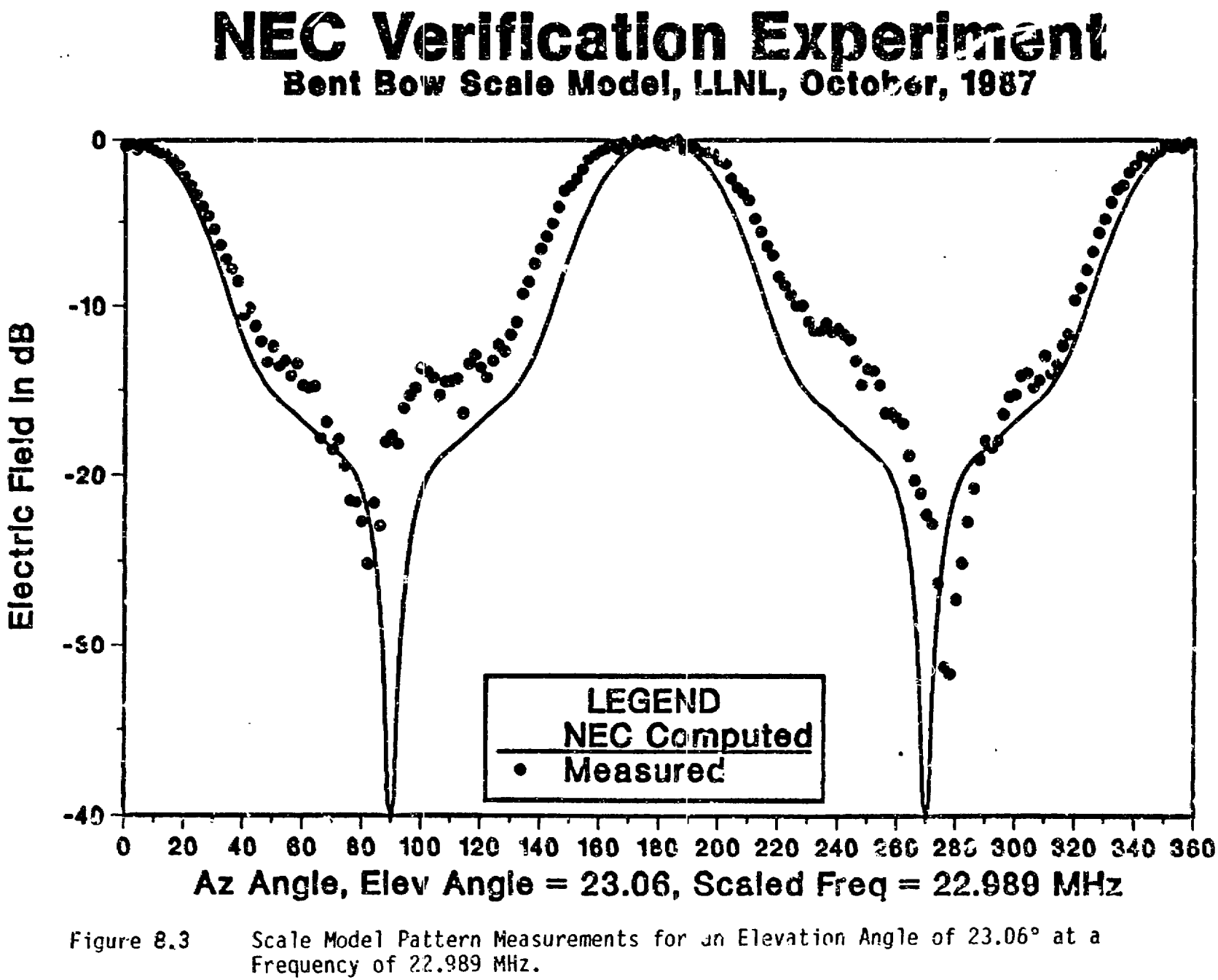


Figure 8.3 Scale Model Pattern Measurements for an Elevation Angle of 23.06° at a Frequency of 22.989 MHz.

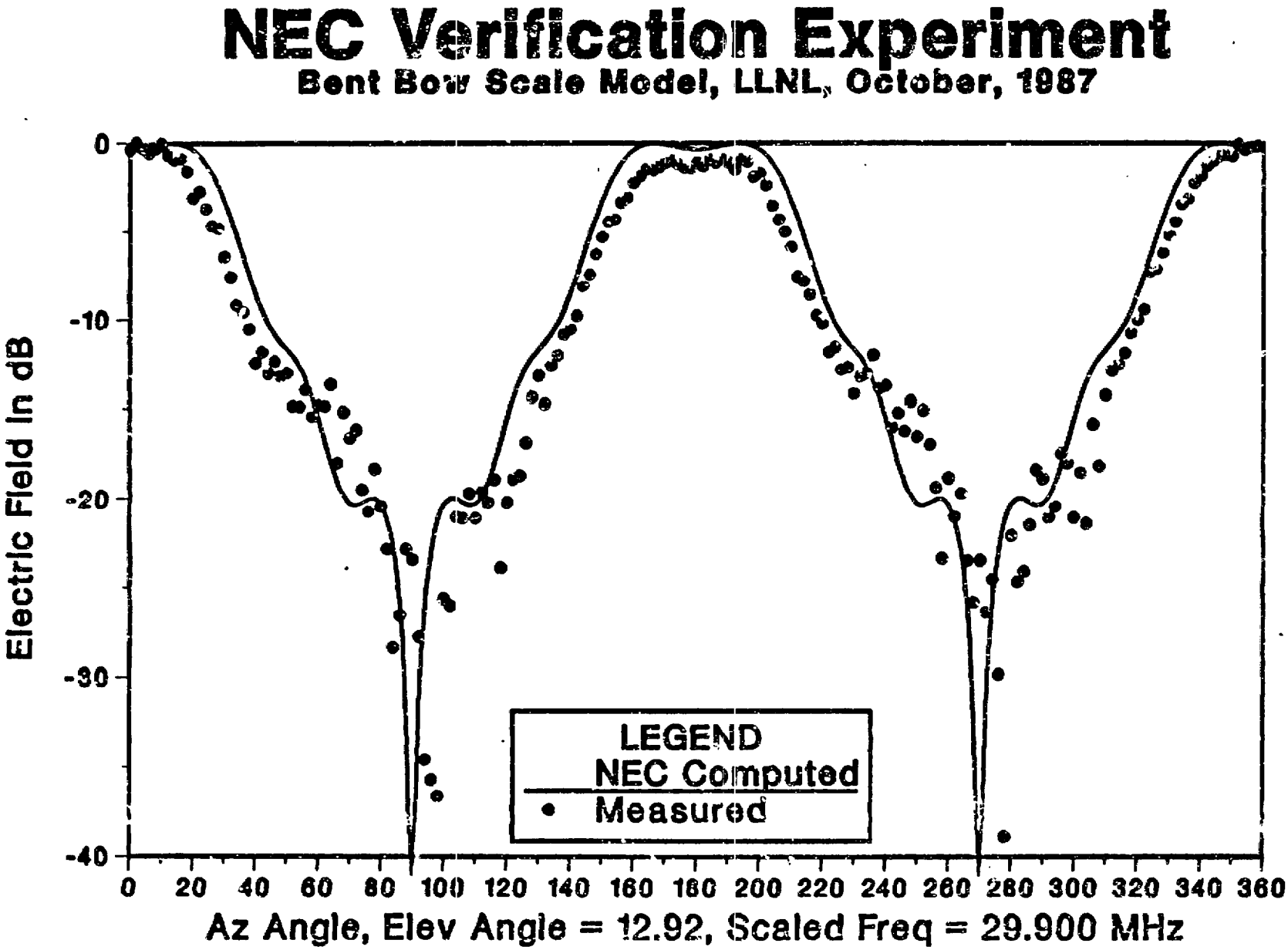


Figure 8.4 Scale Model Pattern Measurements for an Elevation Angle of 12.92° at a Frequency of 29.900 MHz.

NEC MODELING
of
HF MONOPOLE ANTENNAS
with
ELEVATED RADIALS

by

Al Christman & Roger Radcliff
Department of Electrical & Computer Engineering
Ohio University
Athens, OH 45701

and

Jim Breakall, L-156
Lawrence Livermore National Laboratory
Box 808
Livermore, CA 94550

ABSTRACT

The Numerical Electromagnetics Code (NEC) was used to model a 32-foot vertical radiator operating at several frequencies throughout the HF band. The radiator was elevated to a number of different heights above ground level, and was used with 4 elevated horizontal radials of various lengths. Two separate methods of feeding the antenna were modeled, and its performance was evaluated in terms of ground-wave field strength and far-field power gain.

INTRODUCTION

Personnel at LLNL were asked by the U.S. Army Communications Electronics Command (CECOM) to model vertical monopole antennas with several different types of ground systems in order to determine relative performance characteristics. Since HF radio channels are used by the Armed Forces to supply communications in a wide variety of tactical (field) environments, a single all-purpose antenna is highly desirable. The ideal antenna would be simple in design and should be quickly and easily erectable by personnel with minimal skills and few tools. In addition, it would have a low profile and not cover vast amounts of land area. Finally, this ideal antenna would have a wide bandwidth, while providing both ground-wave and sky-wave coverage. A "perfect radiator" such as the one delineated above probably does not exist, but NEC modeling indicates that an elevated vertical radiator with four elevated horizontal radials can provide surprisingly good results.

Several options are available for modeling antennas which are located near the ground. Either perfect ground or imperfect ground may be specified, with the user supplying values for conductivity (σ) and relative permittivity (ϵ_r) in the case of finite ground. The finite-ground solution may be performed in one of two ways, either as a reflection-coefficient approximation (which is fast but less accurate), or by using a Sommerfeld-Norton method which is slower and requires more memory storage space but is more precise. The Sommerfeld-Norton option requires that a separate computer program (SOMNTXD) be run prior to the NEC3D program in order to generate and store a "ground interaction matrix" which is then called by NEC3D. To give the best possible accuracy, the CECOM antennas were modeled using the Sommerfeld/Norton option. The ground constants (conductivity and relative permittivity) used throughout this study were "average" values typical of many rural sites.

NEC MODELS

NEC was used to model a simple vertical radiator at five different frequencies, in combination with a wide variety of ground system configurations. Table I shows the extensive number of antennas which were analyzed, including the frequencies of operation and a description of the ground systems. At each frequency, the simplest ground system was always a 2-foot ground rod, which served as the "worst-case" model. Then a number of different four-radial antennas were studied, in which the height

THE NUMERICAL ELECTROMAGNETICS CODE

NEC-3D (the D indicates double-precision) is a user-oriented computer program which can be used to design or analyze the electromagnetic characteristics of an antenna or other metallic structure. The code operates by solving a set of integral equations for the currents induced on the structure by incident fields or sources. A magnetic-field integral equation is used for modeling smooth surfaces, while an electric-field integral equation formulated especially for wires is also included, thus providing the user with the ability to model a wide variety of devices.

Radiating systems can be modeled in free space or over ground, which may be either a perfect or an imperfect conductor. The structure may be isolated from the ground plane or may touch or penetrate the earth/air interface. The model may include lumped-element loading, perfect or imperfect conductors, non-radiating networks, or transmission lines interconnecting various parts of the system.

Excitation may include incident plane waves of either linear or elliptical polarization, or voltage sources located at arbitrary points on the structure. The output may consist of currents or charges on wire segments, radiation patterns, near and far electric and magnetic fields, and antenna feed-point parameters.

Table I. Listing of vertical monopole antenna systems which were modeled using NEC.

ANTENNA No.	FREQUENCY (MHz)		GROUND SYSTEM DESCRIPTION
HF 1	2		2-foot Ground Stake ONLY
HF 21	2	4	32-foot Radials buried 2 inches deep, direct feed
HF 2	2	4	32-foot Radials, entire antenna elevated 1 meter, direct feed
HF 3	2	4	32-foot Radials, entire antenna elevated 3 meters, direct feed
HF 4	2	4	32-foot Radials, entire antenna elevated 5 meters, direct feed
HF 58	2	4	32-foot Radials, entire antenna elevated 1 meter, isolated feed
HF 59	2	4	32-foot Radials, entire antenna elevated 3 meters, isolated feed
HF 60	2	4	32-foot Radials, entire antenna elevated 5 meters, isolated feed
HF 41	2	4	123-foot Radials, buried 2 inches deep, direct feed
HF 42	2	4	123-foot Radials, entire antenna elevated 1 meter, direct feed
HF 43	2	4	123-foot Radials, entire antenna elevated 3 meters, direct feed
HF 44	2	4	123-foot Radials, entire antenna elevated 5 meters, direct feed
HF 64	2	4	123-foot Radials, entire antenna elevated 1 meter, isolated feed
HF 65	2	4	123-foot Radials, entire antenna elevated 3 meters, isolated feed
HF 66	2	4	123-foot Radials, entire antenna elevated 5 meters, isolated feed
HF 5	4		2-foot Ground Stake ONLY
HF 22	4	4	32-foot Radials, buried 2 inches deep, direct feed
HF 6	4	4	32-foot Radials, entire antenna elevated 1 meter, direct feed
HF 7	4	4	32-foot Radials, entire antenna elevated 3 meters, direct feed
HF 8	4	4	32-foot Radials, entire antenna elevated 5 meters, direct feed
HF 61	4	4	32-foot Radials, entire antenna elevated 1 meter, isolated feed
HF 62	4	4	32-foot Radials, entire antenna elevated 3 meters, isolated feed
HF 63	4	4	32-foot Radials, entire antenna elevated 5 meters, isolated feed
HF 45	4	4	61.5-foot Radials buried 2 inches deep, direct feed
HF 46	4	4	61.5-foot Radials, entire antenna elevated 1 meter, direct feed
HF 47	4	4	61.5-foot Radials, entire antenna elevated 3 meters, direct feed
HF 48	4	4	61.5-foot Radials, entire antenna elevated 5 meters, direct feed
HF 67	4	4	61.5-foot Radials, entire antenna elevated 1 meter, isolated feed
HF 68	4	4	61.5-foot Radials, entire antenna elevated 3 meters, isolated feed
HF 69	4	4	61.5-foot Radials, entire antenna elevated 5 meters, isolated feed

Table I. Listing of vertical monopole antenna systems which were modeled using NEC, continued.

ANTENNA No.	FREQUENCY (MHz)		GROUND SYSTEM DESCRIPTION
HF 3	8		2-foot Ground Stake ONLY
HF 23	8	4	32-foot Radials buried 2 inches deep, direct feed
HF 10	8	4	32-foot Radials, entire antenna elevated 1 meter, direct feed
HF 11	8	4	32-foot Radials, entire antenna elevated 3 meters, direct feed
HF 12	8	4	32-foot Radials, entire antenna elevated 5 meters, direct feed
HF 49	8	4	32-foot Radials, entire antenna elevated 1 meter, isolated feed
HF 50	8	4	32-foot Radials, entire antenna elevated 3 meters, isolated feed
HF 51	8	4	32-foot Radials, entire antenna elevated 5 meters, isolated feed
HF 13	16		2-foot Ground Stake ONLY
HF 24	16	4	32-foot Radials buried 2 inches deep, direct feed
HF 14	16	4	32-foot Radials, entire antenna elevated 1 meter, direct feed
HF 15	16	4	32-foot Radials, entire antenna elevated 3 meters, direct feed
HF 16	16	4	32-foot Radials, entire antenna elevated 5 meters, isolated feed
HF 52	16	4	32-foot Radials, entire antenna elevated 1 meter, isolated feed
HF 53	16	4	32-foot Radials, entire antenna elevated 3 meters, isolated feed
HF 54	16	4	32-foot Radials, entire antenna elevated 5 meters, isolated feed
HF 17	24		2-foot Ground Stake ONLY
HF 25	24	4	32-foot Radials buried 2 inches deep, direct feed
HF 18	24	4	32-foot Radials, entire antenna elevated 1 meter, direct feed
HF 19	24	4	32-foot Radials, entire antenna elevated 3 meters, direct feed
HF 20	24	4	32-foot Radials, entire antenna elevated 5 meters, direct feed
HF 55	24	4	32-foot Radials, entire antenna elevated 1 meter, isolated feed
HF 56	24	4	32-foot Radials, entire antenna elevated 3 meters, isolated feed
HF 57	24	4	32-foot Radials, entire antenna elevated 5 meters, isolated feed

above ground, the length of the radials, and the type of feed system were varied. The monopole length in all cases was fixed at 32 feet, while operating frequencies of 2,4,8,16, and 24 MHz were utilized. The minimum radial length was held at 32 feet, but longer (0.25 wavelength) radials were also examined at those frequencies where the 32-foot radials were shorter than a quarter-wavelength. In the "direct-feed" method, the inner end of each radial and the outer shield conductor of the coaxial transmission line are both tied directly to the metallic structure which supports the vertical radiator; the "isolated-feed" system eliminates this connection to the supporting structure. Figure 1 is a computer-generated illustration of a typical elevated-radial vertical monopole antenna system.

Special software written at LLNL takes the NEC output for a particular antenna model and reduces the 20-plus pages of numerical listings into a concise, user-friendly, three-page summary which contains the following information:

1. A title block with the number of the antenna and a short description of its geometry.
2. A drawing of the antenna showing compass directions and a scale of distances.
3. Operating frequency in megahertz.
4. Ground conductivity in Siemens per meter.
5. Relative permittivity of the ground.
6. Input impedance in ohms.
7. VSWR with respect to 50 ohms.
8. Azimuthal-plane plot of vertical ground-wave field

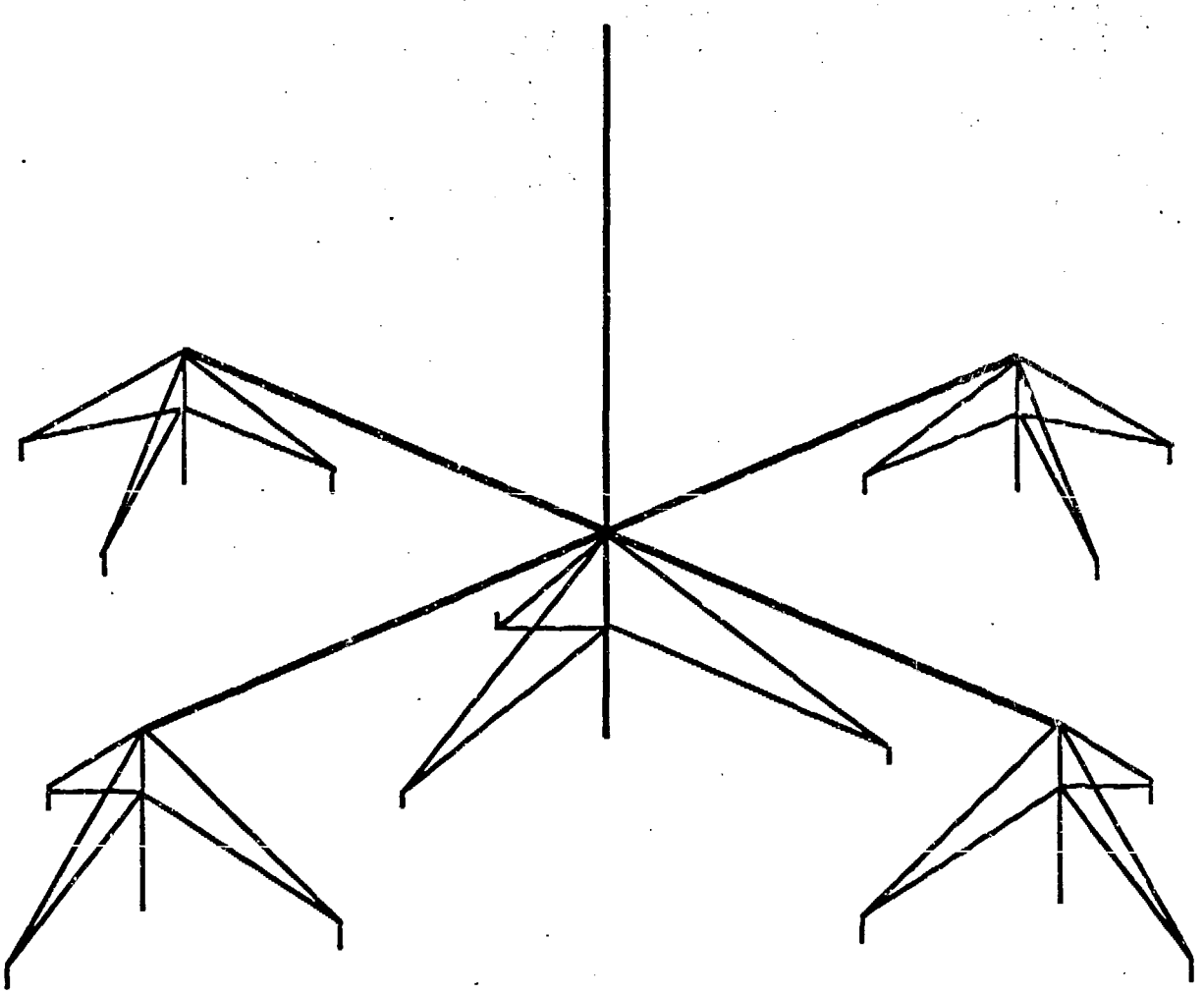


Figure 1. Drawing of elevated-radial antenna showing support masts and guy ropes.

strength in dBmV/m, for 15 watts power input.

9. Azimuthal-plane plot of horizontal ground-wave field strength in dBmV/m, for 15 watts power input.

10. Azimuthal-and elevation-plane power patterns at 10-degree increments in elevation angle.

Figure 2 is the three-page summary for antenna #HF57, which is a 32-foot monopole with four 32-foot radials operating at 24 MHz; the entire antenna is elevated to a height of 5 meters above the ground, and an isolated feed system is used.

CONCLUSIONS

It is not possible to include the complete three-page summary for each of the many antennas which were modeled, but a careful study of these results has led to the following general conclusions:

A. At 2 MHz, the 32-foot vertical monopole and radials are quite short compared to the wavelength, so several examples using 123-foot (0.25 λ) radials were modeled. A review of the NEC output shows:

   1. When using 32-foot radials, isolated feed works much better than direct feed.
   2. When using 123-foot (0.25 λ) radials, direct feed and isolated feed both perform about the same.
   3. When using direct feed, full-size (0.25 λ) radials are much better than shorter ones.
   4. When using isolated feed, short radials are slightly better than full-size (0.25 λ) ones.

Figure 2. HF57: 32-FT WHIP & 4 32-FT RADIALS UP 5 METERS, ISOLATED

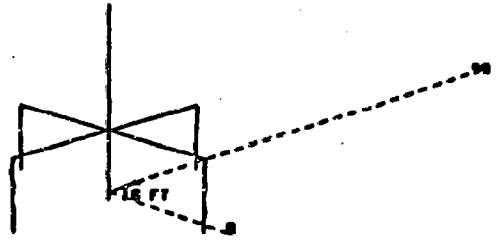
FREQUENCY(MHZ) : 24.00

GROUND CONDUCTIVITY (MHOS): 0.01200

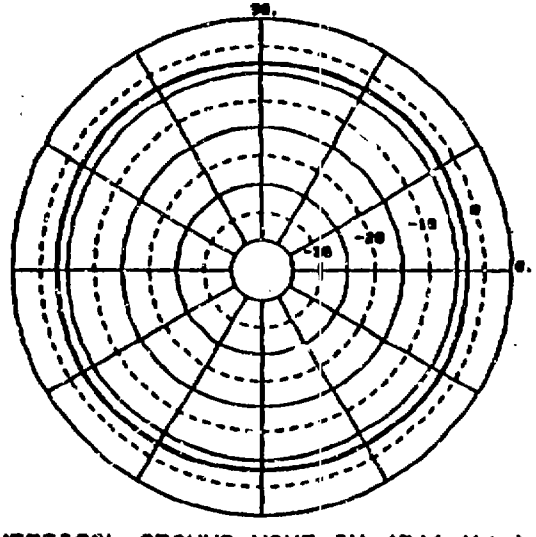
GROUND DIELECTRIC CONSTANT (REL) : 12.00

INPUT IMPEDANCE : 60.16 +j 97.44

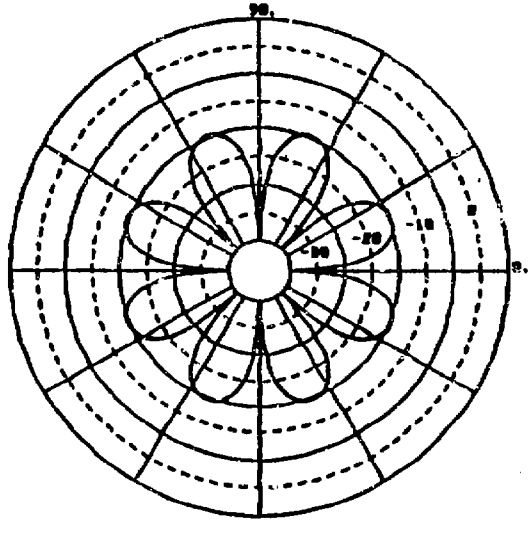
VSWR (FOR 50 OHMS) : 4.662



3-D PLOT



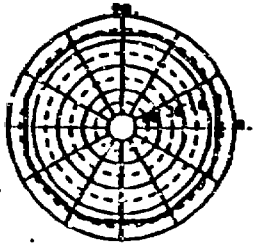
VERTICAL GROUND WAVE IN dB(1mV/m)



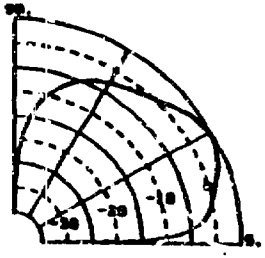
HORIZONTAL GROUND WAVE IN dB(1mV/m)

Figure 2. HF57: 32-FT WHIP & 4 32-FT RADIALS UP 5 METERS, ISOLATED, continued.

TOTAL GAIN IN dBi

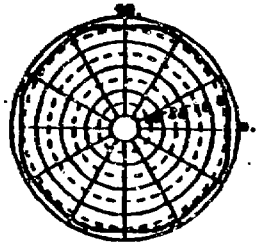


AZIMUTH PLOT AT
18 DEGS
IN ELEVATION

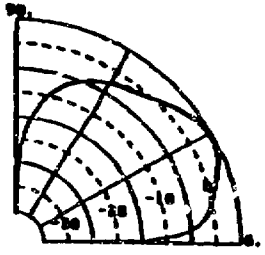


ELEVATION PLOT AT
22 DEGS
IN AZIMUTH

TOTAL GAIN IN dBi

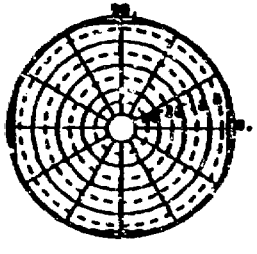


AZIMUTH PLOT AT
20 DEGS
IN ELEVATION

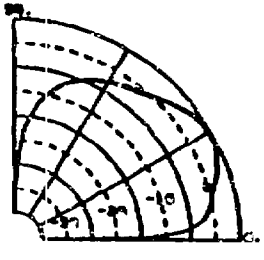


ELEVATION PLOT AT
23 DEGS
IN AZIMUTH

TOTAL GAIN IN dBi

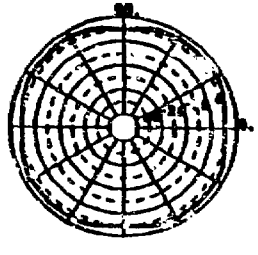


AZIMUTH PLOT AT
30 DEGS
IN ELEVATION

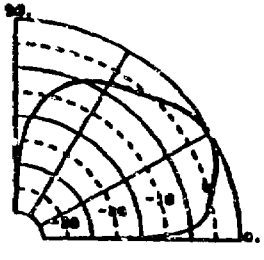


ELEVATION PLOT AT
27 DEGS
IN AZIMUTH

TOTAL GAIN IN dBi



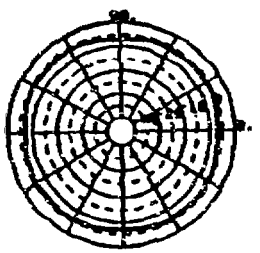
AZIMUTH PLOT AT
40 DEGS
IN ELEVATION



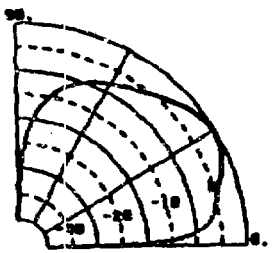
ELEVATION PLOT AT
31 DEGS
IN AZIMUTH

Figure 2. HF57: 32-FT WHIP & 4 32-FT RADIALS UP 5 METERS, ISOLATED, continued.

TOTAL GAIN IN dBi

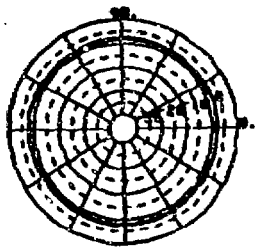


AZIMUTH PLOT AT
50 DEGS
IN ELEVATION

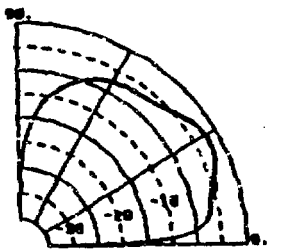


ELEVATION PLOT AT
29 DEGS
IN AZIMUTH

TOTAL GAIN IN dBi

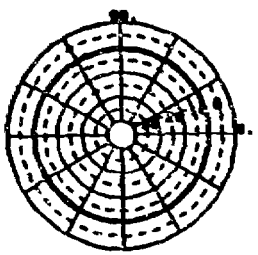


AZIMUTH PLOT AT
60 DEGS
IN ELEVATION

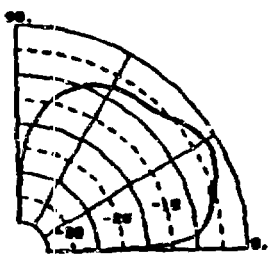


ELEVATION PLOT AT
0 DEGS
IN AZIMUTH

TOTAL GAIN IN dBi

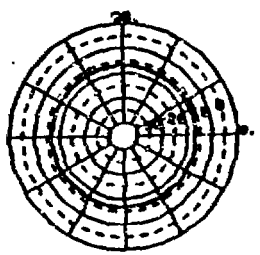


AZIMUTH PLOT AT
70 DEGS
IN ELEVATION

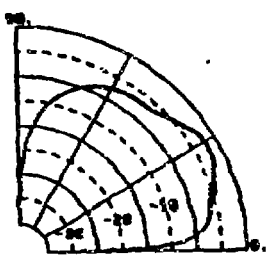


ELEVATION PLOT AT
0 DEGS
IN AZIMUTH

TOTAL GAIN IN dBi



AZIMUTH PLOT AT
80 DEGS
IN ELEVATION



ELEVATION PLOT AT
0 DEGS
IN AZIMUTH

5. When using elevated radials, higher is better.
6. The best performance was obtained from an isolated-feed system using 4 32-foot radials at a height of 5 meters.

B. At an operating frequency of 4 MHz, the 32-foot antenna system is still small in terms of wavelength, so both 32-foot and 61.5-foot (0.25 λ) radials were tried. Analysis of the computer output reveals that:

1. When using 32-foot radials, isolated feed works much better than direct feed.
2. When using 61.5-foot (0.25 λ) radials, direct feed and isolated feed both perform about the same.
3. When using direct feed, full-size (0.25 λ) radials are much better than shorter ones.
4. When using isolated feed, short radials are slightly worse than full-size (0.25 λ) ones.
5. When using elevated radials, higher is better, except for the case of 32-foot radials and direct feed.
6. The best performance was obtained from an isolated-feed system using 4 61.5-foot radials (0.25 λ) at a height of 5 meters.

C. The antenna system is essentially full-size (0.25 λ) at a frequency of 8 MHz, and the following conclusions may be drawn:

1. At a fixed height, both isolated and direct-feed methods perform in a similar fashion.

2. When using elevated radials, higher is better.

3. The best performance was obtained using 4 elevated radials at a height of 5 meters, with either the isolated or direct feed techniques.

D. At 16 MHz the 32-foot monopole and radials are now about 0.5 λ in size, and the performance may be summarized as follows:

1. With elevated radials, a secondary (high-angle) lobe starts to develop as the height above ground increases, and this secondary lobe begins to dominate the elevation-plane pattern as the antenna is raised more than 3 meters above ground.

2. The isolated-feed system works slightly better than direct feed.

E. The antenna system is rather large in terms of wavelength at an operating frequency of 24 MHz, and the computer output reveals:

1. For elevated radials, higher is better; as height increases, the power gain remains about the same, but the elevation angle of the single (relatively high-angle) lobe becomes steadily lower.

2. Both direct and isolated feed methods provide similar performance.

Throughout this paper it has been implicitly assumed that the results produced by NEC are correct. While NEC is probably the most widely-used electromagnetics program available today for the sophisticated user, little has been done to verify the

accuracy of NEC-3 when used to analyze wire antennas which penetrate or lie in close proximity to lossy earth. More field research needs to be conducted in this area, so that code users can be fully confident in the validity of their work.

FIELD TESTS of HF MONOPOLE ANTENNAS with ELEVATED RADIALS

by

Al Christman & Roger Radcliff
Ohio University
Department of Electrical and Computer Engineering
Stocker Center
Athens, Ohio 45701-2979

and

Jim Breakall, L-156
Lawrence Livermore National Laboratory
Box 808
Livermore, CA 94550

ABSTRACT

Computer analysis performed at Lawrence Livermore National Laboratory (LLNL) in the summer of 1986 indicated that an elevated vertical monopole with 4 elevated horizontal radials could outperform a conventional ground-mounted monopole with 120 buried radials. In the fall of 1987, field tests were carried out on several elevated-radial configurations as well as typical ground-mounted vertical antennas using as many as 120 radials in an attempt to confirm the computer predictions. The results of input-impedance and field-strength measurements are contained herein.

INTRODUCTION

Computer modeling studies performed at LLNL during the summer of 1986 indicated that an elevated vertical monopole antenna with four elevated horizontal radials could provide low-angle power gain that was equal to or better than that which was attainable from a conventional ground-mounted radiator with 120 buried radials. In 1987, the U.S. Army Communications Electronics Command at Ft. Monmouth, New Jersey, provided funding to conduct a limited outdoor test of this concept in order to determine its validity. Measurements of input impedance and electric field intensity were made on 8 separate vertical-monopole antenna systems which were constructed sequentially on a large flat site immediately adjacent to the laboratory facility.

METHODOLOGY

Several different types of ground systems were constructed in the field and used in conjunction with a 32-foot tapered aluminum vertical radiator. The radiator is self-supporting, but was lightly guyed with nylon string in order to ensure verticality. The following ground system configurations were utilized:

1. 120 32-foot radials laid on top of the soil, direct feed
2. 4 32-foot radials laid on top of the soil, direct feed
3. 2-foot ground rod driven completely into the soil, direct feed
4. 4 32-foot radials, system elevated 1 meter above the earth, direct feed
5. 4 32-foot radials, system meters above the earth, direct feed
6. 4 32-foot radials, system vated 5 meters above the earth, direct feed

7. 4 32-foot radials, system elevated 3 meters above the earth, isolated feed

8. 4 32-foot radials, system elevated 5 meters above the eartn, isolated feed

For the "direct feed" method, the interior ends of the radials and the outer conductor (shield) of one end of a 20-foot section of RG-213 coaxial cable were joined directly to the metallic mast which was supporting the base of the vertical radiator. The center conductor of the coax was terminated with a solder lug which attached to a stainless-steel bolt at the base of the radiator. The vertical radiator was insulated from its support structure by a large sturdy spacer made of Delrin. When using four elevated horizontal radials, the outer end of each radial was isolated from its associated mast by an insulator and a length of nylon string. An additional 100-foot section of RG-213 coax was used to complete the cable run from the antenna back to the transmitter.

The "isolated feed" method utilized a 1:1 "W2DU" balun at the feedpoint in an effort to prevent the flow of "antenna current" on the outer surface of the shield (outer conductor) of the coaxial cable. The W2DU device is a "choke" balun; it contains ferrite rings which surround the outer circumference of the feeder and are designed to "choke off" any RF current which might otherwise be present. One of the balun output terminals has an alligator clip on it for connection to the four radials; the other terminal has a solder lug which attaches to the bolt at the base of the vertical radiator. A 20-foot length of RG-213 transmission line which is equipped with PL259 connectors on both ends is substituted for the

20-foot line used in the "direct" method. Four 32-foot copper radials are used, all of which have insulators on both ends in order to provide electrical isolation from the metallic support mast. The inner ends each have an alligoator clip, so that every radial may be joined to its neighbor. Figure 1 illustrates the physical arrangement of the masts, guy ropes, monopole, and radials for a typical elevated-radial antenna-test configuration.

RESULTS AND DISCUSSION

Input Impedance

The input impedance of each antenna configuration tested in the field is presented in Tables I through VIII. The impedance values were measured at the transmitter end of 120 feet of coaxial cable and then transformed to their equivalent antenna feed-point values through use of the classical transmission-line equations. It should be noted that slight inaccuracies in either the measured impedance values or the measured velocity factor of the coaxial cable can lead to large changes in the calculated feed-point impedances, so the "antenna end" values may be less precise than the "transmitter end" data.

Because the 32-foot whip is quarter-wave-resonant at a frequency just below 8 MHz, it is helpful to examine the "antenna end" input-impedance values for all of the various antenna configurations when measured at 8 MHz; this information is listed in Table IX. Notice that, as one would expect, the input resistance for the 120-radial system is about 40 ohms,

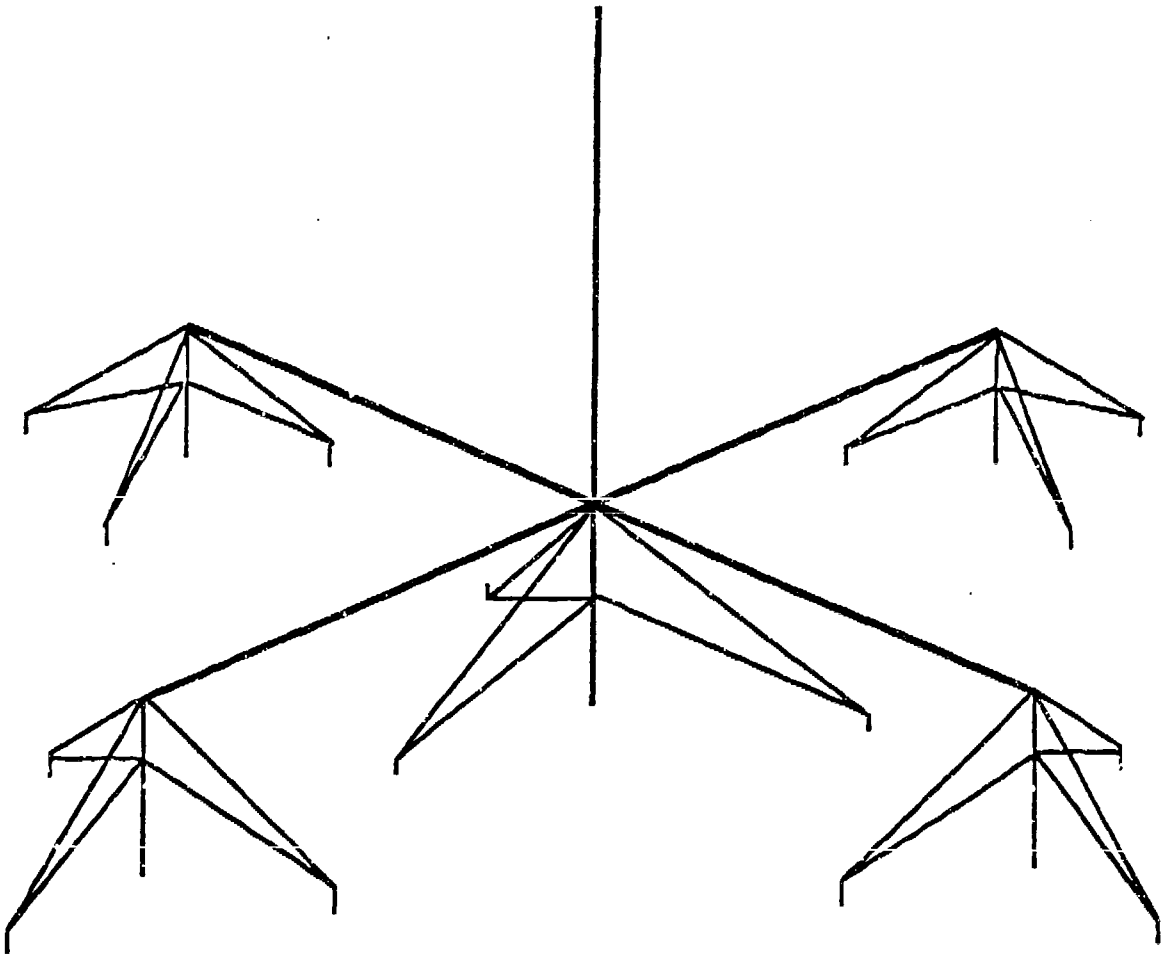


Figure 1. Drawing of elevated-radial antenna showing support masts and guy ropes.

Table I. Input impedance of a 32-foot vertical monopole antenna with 120 32-foot radials laid on the surface of the earth. Impedance values are given at the transmitter and at the antenna feed-point, which are separated by 120 feet of RG-213 50-ohm coaxial cable.

	----------INPUT IMPEDANCE (Ohms) ----------			
	Transmitter End		Antenna End	
FREQUENCY (MHz)	Real	Imaginary	Real	Imaginary
2.0	5.57	53.00	443.00	-475.41
4.0	3.31	3.68	171.86	-314.71
8.0	37.25	27.16	41.67	30.62
16.0	46.50	109.54	134.78	166.21
32.0	18.93	41.16	47.52	81.67

Table II. Input impedance of a 32-foot vertical monopole antenna with 4 32-foot radials laid on the surface of the earth. Impedance values are given at the transmitter and at the antenna feed-point, which are separated by 120 feet of RG-213 50-ohm coaxial cable.

	----------INPUT IMPEDANCE (Ohms) ----------			
	Transmitter End		Antenna End	
FREQUENCY (MHz)	Real	Imaginary	Real	Imaginary
2.0	5.72	52.69	467.78	-461.35
4.0	3.69	3.24	202.15	-308.08
8.0	66.36	40.99	77.56	38.95
16.0	43.26	105.47	120.68	161.75
32.0	17.90	39.10	43.07	78.17

Table III. Input impedance of a 32-foot vertical monopole antenna with only a 2-foot ground stake. Impedance values are given at the transmitter and at the antenna feed-point, which are separated by 120 feet of RG-213 50-ohm coaxial cable.

FREQUENCY (MHz)	----------INPUT IMPEDANCE (Ohms) ----------			
	Transmitter End		Antenna End	
	Real	Imaginary	Real	Imaginary
2.0	5.97	52.36	490.81	-436.42
4.0	4.69	2.43	257.76	-264.56
8.0	88.10	31.89	97.81	21.32
16.0	41.89	105.27	117.14	163.29
32.0	17.64	38.89	42.30	77.96

Table IV. Input impedance of a 32-foot vertical monopole antenna with 4 radials, antenna elevated 1 meter above the ground, direct feed. Impedance values are given at the transmitter and at the antenna feed-point, which are separated by 120 feet of RG-213 50-ohm coaxial cable.

	----------INPUT IMPEDANCE (Ohms) ----------			
	Transmitter End		Antenna End	
FREQUENCY (MHz)	Real	Imaginary	Real	Imaginary
2.0	5.77	52.28	501.14	-451.41
4.0	4.08	2.37	257.75	-300.68
8.0	37.04	27.11	41.42	30.60
16.0	39.62	105.40	111.83	166.84
32.0	16.87	38.79	40.50	78.47

Table V. Input impedance of a 32-foot vertical monopole antenna with 4 radials, antenna elevated 3 meters above the ground, direct feed. Impedance values are given at the transmitter and at the antenna feed-point, which are separated by 120 feet of RG-213 50-ohm coaxial cable.

FREQUENCY (MHz)	----------INPUT IMPEDANCE (Ohms) ----------			
	Transmitter End		Antenna End	
	Real	Imaginary	Real	Imaginary
2.0	5.95	52.26	499.27	-436.06
4.0	4.86	1.91	286.98	-253.72
8.0	31.32	20.81	34.20	24.58
16.0	38.59	103.76	107.07	164.24
32.0	15.77	37.52	36.96	76.65

Table VI. Input impedance of a 32-foot vertical monopole antenna with 4 radials, antenna elevated 5 meters above the ground, direct feed. Impedance values are given at the transmitter and at the antenna feed-point, which are separated by 120 feet of RG-213 50-ohm coaxial cable. As noted in the text, all of these values are questionable.

	----------INPUT IMPEDANCE (Ohms) ----------			
	Transmitter End		Antenna End	
FREQUENCY (MHz)	Real	Imaginary	Real	Imaginary
2.0	9.94	27.03	90.60	140.14
4.0	34.55	-59.84	19.28	34.47
8.0	7.98	-7.21	7.83	-2.44
16.0	44.77	108.09	128.31	165.62
32.0	20.89	43.22	54.41	83.98

Table VII. Input impedance of a 32-foot vertical monopole antenna with 4 radials, antenna elevated 3 meters above the ground, isolated feed. Impedance values are given at the transmitter and at the antenna feed-point, which are separated by 120 feet of RG-213 50-ohm coaxial cable.

	----------INPUT IMPEDANCE (Ohms) ----------			
	Transmitter End		Antenna End	
FREQUENCY (MHz)	Real	Imaginary	Real	Imaginary
2.0	6.45	54.12	367.44	-417.29
4.0	3.50	4.36	150.37	-289.21
8.0	37.51	40.36	44.31	45.56
16.0	141.93	177.16	365.62	-54.82
32.0	63.72	88.68	214.35	-8.75

Table VIII. Input impedance of a 32-foot vertical monopole antenna with 4 radials, antenna elevated 5 meters above the ground, isolated feed. Impedance values are given at the transmitter and at the antenna feed-point, which are separated by 120 feet of RG-213 50-ohm coaxial cable.

	----------INPUT IMPEDANCE (Ohms) ----------			
	Transmitter End		Antenna End	
FREQUENCY (MHz)	Real	Imaginary	Real	Imaginary
2.0	6.51	53.81	385.36	-413.39
4.0	3.53	4.12	159.86	-294.09
8.0	33.77	43.54	40.47	49.97
16.0	125.47	165.90	357.76	-1.35
32.0	47.06	80.21	205.82	62.42

and the input reactance is inductive (the antenna is slightly "long" at 8 MHz). When just 4 radials are used, the ground losses are much higher, as revealed by the 36-ohm increase in the feed-point resistance. Earth losses are greater still when only a single 2-foot ground rod is used! Notice what happens when 4 elevated radials are used: at a height of 1 meter above ground, the input impedance is virtually identical to that of the ground-mounted 120-radial system. This would seem to indicate that these two systems are very similar electrically, and NEC studies predict nearly-equal values of radiated field strength from both antennas. The elevated system at a height of 3 meters has values of resistance and reactance which are somewhat lower than those of the previous elevated antenna, but the

Table IX. Input impedance values for a 32-foot vertical monopole antenna with a variety of ground systems. The values shown were derived by taking data at the end of 120 feet of RG-213 50-ohm coaxial cable and transforming them to the antenna feed-point through use of the transmission-line equations. Frequency = 8 MHz. Radial length = 32 feet.

Ground System Configuration	Feed Method	Input Impedance (Ohms) Real	Imaginary
120 radials on the ground	direct	41.67	30.62
4 radials on the ground	direct	77.56	38.95
2-foot ground rod only	direct	97.81	21.32
4 radials elevated 1 meter	direct	41.42	30.60
4 radials elevated 3 meters	direct	34.20	24.58
4 radials elevated 5 meters	direct	7.83	-2.44
4 radials elevated 3 meters	isolated	44.31	45.56
4 radials elevated 5 meters	isolated	40.47	49.97

numbers seem reasonable. The next line of data, for the direct-feed elevated-radial system at a height of 5 meters, appears to be totally wrong, and should probably be discarded. The indicated value of only 8 ohms for the input resistance is very far out of line, and disagrees with the trend established by the earlier data. It is probable that some kind of wiring error was made in the field test apparatus, leading to an artificially-low value of input impedance. The last two Table entries, for an isolated-feed system at heights of 3 meters and 5 meters above ground, show that both the input resistance and reactance are somewhat higher when using isolated feed than with direct feed. This could indicate a reduction in efficiency caused by the isolated-feed method, or it could be an artifact of the balun. NEC modeling experience indicates that changing from "direct" to "isolated" feed should cause only a modest shift of the input impedance values.

Field Intensity

NEC studies indicate that an elevated vertical monopole antenna with 4 elevated horizontal radials can out-perform a conventional ground-mounted antenna with 120 buried radials when the elevated antenna is raised only a few meters above the earth. The low-angle field strength is shown to increase continually as the antenna is lifted further and further away from ground. In addition, NEC predicts that the "isolated feed" system should provide a slight improvement over the "direct feed" method at any height above the earth.

For the field tests, a synthesized transmitter (f = 8.040 MHz) was used as the signal source, along with a digital watt-meter for measuring

forward and reflected power. A battery-powered calibrated portable receiver was used to determine the vertical component of the electric field intensity at three separate locations in the far-field of the antenna. This hand-held instrument is enclosed in a metal case and contains a collapsible 1-meter whip antenna which is used to sense the vertical component of an incident electric field. Preliminary tests indicated that repeatable and reliable measurements could be made with this instrument.

Table X is a summary of all the field-strength readings taken during three man-weeks of effort at the test site. All of the field intensities shown in the Table were adjusted to allow for losses in the transmission line (and balun if present) and were normalized for a power input of 15 watts at the feed-point of the antenna. Unfortunately, the data proved to be inconclusive, and no strong trends were observed. Although computer analysis shows that the elevated-radial technique is promising, there was so much variability in the experimental results that no conclusive evidence was found to either confirm or deny the hypothesis. It is not known whether the discrepancies are due to equipment malfunction, operator error, or shortcomings in the NEC computer program. Scattered showers which occurred in the area during the course of the outdoor testing may have altered the ground constants from one day to the next, so that field strength data taken from one antenna configuration may not be comparable to data taken on another configuration. On one occasion the field-strength receiver ceased operation altogether, but mysteriously recovered a few minutes later. It appears that a combination of all of these factors may have acted in concert, leading to a collection of data points which have little or no meaning in relation to each other.

Table X. Vertical electric field strength for a 32-foot vertical monopole antenna with various types of ground systems. In all cases the frequency is 8.040 MHz and the input power at the antenna feed-point is 15 Watts. All radials are 32 feet in length.

* As noted in the text, all of the values on this line may be incorrect.

	----------VERTICAL ELECTRIC FIELD INTENSITY (dBuV/m)----------		
GROUND CONFIGURATION	DISTANCE = 250 FEET	DISTANCE = 500 FEET	DISTANCE = 4398 FEET
120 radials laid on earth's surface, direct feed	106.5	98.5	69.5
4 radials laid on earth's surface, direct feed	102.5	94.	64.5
2-foot ground stake, direct feed	100.	92.5	64.5
4 radials, antenna elevated 1 meter, direct feed	104.5	95.	69.
4 radials, antenna elevated 3 meters, direct feed	105.5	99.	70.
* 4 radials, antenna elevated 5 meters, direct feed	91.	83.5	55.
4 radials, antenna elevated 3 meters, isolated feed	78.5	96.5	69.5
4 radials, antenna elevated 5 meters, isolated feed	105.	98.	69.

Nevertheless, an attempt will be made to analyze the data contained in Table X on a line-by-line basis. In those cases involving a ground-mounted monopole with radials, the radial wires were strung out on top of the soil after all surface vegetation had been cleared away. The original plan required that these radials be buried in the soil to a depth of about two inches, but the dirt at the test site proved to be extremely hard and compacted, so this strategy was abandoned. The first design included a 120-radial ground system, similar (except for burial) to those used in the AM radio broadcast industry, which will be used as the "standard reference" throughout this study. The data in the first line of Table X shows that the resulting field intensity is quite high at a location 250 feet from the antenna and decreases smoothly with increasing distance from the radiator. A second test was performed using only four radials, which were also rolled out on top of the ground and their ends "nailed" into the soil. As may be seen, the field strength again falls off monotonically with increasing distance, as expected, although the 4-radial system is some 4 to 5 dB inferior to the monopole with 120 radials. This decrease in field intensity is caused by higher ground losses in the 4-radial system, as was shown by the increased value of input resistance displayed by this antenna. When the vertical radiator was driven against a 2-foot ground rod, with no radials at all, the field strength values were even lower than with the 4-radial system, except at the most distant measuring point (where the two ground systems produced equal field intensities). This further decrease in field strength is also expected, based upon the very large ground losses which exist in the "ground-rod-only" antenna system.

The elevated 4-radial direct-feed system at a height of 1 meter was the next to be constructed and measured. The field-strength values decrease as one moves farther from the antenna, but the absolute values are somewhat lower than those which were obtained from the 120-radial "reference" system. The elevated direct-feed antenna at a height of 3 meters is slightly inferior to the reference antenna at the 250-foot measuring point, but marginally better than the reference at both of the more-distant measurement locations. It should be noted here that the specified accuracy of the field-strength receiver is plus-or-minus 2 dB, so that from a practical standpoint, the performance of the 4-elevated-radial direct-feed antenna system at a height of either 1 meter or 3 meters is equal to that of the ground-mounted reference system with 120 radials. The next line of Table X contains data which is very curious and which may be erroneous, as noted in the earlier discussion on input impedances.

The last two field experiments were intended to check the performance of the "isolated feed" system versus that of the more conventional "direct-feed" method. (Recall that NEC modeling indicates an advantage with isolated feed.) The expected increase in performance from use of the "isolated feed" system did not materialize, as evidenced by a comparison of the "direct feed" and isolated feed" values for the antenna at a height of 3 meters. At a distance of 250 feet from the antenna, the direct-feed system is far superior to the isolated-feed method, while the gap between the two techniques narrows steadily as one moves farther and farther away from the radiator. In this case it appears that the ground constants may have changed during the interval of time between the two tests, possibly

due to rain showers, which would explain the enormous spread in the measured field intensity values. Alternatively, it may be that the value of 78.5 dBuV/m which was measured at the 250-foot distance is incorrect. Since the field-strength values observed with the direct-feed system at a height of 5 meters are already suspect, it is fallacious to attempt to compare them with the field intensities obtained from the isolated-feed system at the same height. A check of the balun showed that its efficiency at 8 MHz was in excess of 98 percent, but this was already taken into account when the field data was normalized for inclusion in the Table, so this factor alone cannot explain the disappointing performance of the isolated-feed antenna systems. It is possible that the balun which was used in the field studies did not actually provide the expected degree of isolation, and that some additional methods of achieving this goal should be found.

CONCLUSIONS

Field tests of the elevated-radial vertical monopole antenna system were inconclusive, with only one or two elevated-radial configurations being shown to be competitive with a conventional ground-mounted antenna with 120 radials. It is believed that this poor showing by the elevated-radial antenna systems was due to equipment problems and adverse weather conditions rather than to any inherent weakness in the technique itself. Much more work needs to be done in order to verify the true performance of the elevated-radial antenna at a variety of heights above the ground, and to ascertain the performance of the antenna over the entire HF band, rather than at a single frequency as was done here. In addition, field-

intensity measurements should be taken at several different azimuths, as a function of distance, in order to determine how well the antenna radiates in directions other than those which are directly off the end of a radial wire. Other means for achieving an "isolated feed" need to be investigated, such as wrapping several large turns of the coaxial transmission line into a coil at the feed-point, or perhaps by using other types of baluns. The elevated-radial technique appears to work (according to NEC) at frequencies from the lower part of the HF spectrum downward into the standard AM broadcast band, and experimental verification of this technique is needed.

A separate, but related, issue which needs to be raised in this paper is that of the validity of NEC itself. The special virtue of NEC-3 is its ability to model metallic structures which penetrate the air-earth interface, such as vertical monopole antennas with buried radials. Verification tests need to be carried out, either on full-size antennas erected and measured in the field or on carefully-constructed scale models which can be analyzed in a laboratory setting. Users will be able to place their complete trust in NEC-3 only when all of its unique capabilities have been fully confirmed.

A SIMPLIFIED MODEL OF THE TERMINATED, SLOPING, LONG-WIRE (AFWONXX) ANTENNA

Prepared by

B. Campbell and W. Stuart

for Submission to the
Applied Computational
Electromagnetics Society

A SIMPLIFIED MODEL OF THE TERMINATED, SLOPING, LONG-WIRE (AFWONXX) ANTENNA

Brenton P. Campbell, William D. Stuart
IIT Research Institute
Electromagnetic Compatibility Analysis Center (ECAC)
Annapolis, MD

ABSTRACT

To obtain a simple computer model for the terminated, sloping, long-wire (AFWONXX) antenna for use in electromagnetic compatibility analyses (EMC) at ECAC, a current distribution as a function of frequency and length and an impedance were assumed. Analytic expressions for the far field were developed and programmed. The model results for a standard terminated sloping long-wire antenna were compared with outputs from the Numerical Electromagnetics Code (NEC) - Method of Moments (MOM) version 3. The difference was considerably less than the variability of propagation loss. Selected comparisons are presented herein. The model has been incorporated into an existing ECAC program termed the Accessible Antenna Package (APACK). APACK is used to support propagation programs requiring antenna analysis capabilities.

BACKGROUND

On numerous occasions, far-field antenna gain values at many frequencies in many directions are needed to evaluate potential sky-wave and ground-wave interference in the HF and VHF bands. These interference analyses normally must be performed in a limited amount of time. There is usually insufficient calendar and/or computer time to perform a detailed analysis with a Numerical Electromagnetics Code (NEC) - Method of Moments (MOM) program. Because of the need of systems engineers for rapid, simple models, a set of computer subroutines termed the Accessible Antenna Package (APACK) [1,2,3] was developed at ECAC. The models for sky-wave behavior of antennas, as discussed by Ma [4,5], were extended to include surface wave terms. APACK is called by various propagation models to give a quick estimate of antenna performance as needed. In the APACK subroutines a current distribution--either sinusoidal or exponential (as appropriate)--is assumed, and the magnitude of the

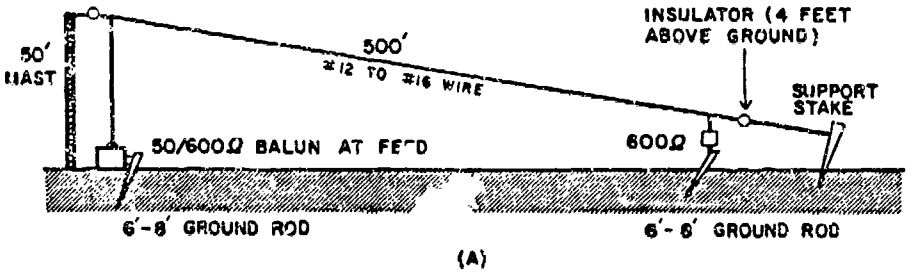
current is determined with the aid of a suitable approximation for the impedance. The antenna is then decomposed into Hertzian dipoles, each weighted by the appropriate magnitude and phase of the current, and the far-field is determined by summing the contributions of the Hertzian dipoles [6]. An analytic expression can be developed for this sum for most of the APACK antennas. The result is a computer program that evaluates approximately the far field, in-design-band, antenna performance with considerably less computer time than the NEC-MOM code. The APACK routines require only the geometry of the antenna as input and are considerably easier to apply for system engineers with little antenna analysis experience. In some cases, the APACK computer run times are about one-one thousandth of the NEC-MOM run time with reasonable accuracy.

ANALYSIS OF TERMINATED, SLOPING, LONG-WIRE ANTENNA

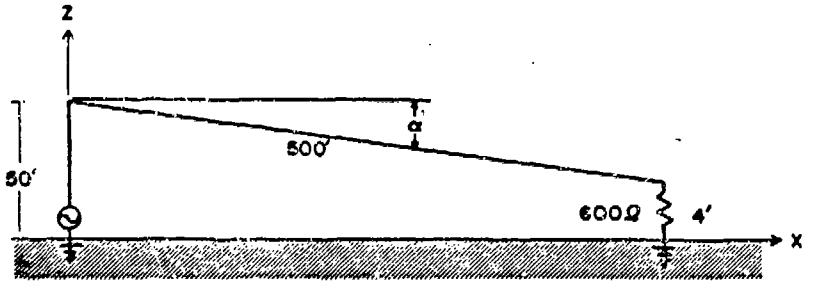
Because of the likelihood of frequent deployment of the terminated sloping long wire (AFWONXX) antenna [7], the decision was made to add it to the APACK set of subroutines. The terminated, sloping, long-wire antenna was developed to be a simple, easily erected antenna that would provide useful directivity and gain for path lengths greater than 500 miles. The physical dimensions of the antenna are approximately the same as for the sloping-vee antenna for the same frequency range of operation. Figure 1(a) illustrates the construction of the antenna. The radiating wire rises vertically from the grounded feed source to the top of the supporting mast and slopes toward the ground where it is terminated in a grounded load resistance. Insulators are used to isolate the radiating element from the support structure. Figure 1(b) shows the electrical operation of the antenna and the analysis coordinates.

The distribution of current on the antenna is assumed to take the form of a traveling wave. A time dependence of $\exp(j\omega t)$ is assumed and suppressed. For the vertical portion of the antenna, using the coordinate system of Figure 2, the current $I_v(z)$ is assumed to have the form

$$I_v(z) = I_m e^{-jkz} \quad \text{for } z > 0 \qquad (1)$$



(A)



(B)

Figure 1. Terminated, sloping, long-wire antenna.

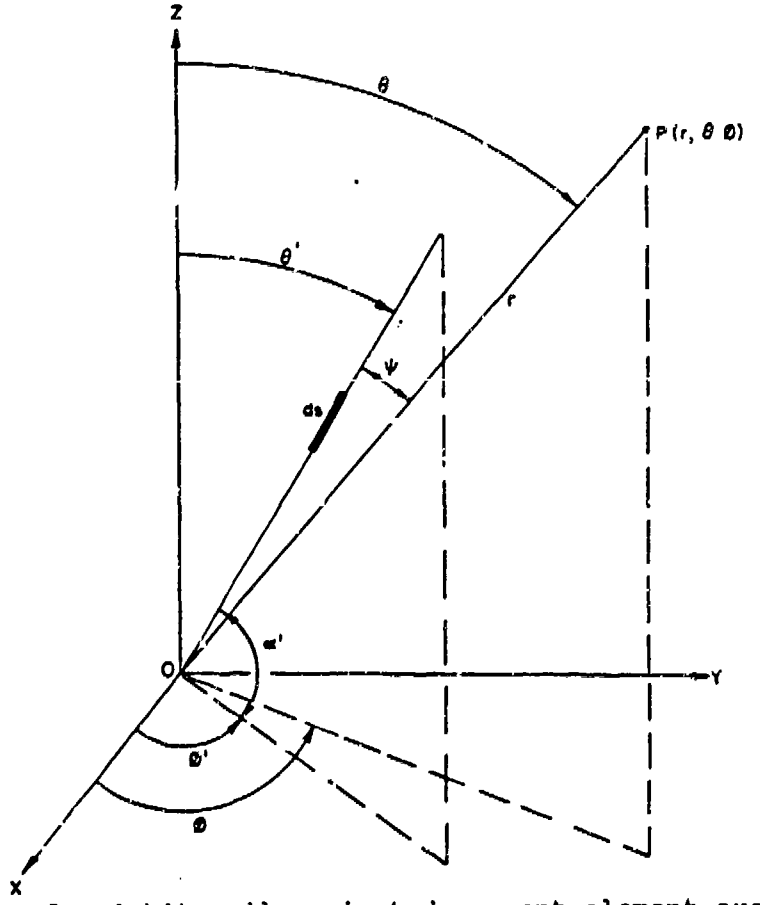


Figure 2. Arbitrarily oriented current element over lossy planar earth.

where I_m is the peak value of the current,

$k = 2\pi/\lambda$
λ = wavelength, in meters
z = height, in meters

It is seen that, due to cylindrical symmetry,

$$E_{\phi v} = 0 \tag{2}$$

where

$E_{\phi v}$ is the ϕ- component of the electric far field, in volts/meter due to the vertical antenna portion.

The theta component $E_{\theta v}$ caused by the vertical antenna portion is computed from the contributions of the elementary current element (in terms of the coordinate system illustrated in Figure 2) over the assumed current distribution, resulting in

$$E_{\theta v} = -j30k\, I_m \frac{e^{-jkr}}{r} \sin\theta \left[J_1 + R_v J_2 + (1-R_v)\left(\sin^2\theta - \frac{\sqrt{n^2-\sin^2\theta}}{n^2}\cos\theta\right)(J_2 + J_3)\right] \tag{3}$$

where

r = radial distance from the origin to the far-field point $P(r,\theta,\phi)$ of Figure 2, in meters
R_v = the Fresnel reflection coefficient of the ground for vertical polarization

$$J_1 = \frac{1 - e^{-jkH(1-\cos\theta)}}{jk\,(1-\cos\theta)}$$

$$J_2 = \frac{1 - e^{-jkH(1+\cos\theta)}}{jk\,(1+\cos\theta)}$$

$$J_3 = \frac{2\sqrt{n^2-\sin^2\theta}}{1 - R_v} \left[\exp[-jkH(1 + \cos\theta)] - 1\right]$$

$$\left[(1 - \cos\theta)\, J_{31} + \frac{1}{kn^2 \sin^2\theta_r}\right]$$

H is the height of the origin above the ground plane (also the length of the vertical portion).

n is the refractive index of the ground under the antenna

$$J_{31} = \frac{\sqrt{-jr\lambda}}{2n^2 \sin\theta_r} e^{-\omega_1} \operatorname{erfc}(j\sqrt{\omega_1})$$

and

$$\omega_1 = \frac{-jkr}{2\sin^2\theta_r}\left(\cos\theta + \frac{H}{r} + \frac{\sqrt{n^2-\sin^2\theta_r}}{n^2}\right)^2$$

The theta component of the field $E_{\theta s}$ created by the sloping portion of the antenna is evaluated in terms of the coordinate system in Figure 2, in which case,

$$\theta' = \frac{\pi}{2} - \alpha', \quad \phi' = 0$$

$$\cos\psi_2 = \cos\theta \sin\alpha' + \sin\theta \cos\alpha' \cos\phi$$

α' is the angle between the antenna element and its projection on the X Y plane or the complement of θ' illustrated in Figure 2.

The current distribution along the sloping portion is assumed as

$$I_s = I_m e^{-jk(H+s)} \qquad (4)$$

where s is the distance along the sloping portion of the antenna.

When the observer is far enough away such that:

$$r \sim r' + H\cos\theta$$

where r is the distance to the observer from the feed point on the ground plane and r' is the distance to the observer from the top of the mast, then the theta component for the sloping portion may be written as

$$E_{\theta 3} = 30\, I_m \frac{e^{-jkr}}{r}\, e^{+jkH(\cos\theta-1)} \left[Q_1\{F_1 - R_v F_2 G_4 + (1-R_v)\, G_2 G_3 G_4 F_2\} - Q_2\{F_1 + R_v F_2 G_4 + (1-R_v)\, G_3 G_4 F_2\}\right] \quad (5)$$

where the following definitions are used for simplification,

$$G_2 = \frac{\sqrt{n^2 - \sin^2\theta}}{n^2\cos\theta}$$

$$G_3 = F_v\,(\sin^2\theta - G_2\cos^2\theta)$$

$$G_4 = e^{-j2kH\cos\theta}$$

F_v is the surface wave attenuation for vertical polarization

$$Q_1 = \cos\alpha'\cos\phi\cos\theta$$

$$Q_2 = \sin\alpha'\sin\theta$$

and we define a new variable ψ_2' such that

$$\cos\psi_2' = \cos\psi_2 - 2\cos\theta\sin\alpha'$$

and

$$F_1 = \frac{1 - e^{-jkL(1-\cos\psi_2)}}{(1-\cos\psi_2)}$$

$$F_2 = \frac{1 - e^{-jkL(1-\cos\psi_2')}}{(1-\cos\psi_2')}$$

where L is the total length of the sloping portion of the antenna.

Assuming that the surface wave attenuation for horizontal polarization, F_m, is constant over the range of integration, the phi component of the field created by the sloping portion of the antenna is $E_{\phi s}$.

$$E_{\phi s} = -30\, I_m \frac{e^{-jkr}}{r} e^{jkH(\cos\theta-1)} \cos\alpha' \sin\phi$$
$$[F_1 + R_H F_2 G_4 + (1-R_H) G_4 F_m F_2] \qquad (6)$$

where R_H is the Fresnel reflection coefficient of the ground for horizontal polarization.

The analytic expressions for the electromagnetic fields given in Equations 3, 5 and 6 all have a multiplicative factor of 1/r. The gain of the antenna can be expressed as the square of the total field times r^2 divided by the total power input to the antenna. Thus, the gain of the antenna is independent of r wherever the surface wave term is neglected. This independence of distance limits APACK to far-field gain calculations since gain varies with distance at distances less than that for which the far-field criterion is satisfied. Since it is useful to express the gain of the antenna relative to that of an isotropic antenna, it is necessary to divide by 30 (the ratio of the impedance of free space to 4π steradians).

In order to relate the power input to the antenna to the current I_m, it is necessary to determine the impedance of the antenna. The impedance of the antenna is estimated to be approximately 600 ohms when the length of the terminated, sloping, long-wire

antenna is between 2 and 8 λ and is approximately 10 times the height of the mast [7]. Models of the antenna at different frequencies were constructed for a design length of 500 feet and mast height of 50 feet employing NEC-3 [8]. The results of NEC calculations can be linearly approximated by the following formula for the region around 10 MHz.

$$R_{in} = 521 + 24\ (10 - f_{MHz}) \qquad (7)$$

where

R_{in} = input impedance of the antenna in ohms
f_{MHz} = operating frequency in MHz.

However, comparisons of APACK and NEC calculations for field strengths and gain were found to be in closer agreement when the constant value of 600 ohms is used for the input impedance. This is possibly due to the fact that the amplitude of the current computed by NEC becomes increasingly smaller with either an increase in distance along the antenna from the feed or an increase in the frequency, whereas a constant value of current is assumed in APACK. Therefore, using the value of 600 ohms at higher frequencies allows the APACK model to compensate somewhat for the fact that the amplitude of the current along the antenna is not really constant.

NEC AND APACK MODEL PREDICTIONS

NEC models of the terminated, sloping, long-wire antenna for typical operating conditions were constructed and compared with APACK model results. Since the APACK model of this antenna is an approximation of the more rigorous techniques used in NEC, the NEC models of the antenna were viewed as the standards by which modeling performance could be assessed. Differences in the predictions of the NEC and APACK models are mainly attributed to the more fundamental ability of the NEC program to model amplitude and phase of the current along the antenna.

Figure 3 shows a 3-dimensional plot of the NEC predictions of the antenna radiation pattern for the total gain for an antenna above a ground with a relative dielectric constant ε of 10 and a conductivity σ of 0.01 mhos per meter. Such plots are, in general, great aids in visualizing the patterns and in verifying that the antenna has indeed been modeled properly. Figure 4 presents the top view of Figure 3. The coordinate axes accompanying each plot are provided to show the orientation of the axes only, and therefore do not depict the coordinate origin, which lies within each plot. The oblique view of Figure 3 places the observer at ϕ = 25 degrees and θ = 60 degrees. The terminated sloping longwire antenna lies completely in the X-Z plane and is excited at a frequency of 10 MHz. The complex lobing pattern is also evident in Figure 4. The total gain pattern was found to be very similar to the gain pattern for vertical polarization (not shown), which indicates that the total gain is most heavily influenced by the vertical component. Figure 3 indicates that, for a given elevation angle (e.g., 30 degrees), the maximum gain lies on either side of the plane of symmetry (X-Z plane).

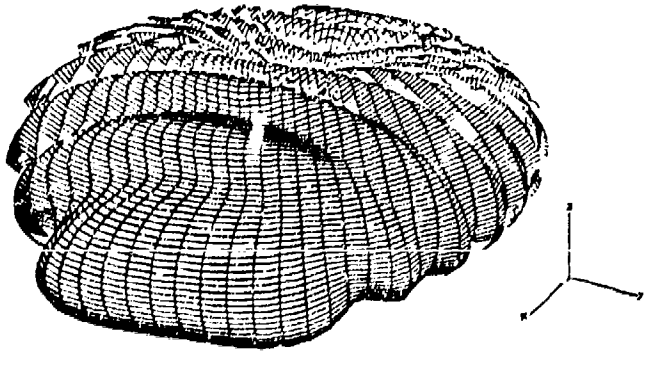


Figure 3. Three dimensional plot of the total gain of terminated, sloping, long-wire antenna.

Comparisons of NEC and APACK predictions at specific pattern cuts for the space wave (direct & reflected) antenna patterns of the terminated sloping longwire antenna are shown in Figures 5 through 7. The general behavior of the pattern for the APACK predictions agrees with those predicted by use of NEC-3. For practical applications, these results are quite satisfactory. The groundwave is considered the complex vector sum of the space wave and the surface

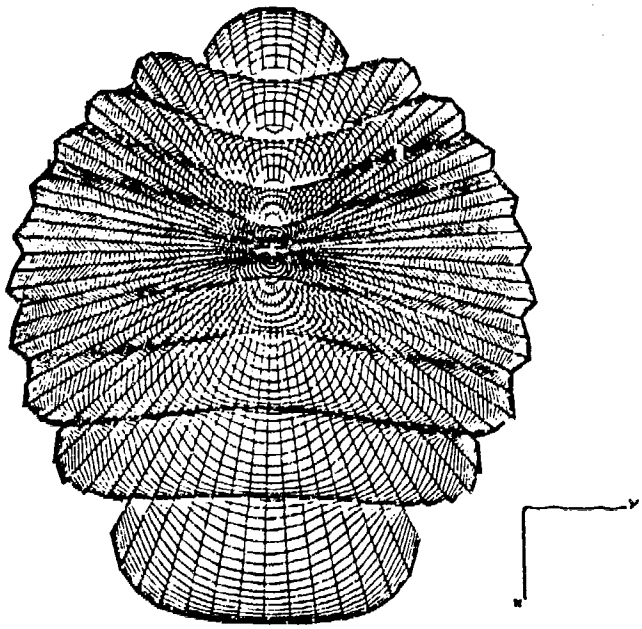


Figure 4. Plot of the top view of the total gain of of terminated, sloping, long-wire antenna.

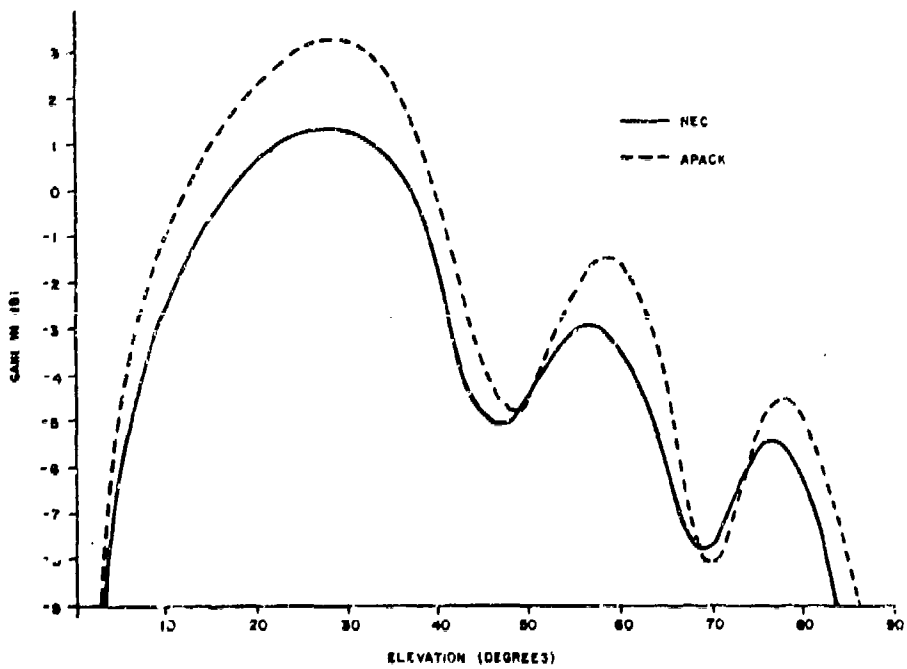


Figure 5. Total gain of terminated, sloping, long-wire antenna in X-Z plane (freq. = 6 MHz, ϕ = 0., ε = 10., σ = .01, power = 1 kW).

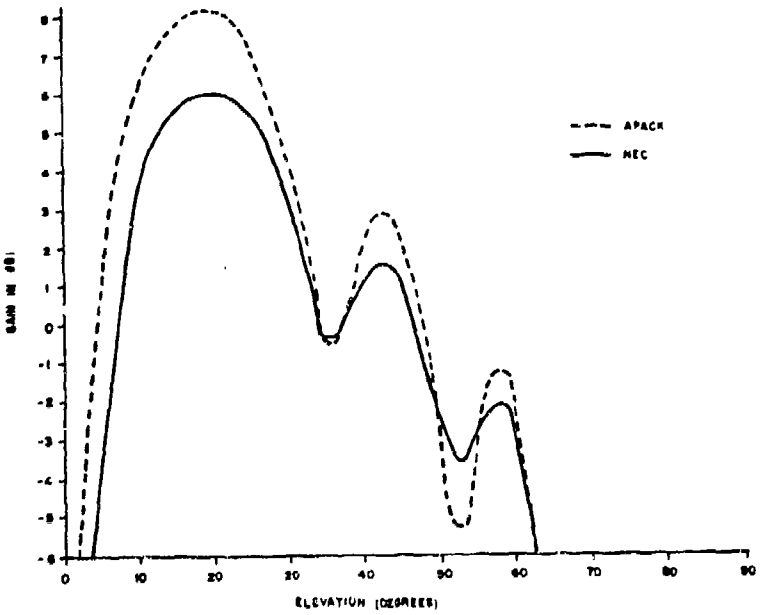


Figure 6. Total gain of terminated, sloping, long-wire antenna in X-Z plane (freq. = 10 MHz, ϕ = 0., ϵ = 10., σ = .01, power = 1 kW).

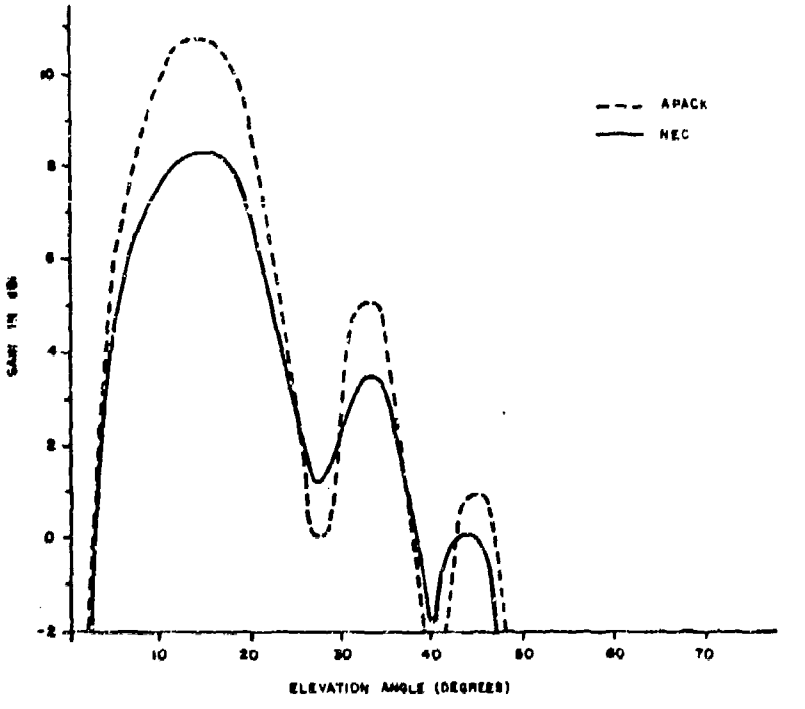


Figure 7. Total gain of terminated, sloping, long-wire antenna in X-Z plane (freq. = 15 MHz, ϵ = 10., σ = .01, power = 1 kW).

wave. The groundwave field strength comparisons in Figures 8 through 10 are considered excellent since they differ by no more than 1 dB.

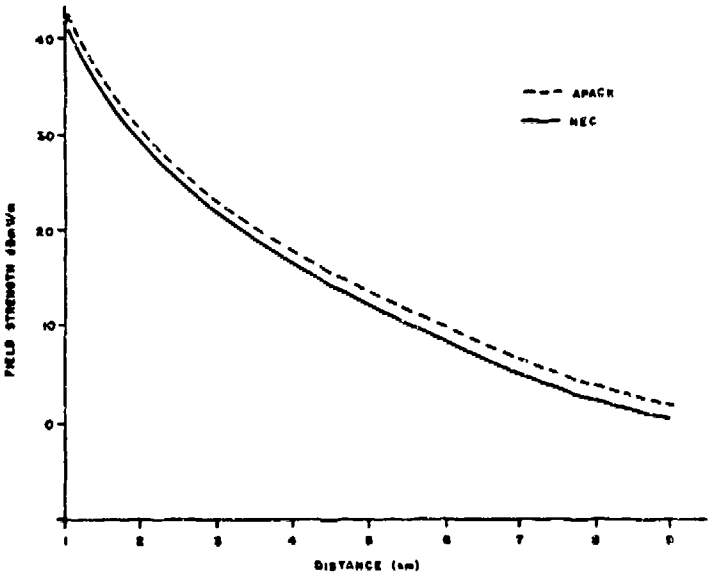


Figure 8. Comparison of groundwave field strength predictions along X axis of terminated, sloping, long-wire antenna (freq. = 6 MHz, Observer height = 1 m, ε = 10., σ = .01, ϕ = 0, power = 1 kW).

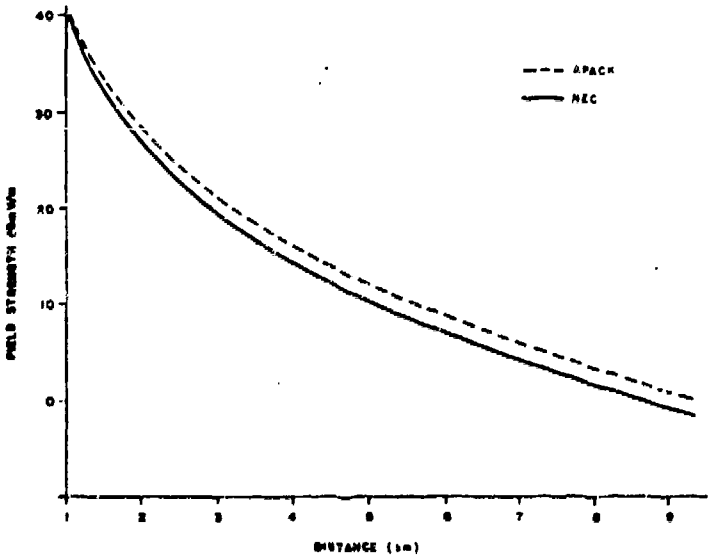


Figure 9. Comparison of groundwave field strength predictions along X axis of terminated, sloping, long-wire antenna (freq. = 10 MHz, Observer height = 1 m, ε = 10., σ = .01, ϕ = 0, power = 1 kW).

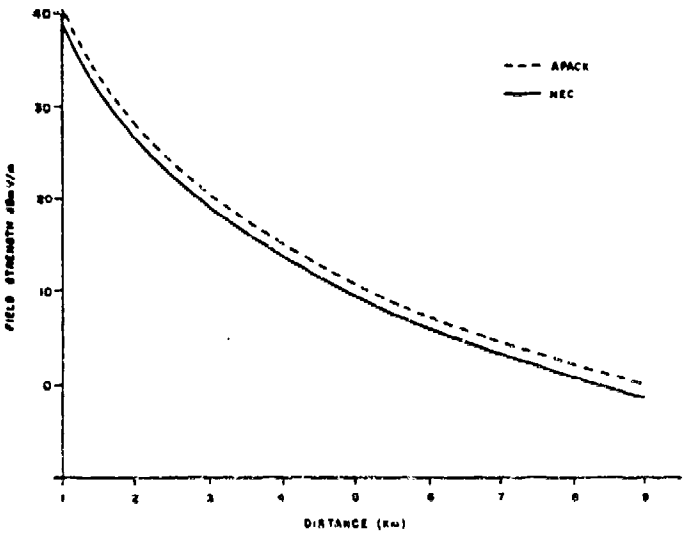


Figure 10. Comparison of groundwave field strength predictions along X axis of terminated, sloping, long-wire antenna (freq., = 15 MHz, Observer height = 1 m, ε = 10., σ = .01, ϕ = 0, power = 1 kW).

SUMMARY

Analytical equations (Equations 2, 3, 5 and 6) have been developed for far-field and in-band conditions, that enable rapid computer predictions of the gains and field strengths as well as the groundwave over flat or spherical smooth earth for the terminated, sloping, long-wire antenna. These equations have been programmed and tested for use in the Accessible Antenna Package (APACK), a collection of computer subroutines, which is used at the Electromagnetic Compatibility Analysis Center (ECAC) to support propagation programs requiring antenna analysis capabilities. Computer predictions based on the equations have been compared with those of the more rigorous Numerical Electromagnetics Code (NEC) and have been found to provide satisfactory agreement.

Comparisons of the groundwave field strength at a height of 1 meter differed by no more than 1 dB for distances from 1 km to 8 km. The APACK predictions for the peak gains of the terminated, sloping, long-wire antenna were within 2 dB in the main lobe region.

Errors of this magnitude are considerably less than the variability of propagation loss.

REFERENCES

1. Chang, S., "A New Combined Antenna and Propagation Model," 1980 International Symposium Digest, Antennas and Propagation, IEEE, Quebec, Canada, pp 308-311, June 1980.

2. Campbell, B. P., "Accessible Antenna Package (APACK)," Paper presented at IEEE International Symposium on Electromagnetic Compatibility, Baltimore, MD, 1980.

3. Chang, S., and Maddocks, H. C., APACK, A Combined Antenna and Propagation Model, ESD-TR-80-102, DoD ECAC, Annapolis, MD, March 1981, A102622.

4. Ma, M. T., and Walters, L. C., Power Gains for Antennas Over Lossy Plane Ground, ESSA/US Dept. Commerce, ERL 104-ITS 74, April 1969.

5. Ma, M. T., Theory and Application of Antenna Arrays, Wiley and Sons, New York, NY, 1974.

6. Laitinen, P., Linear Communication Antennas, Technical Report No. 7, US Army Signal Radio Propagation Agency, Fort Monmouth, NJ, 1949, AD081071.

7. Christinsin, A. S., "The AFWONXX Longwire," Anthology, 1970-1976, Spectrum Management Division, Directorate of Systems Evaluation, DCS/Operation Headquarters, Air Force Communications Service, 1976.

8. Burke, G. J., Numerical Electromagnetics Code - Method of Moments User's Guide Supplement for NEC-3 for Modeling Buried Wires, UCID-19918, Lawrence Livermore Laboratory, Livermore, CA, October 1983, DE84002195.